Second edition

Superconductivity

Charles P. Poole Jr.

Horacio A. Farach

Richard J. Creswick

Ruslan Prozorov

Superconductivity

This page intentionally left blank

Superconductivity

Charles P. Poole, Jr.
Horacio A. Farach
Richard J. Creswick

Department of Physics and Astronomy
University of South Carolina
Columbia, South Carolina

Ruslan Prozorov

Ames Laboratory
Department of Physics and Astronomy
Iowa State University
Ames Iowa

ELSEVIER

Amsterdam – Boston – Heidelberg – London – New York – Oxford
Paris – San Diego – San Francisco – Singapore – Sydney – Tokyo

Academic Press is an imprint of Elsevier

Academic Press is an imprint of Elsevier
84 Theobald's Road, London WC1X 8RR, UK
Radarweg 29, PO Box 211, 1000 AE Amsterdam, The Netherlands
Linacre House, Jordan Hill, Oxford OX2 8DP, UK
30 Corporate Drive, Suite 400, Burlington, MA 01803, USA
525 B Street, Suite 1900, San Diego, CA 92101-4495, USA

First edition 1995
Second edition 2007

ISBN: 0-12-561456-X first edition (1995)
ISBN: 978-0-12-088761-3 second edition (revised version)

For information on all Academic Press publications visit our website at books.elsevier.com

Printed and bound in The Netherlands

07 08 09 10 11 10 9 8 7 6 5 4 3 2 1

One of us wishes to dedicate this book to the memory of his wife of 51 years
Kathleen Theresa Walsh Poole (November 12, 1932–November10, 2004)

This page intentionally left blank

Contents

9 *Unconventional Superconductors*

12 *Type II Superconductivity*

13 Irreversible Properties

14 Magnetic Penetration Depth

15 Energy Gap and Tunneling

16 Transport Properties

17 Spectroscopic Properties

This page intentionally left blank

Preface to the First Edition

When we wrote our 1988 book, *Cooper Oxide Superconductors*, our aim was to present an early survey of the experimental aspects of the field of high temperature superconductivity as an aid to researchers who were then involved in the worldwide effort to (a) understand the phenomenon of cuprate superconductivity and (b) search for ways to raise the critical temperature and produce materials suitable for the fabrication of magnets and other devices. A great deal of experimental data are now available on the cuprates, and their superconducting properties have been well characterized using high quality untwinned monocrystals and epitaxial thin films. Despite this enormous research effort, the underlying mechanisms responsible for the superconducting properties of the cuprates are still open to question. Nevertheless, we believe that the overall picture is now clear enough to warrant the writing of a text-book that presents our present-day understanding of the nature of the phenomenon of superconductivity, surveys the properties of various known superconductors, and shows how these properties fit into various theoretical frameworks. The aim is to present this material in a format suitable for use in a graduate-level course.

An introduction to superconductivity must be based on a background of fundamental principles found in standard solid state physics texts, and a brief introductory chapter provides this background. This initial chapter on the properties of normal conductors is limited to topics that are often referred to throughout the remainder of the text: electrical conductivity, magnetism, specific heat, etc. Other background material specific to particular topics is provided in the appropriate chapters. The presence of the initial normal state chapter makes the remainder of the book more coherent.

The second chapter presents the essential features of the superconducting state—the phenomena of zero resistance and

perfect diamagnetism. Super current flow, the accompanying magnetic fields, and the transition to this ordered state that occurs at the transition temperature T_c are described. The third chapter surveys the properties of the various classes of superconductors, including the organics, the buckminsterfullerenes, and the precursors to the cuprates, but not the high temperature superconductors themselves. Numerous tables and figures summarize the properties of these materials.

Having acquired a qualitative understanding of the nature of superconductivity, we now proceed, in five subsequent chapters, to describe various theoretical frameworks which aid in understanding the facts about superconductors. Chapter 4 discusses superconductivity from the view-point of thermodynamics and provides expressions for the free energy—the thermodynamic function that constitutes the starting point for the formulations of both the Ginzburg–Landau (GL) and the BCS theories. The GL theory is developed in Chapter 5 and the BCS theory in Chapter 6. GL is a readily understandable phenomenological theory that provides results that are widely used in the interpretation of experimental data, and BCS in a more fundamental, and mathematically challenging, theory that makes predictions that are often checked against experimental results. Most of Chapter 5 is essential reading, whereas much of the formalism of Chapter 6 can be skimmed during a first reading.

The theoretical treatment is interrupted by Chapter 7, which presents the details of the structures of the high temperature superconductors. This constitutes important background material for the band theory sections of Chapter 8, which also presents the Hubbard and related models, such as RVB and *t–J*. In addition, Chapter 8 covers other theoretical approaches involving, for example, spinons, holons, slave bosons, anyons, semions, Fermi liquids, charge and spin density waves, spin bags, and the Anderson interlayer tunneling scheme. This completes the theoretical aspects of the field, except for the additional description of critical state models such as the Bean model in Chapter 12. The Bean model is widely used for the interpretation of experimental results.

The remainder of the text covers the magnetic, transport, and other properties of superconductors. Most of the examples in these chapters are from the literature on the cuprates. Chapter 9 introduces Type II superconductivity and describes magnetic properties, Chapter 10 continues the discussion of magnetic properties, Chapter 11 covers the intermediate and mixed states, and Chapter 12, on critical state models, completes the treatment of magnetic properties. The next two chapters are devoted to transport properties. Chapter 13 covers various types of tunneling and the Josephson effect, and Chapter 14 presents the remaining transport properties involving the Peltier, Seebeck, Hall, and other effects.

When the literature was surveyed in preparation for writing this text, it became apparent that a very significant percentage of current research on superconductivity is being carried out by spectroscopists, and to accommodate this, Chapter 15 on spectroscopy was added. This chapter lets the reader know what the individual branches of spectroscopy can reveal about the properties of superconductors, and in addition, it provides an entrée to the vast literature on the subject.

This book contains extensive tabulations of experimental data on various superconductors, classical as well as high T_c types. Figures from research articles were generally chosen because they exemplify principles described in the text. Some other figures, particularly those in Chapter 3, provide correlations of extensive data on many samples. There are many cross-references between the chapters to show how the different topics fit together as on unified subject.

Most chapters end with sets of problems that exemplify the material presented and

sets of references for additional reading on the subject. Other literature citations are scattered throughout the body of each chapter. Occasional reference is made to our earlier work, *Copper Oxide Superconductors*, for supplementary material.

One of us (C.P.P.) taught a graduate-level superconductivity course three times using lecture notes which eventually evolved into the present text. It was exciting to learn with the students while teaching the course and simultaneously doing research on the subject.

We thank the following individuals for their helpful discussions and comments on the manuscript: C. Almasan, S. Aktas, D. Castellanos, T. Datta, N. Fazyleev, J. B. Goodenough, K. E. Gray, D. U. Gubser, D. R. Harshman, A. M. Herman, Z. Iqbal, E. R. Jones, A. B. Kaiser, D. Kirvin, O. Lopez, M. B. Maple, A. P. Mills, Jr., S. Misra, F. J. Owens, M. Pencarinha, A. Petrile, W. E. Pickett, S. J. Poon, A. W. Sleight, O. F. Schuette, C. Sisson, David B. Tanner, H. Testardi, C. Uher, T. Usher, and S. A. Wolf. We also thank the graduate students of the superconductivity classes for their input, which improved the book's presentation. We appreciate the assistance given by the University of South Carolina (USC) Physics Department; our chairman, F. T. Avignone; the secretaries, Lynn Waters and Cheryl Stocker; and especially by Gloria Phillips, who is thanked for her typing and multiple emendations of the BCS chapter and the long list of references. Eddie Josie of the USC Instructional Services Department ably prepared many of the figures.

This page intentionally left blank

Preface to the Second Edition

It has been an exciting two decades spending most of my time playing a relatively minor role in the exciting world-wide Superconductivity Endeavor. My involvement began on March 18th, 1987, when I attended what became known later as the "Woodstock of Physics", the "Special Panel Discussion on Novel High Temperature Superconductivity" held at the New York meeting of the American Physical Society. I came a half hour early and found the main meeting room already full, so several hundred physicists and I watched the proceedings at one of the many TV monitors set up in the corridors of the hotel. That evening in the hotel room my colleague Timir Datta said to me "Why don't we try to write the first book on high temperature superconductivity?" When we arrived back in Columbia I enlisted the aid of Horacio, my main collaborator for two prior decades, and the work began. Timir and I spent many nights working until two or three in the morning gathering together material, collating, and writing. We had help from two of our USC students M. M. Rigney and C. R. Sanders. In this work *Copper Oxide Superconductors* we managed to comment on, summarize, and collate the data by July of 1988, and the book appeared in print toward the end of that year.

By the mid 1990's the properties of the cuprates had become well delineated by measurements carried out with high quality untwinned single crystals and epitaxial thin films. There seemed to be a need to assemble and characterize the enormous amount of accumulated experimental data on a multitude of superconducting types. To undertake this task and acquire an understanding of the then current status of the field, during 1993 and 1994 I mailed postcards to researchers all over the world requesting copies of their work on the subject. This was supplemented by xerox copies of additional articles made in our library, and provided a collection of over 2000 articles on superconductivity.

These reprints and xeroxes were sorted into categories which became chapters and sections of the first edition of this present book. For several months the floor of my study at home remained covered with piles of reprints as I proceeded to sort, peruse, and transpose data and information from them. This was a tedious, but nonetheless very exciting task.

There were some surprises, such as the relatively large number of articles on spectroscopy, most of which were very informative, and they became Chap. 15. This chapter contained material that most closely matched my pre-superconductivity era research endeavors, and I was pleased to learn how much spectroscopy had contributed to an understanding of the nature of superconductors. There were also many articles on magnetic properties, critical states, tunneling, and transport properties, which became Chapters 10, 12, 13, and 14, respectively. Most of the relatively large number of articles on the Hubbard Model did not, in my opinion, add very much to our understanding of superconductivity. Some of them were combined with more informative articles on band structure to form Chap. 8. There was a plethora of articles on the crystallographic structures of various cuprates, with a great deal of redundancy, and the information culled from them constituted Chap. 7. Chapter 9, Type II Superconductivity, summarized information from a large number of reprints.

The Intermediate and Mixed States Chapter 11 depended much less on information garnered from the reprints, and much more on classical sources. The same was true of Chap. 3 Classical Superconductors, Chap. 4 Thermodynamic Properties, Chap. 5 Ginzburg-Landau Theory, and Chap. 6 BCS Theory written by Rick. Finally the beginning of the First Edition text, namely Chap. 1 Properties of the Normal State, and Chap. 2 The Phenomenon of Superconductivity, were introductory in nature, and relied very little on material garnered from the reprint collection. Thus our first edition provided an overall coverage of the field as it existed at the end of 1994.

In 1996 and 1999, respectively, the books *The New Superconductors* and *Electromagnetic Absorption in Superconductors* were written in collaboration with Frank J. Owens as the principal author.

The next project was the *Handbook of Superconductivity*, published during the millennial year 2000. It assembled the experimental data that had accumulated up to that time. Chapters in this volume were written by various researchers in the field. Of particular importance in this work were Chapters 6 and 8 by Roman Gladyshevski and his two coworkers which tabulated and explicated extensive data on, respectively, the Classical and the Cuprate Superconductors. His classification of the cuprate materials is especially incisive.

Seven years have now passed since the appearance of the Handbook, and our understanding of the phenomenon of Superconductivity is now more complete. Much of the research advances during this period have been in the area of magnetism so I enlisted Ruslan Prozorov, who was then a member of our Physics Department at USC, and an expert on the magnetic properties of superconductors, to join Horacio, Rick, and myself in preparing a second edition of our 1995 book. In the preparation of this edition some of the chapters have remained close to the original, some have been shortened, some have been extensively updated, and some are entirely new. The former Chap. 10, Magnetic Properties, has been moved earlier and becomes Chap. 5. Aside from this change, the first six chapters are close to what they were in the original edition. Chapter 7, BCS Theory, has been rewritten to take into account advances in some topics of recent interest such as d-wave and multiband superconductivity. Chapter 8, on the Structures of the Cuprates, has material added to it on the superconductor Sr_2RuO_4, layerng schemes, and infinite layer phases.

Chapter 9 on Nonclassical Superconductors describes superconducting materials which do not fit the categories of Chap. 3. It discusses the properties of the relatively recently discovered superconductor magnesium diboride, MgB_2, as well as borocarbides, boronitrides, perovskites such as $MgCNi_3$, charge transfer organics, heavy electron systems, and Buckminsterfullerenes. The chapter ends with a discussion of the symmetry of the order parameter, and a section that treats magnetic superconductors and the coexistence of superconductivity and magnetism. The coverage of the Hubbard Model and Band Structure in Chap. 10 is significantly shorter than it was in the first edition. Chapter 11, Type I Superconductors and the Intermediate State, includes some recent developments in addition to what was covered in the first edition. Chapter 12 describes the nature and properties of Type II Superconductors, and is similar to its counterpart in the first edition. Chapter 13, Irreversible Properties, discusses critical states and the Bean model, the treatment of the latter being much shorter than it was in the first edition. In addition there are sections on current-magnetic moment conversion formulae, and susceptibility measurements of a perfect superconductor.

Chapter 14, Magnetic Penetration Depth, written by Ruslau is entirely new. It covers the topics of isotropic London electrodynamics, the superconductivity gap and Fermi surfaces, the semiclassical model for superfluid density, mixed gaps, s- and d-wave pairing, the effect of disorder on the penetration depth, surface Andreev bound states, nonlocal electrodynamics of nodal superconductors, the nonlinear Meissner Effect, the Campbell penetration depth, and proximity effect identification. Chapter 15, Energy Gap and Tunneling, includes a new section on tunneling in unconventional superconductors. Finally Chapters 16 and 17 discuss, respectively, transport properties and spectroscopic properties of superconductors, and are similar in content to their counterparts in the first edition. Recent data on superconducting materials have been added to the tables that appeared in various chapters of the first edition, and there are some new tables of data. References to the literature have been somewhat updated.

Two of us (Horacio and I) are now octogenarians, but we continue to work. Over the decades Horacio has been a great friend and collaborator. It is no longer "publish or perish" but "stay active or perish." We intend to remain active, *deo volente*.

Professor Prozorov would like to acknowledge partial support of NSF grants numbered DMR-06-03841 and DMR-05-53285, and also the Alfred P. Sloan Foundation. He wishes to thank his wife Tanya for her support, and for pushing him to finish his chapters. He also affirms that: "In my short time with the USC Department of Physics, one of the best things that happened was to get to know Charles Poole Jr., Horacio Farach, Rick Creswick, and Frank Avignone III whose enthusiasm was contagious, and I will always cherish the memory of our discussions."

Charles P. Poole, Jr.
June 2007

This page intentionally left blank

1

Properties of the Normal State

I. INTRODUCTION

This text is concerned with the phenomenon of superconductivity, a phenomenon characterized by certain electrical, magnetic, and other properties, many of which will be introduced in the following chapter. A material becomes superconducting below a characteristic temperature, called the *superconducting transition temperature* T_c, which varies from very small values (millidegrees or microdegrees) to values above 100 K. The material is called normal above T_c, which merely means that it is not superconducting. Elements and compounds that become superconductors are conductors—but not good conductors—in their normal state. The good conductors, such as copper, silver, and gold, do not superconduct.

It will be helpful to survey some properties of normal conductors before discussing the superconductors. This will permit us to review some background material and to define some of the terms that will be used throughout the text. Many of the normal state properties that will be discussed here are modified in the superconducting state. Much of the material in this introductory chapter will be referred to later in the text.

II. CONDUCTING ELECTRON TRANSPORT

The electrical conductivity of a metal may be described most simply in terms of the constituent atoms of the metal. The atoms, in this representation, lose their valence electrons, causing a background lattice of

Table 1.1 Characteristics of Selected Metallic Elements[a]

Z	Element	Valence	Radius (Å)	Xtal type	a(Å)	$n_e\left(\frac{10^{22}}{cm^3}\right)$	r_s(Å)	$\rho, 77K$ ($\mu\Omega$ cm)	$\rho, 273K$ ($\mu\Omega$ cm)	$\tau, 77K$ (fs)	$\tau, 273K$ (fs)	$K_{th}\left(\frac{W}{cm\ K}\right)$
11	Na	1	0.97	bcc	4.23	2.65	2.08	0.8	4.2	170	32	1.38
19	K	1	1.33	bcc	5.23	1.40	2.57	1.38	6.1	180	41	1.0
29	Cu	1	0.96	fcc	3.61	8.47	1.41	0.2	1.56	210	27	4.01
47	Ag	1	1.26	fcc	4.09	5.86	1.60	0.3	1.51	200	40	4.28
41	Nb	1	1.0	bcc	3.30	5.56	1.63	3.0	15.2	21	4.2	0.52
20	Ca	2	0.99	fcc	5.58	4.61	1.73		3.43		22	2.06
38	Sr	2	1.12	fcc	6.08	3.55	1.89	7	23	14	4.4	≈ 0.36
56	Ba	2	1.34	bcc	5.02	3.51	1.96	17	60	6.6	1.9	≈ 0.19
13	Al	3	0.51	fcc	4.05	18.1	1.10	0.3	2.45	65	8.0	2.36
81	Tl	3	0.95	bcc	3.88	10.5	1.31	3.7	15	9.1	2.2	0.5
50	Sn(W)	4	0.71	tetrg	$a = 5.82$ $c = 3.17$	14.8	1.17	2.1	10.6	11	2.3	0.64
82	Pb	4	0.84	fcc	4.95	13.2	1.22	4.7	19.0	5.7	1.4	0.38
51	Sb	5	0.62	rhomb	4.51	16.5	1.19	8	39	2.7	0.55	0.18
83	Bi	5	0.74	rhomb	4.75	14.1	1.13	35	107	0.72	0.23	0.09

[a] Notation: a, lattice constant; n_e, conduction electron density; $r_s = (3/4\pi n_e)^{1/3}$; ρ, resistivity; τ, Drude relaxation time; K_{th}, thermal conductivity; $L = \rho K_{th}/T$ is the Lorentz number; γ, electronic specific heat parameter; m^*, effective mass; R_H, Hall constant; Θ_D, Debye temperature; ω_p, plasma frequency in radians per femtosecond (10^{-15} s); IP, first ionization potential; WF, work function; E_F, Fermi energy; T_F, Fermi temperature in kilokelvins; k_F, Fermi wavenumber in mega reciprocal centimeters; and v_F, Fermi velocity in centimeters per microsecond.

positive ions, called *cations*, to form, and the now delocalized conduction electrons move between these ions. The number density n (electrons/cm^3) of conduction electrons in a metallic element of density ρ_m(g/cm^3), atomic mass number A (g/mole), and valence Z is given by

$$n = \frac{N_A Z \rho_m}{A}, \tag{1.1}$$

where N_A is Avogadro's number. The typical values listed in Table 1.1 are a thousand times greater than those of a gas at room temperature and atmospheric pressure.

The simplest approximation that we can adopt as a way of explaining conductivity is the Drude model. In this model it is assumed that the conduction electrons

1. do not interact with the cations ("free-electron approximation") except when one of them collides elastically with a cation which happens, on average, $1/\tau$ times per second, with the result that the velocity v of the electron abruptly and randomly changes its direction ("relaxation-time approximation");
2. maintain thermal equilibrium through collisions, in accordance with Maxwell–Boltzmann statistics ("classical-statistics approximation");
3. do not interact with each other ("independent-electron approximation").

This model predicts many of the general features of electrical conduction phenomena, as we shall see later in the chapter, but it fails to account for many others, such as tunneling, band gaps, and the Bloch T^5 law. More satisfactory explanations of electron transport relax or discard one or more of these approximations.

Ordinarily, one abandons the free-electron approximation by having the electrons move in a periodic potential arising from the background lattice of positive ions. Figure 1.1 gives an example of a simple potential that is negative near the positive

$\left(\frac{\mathbf{L}}{\mu\Omega\,\mathbf{W}}{\mathbf{K}^2}\right)$	$\left(\frac{\gamma}{\mathbf{mJ}}{\mathbf{mole\ K}^2}\right)$	$\frac{m^*}{m_e}$	$\frac{1}{R_H ne}$	Θ_D (K)	$\left(\frac{\omega_p}{\mathbf{rad}}{\mathbf{fs}}\right)$	IP (eV)	WF (eV)	E_F (eV)	T_F (kK)	k_F (M cm^{-1})	$\left(\frac{\nu_F}{\mathbf{cm}}{\mu\,\mathbf{s}}\right)$
0.021	1.5	1.3	−1.1	150	8.98	5.14	2.75	3.24	37.7	92	107
0.022	2.0	1.2	−1.1	100	5.98	4.34	2.3	2.12	24.6	75	86
0.023	0.67	1.3	−1.4	310	3.85	7.72	4.6	7.0	81.6	136	157
0.023	0.67	1.1	−1.2	220		7.57	4.3	5.49	63.8	120	139
0.029	8.4	12		265		6.87	4.3	5.32	61.8	118	137
0.026	2.7	1.8	−0.76	230		6.11	2.9	4.69	54.4	111	128
0.030	3.6	2.0		150		5.69	2.6	3.93	45.7	102	118
0.042	2.7	1.4		110		5.21	2.7	3.64	42.3	98	113
0.021	1.26	1.4	+1.0	394	14.5	5.99	4.3	11.7	136	175	203
0.028	1.5	1.1		96		6.11	3.8	8.15	94.6	146	169
0.025	1.8	1.3		170		7.34	4.4	10.2	118	164	190
0.026	2.9	1.9		88		7.41	4.3	9.47	110	158	183
0.026	0.63	0.38		200		8.64	4.6	10.9	127	170	196
0.035	0.084	0.047		120		7.29	4.2	9.90	115	161	187

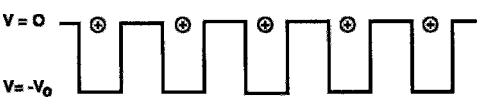

Figure 1.1 Muffin tin potential has a constant negative value $-V_0$ near each positive ion and is zero in the region between the ions.

ions and zero between them. An electron moving through the lattice interacts with the surrounding positive ions, which are oscillating about their equilibrium positions, and the charge distortions resulting from this interaction propagate along the lattice, causing distortions in the periodic potential. These distortions can influence the motion of yet another electron some distance away that is also interacting with the oscillating lattice. Propagating lattice vibrations are called *phonons*, so that this interaction is called the *electron-phonon interaction*. We will see later that two electrons interacting with each other through the intermediary phonon can form bound states and that the resulting bound electrons, called *Cooper pairs*, become the carriers of the super current.

The classical statistics assumption is generally replaced by the Sommerfeld approach. In this approach the electrons are assumed to obey Fermi-Dirac statistics with the distribution function

$$f_0(\mathbf{v}) = \frac{1}{\exp[(mv^2/2-\mu)/k_B T]+1}, \quad (1.2)$$

(see the discussion in Section IX), where k_B is Boltzmann's constant, and the constant μ is called the *chemical potential*. In Fermi–Dirac statistics, noninteracting conduction electrons are said to constitute a Fermi gas. The chemical potential is the energy required to remove one electron from this gas under conditions of constant volume and constant entropy.

The relaxation time approximation assumes that the distribution function $f(\mathbf{v}, t)$ is time dependent and that when $f(\mathbf{v}, t)$ is disturbed to a nonequilibration configuration f^{col}, collisions return it back to its equilibrium state f^0 with time constant τ in accordance with the expression

$$\frac{df}{dt} = -\frac{f^{\text{col}} - f^0}{\tau}. \quad (1.3)$$

Ordinarily, the relaxation time τ is assumed to be independent of the velocity, resulting in a simple exponential return to equilibrium:

$$f(\mathbf{v}, t) = f^0(\mathbf{v}) + [f^{\text{col}}(\mathbf{v}) - f^0(\mathbf{v})]e^{-t/\tau}. \quad (1.4)$$

In systems of interest $f(\mathbf{v}, t)$ always remains close to its equilibrium configuration (1.2). A more sophisticated approach to collision dynamics makes use of the Boltzmann equation, and this is discussed in texts in solid state physics (e.g., Ashcroft and Mermin, 1976; Burns, 1985; Kittel, 1976) and statistical mechanics (e.g., Reif, 1965).

It is more realistic to waive the independent-electron approximation by recognizing that there is Coulomb repulsion between the electrons. In the following section, we will show that electron screening makes electron–electron interaction negligibly small in good conductors. The use of the Hartree–Fock method to calculate the effects of this interaction is too complex to describe here; it will be briefly discussed in Chapter 10, Section VII.

When a method developed by Landau (1957a, b) is employed to take into account electron–electron interactions so as to ensure a one-to-one correspondence between the states of the free electron gas and those of the interacting electron system, the conduction electrons are said to form a Fermi liquid. Due to the Pauli exclusion principle, momentum-changing collisions occur only in the case of electrons at the Fermi surface. In what are called *marginal Fermi liquids* the one-to-one correspondence condition breaks down at the Fermi surface. Chapter 10, Section VII provides a brief discussion of the Fermi liquid and the marginal Fermi liquid approaches to superconductivity.

III. CHEMICAL POTENTIAL AND SCREENING

Ordinarily, the chemical potential μ is close to the Fermi energy E_F and the conduction electrons move at speeds v_F corresponding to kinetic energies $\frac{1}{2}mv_F^2$ close to $E_F = k_B T_F$. Typically, $v_F \approx 10^6$ m/s for good conductors, which is 1/300 the speed of light; perhaps one-tenth as great in the case of high-temperature superconductors and $A15$ compounds in their normal state. If we take τ as the time between collisions, the mean free path l, or average distance traveled between collisions, is

$$l = v_F \tau. \tag{1.5}$$

For aluminum the mean free path is 1.5×10^{-8} m at 300 K, 1.3×10^{-7} m at 77 K, and 6.7×10^{-4} m at 4.2 K.

To see that the interactions between conduction electrons can be negligible in a good conductor, consider the situation of a point charge Q embedded in a free electron gas with unperturbed density n_0. This negative charge is compensated for by a rigid background of positive charge, and the delocalized electrons rearrange themselves until a static situation is reached in which the total force density vanishes everywhere. In the presence of this weak electrostatic interaction the electrons constitute a Fermi liquid.

The free energy F in the presence of an external potential is a function of the local density $n(r)$ of the form

$$F[n] = F_0[n] - e \int n(r)\Phi(r) d^3 r, \tag{1.6}$$

where $\Phi(r)$ is the electric potential due to both the charge Q and the induced screening charge and $F_0[n]$ is the free energy of a non-interacting electron gas with local density n. Taking the functional derivative of $F[n]$ we have

$$\frac{\delta F[n]}{\delta n(r)} = \mu_0(r) - e\Phi(r) \tag{1.7}$$

$$= \mu, \tag{1.8}$$

where $\mu_0(r)$ is the local chemical potential of the free electron gas in the absence of charge Q and μ is a constant. At zero temperature, which is a good approximation because $T \ll T_F$, the local chemical potential is

$$\mu_0 = \frac{\hbar^2}{2m}(3\pi^2 n)^{2/3}. \tag{1.9}$$

Solving this for the density of the electron gas, we have

$$n(r) = \frac{1}{3\pi^2}\left\{\frac{2m}{\hbar^2}[\mu + e\Phi(r)]\right\}^{3/2}. \quad (1.10)$$

Typically the Fermi energy is much greater than the electrostatic energy so Eq. (1.10) can be expanded about $\Phi = 0$ to give

$$n(r) = n_0\left(1 + \frac{3}{2}\cdot\frac{e\Phi}{\mu}\right), \quad (1.11)$$

where $n_0 = [2m\mu/\hbar^2]^{3/2}/3\pi^2$. The total induced charge density is then

$$\begin{aligned}\rho_i(r) &= e[n_0 - n(r)] \\ &= -\frac{3}{2}\cdot\frac{n_0 e^2\Phi(r)}{\mu}. \end{aligned} \quad (1.12)$$

Poisson's equation for the electric potential can be written as

$$\nabla^2\Phi(r) - \lambda_{sc}^{-2}\Phi(r) = -4\pi Q\delta(r), \quad (1.13)$$

where the characteristic distance λ_{sc}, called the *screening length*, is given by

$$\lambda_{sc}^2 = \frac{1}{6\pi}\cdot\frac{\mu}{n_0 e^2}. \quad (1.14)$$

Equation (1.13) has the well-known Yukawa solution

$$\rho_i(r) = -\frac{Q}{r}e^{-r/\lambda_{sc}}. \quad (1.15)$$

Note that at large distances the potential of the charge falls off exponentially, and that the characteristic distance λ_{sc} over which the potential is appreciable decreases with the electron density. In good conductors the screening length can be quite short, and this helps to explain why electron–electron interaction is negligible. Screening causes the Fermi liquid of conduction electrons to act like a Fermi gas.

IV. ELECTRICAL CONDUCTIVITY

When a potential difference exists between two points along a conducting wire, a uniform electric field E is established along the axis of the wire. This field exerts a force $F = -eE$ that accelerates the electrons:

$$-eE = m\left(\frac{dv}{dt}\right), \quad (1.16)$$

and during a time t that is on the order of the collision time τ the electrons attain a velocity

$$v = -\left(\frac{eE}{m}\right)\tau. \quad (1.17)$$

The electron motion consists of successive periods of acceleration interrupted by collisions, and, on average, each collision reduces the electron velocity to zero before the start of the next acceleration.

To obtain an expression for the current density $\mathbf{J}$,

$$\mathbf{J} = ne\mathbf{v}_{av}, \quad (1.18)$$

we assume that the average velocity $\mathbf{v}_{av}$ of the electrons is given by Eq. (1.17), so we obtain

$$\mathbf{J} = \left(\frac{ne^2\tau}{m}\right)\mathbf{E}. \quad (1.19)$$

The dc electrical conductivity σ_0 is defined by Ohm's law,

$$\mathbf{J} = \sigma_0\mathbf{E} \quad (1.20)$$

$$= \frac{\mathbf{E}}{\rho_0}, \quad (1.21)$$

where $\rho_0 = 1/\sigma_0$ is the resistivity, so from Eq. (1.19) we have

$$\sigma_0 = \frac{ne^2\tau}{m}. \quad (1.22)$$

We infer from the data in Table 1.1 that metals typically have room temperature

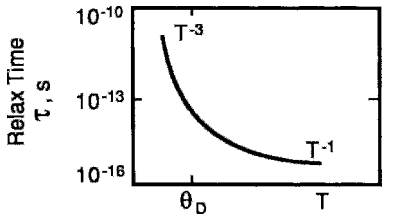

Figure 1.2 Typical temperature dependence of the conduction electron relaxation time τ.

resistivities between 1 and 100 $\mu\Omega$ cm. Semiconductor resistivities have values from 10^4 to $10^{15}\,\mu\Omega$ cm, and for insulators the resistivities are in the range from 10^{20} to $10^{28}\,\mu\Omega$ cm.

Collisions can arise in a number of ways, for example, from the motion of atoms away from their regular lattice positions due to thermal vibrational motion—the dominant process in pure metals at high temperatures (e.g., 300 K), or from the presence of impurities or lattice imperfections, which is the dominant scattering process at low temperatures (e.g., 4 K). We see from a comparison of the data in columns 11 and 12 of Table1.1 that for metallic elements the collision time decreases with temperature so that the electrical conductivity also decreases with temperature, the latter in an approximately linear fashion. The relaxation time τ has the limiting temperature dependences

$$\tau \approx \begin{cases} T^{-3} & T \ll \Theta_D \\ T^{-1} & T \gg \Theta_D \end{cases}, \tag{1.23}$$

as shown in Figure 1.2; here Θ_D is the Debye temperature. We will see in Section VI that, for $T \ll \Theta_D$, an additional phonon scattering correction factor must be taken into account in the temperature dependence of σ_0.

V. FREQUENCY DEPENDENT ELECTRICAL CONDUCTIVITY

When a harmonically varying electric field $E = E_0 e^{-i\omega t}$ acts on the conduction electrons, they are periodically accelerated in the forward and backward directions as E reverses sign every cycle. The conduction electrons also undergo random collisions with an average time τ between the collisions. The collisions, which interrupt the regular oscillations of the electrons, may be taken into account by adding a frictional damping term $\mathbf{p}/\tau$ to Eq. (1.16),

$$\frac{d\mathbf{p}}{dt} + \frac{\mathbf{p}}{\tau} = -e\mathbf{E}, \tag{1.24}$$

where $\mathbf{p} = m\mathbf{v}$ is the momentum. The momentum has the same harmonic time variation, $\mathbf{p} = m\mathbf{v}_0 e^{-i\omega t}$. If we substitute this into Eq. (1.24) and solve for the velocity $\mathbf{v}_0$, we obtain

$$\mathbf{v}_0 = \frac{-e\mathbf{E}_0}{m} \cdot \frac{\tau}{1 - i\,\omega\tau}. \tag{1.25}$$

Comparing this with Eqs. (1.18) and (1.22) with $\mathbf{v}_0$ playing the role of $\mathbf{v}_{av}$ gives us the ac frequency dependent conductivity:

$$\sigma = \frac{\sigma_0}{1 - i\,\omega\tau}. \tag{1.26}$$

This reduces to the dc case of Eq. (1.22) when the frequency is zero.

When $\omega\tau \ll 1$, many collisions occur during each cycle of the E field, and the average electron motion follows the oscillations. When $\omega\tau \gg 1$, E oscillates more rapidly than the collision frequency, Eq. (1.24) no longer applies, and the electrical conductivity becomes predominately imaginary, corresponding to a reactive impedance. For very high frequencies, the collision rate becomes unimportant and the electron gas behaves like a plasma, an electrically neutral ionized gas in which the negative charges are mobile electrons and the positive charges are fixed in position. Electromagnetic wave phenomena can be described in terms of the frequency-dependent dielectric constant $\epsilon(\omega)$,

$$\epsilon(\omega) = \epsilon_0 \left(1 - \frac{\omega_p^2}{\omega^2}\right), \tag{1.27}$$

where ω_p is the plasma frequency,

$$\omega_p = \left(\frac{ne^2}{\epsilon_0 m}\right)^{1/2}. \qquad (1.28)$$

Thus ω_p is the characteristic frequency of the conduction electron plasma below which the dielectric constant is negative—so electromagnetic waves cannot propagate—and above which ϵ is positive and propagation is possible. As a result metals are opaque when $\omega < \omega_p$ and transparent when $\omega > \omega_p$. Some typical plasma frequencies $\omega_p/2\pi$ are listed in Table1.1. The plasma wavelength can also be defined by setting $\lambda_p = 2\pi c/\omega_p$.

VI. ELECTRON–PHONON INTERACTION

We will see later in the text that for most superconductors the mechanism responsible for the formation of Cooper pairs of electrons, which carry the supercurrent, is electron–phonon interaction. In the case of normal metals, thermal vibrations disturb the periodicity of the lattice and produce phonons, and the interactions of these phonons with the conduction electrons cause the latter to scatter. In the high-temperature region ($T \gg \Theta_D$), the number of phonons in the normal mode is proportional to the temperature (cf. Problem 6). Because of the disturbance of the conduction electron flow caused by the phonons being scattered, the electrical conductivity is inversely proportional to the temperature, as was mentioned in Section IV.

At absolute zero the electrical conductivity of metals is due to the presence of impurities, defects, and deviations of the background lattice of positive ions from the condition of perfect periodicity. At finite but low temperatures, $T \ll \Theta_D$, we know from Eq. (1.23) that the scattering rate $1/\tau$ is proportional to T^3. The lower the temperature, the more scattering in the forward direction tends to dominate, and this introduces another T^2 factor, giving the Bloch T^5 law,

$$\sigma \approx T^{-5} \quad T \ll \Theta_D, \qquad (1.29)$$

which has been observed experimentally for many metals.

Standard solid-state physics texts discuss Umklapp processes, phonon drag, and other factors that cause deviations from the Bloch T^5 law, but these will not concern us here. The texts mentioned at the end of the chapter should be consulted for further details.

VII. RESISTIVITY

Electrons moving through a metallic conductor are scattered not only by phonons but also by lattice defects, impurity atoms, and other imperfections in an otherwise perfect lattice. These impurities produce a temperature-independent contribution that places an upper limit on the overall electrical conductivity of the metal.

According to Matthiessen's rule, the conductivities arising from the impurity and phonon contributions add as reciprocals; that is, their respective individual resistivities, ρ_0 and ρ_{ph}, add to give the total resistivity

$$\rho(T) = \rho_0 + \rho_{ph}(T). \qquad (1.30)$$

We noted earlier that the phonon term $\rho_{ph}(T)$ is proportional to the temperature T at high temperatures and to T^5 via the Bloch law (1.29) at low temperatures. This means that, above room temperature, the impurity contribution is negligible, so that the resistivity of metallic elements is roughly proportional to the temperature:

$$\rho(T) \approx \rho(300\,\mathrm{K})\left[\frac{T}{300}\right] \quad 300\,\mathrm{K} < T. \qquad (1.31)$$

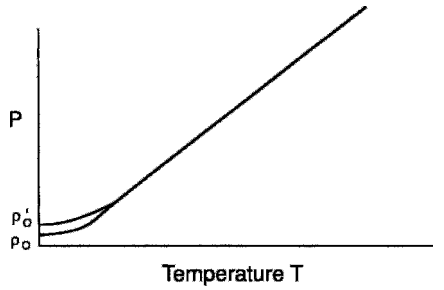

Figure 1.3 Temperature dependence of the resistivity ρ of a pure (ρ_0) and a less pure conductor. Impurities limit the zero temperature resistivity (ρ_0') in the latter case.

At low temperatures far below the Debye temperature, the Bloch T^5 law applies to give

$$\rho(T) = \rho_0 + AT^5 \quad T \ll \Theta_D. \qquad (1.32)$$

Figure 1.3 shows the temperature dependence of the resistivity of a high-purity (low ρ_0) and a lower-purity (larger ρ_0') good conductor.

Typical resistivities at room temperature are 1.5 to 2 $\mu\Omega$ cm for very good conductors (e.g., Cu), 10 to 100 for poor conductors, 300 to 10,000 for high-temperature superconducting materials, 10^4 to 10^{15} for semiconductors, and 10^{20} to 10^{28} for insulators. We see from Eqs. (1.31) and (1.32) that metals have a positive temperature coefficient of resistivity, which is why metals become better conductors at low temperature. In contrast, the resistivity of a semiconductor has a negative temperature coefficient, so that it increases with decreasing temperature. This occurs because of the decrease in the number of mobile charge carriers that results from the return of thermally excited conduction electrons to their ground states on donor atoms or in the valence band.

VIII. THERMAL CONDUCTIVITY

When a temperature gradient exists in a metal, the motion of the conduction electrons provides the transport of heat (in the form of kinetic energy) from hotter to cooler regions. In good conductors such as copper and silver this transport involves the same phonon collision processes that are responsible for the transport of electric charge. Hence these metals tend to have the same thermal and electrical relaxation times at room temperature. The ratio $K_{th}/\sigma T$, in which both thermal (K_{th}, $\mathbf{J}\,\mathrm{cm}^{-1}\,\mathrm{s}^{-1}\,\mathrm{K}^{-1}$) and electrical ($\sigma$, $\Omega^{-1}\,\mathrm{cm}^{-1}$) conductivities occur (see Table1.1 for various metallic elements), has a value which is about twice that predicted by the law of Wiedermann and Franz,

$$\frac{K_{th}}{\sigma T} = \frac{3}{2}\left(\frac{k_B}{e}\right)^2 \qquad (1.33)$$

$$= 1.11 \times 10^{-8}\,\mathrm{W}\Omega/\mathrm{K}^2, \qquad (1.34)$$

where the universal constant $\frac{3}{2}(k_B/e)^2$ is called the Lorenz number.

IX. FERMI SURFACE

Conduction electrons obey Fermi–Dirac statistics. The corresponding F–D distribution function (1.2), written in terms of the energy E,

$$f(E) = \frac{1}{\exp[(E-\mu)/k_BT]+1}, \qquad (1.35)$$

is plotted in Fig 1.4a for $T = 0$ and in Fig 1.4b for $T > 0$. The chemical potential μ corresponds, by virtue of the expression

$$\mu \approx E_F = k_BT_F, \qquad (1.36)$$

to the Fermi temperature T_F, which is typically in the neighborhood of 10^5 K. This means that the distribution function $f(E)$ is 1 for energies below E_F and zero above E_F, and assumes intermediate values only in a region k_BT wide near E_F, as shown in Fig. 1.4b.

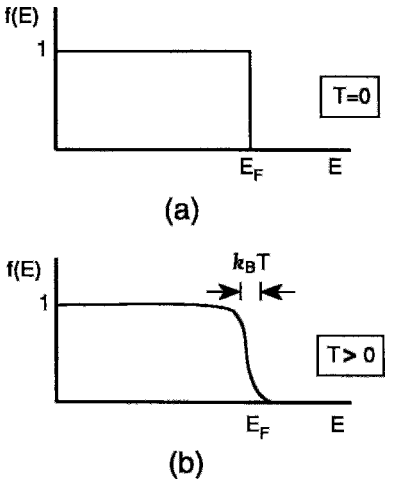

Figure 1.4 Fermi-Dirac distribution function $f(E)$ for electrons (a) at $T = 0$ K, and (b) above 0 K.

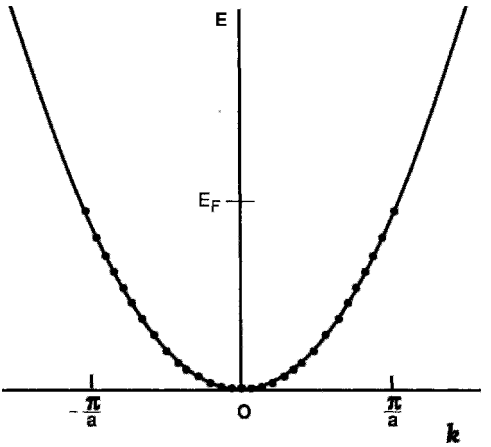

Figure 1.5 One-dimensional free electron energy band shown occupied out to the first Brillouin zone boundaries at $k = \pm\pi/a$.

The electron kinetic energy can be written in several ways, for example,

$$E_{\mathrm{k}} = \frac{1}{2}mv^2 = \frac{p^2}{2m} = \frac{\hbar^2 k^2}{2m} = \frac{\hbar^2}{2m}(k_x^2 + k_y^2 + k_z^2), \qquad (1.37)$$

where $p = \hbar k$, and the quantization in k-space, sometimes called reciprocal space, means that each Cartesian component of $\mathbf{k}$ can assume discrete values, namely $2\pi n_x/L_x$ in the x direction of length L_x, and likewise for the y and z directions of length L_y and L_z, respectively. Here n_x is an integer between 1 and L_x/a, where a is the lattice constant; n_y and n_z are defined analogously. The one-dimensional case is sketched in Fig. 1.5. At absolute zero these k-space levels are doubly occupied by electrons of opposite spin up to the Fermi energy E_{F},

$$E_{\mathrm{F}} = \frac{\hbar^2 k_{\mathrm{F}}^2}{2m}, \qquad (1.38)$$

as indicated in the figure. Partial occupancy occurs in a narrow region of width $k_{\mathrm{B}}T$ at E_{F}, as shown in Fig. 1.4b. For simplicity we will assume a cubic shape, so that $L_x = L_y = L_z = L$. Hence the total number of electrons N is given as

$$N = 2\frac{\text{occupied } k\text{-space volume}}{k\text{-space volume per electron}} = 2\frac{4\pi k_{\mathrm{F}}^3/3}{(2\pi/L)^3}. \qquad (1.39)$$

The electron density $n = N/V = N/L^3$ at the energy $E = E_{\mathrm{F}}$ is

$$n = \frac{k_{\mathrm{F}}^3}{3\pi^2} = \frac{1}{3\pi^2}\left(\frac{2mE_{\mathrm{F}}}{\hbar^2}\right)^{3/2}, \qquad (1.40)$$

and the density of states $D(E)$ per unit volume, which is obtained from evaluating the derivative dn/dE of this expression (with E_{F} replaced by E), is

$$D(E) = \frac{d}{dE}n(E) = \frac{1}{2\pi^2}\left(\frac{2m}{\hbar^2}\right)^{3/2} E^{1/2} = D(E_{\mathrm{F}})(E/E_{\mathrm{F}})^{1/2}, \qquad (1.41)$$

and this is shown sketched in Fig. 1.6. Using Eqs. (1.36) and (1.38), respectively, the density of states at the Fermi level can be written in two equivalent ways,

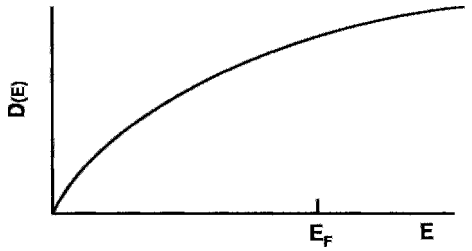

Figure 1.6 Density of states $D(E)$ of a free electron energy band $E = \hbar^2 k^2/2m$.

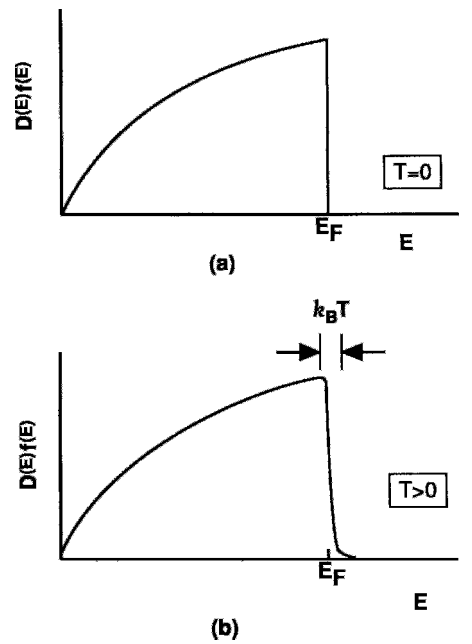

Figure 1.7 Energy dependence of occupation of a free electron energy band by electrons (a) at 0 K and (b) for $T > 0$ K. The products $D(E)f(E)$ are calculated from Figs. 1.4 and 1.6.

$$D(E_F) = \begin{cases} \dfrac{3n}{2k_B T_F} \\ \dfrac{mk_F}{\hbar^2 \pi^2} \end{cases}, \tag{1.42}$$

for this isotropic case in which energy is independent of direction in k-space (so that the Fermi surface is spherical). In many actual conductors, including the high-temperature superconductors in their normal states above T_c, this is not the case, and $D(E)$ has a more complicated expression.

It is convenient to express the electron density n and the total electron energy E_T in terms of integrals over the density of states:

$$n = \int D(E) f(E) dE, \tag{1.43}$$

$$E_T = \int D(E) f(E) E dE. \tag{1.44}$$

The product $D(E)f(E)$ that appears in these integrands is shown plotted versus energy in Fig. 1.7a for $T = 0$ and in Fig. 1.7b for $T > 0$.

X. ENERGY GAP AND EFFECTIVE MASS

The free electron kinetic energy of Equation (1.37) is obtained from the plane wave solution $\phi = e^{-i\mathbf{k}\cdot\mathbf{r}}$ of the Schrödinger equation,

$$-\left(\frac{\hbar^2}{2m}\right)\nabla^2\phi(\mathbf{r}) + V(\mathbf{r})\phi(\mathbf{r}) = E\phi(\mathbf{r}), \tag{1.45}$$

with the potential $V(\mathbf{r})$ set equal to zero. When a potential, such as that shown in Fig. 1.1, is included in the Schrödinger equation, the free-electron energy parabola of Fig. 1.5 develops energy gaps, as shown in Fig 1.8. These gaps appear at boundaries $k = \pm n\pi/a$ of the unit cell in k-space, called the *first Brillouin zone*, and of successively higher Brillouin zones, as shown. The energies levels are closer near the gap, which means that the density of states $D(E)$ is larger there (see Figs. 1.9 and 1.10). For weak potentials, $|V| \ll E_F$, the density of states is close to its free-electron form away from the gap, as indicated in the figures. The number of points in k-space remains the same, that is, it is *conserved*, when the gap forms; it is the density *D(E)* that changes.

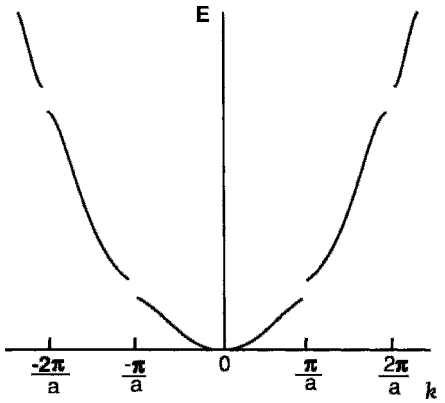

Figure 1.8 A one-dimensional free electron energy band shown perturbed by the presence of a weak periodic potential $V(x) \ll \hbar^2\pi^2/2ma^2$. The gaps open up at the zone boundaries $k = \pm n\pi/a$, where $n = 1, 2, 3, \ldots$.

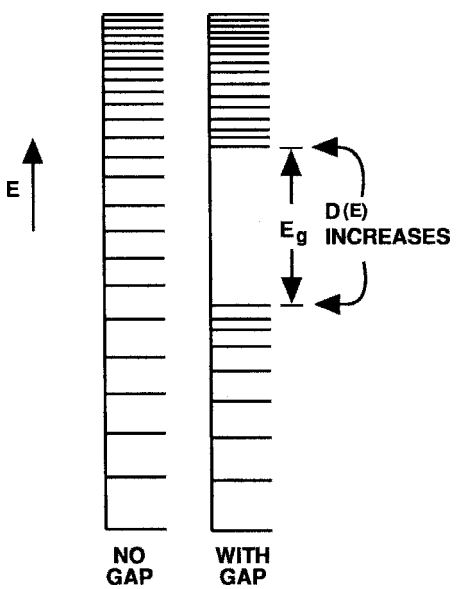

Figure 1.9 Spacing of free electron energy levels in the absence of a gap (left) and in the presence of a small gap (right) of the type shown in Fig. 1.8. The increase of *D(E)* near the gap is indicated.

If the kinetic energy near an energy gap is written in the form,

$$E_k = \frac{\hbar^2 k^2}{2m^*}, \tag{1.46}$$

the effective mass $m^*(k)$, which is different from the free-electron value m, becomes a function of k, which takes into account bending of the free-electron parabola near the gap. It can be evaluated from the second derivative of E_k with respect to k:

$$\frac{1}{m^*} = \frac{1}{\hbar^2}\left(\frac{d^2E_k}{dk^2}\right)_{E_F}. \tag{1.47}$$

This differentiation can be carried out if the shapes of the energy bands near the Fermi level are known. The density of states $D(E_F)$ also deviates from the free-electron value near the gap, being proportional to the effective mass m^*,

$$D(E_F) = \frac{m^* k_F}{\hbar^2\pi^2}, \tag{1.48}$$

as may be inferred from Eq. (1.42).

There is a class of materials called heavy fermion compounds whose effective conduction electron mass can exceed 100 free electron masses. Superconductors of this type are discussed in Sect. 9.II.

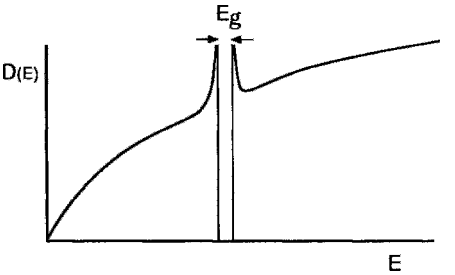

Figure 1.10 Energy dependence of the density of states $D(E)$ corresponding to the case of Fig. 1.9 in the presence of a gap.

XI. ELECTRONIC SPECIFIC HEAT

The specific heat C of a material is defined as the change in internal energy U brought about by a change in temperature

$$C = \left(\frac{dU}{dT}\right)_V. \tag{1.49}$$

We will not make a distinction between the specific heat at constant volume and the specific heat at constant pressure because for solids these two properties are virtually indistinguishable. Ordinarily, the specific heat is measured by determining the heat input dQ needed to raise the temperature of the material by an amount dT,

$$dQ = CdT. \tag{1.50}$$

In this section, we will deduce the contribution of the conduction electrons to the specific heat, and in the next section we will provide the lattice vibration or phonon participation. The former is only appreciable at low temperatures while the latter dominates at room temperature.

The conduction electron contribution C_e to the specific heat is given by the derivative dE_τ/dT. The integrand of Eq. (1.44) is somewhat complicated, so differentiation is not easily done. Solid-state physics texts carry out an approximate evaluation of this integral, to give

$$C_e = \gamma T, \tag{1.51}$$

where the normal-state electron specific heat constant γ, sometimes called the Sommerfeld constant, is given as

$$\gamma = \left(\frac{\pi^2}{3}\right) D(E_F) k_B^2. \tag{1.52}$$

This provides a way to experimentally evaluate the density of states at the Fermi level. To estimate the electronic specific heat per mole we set $n = N_A$ and make use of Eq. (1.42) to obtain the free-electron expression

$$\dot{\gamma}_0 = \frac{\pi^2 R}{2T_F}, \tag{1.53}$$

where $R = N_A k_B$ is the gas constant. This result agrees (within a factor of 2) with experiment for many metallic elements.

A more general expression for γ is obtained by applying $D(E_F)$ from Eq. (1.48) instead of the free-electron value of (1.42). This gives

$$\gamma = \left(\frac{m^*}{m}\right) \gamma_0, \tag{1.54}$$

where γ_0 is the Sommerfeld factor (1.53) for a free electron mass. This expression will be discussed further in Chapter 9, Section II, which treats heavy fermion compounds that have very large effective masses.

XII. PHONON SPECIFIC HEAT

The atoms in a solid are in a state of continuous vibration. These vibrations, called *phonon modes*, constitute the main contribution to the specific heat. In models of a vibrating solid nearby atoms are depicted as being bonded together by springs. For the one-dimensional diatomic case of alternating small and large atoms, of masses m_s and m_1, respectively, there are low-frequency modes called *acoustic* (A) *modes*, in which the two types of atoms vibrate in phase, and high-frequency modes, called *optical* (O) *modes*, in which they vibrate out of phase. The vibrations can also be longitudinal, i.e., along the line of atoms, or transverse, i.e., perpendicular to this line, as explained in typical solid-state physics texts. In practice, crystals are three-dimensional and the situation is more complicated, but these four types of modes are observed. Figure 1.11 presents a typical wave vector dependence of their frequencies.

It is convenient to describe these vibrations in k-space, with each vibrational mode having energy $E = \hbar\omega$. The Planck distribution function applies,

$$f(E) = \frac{1}{\exp(E/k_B T) - 1}, \tag{1.55}$$

where the minus one in the denominator indicates that only the ground vibrational level is occupied at absolute zero. There is no chemical potential because the number of phonons

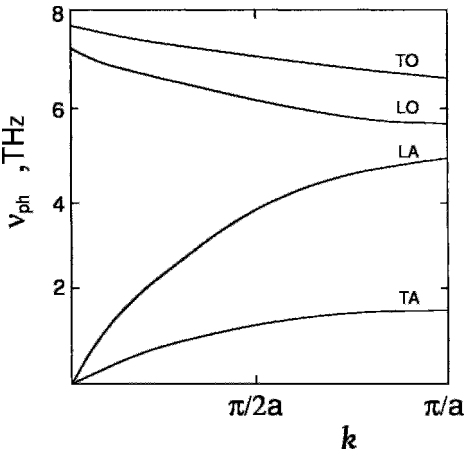

Figure 1.11 Typical dependence of energy E on the wave vector k for transverse (T), longitudinal (L), optical (O), and acoustic (A) vibrational modes of a crystal.

is not conserved. The total number of acoustic vibrational modes per unit volume N is calculated as in Eq. (1.39) with the factor 2 omitted since there is no spin,

$$N = \frac{\text{occupied } k\text{-space volume}}{k\text{-space volume per atom}} = \frac{4\pi k_D^3/3}{(2\pi/L)^3}, \tag{1.56}$$

where L^3 is the volume of the crystal and k_D is the maximum permissible value of k. In the Debye model, the sound velocity v is assumed to be isotropic ($v_x = v_y = v_z$) and independent of frequency,

$$v = \frac{\omega}{k}. \tag{1.57}$$

Writing $\omega_D = vk_D$ and substituting this expression in Eq. (1.56) gives, for the density of modes $n = N/L^3$,

$$n = \frac{\omega_D^3}{6\pi^2 v^3}, \tag{1.58}$$

where the maximum permissible frequency ω_D is called the *Debye frequency*.

The vibration density of states per unit volume $D_{ph}(\omega) = dn/d\omega$ is

$$D_{ph}(\omega) = \frac{\omega^2}{2\pi^2 v^3}, \tag{1.59}$$

and the total vibrational energy E_{ph} is obtained by integrating the phonon mode energy $\hbar\omega$ times the density of states (1.59) over the distribution function (1.55) (cf. de Wette *et al.*, 1990)

$$E_{ph} = \int_0^{\omega_D} \left(\frac{\omega^2}{2\pi^2 v^3}\right) \frac{\hbar\,\omega\, d\,\omega}{e^{\hbar\omega/k_B T} - 1}. \tag{1.60}$$

The vibrational or phonon specific heat $C_{ph} = dE_{ph}/dT$ is found by differentiating Eq. (1.60) with respect to the temperature,

$$C_{ph} = 9R\left(\frac{T}{\Theta_D}\right)^3 \int_0^{\Theta_D} \frac{x^4 e^x dx}{(e^x - 1)^2}, \tag{1.61}$$

and Fig. 1.12 compares this temperature dependence with experimental data for Cu and Pb. The molar specific heat has the respective low- and high-temperature limits

$$C_{ph} = \left(\frac{12\pi^4}{5}\right) R\left(\frac{T}{\Theta_D}\right)^3 \quad T \ll \Theta_D \tag{1.62a}$$

$$C_{ph} = 3R \quad T \gg \Theta_D \tag{1.62b}$$

far below and far above the Debye temperature

$$\Theta_D = \frac{\hbar\,\omega_D}{k_B}, \tag{1.63}$$

and the former limiting behavior is shown by the dashed curve in Fig. 1.12. We also see from the figure that at their superconducting transition temperatures T_c the element Pb and the compound LaSrCuO are in the T^3 region, while the compound YBaCuO is significantly above it.

Since at low temperatures a metal has an electronic specific heat term (1.51) that is linear in temperature and a phonon term (1.62a)

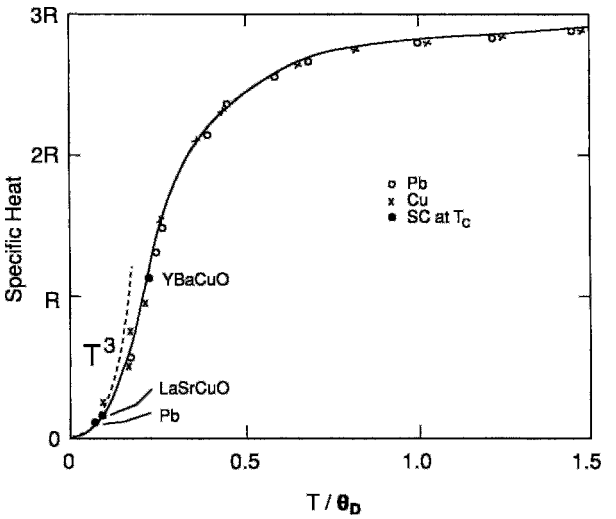

Figure 1.12 Temperature dependence of the phonon-specific heat in the Debye model compared with experimental data for Cu and Pb. The low-temperature T^3 approximation is indicated by a dashed curve. The locations of the three superconductors Pb, $(La_{0.925}Sr_{0.075})_2CuO_4$, and $YBa_2Cu_3O_{7-\delta}$ at their transition temperature T_c on the Debye curve are indicated (it is assumed that they satisfy Eq. (1.61)).

that is cubic in T, the two can be experimentally distinguished by plotting $C_{\rm exp}/T$ versus T^2, where

$$\frac{C_{\rm exp}}{T} = \gamma + AT^2, \qquad (1.64)$$

as shown in Fig. 1.13. The slope gives the phonon part A and the intercept at $T = 0$ gives the electronic coefficient γ

Materials with a two-level system in which both the ground state and the excited state are degenerate can exhibit an extra contribution to the specific heat, called the *Schottky term*. This contribution depends on the energy spacing $E_{\rm Sch}$ between the ground and excited states. When $E_{\rm Sch} \ll k_{\rm B}T$, the Schottky term has the form aT^{-2} (Crow and Ong, 1990). The resulting upturn in the observed specific heat at low temperatures, sometimes called the *Schottky anomaly*, has been observed in some superconductors.

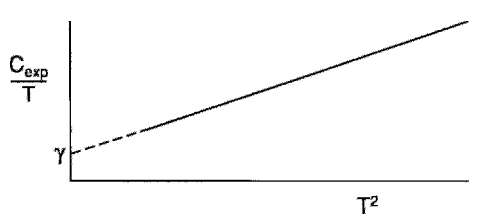

Figure 1.13 Typical plot of $C_{\rm exp}/T$ versus T^2 for a conductor. The phonon contribution is given by the slope of the line, and the free electron contribution γ is given by the intercept obtained by the extrapolation $T \to 0$.

XIII. ELECTROMAGNETIC FIELDS

Before discussing the magnetic properties of conductors it will be helpful to say a few words about electromagnetic fields, and to write down for later reference several of the basic equations of electromagnetism.

These equations include the two homogeneous Maxwell's equations

$$\nabla \cdot \mathbf{B} = 0, \qquad (1.65)$$

$$\nabla \times \mathbf{E} + \frac{\partial \mathbf{B}}{\partial t} = 0, \tag{1.66}$$

and the two inhomogeneous equations

$$\nabla \cdot \mathbf{D} = \rho, \tag{1.67}$$

$$\nabla \times \mathbf{H} = \mathbf{J} + \frac{\partial \mathbf{D}}{\partial t}, \tag{1.68}$$

where ρ and $\mathbf{J}$ are referred to as the free charge density and the free current density, respectively. The two densities are said to be 'free' because neither of them arises from the reaction of the medium to the presence of externally applied fields, charges, or currents. The $\mathbf{B}$ and $\mathbf{H}$ fields and the $\mathbf{E}$ and $\mathbf{D}$ fields, respectively, are related through the expressions

$$\mathbf{B} = \mu\mathbf{H} = \mu_0(\mathbf{H} + \mathbf{M}), \tag{1.69}$$

$$\mathbf{D} = \epsilon\mathbf{E} = \epsilon_0\mathbf{E} + \mathbf{P}, \tag{1.70}$$

where the medium is characterized by its permeability μ and its permittivity ϵ, and μ_0 and ϵ_0 are the corresponding free space values. These, of course, are SI formulae. When cgs units are used, $\mu_0 = \epsilon_0 = 1$ and the factor 4π must be inserted in front of $\mathbf{M}$ and $\mathbf{P}$.

The fundamental electric ($\mathbf{E}$) and magnetic ($\mathbf{B}$) fields are the fields that enter into the Lorentz force law

$$\mathbf{F} = q(\mathbf{E} + \mathbf{v} \times \mathbf{B}) \tag{1.71}$$

for the force $\mathbf{F}$ acting on a charge q moving at velocity $\mathbf{v}$ in a region containing the fields $\mathbf{E}$ and $\mathbf{B}$. Thus $\mathbf{B}$ and $\mathbf{E}$ are the macroscopically measured magnetic and electric fields, respectively. Sometimes $\mathbf{B}$ is called the magnetic induction or the magnetic flux density.

It is convenient to write Eq. (1.68) in terms of the fundamental field $\mathbf{B}$ using Eq. (1.69)

$$\nabla \times \mathbf{B} = \mu_0(\mathbf{J} + \nabla \times \mathbf{M}) + \mu_0 \frac{\partial \mathbf{D}}{\partial t}, \tag{1.72}$$

where the displacement current term $\partial\mathbf{D}/\partial t$ is ordinarily negligible for conductors and superconductors and so is often omitted. The reaction of the medium to an applied magnetic field produces the magnetization current density $\nabla \times \mathbf{M}$ which can be quite large in superconductors.

XIV. BOUNDARY CONDITIONS

We have been discussing the relationship between the $\mathbf{B}$ and $\mathbf{H}$ fields within a medium or sample of permeability μ. If the medium is homogeneous, both μ and $\mathbf{M}$ can be constant throughout, and Eq. (1.69), with $\mathbf{B} = \mu\mathbf{H}$, applies. But what happens to the fields when two media of respective permeabilities μ' and μ'' are in contact? At the interface between the media the $\mathbf{B}'$ and $\mathbf{H}'$ fields in one medium will be related to the $\mathbf{B}''$ and $\mathbf{H}''$ fields in the other medium through the two boundary conditions illustrated in Fig. 1.14, namely:

1. The components of $\mathbf{B}$ normal to the interface are continuous across the boundary:

$$\mathbf{B}'_\perp = \mathbf{B}''_\perp. \tag{1.73}$$

2. The components of $\mathbf{H}$ tangential to the interface are continuous across the boundary:

$$\mathbf{H}'_\parallel = \mathbf{H}''_\parallel. \tag{1.74}$$

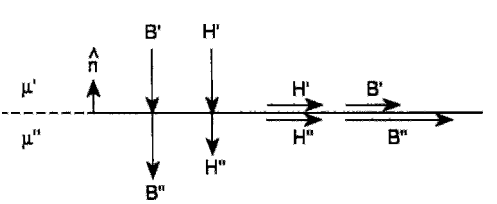

Figure 1.14 Boundary conditions for the components of the $\mathbf{B}$ and $\mathbf{H}$ magnetic field vectors perpendicular to and parallel to the interface between regions with different permeabilities. The figure is drawn for the case $\mu'' = 2\mu'$.

If there is a surface current density $\mathbf{J}_{\text{surf}}$ present at the interface, the second condition must be modified to take this into account,

$$\hat{\mathbf{n}} \times (\mathbf{H}' - \mathbf{H}'') = \mathbf{J}_{\text{surf}}, \tag{1.75}$$

where $\mathbf{n}$ is a unit vector pointing from the double primed ($''$) to the primed region, as indicated in Fig. 1.14, and the surface current density $\mathbf{J}_{\text{surf}}$, which has the units ampere per meter, is perpendicular to the field direction. When $\mathbf{H}'$ and $\mathbf{H}''$ are measured along the surface parallel to each other, Eq. (1.75) can be written in scalar form:

$$H'_{\parallel} - H''_{\parallel} = J_{\text{surf}}. \tag{1.76}$$

In like manner, for the electric field case the normal components of D and the tangential components of E are continuous across an interface, and the condition on D must be modified when surface charges are present.

XV. MAGNETIC SUSCEPTIBILITY

It is convenient to express Eq. (1.69) in terms of the dimensionless magnetic susceptibility χ,

$$\chi = \frac{\mathbf{M}}{\mathbf{H}}, \tag{1.77}$$

to give

$$\mathbf{B} = \mu_0 \mathbf{H}(1 + \chi_{\text{SI}}) \quad \text{SI units} \tag{1.78a}$$

$$\mathbf{B} = \mathbf{H}(1 + 4\pi\chi_{\text{cgs}}) \quad \text{cgs units.} \tag{1.78b}$$

The susceptibility χ is slightly negative for diamagnets, slightly positive for paramagnets, and strongly positive for ferromagnets. Elements that are good conductors have small susceptibilities, sometimes slightly negative (e.g., Cu) and sometimes slightly positive (e.g., Na), as may be seen from Table 1.2. Nonmagnetic inorganic compounds are weakly diamagnetic (e.g., NaCl), while magnetic compounds containing transition ions can be much more strongly paramagnetic (e.g., $CuCl_2$).

The magnetization in Eq. (1.77) is the magnetic moment per unit volume, and the susceptibility defined by this expression is dimensionless. The susceptibility of a material doped with magnetic ions is proportional to the concentration of the ions in the material. In general, researchers who study the properties of these materials are more interested in the properties of the ions themselves than in the properties of the material containing the ions. To take this into account it is customary to use molar susceptibilities χ^{M}, which in the SI system have the units m^3 per mole.

Table 1.2 cgs Molar Susceptibility (χ_{cgs}) and Dimensionless SI Volume Susceptibility (χ) of Several Materials

Material	MW g/mole	Density g/cm^3	χ_{cgs} cm^3/mole	χ —
Free space	—	0.0	0	0
Na	22.99	0.97	1.6×10^{-5}	8.48×10^{-6}
NaCl	58.52	2.165	-3.03×10^{-5}	-1.41×10^{-5}
Cu	63.54	8.92	-5.46×10^{-6}	-9.63×10^{-6}
$CuCl_2$	134.6	3.386	1.08×10^{-3}	3.41×10^{-4}
Fe alloy	≈ 60	7–8	10^3–10^4	10^3–10^4
Perfect SC	—	—	—	-1

It is shown in solid-state physics texts (e.g., Ashcroft and Mermin, 1976; Burns, 1985; Kittel, 1976) that a material containing paramagnetic ions with magnetic moments μ that become magnetically ordered at low temperatures has a high-temperature magnetic susceptibility that obeys the Curie–Weiss Law:

$$\chi^{\mathrm{M}} = \frac{n\mu^2}{3k_{\mathrm{B}}(T-\Theta)}, \tag{1.79a}$$

$$= \frac{C}{(T-\Theta)}, \tag{1.79b}$$

where n is the concentration of paramagnetic ions and C is the Curie constant. The Curie–Weiss temperature Θ has a positive sign when the low-temperature alignment is ferromagnetic and a negative sign when it is antiferromagnetic. Figure 1.15 shows the temperature dependence of χ^{M} for the latter case, in which the denominator becomes $T + |\Theta|$. The temperature T_{N} at which antiferromagnetic alignment occurs is referred to as the *Néel temperature*, and typically $T_{\mathrm{N}} \neq \Theta$. When $\Theta = 0$, Eq. (1.79) is called the Curie law.

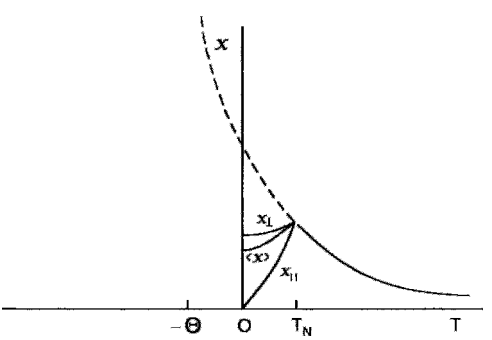

Figure 1.15 Magnetic susceptibility of a material that is paramagnetic above the Néel transition temperature T_{N} and antiferromagnetic with axial symmetry below the transition. The extrapolation of the paramagnetic curve below $T = 0$ provides the Curie-Weiss temperature Θ.

For a rare earth ion with angular momentum $J\hbar$ we can write

$$\mu^2 = g^2\mu_{\mathrm{B}}^2 J(J+1), \tag{1.80}$$

where $J = L + S$ is the sum of the orbital (L) and spin (S) contributions, $\mu_{\mathrm{B}} = e\hbar/2m$ is the Bohr magneton, and the dimensionless Landé g factor is

$$g = \frac{3}{2} + \frac{S(S+1) - L(L+1)}{2J(J+1)}. \tag{1.81}$$

For a first transition series ion, the orbital angular momentum $L\hbar$ is quenched, which means that it is uncoupled from the spin angular momentum and becomes quantized along the crystalline electric field direction. Only the spin part of the angular momentum contributes appreciably to the susceptibility, to give the so-called spin-only result

$$\mu^2 = g^2\mu_{\mathrm{B}}^2 S(S+1), \tag{1.82}$$

where for most of these ions $g \approx 2$.

For conduction electrons the only contribution to the susceptibility comes from the electrons at the Fermi surface. Using an argument similar to that which we employed for the electronic specific heat in Section XI we can obtain the temperature-independent expression for the susceptibility in terms of the electronic density of states,

$$\chi = \mu_{\mathrm{B}}^2 D(E_{\mathrm{F}}), \tag{1.83}$$

which is known as the *Pauli susceptibility*. For a free electron gas of density n we substitute the first expression for $D(E_{\mathrm{F}})$ from Eq. (1.42) in Eq. (1.83) to obtain, for a mole,

$$\chi^{\mathrm{M}} = \frac{3n\mu_{\mathrm{B}}^2}{2k_{\mathrm{B}}T_{\mathrm{F}}}. \tag{1.84}$$

For alkali metals the measured Pauli susceptibility decreases with increasing atomic number from Li to Cs with a typical value $\approx 1 \times 10^{-6}$. The corresponding free-electron

values from Eq. (1.84) are about twice as high as their experimental counterparts, and come much closer to experiment when electron–electron interactions are taken into account. For very low temperatures, high magnetic fields, and very pure materials there is an additional dia-magnetic correction term χ_{Landau}, called *Landau diamagnetism*, which arise from the orbital electronic interaction with the magnetic field. For the free-electron this correction has the value

$$\chi_{\text{Landau}} = -\tfrac{1}{3}\chi_{\text{Pauli}}. \tag{1.85}$$

In preparing Table 1.2 the dimensionless SI values of χ listed in column 5 were calculated from known values of the molar cgs susceptibility $\chi^{\text{M}}_{\text{cgs}}$, which has the units cm^3 per mole, using the expression

$$\chi = 4\pi\left(\frac{\rho_m}{\text{MW}}\right)\chi^{\text{M}}_{\text{cgs}}, \tag{1.86}$$

where ρ_m is the density in g per cm^3 and MW is the molecular mass in g per mole. Some authors report per unit mass susceptibility data in emu/g, which we are calling $\chi^{\text{g}}_{\text{cgs}}$. The latter is related to the dimension-less χ through the expression

$$\chi = 4\pi\rho_m\chi^{\text{g}}_{\text{cgs}}. \tag{1.87}$$

The ratio of Eq. (1.52) to Eq. (1.83) gives the free-electron expression

$$\frac{\gamma}{\chi^{\text{M}}} = \frac{1}{3}\left(\frac{\pi k_{\text{B}}}{\mu_{\text{B}}}\right)^2, \tag{1.88}$$

where χ^{M} is the susceptibility arising from the conduction electrons. An experimental determination of this ratio provides a test of the applicability of the free-electron approximation.

This section has been concerned with dc susceptibility. Important information can also be obtained by using an ac applied field $B_0\cos\omega t$ to determine $\chi_{\text{ac}} = \chi' + i\chi''$, which has real part χ', called dispersion, in phase with the applied field, and an imaginary lossy part χ'', called absorption, which is out of phase with the field (Khode and Couach, 1992). D. C. Johnston (1991) reviewed normal state magnetization of the cuprates.

XVI. HALL EFFECT

The Hall effect employs crossed electric and magnetic fields to obtain information on the sign and mobility of the charge carriers. The experimental arrangement illustrated in Fig. 1.16 shows a magnetic field B_0 applied in the z direction perpendicular to a slab and a battery that establishes an electric field E_y in the y direction that causes a current $I = JA$ to flow, where $J = nev$ is the current density. The Lorentz force

$$\mathbf{F} = q\mathbf{v}\times\mathbf{B}_0 \tag{1.89}$$

of the magnetic field on each moving charge q is in the positive x direction for both positive and negative charge carriers, as shown in Figs. 1.17a and 1.17b, respectively. This causes a charge separation to build up on the sides of the plate, which produces an electric field E_x perpendicular to the directions of the current (y) and magnetic (z) fields. The induced electric field is in the negative x direction for positive q, and in the positive x direction for negative q, as shown in Figs. 1.17c and 1.17d, respectively. After the charge separation has built up, the electric force $q\mathbf{E}_x$ balances the magnetic force $q\mathbf{v}\times\mathbf{B}_0$,

$$q\mathbf{E}_x = q\mathbf{v}\times\mathbf{B}_0, \tag{1.90}$$

and the charge carriers q proceed along the wire undeflected.

The Hall coefficient R_{H} is defined as a ratio,

$$R_{\text{H}} = \frac{E_x}{J_y B_z}. \tag{1.91}$$

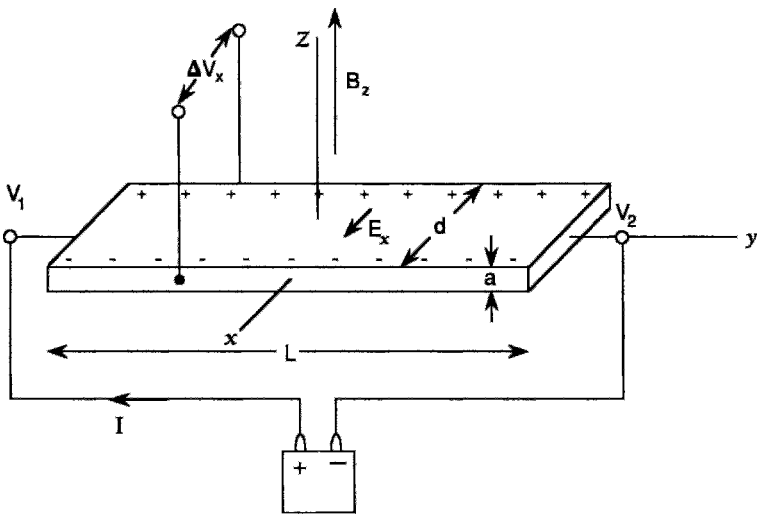

Figure 1.16 Experimental arrangement for Hall effect measurements showing an electrical current I passing through a flat plate of width d and thickness a in a uniform transverse magnetic field B_z. The voltage drop $V_2 - V_1$ along the plate, the voltage difference ΔV_x across the plate, and the electric field E_x across the plate are indicated. The figure is drawn for negative charge carriers (electrons).

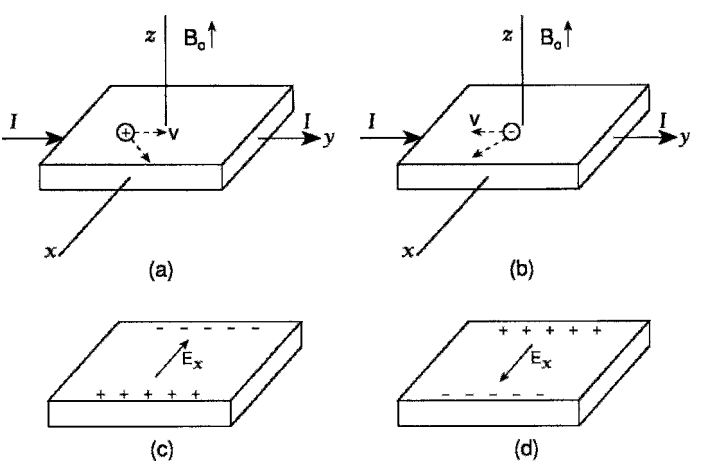

Figure 1.17 Charge carrier motion and transverse electric field direction for the Hall effect experimental arrangement of Fig. 1.16. Positive charge carriers deflect as indicated in (a) and produce the transverse electric field E_x shown in (c). The corresponding deflection and resulting electric field for negative charge carriers are sketched in (b) and (d), respectively.

Substituting the expressions for $\mathbf{J}$ and $\mathbf{E}_x$ from Eqs. (1.18) and (1.90) in Eq. (1.91) we obtain for holes ($q = e$) and electrons ($q = -e$), respectively,

$$R_{\mathrm{H}} = \frac{1}{ne} \quad \text{(holes)} \tag{1.92a}$$

$$R_{\mathrm{H}} = -\frac{1}{ne} \quad \text{(electrons)}, \tag{1.92b}$$

where the sign of R_{H} is determined by the sign of the charges. The Hall angle Θ_{H} is defined by

$$\tan \Theta_{\mathrm{H}} = \frac{E_x}{E_y}. \tag{1.93}$$

Sometimes the dimensionless Hall number is reported,

$$\text{Hall \#} = \frac{V_0}{R_{\mathrm{H}} e}, \tag{1.94}$$

where V_0 is the volume per chemical formula unit. Thus the Hall effect distinguishes electrons from holes, and when all of the charge carriers are the same this experiment provides the charge density n. When both positive and negative charge carriers are present, partial (or total) cancellation of their Hall effects occurs.

The mobility μ is the charge carrier drift velocity per unit electric field,

$$\mu = \frac{|v_{\mathrm{av}}|}{E}, \tag{1.95}$$

and with the aid of Eqs. (1.18), (1.21), and (1.92) we can write

$$\mu_{\mathrm{H}} = \frac{R_{\mathrm{H}}}{\rho}, \tag{1.96}$$

where the Hall mobility μ_{H} is the mobility determined by a Hall effect measurement. It is a valid measure of the mobility (1.95) if only one type of charge carrier is present.

By Ohm's law (1.21) the resistivity is the ratio of the applied electric field in the direction of current flow to the current density,

$$\rho = \frac{E_y}{J}, \tag{1.97}$$

In the presence of a magnetic field, this expression is written

$$\rho_{\mathrm{m}} = \frac{E_y}{J}, \tag{1.98}$$

where ρ_{m} is called the *transverse magnetoresistivity*. There is also a longitudinal magnetoresistivity defined when E and B_0 are parallel. For the present case the resistivity does not depend on the applied field, so $\rho_{\mathrm{m}} = \rho$. For very high magnetic fields ρ_{m} and ρ can be different. In the superconducting state ρ_{m} arises from the movement of quantized magnetic flux lines, called vortices, so that it can be called the flux flow resistivity ρ_{ff}. Finally, the Hall effect resistivity ρ_{xy} (Ong, 1991) is defined by

$$\rho_{xy} = \frac{E_x}{J}. \tag{1.99}$$

FURTHER READING

Most of the material in this chapter may be found in standard textbooks on solid state physics (e.g., Ashcroft and Mermin, 1976; Burns, 1985; Kittel, 1996).

PROBLEMS

1. Show that Eq. (1.61) for the phonon specific heat has the low- and high-temperature limits (1.62a) and (1.62b), respectively.
2. Aluminum has a magnetic susceptibility $+16.5 \times 10^{-6}$ cgs, and niobium, 195×10^{-6} cgs. Express these in dimensionless SI units. From these values estimate the density of states and the electronic specific heat constant γ for each element.

3. Copper at room temperature has 8.47×10^{22} conduction electrons/cm^3, a Fermi energy of 7.0 eV, and $\tau = 2.7 \times 10^{-14}$ s. Calculate its Hall coefficient, average conduction electron velocity in an electric field of 200 V/cm, electrical resistivity, and mean free path.
4. Calculate the London penetration depth, resistivity, plasma frequency, and density of states of copper at room temperature.
5. It was mentioned in Section 1. II that the chemical potential μ is the energy required to remove one electron from a Fermi gas under the conditions of constant volume and constant entropy. Use a thermodynamic argument to prove this assertion, and also show that μ equals the change in the Gibbs free energy when one electron is removed from the Fermi gas under the conditions of constant temperature and constant pressure.
6. Show that well above the Debye temperature the number of phonons in a normal mode of vibration is proportional to the temperature.
7. For the two-dimensional square lattice draw the third Brillouin zone in (a) the extended zone scheme and (b) the reduced zone scheme in which the third zone is mapped into the first zone. Show where each segment in the extended scheme goes in the first zone. Draw constant energy lines for $\epsilon = 2\epsilon_0$, $3\epsilon_0$, $4\epsilon_0$, $5\epsilon_0$. Sketch the Fermi surface for $\epsilon_F = 4.5\epsilon_0$. Indicate the electron-like and hole-like regions.

This page intentionally left blank

2

Phenomenon of Superconductivity

I. INTRODUCTION

A perfect superconductor is a material that exhibits two characteristic properties, namely zero electrical resistance and perfect diamagnetism, when it is cooled below a particular temperature T_c, called the *critical temperature*. At higher temperatures it is a normal metal, and ordinarily is not a very good conductor. For example, lead, tantalum, and tin become superconductors, while copper, silver, and gold, which are much better conductors, do not super-conduct. In the normal state some super-conducting metals are weakly diamagnetic and some are paramagnetic. Below T_c they exhibit perfect electrical conductivity and also perfect or quite pronounced diamagnetism.

Perfect diamagnetism, the second characteristic property, means that a superconducting material does not permit an externally applied magnetic field to penetrate into its interior. Those superconductors that totally exclude an applied magnetic flux are known as Type I superconductors, and they constitute the subject matter of this chapter. Other superconductors, called Type II superconductors, are also perfect conductors of electricity, but their magnetic properties are more complex. They totally exclude magnetic flux when the applied magnetic field is low, but only partially exclude it when the applied field is higher. In the region of higher magnetic fields their diamagnetism is not perfect, but rather of a mixed type. The basic properties of these mixed magnetism superconductors are described in Chapters 5 and 12.

II. BRIEF HISTORY

In 1908, H. Kamerlingh Onnes initiated the field of low-temperature physics by liquifying helium in his laboratory at Leiden. Three years later he found that below 4.15 K of the dc resistance of mercury dropped to zero (Onnes, 1911). With that finding the field of superconductivity was born. The next year Onnes discovered that the application of a sufficiently strong axial magnetic field restored the resistance to its normal value. One year later, in 1913, the element lead was found to be superconducting at 7.2 K (Onnes, 1913). Another 17 years were to pass before this record was surpassed, by the element niobium ($T_c = 9.2\,K$) (vide Ginzburg and Kitzhnits, 1977, p. 2).

A considerable amount of time went by before physicists became aware of the second distinguishing characteristic of a superconductor—namely, its perfect diamagnetism. In 1933, Meissner and Ochsenfeld found that when a sphere is cooled below its transition temperature in a magnetic field, it excludes the magnetic flux.

The report of the Meissner effect led the London brothers, Fritz and Heinz, to propose equations that explain this effect and predict how far a static external magnetic field can penetrate into a superconductor. The next theoretical advance came in 1950 with the theory of Ginzburg and Landau, which described superconductity in terms of an order parameter and provided a derivation for the London equations. Both of these theories are macroscopic in character and will be described in Chapter 6.

In the same year it was predicted theoretically by H. Fröhlich (1950) that the transition temperature would decrease as the average isotopic mass increased. This effect, called the *isotope effect*, was observed experimentally the same year (Maxwell, 1950; Reynolds *et al.*, 1950). The isotope effect provided support for the electron–phonon interaction mechanism of superconductivity.

Our present theoretical understanding of the nature of superconductivity is based on the BCS microscopic theory proposed by J. Bardeen, L. Cooper, and J. R. Schrieffer in 1957 (we will describe it in Chapter 7). In this theory it is assumed that bound electron pairs that carry the super current are formed and that an energy gap between the normal and superconductive states is created. The Ginzburg–Landau (1950) and London (1950) results fit well into the BCS formalism. Much of the present theoretical debate centers around how well the BCS theory explains the properties of the new high-temperature superconductors.

Alloys and compounds have been extensively studied, especially the so-called *A*15 compounds, such as Nb_3Sn, Nb_3Ga, and Nb_3Ge, which held the record for the highest transition temperatures from 1954 to 1986, as shown in Table 2.1.

Table 2.1 Superconducting Transition Temperature Records through the Years[a]

Material	T_c (K)	Year
Hg	4.1	1911
Pb	7.2	1913
Nb	9.2	1930
$NbN_{0.96}$	15.2	1950
Nb_3 Sn	18.1	1954
$Nb_3(Al_{\frac{3}{4}}Ge_{\frac{1}{4}})$	20–21	1966
Nb_3Ga	20.3	1971
Nb_3Ge	23.2	1973
$Ba_xLa_{5-x}Cu_5O_y$	30–35	1986
$(La_{0.9}Ba_{0.1})_2CuO_{4-\delta}$ at 1 GPa	52	1986
$YBa_2Cu_3O_{7-\delta}$	95	1987
$Bi_2Sr_2Ca_2Cu_3O_{10}$	110	1988
$Tl_2Ba_2Ca_2Cu_3O_{10}$	125	1988
$Tl_2Ba_2Ca_2Cu_3O_{10}$ at 7 GPa	131	1993
$HgBa_2Ca_2Cu_3O_{8+\delta}$	133	1993
$HgBa_2Ca_2Cu_3O_{8+\delta}$ at 25 GPa	155	1993
$Hg_{0.8}Pb_{0.2}Ba_2Ca_2Cu_3O_x$	133	1994
$HgBa_2Ca_2Cu_3O_{8+\delta}$ at 30 GPa	164	1994

[a] cf. Ginzburg and Kirzhnits, 1977.

Many other types of compounds have been studied in recent years, particularly the so-called heavy fermion systems in which the superconducting electrons have high effective masses of $100m_e$ or more. Organic superconductors have shown a dramatic rise in transition temperatures during the past decade.

On April 17, 1986, a brief article, entitled "Possible High T_c Superconductivity in the Ba–La–Cu–O System," written by J. G. Bednorz and K. A. Müller was received by the *Zeitschrift für Physik*, initiating the era of high-temperature superconductivity. When the article appeared in print later that year, it met with initial skepticism. Sharp drops in resistance attributed to "high-T_c" superconductivity had appeared from time to time over the years, but when examined they had always failed to show the required diamagnetic response or were otherwise unsubstantiated. It was only when a Japanese group (Uchida *et al.*, 1987) and Chu's group in the United States (Chu *et al.*, 1987b) reproduced the original results that the results found by Bednorz and Müller began to be taken seriously. Soon many other researchers became active, and the recorded transition temperature began a rapid rise.

By the beginning of 1987, scientists had fabricated the lanthanum compound, which went superconducting at close to 40 K at atmospheric pressure (Cava *et al.*, 1987; Tarascon *et al.*, 1987c) and at up to 52 K under high pressure (Chu *et al.*, 1987a). Soon thereafter, the yttrium–barium system, which went superconducting in the low 90s (Chu *et al.*, 1988a; Zhao *et al.*, 1987), was discovered. Early in 1988, superconductivity reached 110 K with the discovery of BiSrCaCuO (Chu *et al.*, 1988b; Maeda *et al.*, 1988; Michel *et al.*, 1987), and then the 120–125 K range with TlBaCaCuO (Hazen *et al.*, 1988; Sheng and Herman, 1988; Sheng *et al.*, 1988). More recently, Berkley *et al.* (1993) reported

$$T_c = 131.8\,\text{K for } Tl_2Ba_2Ca_2Cu_3O_{10-x}$$

at a pressure of 7 GPa. Several researchers have reported T_c above 130 K for the Hg series of compounds $HgBa_2Ca_nCu_{n+1}O_{2n+4}$ with $n = 1, 2$, sometimes with Pb doping for Hg (Chu *et al.*, 1993a; Iqbal *et al.*, 1994; Schilling *et al.*, 1993, 1994a). The transition temperature of the Hg compounds increases with pressure (Chu, 1994; Klehe *et al.*, 1992, 1994; Rabinowitz and McMullen, 1994) in the manner shown in Fig. 2.1a (Gao *et al.*, 1994) and onset T_c values in the 150 K range are found for pressures above 10 GPa (Chu *et al.*, 1993b, Ihara *et al.*, 1993). We see from Fig. 2.1b that the transitions are broad, with midpoint T_c located 7 or 8 K below the onset, and the zero resistivity point comes much lower still (Gao *et al.*, 1994).

This rapid pace of change and improvement in superconductors exceeds that of earlier decades, as the data listed in Table 2.1 and plotted in Fig. 2.2 demonstrate. For 56 years the element niobium and its compounds had dominated the field of superconductivity. In addition to providing the highest T_c values, niobium compounds such as NbTi and Nb_3Sn are also optimal magnet materials: for NbTi, $B_{c2} = 10$ T and for Nb_3Sn, $B_{c2} = 22$ T at 4.2 K, where B_{c2} is the upper-critical field of a Type II superconductor, in the sense that it sets a limit on the magnetic field attainable by a magnet; thus application of an applied magnetic field in excess of B_{c2} drives a superconductor normal. The period from 1930 to 1986 can be called the Niobium Era of superconductivity. The new period that began in 1986 might become the Copper Oxide Era because, thus far, the presence of copper and oxygen has, with rare exceptions, been found essential for T_c above 40 K. It is also interesting to observe that Hg was the first known superconductor, and now a century later mercury compounds have become the best!

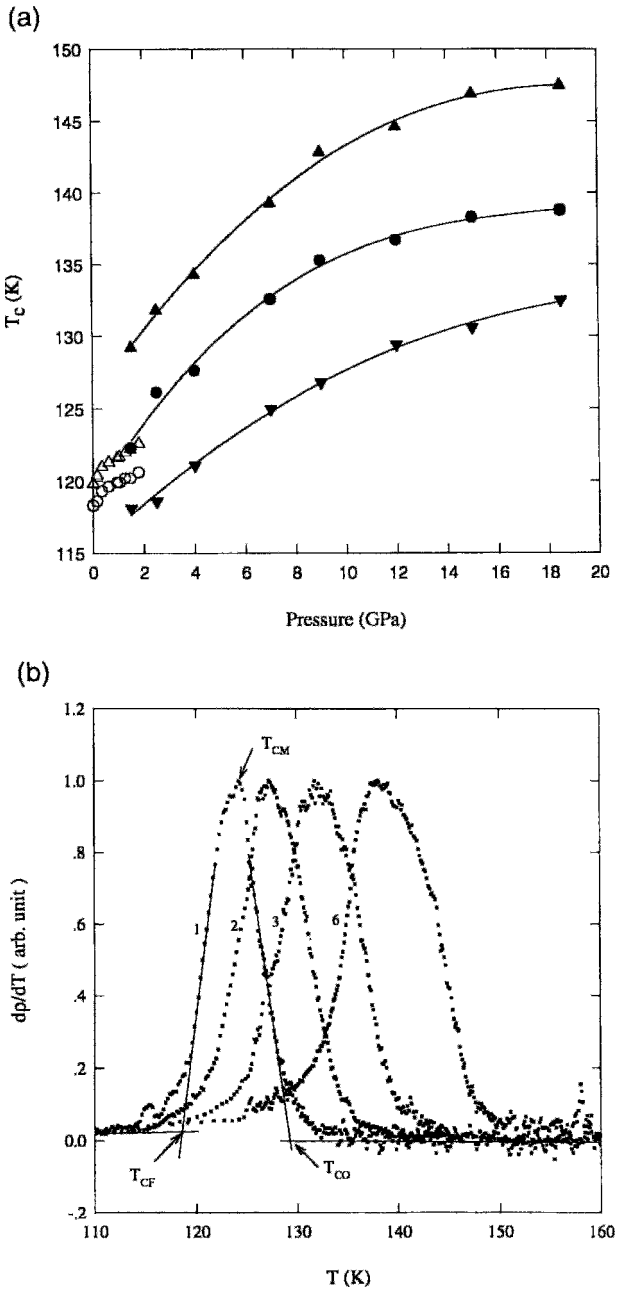

Figure 2.1 Effect of pressure on the transition temperature of the superconductor $HgBa_2Ca_2Cu_3O_{8+\delta}$ showing (a) pressure dependence of the onset (upper curve), midpoint (middle curve), and final off-set (lower curve) values of T_c, and (b) temperature dependence of the resistivity derivative dp/dT at 1.5 (1), 4 (2), 7 (3), and 18.5 GPa (6). Definitions of T_{co} onset, T_{cm} midpoint, and T_{cf} final offset that are plotted in (a) are given in (b) (Gao *et al.*, 1993).

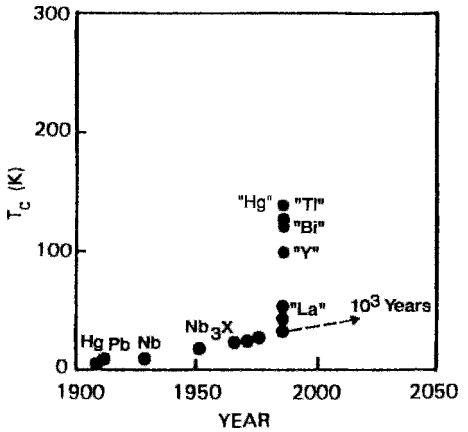

Figure 2.2 Increase in the superconducting transition temperature with time. A linear extrapolation of the data before 1986 predicts that room temperature would be reached in about 1000 years. From left to right $X =$ Sn, $Al_{0.75}Ge_{0.25}$, Ga, and Ge for the data points of the $A15$ compound Nb_3X (Adapted from Fig. I-1, Poole *et al.*, 1988).

III. RESISTIVITY

Before beginning the discussion of super currents, we will examine the resistivity of superconducting materials in their normal state above the transition temperature T_c; we will then make some comments on the drop to zero resistance at T_c; finally, we will describe the measurements that have set upper limits on resistivity below T_c.

A. Resistivity above T_c

In Chapter 1, Section VII, we explained, and now we illustrate in Figs. 2.3–2.6, how the resistivity of a typical conductor depends linearly on temperature at high temperatures and obeys the T^5 Bloch law at low temperatures. Classical or low-temperature superconductors are in the Bloch law region if the transition temperature is low enough, as illustrated in Fig. 2.3a. High-temperature superconductors have transition temperatures that are in the linear region, corresponding to the resistivity plot of Fig. 2.3b. However, the situation is actually more complicated because the resistivity of single crystals of high-temperature superconductors is strongly anisotropic, as we will show later. Several theoretical treatments of the resistivity of cuprates have appeared (e.g., Griessen, 1990; Micnas *et al.*, 1987; Song and Gaines, 1991; Wu *et al.*, 1989; Zeyhe, 1991).

Good conductors such as copper and silver have room temperature resistivities of about $1.5\,\mu\Omega\,\text{cm}$, whereas at liquid nitrogen temperatures the resistivity typically decreases by a factor in the range 3–8, as shown by the data in Table 1.1. The elemental superconductors, such as Nd, Pb, and Sn, have room temperature resistivities a factor of 10 greater than good conductors. The metallic elements Ba, Bi,

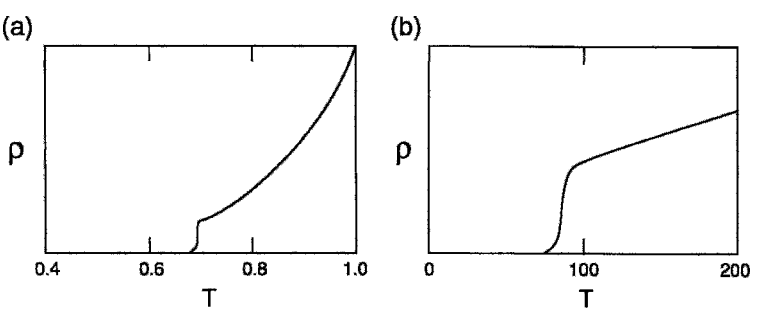

Figure 2.3 Abrupt drop of the resistivity to zero at the superconducting transition temperature T_c (a) for a low-temperature superconductor in the Bloch T^5 region and (b) for a high-temperature superconductor in the linear region.

La, Sr, Tl, and Y, which are also present in oxide superconductors, have room temperature resistivities 10 to 70 times that of Cu.

The copper-oxide superconductors have even higher room temperature resistivities, more than three orders of magnitude greater than that of metallic copper, which puts them within a factor of 3 or 4 of the semiconductor range, as shown by the data in Table 2.2. The resistivity of these materials above T_c decreases more or less linearly with decreasing temperature down to the neighborhood of T_c, with a drop by a factor of 2 or 3 from room temperature to this point, as shown in Fig. B. and by the data in Table 2.2. Figure 2.5 shows that the linearity extends far above room temperature, especially for the lanthanum compound (Gurvitch and Fiory, 1987a, b, c; Gurvitch *et al.*, 1988). It has been linked to the two-dimensional character of electron transport (Micnas *et al.*, 1990).

We see from the figure that

$$YBa_2Cu_3O_{7-\delta}$$

begins to deviate from linearity at about 600–700 K, near the orthorhombic-to-tetragonal phase transformation (cf. Chapter 8, Section IV.D) where it changes from a metallic material below the transition to a semiconductor above. Heating causes a loss of oxygen, as shown in Fig. 2.6 which presents the dependence of resistivity on the oxygen partial pressure (Grader *et al.*, 1987). The temperature dependence of resistivity has been related to the loss of oxygen [cf. Eq. (X-1) from Poole *et al.*, 1988; cf. Chaki and Rubinstein, 1987; Fiory *et al.*, 1987].

The resistivity of poor metals at high temperatures tends to saturate to a temperature-independent value when the mean free path l approaches the wavelength $\lambda_F = 2\pi/k_F$ associated with the Fermi level, where k_F is the Fermi wave vector. The Ioffe–Regel criterion for the onset of this saturation is $k_F l \approx 1$. The quantity $k_F l$ for $YBa_2Cu_3O_{7-\delta}$ has been estimated to have a value of 30 for $T = 100\,K$ (Hagen *et al.*, 1988) and 3 for $T = 1000\,K$ (Crow and Ong, 1990). These considerations, together with the curves in Fig. 2.5, indicate that, in practice, the Ioffe–Regel criterion does not cause the resistivity to saturate in high-temperature superconductors. The *A*15 compound V_3Si, whose crystal structure is stable up to 1950°C, does exhibit saturation in its resistivity-versus-temperature plot.

B. Resistivity Anisotropy

The resistivity of $YBa_2Cu_3O_{7-\delta}$ is around two orders of magnitude greater along the *c*-axis than parallel to the *a*, *b*-plane; thus $\rho_c/\rho_{ab} \approx 100$ and for

$$Bi_{2+x}Sr_{2-y}CuO_{6+\delta},$$

$\rho_c/\rho_{ab} \approx 10^5$ (Fiory *et al.*, 1989). The temperature dependence of these resistivities, measured by the method described in the following section, exhibits a peak near T_c in the case of ρ_c, and this is shown in Fig. 2.7. When the data are fitted to the expressions (Anderson and Zou, 1988)

$$\rho_{ab} = \frac{A_{ab}}{T} + B_{ab}T, \tag{2.1}$$

$$\rho_c = \frac{A_c}{T} + B_c T, \tag{2.2}$$

by plotting $\rho_{ab}T$ and $\rho_c T$ from the data of Fig. 2.7 versus T^2, a good fit is obtained, as shown in Fig. 2.8. The angular dependence of the resistivity is found to obey the expression (Wu *et al.*, 1991b)

$$\rho(\Theta) = \rho_{ab}\sin^2\Theta + \rho_c\cos^2\Theta \tag{2.3}$$

where Θ is the angle of the current direction relative to the *c* axis.

Typical measured resistivities of polycrystalline samples are much closer to the in-plane values. The anisotropy ratio $\rho_c/\rho_{ab} \approx 100$ is so large that the current encounters less resistance when it follows a longer path

Table 2.2 Resistivity Data on Superconducting Single Crystals Slightly above T_c and near Room Temperature. The Slopes $\Delta\rho/\Delta T$ Are Averages for the Typical Range from 150 K to 290 K. (Earlier data on mostly polycrystalline samples are given in Table X-1 of Poole *et al.* (1988)[a])

Material	T K	ρ_{ab} $\mu\Omega$ cm	ρ_c mΩ cm	ρ_c/ρ_{ab}	$\Delta\rho_{ab}/\Delta T$ $\mu\Omega$ cm/K	$\Delta\rho_c/\Delta T$ mΩ cm/K	Reference
Re	50	0.8	0.0005	0.6	0.075	0.055	Volkenshteyn *et al.* (1978)
Re	275	17.5	0.013	0.7			Volkenshteyn *et al.* (1978)
TaS_2				450			Wattamaniuk *et al.* (1975)
2H–$TaSe_2$	4			1200			Martin *et al.* (1990)
							Pfalzgraf and Spreckels (1987)
K_3C_{60} thin film[e]	290	[2.5 mΩ cm]					Palstra *et al.* (1992)
			19				
$(La_{0.925}Sr_{0.075})_2CuO_4$	50	2500			13		Preyer *et al.* (1991)
$(La_{0.925}Sr_{0.075})_2CuO_4$	290	5000					Preyer *et al.* (1991)
$(Nd_{0.925}Ce_{0.075})_2CuO_4$	30	1700	500	300	19	3.7	Crusellas *et al.* (1991)
$(Nd_{0.925}Ce_{0.075})_2CuO_4$	273	4800	1300	270	2.0		Crusellas *et al.* (1991)
$YBa_2Cu_3O_{7-\delta}$	290	$\sim$ 380	$\sim$ 15	$\sim$ 45			averages
$YBa_2Cu_3O_{7-\delta}$	100	$\sim$ 180	$\sim$ 15	$\sim$ 90	$\sim$ 08	$\sim$ 02	averages
$Bi_2Sr_2CuO_{6\pm\delta}$	25	90	14,000	1.6×10^5	0.9	-6	Martin *et al.* (1990)
$Bi_2Sr_2CuO_{6\pm\delta}$	290	275	6000	2.2×10^4			Martin *et al.* (1990)
$Bi_2Sr_{2.2}CaCu_2O_8$	100	55[b]	5200	9.5×10^4	0.46	15	Martin *et al.* (1998)
$Bi_2Sr_{2.2}CaCu_2O_8$	300	150[c]	8880	5.9×10^4			Martin *et al.* (1998)
$Tl_2Ba_2CuO_6$	110	900					Mukaida *et al.* (1990)
$Tl_2Ba_2CaCu_2O_8$	110	3500					Mukaida *et al.* (1990)

[a] Typical semiconductors range from 10^4 to 10^{15} $\mu\Omega$ cm and insulators from 10^{20} to 10^{28} $\mu\Omega$ cm.
[b] Averages of $\rho_a = 60$, $\rho_b = 50$ $\mu\Omega$ cm at 100 K, and $\rho_a = 180$, $\rho_b = 120$ $\mu\Omega$ cm at 300 K.

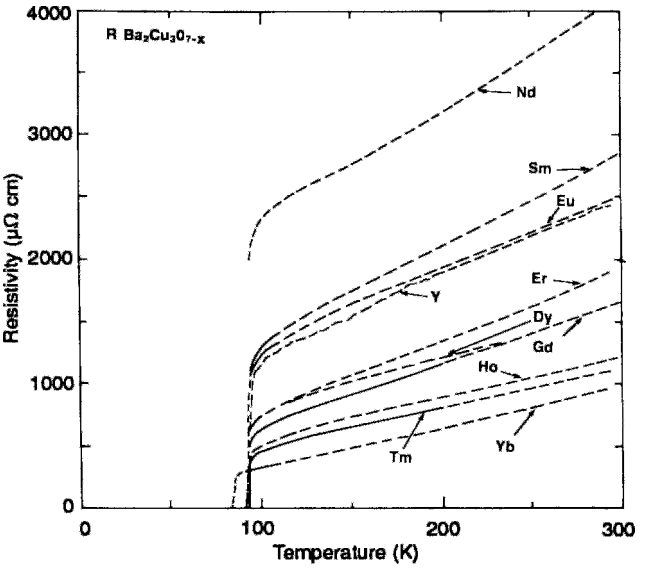

Figure 2.4 Temperature dependence of resistivity for various rare earth substituted $RBa_2Cu_3O_7$ compounds. For these compounds T_c is in the linear region (Tarascon *et al.*, 1987b).

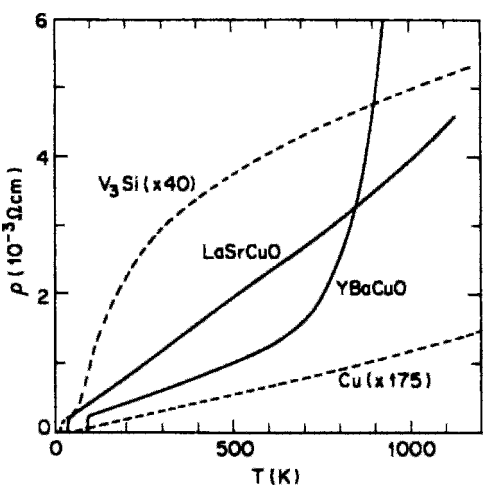

Figure 2.5 Comparison of the resistivities of $(La_{0.9125}Sr_{0.0825})_2CuO_4$ and $YBa_2Cu_3O_{7-\delta}$ with those of the $A15$ compound $V_3Si(T_c = 17.1\,K)$, and with nonsuperconducting copper (Gurvitch and Fiory, 1987a, b, c).

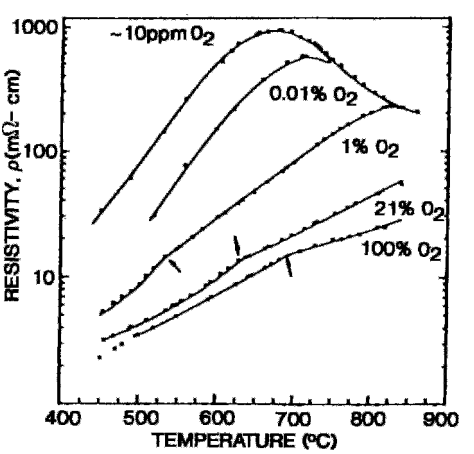

Figure 2.6 Temperature dependence of the resistivity of $YBa_2Cu_3O_{7-\delta}$ for various oxygen partial pressures (Grader *et al.*, 1987).

in the planes than when it takes the shorter path perpendicular to the planes, so it tends to flow mainly along the crystallite planes. Each individual current zigzags from one crystallite to the next, so that its total path is longer than it would be if all of the crystallites were aligned with their planes parallel to the direction of the current. The increase in the resistivity of a polycrystalline sample beyond ρ_{ab} can be a measure of how much the average path length increases.

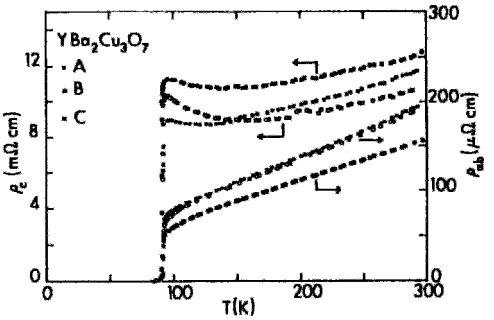

Figure 2.7 Resistivity for current flow parallel (ρ_{ab}) and perpendicular (ρ_c) to the CuO planes of $YBa_2Cu_3O_7$. Data are given for three samples *A*, *B*, and *C*. Note from the change in scale that $\rho_{ab} \ll \rho_c$ (Hagen *et al.*, 1988).

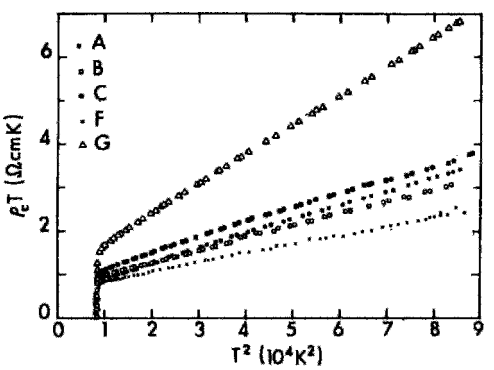

Figure 2.8 Plot of $\rho_c T$ versus T^2 to test the validity of Eq. (2.2) for five single crystals of $YBa_2Cu_3O_{7-\delta}$ (Hagen *et al.*, 1988).

Polycrystalline samples should be compacted or pressed into pellets before resistivity measurements are made, in order to reduce the number of voids in the sample and minimize intergrain contact problems. Such compacted samples require appropriate heat treatments to maintain the proper oxygen content. Uniaxial compression tends to align the grains with their *c*-axes parallel so that the resulting compressed pellets have different resistivities when measured parallel to the compression direction compared to when they are measured perpendicular to this direction.

Hysteresis effects have been seen in the resistance-versus-temperature curves, as illustrated in Fig. X-1 of the monograph by Poole *et al.* (1988), for

$$(Y_{0.875}Ba_{0.125})_2CuO_{4-\delta}$$

(Tarascon *et al.*, 1987a). These hysteresis effects occur in the presence of both magnetic fields and transport currents, with the latter illustrated in Figure X-1.

C. Anisotropy Determination

The most common way of measuring the resistivity of a sample is the four-probe method sketched in Fig. 2.9. Two leads or probes carry a known current into and out of the ends of the sample, and two other leads separated by a distance L measure the voltage drop at points nearer the center where the current approximates uniform, steady-state flow. The resistance R between measurement points 3 and 4 is given by the ratio V/I of the measured voltage to the input current,

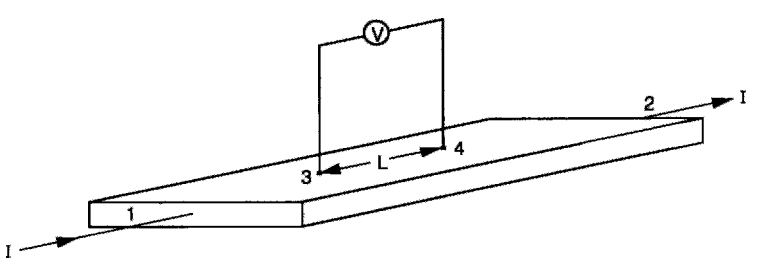

Figure 2.9 Experimental arrangement for the four-probe resistivity determination.

and the resistivity ρ is calculated from the expression

$$R = \frac{\rho L}{A}, \tag{2.4}$$

where A is the cross-sectional area. This four-probe technique is superior to a two-probe method in which uniform, steady-state current flow is not assured, and errors from lead and contact resistance are greater.

The four-probe method is satisfactory for use with an anisotropic sample if the sample is cut with one of its principal directions along the direction of current flow and if the condition $L \gg \sqrt{A}$ is satisfied. For a high-temperature superconductor, this requires two samples for the resistivity determination, one with the c-axis along the current flow direction and one with the c-axis perpendicular to this direction.

Transverse and longitudinal resistance determinations, R_t and R_l respectively, can both be made on a sample cut in the shape of a rectangular solid with $a = b$, with the shorter c-axis along the current direction, as shown in Fig. 2.10 (Hagen *et al.*, 1988). These resistances R_t and R_l are used to calculate the resistivity ρ_{ab} in the a, b-plane and the resistivity and ρ_c perpendicular to this plane, i.e., along c. The expressions

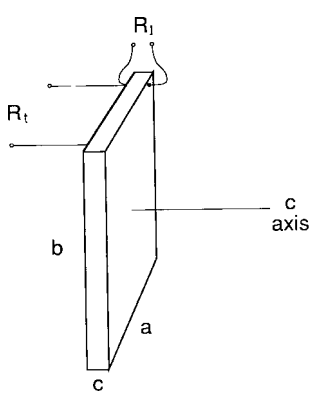

Figure 2.10 Experimental arrangement for measuring anisotropic resistivities (see explanation in text) (Hagen *et al.*, 1988).

that relate the resistances depend on the parameter x,

$$x = \frac{c}{a}\left(\frac{\rho_c}{\rho_{ab}}\right)^{1/2}, \tag{2.5}$$

where $\rho_c/\rho_{ab} \approx 100$ for $YBa_2Cu_3O_{7-\delta}$. For the limiting case $x \ll 1$, the measured resistances are given by (Montgomery, 1971):

$$R_t = \frac{a}{bc}\rho_{ab}\left[1 - \frac{4 \ln 2}{\pi}\right] \quad x \ll 1, \tag{2.6}$$

$$R_l = \frac{c}{ab}\rho_c\left[\frac{16 \exp(-\pi/x)}{\pi x}\right] \quad x \ll 1. \tag{2.7}$$

and for the opposite limit $x \gg 1$ we have

$$R_t = \frac{a}{bc}\rho_{ab}\left[\frac{16x \exp(-\pi x)}{\pi}\right] \quad x \gg 1, \tag{2.8}$$

$$R_l = \frac{c}{ab}\rho_c\left[1 - \frac{4 \ln 2}{\pi x}\right] \quad x \gg 1. \tag{2.9}$$

Both the resistance with the exponential factor and the correction term containing the factor $4 \ln 2/\pi$ are small.

Contributions to the electrical conductivity in the normal state near T_c arising from fluctuations of regions of the sample into the superconducting state, sometimes called paraconductivity, have been observed and discussed theoretically (X. F. Chem *et al.*, 1993; Friedman *et al.*, 1989; Lawrence and Doniach, 1971; Shier and Ginsberg, 1966). Several more theoretical articles treating resistivity have appeared (e.g., Gijs *et al.*, 1990a; Hopfengärtner *et al.*, 1991; Kumar and Jayannavar, 1992; Sanborn *et al.*, 1989; Yel *et al.*, 1991).

D. Sheet Resistance of Films: Resistance Quantum

When a current flows along a film of thickness d through a region of surface with dimensions $a \times a$, as shown in Fig. 2.11,

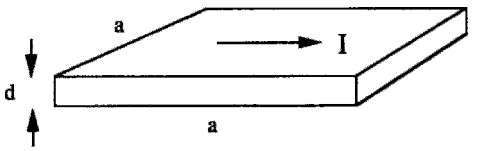

Figure 2.11 Geometrical arrangement and current flow direction for sheet resistance determination.

it encounters the resistance R_s which, from Eq. (2.4), is given by

$$R_s = \frac{\rho a}{ad} = \frac{\rho}{d}. \tag{2.10}$$

The resistance ρ/d is called the *sheet resistance*, or the *resistance per square*, because it applies to a square section of film, as shown in Fig. 2.11, and is independent of the length of the side a. It is analogous to the surface resistance $R_s = \rho/\delta$ of a metallic surface interacting with an incident high-frequency electromagnetic wave, where δ is the skin depth of the material at the frequency of the wave.

There is a quantum of resistance $h/4e^2$ with the value

$$\frac{h}{4e^2} = 6.45\,\text{k}\Omega, \tag{2.11}$$

where the charge is $2e$ per pair. When the films are thin enough so that their sheet resistance in the normal state just above T_c exceeds this value, they no longer become superconducting (Hebard and Paalanen, 1990; Jaeger *et al.*, 1989; Lee and Ketterson, 1990; Li *et al.*, 1990; Pyun and Lemberger, 1991; Seidler *et al.*, 1992; Tanda *et al.*, 1991; Valles *et al.*, 1989; T. Wang *et al.*, 1991). It has been found experimentally (Haviland *et al.*, 1989) that bismuth and lead films deposited on germanium substrates become superconducting only when they have thicknesses greater than 0.673 nm and 0.328 nm, respectively. The variation in T_c with the sheet resistance for these two thin films is shown in Fig. 2.12. Figure 2.13 shows the sharp drop in resistivity at T_c for bismuth films with a range

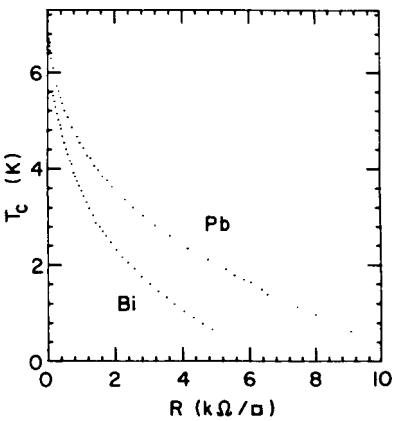

Figure 2.12 Dependence of the transition temperature T_c of Bi and Pb films on the sheet resistance (Haviland *et al.*, 1989).

of thickness greater than 0.673 nm. Thinner films exhibit resistivity increases down to the lowest measured temperatures, as shown in the figure. The ordinary transition temperatures, which occur for the limit $\rho/d \ll h/4e^2$, are 6.1 K for Bi films and 7.2 K for Pb.

Copper-oxide planes in high-temperature superconductors can be considered thin conducting layers, with thickness c for $YBa_2Cu_3O_{7-\delta}$ corresponding to a sheet resistance $\rho_{ab}/\frac{1}{2}c$. Using this layer approximation, the Ioffe–Regel parameter $k_F l$ mentioned in Section A can be estimated from the expression

$$k_F l = \frac{\text{conductance per square}}{\text{conductance quantum}} \tag{2.12}$$

$$= \frac{h/4e^2}{2\rho_{ab}/\frac{1}{2}c}, \tag{2.13}$$

where the conductances are the reciprocals of the resistances. Note that the two reported $k_F l$ values for $YBa_2Cu_3O_{7-\delta}$ calculated by this method and referred to earlier assumed $k_F = 4.6 \times 10^7\,\text{cm}^{-1}$.

It is of interest that metallic contacts of atomic size exhibit conduction jumps at integral multiples of $2e^2/h$ (Agraït

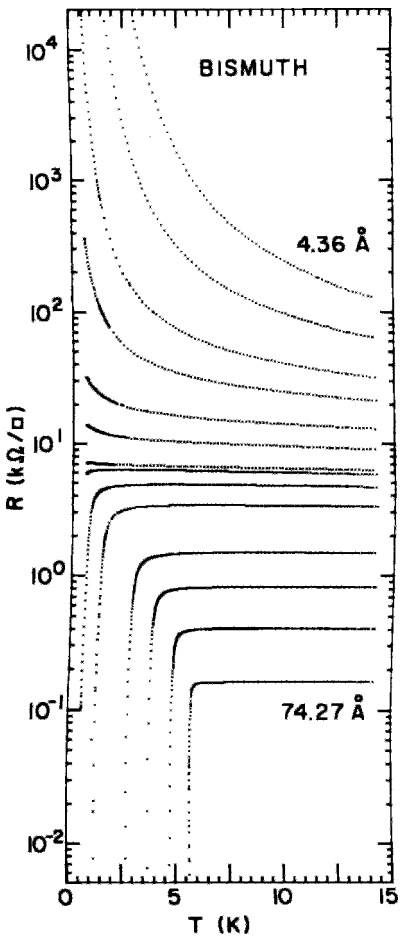

Figure 2.13 Temperature dependence of the sheet resistance of films of Bi deposited on Ge as a function of film thickness in the range from 4.36 Å to 74.27 Å (Haviland *et al.*, 1989).

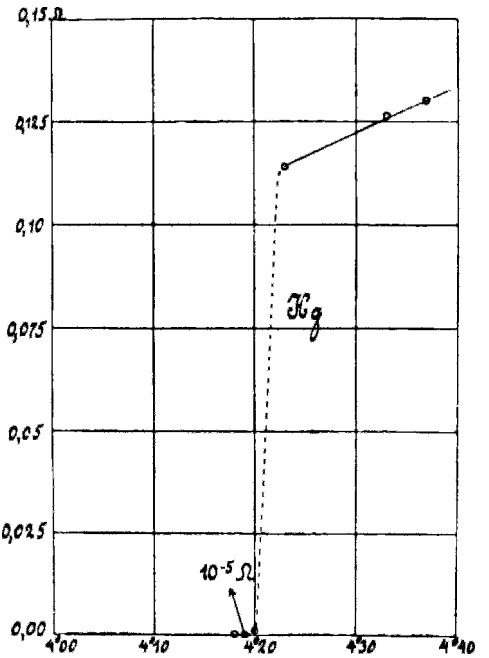

Figure 2.14 Resistivity-versus-temperature plot obtained by Kamerlingh Onnes when he discovered superconductivity in Leiden in 1911.

et al., 1993), and that the Hall effect resistance in one-dimensional objects, so-called *quantum wires*, is quantized to $h/2Ne^2$, where $N = 1, 2, 3, \ldots$ (Akera and Andu, 1989).

IV. ZERO RESISTANCE

In 1911, when Onnes was measuring the electrical resistance of mercury, he expected to find a temperature dependence of the type given by Eq. (1.30). Instead, to his surprise, he found that below 4.2 K the electrical resistance dropped to zero, as shown in Fig. 2.14. He had discovered superconductivity! At this temperature mercury transforms from the normal metallic state to that of a superconductor. Figure 2.3a shows the abrupt change to zero resistance for the case of an old superconductor, where T_c is in the low-temperature Bloch T^5 region, while Fig. 2.3b shows what happens in the case of a high-temperature superconductor where T_c is in the linear region.

A. Resistivity Drop at T_c

Figures 2.3a, 2.3b, 2.7, and 2.8 show the sharp drop in resistance that occurs at T_c. We will see later in the chapter that there is an analogous drop in susceptibility at T_c.

A susceptibility measurement is a more typical thermodynamic indicator of the superconducting state because magnetization is a thermodynamic state variable. Resistivity, on the other hand, is easier to measure, and can be a better guide for applications. Generally, the T_c value determined from the resisitivity drop to zero occurs at a somewhat higher temperature than its susceptibility counterpart. This is because any tiny part of the material going superconductive loses its resistance, and $R = 0$ when one or more continuous superconducting paths are in place between the measuring electrodes. In contrast, diamagnetism measurements depend on macroscopic current loops to shield the **B** field from an appreciable fraction of the sample material, and this happens when full superconducting current paths become available. Therefore, filamentary paths can produce sharp drops in resistivity at temperatures higher than the temperatures at which there are pronounced drops in diamagnetism, which also require extensive regions of superconductivity. Such filamentary behavior can be described in terms of percolation thresholds (Gingold and Lobb 1990; Lin, 1991; Phillips, 1989b; Tolédano *et al.*, 1990; Zeng *et al.*, 1991).

B. Persistent Currents below T_c

To establish a transport current in a loop of superconducting wire, the ends of the wire may be connected to a battery in series with a resistor, thus limiting the current, as shown in Fig. 2.15. When switch S_2 is closed, current commences to flow in the loop. When switch S_1 is closed in order to bypass the battery and S_2 opened in order to disconnect the battery, the loop resistance drops to zero and the current flow enters the persistent mode. The zero resistance property implies that the current will continue flowing indefinitely.

Many investigators have established currents in loops of superconducting wire and have monitored the strength of the associated magnetic field through the loop over prolonged periods of time using, for example, a magnetometer with a pickup coil, as shown in Fig. 2.15. In experiments it was found that there is no detectable decay of the current for periods of time on the order of several years. The experiments established lower limits on the life-time of the current and upper limits on the possible resistivity of superconducting materials. Currents in copper oxide superconductors persist for many months or in excess of a year, and resistivity limits have been reported as low as 10^{-18} (Yeh *et al.*,

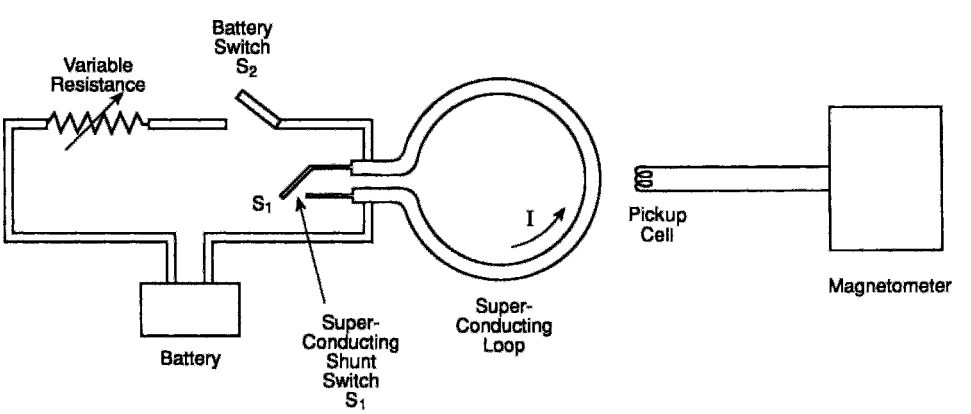

Figure 2.15 Experimental arrangement for establishing and measuring a persistent current. Switch S_2 is closed to send current through the loop and S_1 is closed to confine the current flow to the loop. The magnetometer measures the magnetic field through the loop and thereby determines the current.

1987) and $10^{-22}\,\Omega\,\mathrm{cm}$ (Kedve *et al.*, 1987). Super current lifetimes of low-temperature superconductors are also greater than a year for $\rho < 10^{-23}\,\Omega\,\mathrm{cm}$ (Chandrasekhar, 1969). Persistent current flow has also been treated theoretically (e.g., Ambegaokar and Eckern, 1991; Cheun *et al.*, 1988; Kopietz, 1993; Riedel *et al.*, 1989; von Oppen and Riedel, 1991).

It will be instructive to estimate the minimum resistivity of a simple loop of superconducting wire of loop radius r and wire radius a. The inductance L of the loop is given by

$$L \approx \mu_0 r[\ln(8r/a) - 2]. \tag{2.14}$$

The loop has 'length' $2\pi r$ and cross-sectional area πa^2, so that its resistance R is

$$R = \frac{2r\rho}{a^2}. \tag{2.15}$$

This gives it a time constant $\tau = L/R$. Combining Eqs. (2.14) and (2.15) gives the product

$$\rho\tau \approx \tfrac{1}{2}\mu_0 a^2[0.0794 + \ln(r/a)]. \tag{2.16}$$

Using $\mu_0 = 4\pi \times 10^{-7}\,\mathrm{H/m}$ and typical loop dimensions of $a = 1.5\,\mathrm{mm}$ and $r = 15\,\mathrm{cm}$ gives

$$\rho\tau \approx 6.6 \times 10^{-10}\,\Omega\,\mathrm{cm\,s} \tag{2.17}$$

for the product $\rho\tau$.

A super current I_s can be made to flow in the loop by subjecting it to a changing magnetic field below T_c, in accordance with Faraday's and Lenz' laws. The magnitude of the current that is flowing can be determined by measuring the induced magnetic field. At a point P along the axis a distance z above the loop, as shown in Fig. 2.16, this magnetic field has the following value, as given in standard general physics texts:

$$B(z) = \frac{\mu_0 I_s r^2}{2(r^2 + z^2)^{3/2}}, \tag{2.18}$$

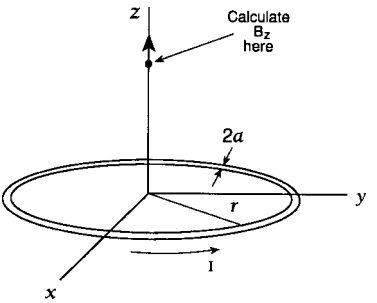

Figure 2.16 Magnetic field B_z along the axis of a circular loop of wire of radius r carrying the current I. The wire itself has radius a.

and once $B(z)$ is measured, I_s can be calculated.

If the super current persists unchanged for over a year ($\tau > 3.16 \times 10^7\,\mathrm{s}$) without any appreciable decrease (we are assuming that a 1% decrease is easily detectable), Eq. (2.17) can be used to place an upper limit on the resistivity:

$$\rho < 2.1 \times 10^{-17}\,\Omega\,\mathrm{cm}, \tag{2.19}$$

which is in the range mentioned earlier, and is 11 orders of magnitude less than the resistivity of copper ($\rho = 1.56\,\mu\,\Omega\,\mathrm{cm}$). A similar loop of copper wire at room temperature has $\tau \approx 0.42\,\mathrm{ms}$, so that the current will be gone after several milli-seconds.

We will see in Section XIV that the drop to zero resistance can be explained in terms of a two–fluid model in which some of the normal electrons turn into super electrons which move through the material without resistance. The current carried by the flow of super electrons is then assumed to short circuit the current arising from the flow of normal electrons, causing the measured resistance to vanish.

V. TRANSITION TEMPERATURE

Before proceeding to the discussion of magnetic and transport properties of superconductors, it will be helpful to say a few

words about the transition temperature. We will discuss it from the viewpoint of the resistivity change even though the onset of the energy gap and pronounced diamagnetism are more fundamental indices of T_c. Pechan and Horvath (1990) described a fast and inexpensive method for accurate determination of transition temperatures above 77 K.

Although the theoretical transition from the normal to the superconducting state is very sharp, experimentally it sometimes occurs gradually and sometimes abruptly. Figure 2.17 shows the gradual decrease in resistivity near T_c that was reported by Bednorz and Müller (1986) in the first published article on the new superconductors. We see from this figure that the range of temperatures over which the resistivity changes from its normal-state value to zero is comparable with the transition temperature itself. An example of a narrow transition centered at 90 K with width of ≈ 0.3 K is shown in Fig. 2.18. These two cases correspond to $\Delta T/T_c \approx 1/2$ and $\Delta T/T_c \approx 0.003$, respectively.

The sharpness of the drop to zero resistance is a measure of the goodness or purity of the sample. Figure 2.19 shows how the drop to zero in pure tin becomes broader and shifts to a higher temperature in an impure specimen. In a sense impure tin is a better superconductor because it has a higher T_c but worse because it has a broader transition. When high-temperature superconductors are

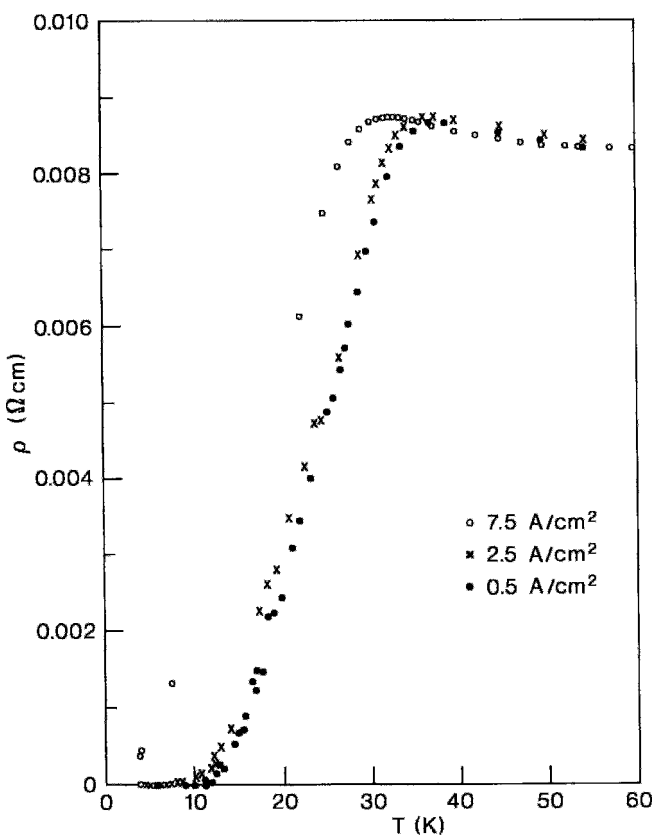

Figure 2.17 First reported drop to zero resistance for a high-temperature superconductor (Bednorz and Müller, 1986).

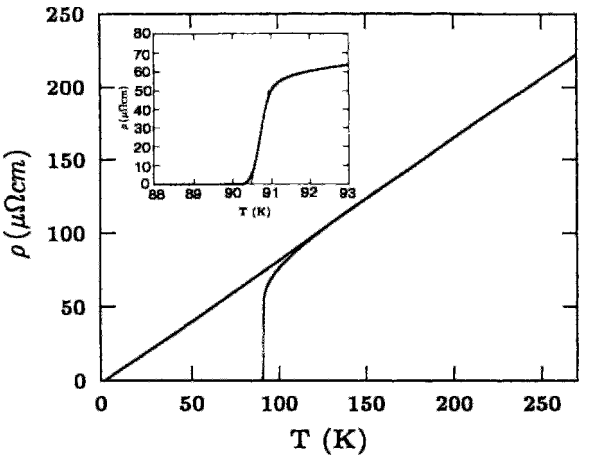

Figure 2.18 Sharp drop to zero resistance of a $YBa_2Cu_3O_7$ epitaxial film (Hopfengärtner *et al.*, 1991).

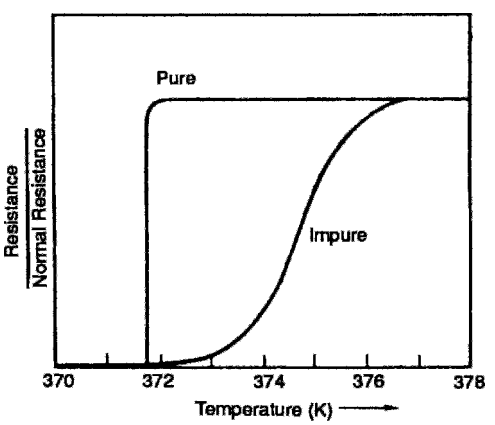

Figure 2.19 Narrow and broad superconducting resistivity drop in pure and impure tin, respectively. Reprinted from Rose Innes and Rhoderick (1978), p. 7, with kind permission of Pergamon Press, Headington Hill Hall, Oxford OX3 0BW, UK.

doped with paramagnetic ions at copper sites, the transition temperature both shifts to lower values and broadens, whereas doping at the yttrium sites of YBaCuO has very little effect on T_c, as may be seen by comparing the data plotted in Figs. 2.20 and 2.4, respectively. This can be explained in terms of delocalization of the super electrons on the copper oxide planes.

There are various ways of defining the position and sharpness, or width, of the superconducting transition temperature, and the literature is far from consistent on this point. Authors talk in terms of the onset, 5%, 10%, midpoint, 90%, 95%, and zero resistance points, and Fig. 2.21 shows some of these on an experimental resistivity curve. The onset, or 0% point, is where the experimental curve begins to drop below the extrapolated high-temperature linear behavior of Eq. (1.30), indicated by the dashed line in the figure. The T_c values that we cite or list in the tables are ordinarily midpoint values at which $\rho(T)$ has decreased by 50% below the onset. Many of the published reports of unusually high transition temperatures actually cited onset values, which can make them suspect. The current density can influence the resistive transition (Goldschmidt, 1989).

The point at which the first derivative of the resistivity curve, shown in Fig. 2.22b, reaches its maximum value could be selected as defining T_c, since it is the inflection point on the original curve (Azoulay, 1991; Datta *et al.*, 1988; Nkum and Datars, 1992; Poole and Farach, 1988). The width ΔT between the half-amplitude points of the first derivative curve, or the peak-to-peak width ΔT_{pp}

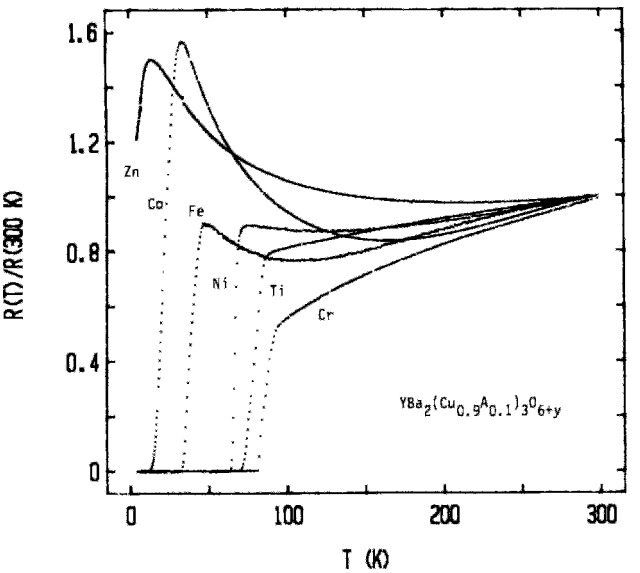

Figure 2.20 Influence of doping $YBa_2(Cu_{0.9}M_{0.1})_3O_{6+y}$ with the first transition series ions M = Ti, Cr, Fe, Co, Ni, and Zn on the resistivity transition near T_c (Xiao *et al.*, 1987a).

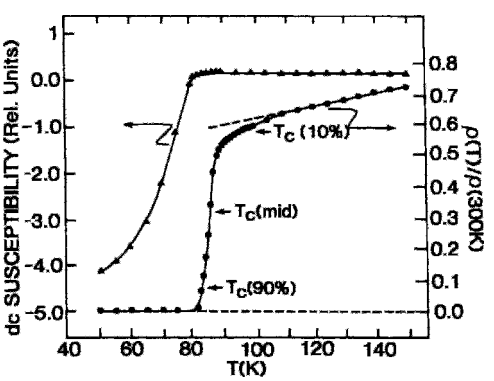

Figure 2.21 Temperature dependence of the resistivity and zero-field-cooled magnetization of $HoBa_2Cu_3O_7$. The 10%-drop, midpoint, and 90%-drop points are indicated on the resistivity curve (Ku *et al.*, 1987).

of the second derivative curve sketched in Fig. 2.22c, are both good quantitative measures of the width of the transition. An asymmetry parameter, equal to $[(A-B)/(A+B)]$, may also be evaluated from Fig. 2.22c.

There appear to be enough data points near the midpoint of Fig. 2.22a to accurately define the transition, but the first and second derivative curves of Figs. 2.22b and 2.22c, respectively, show that this is not the case. This need for additional data points demonstrates the greater precision of the derivative method.

Phase transitions in general have finite widths, and a typical approach is to define T_c in terms of the point of most rapid change from the old to the new phase. Critical exponents are evaluated in this region near T_c. Ordinarily, less account is taken of the more gradual changes that take place at the onset or during the final approach to the new equilibrium state. The onset of superconductivity is important from a physics viewpoint because it suggests that superconducting regions are being formed, whereas the zero point is important from an engineering viewpoint because it is where the material can finally carry a super current.

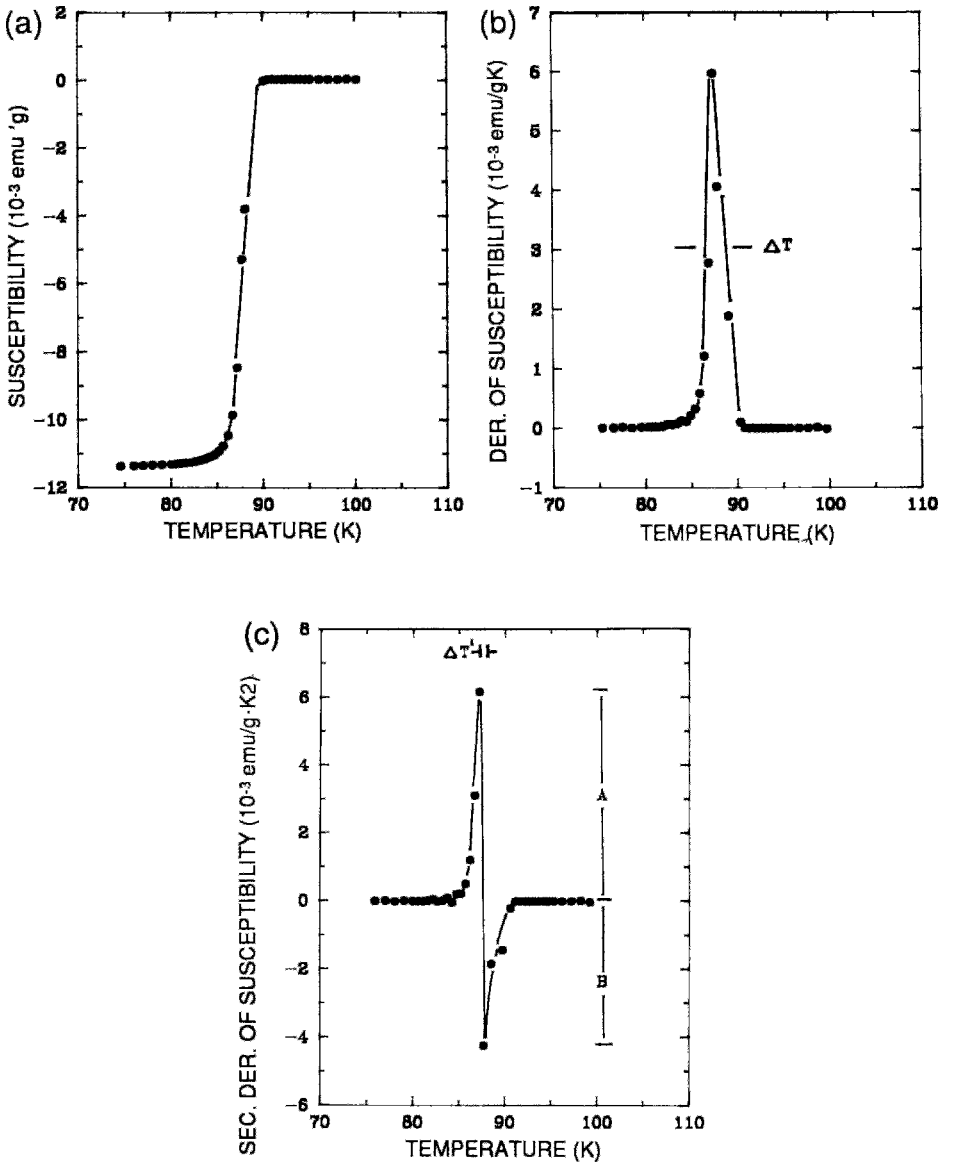

Figure 2.22 Zero-field-susceptibility of $YBa_2Cu_3O_7$ as a function of temperature in a magnetic field of 0.1 mT: (a) usual susceptibility plot χ; (b) first derivative plot d_χ/dT; and (c) second derivative plot $d^2\chi/d^2T$ (Almasan *et al.*, 1988).

VI. PERFECT DIAMAGNETISM

The property of perfect diamagnetism, which means that the susceptibility $\chi = -1$ in Eq. (1.78a),

$$\mathbf{B} = \mu_0\mathbf{H}(1+\chi), \tag{2.20}$$

$$= \mu_0(\mathbf{H}+\mathbf{M}), \tag{2.21}$$

is equivalent to the assertion that there can be no **B** field inside a perfect diamagnet because

the magnetization **M** is directed opposite to the **H** field and thereby cancels it:

$$\mathbf{M} = -\mathbf{H}. \tag{2.22}$$

When a superconductor is placed between the pole pieces of a magnet, the **B** field lines from the magnet go around it instead of entering, and its own internal field remains zero, as shown in Fig. 2.23. This field distribution is the result of the super-position of the uniform applied field and a dipole field from the reversely magnetized superconducting sphere, as illustrated in Fig. 2.24 (Jackson, 1975; cf. Section 5–10).

There are two aspects to perfect diamagnetism in superconductors. The first is flux exclusion: If a material in the normal state is zero field cooled (ZFC), that is, cooled below T_c to the superconducting state without any magnetic field present, and is then placed in an external magnetic field, the field will be excluded from the superconductor. The second aspect is flux expulsion: If the same material in its normal state is placed in a magnetic field, the field will penetrate and have almost the same value inside and outside because the permeability μ is so close to the free-space value μ_0. If this material is then field cooled (FC), that is, cooled below T_c in the presence of this field, the field will be expelled from the material, a phenomenon called the *Meissner effect*. These two processes are sketched on the left side of Fig. 2.25. Although ZFC and FC lead to the same result (absence of magnetic flux inside the sample below T_c), nevertheless the two

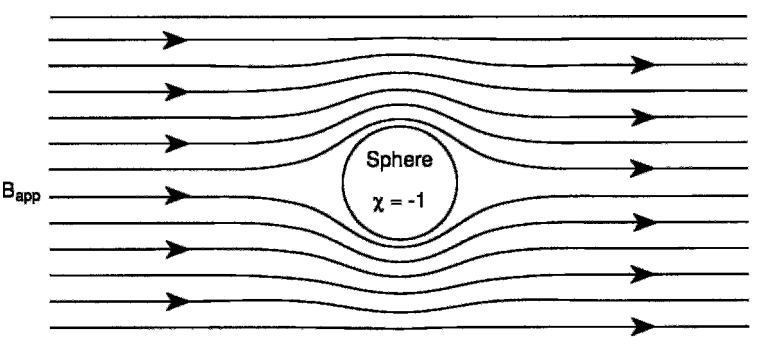

Figure 2.23 Curvature of magnetic field lines around a superconducting sphere in a constant applied field.

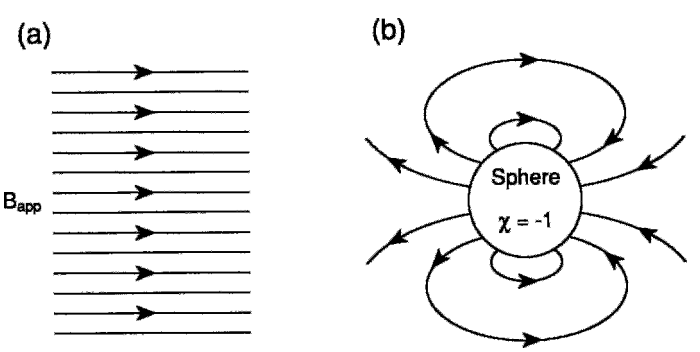

Figure 2.24 Sketch of constant applied magnetic field (a) and dipole field (b) that superimpose to provide the magnetic field lines shown in Fig. 2.23 (Jackson, 1975).

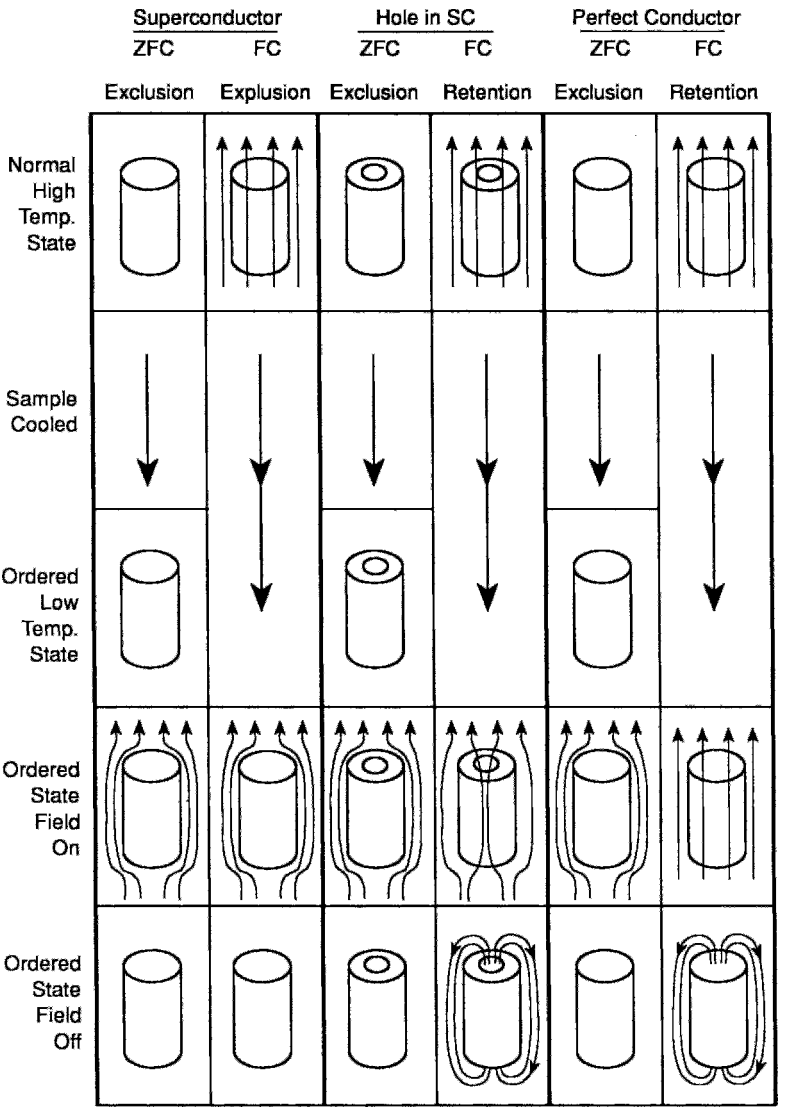

Figure 2.25 Effect of zero field cooling (ZFC) and field cooling (FC) of a solid superconducting cylinder (left), a superconducting cylinder with an axial hole (center), and a perfect conductor (right).

processes are not equivalent, as we will see in Section IX.

Thompson *et al.* (1991) found that for a "defect-free" high-purity niobium sphere the ZFC and FC susceptibilities are almost identical. A second high-purity sphere of similar composition that exhibited strong pinning was also examined and the same ZFC results were obtained, except that no Meissner flux expulsion following field cooling was observed. The pinning was so strong that the vortices could not move out of the sample. Figure 2.25 is drawn for the case of very weak pinning, in which virtually all of the flux is expelled from the superconducting material following field cooling.

VII. MAGNETIC FIELDS INSIDE A SUPERCONDUCTOR

To further clarify the magnetic field configurations inside a superconductor, consider a long cylindrical sample placed in a uniform applied magnetic field with its axis in the field direction, as indicated in Fig. 2.26. Since there are no applied currents, the boundary condition at the surface given in Chapter 1, Section XIV,

$$H'_{\parallel} = H''_{\parallel}, \tag{2.23}$$

shows that the H field is uniform inside with the same value as the applied field:

$$H_{\text{app}} = H_{\text{in}} \tag{2.24}$$

The B field has only a z component with value $B_{\text{app}} = \mu_0 H_{\text{app}}$ outside and zero inside, $B_{\text{in}} = 0$. There is, however, a transition layer of thickness λ, called the *penetration depth*, at the surface of the superconductor where the B field drops exponentially from its value B_{app} on the outside to zero inside, in accordance with the expression

$$B(r) \approx B_{\text{app}} \exp[-(R-r)/\lambda], \tag{2.25}$$

as shown in Fig. 2.27. Thus the B field exists only in the surface layer, and not in the bulk. Since

$$B_{\text{in}}(r) = \mu[H_{in} + M(r)] \tag{2.26}$$

with $H_{\text{in}} = H_{\text{app}}$, we have for $M(r)$

$$M(r) = -H_{\text{app}} \left\{ 1 - \exp\left[-\frac{(R-r)}{\lambda} \right] \right\}, \tag{2.27}$$

again subject to the assumption that $\lambda \ll R$, and this is also sketched in Fig. 2.27.

We will show later in Chapter 6, Sections VII and VIII, that this exponential decay process arises naturally in the Ginzburg–Landau and London theories, and that these theories provide an explicit

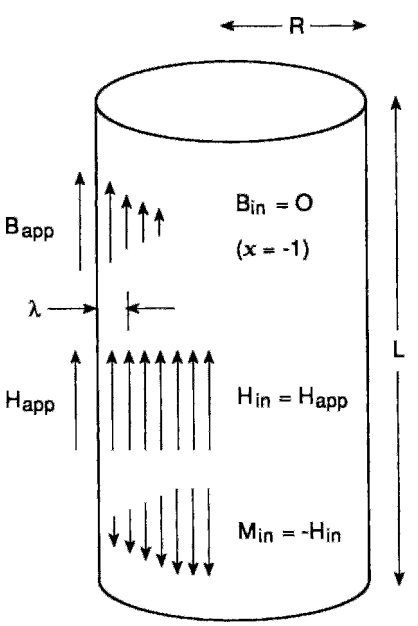

Figure 2.26 Boundary region and internal fields for a superconducting cylinder in an axial external magnetic field B_{app}.

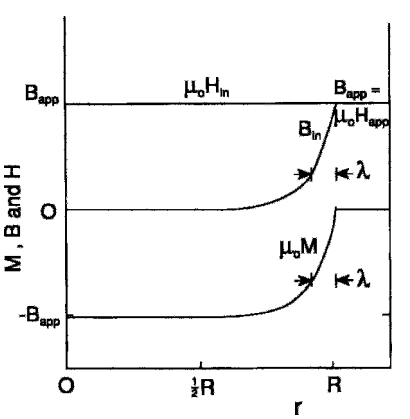

Figure 2.27 Plot of the fields B and $\mu_0 H$ and of the magnetization $\mu_0 M$ outside ($r > R$) and inside ($r < R$) a superconducting cylinder of radius R in an axial applied field B_{app}. At the center of the sphere r = 0.

formula for what is called the *London penetration depth* λ_L, namely

$$\lambda_L = \left(\frac{m}{\mu_0 n_s e^2}\right)^{1/2}. \tag{2.28}$$

where n_s is the density of superconducting electrons.

VIII. SHIELDING CURRENT

In the absence of any applied transport current we set $\mathbf{J} = 0$ (also $\partial D/\partial t = 0$) in Maxwell's equation, Eq. (1.72), to obtain

$$\nabla \times \mathbf{B}_{in} = \mu_0 \nabla \times \mathbf{M} \tag{2.29a}$$

$$= \mu_0 \mathbf{J}_{sh} \tag{2.29b}$$

where $\mathbf{J}_{sh}$ is called the *shielding or demagnetization current density*:

$$\mathbf{J}_{sh} = \nabla \times \mathbf{M}. \tag{2.30}$$

Since $\mathbf{B}_{in}$ has only a z or axial component, the curl, expressed in terms of cylindrical coordinates, gives the following shielding current density flowing around the cylinder in the negative ϕ direction:

$$\mathbf{J}_{sh}(r) = -\frac{1}{\mu_0} \cdot \frac{d\mathbf{B}}{dr} \tag{2.31}$$

$$\approx -\left(\frac{\mathbf{B}_{app}}{\mu_0 \lambda}\right) \exp\left[-\frac{(R-r)}{\lambda}\right] \tag{2.32}$$

$$\approx -\mathbf{J}_0 \exp\left[-\frac{(R-r)}{\lambda}\right], \tag{2.33}$$

where

$$\mathbf{B}_{app} = \mu_0 \lambda \mathbf{J}_0, \tag{2.34}$$

again with $\lambda \ll R$, and this circular current flow is sketched in Fig. 2.28 and graphed in Fig. 2.29. In other words, the vectors $\mathbf{B}$ and $\mathbf{J}_{sh}$ do not exist in the bulk of the superconductor but only in the surface layer where

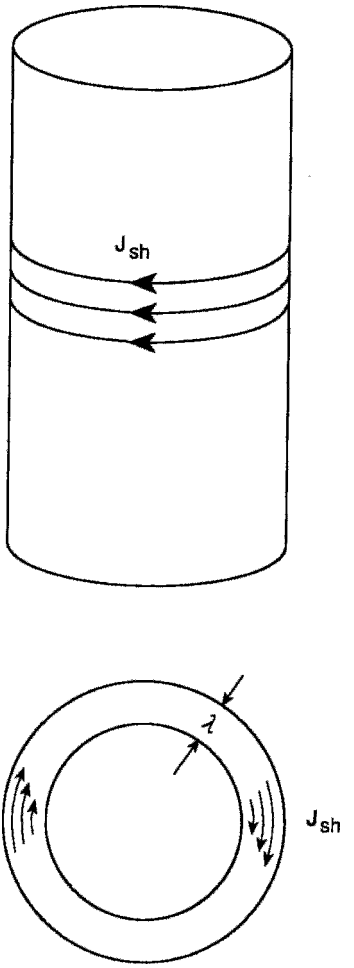

Figure 2.28 Shielding current flow J_{sh} in a surface layer of thickness λ around a superconducting cylinder in an axial applied magnetic field B_{app}.

they are perpendicular to each other, with $\mathbf{B}$ oriented vertically and $\mathbf{J}_{sh}$ flowing around the cylinder in horizontal circles. It may be looked upon as a circulating demagnetizing current that shields or screens the interior of the superconductor by producing a negative $\mathbf{B}$ field that cancels $\mathbf{B}_{app}$ so that $\mathbf{B}_{in} = 0$ inside.

Thus we see that the superconducting medium reacts to the presence of the applied field by generating shielding currents that cancel the interior $\mathbf{B}$ field. The reaction of the

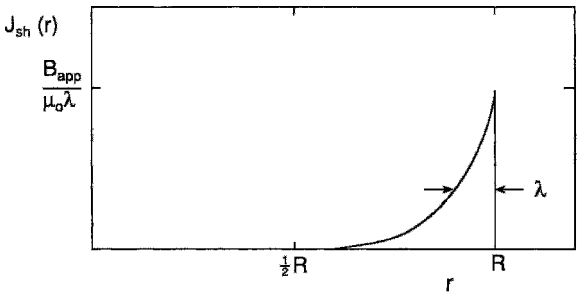

Figure 2.29 Dependence of the shielding current density J_{sh} on the position inside a superconducting cylinder of radius R in an applied axial field B_{app}. Note that J_{sh} has the value H_{app}/λ at the surface.

medium may also be looked upon as generating a magnetization **M** that cancels the interior **B** field, as was explained above. These are two views of the same phenomenon, since the shielding current density $\mathbf{J}_{sh}$ and the compensating magnetization **M** are directly related through Eq. (2.30). The negative **B** field that cancels $\mathbf{B}_{app}$ is really a magnetization in the negative z direction.

It is instructive to see how Eq. (2.34) is equivalent to the well-known formula

$$B_0 = \frac{\mu_0 NI}{L} \tag{2.35}$$

for the magnetic field B_0 of an N-turn solenoid of length L. Since each turn carries the current I, the total current is NI. This total current also equals the current density $\mathbf{J}_0$ times the area λL, corresponding to

$$NI = \lambda L J_0. \tag{2.36}$$

Substituting NI from this expression in Eq. (2.35) gives Eq. (2.34). Thus the circulating shielding current is equivalent to the effect of a solenoid that cancels the applied **B** field inside the superconductor.

The dipole field of the superconducting sphere sketched in Fig. 2.24 may be considered as arising from demagnetizing currents circulating in its surface layers, as shown in Fig. 2.30. These demagnetizing currents provide the reverse magnetization that cancels the applied field to make $\mathbf{B} = 0$ inside, just as in the case of a cylinder.

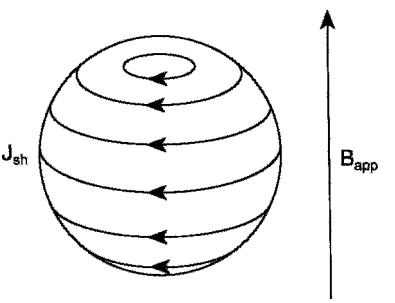

Figure 2.30 Shielding current flow around the surface of a superconducting sphere in an applied magnetic field B_{app}.

IX. HOLE IN SUPERCONDUCTOR

As an example of how ZFC and FC can lead to two different final states of magnetism let us examine the case of a hole inside a superconductor.

Consider a cylindrical superconducting sample of length L and radius R with a concentric axial hole through it of radius r, as shown in Fig. 2.31. This will be referred to as an "open hole" because it is open to the outside at both ends. If this sample is zero-field-cooled in the manner described in Section VI, an axial magnetic field applied after cooling below T_c will be excluded from the superconductor and also from the open axial hole.

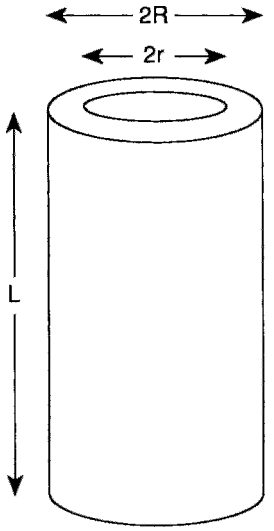

Figure 2.31 Superconducting tube of radius R with an axial hole of radius r.

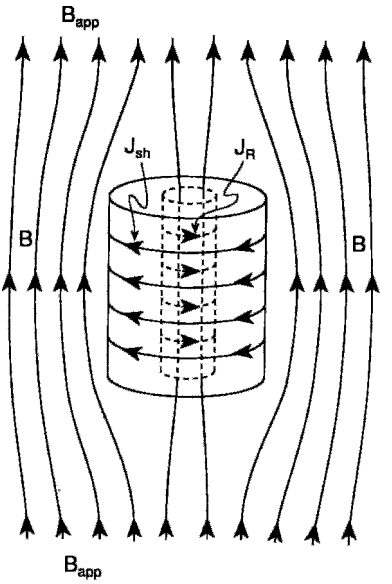

Figure 2.32 Magnetic field lines, shielding current flow J_{sh} on the outside surface, and reverse-direction shielding current flow J_R on the inside surface of a superconducting tube in an applied axial magnetic field. The magnetic field lines pass through the hole because the cylinder has been field cooled.

Surface currents shield the superconducting regions from the external field and bring about the flux exclusion shown in Fig. 2.25. These same surface currents also shield the hole from the applied field. This means that the superconductor plus the hole act like a perfect diamagnet under zero-field cooling. The entire volume $\pi R^2 L$, including the open hole volume $\pi r^2 L$, has an effective susceptibility of -1,

$$\chi_{\text{eff}} = -1. \tag{2.37}$$

If this same sample, still with an open hole, is field cooled, once it attains the superconducting state the magnetic flux will be expelled from the superconducting material, but will remain in the hole. The same outer surface currents flow to shield the superconductor from the applied field, but the surface currents flowing in the reverse direction around the inside surface of the cylinder, i.e., around the hole periphery as indicated in Fig. 2.32, cancel the effect of the outside surface currents and sustain the original magnetic flux in the hole. The volume of the superconducting material, $(\pi R^2 - \pi r^2)L$, has a susceptibility of -1, but the space in the open hole, $\pi r^2 L$, does not exhibit diamagnetism, so that for the hole $\chi = 0$. The effective susceptibility of the cylinder with the hole is the average of -1 for the superconducting material and 0 for the hole, corresponding to

$$\chi_{\text{eff}} = -\left[1 - \left(\frac{r}{R}\right)^2\right], \tag{2.38}$$

which reduces to -1 for no hole ($r = 0$) and to 0 for $r = R$. This experimentally measurable result is different from the ZFC open hole case (2.37). Experimentally, it is found that the magnetic susceptibility is less negative for field-cooled samples than for zero-field-cooled samples, as shown by the data in Fig. 2.33. Mohamed *et al.* (1990) give plots of the ZFC and FC magnetic field distributions of a 16-mm diameter, 2-mm thick superconducting disk with a 3-mm diameter axial hole.

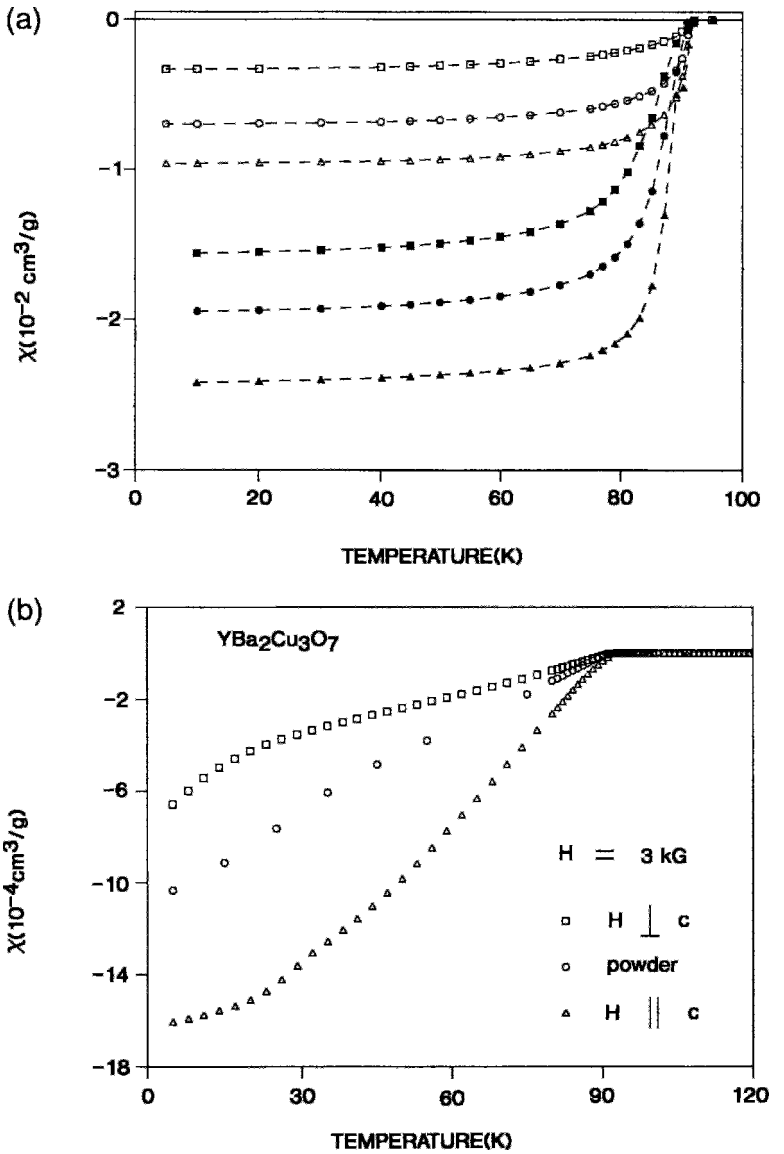

Figure 2.33 Zero-field-cooled (closed symbols) and field-cooled (open symbols) magnetic susceptibility of $YBa_2Cu_3O_7$ nonaligned powder (circles) and grain-aligned samples with the applied field parallel to the *c*-axis (triangles) and perpendicular to the *c*-axis (squares). Results are shown in an applied field of (a) 5 mT and (b) 0.3 T. Note the change in abscissa and ordinate scales between the two figures (Lee and Johnston, 1990).

Another important case to consider is that of a totally enclosed hole of the type shown in Fig. 2.34, which we call a closed hole or cavity. It is clear that for ZFC the closed hole behaves the same as the open hole, that is, flux is excluded from it, with $\chi_{\text{eff}} = -1$, as shown in the fifth column of Fig. 2.25. Flux is also excluded for field cooling. To see this, we recall that the **B** field lines must be continuous and can only

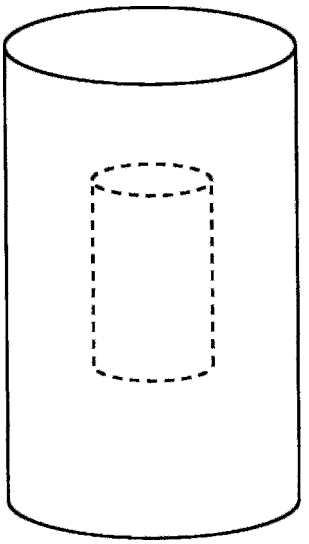

Figure 2.34 Superconducting cylinder with a totally enclosed hole.

begin or end at the poles of a magnet. In the open hole case, the **B** field lines in the hole either join to the externally applied field lines or form loops that close outside the sample, as shown at the bottom of column 4 of Fig. 2.25. The **B** field lines have no way of leaving a closed hole to connect with the external field or to form closed loops outside, so such lines cannot exist inside a cavity completely surrounded by a superconducting material. Therefore, flux is expelled during field cooling, so again $\chi_{\text{eff}} = -1$. Thus a superconductor with a cavity behaves like a solid superconductor with the difference that magnetization can exist only in the superconductor, not in the cavity.

In this section we have discussed the cases of open and closed holes in superconductors. We showed in Table 1.2 that the susceptibility of typical diamagnetic and paramagnetic samples is quite close to zero, so that the empty hole results also apply to holes filled with typical nonsuper conducting materials. Experimentally, we deal with samples with a known overall or external volume, but with an unknown fraction of this volume taken up by holes, intergranular spaces, and nonsuperconducting material that could respond to ZFC and FC preconditioning the same way as a hole.

If a sample is a mixture of a superconducting material and a non-superconducting material with the nonsuperconducting part on the outside so that the applied magnetic field can penetrate it under both ZFC and FC conditions, the average sample susceptibility will be the average of $\chi = 0$ for the normal material and $\chi = -1$ for the superconducting part. Thus both the ZFC and the FC measurement will give values of χ_{eff} that are less negative than -1. A granular superconducting sample can have an admixture of normal material on the outside or inside and space between the grains that produce ZFC and FC susceptibilities of the type shown in Fig. 2.33, where, typically, the measured susceptibilities are $\chi_{\text{zfc}} \approx -0.7$ and $\chi_{\text{fc}} \approx -0.3$.

X. PERFECT CONDUCTIVITY

We started this chapter by describing the perfect conductivity property of a superconductor—namely, the fact that it has zero resistance. Then we proceeded to explain the property of perfect diamagnetism exhibited by a superconductor. In this section we will treat the case of a perfect conductor, i.e., a conductor that has zero resistivity but the susceptibility of a normal conductor, i.e., $\chi \approx 0$. We will examine its response to an applied magnetic field and see that it excludes magnetic flux, but does not expel flux, as does a superconductor. We will start with a good conductor and then take the limit, i.e., letting its resistance fall to zero so that it becomes a hypothetical perfect conductor.

A static magnetic field penetrates a good conductor undisturbed because its magnetic permeability μ is quite close to the magnetic permeability of free space μ_0, as the susceptibility data of Table 1.2 indicate. Therefore,

a good conductor placed in a magnetic field leaves the field unchanged, except perhaps for current transients that arise while the field is turned on and die out rapidly. In Section IV we estimated the decay time constant for a loop of copper wire 15 cm in diameter to be 0.42 ms.

Consider a closed current path within the conductor. When the magnetic field $\mathbf{B}_{app}$ is applied, the magnetic flux through this circuit $\Phi = \mathbf{A} \cdot \mathbf{B}_{app}$ changes, so that by Lenz' law a voltage $-\mathbf{A} \cdot d\mathbf{B}_{app}/dt$ is induced in the circuit and a current I flows, as indicated in Fig. 2.35, in accordance with the expression

$$-\mathbf{A} \cdot \frac{d\mathbf{B}_{app}}{dt} = RI + L\frac{dI}{dt}. \qquad (2.39)$$

The current rapidly dies out with time constant L/R. For a perfect conductor the resistance term in Eq. (2.39) vanishes. Solving the resultant equation,

$$-\mathbf{A} \cdot \frac{d\mathbf{B}_{app}}{dt} = L\frac{dI}{dt}, \qquad (2.40)$$

gives

$$LI + \mathbf{A} \cdot \mathbf{B}_{app} = \Phi_{Total}, \qquad (2.41)$$

which means that the total flux $LI + \mathbf{A} \cdot \mathbf{B}_{app}$ remains constant when the field is applied. If no fields or currents are present and the field $\mathbf{B}_{app}$ is applied, the flux LI will be induced to cancel that from the applied field and maintain the $\mathbf{B} = 0$ state inside the perfect conductor. In real conductors the induced currents die out so rapidly that the internal $\mathbf{B}$ field builds up immediately to the applied field value. Hence a perfect conductor exhibits flux exclusion since a magnetic field turned on in its presence does not penetrate it. It will, however, not expel flux already present because flux that is already there will remain forever. In other words, an FC-perfect conductor retains magnetic flux.

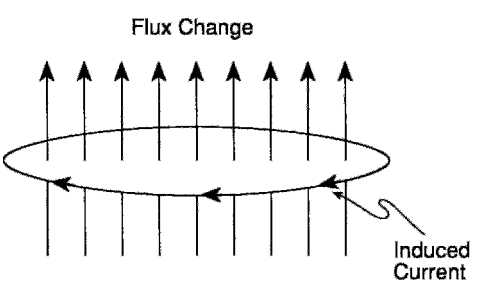

Figure 2.35 Magnetic field B rapidly established through a loop of wire and induced current I. which, by Lenz' law, flows in a direction to oppose the establishment of this field.

Thus we find that a ZFC-perfect conductor excludes magnetic flux just like a ZFC superconductor. The two, however, differ in their field-cooled properties, the perfect conductor retaining flux and a superconductor excluding flux after FC. A perfect conductor acts like an open hole in a superconductor!

We do not know of any examples of perfect conductors in nature. The phenomenon has been discussed because it provides some insight into the nature of superconductivity.

XI. TRANSPORT CURRENT

In the previous section we discussed the shielding currents induced by the presence of applied magnetic fields. We saw how a field applied along the cylinder axis gives rise to currents circulating around this axis. When a current is applied from the outside and made to flow through a superconductor, it induces magnetic fields near it. An applied current is called transport current, and the applied current density constitutes the so-called "free" current density term on the right side of Maxwell's inhomogeneous equation (1.68).

Suppose that an external current source causes current I to flow in the direction of the axis of a superconducting cylinder of radius R, in the manner sketched in Fig. 2.36. We know from general physics that the wire has a circular B field around it, as indicated in the figure, and that this field decreases with distance r from the wire in accordance with the expression

$$B = \frac{\mu_0 I}{2\pi r} \quad r \geq R, \qquad (2.42)$$

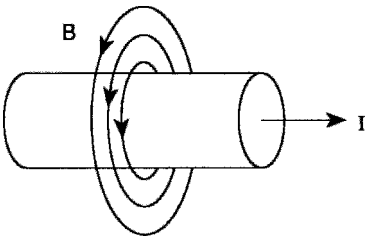

Figure 2.36 Magnetic field lines B around a wire carrying a current I.

as shown sketched in Fig. 2.37, with the following value on the surface:

$$B_{\text{surf}} = \frac{\mu_0 I}{2\pi R}. \tag{2.43}$$

We also know that if the current density were uniform across the cross section of the wire, the B field inside would be proportional to the distance from the axis, $B = B_{\text{surf}}(r/R)$, as shown in Fig. 2.37.

Since magnetic flux is excluded from inside a superconducting wire, the current density cannot be uniform, and instead the transport current must flow in a surface layer of thickness λ, as shown in Fig. 2.38, to maintain the B field equal to zero inside. This current density $J(r)$ must have the same

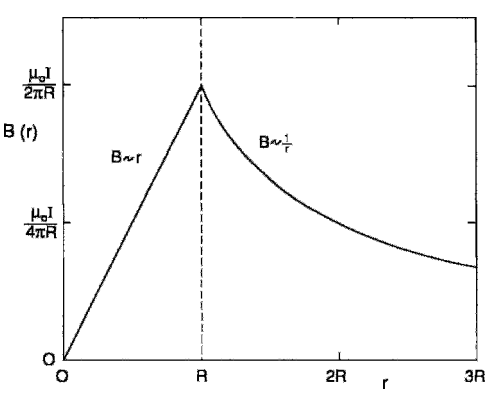

Figure 2.37 Dependence of the internal ($r < R$) and external ($r > R$) magnetic field on distance from the center of a normal conductor wire carrying a current of uniform density.

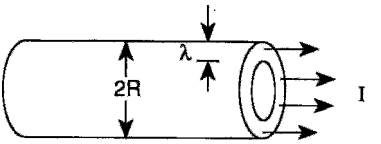

Figure 2.38 Transport current flow in a surface layer of thickness λ of a Type I superconducting wire of radius R.

exponential dependence on distance as given by Eq. (2.31) for the case of the shielding current:

$$J(r) = \frac{B_{\text{surf}}}{\mu_0 \lambda} \exp\left[-\frac{(R-r)}{\lambda}\right] \tag{2.44}$$

$$= \frac{I}{2\pi R\lambda} \exp\left[-\frac{(R-r)}{\lambda}\right]. \tag{2.45}$$

Figure 2.39 shows how the current distribution changes at the junction between a normal wire and a superconducting wire from uniform density flow in the normal conductor to surface flow in the superconductor. The total current I is the integral of the current density $J(r)$ from Eq. (2.45) over the cross section of the superconducting wire, with value

$$I = 2\pi R\lambda J, \tag{2.46}$$

where $J = J(R)$ is the maximum value of $J(r)$, which is attained at the surface, and the quantity $2\pi R\lambda$ is the effective cross-sectional area of the surface layer. Substituting the expression for I from Eq. (2.46) in Eq. (2.43) gives

$$B_{\text{surf}} = \mu_0 \lambda J, \tag{2.47}$$

which is the same form as Eq. (2.34) for the shielding current.

Comparing Eqs. (2.32) and (2.44) we obtain for the magnetic field inside the wire

$$B(r) = B_{\text{surf}} \exp\left[-\frac{(R-r)}{\lambda}\right] \quad r \le R, \tag{2.48}$$

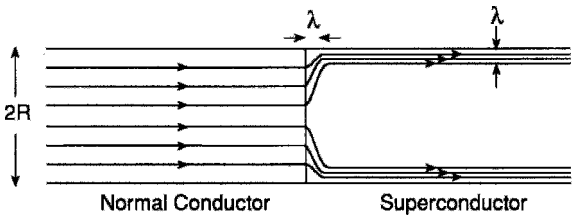

Figure 2.39 Current flow through a wire that is normal on the left and Type I superconducting on the right. Note that the penetration depth λ determines the thickness of both the transition region at the interface and that of the surface layer.

as shown sketched in Fig 2.40. In Chapter 5, Sections VII and IX, we show how to derive these various exponential decay expressions from the Ginzburg–Landau and London theories. Outside the wire the magnetic field exhibits the same decline with distance in both the normal and superconducting cases, as can be seen by comparing Figs. 2.37 and 2.40.

There is really no fundamental difference between the demagnetizing current and the transport current, except that in the present case of a wire their directions are orthogonal to each other. When a current is impressed into a superconductor it is called a transport current, and it induces a magnetic field. When a superconductor is placed in an external magnetic field, the current induced by this field is called *demagnetization current or shielding current*. The current–field relationship is the same in both cases. This is why Eqs. (2.25) and (2.48) are the same.

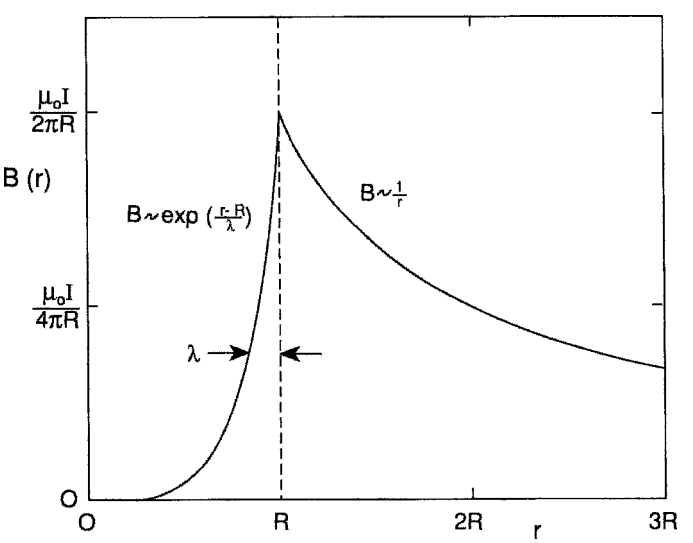

Figure 2.40 Dependence of the internal ($r < R$) and external ($r > R$) magnetic field on distance from the center of a superconducting wire carrying a current that is confined to the surface layer. This figure should be compared with Fig. 2.37.

XII. CRITICAL FIELD AND CURRENT

We noted in Section II that application of a sufficiently strong magnetic field to a superconductor causes its resistance to return to the normal state value, and each superconductor has a critical magnetic field B_c above which it returns to normal. There is also a critical transport current density J_c that will induce this critical field at the surface and drive the superconductor normal. Comparing Eqs. (2.34) and (2.47), respectively, we have for both the demagnetizing and transport cases

$$B_c(T) = \mu_0 \lambda(T) J_c(T), \tag{2.49}$$

where all three quantities are temperature dependent in a way that will be described in the following section. Either an applied field or an applied current can destroy the superconductivity if either exceeds its respective critical value. At absolute zero, we have

$$B_c(0) = \mu_0 \lambda(0) J_c(0), \tag{2.50}$$

and this is often written

$$B_c = \mu_0 \lambda J_c, \tag{2.51}$$

where $T = 0$ is understood.

A particular superconducting wire of radius R has a maximum current, called the critical current I_c, which, by Eq. (2.46), has the value

$$I_c = 2\pi R \lambda J_c. \tag{2.52}$$

Using Eq. (2.51), the value of the critical current may be written as

$$I_c = \frac{2\pi R B_c}{\mu_0} \tag{2.53a}$$

$$= 5 \times 10^6 \, R H_c. \tag{2.53b}$$

The transformation of a superconducting wire to the normal state when the current passing through it exceeds the critical value is called the *Silsbee effect*.

In Type I superconductors with thicknesses much greater than the penetration depth λ, internal magnetic fields, shielding currents, and transport currents are able to exist only in a surface layer of thickness λ. The average current carried by a superconducting wire is not very high when most of the wire carries zero current. To achieve high average super current densities, the wire must have a diameter less than the penetration depth, which is typically about 50 nm for Type I superconductors. The fabrication of such filamentary wires is not practical, and Type II superconductors are used for this application.

XIII. TEMPERATURE DEPENDENCES

In the normal region above the transition temperature there is no critical field ($B_c = 0$) and there is total magnetic field penetration ($\lambda = \infty$). As a superconductor is cooled down through the transition temperature T_c, the critical field gradually increases to its maximum value $B_c(0)$ at absolute zero ($T = 0$), while the penetration depth decreases from infinity to its minimum value $\lambda(0)$ at absolute zero. The explicit temperature dependences of $B_c(T)$ and $\lambda(T)$ are given by the Ginzburg–Landau theory that will be presented in Chapter 6, where $\lambda(0) = \lambda_L$ as given by Eq. (2.28),

$$\lambda(0) = \left(\frac{m}{\mu_0 n_s e^2} \right)^{1/2}, \tag{2.54}$$

which assumes that all of the conduction electrons are super electrons at $T = 0$. The critical current density may be written as the ratio

$$J_c(T) = \frac{B_c(T)}{\mu_0 \lambda(T)} \tag{2.55}$$

given in Eq. (2.49) in order to obtain the temperature dependence of $J_c(T)$. These temperature dependences have the form

$$B_c = B_c(0)\left[1-\left(\frac{T}{T_c}\right)^2\right], \tag{2.56}$$

$$\lambda = \lambda(0)\left[1-\left(\frac{T}{T_c}\right)^4\right]^{-1/2}, \tag{2.57}$$

$$J_c = J_c(0)\left[1-\left(\frac{T}{T_c}\right)^2\right]\left[1-\left(\frac{T}{T_c}\right)^4\right]^{1/2}, \tag{2.58}$$

and are sketched in Figs. 2.41, 2.42, and 2.43. Also shown by dashed lines in the figures are the asymptotic behaviors near the transition temperature $T \approx T_c$ (Nicol and Carbotte, 1991):

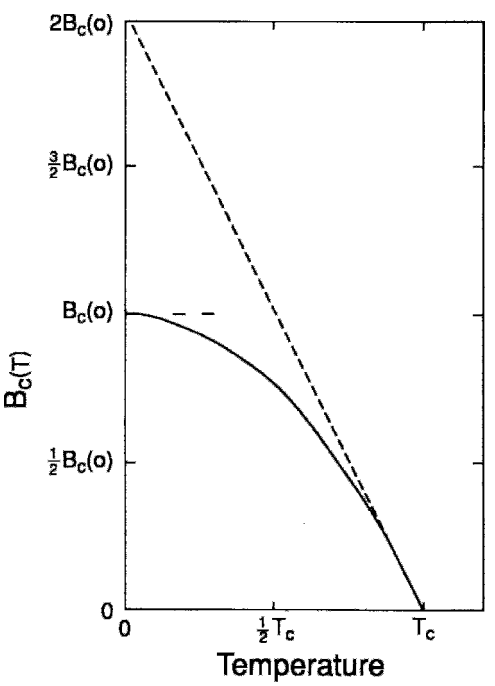

Figure 2.41 Temperature dependence of the critical field $B_c(T)$ corresponding to the behavior expressed by Eq. (2.56). The asymptotic behaviors near $T = 0$ and $T = T_c$ are indicated by dashed lines.

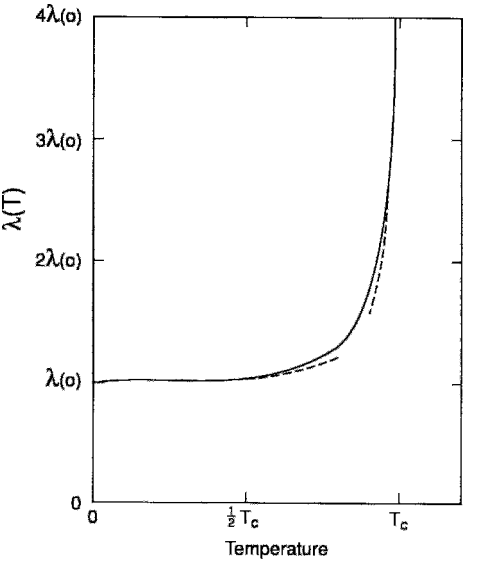

Figure 2.42 Temperature dependence of the penetration depth $\lambda(T)$ corresponding to Eq. (2.57). The asymptotic behaviors near $T = 0$ and $T = T_c$ are indicated by dashed lines.

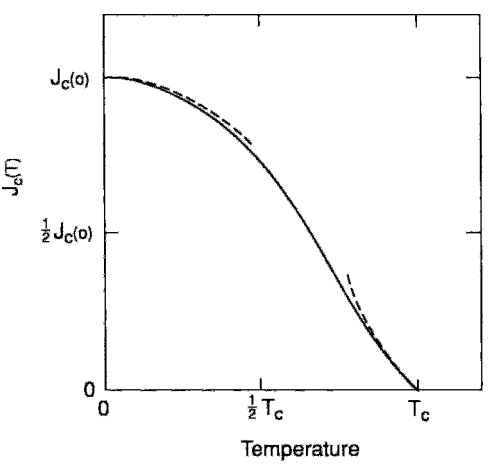

Figure 2.43 Temperature dependence of the critical current density $J_c(T)$ in accordance with Eq. (2.58). The asymptotic behavior near $T = 0$ and $T = T_c$ is indicated by dashed lines.

$$B_c \approx 2B_c(0)\left[1-\frac{T}{T_c}\right], \tag{2.59}$$

$$\lambda \approx \tfrac{1}{2}\lambda(0)\left[1-\frac{T}{T_c}\right]^{-1/2}, \tag{2.60}$$

$$J_c \approx 4J_c(0)\left[1-\frac{T}{T_c}\right]^{3/2}. \qquad (2.61)$$

Jiang and Carbotte (1992) give plots of $\lambda(0)/\lambda(T)$ for various theoretical models and anisotropies. The asymptotic behaviors near absolute zero, $T \to 0$, are as follows:

$$B_c = B_c(0)\left[1-\left(\frac{T}{T_c}\right)^2\right], \qquad (2.62)$$

$$\lambda \approx \lambda(0)\left[1+\frac{1}{2}\left(\frac{T}{T_c}\right)^4\right], \qquad (2.63)$$

$$J_c \approx J_c(0)\left[1-\left(\frac{T}{T_c}\right)^2\right], \qquad (2.64)$$

which are proven in Problems 5 and 6, respectively. Note that Eq. (2.62) is identical to Eq. (2.56). Some authors report other values of the exponents or expressions related to Eqs. (2.56)–(2.64) for B_c (Miu, 1992; Miu *et al.*, 1990), λ (Däumling and Chandrashekhar, 1992; Hebard *et al.,* 1989; Kanoda *et al.,* 1990; Kogan *et al.,* 1988), and J_c (Askew *et al.,* 1991; Freltoft *et al.,* 1991).

For later reference we give here the temperature dependence of the superconducting energy gap E_g in the neighborhood of T_c:

$$E_g \approx 3.52\, k_B T_c\left[1-\frac{T}{T_c}\right]^{1/2} \qquad (2.65)$$

(cf. Section VI, Chapter 7 for an explanation of the energy gap and a plot (Fig. 7.7) of this expression). Another length parameter that is characteristic of the superconducting state is the coherence length ξ; this parameter will be introduced in Chapter 6 and referred to frequently throughout the remainder of the text. It is reported to have a $[1-T/T_c]^{-n}$ dependence, with $n = 1/2$ expected; the penetration depth also depends on $[1-(T/T_c)]^{-n}$ near T_c (Chakravarty *et al.*, 1990; Duran *et al.*, 1991; Schneider, 1992).

XIV. TWO FLUID MODEL

Many properties of superconductors can be described in terms of a two-fluid model that postulates a fluid of normal electrons mixed with a fluid of superconducting electrons. The two fluids interpenetrate but do not interact. A similar model of interpenetrating fluids consisting of normal and superfluid atoms is used to explain the properties of He^4 below its lambda point. When a superconductor is cooled below T_c, normal electrons begin to transform to the super electron state. The densities of the normal and the super electrons, n_n and n_s, respectively, are temperature dependent, and sum to the total density n of the conduction electrons,

$$n_n(T) + n_s(T) = n, \qquad (2.66)$$

where at $T = 0$ we have $n_n(0) = 0$ and $n_s(0) = n$.

If we assume that Eq. (2.54) is valid for any temperature below T_c,

$$\lambda(T) = \left(\frac{m}{\mu_0 n_s(T) e^2}\right)^{1/2}, \qquad (2.67)$$

then $\lambda(0) = (m/\mu_0 n e^2)^{1/2}$, and we can write

$$\frac{n_s}{n} = \left[\frac{\lambda(0)}{\lambda(T)}\right]^2, \qquad (2.68)$$

which becomes, with the aid of Eq. (2.57),

$$n_s \approx n\left[1-\left(\frac{T}{T_c}\right)^4\right]. \qquad (2.69)$$

Figure 2.44 shows a sketch of n_s versus temperature. Substituting the latter in Eq. (2.66) gives for the normal electron density

$$n_n \approx n\left(\frac{T}{T_c}\right)^4. \qquad (2.70)$$

Equation (2.68) is useful for estimating super electron densities.

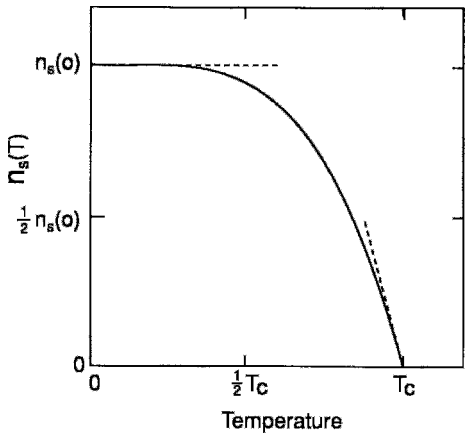

Figure 2.44 Temperature dependence of the density of superconducting electrons n_s as given by Eq. (2.69). The dashed lines show the slope $dn_s/dT = 0$ at $T = 0$ and -4 at T_c.

XV. CRITICAL MAGNETIC FIELD SLOPE

We showed in the previous section that the critical magnetic field has the parabolic dependence on temperature given by Eq. (2.56), and this is plotted in Fig. 2.41. The slope of the curve near T_c is given by Eq. (2.59) and may also be written

$$\frac{dB_c(T)}{dT} = -\frac{2B_c(0)}{T_c}. \qquad (2.71)$$

For most Type I superconductors this ratio varies between -15 and $-50\,\mathrm{mT/K}$; for example, it has a value of $-22.3\,\mathrm{mT/K}$ for lead.

A Type II superconductor has two critical fields, a lower-critical field B_{c1} and an upper-critical field B_{c2}, where $B_{c1} < B_{c2}$, as we will see in Chapter 12. These critical fields have temperature dependences similar to that of Eq. (2.71). Typical values of these two slopes for a high-temperature superconductor are (see Fig. 12.8, Table 12.5)

$$\frac{dB_{c1}}{dT} = -\frac{2B_{c1}(0)}{T_c} \approx -1\,\mathrm{mT/K}, \qquad (2.72)$$

$$\frac{dB_{c2}}{dT} = -\frac{2B_{c2}(0)}{T_c} \approx -1.83\,\mathrm{T/K}. \qquad (2.73)$$

For high-temperature superconductors the slopes of Eqs. (2.72) and (2.73) near T_c can be quite anisotropic.

XVI. CRITICAL SURFACE

The critical behavior of a superconductor may be described in terms of a critical surface in three-dimensional space formed by the applied magnetic field B_{app}, applied transport current J_{tr}, and temperature T, and this is shown in Fig. 2.45. The surface is bounded on the left by the $B_c(T)$ versus T curve (d–c–b–a) drawn for $J_{tr} = 0$; this curve also appears in Figs. 2.41 and 2.46. The surface is bounded on the right by the $J_c(T)$ versus T curve (g–h–i–a) drawn for $B_{app} = 0$, which also appears in Figs. 2.43 and 2.47. Figure 2.46 shows three $B_c(T)$ versus T curves projected onto the $J_{tr} = 0$ plane, while Fig. 2.47 presents three $J_c(T)$ versus T curves projected onto the $B_{app} = 0$ plane. Finally, Fig. 2.48 gives projections of

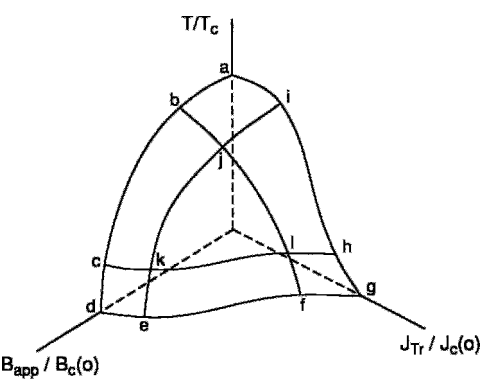

Figure 2.45 Critical surface of a superconductor. Values of applied field B_{app}, transport current J_{tr}, and temperature T corresponding to points below the critical surface, which are in the superconducting region, and points above the critical surface, which are in the normal region. The points on the surface labeled A, B , . . . , L also appear in Figs. 2.46–2.49.

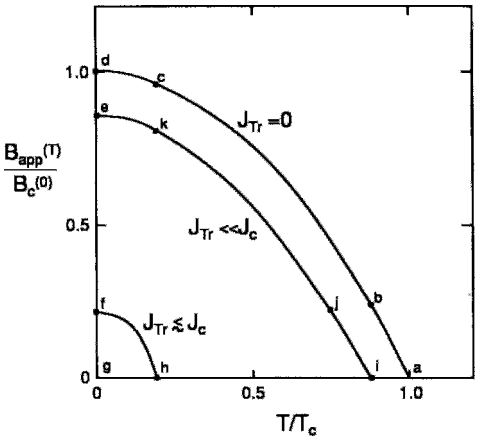

Figure 2.46 Projection of constant current curves of the critical surface of Fig. 2.45 on the B_{app}, T-plane. Projections are shown for $J_{tr} = 0$, $J_{tr} \ll J_c$, and $J_{tr} \approx J_c$. The $J_{tr} = 0$ curve is calculated from Eq. (2.56). The other two curves are drawn so as to have the same shape as the curve for $J_{tr} = 0$.

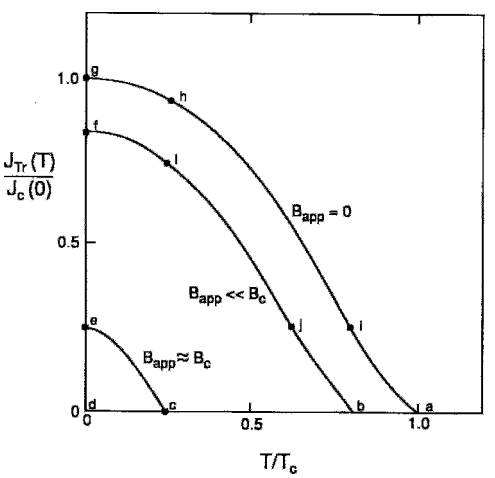

Figure 2.47 Projection of constant applied field curves of the critical surface of Fig. 2.45 onto the J_{tr}, T plane. Projections are shown for $B_{app} = 0$, $B_{app} \ll B_c$, and $B_{app} \approx B_c$. The $B_{app} = 0$ curve is calculated from Eq. (2.58). The other two curves are drawn to have the same shape as the curve for $B_{app} = 0$.

three $J_c(T)$ versus $B_c(T)$ curves onto the $T = 0$ plane. The points a, b , . . . , 1 in the various figures are meant to clarify how the projections are made. The notation $B_c(0) = B_c$ and $J_c(0) = J_c$ is used in these figures.

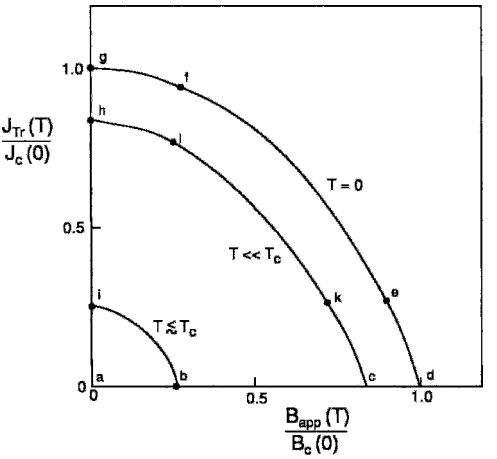

Figure 2.48 Projection of constant-temperature curves of the critical surface of Fig. 2.45 onto the J_{tr}, B_{app} plane. Projection isotherms are shown for $T = 0$, $T \ll T_c$, and $T \approx T_c$. The shapes given for these curves are guesses.

The x- and y-coordinates of this surface are, respectively, the applied magnetic field B_{app} and the applied transport current J_{tr}. The former does not include the magnetic fields that are induced by the presence of transport currents, while the latter does not include shielding currents arising from the applied fields. What the critical surface means is that at a particular temperature T there is a characteristic critical field $B_c(T)$ that will drive the superconductor normal if applied in the absence of a transport current. Similarly there is a critical current density $J_c(T)$ that will drive the superconductor normal if it is applied in zero field. In the presence of an applied field a smaller transport current will drive the superconductor normal, and if a transport current is already passing through a superconductor, a smaller applied magnetic field will drive it normal. This is evident from the three constant temperature $B_c(T)$ versus $J_c(T)$ curves shown in Fig. 2.48. One of these (h–l–k–c) is redrawn in Fig. 2.49.

It will be instructive to illustrate the significance of Figs. 2.48 and 2.49 by an example. Consider the case of a long, cylindrical superconductor of radius $R \ll L$ with

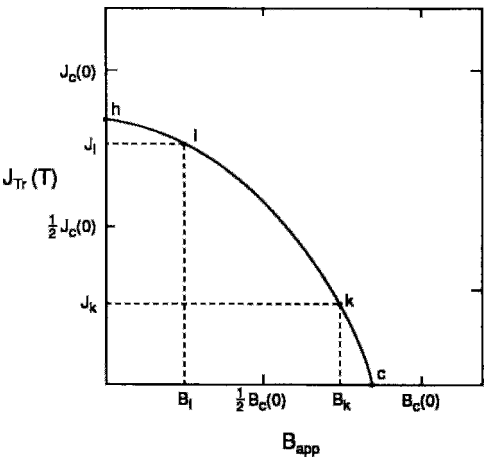

Figure 2.49 Projection of the h-l-k-c curve of Fig. 2.45 onto the $J_c(T)$ versus B_{app} plane showing the critical fields and current densities at the points k and l.

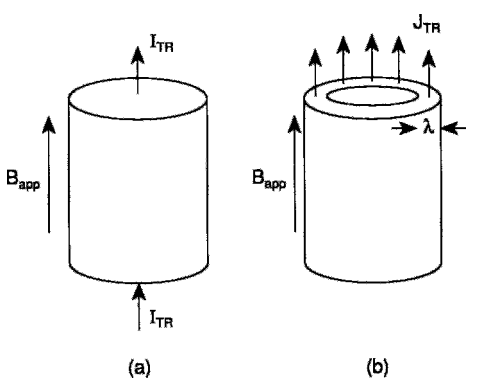

Figure 2.50 Type I superconducting cylinder (a) carrying a transport current I_{tr} of density J_{tr} in an applied magnetic field B_{app}, and (b) flow of this transport current in a surface layer of thickness λ.

an applied transport current I_{tr} flowing along its axis and located in a magnetic field B_{app} along its axis, as indicated in Fig. 2.50. This situation is analyzed by taking into account the magnetic field produced at the surface by the transport current, assuming that $J_c(T)/J_c(0) = B_c(T)/B_c(0)$ and that the normalized $J_c(T)$-versus-$B_c(T)$ curve of Fig. 2.49 is an arc of a circle.

We can see from Eq. (2.43) that the transport current produces the magnetic

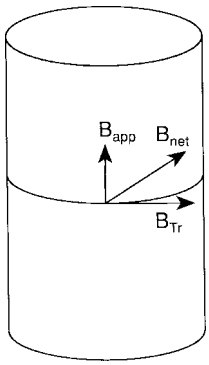

Figure 2.51 Net magnetic field B_{net} on the surface of a superconducting cylinder resulting from vector addition of the applied field B_{app} and the field B_{tr} produced by the transport current.

field B_{tr},

$$B_{tr} = \frac{\mu_0 I_{tr}}{2\pi R} \tag{2.74}$$

at the surface of the cylinder. This magnetic field is at right angles to B_{app} at the surface, as shown in Fig. 2.51, so that the net field B_{net} at the surface is the square root of the sum of the squares of B_{app} and B_{tr}:

$$B_{net} = (B_{app}^2 + B_{tr}^2)^{1/2}. \tag{2.75}$$

Using Eq. (2.74) this equation can be written explicitly in terms of the transport current:

$$B_{net} = \left[B_{app}^2 + \left(\frac{\mu_0 I_{tr}}{2\pi R} \right)^2 \right]^{1/2}. \tag{2.76}$$

The superconductor will go normal when the combination of B_{app} and I_{tr} is high enough to make B_{net} equal $B_c(T)$, the critical field for this temperature in the absence of transport currents:

$$B_c(T) = \left[B_{app}^2 + \left(\frac{\mu_0 I_{tr}}{2\pi R} \right)^2 \right]^{1/2}. \tag{2.77}$$

If we consider the case of the superconductor going normal at the point k of Fig. 2.49 then,

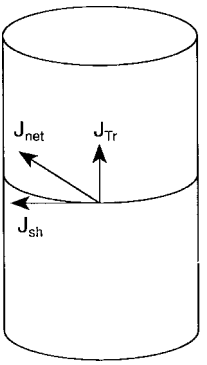

Figure 2.52 Net current density J_{net} flowing on the surface of a superconducting cylinder resulting from vector addition of the transport current density J_{tr} and the shielding current density J_{sh}.

in the notation of that figure, we have at this point,

$$B_{app} = B_k, \tag{2.78}$$

$$I_{tr} = 2\pi R\lambda J_k, \tag{2.79}$$

where in a typical experimental situation the applied quantities B_{app} and I_{tr} are often known.

This analysis was carried out by equating the vector sum of the applied field and the field arising from the transport current to the critical field $B_c(T)$. An alternate way of analyzing this situation is to equate the vector sum of the transport current density and the shielding current density to the critical current density $J_c(T)$ at the same temperature. This can be done with the aid of Fig. 2.52 to give the expression

$$J_c(T) = \left[\left(\frac{B_{app}}{\mu_0\lambda}\right)^2 + \left(\frac{I_{tr}}{2\pi R\lambda}\right)^2\right]^{1/2}, \tag{2.80}$$

which is the counterpart of Eq. (2.77).

In this section we assumed axially applied fields and currents and neglected demagnetizing effects that depend on the shape of the sample. More general cases are far more difficult to analyze.

FURTHER READING

Several superconductivity texts cover the material found in this chapter. Five of them may be cited: Kresin and Wolf, 1990; Orlando and Delin, 1991; Rose-Innes and Rhoderick, 1994; Tilley and Tilley, 1986; Tinkham, 1985. Ott (1993) surveyed the progress in superconductivity from 1980 to 1990 and provided a collection of reprinted articles. Other sources of introductory material are Hettinger and Steel (1994), Sheahan (1994), and Shi (1994). There are Landolt–Börnstein data tabulations on the classic superconductors by Flükiger and Klose (1993) and on the cuprates and related compounds by Kazei and Krynetskii (1993). The book by Hermann and Yakhmi (1993) is devoted to the thallium compounds. The Handbook of superconductivity edited by Poole (2000) contains much pertinent information.

PROBLEMS

1. A wire with a radius of 1 cm is produced from a superconductor with a transition temperature of 120 K. It is in a longitudinal magnetic field of 40 T at 60 K, and it is found that increasing the applied current to 10^3 A drives it normal. What are the values of the upper critical field, the critical current, and the critical current density for the wire at 60 K and in the limit $T \to 0$ K? Assume that B_c and B_{c2} exhibit the same temperature behavior.
2. A cylindrical superconductor of radius 200 cm with an axial hole in the center of radius 100 cm is located in a parallel magnetic field of 2 T at 300 K. It has a penetration depth of 2000 Å. What amount of flux is stored in the superconducting material and in the hole if the sample is cooled to 40 K, well below $T_c = 90$ K. If the applied field is reduced to 0.5 T, how will these stored fluxes change? What is the value of the current density on the outside surface and on the inside surface for these two cases?
3. What is the resistance of a 50-cm length of niobium wire of diameter 3 mm at 300 K? How much longer would a wire made of copper have to be in order to have the same resistance?

4. A superconducting wire 4 mm in diameter is formed into a loop of radius 7 cm. If a super current persists unchanged in this wire for 12 years, what is the approximate upper limit on the resistivity?
5. Show that Eqs. (2.59)–(2.61) provide the limiting behaviors of Eqs. (2.56)–(2.58), respectively, in the limit $T \to T_c$.
6. Show that Eqs. (2.62)–(2.64) provide the limiting behaviors of Eqs. (2.56)–(2.58), respectively, as the temperature approaches absolute zero.
7. Explain how the analysis of Fig. 2.49 that is given in Section XVI is based on the assumptions that were made concerning $J_c(T)$, $B_c(T)$, and the shape of the curve in the figure.
8. Derive Eq. (2.80).
9. Give the location of point ℓ in Fig. 2.46, of point k in Fig. 2.47, and of point j in Fig. 2.48.
10. What is the concentration of super electrons at $T = 0\,K$, $T = \frac{1}{4}T_c$, $T = \frac{1}{2}T_c$, and $T = 1.1T_c$ in a superconductor with a penetration depth of 150 nm? What is the concentration of normal conduction electrons at these temperatures?
11. A Type I superconductor has a critical field $B_c = 0.3\,T$ and a critical current density $J_c = 2 \times 10^4\,A/cm^2$ at 0 K. Find B_c, J_c, λ, and n_s at $T = \frac{1}{2}T_c$.
12. If a transport current density of $9000\,A/cm^2$ is flowing through the super-conductor of Problem 11 at 0 K, what magnetic field will drive it normal?
13. A Type I superconducting wire 3 mm in diameter has a critical field $B_c = 0.4\,T$ and a critical current density $J_c = 3 \times 10^4\,A/cm^2$ at 0 K. What is the maximum transport current that can flow through it at 0 K in an applied field of 0.35 T?
14. A Type I superconductor with $T_c = 7\,K$ has slope $dB_c/dT = 25\,mT/K$ at T_c. Estimate its critical field at $T = 6\,K$.
15. Show that for a particular temperature T a plot of the critical surface B_{app} versus $\mu_0 \lambda J_{tr}$ is an arc of a circle a distance $B_c(T)$ from the origin.
16. If it is assumed that the a direction electrical conductivity arises from the planes and that the b direction conductivity is the sum of the contributions from the planes and chains (as explained in Section 7.VI), find σ_{plane} and σ_{chain} for $YBa_2Cu_3O_7$ at 100 K and 275 K.

This page intentionally left blank

3

Classical Superconductors

I. INTRODUCTION

In this chapter we will survey the properties of various classes of elements and compounds that are superconductors below about 25 K. We will begin with the simplest group, namely the elements, and will proceed to discuss the binary, ternary, and larger compounds. Then we will treat the $A15$ compounds such as Nb_3Sn that, until the discovery of the high T_c types, produced the highest transition temperatures of all. Following this discussion we will review the Laves phases, the Chevrel phases, the chalcogenides, and the oxides.

II. ELEMENTS

Superconductivity was first observed in 1911 in the element mercury with $T_c = 4.1$ K, as shown in Fig. 2.2. Two years later lead surpassed mercury with $T_c = 7.2$ K. Niobium with $T_c = 9.25$ K held the record for highest T_c for the longest period of time, from 1930 to 1954 when the $A15$ compounds came to prominence. Other relatively high-T_c elements are Tl (2.4 K), In (3.4 K), Sn (3.7 K), Ta (4.5 K), V (5.4 K), La (6.3 K), and Tc (7.8 K), as shown in Table 3.1. Figure 3.1 shows how the super-conducting elements are clustered in two regions of the periodic table, with the transition metals on the left and the nontransition metals on the right. Some elements become superconducting only as thin films, only under pressure, or only after irradiation, as indicated in the figure.

We see from Table 3.1 that the great majority of the superconducting elements

Table 3.1 Properties of the Superconducting Elements[a]

Z	Element[b]	N_e	Crystal Structure[c]	T_c (K)	Θ_D (K)	B_c (mT)	$2B_c/T_c$ (mT/K)	γ $\left(\frac{\text{mJ}}{\text{mole K}^2}\right)$	$\chi \times 10^6$ (cm^3/mole)	λ	μ_c^*
4	Be	2	hcp	0.026	940			0.21			
13	Al	3	fcc	1.18	420	10.5	18	1.4			
21	Sc	3	hcp	0.01	470			10.9			
22	Ti	4	hcp	0.40	415	5.6	28	3.3	155	0.38	0.17
23	V	5	bcc	5.40	383	141.0	52	9.82	300	0.60	0.17
30	Zn	12	hcp	0.85	316	5.4	12	0.66			
31	Ga	3	orthr	1.08	325	5.83	11	0.60			
40	Zr	4	hcp	0.61	290	4.7	15	2.77	129	0.41	0.15
41	Nb	5	bcc	9.25	276	206.0	45	7.80	212	0.82	0.15
42	Mo	6	bcc	0.92	460	9.6	21	1.83	89	0.41	0.10
43	Tc	7	hcp	7.8	411	141.0	36	6.28	270		
44	Ru	8	hcp	0.49	580	6.9	28	2.8	39	0.38	0.14
48	Cd	12	hcp	0.517	210	2.8	11	0.69			
49	In	3	tetrg	3.41	108	28.2	17	1.67			
50	Sn(w)	4	tetrg	3.72	195	30.5	16	1.78			
57	La(α)	3	hcp	4.88	152	80.0	33	9.8			
57	La(β)	3	fcc	6.3	140	110.0	37	11.3			
71	Lu	3	hcp	0.1		<35.0					
72	Hf	4	hcp	0.13	252	1.27	20	2.2	70	0.14	
73	Ta	5	bcc	4.47	258	82.9	37	6.15	162	0.75	
74	W	6	bcc	0.015	383	0.12	16	0.90	53	0.25	
75	Re	7	hcp	1.70	415	20.0	24	2.35	68	0.37	0.10
76	Os	8	hcp	0.66	500	7.0	21	2.35	13	0.44	0.12
77	Ir	9	fcc	0.11	425	1.6	29	3.2	24	0.35	
80	Hg(α)	12	trig	4.15	88	41.1	20	1.81			
80	Hg(β)	12	tetrg	3.9	93	33.9	17	1.37			
81	Tl	3	hcp	2.38	79	17.8	15	1.47		0.80	
82	Pb	4	fcc	7.20	96	80.3	22	3.1		1.55	
90	Th	4	fcc	1.38	165	16.0	23	4.32			
91	Pa	5		1.4							
95	Am	9	fcc	1.0							

[a] N_c is as defined in Fig. 3.1; Θ_D, Debye temperature; B_c, critical field; γ, electronic specific heat parameter; χ, susceptibility; λ, electron–phonon coupling constant; μ_c^*, Coulomb pseudopotential; P, pressure; WF, work function E_q, energy gap; and $D(E_F)$, density of states at the Fermi level.
Most of the data in the table come from Roberts (1976), Vonsovsky *et al*. (1982), and *Handbook of Chemistry as Physics*, 70th edition (1989–1990).

[b] Sn is the gray diamond structure α form below 13.2 °C, and the white tetragonal β form above; La is the fcc β form above 310 °C, and the hcp α form at lower temperatures.

have crystallographic structures of very high symmetry, either face-centered cubic (10, fcc), hexagonal close-packed (15, hcp), or body-centered cubic (11, bcc), with the unit cells sketched in Fig. 3.2. The fcc and hcp structures provide the densest possible crystallographic packing, with each atom surrounded by 12 equidistant nearest neighbors. Other cases include trigonal Hg, tetragonal In, tetragonal (white) Sn, and orthorhombic Ga.

Slightly more than half of the elements that are superconducting are members of different transition series, for exam-

dT_c/dP (K/GPa)	P (GPa)	α	WF (eV)	$E_g = 2\Delta$ (meV)	E_g/kT_c	$D(E_F)$ (states, atom eV)	Z
			5.0				4
			4.3	0.35	3.4		13
			5.9				21
0.6	0–1.4		4.33			≈1.4	22
6.3	0–2.5		4.3	1.6	3.4	≈2.1	23
		0.45	4.3	0.23	3.2		30
				0.33	3.5		31
15.0	0–2.0	0	4.05			≈0.8	40
−2.0	0–2.5		4.3	3.0	3.8	≈2.1	41
−1.4	0–2.5	0.37	4.6	0.26	3.4	0.65	42
−12.5	0–1.5		5.0	2.4	3.6		43
−2.3	0–1.8	0	4.7	0.15	3.5	0.91	44
		0.5	4.2	0.14	3.2		48
			3.8	1.05	3.6		49
		0.47	4.38	1.4	4.4		50
190	0–2.3			1.5	3.5		57
110							57
				0.028	3.3		71
−2.6	0–1.0			0.044	3.9	0.83	72
−2.6				≈1.7	≈3.5	≈1.7	73
			4.5	≈0.006	≈4.5	≈0.5	74
−2.3	0–1.8	0.23		0.78	3.4	0.76	75
−1.8		0.20		0.29	4.8	0.70	76
				0.048	5.6		77
		0.50	4.52	1.7	4.6		80
							80
		0.50	3.7	0.79	3.8		81
		0.48	4.3	2.7	4.3		82
				0.41	3.4		90
							91
							95

ple, the first transition series from scandium to zinc (5), which has an incomplete $3d^n$ electron shell; the second transition series from yttrium to cadmium (8), with $4d^n$ electrons; the third such series from lutecium to mercury (8), with $5d^n$ electrons; the rare earths from lanthanum to ytterbium (3), which have an incomplete $4f^n$ electron shell; and the actinides from actinium to lawrencium (4), with $5f^n$ electrons (the number of superconductors in each class is given in parenthesis).

Among the elements niobium has the highest transition temperature, and perhaps not coincidentally it is also a constituent of higher T_c compounds such as Nb_3Ge. Niobium has not appeared prominently in the newer copper oxide superconductors.

Of the transition elements most commonly found in the newer ceramic-type superconductors, lanthanum is superconducting with a moderately high T_c (4.88 K for the α or hcp form and 6.3 K for the β or fcc form), yttrium becomes superconducting only under pressure ($T_c \approx 2$ K for pressure P in the range $110 \leq P \leq 160$ kbar), and copper is not known to super conduct. Studies of the transition temperature of copper alloys as a function of copper content have provided an extrapolated value of $T_c = 6 \times 10^{-10}$ K for

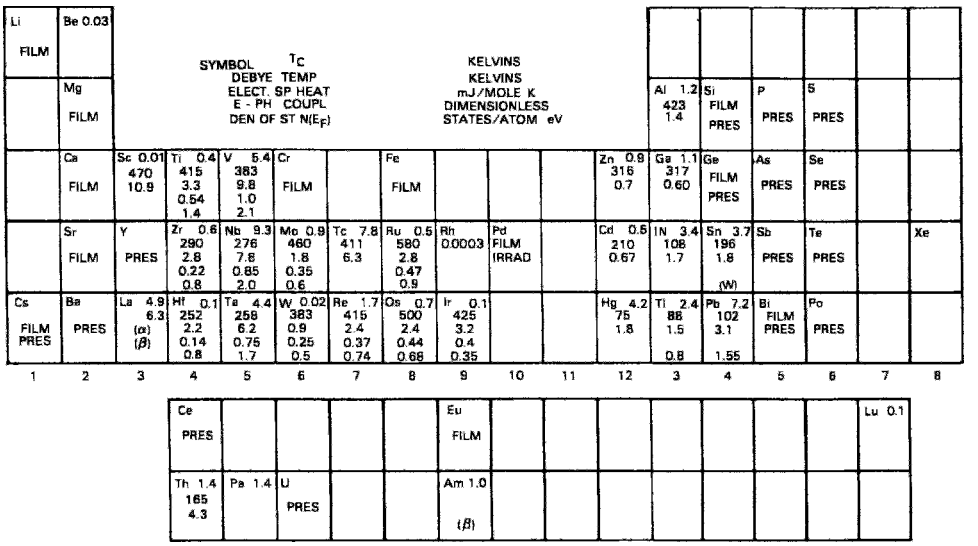

Figure 3.1 Periodic table showing the superconducting elements together with their transition temperatures T_c and some of their properties (Poole *et al.*, 1988).

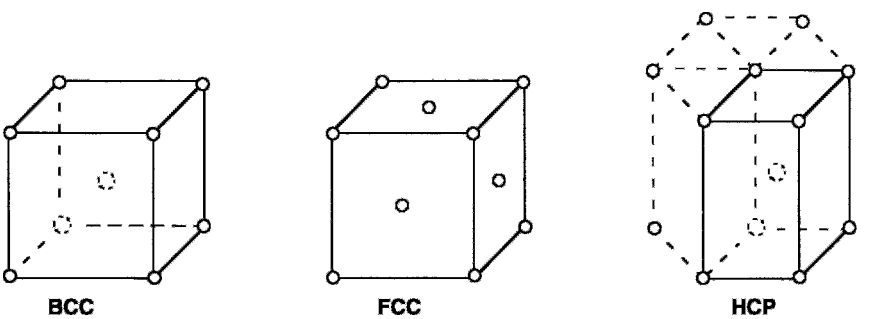

Figure 3.2 Body-centered cubic, face-centered cubic, and hexagonal close-packed unit cells.

Cu which, while nonzero, cannot be achieved experimentally. The nontransition elements oxygen and strontium present in these compounds do not superconduct, barium does so only under pressure ($T_c = 1\,\mathrm{K}$ to $5.4\,\mathrm{K}$ under pressures from 55 to 190 kbar), bismuth likewise superconducts under pressure, and thallium is a superconductor with $T_c = 2.4\,\mathrm{K}$. Lead, added in low concentrations to stabilize the bismuth and thallium high-T_c compounds, is also a well-known elemental superconductor. Thus the superconducting properties of the elements are not always indicative of the properties of their compounds, although niobium seems to be an exception.

III. PHYSICAL PROPERTIES OF SUPERCONDUCTING ELEMENTS

Figure 3.1 gives the transition temperature T_c, Debye temperature Θ_D, Sommerfeld constant, or normal-state electronic specific heat constant γ from Eq. (1.51), $C_e = \gamma T$, dimensionless electron–phonon coupling constant λ (cf. Chapter 6), and density of states $D(E_F)$ at the Fermi level (1.42)

for different elemental superconductors. The columns of the periodic table are labeled with the number of (valence) electrons N_e outside the closed shells. Table 3.1 lists various properties of some of these elements.

When an element has more than one isotope, the transition temperature often decreases with increasing isotopic mass M in accordance with the relation

$$M^{\alpha}T_c = \text{constant}, \qquad (3.1)$$

where $\alpha = 1/2$ for the simplified BCS model described in Chapter 7. This is to be expected for a simple metal because the phonon frequency is proportional to the square root of the atom's mass. However electron–phonon coupling can also be mass dependent, and deviations from Eq. (3.1) are not unusual.

Some elemental superconductors have isotope effect coefficients α close to 1/2, such as Hg (0.50), Pb (0.48), Sn (0.47), and Zn (0.45). Most values of α listed in Table 3.1 for the transition metal superconductors are less than this BCS-theory estimate. For the two metals zirconium and ruthenium, both with $T_c < 0.1\,\text{K}$, α is zero to within experimental error.

The BCS theory predicts that twice the energy gap 2Δ of a superconductor is 3.52 times $k_B T_c$ (cf. Chapter 7, Section VI) and from the data in Table 3.1 it is clear that this prediction is fairly well satisfied for the elements. In rhenium the energy gap is anisotropic, varying between 2.9 and $3.9\,k_B T_c$, depending upon the direction. The anisotropies found for molybdenum and vanadium are half as large and almost within the experimental accuracy.

It has been found that some of the properties of an element correlate with the number N_e of its valence electrons in the same manner as the transition temperature (Vonsovsky *et al.*, 1982). Here N_e is the number of electrons outside the filled shells corresponding to the configuration of the next lower noble gas. Figure 3.3 shows that T_c is a maximum for transition metals with five and seven valence electrons; Figs. 3.4, 3.5, 3.6, and 3.7 show that the Sommerfeld factor γ of the conduction-electron heat capacity $C_e = \gamma T$, the magnetic susceptibility $\chi = M/\mu_0 H$, the square of the

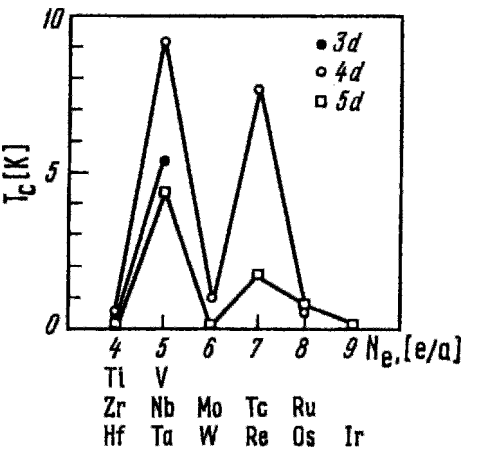

Figure 3.3 Dependence of transition temperature on the number of valence electrons N_e in the superconducting transition elements (Vonsovsky *et al.*, 1982, p. 184).

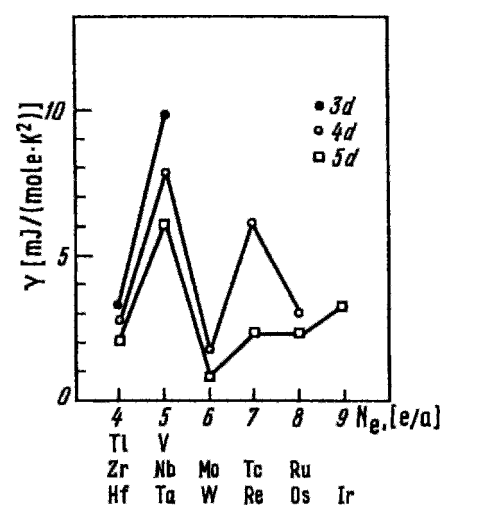

Figure 3.4 Dependence of electronic specific heat γ on N_e, as in Fig. 3.3 (Vonsovsky *et al.*, 1982, p. 184).

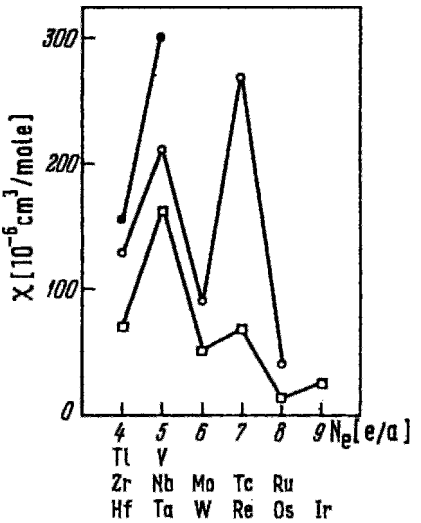

Figure 3.5 Dependence of magnetic susceptibility χ on N_e, as in Fig. 3.3 (Vonsovsky *et al.*, 1982, p. 185).

inverse of the Debye temperature Θ_D, and the electron–phonon coupling constant λ defined by Eq. (7.96) all exhibit similar behavior. These quantities, together with the dimensionless screened Coulomb interaction

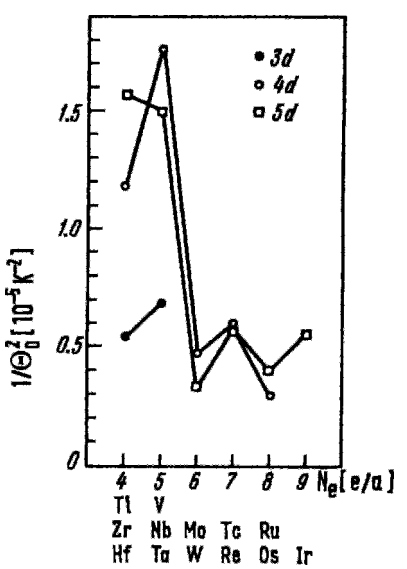

Figure 3.6 Dependence of inverse Debye temperature squared $1/\Theta_D^2$ on N_e, as in Fig. 3.3 (Vonsovsky *et al.*, 1982, p. 185).

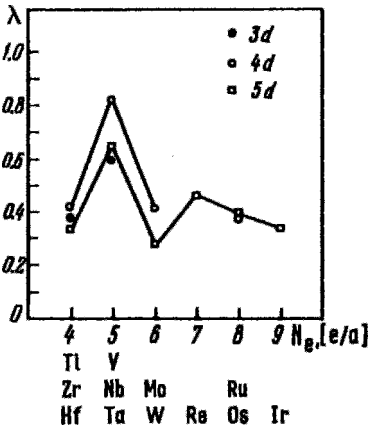

Figure 3.7 Dependence of electron–phonon coupling constant λ on N_e, as in Fig. 3.3 (Vonsovsky *et al.*, 1982, p. 211).

parameter μ_C^* (cf. Chapter 6), are tabulated in Table 3.1 for the superconducting elements. The correlation of the melting points of the transition metals, as plotted in Fig. 3.8, with the number of valence electrons N_e tends to be opposite to the correlation of T_c with N_e—thus the highest melting points occur for six valence electrons for which T_c is the lowest in each series.

The chemical bonding of the transition metals is mainly ionic, but there can also be contributions of a covalent type. The

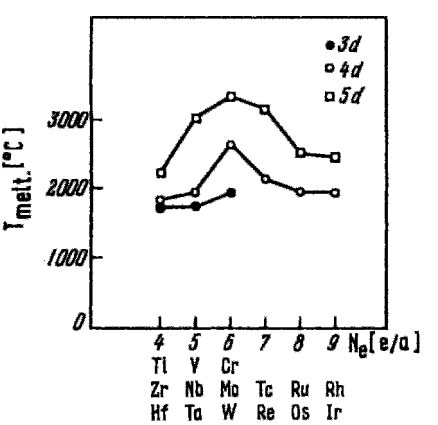

Figure 3.8 Dependence of melting temperature on N_e, as in Fig. 3.3 (Vonsovsky *et al.*, 1982, p. 186).

amount of covalency is particularly strong in the two metals molybdenum and tungsten, each of which has five valence electrons. This fact has been used to account for the low- transition temperatures of these tw elements.

Another important electronic parameter of a metal is its density of states $D(E_F)$ at the Fermi level, and Table 3.1 lists values of $D(E_F)$ for different elements. In several cases the value in the table is an average of several determinations with a large amount of scatter. For example, four reported values for niobium of 1.6, 1.8, 2.1, and 2.7 are given by Vonsovsky *et al*. (1982, p. 202) along with a rounded-off average of 2.1 states/atom eV. These large scatters lead one to suspect the accuracy of cases in which only one determination is available. The *d* electrons dominate this density of states, with small contributions from the remaining valence electrons. For example, in vanadium the percentage contributions to $D(E_F)$ from the *s, p, d*, and *f* electrons are 1%, 14%, 84%, and 1%, respectively, while for niobium the corresponding percentages are 3%, 14%, 81%, and 2%.

When a metal is subjected to high pressure, the density of states at the Fermi level changes. This change may be detected by the change in the conduction-electron heat capacity factor γ, since from Eq. (1.52) γ is proportional to $D(E_F)$. Sometimes the derivative dT_c/dP is positive, as in the case of vanadium (see curve for vanadium plotted in Fig. 3.9), so that here T_c increases with increasing pressure, and sometimes it is negative, as with tantalum (cf. Fig. 3.9), where high pressures lead to lower values of T_c. With some elements the situation is more complicated. For example, when niobium is subjected to high pressure T_c decreases until about 40 kbar is reached, then it begins to increase with increasing pressure and, eventually, above 150 kbar, surpasses its atmospheric value, as indicated in Fig. 3.9. Finally some elements, such as P, As, Se, Y, Sb, Te, Ba, Ce, and U, become superconducting only when subjected to high pressure.

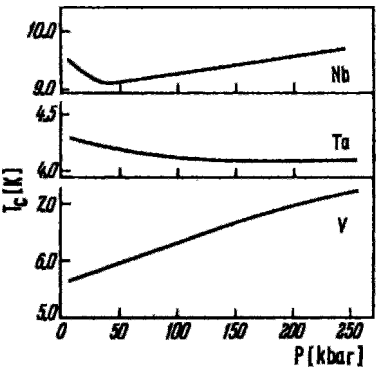

Figure 3.9 Dependence of transition temperature T_c on pressure for the elements Nb, Ta, and V (Vonsovsky *et al*., 1982, p. 188).

T_c of some transition metals rises dramatically when the metal is in the form of thin films made by ion sputtering on various substrates. For example, the transition temperature of tungsten (bulk value 0.015 K) rises to 5.5 K in a film, that for molybdenum (bulk value 0.915 K) rises to 7.2 K, and that for titanium (bulk value 0.40 K) rises to 2.52 K. Chromium and lithium only superconduct in the thin-film state, while other nonsuperconductors such as Bi, Cs, Ge, and Si can be made to superconduct either by applying pressure or by preparing them as thin films. Figure 3.1 summarizes this information.

IV. COMPOUNDS

Superconductivity workers sometimes use the old Strukturbericht notation which uses the letter *A* to denote elements, *B* for *AB* compounds, *C* for AB_2 compounds, and *D* for A_mB_n binary compounds, with additional letters assigned to compounds containing three or more dissimilar atoms. Superconductors of the class Nb_3Sn were originally assigned to the β-W structure (Wyckoff, 1963, p. 42), which has

two types of tungsten atoms, one type in the center and the other six on the faces of the cubic unit cell; these A_3B compounds came to be called the *A*15 compounds. The notation has endured despite the fact that other compounds such as UH_3 and Cr_3Si had been assigned to this structure (Wyckoff, 1964, p. 119) before Pearson described the notation in the 1958 Handbook. This notation is no longer widely used outside the superconducting community.

Several structures contain a large number of superconductors. Table 3.2 presents data on the principal superconductors, together with the transition temperature of a representative compound from each group. The table provides the Strukturbericht symbol, T_c of a prototype compound, and the number of superconducting compounds that are found in the listings of Phillips (1989a) and Vonsovsky *et al*. (1982) for each group.

All of the known nonradioactive elements are constituents of at least one superconducting compound, as Table 3.3 shows. The table catalogs the structure types with binary superconducting compounds, and gives the value of

Table 3.2 Structure Types and Transition Temperatures of Representative Compounds of each Type[a]

Structure and Type	Example	T_c (K)	Nbr	Type	Reference[c]
*B*1, NaCl, fc cubic	MoC	14.3	26	a	Ph, 336, 369; Vo, 393
*B*2, CsCl, bc cubic	VRu	5.0	10	b	Ph, 362; Vo, 385
*B*13, MnP, *ortho*	GeIr	4.7	10	c	Ph, 341
*A*12, α-Mn, bc cubic	$Nb_{0.18}Re_{0.82}$	10	15	d	Ph, 368; Vo, 388
$B8_1$, NiAs, hex	$Pd_{1.1}Te$	4.1	18	e	Ph, 354
$D10_2$, Fe_3Th_7, hex, 3–7 compound	B_3Ru_7	2.6	12	f	Ph, 359
$D8_b$, CrFe, tetrag, σ-phase	$Mo_{0.3}Tc_{0.7}$	12.0	27	g	Ph, 347, Vo, 388
*C*15, $MgCu_2$, fc cubic, Laves	HfV_2	9.4	40	h	Ph, 370; Vo, 375
*C*14, $MgZn_2$, hex, Laves	$ZrRe_2$	6.8	19	i	Ph, 357; Vo, 375
*C*16, Al_2Cu, bc tetrag	$RhZr_2$	11.3	16	j	Ph, 350
*A*15, UH_3[b], cubic	Nb_3Sn	18	60	k	Ph, 336, 363; Vo, 259
LI_2, $AuCu_3$, cubic	La_3Tl	8.9	24	l	Ph, 362
Binary heavy fermions	UBe_{13}	0.9	9	m	Table 3.10
Miscellaneous binary compounds	MoN	14.8	170	n	Ph, Appendix C
*C*22, Fe_2P, Trig	HfPRu	9.9	11	o	Ph, 357
$E2_1$, $CaTiO_3$, cubic, perovskite	$SrTiO_3$	0.3		p	
HI_1, $MgAl_2O_4$, cubic, spinel	$LiTi_2O_4$	13.7	3	q	Ph, 339; Vo, 431
B_4CeCo_4, tetrag, ternary boride	YRh_4B_4	11.9	10	r	Ph, 347; Vo, 415
$PbMo_6S_8$, trig, Chevrel	$LaMo_6Se_8$	11.4	88	s	Ph, 361; Vo, 418
$Co_4Sc_5Si_{10}$, tetrag	$Ge_{10}As_4Y_5$	9.1	11	t	Ph, 348
fcc, buckminsterfullerene	$C_{60}Rb_2Cs$	31	12	u	

[a] The at one time important but now antiquated Pearson (1958) symbols (e.g., *A*15) are given for most of the structures. The numbers of compounds listed in column 4 were deduced from data given in the references of column 6.

[b] *A*15 is sometimes called the β-Mn or the Cr_3Si structure.

[c] Ph and Vo followed by page numbers denote the references Phillips (1989a) and Vonsovsky *et al*. (1982), respectively. Additional data may be found in Roberts (1976).

Table 3.3 Number of Superconducting Binary Compounds A_mB_n of the Elements Discussed in the Literature, and T_c of a Representative Compound of each Element among the Classical Superconductors (see column 5 of Table 3.2 for key to the compound types)

Element			Binary Compounds		Representative Compound		
Z	**Symbol**	**T_c (K)[a]**	**Number**	**Types**	**Compound**	**T_c (K)**	**Type**
1	H	—	1	n	HNb_2	7.3	n
2	Li	—	2	n	$LiTi_2O_4$	13.7	q
11	Na	—	3	n u	$Na_2Mo_6S_8$	8.6	s
19	K	—	2	h u	Bi_2K	3.58	h
37	Rb	—	2	h u	$C_{60}Rb_2K$	24	u
55	Cs	1.5^P	2	h u	Bi_2Cs	4.8	h
4	Be	8.6^F	1	n	BeTc	5.2	n
12	Mg	—	7	b n	HgMg	1.4	b
20	Ca	0.52	6	h l n	Au_5Ca	0.38	n
38	Sr	—	2	h	Rh_2Sr	6.2	h
56	Ba	5.0^P	3	n	$BaBi_{0.2}O_3Pb_{0.8}$	4.5	p
5	B	—	12	a f j r n	B_4LuRh_4	11.7	r
13	Al	1.18	17	d g h j k l m n	Nb_3Al	19	k
31	Ga	1.08	13	c j k l n	Nb_3Ga	21	k
49	In	3.41	9	a c k l n	V_3In	13.9	k
81	Tl	2.38	6	l n	$TlMo_6Se_8$	12.2	s
6	C	—	14	a n u	$C_{60}Rb_2Cs$	32	u
14	Si	6.7	14	c h k n	Nb_3Si	19	k
32	Ge	5.3	18	a c k m n	Nb_3Ge	23.2	k
50	Sn	3.7	16	a c k l m n	Nb_3S_n	18	k
82	Pb	7.20	13	h j k l n	Ta_3Pb	17	k
7	N	—	11	a n	NbN	17.3	a
5	P	5.8^P	6	n	PbP	7.8	n
33	As	0.5^P	9	c k n	$Ge_{10}As_4Y_5$	9.1	t
51	Sb	2.7^P	8	k n	Ti_3Sb	5.8	k
83	Bi	6.1^F	25	c e h l n	$BaBi_{0.2}O_3Pb_{0.8}$	4.5	p
8	O	—	4	a n	$LiTi_2O_4$	13.7	q
16	S	—	7	a n	$Sn_{0.6}Mo_6S_4$	14.2	s
34	Se	6.9^P	7	a n	$TlMo_6Se_8$	12.2	s
52	Te	3.9^P	12	a e i n	$Mo_6S_{4.8}Te_{3.2}$	2.5	s
9	F	—	0	—	$F_{0.12}K_{0.1}Li_{0.02}O_{2.88}W$	1.1	n
17	Cl	—	0	—	$Cl_3Mo_6Se_8$	9.1	s
35	Br	—	0	—	$Br_2Mo_6S_6$	13.8	s
53	I	—	0	—	$I_2Mo_6S_6$	14.0	s
21	Sc	0.01	10	b d h i n	$ScMo_6S_8$	3.6	s
22	Ti	0.40	10	a b d k n	$LiTi_2O_4$	13.7	q
23	V	5.40	21	a b g h k	V_3Si	17.2	k
24	Cr	—	7	g h k	Cr_3Os	4.68	k
25	Mn	—	9	b c j k m n	Mn_3Si	12.5	k
26	Fe	—	5	f g n	Fe_3Re_2	6.6	g
27	Co	—	12	d f g j n	$CoZr_2$	6.3	j
28	Ni	—	5	f j k n	Ni_3Th_7	1.98	f
29	Cu	—	8	b j m n	$Cu_{1.8}Mo_6S_8$	10.8	s
30	Zn	0.85	5	n	$Mo_{6.6}S_8Zn_{11}$	3.6	s
39	Y	2.5^P	20	a b f h i l n	B_4YRh_4	11.3	r

(*Continued*)

Table 3.3 (*Continued*)

Element			Binary Compounds		Representative Compound		
Z	**Symbol**	**T_c (K)[a]**	**Number**	**Types**	**Compound**	**T_c (K)**	**Type**
40	Zr	0.61	25	a d g h i j k l n	ZrN	10.7	a
41	Nb	9.25	41	a c d g h j k n	Nb_3Ge	23.2	k
42	Mo	0.92	24	a d g h k m n	Tc_3Mo	15.8	g
43	Tc	7.8	6	d g k n	Tc_3Mo	15.8	g
44	Ru	0.49	18	b f g h i k n	HfPRu	9.9	o
45	Rh	—	32	c f g h j k n	B_4LuRh_4	11.7	r
46	Pd	—	28	c d e g j k n	Bi_2Pd_3	4.0	e
47	Ag	—	6	n	$Ag_{1.6}Mo_{6.4}S_8$	9.1	s
48	Cd	0.517	1	n	CdHg	1.77	n
71	Lu	1.0	6	b h i l n	B_4LuRh_4	11.7	r
72	Hf	0.13	10	a d h i n	HfV_2	9.4	h
73	Ta	4.47	18	a c d g j k n	Ta_3Pb	17	k
74	W	0.015	12	a d g k n	W_3Re	11.4	k
75	Re	1.7	24	a d f g h i k n	Mo_3Re	15	k
76	Os	0.66	20	b d f g h i j k	$LaOs_2$	6.5	i
77	Ir	0.11	30	d f g h i k m n	$Ir_{0.4}Nb_{0.6}$	10	d
78	Pt	—	23	b c e f g h k m n	Nb_3Au	11.5	k
79	Au	—	17	b c h j k n	Ta_3Au	16	k
80	Hg	4.15	10	n	Hg_2Mg	4.0	n
57	La	4.9	21	a h n	$LaMo_6S_8$	7.1	s
58	Ce	1.7^P	4	h m n	B_4LuRh_4	11.7	r
59	Pr	—	0		$PrMo_6S_8$	4.0	s
60	Nd	—	0		$NdMo_6Se_8$	8.2	s
61	Pm	—	0				
62	Sm	—	0		B_4SmRh_4	2.7	r
63	Eu	—	1	n	$Eu_{0.012}La_{0.988}$	0.2	n
64	Gd	—	0		$GdMo_6Se_8$	5.6	s
65	Tb	—	0		$TbMo_6Se_8$	5.7	s
66	Dy	—	0		$Dy_{1.2}Mo_6Se_8$	8.2	s
67	Ho	—	0		$Ho_{1.2}Mo_6Se_8$	6.1	s
68	Er	—	0		B_4ErRh_4	8.7	r
69	Tm	—	0		B_4TmRh_4	9.8	r
70	Yb	—	0		$Yb_{1.2}Mo_6Se_8$	6.2	s
90	Th	1.38	27	a f h i j l n	Pb_3Th	5.55	l
91	Pa	1.4	0				
92	U	1.0	9	l m n	UPt_3	0.43	m

[a] P denotes T_c measured under pressure, and F indicates measurement on thin film.

T_c for a representative superconductor of each element. It is clear that transition temperatures above 10 K are widely distributed among the elements and compounds.

On the whole, there is a tendency for the superconducting materials to be stoichiometric, i.e., with ratios of the constituent elements generally integral. Even some of the solid solutions, such as $Nb_{0.75}Zr_{0.25}$ and $Nb_{0.75}Ti_{0.25}$, have atom ratios that are easily expressed in terms of integers (Nb_3Zr and Nb_3Ti), though others, such as $Mo_{0.38}Re_{0.62}$, do not fit this format. Indeed, T_c is often sensitive to stoichiometry, and experiments in which Nb_3Ge gradually approached stoichiometry raised its measured T_c from 6 K

to 17 K and, finally, to the previous record value of 23.2 K. Other materials have undergone the same evolution with the approach to ideal stoichiometry, such as Nb_3Ga (T_c going from 14.9 to 20.3 K), V_3Sn (T_c from 3.8 to 17.9 K), and V_3Ge (T_c increasing from 6.0 to 11.2 K). In contrast, there are compounds, such as Cr_3Os, Mo_3Ir, Mo_3Pt, and V_3Ir, in which the highest T_c does not occur at the ideal stoichiometric composition and in which T_c is generally less dependent on composition. For example $T_c = 0.16$ K in stoichiometric Cr_3Ir but $T_c = 0.75$ K in $Cr_{0.82}Ir_{0.18}$. Although less prevalent among the older superconducting types, this phenomenon is not unusual among the newer superconductors (cf. Vonsovsky *et al.*, 1982, for more details).

V. ALLOYS

An alloy is a solid solution or mixture in which the constituent atoms are randomly distributed on the lattice sites. An intermetallic compound, on the other hand, contains definite ratios of atoms that are crystallographically ordered in the sense that there is a unit cell that replicates itself throughout space to generate the lattice. Some alloys become ordered for particular ratios of atoms. Both random and ordered materials can become superconducting.

First we will consider the random binary alloys. In these types of alloys two transition elements are mixed in all proportions. There are several possibilities for the transition temperature of such an alloy: it can be higher than that of both elements, between the T_c values of the constituents, or lower than either constituent taken by itself. The curve of T_c versus binary alloy concentration can be close to a straight line, concave downwards with a minimum, or concave upwards with an intermediate maximum value. These three alternatives are illustrated in Fig. 3.10. The figure shows how T_c varies with Nb content when niobium is alloyed with any one of the transition elements V, Zr, Mo, Ta, or W, with the plots arranged in the order in which the five transition elements are distributed around niobium in the periodic table. We see from Fig. 3.10 that the transition temperature reaches a maximum with an alloy containing 25 at-% zirconium. The figure also shows that it can be very small for alloys with Zr, Mo, or W.

To gain some understanding of the shapes of these curves systematic studies involving sequences of transition metals that are adjacent to each other in the periodic table have been carried out. (See Vonsovsky *et al.*, 1982.) The results indicate that T_c varies with the number of valence electrons N_e in the manner illustrated in Fig. 3.11. The curves have two maxima of T_c, one near $N_e = 4.7$ and one near $N_e = 6.5$. The peak in the Nb versus Zr plot of Fig. 3.10 occurs close to $N_e = 4.7$. Amorphous alloys exhibit only one maximum for each series, as indicated in Fig. 3.12. Other properties, such as the electronic specific-heat factor γ that was defined in Eq. (1.51), magnetic susceptibility χ, and pressure derivative dT_c/dP have the dependences on electron concentration that are illustrated in Figs. 3.13, 3.14, and 3.15, respectively. The specific heat and susceptibility plots are similar to the T_c versus N_e graph of Fig. 3.11.

In addition to the correlation of the transition temperature with the valence electron concentration, there is also a correlation with the lattice properties. The body-centered cubic structure is the stable one for Ne in the range from 4.5–6.5, with hcp the stable structure outside this range, as shown in Fig. 3.16. The peaks in the plot of T_c versus N_e occur at the boundaries of instability—i.e., where a lattice rearrangement transition can occur between the two structure types. The lowest T_c occurs (Fig. 3.11) for $N_e \approx 5.5$–6, which is also where the bcc structure is most stable.

The alloy types listed in Table 3.2 are binary; most of them having their component elements in an atom ratio of 1 : 1, 1 : 2,

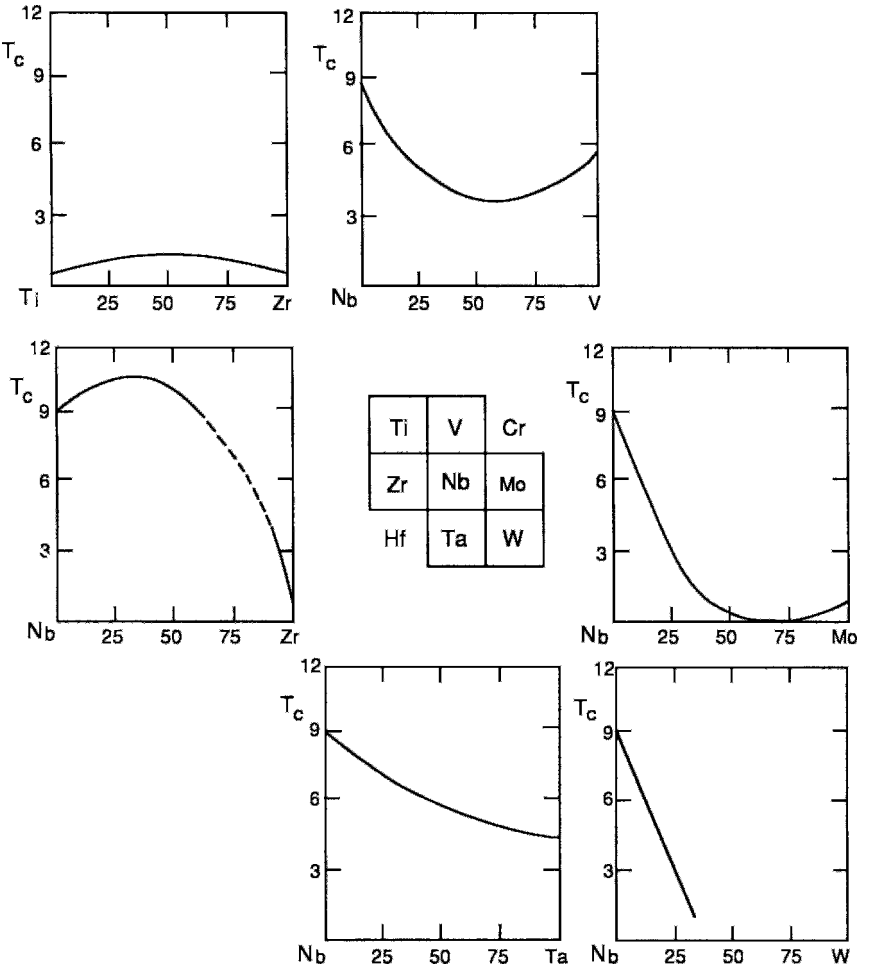

Figure 3.10 Dependence of transition temperature T_c on concentration for binary alloys of Nb with adjacent transition elements in the periodic table. The abscissae are expressed in percentages (adapted from Vonsovsky *et al.*, 1982, pp. 234, 235).

or 1 : 3. In most cases at least one constituent is an elemental superconductor, and sometimes (e.g., $NbTc_3$, VRu) both elements superconduct. Occasionally, more than one intermetallic stoichiometry (e.g., $RhZr_2$ and $RhZr_3$, Nb_3Ge and $NbGe_2$) is superconducting. The binary superconductors in Table 3.2 have T_c values higher than the highest T_c of their constituents, although even here VRu is an exception. The high-T_c semiconducting and layered compounds tend to be binary also. Some of the compounds in Table 3.2 are ternary types and even $Lu_{0.75}Th_{0.25}Rh_4B_4$ is really the ternary compound MRh_4B_4 with Lu occupying three-quarters and Th one-quarter of the M sites.

VI. MIEDEMA'S EMPIRICAL RULES

Matthias (1953, 1955) interpreted the shape of the curve of T_c versus N_e as indicating the presence of favorable and unfavorable regions of N_e and suggested rules

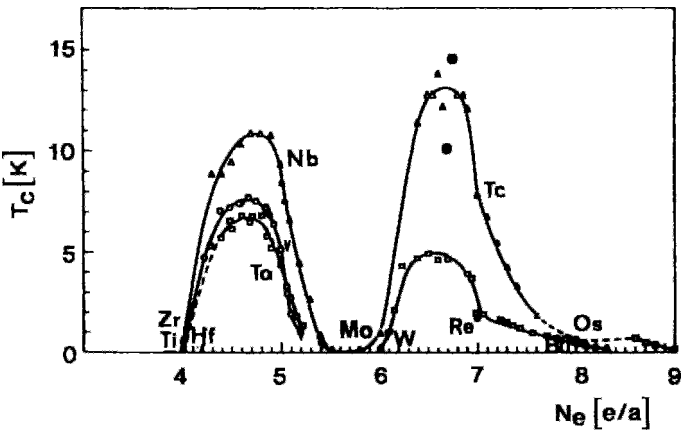

Figure 3.11 Dependence of transition temperature T_c on the number of valence electrons N_e in solid solutions of adjacent $3d(\bigcirc)$, $4d(\Delta)$, and $5d(\square)$ elements in the periodic table. Dark symbols are for pure elements (Vonsovsky *et al.*, 1982, p. 239).

for explaining the T_c-versus-concentration curves. One rule, for example, explains the increase of T_c in terms of the shift of N_e toward more favorable values; thus $N_e = 5$(V, $T_c = 5.4$ K; Nb, $T_c = 9.3$ K; Ta, $T_c = 4.5$ K) and $N_e = 7$ (Tc, $T_c = 7.8$ K, Re, $T_c = 1.7$ K).

Miedema (1973, 1974) proposed an empirical method of correlating the concentration dependence of the transition temperature and other physical characteristics of alloys. The method assumes that the density of states $D(E_F)_{AB} = D_{AB}$ at the Fermi level of an alloy AB is an additive function of its constituents,

$$D_{AB} = f_A D_A(N_A) + f_B D_B(N_B), \qquad (3.2)$$

where f_A and f_B are the mole fractions of the components A and B, and the densities of states D_A and D_B depend on the number of valence electrons N_A and N_B of atoms A and B, respectively (cf. Vonsovsky *et al.* (1982, Section 5.4) for evaluation of the

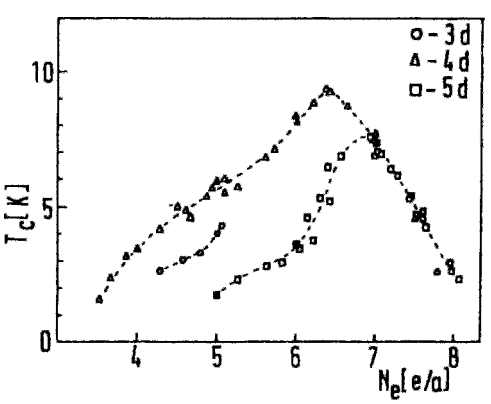

Figure 3.12 Dependence of transition temperature T_c on the number of valence electrons N_e in amorphous alloys of $3d$, $4d$, and $5d$ elements, using the notation of Fig. 3.11 (Vonsovsky *et al.*, 1982, p. 241).

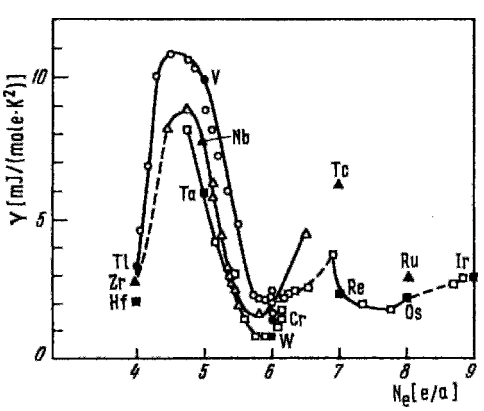

Figure 3.13 Dependence of electronic specific heat γ on N_e, as in Fig. 3.11 (Vonsovsky *et al.*, 1982, p. 237).

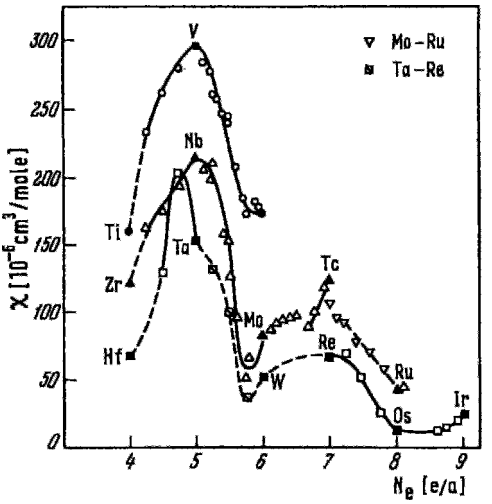

Figure 3.14 Dependence of magnetic susceptibility χ on N_e, as in Fig. 3.11. Points are plotted for Mo–Ru instead of Tc–Ru, and for Ta–Re instead of Ta–W for the same N_e, since data were not available for the preferred adjacent elements (Vonsovsky *et al.*, 1982, p. 242).

N_i dependences of the functions D_i and γ_i in Eq. (3.2)). Equation (1.52) permits us to write a similar expression for the electronic heat capacity factor γ:

$$\gamma_{AB} = f_A \gamma_A(N_A) + f_B \gamma_B(N_B). \qquad (3.3)$$

The density of states and γ depend upon the number of valence electrons per atom N_i in a similar manner for the $3d$, $4d$, and $5d$ transition ion series. Some electron concentration is transferred between the atoms during alloying, so that the number of valence electrons of the ith component N_i differs from its free atom value N_{ei} by the factor

$$N_i = N_{ei} + K\Delta\phi(1 - f_i), \qquad (3.4)$$

where $\Delta\phi$ is the difference between the work functions (cf. Chapter 15, Section II, A) of the two pure metals involved in the alloy. Table 3.1 lists the work functions of the superconducting elements. Empirical expressions similar to Eqs. (3.2) and (3.3) have been written for the electron–phonon coupling constant λ_{AB},

$$\lambda_{AB} = f_A \lambda_A(N_A) + f_B \lambda_B(N_B), \qquad (3.5)$$

and for the quantity $[\ln(T_c/\Theta_D)]^{-1}$ for the binary alloys,

$$\frac{1}{[\ln(T_c/\Theta_D)]_{AB}} = \frac{f_A}{[\ln(T_c/\Theta_D)]_A} + \frac{f_B}{[\ln(T_c/\Theta_D)]_B}. \qquad (3.6)$$

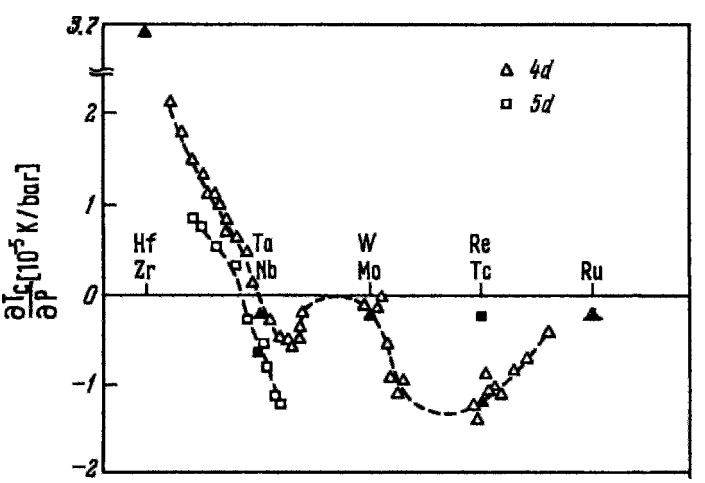

Figure 3.15 Dependence of pressure derivative dT_c/dP on N_e in alloys of adjacent $4d$ and $5d$ elements, following Fig. 3.11 (Vonsovsky *et al.*, 1982, p. 238).

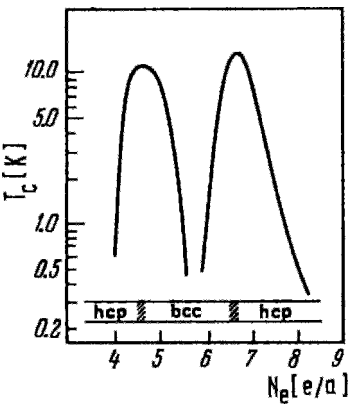

Figure 3.16 Sketch of the structure dependence of the transition temperature for alloys of adjacent transition elements, showing how T_c peaks at the boundaries between structure types (Vonsovsky *et al.*, 1982, p. 245).

Figure 3.17 shows that the agreement of Eqs. (3.3) and (3.6) with experiment is good for four isoelectronic alloy systems over the entire solid solution range. We see from this figure that the linear approximation obtained by setting $K = 0$ in Eq. (3.4), hence replacing N_i by N_{ei} in Eqs. (3.2)–(3.6), does not agree with experiment.

VII. COMPOUNDS WITH THE NaCl STRUCTURE

The $B1$ class of AB superconductors has the metallic atoms A and nonmetallic atoms B arranged on a sodium chloride-type lattice that consists of two interpenetrating fcc lattices with each atom of one type in the center of an octahedron whose vertices are occupied by atoms of the other type, as indicated in Fig. 3.18. As of 1981, 26 $B1$ compounds (out of the 40 $B1$ compounds that had been tested) had been found to be superconducting. The carbides AC and nitrides AN, such as NbN with $T_c = 17\,\mathrm{K}$ (Kim and Riseborough, 1990), had the 12 highest transition temperatures, while the metallic A atoms with T_c values above 10 K were Nb, Mo, Ta, W, and Zr. Niobium always seems to be the best! Three examples of superconducting NaCl-type compounds are given in Tables 3.2 and 3.3.

The NaCl-type superconductors are compositionally stoichiometric but not structurally so. In other words, these compounds have a small to moderate concentration of vacancies in the lattice, as indicated in Table 3.4. We see from the table that YS has

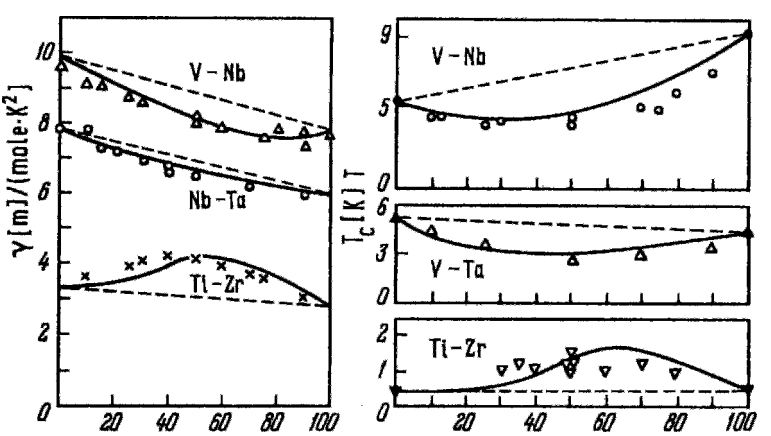

Figure 3.17 Comparison of calculated (—) and experimental (symbols) values of the specific heat coefficient γ and the transition temperature T_c for four isoelectronic binary alloys. The linear approximation (- - - -), which is obtained by setting $N_i = N_{ei}$ in Eqs. (3.3) and (3.6), does not fit the data very well (Vonsovsky *et al.*, 1982, p. 250).

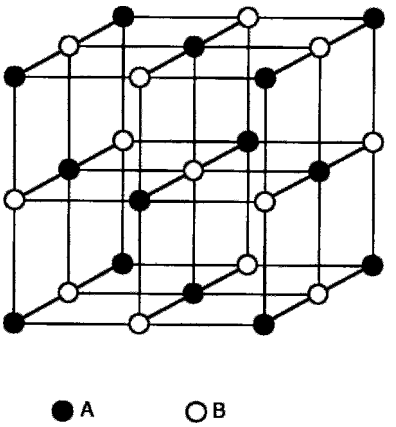

Figure 3.18 Structure of NaCl in which each atom of one type (○ or ●) is in the center of an octahedron whose vertices are occupied by atoms of the other type (● or ○).

10% vacancies, which means that its chemical formulae should properly be written $Y_{0.9}S_{0.9}$. Nonstoichiometric NaCl-type compounds, such as $Ta_{1.0}C_{0.76}$, also exist.

Ordinarily the vacancies are random, but sometimes they are ordered on the metalloid (e.g., $Nb_{1.0}C_{0.75}$) or on the metallic (e.g., $V_{0.763}O_{1.0}$) sublattice, and can also produce a larger unit cell in, for example, $Ti_{1.0}O_{0.7}$. The vacancies can also be ordered on both sublattices in stoichiometric compounds, such as $Nb_{0.75}O_{0.75}$. Table 3.5 lists several NaCl-type compounds with ordering of the vacancies. It has been found that the metallic and nonmetallic atoms can be absent over broad composition ranges.

Table 3.4 Percentage of Vacancy Concentration $100(1-x)$ in Stoichiometric Compounds A_xB_x with NaCl Structure[a]

A_x \ B_x	C	N	O	S	Se
Ti	2	4.0	15		
V	8.5	1.0	11–15		
Y				10	
Zr	3.5	3.5		20	16
Nb	0.5–3.0	1.3	25		
Hf	4				
Ta	0.5	2.0			

[a] After Vonsovsky *et al.*, 1982.

Table 3.5 Nonstoichiometric Compounds A_xB_y with NaCl Structure with Vacancy Ordering on One Sublattice and Stoichiometric Compounds A_xB_x with this Structure (shown in square brackets) with Vacancy Ordering on Two Sublattices[a]

A_x \ B_x	C	N	O
Ti			$Ti_{1.0}O_{0.7}$ $[Ti_{0.85}O_{0.85}]$
V	$V_{1.0}C_{0.84}$	$V_{1.0}N_{0.75}$	$V_{0.763}O_{1.0}$
Nb	$Nb_{1.0}C_{0.75}$		$[Nb_{0.75}O_{0.75}]$
Ta	$Ta_{1.0}C_{0.76}$		

[a] After Vonsovsky *et al.*, 1982, p. 394.

VIII. TYPE A15 COMPOUNDS

The highest transition temperatures for the older superconductors were obtained with the *A*15 intermetallic compounds A_3B, and extensive data are available on these compounds. Nb_3Sn can be considered the prototype of this class. These compounds have the (simple) cubic structure (Pm3n, O_h^3) sketched in Fig. 3.19 with the two *B* atoms in the unit cell at the body center $(\frac{1}{2}, \frac{1}{2}, \frac{1}{2})$ and apical (0, 0, 0) positions, and the six *A* atoms paired on each face at the sites $(0, \frac{1}{2}, \frac{1}{4})$; $(0, \frac{1}{2}, \frac{3}{4})$; $(\frac{1}{2}, \frac{1}{4}, 0)$; $(\frac{1}{2}, \frac{3}{4}, 0)$; $(\frac{1}{4}, 0, \frac{1}{2})$; $(\frac{3}{4}, 0, \frac{1}{2})$, a configuration that amounts to the presence of chains of *A* atoms with spacing of one-half the lattice constant *a*. The *A* atom is any one of the transition elements (but not Hf) shown in the center of Fig. 3.10. The *B* element is either a transition element or is in row III (Al, Ga, In, Tl), row IV (Si, Ge, Sn, Pb), row V (P, As, Sb, Bi), or row VI (Te) of the periodic table. High transition temperatures occur when *B* is either a metal (Al, Ga, Sn)

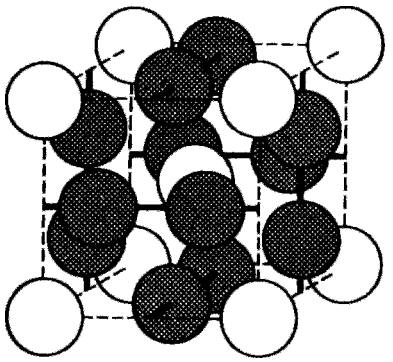

Figure 3.19 The unit cell of the *A*15 compound A_3B showing *B* atoms at the apical and body center positions and *A* atoms in pairs on the faces of the cube (Vonsovsky *et al*., 1982, p. 260; see also Wyckoff, 1964, p. 119).

or a nonmetal (Si, Ge), but not a transition element. Table 3.6 shows seven *A* elements and 20 *B* elements for a total of 140 possibilities, 60 of which superconduct. Two additional *A*15 superconductors are V_3Ni with $T_c = 0.3\,K$ and W_3Os with $T_c = 11.4\,K$.

Stoichiometry is important, and paying attention to it has produced higher transition temperatures, as was explained in Section IV. Typical *A*15 compounds $A_{3+x}B_{1-x}$ have narrow ranges of homogeneity. They are homogeneous toward *A*, with deviations from stoichiometry, $x > 0$, that tend to maintain the chains intact. Some atypical compounds, such as $A_{3-x}B_{1+x}$, are homogeneous toward *B* so that the chains are affected, and can have their highest T_c values when they deviate from ideal stoichiometry. Figure 3.20 shows that there is a close correlation between the transition temperature and the valence electron concentration N_e. We see that high values of T_c occur for $N_e = 4.5$ (Nb_3Ga, $T_c = 20.3\,K$), $N_e = 4.75$ (Nb_3Ge, $T_c = 23.2\,K$), $N_e = 6.25$ (Nb_3Pt, $T_c = 10.9\,K$), and $N_e = 6.5$ (TaAu, $T_c = 13\,K$). The specific-heat factor γ plotted in Fig. 3.21 and the magnetic susceptibility χ (Vonsovsky *et al*., 1982) show the same correlation (cf. Hellman and Geballe, 1987). The Villars–Phillips approach (1988, Phillips 1989a, p. 324) adds two additional parameters for high-T_c values. For further details see Sect. XIII of Chap. 7 of the first edition of this work.

Table 3.6 Superconducting transition temperatures T_c of some A15 compounds A_3B. The number of valence electrons is given for each element. Data are from Phillips (1989a) and Vonsovsky et al. (1982).

B \ A_3	Ti 4	Zr 4	V 5	Nb 5	Ta 5	Cr 6	Mo 6
Al 3			11.8	18.8			0.6
Ga 3			16.8	20.3			0.8
In 3			13.9	9.2			
Tl 3				9			
Si 4			17.1	19			1.7
Ge 4			11.2	23.2	8.0	1.2	1.8
Sn 4	5.8	0.9	7.0	18.0	8.4		
Pb 4		0.8		8.0	17		
As 5			0.2				
Sb 5	5.8		0.8	2.2	0.7		
Bi 5		3.4		4.5			
Tc 7							15.0
Re 7							15.0
Ru 8						3.4	10.6
Os 8			5.7	1.1		4.7	12.7
Rh 9			1.0	2.6	10.0	0.3	
Ir 9	5.4		1.7	3.2	6.6	0.8	9.6
Pd 10			0.08				
Pt 10	0.5		3.7	10.9	0.4		8.8
Au 11		0.9	3.2	11.5	16.0		

The superconducting energy gap data vary over a wide range, with $2\Delta/k_BT_c$ in the range 0.2–4.8, low values probably representing poor junctions. The *A*15 group has some weak-coupled, BCS-like compounds, such as V_3Si with $2\Delta/k_BT_c \approx 3.5$, and some strong coupled compounds, such as Nb_3Sn with $2\Delta/k_BT_c \approx 4.3$ and Nb_3Ge with $2\Delta/k_BT_c \approx 4.3$. The electron–phonon coupling constant λ has been reported to vary between the weak coupling value of 0.1 and the strong coupling value of 2.0 (see Table 7.3).

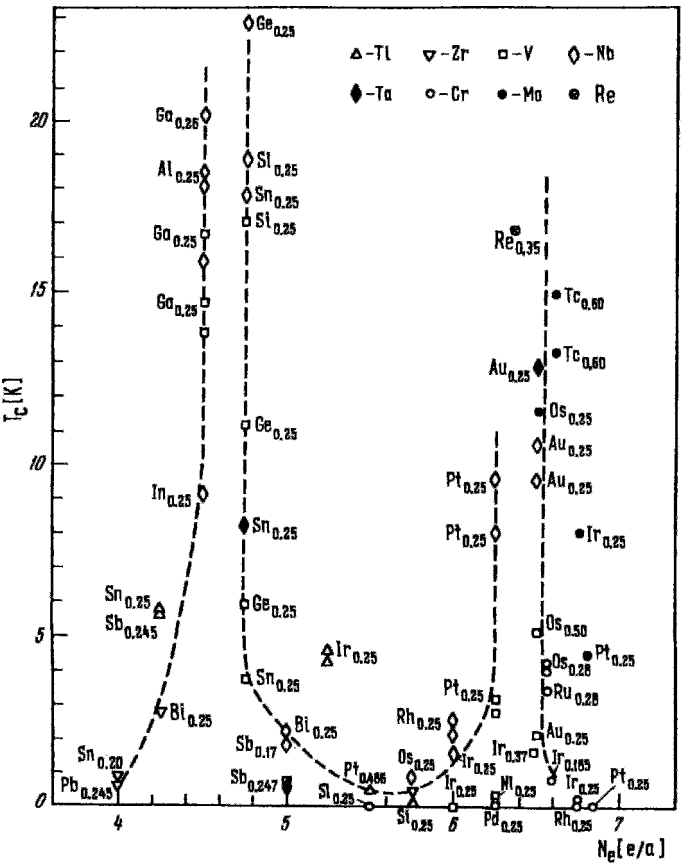

Figure 3.20 Dependence of transition temperature T_c on the number of valence electrons N_e in $A_{0.75}B_{0.25}$ compounds with the $A15$ structure. The A element is specified by the symbol at the top right, and the B element (see Fig. 3.19) is indicated at the experimental points (Vonsovsky *et al.*, 1982, p. 269).

Some $A15$ compounds undergo a reversible structural phase transformation above T_c from a high-temperature cubic phase to a low-temperature tetragonal phase that deviates very little from cubic ($|c-a|/a \approx 3\times10^{-3}$). At the transformation each atom remains close to its original site and the volume of the unit cell remains the same. Table 3.7 lists some transformation temperatures and $(c-a)/a$ ratios.

There is no isotope effect in this class of compounds, meaning that $\alpha = 0$ in Eq. (3.1). In addition there is a large scatter in the data on the change of T_c with pressure, dT_c/dP, as Fig. 3.22 indicates (cf. Ota, 1987).

IX. LAVES PHASES

There are several dozen metallic AB_2 compounds called Laves phases which are superconducting; the transition temperatures of some of these compounds are listed in Table 3.8. The $C15$ Laves phases have the cubic (Fd3m, O_h^7) structure sketched in Fig. 3.23, and the $C14$ phases are hexagonal,

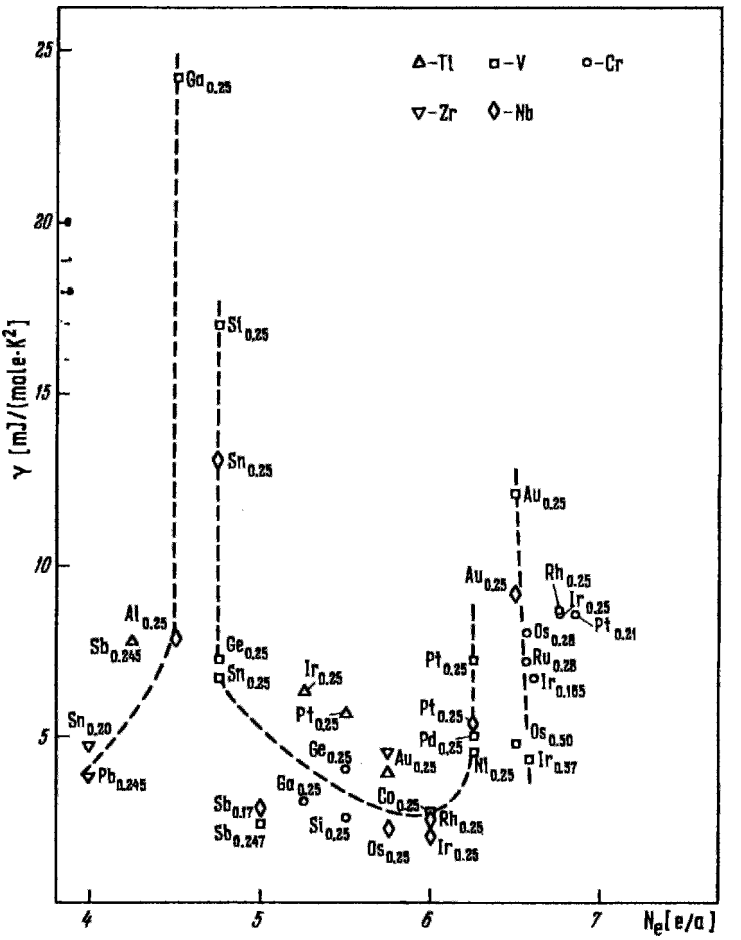

Figure 3.21 Dependence of electronic specific heat γ on N_e in *A*15 compounds, using the notation of Fig. 3.20 (Vonsovsky *et al*., 1982, p. 271). The dependence of the magnetic susceptibility χ on N_e produces a similar plot (Vonsovsky *et al*., 1982, p. 271).

Table 3.7 Structural Transformation Temperature T_{str} and Anisotropy $(c-a)/a$ in the Low-Temperature Tetragonal Phase of Several *A*15 type Superconductors[a]

Compound	T_{str} (K)	T_c (K)	Anisotropy $(c-a)/a$	Reference
V_3Si	21	17	0.0024	Batterman and Barrett (1964)
Nb_3Sn	43	18	−0.0061	Mailfert *et al*. (1967)
V_3Ga	>50	14.5	—	Nembach *et al*. (1970)
Nb_3Al	80	17.9	—	Kodess (1973, 1982)
$Nb_3(Al_{0.75}Ge_{0.25})$	105	18.5	−0.003	Kodess (1973, 1982)
$Nb_{3.1}(Al_{0.7}Ge_{0.3})$	130	17.4	—	Kodess (1973, 1982)

[a] cf. Vonsovsky *et al*., 1982, p. 278.

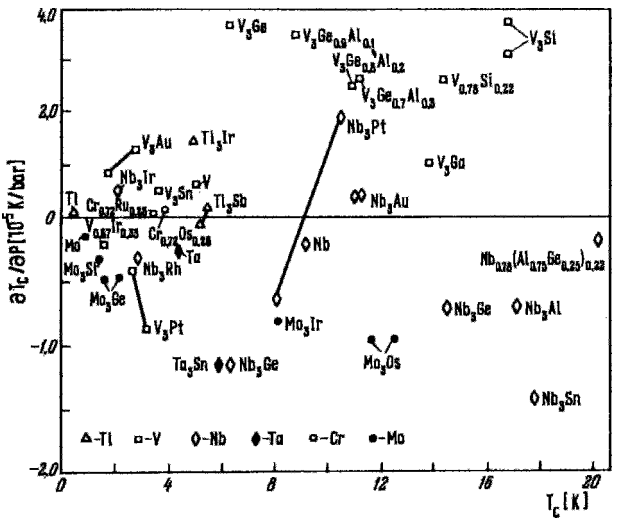

Figure 3.22 Dependence of pressure derivative dT_c/dP on N_e in $A15$ compounds, following Fig. 3.20 (Vonsovsky *et al.*, 1982, p. 288).

Table 3.8 Superconducting transition temperatures Tc of selected Laves phase (AB_2) compounds. Those labeled with an asterisk (∗) are hexagonal, and the remaining ones are cubic. The data are from Phillips (1989a) and Vonsovsky et al. (1982).

A \ B_2	V 6	Mo 6	Te 6	Re 7	Ru 8	Os 8	Rh 9	Ir 9	Pt 16
Ca 2							6.4	6.2	
Sr 2							6.2	5.7	
Sc 3				4.2*	2.3*	4.6*	6.2	2.5	0.7
Y 3				1.8*	2.4*	4.7*		2.1	0.5
La 3					4.4	8.9		0.5	
Zl 4	9.6	0.13	7.6*	6.8*	1.8*	3.0*		4.1	
Hf 4	9.4	0.07*	5.6*	5.6*		2.7*			
Th 4				5.0*	3.5			6.5	
Lu -					0.9*	3.5*	1.3	2.9	

as noted in Table 3.2. One additional Laves superconductor $HfMo_2$ has the $C36$ hexagonal structure with a larger unit cell. Some have critical temperatures above 10 K and high critical fields. For example, $Zr_{\frac{1}{2}}Hf_{\frac{1}{2}}V_2$ has $T_c = 10.1\,\mathrm{K}$, $B_{c2} = 24\,\mathrm{T}$, and a compound with a different Zr/Hf ratio has similar T_c and B_{c2} values with $J_c \approx 4 \times 10^5\,\mathrm{A/cm^2}$. These materials also have the advantage of not being as hard and brittle as some other intermetallics and alloys with comparable transition temperatures.

X. CHEVREL PHASES

The Chevrel phases $A_xMo_6X_8$ are mostly ternary transition metal chalcogenides, where X is S, Se, or Te and A can be almost any element (Fischer, 1978). These compounds have relatively high transition temperatures and critical fields B_{c2} of several teslas. However, the critical currents, typically 2 to $500\,\mathrm{A/cm^2}$, are rather low. Substituting oxygen for sulphur in $Cu_{1.8}Mo_6S_8$ raises T_c (Wright *et al.*, 1987). Table 3.9

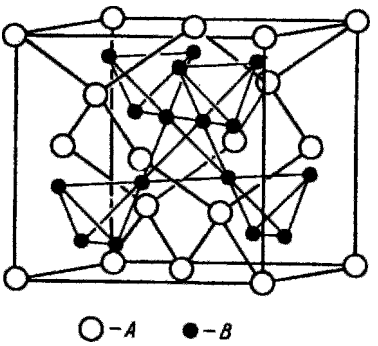

Figure 3.23 Crystal structure of the Laves phase (Vonsovsky *et al*., 1982, p. 376).

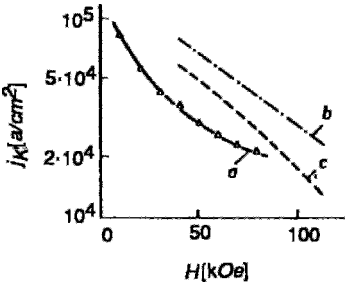

Figure 3.24 Comparison of the critical current densities on the applied field for a, $SnGa_{0.25}Mo_6S_8$, b, V_3Ga, and c, Nb_3Sn (Alekseevskii *et al*., 1977).

lists several dozens of these superconductors and their transition temperatures. Figure 3.24 compares the critical currents (see Fig. 5.26 for a comparison of the critical fields for several superconductors).

The trigonal structure sketched in Fig. 3.25, with space group R3, C_{3i}^2, is a simple cubic arrangement slightly distorted along the (111) axis of the Mo_6X_8-group building blocks, each consisting of a deformed cube with large X atoms at the vertices and small Mo atoms at the centers of the faces. The Mo_6X_8 group may be looked on as an Mo_6 octahedron inscribed in an X_8 cube. Mo_6X_{12}-group building blocks

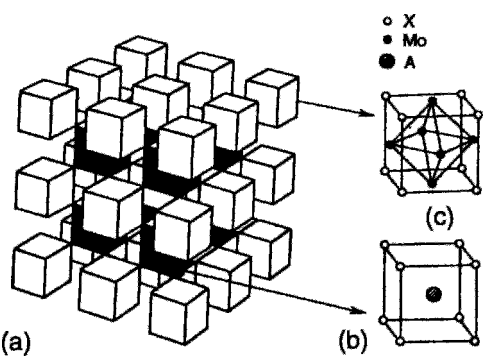

Figure 3.25 Structure of the Chevrel phase $A_xMo_6X_8$ (Vonsovsky *et al*., 1982, p. 431).

Table 3.9 Superconducting Transition Temperatures of some Chevrel compounds[a]

$A_xMo_6S_8$	T_c(K)	$A_xMo_6Se_8$	T_c(K)	Misc. Compounds	T_c(K)
Mo_6S_8	1.85	Mo_6Se_8	6.5	$Pb_{0.9}Mo_6S_{7.5}$	15.2
$Cu_2Mo_6S_8$	10.7	$Cu_2Mo_6Se_8$	5.9	$PbGd_{0.2}Mo_6S_8$	14.3
$LaMo_6S_8$	7.0	$La_2Mo_6Se_8$	11.7	$PbMo_6S_8$	12.6
$PrMo_6S_8$	2.6	$PrMo_6Se_8$	9.2	$Sn_{1.2}Mo_6S_8$	14.2
$NdMo_6S_8$	3.5	$NdMo_6Se_8$	8.4	$SnMo_6S_8$	11.8
$Sm_{1.2}Mo_6S_8$	2.4	$Sm_{1.2}Mo_6Se_8$	6.8	$LiMo_6S_8$	4.0
$Tb_{1.2}Mo_6S_8$	1.4	$Tb_{1.2}Mo_6Se_8$	5.7	$NaMo_6S_8$	8.6
$Dy_{1.2}Mo_6S_8$	1.7	$Dy_{1.2}Mo_6Se_8$	5.8	KMo_6S_8	2.9
$Ho_{1.2}Mo_6S_8$	2.0	$Ho_{1.2}Mo_6Se_8$	6.1	$Br_2Mo_6S_6$	13.8
$Er_{1.2}Mo_6S_8$	2.0	$Er_{1.2}Mo_6Se_8$	6.2	$I_2Mo_6Se_7$	14.0
$Tm_{1.2}Mo_6S_8$	2.0	$Tm_{1.2}Mo_6Se_8$	6.3	$BrMo_6Se_7$	7.1
$Yb_{1.2}Mo_6S_8$	≈ 8.7	$Yb_{1.2}Mo_6Se_8$	5.8	IMo_6Se_7	7.6
$Lu_{1.2}Mo_6S_8$	2.0	$Lu_{1.2}Mo_6Se_8$	6.2	$I_2Mo_6Te_6$	2.6

[a] See Phillips (1989a, pp. 339, 361) and Vonsovsky *et al*. (1982, p. 419) for more complete listings.

are also found. The distortions are not shown in the figure. The parameter x in the formula $A_xMo_6X_8$ assumes various values such as $x = 1$ (e.g., YMo_6S_8, $LaMo_6S_8$), $x = 1.2$ (e.g., $V_{1.2}Mo_6Se_8$), $x = 1.6$ (e.g., $Pb_{1.6}Mo_6S_8$), and $x = 2$ (e.g., $Cu_2Mo_6Se_8$). This parameter can vary because of the large number of available sites between the cubes for the A cations. Most of the space is occupied by the large chalcogenide anions, which have radii of 0.184 nm (S), 0.191 nm (Se), and 0.211 nm (Te).

The electronic and superconducting properties depend mainly on the Mo_6X_8 group. No correlations are evident between the type of A ion and the superconducting properties. Magnetic order and superconductivity are known to coexist in Chevrel phase compounds. When A is a rare earth its magnetic state does not influence the superconducting properties, but when A is a transition metal ion the magnetic properties suppress the superconductivity. This may be explained on structural grounds by pointing out that the large rare earths occupy sites between the Mo_6X_8 groups, as shown in Fig. 3.25, where they are remote from the molybdenums with only X as nearest neighbors. The smaller transition ions, on the other hand, can fit into octahedral sites with six Mo as their nearest neighbors (Ø. Fischer, 1990).

XI. CHALCOGENIDES AND OXIDES

Many of the classical superconductors (for example, the Chevrel phases discussed in Section X) contain an element of row VI in the periodic table, namely O, S, Se, or Te, with oxygen by far the least represented among the group. The newer superconductors in contrast, are oxides. Since the presence of lighter atoms tends to raise the Debye temperature, oxides are expected to have higher Debye temperatures than the other chalcogenides (Gallo *et al.*, 1987, 1988). Thus the presence of group VI elements is a commonality that links the older and the newer superconductors.

The two oxide compounds listed in Table 3.2 are cubic and ternary. One is the well-known ferroelectric perovskite $SrTiO_3$, which has a very low transition temperature (0.03–0.35 K). Nb-doped $SrTiO_3$, with its small carrier concentration $N_e \approx 2 \times 10^{20}$ and high electron–phonon coupling, has $T_c = 0.7$ K (Baratoff and Binnig, 1981; Binnig *et al.*, 1980). The other cubic ternary oxide is the spinel $LiTi_2O_4$ with moderately high $T_c = 13.7$ K (Johnston *et al.*, 1973). The system $Li_xTi_{3-x}O_4$ is superconducting in the range $0.8 \leq x \leq 1.33$ with T_c in the range 7–13 K. It is interesting to note that the stoichiometric compound with $x = 1$ is near the composition where the metal-to-insulator transition occurs. A band structure calculation of this Li–Ti spinel (Satpathy and Martin, 1987) is consistent with resonance valence bond superconductivity (Chapter 10, Section III, F) and a large electron–phonon coupling constant ($\lambda \approx 1.8$). Only three more of the 200 known spinels superconduct—namely, $CuRh_2Se_4$ with $T_c = 3.5$ K, CuV_2S_4 with $T_c = 4.5$, and $CuRh_2S_4$ with $T_c = 4.8$—so $LiTi_2O_4$ turns out to be the only spinel oxide superconductor.

PROBLEMS

1 Show why the alloys of Fig. 3.17 contain isoelectronic elements.

2 Consider the following expression as an alternate to Eq. (3.3) for describing the electronic specific heat of alloys:

$$\gamma_{AB} = f_A\gamma_A(N_{eA}) + f_B\gamma_B(N_{eB}) + \alpha f_A f_B.$$

Evaluate the constant α for the three cases of Fig. 3.17, and compare the goodness of fit to the data with the results obtained from Eq. (3.3), as plotted in Fig. 3.17.

4

Thermodynamic Properties

I. INTRODUCTION

The first three chapters surveyed normal state conductivity, properties characteristic of superconductivity, and the principal types of superconducting materials. But none of the theoretical ideas that have been proposed to account for these phenomena were developed. In the present chapter we will refer to certain principles of thermodynamics as a way of providing some coherence to our understanding of the material that has been covered so far. In Chapters 6, 7 and 10 we will deepen our understanding by examining in succession the London approach, the Ginzburg–Landau phenomenological theory, the microscopic theory of Bardeen, Cooper, and Schrieffer (BCS), the Hubbard model, and the band structure. Then, after having acquired some understanding of the theory, we will proceed to examine other aspects of superconductivity from the perspective of the theoretical background, with an emphasis on the high-transition temperature cuprates.

The overall behavior of the heat absorption process that will be examined in this chapter can be understood by deriving the thermodynamic functions of the normal state from the known specific heat–temperature dependence. The corresponding superconducting-state thermodynamic functions can then be deduced from the critical field dependence of the Gibbs free energy. We will begin by presenting experimental results on specific heat, following that with a derivation of the different thermodynamic functions associated with specific heat in the normal and superconducting states.

A specific heat determination is of interest because it provides a good measure of the range of applicability of the phonon-mediated BCS theory (cf. Chapter 7, Section VI, E). This theory predicts characteristics of the discontinuity in specific heat at T_c.

II. SPECIFIC HEAT ABOVE T_C

One of the most extensively studied properties of superconductors is the specific heat. It represents a "bulk" measurement that sees the entire sample since all of the sample responds. Many other measurements are sensitive to only part of the sample, for example, microscopy in which only the surface is observed.

Above the transition temperature T_c the specific heat C_n of high-temperature superconductors tends to follow the Debye theory described in Chapter 1, Section XII (cf. Fig. 1.12, which shows the positions of the lanthanum and yttrium compounds on the Debye plot at their transition temperatures). We know from Eq. (1.64) that C_n of a normal metal far below the Debye temperature Θ_D is the sum of a linear term $C_e = \gamma T$ arising from the conduction electrons, a lattice vibration or phonon term $C_{ph} = AT^3$, and sometimes an additional Schottky contribution aT^{-2} (Crow and Ong, 1990) (cf. Chapter 1, Section XII).

$$C_n = aT^{-2} + \gamma T + AT^3. \qquad (4.1)$$

For the present we will ignore the Schottky term aT^{-2}. The C_{exp}/T versus T^2 plot of Fig. 4.1 shows how the yttrium compound obeys Eq. (4.1) at low temperatures and then deviates from it at higher temperatures, as expected for the Debye approximation. The normalized specific heat plots of Fig. 4.2 compare for the case of several metals the electronic and photon contributions to the specific heat at low temperatures.

In the free-electron approximation the electronic contribution to the specific heat per mole of conduction electrons is given by Eqs. (1.51) and (1.53), which we combine as follows:

$$C_e = \gamma T = \tfrac{1}{2}\pi^2 R\left(\frac{T}{T_F}\right) = 4.93R\left(\frac{T}{T_F}\right). \qquad (4.2)$$

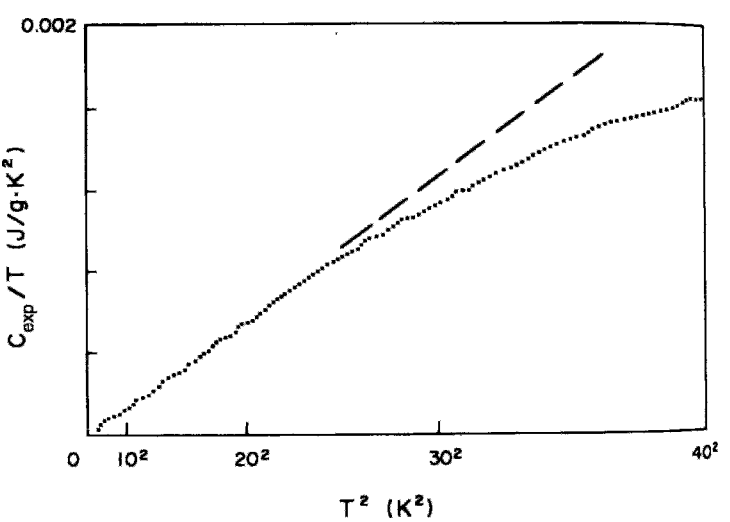

Figure 4.1 Plot of C_{exp}/T versus T^2 for $YBa_2Cu_3O_{7-\delta}$ showing how the deviation from linearity begins far below the transition temperature $T_c = 90\,K$ (Zhaojia *et al.*, 1987).

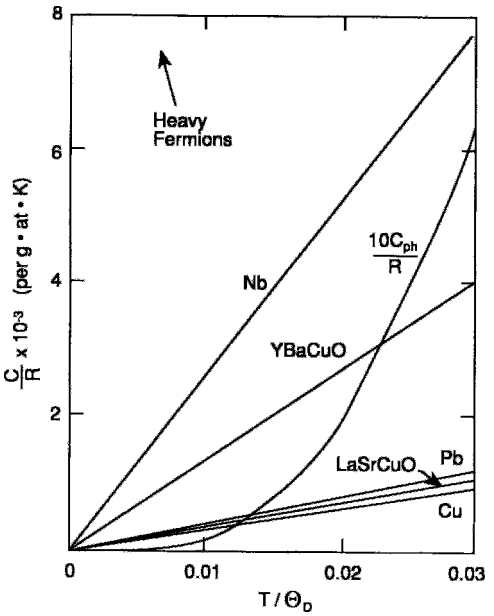

Figure 4.2 Comparison of the electronic specific heat $C_e = \gamma T$ of several conductors and superconductors at low temperature. The low-temperature Debye approximation $C_{ph} \approx AT^3$, multiplied by 10, is shown for comparison. The specific heats are normalized relative to the gas constant R and are expressed in terms of gram atoms. The heavy fermions are off scale on the upper left.

In the Debye approximation the phonon contribution to the specific heat per gram atom is given by Eq. (1.62a),

$$C_{ph} = AT^3 = \left(\frac{12\pi^4}{5}\right) R \left(\frac{T}{\Theta_D}\right)^3 = 234R\left(\frac{T}{\Theta_D}\right)^3, \tag{4.3}$$

where $R = k_B N_A$ is the gas constant and T_F the Fermi temperature. For a typical high-temperature superconductor we see from Table 4.1 that $\gamma \approx 10\,\text{mJ/mole Cu K}^2$, and Eq. (4.2) gives $T_F \approx 4.0 \times 10^3\,\text{K}$. This is much smaller than typical good conductor values, such as $8.2 \times 10^4\,\text{K}$ for Cu, as listed in Table 1.1. This discrepancy can be accounted for in terms of effective masses, as will be explained subsequently.

The vibrational and electronic contributions to the specific heat at $T = T_c$ may be compared with the aid of Eqs. (4.2) and (4.3),

$$\frac{C_{ph}}{C_e} = \frac{AT_c^2}{\beta\gamma} \tag{4.4}$$

$$= \left(\frac{47.5}{\beta} \cdot \frac{T_F}{\Theta_D^3}\right) T_c^2, \tag{4.5}$$

where the factor β, which is the ratio of the number of conduction electrons to the number of atoms in the compound, is needed when C_e is expressed in terms of moles of conduction electrons and C_{ph} in terms of moles of atoms. When both specific heats are in the same units, β is set equal to 1. Typical values of the Fermi and Debye temperatures are $10^5\,\text{K}$ and $350\,\text{K}$, respectively.

For most low-temperature superconductors the transition temperature T_c is sufficiently below Θ_D so that the electronic term in the specific heat is appreciable in magnitude, and sometimes dominates. This is not the case for high-temperature superconductors, however. Using measured values of γ and A we have shown in our earlier work (Poole *et al.*, 1988), that $AT_c^2 \gg \gamma$ for

$$(La_{0.9}Sr_{0.1})_2CuO_{4-\delta} \text{ and } YBa_2Cu_3O_{7-\delta},$$

so for oxide superconductors the vibrational term dominates at T_c, in agreement with the data plotted in Figs. 4.1 and 4.3.

If the conduction electrons have effective masses m^* that differ from the free-electron mass m, the conduction-electron specific heat coefficient γ is given by Eq. (1.54),

$$\gamma = \left(\frac{m^*}{m}\right)\gamma_0, \tag{4.6}$$

Table 4.1 Debye temperature Θ_D, Density of States $D(E_F)$, and Specific Heat Data[a]

Material	T_c (K)	Θ_D (K)	γ_n $\left(\frac{mJ}{mole\,K^2}\right)$	$(C_s - C_n)/\gamma T_c$	A (mJ/mole K^4)	$D(E_F)$ (states/eV)	Reference
Cd	0.55	252	0.67	1.36			
Al	1.2	423	1.36	1.45			
Sn, white	3.72	196	1.78	1.60			
Pb	7.19	102	3.14	2.71		1.55	
Nb	9.26	277	7.66	1.93		2.0	
$Zr_{0.7}Ni_{0.3}$	2.3	203	4.04	$\approx$1.65	0.23		Sürgers *el al.* (1989)
$V_3Ge(A15)$	11.2		7				Vonsovsky *et al.* (1982, pp. 269ff.)
$V_3Si(A15)$	17.1		17				Vonsovsky *et al.* (1982, pp. 269ff.)
$Nb_3Sn(A15)$	18.0		13				Vonsovsky *et al.* (1982, pp. 269ff.)
HfV_2 (laves)	9.2	187	21.7			2.30	Vonsovsky *et al.* (1982, p. 379)
$(Hf_{0.5}Zr_{0.5})V_2$ (laves)	10.1	197	28.3			2.97	Vonsovsky *et al.* (1982, p. 379)
ZrV_2 (laves)	8.5	219	16.5			1.86	Vonsovsky *et al.* (1982, p. 379)
$PbMo_6S_8$ (chevrel)	12.6		79				Vonsovsky *et al.* (1982, p. 420)
$PbMo_6Se_8$ (chevrel)	3.8		28				Vonsovsky *et al.* (1982, p. 420)
$SnMo_6S_8$ (chevrel)	11.8		105				Vonsovsky *et al.* (1982, p. 420)
YMo_6S_7 (chevrel)	6.3		34				Vonsovsky *et al.* (1982, p. 420)
UPt_3 (heavy fermion)	0.46		460	$\approx$0.9	1525		Ellman *et al.* (1990); Fisher *et al.* (1989); Schuberth *et al.* (1992)
UCd_{11} (heavy fermion)	5	200	290		115		deAndrade *et al.* (1991)
URu_2Si_2 (heavy fermion)	1.1		31	0.42			Ramirez *et al.* (1991)
$CeRu_2Si_2$ (heavy fermion)	$\approx$0.8		340	3.5			van de Meulen *et al.* (1991)
$(TMTSF)_2ClO_4$ (organic)	1.2	213	10.5	1.67	11.4		Garohce *et al.* (1982)
K-$(ET)_2$ $Cu(NCS)_2$ (organic)	9.3		34				Graebner *et al.* (1990)

K_3C_{60} (buckyball)	19	70				9.3	Ramir *et al.* (1992b); Novikov *et al.* (1992)
Rb_3C_{60} (buckyball)	30.5					10.9	Novikov *et al.* (1992)
Cs_3C_{60} (buckyball)	47.4					12.7	Novikov *et al.* (1992)
$BaPb_{1-x}Bi_xO_3$ (perovskite)	10		0.6	8		0.24	Junod (1990)
$(La_{0.925}Sr_{0.075})_2CuO_4$	37	360	4.5	2.0		1.9	Junod (1990); Sun *et al.* (1991)
$(La_{0.925}Ba_{0.075})_2CuO_4$	27	370		1.1			Junod (1990)
$YBa_2Cu_3O_7$ (orthorhombic)	92	410	4−10	3.6	0.035	2.0	Collocott *et al.* (1990a); Junod (1990); Stupp *et al.* (1991)
$YBa_2Cu_4O_{8.5}$	80	350	4.9		2.1	2.1	Junod (1990); Junod *et al.* (1991)
$Bi_2Sr_2CaCu_2O_8$	95	250	≈8				Junod (1990); Fisher and Huse (1988); Urbach *et al.* (1989)
$Bi_2Sr_2Ca_2Cu_3O_{10}$	110	260					Junod (1990)
$Tl_2Ba_2CaCu_2O_8$	110	260		>2.8			Junod (1990)
$Tl_2Ba_2Ca_2Cu_3O_{10}$	125	280			2.0		Junod (1990); Urbach *et al.* (1989)
$HgBa_2Ca_2Cu_3O_8$	133						Schilling *et al.* (1994a, b)

[a] Some of the high-temperature superconductor values are averages from Junod (1990), in many cases with a wide scatter of the data. The density of states is expressed per atom for the elements and per copper atom for the high-temperature superconductors. For the latter γ_n is the electronic specific heat factor determined from normal state measurements, and γ_n^* is the value obtained from the limit $T \to 0$, as explained by Junod. The BCS theory predicts $(C_s - C_n)/\gamma_n T_c = 1.43$.

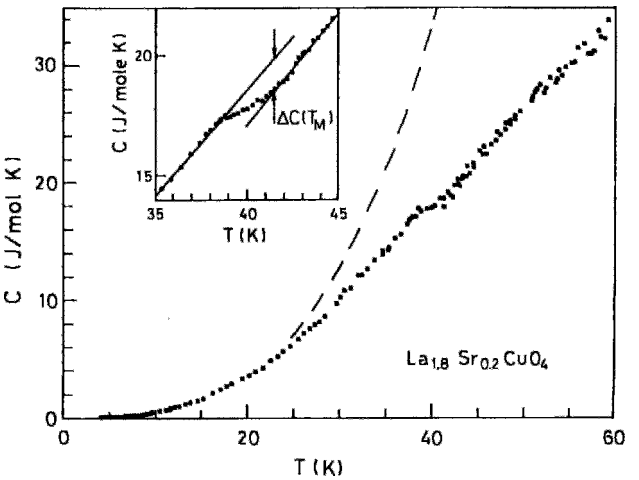

Figure 4.3 Discontinuity in the specific heat of $(La_{0.9}Sr_{0.1})_2CuO_4$ near 40 K. The inset shows the magnitude of the jump. The AT^3 behavior indicated by the dashed curve shows that the transition occurs beyond the region where the T^3 approximation is valid (Nieva *et al.*, 1987).

where γ_0 is the ordinary electron counterpart of γ from Eq. (1.51). In the free-electron approximation we have from Eq. (4.2)

$$\gamma_0 = \frac{\frac{1}{2}\pi^2 R}{T_F}, \tag{4.7}$$

which gives for the effective mass ratio

$$\frac{m^*}{m} = \frac{\gamma T_F}{\frac{1}{2}\pi^2 R}. \tag{4.8}$$

Table 1.1 lists effective mass ratios for the elemental superconductors calculated from this expression. The unusually low estimate of T_F given following Eq. (4.3) for a high-temperature superconductor can be explained in terms of a large effective mass. We see from Table 9.1 and Fig. 4.2 that large effective masses make the electronic term γ very large for the heavy fermions. The plot of T_c versus γ in Fig. 4.4 shows that the points for

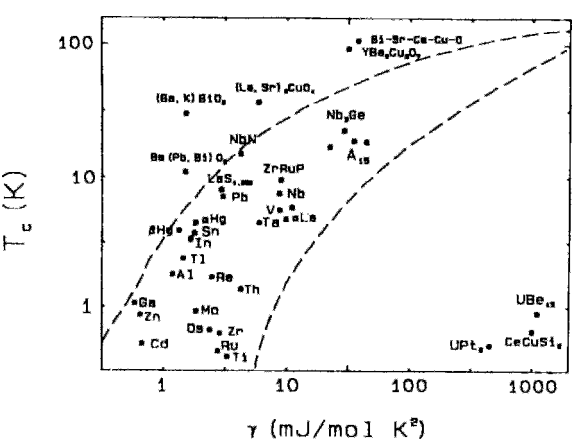

Figure 4.4 Comparison of the electronic specific-heat factor γ for a selection of superconductors and superconducting types over a wide range of T_c values. The dashed lines delimit the region of phonon-mediated superconductivity (Crow and Ong, 1990, p. 239).

BCS phonon-mediated superconductors cluster in a region delimited by the dashed lines. The heavy fermions lie far to the right, as expected, while the oxide and cuprate compounds lie somewhat above those in the main group. A diagram similar to Fig. 4.4 may be found in Batlogg *et al.* (1987).

We have seen that the specific heat is a measure of how effectively the introduction of heat into a material, and it raises its temperature. A related quantity is the thermal conductivity which is a measure of how easily heat flows through a material from a region at a high temperature to a region at a low temperature. Thermal conduction and the flow of heat through materials will be discussed in Sect. VII of Chap. 16.

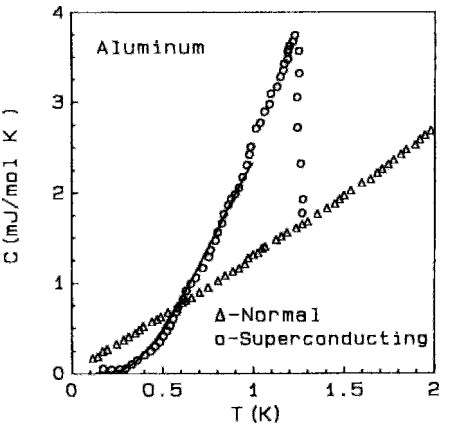

Figure 4.5 Specific heat jump in superconducting Al compared with the normal-state specific heat (Phillips, 1959; see Crow and Ong, 1990, p. 225).

III. DISCONTINUITY AT T_C

The transition from the normal to the superconducting state in the absence of an applied magnetic field is a second-order phase transition, as we will show in Section XIV. This means that there is no latent heat, but nevertheless a discontinuity in the specific heat. The BCS theory, which will be explained in Chapter 7, predicts that the electronic specific heat jumps abruptly at T_c from the normal state value γT_c to the superconducting state value C_s with ratio

$$\frac{C_s - \gamma T_c}{\gamma T_c} = 1.43. \qquad (4.9)$$

Figure 4.5, as well as Fig. IX-12 of our earlier work (Poole *et al.*, 1988) show details of this jump for an element and for a high-temperature superconductor, respectively. For the latter case the magnitude of the jump is small compared to the magnitude of the total specific heat because it is superimposed on the much larger AT^3 vibrational term, as indicated in Fig. 4.3. This is seen if Eq. (4.9) is used to express Eq. (4.5) in the form

$$\frac{AT_c^3}{C_e - \gamma T_c} = \left(\frac{67.9}{\beta} \cdot \frac{T_F}{\Theta_D^3}\right) T_c^2. \qquad (4.10)$$

Figure 4.6 illustrates how the small change at T_c is resolved by superimposing curves of C/T versus T^2 obtained in zero field and in a magnetic field large enough ($B_{app} > B_{c2}$) to destroy the superconductivity. It is clear from the figure that the data in the superconducting state extrapolate to zero, and that the normal state data extrapolate to γ at 0 K.

Many researchers have observed the jump in the specific heat at T_c (cf. Table 4.1 for results from a number of studies). Table 4.1 also lists experimental values of T_c, Θ_D, and γ, together with the ratios $(C_s - C_n)/T_c$ and $(C_s - C_n)/\gamma T_c$, for several elements and a number of copper oxide superconductors. Some of the elements are close to the BCS value of 1.43, but the strongly coupled ones, Pb and Nb, which have large electron–phonon coupling constants λ, are higher. Several experimental results for YBaCuO are close to 1.43, as indicated in the table. Some researchers have failed to observe a specific heat discontinuity, however.

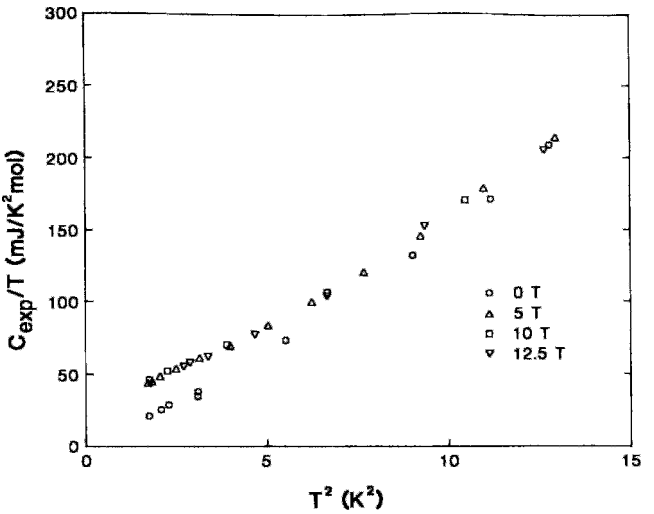

Figure 4.6 Plot of C_{exp}/T versus T^2 for monocrystals of the organic superconductor K–$(ET)_2Cu(NCS)_2$ in the superconducting state with no applied magnetic field, and also in the presence of applied fields that destroy the superconductivity. The superconducting state data extrapolate to a value $\gamma = 0$, while the normal-state extrapolation indicates $\gamma \approx 25\,\text{mJ/mole K}^2$ (Andraka *et al.*, 1989).

IV. SPECIFIC HEAT BELOW T_C

For $T \ll T_c$ BCS theory predicts that the electronic contribution to the specific heat C_e will depend exponentially on temperature,

$$C_s \approx a \exp\left(-\frac{\Delta}{k_B T}\right), \tag{4.11}$$

where 2Δ is the energy gap in the superconducting density of states. We see from Fig. 4.5 that the fit of this equation to the data for aluminum is good, with the specific heat falling rapidly to zero far below T_c, as predicted. The vibrational term AT^3 also becomes negligible as 0 K is approached, and other mechanisms become important, for example, antiferromagnetic ordering and nuclear hyperfine effects, two mechanisms that are utilized in cryogenic experiments to obtain temperatures down to the microdegree region.

V. DENSITY OF STATES AND DEBYE TEMPERATURE

The density of states at the Fermi level $D(E_F)$ can be estimated from Eq. (1.52):

$$D(E_F) = \frac{3}{\pi^2} \cdot \frac{\gamma}{R} \cdot \frac{1}{k_B}. \tag{4.12}$$

For a typical high-temperature superconductor with $\gamma \approx 0.01\,\text{J/mole Cu K}$ we obtain

$$D(E_F) \approx \frac{4.5\ \text{states}}{\text{eV Cu atom}}. \tag{4.13}$$

The Debye temperature may be estimated from the slope of the normal state C_n/T-versus-T^2 curve sketched in Fig. 1.13, since with the aid of Eq. (1.62a) we can write

$$\Theta_D^3 = \frac{12\pi^4 R}{\{5[\text{slope}]\}}. \tag{4.14}$$

Typical values for Θ_D are from 200 to 350 K.

We have been using formulae that involve the free-electron approximation. To estimate the validity of this approximation we can make use of Eq. (1.88), which gives the ratio of γ to the magnetic susceptibility χ arising from the conduction electrons,

$$\frac{\gamma}{\chi} = \frac{1}{3}\left(\frac{\pi k_B}{\mu_B}\right)^2, \qquad (4.15)$$

in terms of well-known physical constants.

VI. THERMODYNAMIC VARIABLES

We have been discussing the specific heat of a superconductor in its normal and superconducting states in the absence of an applied magnetic field. When a magnetic field is present the situation is more complicated, and we must be more careful in describing the specific heat as the result of a thermodynamic process. In this section we will develop some of the necessary background material required for such a description, and in the following sections we will apply the description to several cases.

Later on, in Chapter 5, Section X, we will learn why the magnetic energy of a superconducting sample in a magnetic field depends on its shape and orientation. In the present chapter we will not be concerned with these demagnetization effects and will instead assume that the sample is in the shape of a cylinder and that the internal magnetization **M** is directed along the axis of the cylinder, as illustrated in Fig. 2.26. If an external field $\mathbf{B}_{app}$ is applied, it will also be directed along this axis. This means that the applied **B** field is related to the internal **H** field by means of the expression

$$\mathbf{B}_{app} = \mu_0 \mathbf{H}_{in}. \qquad (4.16)$$

This geometry simplifies the mathematical expressions for the free energy, enthalpy, and other properties of a superconductor in the presence of a magnetic field. In the next few sections we will simplify the notation by using the symbol **B** instead of $\mathbf{B}_{app}$ for the applied magnetic field, but throughout the remainder of the text the symbol $\mathbf{B}_{app}$ will be used.

In treating the superconducting state it is convenient to make use of the free energy because (1) the superconductivity state is always the state of lowest free energy at a particular temperature, and (2) the free energies of the normal and superconducting states are equal at the transition temperature. We will use the Gibbs free energy $G(T, P, B) = G(T, B)$ rather than the Helmholtz free energy

$$F(T, V, M) = F(T, M),$$

where the variables P and V are omitted because pressure–volume effects are negligible for superconductors. The Gibbs free energy $G(T, B)$ is selected because the experimenter has control over the applied magnetic field B, whereas the magnetization $M(T, B)$ is produced by the presence of the field. The remaining thermodynamic functions will be expressed in terms of the two independent variables T and B.

In the treatment that follows we will be dealing with thermodynamic quantities on a per-unit-volume basis, so that G will denote the Gibbs free energy density and S the entropy density. For simplicity, we will generally omit the term density by, for example, calling G the Gibbs free energy.

The first law of thermodynamics for a reversible process expresses the conservation of energy. For a magnetic material the differential of the internal energy dU may be written in terms of the temperature T, the entropy S, the applied magnetic field **B**, and the magnetization **M** of the material as

$$dU = TdS + \mathbf{B} \cdot d\mathbf{M}, \qquad (4.17)$$

where the usual $-PdV$ term for the mechanical work is negligible and hence omitted,

while the $+\mathbf{B}\cdot d\mathbf{M}$ term for the magnetic work is included. (Work is done when an applied pressure P decreases the volume of a sample or an applied magnetic field $\mathbf{B}$ increases its magnetization.) So these two work terms are opposite in sign. The work term $\mu_0\mathbf{H}\cdot d\mathbf{M}$ that appears in Eq. (4.17) is positive. This equation does not include the term $d(\mathbf{B}^2/2\mu_0) = \mu_0^{-1}\mathbf{B}\cdot d\mathbf{B}$ for the work involved in building up the energy density of the applied field itself since we are only interested in the work associated with the superconductor.

We will be concerned with a constant applied field rather than a constant magnetization, so it is convenient to work with the enthalpy H' rather than the internal energy U,

$$H' = U - \mathbf{B}\cdot\mathbf{M}, \tag{4.18}$$

with differential form

$$dH' = TdS - \mathbf{M}\cdot d\mathbf{B}. \tag{4.19}$$

The second law of thermodynamics permits us to replace TdS by CdT for a reversible process, where C is specific heat,

$$CdT = TdS, \tag{4.20}$$

which gives for the differential enthalpy

$$dH' = CdT - \mathbf{M}\cdot d\mathbf{B}. \tag{4.21}$$

Finally we will be making use of the Gibbs free energy

$$G = H' - TS, \tag{4.22}$$

and its differential form

$$dG = -SdT - \mathbf{M}\cdot d\mathbf{B}. \tag{4.23}$$

Note the prime in the symbol H' for enthalpy to distinguish it from the symbol H for the magnetic field. For the balance of the chapter we will also be assuming that the vectors $\mathbf{B}$, $\mathbf{H}$, and $\mathbf{M}$ are parallel and write, for example, MdB instead of $\mathbf{M}\cdot d\mathbf{B}$.

The fundamental thermodynamic expressions (4.17)–(4.23) provide a starting point for discussing the thermodynamics of the superconducting state. Two procedures will be followed in applying these expressions to superconductors. For the normal state we will assume a known specific heat (4.1) and then determine the enthalpy by integrating Eq. (4.21), determine the entropy by integrating Eq. (4.20), and finally find the Gibbs free energy from Eq. (4.22). For the superconducting case we will assume a known magnetization and critical field, and determine the Gibbs free energy by integrating Eq. (4.23), the entropy by differentiating Eq. (4.23), the enthalpy from Eq. (4.22), and finally the specific heat by differentiating Eq. (4.21). The first procedure, called the specific heat-to-free energy procedure, goes in the direction $\mathrm{C}\rightarrow\mathrm{H}'\rightarrow\mathrm{S}\rightarrow\mathrm{G}$ and the second, called the free energy-to-specific heat procedure, goes in the opposite direction $\mathrm{G}\rightarrow\mathrm{S}\rightarrow\mathrm{H}'\rightarrow\mathrm{C}$. The former procedure will be presented in the following section and the latter in the succeeding three sections. We will assume specific expressions for C and M, respectively, to obtain closed-form expressions for the temperature dependences of the difference thermodynamic variables. This will give us considerable physical insight into the thermodynamics of the superconducting state. These assumptions also happen to approximate the behavior of many real superconductors.

VII. THERMODYNAMICS OF A NORMAL CONDUCTOR

In this section we will use the specific heat-to-free energy procedure. We deduce in succession the enthalpy, entropy, and Gibbs free energy of a normal conductor by assuming that its low-temperature specific heat C_{n}

is given by Eq. (4.1) with the Schottky term omitted:

$$C_n = \gamma T + AT^3. \tag{4.24}$$

The enthalpy at zero magnetic field is obtained by setting $MdB = 0$,

$$MdB = \mu_0^{-1}\chi_n BdB \approx 0, \tag{4.25}$$

where $\chi_n = \mu_0 M/B$. Integrating Eq. (4.21), we find that

$$\int dH_n' = \int_0^T [\gamma T + AT^3]dT, \tag{4.26}$$

$$H_n'(T) = \tfrac{1}{2}\gamma T^2 + \tfrac{1}{4}AT^4, \tag{4.27}$$

where it is assumed that γ and A are independent of temperature, and that $H_n'(0) = 0$. A similar calculation for the entropy involves integrating Eq. (4.20),

$$\int dS_n = \int_0^T [\gamma T + AT^3]\frac{dT}{T}, \tag{4.28}$$

$$S_n(T) = \gamma T + \tfrac{1}{3}AT^3, \tag{4.29}$$

where $S_n(0) = 0$. The normal-state Gibbs free energy at zero field may be determined either from Eq. (4.22) or by integrating Eq. (4.23) with MdB set equal to zero. It has the following temperature dependence:

$$G_n(T) = -\tfrac{1}{2}\gamma T^2 - \tfrac{1}{12}AT^4. \tag{4.30}$$

The normal-state specific heat, entropy, enthalpy, and Gibbs free energy from Eqs. (4.24), (4.29), (4.27), and (4.30) are plotted in Figs. 4.7, 4.8, 4.9, and 4.10, respectively, for the very-low-temperature region.

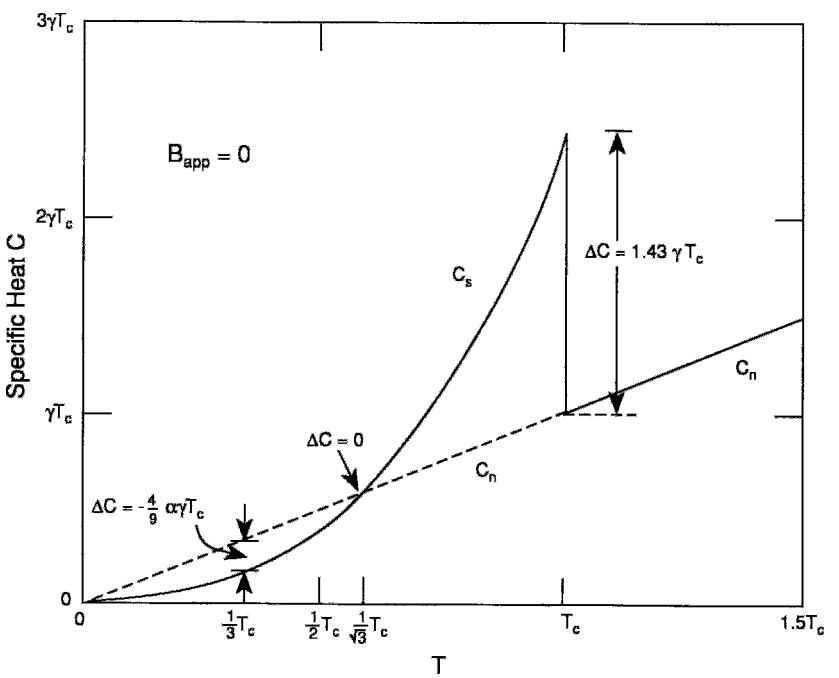

Figure 4.7 Temperature dependence of the normal-state C_n (- - -) and superconducting-state C_s (—) specific heats. The figure shows the specific heat jump $1.43\gamma T_c$ of Eq. (4.9) that is predicted by the BCS theory, the crossover point at $T = T_c/\sqrt{3}$, and the maximum negative jump $0.44\alpha\gamma T_c$ at $T = T_c/3$. In this and the following 12 figures it is assumed that only the linear electronic term γT exists in the normal state (i.e, $AT^3 = 0$).

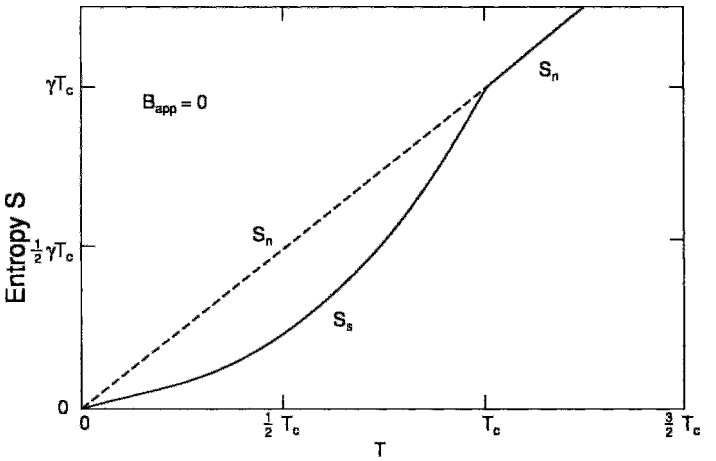

Figure 4.8 Temperature dependence of the normal-state S_n (---) and superconducting-state S_s (—) entropies. The transition is second order so there is no discontinuity in entropy at T_c.

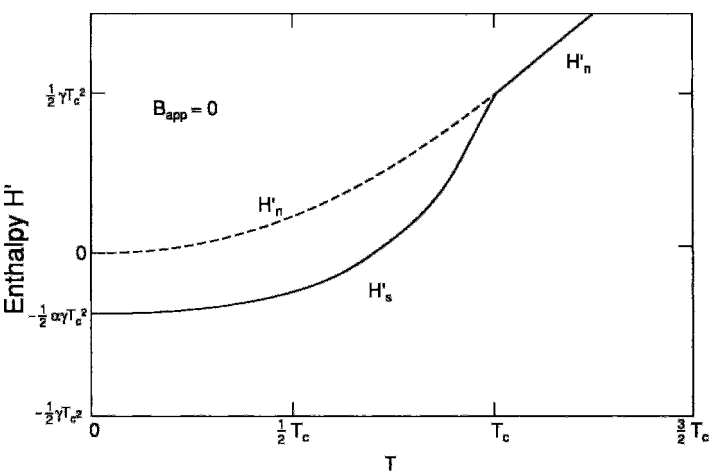

Figure 4.9 Temperature dependence of the normal state H_n (---) and superconducting state H_s (—) enthalpies. The transition is second order so there is no discontinuity in enthalpy, and hence no latent heat at T_c.

Here the AT^3 term is negligible, and only the γT term is appreciable in magnitude.

In this section we have derived several thermodynamic expressions for a normal conductor in the absence of a magnetic field. The permeability μ of such a conductor is so close to that of free space μ_0 (cf. Chapter 1, Section XV, and Table 1.2), that the magnetic susceptibility χ_n is negligibly small and $M \approx 0$. Therefore, the thermodynamic quantities (4.24), (4.27), (4.29), and (4.30) are not appreciably influenced by a magnetic field, and we will assume that they are valid even when there is a magnetic field present. For example, we assume that

$$G_n(T, B) \approx G_n(T, 0) \tag{4.31}$$

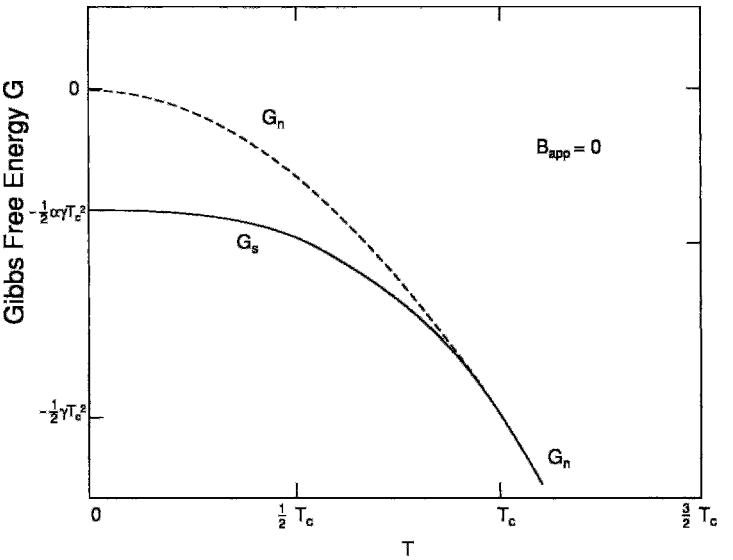

Figure 4.10 Temperature dependence of the normal-state G_n (---) and superconducting-state G_s (—) Gibbs free energies. Since the transition is second order, both G and its first derivative are continuous at T_c.

and it is convenient to simplify the notation by writing

$$G_n(T, B) \approx G_n(T). \tag{4.32}$$

Thus all of the equations derived in this section are applicable when a magnetic field is also present.

VIII. THERMODYNAMICS OF A SUPERCONDUCTOR

If we had a well-established expression for the specific heat C_s of a superconductor below T_c it would be easy to follow the same $C \rightarrow H' \rightarrow S \rightarrow G$ procedure to obtain the quantities H_s', S_s, and G_s, as in the case of a normal conductor. Unfortunately, there is no such expression, although many experimental data far below T_c have been found to follow the BCS expression (4.11). Equation (4.11) does not cover the entire temperature range of the superconducting region, however, and, in addition it does not integrate in closed form. Another complication is that the thermodynamic properties of the superconducting state are intimately related to its magnetic properties, as we will demonstrate below, and the specific heat relation (4.11) does not take magnetism into account.

Because of the close relationship between superconductivity and magnetism we will adopt the free energy-to-specific heat procedure and examine the Gibbs free energy of a superconductor in the presence of an applied magnetic field B. We will not resort to any model for the temperature dependence of the specific heat or that of the critical field, so the results that will be obtained will be general. Then in the following two sections we will return to the specific model based on Eq. (4.24) to obtain more practical results.

We begin by seeking an expression for the free-energy difference $G_s(T, B) - G_n(T, B)$ between the superconducting and normal states to allow us to deduce S_s and H_s' by differentiation. To accomplish this we

write down the differential of the Gibbs free energy from Eq. (4.23) assuming isothermal conditions ($dT = 0$),

$$dG = -MdB, \tag{4.33}$$

and examine its magnetic field dependence in the superconducting and normal states.

We treat the case of a Type I superconductor that has the magnetization given by Eq. (2.22), $M = -H = -B/\mu_0$, and assume that surface effects involving the penetration depth are negligible. Demagnetization effects are also inconsequential, as explained in Section VI, so Eq. (4.33) becomes

$$dG_s = \mu_0^{-1} B dB. \tag{4.34}$$

If this expression is integrated from $B = 0$ to a field B we obtain

$$G_s(T, B) = G_s(T, 0) + \tfrac{1}{2}\mu_0^{-1} B^2, \tag{4.35}$$

where, of course, the magnetic energy density $B^2/2\mu_0$ is independent of temperature. When the applied field B equals the critical field $B_c(T)$ for a particular temperature $T < T_c$, the free energy becomes

$$G_s(T, B_c(T)) = G_s(T, 0) + \tfrac{1}{2}\mu_0^{-1} B_c(T)^2 \qquad T = T_c(B), \tag{4.36}$$

and recalling that this is a phase transition for which $G_s = G_n$, we have

$$G_n(T) = G_s(T, 0) + \tfrac{1}{2}\mu_0^{-1} B_c(T)^2 \qquad T = T_c(B), \tag{4.37}$$

where $\frac{1}{2}\mu_0^{-1} B_c(T)^2$ is the magnetic-energy density associated with the critical field, and, from Eq. (4.32), $G_n(T)$ does not depend on the field. Subtracting Eq. (4.35) from Eq. (4.37) gives

$$G_s(T, B) = G_n(T) - \tfrac{1}{2}\mu_0^{-1}(B_c(T)^2 - B^2), \tag{4.38}$$

where, of course, $B < B_c(T)$. In the absence of an applied field Eq. (4.38) becomes

$$G_s(T, 0) = G_n(T) - \tfrac{1}{2}\mu_0^{-1} B_c(T)^2 \ (B = 0), \tag{4.39}$$

so the Gibbs free energy in the superconducting state depends on the value of the critical field at that temperature. This confirms that there is indeed a close relationship between superconductivity and magnetism. Figure 4.11 shows that the curves for $G_s(T, 0)$ and $G_n(T)$ intersect at the temperature T_c, while those for $G_s(T, B)$ and $G_n(T)$ intersect at the temperature $T_c(B)$. The figure also shows that $\frac{1}{2}\mu_0^{-1} B_c^2$ is the spacing between the curves of $G_s(T, 0)$ and $G_n(T)$, and that $\frac{1}{2}\mu_0^{-1} B^2$ is the spacing between the curves of $G_s(T, B)$ and $G_s(T, 0)$. The figure is drawn for a particular value of the applied field corresponding to $T_c(B) = \frac{1}{2}T_c$.

Since we know that the Gibbs free energy of the superconducting state depends only on the applied magnetic field and the temperature, we can proceed to write down general expressions for the other thermodynamic functions that can be obtained through differentiation of $G_s(T)$ with respect to the temperature when the applied field B is kept constant. The value of B, of course, does not depend on T.

For the entropy we have, using Eq. (4.23),

$$S_s - S_n = -\frac{d}{dT}[G_s - G_n], \tag{4.40}$$

and for the free energy, from Eq. (4.38),

$$S_s(T) = S_n(T) + \frac{B_c(T)}{\mu_0}\frac{d}{dT}B_c(T). \tag{4.41}$$

The entropy $S_s(T, B)$ does not depend explicitly on the applied field, so it is denoted $S_s(T)$. From this expression, together with

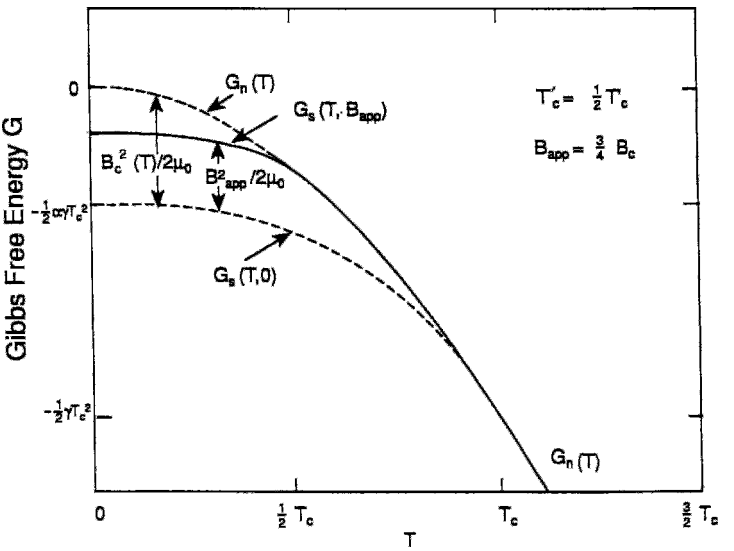

Figure 4.11 Effect of an applied magnetic field $B_{app} = 0.75B_c$ on the Gibbs free energy $G_s(T, B)$ in the superconducting state. In this and the succeeding figures dashed curves are used to indicate both the normal-state extrapolation below T_c' and the zero-field superconducting state behavior, where T_c' denotes the transition temperature when there is a field present.

Eqs. (4.22) and (4.39), we can write down the enthalpy at constant field,

$$H_s'(T, B) = H_n'(T) - \tfrac{1}{2}\mu_0^{-1}[B_c(T)^2 - B^2] + \frac{TB_c(T)}{\mu_0}\frac{d}{dT}B_c(T), \quad (4.42)$$

which shows that the enthalpy does depend on the magnetic energy $B^2/2\mu_0$. We see from Eq. (4.21) that the enthalpy can be differentiated to provide the specific heat at constant field:

$$C_s(T) = C_n(T) + \mu_0^{-1}TB_c(T)\frac{d^2}{dT^2}B_c(T) + \frac{T}{\mu_0}\left|\frac{d}{dT}B_c(T)\right|^2. \quad (4.43)$$

The specific heat does not depend explicitly on the applied field, so we write $C_s(T)$ instead of $C_s(T, B)$. We will see below that the terms in this expression that depend on $B_c(T)$ become negative at the lowest temperatures, making $C_s(T)$ less than $C_n(T)$. At zero field ($B = 0$) the transition temperature is T_c itself, and we know (e.g., from Eq. (4.45) in Section IX) that $B_c(T_c) = 0$, so that only the second term on the right exists under this condition:

$$C_s(T) = C_n(T) + \frac{T}{\mu_0}\left|\frac{d}{dT}B_c(T)\right|^2 \quad T = T_c. \quad (4.44)$$

This is known as Rutger's formula. It provides the jump in the specific heat at T_c that is observed experimentally, as shown in Figs. 4.3, 4.5, and 4.6. We will show in Section XIII how this expression can be used to evaluate the electronic specific-heat factor γ.

IX. SUPERCONDUCTOR IN ZERO FIELD

We will develop the thermodynamics of a Type I superconductor in the absence of

a magnetic field using the free energy-to-specific heat procedure G → S → H′ → C. We apply the general expression (4.39) to the particular case in which the free energy of the normal state is given by Eq. (4.30) and the critical magnetic field $B_c(T)$ has a parabolic dependence on temperature,

$$B_c(T) = B_c(0)\left[1 - \left(\frac{T}{T_c}\right)^2\right], \qquad (4.45)$$

given by Eq. (2.56). Substituting these expressions in Eq. (4.39) gives

$$G_s(T,0) = -\tfrac{1}{2}\gamma T^2 - \tfrac{1}{12}AT^4 - \tfrac{1}{2}\mu_0^{-1}B_c(0)^2 \times \left[1 - \left(\frac{T}{T_c}\right)^2\right]^2, \qquad (4.46)$$

which is plotted in Fig. 4.10 with A set equal to zero.

The difference between the entropies in the normal and superconducting states is obtained by substituting the expressions from Eqs. (4.29) and (4.45) in Eq. (4.41) and carrying out the differentiation:

$$S_s(T) = \gamma T + \tfrac{1}{3}AT^3 - 2\mu_0^{-1}B_c(0)^2 \times \left(\frac{T}{T_c^2}\right)\left[1 - \frac{T^2}{T_c^2}\right]. \qquad (4.47)$$

The last term on the right is zero for both $T = 0$ and $T = T_c$, so $S_s = S_n$ for both limits. The former result is expected from the third law of thermodynamics. Differentiation shows that the last term on the right is a maximum when $T = T_c/\sqrt{3}$, so that the difference $S_s - S_n$ is a maximum for this temperature. The entropy S_s with $A = 0$ is plotted in Fig. 4.8.

The enthalpy $H_s'(T,0)$ of the superconducting state in zero field is obtained from Eq. (4.22),

$$H_s'(T,0) = \tfrac{1}{2}\gamma T^2 + \tfrac{1}{4}AT^4 - \tfrac{1}{2}\mu_0^{-1}B_c(0)^2 \times \left[1 - \frac{T^2}{T_c^2}\right]\left[1 + 3\frac{T^2}{T_c^2}\right], \qquad (4.48)$$

and the specific heat of the superconducting state from Eq. (4.20),

$$C_s = T\left(\frac{dS_s}{dT}\right)_H, \qquad (4.49)$$

by differentiating Eq. (4.47) at constant field, to give

$$C_s(T) = \gamma T + AT^3 + 2\mu_0^{-1}B_c(0)^2 \times \left(\frac{T}{T_c^2}\right)\left[3\frac{T^2}{T_c^2} - 1\right]. \qquad (4.50)$$

The last term on the right changes sign at $T = T_c/\sqrt{3}$. Expressions (4.48) and (4.50) are plotted in Figs. 4.9 and 4.7, respectively, with the AT^3 term set equal to zero.

The results given in this section are for a Type I superconductor in zero field with electronic specific heat given by Eq. (4.24) and a critical field with the temperature dependence of Eq. (4.45). Figures 4.7, 4.8, 4.9, and 4.10 show plots of the temperature dependence of the thermodynamic functions C_s, S_s, H_s', and G_s under the additional assumption $A = 0$.

X. SUPERCONDUCTOR IN A MAGNETIC FIELD

In the previous section we derived Eq. (4.38) for the Gibbs free energy $G_s(T,B)$ of the superconducting state in the absence of an applied magnetic field B. With the aid of Eqs. (4.30), (4.38), and (4.45) this can be written in the following form for the case of an applied field:

$$G_s(T,B) = -\tfrac{1}{2}\gamma T^2 - \tfrac{1}{12}AT^4 - \tfrac{1}{2}\mu_0^{-1} \times \left[B_c(0)^2\left(1 - \frac{T^2}{T_c^2}\right)^2 - B^2\right]. \qquad (4.51)$$

Since the applied field B does not depend on the temperature, the entropy obtained from

Eq. (4.40) by differentiating the Gibbs free energy (4.51) assuming the presence of a field is the same as in the case where there is no magnetic field present,

$$S_s(T) = \gamma T + \tfrac{1}{3}AT^3 - 2\mu_0^{-1}B_c(0)^2 \times \frac{T}{T_c^2}\left[1 - \frac{T^2}{T_c^2}\right]. \quad (4.52)$$

The enthalpy obtained from Eq. (4.22) does depend explicitly on this field,

$$H_s'(T,B) = \tfrac{1}{2}\gamma T^2 + \tfrac{1}{4}AT^4 - \tfrac{1}{2}\mu_0^{-1}B_c(0)^2\left(1 - \frac{T^2}{T_c^2}\right) \times \left(1 + 4\frac{T^2}{T_c^2}\right) + \tfrac{1}{2}\mu_0^{-1}B^2, \quad (4.53)$$

but the specific heat from Eq. (4.20) does not,

$$C_s(T) = \gamma T + AT^3 + 2\mu_0^{-1}B_c(0)^2 \times \frac{T}{T_c^2}\left(3\frac{T^2}{T_c^2} - 1\right), \quad (4.54)$$

where Eqs. (4.52) and (4.54) are the same as their zero-field counterparts (4.47) and (4.50), respectively. The field-dependent G_s and H_s' terms of Eqs. (4.51) and (4.53), on the other hand, differ from their zero-field counterparts (4.46) and (4.48) by the addition of the magnetic-energy density $B^2/2\mu_0$.

In a magnetic field the sample goes normal at a lower temperature than in zero field. We denote this magnetic-field transition temperature by $T_c(B) = T_c'$, where, of course, $T_c(0) = T_c$ and $T_c' < T_c$. This transition from the superconducting to the normal state occurs when the applied field H equals the critical field $B_c(T)$ given by Eq. (4.45) at that temperature. Equation (4.45) may be rewritten in the form

$$T_c' = T_c\left[1 - \frac{B}{B_c(0)}\right]^{1/2} \quad (4.55)$$

to provide an explicit expression for the transition temperature T_c' in an applied field B. We show in Problem 7 that this same expression is obtained by equating the Gibbs free energies $G_s(T,B)$ and $G_n(T)$ for the superconducting and normal states at the transition point,

$$G_s(T,B) = G_n(T) \quad T = T_c', \quad (4.56)$$

At the transition temperature $T_c' = T_c(B)$ the superconducting and normal state entropies (4.52) and (4.29), respectively, differ. Their difference gives the latent heat L of the transition by means of the standard thermodynamic expression

$$L = (S_n - S_s)T_c(B) \quad (4.57)$$

$$= 2\mu_0^{-1}B_c^2\left[\frac{T_c(B)}{T_c}\right]^2 \times \left\{1 - \left[\frac{T_c(B)}{T_c}\right]^2\right\}. \quad (4.58)$$

We show in Problem 9 that this same result can be obtained from the enthalpy difference $L = H_n' - H_s'$. The latent heat is a maximum at the particular transition temperature $T_c(B) = T_c/\sqrt{2}$, as may be shown by setting the derivative of Eq. (4.58) with respect to temperature equal to zero. We see from this equation that there is no latent heat when the transition occurs in zero field, i.e., when $T = T_c$, or at absolute zero, $T = 0$. In addition to the latent heat, there is also a jump in the specific heat at $T_c(B)$ which will be discussed in the following section.

Figures 4.12, 4.13, 4.14, and 4.15 show the temperature dependences of the thermodynamic functions C, S, H', and G, respectively, for high applied fields in which $T_c(B)$ is far below T_c. Figures 4.16, 4.17, 4.18, and 4.19 show these same plots for low applied fields in which $T_c(B)$ is slightly below T_c. All of these plots are for the case $A = 0$. We see from Figs. 4.12, 4.16, 4.13, and 4.17, respectively, that the specific heat C_s and entropy S_s

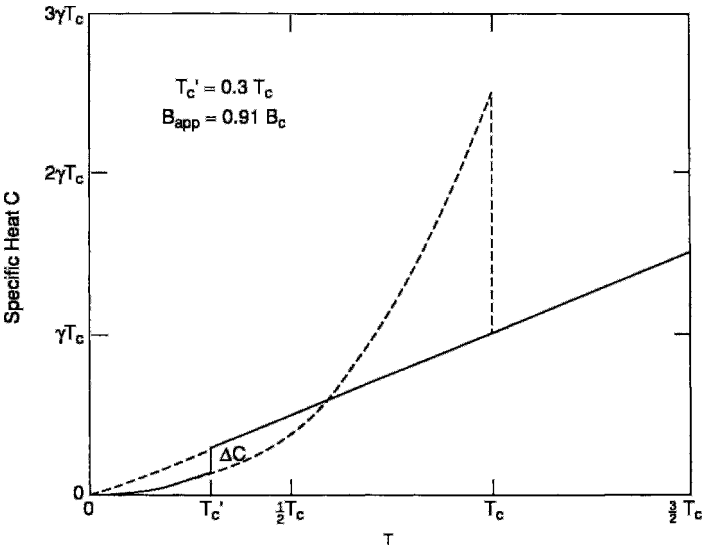

Figure 4.12 Temoerature dependence of the specific heat in the normal and superconducting states in the presence of a strong applied magnetic field. The downward jump in specific heat ΔC at T_c' is indicated.

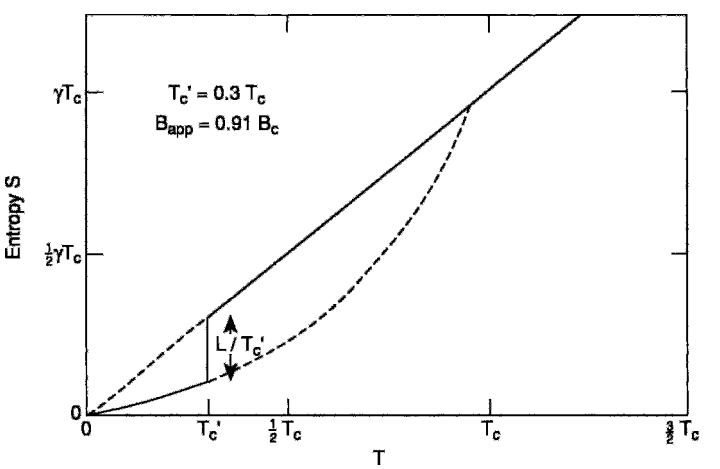

Figure 4.13 Temperature dependence of the entropy in the normal and superconducting states in the presence of a strong applied magnetic field. The latent heat factor L/T_c' of the jump in entropy at T_c' is indicated.

curves (assuming the presence of a magnetic field) coincide with their zero-field counterparts below $T_c(B)$ and with their normal-state counterparts above $T_c(B)$. In contrast, from Figs. 4.14, 4.18, 4.15, and 4.19 it is clear that the enthalpy H_s' and Gibbs free energy G_s curves in a magnetic field lie between their normal-state and zero-field superconducting state counterparts below the transition point $T_c(B)$, and coincide with the normal-state curves above the transition. These plots also show the jumps associated with the specific heat and the latent heat as well as the continuity of the Gibbs free energy at the transition.

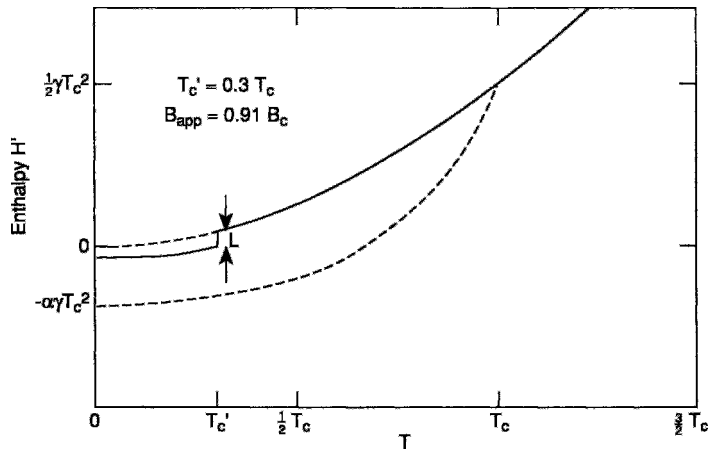

Figure 4.14 Temperature dependence of the enthalpy in the normal and superconducting states in the presence of a strong applied magnetic field. The jump in entropy at the transition temperature T_c' is equal to the latent heat L, as indicated.

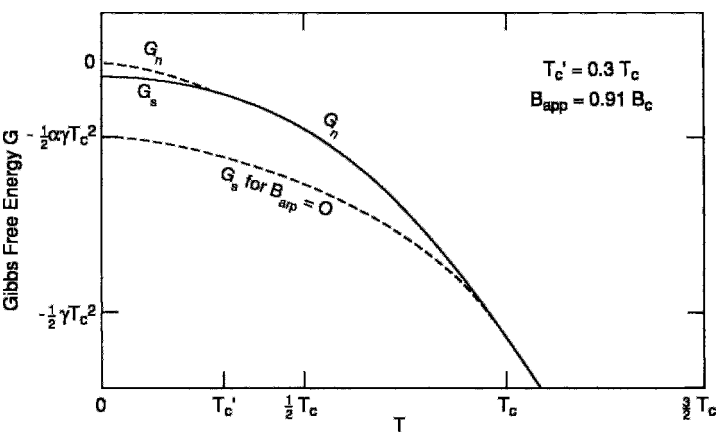

Figure 4.15 Temperature dependence of Gibbs free energy in the normal and superconducting states in the presence of a strong applied magnetic field. The transition is first order so that there is no discontinuity in free energy at the transition temperature T_c', but there is a discontinuity in the derivative. The normal (G_n) and superconducting (G_s) branches of the upper curve are indicated. The lower dashed (- - -) curve shows the Gibbs free energy in the superconducting state at zero field ($B_{app} = 0$) for comparison.

Figure 4.20 shows the experimentally determined Gibbs free-energy surface of $YBa_2Cu_3O_7$ obtained by plotting $G(T, B) - G(T, 0)$ versus temperature and the applied field close to the superconducting transition temperature (Athreya *et al.*, 1988). The free-energy differences are obtained by integrating Eq. (4.33) using measured magnetization data for $M(T, B)$:

$$G(T, 0) - G(T, B) = MdB'. \qquad (4.59)$$

This procedure is possible because close to the transition temperature magnetic flux

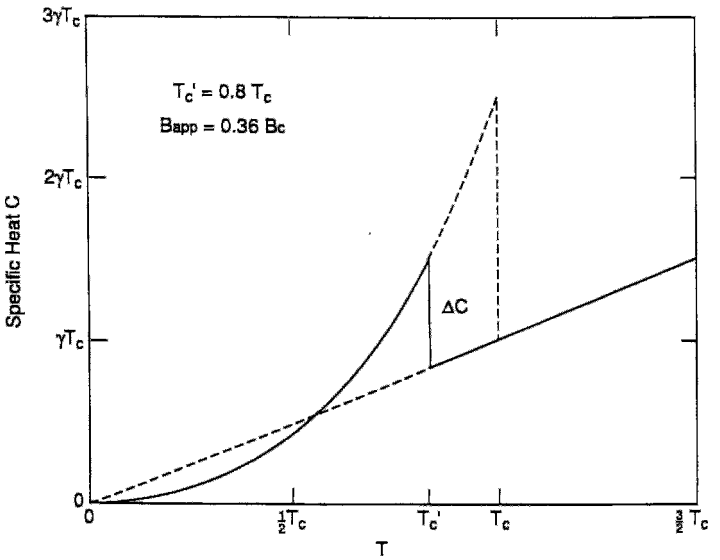

Figure 4.16 Temperature dependence of specific heat in the normal and superconducting states in the presence of a weak applied magnetic field. The jump in specific heat ΔC at T_c' is upward, in contrast to the downward jump shown in Fig. 4.12 for the high-field case.

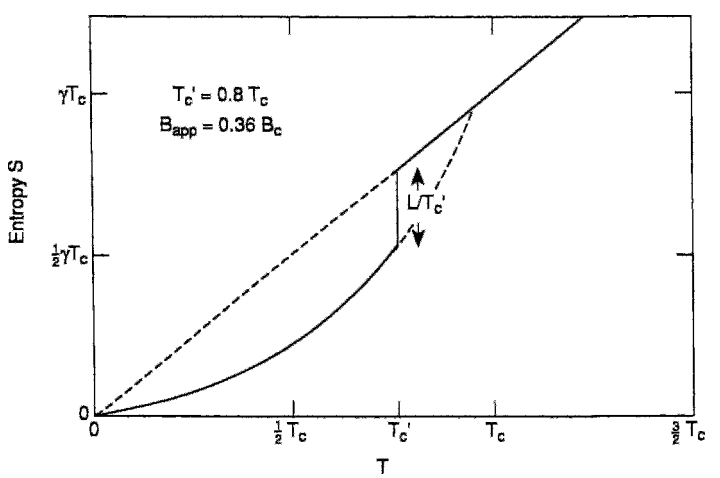

Figure 4.17 Temperature dependence of entropy in the normal and superconducting states in the presence of a weak applied magnetic field showing the jump in entropy L/T_c' at T_c', as expected for a first-order transition.

moves easily and reversibly into and out of the material, which makes the magnetization a thermodynamic variable. Magnetization is linear in $(T_c - T)^2$ near T_c. The free-energy surface varies with the magnetic field all the way up to 92 K. Fang *et al.* (1989) determined free-energy surfaces for thallium-based superconductors.

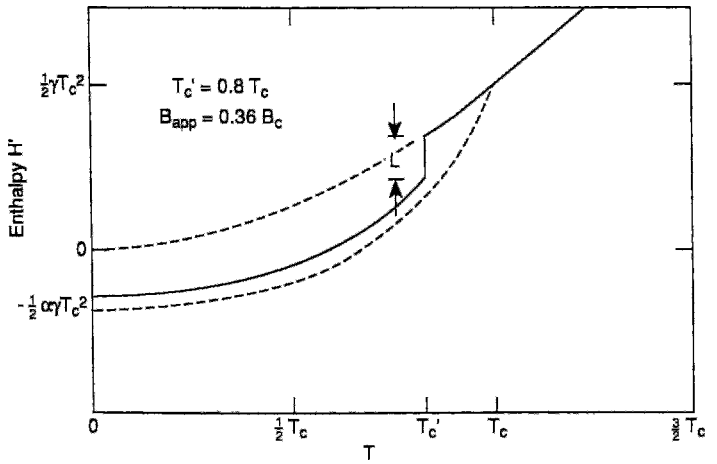

Figure 4.18 Temperature dependence of enthalpy in the normal and superconducting states in the presence of a weak applied magnetic field, showing the presence of a latent heat jump L at the transition temperature T_c', indicating a first-order transition.

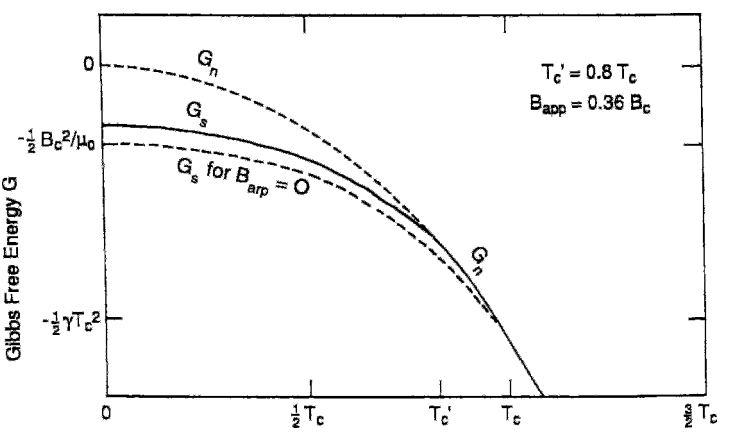

Figure 4.19 Temperature dependence of Gibbs free energy in the normal and superconducting states in the presence of a weak applied magnetic field using the notation of Fig. 4.15. The transition is first order so that the change in G at T_c' is continuous, but the change in its derivative is discontinuous (cf. Athreya *et al.*, 1988).

XI. NORMALIZED THERMODYNAMIC EQUATIONS

The equations for $G_s(T, B)$, $S_s(T)$, and $C_s(T)$ given in the previous section, together with $H_s'(T, B)$ of Problem 9, can be written in normalized form by defining two dimensionless independent variables,

$$t = \frac{T}{T_c} \qquad b = \frac{B}{B_c} \tag{4.60}$$

and two dimensionless parameters,

$$a = \frac{AT_c^2}{\gamma} \qquad \alpha = \frac{B_c^2}{\mu_0 \gamma T_c^2}. \tag{4.61}$$

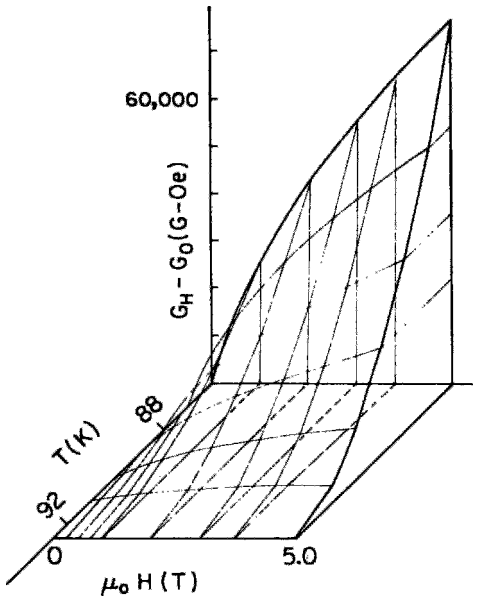

Figure 4.20 Free-energy surface for $YBa_2Cu_3O_7$ close to the transition temperature (Athreya *et al.*, 1988).

The resulting normalized expressions for g_s, s_s, and h'_s are given in Table 4.2. Also given in the table are the normalized specific heat jump $\Delta C/\gamma T_c$ and the normalized latent heat $L/\gamma T_c^2$. These expressions are valid under the condition

$$t^2 + b < 1. \tag{4.62}$$

The sample becomes normal when either t or b are increased to the point where $t^2 + b = 1$, and the value of t that satisfies this expression is called t':

$$t'^2 + b = 1. \tag{4.63}$$

This is the normalized equivalent of Eq. (4.55), where $t' = T'_c/T_c$ is the normalized transition temperature in a magnetic field.

The normalized specific heat jump has the following special values:

$$\frac{\Delta C}{\gamma T_c} = 2\alpha t'(3t'^2 - 1)$$

Table 4.2 Normalized Equations for the Thermodynamic Functions of a Superconductor in an Applied Magnetic Field B[a]

Gibbs Free Energy	$g_s = \dfrac{G_s}{\gamma T_c^2} = -\frac{1}{2}t^2 - \frac{1}{12}at^4 - \frac{1}{2}\alpha[(1-t^2)^2 - b^2]$
Entropy	$s_s = \dfrac{S_s}{\gamma T_c} = t + \frac{1}{3}at^3 - 2\alpha t(1-t^2)$
Specific Heat	$c_s = \dfrac{C_s}{\gamma T_c} = t + at^3 + 2\alpha t(3t^2 - 1)$
Enthalpy	$h'_s = \dfrac{H'_s}{\gamma T_c^2} = \frac{1}{2}t^2 + \frac{1}{4}at^4 - \frac{1}{2}\alpha[(1-t^2)(1+3t^3-b^2)]$
Specific Heat Jump	$\dfrac{\Delta C}{\gamma T_c} = 2\alpha t'(3t'^2 - 1)$
Latent Heat	$\dfrac{L}{\gamma T_c^2} = 2\alpha t'^2(1 - t'^2)$

Definitions of normalized variables (t, b) and parameters:

$t = \dfrac{T}{T_c}$	$b = \dfrac{B}{B_c(0)}$	$a = \dfrac{AT_c^2}{\gamma}$
$t' = \dfrac{T'}{T_c}$	$b' = \dfrac{B_c(T')}{B_c(0)}$	$\alpha = \dfrac{[B_c(0)]^2}{\mu_0 \gamma T_c^2}$

[a] The first four expressions are valid under the condition $t^2 + b < 1$ of Eq. (4.62), and the last two are valid at the transition point given by $t'^2 + b = 1$ from Eq. (4.63).

$$= \begin{cases} 0 & t' = 0 \\ -\dfrac{4\alpha}{9} & t' = \frac{1}{3} \\ 0 & t' = \frac{1}{\sqrt{3}} \\ 4\alpha & t' = 1 \end{cases} \quad \text{(max)}, \quad (4.64)$$

where $4\alpha/9$ is its maximum magnitude of $\Delta C/\gamma T_c$ for reduced temperatures in the range $0 < t' < 1/\sqrt{3}$, as indicated in Fig. 4.12. The normalized latent heat has the special values

$$\frac{L}{\gamma T_c^2} = 2\alpha t'^2(1 - t'^2)$$

$$= \begin{cases} 0 & t' = 0 \\ \frac{1}{2}\alpha & t' = \frac{1}{\sqrt{2}} \\ 0 & t' = 1 \end{cases} \quad \text{(max)}, \quad (4.65)$$

where its maximum $\frac{1}{2}\alpha$ is at $t' = 1/\sqrt{2}$.

XII. SPECIFIC HEAT IN A MAGNETIC FIELD

A number of authors have measured or calculated the specific heat of high-temperature superconductors in a magnetic field (Hikami and Fujita, 1990a,b; Riecke *et al.*, 1989; Quade and Abrahams, 1988; Watson *et al.*, 1989). Reeves *et al.*, (1989) found that the quantity C/T of $YBa_2Cu_3O_{7-\delta}$ in an applied magnetic field is linear in T^2 in the range $4\,\mathrm{K} < T < 6\,\mathrm{K}$ in accordance with the expression

$$C = [\gamma + \gamma'(B)]T + [A - A'(B)]T^3, \quad (4.66)$$

which is compared in Fig. 4.21 with experimental data for applied fields up to 3 T. It was also found that $\gamma = 4.38\,\mathrm{mJ/mole\,K^2}$ and $A = 0.478\,\mathrm{mJ/mole\,K^4}$, with the coefficients $\gamma'(B)$ and $A'(B)$ increasing as the applied magnetic field was increased.

At the highest measured field of 3 T, it turned out that

$$\frac{\gamma}{\gamma'} = 0.54, \qquad \frac{A}{A'} = 0.11. \quad (4.67)$$

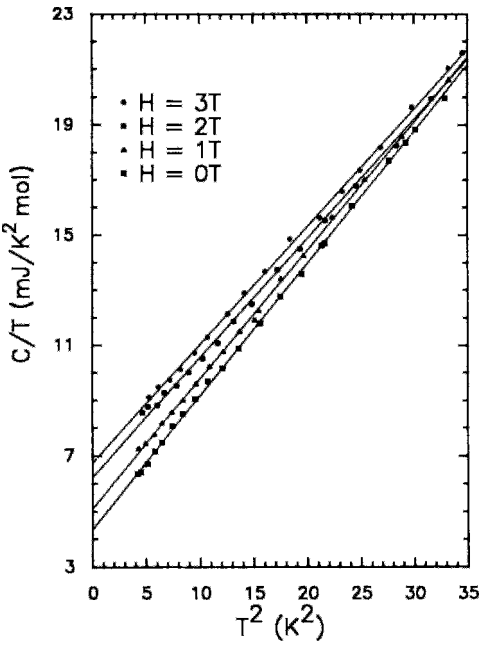

Figure 4.21 Low-temperature specific heat of $YBa_2Cu_3O_{7-\delta}$ in a magnetic field. The straight lines are fits of Eq. (4.66) to the data for each field value (Reeves *et al.*, 1989).

Reeves *et al.*, also mention that other workers have obtained results that differ from those described by Eq. (4.66).

Bonjour *et al.* (1991), Inderhees *et al.* (1991), and Ota *et al.* (1991) measured the magnetic-field dependence of the anisotropies in the specific heat near T_c. The results obtained by Inderhees *et al.* for untwinned $YBa_2Cu_3O_{7-\delta}$, which are presented in Fig. 4.22, turned out to be similar to those obtained by the other two groups. We see that increasing the magnetic field shifts the specific-heat jump to lower temperatures and broadens it, especially for an applied field parallel to the c-axis. Ebner and Stroud (1989) obtained a good approximation to the specific heat curves of Fig. 4.22 with $B \parallel c$ by including fluctuations in the Ginzburg–Landau free energy (cf. Chapter 6, Section III) and carrying out Monte–Carlo simulations. Figure 4.23 shows how the difference between the specific heat measured

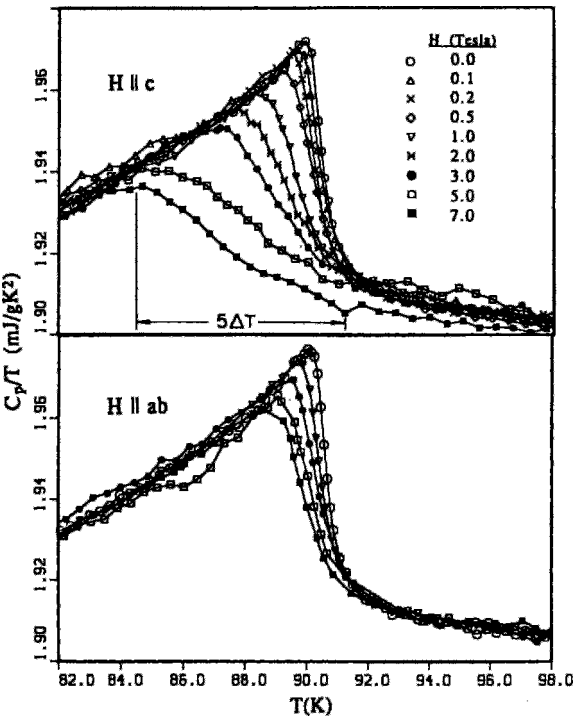

Figure 4.22 Specific heat jump of untwinned $YBa_2Cu_3O_{7-\delta}$ near T_c for different applied magnetic fields aligned parallel (top) and perpendicular (bottom) to the c-axis (Inderhees *et al.*, 1991).

at zero field C_0 and that measured in the field C_H depends on the value of the applied field at a temperature of 88 K, which is close to T_c. The difference is about five times larger in the parallel field orientation than in the perpendicular field orientation.

Bonjour *et al.* (1991) used their own specific heat data to determine the dependence of the entropy difference $S_0 - S_H$ on the applied field, where $S_0(T)$ is the entropy in the absence of the field and $S_H(T, B)$ the entropy assuming the presence of a field; their results are given in Fig. 4.24. They were aided by recent magnetic data of Welp *et al.* (1989; cf. Hake, 1968) in deducing the experimental entropy. Bonjour *et al.* compared their measured entropies with the following generalization of Eq. (4.41) to the mixed state of a Type II superconductor:

$$S_H(T, B) = S_n(T) + \chi'(T) \times \frac{B_{c2}(T) - B}{\mu_0} \cdot \frac{d}{dT} B_{c2}(T), \tag{4.68}$$

where $\chi' = \mu_0 dM/dB$ is called the 'differential susceptibility.' This gives

$$S_0(T_i) - S_H(T_i, B) = \chi'(T_i) \times \frac{B}{\mu_0} \cdot \frac{d}{dT} B_{c2}(T_i), \tag{4.69}$$

where $T_i = 80\,\mathrm{K}$ is the temperature at which all the specific heat curves are still superimposed. The values for $B = 5\,\mathrm{T}$ calculated from Eq. (4.68) using the data of Welp *et al.* are reasonably close to the measured values, as indicated in the figure.

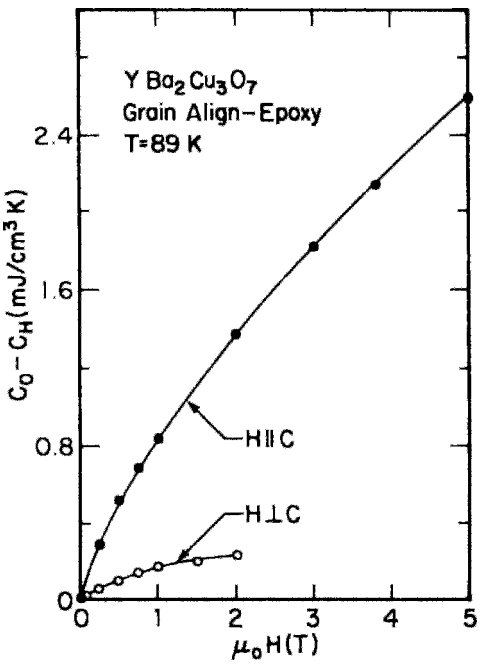

Figure 4.23 Magnetic field dependence of the specific heat difference for parallel and perpendicular fields (Athreya *et al.*, 1988).

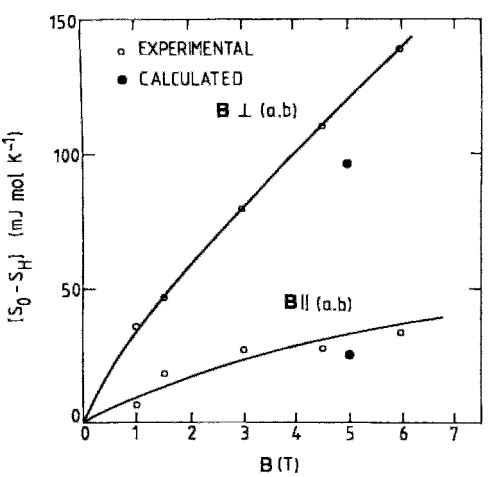

Figure 4.24 Magnetic field dependence of the entropy difference of parallel and perpendicular fields showing measured (○) and calculated (●) values for $YBa_2Cu_3O_7$ (Bonjour *et al.*, 1991).

XIII. FURTHER DISCUSSION OF THE SPECIFIC HEAT

Earlier in the chapter we mentioned the jump in the specific heat in zero field (4.44), in a magnetic field (4.43), and as predicted by the BCS theory (4.9). We also gave expressions for the temperature dependence of the specific heat in the superconducting state, one of which (Eq. (4.11)) appeared to be incompatible with the other two expressions (Eqs. (4.50) and (4.54)). In this section we compare these results and use them to evaluate the electronic specific-heat coefficient γ for zero field, after which we will write down an expression for the jump in the specific heat in a magnetic field.

At the transition temperature $T = T_c$ in zero field, Eq. (4.50), with $A = 0$, simplifies to

$$C_s(T_c) - C_n(T_c) = \frac{4[B_c(0)]^2}{\mu_0 T_c}, \qquad (4.70)$$

where $C_n(T_c) = \gamma T_c$. If the BCS prediction (4.9) is substituted in Eq. (4.70), we obtain for the normalized specific heat factor α of Eq. (4.61)

$$\alpha = 0.357. \qquad (4.71)$$

The curves of Figs. 4.7–4.9 were drawn for this value. Since $B_c^2/2\mu_0$ is an energy density expressed in units J/m^3 and γ is given in units mJ/mole K, it is necessary to multiply γ by the density ρ and divide it by the molecular weight (MW) in Eq. (4.71), giving us the BCS dimensionless ratio

$$R_{BCS} = \frac{[B_c(0)]^2(\mathrm{MW})}{\mu_0 T_c^2 \rho \gamma} = 449, \qquad (4.72)$$

where B_c is expressed in units mT, γ in mJ/mole K^2, ρ in g/cm^3, and T_c in degrees Kelvin. It is reasonable to assume that this expression will be a good approximation for Type I superconductors, and we see from the last column of Table 4.3 that this is indeed

Table 4.3 Variation of the Dimensionless Ratio $R = B_c^2\,(\mathrm{MW})/\mu_0 T_c^2 \rho\gamma$ of Several Elemental Superconductors[a]

Element	T_c K	$\frac{B_c^2(\mathrm{MW})}{\mu_0 T_c^2 \rho\gamma}$ $\frac{\mathrm{mT^2\,cm^3}}{\mathrm{mJ}}$	R/R_{BCS}
W	0.015	676	1.51
Ir	0.11	569	1.27
Ru	0.49	577	1.29
Zr	0.61	300	0.67
Os	0.66	403	0.90
Re	1.7	522	1.16
Sn	3.72	615	1.37
V	5.4	571	1.27
Pb	7.20	733	1.63
Tc	7.80	443	0.99
Nb	9.25	697	1.55
BCS theory	—	449	1.00

[a] $B_c = B_c(0)$, MW is molecular weight, ρ density, and γ electronic specific heat.

the case for the elemental superconductors. Equation (4.72) was derived for materials in which the number density of the conduction electrons is the same as the number density of the atoms. For materials in which this is not the case, the effective electron density $\beta\rho$ can be used, where β is the factor introduced in Eq. (4.4), to give

$$\frac{[B_c(0)]^2(\mathrm{MW})}{\mu_0 T_c^2 \beta\rho\gamma} = 449. \tag{4.73}$$

Equations (4.54) and (4.11) constitute entirely different dependences of $C_s(T)$ on temperature, and it is of interest to compare them. In normalized form, with A set equal to zero, they are

$$\frac{C_s(T)}{\gamma T_c} = \frac{T}{T_c}\left[0.285 + 2.145\left(\frac{T}{T_c}\right)^2\right], \tag{4.74}$$

$$\frac{C_s(T)}{\gamma T_c} = 14\,\exp\left(-1.76\frac{T_c}{T}\right), \tag{4.75}$$

where α has the BCS value 0.357 and the coefficient 1.76 in the exponential expression is chosen because the BCS theory predicts $\Delta = 1.76\,kT_c$ in Eq. (4.11). The coefficient 14 is selected to normalize Eq. (4.75) to the BCS value (4.11); i.e., $C_s(T_c) = 2.43\gamma T_c$ at the transition point. Figure 4.25 compares the temperature dependence of (4.74) and (4.75), and shows that they are close at all but the lowest temperatures. Equation (4.74) is slightly lower for T near T_c and Eq. (4.75) is significantly lower for $T \ll T_c$.

The first of these expressions for $C_s(T)$, i.e., Eq. (4.74), is based on Eq. (4.45), which is a good approximation to the tempera-

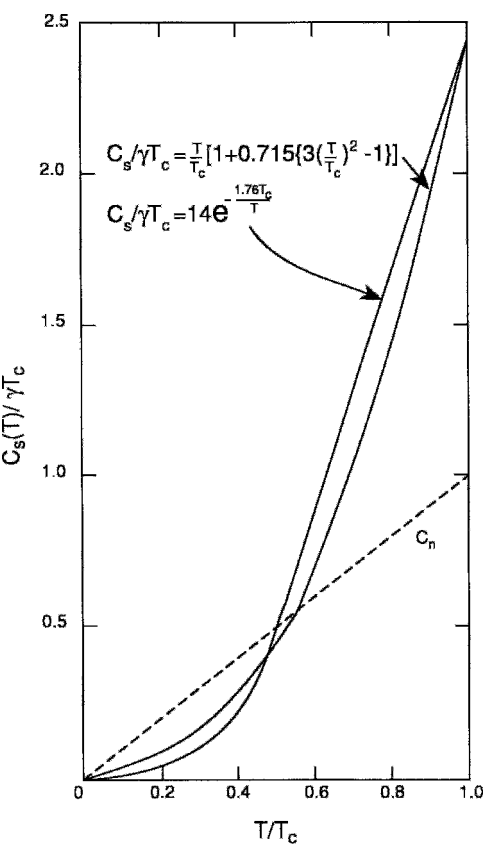

Figure 4.25 Comparison of the thermodynamic and BCS expressions (4.74) and (4.75), respectively, for the specific heat ratio $C_s/\gamma T_c$ normalized to the same value at $T = T_c$.

ture dependence of the critical field $B_c(T)$ near the critical temperature. However, the temperature derivatives of Eq. (4.45) that enter into the $C_s(T)$ expression (4.43) are not expected to be valid quantitatively far below T_c. The second expression, Eq. (4.75), on the other hand, is based on excitation of quasiparticles to energies above the superconducting ground state, and is valid at temperatures far below T_c where most of the electrons that contribute to the superconductivity are condensed as Cooper pairs in the ground-energy state. Therefore, we might expect an experimental $C_s(T)$-versus-T curve to approximate Eq. (4.75) far below T_c, as in the case of the superconducting Al data shown in Fig. 4.5.

Now that we have found explicit expressions for the specific heat in the superconducting state in the absence of a magnetic field, let us examine the case when there is a field present. We will continue to assume that $\gamma T = C_n(T)$ and $A = 0$, and that the BCS expression (4.10) is valid in zero field at T_c. Thus, in a magnetic field Eq. (4.74) can be written

$$C_s(T) - C_n(T) = 0.715\gamma T\left[3\left(\frac{T}{T_c}\right)^2 - 1\right], \tag{4.76}$$

and the jump in specific heat at the transition temperature T_c' in a magnetic field is given by

$$C_s(T_c') - C_n(T_c') = 0.175\gamma T\left[3\left(\frac{T_c'}{T_c}\right)^2 - 1\right]. \tag{4.77}$$

This change in specific heat $C_s - C_n$ is negative for $T_c' < T_c/\sqrt{3}$ and positive for $T_c' > T_c/\sqrt{3}$. This means that with increasing temperature there is an upward jump in the specific heat for $T_c' < T_c/\sqrt{3}$ and a downward jump for $T_c' > T_c/\sqrt{3}$, as shown in Figs. 4.12, and 4.16, respectively. We also see that no jump at all occurs at the crossover point of the normal-state and superconducting curves, where $T_c' = T_c/\sqrt{3}$. In addition to the jump in specific heat, there is also latent heat present, Eq. (4.57), in the presence of a magnetic field.

XIV. ORDER OF THE TRANSITION

We mentioned in Section III that the transition from the normal to the superconducting state in the absence of a magnetic field is a second-order phase transition, which means that the Gibbs free energy and its temperature derivative are continuous at the transition:

$$G_s(T_c) = G_n(T_c), \tag{4.78}$$

$$\frac{dG_s}{dT} = \frac{dG_n}{dT}. \tag{4.79}$$

This can be seen from Eq. (4.39), using the condition $B_c(T_c) = 0$ from Eq. (4.45). Therefore, there is no latent heat, but there is a discontinuity in the specific heat given, for example, by Eqs. (4.44) and (4.70).

We showed in Section X that the transition from the superconducting to the normal state in the presence of a magnetic field does have a latent heat given by Eq. (4.58) and, therefore, is a first-order phase transition.

XV. THERMODYNAMIC CONVENTIONS

There are several conventions in vogue for formulating the thermodynamic approach to superconductivity. Some of these conventions make use of the total internal energy U_{tot}, which includes the energy of the magnetic field $B^2/2\mu_0 = \frac{1}{2}\mu_0 H^2$ that would be present in the absence of the superconductor, whereas others, including the one adopted in the present work, use the internal energy U, which excludes this field energy. The

total internal energy and internal energy are related through the expressions

$$U_{\text{tot}} = U + \frac{B^2}{2\mu_0}, \tag{4.80}$$

$$dU_{\text{tot}} = TdS + \mathbf{H}\cdot d\mathbf{B}, \tag{4.81}$$

$$= dU + d\left(\frac{B^2}{2\mu_0}\right). \tag{4.82}$$

Some authors, including ourselves, deduce the properties of superconductors with the aid of the Gibbs free energy G defined in Eq. (4.22), while others resort to G_{tot}, where

$$G_{tot} = H'_{\text{tot}} - TS. \tag{4.83}$$

Still other authors instead employ the Helmholtz free energy F or F_{tot}, where

$$F = U - TS, \tag{4.84}$$

$$F_{\text{tot}} = U_{\text{tot}} - TS \tag{4.85}$$

$$= F + \frac{B^2}{2\mu_0}. \tag{4.86}$$

An added complication in making comparison between results arrived at by different authors arises because some authors use the cgs system instead of SI units.

XVI. CONCLUDING REMARKS

In the beginning of this chapter we discussed the experimental results of specific heat measurements, and then proceeded to develop the thermodynamic approach to superconductivity, an approach in which the specific heat plays a major role. Some of the expressions that were derived are fairly general. Others, however, are for the particular model in which the specific heat (4.24) in the normal state obeys the linear low-temperature relation γT and the critical field (4.45) has a simple parabolic dependence $[1-(T/T_c)^2]$ on temperature. Some expressions make use of the additional assumption that the BCS expression $C_s(T_c) = 2.43\gamma T_c$ of Eq. (4.9) is also valid. It is believed that these models provide a good physical picture of the thermodynamics of the superconducting state. A more appropriate description for the high-temperature superconductors would include the AT^3 term in the specific heat. It is, of course, also true that real superconductors have more complex temperature dependences than is implied by these simple models. The theoretical approaches presented in the following two chapters are needed to achieve a more basic understanding of the nature of superconductivity.

PROBLEMS

1. Consider a metallic element such as copper that contributes one electron per atom to the conduction band. Show that in the free-electron approximation the electronic and phonon contributions to the specific heat will be equal at the temperature

$$T = \Theta_D(5/24\pi^2)^{1/2}\left(\frac{\Theta_D}{T_F}\right)^{1/2}$$

2. Show that the factor β in Eq. (4.5) has the value 1 for an element, 1/7 for the LaSrCuO compound, and 3/13 for the YBaCuO compound.
3. A superconductor has a Fermi energy of 3 eV. What is the density of states at the Fermi level and the electronic specific-heat factor γ. If this superconductor has an effective mass m^* of 81, what will be the value of these quantities? What other measurable quantities depend on the effective mass?
4. Consider a BCS-type superconductor with transition temperature $T_c = 20\,\text{K}$ and a critical field $B_c(0) = 0.2\,\text{T}$. What is its electronic specific-heat factor γ? What are the values of its specific heat, entropy, Gibbs free energy, and enthalpy

in the superconducting state at 10 K, both in zero field and in an applied magnetic field of 0.1 T? (Ignore the vibrational contribution to the specific heat.)

5. With the initial conditions of the previous problem, what applied magnetic field will drive the superconductor normal at 10 K? What will be the latent heat? What will be the change in the specific heat at the transition? (Ignore the vibrational contribution to the specific heat.)
6. Show that the following expressions for the enthalpy are valid:

$$\begin{aligned} H'_{\text{tot}} &= U_{\text{tot}} - H \cdot B \\ &= H' - \tfrac{1}{2}\mu_0 H^2 \\ dH'_{\text{tot}} &= TdS - B \cdot dH \\ &= dH' - d\left(\tfrac{1}{2}\mu_0 H^2\right). \end{aligned}$$

7. Show that equating the superconducting- and normal-state Gibbs free energies $G_s(T, H) = G_n(T)$ at the critical temperature leads to Eq. (4.55):

$$T'_c = T_c \left[1 - \frac{B}{B_c(0)}\right]^{1/2}.$$

8. Calculate the transition temperature T'_c, jump in specific heat, jump in entropy, jump in enthalpy, and the values of the Gibbs and Helmholtz free energies at the temperature $T = T'_c$ of a Type I superconductor in an applied magnetic field $B_{\text{app}} = \frac{1}{2}B_c$. Express your answers in terms of γ and T_c, assuming that $\alpha = 4.0$ and $A = \gamma/3T_c^2$.
9. We know from thermodynamics that at the transition temperature $T = T_c(B)$ in an applied magnetic field B, the latent heat equals the difference in enthalpy, $L = H'_n - H'_s$. Show that this difference gives Eq. (4.57).
10. Derive the expression for the enthalpy of a superconductor in a magnetic field, and show that in its normalized form it agrees with the expression $H'_s/\gamma T_c^2$ in Table 4.2.
11. Show that the specific heat jump in a magnetic field has the maximum $4\alpha\gamma T_c/9$ in the range $0 < T_c < 1/\sqrt{3}$, and that the latent heat has the maximum $\frac{1}{2}\alpha\gamma T_c^2$.
12. Show that the following normalized thermodynamic expressions are valid,

$$\begin{aligned} du &= tds + b \cdot dm, \\ cdt &= tds, \\ h' &= u - b \cdot m, \\ g &= h' - ts, \end{aligned}$$

and write down expressions for the normalized internal energy u and magnetization m.

13. Derive Eq. (4.70) from Rutger's formula.
14. Sketch a three-dimensional Gibbs free energy surface analogous to the surface presented in Fig. 4.20 using the equations in Section X.

This page intentionally left blank

5

Magnetic Properties

I. INTRODUCTION

Superconductivity can be defined as the state of perfect diamagnetism, and consequently researchers have always been interested in the magnetic properties of superconductors. In the second chapter we explained how magnetic fields are excluded from and expelled from superconductors. Then in the previous chapter we examined the thermodynamics of the interactions of a superconductor with a magnetic field. The present chapter will extend the discourse to a number of additional magnetic properties.

We begin with a discussion of magnetization, zero field cooling, and field cooling, with comments on the granularity and porosity of high-temperature superconductors. Next we will explain how magnetization depends on the shape of the material and how this shape dependence affects the measured susceptibility. Both ac and dc susceptibilities will be treated. Finally, we will show how samples can be categorized in terms of traditional magnetic behavior, such as diamagnetism, paramagnetism, and antiferromagnetism. The chapter will conclude with remarks on ideal Type II superconductors and on magnets.

In the present chapter we do not always distinguish between Type I and Type II superconductors since many of the results that will be obtained here apply to both types of superconductors.

In later chapters we will discuss additional magnetic properties of superconductors, such as, in Chapter 11, the intermediate and mixed states of Type I and Type II

superconductors, respectively. In Chapter 13 we will present the Bean model which provides a good description of some magnetic properties, especially hysteresis loops.

II. SUSCEPTIBILITY

A material in the mixed state of a Type II superconductor contains magnetic flux in vortices that are embedded in a superconducting matrix with $\chi = -1$. From a macroscopic perspective we average over this structure and consider the material to be homogeneous with a uniform susceptibility having a value that is constant throughout the volume. The internal fields B_{in}, H_{in}, and M are also averages that are uniform at this level of observation. In this chapter we will be working with these average quantities and ignore the underlying mesoscopic vortex structure.

We saw in Chapter 1 how the B and H fields within a homogeneous medium are related to the magnetization M and the susceptibility χ through Eqs. (1.69), (1.77), and (1.78a),

$$B_{\text{in}} = \mu_0(H_{\text{in}} + M) \tag{5.1}$$

$$= \mu_0 H_{\text{in}}(1 + \chi) \tag{5.2}$$

$$\chi = \frac{M}{H_{\text{in}}} \tag{5.3}$$

where μ_0 is the permeability of free space and χ is an intrinsic property of the medium.

In the general case the susceptibility is a symmetric tensor with components χ_{ij} because of the off-diagonal components ($i \neq j$) the vector fields $\mathbf{B}_{\text{in}}$, $\mathbf{H}_{\text{in}}$, and $\mathbf{M}$ are in different directions. In the principal coordinate system the susceptibility tensor is diagonal with components χ_x, χ_y, and χ_z along the three orthogonal principle directions. High-temperature superconductors are planar with values $\chi_a \approx \chi_b$ in the plane of the CuO_2 layers different from χ_c, which is measured along the c direction perpendicular to the layers. This axial anisotropy manifests itself in the large difference in the critical fields of single crystals when measured parallel to and perpendicular to the CuO_2 layers, as shown in Table 12.5. Several figures in the present chapter will illustrate this anisotropy. However, for the present we will restrict our attention to the isotropic case, for which $\chi = \chi_x = \chi_y = \chi_z$.

III. MAGNETIZATION AND MAGNETIC MOMENT

The magnetization $\mathbf{M}$ is the magnetic moment per unit volume. This means that the overall magnetic moment $\boldsymbol{\mu}$ of a sample is the volume integral of $\mathbf{M}$ throughout it,

$$\boldsymbol{\mu} = \int \mathbf{M}\, dV. \tag{5.4}$$

Many magnetic studies of superconductors are carried out using samples with shapes that can be approximated by ellipsoids. When the magnetic field $\mathbf{B}_{\text{app}} = \mu_0 \mathbf{H}_{\text{app}}$ is applied along or perpendicular to the symmetry axis of such a sample, the internal fields $\mathbf{B}_{\text{in}}$ and $\mathbf{H}_{\text{in}}$, and the magnetization $\mathbf{M}$ as well, are uniform and parallel to the applied field, with M given by

$$M = \frac{\mu}{V}, \tag{5.5}$$

where V is the sample volume. Long thin cylinders and thin films are limiting cases of this general ellipsoidal geometry.

We begin by analyzing the parallel geometry case of a superconductor in the shape of a long cylinder located in an applied field directed along its axis, as shown in Fig. 12.1. For this case the fields can be written as scalars. We wish to express the internal fields in terms of the known applied field B_{app}:

$$B_{\text{app}} = \mu_0 H_{\text{app}}. \tag{5.6}$$

For this particular geometry the boundary condition (1.74) shows that the internal field H_{in} equals H_{app}. From Eqs. (5.2) and (5.3) the internal fields are given by

$$B_{in} = B_{app}(1+\chi), \tag{5.7}$$

$$H_{in} = \frac{B_{app}}{\mu_0}, \tag{5.8}$$

$$M = \frac{\chi B_{app}}{\mu_0}. \tag{5.9}$$

Experimentally, it is the magnetic moment μ, given by

$$\mu = \frac{\chi V B_{app}}{\mu_0}, \tag{5.10}$$

which is measured, for example, by a Superconducting Quantum Interference Device (SQUID) magnetometer. Since V and B_{app} are known, Eqs. (5.10) and (5.9) can be used to determine the susceptibility and magnetization, respectively. In these expressions χ is the volume susceptibility corresponding to the magnetic moment per unit field per unit volume. We assume that χ is independent of the applied field B_{app}, and that M is proportional to B_{app} through Eq. (5.9).

For an ideal superconductor the property of perfect diamagnetism means that $\chi = -1$, so that Eqs. (5.7)–(5.10) become, respectively,

$$B_{in} = 0, \tag{5.11}$$

$$H_{in} = \frac{B_{app}}{\mu_0}, \tag{5.12}$$

$$M = -\frac{B_{app}}{\mu_0}, \tag{5.13}$$

$$\mu = -\frac{V B_{app}}{\mu_0}, \tag{5.14}$$

and we see that the internal field B_{in} vanishes. This is the case illustrated in Fig. 12.1. The fact that B_{in} vanishes can also be explained in terms of the shielding currents (see Fig. 6.19) which flow on the surface and act like a solenoid to produce a field B_{in} which cancels B_{app}. This was discussed at length in Chapter 2, Section VIII.

Figure 5.1 shows the experimentally measured magnetization curve for

$$(La_{0.9}Sr_{0.1})_2CuO_4$$

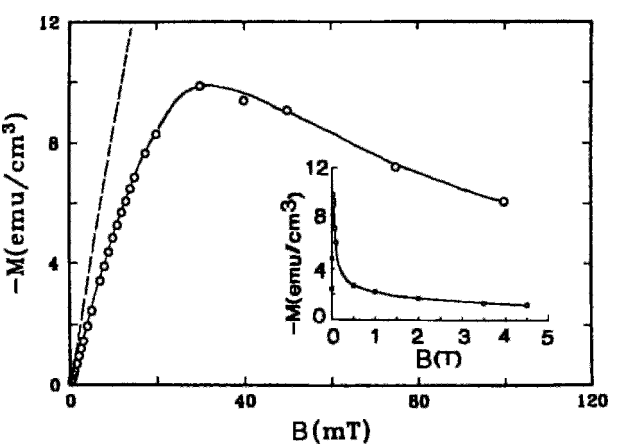

Figure 5.1 Zero-field magnetization of annealed $(La_{0.9}Sr_{0.1})_2CuO_4$ in applied magnetic fields up to 100 mT at a temperature of 5 K. The maximum of the curve occurs near the lower-critical field $B_{cl} \approx 30$ mT. The dashed line is the low-field asymptote for perfect diamagnetic shielding (Maletta *et al.*, 1987). The inset shows the magnetization in applied fields up to 4.5 T.

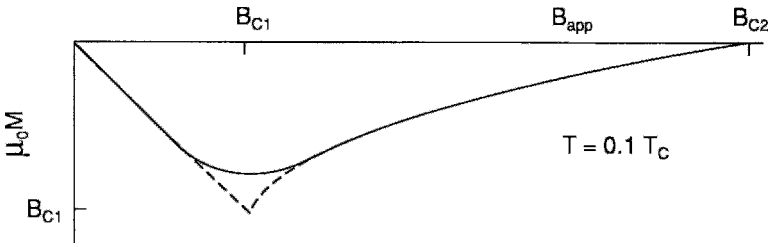

Figure 5.2 Typical magnetization curve for $T = 0.1T_c$ (cf. Fig. 5.3, which is drawn to the same scale).

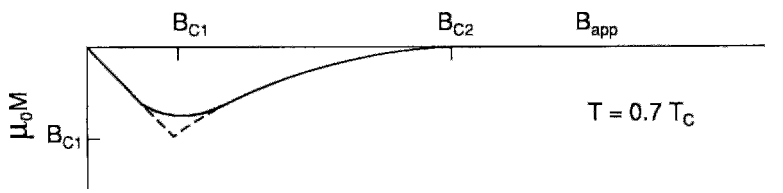

Figure 5.3 Typical magnetization curve for $T = 0.7\,T_c$ drawn to the same scale as Fig. 5.2.

plotted against the applied field. The applied field reaches a maximum at 30 mT, which is approximately the lower critical field B_{c1} (Maletta *et al.*, 1987; see Müller *et al.*, 1987). The upper critical field is well beyond the highest field used, 4.5 T, as shown in the inset to the figure. Note that the abscissa scale is in terms of milliteslas for the main figure, and in terms of teslas for the inset.

We see in Fig. 12.36 that the critical fields B_{c1} and B_{c2} are highest at 0 K and that they decrease continuously with increasing temperature until they become zero at the transition temperature T_c. Thus, a magnetization curve, such as that presented in Fig. 10.1, contracts as temperature increases. This situation is illustrated graphically by Figs. 10.2 and 10.3, which show sketches of magnetization curves at two temperatures $T = 0.1T_c$ and $T = 0.7T_c$.

IV. MAGNETIZATION HYSTERESIS

Many authors have reported hysteresis in the magnetization of superconductors, meaning that the magnetization depends on the previous history of how magnetic fields were applied. Hysteresis is observed when the magnetic field is increased from zero to a particular field, then scanned back through zero to the negative of this field, and finally brought back to zero again. Figure 5.4 sketches a low-field hysteresis loop showing the coercive field B_{coer}, or value of the applied field that reduces the magnetization to zero, and the remanent magnetization M_{rem}, or magnitude of the magnetization when the applied field passes through zero.

Figures 5.5 and 5.6, respectively, show how low-field hysteresis loops vary with changes in the scanning-field range and temperature. It is clear from these figures that the hysteresis loop is thin and close to linear when the scan range is much less than the lower-critical field and when the temperature is close to T_c. Decreasing the temperature broadens the loop. The larger the magnetic field excursion, the more the loop becomes elongated horizontally, which increases the ratio $B_{coer}/\mu_0 M_{rem}$ between the coercive field and the remanent magnetization.

Figure 5.7 shows how hysteresis loops traversed over a broad field range vary with

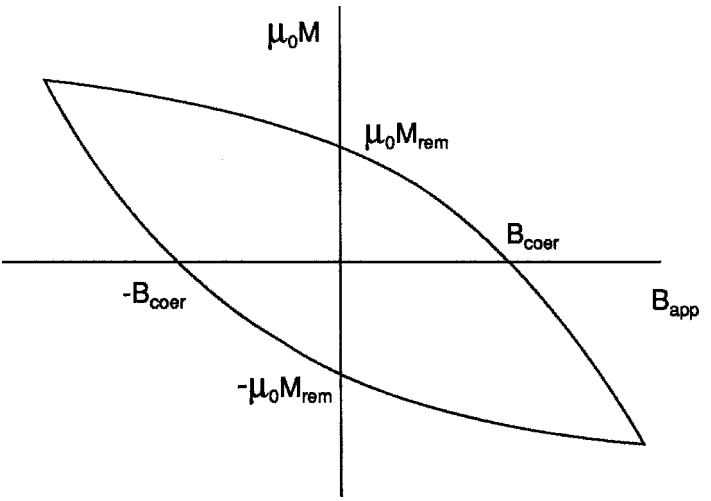

Figure 5.4 Typical low-field hysteresis loop showing the coercive field B_{coer}, where magnetization is zero, and the remanent magnetization M_{rem} which remains when the applied field is reduced to zero.

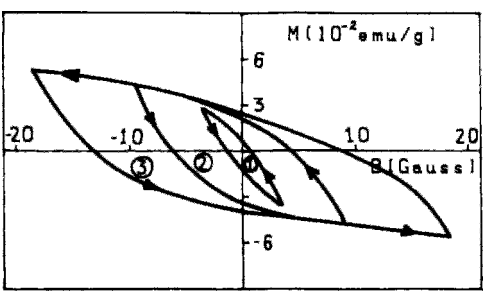

Figure 5.5 Low-field hysteresis loops of $(La_{0.9}Sr_{0.1})_2CuO_4$ at 4.5 K cycled over different ranges of field up to 2 mT (Marcus *et al.*, 1987).

the temperature. Each loop has a peak near the lower-critical field B_{c1}. Beyond this point flux penetrates and the magnetization begins to decrease gradually. Ideally, no flux penetrates below B_{c1}, but in practice some of it does, as Fig. 5.1 suggests. The large hysteresis is indicative of flux pinning. It is observed that as the temperatures is lowered, the loop increases in area, as shown in the figures. Paranthaman *et al.* (1993) obtained similar results with the superconductor

$$HgBaCuO_{4+\delta}.$$

Chapter 13 will present a model, called the critical-state model, which provides an explanation for the shapes of many hysteresis loops.

V. ZERO FIELD COOLING AND FIELD COOLING

In Chapter 2 we discussed the magnetic properties of a perfectly diamagnetic material with a hole that is either open or closed to the outside. We examined these two cases for the conditions of (a) zero field cooling (ZFC), a condition characterized by flux exclusion from both the open hole and the enclosed cavity, a phenomenon called *diamagnetic shielding*, and (b) field cooling (FC), a condition characterized by flux expulsion from the cavity but not from the hole, a phenomenon called the *Meissner effect*. For both cases, the flux is absent from the superconducting portion. Hence, the overall sample can exclude more flux when it is zero field cooled than it expels when it is is field cooled. The difference between the amount of excluded

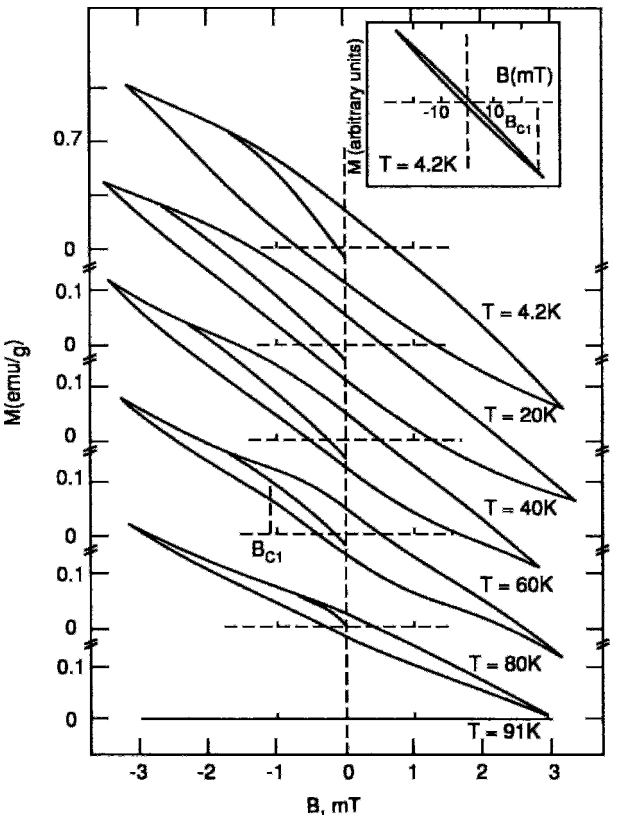

Figure 5.6 Low-field hysteresis loops of $YBa_2Cu_3O_7$ cycled over the same field scan, $-3\,\text{mT} \leq B_{\text{app}} \leq 3\,\text{mT}$, over a range of temperatures. The loops gradually collapse as the temperature increases. The virgin curve for the initial rise in magnetization is given for each loop (Senoussi *et al.*, 1988).

flux and the amount of expelled flux is the *trapped flux*.

To clarify some of the principles involved in ZFC and FC experiments, we will examine the rather idealized case of a cylindrical sample of total volume V_T that contains a volume V_s of perfectly superconducting material ($\chi = -1$), a cylindrical hole of volume V_h open at the top and bottom, and a totally enclosed cylindrical cavity of volume V_c,

$$V_T = V_s + V_h + V_c, \tag{5.15}$$

as shown in Fig. 5.8. The hole and cavity could either be empty or contain normal material; since the effect in the two cases is the same, we will consider them empty. The magnetic field B_{app} is applied parallel to the cylinder axis, as indicated in Fig. 5.9; demagnetizing effects arising from the lack of cylindrical symmetry will not be taken into account.

For this composite sample the measured or effective magnetic moment μ_{eff} can receive contributions from three individual components,

$$\mu_{\text{eff}} = \mu_s + \mu_h + \mu_c, \tag{5.16}$$

with μ_s due to the superconducting material itself, μ_h resulting from the presence of

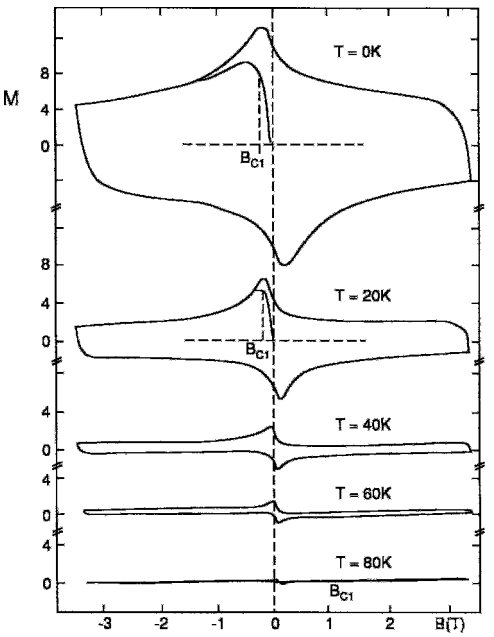

Figure 5.7 High-field hysteresis loops of $YBa_2Cu_3O_7$ cycled over the same field scan, $-3\,\mathrm{T} \le B_{\mathrm{app}} \le 3\,\mathrm{T}$, over a range of temperatures. The loops gradually collapse as the temperature increases. The deviation of the virgin curve from linearity occurs near the lower-critical field $\mathbf{B}_{c1}$, which increases as the temperature is lowered (Senoussi *et al.*, 1988).

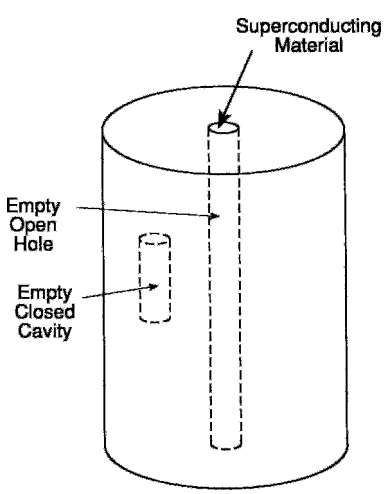

Figure 5.8 Cylindrical superconducting sample with hole of volume V_{h} open at the top and bottom, and a totally enclosed cavity of volume V_{c}.

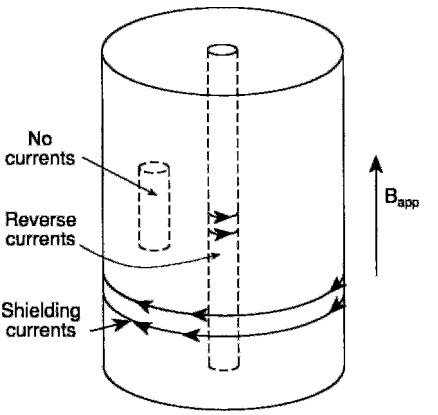

Figure 5.9 The superconducting cylinder sketched in Fig. 5.10 after field cooling in an axial applied field, showing the shielding currents flowing around the outside, the reverse-direction current flow around the walls of the open hole, and the absence of currents in the enclosed cavity.

the open hole, and μ_{c} due to the enclosed cavity. In the case of zero field cooling, the circulating surface currents shield the superconductor, hole, and cavity, so Eq. (5.10), with $\chi = -1$, becomes

$$\mu_{\mathrm{zfc}} = -(V_{\mathrm{s}} + V_{\mathrm{h}} + V_{\mathrm{c}})\frac{B_{\mathrm{app}}}{\mu_0}. \qquad (5.17)$$

For field cooling, the magnetic field is trapped in the open hole, while surface currents shield the superconductor itself and the enclosed cavity from this field, which gives for the magnetic moment

$$\mu_{\mathrm{fc}} = -(V_{\mathrm{s}} + V_{\mathrm{c}})\frac{B_{\mathrm{app}}}{\mu_0}. \qquad (5.18)$$

Associated with the effective magnetic moment (5.16) there is an effective magnetization M_{eff} defined by Eq. (5.5) in terms of the total volume (5.15)

$$M_{\mathrm{eff}} = \frac{\mu_{\mathrm{eff}}}{V_{\mathrm{T}}} = \chi_{\mathrm{eff}}\frac{B_{\mathrm{app}}}{\mu_0}. \qquad (5.19)$$

which can be employed to write down the ZFC and FC magnetization, respectively.

The corresponding susceptibilities χ_{zfc} and χ_{fc} are determined in Problem 1. We know from Eqs. (5.9) and (5.10) and the above expressions that the ratios between the FC and ZFC moments, magnetizations, and susceptibilities all have the same value,

$$\frac{\mu_{fc}}{\mu_{zfc}} = \frac{M_{fc}}{M_{zfc}} = \frac{\chi_{fc}}{\chi_{zfc}} = \frac{V_s + V_c}{V_s + V_h + V_c}, \tag{5.20}$$

and that this value is independent of the units used.

If field cooling is carried out in an applied field $B_{fc} = \mu_0 H_{fc}$ that differs from the field B_{app} which is applied to measure the magnetic moment, we obtain, neglecting hysteresis (see Problem 3),

$$\mu_0 \mu_{fc} = -(V_s + V_c) B_{app} + (B_{fc} - B_{app}) V_h, \tag{5.21}$$

which reduces to Eq. (5.18) when $B_{app} = B_{fc}$. Thus, the field trapped in the hole acts like a magnetization with the same magnitude and direction as the quantity $(B_{fc} - B_{app})$. Ordinarily, field cooling is carried out in the same field as the susceptibility measurements, so that $B_{app} = B_{fc}$ and Eq. (5.18) applies.

As long as the sample is kept below T_c the field B_{fc} remains in the open hole irrespective of whether the outside field is turned off or another applied field is turned on. B_{fc} is maintained in the hole by surface currents circulating in opposite directions around the inside of the superconducting tube, as shown in Fig. 5.9 and explained in Chapter 2, Sections VIII and IX. This trapped flux subtracts from the diamagnetic response to make the measured susceptibility and magnetization less negative for the Meissner effect (FC) than for diamagnetic shielding (ZFC). This is shown in Fig. 5.10 for the rubidium fullerene compound (C.-C. Chen *et al.*, 1991; Politis *et al.*, 1992), where the ZFC data points are far below the corresponding FC data, as expected from Eq. (5.20). The earliest HgBaCaCuO compound samples produced FC susceptibilities that were far above

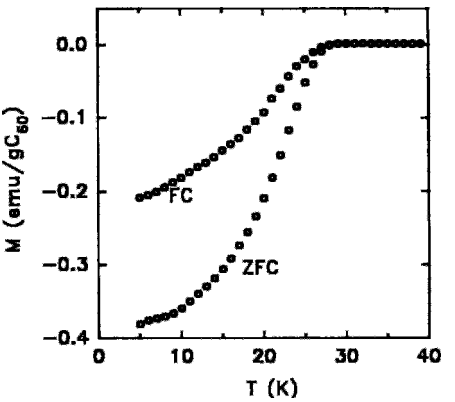

Figure 5.10 Rb_3C_{60} powder sample showing that the zero-field-cooled magnetic susceptibility is more negative than its field-cooled counterpart (C.-C. Chen *et al.*, 1991).

ZFC ones (Adachi *et al.*, 1993; Gao *et al.*, 1993; Meng *et al.*, 1993b, Schilling *et al.*, 1993).

Clem and Hao (1993) examined the four cases of ZFC, FC with data collected on cooling (FCC), FC with data collected on warming (FCW), and remanence. In the fourth case the applied field is turned off after the specimen has been FC, and the remanent magnetization is measured as a function of increasing temperature.

VI. GRANULAR SAMPLES AND POROSITY

The analysis of the previous section can help us understand experimental susceptibility data on granular samples. The grains sometimes consist of a mixture of superconducting and normal material of about the same density, with empty space between and perhaps within the material. The two densities can be comparable when the sample preparation procedure does not completely transform the starting materials into the superconducting phase. A well-made granular superconductor does not contain any

normal material, but it does have intergranular and perhaps intragranular spaces, either of which can trap flux. The field-cooled moment can be significantly less than the zero-field-cooled moment, as shown by the data in Table VIII.1 of previous work (Poole *et al.*, 1988).

A quantitative measure of the degree of granularity of a sample is its porosity P, which is defined by

$$P = (1 - \rho/\rho_{\text{x-ray}}), \tag{5.22}$$

where the density ρ of the sample is

$$\rho = \frac{m}{V_{\text{T}}} \tag{5.23}$$

and the x-ray density is calculated from the expression

$$\rho_{\text{x-ray}} = \frac{[\text{MW}]}{V_0 N_{\text{A}}} \tag{5.24}$$

where N_{A} is Avogadro's number and V_0 is the volume of the sample per formula unit, with the value

$$V_0 = abc \qquad (YBa_2Cu_3O_{7-\delta}), \tag{5.25}$$

$$V_0 = \tfrac{1}{2}abc$$

$$\text{(LaSrCuO, BiSrCaCuO, TlBaCaCuO)}, \tag{5.26}$$

where a, b, and c are the lattice constants and the La, Bi, and Tl compounds have assigned to them two formula units per unit cell, as explained in Chapter 8.

Porosity is a measure of the proportion of empty spaces or voids within and between the solid material or grains of a sample. Problem 4 shows how V_{s}, V_{h}, and V_{c} can be determined from measurements of ρ, χ_{zfc} and χ_{fc}. The x-ray density calculated from the unit cell dimensions of

$$YBa_2Cu_3O_7$$

is $6.383\,\text{g/cm}^3$. Typical densities of granular samples vary from 4.3 to $5.6\,\text{g/cm}^3$, corresponding to porosities between 33% and 12%, respectively (Blendell *et al.*, 1987; Mathias *et al.*, 1987).

Porosity can be reduced by applying pressure to the material. For example, a sample of $YBa_2Cu_3O_7$ with a 5:1 ratio between flux exclusion and flux expulsion was compressed at 20–30 kbar to a claimed 100% of theoretical density, $\rho = \rho_{\text{x-ray}}$, bringing the measure flux expulsion to within about 11% of the theoretical value (Venturini *et al.*, 1987). Researchers have also found 100% flux shielding and 95% flux expulsion in $YBa_2Cu_3O_7$ at 4.2 K (Larbalestier *et al.*, 1987a). Good single crystals, of course, have a porosity of zero.

VII. MAGNETIZATION ANISOTROPY

The magnetic properties of high-temperature superconductors are highly anisotropic, with magnetization and susceptibility depending on the angle which the applied field makes with the c-axis. We will see in Chapter 12, Section IV, that anisotropy here is a result of the difference in the values of the coherence length, penetration depth, and effective mass measured along the c direction as opposed to values obtained from measurements in the a, b-plane. Particles of anisotropic superconductors in a magnetic field experience a torque which tends to align them with the field (Kogan, 1988). Anisotropy effects can be determined by employing single crystals, epitaxial films, or grain-aligned powders. Epitaxial films are generally single-crystal films with the c-axis perpendicular to the plane. It is, of course, preferable to work with untwinned single crystals or epitaxial films. However, these are not always available, and much good research has been carried out with aligned granular samples.

Grain alignment is a technique that converts a collection of randomly oriented grains into a set of grains with their c-axes preferentially pointing in a particular direction. This

alignment can be brought about by uniaxial compression, by application of a strong magnetic field to grains embedded in, for example, epoxy, or by melting a random powder sample and reforming it in the presence of a temperature gradient (Farrell *et al.*, 1987). It is much easier to fabricate grain-aligned samples than single crystals. Grain-aligned samples, however, cannot compete with single crystals in terms of degree of alignment. Untwinned monocrystals are needed for perfect alignment.

Another technique for preparing samples with monocrystal characteristics is melt-textured growth (L. Gao *et al.*, 1991; Jin *et al.*, 1988; Murakami *et al.*, 1991). In melt-textured growth a granular material is melted and then slowly cooled in a thermal gradient to produce a high degree of texturing. The effect is to reduce weak-link grain boundaries and increase critical currents.

Figure 5.11a shows that both the ZFC and FC susceptibilities of $YBa_2Cu_3O_7$ are greater in magnitude (i.e., more negative) for the applied field aligned parallel to the c-axis than they are for B_{app} aligned perpendicular to c (i.e., along the copper-oxide planes); these measurements were made with grain-aligned samples. The figure shows that the susceptibility data for a nonaligned power are between the results for $B_{app\parallel c}$ and $B_{app\perp c}$. Figure 5.11c shows that the susceptibility is much less for field cooling in the field $B_{fc} = 0.3\,T$, again with the data for $B_{app\parallel c}$ lying below the data for $B_{app\perp c}$.

VIII. MEASUREMENT TECHNIQUES

Experimentally, susceptibility, a dimensionless quantity, is determined from the measured magnetic moment μ of the sample with the aid of Eq. (5.10),

$$\chi = \frac{\mu_0 \mu}{V_T B_{app}}. \tag{5.27}$$

For a small sample the overall volume V_T can be estimated by viewing it under a microscope. This is sometimes called the volume susceptibility, although in actuality the parameter is dimensionless. Many investigators determine sample size by weighting and report what is sometimes called the mass susceptibility χ_{mass}, defined by

$$\chi_{mass} = \frac{\chi}{\rho} = \frac{\mu_0 \mu}{(\rho V_T) B_{app}} \tag{5.28}$$

where ρV_T is the mass of the sample. This quantity has the dimensions m^3/kg in the SI system and cm^3/g in the cgs system.

Many susceptibility and magnetism measurements are carried out with a SQUID, a dc measuring instrument (see Section III). In this device, which is sketched in Fig. 5.12, a magnetized sample that has been moved into a sensor coil causes the flux through the coil to change. The current produced by this flux change is passed to the multiturn coil on the left side of the figure where it is amplified by the increase in the number of turns. The SQUID ring with its weak links detects this flux change in a manner that will be discussed in Chapter 15, Section VIII.1. The change in flux provides the magnetic moment by the expression

$$\mu_0 \mu = \Delta\Phi, \tag{5.29}$$

and from Eq. (5.27) we have for the susceptibility,

$$\chi = \Delta\Phi / V B_{app}. \tag{5.30}$$

The data presented in Figs. 5.10 and 5.11 were obtained with a SQUID magnetometer. More classical techniques, such as the vibrating sample magnetometer or perhaps the Gouy or Faraday balance, are less frequently employed. One can make ac susceptibility measurements using a low-frequency mutual inductance bridge operating at, for example, 200 Hz.

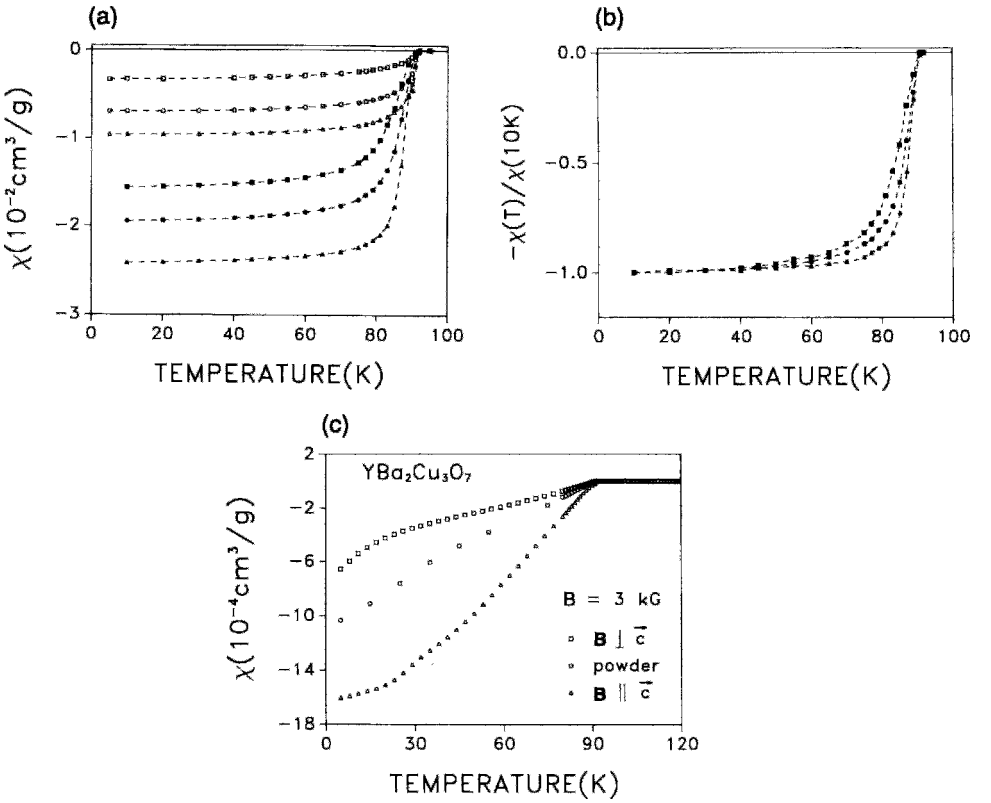

Figure 5.11 (a) Zero-field-cooled (closed symbols) and field-cooled (open symbols) susceptibility versus temperature for nonaligned powder (circles) and grain-aligned samples of $YBa_2Cu_3O_7$ in a field of 5 mT with $B_{app\|c}$ (triangles) and $B_{app\perp c}$ (squares), (b) normalized susceptibilities for the zero-field-cooled samples of (a), (c) field-cooled measurements in 0.3 T, plotted with the same symbol convention (Lee and Johnston, 1990).

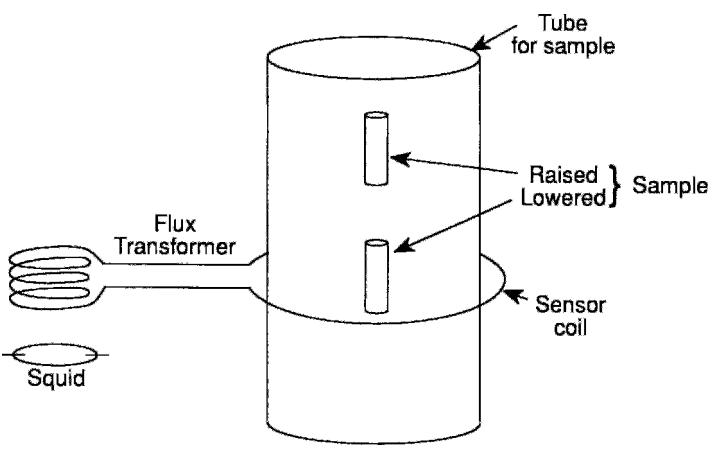

Figure 5.12 The change of magnetic flux in a sensor coil loop that has been produced by raising or lowering a sample induces a current which is transferred to a multiloop coil where it is measured by a Superconducting Quantum Interference Device (SQUID).

IX. COMPARISON OF SUSCEPTIBILITY AND RESISTIVITY RESULTS

We saw in Section V that the susceptibility of a composite sample is a linear combination of the contributions from its component parts. Thus, susceptibility measurements determine the magnetic state of an entire sample, and also give a better indication of the degree to which the sample has transformed to the super-conducting state. Resistivity measurements, on the other hand, merely show whether or not continuous superconducting paths are in place. In addition, while a dc susceptibility measurement provides a better experimental indicator of the overall superconducting state, a resistivity measurement is a better practical guide for application purposes. We should also note that magnetization is a thermodynamic state variable (cf. Chapter 4, Section VI), whereas resistivity is not. The properties of zero resistance and perfect diamagnetism are the two classic ways of defining superconductivity. In an ideal homogeneous material both measurements should provide the same transition temperature.

The transition temperatures determined by magnetic susceptibility and resistivity measurements sometimes differ somewhat. When the transition is sharp, resistivity can drop sharply to zero at a temperature slightly above the onset of the susceptibility or magnetization transition, as shown in Fig. 2.21. When the transition is broad, the χ-versus-T and ρ-versus-T curves often overlap considerably. Many articles provide susceptibility and resistivity curves for the same sample. Figure III-5 from our previous work (Poole *et al.*, 1988) compares the resistivity, Meissner magnetization, ac susceptibility, and specific heat transitions for the same

$$YBa_2Cu_3O_7$$

sample (Junod *et al.*, 1988).

X. ELLIPSOIDS IN MAGNETIC FIELDS

In Section III we treated the case of a cylindrically shaped sample in a parallel magnetic field, noting that this geometry was chosen to avoid demagnetization effects that could complicate the calculation of the internal magnetic field and magnetization. Some commonly used superconductor arrangements in magnetic fields, such as thin films in perpendicular fields, have very pronounced demagnetization effects. In practice, these arrangements constitute limiting cases of ellipsoids, so that in the present section we will analyze the case of an ellipsoid in an applied field. Then we will show how some common geometries are good approximations to elongated and flattened ellipsoids. Many of the results of this and the following few sections are applicable to both Type I and Type II superconductors.

When an ellipsoid with permeability μ is placed in a uniform externally applied magnetic field $\mathbf{B}_{app}$ oriented along one of its principal directions, its internal fields $\mathbf{B}_{in}$ and $\mathbf{H}_{in}$ will be parallel to the applied field, and hence all of the fields can be treated as scalars. Their values will be determined by applying Eqs. (5.1) and (5.2) to the internal fields

$$\begin{aligned} B_{in} &= \mu H_{in} = \mu_0 (H_{in} + M) \\ &= (1+\chi)\mu_0 H_{in} \end{aligned} \tag{5.31}$$

and the applied fields

$$B_{app} = \mu_0 H_{app}, \quad M_{app} = 0 \tag{5.32}$$

and utilizing the demagnetization expression

$$\frac{NB_{in}}{B_{app}} + \frac{(1-N)H_{in}}{H_{app}} = 1, \tag{5.33}$$

where N is the demagnetization factor, to relate the internal and applied fields. The

demagnetization factors along the three principal directions of the ellipsoid are geometrical coefficients that obey the normalization condition

$$N_x + N_y + N_z = 1, \tag{5.34}$$

with the largest value along the shortest principal axis and the smallest value along the longest principal axis. We will confine our attention to situations in which the external field is oriented along a principal direction since all the other orientations are much more complicated to analyze. In the following section we will give explicit expressions for the demagnetization factors associated with a sphere, a disk, and a rod.

Solving for B_{in}, H_{in}, and M in Eqs. (5.31) and (5.33) gives

$$B_{\text{in}} = B_{\text{app}} \frac{1+\chi}{1+\chi N}, \tag{5.35}$$

$$H_{\text{in}} = \frac{B_{\text{app}}/\mu_0}{1+\chi N}, \tag{5.36}$$

$$M = \frac{B_{\text{app}}}{\mu_0} \cdot \frac{\chi}{1+\chi N} \tag{5.37}$$

for the internal fields and magnetization expressed in terms of the applied fields. We should bear in mind that the susceptibility χ is negative for a superconductor, so that the denominators in these expressions become small when χ approaches -1 and N approaches 1.

For an ideal superconducting material $\chi = -1$. Equations (5.35)–(5.37) now assume a simpler form:

$$B_{\text{in}} = 0, \tag{5.38}$$

$$H_{\text{in}} = \frac{B_{\text{app}}/\mu_0}{1-N}, \tag{5.39}$$

$$M = -\frac{B_{\text{app}}/\mu_0}{1-N}. \tag{5.40}$$

These expressions are applicable to Type I superconductors subject to the condition $B_{\text{app}} < (1-N)B_{\text{c}}$, as will be explained in Chapter 11, Section IV. They apply to Type II superconductors when $B_{\text{app}} < (1-N)B_{\text{c1}}$, but for higher applied fields Eqs. (5.35)–(5.37) must be used since $-1 < \chi < 0$. Sometimes the transition from the Meissner to the vortex state is not sharply defined and a precise value of B_{c1} cannot be determined.

XI. DEMAGNETIZATION FACTORS

It will be helpful to write down formulae for the demagnetization factors for sample shapes that are often encountered in practice. For a sphere all three factors are the same, $a = b = c$ and $N_x = N_y = N_z$, so that from the normalization condition (5.34) we obtain

$$N = \frac{1}{3} \quad \text{(sphere)}. \tag{5.41}$$

For an ellipsoid of revolution with the z direction selected as the symmetry axis, the semi-major axes $a = b \neq c$ along the x-, y-, and z-axes, and the demagnetization factors are $N_\parallel = N_z$ and $N_\perp = N_x = N_y$, subject to the normalization condition

$$N_\parallel + 2N_\perp = 1 \tag{5.42}$$

of Eq. (5.34). An oblate ellipsoid, i.e., one flattened in the x, y-plane, has $c < a$ with $N_\parallel > N_\perp$, and von Hippel (1954) gives (cf. Osborn, 1945; Stone, 1945; Stratton, 1941),

$$N_\parallel = \frac{1}{\epsilon^2} - \frac{[1-\epsilon^2]^{1/2}}{\epsilon^3} \sin^{-1}\epsilon \quad c < a, \tag{5.43}$$

where the oblate eccentricity ϵ is

$$\epsilon = [1-(c^2/a^2)]^{1/2} \quad c < a. \tag{5.44}$$

For a prolate ellipsoid, i.e., one elongated along its symmetry axis so that $c > a$ and $N_\parallel < N_\perp$, we have again from von Hippel (1954)

$$N_\parallel = \frac{1-\epsilon^2}{\epsilon^2}\left[\frac{1}{2\epsilon}\ln\left(\frac{1+\epsilon}{1-\epsilon}\right) - 1\right] \quad c > a, \tag{5.45}$$

where the prolate eccentricity ϵ is

$$\epsilon = [1 - (a^2/c^2)]^{1/2} \quad c > a. \qquad (5.46)$$

Of especial interest are samples in the shape of a disk, which may be considered the limiting case of a very flattened oblate ellipsoid, $c \ll a$, with the demagnetization factors

$$N_\parallel \approx 1, \quad N_\perp \approx 0, \quad \text{(flat disk)}, \qquad (5.47)$$

or in the shape of a rod, which is the limit of an elongated prolate ellipsoid, $c \gg a$, with the values

$$N_\parallel \approx 0, \quad N_\perp \approx \frac{1}{2} \quad \text{(long cylinder)}. \qquad (5.48)$$

Correction factors δ_i to the limiting values of N_i given in Eqs. (5.47) and (5.48) are shown in Figs. 5.13 and 5.14, respectively, and listed in Table 5.1. Problems 6 and 7 give explicit expressions for these factors. Figure 5.15 shows how the parallel and perpendicular components of N depend on the length-to-diameter ratio of the ellipsoid. D.-X. Chen *et al.* (1991) reviewed demagnetization factors for cylinders; other pertinent articles are Bhagwat and Chaddah (1992), Kunchur and Poon (1991), and Trofimov *et al.* (1991). The electric case of depolarization factors is mathematically equivalent (Stratton, 1941).

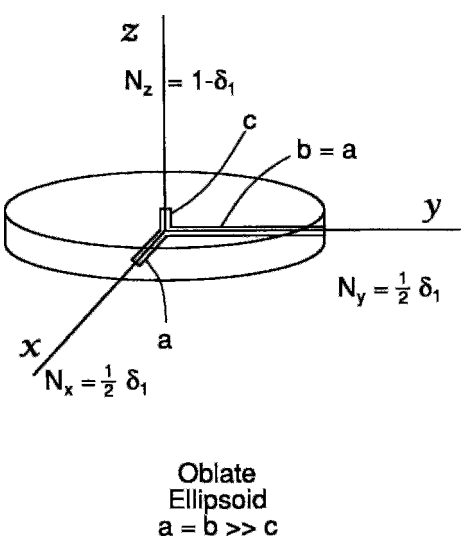

Figure 5.13 Demagnetization factors $N_x = N_y = \frac{1}{2}\delta_1 \ll 1$ and $N_z = 1 - \delta_1$ of an oblate ellipsoid with semi-major axes $a = b \gg c$ along the x, y, and z directions, respectively.

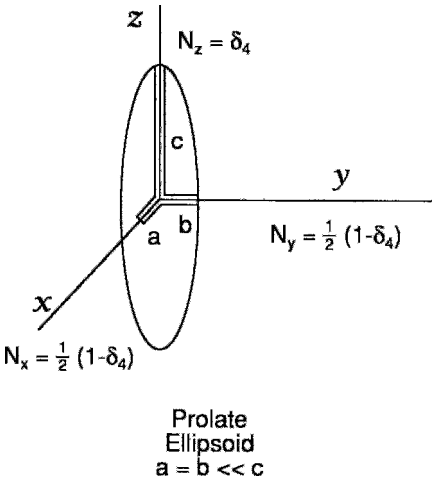

Figure 5.14 Demagnetization factors $N_x = N_y = \frac{1}{2}(1 - \delta_4)$ and $N_z = \delta_4 \ll 1$ of a prolate ellipsoid with $a = b \ll c$, using the notation of Fig. 5.13.

Table 5.1 Demagnetization Factors for Ellipsoids of Revolution with Semi-axes $a = b$ and c for the Case of a Disk (oblate, $c < a$), Sphere ($c = a$), or Rod (prolate, $c > a$)[a]

Shape	Condition	$N_\perp$	$N_\parallel$
disk limit	$c \to 0$	0	1
flat disk	$c \ll a$	$\frac{1}{2}\delta_1$	$1 - \delta_1$
oblate	$c \approx a$	$\frac{1}{3} - \frac{1}{2}\delta_2$	$\frac{1}{3} + \delta_2$
sphere	$c = a$	$\frac{1}{3}$	$\frac{1}{3}$
prolate	$c \approx a$	$\frac{1}{3} + \frac{1}{2}\delta_3$	$\frac{1}{3} - \delta_3$
long rod	$c \gg a$	$\frac{1}{2} - \frac{1}{2}\delta_4$	δ_4
rod limit	$c \to \infty$	$\frac{1}{2}$	0

[a] Values of the correction factors δ_i are given in Problems 6 and 7.

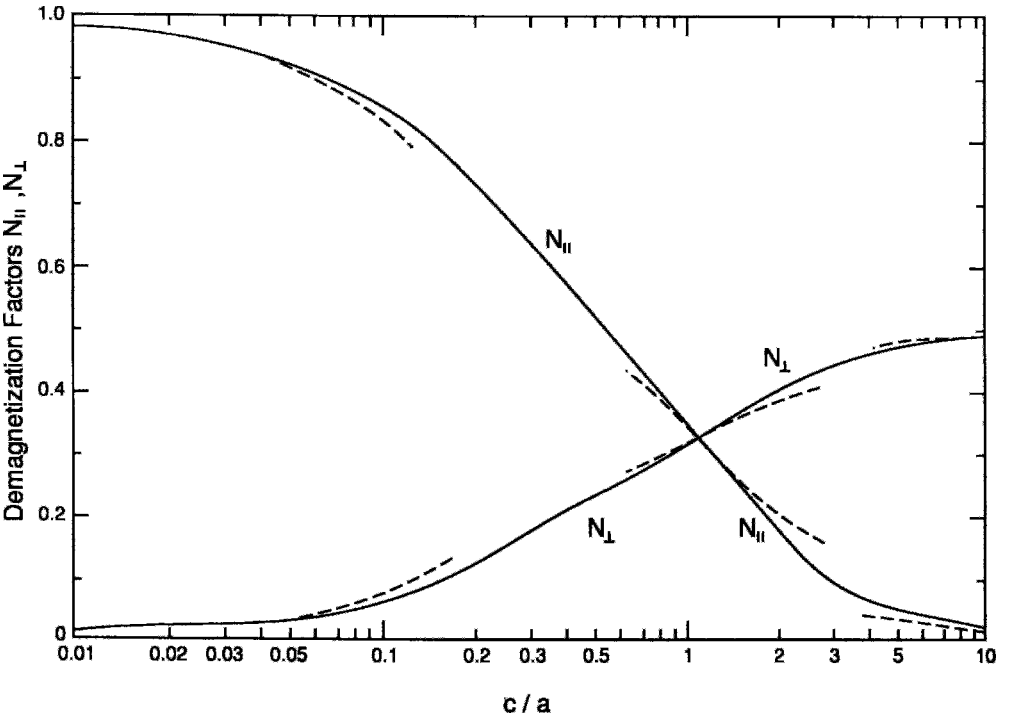

Figure 5.15 Dependence on the ratio c/a of the demagnetization factors $N_\perp = N_x = N_y$ perpendicular to the axis of an ellipsoid with semi-major axes $a = b \neq c$ and $N_\parallel = N_z$ along the axis. The solid lines were calculated using the exact expressions (5.42) to (5.46), and the dashed lines from the approximation formulae of Table 5.1 and Problems 6 and 7.

XII. MEASURED SUSCEPTIBILITIES

From the theoretical viewpoint the magnetic susceptibility χ is a fundamental property of a material. It can be anisotropic, but for the present we will treat the isotropic case. It is defined by Eq. (5.3) as the ratio between the two quantities M and H_{in} in the interior of a superconductor,

$$\chi = M/H_{\text{in}}. \tag{5.49}$$

In practice, research workers often report an experimentally determined susceptibility χ_{exp} that has been calculated from measured values of the magnetization and the applied field B_{app}, as follows:

$$\chi_{\text{exp}} = \mu_0 M/B_{\text{app}}. \tag{5.50}$$

This is the definition of susceptibility that often appears in solid state physics books. Equations (5.49) and (5.50) are only equivalent for the case of "parallel geometry," in which the applied field is along the axis of a cylinder and the demagnetization factor N is zero: $H_{\text{in}} = B_{\text{app}}/\mu_0$.

When N is not zero, Eq. (5.49) is still valid because χ is a property of the material independent of its shape. Substituting Eq. (5.37) in Eq. (5.50) gives the expression

$$\chi_{\text{exp}} = \chi/(1 + N\chi), \tag{5.51}$$

which may be solved for the intrinsic susceptibility in terms of the experimentally measured value

$$\chi = \chi_{\text{exp}}/(1 - N\chi_{\text{exp}}). \tag{5.52}$$

The susceptibility must be in dimensionless units (SI units) to apply this expression. Equation (10.52) shows that $|\chi| \leq |\chi_{exp}|$, where both χ and χ_{exp} are negative. Some authors set $N_\chi = -N$ in Eq. (5.52) so as to write the approximate expression

$$\chi \approx \chi_{exp}(1-N), \tag{5.53}$$

which, however, underestimates the magnitude of χ, especially when N is appreciable and $|\chi|$ is small.

XIII. SPHERE IN A MAGNETIC FIELD

In this section we will examine a case that is commonly treated in electromagnetic theory and solid-state physics texts—that of a sphere in a magnetic field. This will provide us with closed-form expressions for the fields and the magnetization, both inside and outside the sphere as well as on its surface.

We mentioned in the previous section that for a sphere $N = 1/3$, so that using Eqs. (5.35)–(5.37) and (5.52) we have, respectively, for the two internal fields, magnetization, and susceptibility,

$$B_{in} = B_{app}\frac{3(1+\chi)}{3+\chi}, \tag{5.54}$$

$$H_{in} = \frac{3B_{app}/\mu_0}{3+\chi}, \tag{5.55}$$

$$M = \frac{B_{app}}{\mu_0}\cdot\frac{3\chi}{3+\chi}, \tag{5.56}$$

$$\chi = \frac{3\chi_{exp}}{3-\chi_{exp}}. \tag{5.57}$$

The B field immediately outside a superconducting sphere of radius a placed in a uniform external magnetic field B_{app} may be calculated from the standard formula for the magnetic scalar potential Φ_{out} given in electrodynamics texts (e.g., Jackson, 1975, p. 150),

$$\Phi_{out} = -\left[r - \frac{\chi}{\chi+3}\cdot\frac{a^3}{r^2}\right]B_{app}\cos\Theta, \tag{5.58}$$

where Θ is the angle of the position vector $\mathbf{r}$ relative to the applied field direction. This is the solution to Laplace's equation

$$\nabla^2\Phi = 0, \tag{5.59}$$

which for the case of axial symmetry in spherical coordinates has the form

$$\frac{1}{r^2}\frac{d}{dr}\left(r^2\frac{d\Phi}{dr}\right) + \frac{1}{r^2\sin\Theta}\cdot\frac{d}{d\Theta}\left(\sin\Theta\frac{d\Phi}{d\Theta}\right) = 0, \tag{5.60}$$

where the potential $\Phi_{out}(r, \Theta)$ depends on the polar angle Θ, but not on the azimuthal angle ϕ. This solution is subject to two boundary conditions, first, that B_r and H_Θ are continuous across the surface at $r = a$, and second, that $B = B_{app}$ far from the sphere where $r \gg a$.

The first term of Eq. (10.58),

$$rB_{app}\cos\Theta = zB_{app},$$

corresponds to the potential of the uniform applied field. The second term is known to be the magnetic field produced by a magnetic dipole of moment $\mu = a^3H_{app}\chi/(\chi+3)$. The radial component B_r of the field outside,

$$B_r = -\frac{\partial\Phi_{out}}{\partial r} \tag{5.61}$$

$$= \left[1 + \frac{2\chi}{\chi+3}\cdot\frac{a^3}{r^3}\right]B_{app}\cos\Theta, \tag{5.62}$$

has a value at the surface $r = a$ of

$$B_r = \left[\frac{3(\chi+1)}{\chi+3}\right]B_{app}\cos\Theta. \tag{5.63}$$

Setting $\chi = -1$ shows that this radial field vanishes at the surface for a perfect diamagnet. The polar angle component B_Θ outside,

$$B_\Theta = -\frac{1}{r} \cdot \frac{\partial \Phi_{\text{out}}}{\partial \Theta} \tag{5.64}$$

$$= \left[1 - \frac{\chi}{\chi + 3} \cdot \frac{a^3}{r^3}\right] B_{\text{app}} \sin \Theta, \tag{5.65}$$

has a value at the surface of

$$B_\Theta = \left[\frac{3}{\chi + 3}\right] B_{\text{app}} \sin \Theta. \tag{5.66}$$

This field reaches a maximum along the equator, i.e., when $\Theta = \pi/2$. The magnetic field lines around the sphere, which are sketched in Fig. 2.23, are closest together at this maximum field position along the equator.

Equations (5.63) and (5.66) show that for the case $\chi = -1$ of perfect diamagnetism, the external field is parallel to the surface with no radial component. This field may be looked upon as inducing a current density in the surface of the sphere that circulates along circles of longitude that are oriented perpendicular to the z-axis, as illustrated in Fig. 2.30. These currents serve to cancel the B field that would otherwise be present inside the sphere. The presence of the factor $\sin \Theta$ in Eq. (5.66) means that the current density along a particular longitude circle at the latitude Θ is proportional to the radius ρ of the circle on which it flows, where $\rho = r \sin \Theta$, as indicated in Fig. 5.16. This causes each such current element to produce the same magnitude of magnetic field within the sphere, as expected.

We will see in Chapter 11, Section XI, that the results of this section apply directly to a sphere in the mixed state of a Type II superconductor for applied fields in the range $\frac{2}{3}B_{c1} < B_{\text{app}} < B_{c2}$. For applied fields below $\frac{2}{3}B_{c1}$ the Meissner state exists with $\chi = -1$. For a Type I superconductor in the applied field range $\frac{2}{3}B_c < B_{\text{app}} < B_c$, the formalism applies with χ chosen so that

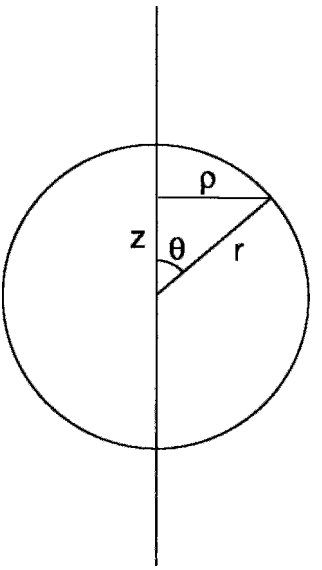

Figure 5.16 Coordinates for describing current flow along the surface of a sphere in a magnetic field applied along the z direction.

$H_{\text{in}} = B_c/\mu_0$. For the condition $B_{\text{app}} < \frac{2}{3}B_c$ we have $\chi = -1$, as will be clear from the discussion in Chapter 11, Section IV.

XIV. CYLINDER IN A MAGNETIC FIELD

On several occasions we have discussed the case of a long diamagnetic cylinder in an axially applied magnetic field, as shown in Fig. 12.1. In this "parallel geometry" the demagnetization factor N is zero. Inserting $N = 0$ in Eqs. (5.35)–(5.37) gives Eqs. (5.7)–(5.9), which we have already obtained for this case. These reduce to Eqs. (5.11)–(5.13), respectively, for the ideal Type I superconductor with $\chi = -1$. Since $N = 0$, the boundary condition—i.e., that H is continuous

$$H_{\text{in}} = H_{\text{app}}$$

across the interface—leaves the H field undisturbed by the presence of the

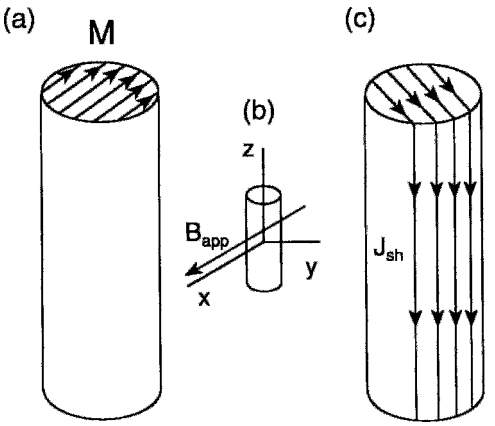

Figure 5.17 Magnetization M (a) and shielding current flow J (c) of a superconducting rod located in an applied magnetic field with the perpendicular geometry arrangement (b).

superconductor. The fields outside the cylinder are then

$$B_{\text{out}} = B_{\text{app}} \tag{5.67}$$

$$H_{\text{out}} = B_{\text{app}}/\mu_0, \tag{5.68}$$

independent of position.

An alternate arrangement that sometimes occurs in practice is the perpendicular geometry sketched in Fig. 5.17, whereby the cylinder axis remains in the z direction but the magnetic field is applied along x. For this case we see from Table 5.1 that $N = \frac{1}{2}$ so that the fields inside are, from Eqs. (5.35)–(5.37),

$$B_{\text{in}} = B_{\text{app}} \frac{2(1+\chi)}{2+\chi}, \tag{5.69}$$

$$H_{\text{in}} = \frac{B_{\text{app}}}{\mu_0} \frac{2}{2+\chi}, \tag{5.70}$$

$$M = \frac{B_{\text{app}}}{\mu_0} \frac{2\chi}{2+\chi}. \tag{5.71}$$

$$\chi = \frac{2\chi_0\chi_1^0}{2-\chi_{\text{exp}}}.$$

The calculation of the fields outside for this geometry is more complicated. There is no z dependence, so this is a two-dimensional problem in which Laplace's equation is solved in cylindrical coordinates with the $\partial^2/\partial z^2$ term omitted,

$$\frac{1}{\rho} \cdot \frac{d}{d\rho}\left(\rho \frac{\partial \Phi}{\partial \rho}\right) + \frac{1}{\rho^2} \cdot \frac{\partial^2 \Phi}{\partial \phi^2} = 0, \tag{5.72}$$

subject to two boundary conditions—first that H parallel to the surface and B perpendicular to the surface are both continuous; second, that far from the sample B is in the x direction with the magnitude B_{app}. The solution for the magnetic scalar potential $\Phi(\rho, \phi)$ is

$$\Phi_{\text{out}} = -\left[\rho - \frac{\chi}{\chi+2} \cdot \frac{a^2}{\rho}\right] B_{\text{app}} \cos\phi, \tag{5.73}$$

which is similar to the case of the sphere given in Eq. (5.58). The differences arise from the particular forms of the differential operators in Eqs. (5.60) and (5.72). The first term in this potential,

$$\rho B_{\text{app}} \cos\phi = x B_{\text{app}},$$

corresponds to the potential of the uniform applied field, where $x = \rho\cos\phi$.

The radial component B_ρ of the field outside,

$$B_\rho = -\frac{\partial \Phi_{\text{out}}}{\partial \rho} \tag{5.74}$$

$$= \left[1 + \frac{\chi}{\chi+2} \cdot \frac{a^2}{\rho^2}\right] B_{\text{app}} \cos\phi, \tag{5.75}$$

has a value at the surface of

$$B_\rho = \left[\frac{2(\chi+1)}{\chi+2}\right] B_{\text{app}} \cos\phi, \tag{5.76}$$

which vanishes for the perfect superconductor case of $\chi = -1$. The azimuthal component B_ϕ outside,

$$B_\phi = -\frac{1}{\rho} \cdot \frac{\partial \Phi_{\text{out}}}{\partial \phi} \tag{5.77}$$

$$= \left[1 - \frac{\chi}{\chi+2} \cdot \frac{a^2}{\rho^2}\right] B_{\text{app}} \sin\phi, \tag{5.78}$$

becomes at the surface

$$B_\phi = \left[\frac{2}{\chi+2}\right] B_{\text{app}} \sin\phi. \qquad (5.79)$$

This surface field is zero along x and reaches a maximum value along the y direction, where $\phi = \pi/2$ and $B_\phi/\mu_0 = H_{\text{in}}$ (cf. Eq. (5.70)). A sketch of the magnetic field lines around the cylinder would resemble that of Fig. 2.23. This case is equivalent to a two-dimensional problem with all of the field lines lying in the x, y-plane.

For perfect diamagnetism, $\chi = -1$, we see from Eqs. (5.76) and (5.79) that immediately outside the cylinder the external magnetic field is parallel to the surface with no radial component. Longitudinal surface currents J_z flow along the surface in the $+z$ direction on one side and in the $-z$ direction on the other, forming closed loops at the ends that sustain the magnetization inside, as indicated in Fig. 5.17. These currents serve to cancel the B field that would otherwise be present inside the cylinder. The factor $\sin\phi$ in Eq. (5.78) causes the surface-current density to produce the uniform magnetic field of Eq. (5.69) inside the cylinder.

XV. ac SUSCEPTIBILITY

Earlier in the chapter we discussed susceptibilities determined in constant magnetic fields. Now let us consider what happens when the external field varies harmonically in time (D.-X. Chen *et al.*, 1990c; vide Q. Y. Chen, 1992; Hein *et al.*, 1992; Khode and Couach, 1992). An ac field $B_0 \cos\omega t$ applied to the sample causes the magnetization $M(t)$ to trace out a magnetic hysteresis loop in the course of every cycle of the applied field. The initial loop for the first cycle will be different from all the other cycles, as suggested by the initial curves starting from the middle of the loops of Figs. 5.6 and 5.7, but after several cycles a state of dynamic equilibrium is attained in which the magnetization $M(t)$ repeatedly traces out the same curve, perhaps of the types shown in Figs. 5.5 or 5.6, during every period of oscillation.

If the magnetization were to change linearly with the applied field, the response would be $M(t) = M_0 \cos\omega t$ in phase with the applied field, with $M_0 = \chi B_0/\mu_0$. The shape of the loop causes $M(t)$ to become distorted in shape and shift in phase relative to the applied field, causing it to acquire an out-of-phase component that varies as $\sin\omega t$. We can define the inphase dispersion χ' and the out-of-phase (quadrature) absorption χ'' susceptibilities (Matsumoto *et al.*, 1991):

$$\chi' = \frac{\mu_0}{\pi B_0} \int M(t) \cos\omega t \, d\,\omega t, \qquad (5.80a)$$

$$\chi'' = \frac{\mu_0}{\pi B_0} \int M(t) \sin\omega t \, d\,\omega t. \qquad (5.80b)$$

Higher harmonic responses χ_n' and χ_n'' at the frequencies $n\omega t$ have also been studied (Ghatak *et al.*, 1992; Ishida and Goldfarb, 1990; Ishida *et al.*, 1991; Jeffries *et al.*, 1989; Ji *et al.*, 1989; Johnson *et al.*, 1991; Yamamoto *et al.*, 1992). Note that the absorption susceptibility is proportional to the energy dissipation. Unfortunately, in practice it is not practical to measure $M(t)$, so that a different approach must be followed.

The usual mutual inductance method for determining χ' and χ'' involves placing the sample in the coil of an LC tuned circuit to establish an alternating magnetic field $B_0 \cos\omega t$ in the superconductor and to detect the voltage induced in a detector pickup coil coupled to the coil of the LC circuit. The presence of the sample changes the effective inductance and resistance of the LC circuit, and this change is reflected in the form of the current induced in the detector coil. The component of the induced signal which is in phase with the applied field is proportional to the dispersion χ', while the out-of-phase component is proportional

to the absorption χ''. These two responses can be separated instrumentally by a lock-in detector that compares the phase of the output signal with that of the reference signal $B_0 \cos \omega t$.

Figures 5.18 and 5.19 present the temperature dependence of the dispersion χ' and absorption χ'' components of the ac susceptibility determined for applied fields of the form

$$B_{\text{app}} = B_{\text{dc}} + B_0 \cos \omega t \tag{5.81}$$

at the frequency $\omega/2\pi = 73$ Hz. Figure 5.18 shows the results for three alternating field amplitudes B_0 with $B_{\text{dc}} = 0$, and Fig. 5.19 illustrates the effect of simultaneously applying a dc field. We see from the figures that for a particular applied field, χ' decreases continuously as the temperature is lowered, also that the drop in χ' is sharper and occurs closer to T_c for lower values of B_0 and B_{dc}. The peak in the χ''-versus-temperature curve is near the center of the sharp diamagnetic change in χ', as expected, inasmuch as magnetic susceptibilities, like dielectric constants, obey Kramers–Kronig relations (cf. Chapter 15, Section II.E; Poole and Farach, 1971, Chapter 20). Recent data on $HgBa_2CuO_{4+\delta}$ at high pressure exhibit this behavior (Klehe *et al.*, 1992). These K–K relations permit χ' to be calculated from knowledge of the frequency dependence of $\chi''(\omega)$, and vice versa. Increasing the applied field shifts the χ'' peak to lower temperatures and broadens it (D.-X. Chen *et al.*, 1988; Goldfarb *et al.*, 1987a, b; Ishida and Goldfarb, 1990; Puig *et al.*, 1990; K. V. Rao *et al.*, 1987). These χ_{ac} response curves depend only slightly on frequency below 1 kHz so that the magnetization is able to follow the variation in the applied field.

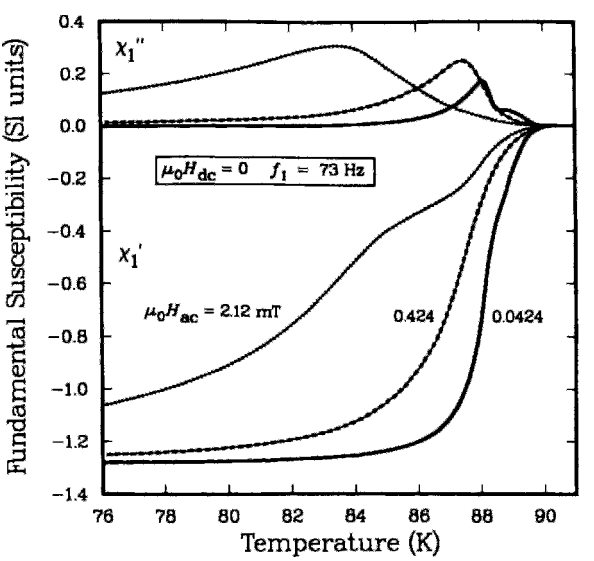

Figure 5.18 Real (χ') and imaginary (χ'') components of the susceptibility of $YBa_2Cu_3O_{7-\delta}$ measured in the applied ac magnetic fields with $\mu_0 H_{\text{ac}} = 0.0424$, 0.424, and 2.12 mT as a function of the temperature below T_c for a frequency of 73 Hz. For this experiment $\mu_0 H_{\text{dc}} = 0$; the data were not corrected for the demagnetization factor (Ishida and Goldfarb, 1990).

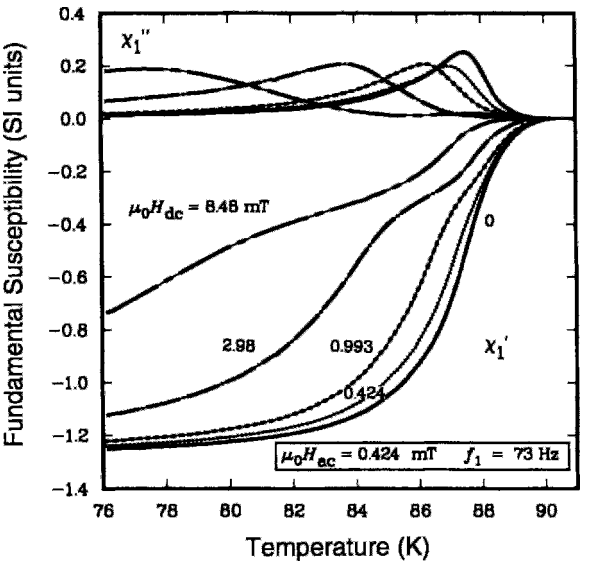

Figure 5.19 Real (χ') and imaginary (χ'') components of the susceptibility of $YBa_2Cu_3O_{7-\delta}$ measured in superimposed ac and dc magnetic fields as a function of the temperature below T_c for a frequency of 73 Hz. The conditions were $\mu_0 H_{ac} = 0.424$ mT, $\mu_0 H_{dc} = 0$, 0.424, 0.993, 2.98, and 8.48 mT; the data were not corrected for the demagnetization factor (Ishida and Goldfarb, 1990).

The ac susceptibility results can be thought of in terms of the temperature dependence of the lower-critical field $B_{c1}(T)$ (cf. Figs. 12.36 and 5.28). A low applied field at low temperature will be far below $B_{c1}(T)$, thus in Fig. 5.18 the χ' curve for $B_0 = 0.0424$ approaches total dia-magnetic shielding. A high applied field near but still below T_c will exceed $B_{c1}(T)$ so that χ', will be smaller in magnitude and closer to its normal state value, as shown in Fig. 5.19.

It is more customary to interpret ac susceptibility data in terms of one of the critical-state models that will be introduced in Chapter 13 (Chen and Sanchez, 1991) with a temperature-dependent critical current (Ishida and Goldfarb, 1990; Johnson *et al.*, 1991; LeBlanc and LeBlanc, 1992). Ji *et al.* (1989) assumed the two-fluid model temperature dependence of Eq. (2.56). Here magnetic flux in the form of vortices alternately enters and leaves the sample as the magnetization cycles around the hysteresis loop. The maximum of χ'' can be interpreted as occurring near the applied field $B_{app} = B^*$, where the critical current and internal field just reach the center of the sample. Sample geometry (Forsthuber and Hilscher, 1992) and size effects (Skumryev *et al.*, 1991) have also been reported.

Clem (1992) suggested that there are three main mechanisms responsible for ac susceptibility losses: (a) flux flow losses, which can also be called eddy current losses or viscous losses, arising in the absence of pinning centers, when time-varying currents arising from the oscillating applied magnetic field induce fluxons to move, (b) hysteresis losses occuring near pinning centers that impede the flux motion, as well as wherever vortices of opposite sense annihilate each other, and (c) surface pinning losses arising from a surface barrier to vortex entry and exit (Hocquet *et al.*, 1992; Mathieu and Simon, 1988). An additional complication in granular superconductors is the presence of

both intergranular and intragranular shielding currents.

In a granular superconductor the ac susceptibility is expected to receive contributions from intergranular current flow in loops through Josephson junctions at the boundaries between grains as well as from intragranular shielding current flow within the individual grains (J. H. Chen, 1990a, b; Lam *et al.*, 1990; Lera *et al.*, 1992; Müller and Pauza, 1989). The χ''-versus-T curves can exhibit both intergranular and intragranular peaks. Coreless Josephson vortices at the junctions and the more common Abrikosov vortices inside the grains alternately sweep in and out of the sample during each cycle around the hysteresis loop.

XVI. TEMPERATURE-DEPENDENT MAGNETIZATION

Diamagnetism is an intrinsic characteristic of a superconductor. Superconductors exhibit other types of magnetic behavior as well, due to, for example, the presence of paramagnetic rare earth and transition ions in their structure.

Susceptibility above T_c can have a temperature-independent contribution χ_0 arising from the conduction electrons along with a temperature-dependent Curie–Weiss term due to the presence of para-magnetic ions,

$$\chi = \chi_0 + \frac{K\mu^2}{3k_B(T-\Theta)} \tag{5.82}$$

$$= \chi_0 + \frac{C}{T-\Theta}, \tag{5.83}$$

where μ is the magnetic moment of the paramagnetic ions, K is a parameter that incorporates the concentration of para-magnetic ions and the conversion factor (1.86) for volume susceptibility, and C is the Curie constant. The Curie–Weiss temperature Θ is negative for ferromagnetic coupling between the magnetic ions and positive for antiferromagnetic coupling. Below T_c the large diamagnetism generally overwhelms the much smaller terms of Eq. (5.82), and they become difficult to detect.

A. Pauli Paramagnetism

The constant term χ_0 in Eq. (5.82) is often Pauli-like, arising from the conduction electrons (cf. Eq. (1.84)). We see from Eq. (1.83) that χ_{Pauli} provides an estimate of the density of states $D(E_F)$ at the Fermi level.

B. Paramagnetism

Most superconductors are paramagnetic above T_c. For example, it has been found (Tarascon *et al.*, 1987b) that the susceptibility of $YBa_2Cu_3O_{7-\delta}$ above T_c has a temperature dependence that obeys the Curie–Weiss law 1.79, with $\mu \approx 0.3\,\mu_B$/mole of Cu and $\Theta \approx -20$ to -30 K for oxygen contents δ in the range 0–0.6. Removing more oxygen increases μ and decreases Θ, but the samples no longer superconduct. These measured moments are less than the Cu^{2+} spin-only value of $1.9\mu_B$ given by Eq. (1.82),

$$\mu = g[S(S+1)]^{1/2}\mu_B = 1.9\mu_B, \tag{5.84}$$

where $S = \frac{1}{2}$ and $g \approx 2.2$.

Oxide materials in which magnetic rare earths replace lanthanum or yttrium provide linear plots of $1/\chi$ versus T above T_c as shown by the solid curves in Fig. 5.20, indicating paramagnetic behavior. For some compounds the temperature-independent term χ_0 of Eq. (5.82) is zero. Vacuum annealing of the samples destroyed the superconductivity and gave linear Curie–Weiss plots below T_c, shown by the dashed curves in the figure, which provide Θ from the extrapolated intercept at $T = 0$. The magnetic moments μ were very close to the values $g(J(J+1))^{1/2}$ expected from Eq. (1.80)

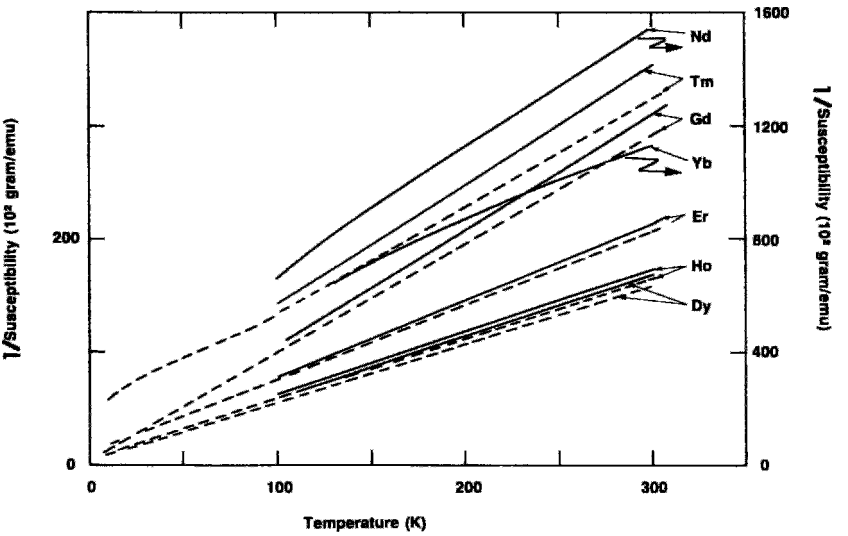

Figure 5.20 Temperature dependence of the reciprocal susceptibility $(1/\chi)$ for a series of rare earth (R) substituted $R\mathrm{Ba_2Cu_3O_{7-\delta}}$ superconductors over the temperature range 100–300 K in a field of 1 T (solid lines). Data for the corresponding nonsuperconducting vacuum-annealed compounds (dashed lines) are shown for comparison. The linear behavior is indicative of paramagnetism (Tarascon *et al.*, 1987b).

for rare earth ions. The positive sign for Θ indicates that these ions interact antiferromagnetically, with the susceptibility behavior above T_c corresponding to Fig. 1.15. The results suggest nearly complete decoupling of the Cu–O planes responsible for the superconducting properties from the planes containing the rare earth ions responsible for the magnetic properties. Such decoupling of the magnetic and superconducting properties was observed in Chapter 3, Section X, for the Chevrel phases; it also occurs with the heavy fermions (Jee *et al.*, 1990; Konno and Veda, 1989).

The paramagnetic contribution to χ arising from the Curie–Weiss law below T_c should appear as a rise in χ or M near $T = \Theta$. Such a rise is indeed noticeable at temperatures low enough for the diamagnetic contribution to have already come close to the asymptotic value $\chi(0)$ expected experimentally at absolute zero. In practice, this paramagnetism is often too weak to observe. However, we see from that data shown in Fig. 5.21 that it is enhanced at high applied fields. In fact, the highest fields used, $B_{app} > 1.5\,\mathrm{T}$, are strong enough to overwhelm the diamagnetic contribution and drive the magnetization positive. This rise in M is also partly due to the decrease in the diamagnetism as B_{app} is increased. The inset to this figure shows how the Meissner fraction, which is the value of χ_{fc} expressed as a percentage of its value (-1) for perfect diamagnetism, depends on the applied field.

The susceptibility above T_c of the series of compounds $\mathrm{YBa_2(Cu_{0.9}}A_{0.1})_3\mathrm{O_{7-\delta}}$, where A is a first transition series element, is an average of the contributions from the A and Cu ions. It has been found to obey Eq. (5.82) with an effective magnetic moment given by (Xiao *et al.*, 1987a, b),

$$\mu_{\mathrm{eff}}^2 = 0.1\mu_A^2 + 0.9\mu_{\mathrm{Cu}}^2, \tag{5.85}$$

where μ_A and μ_{Cu} are the moments of the A and Cu atoms, respectively. We see from Fig. 5.22 that the depression of T_c correlates

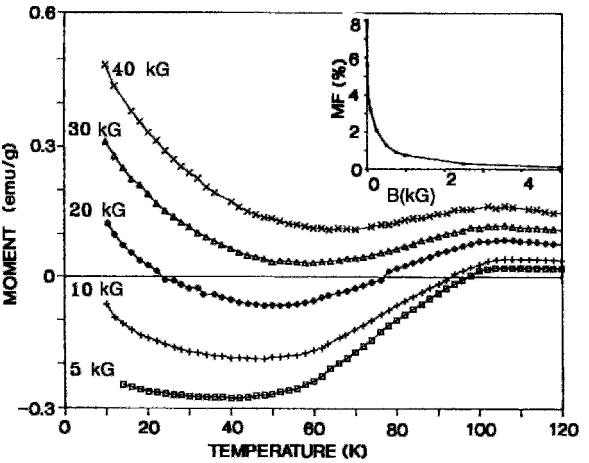

Figure 5.21 Appearance of a paramagnetic contribution at the low-temperature end of a field-cooled magnetization determination. The contribution becomes dominant as the field B_{fc} was increased from 0.5 to 4 T (i.e., from 5 to 40 kG), as shown. The inset gives the Meissner fraction (MF) as a function of the applied field from 0 to 0.5 T (Wolfus *et al.*, 1989).

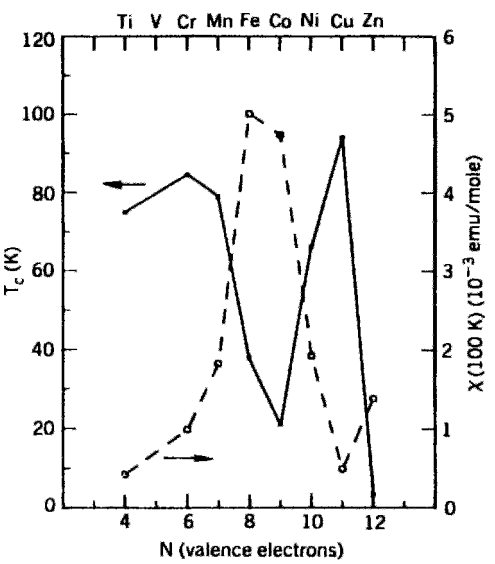

Figure 5.22 Dependence of the transition temperature T_c (—) and magnetic susceptibility at 100 K (– – –) on the number of valence electrons for the series of compounds $YBa_2(Cu_{0.9}A_{0.1})_3O_{7-\delta}$, where A is a 3*d* transition element, as shown (Xiao *et al.*, 1987a).

with the size of the magnetic moment of the substituted transition ion—the larger the moment, the lower the T_c value. Others have reported similar results (e.g., Maeno *et al.*, 1987; Oseroff *et al.*, 1987).

C. Antiferromagnetism

Cuprate superconductors generally have a negative Curie–Weiss temperature Θ indicative of antiferromagnetic coupling (Chapter 1, Section XV). The undoped compound La_2CuO_4 is an antiferromagnet below the Néel temperature $T_N \approx 245$ K, which is considerably lower than the tetragonal-to-orthorhombic transition temperature $T_{t-o} = 525$ K. The copper spins are ordered in the CuO_2 planes in the manner shown in Fig. VIII-18 of our earlier book (1988; cf. also Freltoft *et al.*, 1988; Kaplan *et al.*, 1989; Thio *et al.*, 1988; Yamada *et al.*, 1989). Antiferromagnetic spin fluctuations in these CuO_2 planes, called *antiparamagnons*, have also been discussed (Statt and Griffin, 1993).

Compounds formed by replacing the yttrium in $YBa_2Cu_3O_{7-\delta}$ by a rare-earth ion tend to align antiferromagnetically at low

temperature (Lynn, 1992). For example, the Er moments $\mu = 4.8\mu_B$ in $ErBa_2Cu_3O_{7-\delta}$ order in the a,b-plane with antiferromagnetic coupling along a and ferromagnetic coupling along b and c, in the manner shown in Fig. 5.23. The neutron-magnetic reflection intensity plotted in Fig. 5.24 versus temperature provided the Néel temperature $T_N \approx 0.5\,K$ (Chattopadhyay *et al.*, 1989; Lynn *et al.*, 1989; Paul *et al.*, 1989). Below $T_N \approx 2.2\,K$, the Gd moments in $GdBa_2Cu_3O_{7-\delta}$ align along the c-axis with antiferromagnetic coupling to all Gd nearest neighbors, as illustrated in Fig. VIII-19 of our earlier work (1988; cf. also Dunlap *et al.*, 1988; Mook *et al.*, 1988; Niedermayer *et al.*, 1993; Paul *et al.*, 1988; Watson *et al.*, 1989). Other magnetic ions, such as Dy, Ho, Nd, Pr, and Sm, when substituted for Y, also produce antiferromagnetic ordering (Dy: Fischer *et al.*, 1988; Zhang *et al.*, 1992; Ho: Fischer *et al.*, 1988; Nd: Yang *et al.*, 1989; Pr: Kebede *et al.*, 1989; Sm: Yang *et al.*, 1989). For $x < 6.4$ the undoped compound $YBa_2Cu_3O_x$ is an antiferromagnetic non-superconductor with aligned Cu ions, and $T_N \approx 500\,K$ for $x \approx 6$ (Miceli *et al.*, 1988; Rossat-Mignod *et al.*, 1988; Tranquada, 1990; Tranquada *et al.*, 1992).

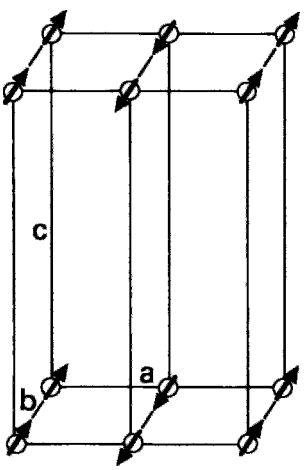

Figure 5.23 Magnetic spin structure of ordered Er ions in antiferromagnetic $ErBa_2Cu_3O_{7-\delta}$ determined by neutron diffraction (Chattopadhyay *et al.*, 1989)

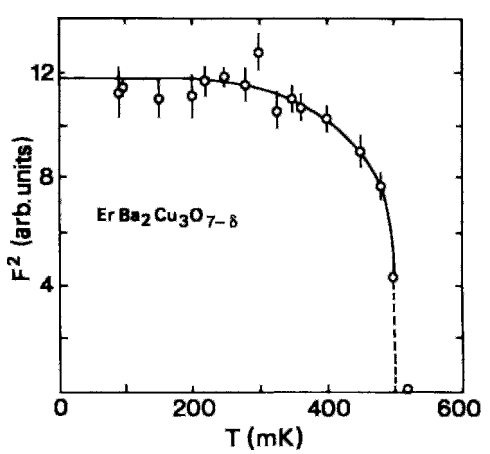

Figure 5.24 Temperature dependence of the intensity of reflected neutrons from the $ErBa_2Cu_3O_{7-\delta}$ sample of Fig. 5.23 showing the Néel temperature $T_N \approx 0.5\,K$ far below $T_c = 88\,K$ (Chattopadhyay *et al.*, 1989).

XVII. PAULI LIMIT AND UPPER CRITICAL FIELD

An electron spin in a magnetic field has the Zeeman energy

$$E = g\mu_B \mathbf{B}_{app} \cdot S, \tag{5.86}$$

$$E_{\pm} = \pm\frac{1}{2} g\,\mu_B B_{app} \tag{5.87}$$

shown in Fig. 5.25, where $\mu = g\mu_B \mathbf{S}$ is the spin magnetic moment, $g = 2.0023$ for a free electron, and μ_B is the Bohr magneton. We will approximate the g-factor by 2, and, of course, $S = \frac{1}{2}$. If the Zeeman energy level splitting (Poole and Farach, 1987) indicated in the figure,

$$E_+ - E_- = 2\mu_B B_{app}, \tag{5.88}$$

becomes comparable with the energy gap E_g, the field will be strong enough to break up the Cooper pairs and destroy the superconductivity. The magnetic field B_{Pauli} that brings this about is called the Pauli limiting field. It has the value

$$B_{Pauli} = \frac{E_g}{2\sqrt{2}\mu_B}, \tag{5.89}$$

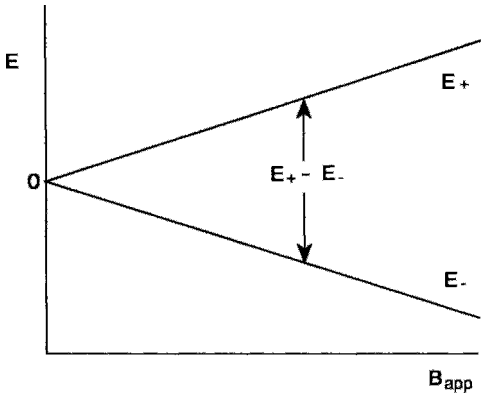

Figure 5.25 Zeeman energy level splitting $E_+ - E_-$ of electrons resulting in the breakup of Cooper pairs by becoming comparable to the energy gap 2Δ when B_{app} reaches the value B_{c2}.

where the factor $\sqrt{2}$ comes from a more detailed calculation. Inserting the BCS gap ratio $E_g = 3.53k_BT_c$, this becomes

$$B_{Pauli} = 1.83T_c. \tag{5.90}$$

The data in Table 5.2 demonstrate that this provides an approximation to experimentally determined upper-critical fields B_{c2}. This limiting field has also been called the paramagnetic limit or the Clogston–Chandrasekhar limit (Chandrasekhar, 1962; Clogston, 1962; Pérez-González and Carbotte, 1992).

For many Type II superconductors both the ratio $B_{c2}(0)/T_c$ and the slope dB_{c2}/dT at T_c are close to the Pauli value 1.83 T/K, as shown by the data listed on Table 5.2 and plotted in Fig. 5.26. The zero-temperature upper-critical fields $B_{c2}(0)$ of high-temperature superconductors are generally too high to measure directly, but they can be estimated from the Pauli limit or from the empirical expression $B_{c2} \approx (2T_c/3)dB_{c2}/dT$, which can be deduced from the data in Table 5.2.

Upper critical fields $B_{c2}(T)$ and their temperature derivatives dB_{c2}/dT often depend on the orientation of the applied magnetic field. This is especially true for the high-temperature superconductors because of their planar structures. These types of critical fields and their temperature derivatives at T_c are larger when the external field is applied perpendicular to the c-axis (i.e., parallel to the Cu–O planes) than when it is applied parallel to this axis, as shown in Fig. 5.27. This order is reversed for the lower critical field, as shown in Fig. 5.28; in other words, $B_{c1\perp c} < B_{c1\parallel c} \ll B_{c2\parallel c} < B_{c2\perp c}$.

This reversal is associated with the reversal in the order of sizes of the penetration depths and coherence lengths given by Eq. (12.46), $\xi_c < \xi_{ab} \ll \lambda_{ab} < \lambda_c$. Therefore, we have, from Eqs. (12.51) and (12.52), the lower critical field ratio

$$\frac{B_{c1\perp c}}{B_{c1\parallel c}} = \frac{\lambda_{ab}}{\lambda_c} = \frac{\ln \kappa_{ab}}{\ln \kappa_c} < 1 \tag{5.91}$$

Table 5.2 Comparison of Upper-Crititcal Feild $B_{c2}(0)$, Slope dB_{c2}/dT at T_c, and Pauli Limiting Fields $B_{Pauli} = 1.83T_c$ of Selected Type II Superconductors

Material	T_c (K)	B_{c2} (T)	B_{c2}/T_c (T/K)	$-dB_{c2}/dT$ (T/K)	B_{Pauli} (T)	$\frac{2}{3}T_c\left(\frac{dB_{c2}}{dT}\right)$
$CeCu_2Si_2$ (heavy fermion)	0.5	2.4	4.8	23	0.9	7.67
UBe_{13} (heavy fermion)	0.9	6	6.7	44	1.7	26.4
Nb(44%)–Ti (alloy)	9.3	15	1.6	2.4	17	14.9
$Gd_{0.2}PbMo_6S_8$ (Chevrel)	14	61	4.4	6.8	26	63.4
Nb_3Sn ($A15$)	18	28	1.6	2.5	33	30.0
$Nb_3(Al_{0.75}Ge_{0.25})$ ($A15$)	20.7	43.5	2.1	3.0	38	41.4
Nb_3Ge ($A15$)	23.1	38	1.7	2.3	42	35.4
$YBa_2Cu_3O_7$ (HTSC)	92	120–200	1.3–2.2	0.7–4.6	168	42.9–282

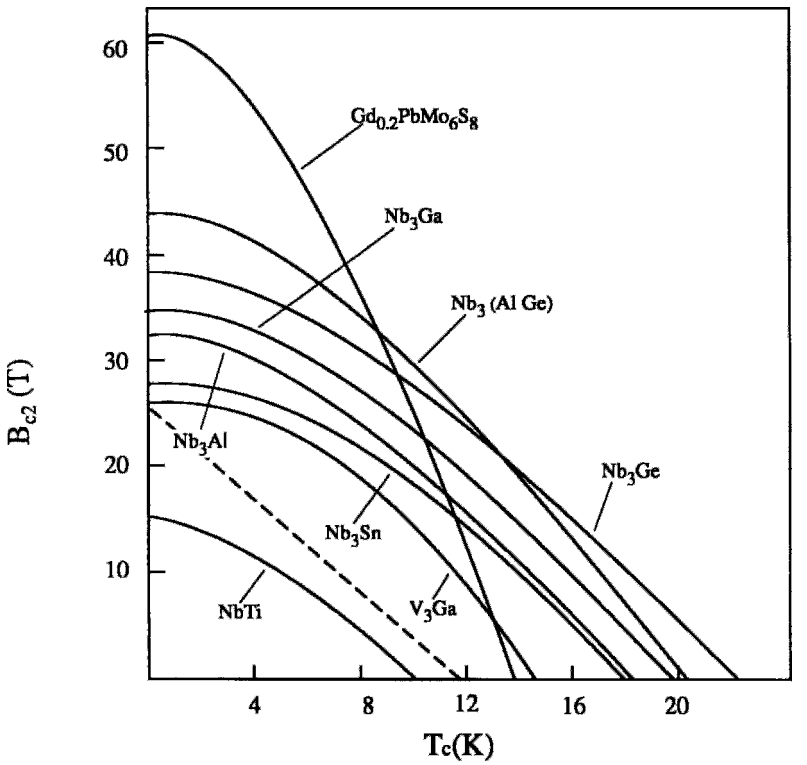

Figure 5.26 Relation between upper-critical field B_{c2} and temperature for the best classical superconductors, some of which are used for fabricating commercial magnets. In the high-temperature limit ($2/3T_c < T < T_c$) many of the curves have a slope that is close to the value 1.83 T/K of the Pauli limit (dashed curve) (Wilson, 1983, p. 302).

and its upper critical field counterpart

$$\frac{B_{c2\perp c}}{B_{c2\parallel c}} = \frac{\xi_{ab}}{\xi_c} > 1, \qquad (5.92)$$

where κ_{ab} and κ_c are given by Eqs. (12.48) and $\kappa_{ab} > \kappa_c$. These inequalities may be verified from the data in Tables 12.4 and 12.5.

Tesanovic (1991), Tesanovic and Rasolt (1989), and Tesanovic *et al.* (1991) discussed the possibility of reentrant superconducting behavior in applied fields far exceeding B_{c2}.

XVIII. IDEAL TYPE II SUPERCONDUCTOR

A Type II superconductor has several characteristic parameters, such as its Ginzburg–Landau parameter κ, transition temperature T_c, energy gap E_g, coherence length ξ, penetration depth λ, upper-critical field B_{c2}, lower critical field B_{c1}, thermodynamic critical field B_c, and critical current density J_c. We have seen how these various parameters are related by simple theoretical expressions, so that if any two of them are specified, the others can be estimated. This suggests defining an ideal isotropic Type II superconductor as one whose parameters have "ideal" relationships with each other.

Consider such a Type II superconductor with $\kappa = 100$ and $T_c = 90\,\text{K}$. Its energy gap is obtained from the BCS relation (7.79)

$$E_g = 3.528 k_B T_c = 27.5\,\text{meV}. \qquad (5.93)$$

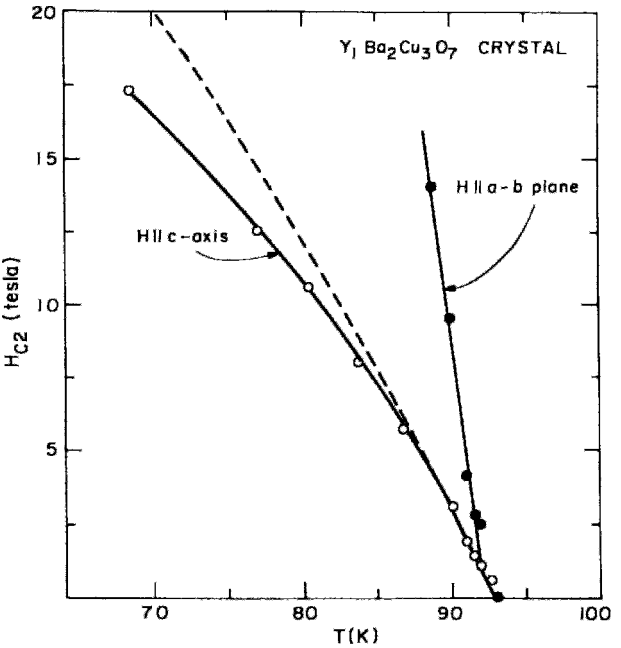

Figure 5.27 Anisotropy in the upper-critical fields of $YBa_2Cu_3O_7$. The initial slope $dB_{c2\|c}/dT$ at T_c (– – –) is $-0.96\,T/K$, while its counterpart $dB_{c2\perp c}/dT$ at T_c is $-4\,T/K$ (Moodera *et al.*, 1988).

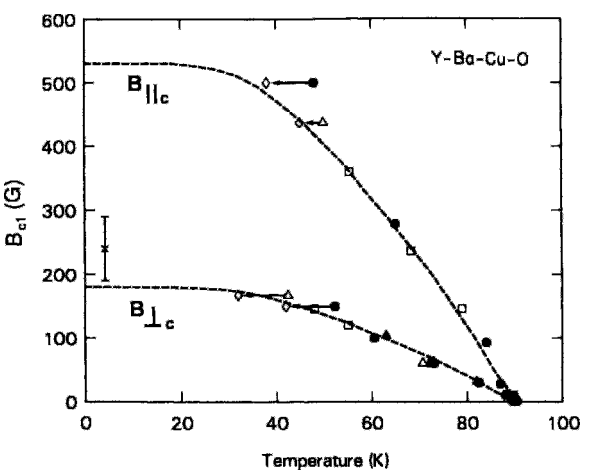

Figure 5.28 Anisotropy in the lower-critical fields of $YBa_2Cu_3O_7$. The initial slope $dB_{c1\|c}/dT$ at T_c is $-1.4\,mT/K$, and that of $dB_{c1\perp c}/dT$ at T_c is $-0.40\,mT/K$. The low-temperature extrapolations give $53 \pm 5\,mT$ for the applied field parallel to c and $18 \pm 2\,mT$ for B_{app} perpendicular to c. Yeshuran *et al.* (1988) obtained the 6 K values, $B_{c1\|c} = 90 \pm 10\,mT$ (not shown) and $B_{c1\perp c} = 25 \pm 5\,mT$ (shown as $\times$ with vertical error bar). The dashed curves are BCS fits to the data (Krusin-Elbaum *et al.*, 1989). Recall that $10G = 1\,mT$.

The Pauli limit (5.90) provides an estimate of the upper-critical field,

$$B_{c2} = 1.83 T_c = 165\,\mathrm{T}. \tag{5.94}$$

Equation (12.9) gives the coherence length ξ,

$$\xi = \left(\frac{\Phi_0}{2\pi B_{c2}}\right)^{1/2} = 1.26\,\mathrm{nm}, \tag{5.95}$$

and from the definition (12.6) of the Ginzburg–Landau parameter we obtain the penetration depth λ,

$$\lambda = \kappa\xi = 126\,\mathrm{nm}. \tag{5.96}$$

Equations (12.10) and (12.11), respectively, give the thermodynamic and lower critical fields,

$$B_c = \frac{B_{c2}}{\sqrt{2}\,\kappa} = 1.16\,\mathrm{T}, \tag{5.97}$$

$$B_{c1} = \frac{B_c \ln\kappa}{\sqrt{2}\,\kappa} = 37.9\,\mathrm{mT}. \tag{5.98}$$

The critical current density J_c at 0 K is given by Eq. (2.51):

$$J_c = B_c/\mu_0\,\lambda = 6.95 \times 10^8\,\mathrm{A/cm^2}. \tag{5.99}$$

This approximates what has been called the depairing current density.

$$J_{\mathrm{depair}} = 10 B_c/4\pi\lambda\mu_0 \tag{5.100}$$

$$= 5.53 \times 10^8\,\mathrm{A/cm^2} \tag{5.101}$$

where for YBaCuO the thermodynamic field $B_c \approx 1\,\mathrm{T}$, penetration depth $\lambda \approx 0.2\,\mu\mathrm{m}$, and $T_c \approx 92\,\mathrm{K}$. These "ideal" values are good approximations to the experimentally determined values for typical high-temperature superconductors.

XIX. MAGNETS

Superconducting magnet design requires simultaneously achieving high critical fields, high critical currents, and suitably malleable wire. The slope $dB_{c2}/dT \approx -2\,\mathrm{T/K}$ of YBaCuO is typical, and gives a critical field of 30 T at the temperature of liquid nitrogen, as shown in Fig. 12.8, and in Table I-2 of our previous work (Poole *et al.*, 1988). This high critical field is for the case of the externally applied field **B** aligned perpendicular to the *c*-axis, i.e., parallel to the crystallographic conducting planes. When $\mathbf{B}_{\mathrm{app}}$ is parallel to the *c*-axis, the critical field is four or five times lower, as already noted in Section XVII.

The standard magnet materials Nb_3Sn and Nb–Ti have critical fields of about 24 T and 10 T, respectively, at 4.2 K, which are not much lower than that of YBaCuO at 77 K. Operating YBaCuO at temperatures much below 77 K will, of course, provide higher critical fields, and TlBaCaCuO, with its much higher T_c (125 K), is even better at 77 K. The problem is to obtain high-T_c superconductors that can carry large transport currents and in addition, have the proper ductility and possess the appropriate mechanical properties. This, however, has yet to be achieved. Vortex pinning must also be optimized to control flux creep.

A better approximation than Eq. (5.99) to the upper limit of the critical current density is given by the Ginzburg–Landau expression

$$J_{\mathrm{cmax}} = \left[\frac{2}{3}\left(1 - \frac{T}{T_c}\right)\right]^{3/2} J_{\mathrm{depair}}. \tag{5.102}$$

This gives $J_c \approx 3 \times 10^8\,\mathrm{A/cm^2}$ at 0 K and $J_c \approx 1.2 \times 10^7$ at 77 K, respectively. Jiang *et al.* (1991) reported $J_c \approx 1.3 \times 10^9\,\mathrm{A/cm^2}$ for microbridges of

$$YBa_2Cu_3O_{7-\delta}$$

films. Achievable critical currents are typically one-tenth the limiting values calculated from Eq. (5.102), as indicated by the data in Table I-2 of our earlier work (Poole *et al.*, 1988).

PROBLEMS

1. Show that a superconductor containing a volume V_{ex} of voids which cannot store any flux has the following ZFC and FC susceptibilities and porosity:

$$\chi_{zfc} = -\frac{V_s + V_h + V_c}{V_s + V_h + V_c + V_{ex}},$$

$$\chi_{fc} = -\frac{V_s + V_c}{V_s + V_h + V_c + V_{ex}},$$

$$P = \frac{V_h + V_c + V_{ex}}{V_s + V_h + V_c + V_{ex}}.$$

2. A granular, 10-mg sample of $YBa_2Cu_3O_{7-\delta}$ has a density of $3.19\,g/cm^3$ and the susceptibilities $\chi_{zfc} = -0.8$ and $\chi_{fc} = -0.4$. Find the porosity and the volumes of the purely superconducting, normal material, open hole-like, enclosed cavity-like and non-flux storing portions of the sample. Assume that there is no normal material present.
3. Show that the measured magnetic moment is given by Eq. (5.21),

$$\mu_0 \mu_{fc} = -(V_s + V_c)B_{app} + (B_{fc} - B_{app})V_h,$$

when field cooling is carried out in a magnetic field B_{fc} that differs from the field B_{app} applied for the measurement.
4. Show that the sample of Problem 1 has the following superconducting, open-hole, closed-cavity, and non-flux storing volumes given by, respectively,

$$V_s = (1-P)V_T,$$

$$V_h = -(\chi_{zfc} - \chi_{fc})V_T,$$

$$V_c = (P - 1 - \chi_{fc})V_T,$$

$$V_{ex} = (1 + \chi_{zfc})V_T,$$

where, of course, χ_{zfc} and χ_{fc} are both negative.
5. Show that Eqs. (5.43) and (5.45) both have the limiting behavior $N_{\|} \to 1/3$ as $\epsilon \to 0$.
6. Show that δ_1 and δ_2 of Table 5.1 are given by

$$\delta_1 = \frac{1}{2}\pi\frac{c}{a},$$

$$\delta_2 = \frac{4}{15}\left(1 - \frac{c}{a}\right).$$

7. Show that δ_3 and δ_4 of Table 5.1 are equal to

$$\delta_3 = \frac{4}{15}\left(1 - \frac{a}{c}\right).$$

$$\delta_4 = \left[\frac{1}{2}\ln\left(2\frac{c^2}{a^2}\right) - 1\right]\frac{a^2}{c^2}.$$

8. Show that the expressions that were deduced in this chapter for the magnetic fields inside and outside a sphere obey the boundary conditions (1.73) and (1.74) at the surface $r = a$.
9. Show that the expressions that were deduced in this chapter for the magnetic fields inside and outside a cylinder in a perpendicular magnetic field obey the boundary conditions (1.73) and (1.74) at the surface.
10. Show that the Curie law, which is based on the assumption that $g\mu_B B_{app}/k_B T \ll 1$, is still applicable for the highest-field, lowest-temperature data of Fig. 5.26. What is the value of the ratio B_{app}/T for which $g\mu_B B_{app}/k_B T = 1$ for $g = 2.0$?
11. Show that for the condition $\chi_\infty = 0$, a plot of χ'' versus χ' over the frequency range $\omega_0 \le \omega \le \infty$ is a semicircle of radius $\frac{1}{2}\chi_0$. Identify the five points at which $(\omega - \omega_0)\tau$ is equal to 0, $\frac{1}{2}$, 1, 4, and ∞ on the semicircle. How would the plot change for $\chi_\infty = \frac{1}{4}\chi_0$?

6

Ginzburg–Landau Theory

I. INTRODUCTION

In Chapter 4 we presented the thermodynamic approach to the phenomenon of superconductivity. We used the Gibbs free energy since in the absence of a magnetic field the Gibbs free energy is continuous across the superconducting-to-normal-state transition. The situation below the transition temperature T_c was handled by assuming a known magnetization and a known critical field, which were then used to calculate the various thermodynamic functions. This approach cannot really be called a theory because it simply incorporates known properties of superconductors into a standard treatment of thermodynamics in the presence of an applied magnetic field.

To gain more understanding of the phenomenon of superconductivity let us examine some simple but powerful theories that have been developed in efforts to explain it. In the present chapter we will consider the phenomenological approach proposed by Ginzburg and Landau (GL) in 1950. This approach begins by adopting certain simple assumptions that are later justified by their successful prediction of many properties of superconducting materials. The assumptions describe superconductivity in terms of a complex order parameter ϕ the physical significance of which is that $|\phi|^2$ is proportional to the density of super electrons. The order parameter is minimally coupled to the electromagnetic field, and in the presence of a magnetic field $\mathbf{B} = \boldsymbol{\nabla} \times \mathbf{A}$ the momentum operator $-i\hbar\boldsymbol{\nabla}\phi$ becomes $[-i\hbar\boldsymbol{\nabla}\phi + e^*\mathbf{A}]$,

where e^* is the charge associated with the "super electrons." The free energy is a minimum with respect to variations of both ϕ and $\mathbf{A}$. The London equations, dating from 1935, follow as a natural consequence of the GL theory, as we show in Section IX (London and London, 1935).

In the next chapter we will examine the more fundamental Bardeen–Cooper–Schrieffer (BCS) microscopic theory that first appeared in 1957. Soon after this theory was published, its correct prediction of many observable properties of superconductors was recognized. The earlier GL theory, on the other hand, was not widely accepted outside the Soviet Union until Gor'kov showed in 1959 that it is derivable from the BCS theory.

This chapter will concentrate on the case of isotropic superconductors. Formulations of the GL theory and of the London Model are also available for the anisotropic case (e.g., Coffey, 1993; Doria *et al*., 1990; Du *et al*., 1992; Klemm, 1993, 1994; Wang and Hu, 1991), and more specifically for the cuprates (Horbach *et al*., 1994; Schneider, *et al*., 1991; Wilkin and Moore, 1993). Time dependent processes have also been treated (Malomed and Weber, 1991; Stoof, 1993).

II. ORDER PARAMETER

Many phenomena in nature, such as the boiling of liquids and ferromagnetism, involve a transition from an ordered to a disordered phase. Each of these transitions can be characterized by an appropriate order parameter that has one value in the high-temperature disordered state and another in the low-temperature ordered state. The order parameter may be thought of as characterizing the extent to which the system is "aligned."

In the case of boiling, the order parameter might be the density, which is high in the liquid state and low in the gaseous state. The magnetic order parameter is often taken as the magnetization; it is zero in the high-temperature paramagnetic region, where the spins are randomly oriented, and nonzero at low temperatures, where the spins are ferromagnetically aligned.

In the normal conduction state the electric current is carried by a Fermi gas of conduction electrons, as was explained in Chapter 1. The GL theory assumes that in the superconducting state the current is carried by super electrons of mass m^*, charge e^*, and density n^* which are connected by the relationships

$$m^* = 2m, \tag{6.1a}$$

$$e^* = \pm 2e, \tag{6.1b}$$

$$n_s^* = \frac{1}{2} n_s \tag{6.1c}$$

with their electron counterparts m, e, and n_s, respectively. The actual "mass" here is the *effective* mass, and it need not be twice the mass of a free electron. The charge is negative for electron-type charge carriers, as is the case with many classical superconductors, and positive for hole conduction, as with most of the high-temperature superconductors. The super electrons begin to form at the transition temperature and become more numerous as the temperature falls. Therefore, their density n_s^* is a measure of the order that exists in the superconducting state. This order disappears above T_c, where $n_s^* = 0$, although fluctuations in n_s^* can occur above T_c. More generally $n_s^* \leq \frac{1}{2} n_s$, and Eq. (6.1c) gives us the limiting value of n_s^* for $T = 0$.

The Ginzburg–Landau theory, to be described in the following section, is formulated in terms of the complex order parameter $\phi(\mathbf{r})$, which may be written in the form of a product involving a phase factor Θ and a modulus $|\phi(\mathbf{r})|$,

$$\phi(\mathbf{r}) = |\phi(\mathbf{r})| e^{i\Theta} \tag{6.2}$$

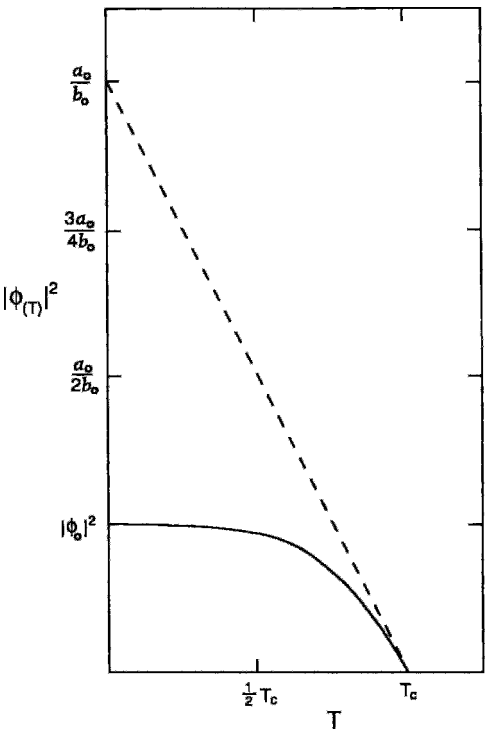

Figure 6.1 Temperature dependence of the order parameter $|\phi|^2$ showing its value $|\phi_0|^2$ at $T = 0$, and the linear behavior (---) near T_c, which extrapolates to the ordinate value a_0/b_0. This figure is drawn under the assumption $|\phi_0|^2 = \frac{1}{4}a_0/b_0$ to agree with Fig. 2.44.

whose square, $|\phi|^2$, is the super electron density,

$$n_s^* = |\phi|^2. \tag{6.3}$$

The parameter ϕ is zero above T_c and increases continuously as the temperature falls below T_c, as shown in Fig. 6.1.

III. GINZBURG–LANDAU EQUATIONS

We saw in the previous chapter that the thermodynamic properties of the superconducting state can be described in terms of the Gibbs free energy density G. Ginzburg and Landau assumed that, close to the transition temperature below T_c, the Gibbs free energy per unit volume $G_s[\phi]$ may be expanded as a local functional of the order parameter,

$$\begin{aligned} G_s[\phi] = G_n + \frac{1}{V}\int d^3\mathbf{r}\Bigg[& \frac{1}{2m^*} \\ & \times (-i\hbar\boldsymbol{\nabla} + e^*\mathbf{A})\phi^* \cdot (i\hbar\boldsymbol{\nabla} + e^*\mathbf{A})\phi \\ & + \left(\frac{1}{2\mu_0}\right) B^2(\mathbf{r}) \\ & - \mu_0 \mathbf{H}(\mathbf{r}) \cdot \mathbf{M}(\mathbf{r}) + a\phi\phi^* \\ & + \frac{1}{2} b\phi\phi^*\phi\phi^* + \cdots \Bigg], \end{aligned} \tag{6.4}$$

where G_n is the free-energy density of the normal state, $\mathbf{A}$ is the magnetic vector potential, and a and b are functions of the temperature only. If the material is normal, $\mathbf{B} = \mu_0 \mathbf{H}$, $\mathbf{M} = 0$, and the magnetic contribution is $\frac{1}{2}\mu_0 H^2$. In regions of perfect superconductivity $\mathbf{B} = 0$ and $\mathbf{M} = -\mathbf{H}$, and the magnetic contribution is $\mu_0 H^2$. In equilibrium the superconductor distributes currents in such a way as to minimize the total free energy.

The assumption is made that over a small range of temperatures near T_c the parameters a and b have the approximate values

$$a(T) \approx a_0\left[\frac{T}{T_c} - 1\right], \tag{6.5a}$$

$$b(T) \approx b_0, \tag{6.5b}$$

where a_0 and b_0 are both defined as positive, so that $a(T)$ vanishes at T_c and is negative below T_c.

To determine $\phi(\mathbf{r})$ we require that the free energy be a minimum with respect to variations in the order parameter. Taking the variational derivative (Arfken, 1985, Chapter 17) of the integrand in (6.4) with respect to ϕ^* with ϕ held constant gives the first GL equation:

$$\frac{1}{2m^*}(i\hbar\boldsymbol{\nabla} + e^*\mathbf{A})^2\phi + a\phi + b|\phi|^2\phi = 0. \tag{6.6}$$

In the London-Landau gauge (sometimes called the Coulomb or radiation gauge)

$$\nabla \cdot \mathbf{A} = 0, \tag{6.7}$$

the first GL equation can be expanded into the form

$$\frac{1}{2m^*}(\hbar^2\nabla^2\phi - 2i\hbar e^*\mathbf{A}\cdot\nabla\phi - e^{*2}\mathbf{A}^2\phi) - a\phi - b|\phi|^2\phi = 0. \tag{6.8}$$

The free energy is also a minimum with respect to variations in the vector potential $\mathbf{A}$, where

$$\mathbf{B} = \nabla \times \mathbf{A}. \tag{6.9}$$

Taking the variational derivative of G with respect to $\mathbf{A}$ we obtain the second GL equation:

$$\nabla \times (\nabla \times \mathbf{A}) + \frac{i\hbar e^*}{2m^*}(\phi^*\nabla\phi - \phi\nabla\phi^*) + \frac{e^{*2}}{m^*}\mathbf{A}|\phi|^2 = \mathbf{0}. \tag{6.10}$$

In Cartesian coordinates this equation, expressed in terms of the London-Landau gauge (6.7), can be simplified by writing $-\nabla^2\mathbf{A}$ in place of $\nabla \times (\nabla \times \mathbf{A})$ (see Problem 7). If we substitute the expression for $\mathbf{B}$ from Eq. (6.9) into the Maxwell expression (Ampère's law),

$$\nabla \times \mathbf{B} = \mu_0\mathbf{J}, \tag{6.11}$$

and compare the result with Eq. (6.10), we find the following proper gauge-invariant expression for the current density:

$$\mu_0\mathbf{J} = -\frac{i\hbar e^*}{2m^*}(\phi^*\nabla\phi - \nabla\phi^*\phi) - \frac{e^{*2}}{m^*}\mathbf{A}|\phi|^2. \tag{6.12}$$

Thus the Ginzburg-Landau theory gives us two coupled differential equations, (6.8) and (6.10), involving the order parameter and vector potential, which can be solved to determine the properties of the superconducting state. For most applications the equations must be solved numerically. However, there are some simple cases in which exact closed-form solutions can be found, and others in which useful approximate solutions can be obtained. We will examine some of these cases, and then transform the GL equations to a normalized form and discuss the solution for more complex cases. When these equations are written in a normalized form, the coherence length, penetration depth, and quantum of magnetic flux, called the *fluxoid*, appear as natural parameters in the theory.

IV. ZERO-FIELD CASE DEEP INSIDE SUPERCONDUCTOR

To get a feeling for the behavior of ϕ, let us first consider the zero-field case ($\mathbf{A} = \mathbf{0}$) with homogeneous boundary conditions (zero gradients, $\nabla^2\phi = 0$). The absence of gradients corresponds to a region deep inside a superconductor where the super electron density does not vary with position. Integration of Eq. (6.4) can be carried out directly for this zero field–zero gradient case, to give for the Gibbs free energy density G_s of the superconductor

$$G_s = G_n + a|\phi|^2 + \frac{1}{2}b|\phi|^4, \tag{6.13}$$

where from Eqs. (6.5) b is positive and a negative below T_c. The GL equation (6.8) provides the minimum for this free energy,

$$a\phi + b|\phi|^2\phi = 0, \tag{6.14}$$

and all of the terms of the second GL equation (6.10) vanish. The phase of ϕ is arbitrary, so we can take ϕ to be real. Equation (6.14) has one solution, $\phi = 0$, corresponding to the normal state and one solution for $a < 0$ at $T < T_c$, with lower free energy:

$$|\phi|^2 = -\frac{a}{b} = \frac{|a|}{b}. \tag{6.15}$$

Using the approximations (6.5a) and (6.5b) for a and b, respectively, we have

$$|\phi|^2 = \frac{a_0}{b_0}\left(1 - \frac{T}{T_c}\right), \tag{6.16}$$

and this linear temperature dependence is shown in Fig. 6.1 for the region near $T \approx T_c$. For lower temperatures $|\phi|^2$ is expected to deviate from linearity on its approach to its 0 K value, $|\phi_0|^2 < a_0/b_0$, as shown in the figure. From Eq. (6.3) we have for the super electron density

$$n_s^* = \frac{a_0}{b_0}\left[1 - \frac{T}{T_c}\right], \tag{6.17}$$

which agrees with Eq. (2.69) in the superconducting region near T_c.

When the expressions for ϕ from Eqs. (6.15) and (6.16) are substituted into Eq. (6.13), we obtain for the minimum Gibbs free energy density

$$G_s = G_n - \frac{1}{2}\left(\frac{a^2}{b}\right) = G_n - \frac{1}{2}\left(\frac{a_0^2}{b_0}\right)\left[1 - \frac{T}{T_c}\right]^2, \tag{6.18}$$

where $\frac{1}{2}(a^2/b)$, called the condensation energy per unit volume of the super electrons, is the energy released by transformation of normal electrons to the super electron state. The condensation energy can be expressed in terms of the thermodynamic critical field $\mathbf{B}_c$ as follows:

$$\frac{1}{2}\left(\frac{a^2}{b}\right) = \frac{B_c^2}{2\mu_0}. \tag{6.19}$$

Figure 6.2 presents a plot of $G_s - G_n$ from Eq. (6.13) versus ϕ for the three ratios of temperatures $T/T_c = 1$, 0.9, and 0.8.

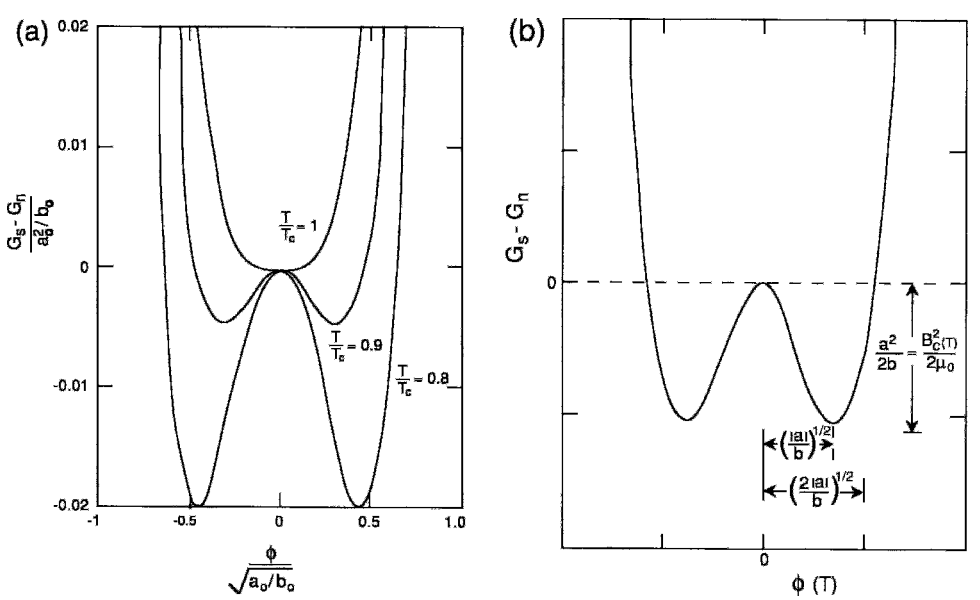

Figure 6.2 Dependence of the difference $G_s - G_n$ between the Gibbs free energy in the normal and superconducting states on the order parameter ϕ. (a) Normalized plots for $T/T_c = 1$, 0.9, and 0.8, and (b) Plot for $T/T_c = 0.85$ showing the minimum free-energy difference $G_s - G_n = a^2/2b$, which occurs for $\phi = (|a|/b)^{1/2}$, and the zero, $G_s - G_n = 0$, at $\phi = (2|a|/b)^{1/2}$.

The minimum for each curve occurs at $\phi = (|a|/b)^{1/2}$ given by Eq. (6.15), and $G_s - G_n = 0$ at $\phi = (2|a|/b)^{1/2}$. These coordinates for the minimum and crossover points of the $T/T_c = 0.8$ curve are indicated in the figure. The equilibrium superconducting state exists at the minimum of each curve. The minimum gets deeper, and the order parameter ϕ for the minimum increases, as the temperature is lowered, as shown. The magnitude of the free-energy minimum at 0 K cannot be written down because the temperature dependence of Eq. (6.16) can only be a good approximation near T_c.

V. ZERO-FIELD CASE NEAR SUPERCONDUCTOR BOUNDARY

Next we consider the case of zero field with inhomogeneous boundary conditions, which means that gradients can exist. Setting $\mathbf{A} = \mathbf{0}$ in the second GL equation (6.10) gives

$$\phi^* \nabla \phi = \phi \nabla \phi^*, \tag{6.20}$$

which means, from Eq. (6.2), that the phase Θ of the order parameter is independent of position. The first GL equation, Eq. (6.8), with $\mathbf{A}$ set equal to zero, provides us with a differential equation for the order parameter:

$$-\frac{\hbar^2}{2m^*}\nabla^2\phi + a\phi + b|\phi|^2\phi = 0. \tag{6.21}$$

Since the phase of the order parameter is constant we select ϕ to be real.

We assume that the right half-space, $x > 0$, is filled with a superconductor and that the left half-space, $x < 0$, is a vacuum or normal material, as shown in Fig. 6.3. Therefore, ϕ is a function of x, the gradient operator ∇ only has an x component, and we can write Eq. (6.21) in one-dimensional form:

$$-\frac{\hbar^2}{2m^*}\frac{d^2\phi}{dx^2} + a\phi + b|\phi|^2\phi = 0. \tag{6.22}$$

When we change variables by letting

$$\phi = \left(\frac{|a|}{b}\right)^{1/2} f, \tag{6.23}$$

the normalized order parameter f satisfies the "nonlinear Schrödinger equation"

$$\frac{\hbar^2}{2m^*|a|}\cdot\frac{d^2f}{dx^2} + f(1 - f^2) = 0. \tag{6.24}$$

If we define the dimensionless variable η as

$$\eta = \frac{x}{\xi}, \tag{6.25}$$

where

$$\xi^2 = \frac{\hbar^2}{2m^*|a|}, \tag{6.26}$$

Eq. (6.24) assumes the simplified dimensionless form

$$\frac{d^2f}{d\eta^2} + f(1 - f^2) = 0. \tag{6.27}$$

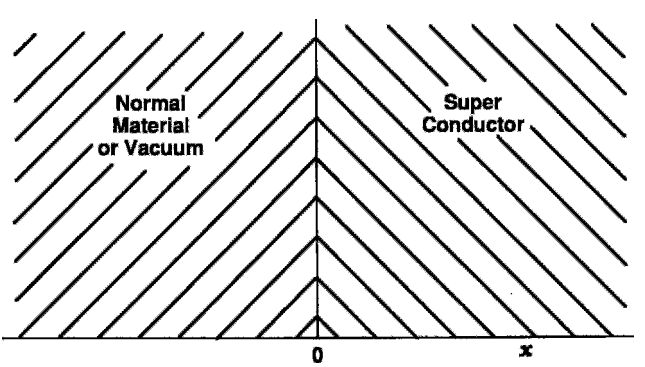

Figure 6.3 Interface between a normal material on the left ($x < 0$) and a superconductor on the right ($x > 0$).

It may be easily verified by direct substitution that Eq. (6.27) has the solution

$$f = \tanh \frac{\eta}{\sqrt{2}}. \tag{6.28}$$

This can be written in terms of the original variable ϕ,

$$\phi = \phi_\infty \tanh \frac{x}{\sqrt{2}\xi}, \tag{6.29}$$

where

$$\phi_\infty = \left(\frac{|a|}{b}\right)^{1/2}, \tag{6.30}$$

with $\phi \to 0$ as $x \to 0$ and $\phi \to \phi_\infty$ as $x \to \infty$. Therefore, ξ is the characteristic length over which ϕ can vary appreciably. The parameter ξ, called the *coherence length*, is one of the two fundamental length scales associated with superconductivity. Its significance is shown graphically in Fig. 6.4, in which we see that ϕ is close to ϕ_∞ far inside the superconductor, is zero at the interface with the normal material, and has intermediate values in a transition layer near the interface with a width on the order of ξ.

Substituting Eq. (6.20) in Eq. (6.12) shows that for $\mathbf{A} = \mathbf{0}$ the current density $\mathbf{J}$ vanishes. This is to be expected since from the Maxwell expression (6.11) we know that electric currents cannot exist if there are no associated magnetic fields present.

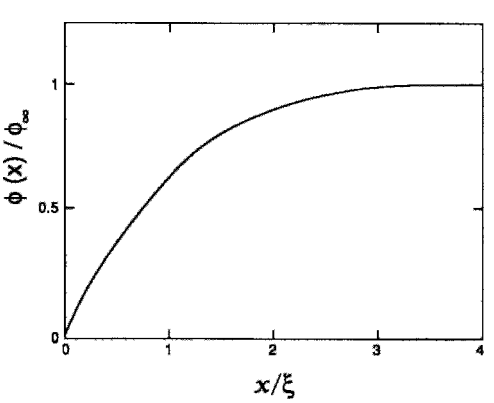

Figure 6.4 Dependence of the order parameter $\phi(x)$ on distance x inside a superconductor. The order parameter is large for $x > \xi$, where ξ is the coherence length.

The BCS theory presented in the next chapter gives an alternate expression

$$\xi_P = \frac{\hbar V_F}{\pi \Delta} = \frac{0.1804 \hbar V_F}{k_B T_C}$$

For what is called the BCS or Pippard coherence length, where $2\Delta = \mathrm{Eg}$ is the superconducting energy gap, and V_F is the Fermi, velocity. The second equation comes from the BCS dimensionless ratio.

$$\frac{2\Delta}{k_B T_C} = 3.528$$

VI. FLUXOID QUANTIZATION

Now that we have determined the order parameter ϕ for the case $B = 0$, we will proceed to investigate the situation when there is an applied magnetic field. In the presence of such a field an interesting result follows from Eq. (6.12). If we write $\phi(\mathrm{r})$ as the product of a modulus and a phase factor, as in Eq. (6.2), the gradient of ϕ will have the form

$$\nabla\phi = i\phi\nabla\Theta + e^{i\Theta}\nabla|\phi(\mathbf{r})|, \tag{6.31}$$

and the total current from Eq. (6.12) will be given by

$$\mu_0 \mathbf{J} = \frac{\hbar e^*}{m^*}|\phi|^2\nabla\Theta - \frac{e^{*2}}{m^*}|\phi|^2\mathbf{A}. \tag{6.32}$$

Dividing Eq. (6.32) by $\hbar e^*|\phi|^2/m^*$ and taking the line integral around a closed contour gives

$$\frac{m^*}{e^{*2}}\oint \frac{\mu_0 \mathbf{J}}{|\phi|^2}\cdot d\mathbf{1} = \frac{\hbar}{e^*}\oint \nabla\Theta \cdot d\mathbf{1} - \oint \mathbf{A}\cdot d\mathbf{1}. \tag{6.33}$$

For the order parameter to be single valued the line integral over the phase Θ around a closed path must be a multiple of 2π,

$$\oint \nabla\Theta \cdot d\mathbf{l} = 2\pi n, \tag{6.34}$$

where n is an integer. Equation (6.33) can now be written

$$\frac{m^*}{e^{*2}} \oint \frac{\mu_0 \mathbf{J}}{|\phi|^2} \cdot d\mathbf{l} + \oint \mathbf{A} \cdot d\mathbf{l} = n\Phi_0, \tag{6.35}$$

where the quantum of flux Φ_0 has the value

$$\Phi_0 = \frac{h}{e^*}, \tag{6.36}$$

in agreement with experiment (e.g., Cabrera *et al.*, 1989; Gough *et al.*, 1987; S. Hasegawa *et al.*, 1992).

It is convenient to express the line integral of $\mathbf{A}$ in Eq. (6.35) in terms of the magnetic flux Φ through the closed contour. Applying Stokes' theorem we find

$$\oint \mathbf{A} \cdot d\mathbf{l} = \int \mathbf{B} \cdot d\mathbf{S} \tag{6.37}$$

$$= \Phi, \tag{6.38}$$

and Eq. (6.35) becomes

$$\frac{m^*}{e^{*2}} \oint \frac{\mu_0 \mathbf{J}}{|\phi|^2} \cdot d\mathbf{l} + \Phi = n\Phi_0. \tag{6.39}$$

This expression is valid for all superconductors, and can be applied to the intermediate and mixed states described in Chapter 11. Equation (6.39) expresses the condition whereby the sum of the enclosed flux Φ and the line integral involving the current density $\mathbf{J}$ is quantized.

We will see later that for Type II superconductors quantized flux occurs in vortices, which have a core region of very high field, and a field outside which decreases with distance in an approximately exponential manner far from the core. Figure 6.5 sketches two such vortices. When a contour is taken in a region of space that contains vortices, the integer n in Eq. (6.39) corresponds to the number of cores included within the path of integration. Figure 6.5 shows contours enclosing $n = 0$, 1, and 2 core regions. Here we are assuming that all the vortices have the same polarity, i.e., the magnetic field points in the same direction in all the vortices. Equation (6.39) is easily generalized to include the presence of positively and negatively directed vortices.

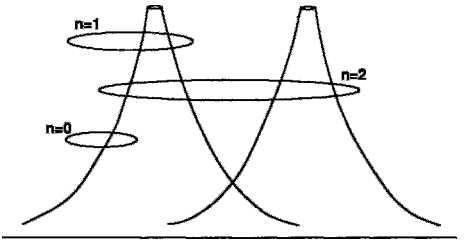

Figure 6.5 Integration paths for Eq. (6.35) encircling no cores ($n = 0$), encircling one core ($n = 1$), and encircling two cores ($n = 2$).

The Little–Parks (1962, 1964) experiment demonstrated this flux quantization by measuring the magnetic field dependence of the shift in T_c of a thin-walled superconducting cylinder in an axial applied field.

VII. PENETRATION DEPTH

In Section V we found how the order parameter changes with distance in the neighborhood of the boundary of a superconductor, and this provided us with the first fundamental length scale—the coherence length ξ. In this section we will investigate the behavior of the internal magnetic field in the neighborhood of a boundary when there is an applied field outside. This will give us the penetration depth λ_L, the second of the two fundamental length scales of superconductivity.

We begin by returning to the semi-infinite geometry of Fig. 6.3 with a uniform magnetic field oriented in the z direction.

In the London-Landau gauge (6.7) the vector potential for a constant magnetic field B_0 outside the superconductor ($x < 0$) is

$$\mathbf{A} = A_y(x)\hat{\mathbf{j}} \tag{6.40}$$

with

$$A_y(x) = xB_0 + A_0 \quad x < 0, \tag{6.41}$$

where the constant A_0 is selected for continuity with the solution $A_y(x)$ inside the superconductor, as shown in Fig. 6.6. This constant does not affect the field $\mathbf{B}(x)$.

In order to determine how the phase of the order parameter varies throughout the interior of the superconductor, let us evaluate the line integrals of Eq. (6.35) along a rectangular contour in the *x,y*- plane that is closed at $x = x_0$ and $x_1 \to \infty$, as indicated in Fig. 6.7. This is done for a contour of arbitrary width L, as shown. Since $\mathbf{A}$ is a vector in the y direction, it is perpendicular to the upper and lower horizontal parts of the contour, which are along x, so that the integral of $\mathbf{A} \cdot d\mathbf{l}$ vanishes along these paths. We also observe that no current flows into the superconductor, so that $J_x = 0$ and the line integrals of $\mathbf{J} \cdot d\mathbf{l}$ along these same upper and lower horizontal paths vanish. When we take the limit $x_1 \to \infty$ the two line integrals along this vertical x_1 path vanish because $\mathbf{A}$ and $\mathbf{J}$ are zero far inside the superconductor. As a result only the line integrals along the x_0 vertical path contribute, and they may be written down immediately because there is no y dependence for the fields and currents:

$$L \cdot \left[\frac{m^* J_y(x_0)}{e^{*2}|\phi(x_0)|^2} + A_y(x_0) \right] = n\Phi_0. \tag{6.42}$$

Since the width L is arbitrary and n is quantized, it follows that $n = 0$. Then, from the

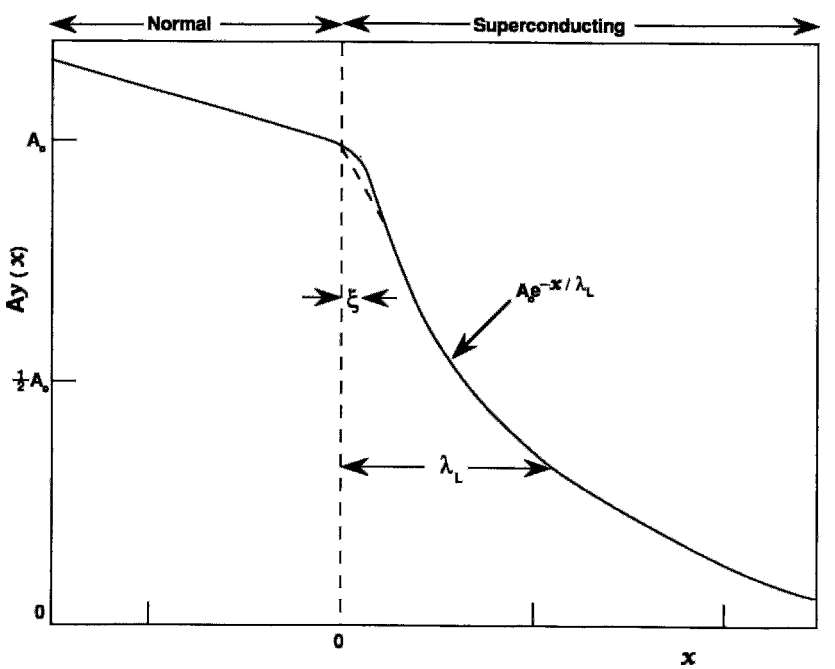

Figure 6.6 Dependence of the vector potential *A(x)* on distance x for the case of Fig. 6.3. *A(x)* depends linearly on x outside the superconductor (left), where there is a constant applied magnetic field, and decays exponentially inside the superconductor (right), becoming very small for $x \gg \lambda_L$, where λ_L is the London penetration depth.

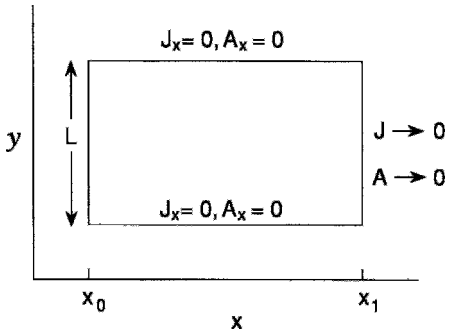

Figure 6.7 Integration path inside a superconductor for determining the phase Θ of the order parameter ϕ.

quantization condition (6.34) and the arbitrariness of the path, we conclude that the phase Θ of the order parameter (6.2) is constant everywhere throughout the superconductor, and we set it equal to 0. Furthermore, since x_0 in Eq. (6.42) is arbitrary, it follows that

$$J_y(x) = \frac{e^{*2}|\phi(x)|^2}{m^*} A_y(x), \qquad (6.43)$$

which tells us how $\mathbf{J}$ is related to $\mathbf{A}$.

To determine the x dependence of A_y, note that Eq. (6.20) is valid for a constant phase and that the second GL equation (6.10) reduces to the expression

$$\frac{d^2}{dx^2} A_y(x) = \frac{\mu_0 e^{*2}|\phi(x)|^2}{m^*} A_y(x). \qquad (6.44)$$

We seek to solve this equation far enough inside the superconductor, $x \gg \xi$, so that the order parameter attains its asymptotic value, $\phi \to \phi_\infty$, independent of x. It is convenient to define the London penetration depth λ_L, the second of the two fundamental length scales of a superconductor:

$$\lambda_L^2 = \frac{m^*}{\mu_0 e^{*2}|\phi_\infty|^2}. \qquad (6.45)$$

This permits us to write Eq. (6.44) in the form

$$\frac{d^2}{dx^2} A_y(x) = \frac{A_y(x)}{\lambda_L^2}, \qquad (6.46)$$

which has a simple exponential solution inside the superconductor,

$$A_y(x) = A_0 \exp(-x/\lambda_L) \qquad x > 0, \quad (6.47)$$

for the case $\xi \ll \lambda_L$ which is plotted in Fig. 6.6. The preexponential factor A_0 makes $A_y(x)$ from Eqs. (6.41) and (6.47) match continuously across the boundary at $x = 0$.

In writing Eq. (6.46) we implicitly assumed that the London penetration depth λ_L is greater than the coherence length ξ. For distances from the surface x in the range $0 < x \ll \xi$ we know from Eq. (6.29) and the power series expansion of $\tanh(x/\sqrt{2}\xi)$ for small values of the argument that

$$\phi(x) \approx \phi_\infty \frac{x}{\sqrt{2}\xi} \qquad 0 \ll x \ll \xi, \quad (6.48)$$

so that $\phi(x)$ is much less than ϕ_∞. In this range the effective penetration depth exceeds the London value (6.45), so $A_y(x)$ decays more gradually there, as indicated in Fig. 6.6.

To obtain the fields from the potentials we apply the curl operation $\mathbf{B} = \nabla \times \mathbf{A}$. Only the z component exists, as assumed initially,

$$B_z(x) = B_0 \qquad x < 0, \qquad (6.49)$$

$$B_z(x) = \frac{-A_0}{\lambda_L} \exp(-x/\lambda_L) \quad \xi < x < \infty,$$
$$= B_0 \exp(-x/\lambda_L) \qquad (6.50)$$

where $A_0 = -\lambda_L B_0$ from the boundary condition at the surface ($x = 0$). The distance dependences of Eqs. (6.48) and (6.49), together with the more gradual decay in the range $0 < x < \xi$, are shown in Fig. 6.8. We conclude that for this case the applied field has the constant value $\mathbf{B}_0$ outside the superconductor, decays exponentially with distance inside, and becomes negligibly small beyond several penetration depths within, as shown.

From Eq. (6.43) we find that far inside the superconductor

$$\mu_0 \lambda_L^2 J_y(x) = -A_y(x) \qquad \xi \ll x < \infty, \qquad (6.51)$$

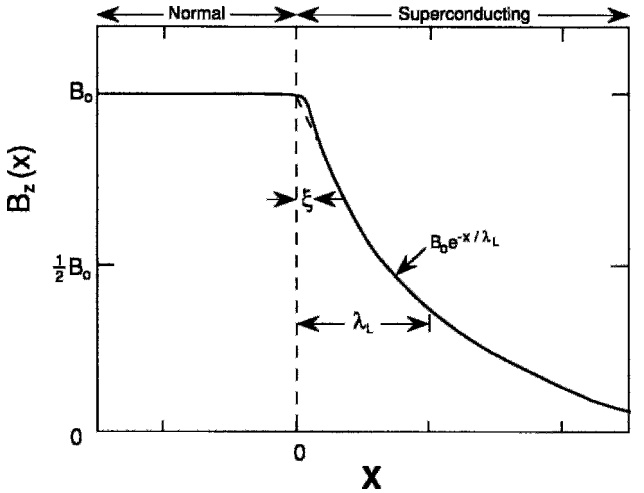

Figure 6.8 Exponential decay of a constant applied magnetic field $B_z(x)$ inside a superconductor for the case $\lambda_L > \xi$. Note the small deviation from exponential behavior within a coherence length ξ of the surface.

as $\phi(x) \to \phi_\infty$, and hence that $J_y(x)$ also satisfies Eq. (6.46) with the distance dependence

$$J_y(x) = \frac{A_0}{\mu_0 \lambda_L^2} \exp(-x/\lambda_L)$$
$$= J_0 \exp(-x/\lambda_L) \qquad \xi < x < \infty, \tag{6.52}$$

which is the same as $A_y(x)$ of Eq. (6.47). In the range $0 < x < \xi$, which is near the surface, we see from Eq. (6.43) that $J_y(x)$ is less than this value, as indicated in Fig. 6.9. Thus, we see that $B_z(x)$ decays less and that the current density $J_y(x)$ has a magnitude less than its value beyond the coherence length.

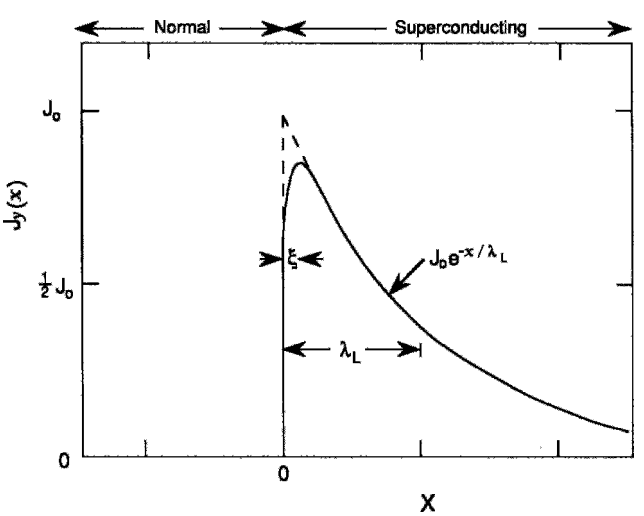

Figure 6.9 Dependence of the current density $J_y(x)$ on distance x inside a superconductor for the case $\lambda_L > \xi$.

In the remainder of the chapter we will ignore these surface effects for $x < \xi$ and only take into account the exponential decay in terms of the penetration-depth distance parameter.

VIII. CRITICAL CURRENT DENSITY

An electric current is accompanied by a magnetic field. To obtain an expression for the current density independent of the magnetic field, the vector potential can be eliminated between the current density equation and the second GL equation. We will do this deep inside the superconductor where the order parameter $\phi(\mathbf{r})$ depends on position only through the phase $\Theta(\mathbf{r})$.

For this situation the order parameter, written in the form

$$\phi(\mathbf{r}) = \phi_0 e^{i\Theta(r)}, \tag{6.53}$$

has the gradient

$$\nabla\phi(\mathbf{r}) = i\phi\nabla\Theta(r), \tag{6.54}$$

and the current density (6.12) is

$$\mathbf{J} = \frac{\hbar e^*}{m^*}\phi_0^2\left(\nabla\Theta - \frac{2\pi}{\Phi_0}\mathbf{A}\right), \tag{6.55}$$

where Φ_0 is given by Eq. (6.36). Substituting the expression for the order parameter from (6.53) in Eq. (6.8) and multiplying on the left by $e^{-i\Theta}$ gives

$$\frac{\hbar^2}{2m^*|a|}\phi_0 e^{-i\Theta}\left(i\nabla + \frac{2\pi}{\Phi_0}\mathbf{A}\right)^2 e^{i\Theta} + \phi_0 - \left(\frac{b}{|a|}\right)\phi_0^3 = 0. \tag{6.56}$$

If the Laplacian $\nabla^2\phi$ is negligible, this becomes

$$\frac{\hbar^2}{2m^*|a|}\left(\nabla\Theta - \frac{2\pi}{\Phi_0}\mathbf{A}\right)^2 + 1 - \frac{\phi_0^2}{(|a|/b)} = 0. \tag{6.57}$$

The factor $[\nabla\Theta - (2\pi/\Phi_0)\mathbf{A}]$ can be eliminated between Eqs. (6.55) and (6.57) to give for the current density

$$J_s = \frac{\Phi_0}{2\pi\mu_0\lambda_L^2\xi}f^2(1-f^2)^{1/2}, \tag{6.58}$$

where f is given by Eq. (6.23) (we have used Eqs. (6.26) and (6.45) here). Figure 6.10 shows how J_s depends on f. The largest possible current density shown in the figure, called the *critical current density* J_c, is obtained by maximizing Eq. (6.58) through differentiation with respect to f^2. This gives $f^2 = \frac{2}{3}$, and we obtain what is sometimes called the Ginzburg–Landau critical current density,

$$J_c = \frac{\Phi_0}{3\sqrt{3}\pi\mu_0\lambda_L^2\xi}. \tag{6.59}$$

This can also be written in terms of the thermodynamic critical field (12.10).

$$J_c = \frac{2\sqrt{2}B_c}{3\sqrt{3}\mu_0\lambda_L}. \tag{6.60}$$

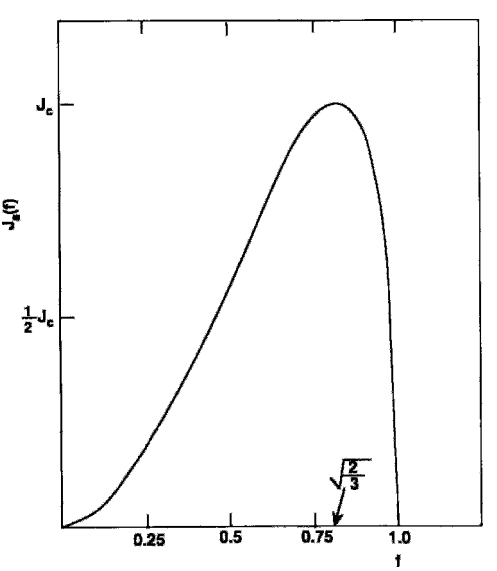

Figure 6.10 Dependence of the super current density $\mathbf{J}_s$ on the normalized order parameter f. $\mathbf{J}_s(f)$ reaches a maximum at $f = (2/3)^{1/2}$.

From Eq. (2.61) this has the following temperature dependence near T_c:

$$J_c = \frac{8\sqrt{2}B_c(0)}{3\sqrt{3}\mu_0\lambda_L(0)}\left(1-\frac{T}{T_c}\right)^{3/2}. \quad (6.61)$$

Thus J_c becomes zero at the critical temperature, and we know from Eq. (2.58) that it is a maximum at $T = 0$.

IX. LONDON EQUATIONS

In 1935 the London brothers, Fritz and Heinz, proposed a simple theory to explain the Meissner effect, which had been discovered two years earlier. They assumed that the penetration depth λ_L is a constant independent of position. The equations which they derived, now called the first London equation,

$$\mathbf{E} = \mu_0\lambda_L^2\frac{d}{dt}\mathbf{J}, \quad (6.62)$$

and the second London equation,

$$\mathbf{B} = -\mu_0\lambda_L^2\nabla\times\mathbf{J}, \quad (6.63)$$

were used to explain the properties of superconductors.

These two equations are easily obtained from the GL theory with the aid of Eq. (6.51) expressed in vector form:

$$\mu_0\lambda_L^2\mathbf{J} = -\mathbf{A}. \quad (6.64)$$

If the vector potential expression (6.9) is substituted in Maxwell's equation (1.66), we obtain

$$\nabla\times\left(\mathbf{E}+\frac{d\mathbf{A}}{dt}\right) = 0, \quad (6.65)$$

and with the aid of Eq. (6.51) we can then write down the first London equation (6.62). The second London equation (6.63) is obtained by substituting the expression for $\mathbf{A}$ from Eq. (6.64) in Eq. (6.9). It should be compared with Eq. (1.72), which, in the absence of magnetization and displacement currents, becomes Ampère's law:

$$\nabla\times\mathbf{B} = \mu_0\mathbf{J}. \quad (6.66)$$

Thus we see that Maxwell's and London's equations link the magnetic field $\mathbf{B}$ and the current density $\mathbf{J}$ in such a way that if one is present in the surface layer so is the other.

If the expression for the current density $\mathbf{J}$ from Eq. (6.66) is substituted in Eq. (6.63) we obtain

$$\nabla^2\mathbf{B} = \frac{\mathbf{B}}{\lambda_L^2}, \quad (6.67)$$

and eliminating $\mathbf{B}$ between these same two expressions gives

$$\nabla^2\mathbf{J} = \frac{\mathbf{J}}{\lambda_L^2}. \quad (6.68)$$

Thus, recalling (6.46), we see that $\mathbf{A}$, $\mathbf{B}$, and $\mathbf{J}$ all obey the same differential equation. In Cartesian coordinates, Eqs. (6.67) and (6.68) correspond to the Helmholtz equation well known from mathematical physics (Arfken, 1985). In the following section we will provide applications of these equations to the phenomena of magnetic field penetration and surface current flow.

X. EXPONENTIAL PENETRATION

In Section VII we deduced the exponential decay of the magnetic field $\mathbf{B}$ and the current density $\mathbf{J}$, Eqs. (6.50) and (6.52), respectively, inside a superconductor in the presence of an external magnetic field $\mathbf{B}_0$, and in the previous section we wrote down the Helmholtz equations (6.67) and (6.68), respectively, for these same two cases. In the present section we will apply these equations to several practical situations involving magnetic field penetration and surface current flow in superconductors with rectangular

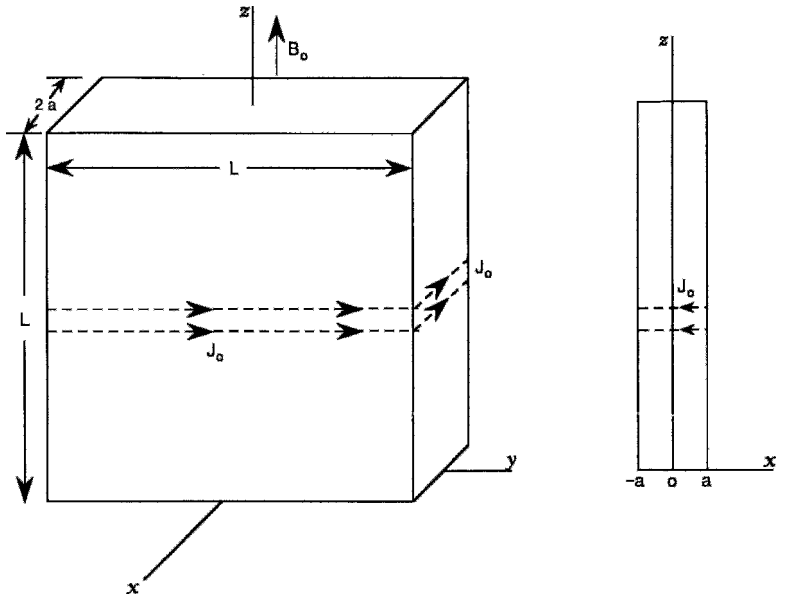

Figure 6.11 Flat superconducting slab with thickness $2a$ much less than the two broad dimensions L. The applied magnetic field $\mathbf{B}_0$ and super current flow $\mathbf{J}_0$ have the indicated directions. The thickness parameter a should not be confused with the GL parameter a of Eq. 6.4.

and cylindrical shapes. Both shielding and transport currents will be discussed.

Consider a flat superconducting slab oriented in the y, z-plane in the presence of an applied magnetic field $\mathbf{B}_0$ in the z direction, as illustrated in Fig. 6.11. The slab is of length L, width L, and thickness $2a$, as indicated in the figure; we assume that $a \ll L$. The solution to Helmholtz equation (6.67) which satisfies the boundary conditions $B_z(-a) = B_z(a) = \mathbf{B}_0$ at the edges is

$$B_z(x) = \frac{B_0 \cosh\left(\dfrac{x}{\lambda_L}\right)}{\cosh\left(\dfrac{a}{\lambda_L}\right)} \qquad -a < x < a. \tag{6.69}$$

This is sketched in Fig. 6.12 for $\lambda_L \ll a$ and in Fig. 6.13 for $\lambda_L \gg a$. For the former case we have

$$B_z(x) \approx B_0 \exp\left(\frac{-(a-|x|)}{\lambda_L}\right) \qquad \lambda_L \ll a. \tag{6.70}$$

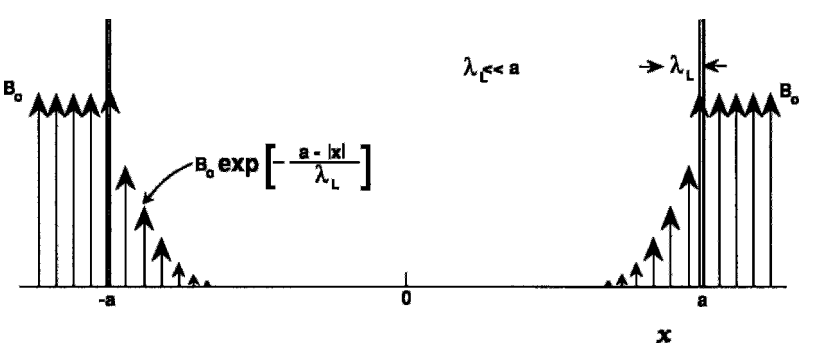

Figure 6.12 Exponential decay of a magnetic field inside a superconductor for the case $\lambda_L \ll a$. Both this figure and Fig. 6.13 are symmetric about the midpoint $x = 0$.

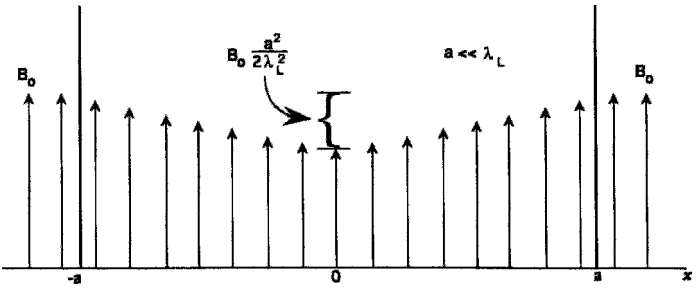

Figure 6.13 Decrease of the magnitude of a magnetic field inside a superconductor for the case $\lambda_L \gg a$. The field in the center is $[1-\frac{1}{2}(a/\lambda_L)^2]$ times the field $\mathbf{B}_0$ outside.

We show in Problem 5 that in the latter case the penetration is linear near each boundary,

$$B_z(x) \approx B_0\left[1-\frac{a(a-x)}{\lambda_L^2}\right] \qquad \lambda_L \gg a, \quad 0 \ll x < a, \quad (6.71a)$$

and

$$B_z(x) \approx B_0\left[1-\frac{a(a+x)}{\lambda_L^2}\right] \qquad \lambda_L \gg a, \quad -a < x \ll 0, \quad (6.71b)$$

with the value in the center

$$B_z(0) \approx B_0\left[1-\frac{a^2}{2\lambda_L^2}\right] \qquad x = 0, \quad (6.72)$$

as indicated in Fig. 6.13.

To derive the corresponding expressions for the current density we find from Eq. (6.11) that for this case **J** and **B** are related through the expression

$$\mu_0 J_y = \frac{dB_z}{dx}, \quad (6.73)$$

and differentiating $B_z(x)$ in Eq. (6.69) gives

$$\mu_0 J_y(x) = \frac{B_0}{\lambda_L}\cdot\frac{\sinh\dfrac{x}{\lambda_L}}{\cosh\dfrac{a}{\lambda_L}} \qquad -a < x < a. \quad (6.74)$$

Thus the magnetic field **B** and the current density **J** are mutually perpendicular, as indicated in Fig. 6.11. The current density flows around the slab in the manner shown in Fig. 6.14, and is positive on one side and negative on the other. It has the maximum magnitude $J_y(0) = J_0$ on the surface, $x = \pm a$, where

$$J_0 = \frac{B_0}{\mu_0\lambda_L}\tanh\frac{a}{\lambda_L}, \quad (6.75)$$

and this gives for $J_y(x)$

$$J_y(x) = J_0\frac{\sinh\left(\dfrac{x}{\lambda_L}\right)}{\sinh\left(\dfrac{a}{\lambda_L}\right)} \qquad -a < x < a. \quad (6.76)$$

This expression for the current density satisfies Helmholtz equation (6.68), as expected.

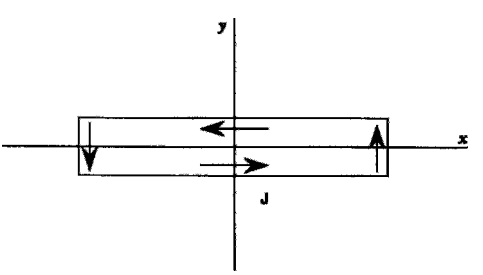

Figure 6.14 Cross section in the x, y-plane of the slab of Fig. 6.11 showing the shielding super current flow for an applied magnetic field $\mathbf{B}_0$ in the z direction.

For $a \gg \lambda_L$ the current density flows in a surface layer of thickness λ_L, while for the opposite limit, $a \ll \lambda_L$, it flows through the entire cross section, in accordance with Figs. 6.15 and 6.16, respectively. In the latter case the distance dependence is linear such that

$$J(x) \approx \frac{J_0 x}{a} \qquad -a < x < a, \qquad (6.77)$$

as shown in Fig. 6.16.

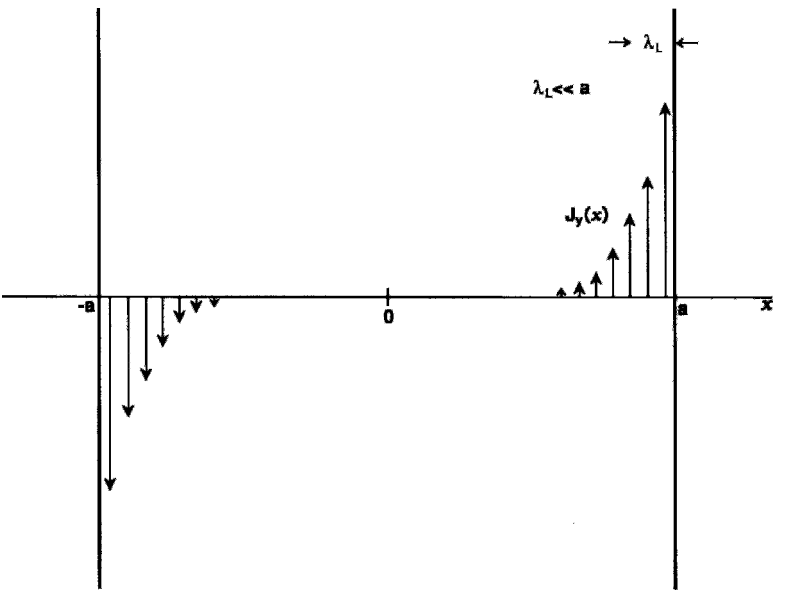

Figure 6.15 Current density $J_y(x)$ inside the superconducting slab for the case $a \gg \lambda_L$. This figure and Fig. 6.16 are antisymmetric about the origin $x = 0$.

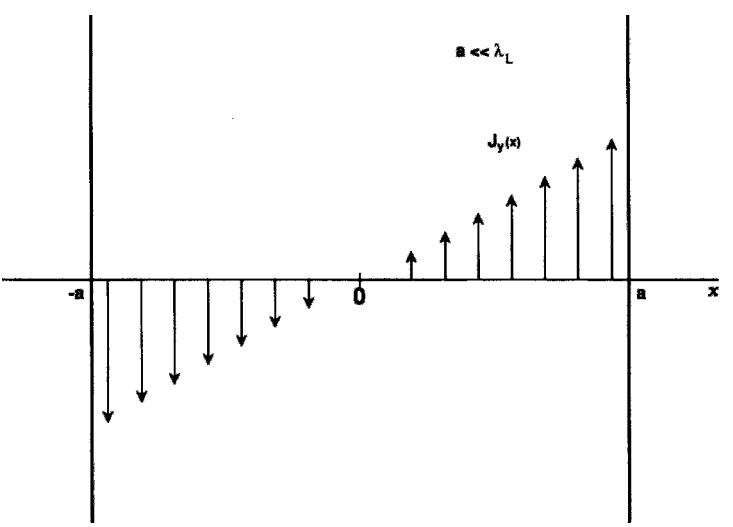

Figure 6.16 Current density $J_y(x)$ inside the superconducting slab for the case $a \ll \lambda_L$. Note that the magnitude of $\mathbf{J}(x)$ decreases linearly with distance x.

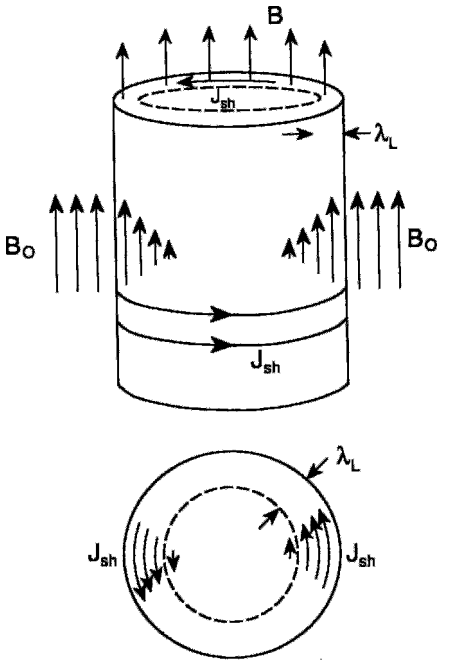

Figure 6.17 Sketch of a Type I superconducting cylinder in an external magnetic field $\mathbf{B}_{app} = \mathbf{B}_0$ directed along its axis, an arrangement referred to as parallel geometry. The penetration of the magnetic field **B** into the superconductor and the current flow $\mathbf{J}_{sh}$ near the surface are shown. The London penetration depth λ_L is also indicated.

The super current which flows in the surface layer may be looked upon as generating a magnetic field in the interior that cancels the applied field there. Thus the encircling currents are called *shielding currents* in that they shield the interior from the applied field.

The case of the long superconducting cylinder shown in Fig. 6.17 in an external axial magnetic field B_0 is best treated in cylindrical coordinates, and, as we show in Chapter 12; Section III.B, the solutions are modified Bessel functions. In the limit $\lambda_L \ll R$, the surface layer approximates a planar layer, and the penetration is approximately exponential,

$$B_z(r) \approx B_0 \exp\left[\frac{-(R-r)}{\lambda_L}\right] \qquad \lambda_L \ll R \quad 0 < r < R, \quad (6.78)$$

as illustrated in Fig. 6.18, and expected on intuitive grounds. Figure 6.17 presents three-dimensional sketches of the fields and currents.

Another example to consider is a flow of transport current moving in a surface layer in the axial direction, as shown in Fig. 6.19. Note the magnetic field lines encircling the wire outside and decaying into the surface layer. Figures 6.17 and 6.19 compare these shielding and transport current cases. The figures are drawn for the limit $a \gg \lambda_L$ and apply to Type I superconductors that exclude the **B** field and current flow from the interior. They also apply to Type II superconductors in low applied fields below but near the transition temperature, $T < T_c$, since in this case

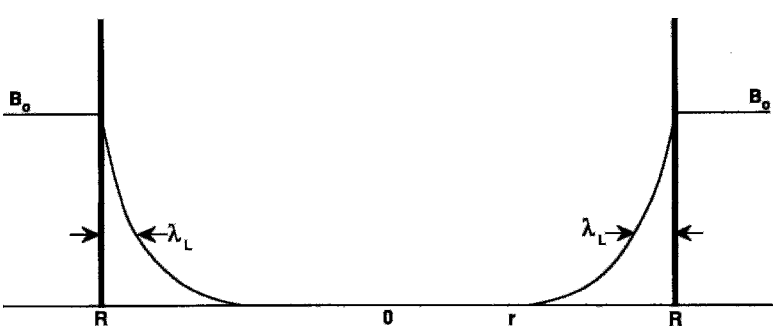

Figure 6.18 Magnetic field $\mathbf{B}(\mathbf{r})$ inside the Type I superconducting cylinder of Fig. 6.17 for the case $\lambda \ll R$.

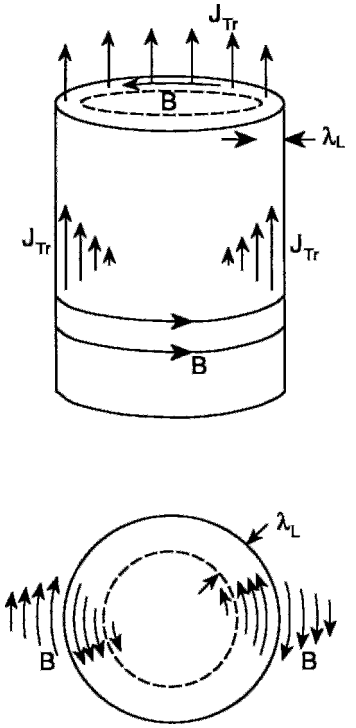

Figure 6.19 Sketch of the current density $\mathbf{J}_{tr}$ and magnetic field $\mathbf{B}$ near the surface of a Type I superconducting cylinder carrying a transport current.

the internal field $\mathbf{B}_{in}$ is small and the behavior approximates Type I.

XI. NORMALIZED GINZBURG–LANDAU EQUATIONS

In Section IV we wrote down the one-dimensional zero field GL equation normalized in terms of a dimensionless coordinate (6.25) and a dimensionless order parameter (6.23), and this simplified the process of finding a solution. Before proceeding to more complex cases it will be helpful to write down the general GL equations (Eqs. (6.6) and (6.10)) in fully normalized form in terms of the coherence length (6.26), London penetration depth (6.45), and flux quantum (6.36).

To accomplish this we express the coordinates as dimensionless variables divided by the coherence length ξ. Thus we have, for example, ρ/ξ, ϕ, z/ξ in cylindrical coordinates, and use the differential operator symbols $\boldsymbol{\nabla}$ and $\boldsymbol{\nabla}^2$,

$$\boldsymbol{\nabla} \to \xi \boldsymbol{\nabla}, \tag{6.79}$$

$$\boldsymbol{\nabla}^2 \to \xi^2 \boldsymbol{\nabla}^2, \tag{6.80}$$

to designate differentiation with respect to these normalized coordinates. The order parameter ϕ is normalized as in Eq. (6.23),

$$\phi = \left(\frac{|a|}{b}\right)^{1/2} f, \tag{6.81}$$

the vector potential $\mathbf{A}$ is normalized in terms of the flux quantum Φ_0,

$$\mathbf{A} = \left(\frac{\Phi_0}{2\pi\xi}\right) \mathscr{A}, \tag{6.82}$$

and we make use of the Ginzburg–Landau parameter κ, which is defined as the ratio of the penetration depth to the coherence length,

$$\kappa = \frac{\lambda_L}{\xi}. \tag{6.83}$$

Using this notation the GL equations (6.6) and (6.10), respectively, expressed in the London–Landau gauge (6.7), $\boldsymbol{\nabla} \cdot \mathscr{A} = 0$, assume the normalized forms

$$-(i\boldsymbol{\nabla} - \mathscr{A})^2 f + f(1 - f^2) = 0, \tag{6.84a}$$

$$\kappa^2 \boldsymbol{\nabla} \times (\boldsymbol{\nabla} \times \mathscr{A}) + \tfrac{1}{2} i (f^* \boldsymbol{\nabla} f - f \boldsymbol{\nabla} f^*) + \mathscr{A} f^2 = 0. \tag{6.84b}$$

We can also define a dimensionless current density $\mathbf{j}$ from

$$\mathbf{J} = \frac{\Phi_0}{2\pi\lambda_L^2 \xi \mu_0} \mathbf{j}, \tag{6.85}$$

which gives us

$$\mathbf{j} = \kappa^2 \boldsymbol{\nabla} \times (\boldsymbol{\nabla} \times \mathscr{A}). \tag{6.86}$$

Equation (6.84a) can be expanded and Eq. (6.84b) written as follows:

$$\nabla^2 f - 2i\mathcal{A}\cdot\nabla f - \mathcal{A}^2 f + f(1-f^2) = 0, \quad (6.87a)$$

$$\mathbf{j} = -\tfrac{1}{2}i(f^*\nabla f - f\nabla f^*) - \mathcal{A}f^2. \quad (6.87b)$$

Thus the coherence length, penetration depth, and flux quantum are the natural normalization parameters for transforming the GL equations into dimensionless form. In the following section we will use these normalized equations to elucidate various properties of superconductors.

XII. TYPE I AND TYPE II SUPERCONDUCTIVITY

In Chapter 11 we will discuss how bulk normal and superconducting phases coexist in equilibrium in an external magnetic field $\mathbf{B}_{\text{app}}$. We now wish to investigate this "mixed state" by considering a plane interface between a normal phase filling the left half-space $z<0$ and a superconducting phase in the right half-space $z>0$, as indicated in Fig. 6.3.

We expect the superconducting order parameter to vanish at the interface and, as we have seen, begin approaching its bulk equilibrium value within a characteristic length ξ. On the other hand, surface currents flow in a surface layer of width $\approx \lambda_{\text{L}}$, and full exclusion of magnetic flux occurs only deep inside the superconductor. Here we are interested in calculating the effect of the interface on the free energy of the state. This, in turn, leads naturally to the idea of a "surface tension" between the superconducting and normal phases.

Deep within either of the homogeneous phases the free-energy density at the critical field $B_{\text{app}} = \mu_0 H_{\text{c}}$ is equal to $G_{\text{n0}} + \frac{1}{2}\mu_0 H_{\text{c}}^2$. The free-energy density of the associated mixed state, including the interface, is

$$G(z) = \begin{cases} G_{\text{n0}} + \frac{1}{2}\mu_0 H_{\text{c}}^2 & z<0 \\ G_{\text{n0}} - \frac{1}{2}b|\phi|^4 + \dfrac{1}{2\mu_0} \times (B^2 - 2\mu_0^2 \mathbf{H}_{\mathbf{c}}\cdot\mathbf{M}) & z>0 \end{cases} \quad (6.88)$$

where we have used Eq. (6.4) subject to the minimization restriction (6.6) for the half-space $z>0$. The surface tension σ_{ns} is defined as the difference in free energy per unit area between a homogeneous phase (either all normal or all superconducting) and a mixed phase. Therefore, we can write

$$\sigma_{\text{ns}} = \int dz \left[-\tfrac{1}{2}b|\phi|^4 + \frac{1}{2\mu_0} \times (B^2 - 2\mu_0^2 \mathbf{H}_{\mathbf{c}}\cdot\mathbf{M}) - \tfrac{1}{2}\mu_0 \mathbf{H}_{\mathbf{c}}^2 \right], \quad (6.89)$$

since the integrand vanishes for $z<0$. With the aid of the expression $B = \mu_0(H+M)$ this becomes

$$\sigma_{\text{ns}} = \int dz \left[-\tfrac{1}{2}b|\phi|^4 + \tfrac{1}{2}\mu_0 M^2 \right]. \quad (6.90)$$

Note that as $z\to\infty$, $M\to -H_{\text{c}}$, and by Eq. (6.15), $|\phi|^2 \to |a|/b$, so from Eq. (6.19) the integrand vanishes far inside the superconductor where $z > \lambda_{\text{L}}$, and the principal contribution to the surface tension comes from the region near the boundary.

If $\sigma_{\text{ns}} > 0$, the homogeneous phase has a lower free energy than the mixed phase, and therefore the system will remain superconducting until the external field exceeds B_{c}, at which point it will turn completely normal. Superconductors of this variety are called Type I. However, if $\sigma_{\text{ns}} < 0$, the superconductor can lower its free energy by spontaneously developing normal regions that include some magnetic flux. Since the greatest saving in free energy is achieved by maximizing the surface area: flux ratio, these normal regions will be as small as possible

consistent with the quantization of fluxoid. Thus the flux enters in discrete flux quanta.

Returning to Eq. (6.90), the first term represents the free energy gained by condensation into the superconducting state, while the second is the cost of excluding flux from the boundary layer. Roughly speaking, the order parameter attains its bulk value over a characteristic length ξ, while the super currents and magnetic flux are confined to a distance on the order of λ_L from the surface. If we define the dimensionless magnetization m by

$$M^2 = \left(\frac{a^2}{\mu_0 b}\right) m^2 \tag{6.91}$$

and make use of the dimensionless order parameter (6.81), Eq. (6.90) becomes

$$\sigma_{ns} = \frac{a^2}{2b} \int dz(-f^4 + m^2), \tag{6.92}$$

which can be written

$$\sigma_{ns} = \frac{a^2}{2b} \int dz[(1 - f^4) - (1 - m^2)]. \tag{6.93}$$

Equation (6.28) gives $f = \tanh(z/\sqrt{2}\,\xi)$ (see Problem 10 for an expression for the distance dependence of m). We can estimate σ_{ns} by observing that $f^4 = m^2 = 1$ in the bulk, that f^4 is small only over a distance on the order of ξ, and that m^2 is small only over a distance on the order of λ_L. This gives the approximate result

$$\sigma_{ns} \approx \frac{B_c^2}{2\mu_0}(\xi - \lambda_L), \tag{6.94}$$

where we have used Eq. (6.19). The value of the integral is the difference between the area under the two terms of the integrand, as shown plotted in Fig. 6.20. If $\xi > \lambda_L$, the surface tension is positive and we have Type I behavior. On the other hand, for $\xi < \lambda_L$, σ_{ns} is negative, and the superconductor is unstable with respect to the formation of a normal–superconducting interface, i.e., vortices form and Type II behavior appears.

We could also argue that λ_L is basically the width of an included vortex, i.e., the radius within which most of the flux is confined, and ξ is the distance over which the super electron density rises from $n_s = 0$ at the center of the vortex to its full bulk value, i.e., the distance needed to "heal the wound." A long coherence length ξ prevents the superconductor's n_s from rising quickly enough to provide the shielding current required to contain the flux, so no vortex can form.

Ginzburg and Landau (1950) showed that σ_{ns} vanishes for $\kappa = \lambda_L/\xi = 1/\sqrt{2}$, so as a convention we adopt the following criterion:

$$\begin{aligned} \kappa &< \frac{1}{\sqrt{2}} \qquad \text{Type I} \\ \kappa &> \frac{1}{\sqrt{2}} \qquad \text{Type II.} \end{aligned} \tag{6.95}$$

For Type II superconductors in very weak applied fields, $B_{app} \ll B_c$, the Meissner effect will be complete, but as B_{app} is increased above the lower critical field B_{c1}, where $B_{c1} < B_c$, vortices will begin to penetrate the sample. The magnetization of the sample then increases until the upper critical field B_{c2} is reached, at which point the vortex cores almost overlap and the bulk superconductivity is extinguished. Superconductivity may persist in a thin sheath up to an even higher critical field B_{c3}, where the sample goes completely normal.

XIII. UPPER CRITICAL FIELD B_{C2}

To calculate the upper critical field B_{c2} of a Type II superconductor we will examine the behavior of the normalized GL equation (6.87a) in the neighborhood of this field. For this case the order parameter is small and we can assume $B_{in} \approx B_{app}$. This suggests neglecting the nonlinear term f^3 in

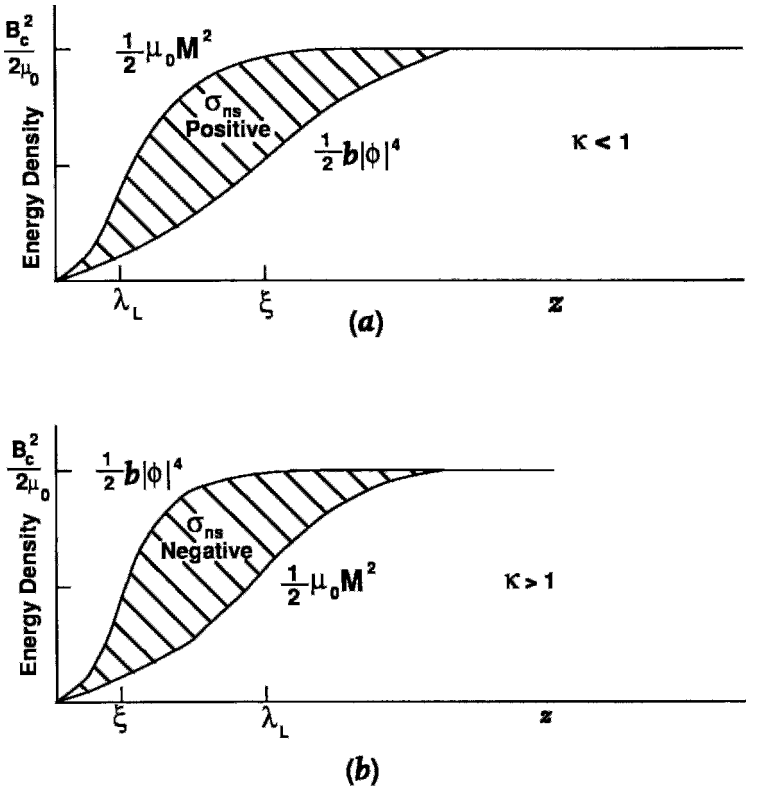

Figure 6.20 Order parameter $|\phi|$ and magnetization **M** inside a superconductor which is Type I ($\kappa < 1$, a) and inside a superconductor which is Type II ($\kappa > 1$, b), where $\kappa = \lambda_L/\xi$. The surface energy σ_{ns} is positive for the Type I case and negative for Type II.

Eq. (6.87a) and following Eq. (6.41), taking for the normalized vector potential

$$\mathscr{A} = b_0 u, \tag{6.96}$$

where u is a dimensionless Cartesian coordinate perpendicular to the directions of both the applied field and the vector potential. From Eq. (6.82) we have for the magnitude of b_0,

$$b_0 = \left(\frac{2\pi\xi^2}{\Phi_0}\right) B_{\text{app}}. \tag{6.97}$$

Deep inside the superconductor the normalized order parameter f is independent of position so that the term $\mathscr{A} \cdot \nabla f$ in the GL equation (6.87a) is zero.

The linearized GL equation now has the form

$$\nabla^2 f - \mathscr{A}^2 f + f = 0. \tag{6.98}$$

This equation has bounded solutions only for special values of b_0. By analogy with the harmonic-oscillator Schrödinger equation from quantum mechanics, we can take $f \approx e^{\alpha u/2}$, which on substitution in (6.98) gives $\alpha = 2 = b_0$. Solutions can be found for larger values of b_0, but these are not of physical interest. Identifying the upper critical field with the applied field of Eq. (6.97) for this solution, we have

$$B_{c2} = \frac{\Phi_0}{\pi\xi^2}. \tag{6.99}$$

This expression has an appealing physical explanation. If we assume that in the upper critical field the cores of the vortices are nearly touching and that the flux contained in each core is $\approx \Phi_0$, the average magnetic field is $B_{c2} \approx \Phi_0/\pi\xi^2$.

Obviously, the existence of an upper critical field requires that $B_{c2} > B_c$, the thermodynamic critical field. By Eq. (12.12) the ratio of B_{c2} to B_c is

$$\frac{B_{c2}}{B_c} = \sqrt{2}\,\kappa. \tag{6.100}$$

Therefore, for $\kappa < 1/\sqrt{2}$, $B_{c2} < B_c$ and no vortex state exists. In this way we can see that the condition for a superconductor to be Type II is $\kappa > 1/\sqrt{2}$.

XIV. STRUCTURE OF A VORTEX

For the case of a semi-infinite superconductor in a magnetic field it was found, by the arguments of Section VII, that the phase Θ of the order parameter remains fixed throughout the superconductor. Here we will consider a different geometry in which the phase of the order parameter is nontrivial.

In Type II superconductors it is observed that magnetic flux is completely excluded only for external fields $B < B_{c1}$. Above the lower-critical field, B_{c1}, flux penetrates in discrete flux quanta in the form of flux tubes, or vortices. In this section we will obtain approximate expressions for the fields associated with such a vortex, both in the core region and far outside the core. We assume that the external magnetic field B_{app} is applied along the z direction, parallel to the surface, and that currents flow at the surface, canceling the field inside. We are concerned with a vortex that is far enough inside the superconductor so that exponential decay of the external fields, as given by Eq. (6.50), drops essentially to zero.

States with more than one quantum of flux are also possible (Sachdev, 1992), but the energy scales as n^2, so single-flux quanta are energetically favored. This is because, according to Eq. (6.15), the parameter a scales as n, from Eq. (6.12) J scales as n, and from Eq. (6.11) B scales as n. Therefore n noninteracting vortices have n times the energy of a single vortex, but one multiquantum vortex has a magnetic energy $(nB)^2$, which scales as n^2.

A. Differential Equations

To treat this case we assume that there is no flux far inside the superconductor. If the applied field $B_{app} \approx B_{c1}$ a single quantum of flux Φ_0 enters in the form of a vortex with axis parallel to the applied field. The simplest assumption we could make about the shape of the vortex is to assume that it is cylindrically symmetric, so that in its vicinity the order parameter (6.81) has the form of Eq. (6.2), corresponding to

$$f(x, \Theta) = f(x)e^{i\Theta}, \tag{6.101}$$

where $(x, \Theta) = (\rho/\xi, \Theta)$ are normalized polar coordinates. The vector potential has the form $\mathbf{A} = A(x)\hat{\Theta}$, so that we can write for its normalized counterpart (6.82)

$$\mathcal{A}(x) = \mathcal{A}(x)\hat{\Theta}. \tag{6.102}$$

This is a two-dimensional problem since neither $f(x)$ nor $\mathcal{A}(x)$ have a z dependence. It is easy to show that $\boldsymbol{\nabla} \times \mathcal{A}$ has only a z component (this we do by working out the curl operation in cylindrical coordinates), which is to be expected, since the magnetic field $\mathbf{B} = \boldsymbol{\nabla} \times \mathbf{A}$ is known to be parallel to z.

If we substitute these functions in the two GL equations (6.84) and perform the Laplacian and double curl operations in cylindrical coordinates, we obtain

$$\left[\frac{1}{x}\frac{d}{dx}\left(x\frac{df}{dx}\right) - \frac{f}{x^2} + \left(\frac{2\mathcal{A}}{x}\right) f - \mathcal{A}^2 f\right] + f(1 - f^2) = 0, \tag{6.103}$$

$$\frac{d}{dx}\left[\frac{1}{x}\cdot\frac{d}{dx}(x\mathscr{A})\right] + \frac{1}{\kappa^2}f^2\left(\frac{1}{x}-\mathscr{A}\right)=0, \tag{6.104}$$

where $x=\rho/\xi$ and the current density equation (6.87b) becomes

$$j=f^2\left(\frac{1}{x}-\mathscr{A}\right)=0. \tag{6.105}$$

In constructing a solution to Eqs. (6.103) and (6.104) we must be guided by two requirements, first that the magnetic field and current density must be finite everywhere and, second, that the solution must have a finite free energy per unit length along the z-axis. If the free energy per unit length were infinite, the total free energy would diverge and render the solution unphysical. Further, we anticipate from the Meissner effect and Eqs. (6.50) and (6.52), that the magnetic field and the current density will decay exponentially far from the axis of the vortex.

B. Solutions for Short Distances

We seek to solve Eqs. (6.103) and (6.105) for the short-distance limit, namely in the core where $x<1$. Since the first term in Eq. (6.105) has the factor $1/x$, it is necessary for the order parameter f to vanish as $x\to 0$ in order for the current density to remain finite in the core. By symmetry and continuity, the current density must vanish on the axis of the vortex, and it is expected to be small everywhere in the core. Maxwell's equation, Eq. (6.11), tells us that in this situation the magnetic field **B** is approximately constant in the core and we can write

$$\mathbf{A}=\tfrac{1}{2}B_0\rho\hat{\Theta}, \tag{6.106}$$

or, in dimensionless units, with $x=\rho/\xi$

$$\mathscr{A}=\tfrac{1}{2}xb_0\hat{\Theta}, \tag{6.107}$$

recalling Eq. 6.82, and from Eq. (6.97),

$$b_0=\frac{2\pi\xi^2}{\Phi_0}B_0. \tag{6.108}$$

If we now use this approximate solution (6.107) for the vector potential in Eq. (6.103) and neglect the f^3 term because we expect $f\ll 1$ in the core, we will have

$$\frac{1}{x}\frac{d}{dx}\left(x\frac{df}{dx}\right) + \left[(b_0+1)-\tfrac{1}{4}b_0^2x^2-\frac{1}{x^2}\right]f=0. \tag{6.109}$$

This equation has exactly the form of Schrödinger's equation for the two-dimensional harmonic oscillator. We know from quantum mechanics texts (e.g., Pauling and Wilson, 1935, p. 105) that the constant term in the square brackets (b_0+1) is the eigenvalue, the coefficient of the x^{-2} term is the z component of the angular momentum, i.e., $m=1$, and, for the lowest eigenvalue, the coefficient of the x^2 term is related to the other two terms by the expression

$$(b_0+1)=2(m+1)(\tfrac{1}{4}b_0^2)^{1/2}. \tag{6.110}$$

Solving this for b_0 gives

$$b_0=1. \tag{6.111}$$

Substituting Eq. (6.111) in Eq. (6.108) gives the magnetic field on the axis of the vortex:

$$B_0=\frac{\Phi_0}{2\pi\xi^2}. \tag{6.112}$$

The solution to the 'Schrödinger' equation, Eq. (6.109), is

$$f=Cxe^{-x^2/4}, \tag{6.113}$$

where C is a constant. This function reaches its maximum at $x=\sqrt{2}$, which is outside the

core, so, to a first approximation, f continuously increases in magnitude with increasing radial distance throughout the core region. This behavior is shown by the dashed curve in and near the core region of Fig. 6.21.

We can use the results of Problem 8 to obtain a better approximation to the vector potential and magnetic field in the core region,

$$\mathbf{A}(\rho) = \tfrac{1}{2}B_0\left[\rho - \alpha\left(\frac{\rho^3}{\xi^2}\right)\right]\hat{\Theta}, \quad (6.114)$$

$$\mathbf{B}(\rho) = B_0\left[1 - 3\alpha\left(\frac{\rho}{\xi}\right)^2\right]\hat{\mathrm{k}}, \quad (6.115)$$

where $\alpha \ll 1$. These expressions are plotted as dashed curves in the core regions of Figs. 6.22 and 6.23, respectively.

C. Solution for Large Distances

To obtain a solution far from the vortex core, $x \gg 1$, it is convenient to simplify Eqs. (6.103) to (6.105) by means of a change of variable,

$$\mathscr{A}' = \mathscr{A} - \frac{1}{x}, \quad (6.116)$$

which gives

$$\frac{d^2f}{dx^2} + \frac{1}{x}\cdot\frac{df}{dx} - \mathscr{A}'^2 f + f(1-f^2) = 0. \quad (6.117)$$

$$\frac{d^2\mathscr{A}'}{dx^2} + \frac{1}{x}\cdot\frac{d\mathscr{A}'}{dx} - \frac{\mathscr{A}'}{x^2} - \frac{f^2\mathscr{A}'}{\kappa^2} = 0, \quad (6.118)$$

$$j = -f^2\mathscr{A}', \quad (6.119)$$

where the derivatives have been multiplied out. It should be pointed out that the curl of $(1/x)\hat{\Theta}$ vanishes in the region under consideration, so that $\nabla \times \mathscr{A}' = \nabla \times \mathscr{A}$, and hence

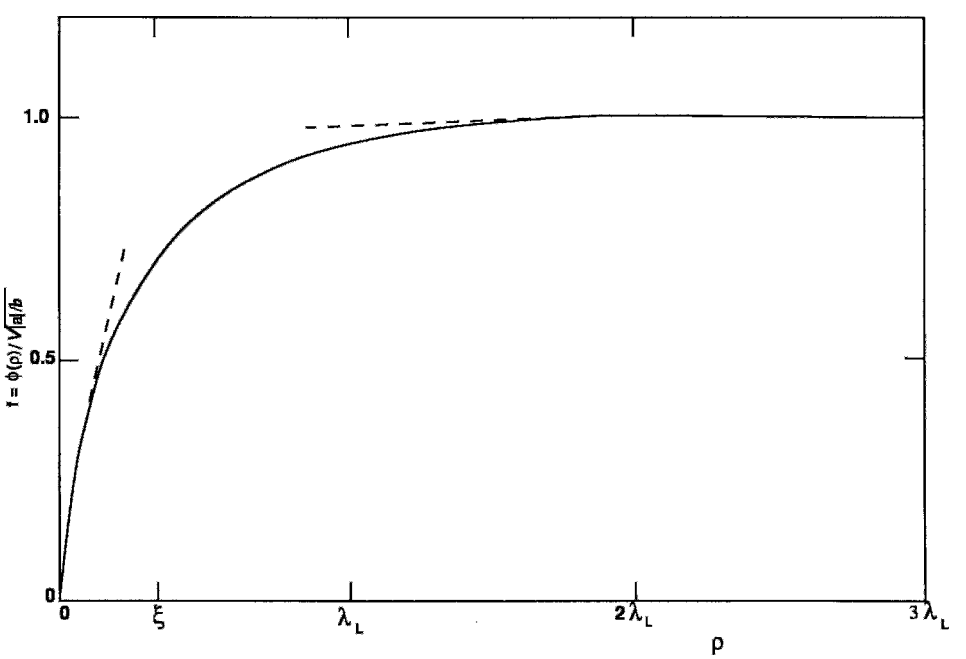

Figure 6.21 Dependence of the order parameter $|\phi|$ on distance ρ from the core of a vortex. The asymptotic behaviors near the core and far from the core are indicated by dashed lines.

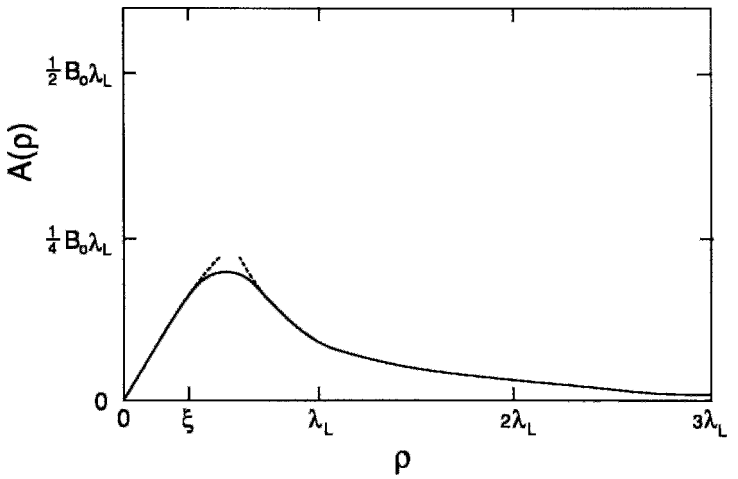

Figure 6.22 Distance dependence of the vector potential $\mathbf{A}(\rho)$ associated with a vortex in the notation of Fig. 6.21.

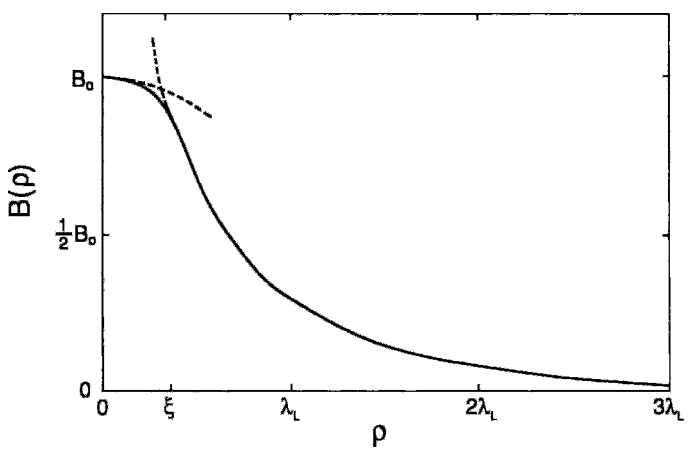

Figure 6.23 Distance dependence of the magnetic field $\mathbf{B}(\rho)$ encircling a vortex in the notation of Fig. 6.21.

the $1/x$ term of Eq. (6.116) does not contribute to the magnetic field (see, however, Problem 9).

For the approximation $f \approx 1$, the change of variable $x = \kappa y$ puts Eq. (6.118) into the form of a first-order ($n = 1$) modified Bessel equation:

$$y^2 \frac{d^2\mathscr{A}'}{dy^2} + y\frac{d\mathscr{A}'}{dy} - (y^2+1)\mathscr{A}' = 0. \tag{6.120}$$

The solution to this equation which satisfies the boundary conditions $\mathscr{A}'(y) \to 0$ as $y \to \infty$ is

$$\mathscr{A}'(y) = A'_\infty K_1(y), \tag{6.121}$$

where $K_1(y)$ is a modified first-order Bessel function. For large distances, $x \gg \kappa$, it has the asymptotic form

$$\mathscr{A}'(x) = A_\infty \frac{e^{-x/\kappa}}{\sqrt{x}}, \tag{6.122}$$

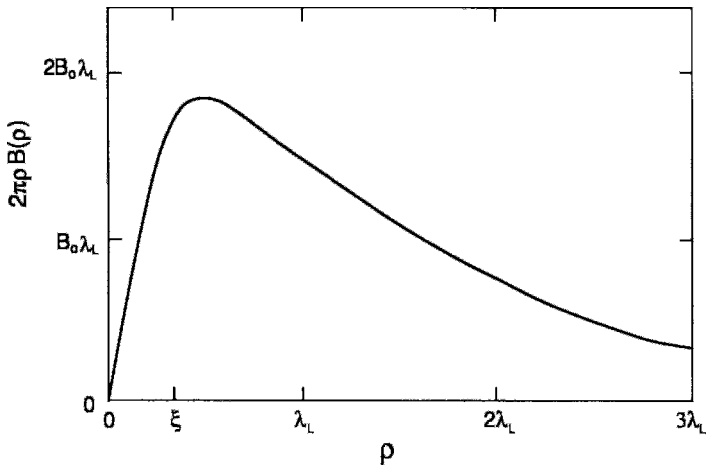

Figure 6.24 Distance dependence of the function $2\pi\rho\mathbf{B}(\rho)$ in the notation of Fig. 5.21. This function is proportional to the amount of magnetic flux at a distance ρ from the origin, and the integrated area under the curve is one fluxoid, $h/2e$.

where $A'_\infty = (2/\pi\kappa)^{1/2}A_\infty$. Figure 6.22 shows the asymptotic long-distance behavior of $A(\rho)$.

Taking the curl $\mathbf{B} = \boldsymbol{\nabla} \times \mathbf{A}$ in cylindrical coordinates (cf. Eq. (6.86)) provides the corresponding magnetic field for $x \gg \kappa$,

$$B_z(\rho) \approx \frac{e^{-\rho/\lambda_L}}{(\rho/\xi)^{1/2}} \qquad \rho \gg \lambda_L, \quad (6.123)$$

where we have restored the original coordinate $\rho = x\xi = y\lambda_L$. Figure 6.23 shows a plot of $B_z(\rho)$ versus ρ for large ρ and indicates the $\rho = 0$ value of Eq. (6.115).

To find the radial dependence of the order parameter far from the core, where the material is in the superconducting state, we have $f \approx 1$, so we can write

$$f(x) = 1 - g(x), \quad (6.124)$$

where $g(x) \ll 1$, and hence $f(1 - f^2) \approx 2g$ As a result Eq. (6.117) assumes the form

$$\frac{d^2}{dx^2}g(x) + \frac{1}{x}\cdot\frac{d}{dx}g(x) + \mathscr{A}' - 2g(x) = 0. \quad (6.125)$$

Far from the core, $x \gg \kappa$, the behavior of $g(x)$ for $\kappa \gg 1$ is determined by that of $\mathscr{A}'(x)$, and we have

$$g(x) \approx g_\infty \frac{e^{-2x/\kappa}}{x}, \quad (6.126)$$

where g_∞ is positive.

Comparing Figs. 6.22 and 6.23 we see that A increases in the core region, reaches a maximum near the inflection point of the B curve, and decreases outside the core. The quantity $2\pi\rho\mathbf{B}(\rho)$ is proportional to the amount of magnetic flux at a particular distance from the vortex axis; it is shown plotted against ρ in Fig. 6.24. The integrated area under this curve equals one fluxoid, $h/2e$.

FURTHER READING

The GL theory was first proposed by Ginzburg and Landau in 1950. Its value became more apparent after Gor'kov (1959) showed that it is a limiting case of the BCS theory. The theory was extended to the limit of high κ by Abrikosov (1957) in the same year that the BCS theory was proposed. The London and London (1935), London (1950), and related Pippard (1953) equations follow from the GL theory.

The first edition of this book mentions some articles that apply GL theory to the cuprate super conductors.

PROBLEMS

1. Derive the first GL equation, Eq. (6.6), from the Gibbs free energy integral (6.4).
2. Show that minimizing the term $B^2/2\mu_0$ with respect to the vector potential $\mathbf{A}$ in Eq. (6.4) gives the expression $\boldsymbol{\nabla}^2\mathbf{A}/\mu_0$ that is found in Eq. (6.10). Hint: write

$$\frac{\partial}{\partial A_n(x)}\left[\epsilon_{ijk}\epsilon_{ilm}\int \partial_j A_k(y)\partial_l A_m(y)d^2y\right],$$

bring the partial differentiation inside the integral, and integrate by parts.
3. Show that $f(\eta) = \coth(\eta/\sqrt{2})$ is also a solution to Eq. (6.27), and explain why it is not used.
4. Show that Eq. (6.17) is consistent with Eq. (2.69) in the superconducting region near T_c, and express the ratio a_0/b_0 in terms of the density n of conduction electrons.
5. Derive Eqs. (6.71a) and (6.71b).
6. Justify Eq. (6.97): $b_0 = (2\pi\xi^2/\Phi_0)B_{\text{app}}$.
7. Show that $\boldsymbol{\nabla}\times(\boldsymbol{\nabla}\times\mathbf{A}) = -\boldsymbol{\nabla}^2\mathbf{A}$ in Cartesian coordinates, assuming the London-Landau gauge. Why is this not true when the coordinate system is non-Cartesian?
8. Assume the following power series solutions to Eqs. (6.103) and (6.104) in the region of the core:

$$f(x) \approx \Sigma a_n x^n \qquad x \ll 1,$$
$$f(x) \approx \Sigma f_n x^n \qquad x \ll 1.$$

   (a) Show that the lowest-order terms that exist are f_1 and a_1, that the even order terms vanish, and that

$$a_3 = -\frac{f_1^2}{8\kappa^2},$$
$$f_3 = -\tfrac{1}{4}(a_1 + \tfrac{1}{2})f_1.$$

   (b) Show that the distance dependence of the order parameter, vector potential, magnetic field, and current density in the neighborhood of the origin are given by

$$|\phi(\rho)| \approx \left(\frac{|a|}{b}\right)^{1/2} \times\left[f_1\left(\frac{\rho}{\xi}\right) - |f_3|\left(\frac{\rho}{\xi}\right)^3\right] \quad \rho \ll \xi,$$
$$A_\phi(\rho) \approx \left(\frac{\Phi_0}{2\pi\xi}\right) \times\left[a_1\left(\frac{\rho}{\xi}\right) - |a_3|\left(\frac{\rho}{\xi}\right)^3\right] \quad \rho \ll \xi,$$
$$B_z(\rho) \approx \left(\frac{\Phi_0}{\pi\xi^2}\right) \times\left[a_1 - 2|a_3|\left(\frac{\rho}{\xi}\right)^2\right] \quad \rho \ll \xi.$$

   (c) Show that the expression for $|\phi(\rho)|$ agrees with Eq. (6.113).
9. Show that $\oint \mathscr{A}' \cdot d\mathbf{l} = 0$, whereas $\oint \mathscr{A} \cdot d\mathbf{l} = 2\pi$ for contours at infinity. What is the significance of the $1/x$ term in Eq. (6.116)?
10. Show that the dimensionless magnetization m defined by Eq. (6.125) can be written

$$m = \frac{M}{H_c},$$

and has the distance dependence

$$m = -(1 - e^{-z/\lambda_L}).$$

in Eq. (6.93) (assume zero demagnetization factor).
11. Derive Eq. (6.123) for the magnetic field far from a vortex. Find the first higher-order term that is neglected in writing out this expression.

This page intentionally left blank

7

BCS Theory

I. INTRODUCTION

Chapter 6 presents the Ginzburg–Landau (GL) theory, which originated in 1950. Despite the fact that it is a phenomenological theory, it has had surprising success in explaining many of the principal properties of superconductors. Nevertheless, it has limitations because it does not explain the microscopic origins of super-conductivity. In 1957 Bardeen, Cooper, and Schrieffer (BCS) proposed a microscopic theory of superconductivity that predicts quantitatively many of the properties of elemental superconductors. In addition, the Landau–Ginzburg theory can be derived from the BCS theory, with the added bonus that the charge and mass of the "particle" involved in the superconducting state emerge naturally as $2e$ and $2m_e$, respectively.

With the discovery of the heavy fermion and copper-oxide superconductors it is no longer clear whether the BCS theory is satisfactory for all classes of superconductors. The question remains open, although there is no doubt that many of the properties of high-temperature superconductors are consistent with the BCS formalism.

To derive the BCS theory it is necessary to use mathematics that is more advanced than that which is employed elsewhere in this book, and the reader is referred to standard quantum mechanics texts for the details of the associated derivations. If the chapter is given a cursory initial reading without working out the intermediate steps in the development, an overall picture of BCS can be obtained. For didactic purposes we will end the chapter by describing the simplified case of a square well electron–electron interaction

potential, which is also the case treated in the original formulation of the theory.

II. COOPER PAIRS

One year before publication of the BCS theory, Cooper (1956) demonstrated that the normal ground state of an electron gas is unstable with respect to the formation of "bound" electron pairs. We have used quotation marks here because these electron pairs are not bound in the ordinary sense, and the presence of the filled Fermi sea is essential for this state to exist. Therefore this is properly a many-electron state.

In the normal ground state all one-electron orbitals with momenta $k < k_F$ are occupied, and all the rest are empty. Now, following Cooper, let us suppose that a weak attractive interaction exists between the electrons. The effect of the interaction will be to scatter electrons from states with initial momenta (k_1, k_2) to states with momenta (k_1', k_2'). Since all states below the Fermi surface are occupied, the final momenta (k_1', k_2') must be above k_F. Clearly, these scattering processes tend to increase the kinetic energy of the system. However, as we shall now see, the increase in kinetic energy is more than compensated by a decrease in the potential energy if we allow states above k_F to be occupied in the many-electron ground state.

We begin by considering the Schrödinger equation for two electrons interacting via the potential V,

$$\left[-\frac{\hbar^2}{2m}(\nabla_1^2+\nabla_2^2)+V(r_1-r_2)\right]\Psi(r_1,r_2) = (E+2E_F)\Psi(r_1,r_2). \tag{7.1}$$

In (7.1) the spin part of the wavefunction has been factored out and the energy. eigenvalue E is defined relative to the Fermi level $(2E_F)$. Most superconductors are spin-singlet so the orbital part to the wavefunction, $\Psi(r_1, r_2)$, must be symmetric.

As with any two-body problem, we begin by defining the center of mass coordinate,

$$R = \tfrac{1}{2}(r_1 + r_2), \tag{7.2}$$

and the relative coordinate,

$$r = r_1 - r_2. \tag{7.3}$$

In terms of these coordinates (7.1) becomes

$$\left[-\frac{\hbar^2}{4m}\nabla_R^2 - 2\frac{\hbar^2}{2m}\nabla_r^2\right]\Psi(R,r) + V(r)\Psi(R,r) = (E+2E_F)\Psi(R,r). \tag{7.4}$$

The center of mass and relative coordinates now separate and we can write

$$\Psi(R,r) = \Phi(R)\Psi(r). \tag{7.5}$$

$\Phi(R)$ is simply a plane wave,

$$\Phi(R) = e^{iK\cdot R}, \tag{7.6}$$

while for the relative coordinate wavefunction $\Psi(r)$ we have

$$\left[-2\frac{\hbar^2}{2m}\nabla_r^2 + V(r)\right]\Psi(r) = \left(E+2E_F-\frac{\hbar^2K^2}{4m}\right)\Psi(r). \tag{7.7}$$

Since we are interested in the ground state, we can set $K = 0$. There are solutions for $K \neq 0$ that lie close to the $K = 0$ states and are needed to describe states in which a persistent current flows.

We now express $\Psi(r)$ as a sum over states with momenta $p > k_F$,

$$\Psi(r) = \frac{1}{\sqrt{V}}\sum_p{}' a(p)e^{ip\cdot r}. \tag{7.8}$$

In (7.8) Σ_p' denotes a summation over all $|p| > k_F$. Substitution of the expression for

$\Psi(r)$ from (7.8) in (7.7) then gives the Schrödinger equation in momentum space,

$$[2(\mathscr{E}_p - E_F) - E]a(p) + \sum_{p'} V(p, p')a(p') = 0, \quad (7.9)$$

where

$$V(p, p') = \frac{1}{V}\int d^3 r e^{-i(p-p')\cdot r} V(r). \quad (7.10)$$

In order to simplify the solution of (7.9) we assume that

$$V(p, p') = \begin{cases} -V_0 & 0 \le \mathscr{E}_p - E_F \le \hbar\ \omega_D \\ & \text{and } 0 \le \mathscr{E}_{p'} - E_F \le \hbar\ \omega_D \\ 0 & \text{otherwise.} \end{cases} \quad (7.11)$$

In (7.11), $\hbar\omega_D$ is a typical phonon energy, which reflects the idea that attraction between electrons arises via exchange of virtual phonons.

With the potential (7.11) the interaction term in (7.9) becomes

$$\sum_{p'}{}' V(p, p')a(p') = -V_0 K \Theta(\hbar\omega_D - E_F - \mathscr{E}_p), \quad (7.12)$$

where $\Theta(x)$ is the ordinary step function and

$$K = \sum_p{}' a(p) \quad (7.13)$$

is a constant. Solving (7.9) for $a(p)$, we have

$$a(p) = \frac{V_0 K}{2(\mathscr{E}_p - E_F) - E} \times \Theta(\hbar\omega_D - E_F - \mathscr{E}_p). \quad (7.14)$$

Note that our Cooper pair involves momenta only in the narrow region $\mathscr{E}_p - E_F \le \hbar\ \omega_D$ just above the Fermi surface.

We can now self-consistently evaluate the constant K in (7.13),

$$K = V_0 K \sum_p{}' \frac{1}{2(\mathscr{E}_p - E_F) - E} \times \Theta(\hbar\ \omega_D - E_F - \mathscr{E}_p). \quad (7.15)$$

If we assume that $K \neq 0$, this leads to an implicit equation for the eigenvalue E,

$$1 = V_0 \sum_p{}' \frac{1}{2(\mathscr{E}_p - E_F) - E} \times \Theta(\hbar\omega_D - E_F - \mathscr{E}_p). \quad (7.16)$$

The sum over the momenta can be expressed as an integral over the energies in terms of the density of states $D(\mathscr{E})$. Since typically $\hbar\ \omega_D \ll E_F$, $D(\mathscr{E})$ is well approximated inside the integral by its value at the Fermi surface, $D(E_F)$. Thus we have

$$1 = V_0 D(E_F)\int_{E_F}^{E_F + \hbar\ \omega_p} \frac{1}{2(\mathscr{E} - E_F) - E} d\mathscr{E} = \tfrac{1}{2} V_0 D(E_F) \ln\left(\frac{E - 2\hbar\omega_D}{E}\right). \quad (7.17)$$

Solving for E we have

$$E = -\frac{2\hbar\omega_D}{\exp[2/V_0 D(E_F)] - 1}. \quad (7.18)$$

In the weak-coupling limit $V_0 D(E_F) \ll 1$ and the exponential dominates the denominator in (7.18) so that

$$E \approx -2\hbar\omega_D \exp\left(-\frac{2}{V_0 D(E_F)}\right). \quad (7.19)$$

This result is remarkable in several ways. First, it tells us that the pair state we have constructed will always have a lower energy than the normal ground state no matter how small the interaction V_0. This is why we say the normal ground state is unstable with respect to the formation of Cooper pairs. Second, we see in (7.18) a hierarchy of very different energy scales,

$$E_F \gg \hbar\omega_D \gg |E|, \quad (7.20)$$

which, if we assume that $k_B T_c \cong |E|$, explains why the superconducting transition temperature is so small compared with the Debye temperature,

$$\theta_D = \frac{\hbar\omega_D}{k_B}.$$

If one Cooper pair lowers the ground state by $-|E|$, then, clearly many pairs will lower the energy even further, and one might be tempted to conclude that all the electrons should pair up in this fashion. Such a state would then resemble a Bose–Einstein condensate of Cooper pairs. However, we must keep in mind that if we do away entirely with the normal Fermi sea the state we have constructed collapses. We can use these intuitive ideas to guide our thinking, but to arrive at the true BCS ground state we must go beyond simple one- and even two-electron pictures and realize that the superconducting state is a highly correlated many-electron state.

III. THE BCS ORDER PARAMETER

In this section and those that follow we will present the formal details of the BCS theory. The most natural mathematical language to use in this case is "second quantization", where all observables are expressed in terms of the electron operators $a_{n\sigma}(\mathbf{k})$, and their Hermitian conjugates. The operator $a_{n\sigma}(\mathbf{k})$ annihilates an electron with band index n, z-component of the spin σ and Bloch wavevector $\mathbf{k}$. The electron operators have the anticommutation relations,

$$\begin{aligned}\left\{a_{n\sigma}(\mathbf{k}), a^\dagger_{m\tau}(\mathbf{k}')\right\} &= \delta_{nm}\delta_{\sigma\tau}\delta(\mathbf{k},\mathbf{k}')\\ \{a_{n\sigma}(\mathbf{k}), a_{m\tau}(\mathbf{k}')\} &= 0\end{aligned} \qquad (7.21)$$

In order to reduce the complexity of the equations we will encounter, the band index, n, and the spin index, σ, will be combined into a single discrete index, $(\sigma, n) \to \sigma$.

As in any theory of a phase transition the first task is to identify the "order parameter", which vanishes in the high temperature, disordered phase and is non-zero in the low temperature, ordered phase. We have seen that the normal ground state is unstable with respect to the formation of "Cooper pairs" if there is an attractive interaction between electrons at the Fermi surface. This leads us to consider the BCS order parameter

$$\Psi_{\alpha\beta}(\mathbf{k}_1, \mathbf{k}_2) = \langle a_\alpha(\mathbf{k}_1) a_\beta(\mathbf{k}_2)\rangle \qquad (7.22a)$$

The BCS order parameter is in general a two-by two complex matrix. We will find it useful to define the Hermitian conjugate of the order parameter,

$$\Psi_{\alpha\beta}(\mathbf{k}_1, \mathbf{k}_2)^* = \langle a^\dagger_\alpha(\mathbf{k}_2) a^\dagger_\alpha(\mathbf{k}_1)\rangle \qquad (7.22b)$$

It is easy to see that the order parameter vanishes in the normal state. The average in (7.22a) is

$$\begin{aligned}&\langle a_\alpha(\mathbf{k}_1) a_\beta(\mathbf{k}_2)\rangle\\ &\quad = Z^{-1} Tr\left[e^{-\beta H} a_\alpha(\mathbf{k}_1)\alpha_\beta(\mathbf{k}_2)\right]\end{aligned} \qquad (7.23)$$

where $\beta = 1/k_B T$, H is the Hamiltonian for the normal state, and Z is the partition function. This Hamiltonian is invariant under the (unitary) global gauge transformation,

$$U^\dagger(\varphi) a_\alpha(\mathbf{k}) U(\varphi) = e^{-i\varphi} a_\alpha(\mathbf{k}) \qquad (7.24a)$$

$$U^\dagger(\varphi) H U(\varphi) = H \qquad (7.24b)$$

If we apply this transformation inside the trace in (7.23), we have

$$\begin{aligned}&\langle a_\alpha(\mathbf{k}_1) a_\beta(\mathbf{k}_2)\rangle\\ &\quad = Z^{-1} Tr[U(\varphi)U^\dagger(\varphi) e^{-\beta H} a_\alpha(\mathbf{k}_1) a_\beta(\mathbf{k}_2)]\\ &\quad = Z^{-1} Tr[U^\dagger(\varphi) e^{-\beta H} U(\varphi) U^\dagger(\varphi) a_\alpha(\mathbf{k}_1)\\ &\qquad \times U(\varphi) U^\dagger(\varphi) a_\beta(\mathbf{k}_2) U(\varphi)]\\ &\quad = e^{-2i\varphi}\langle a_\alpha(\mathbf{k}_1) a_\beta(\mathbf{k}_2)\rangle\end{aligned} \qquad (7.25)$$

In the first and second lines of (7.25) we have used the fact that $U(\varphi)U^{\dagger}(\varphi) = 1$, and in the second line we have also used the cyclic property of the trace, $Tr[ABC] = Tr[BCA]$. Since φ is an arbitrary phase angle, the only possible solution to (7.25) is that $\langle a_{\alpha}(\mathbf{k}_1)a_{\beta}(\mathbf{k}_2)\rangle = 0$, as expected in the normal state.

If the order parameter is to be different from zero, it is clear from the above argument that the statistical operator cannot be invariant under a global gauge transformation. In the general theory of phase transitions this is called *spontaneous symmetry breaking*: the statistical operator has a lower symmetry in the ordered state than in the normal, or disordered, state. In the case of a ferromagnet, the normal state is rotationally invariant and the thermal average of the magnetization, which is a vector, vanishes. Below the Curie temperature, however, there is a spontaneous magnetization that clearly breaks the rotational symmetry of the high temperature phase. The phenomenon of superconductivity is characterized by the breaking of global gauge symmetry.

The normal state may exhibit other symmetries that are characteristic of the crystal structure of the solid. If the superconducting state breaks one of the symmetries of the normal state in addition to global gauge symmetry then we say the superconductor is "unconventional". For example, in "p-wave" superconductors, the order parameter has a vector character much like the magnetization in a ferromagnet. We will assume that the translational symmetry of the superconducting phase is the same as that of the normal state. Under a translation by a lattice vector $\mathbf{R}$ the electron operator transforms as

$$T^{\dagger}(\mathbf{R})a_{\alpha}(\mathbf{k})T(\mathbf{R}) = e^{i\mathbf{k}\cdot\mathbf{R}}a_{\alpha}(\mathbf{k}) \qquad (7.26)$$

Assuming the statistical operator for the superconducting state is invariant under translations, it follows, (by an argument very much like the preceding one) that

$$\Psi_{\alpha\beta}(\mathbf{k}_1, \mathbf{k}_2) = e^{i(\mathbf{k}_1+\mathbf{k}_2).\mathbf{R}}\Psi_{\alpha\beta}(\mathbf{k}_1, \mathbf{k}_2) \quad (7.27)$$

From this we conclude that the order parameter vanishes unless $\mathbf{k}_1 = -\mathbf{k}_2$. We can use this fact to simplify things somewhat and define an order parameter that is a function of only one wavevector,

$$\Psi_{\alpha\beta}(\mathbf{k}) \equiv \Psi_{\alpha\beta}(\mathbf{k}, -\mathbf{k}) \qquad (7.28)$$

Finally, the anticommutation relations, (7.21), imply that the order parameter is antisymmetric under exchange of all its arguments,

$$\Psi_{\alpha\beta}(\mathbf{k}_1, \mathbf{k}_2) = -\Psi_{\beta\alpha}(\mathbf{k}_2, \mathbf{k}_1) \qquad (7.29a)$$

or, in the case of translational invariance,

$$\Psi_{\alpha\beta}(\mathbf{k}) \equiv -\Psi_{\beta\alpha}(-\mathbf{k}) \qquad (7.29b)$$

If the electron spin commutes with the normal state statistical operator (no spin-orbit interaction), then the order parameter must transform either as a spin singlet or a spin triplet. In the singlet case, which is the most common, we can write

$$\Psi_{\alpha\beta}(\mathbf{k}) = \varepsilon_{\alpha\beta}\psi(\mathbf{k}) \qquad (7.30)$$

where $\varepsilon_{\alpha\beta} = -\varepsilon_{\beta\alpha}$ and $\psi(\mathbf{k}) = \psi(-\mathbf{k})$. In the triplet case we have

$$\Psi_{\alpha\beta}(\mathbf{k}) = \begin{pmatrix} -[\psi_1(\mathbf{k}) + i\psi_2(\mathbf{k})]/\sqrt{2} & \psi_3(\mathbf{k}) \\ \Psi_3(\mathbf{k}) & [\psi_1(\mathbf{k}) - i\psi_2(\mathbf{k})]/\sqrt{2} \end{pmatrix} \qquad (7.31)$$

where the three spatial components of the order parameter, $(\psi_1(\mathbf{k}), \psi_2(\mathbf{k}), \psi_3(\mathbf{k}))$ are odd functions of the wavevector,

$$\psi_i(\mathbf{k}) = -\psi_i(-\mathbf{k}) \qquad (7.32)$$

The three components of the triplet order parameter defined by (7.31) transform under

rotations in spin-space as a vector, and clearly break the invariance of the normal state under such rotations. Therefore, the triplet order parameter is unconventional, and the singlet is conventional.

IV. THE BCS HAMILTONIAN

We have argued that in order for the order parameter to differ from zero the statistical operator must break global gauge symmetry. The simplest way to construct such a statistical operator is to assume the order parameter is not zero and that the fluctuations about the order parameter are small. Thus we write

$$\begin{aligned} a_\alpha(\mathbf{k}_1)a_\beta(\mathbf{k}_2) = &\langle a_\alpha(\mathbf{k}_1)a_\beta(\mathbf{k}_2)\rangle \\ &+ [a_\alpha(\mathbf{k}_1)a_\beta(\mathbf{k}_2) \\ &- \langle a_\alpha(\mathbf{k}_1)a_\beta(\mathbf{k}_2)\rangle] \end{aligned} \tag{7.33}$$

in the Hamiltonian, and expand in powers of the fluctuation.

We begin with a Hamiltonian that includes the one-electron band structure and a two-body interaction between electrons,

$$\begin{aligned} H = &\sum_{\sigma,\mathbf{k}} E_\sigma(\mathbf{k})a^\dagger_\sigma(\mathbf{k})a_\sigma(\mathbf{k}) \\ &+ \frac{1}{2}\sum_{\{\mathbf{k}_1,\mathbf{k}_2,\mathbf{k}_3,\mathbf{k}_4\}} a^\dagger_\alpha(\mathbf{k}_1)a^\dagger_\beta(\mathbf{k}_2) \\ &\times V_{\alpha\beta\gamma\delta}(\mathbf{k}_1,\mathbf{k}_2;\mathbf{k}_3,\mathbf{k}_4)\alpha_\gamma(\mathbf{k}_3)a_\delta(\mathbf{k}_4) \end{aligned} \tag{7.34}$$

Under translation by a lattice vector the interaction transforms as

$$\begin{aligned} V_{\alpha\beta\gamma\delta}(\mathbf{k}_1,\mathbf{k}_2;\mathbf{k}_3,\mathbf{k}_4) = &e^{-i(\mathbf{k}_1+\mathbf{k}_2-\mathbf{k}_3-\mathbf{k}_4)\cdot\mathbf{R}} \\ &\times V_{\alpha\beta\gamma\delta}(\mathbf{k}_1,\mathbf{k}_2;\mathbf{k}_3,\mathbf{k}_4) \end{aligned} \tag{7.35}$$

which requires $\mathbf{k}_1+\mathbf{k}_2-\mathbf{k}_3-\mathbf{k}_4=\mathbf{G}$, where $\mathbf{G}$ is a reciprocal lattice vector.

If we now insert the expansion, (7.33), into the interaction term in (7.34) and keep only terms first order in the fluctuations, we have

$$\begin{aligned} &\sum_{\{\mathbf{k}_1,\mathbf{k}_2,\mathbf{k}_3,\mathbf{k}_4\}} a^\dagger_\alpha(\mathbf{k}_1)a^\dagger_\beta(\mathbf{k}_2)V_{\alpha\beta\gamma\delta}(\mathbf{k}_1,\mathbf{k}_2;\mathbf{k}_3,\mathbf{k}_4)a_\gamma(\mathbf{k}_3) \\ &\times a_\delta(\mathbf{k}_4) = \sum_{\{\mathbf{k}_1,\mathbf{k}_2,\mathbf{k}_3,\mathbf{k}_4\}} \{\langle a^\dagger_\alpha(\mathbf{k}_1)a^\dagger_\beta(\mathbf{k}_2)\rangle \\ &+ [a_\alpha(\mathbf{k}_1)a_\beta(\mathbf{k}_2) - \langle a^\dagger_\alpha(\mathbf{k}_1)a^\dagger_\beta(\mathbf{k}_2)\rangle]\} \\ &\times V_{\alpha\beta\gamma\delta}(\mathbf{k}_1,\mathbf{k}_2;\mathbf{k}_3,\mathbf{k}_4)\{\langle a_\gamma(\mathbf{k}_3)a_\delta(\mathbf{k}_4)\rangle \\ &+ [a_\gamma(\mathbf{k}_3)a_\delta(\mathbf{k}_4) - \langle a_\gamma(\mathbf{k}_3)a_\delta(\mathbf{k}_4)\rangle]\} \\ &\approx -\sum_{\{\mathbf{k}_1,\mathbf{k}_2,\mathbf{k}_3,\mathbf{k}_4\}} \langle a^\dagger_\alpha(\mathbf{k}_1)a^\dagger_\beta(\mathbf{k}_2)\rangle V_{\alpha\beta\gamma\delta}(\mathbf{k}_1,\mathbf{k}_2;\mathbf{k}_3,\mathbf{k}_4) \\ &\times \langle a_\gamma(\mathbf{k}_3)a_\delta(\mathbf{k}_4)\rangle + \sum_{\{\mathbf{k}_1,\mathbf{k}_2,\mathbf{k}_3,\mathbf{k}_4\}} \langle a^\dagger_\alpha(\mathbf{k}_1)a^\dagger_\beta(\mathbf{k}_2)\rangle \\ &\times V_{\alpha\beta\gamma\delta}(\mathbf{k}_1,\mathbf{k}_2;\mathbf{k}_3,\mathbf{k}_4)a_\gamma(\mathbf{k}_3)a_\delta(\mathbf{k}_4) \\ &+ \sum_{\{\mathbf{k}_1,\mathbf{k}_2,\mathbf{k}_3,\mathbf{k}_4\}} a^\dagger_\alpha(\mathbf{k}_1)a^\dagger_\beta(\mathbf{k}_2)V_{\alpha\beta\gamma\delta}(\mathbf{k}_1,\mathbf{k}_2;\mathbf{k}_3,\mathbf{k}_4) \\ &\times \langle a_\gamma(\mathbf{k}_3)a_\delta(\mathbf{k}_4)\rangle \end{aligned} \tag{7.36}$$

We now use the definition of the order parameter, (7.25) and (7.35) to get

$$\begin{aligned} H_{BCS} = &\frac{1}{2}\sum_{\mathbf{k}\mathbf{k}'} \Psi^*_{\alpha\beta}(\mathbf{k})V_{\alpha\beta;\gamma\delta}(\mathbf{k};\mathbf{k}')\Psi_{\gamma\delta}(\mathbf{k}') \\ &+ \sum_{\sigma,\mathbf{k}} E_\sigma(\mathbf{k})a^\dagger_\sigma(\mathbf{k})a_\sigma(\mathbf{k}) + \\ &- \frac{1}{2}\sum_{\mathbf{k}\mathbf{k}'} \Psi^*_{\alpha\beta}(\mathbf{k})V_{\alpha\beta;\gamma\delta}(\mathbf{k};\mathbf{k}')a_\gamma(\mathbf{k}')a_\delta(-\mathbf{k}') \\ &+ \frac{1}{2}\sum_{\mathbf{k}\mathbf{k}'} a^\dagger_\alpha(\mathbf{k})a^\dagger_\beta(-\mathbf{k})V_{\alpha\beta;\gamma\delta}(\mathbf{k};\mathbf{k}')\Psi_{\gamma\delta}(\mathbf{k}') \end{aligned} \tag{7.37}$$

where we've introduced the shorthand $V_{\alpha\beta;\gamma\delta}(\mathbf{k};\mathbf{k}') \equiv V_{\alpha\beta;\gamma\delta}(\mathbf{k},-\mathbf{k};\mathbf{k}',-\mathbf{k}')$.

The leading term in (7.37) is just a complex number, the next term is the normal state one-electron band structure, and the final two terms are new.

The BCS Hamiltonian can be simplified even further if we define the *gap function*,

$$\Delta_{\alpha\beta}(\mathbf{k}) = \sum_{\mathbf{k}'} V_{\alpha\beta\gamma\delta}(\mathbf{k};\mathbf{k}')\Psi_{\gamma\delta}(\mathbf{k}') \tag{7.38}$$

so that (7.37) now becomes

$$H_{BCS} = \frac{1}{2}\sum_{\mathbf{k}\mathbf{k}'} \Psi^*_{\alpha\beta}(\mathbf{k}) V_{\alpha\beta\gamma\delta}(\mathbf{k};\mathbf{k}')\Psi_{\gamma\delta}(\mathbf{k}') + \sum_{\sigma,\mathbf{k}} E_\sigma(\mathbf{k}) a^\dagger_\sigma(\mathbf{k}) a_\sigma(\mathbf{k}) + \frac{1}{2}\sum_{\mathbf{k}} \left[a^\dagger_\alpha(\mathbf{k})\Delta_{\alpha\beta}(\mathbf{k}) a^\dagger_\beta(-\mathbf{k}) - a_\alpha(\mathbf{k})\Delta^*_{\alpha\beta}(\mathbf{k})\, a_\beta(-\mathbf{k})\right] \quad (7.39)$$

Note that the gap function has the same symmetries as the order parameter itself. In particular it is antisymmetric under exchange of labels,

$$\begin{aligned}\Delta_{\beta\alpha}(-\mathbf{k}) &= \sum_{\mathbf{k}'\gamma\delta} V_{\beta\alpha;\gamma\delta}(-\mathbf{k};\mathbf{k}')\Psi_{\gamma\delta}(\mathbf{k}') \\ &= \sum_{\mathbf{k}'\gamma\delta} V_{\alpha\beta;\delta\gamma}(-\mathbf{k};-\mathbf{k}')\Psi_{\gamma\delta}(\mathbf{k}') \\ &= \sum_{\mathbf{k}'\gamma\delta} V_{\alpha\beta;\gamma\delta}(-\mathbf{k};-\mathbf{k}')\Psi_{\delta\gamma}(-\mathbf{k}') \\ &= -\Delta_{\alpha\beta}(\mathbf{k}) \end{aligned} \quad (7.40)$$

V. THE BOGOLIUBOV TRANSFORMATION

The BCS Hamiltonian, (7.39), is bilinear in the electron operators, and so it can be diagonalized by a unitary transformation, called the Bogoliubov transformation, that mixes electron creation and annihilation operators.

The generator for the Bogoliubov transformation is the anti-hermitian operator

$$B = \frac{1}{2}\sum_{\mathbf{k}} \left[\Theta_{\alpha\beta}(\mathbf{k}) a^\dagger_\alpha(\mathbf{k}) a^\dagger_\beta(-\mathbf{k}) + \Theta^*_{\alpha\beta}(\mathbf{k}) a_\alpha(\mathbf{k})\, a_\beta(-\mathbf{k})\right] \quad (7.41)$$

Since the electron operators anticommute, the coefficients $\Theta_{\alpha\beta}(\mathbf{k})$ must be antisymmetric under exchange of spin and band indices and $\mathbf{k} \to -\mathbf{k}$,

$$\Theta_{\alpha\beta}(\mathbf{k}) = -\Theta_{\beta\alpha}(-\mathbf{k}) \quad (7.42)$$

The action of the Bogoliubov transformation on the electron operators is

$$\begin{aligned} e^B a_\alpha(\mathbf{k}) e^{-B} &= U_{\alpha\beta}(\mathbf{k}) a_\beta(\mathbf{k}) - V_{\alpha\beta}(\mathbf{k}) a^\dagger_\beta(-\mathbf{k}) \\ &\equiv b_\alpha(\mathbf{k}) \end{aligned} \quad (7.43)$$

which defines the quasiparticle operators $b_\alpha(\mathbf{k})$. The coefficients $U_{\alpha\beta}(\mathbf{k})$ and $V_{\alpha\beta}(\mathbf{k})$ are given by

$$U_{\mu\nu}(\mathbf{k}) = \delta_{\mu\nu} + \frac{1}{2!}\Theta_{\mu\alpha}(\mathbf{k})\Theta_{\alpha\nu}(-\mathbf{k})^* + \frac{1}{4!}\Theta_{\mu\alpha}(\mathbf{k})\Theta_{\alpha\beta}(-\mathbf{k})^* \Theta_{\beta\gamma}(\mathbf{k})\Theta_{\gamma\nu}(-\mathbf{k})^* + \cdots \quad (7.44a)$$

$$V_{\mu\nu}(\mathbf{k}) = \Theta_{\mu\nu}(\mathbf{k}) + \frac{1}{3!}\Theta_{\mu\alpha}(\mathbf{k})\Theta^*_{\alpha\beta}(-\mathbf{k})\Theta_{\beta\nu}(\mathbf{k}) + \cdots \quad (7.44b)$$

The $V_{\mu\nu}(\mathbf{k})$ have the same symmetry as $\Theta_{\mu\nu}(\mathbf{k})$ itself,

$$V_{\mu\nu}(\mathbf{k}) = V_{\nu\mu}(-\mathbf{k}) \quad (7.45a)$$

whereas for the U's we have

$$U^*_{\nu\mu}(\mathbf{k}) = U_{\mu\nu}(\mathbf{k}) \quad (7.45b)$$

The Bogoliubov transformation preserves the canonical commutation relations for the electron operators, (7.21), which lead to the following relations:

$$U_{\alpha\mu}(\mathbf{k})V_{\mu\beta}(\mathbf{k}) - V_{\alpha\mu}(\mathbf{k})U^*_{\mu\beta}(-\mathbf{k}) = 0 \quad (7.46a)$$

$$U_{\alpha\mu}(\mathbf{k})U^*_{\mu\beta}(\mathbf{k}) - V_{\alpha\mu}(\mathbf{k})V^*_{\mu\beta}(-\mathbf{k}) = \delta_{\alpha\beta} \quad (7.46b)$$

The coefficients $\Theta_{\alpha\beta}(\mathbf{k})$, or equivalently the Bogoliubov amplitudes, are chosen so that the "off-diagonal" terms, i.e. the terms that involve the product of two creation or two annihilation operators, vanish. In order

to facilitate the calculation of the Bogoliubov amplitudes it is useful to define a two-component operator

$$A_\alpha(\mathbf{k}) = \begin{pmatrix} a_\alpha(\mathbf{k}) \\ a^\dagger_\alpha(-\mathbf{k}) \end{pmatrix} \tag{7.47}$$

The BCS Hamiltonian can then be written in the compact form

$$H_{BCS} = \frac{1}{2}\sum_{\mathbf{k}} A^\dagger_\alpha(\mathbf{k}) \cdot \mathrm{H}_{\alpha\beta}(\mathbf{k}) \cdot A_\beta(\mathbf{k}) + E_0' \tag{7.48}$$

where the 2×2 matrix $\mathrm{H}_{\alpha\beta}(\mathbf{k})$ is

$$\mathrm{H}_{\alpha\beta}(\mathbf{k}) = \begin{pmatrix} E_{\alpha\beta}(\mathbf{k}) & \Delta_{\alpha\beta}(\mathbf{k}) \\ -\Delta^*_{\alpha\beta}(-\mathbf{k}) & -E_{\alpha\beta}(-\mathbf{k}) \end{pmatrix} \tag{7.49}$$

The constant E_0' arises from reordering the electron operators,

$$E_0' = \frac{1}{2}\sum_{\alpha\mathbf{k}} E_\alpha(\mathbf{k}) \tag{7.50}$$

and $E_{\alpha\beta}(\mathbf{k})$ is the diagonal matrix $E_{\alpha\beta}(\mathbf{k}) = E_\alpha(\mathbf{k})\delta_{\alpha\beta}$.

The action of the Bogoliubov transformation, (7.43), on the BCS Hamiltonian (7.48) is

$$\begin{aligned} & e^B A^\dagger_\alpha(\mathbf{k}) \cdot \mathrm{H}_{\alpha\beta}(\mathbf{k}) \cdot A_\beta(\mathbf{k}) e^{-B} \\ & = A^\dagger_\mu(\mathbf{k}) \begin{pmatrix} U_{\mu\alpha}(\mathbf{k}) & V_{\mu\alpha}(\mathbf{k}) \\ V^*_{\mu\alpha}(-\mathbf{k}) & U^*_{\mu\alpha}(-\mathbf{k}) \end{pmatrix} \mathrm{H}_{\alpha\beta}(\mathbf{k}) \\ & \quad \times \begin{pmatrix} U_{\beta\nu}(\mathbf{k}) & -V_{\beta\nu}(\mathbf{k}) \\ -V^*_{\beta\nu}(-\mathbf{k}) & U^*_{\beta\nu}(-\mathbf{k}) \end{pmatrix} A_\nu(\mathbf{k}) \end{aligned} \tag{7.51}$$

We see from this that the Bogoliubov transformation acting on the electron operators induces a unitary transformation of the matrix $\mathrm{H}_{\alpha\beta}(\mathbf{k})$. In the usual way, the unitary matrix that diagonalizes $\mathrm{H}_{\alpha\beta}(\mathbf{k})$ can be constructed from its eigenvectors. By inspection of (7.51) we see that the BCS Hamiltonian is diagonalized if the Bogoliubov amplitudes satisfy the eigenvalue equation

$$\begin{aligned} & \begin{pmatrix} E_{\alpha\beta}(\mathbf{k}) & -\Delta_{\alpha\beta}(\mathbf{k}) \\ -\Delta^*_{\alpha\beta}(-\mathbf{k}) & -E_{\alpha\beta}(-\mathbf{k}) \end{pmatrix} \begin{pmatrix} U_{\beta\nu}(\mathbf{k}) \\ -V^*_{\beta\nu}(-\mathbf{k}) \end{pmatrix} \\ & = \lambda_\nu(\mathbf{k}) \begin{pmatrix} U_{\beta\nu}(\mathbf{k}) \\ -V^*_{\beta\nu}(-\mathbf{k}) \end{pmatrix} \end{aligned} \tag{7.52a}$$

It should be noted that by introducing the two-component operator $A_\alpha(\mathbf{k})$ we have doubled the size of the vector space. As a consequence, for every eigenvector with eigenvalue $\lambda_\nu(\mathbf{k})$ there is a second eigenvector with eigenvalue $-\lambda_\nu(\mathbf{k})$ given by

$$\begin{aligned} & \begin{pmatrix} E_{\alpha\beta}(\mathbf{k}) & \Delta_{\alpha\beta}(\mathbf{k}) \\ -\Delta^*_{\alpha\beta}(-\mathbf{k}) & -E_{\alpha\beta}(-\mathbf{k}) \end{pmatrix} \begin{pmatrix} -V_{\beta\nu}(\mathbf{k}) \\ U^*_{\beta\nu}(-\mathbf{k}) \end{pmatrix} \\ & = -\lambda_\nu(\mathbf{k}) \begin{pmatrix} -V_{\beta\nu}(\mathbf{k}) \\ U^*_{\beta\nu}(-\mathbf{k}) \end{pmatrix} \end{aligned} \tag{7.52b}$$

If we use (7.52a,b), the Hamiltonian takes the diagonal form

$$H_{BCS} = A^\dagger_\mu(\mathbf{k}) \begin{pmatrix} \lambda_\mu(\mathbf{k})\delta_{\mu\nu} & 0 \\ 0 & -\lambda_\mu(\mathbf{k})\delta_{\mu\nu} \end{pmatrix} A_\nu(\mathbf{k}) \tag{7.53}$$

which can be expressed in terms of the electron operators as

$$H_{BCS} = \sum_{\mu\mathbf{k}} \lambda_\mu(\mathbf{k}) b^\dagger_\mu(\mathbf{k}) b_\mu(\mathbf{k}) + E_0' - E_0'' \tag{7.54}$$

where

$$E_0'' = \frac{1}{2}\sum_{\mathbf{k},n} \lambda_n(\mathbf{k}) \tag{7.55}$$

is a constant that arises when the quasiparticle operators are normal ordered. The eigenvalues $\lambda_\nu(\mathbf{k})$ appearing in (7.52) are the quasiparticle energies.

VI. THE SELF-CONSISTENT GAP EQUATION

By treating order parameter in the mean-field approximation the BCS Hamiltonian clearly breaks global gauge symmetry, but we must complete the theory by calculating the order parameter in the ordered state,

$$\Psi_{\alpha\beta}(\mathbf{k}) = Z^{-1} Tr\ e^{-\beta H_{BCS}[\Psi]} a_\alpha(\mathbf{k}) a_\beta(-\mathbf{k}) \tag{7.56}$$

Note that the order parameter appears both on the right and on the left-hand side of this equation, so it must be solved self-consistently.

If we apply the Bogoliubov transformation to (7.56), we have

$$\Psi_{\alpha\beta}(\mathbf{k}) = Z^{-1} Tr\ e^{-\beta H_{BCS}} [U_{\alpha\mu}(\mathbf{k}) a_\mu(\mathbf{k}) - V_{\alpha\mu}(\mathbf{k}) a^\dagger_\mu(-\mathbf{k})] \times [U_{\beta\nu}(-\mathbf{k}) a_\nu(-\mathbf{k}) - V_{\beta\nu}(-\mathbf{k}) a^\dagger_\nu(\mathbf{k})] \quad (7.57)$$

The Bogoliubov transformation diagonalizes the BCS Hamiltonian as in (7.54), so the thermal averages in (7.57) can be done immediately, with the result

$$\Psi_{\alpha\beta}(\mathbf{k}) = \sum_\mu \left[U_{\alpha\mu}(\mathbf{k}) V_{\mu\beta}(\mathbf{k}) \left[1 - n(\beta\lambda_\mu)\right] - V_{\alpha\mu}(\mathbf{k})\ U^*_{\mu\beta}(-\mathbf{k}) n(\beta\lambda_\mu) \right] \quad (7.58)$$

where $n(x) = (e^x + 1)^{-1}$ is the usual Fermi-Dirac occupation function.

A. Solution of the Gap Equation Near T_c

In general this nonlinear equation is quite difficult to solve, but near the critical temperature, where the order parameter is small, we can treat the symmetry-breaking terms in H_{BCS} as a perturbation and linearize the gap equation. The details of this calculation are somewhat involved, and so we relegate them to Appendix A. The final result is (A.13)

$$\Psi_{\alpha\beta}(\mathbf{k}) = \frac{1 - n[\beta E_\beta(-\mathbf{k})] - n[\beta E_\alpha(\mathbf{k})]}{E_\alpha(\mathbf{k}) + E_\beta(-\mathbf{k})} \times \Delta_{\alpha\beta}(\mathbf{k}) \quad (7.59)$$

The energy dependent factor in (7.59) has a maximum near $E_\alpha \approx E_\beta \approx 0$, that is for both energies near the Fermi surface. Therefore bands that are far from the Fermi energy will contribute very little to the superconducting order parameter.

If we use the definition of the gap function, (7.38), the gap equation (7.59) can be written entirely in terms of the order parameter,

$$\Psi_{\alpha\beta}(\mathbf{k}) = \frac{1 - n[\beta E_\beta(-\mathbf{k})] - n[\beta E_\alpha(\mathbf{k})]}{E_\alpha(\mathbf{k}) + E_\beta(-\mathbf{k})} \times \sum_{\mathbf{p}} V_{\alpha\beta;\mu\nu}(\mathbf{k};\mathbf{p}) \Psi_{\mu\nu}(\mathbf{p}) \quad (7.60)$$

B. Solution At $T = 0$

The gap equation also simplifies at zero temperature, where the number of quasiparticles vanishes. In this case we have, by (7.46a)

$$\lim_{T\to 0} \Psi_{\alpha\beta}(\mathbf{k}) \to U_{\alpha\mu}(\mathbf{k}) V_{\mu\beta}(\mathbf{k}) = \frac{1}{2} V_{\alpha\beta}[2\Theta(\mathbf{k})] \quad (7.61)$$

which tells us that $V_{\alpha\beta}(\mathbf{k})$ has the same symmetry as the order parameter.

C. Nodes of the Order Parameter

Most of the superconducting materials known before the discovery of the copper-oxide high temperature superconductors by Bednorz and Müller (1986) are of the "s-wave" type, meaning the order parameter is a spin-singlet and positive everywhere in the Brillouin zone. There is convincing evidence that the quasi two-dimensional high-temperature superconductors are "d-wave", with nodal lines along the directions $k_x = \pm k_y$ in the plane perpendicular to the c-axis. Heavy-fermion superconductors like UPt_3 may be "p-wave", or triplet, $\Psi_{\alpha\beta}(\mathbf{k}) = -\Psi_{\alpha\beta}(-\mathbf{k})$, requiring a node at $\mathbf{k} = 0$.

The order parameter must transform as an irreducible representation of the point

group of the crystal structure[1]. If the order parameter has a single component, it must transform as a one-dimensional representation of the point group. Of these one-dimensional representations, there is always the identity representation, which corresponds to the case where the order parameter does not change sign under the operations of the point group. This is referred to as "extended s-wave". It is possible that the order parameter can still have nodes in this case. For example, the order parameter $\psi(\mathbf{k}) = \psi_0 + \psi_1(\cos k_x a + \cos k_y a)$, which is invariant under the point group D_{4h} appropriate to a copper-oxygen plane in the cuprate materials, may have nodal lines near the corners of the Brillouin zone if $\psi_0 < 2\psi_1$.

On the other hand, if the order parameter transforms as one of the other one-dimensional representations of the point group, it *must* change sign under at least one element of the point group, P, $\Psi_{\alpha\beta}(P\mathbf{k}) = -\Psi_{\alpha\beta}(\mathbf{k})$.

D. Single Band Singlet Pairing

In the case of spin-singlet pairing in a single band, the order parameter is

$$\Psi_{\mu\nu}(\mathbf{p}) = \varepsilon_{\mu\nu}\psi(\mathbf{p}) \tag{7.62}$$

where $\varepsilon_{\mu\nu} = -\varepsilon_{\nu\mu}$ and $\psi(\mathbf{p}) = \psi(-\mathbf{p})$ is a complex scalar function. The same is true of the gap function $\Delta_{\mu\nu}(\mathbf{p}) = \varepsilon_{\mu\nu}\Delta(\mathbf{p})$ and the Bogoliubov parameter $\Theta_{\mu\nu}(\mathbf{k}) = \varepsilon_{\mu\nu}\theta(\mathbf{k})$. If we assume the band energies are spin-independent and invariant under parity, the form of the Bogoliubov amplitudes simplify a great deal (note that $\varepsilon_{\mu\alpha}\varepsilon_{\alpha\beta} = -\delta_{\mu\beta}$) and we find

$$\begin{aligned} U_{\alpha\beta}(\mathbf{k}) &= \delta_{\alpha\beta}\cos\theta(\mathbf{k}) \\ V_{\alpha\beta}(\mathbf{k}) &= \varepsilon_{\alpha\beta}\sin\theta(\mathbf{k}) \end{aligned} \tag{7.63}$$

The quasiparticle energies are given by

$$\lambda(\mathbf{k}) = \sqrt{E^2(\mathbf{k}) + |\Delta(\mathbf{k})|^2} \tag{7.64}$$

from which we see why $\Delta(\mathbf{k})$ is referred to as the gap function.

The Bogoliubov amplitudes can be found,

$$\begin{aligned} |u(\mathbf{k})|^2 &= \frac{1}{2}\left(1 + \frac{E(\mathbf{k})}{\lambda(\mathbf{k})}\right) \\ |v(\mathbf{k})|^2 &= \frac{1}{2}\left(1 - \frac{E(\mathbf{k})}{\lambda(\mathbf{k})}\right) \end{aligned} \tag{7.65}$$

and are shown in Fig. 7.1. The expression for the order parameter, (7.58) then takes the very simple form

$$\psi(\mathbf{k}) = -\frac{1 - 2n[\lambda(\mathbf{k})]}{2\lambda(\mathbf{k})}\Delta(\mathbf{k}) \tag{7.66}$$

Close to the transition temperature the order parameter is given by

$$\psi(\mathbf{k}) = -\frac{1 - 2n[\beta E(\mathbf{k})]}{2E(\mathbf{k})}\sum_{\mathbf{p}} V(\mathbf{k},\mathbf{p})\psi(\mathbf{p}) \tag{7.67}$$

E. S-Wave Pairing

To proceed further we need a model for the interaction potential. A simple choice (J. Bardeen, L.N. Cooper and J. R. Schrieffer 1957) that leads to tractable expressions is

$$V(\mathbf{k},\mathbf{p}) = -V_0\,\eta(E(\mathbf{k})/E_0)\,\eta(E(\mathbf{p})/E_0) \tag{7.68}$$

where

$$\eta(x) = \begin{cases} 1 & \text{for } -1 \le x \le 1 \\ 0 & \text{otherwise} \end{cases} \tag{7.69}$$

Note that the choice of sign in (7.68) anticipates that we will find a solution only if the effective interaction is attractive. In the case of phonon-mediated interactions, V_0 is

[1] An exception to this can occur if two order parameters with different symmetry are degenerate. In this case the order parameter is said to be "mixed".

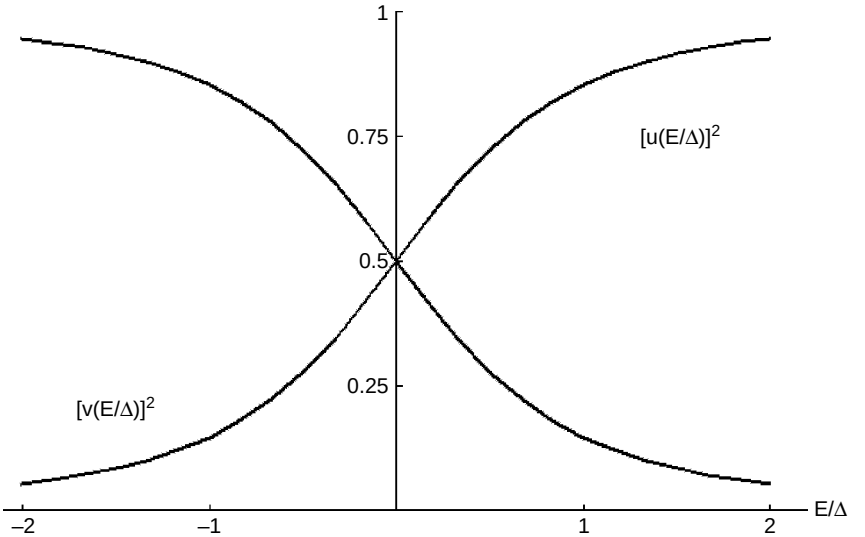

Figure 7.1 Bogoliubov amplitudes in the neighborhood of the Fermi surface.

a measure of the strength of the electron-phonon coupling and $E_0 = \hbar\omega_D$ is a typical phonon energy. We then have

$$\psi(\mathbf{k}) = \kappa V_0 \left(\frac{1 - 2n[\beta E(\mathbf{k})]}{2E(\mathbf{k})} \right) \eta(E(\mathbf{k})/E_0) \tag{7.70}$$

where

$$\kappa = \sum_{\mathbf{p}} \eta(E(\mathbf{p})/E_0)\psi(\mathbf{p}) \tag{7.71}$$

If we substitute (7.70) for the order parameter in (7.71) we get

$$1 = V_0 \sum_{\mathbf{p}} \eta(E(\mathbf{p})/E_0) \left(\frac{1 - 2n[\beta E(\mathbf{p})]}{2E(\mathbf{p})} \right) \tag{7.72}$$

This equation determines the transition temperature, which enters through the Fermi-Dirac function on the right hand side.

The summand in (7.72) is monotonically decreasing with temperature. Above the transition temperature the only solution to the gap equation is $\psi(\mathbf{k}) = 0$. For $T \leq T_c$ a second solution exists with $\psi(\mathbf{k}) \neq 0$.

We can solve (7.72) for the transition temperature if we replace the sum by an integral and assume the density of states in the neighborhood of the Fermi surface is constant, $D(0)$. With these approximations, (7.72) becomes

$$1 = \frac{V_0 D(0)}{2} \int_{-E_0}^{E_0} \left(\frac{1 - 2n(E)]}{E} \right) dE$$

$$= V_0 D(0) \int_0^{E_0} \frac{\tanh\, E/2k_B T_c}{E} dE \tag{7.73}$$

In most simple superconductors $E_0/k_B T_c >> 1$. The integral in (7.73) can then be done by parts, and in the remaining integral the upper limit set to infinity, with the result

$$k_B T_c = \frac{2e^{\gamma}}{\pi} E_0 e^{-1/D(0)V_0} \tag{7.74}$$

The remarkable thing about this result is that no matter how weak the interaction between electrons, there is always a superconducting state. It is also clear that any sort of series expansion in V_0 will suffer from an essential singularity at $V_0 = 0$. Figure 7.2 shows a scatter plot of the density of states and transition

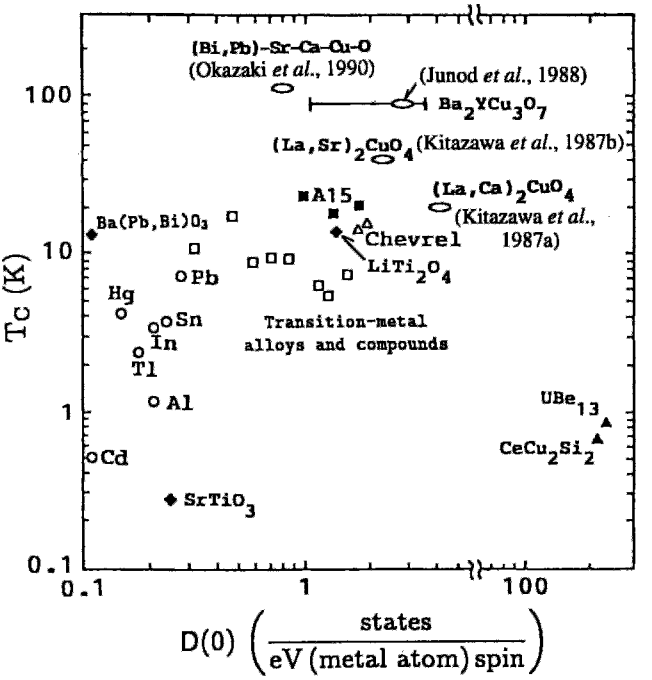

Figure 7.2 Dependence of the superconducting transition temperature T_c on the density of states $D(0)$ for various superconductors (Okazaki *et al.*, 1990)

temperatures for a variety of superconducting materials.

F. Zero-Temperature Gap

At zero temperature there are no quasiparticles and the gap equation becomes

$$\psi(\mathbf{k}) = \frac{V_0}{2\lambda(\mathbf{k})}\eta(E(\mathbf{k})/E_0) \times \sum_{\mathbf{p}} \eta(E(\mathbf{p})/E_0)\psi(\mathbf{p}) \qquad (7.75)$$

Once again we define

$$\kappa = \sum_{\mathbf{p}} \eta(E(\mathbf{p})/E_0)\psi(\mathbf{p}) \qquad (7.76)$$

and, following the same steps that led to the expression for the transition temperature, we find

$$1 = V_0 D_n(0)\sinh^{-1}(E_0/\Delta_0) \qquad (7.77)$$

In the weak-coupling limit, $E_0/\Delta_0 >> 1$, the zero-temperature gap is

$$\Delta_0 = \frac{E_0}{2} e^{-1/V_0 D_n(0)} \qquad (7.78)$$

If we take the ratio of the zero-temperature gap to the critical temperature we find

$$\frac{2\Delta_0}{k_B T_c} = \frac{2\pi}{e^{\gamma}} \approx 3.53 \qquad (7.79)$$

The full temperature dependence of the gap is shown in Fig. 7.3 below.

Table 7.1 lists the transition temperatures and zero-temperature gaps, and the dimensionless ratio $2\Delta_0/k_B T_c$ for several superconductors. Given the crude approximations made in order to calculate the ratio of the zero temperature gap to the transition temperature, it is remarkable that the value of this ratio for some real materials is not too far from the weak-coupling BCS value.

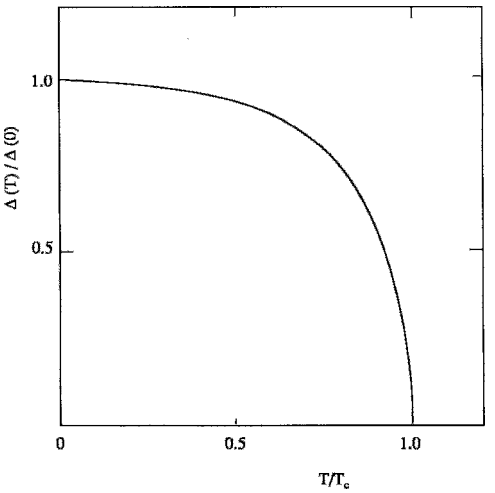

Figure 7.3 Temperature dependence of the BCS gap function Δ.

Many of the physical properties of superconductors depend on the quasiparticle density of states. In particular the presence of the gap is especially important, leading for example, to an exponential behavior in the specific heat. If we assume the density of states in the normal phase is slowly varying in the neighborhood of the Fermi surface, then the density of states in the superconducting state, shown in Fig. 7.4 is

$$D_S = \begin{cases} \dfrac{D_n(0)\lambda}{\sqrt{\lambda^2 - \Delta^2}} & \lambda > \Delta \\ 0 & |\lambda| < \Delta \\ \dfrac{D_n(0)\lambda}{\sqrt{\lambda^2 - \Delta^2}} & \lambda < -\Delta \end{cases} \tag{7.80}$$

Table 7.1 Comparison of Energy Gaps for Various Superconductors[a]

Material	T_c, K	$2\Delta_0$, meV	$2\Delta_0/k_B T_c$
Hf	0.13	0.044	3.9
Cd	0.52	0.14	3.2
Zn	0.85	0.23	3.2
Al	1.2	0.35	3.4
In	3.4	1.05	3.6
Hg	4.2	1.7	4.6
Pb	7.2	2.7	4.3
Nb	9.3	3.0	3.8
$V_3Ge(A15)$	11.2	3.1	3.2
$V_3Si(A15)$	17.1	5.4	3.7
$Nb_3Sn(A15)$	18.1	4.7	3.0
K_3C_{60}	19	5.9	3.6
Rb_3C_{60}	29	7.5	3.0
$Ba_{0.6}K_{0.4}BiO_3$	18.5	5.9	3.7
$(Nd_{0.925}Ce_{0.075})_2CuO_4$	21	7.4	4.4
$(La_{0.925}Sr_{0.075})_2CuO_4$	36	13	4.3
$YBa_2Cu_3O_{7-\delta}$	87	30	4.0
$Bi_2Sr_2Ca_2Cu_3O_{10}$	108	53	5.7
$Tl_2Ba_2CaCu_2O_8$	112	44	4.5
$Tl_2Ba_2Ca_2Cu_3O_{10}$	105	28	3.1
$HgBa_2Ca_2Cu_3O_8$	131	48	4.3

[a] Data on elements from Meservey and Schwartz (1969); data on the *A*15 compounds from Vonsovsky *et al*. (1982); and data on high-temperature superconductors from T. Hasegawa *et al*. (1991). K_3C_{60} and Rb_3C_{60} values are from Degiorgi *et al*. (1992), and $HgBa_2Ca_2Cu_3O_8$ data are from Schilling *et al*. (1994b). Many of the $2\Delta_0/k_BT_c$ ratios are averages of several determinations, sometimes with considerable scatter; the $2\Delta_0$ values are calculated from columns 2 and 4. The BCS value of $2\Delta_0/k_BT_c$ is 3.52. Table 3.1 provides energy gap data for many additional elements.

G. D-Wave Order Parameter

There is a growing consensus that the order parameter in the copper-oxide superconductors is "d-wave". These materials are fairly anisotropic, and many treatments are quasi two-dimensional, focusing on the copper-oxygen planes that form a nearly square lattice. It is also true that many of the parent materials of the cuprates are antiferromagnetic; doping tends to destroy the long-range AF order, but strong short range AF correlations survive in the normal state of superconducting samples. In this section we present a very simple "toy model" that leads to a d-wave order parameter. This model is not intended to be a realistic representation of any material, but merely to illustrate how such a solution to the gap equation can arise.

The point group for the square, D_{4h}, has the parity-even one dimensional representations listed in the following table (D.L Scalapino, 1995),

The order parameter must transform as one of these one-dimensional representations.

The gap equation, (7.66), can be cast in a more symmetric form by defining a rescaled order parameter

$$\psi(\mathbf{k}) = \sqrt{f(\mathbf{k})}\chi(\mathbf{k}) \tag{7.81}$$

and a rescaled two-body potential,

$$W(\mathbf{k},\mathbf{p}) \equiv \sqrt{f(\mathbf{k})}V(\mathbf{k},\mathbf{p})\sqrt{f(\mathbf{p})}$$

where $f(\mathbf{p}) > 0$ is the energy-dependent function

$$f(\mathbf{p}) = \frac{1-2n[\beta\lambda(\mathbf{p})]}{2\beta\lambda(\mathbf{p})} \tag{7.82}$$

The gap equation now has the simple form

$$\chi(\mathbf{k}) = -\beta\sum_{\mathbf{p}} W(\mathbf{k},\mathbf{p})\chi(\mathbf{p}) \tag{7.83}$$

The simple form (7.68) for the interaction potential is insufficient to describe an order parameter that changes sign within the Brillouin zone, since, as one can see from (7.76), the parameter κ vanishes in this case. Therefore let us consider an interaction $W(\mathbf{k},\mathbf{p})$ that is strongly peaked for a momentum transfer $\mathbf{q} = \mathbf{k} - \mathbf{p}$ in the neighborhood of $\mathbf{q}_0 = (\frac{\pi}{a}, \frac{\pi}{a})$,

$$W(\mathbf{k},\mathbf{p}) = V_0\delta(\mathbf{k}-\mathbf{p},\mathbf{q_0}) \tag{7.84}$$

The gap equation then becomes

$$\chi(\mathbf{k}) = -\beta V_0\chi(\mathbf{k}-\mathbf{q}_0) \tag{7.85}$$

If we assume that $V_0 > 0$, that is the effective potential is *repulsive*, it follows that the order parameter must change sign on translation by $\mathbf{q}_0$,

$$\psi(\mathbf{k}) = -\psi(\mathbf{k}-\mathbf{q_0}) \tag{7.86}$$

This rules out the extended s-wave case, $\psi(\mathbf{k}) = \psi_0 + \psi_1(\cos k_x a + \cos k_y a)$, unless $\psi_0 = 0$, and an order parameter that transforms as Γ_4^+, leaving the possibility of order parameters that transform according to the representations Γ_2^+ and Γ_3^+. Contour plots of these two cases are shown in figures 7.5a,b.

Whether the order parameter is extended s-wave, d-wave, or the even more complicated form shown in Fig. 7.5b, is ultimately decided by which one gives the lowest free energy.

Table 7.2 Irreducible one-dimensional representations of the point group D_{4h}. (D.L. Scalapino (1995))

Irreducible one-dimensional representation	**Basis Function**
Γ_1^+	$1, \cos\ k_x a + \cos\ k_y a$
Γ_2^+	$\sin\ k_x a \sin\ k_y a x\ (\cos\ k_x a - \cos\ k_y a)$
Γ_3^+	$\cos\ k_x a - \cos\ k_y a$
Γ_4^+	$\sin\ k_x a \sin\ k_y a$

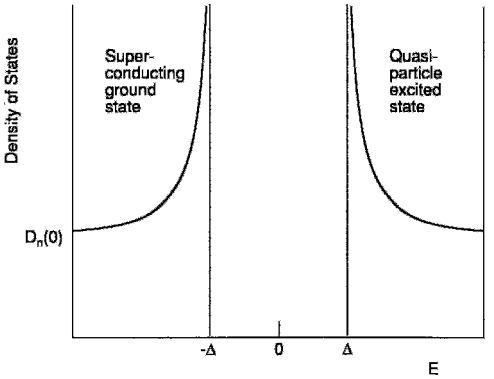

Figure 7.4 Density of states in the superconducting state near the Fermi surface.

H. Multi-Band Singlet Pairing

The superconducting state in MgB_2 is believed to involve more than one band. In order to investigate case where several bands may lie close to the Fermi surface, we return to (7.60) and again assume singlet pairing. We will also assume that the bands are parity invariant so $E_i(\mathbf{k}) = E_i(-\mathbf{k})$. The gap equation (7.60) becomes

$$\Psi_{ij}(\mathbf{k}) = \frac{1 - n[\beta E_i(\mathbf{k})] - n[\beta E_j(\mathbf{k})]}{E_i(\mathbf{k}) + E_j(\mathbf{k})} \times \sum_{\mathbf{p}} V_{ij;mn}(\mathbf{k};\mathbf{p})\Psi_{mn}(\mathbf{p}) \quad (7.87)$$

where the Latin indices label the bands and take the values $i = 1, 2, \ldots n$. We can

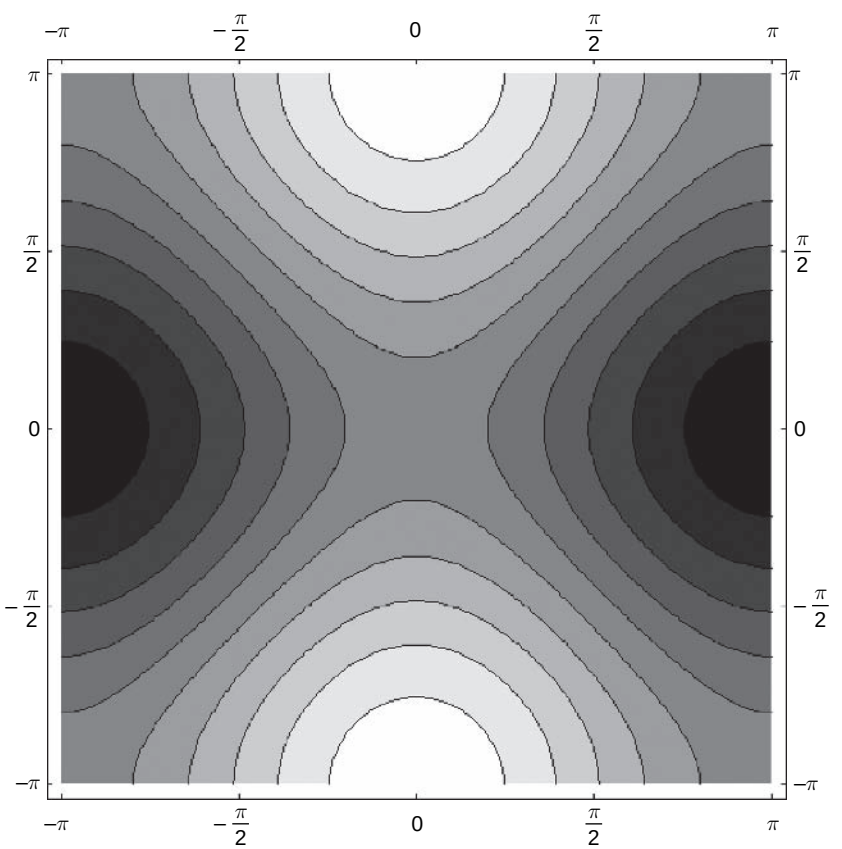

Figure 7.5a Contour plot of k_x versus k_y for the d-wave order parameter belonging to the representation Γ_3^+ of the point group D_{4h}.

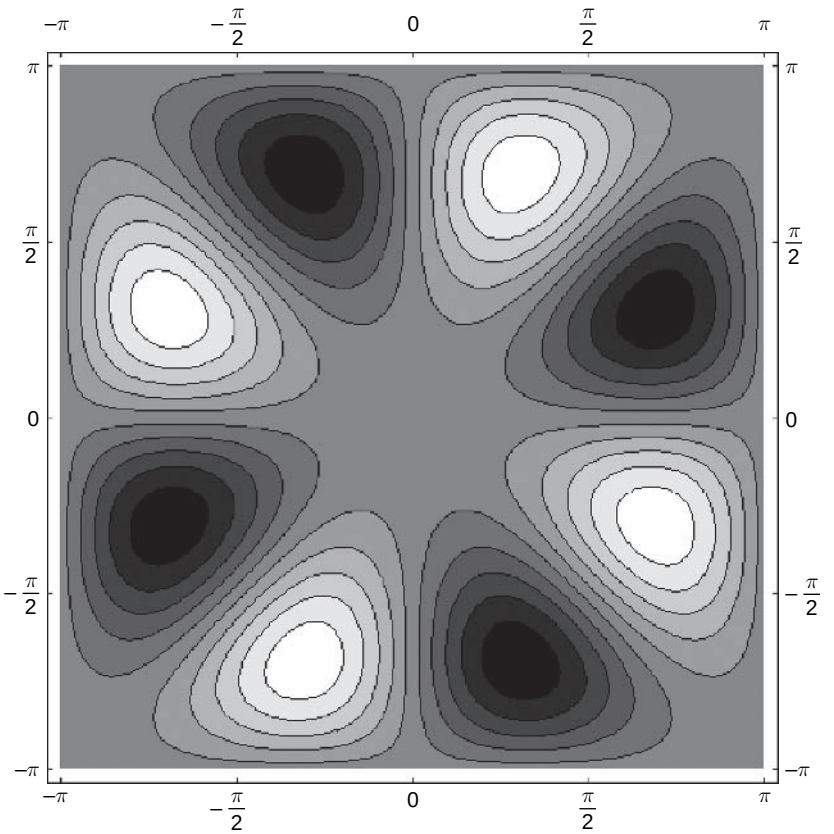

Figure 7.5b Contour plot of k_x versus k_y for the order parameter belonging to the representation Γ_2^+ of the point group D_{4h}.

simplify the structure of (7.87) by defining the function

$$f_{ij}(\mathbf{p}) = \frac{1 - n(\beta E_i(\mathbf{p})) - n(\beta E_i(\mathbf{p}))}{\beta\left(E_i(\mathbf{p}) + E_j(\mathbf{p})\right)} \tag{7.88}$$

Note that $f_{ij}(\mathbf{p}) > 0$, which allows us to define a rescaled order parameter, $\chi_{ij}(\mathbf{p})$,

$$\Psi_{ij}(\mathbf{p}) \equiv \sqrt{f_{ij}(\mathbf{p})}\chi_{ij}(\mathbf{p}) \tag{7.89}$$

and a rescaled two-body potential

$$W_{ij;mn}(\mathbf{k},\mathbf{p}) \equiv \sqrt{f_{ij}(\mathbf{k})}V_{ij;mn}(\mathbf{k},\mathbf{p})\sqrt{f_{mn}(\mathbf{p})} \tag{7.90}$$

The self-consistent gap equation then becomes

$$\chi_{ij}(\mathbf{k}) = \beta \sum_{\mathbf{p}} \sum_{mn} W_{ij;mn}(\mathbf{k},\mathbf{p})\chi_{mn}(\mathbf{p}) \tag{7.91}$$

If we regard this as an eigenvector-eigenvalue equation, we see that the scaled order parameter is an eigenvector of W with eigenvalue $1/\beta$. If the largest eigenvalue of W is $\omega_0(\beta)$, then the critical temperature is the solution of the equation

$$\beta_c \omega_0(\beta_c) = 1 \tag{7.92}$$

Denoting the eigenvector corresponding to the maximum eigenvalue by $\phi_{ij}^{(0)}(\mathbf{k})$, the

order parameter is

$$\Psi_{ij}(\mathbf{k}) \equiv \sqrt{f_{ij}(\mathbf{k})}\phi_{ij}^{(0)}(\mathbf{k}) \tag{7.93}$$

If we assume that the intra-band scattering terms in W are large compared to the inter-band terms, the well-known methods of perturbation theory can be applied to the eigenvalue problem, (7.91). In the usual way W is separated into two parts,

$$W_{ij;mn}(\mathbf{k},\mathbf{p}) = W_{ij;mn}^{(0)}(\mathbf{k},\mathbf{p}) + W_{ij,mn}^{(1)}(\mathbf{k},\mathbf{p}) \tag{7.94}$$

where $W_{ij;mn}^{(0)}(\mathbf{k},\mathbf{p})$ includes all intra-band interactions (and is therefore diagonal in the band indices) and $W_{ij;mn}^{(1)}(\mathbf{k},\mathbf{p})$ contains all inter-band interactions. Following standard perturbation theory, (here the eigenvectors and eigenvalues are understood to be those of $W^{(0)}$) we find the first- correction to the maximum eigenvector is[2]

$$\Delta\phi_{ij}^{(0)} = \sum_{n\neq 0} \frac{\left(\phi^{(n)}, W^{(1)}\phi^{(0)}\right)}{\omega_0 - \omega_n}\phi_{ij}^{(n)} \tag{7.95a}$$

and the shift in the maximum eigenvalue is, to second order (the first order term vanishes),

$$\omega_0^{(2)} = \sum_{n\neq 0} \frac{\left|\left(\phi^{(n)}, W^{(1)}\phi^{(0)}\right)\right|^2}{\omega_0 - \omega_n} > 0 \tag{7.95b}$$

We see that only processes where the number of electrons in each band remains fixed contribute to the change in the order parameter and eigenvalue to lowest order. It is also interesting to note that quite generally the presence of other bands increases the eigenvalue, and therefore the critical temperature.

In the beginning of our discussion we introduced an effective electron-electron potential without saying anything about its origin, other than noting that in the BCS theory the exchange of virtual phonons gives rise to an attractive interaction. A detailed calculation of the electron-phonon coupling is beyond the scope of this book, so we simply refer to the central result of Eliashberg, who defines the dimensionless electron-phonon coupling constant

$$\lambda = 2\int_0^\infty d\omega \frac{\alpha^2(\omega)D_{ph}(\omega)}{\omega} \tag{7.96}$$

Superconductors are characterized according to the magnitude of λ,

$$\begin{aligned} &\lambda << 1 \quad \text{weak coupling} \\ &\lambda \sim 1 \quad \text{intermediate coupling} \\ &\lambda >> 1 \quad \text{strong coupling} \end{aligned} \tag{7.97}$$

In addition to the attractive electron-phonon coupling there is a residual screened Coulomb repulsive interaction characterized by the dimensionless parameter μ_c^*. The net electron-electron interaction is the sum of these two terms, and in the expressions (7.74) and (7.78) we make the substitution

$$D_n(0)V_0 \to \lambda - \mu_c^* \tag{7.98}$$

so the transition temperature is given by

$$T_c = 1.13\theta_D e^{-\frac{1}{\lambda-\mu_c^*}} \tag{7.99}$$

A number of other expressions for the critical temperature have appeared in the literature. McMillan (1968) gives the following empirical formula

$$T_c = \frac{\theta_D}{1.45}\exp\left[-\frac{1.04(1+\lambda)}{\lambda - \mu_c^*(1+062\lambda}\right] \tag{7.100}$$

Values of λ and μ_c^* reported in the literature for various superconductors are listed in Table 7.3.

[2] The inner product notation used in (7.85) involves both sums over band indices and a sum over wavevectors.

Table 7.3 Electron–Phonon Coupling Constants λ and Coulomb Interaction Parameters μ_c^{*a}

Material	T_c(K)	λ	μ_c^*	References
Ru	0.49	0.47	0.15	Table 3.1
Zr	0.61	0.22	0.17	Table 3.1
Os	0.66	0.44	0.12	Table 3.1
Mo	0.92	0.35	0.09	Table 3.1
Re	1.7	0.37	0.1	Table 3.1
Pb	7.2	1.55		Ginzburg and Kirzhnits (1977, p. 171)
Nb	9.3	0.85		Ginzburg and Kirzhnits (1977, p. 171)
NbC	11.1	0.61		Ginzburg and Kirzhnits (1977, p. 171)
TaC	11.4	0.62		Ginzburg and Kirzhnits (1977, p. 171)
V_3Ge	6.1	0.7		Vonsovsky *et al.* (1982, p. 303)
V_3Si	17.1	1.12		Vonsovsky *et al.* (1982, p. 303)
Nb_3Sn	18.1	1.67		Ginzburg and Kirzhnits (1977, p. 171)
Nb_3Ge	23.2	1.80		Vonsovsky *et al.* (1982, p. 303)
K_3C_{60}	16.3	0.51		Novikov *et al.* (1992)
Rb_3C_{60}	30.5	0.61		Novikov *et al.* (1992)
Cs_3C_{60}	47.4	0.72		Novikov *et al.* (1992)
$Ba(Pb,\ Bi)O_3$	12	1.3		Schlesinger *et al.* (1989)
$(La_{0.913}Sr_{0.087})CuO_4$		0.1		Gurvitch and Fiory (1987a,b,c)
$(La_{0.913}Sr_{0.087})CuO_4$	35	2.0	0.18	Rammer (1987)
$YBa_2Cu_3O_7$		0.2		Gurvitch and Fiory (1987a,b,c)
$YBa_2Cu_3O_7$		0.3		Tanner and Timusk (1992, p. 416)
$YBa_2Cu_3O_7$	90	2.5	0.1	Kirtley *et al.* (1987)
$Bi_2Sr_2CuO_6$		0.2		Tanner and Timusk (1992, p. 416)
$Bi_2Sr_2CaCu_2O_8$		0.3		Tanner and Timusk (1992, p. 416)
$Tl_2Ba_2CaCu_2O_8$		0.3		Foster *et al.* (1990)

[a] High and low estimates are given for high-temperature superconductors, some of which are averages of several investigators. Skriver and Mertig (1990) give coupling constants from rare earths.

VII. RESPONSE OF A SUPERCONDUCTOR TO A MAGNETIC FIELD

In this section we consider the behavior of the order parameter in the presence of a weak, slowly varying magnetic field **B** which is given in terms of the vector potential, **A**

$$\mathbf{B} = \nabla \times \mathbf{A} \tag{7.101}$$

Our goal here is to calculate the current density **J** induced by the externally applied magnetic field, and in this way to demonstrate the Meissner effect. To simplify the discussion we will consider singlet pairing in a single free-electron like band characterized by an effective mass m. The BCS Hamiltonian in this model is

$$\begin{aligned} H_{BCS} = & \frac{\hbar^2}{2m}\int d^3r \\ & \times \left(\nabla - \frac{ie}{\hbar}\mathbf{A}\right)\psi_\alpha^\dagger(\mathbf{r}) \cdot \left(\nabla + \frac{ie}{\hbar}\mathbf{A}\right) \\ & \times \psi_\alpha(\mathbf{r}) - \mu\int d^3r \psi_\alpha^\dagger(\mathbf{r})\psi_\alpha(\mathbf{r}) \\ & + \frac{1}{2}\int d^3r \int d^3r' \\ & \times \left[\psi_\alpha^\dagger(\mathbf{r})\psi_\beta^\dagger \Delta_{\alpha\beta}(\mathbf{r},\mathbf{r}') \right. \\ & \left. - \Delta_{\alpha\beta}(\mathbf{r},\mathbf{r}')^*\psi_\alpha(\mathbf{r})\psi_\beta(\mathbf{r}')\right] \end{aligned} \tag{7.102}$$

where μ, the chemical potential, sets the zero-point of the energy scale. Note that the order parameter (and the gap function) is now a function of the coordinates,

$$\Psi_{\alpha\beta}(\mathbf{r},\mathbf{r}') = \langle \psi_\alpha(\mathbf{r})\psi_\beta(\mathbf{r}')\rangle \tag{7.103}$$

Following our earlier treatment, the BCS Hamiltonian can be written up to a c-number (i.e. complex number) in the form

$$H_{BCS} = \frac{1}{2}\int d^3r \times \int d^3r' \Psi^\dagger_\alpha(\mathbf{r}')\mathrm{H}_{\alpha\beta}(\mathbf{r}',\mathbf{r})\Psi_\beta(\mathbf{r}) \tag{7.104}$$

where the two-component field operator is

$$\Psi_\alpha(\mathbf{r}) = \begin{pmatrix}\psi_\alpha(\mathbf{r})\\ \psi^\dagger_\alpha(\mathbf{r})\end{pmatrix} \tag{7.105}$$

and $\mathrm{H}_{\alpha\beta}(\mathbf{r}',\mathbf{r})$ is

$$\mathrm{H}_{\alpha\beta}(\mathbf{r}',\mathbf{r}) = \begin{pmatrix} -\delta_{\alpha\beta}(\mathbf{r}',\mathbf{r}) \times\left[\frac{\hbar^2}{2m}\left(\nabla_\mathbf{r}+\frac{ie}{\hbar}\mathbf{A}\right)^2+\mu\right] & \Delta_{\alpha\beta}(\mathbf{r}',\mathbf{r}) \\ -\Delta_{\alpha\beta}(\mathbf{r}',\mathbf{r})^* & \delta_{\alpha\beta}(\mathbf{r}',\mathbf{r}) \times\left[\frac{\hbar^2}{2m}\left(\nabla_\mathbf{r}-\frac{ie}{\hbar}\mathbf{A}\right)^2+\mu\right] \end{pmatrix} \tag{7.106}$$

As before, the Bogoliubov amplitudes are the components of the eigenvectors of $\mathrm{H}_{\alpha\beta}(\mathbf{r}',\mathbf{r})$, and satisfy the coupled equations

$$\begin{aligned} &\left[-\frac{\hbar^2}{2m}\left(\nabla_\mathbf{r}+\frac{ie}{\hbar}\mathbf{A}\right)^2+\mu\right]U_{\alpha\beta}(\mathbf{r}) - \int d^3r'\Delta_{\alpha\mu}(\mathbf{r},\mathbf{r}')V_{\mu\beta}(\mathbf{r}') = \lambda U_{\alpha\beta}(\mathbf{r}) \\ &\left[\frac{\hbar^2}{2m}\left(\nabla_\mathbf{r}-\frac{ie}{\hbar}\mathbf{A}\right)^2\mu\right]V_{\alpha\beta}(\mathbf{r}) - \int d^3r'\Delta_{\alpha\mu}(\mathbf{r},\mathbf{r}')^*U_{\mu\beta}(\mathbf{r}') = -\lambda V_{\alpha\beta}(\mathbf{r}) \end{aligned} \tag{7.107}$$

In the absence of the magnetic field we recover translational symmetry, and the Bogoliubov amplitudes are

$$\begin{aligned} U_{\alpha\beta}(\mathbf{r}) &= U_{\alpha\beta}(\mathbf{k})e^{i\mathbf{k}\cdot\mathbf{r}} \\ V_{\alpha\beta}(\mathbf{r}) &= V_{\alpha\beta}(\mathbf{k})e^{i\mathbf{k}\cdot\mathbf{r}} \end{aligned} \tag{7.108}$$

Substitution into (7.107) with $\mathbf{A}=0$ gives

$$\begin{aligned} &\left(\frac{\hbar^2k^2}{2m}-\mu\right)U_{\alpha\beta}(\mathbf{k}) - \Delta_{\alpha\mu}(\mathbf{k})V_{\mu\beta}(\mathbf{k}) = \lambda U_{\alpha\beta}(\mathbf{k}) \\ &\left(\frac{\hbar^2k^2}{2m}-\mu\right)V_{\alpha\beta}(\mathbf{k}) - \Delta_{\alpha\mu}(\mathbf{k})^*U_{\mu\beta}(\mathbf{k}) = -\lambda V_{\alpha\beta}(\mathbf{k}) \end{aligned} \tag{7.109}$$

In the presence of a weak, slowly varying magnetic field we can apply the adiabatic approximation, and assume that the amplitudes in (7.108) are slowly varying in space,

$$\begin{aligned} U_{\alpha\beta}(\mathbf{r}) &= U_{\alpha\beta}(\mathbf{k},\mathbf{r})e^{i\mathbf{k}\cdot\mathbf{r}} \\ V_{\alpha\beta}(\mathbf{r}) &= V_{\alpha\beta}(\mathbf{k},\mathbf{r})e^{i\mathbf{k}\cdot\mathbf{r}} \end{aligned} \tag{7.110}$$

and we can drop the term in the kinetic energy operator that is quadratic in A,

$$\left(\nabla_\mathbf{r}+\frac{ie}{\hbar}\mathbf{A}\right)^2 \approx \nabla^2_\mathbf{r}+\frac{2ie}{\hbar}\nabla\cdot\mathbf{A} \tag{7.111}$$

Keeping only the largest terms, (7.109) becomes

$$\begin{aligned} &\left(\frac{\hbar^2k^2}{2m}+\frac{\hbar e}{m}\mathbf{k}\cdot\mathbf{A}(\mathbf{r})-\mu\right)U_{\alpha\beta}(\mathbf{k};\mathbf{r}) - \Delta_{\alpha\mu}(\mathbf{k})V_{\mu\beta}(\mathbf{k};\mathbf{r}) = \lambda U_{\alpha\beta}(\mathbf{k};\mathbf{r}) \\ &\left(\frac{\hbar^2k^2}{2m}-\frac{\hbar e}{m}\mathbf{k}\cdot\mathbf{A}(\mathbf{r})-\mu\right)V_{\alpha\beta}(\mathbf{k};\mathbf{r}) - \Delta_{\alpha\mu}(\mathbf{k})^*U_{\mu\beta}(\mathbf{k};\mathbf{r}) = -\lambda V_{\alpha\beta}(\mathbf{k};\mathbf{r}) \end{aligned} \tag{7.112a}$$

If we move the terms involving the vector potential to the right, we have

$$\left(\frac{\hbar^2 k^2}{2m} - \mu\right) U_{\alpha\beta}(\mathbf{k};\mathbf{r}) - \Delta_{\alpha\mu}(\mathbf{k}) V_{\mu\beta}(\mathbf{k};\mathbf{r})$$
$$= \left(\lambda - \frac{\hbar e}{m}\mathbf{k}\cdot\mathbf{A}(\mathbf{r})\right) U_{\alpha\beta}(\mathbf{k};\mathbf{r})$$
$$\left(\frac{\hbar^2 k^2}{2m} - \mu\right) V_{\alpha\beta}(\mathbf{k};\mathbf{r}) - \Delta_{\alpha\mu}(\mathbf{k})^* U_{\mu\beta}(\mathbf{k};\mathbf{r})$$
$$= -\left(\lambda - \frac{\hbar e}{m}\mathbf{k}\cdot\mathbf{A}(\mathbf{r})\right) V_{\alpha\beta}(\mathbf{k};\mathbf{r}) \quad (7.112b)$$

Comparing this with (7.109), we see that the Bogoliubov amplitudes follow the vector potential adiabatically through their dependence on the eigenvalue

$$\lambda(\mathbf{k},\mathbf{r}) = \lambda(\mathbf{k}) + \frac{\hbar e}{m}\mathbf{k}\cdot\mathbf{A}(\mathbf{r}) \quad (7.113)$$

The current density is given by

$$\mathbf{J}(\mathbf{r}) = \frac{ie\hbar}{2m}\left[\psi_\alpha^\dagger(\mathbf{r})\nabla\psi_\alpha(\mathbf{r}) - \nabla\psi_\alpha^\dagger(\mathbf{r})\psi_\alpha(\mathbf{r})\right] - \frac{e^2}{m}\mathbf{A}(\mathbf{r})\psi_\alpha^\dagger(\mathbf{r})\psi_\alpha(\mathbf{r}) \quad (7.114)$$

and its thermal average is

$$\begin{aligned}\langle\mathbf{J}(\mathbf{r})\rangle = &\frac{ie\hbar}{2m}\sum_n \{[U_\alpha^n(\mathbf{r}^*\nabla U_\alpha^n(\mathbf{r}) \\ &-\nabla U_\alpha^n(\mathbf{r})^* U_\alpha^n(\mathbf{r})]\, n(\lambda) \\ &+[V_\alpha^n(\mathbf{r})^*\nabla U_\alpha^n(\mathbf{r}) - \nabla V_\alpha^n(\mathbf{r})^* U_\alpha^n(\mathbf{r})] \\ &\times[1-n(\lambda)] - \frac{e^2}{m}\mathbf{A}(\mathbf{r})\,[U_\alpha^n(\mathbf{r})^* U_\alpha^n(\mathbf{r}) \\ &\times n(\lambda) + V_\alpha^n(\mathbf{r})^* V_\alpha^n(\mathbf{r})(1-n(\lambda))]\end{aligned} \quad (7.115)$$

Keeping only terms to first order in the vector potential, we have

$$\langle J_i(\mathbf{r})\rangle = -2\left(\frac{e\hbar}{m}\right)^2 \frac{1}{V} \times \sum_{\mathbf{k}} k_i k_j A_j \frac{\partial n}{\partial\lambda} - \frac{e^2 n_e}{m}\mathbf{A}(\mathbf{r}) \quad (7.116)$$

where the total electron density is

$$n_e = \frac{2}{V}\sum_n \Big[|u(\mathbf{k})|^2 n(\lambda) - |v(\mathbf{k})|^2 (1-n(\lambda))\Big] \quad (7.117)$$

The current density induced by the applied field is

$$\langle J_i(\mathbf{r})\rangle = -\frac{e^2 n_s}{m}\mathbf{A}(\mathbf{r}) \quad (7.118)$$

where the "density of super-electrons" is

$$n_s = n_e - \frac{2}{3}\left(\frac{e\hbar}{m}\right)^2 \frac{1}{V}\sum_{\mathbf{k}} k^2\left(-\frac{\partial n}{\partial\lambda}\right) \quad (7.119)$$

and we have used rotational symmetry to write

$$\sum_{\mathbf{k}} k_i k_j \frac{\partial n}{\partial\lambda} = \frac{1}{3}\delta_{ij}\sum_{\mathbf{k}} k^2 \frac{\partial n}{\partial\lambda} \quad (7.120)$$

Note that at zero temperature the second factor in Eq. (7.119) vanishes, and the density of super-electrons is equal to the total density of electrons.

If we substitute our expression (7.118) into Ampere's law, we have London's equation

$$\nabla\times(\nabla\times\mathbf{A}) = \lambda_L^{-2}\mathbf{A} \quad (7.121)$$

where the London penetration depth, λ_L, is given by

$$\lambda_L^{-2} = \mu_0\frac{e^2 n_s}{m} \quad (7.122)$$

The perfect diamagnetism that is characteristic of superconductors is embodied in Eq. (7.121).

APPENDIX A. DERIVATION OF THE GAP EQUATION NEAR T_C

The order parameter is given by

$$\Psi_{\alpha\beta}(\mathbf{k}) = Z^{-1} Tr\; e^{-\beta H} a_\alpha(\mathbf{k}) a_\beta(-\mathbf{k}) \quad (A.1)$$

The BCS Hamiltonian, (7.39), is bilinear in the electron operators, which means thermal averages of the type (A.1) can be calculated by purely algebraic means.
First, we introduce the Bloch operators

$$a_\alpha(\mathbf{k},\tau) = e^{\tau H} a_\alpha(\mathbf{k}) e^{-\tau H} \tag{A.2}$$

The equation for the order parameter can be written as

$$\begin{aligned}\Psi_{\alpha\beta}(\mathbf{k}) &= Z^{-1} Tr\ e^{-\beta H} a_\alpha(\mathbf{k}) e^{-\beta H} e^{\beta H} a_\beta(-\mathbf{k}) \\ &= Z^{-1} Tr\ e^{-\beta H} a_\beta(-\mathbf{k},\beta) a_\alpha(\mathbf{k})\end{aligned} \tag{A.3}$$

where we've used the cyclic property of the trace.

Near the transition temperature the symmetry breaking terms in the BCS Hamiltonian are small and can be treated as a perturbation, so we split the Hamiltonian into two parts, $H = H_0 + H_1$ where

$$H_0 = \sum_{\sigma,\mathbf{k}} E_\sigma(\mathbf{k}) a^+_\sigma(\mathbf{k}) a_\sigma(\mathbf{k}) \tag{A.4}$$

and

$$\begin{aligned}H_1 = \frac{1}{2}\sum_{\mathbf{k}} \big[& a^\dagger_\alpha(\mathbf{k}) \Delta_{\alpha\beta}(\mathbf{k}) a^\dagger_\beta(-\mathbf{k}) \\ & - a_\alpha(\mathbf{k}) \Delta^*_{\alpha\beta}(\mathbf{k}) a_\beta(-\mathbf{k}) \big]\end{aligned} \tag{A.5}$$

In the interaction picture we write

$$e^{-\tau H} = e^{-\tau H_0} K(\tau) \tag{A.6}$$

where $K(\tau)$ satisfies

$$-\frac{dK(\tau)}{d\tau} = H_1(\tau) K(\tau) \tag{A.7}$$

with

$$\begin{aligned}H_1(\tau) &= e^{\tau H_0} H_1 e^{-\tau H_0} \\ &= \frac{1}{2}\sum_{\mathbf{k}\alpha\beta} \Big[e^{\tau\left(E_\alpha(\mathbf{k}) + E_\beta(-\mathbf{k})\right)} a^\dagger_\alpha(\mathbf{k}) a^\dagger_\beta \\ &\quad \times (-\mathbf{k}) \Delta_{\alpha\beta}(\mathbf{k}) + -\Delta_{\alpha\beta}(\mathbf{k})^* \\ &\quad \times e^{-r\left(E_\alpha(\mathbf{k}) + E_\beta(-\mathbf{k})\right)} a_\alpha(\mathbf{k}) a_\beta(-\mathbf{k}) \Big]\end{aligned} \tag{A.8}$$

Integrating (A.7) to first order gives

$$\begin{aligned}K(\tau) &= 1 - \int_0^\tau d\tau' H_1(\tau') \\ &= 1 - \frac{1}{2}\sum_{\mathbf{k}} \Bigg[\frac{e^{\tau\left(E_\alpha(\mathbf{k}) + E_\beta(-\mathbf{k})\right)} - 1}{E_\alpha(\mathbf{k}) + E_\beta(-\mathbf{k})} \\ &\quad \times a^\dagger_\alpha(\mathbf{k}) a^\dagger_\beta(-\mathbf{k}) \Delta_{\alpha\beta}(\mathbf{k}) \\ &\quad - \Delta^*_{\alpha\beta}(\mathbf{k}) \frac{1 - e^{-\tau\left(E_\alpha(\mathbf{k}) + E_\beta(-\mathbf{k})\right)}}{E_\alpha(\mathbf{k}) + E_\beta(-\mathbf{k})} \\ &\quad \times a_\alpha(\mathbf{k}) a_\beta(-\mathbf{k}) \Big]\end{aligned} \tag{A.9}$$

We then have for $a_\alpha(\mathbf{k},\tau)$ to first order

$$\begin{aligned}a_\alpha(\mathbf{k},\tau) &= e^{-\tau E_\alpha(\mathbf{k})} K^{-1}(\tau) a_\alpha(\mathbf{k}) K(\tau) \\ &= e^{-\tau E_\alpha(\mathbf{k})} \Bigg\{ a_\alpha(\mathbf{k}) + \frac{1}{2}\sum_{\mathbf{p}\mu\nu} \frac{e^{\tau\left(E_\mu(\mathbf{p}) + E_\nu(-\mathbf{p})\right)} - 1}{E_\mu(\mathbf{p}) + E_\nu(-\mathbf{p})} \\ &\quad \times \left[a^\dagger_\mu(\mathbf{p}) a^\dagger_\nu(-\mathbf{p}), a_\alpha(\mathbf{k}) \right] \Delta_{\mu\nu}(\mathbf{p}) \Bigg\} = e^{-\tau E_\alpha(\mathbf{k})} a_\alpha \\ &\quad \times (\mathbf{k}) + \frac{1}{2} e^{-\tau E_\alpha(\mathbf{k})} \sum_{\mathbf{p}\mu\nu} \frac{e^{\tau\left(E_\mu(\mathbf{p}) + E_\nu(-\mathbf{p})\right)} - 1}{E_\mu(\mathbf{p}) + E_\nu(-\mathbf{p})} \Delta_{\mu\nu}(\mathbf{p}) \\ &\quad \times \left[a^\dagger_\mu(\mathbf{p}) \delta_{\nu\alpha}(\mathbf{k}, -\mathbf{p}) - \delta_{\mu\alpha}(\mathbf{k}, \mathbf{p}) a^\dagger_\nu(-\mathbf{p}) \right] \\ &= e^{-\tau E_\alpha(\mathbf{k})} a_\alpha(\mathbf{k}) - e^{-\tau E_\alpha(\mathbf{k})} \\ &\quad \times \sum_{\mathbf{p}\mu} \frac{e^{\tau\left(E_\mu(-\mathbf{k}) + E_\alpha(\mathbf{k})\right)} - 1}{E_\mu - (\mathbf{k}) + E_\alpha(\mathbf{k})} \Delta_{\alpha\mu}(\mathbf{k}) a^\dagger_\mu(-\mathbf{p})\end{aligned} \tag{A.10}$$

Inserting this into (A.3) we have

$$\begin{aligned}\Psi_{\alpha\beta}(\mathbf{k}) &= \langle a_\beta(-\mathbf{k},\beta) a_\alpha(\mathbf{k}) \rangle \\ &= e^{-\tau E_\beta(-\mathbf{k})} \Psi_{\beta\alpha}(-\mathbf{k}) - e^{-\tau E_\beta(-\mathbf{k})} \\ &\quad \times \sum_{\mathbf{p}\mu} \frac{e^{\tau\left(E_\alpha(\mathbf{k}) + E_\beta(-\mathbf{k})\right)} - 1}{E_\alpha(\mathbf{k}) + E_\beta(-\mathbf{k})} \Delta_{\beta\alpha}(-\mathbf{k}) n(E_\alpha)\end{aligned} \tag{A.11}$$

where $n(E_\alpha) = \langle a^\dagger_\alpha(\mathbf{p}) a_\alpha(\mathbf{k}) \rangle = (e^{\beta E_\alpha} + 1)^{-1}$ is the usual Fermi-Dirac occupation function.

Using the antisymmetry of the order parameter, (A.11) can be written as

$$\begin{aligned}\Psi_{\alpha\beta}(\mathbf{k}) &= \frac{e^{-\beta E_\beta(-\mathbf{k})}}{1+e^{\tau E_\beta(-\mathbf{k})}} \\ &\quad\times \frac{e^{\beta\left(E_\alpha(\mathbf{k})+E_\beta(-\mathbf{k})\right)}-1}{E_\alpha(\mathbf{k})+E_\beta(\mathbf{k})}\Delta_{\alpha\beta}(\mathbf{k})n(E_\alpha) \\ &= n[E_\beta(-\mathbf{k})]n[E_\alpha(\mathbf{k})] \\ &\quad\times \frac{e^{\beta\left(E_\alpha(\mathbf{k})+E_\beta(-\mathbf{k})\right)-1}}{E_\alpha(\mathbf{k})+E_\beta(\mathbf{k})}\Delta_{\alpha\beta}(\mathbf{k})\end{aligned} \tag{A.12}$$

With a little algebra we have

$$\Psi_{\alpha\beta}(\mathbf{k}) = \frac{1-n[E_\beta(-\mathbf{k})]-n[E_\alpha(\mathbf{k})]}{E_\alpha(\mathbf{k})+E_\beta(-\mathbf{k})}\Delta_{\alpha\beta}(\mathbf{k}) \tag{A.13}$$

If we now use the definition of the gap function, (A.13) becomes Eq. (7.60).

$$\begin{aligned}\Psi_{\alpha\beta}(\mathbf{k}) &= \frac{1-n[E_\beta(-\mathbf{k})]-n[E_\alpha(\mathbf{k})]}{E_\alpha(\mathbf{k})+E_\beta(-\mathbf{k})} \\ &\quad\times \sum_{\mathbf{p}} V_{\alpha\beta;\mu\nu}(\mathbf{k};\mathbf{p})\Psi_{\mu\nu}(\mathbf{p})\end{aligned} \tag{A.14}$$

FURTHER READING

Some of the classical articles on the BCS theory have already been mentioned at the beginning of the chapter. The article by Cooper (1956), predicting the formation of the "pairs" that bear his name, provided the setting for the BCS theory formulated by Bardeen, Cooper, and Schrieffer in 1957, and elaborated upon in the books by de Gennes (1966), Fetter and Walecka (1971), and Schrieffer (1964).

The textbook by Tinkham (1985) provides a good introduction to the BCS theory, and Tilley and Tilley (1986) give a briefer introduction.

Gorkov (1959) showed that the Ginzburg–Landau theory, which was discussed in the previous chapter, follows from the BCS theory. This provided a solid theoretical foundation for the GL theory.

Chapters 4–14 of the book, Theories of High Temperature Superconductivity (Halley, 1988), discuss applications of the BCS theory. Allen (1990) reviewed the BCS approach to electron pairing. The pairing state in $YBa_2Cu_3O_{7-\delta}$ is discussed by Annett *et al*. (1990). We will cite some representative articles.

The weak and strong limits of BCS have been discussed (Carbotte (1990), Cohen, 1987; Cohen and Penn, 1990; Entin-Wohlman and Imry, 1989; Nasu, 1990). There is a crossover between a BCS proper regime of weakly coupled, real space-overlapping Cooper pairs and a Bose–Einstein regime involving a low density boson gas of tightly bound fermion pairs (Pistolesi and Strinati, 1994; Quick *et al*., 1993; Tokumitu *et al*., 1993). The BCS theory has been applied to high temperature superconductors (Berlinsky *et al*., 1993; Ihm and Yu, 1989; Japiassu *et al*., 1992; Jarrell *et al*., 1988; Kitazawa and Tajima, 1990; Lal and Joshi, 1992; Lu *et al*., 1989; Marsiglio, 1991; Marsiglio and Hirsch, 1991; Penn and Cohen, 1992; Pint and Schachinger, 1991; Sachdev and Wang, 1991).

The present chapter, although based in part on the electron–phonon coupling mechanism (Jiang and Carbotte, 1992b; Kirkpatrick and Belitz, 1992; Kresin *et al*., 1993; Marsiglio and Hirsch, 1994; Nicol and Carbotte, 1993; Zheng *et al*., 1994), is nevertheless much more general in its formalism. Unconventional phonon or nonphonon coupling can also occur (Annett *et al*. (1991), Bussmmann-Holder and Bishop, 1991; Cox and Maple, 1995; Dobroliubov and Khlebnikov, 1991; Keller, 1991; Klein and Aharony, 1992; Krüger, 1989; Spathis *et al*., 1992; Tsay *et al*., 1991; Van Der Marel, 1990), involving, for example, excitons (Bala and Olés, 1993; Gutfreund and Little, 1979; Takada, 1989), plasmons (quantized plasma oscillations; Côte and Griflin, 1993; Cui and Tsai, 1991; Ishii and Ruvalds, 1993), polaritons (Lue and Sheng, 1993), polarons (electron plus induced lattice polarization; Kabanov and Mashtakov, 1993; Konior, 1993; Nettel and MacCrone, 1993; Wood and Cooke, 1992) and bipolarons (de Jongh, 1992; Emin, 1994; Khalfin and Shapiro, 1992). Both *s*-wave and *d*-wave pairings have been considered (Anlage *et al*., 1994; Carbotte and Jiang, 1993; Côte and Griflin, 1993; Lenck and Carbotte, 1994; Li *et al*., 1993; Scalapino, 1995; Wengner and Östlund, 1993; Won and Maki, 1994). Kasztin and Leggett (1997) discussed the nonlocality of d-wave superconductivity, Prozovov and Giannetta (2006) examined the electrodynamics of unconventional pairing, and Hirsch feld and Golden feld (1993) commented on the effects of impurities.

Some authors question the applicability of BCS to high temperature superconductors (Collins *et al*., 1991; Kurihara, 1989). Tesanovic and Rasolt (1989) suggested a new type of superconductivity in very high magnetic fields in which there is no upper critical field. The BCS theory has been examined in terms of the Hubbard (Falicov and Proetto, 1993; Micnas *et al*., 1990; Sofo *et al*., 1992) and Fermi liquid (Horbach *et al*., 1993, Ramakumar, 1993) approaches, which are discussed in Chapter 10.

Carbotte (1990) reviewed Eliashberg (1960a, b) theory and its relationship with BCS. Representative articles concern (a) high temperature superconductors (Jin *et al*., 1992; Lu *et al*., 1989; Marsiglio, 1991; Monthoux and Pines, 1994; Sulewski *et al*., 1987; Wermbter and Tewordt, 1991a; Williams and Carbotte, 1991), (b) anisotropies (Combescot, 1991; Lenck *et al*., 1990; Radtke *et al*., 1993; Zhao and Callaway, 1994), (c) transport properties (Kulic and Zeyher, 1994; Ullah and Dorsey, 1991), (d) weak coupling limits (Combescot, 1990; Crisan, 1887), and (e) strong coupling limits (Bulaevskii *et al*., 1988; Heid, 1992 (Pb); Rammer, 1991).

This page intentionally left blank

8

Cuprate Crystallographic Structures

I. INTRODUCTION

Chapter 3 shows that the majority of single-element crystals have highly symmetrical structures, generally fcc or bcc, in which their physical properties are the same along the three crystallographic directions x, y, and z. The NaCl-type and *A*15 compounds are also cubic. Some compounds do have lower symmetries, showing that superconductivity is compatible with many different types of crystallographic structure, but higher symmetries are certainly more common. In this chapter we will describe the structures of the high-temperature superconductors, almost all which are either tetragonal or orthorhombic, but close to tetragonal.

In Chapter 3, we also gave some examples of the role played by structure in determining the properties of superconductors. The highest transition temperatures in alloys of transition metals are at the boundaries of instability between the bcc and hcp forms. The NaCl-type compounds have ordered vacancies on one or another lattice site. The magnetic and superconducting properties of the Chevrel phases depend on whether the large magnetic cations (i.e., positive ions) occupy eightfold sites surrounded by chalcogenide ions, or whether the small magnetic ions occupy octahedral sites surrounded by Mo ions.

The structures described here are held together by electrons that form ionic or covalent bonds between the atoms. No account

is taken of the conduction electrons, which are delocalized over the copper oxide planes and form the Cooper pairs responsible for the superconducting properties below T_c. The later Chapter 10 will be devoted to explaining the role of these conduction electrons within the frameworks of the Hubbard model and band theory. Whereas the present chapter describes atom positions in coordinate space, the Hubbard Model/Band Structure chapter relies on a reciprocal lattice elucidation of these same materials.

We begin with a description of the perovskite structure and explain some reasons that perovskite undergoes various types of distortions. This prototype exhibits a number of characteristics that are common to the high-temperature superconducting cuprates (see Section V). We will emphasize the structural commonalities of these materials and make frequent comparisons between them. Our earlier work (Poole *et al.*, 1988) and the comprehensive review by Yvon and François (1989) may be consulted for more structural detail on the atom positions, interatomic spacings, site symmetries, etc., of these compounds. There have been reports of superconductivity in certain other cuprate structures (e.g., Murphy *et al.*, 1987), but these will not be reported on in this chapter.

There is a related series of layered compounds $Bi_2O_2(M_{m-1}R_mO_{3m+1})$ called Aurivillius (1950, 1951, 1952) phases, with the 12-coordinated $M = $ Ca, Sr, Ba, Bi, Pb, Cd, La, Sm, Sc, etc., and the 6-coordinated transition metal $R =$ Nb, Ti, Ta, W, Fe, etc. The $m = 1$ compound Bi_2NbO_6 belongs to the same tetragonal space group $I4/mmm$, D_{4h}^{17} as the lanthanum, bismuth, and thallium high temperature superconductors (Medvedeva *et al.*, 1993).

We assume that all samples are well made and safely stored. Humidity can affect composition, and Garland (1988) found that storage of $YBa_2Cu_3O_{7-\delta}$ in 98% humidity exponentially decreased the diamagnetic susceptibility with a time constant of 22 days.

II. PEROVSKITES

Much has been written about the high-temperature superconductors being perovskite types. The prototype compound barium titanate, $BaTiO_3$, exists in three crystallographic forms with the following lattice constants and unit cell volumes (Wyckoff, 1964):

cubic:	$a = b = c =$ 4.0118 Å	$V = 64.57$ Å^3	
tetragonal:	$a = b = 3.9947$, $c = 4.0336$	$V = 64.37$ Å^3	(8.1)
ortho rhombic:	$a = 4.009\sqrt{2}$ Å, $b = 4.018\sqrt{2}$ Å, $c = 3.990$ Å	$V = 2(64.26)$ Å^3	

A. Cubic Form

Above 201 °C barium titanate is cubic and the unit cell contains one formula unit $BaTiO_3$ with a titanium atom on each apex, a barium atom in the body center, and an oxygen atom on the center of each edge of the cube, as illustrated in Fig. 8.1. This corresponds to the barium atom, titanium atom, and three oxygen atoms being placed

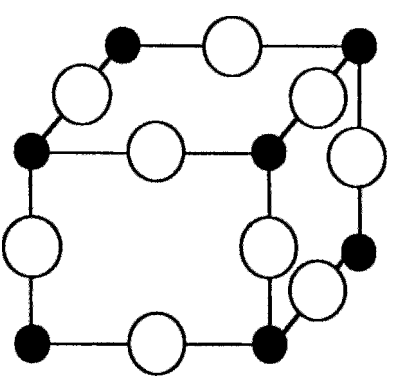

Figure 8.1 Barium titanate ($BaTiO_3$) perovskite cubic unit cell showing titanium (small black circles) at the vertices and oxygen (large white circles) at the edge-centered positions. Ba, not shown, is at the body center position (Poole *et al.*, 1988, p. 73).

in positions with the following x, y, and z coordinates:

E site: Ti	$(0, 0, 0)$	Ti on apex
F site: O	$(0, 0, \frac{1}{2})$; $(0, \frac{1}{2}, 0)$; $(\frac{1}{2}, 0, 0)$	three oxygens centered on edges
C site: Ba	$(\frac{1}{2}, \frac{1}{2}, \frac{1}{2})$	Ba in center.

(8.2)

The barium in the center has 12 nearest-neighbor oxygens, so we say that it is 12-fold coordinated, while the titanium on each apex has 6-fold (octahedral) coordination with the oxygens, as may be seen from the figure. (The notation E for edge, F for face, and C for center is adopted for reasons that will become clear in the discussion which follows.) Throughout this chapter we will assume that the z-axis is oriented vertically, so that the x and y axes lie in the horizontal plane.

Ordinarily, solid-state physics texts place the origin (0, 0, 0) of the perovskite unit cell at the barium site, with titanium in the center and the oxygens at the centers of the cube faces. Our choice of origin facilitates comparison with the structures of the oxide superconductors.

This structure is best understood in terms of the sizes of the atoms involved. The ionic radii of O^{2-} (1.32 Å) and Ba^{2+} (1.34 Å) are almost the same, as indicated in Table 8.1, and together they form a perfect fcc lattice with the smaller Ti^{4+} ions (0.68 Å) located in octahedral holes surrounded entirely by oxygens. The octahedral holes of a close-packed oxygen lattice have a radius of 0.545 Å; if these holes were empty the lattice constant would be $a = 3.73$ Å, as noted in Fig. 8.2a. Each titanium pushes the surrounding oxygens outward, as shown in Fig. 8.2b, thereby increasing the lattice constant. When the titanium is replaced by a larger atom, the lattice constant expands further, as indicated by the data in the last column of Table 8.2. When Ba is

Table 8.1 Ionic Radii for Selected Elements[a]

Small	Cu^{2+}	0.72 Å	Y^{3+}	0.89 Å
	Bi^{5+}	0.74 Å		
Small-Medium	Cu^{+}	0.96 Å	Tl^{3+}	0.95 Å
	Ca^{2+}	0.99 Å	Bi^{3+}	0.96 Å
	Nd^{3+}	0.995 Å		
Medium-Large	La^{3+}	1.06 Å	Sr^{2+}	1.12 Å
	Hg^{2+}	1.10 Å		
Large	Pb^{2+}	1.20 Å	Ag^{+}	1.26 Å
	K^{+}	1.33 Å	O^{2-}	1.32 Å
	Ba^{2+}	1.34 Å	F^{-}	1.33 Å

[a] See Table VI-2 of Poole *et al.* (1988) for a more extensive list.

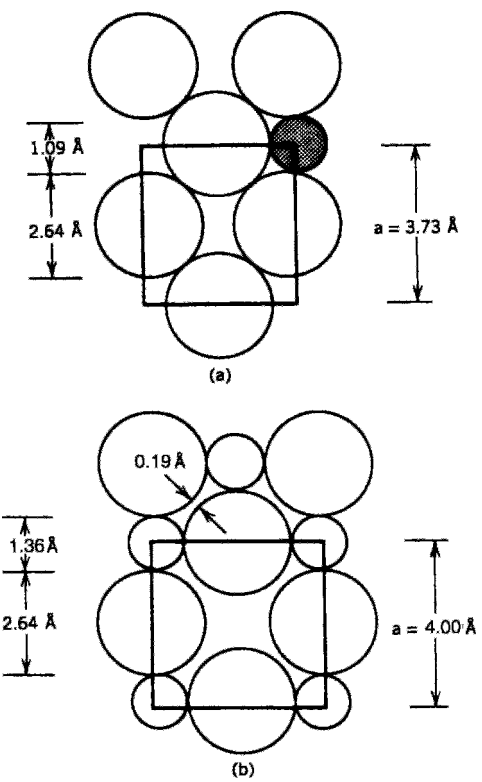

Figure 8.2 Cross section of the perovskite unit cell in the $z = 0$ plane showing (a) the size of the octahedral hole (shaded) between oxygens (large circles), and (b) oxygens pushed apart by the transition ions (small circles) in the hole sites. For each case the lattice constant is indicated on the right and the oxygen and hole sizes on the left (Poole *et al.*, 1988, p. 77).

Table 8.2 Dependence of the Lattice Constants *a* of Selected Perovskites AMO_3 on the Alkaline Earth *A* (right) and the Ionic Radius of Transition Metal Ion *M* (left); the Alkaline Earth Ionic Radii are 0.99 Å (Ca), 1.12 Å (Sr), and 1.34 Å (Ba[a])

Transition metal	Transition metal radius, Å	Lattice constant *a*, Å		
		Ca	Sr	Ba
Ti	0.68	3.84	3.91	4.01
Fe	—	—	3.87	4.01
Mo	0.70	—	3.98	4.04
Sn	0.71	3.92	4.03	4.12
Zr	0.79	4.02	4.10	4.19
Pb	0.84	—	—	4.27
Ce	0.94	3.85	4.27	4.40
Th	1.02	4.37	4.42	4.80

[a] Data from Wyckoff (Vol. 2, 1964, pp. 391ff).

replaced by the smaller Ca (0.99 Å) and Sr (1.12 Å) ions, by contrast, there is a corresponding decrease in the lattice constant, as indicated by the data in columns 3 and 4, respectively, of Table 8.2. All three alkaline earths, Ca, Sr, and Ba, appear prominently in the structures of the high-temperature superconductors.

B. Tetragonal Form

At room temperature barium titanate is tetragonal and the deviation from cubic, $(c-a)/\frac{1}{2}(c+a)$, is about 1%. All of the atoms have the same *x, y* coordinates as in the cubic case, but are shifted along the *z*-axis relative to each other by ≈ 0.1 Å, producing the puckered arrangement shown in Fig. 8.3. The distortions from the ideal structure are exaggerated in this sketch. The puckering bends the Ti–O–Ti group so that the Ti–O distance increases while the Ti–Ti distance remains almost the same. This has the effect of providing more room for the titanium atoms to fit in their lattice sites. We will see later that a similar puckering distortion occurs in the high-temperature superconductors as a way of providing space for the Cu atoms in the planes.

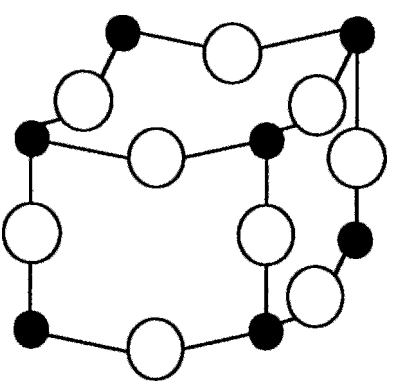

Figure 8.3 Perovskite tetragonal unit cell showing puckered Ti–O layers that are perfectly flat in the cubic cell of Fig. 8.1. The notation of Fig. 8.1 is used (Poole *et al*., 1988, p. 75).

C. Orthorhombic Form

There are two principal ways in which a tetragonal structure distorts to form an orthorhombic phase. The first, shown at the top of Fig. 8.4, is for the *b*-axis to stretch relative to the *a*-axis, resulting in the formation of a rectangle. The second, shown at the bottom of the figure, is for one diagonal of the *ab* square to stretch and the other diagonal to compress, resulting in the formation of a rhombus. The two diagonals are perpendicular, rotated by 45° relative to the

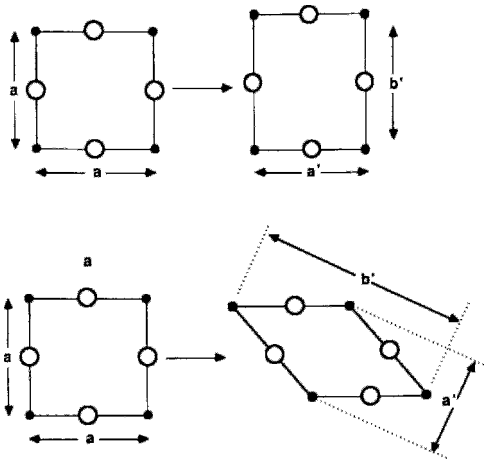

Figure 8.4 Rectangular- (top) and rhombal- (bottom) type distortions of a two-dimensional square unit cell of width a (Poole *et al.*, 1989).

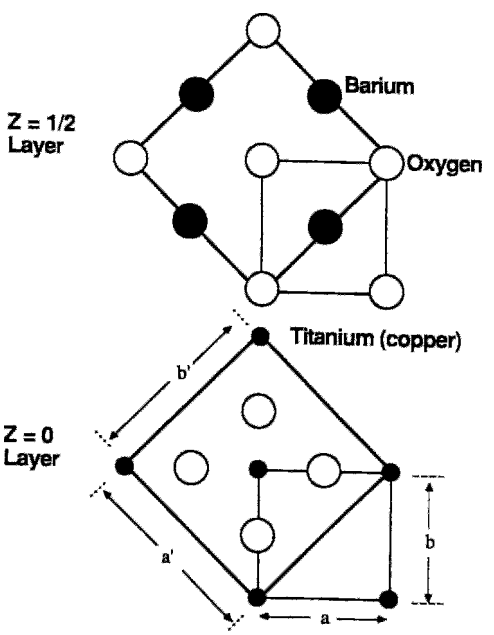

Figure 8.5 Rhombal expansion of monomolecular tetragonal unit cell (small squares, lower right) to bimolecular orthorhombic unit cell (large squares) with new axes 45° relative to the old axes. The atom positions are shown for the $z = 0$ and $z = \frac{1}{2}$ layers (Poole *et al.*, 1988, p. 76).

original axes, and become the a', b' dimensions of the new orthorhombic unit cell, as shown in Fig. 8.5. These a', b' lattice constants are $\approx \sqrt{2}$ times longer than the original constants, so that the volume of the unit cell roughly doubles; thus, it contains exactly twice as many atoms. (The same $\sqrt{2}$ factor appears in Eq. 8.1 in our discussion of the lattice constants for the orthorhombic form of barium titanate.)

When barium titanate is cooled below 5 °C it undergoes a diagonal- or rhombal-type distortion. The atoms have the same z coordinates ($z = 0$ or $\frac{1}{2}$) as in the cubic phase, so the distortion occurs entirely in the x, y-plane, with no puckering of the atoms. The deviation from tetragonality, as given by the percentage of anisotropy,

$$\%\ \text{ANIS} = \frac{100|b-a|}{\frac{1}{2}(b+a)} = 0.22\%, \qquad (8.3)$$

is less than that of most orthorhombic copper oxide superconductors. We see from Fig. 8.5 that in the cubic phase the oxygen atoms in the $z = 0$ plane are separated by 0.19 Å. The rhombal distortion increases this O–O separation in one direction and decreases it in the other, in the manner indicated in Fig. 8.6a, to produce the Ti nearest-neighbor configuration shown in Fig. 8.6b. This arrangement helps to fit the titanium into its lattice site.

The transformation from tetragonal to orthorhombic is generally of the rhombal type for $(La_{1-x}Sr_x)_2CuO_4$ and of the rectilinear type for $YBa_2Cu_3O_{7-\delta}$.

D. Planar Representation

Another way of picturing the structure of perovskite is to think of the atoms as forming horizontal planes. If we adopt the notation [E F C] to designate the occupation of the E, F, and C sites, the sketches of perovskite presented in Figs. 8.1 and 8.3 follow the scheme

$z = 1$	$[TiO_2–]$	Ti at E, O at two F sites
$z = \frac{1}{2}$	[O–Ba]	O at E, Ba at C
$z = 0$	$[TiO_2–]$	Ti at E, O at two F sites

(8.4)

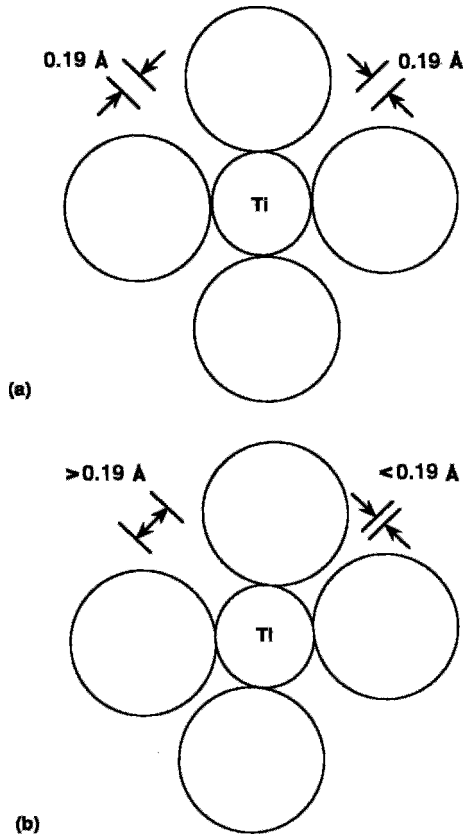

Figure 8.6 Shift of the oxygens (large circles) in the *a, b*-plane around the titanium atom (small circle) of perovskite from the room-temperature tetragonal (and cubic) configuration (a) to the rhombal configuration (b) of its low-temperature orthorhombic structure.

The planes at the heights $z = 0$, $\frac{1}{2}$, and 1 can be labeled using this notation. The usefulness of this labeling scheme will be clarified in Section V.

This completes our treatment of the structure of perovskite. We encountered many features that we will meet again in the analogous superconductor cases, and we established notation that will be useful in describing the structure of the cuprates. In Section V of Chapter 9 we will discuss several cubic and close-to-cubic perovskite superconducting compounds.

III. PEROVSKITE-TYPE SUPERCONDUCTING STRUCTURES

In their first report on high-temperature superconductors Bednorz and Müller (1986) referred to their samples as "metallic, oxygen-deficient . . . perovskite-like mixed-valence copper compounds." Subsequent work has confirmed that the new superconductors do indeed possess these characteristics.

In the oxide superconductors Cu^{2+} replaces the Ti^{4+} of perovskite, and in most cases the TiO_2-perovskite layering is retained as CuO_2 layers, which is common to all of the high-temperature superconductors; such superconductors exhibit a uniform lattice size in the *a*, *b*-plane, as the data in Table 8.3 demonstrate. The compound $BaCuO_3$ does not occur because the Cu^{4+} ion does not form, but this valence constraint is overcome by replacement of Ba^{2+} by a trivalent ion, such as La^{3+} or Y^{3+}, by a reduction in the oxygen content, or by both. The result is a set of "layers" containing only one oxygen per cation located between each pair of CuO_2 layers, or none at all. Each high-temperature superconductor has a unique sequence of layers.

We saw from Eq. (8.2) that each atom in perovskite is located in one of three types of sites. In like manner, each atom at the height z in a high-temperature superconductor occupies either an Edge (E) site on the edge (0, 0, *z*), a Face (F) site on the midline of a face ((0, $\frac{1}{2}$, *z*) or ($\frac{1}{2}$, 0, *z*) or both), or a Centered (C) site centered within the unit cell on the *z*-axis ($\frac{1}{2}$, $\frac{1}{2}$, *z*). The site occupancy notation [E F C] is used because many cuprates contain a succession of [Cu O_2 –] and [– O_2 Cu] layers in which the Cu atom switches between edge and centered sites, with the oxygens remaining at their face positions. Similar alternations in position take place with Ba, O, and Ca layers, as illustrated in Fig. 8.7.

Hauck *et al.* (1991) proposed a classification of superconducting oxide structures

Table 8.3 Crystallographic Characteristics of Oxide Superconducting and Related Compounds[a]

Compound	Code	Symm	Type	Enlarg.	Form. Units	a_0(Å)	c_0(Å)	c_0/Cu	%Anis	T_c(K)	Comments
$BaTiO_3$	—	C	A	1	1	4.012	4.012	—	0	—	T > 200 °C
$BaTiO_3$	—	T	A	1	1	3.995	4.03	—	0	—	20 °C
$BaTiO_3$	—	O	A	$\sqrt{2}$	2	$4.013\sqrt{2}$	3.990	—	0.23	—	T < 5 °C
$BaPbO_3$	—	C	A	1	1	4.273	4.273	—	0	0.4	
$BaPb_{0.7}Bi_{0.3}O_3$	—	T	S	$\sqrt{2}$	4	$4.286\sqrt{2}$	4.304	—	0	12	
$BaBiO_3$	—	M	A	$\sqrt{2}$	2	$4.355\sqrt{2}$	4.335	—	0.13	—	$\beta = 90.17$
$Ba_{0.6}K_{0.4}BiO_3$	—	C	A	1	1	4.293	4.293	—	0	30	
La_2CuO_4	0201	T	S	1	2	3.81	13.18	6.59	0	35	Sr, doped
La_2CuO_4	0201	O	S	$\sqrt{2}$	4	$3.960\sqrt{2}$	13.18	6.59	6.85	35	Sr, doped
$YBa_2Cu_3O_6$	0212	T	A	1	1	3.902	11.94	3.98	0	—	
$YBa_2Cu_3O_8$	0212	O	A	1	1	3.855	11.68	3.89	1.43	92	
$Bi_2Sr_2CaCu_2O_8$	2212	O	S	$5\sqrt{2}$	20	$3.81\sqrt{2}$	30.6	7.65	0	84	
$Bi_2Sr_2Ca_2Cu_3O_{10}$	2223	O	S	$5\sqrt{2}$	20	$3.83\sqrt{2}$	37	6.17	0.57	110	
$Tl_2Ba_2CuO_6$	2201	T	S	1	2	3.83	23.24	11.6	0	90	
$Tl_2Ba_2CaCu_2O_8$	2212	T	S	1	2	3.85	29.4	7.35	0	110	
$Tl_2Ba_2Ca_2Cu_3O_{10}$	2223	T	S	1	2	3.85	35.88	5.98	0	125	
$TlBa_2CuO_5$	1201[b]	T	A	1	1	3.85	9.09	9.09	0	52	
$TlBa_2CaCu_2O_7$	1212	T	A	1	1	3.85	12.7	6.35	0	80	
$TlBa_2Ca_2Cu_3O_9$	1223[c]	T	A	1	1	3.81	15.2	5.1	0	120	
$TlBa_2Ca_3Cu_4O_{11}$	1234	T	A	1	1	3.85	19.0	4.75		114	
$TlBa_2Ca_4Cu_5O_{13}$	1245	T	A	1	1	3.85	22.3	4.42		101	
$HgBa_2CuO_4$	1201	T	A	1	1	3.86	9.5	9.5	0	95	
$HgBa_2CaCu_2O_6$	1212	T	A	1	1	3.86	12.6	6.3	0	122	
$HgBa_2Ca_2Cu_3O_8$	1223	T	A	1	1	3.86	17.7	5.2	0	133	

[a] Code symmetry (cubic C, tetragonal T, orthorhombic O, monclinic M); type (aligned A, staggered S); enlargement in *a, b*-plane (diagona distortion $\sqrt{2}$, superlattice 5); formula units per unit cell; lattice parameters (a_0, c_0, the single layer compound, and c_0 per Cu ion); % anisotropy; and transition temperature T_c. For the orthorhombic compounds tabulated values of a_0 are averages of a_0 and b_0. The single layer compound $Bi_2Sr_2CuO_6$ does not superconduct.

[b] 40% of Ba replaced by La;

[c] 50% of Tl replaced by Pb.

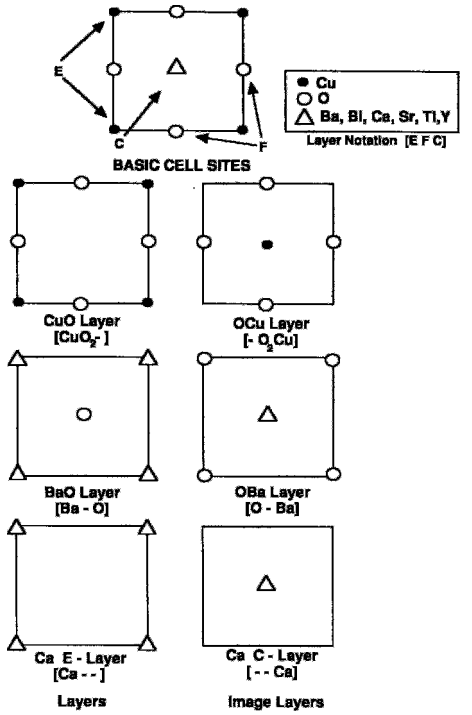

Figure 8.7 Types of atom positions in the layers of a high-temperature superconductor structure, using the edge, face, center notation [*E F C*]. Typical site occupancies are given in the upper right (Poole *et al.*, 1989).

in terms of the sequence (a) superconducting layers [Cu O_2 –] and [– O_2 Cu], (b) insulating layers, such as [Y – –] or [– – Ca], and (c) hole-donating layers, such as [Cu O^b –] or [Bi – O].

The high-temperature superconductor compounds have a horizontal reflection plane ($\perp$ to z) called σ_h at the center of the unit cell and another σ_h reflection plane at the top (and bottom). This means that every plane of atoms in the lower half of the cell at the height z is duplicated in the upper half at the height $1 - z$. Such atoms, of course, appear twice in the unit cell, while atoms right on the symmetry planes only occur once since they cannot be reflected. Figure 8.8 shows a [Cu O_2 –] plane at a height z reflected to the height $1 - z$. Note how the puckering preserves the reflection symmetry operation. Superconductors that have this reflection plane, but lack end-centering and

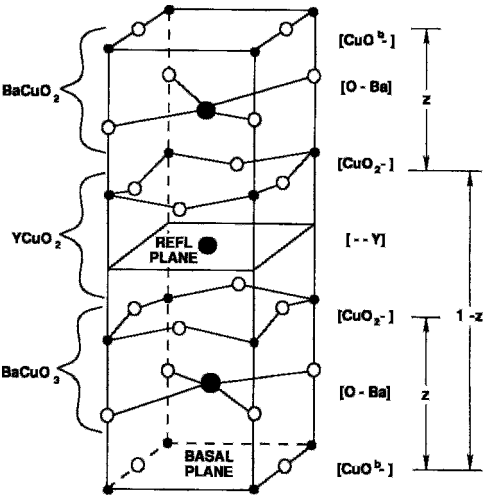

Figure 8.8 Unit cell of $YBa_2Cu_3O_7$ showing the molecular groupings, reflection plane, and layer types.

body-centering operations (see Section VII), are called *aligned* because all of their copper atoms are of one type; either all on the edge (0, 0, z) in E positions or all centered ($\frac{1}{2}$, $\frac{1}{2}$, z) at C sites. In other words, they all lie one above the other on the same vertical lines, as do the Cu ions in Fig. 8.8.

IV. ALIGNED $YBa_2Cu_3O_7$

The compound $YBa_2Cu_3O_7$, sometimes called YBaCuO or the 123 compound, in its orthorhombic form is a superconductor below the transition temperature $T_c \approx 92$ K. Figure 8.8 sketches the locations of the atoms, Fig. 8.9 shows the arrangement of the copper oxide planes, Fig. 8.10 provides more details on the unit cell, and Table 8.4 lists the atom positions and unit cell dimensions (Beno *et al.*, 1987; Capponi *et al.*, 1987; Hazen *et al.*, 1987; Jorgensen *et al.*, 1987; Le Page *et al.*, 1987; Siegrist *et al.*, 1987; Yan and Blanchin, 1991; see also Schuller *et al.*, 1987). Considered as a perovskite derivative, it can be looked upon as a stacking of three perovskite units $BaCuO_3$, $YCuO_2$, and $BaCuO_2$, two of them with a missing oxygen, and this explains why

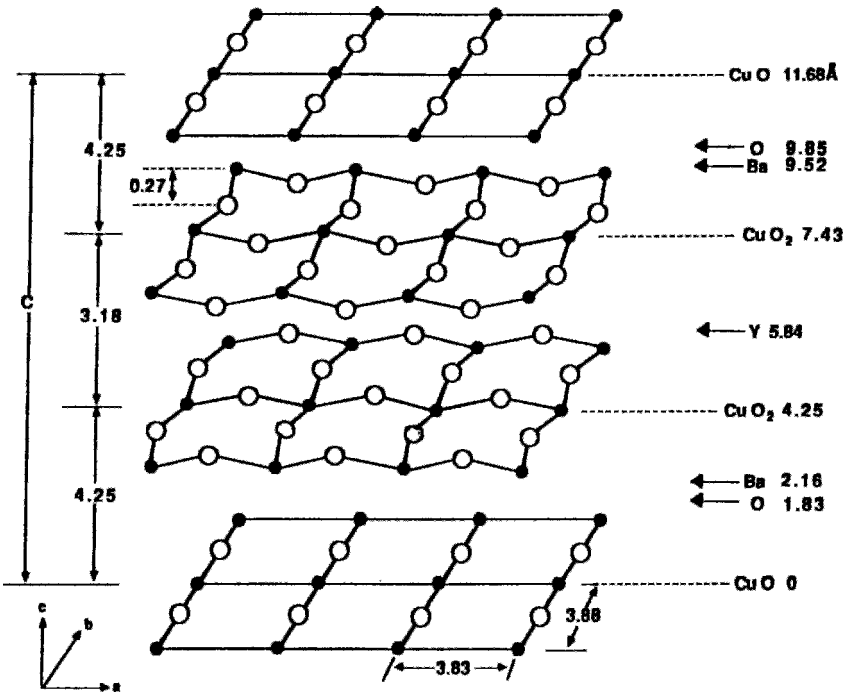

Figure 8.9 Layering scheme of orthorhombic $YBa_2Cu_3O_7$ with the puckering indicated. The layers are perpendicular to the *c*-axis (Poole *et al*., 1988, p. 101).

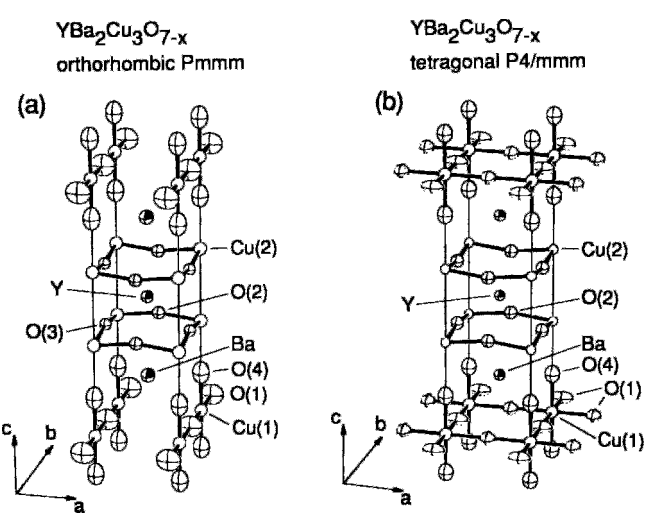

Figure 8.10 Sketches of the superconducting orthorhombic (left) and nonsuperconducting tetragonal (right) YBaCuO unit cells. Thermal vibration ellipsoids are shown for the atoms. In the tetragonal form the oxygen atoms are randomly dispersed over the basal plane sites (Jorgensen *et al*., 1987a, b; also see Schuller *et al*., 1987).

Table 8.4 Normalized Atom Positions in the $YBa_2Cu_3O_7$ Orthorhombic Unit Cell (dimensions $a = 3.83$ Å, $b = 3.88$ Å, and $c = 11.68$ Å)

Layer	Atom	x	y	z
[Cu O –]	Cu(1)	0	0	1
	O(1)	0	$\frac{1}{2}$	1
[O – Ba]	O(4)	0	0	0.8432
	Ba	$\frac{1}{2}$	$\frac{1}{2}$	0.8146
[Cu O_2 –]	Cu(2)	0	0	0.6445
	O(3)	0	$\frac{1}{2}$	0.6219
	O(2)	$\frac{1}{2}$	0	0.6210
[– – Y]	Y	$\frac{1}{2}$	$\frac{1}{2}$	$\frac{1}{2}$
[Cu O_2 –]	O(2)	$\frac{1}{2}$	0	0.3790
	O(3)	0	$\frac{1}{2}$	0.3781
	Cu(2)	0	0	0.3555
[O – Ba]	Ba	$\frac{1}{2}$	$\frac{1}{2}$	0.1854
	O(4)	0	0	0.1568
[Cu O –]	O(1)	0	$\frac{1}{2}$	0
	Cu(1)	0	0	0

$c \approx 3a$. It is, however, more useful to discuss the compound from the viewpoint of its planar structure.

A. Copper Oxide Planes

We see from Fig. 8.9 that three planes containing Cu and O are sandwiched between two planes containing Ba and O and one plane containing Y. The layering scheme is given on the right side of Fig. 8.8, where the superscript b on O indicates that the oxygen lies along the b-axis, as shown. The atoms are puckered in the two [Cu O_2 –] planes that have the [– – Y] plane between them. The third copper oxide plane [Cu O^b –], often referred to as "the chains," consists of –Cu–O–Cu–O– chains along the b axis in lines that are perfectly straight because they are in a horizontal reflection plane σ_h; where no puckering can occur. Note that, according to the figures, the copper atoms are all stacked one above the other on edge (E) sites, as expected for an aligned-type superconductor. Both the copper oxide planes and the chains contribute to the superconducting properties.

B. Copper Coordination

Now that we have described the planar structure of YBaCuO it will be instructive to examine the local environment of each copper ion. The chain copper ion Cu(1) is square planar-coordinated and the two coppers Cu(2) and Cu(3) in the plane exhibit fivefold pyramidal coordination, as indicated in Fig. 8.11. The ellipsoids at the atom positions of Fig. 8.10 provide a measure of

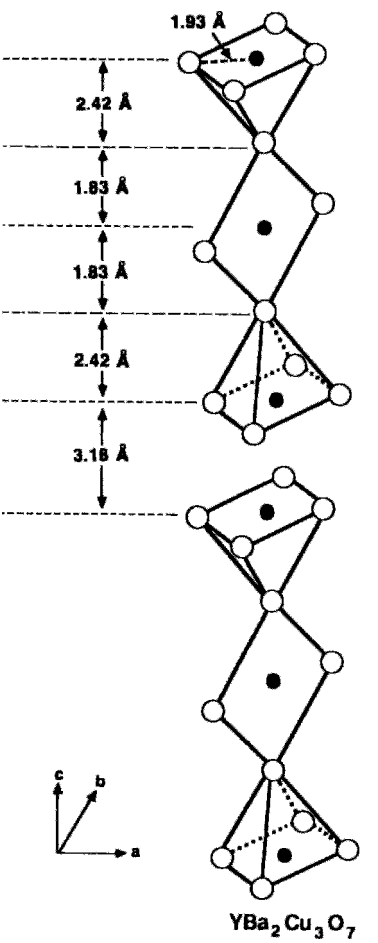

Figure 8.11 Stacking of pyramid, square-planar, and inverted pyramid groups along the c-axis of orthorhombic $YBa_2Cu_3O_7$ (adapted from Poole *et al.*, 1988, p. 100). Minor adjustments to make more room can be brought about by puckering or by distorting from tetragonal to orthorhombic.

the thermal vibrational motion which the atoms experience, since the amplitudes of the atomic vibrations are indicated by the relative size of each of the ellipsoids.

C. Stacking Rules

The atoms arrange themselves in the various planes in such a way as to enable them to stack one above the other in an efficient manner, with very little interference from neighboring atoms. Steric effects prevent large atoms such as Ba (1.34 Å) and O (1.32 Å) from overcrowding a layer or from aligning directly on top of each other in adjacent layers. In many cuprates stacking occurs in accordance with the following two empirical rules:

1. Metal ions occupy either edge or centered sites, and in adjacent layers alternate between E and C sites.
2. Oxygens are found in any type of site, but they occupy only one type in a particular layer, and in adjacent layers they are on different types of sites.

Minor adjustments to make more room can be brought about by puckering or by distorting from tetragonal to orthorhombic.

D. Crystallographic Phases

The $YBa_2Cu_3O_{7-\delta}$ compound comes in tetragonal and orthorhombic varieties, as shown in Fig. 8.10, and it is the latter phase which is ordinarily superconducting. In the tetragonal phase the oxygen sites in the chain layer are about half occupied in a random or disordered manner, and in the orthorhombic phase they are ordered into –Cu–O– chains along the *b* direction. The oxygen vacancy along the *a* direction causes the unit cell to compress slightly so that $a < b$, and the resulting distortion is of the rectangular type shown in Fig. 8.4a. Increasing the oxygen content so that $\delta < 0$ causes oxygens to begin occupying the vacant sites along *a*. Superlattice ordering of the chains is responsible for the phase that goes superconducting at 60 K.

YBaCuO is prepared by heating in the 750–900 °C range in the presence of various concentrations of oxygen. The compound is tetragonal at the highest temperatures, increases its oxygen content through oxygen uptake and diffusion (Rothman *et al.*, 1991) as the temperature is lowered, and undergoes a second-order phase transition of the order-disorder type at about 700 °C to the low-temperature orthorhombic phase, as indicated in Fig. 8.12 (Jorgensen *et al.*, 1987, 1990; Schuller *et al.*, 1987; cf. Beyers and Ahn, 1991; Metzger *et al.*, 1993; Fig. 8). Quenching by rapid cooling from a high temperature can produce at room temperature the tetragonal phase sketched on the right side of Fig. 8.10, and slow annealing favors the orthorhombic phase on the

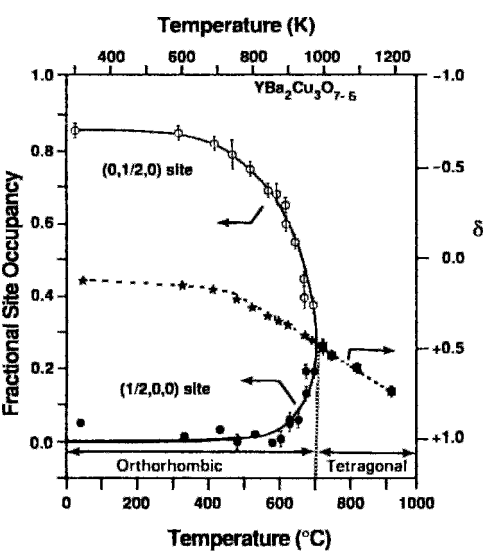

Figure 8.12 Fractional occupancies of the $\left(\frac{1}{2}, 0, 0\right)$ (bottom) and $\left(0, \frac{1}{2}, 0\right)$ (top) sites (scale on left), and the oxygen content parameter δ (center, curve scale on right) for quench temperatures of YBaCuO in the range 0–1000°C. The δ parameter curve is the average of the two site-occupancy curves (adapted from Jorgensen *et al.*, 1987a; also see Schuller *et al.*, 1987; see also Poole *et al.*, 1988).

left. Figure 8.12 shows the fractional site occupancy of the oxygens in the chain site $(0, \frac{1}{2}, 0)$ as a function of the temperature in an oxygen atmosphere. A sample stored under sealed conditions exhibited no degradation in structure or change in T_c four years later (Sequeira *et al.*, 1992). Ultra-thin films tend to be tetragonal (Streiffer *et al.*, 1991).

E. Charge Distribution

Information on the charge distribution around atoms in conductors can be obtained from a knowledge of their energy bands (see description in Chapter 10). This is most easily accomplished by carrying out a Fourier-type mathematical transformation between the reciprocal k_s, k_y, k_z-space (Chapter 8, Section II of the first edition) in which the energy bands are plotted and the coordinate x, y, z-space, where the charge is distributed. We will present the results obtained for $YBa_2Cu_3O_7$ in the three vertical symmetry planes (x, z, and y, z, and diagonal), all containing the z-axis through the origin, shown shaded in the unit cell of Fig. 8.13.

Contour plots of the charge density of the valence electrons in these planes are sketched in Fig. 8.14. The high density at the Y^{3+} and Ba^{2+} sites and the lack of contours around these sites together indicate that these atoms are almost completely ionized, with charges of +3 and +2, respectively. It also shows that these ions are decoupled from the planes above and below. This accounts for the magnetic isolation for the Y site whereby magnetic ions substituted for yttrium do not interfere with the superconducting properties. In contrast, the contours surrounding the Cu and O ions are not characteristic of an ordinary ionic compound. The short Cu–O bonds in the planes and chains (1.93–1.96 Å) increase the charge overlap. The least overlap appears in the Cu(2)–O(4) vertical bridging bond, which is also fairly long (2.29 Å). The Cu, O charge contours can be represented by a model that assigns charges of +1.62

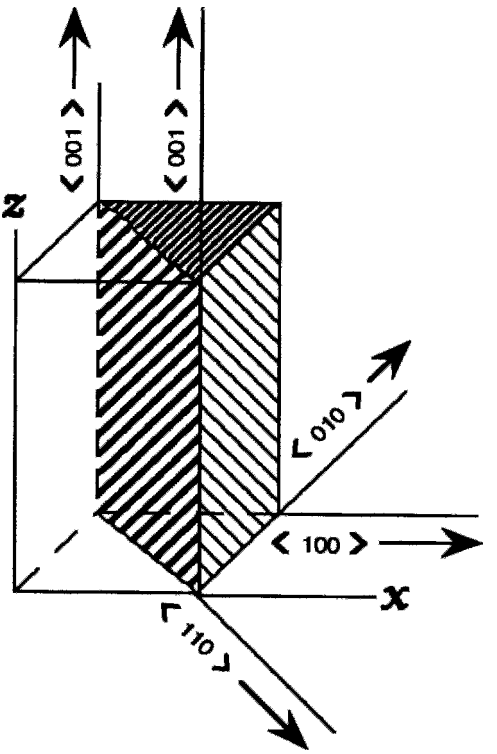

Figure 8.13 Three vertical crystallographic planes (x, z-, and y, z-, and diagonal) of a tetragonal unit cell of $YBa_2Cu_3O_7$, and standard notation for the four crystallographic directions.

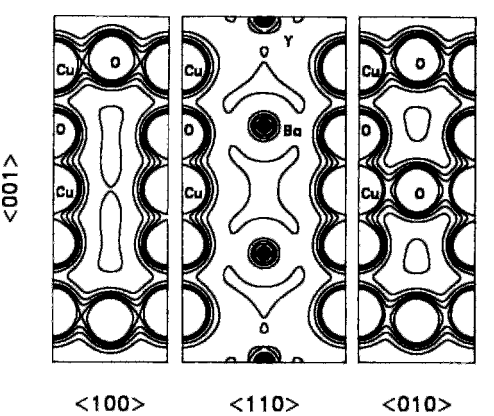

Figure 8.14 Charge density in the three symmetry planes of YBaCuO shown shaded in Fig. 8.13. The x, z, diagonal and the y, z planes are shown from left to right, labeled $\langle 100 \rangle$, $\langle 110 \rangle$, and $\langle 010 \rangle$, respectively. These results are obtained from bandstructure calculations, as will be explained in the following chapter (Krakauer and Pickett, 1988).

and −1.69 to Cu and O, respectively, rather than the values of +2.33 and −2.00 expected for a standard ionic model, where the charge +2.33 is an average of +2, +2, and +3 for the three copper ions. Thus the Cu–O bonds are not completely ionic, but partly covalent.

F. YBaCuO Formula

In early work the formula

$$YBa_2Cu_3O_{9-\delta}$$

was used for YBaCuO because the prototype triple pervoskite $(YCuO_3)(BaCuO_3)_2$ has nine oxygens. Then crystallographers showed that there are eight oxygen sites in the 14-atom YBaCuO unit cell, and the formula $YBa_2Cu_3O_{8-\delta}$ came into widespread use. Finally, structure refinements demonstrated that one of the oxygen sites is systematically vacant in the chain layers, so the more appropriate expression $YBa_2Cu_3O_{7-\delta}$ was introduced. It would be preferable to make one more change and use the formula $Ba_2YCu_3O_{7-\delta}$ to emphasize that Y is analogous to Ca in the bismuth and thallium compounds, but very few workers in the field do this, so we reluctantly adopt the usual "final" notation. In the Bi–Tl compound notation of Section VIII, B, $Ba_2YCu_3O_{7-\delta}$ would be called a 0213 compound. We will follow the usual practice of referring to $YBa_2Cu_3O_{7-\delta}$ as the 123 compound.

G. $YBa_2Cu_4O_8$ and $Y_2Ba_4Cu_7O_{15}$

These two superconductors are sometimes referred to as the 124 compound and the 247 compound, respectively. They have the property that for each atom at position $(x,\ y,\ z)$ there is another identical atom at position $(x,\ y+\frac{1}{2},\ z+\frac{1}{2})$. In other words, the structure is side centered. This property prevents the stacking rules of Section C from applying.

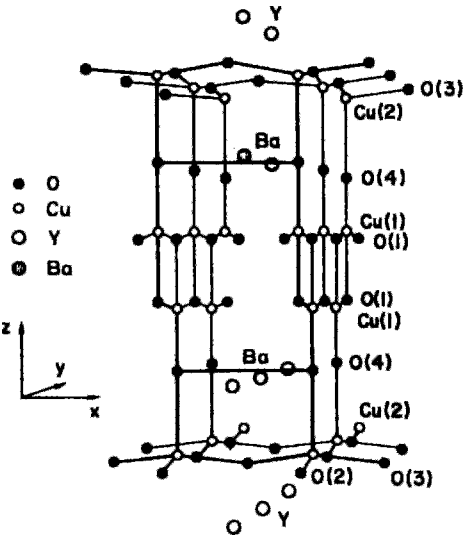

Figure 8.15 Crystal structure of $YBa_2Cu_4O_8$ showing how, as a result of the side-centering symmetry operation, the atoms in adjacent Cu–O chains are staggered along the y direction, with Cu above O and O above Cu (Heyen *et al.*, 1991; modified from Campuzano *et al.*, 1990).

The chain layer of $YBa_2Cu_3O_7$ becomes two adjacent chain layers in $YBa_2Cu_4O_8$, with the Cu atoms of one chain located directly above or below the O atoms of the other, as shown in Fig. 8.15 (Campuzano *et al.*, 1990; Heyen *et al.*, 1990a, 1991; Iqbal, 1992; Kaldis *et al.*, 1989; Marsh *et al.*, 1988; Morris *et al.*, 1989a). The transition temperature remains in the range from 40 K to 80 K when Y is replaced by various rare earths (Morris *et al.*, 1989). The double chains do not exhibit the variable oxygen stoichiometry of the single ones.

The other side-centered compound, $Y_2Ba_4Cu_7O_{15}$, may be considered according to Torardi, "as an ordered 1:1 inter-growth of the 123 and 124 compounds

$$(YBa_2Cu_3O_7 + YBa_2Cu_4O_8 = Y_2Ba_4Cu_7O_{15})"$$

(Bordel *et al.*, 1988, Gupta and Gupta, 1993). The 123 single chains can vary in their oxygen content, and superconductivity onsets up to 90 K have been observed.

This compound has been synthesized with several rare earths substituted for Y (Morris *et al.*, 1989b).

V. ALIGNED HgBaCaCuO

The series of compounds

$$HgBa_2Ca_nCu_{n+1}O_{2n+4},$$

where n is an integer, are prototypes for the Hg family of superconductors. The first three members of the family, with $n = 0, 1, 2$, are often referred to as Hg–1201, Hg–1212, and Hg–1223, respectively. They have the structures sketched in Fig. 8.16 (Tokiwa-Yamamoto *et al.*, 1993; see also Martin *et al.*, 1994; Putilin *et al.*, 1991). The lattice constants are $a = 3.86$ Å for all of them, and $c = 9.5$, 12.6, and 15.7 Å for $n = 0, 1, 2$, respectively. The atom positions of the $n = 1$ compound are listed in Table 8.5 (Hur *et al.*, 1994). The figure is drawn with mercury located in the middle layer of the unit cell, while the table puts Hg at the origin (000) and Ca in the middle ($\frac{1}{2}\frac{1}{2}\frac{1}{2}$). Figure 8.17 presents the unit cell for the $n = 1$ compound $HgBa_2CaCu_2O_{6+\delta}$ drawn with Ca in the middle (Meng *et al.*, 1993a). The symbol δ represents a small excess of oxygen located in the center of the top and bottom layers, at positions $\frac{1}{2}$ $\frac{1}{2}$ 0 and $\frac{1}{2}$ $\frac{1}{2}$ 1 which are labeled "partial occupancy" in the figure. If this oxygen were included the level symbol would be [Hg – O] instead of [Hg – –]. These Hg compound structures are similar to those of the series $TlBa_2Ca_nCu_{n+1}O_{2n+4}$ mentioned above in Section VIII.F.

We see from Fig. 8.16 that the copper atom of Hg–1201 is in the center of a stretched octahedron with the planar oxygens O(1) at a distance of 1.94 Å, and the apical oxygens O(2) of the [O – Ba] layer much further away (2.78 Å). For $n = 1$ each copper atom is in the center of the base of a tetragonal pyramid, and for $n = 2$ the additional CuO_2 layer has Cu atoms which

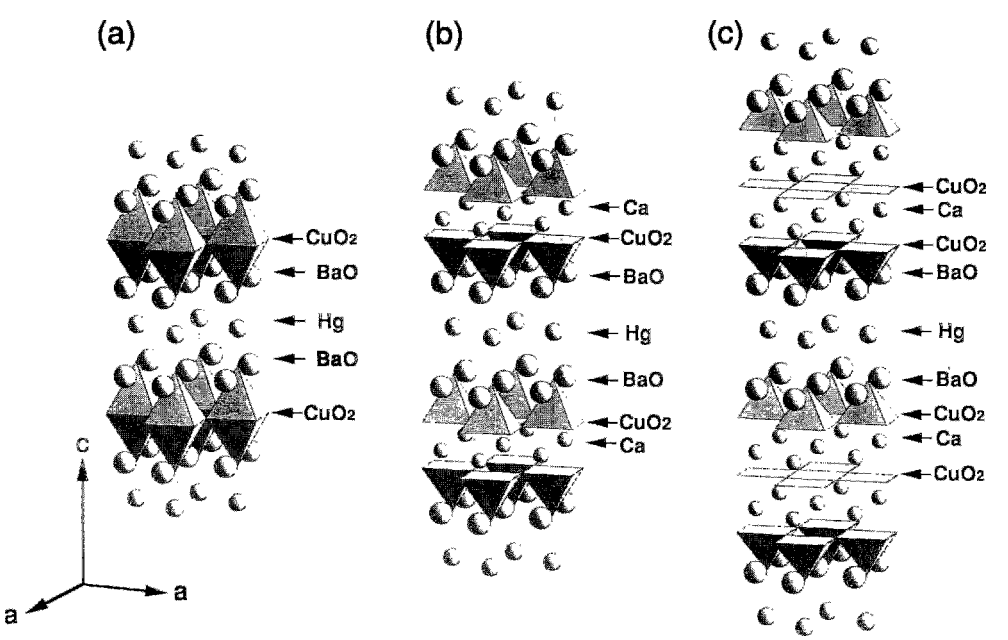

Figure 8.16 Structural models for the series $HgBa_2Ca_nCu_{n+1}O_{2n+4}$. The first three members with $n = 0, 1, 2$ are shown (parts a, b, and c, respectively) (Tokiwa-Yamamoto *et al.*, 1993).

Table 8.5 Normalized Atom Positions in the Tetragonal Unit Cell of $HgBa_2Ca_{0.86}Sr_{0.14}Cu_2O_{6+\delta}$[a]

Layer	Atom	x	y	z
[Hg – –]	Hg	0	0	1
	O(3)	$\frac{1}{2}$	$\frac{1}{2}$	1
[O – Ba]	O(2)	0	0	0.843
	Ba	$\frac{1}{2}$	$\frac{1}{2}$	0.778
	Cu	0	0	0.621
[Cu O_2 –]	O(1)	0	$\frac{1}{2}$	0.627
	O(1)	$\frac{1}{2}$	0	0.627
[– – Ca]	Ca, Sr	$\frac{1}{2}$	$\frac{1}{2}$	$\frac{1}{2}$
	O(1)	$\frac{1}{2}$	0	0.373
[Cu O_2 –]	O(1)	0	$\frac{1}{2}$	0.373
	Cu	0	0	0.379
	Ba	$\frac{1}{2}$	$\frac{1}{2}$	0.222
[O – Ba]	O(2)	0	0	0.157
	O(3)	$\frac{1}{2}$	$\frac{1}{2}$	0
[Hg – –]	Hg	0	0	0

[a] Unit cell dimensions $a = 3.8584$ Å and $c = 12.6646$ Å, space group is $P4/mmm$, D^1_{4h}. The Hg site is 91% occupied and the O(3) site is 11% occupied ($\delta = 0.11$). The data are from Hur *et al.* (1994).

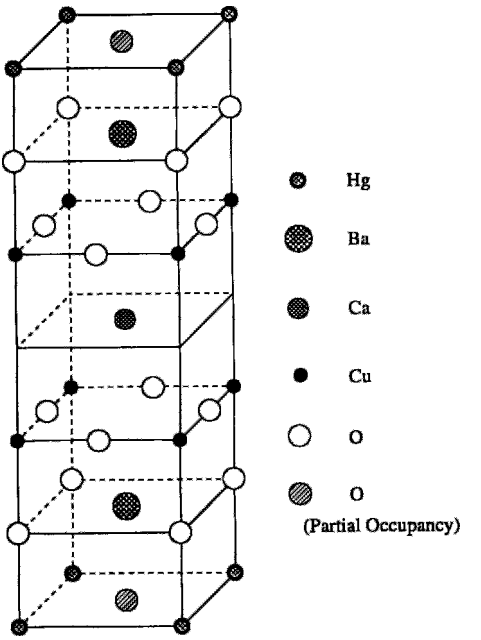

Figure 8.17 Schematic structure of the $HgBa_2CaCu_2O_{6+\delta}$ compound which is also called Hg–1212 (Meng *et al.*, 1993a).

are square planar coordinated. The layering scheme stacking rules of Section IV.C are obeyed by the Hg series of compounds, with metal ions in adjacent layers alternating between edge (E) and centered (C) sites, and oxygen in adjacent layers always at different sites. We see from Table 8.5 that the [O – Ba] layer is strongly puckered and the [Cu O_2 –] layer is only slightly puckered.

The relationships between the layering scheme of the $HgBa_2Ca_nCu_{n+1}O_{2n+4}$ series of compounds and those of the other cuprates may be seen by comparing the sketch of Fig. 8.18 with that of Fig. 8.29. We see that the $n = 1$ compound $HgBa_2CaCu_2O_6$ is quite similar in structure to $YBa_2Cu_3O_7$ with Ca replacing the chains [Cu O –]. More surprising is the similarity between the arrangement of the atoms in the unit cell of each

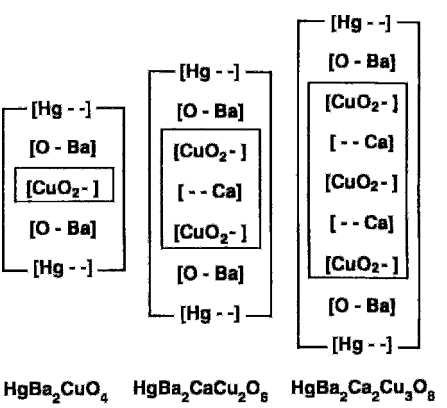

Figure 8.18 Layering schemes of three $HgBa_2Ca_nCu_{n+1}O_{2n+4}$ compounds, using the notation of Fig. 8.29.

$$HgBa_2Ca_nCu_{n+1}O_{2n+4}$$

compound and the arrangement of the atoms in the semi-unit cell of the corresponding

$$Tl_2Ba_2Ca_nCu_{n+1}O_{2n+6}$$

compound. They are the same except for the replacement of the [Tl – O] layer by [Hg – –], and the fact that the thallium compounds are body centered and the Hg ones are aligned.

Supercells involving polytypes with ordered stacking sequences of different phases, such as Hg–1212 and Hg–1223, along the c direction have been reported. The stoichiometry is often

$$Hg_2Ba_4Ca_3Cu_5O_x$$

corresponding to equal numbers of the Hg–1212 and Hg–1223 phases (Phillips, 1993; Schilling *et al*., 1993, 1994).

Detailed structural data have already been reported on various Hg family compounds such as $HgBa_2CuO_{4+\delta}$ (Putlin *et al*., 1993) and the $n = 1$ compound with partial Eu substitution for Ca (Putlin *et al*., 1991). The compound

$$Pb_{0.7}Hg_{0.3}Sr_2Nd_{0.3}Ca_{0.7}Cu_3O_7$$

has Hg in the position (0.065, 0, 0), slightly displaced from the origin of the unit cell (Martin *et al*., 1994). Several researchers have reported synthesis and pretreatment procedures (Adachi *et al*., 1993; Itoh *et al*., 1993; Isawa 1994a; Meng, 1993b; Paranthaman, 1994; Paranthaman *et al*., 1993). Lead doping for Hg has been used to improve the superconducting properties (Iqbal *et al*., 1994; Isawa *et al*., 1993; Martin *et al*., 1994).

VI. BODY CENTERING

In Section V we discussed aligned-type superconductor structures that possess a horizontal plane of symmetry. Most high-temperature superconductor structures have, besides this σ_h plane, an additional symmetry operation called body centering whereby for every atom with coordinates (x, y, z) there is an identical atom with coordinates as determined from the following operation:

$$x \to x \pm \frac{1}{2}, \quad y \to \pm\frac{1}{2}, \quad z \to z \pm \frac{1}{2} \tag{8.5}$$

Starting with a plane at the height z this operation forms what is called an image plane at the height $z \pm \frac{1}{2}$ in which the edge atoms become centered, the centered atoms become edge types, and each face atom moves to another face site. In other words, the body-centering operation acting on a plane at the height z forms a body centered plane, also called an image plane, at the height $z \pm \frac{1}{2}$. The signs in these operations are selected so that the generated points and planes remain within the unit cell. Thus if the initial value of z is greater than $\frac{1}{2}$, the minus sign must be selected, viz., $z \to z - \frac{1}{2}$. Body centering causes half of the Cu–O planes to be [Cu O_2 –], with the copper atoms at edge sites, and the other half to be [– O_2 Cu], with the copper atoms at centered sites.

Let us illustrate the symmetry features of a body-centered superconductor by considering the example of $Tl_2Ba_2CaCu_2O_8$. This compound has an initial plane [Cu O_2 –] with the copper and oxygen atoms at the vertical positions $z = 0.0540$ and 0.0531, respectively, as shown in Fig. 8.19. For illustrative purposes the figure is drawn for values of z closer to 0.1. We see from the figure that there is a reflected plane [Cu O_2 –] at the height $1 - z$, an image (i.e., body centered) plane [– O_2 Cu] of the original plane at the height $\frac{1}{2} + z$, and an image plane [– O_2 Cu] of the reflected plane (i.e., a reflected and body centered plane) at the height $\frac{1}{2} - z$. Figure 8.19 illustrates this situation and indicates how the atoms of the initial plane can be transformed into particular atoms in other planes (see Problem 5). Figure 8.20 shows how the configurations of the atoms in one-quarter of the unit cell, called the *basic subcell,* or subcell I, determine their configuratinon in the other three subcells II, III,

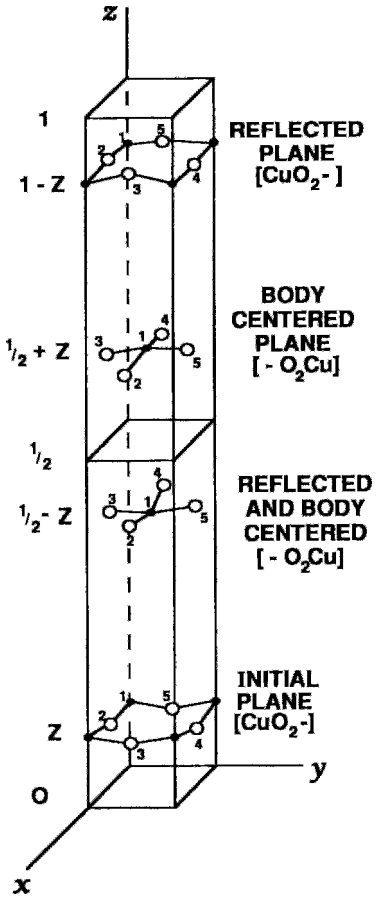

Figure 8.19 Body-centered tetragonal unit cell containing four puckered CuO_2 groups showing how the initial group (bottom) is replicated by reflection in the horizontal reflection plane $\left(z = \frac{1}{2}\right)$, by the body centering operation, and by both.

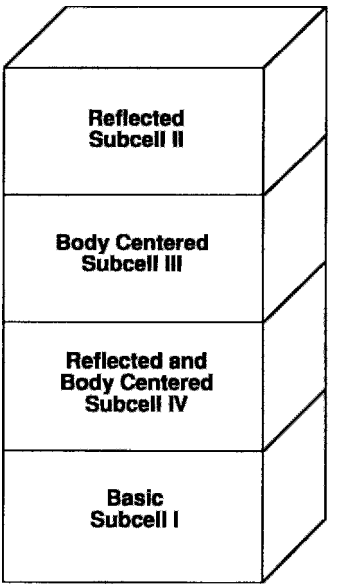

Figure 8.20 Body-centered unit cell divided into four regions by the reflection and body centering operations.

and IV throught the symmetry operations of reflection and body centering.

VII. BODY-CENTERED La_2CuO_4, Nd_2CuO_4 AND Sr_2RuO_4

The body-centered compound

$$M_2CuO_4$$

has three structural variations in the same crystallographic space group, namely the $M = La$ and $M = Nd$ types, and a third mixed variety (Xiao *et al.*, 1989). Table 8.5 lists the atom positions of the first two types, and Fig. 8.21 presents sketches of the structures of all three. The compound Sr_2RuO_4 is isomorphic with La_2CuO_4. Each of these cases will be discussed in turn.

A. Unit Cell of La_2CuO_4 Compound (T Phase)

The structure of the more common La_2CuO_4 variety, often called the T phase, can be pictured as a stacking of CuO_4La_2 groups alternately with image (i.e., body centered) La_2O_4Cu groups along the *c* direction, as indicated on the left side of Fig. 8.21. (Cavaet *et al.*, 1987; Kinoshita *et al.*, 1992; Longo and Raccah, 1973; Ohbayashi *et al.*, 1987; Onoda *et al.*, 1987; Zolliker *et al.*, 1990). Another way of visualizing the structure is by generating it from the group $Cu_{0.5}O_2La$, comprising the layers [O–La] and $\frac{1}{2}$[Cu O_2 –] in subcell I shown on the right side of Fig. 8.22 and also on the left side of

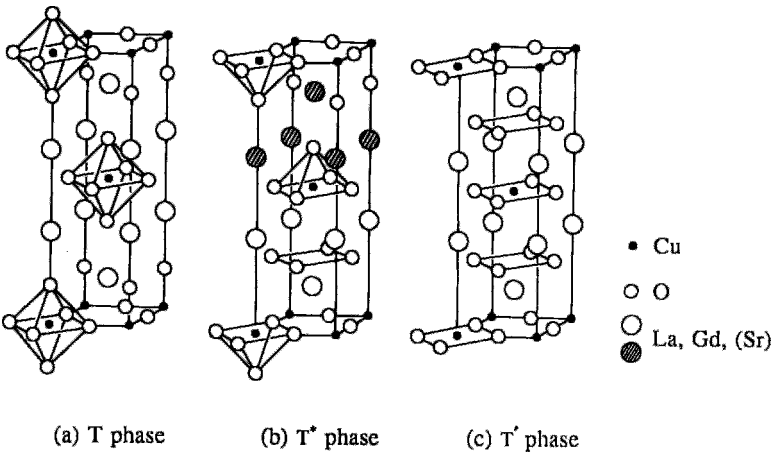

Figure 8.21 (a) Regular unit cell (T phase) associated with hole=type $(La_{1-x}Sr_x)_2CuO_4$ superconductors, (b) hybrid unit cell (T* phase) of the hole-type $La_{2-x-y}R_ySr_xCuO_4$ superconductors, and (c) alternate unit cell (T′ phase) associated with electron-type $(Nd_{1-x}Ce_x)_2CuO_4$ superconductors. The La atoms in the left structure become Nd atoms in the right structure. The upper part of the hybrid cell is T type, and the bottom is T′. The crystallographic space group I4/mmm is the same for all three unit cells (Xiao *et al*., 1989; see also Oguchi, 1987; Ohbayashi *et al*., 1987; Poole *et al*., 1988, p. 83; Tan *et al*., 1990).

Fig. 8.23. (The factor $\frac{1}{2}$ appears here because the [Cu O_2 −] layer is shared by two subcells.) Subcell II is formed by reflection from subcell I, and subcells III and IV are formed from I and II via the body-centering operation in the manner of Figs. 8.19 and 8.20. Therefore, subcells I and II together contain the group CuO_4La_2, and subcells III and IV together contain its image (body centered) counterpart group La_2O_4Cu. The BiSrCaCuO and TlBaCaCuO structures to be discussed in Section VIII can be generated in the same manner, but with much larger repeat units along the *c* direction.

B. Layering Scheme

The La_2CuO_4 layering scheme consists of equally-spaced, flat CuO_2 layers with their oxygens stacked one above the other, the copper ions alternating between the (0, 0, 0) and $\left(\frac{1}{2}, \frac{1}{2}, \frac{1}{2}\right)$ sites in adjacent layers, as shown in Fig. 8.24. These planes are body-centered images of each other, and are perfectly flat because they are reflection planes. Half of the oxygens, O(1), are in the planes, and the other half, O(2), between the planes. The copper is octahedrally coordinated with oxygen, but the distance 1.9 Å from Cu to O(1) in the CuO_2 planes is much leess than the vertical distance of 2.4 Å from Cu to the apical oxygen O(2), as indicated in Fig. 8.25. The La is ninefold coordinated to four O(1) oxygens, to four O(2) at $\left(\frac{1}{2}, \frac{1}{2}, z\right)$ sites, and to one O(2) at a (0, 0, *z*) site.

C. Charge Distribution

Figure 8.26 shows contours of constant-valence charge density on a logarithmic scale drawn on the back *x, z*-plane and on the diagonal plane of the unit cell sketched in Fig. 8.13. These contour plots are obtained from the band structure calculations described in Chapter 10, Section XIV of the first edition. The high-charge density at the lanthanum site and the low charge density around this site indicate an ionic state La^{3+}. The charge density changes in a fairly

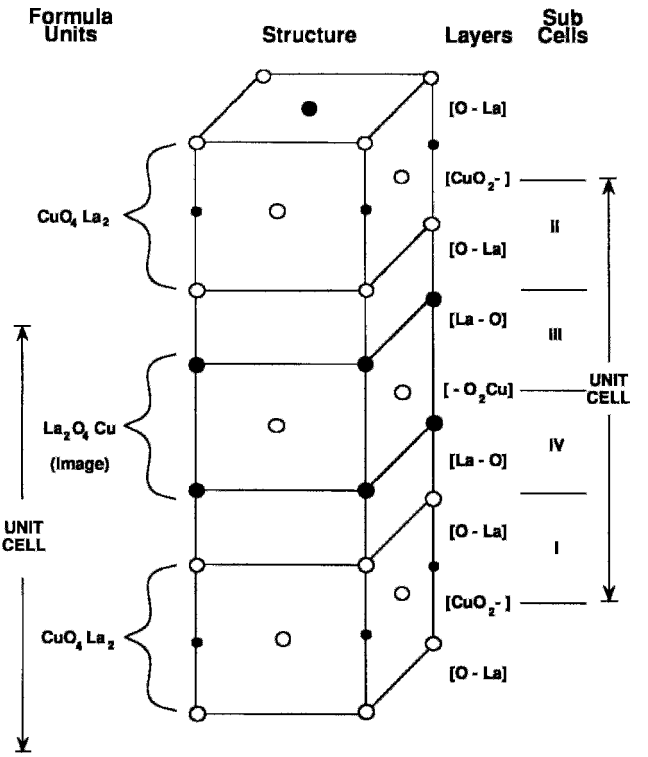

Figure 8.22 Structure of La_2CuO_4 (center), showing the formula units (left) and the level labels and subcell types (right). Two choices of unit cell are indicated, the left-side type unit cell based on formula units, and the more common right-side type unit cell based on copper-oxide layers.

regular manner around the copper and oxygen atoms, both within the CuO_2 planes and perpendicular to these planes, suggestive of covalency in the Cu–O bonding, as is the case with the $YBa_2Cu_3O_7$ compound.

D. Superconducting Structures

The compound La_2CuO_4 is itself an antiferromagnetic insulator and must be doped, generally with an alkaline earth, to exhibit pronounced superconducting properties. The compound $(La_{1-x}M_x)_2CuO_4$, with 3% to 15% of $M = Sr$ or Ba replacing La, are orthorhombic at low temperatures and low M contents and are tetragonal otherwise; superconductivity has been found on both sides of this transition. The orthorhombic distortion can be of the rectangular or of the rhombal type, both of which are sketched in Fig. 8.4. The phase diagram of Fig. 8.27 shows the tetragonal, orthorhombic, superconducting, and antiferromagnetically ordered regions for the lanthanum compound (Weber *et al.*, 1989; cf. Goodenough *et al.*, 1993). We see that the orthorhombic phase is insulating at high temperatures, metallic at low temperatures, and superconducting at very low temperatures. Spin-density waves, to be discussed in Chapter 10, Section IX, occur in the antiferromagnetic region.

E. Nd_2CuO_4 Compound (T′ Phase)

The rarer Nd_2CuO_4 structure (Skantakumar *et al.*, 1989; Sulewski *et al.*,

La_2CuO_4	Sub Cell	Nd_2CuO_4
$[CuO_2-]$	——	$[CuO_2-]$
[O - La]	II	[- - Nd]
[La - O]	——	$[-O_2-]$
	III	[Nd - -]
$[-O_2Cu]$	——	$[-O_2Cu]$
[La - O]	IV	[Nd - -]
[O - La]	——	$[-O_2-]$
	I	[- - Nd]
$[CuO_2-]$	——	$[CuO_2-]$

Figure 8.23 Layering schemes of the La_2CuO_4 (T, left) and Nd_2CuO_4 (T′, right) structures. The locations of the four subcells of the unit cell are indicated in the center column.

1990; Tan *et al.*, 1990) given on the right side of Fig. 8.21 and Table 8.6 has all of its atoms in the same positions as the standard La_2CuO_4 structure, except for the apical O(2) oxygens in the [O–La] and [La–O] layers, which move to form a [– O_2 –] layer between [– – La] and [La – –]. These oxygens, now called O(3), have the same x, y coordinate positions as the O(1) oxygens, and are located exactly between the CuO_2 planes with $z = \frac{1}{4}$ or $\frac{3}{4}$. We see from Fig. 8.21 that the CuO_6 octahedra have now lost their apical oxygens, causing Cu to become square planar-coordinated CuO_4 groups. The Nd is eightfold coordinated to four O(1) and four O(3) atoms, but with slightly different Nd–O distances. The CuO_2 planes, however, are identical in the two structures. Superconductors with this Nd_2CuO_4 structure are of the electron type, in contrast to other high-temperature superconductors, in which the current carriers are holes. In particular, the electron superconductor $Nd_{1.85}Ce_{0.15}CuO_{4-\delta}$ with $T_c = 24\,K$ has been widely studied (Fontcuberta and Fàbrega, 1995, a review

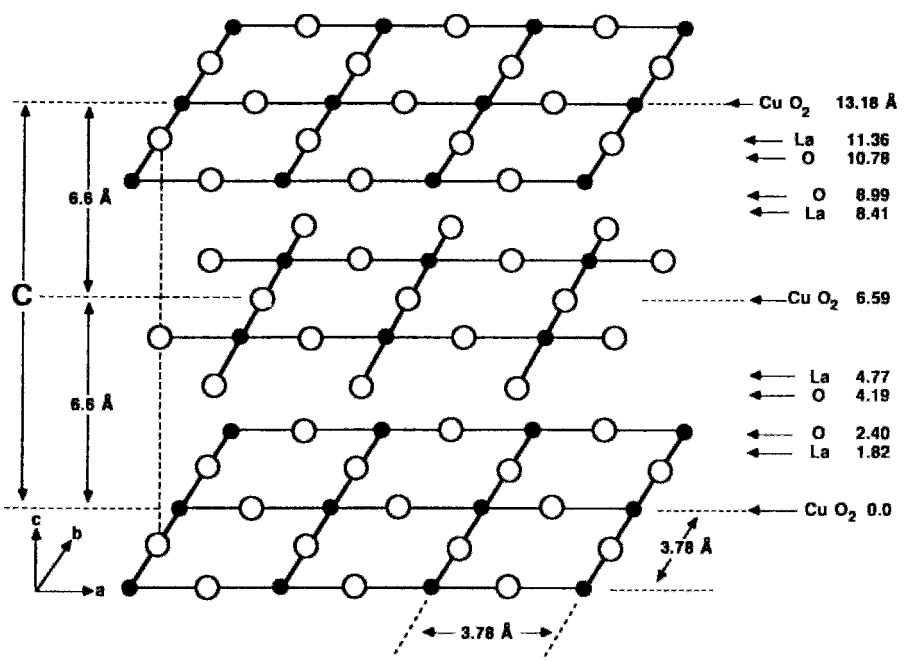

Figure 8.24 CuO_2 layers of the La_2CuO_4 structure showing horizontal displacement of Cu atoms (black dots) in alternate layers. The layers are perpendicular to the *c*-axis (Poole *et al.*, 1988, p. 87).

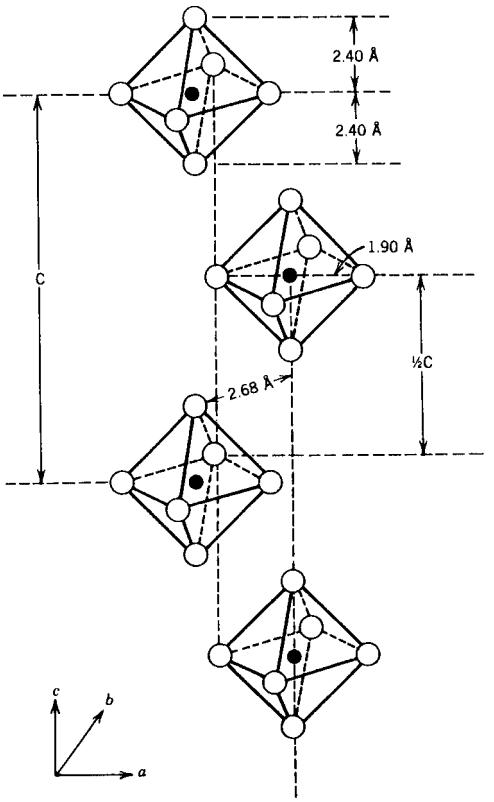

Figure 8.25 Ordering of axially distorted CuO_6 octahedra in La_2CuO_4 (Poole *et al.*, 1988, p. 88).

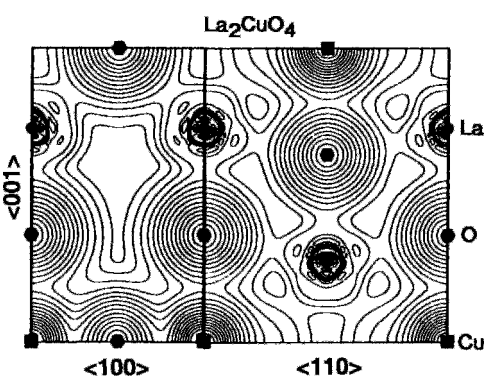

Figure 8.26 Contour plots of the charge density of La_2CuO_4 obtained from band structure calculations. The x, z-crystallographic plane labeled $\langle 100 \rangle$ is shown on the left, and the diagonal plane labeled $\langle 110 \rangle$ appears on the right. The contour spacing is on a logarithmic scale (Pickett, 1989).

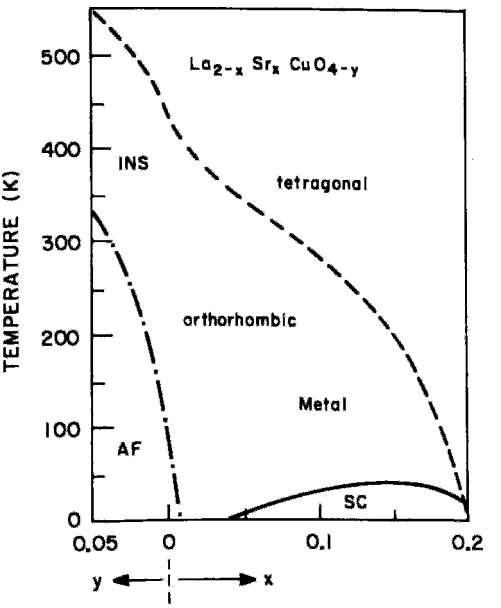

Figure 8.27 Phase diagram for hole-type $La_{2-x}Sr_xCuO_{4-y}$ indicating insulating (INS), antiferromagnetic (AF), and superconducting (SC) regions. Figure VI-6 of Poole *et al.* (1988) shows experimental data along the orthorhombic-to-tetragonal transition line. Spin-density waves (SDW) are found in the AF region (Weber *et al.*, 1989).

chapter; Allen 1990; Alp *et al.*, 1989b; Barlingay *et al.*, 1990; Ekino and Akimitsu, 1989a, b; Lederman *et al.*, 1991; Luke *et al.*, 1990; Lynn *et al.*, 1990; Sugiyama *et al.*, 1991: Tarason *et al.*, 1989a). Other rare earths, such as Pr (Lee *et al.*, 1990) and Sm (Almasan *et al.*, 1992) have replaced Nd.

The difference of structures associated with different signs attached to the current carriers may be understood in terms of the doping process that converts undoped material into a superconductor. Lanthanum and neodymium are both trivalent, and in the undoped compounds they each contribute three electrons to the nearby oxygens,

$$\begin{aligned} \mathrm{La} &\rightarrow \mathrm{La}^{3+} + 3\mathrm{e}^-, \\ \mathrm{Nd} &\rightarrow \mathrm{Nd}^{3+} + 3\mathrm{e}^-, \end{aligned} \tag{8.6}$$

Table 8.6 Atom Positions in the La_2CuO_4 and Nd_2CuO_4 Structures

La_2CuO_4 structure					Nd_2CuO_4 structure				
Layer	**Atom**	x	y	z	**Layer**	**Atom**	x	y	z
	O(1)	$\frac{1}{2}$	0	1		O(1)	$\frac{1}{2}$	0	1
[Cu O_2 –]	Cu	0	0	1	[Cu O_2 –]	Cu	0	0	1
	O(1)	0	$\frac{1}{2}$	1		O(1)	0	$\frac{1}{2}$	1
[La – O]	La	$\frac{1}{2}$	$\frac{1}{2}$	0.862	[– – Nd]	Nd	$\frac{1}{2}$	$\frac{1}{2}$	0.862
	O(2)	0	0	0.818	[– O_2 –]	O(3)	0	$\frac{1}{2}$	$\frac{3}{4}$
						O(3)	$\frac{1}{2}$	0	$\frac{3}{4}$
[La – O]	O(2)	$\frac{1}{2}$	$\frac{1}{2}$	0.682					
	La	0	0	0.638	[Nd – –]	Nd	0	0	0.638
	O(1)	$\frac{1}{2}$	0	$\frac{1}{2}$		O(1)	$\frac{1}{2}$	0	$\frac{1}{2}$
[– O_2 Cu]	Cu	$\frac{1}{2}$	$\frac{1}{2}$	$\frac{1}{2}$	[– O_2 Cu]	Cu	$\frac{1}{2}$	$\frac{1}{2}$	$\frac{1}{2}$
	O(1)	0	$\frac{1}{2}$	$\frac{1}{2}$		O(1)	0	$\frac{1}{2}$	$\frac{1}{2}$
					[Nd – –]	Nd	0	0	0.362
[La – O]	La	0	0	0.362					
	O(2)	$\frac{1}{2}$	$\frac{1}{2}$	0.318	[– O_2 –]	O(3)	$\frac{1}{2}$	0	$\frac{1}{4}$
[O – La]	O(2)	0	0	0.182		O(3)	0	$\frac{1}{2}$	$\frac{1}{4}$
	La	$\frac{1}{2}$	$\frac{1}{2}$	0.138	[– – Nd]	Nd	$\frac{1}{2}$	$\frac{1}{2}$	0.138
	O(1)	0	$\frac{1}{2}$	0		O(1)	0	$\frac{1}{2}$	0
[Cu O_2 –]	Cu	0	0	0	[Cu O_2 –]	Cu	0	0	0
	O(1)	$\frac{1}{2}$	0	0		O(1)	$\frac{1}{2}$	0	0

to produce O^{2-}. To form the superconductors a small amount of La in La_2CuO_4 can be replaced with divalent Sr, and some Nd in Nd_2CuO_4 can be replaced with tetravalent Ce, corresponding to

$$\begin{aligned} \mathrm{Sr} &\rightarrow \mathrm{Sr}^{2+} + 2\mathrm{e}^- \quad (\text{in } \mathrm{La_2CuO_4}) \\ \mathrm{Ce} &\rightarrow \mathrm{Ce}^{4+} + 4\mathrm{e}^- \quad (\text{in } \mathrm{Nd_2CuO_4}) \end{aligned} \tag{8.7}$$

Thus, Sr doping decreases the number of electrons and hence produces hole-type carriers, while Ce doping increases the electron concentration and the conductivity is electron type.

There are also copper-oxide electron superconductors with different structures, such as $Sr_{1-x}Nd_xCuO_2$ (Smith *et al.*, 1991) and $TlCa_{1-x}R_xSr_2Cu_2O_{7-\delta}$, where R is a rare earth (Vijayaraghavan *et al.*, 1989). Electron- and hole-type superconductivity in the cuprates has been compared (Katti and Risbud, 1992; Medina and Regueiro, 1990).

F. $La_{2-x-y}R_xSr_yCuO_4$ Compounds (T^* Phase)

We have described the T structure of La_2CuO_4 and the T′ structure of Nd_2CuO_4. The former has O(2) oxygens and the latter O(3) oxygens, which changes the coordinations of the Cu atoms and that of the La and Nd atoms as well. There is a hybrid structure of hole-type superconducting lanthanum cuprates called the T^* structure, illustrated in Fig. 8.21b, in which the upper half of the unit cell is the T type with O(2) oxygens and lower half the T′ type with O(3) oxygens. These two varieties of half-cells are stacked alternately along the tetragonal c-axis (Akimitsu *et al.*, 1988; Cheong *et al.*, 1989b; Kwei *et al.*, 1990; Tan *et al.*, 1990). Copper, located in the base of an oxygen pyramid, is fivefold-coordinated CuO_5. There are two inequivalent rare earth sites; the ninefold-coordinated site in the T-type

halfcell is preferentially occupied by the larger La and Sr ions, witle the smaller rare earths *R* (i.e., Sm, Eu, Gd, or Tb) prefer the eightfold-coordinated site in the T′ halfcell. Tan *et al*. (1991) give a phase diagram for the concentration ranges over which the T and T^* phases are predominant.

G. Sr_2RuO_4 Compound (T Phase)

Superconductivity was found in the lanthanum and neodymium cuprates during the initial years of the high temperature superconductivity era, but the phenomenon was not found in strontium ruthenate until 1994 (Maeno *et al*.), and did not attract widespread attention until several years later at the arrival of the new millennium. The unit cell dimensions of the three compounds are quite close to each other

$$\begin{array}{lll} La_2CuO_4 & a_0 = 3.79\,\text{Å}, & c_0 = 13.23\,\text{Å} \\ Nd_2CuO_4 & a_0 = 3.94\,\text{Å}, & c_0 = 12.15\,\text{Å} \\ Sr_2RuO_4 & a_0 = 3.87\,\text{Å}, & c_0 = 12.74\,\text{Å} \end{array} \tag{8.8}$$

and the ionic radius of tetravalent ruthenium Ru^{4+} (0.67 Å) is close to that of divalent copper Cu^{2+} (0.72 Å). The two cuprates are insulators, which become conductors and superconductors at 24 K and 35 K, respectively, when they are appropriately doped. Sr_2RuO_4, on the other hand, is a Fermi liquid metal (Wysokinsky *et al*., 2003) without doping, and has a much lower transition temperature $T_c = 1.5\,K$. The c-axis resistivity, however, becomes nonmetallic above $T_M = 130\,K$, with the in-plane resistivity remaining always metallic (Maeno *et al*., 1996). The lanthanum and neodymium compounds are similar to other cuprates in their type of superconductivity, whereas strontium ruthenate is believed to be a more exotic type of superconductor, hence the recent interest in it. Some of the significant properties of Sr_2RuO_4 are: the Sommerfeld specific heat constant $\gamma_0 = 37.5\,\text{mJ/mole K}^2$, the specific heat jump at T_c given by $\Delta C = 27\,\text{mJ/mole}$ (Annett *et al*., 2002), the resistivity anisotropy $\rho_c/\rho_{ab} = 500$ (Wysokinsky *et al*., 2003), the presence of incommensurate spin fluctuations (Sidis *et al*., 1999), and the Pauli limiting field $B_{Pauli} \cong 2T$ (Maki *et al*., 2001).

The Cooper pairs in Sr_2RuO_4 are believed to be odd parity spin triplets (Litak *et al*., 2004), and the compound is said to exhibit time reversal symmetry breaking (Luke *et al*., 1998). Won and Maki (2001) pointed out that the only other spin triplet superconductors found in metals are the heavy Fermion compound UPt_3, and the Bechgaard salt organic conductors $(TMTSF)_2X$ with the structure sketched in Fig. 9.39, where the monovalent counter ion X^- can be, for example, ClO_4^- or PF_6^- (Won and Maaki, 2001). Analogies have been pointed out to the triplet superfluidity found in ^3He (Rice and Sigrist, 1995, Wysokinsky *et al*., 2003). The Fermi surface of Sr_2RuO_4 has the three quasi-two dimensional sheets shown in Fig. 8.28, and these lead to anisotropic resistivity, susceptibility, and other properties. Several researchers have suggested that the superconductivity is of the odd parity p wave or f wave type (e.g. Won and Maki, 2000). The presence of some Ru in the Sr_2RuO_4-Ru eutectic system raises the transition temperature to $T_c \cong 3K$.

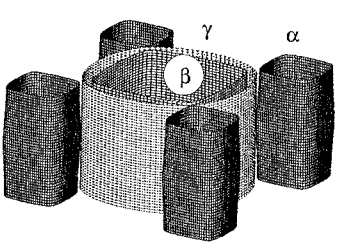

Figure 8.28 Fermi surface of Sr_2RuO_4 calculated by the tight binding method. The three quasi two-dimensional sheets α, β, and γ are indicated. (Wysokinski *et al*., 2003, Fig. 1).

VIII. BODY-CENTERED BiSrCaCuO AND TlBaCaCuO

Early in 1988 two new superconducting systems with transition temperatures considerably above those attainable with YBaCuO, namely the bismuth- and thallium-based materials, were discovered. These compounds have about the same *a* and *b* lattice constants as the yttrium and lanthanum compounds, but with much larger unit cell dimensions along *c*. We will describe their body-centered structures in terms of their layering schemes. In the late 1940s some related compounds were synthesized by the Swedish chemist Bengt Aurivillius (1950, 1951, 1952).

A. Layering Scheme

The $Bi_2Sr_2Ca_nCu_{n+1}O_{6+2n}$ and $Tl_2Ba_2Ca_nCu_{n+1}O_{6+2n}$ compounds, where n is an integer, have essentially the same structure and the same layering arrangement (Barry *et al.*, 1989; Siegrist *et al.*, 1988; Torardi *et al.*, 1988a; Yvon and François, 1989), although there are some differences in the detailed atom positions. Here there are groupings of CuO_2 layers, each separated from the next by Ca layers with no oxygen. The CuO_2 groupings are bound together by intervening layers of BiO and SrO for the bismuth compound, and by intervening layers of TlO and BaO for the thallium compound. Figure 8.29 compares the layering scheme of

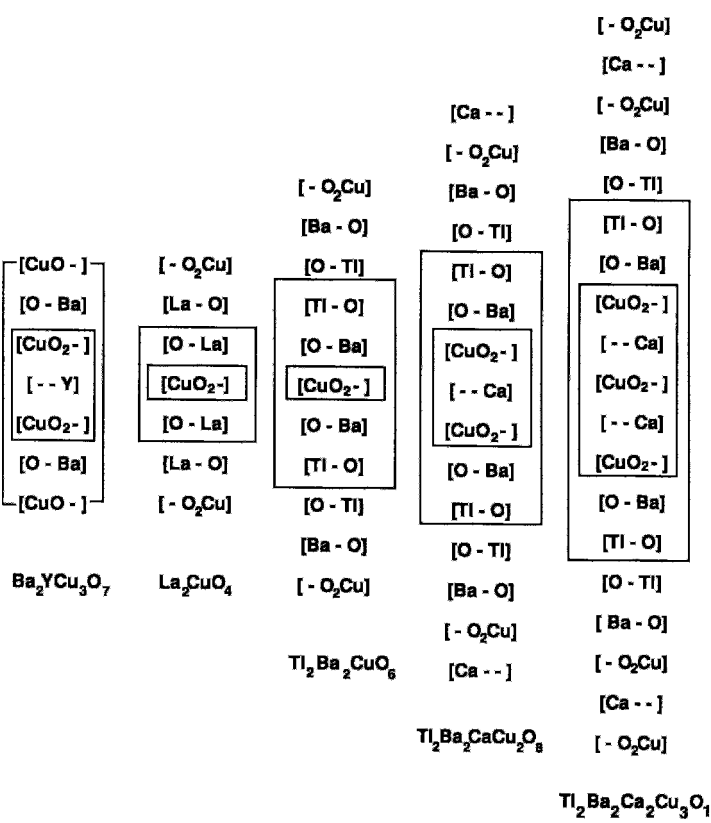

Figure 8.29 Layering schemes of various high-temperature superconductors. The CuO_2 plane layers are enclosed in small inner boxes, and the layers that make up a formula unit are enclosed in larger boxes. The Bi-Sr compounds $Bi_2Sr_2Ca_nCu_{n+1}O_{6+2n}$ have the same layering schemes as their Tl-Ba counterparts shown in this figure.

the $Tl_2Ba_2Ca_nCu_{n+1}O_{6+2n}$ compounds with $n = 0, 1, 2$ with those of the lanthanum and yttrium compounds. We also see from the figure that the groupings of [Cu O_2 −] planes and [− O_2 Cu] image (i.e., body centered) planes repeat along the *c*-axis. It is these copper-oxide layers that are responsible for the superconducting properties.

A close examination of this figure shows that the general stacking rules mentioned in Section VI.C for the layering scheme are satisfied, namely metal ions in adjacent layers alternate between edge (E) and centered (C) sites, and adjacent layers never have oxygens on the same types of sites. The horizontal reflection symmetry at the central point of the cell is evident. It is also clear that $YBa_2Cu_3O_7$ is aligned and that the other four compounds are staggered.

Figure 8.30 (Torardi *et al.*, 1988a) presents a more graphical representation of the information in Fig. 8.29 by showing the positions of the atoms in their layers. The symmetry and body centering rules are also evident on this figure. Rao (1991) provided sketches for the six compounds $Tl_mBa_2Ca_nCu_{n+1}O_x$ similar to those in Fig. 8.30 with the compound containing one ($m = 1$) or two thallium layers ($m = 2$), where $n = 0, 1, 2$, as in the Torardi *et al.* figure.

B. Nomenclature

There are always two thalliums and two bariums in the basic formula for $Tl_2Ba_2Ca_nCu_{n+1}O_{6+2n}$, together with n calciums and $n + 1$ coppers. The first three members of this series for $n = 0,\ 1$, and 2

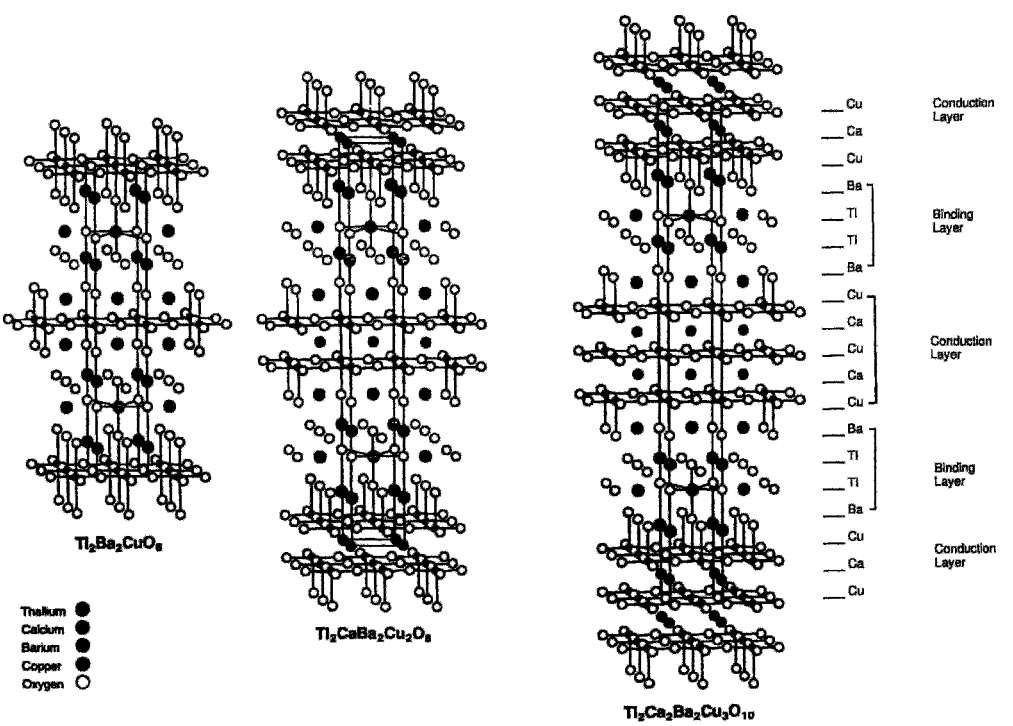

Figure 8.30 Crystal structures of $Tl_2Ba_2Ca_nCu_{n+1}O_{6+2n}$ superconducting compounds with $n = 0,\ 1,\ 2$ arranged to display the layering schemes. The $Bi_2Sr_2Ca_nCu_{n+1}O_{6+2n}$ compounds have the same respective structures (Torardi *et al.*, 1988a).

are called the 2201, 2212, and 2223 compounds, respectively, and similarly for their BiSr analogues $Bi_2Sr_2Ca_nCu_{n+1}O_{6+2n}$. Since Y in $YBa_2Cu_3O_7$ is structurally analogous to Ca in the Tl and Bi compounds, it would be more consistent to write $Ba_2YCu_3O_7$ for its formula, as noted in Section IV.F. In this spirit $Ba_2YCu_3O_{7-\delta}$ might be called the 1212 compound, and $(La_{1-x}M_x)_2CuO_{4-\delta}$ could be called 0201.

C. Bi-Sr Compounds

Now that the overall structures and interrelationships of the BiSr and TlBa high-temperature superconductors have been made clear in Figs. 8.29 and 8.30 we will comment briefly about each compound. Table 8.3 summarizes the characteristics of these and related compounds.

The first member of the BiSr series, the 2201 compound with $n = 0$, has octahedrally coordinated Cu and $T_c \approx 9\,K$ (Torardi *et al.*, 1988b). The second member, $Bi_2(Sr, Ca)_3Cu_2O_{8+\delta}$, is a superconductor with $T_c \approx 90\,K$ (Subramanian *et al.*, 1988a; Tarascon *et al.*, 1988b). There are two [Cu O_2 –] layers separated from each other by the [– – Ca] layer. The spacing from [Cu O –] to [– – Ca] is 1.66 Å, which is less than the corresponding spacing of 1.99 Å between the levels [Cu O_2 –] and [– – Y] of YBaCuO. In both cases the copper ions have a pyramidal oxygen coordination of the type shown in Fig. 8.11. Superlattice structures have been reported along *a* and *b*, which means that minor modifications of the unit cells repeat approximately every five lattice spacings, as explained in Sect. VIII.E. The third member of the series, $Bi_2Sr_2Ca_2Cu_3O_{10}$, has three CuO_2 layers separated from each other by [– – Ca] planes and a higher transition temperature, 100 K, when doped with Pb. The two Cu ions have pyramidal coordination, while the third is square planar.

Charge-density plots of

$$Bi_2Sr_2CaCu_2O_8$$

indicate the same type of covalency in the Cu – O bonding as with the $YBa_2Cu_3O_7$ and La_2CuO_4 compounds. They also indicate very little bonding between the adjacent [Bi – O] and [O – Bi] layers.

D. Tl-Ba Compounds

The TlBa compounds

$$Tl_2Ba_2Ca_nCu_{n+1}O_{6+2n}$$

have higher transition temperatures than their bismuth counterparts (Iqbal *et al.*, 1988b; Torardi *et al.*, 1988a). The first member of the series, namely $Tl_2Ba_2CuO_6$ with $n = 0$, has no [– – Ca] layer and a relatively low transition temperature of $\approx 85\,K$. The second member ($n = 1$), $Tl_2Ba_2CaCu_2O_8$, called the 2212 compound, with $T_c = 110\,K$ has the same layering scheme as its Bi counterpart, detailed in Figs. 8.29 and 8.30. The [Cu O_2 –] layers are thicker and closer together than the corresponding layers of the bismuth compound (Toby *et al.*, 1990). The third member of the series, $Tl_2Ba_2Ca_2Cu_3O_{10}$, has three [Cu O_2 –] layers separated from each other by [– – Ca] planes, and the highest transition temperature, 125 K, of this series of thallium compounds. It has the same copper coordination as its BiSr counterpart. The 2212 and 2223 compounds are tetragonal and belong to the same crystallographic space group as La_2CuO_4.

We see from the charge-density plot of $Tl_2Ba_2CuO_6$ shown in Fig. 8.31 that Ba^{2+} is ionic, Cu exhibits strong covalency, especially in the Cu-O plane, and Tl also appears to have a pronounced covalency. The bonding between the [Tl – O] and [O – Tl] planes is stronger than that between the [Bi – O] and [O – Bi] planes of Bi – Sr.

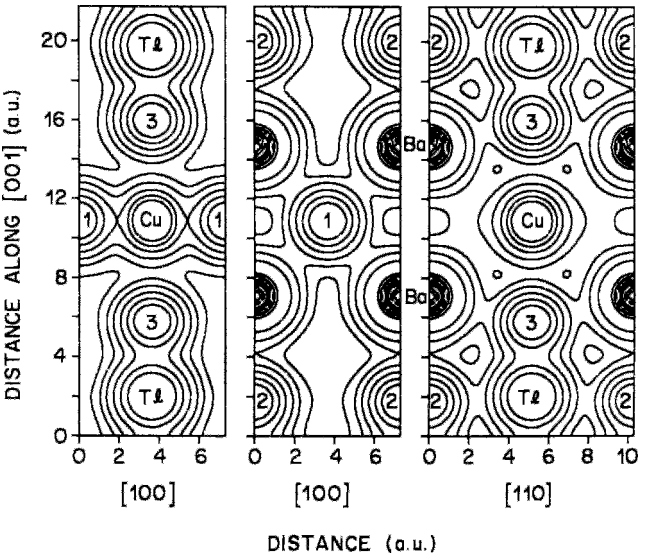

Figure 8.31 Contours of constant charge density on a logarithmic scale in two high-symmetry crystallographic planes of $Tl_2Ba_2CuO_6$. Oxygen atoms O(1), O(2), and O(3) are denoted 1, 2, and 3, respectively. The planar Cu-O(1) binding is strongest (Hamann and Mattheiss, 1988; see Pickett, 1989).

E. Modulated Structures

The x-ray and neutron-diffraction patterns obtained during crystal structure determinations of the bismuth cuprates $Bi_2Sr_2Ca_nCu_{n+1}O_{6+2n}$ exhibit weak satellite lines with spacings that do not arise from an integral multiple of the unit cell dimensions. These satellites have modulation periods of 21 Å, 19.6 Å, and 20.8 Å, respectively, for the $n = 0$, 1, and 2 compounds (Li *et al.*, 1989). Since the lattice constant $a = 5.41$ Å ($b = 5.43$ Å) for all three compounds, this corresponds to a superlattice with unit cell of dimensions $\approx 3.8a$, b, c, with the repeat unit along the a direction equal to $\approx 3.8a$ for all three compounds. A modulation of $4.7b$ has also been reported (Kulik *et al.*, 1990). This structural modulation is called incommensurate because the repeat unit is not an integral multiple of a.

Substitutions dramatically change this modulation. The compound

$$Bi_2Sr_2Ca_{1-x}Y_xCu_2O_y$$

has a period that decreases from about $4.8b$ for $x = 0$ to the commensurate value $4.0b$ for $x = 1$ (Inoue *et al.*, 1989; Tamegai *et al.*, 1989). Replacing Cu by a transition metal (Fe, Mn, or Co) produces nonsuperconducting compounds with a structural modulation that is commensurate with the lattice spacing (Tarascon *et al.*, 1989b). A modulation-free bismuth-lead cuprate superconductor has been prepared (Manivannan *et al.*, 1991). Kistenmacher (1989) examined substitution-induced superstructures in $YBa_2(Cu_{1-x}M_x)_3O_7$. Superlattices with modulation wavelengths as short as 24 Å have been prepared by employing ultra-thin deposition techniques to interpose insulating planes of $PrBa_2Cu_3O_7$ (Jakob *et al.*, 1991; Lowndes *et al.*, 1990; Pennycook *et al.*, 1991; Rajagopal and Mahanti, 1991; Triscone *et al.*, 1990). Tanaka and Tsukada (1991) used the Kronig-Penney model (Tanaka and Tsukada, 1989a, b) to calculate the quasiparticle spectrum of superlattices.

F. Aligned TI-Ba Compounds

A series of aligned thallium-based superconducting compounds that have the general formula $TIBa_2Ca_nCu_{n+1}O_{5+2n}$ with n varying from 0 to 5 has been reported (Ihara *et al.*, 1988; Rona, 1990). These constitute a series from 1201 to 1245. They have superconducting transition temperatures almost as high as the $Tl_2Ba_2Ca_nCu_{n+1}O_{6+2n}$ compounds. Data on these compounds are listed in Table 8.3.

G. Lead Doping

Over the years a great deal of effort has been expended in synthesizing lead-doped superconducting cuprate structures (Itoh and Uchikawa, 1989). Examples involve substituting Pb for Bi (Dou *et al.*, 1989; Zhengping *et al.*, 1990), for Tl (Barry *et al.*, 1989; Mingzhu *et al.*, 1990), or for both Bi and Tl (Iqbal *et al.*, 1990). Different kinds of Pb, Y-containing superconductors have also been prepared (cf. Mattheiss and Hamann, 1989; Ohta and Maekawa, 1990; Tang *et al.*, 1991; Tokiwa *et al.*, 1990, 1991).

IX. SYMMETRIES

Earlier in this chapter we mentioned the significance of the horizontal reflection plane σ_h characteristic of the high-temperature superconductors, and noted that many of these superconductors are body centered. In this section we will point out additional symmetries that are present. Table VI-14 of our earlier work (Poole *et al.*, 1988) lists the point symmetries at the sites of the atoms in a number of these compounds.

In the notation of group theory the tetragonal structure belongs to the point group $4/mmm$ (this is the newer international notation for what in the older Schönflies notation was written D_{4h}). The unit cell possesses the inversion operation at the center, so when there is an atom at position (x, y, z), there will be another identical atom at position $(-x, -y, -z)$. The international symbol $4/mmm$ indicates the presence of a fourfold axis of symmetry C_4 and three mutually perpendicular mirror planes m. The Schönflies notation D_{4h} also specifies the fourfold axis, h signifying a horizontal mirror plane σ_h and D indicating a dihedral group with vertical mirror planes.

We see from Fig. 8.32 that the z-axis is a fourfold (90°) symmetry axis called C_4, and

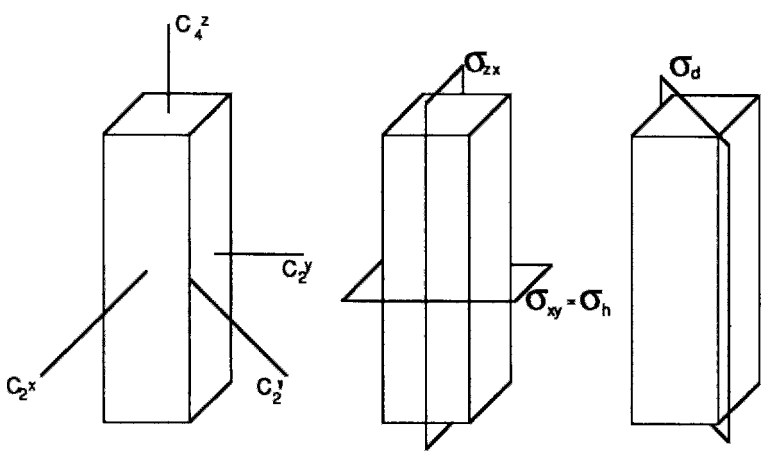

Figure 8.32 Symmetry operations of the tetragonal unit cell showing a fourfold rotation axis C_4, three twofold axes C_2, and reflection planes of the vertical $\sigma_{zx} = \sigma_v$, horizontal $\sigma_{xy} = \sigma_h$; and diagonal σ_d types.

that perpendicular to it are twofold (180°) symmetry axes along the x and y directions, called C_2, and also along the diagonal directions (C_2') in the midplane. There are two vertical mirror planes σ_d which are also vertical, and a horizontal mirror plane σ_h. Additional symmetry operations that are not shown are a 180° rotation C_2^z around the z axis,

$$\mathrm{C}_2^z = \mathrm{C}_4^z\mathrm{C}_4^z, \tag{8.9}$$

and the improper fourfold rotation S_4^z around that corresponds to C_4^z followed by, or preceded by, σ_h,

$$\mathrm{S}_4^z = \mathrm{C}_4^z\sigma_h = \sigma_h\mathrm{C}_4^z \tag{8.10}$$

where C_4^z and σ_h commute.

The orthorhombic structure has mmm, D_{2h} symmetry. We see from Fig. 8.33 that both the rectangular and rhombal unit cells, which correspond to Figs. 8.4a and 8.4b, respectively, have three mutually perpendicular twofold axes, and that they also have three mutually perpendicular mirror planes σ, which are not shown. The two cases differ in having their horizontal axes and vertical planes oriented at 45° to each other.

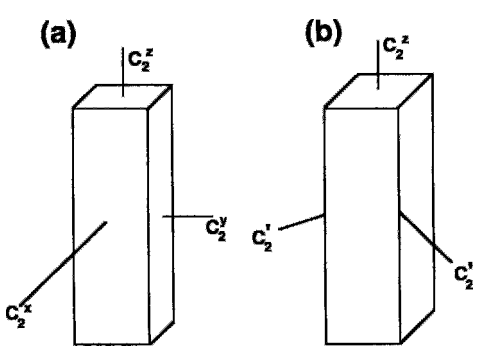

Figure 8.33 Rotational symmetry operations of an orthorhombic unit cell (a) with rectangular distortion, and (b) with rhombal distortion from an originally tetragonal cell.

Cubic structures, being much higher in symmetry, have additional symmetry operations, such as fourfold axes C_4^x, C_4^y, and C_4^z along each coordinate direction, threefold axes C_3 along each body diagonal, and numerous other mirror planes. These can be easily seen from an examination of Fig. 8.1. Buckyballs C_{60} belong to the icosohedral group, which has twofold (C_2), fivefold (C_5), and sixfold (C_6) rotation axes, horizontal reflection planes, inversion symmetry, and sixfold (S_6) and tenfold (S_{10}) improper rotations, for a total of 120 individual symmetry operations in all (Cotton, 1963).

X. LAYERED STRUCTURE OF THE CUPRATES

All cuprate superconductors have the layered structure shown in Fig. 8.34. The flow of supercurrent takes place in conduction layers, and binding layers support and hold together the conduction layers. Conduction layers contain copper-oxide (CuO_2) planes of the type shown in Fig. 8.24 with each copper ion (Cu^{2+}) is surrounded by four oxygen ions (O^{2-}). These planes are held together in the structure by calcium (Ca^{2+}) ions located between them, as indicated in Fig. 8.35. An exception to this is the yttrium compound in which the intervening ions are the element yttrium (Y^{3+}) instead of calcium. These CuO_2 planes are very close to being flat. In the normal state above T_c, conduction electrons released by copper atoms move about on these CuO_2 planes carrying electric current. In the superconducting state below T_c, these same electrons form the Cooper pairs that carry the supercurrent in the planes.

Each particular cuprate compound has its own specific binding layer consisting mainly of sublayers of metal oxides MO, where M is a metal atom; Fig. 8.36 gives the sequences of these sublayers for the

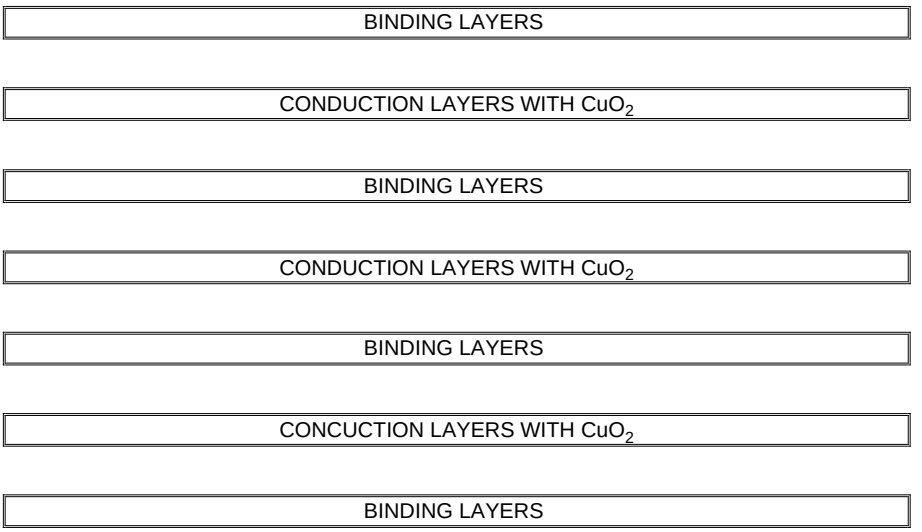

Figure 8.34 Layering scheme of a cuprate superconductor. Figure 8.35 shows details of the conduction layers for different sequences of copper oxide planes, and Fig. 8.36 presents details of the binding layers for several cuprates. (Owens and Poole, 1996, Fig. 8.1).

principal cuprate compounds. These binding layers are sometimes called *charge reservois layers* because they provide the charge for the Cooper pairs that form in the copper-oxide planes. Figure 8.30 presents a three-dimensional perspective of how conduction and binding layers are arranged in the thallium compounds containing one, two, and three copper oxide planes, i.e., having $n = 1,\ 2$, and 3 in the formula $Tl_2Ba_2Ca_{n-1}Cu_nO_{2n+4}$.

The fact that all of the cuprates have structures with alternating conduction layers and binding layers stacked along the z direction led to the adoption of a four digit code for designating their composition and structure. The general formula for a cuprate superconductor with a binding layer $A_jB_kO_{j+k}$, and a conducting layer $S_{n-1}Cu_nO_{2n}$, is $A_jB_kS_{n-1}Cu_nO_{j+k+2n+2}$, and most high temperature superconductors have the more specific formula $A_jB_2S_{n-1}Cu_nO_{j+2n+2}$. A sublayer BO of the binding layer is always adjacent to a CuO_2 sublayer of the conduction layer, with AO sublayers between BO sublayers. The separation atoms S always lie between CuO_2 sublayers of the conduction layer. This means that a CuO_2 sublayers can only have BO or S sublayers adjacent to it. A four digit code jkmn is often employed to designate the structure type $A_jB_kS_mCu_n$.

In typical cases the binding layer consists of oxides of A atoms which are Bi, Tl or Hg, and oxides of B atoms which are Sr or Ba. The separation atoms S of the conduction band are usually Ca, but in the yttrium superconductor they are Y. Using the notation jkmn we have the following examples of four digit codes:

0201	$(La_{1-x}Sr_x)_2CuO_4$
1212	$HgBa_2CaCu_2O_6$
1212	$CuBa_2YCu_2O_7$
	(Usually written $YBa_2Cu_3O_7$)
1223	$TlBa_2Ca_2Cu_3O_9$
2201	$Bi_2Sr_2CuO_6$
2234	$Tl_2Ba_2Ca_3Cu_4O_{12}$

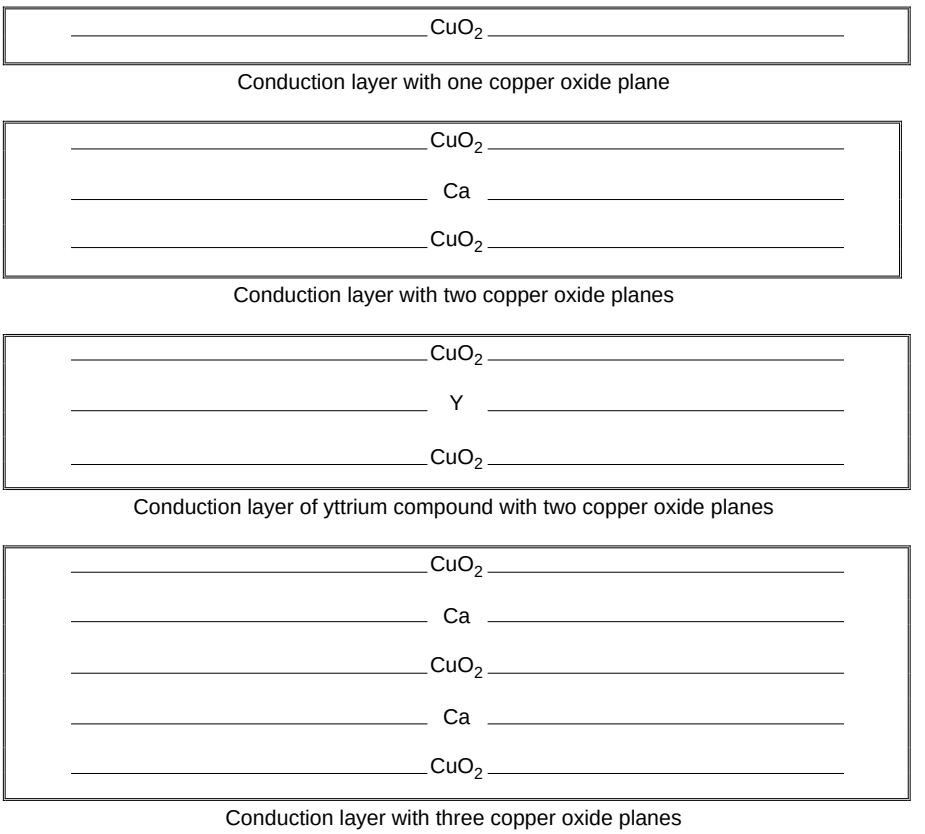

Figure 8.35 Conduction layers of the various cuprate superconductors showing sequences of CuO_2 and Ca (or Y) planes in the conduction layers of Fig. 8.34. (Owens and Poole, 1996, Fig. 8.3).

Sometimes the A atom symbol is used as a prefix to the code, and in this notation five of the above six codes would be written: La-0201, Hg-1212, Tl-1223, Bi-2201, and Tl-2234 to designate the corresponding compounds.

XI. INFINITE-LAYER PHASES

In 1993 superconductivity was discovered in the series of compounds with the general formula $Sr_{n+1}Cu_nO_{2n+1+\delta}$; these compounds represent perhaps the simplest of the copper oxide superconductors containing only two metallic elements, strontium and copper. Like the cuprates these are layered compounds, and the parameter n designates the number of copper oxide layers. The layering scheme is very simple, and it can be visualized from Fig. 8.37. The binding layer Sr_2O for all of these compounds consists of successive Sr, O, and Sr planes, as indicated at the top of Fig. 8.37. This binding layer is much thinner than those of the cuprates; conduction layers are similar to the cuprate ones shown in Fig. 8.35 but with strontium atoms between the CuO_2 planes instead of calcium or yttrium. Thus these compounds may properly be considered as cuprate types.

The $n = 1$ compound has a structure similar to that of La_2CuO_4, discussed earlier and shown in Fig. 8.21. This $n = 1$

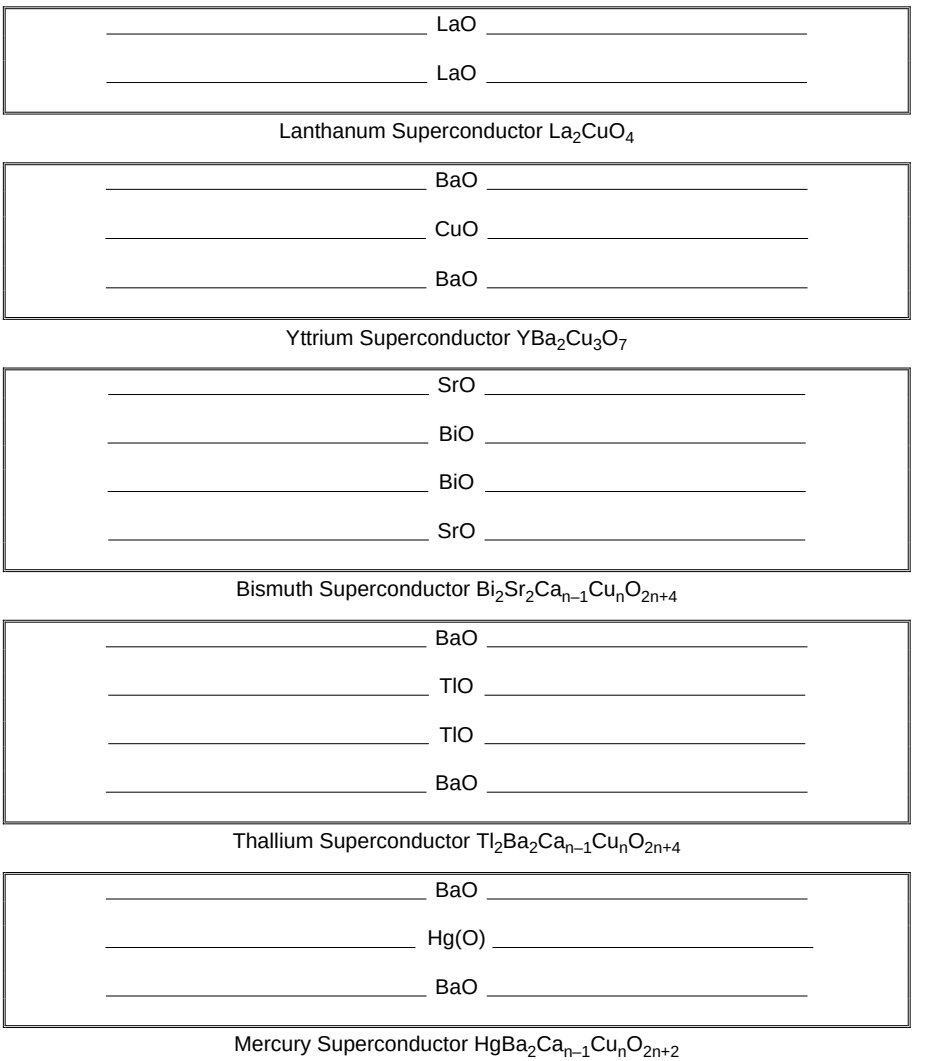

Figure 8.36 Sequences of MO sublayers in the binding layers of Fig. 8.34 where M stands for various metal ions. The parentheses around the oxygen atom O in the lowest panel indicates partial occupancy. (Owens and Poole, 1996, Fig. 8.4).

compound with the formula $Sr_2CuO_{3.1}$ has a large number of vacancies in the binding layers and a transition temperature of 70 K. These vacancies provide the doping mechanism for holes in the CuO planes. The $n = 2$ compound $Sr_3Cu_2O_{5+\delta}$ has a T_c of 100 K.

The limit of the series for very large n is $SrCuO_2$; it has the infinite layer structure shown in Fig. 8.38. This material can be made into an electron-doped superconductor with $T_c = 43$ K by replacing some of the divalent Sr^{2+} with trivalent La^{3+}; this has the effect of putting electron carriers in the copper oxide planes. The large n material doped with holes occurs only in a small fraction of the samples, and it has a transition temperature of 110 K. It is not clear what causes hole doping, but it is believed to involve some kind of defect structure. One idea is that an oxygen atom may be trapped between two Sr

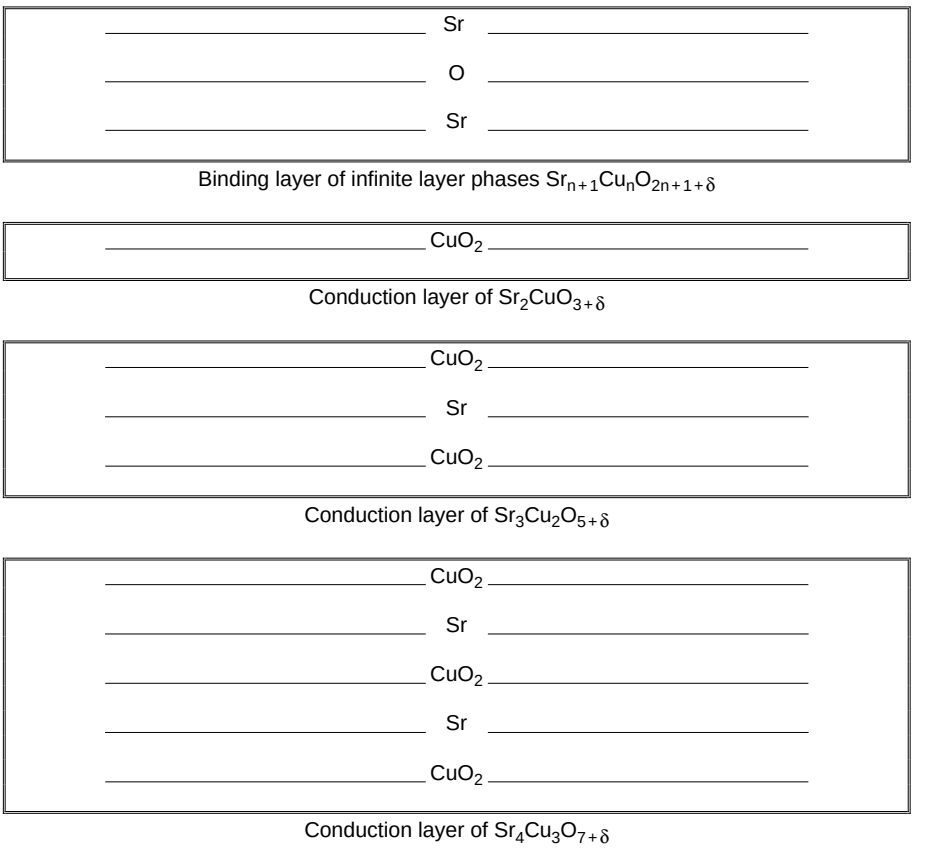

Figure 8.37 Binding layer (top) followed by, in succession, conduction layers of the first three infinite layer phase compounds, namely $Sr_2CuO_{3+\delta}$, $Sr_3Cu_2O_{5+\delta}$ and $Sr_4Cu_3O_{7+\delta}$. The figures are drawn assuming $\delta = 0$. (Owens and Poole, 1996, Fig. 8.17).

atoms, forming an Sr–O–Sr defect. Another proposal is that a corrugated Sr–O layer is substituted for one of the copper oxide layers.

XII. CONCLUSIONS

Almost all the high-temperature oxide superconductors have point symmetry D_{4h} $(a = b)$ or symmetry close to D_{4h} $(a \sim b)$. These superconductors consist of horizontal layers, each of which contains one positive ion and either zero, one, or two oxygens. The copper ions may be coordinated square planar, pyramidal, or octahedral, with some additional distortion. Copper oxide layers are never adjacent to each other, and equivalent layers are never adjacent. The cations alternate sites vertically, as do the oxygens. The copper oxide layers are either flat or slightly puckered, in contrast to the other metal oxide layers, which are generally far from planar. The highest T_c compounds have metal layers (e.g., Ca) with no oxygens between the copper oxide planes.

FURTHER READING

Chapter 8 by R. Gladyshevskii and P. Galez in the Handbook of Superconductivity edited by C. P. Poole, Jr., provides the structures of most of the cuprates. The *International Tables for X-Ray Crystallography* (Henry and Lonsdale, 1965, Vol. 1) provide the atom positions and symmetries for all of the crystallographic space groups.

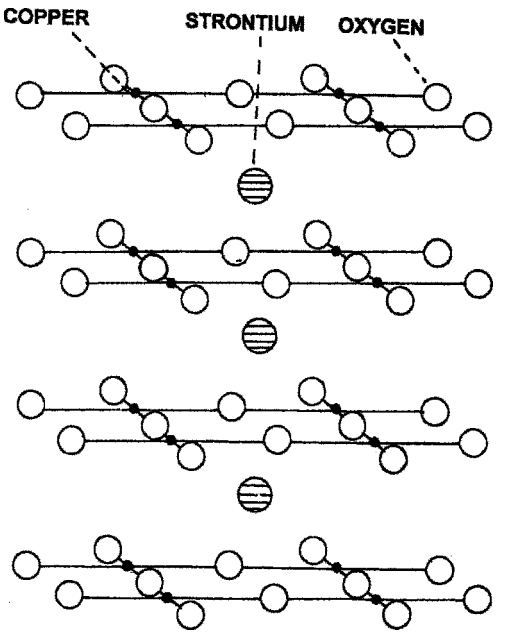

Figure 8.38 Crystal structure of the infinite layer phase $SrCuO_2$. (Owens and Poole, 1996, Fig. 8.18).

PROBLEMS

1. Show that the radius of the octahedral hole in an fcc close-packed lattice of atoms of radius r_0 is equal to $[\sqrt{2}-1]r_0$. What is the radius of the hole if the lattice is formed from oxygen ions?
2. Show that the radius of the tetrahedral hole in an fcc close-packed lattice of atoms of radius r_0 is equal to $\left[(3/2)^{1/2}-1\right]r_0$. What is the radius of the hole if the lattice is formed from oxygen ions?
3. The "image perovskite" unit cell is generated from the unit cell of Fig. 8.1 by shifting the origin from the point (0, 0, 0) to the point $(\frac{1}{2}, \frac{1}{2}, \frac{1}{2})$. Sketch this "image" cell. Show that the planes of atoms in this cell are the image planes related by the body centering operation to those of the original perovskite. This image cell is the one that usually appears as a figure to represent perovskite in solid-state physics texts.
4. Calculate the distance between the yttrium atom and its nearest-neighbor Ba, Cu, and O atoms in the superconductor $YBa_2Cu_3O_7$.
5. Write down the $x,\ y,\ z$ coordinates for the five numbered atoms in the initial plane of Fig. 8.19. Give the explicit symmetry operations, with the proper choice of sign in Eq. (8.5) for each case, that transform these five atoms to their indicated new positions on the other three planes.
6. Explain how the international and Schönflies symbols, *mmm* and D_{2h} respectively, are appropriate for designating the point group for the orthorhombic superconductors.
7. What are the symmetry operations of the *A*15 unit cell of Fig. 3.19?
8. The D_{2h} point group consists of eight symmetry operations that leave an orthorhombic cell unchanged, namely an identity operation E that produces no change, three twofold rotations C_2^i along $I = x,\ y,\ z$, three mirror reflection planes σ_{ij}, and an inversion i. Examples of these symmetry operations are

$$\begin{array}{llll} E & x \to x & y \to y & z \to z \\ C_2^x & x \to x & y \to -y & z \to -z \\ \sigma_{xy} & x \to x & y \to y & z \to -z \\ i & x \to -x & y \to -y & z \to -z \end{array}$$

A group has the property that the successive application of two symmetry operations produces a third. Thus, we have, for example,

$$\begin{aligned} C_2^x \sigma_{xy} &= \sigma_{zx} \\ C_2^y C_2^x &= C_2^z \\ iC_2^y &= \sigma_{zx} \\ \sigma_{zx}\sigma_{yz} &= C_2^x \end{aligned}$$

These four results have been entered into the following multiplication table

	E	C_2^x	C_2^y	C_2^z	i	σ_{xy}	σ_{yz}	σ_{zx}
E								
C_2^x						σ_{zx}		
C_2^y		C_2^z						
C_2^z								
i			σ_{zx}					
σ_{xy}								
σ_{yz}								
σ_{zx}							C_2^z	

for the D_{2h} group. Fill in the remainder of the table. Hint: each element of a group appears in each row and each column of the multiplication table once and only once.

9. Construct the multiplication table for the D_{4h} point group which contains the 16 symmetry elements that leave a tetragonal unit cell unchanged. Which pairs of symmetry elements A and B do not commute, i.e., such that $AB \neq BA$? Hint: follow the procedures used in Problem 8.
10. Draw diagrams analogous to those in Fig. 8.29 for the first two members of the aligned series $TlBa_2Ca_nCu_{n+1}O_{5+2n}$, where $n = 0,\ 1$.
11. Draw the analogue of Fig. 8.22 for the Nd_2CuO_4 compound, showing the location of all of the Cu and O atoms. How do Figs. 8.24 and 8.25 differ for Nd_2CuO_4?
12. Select one of the compounds ($Tl_2Ba_2CuO_6$, $Bi_2Sr_2CaCu_2O_8$, $Bi_2Sr_2Ca_2Cu_3O_{10}$, $Tl_2Ba_2Ca_2Cu_3O_6$) and construct a table for it patterned after Tables 8.5 or 8.6.

This page intentionally left blank

9

Unconventional Superconductors

I. INTRODUCTION

The classical superconductors which are discussed in Chap. 3 consist of elements, alloys, intermetallic compounds, and ionic compounds. They are all s-wave types with properties that are explained well by the standard isotropic BCS theory. The cuprate high temperature superconductors discussed in Chap. 8 exhibit Cooper pairing of a d-wave type, and are anisotropic in their properties. Their symmetries are either tetragonal or orthorhombic, but close to tetragonal. The nonclassical or unconventional nature of their properties arises from their layered structures, as described in Chap. 8. This chapter will cover materials which exhibit other types of unconventional superconductivity. Some of these unconventional superconductors were discussed in the previous edition, such as heavy electron types, charge transfer organics and borocarbides toward the end of Chap. 3, and perovskites and buckministerfuller4enes in both Chap. 3 and Chap. 7 of that edition, while others were discovered in more recent years. The present chapter will cover the properties of all these superconducting materials.

II. HEAVY ELECTRON SYSTEMS

For several years prior to 1987 there was a great deal of interest in the study of heavy-electron superconductors, i.e., superconductors whose effective conduction-electron mass m^* is typically more than 100 electron

masses. Physicists have given these materials a somewhat more pretentious name "heavy fermion superconductors." The first such superconductor, $CeCu_2Si_2$, was discovered in 1979 (Steglich *et al.*, 1979), and some time passed before the phenomenon was confirmed by the discovery of other examples, such as UBe_{13} (Ott *et al.*, 1983) and UPt_3 (Stewart *et al.*, 1984). Since then many additional cases have been found. Many of the investigators who became active in the field of cuprate superconductivity obtained their experience with the heavy-electron types. Work on heavy-electron superconductors has been reviewed in a number of studies (Coles, 1987; Ott, 1987; Stewart, 1984).

The Cooper pairing in the heavy electron systems is of the $\ell = 1$ or p-wave type. Since the superconducting charge carriers are Cooper pairs formed from heavy electrons and since these pairs are bosons, it would be more appropriate to call these compounds "heavy boson superconductors." This, however, is never done, so we will conform to the conventional usage. Ordinary superconductors are not usually called boson superconductors either.

The large effective mass has a pronounced effect on several properties of superconducting materials since it enters into the expression (Eq. (1.41)) for the electron density of states at the Fermi level:

$$D(E_F) = \frac{1}{2\pi^2}\left(\frac{2m^*}{\hbar^2}\right)^{3/2} E_F^{1/2}, \qquad (9.1)$$

Heavy-electron compounds have densities of states that correspond to values of $m^* \approx 200m_e$ in Eq. 9.1, as shown by the data in Table 9.1.

The rare-earth element Ce has two $4f$ electrons and the actinide element U has three $5f$ electrons. In compounds each of these elements has f electron configurations that can mix as linear combinations or hybridize with the conduction electrons and together produce sharp energy bands near the Fermi level. The narrow width of such a band gives it a high density of states, and hence, by Eq. 9.1, a large effective mass. A situation of this type is sketched in Fig. 9.1 in which a narrow hybridization band superimposed on the usual conduction electron expression $D(E)\ \alpha\ \sqrt{E}$ from Fig. 6.5 of the

Table 9.1 Properties of Several Heavy-Electron Superconductors[a]

Compound	T_c (K)	T_N (K)	Θ (K)	$\mu_{eff}/\mu B$	m^*/m_c
$CeAl_3$			−43	2.62	
$CeCu_6$			−88	2.68	
$NpBe_{13}$		3.4	−42	2.76	
UBe_{13}	0.85	8.8	−70	3.1	192
UCd_{11}		5.0	−23	3.45	
UPt_3	0.43	5.0	−200	2.9	187
U_2Zn_{17}		9.7	−250	4.5	
$CeCu_2Si_2$	0.6	0.7	−140	2.6	220
UNi_2Al_3	1.0	4.6			
UPd_2Al_3	≈ 2.0	14.0			
URu_2Si_2	1.3	17.5			

[a] T_c is the superconducting transition temperature; T_N is the Néel temperature; Θ is the Curie-Weiss temperature; μ_{eff} is the effective magnetic moment and m^*/m_c is the ratio of the effective mass to the free electron mass. Some of the data are borrowed from Stewart (1984). Additional data are from Geibel *et al.* (1991a) on UNi_2Al_3, from Geibel *et al.* (1991b and 1991c) on UPd_2Al_2, and Issacs *et al.* (1990) on URh_2Si_2.

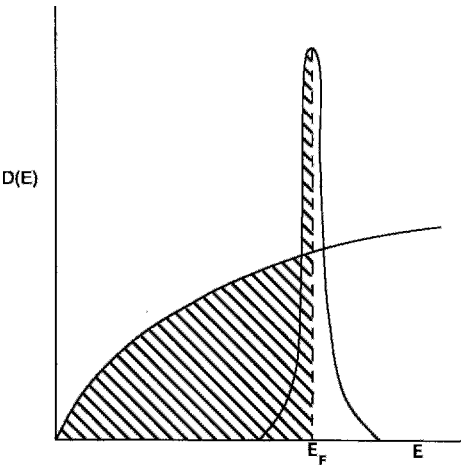

Figure 9.1 Density of states of a heavy fermion compound showing a peaked, narrow, half-occupied band at the Fermi level. (first edition, Fig. 3.26)

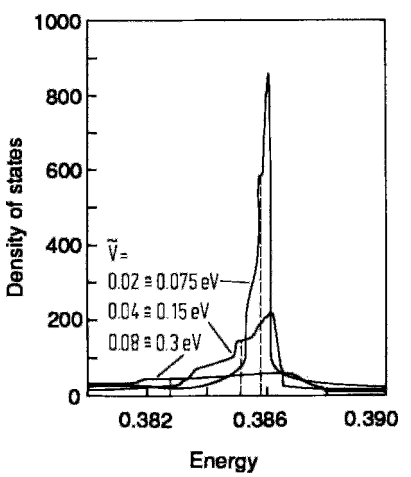

Figure 9.2 Density of states of a narrow hybridization band calculated for three values of the hybridization between a conduction electron and an f electron wave function (Hofmann and Keller, 1989).

first edition. The figure is drawn for the situation where the Fermi level is at the center of the hybridization band. Figure 9.2 shows the density of states at the Fermi level calculated for three values of the effective hybridization between a conduction electron and an f electron wave function (Hofmann and Keller, 1989). We see that the sharpness of the peak in $D(E_F)$ depends on the strength of this interaction. The electrons in these f shells of Ce and U are also responsible for the formation of the superconducting state. Other rare earths and actinides do not form these types of hybridization bands at the Fermi level.

Much of the evidence for the high effective mass comes from experimental observations in the normal state. For example, the conduction-electron contribution to the specific heat from Eq. (1.52)

$$\gamma = \frac{1}{3}\pi^2 D(E_F) k_B^2, \tag{9.2}$$

is proportional to the density of states (9.1) and hence is unusually large for heavy-electron compounds. The electronic specific-heat coefficients γ for heavy-electron superconductors are, on average, more that 10 times larger than those of other superconducting compounds, as may be seen by consulting Table 4.1. The discontinuity $(C_c - \gamma T_c)$ in the specific heat at the transition temperature is also correspondingly large for heavy-electron compounds, so the ratio $(C_s - \gamma T_c)/\gamma T_c$ is close to the usual BCS value of 1.43, as may be seen from the same table. Figure 9.3 shows a measurement of this discontinuity in the compound UPt_3.

Heavy-electron systems often exhibit two ordering transitions, a superconducting transition at T_c and an antiferromagnetic ordering transition at the Néel temperature T_N, with typical values given in Table 9.1. The superconducting transition is illustrated by the drop in magnetic susceptibility at T_c (shown in Fig. 9.4 for URu_2Si_2). When the magnetic moments of the ions couple antiferromagnetically, the magnetic susceptiblility often exhibits Curie-Weiss behavior (cf. Eq. (1.79)). Many of these compounds have effective magnetic moments exceeding the

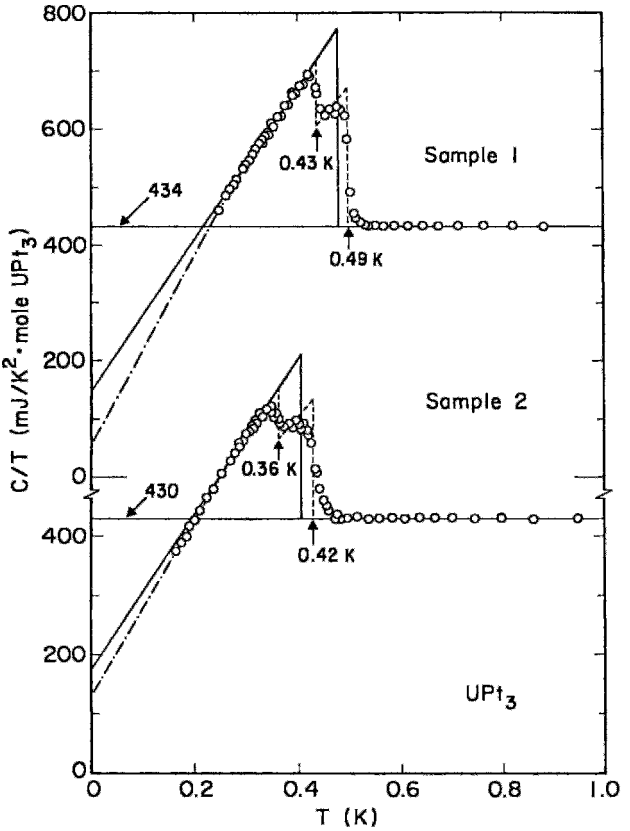

Figure 9.3 Specific heat of the heavy fermion compound UPt_3 in the neighborhood of the transition temperature. The solid lines correspond to a single ideally sharp transition while the dashed lines are fits to the data with two adjacent sharp transitions (Fisher *et al.*, 1989).

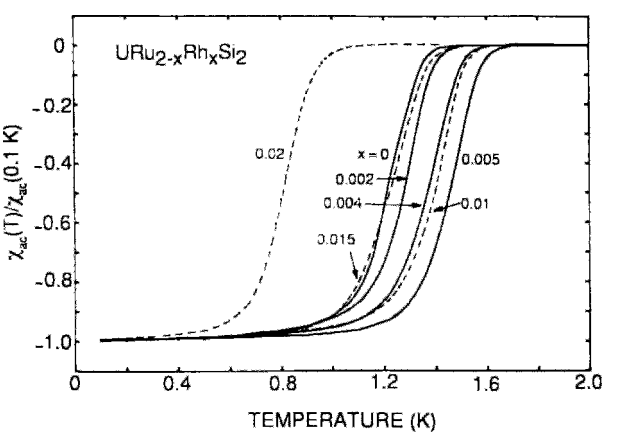

Figure 9.4 Dependence of magnetic susceptibility χ on temperature for the heavy fermion compounds $URu_{2-x}Rh_xSi_2$, with χ in the range $0 \leq \chi \leq 0.02$ (Dalichaouch *et al.*, 1990).

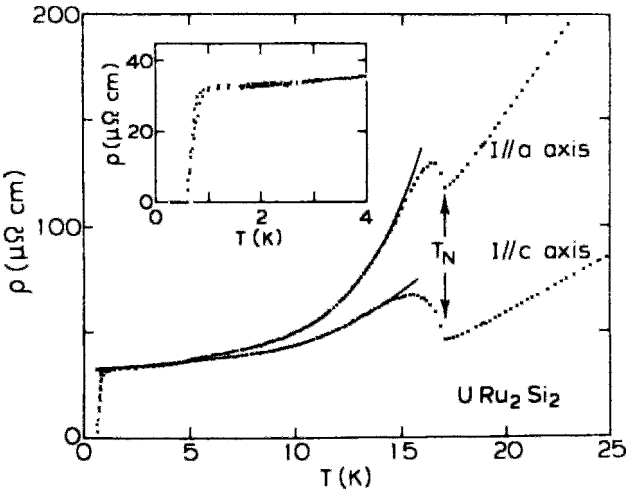

Figure 9.5 Peak near 16K in the resistivity-versus-temperature plot of the heavy fermion compound URu_2Si. The inset shows the superconducting transition below 1K in an expanded scale (Mydosh, 1987; see also Palst *et al.*, 1987).

Bohr magneton, as shown in Table 9.1. The table lists several other properties of these materials.

The heavy-electron superconductors have anisotropic properties that become apparent in such measurements as those for the critical fields, electrical resistivity, ultrasonic attenuation, thermal conductivity, and NMR relaxation. Figures 9.5 and 9.6, respectively, show typical anisotropies in the resistivity (Coles, 1987; Mydosh, 1987; Palst *et al.*, 1987) and upper-critical field (Assmus *et al.*, 1984; Stewart, 1984). The presence of a peak in the resistivity shown in Fig. 9.5 is characteristic of the heavy fermions.

The lower-critical fields B_{c1} are several mT at 0 K, while the upper-critical fields B_{c2} at 0 K approach 1 or 2 tesla as shown by the example in Fig. 9.6. The critical field derivatives dB_{c2}/dT are high in absolute magnitude, such as $-10\,\mathrm{T/K}$ for $CeCu_2Si_2$ and $-44\,\mathrm{T/K}$ for UBe_{13}.

The London penetration depth λ_L is several thousand angstroms, consistent with the large effective mass m^*, which enters as a

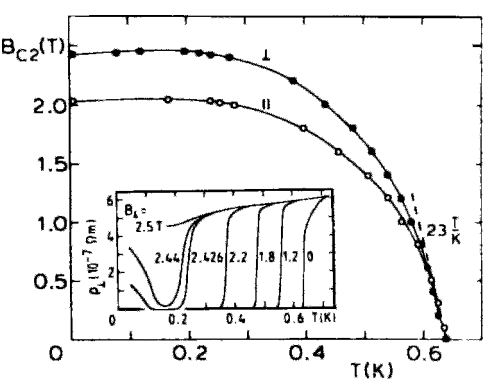

Figure 9.6 Upper critical-field anisotropy in tetragonal heavy fermion superconductor $CeCu_2Si_2$ parallel to, respectively perpendicular to, the Ce planes. Note the lack of anisotropy at T_c where both orientations have the same slope, $-23\mathrm{T/K}$, as given by the dashed line. The inset shows the temperature dependence of the resistivity under various applied fields (Assmus *et al.*, 1984).

square root factor in the classical expression in (2.28)

$$\lambda_L = \left(\frac{m^*}{\mu_0 n_s e^2}\right)^{1/2} \tag{9.3}$$

In ordinary superconductors magnetic impurities suppress the superconducting state

due to the pair-breaking effect of the magnetic moments. In anisotropic superconductors, on the other hand, any kind of impurity is pair breaking. In particular, small amounts of nonmagnetic impurities replacing, for example, uranium, beryllium, or platinum, bring about a pronounced lowering of T_c. Some researchers have suggested that the heavy-electron materials exhibit an unconventional type of superconductivity that does not involve the ordinary electron-phonon interaction (Bishop *et al.*, 1984; Coles, 1987; Gumhalter and Zlatic, 1990; D. W. Hess *et al.*, 1989; Ott, 1987; Ozaki and Machida, 1989; Rodriguez, 1987; Stewart, 1984).

There have also been reports of high effective masses in the oxide superconductors, with, for example, $m^*/m \approx 12$ (Matsura and Miyake, 1987) in LaSrCuO, and $m^*/m \approx 5$ (Gottwick *et al.*, 1987), $m^*/m = 9$ (Salamon and Bardeen, 1987), and $m^*/m \approx 10^2$ in YBaCuO (Kresin and Wolf, 1987). Some more recently discovered heavy-electron superconductors are $Ce_3Bi_4Pt_3$ (Riseborough, 1992), UNi_2Al_3 (Geibel *et al.*, 1991a; Krimmel *et al.*, 1992), UPd_2Al_3 (Geibel *et al.*, 1991b, c; Krimmel *et al.*, 1992; Sato *et al.*, 1992), and YBiPt (Fisk *et al.*, 1991).

III. MAGNESIUM DIBORIDE

Superconductivity in magnesium diboride was discovered by Nagamatsu et al. in 2001. MgB_2 is a simple intermetallic compound with a hexagonal unimolecular unit cell. It was a surprise to find that its transition temperature $T_c \cong 39K$ is so far above that of all other intermetallic compounds. Its superconductivity is the simple BCS phonon mediated s-wave type, but complicated by the presence of two energy gaps. During the year after its discovery the superconducting community of scientists embarked on a worldwide concentrated effort to unravel the reasons why such a simple compound could be such a good superconductor. Two years later the journal Physica C devoted a special issue to the topic (Vol. 385, Nos. 1–2, March 2003), which we will denote by PhC.

A. Structure

Magnesium diboride has the AlB_2 hexagonal structure sketched in Fig. 9.7, with $a_0 = 0.3084\,nm$ and $c_0 = 0.3262\,nm$, corresponding to crystallographic space group $P\bar{3}ml(D_{3d}{}^3)$. Mg is in the special position 000, and B is in the two special positions $^1/_3{}^2/_3{}^1/_2$ and $^2/_3{}^1/_3{}^1/_2$ in the unit cell. There are alternating layers of magnesium and boron atoms perpendicular to the c axis, with the Mg adopting a close packed planar hexagonal arrangement, and the B atoms in a graphite- type hexagonal arrangement. Each boron atom has a triangular array of magnesiums above and below it, and each magnesium has an array of six borons above and six below, as is clear from the figure. The nearest neighbor distances are

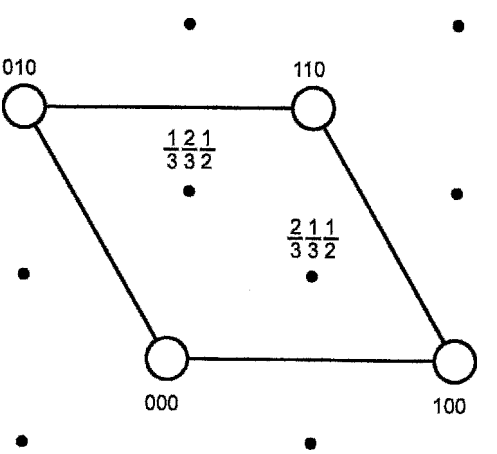

Figure 9.7 Arrangement of magnesium atoms (large open circles) in planes $z = 0$ and $z = c$, with a planar hexagonal arrangement of boron atoms (solid dots) at the height $z = {}^1/_2c$ between these planes. (Thanks are due to Michael A. Poole for preparing this figure).

$$d_{B\text{-}B} = 0.177\,\text{nm}$$
$$d_{Mg\text{-}B} = 0.250\,\text{nm} \qquad (9.4)$$
$$d_{mg\text{-}Mg} = 0.308\,\text{nm}$$

Since boron has the valence electron configuration $2s^2p$ and magnesium has $3s^2$, only s and p electrons are involved in the electronic structure and the Cooper pairing. Within the boron layers the bonding is strongly covalent, and between the boron and magnesium layers the bonding is more metallic-like, involving some electron delocalization [Mazin and Antropov, 2003].

Boron has two naturally occurring isotopes: $^{10}B(19.78\%)$ and $^{12}B(80.22\%)$, and magnesiusm has three: $^{24}Mg(78.99\%)$, $^{25}Mg(10.00\%)$, and $^{26}Mg(11.01\%)$. When T_c was measured with isotopically enriched samples it was found that the isotope effect exponent $\alpha = 0.32$ for boron, somewhat below the theoretical BCS value of $\alpha = 0.5$. Figure 9.8 shows the isotopic shift determined by magnetization and resistivity measurements. The shift for magnesium enrichment was negligible. This indicates that the phonons involved in the Cooper-pairing were mainly from vibrations of the lighter boron atoms, with phonons arising from Mg vibrations making very little contribution.

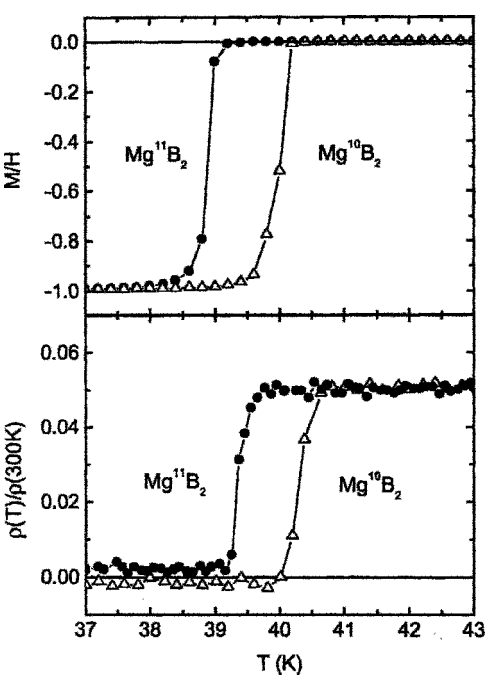

Figure 9.8 Isotope shift determined by magnetization (upper panel) and resistivity (lower panel) measurements. (Canfield et al., 2003, Fig. 1).

B. Physical Properties

In the special issue of the journal Physica C mentioned above Canfield et al., (2003) wrote an introductory article which summarized the basic physical properties of MgB_2, and a number of these properties are listed in Table 9.2. Some of these data are averages, and do not take into account the presence of two gaps in the energy bands. Figure 9.9 shows the temperature dependence of the resistivity in zero field and in applied magnetic fields between 2.5T and 18T. We see that the transition temperature is lowered and the transition is broadened for increasing fields, as expected. Figure 9.10 presents the temperature dependence of the magnetization of aligned single crystals in a magnetic field of 0.5mT applied along the c crystallographic direction. We see that the magnetization below T_c is much more negative for zero field cooling (ZFC) than it is for field cooling (FC). The hysteresis loop in the inset obtained at a temperature of 10K corresponds to a critical current density $J_c < 10^5\,A/cm^2$.

C. Anisotropies

Magnesium diboride has the layered crystal structure illustrated in Fig. 9.7 and this causes some of its physical properties to be anisotropic, with values that differ for measurements made in the a, b plane and along the c direction. The temperature dependence of the penetration depth factor $\Delta\lambda$

Table 9.2 Basic physical properties of the superconductor MgB_2. Some parameters are anisotropic, with only average values listed here.

Superconducting transition temperature T_c	39K*
Coherence length ξ_0	5 nm*
Penetration depth λ	140 nm*
Ginzburg-Landau parameter κ	$\cong 25$
electron mean free path ℓ	$\cong 60$ nm*
Residual resistivity ratio RRR = $\rho(300K)/\rho(42K)$	$\cong 20$
Debye temperature Θ_D	340K
Fermi surface electron velocity V_F	4.8×10^5 m/sec*
Isotope effect constant α	0.32
Upper critical field B_{c2}, clean sample ($\ell \gg \xi_0$)	16T*
dirty sample ($\ell \ll \xi_0$)	30T*
Irreversibility field B_{irr}, clean sample	7T*
dirty sample	15T*
Thermodynamic critical field B_c	0.43T
Lower critical field B_{c1}	30mT
Critical current density J_c	$\cong 4 \times 10^5$ A/cm^{2*}

* Values obtained from Canfield et al. (2003) article cited above.

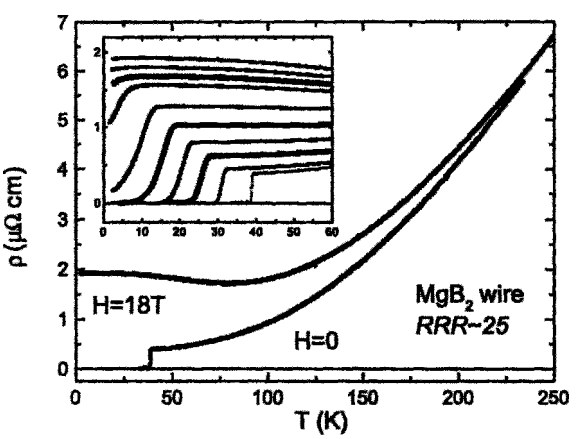

Figure 9.9 Temperature dependence of the resistivity of MgB_2 crystals in zero field and in an 18T applied magnetic field. The inset presents low field data for applied fields, from bottom to top, of 0, 2.5, 5, 7.5, 10, 12.5, 15, 16, 17, and 18T. (Canfield et al., 2003, Fig. 2).

$$\Delta\lambda = \lambda(T) - \lambda(0) \qquad (9.5)$$

presented in Fig. 9.11, shows that $\Delta\lambda$ is larger for a magnetic field applied along the c direction than it is for the field applied in the a, b plane. These measurements were made using a sensitive radio frequency technique, and the inset to the figure gives the ratio of the observed frequency shifts for the applied field perpendicular to and parallel to the c axis. The second critical field B_{c2} is also anisotropic, being about six times larger for fields applied in the a, b plane than for fields along the c axis, as shown in Fig. 9.12a.

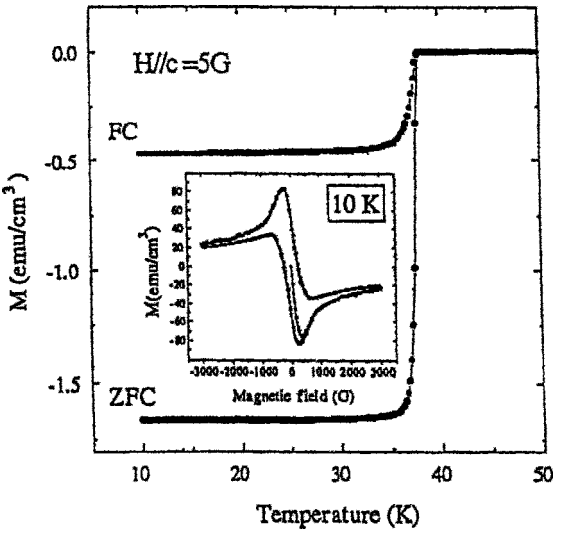

Figure 9.10 Temperature dependence of the magnetization for field cooled (FC) and zero field cooled (ZFC) measurements in an applied field along the crystallographic c direction with $B_{app} = 0.5\,mT$. The inset shows a hysteresis loop of a MgB_2 single crystal at 10K with $B_{app} \parallel c$. (Lee, 2003, Fig. 3).

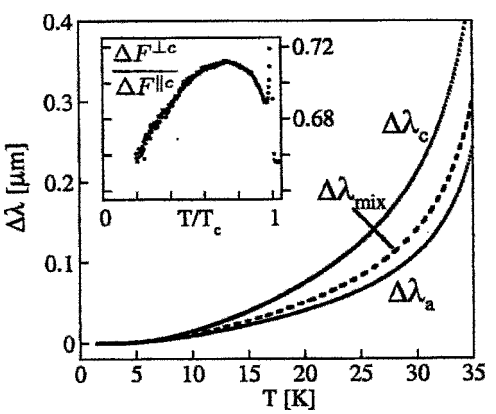

Figure 9.11 Temperature dependence of the penetration depth factor $\Delta\lambda = \lambda(T) - \lambda(0)$ for measurements made in the ab plane ($\Delta\lambda_a$) and in the axial direction ($\Delta\lambda_c$). The insert shows the ratio of changes in the circuit resonant frequency ΔF for the magnetic field applied in the a, b plane and parallel to the c axis. (Fletcher et al., 2005, Fig. 1).

The temperature dependence of the critical field anisotropy factor $\gamma_H = B_{c2}{}^{ab}/B_{c2}{}^{c}$ is indicated in Fig. 9.12b. Since we know from Eq. (12.56b) that $B_{c2}{}^{i} = \Phi_0/2\pi\xi_j\xi_k$ it follows that $\gamma_H = \xi_{ab}/\xi_c$. Equation (12.43) shows that the product $\lambda_i\xi_i$ for all three directions i, j, k = a, b, c is expected to be constant for each superconductor, which means that the critical field anisotropy factor can also be written in the form $\gamma_H = \lambda_c/\lambda_{ab}$. The self-consistency of these three expressions for γ_H can be checked experimentally.

D. Fermi Surfaces

A sketch of the configuration of the Fermi surface of MgB_2 published in the above mentioned special issue of Physica C by Kogan and Bud'ko (2003) is presented in Fig. 9.13, and Cooper et al. (2003) provide a similar sketch in the same issue. The three energy bands (#3,4 and 5) that cross the Fermi level give rise to four Fermi surface sheets, two axial quasi two-dimensional σ-band sheets, and two contorted three-dimensional π-band sheets, as shown in the figure. The σ-bands originate from the boron

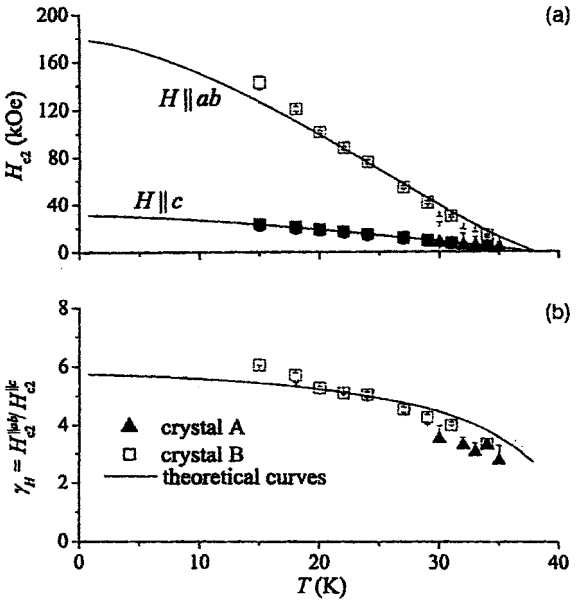

Figure 9.12 (a) Temperature dependence of the upper critical field for measurements made in the a, b plane (lower data set) and parallel to the c axis (upper data). Squares and triangles represent measurements made using two different samples and two different measurement techniques. (b) Temperature dependence of the upper critical field anisotropy given by the factor $\gamma_H = B_{c2}{}^{ab}/B_{c2}{}^{c}$ in the notation used in the text. The full lines are theoretical curves calculated by the method of Miranvoic et al. (Angst. et al., 200, Fig. 3).

valence electron in-plane sp^2 hybridization involving bonding p_x and p_y orbitals that are somewhat weakly coupled [see Samuely *et al.*, 2003], and form two concentric nearly cylindrical sheets along the Γ–A–Γ axis in the k_z direction of the Brillouin zone, as shown in the figure. Because of their cylindrical shape these sheets have a two dimensional character. Conduction electrons can move in the k_z direction on these σ-band surfaces from one Brillouin zone to the next since eight adjacent zones join together at the special point Γ, and the σ cylindrical surfaces are continuous across the boundary.

It is clear from the figure that the π-bands, which arise from aromatically hybridized (covalent) bonding and antibonding p_z orbitals of boron that are more strongly coupled, form very convoluted surfaces that are three dimensional in character. The sheet from band 3 involves electron-type antibonding, and that from band 4 is hole-type bonding. We see from Fig. 9.13 that the surface of π-band No.5 crosses into the next Brillouin zone along the k_x and k_y directions at the special points L, and the surface of π-band No. 4 crosses the zone boundaries at special points M. All of these π-band crossings correspond to electron flow in the k_x, k_y, plane. As a result of these geometric characteristics of the Fermi surface electrical properties such as the resistivity, and other properties of magnesium diboride are anisotropic, and hence depend on the direction of an applied magnetic field.

Lee et al. (2001) provide sketches of extremal orbits of electrons encircling spe-

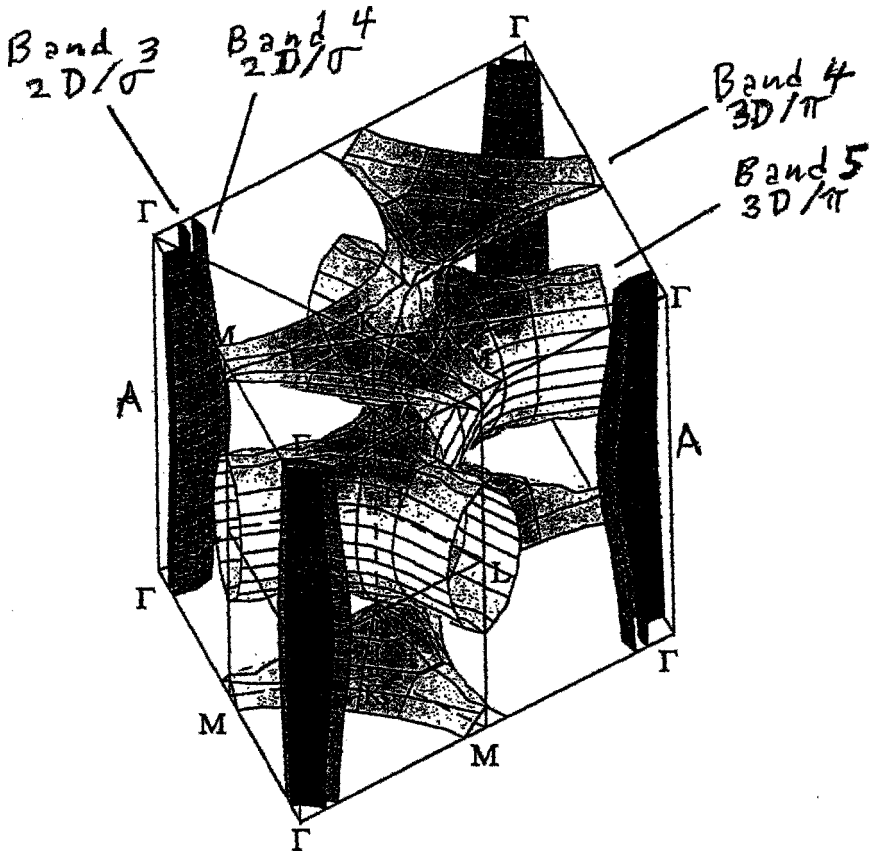

Figure 9.13 Fermi surface of MgB_2 calculated by Choi et al., 2002. Four sheets formed from three energy bands, and points of special symmetry in the tetragonal Brillouin zone, are indicated. (Kogan and Bud'ko, 2003, Fig. 4). Cooper et al. (2003) identify the bands.

cial points Γ, A, K, L, and M on the Fermi surface. De Haas-van Alphen experiments can be carried out with preferentially oriented applied magnetic fields to determine the areas enclosed by these orbits in k-space, and thereby confirm the configuration of these various energy surfaces in k-space (Cooper et al., 2003).

E. Energy Gaps

The superconducting energy gap differs for the two σ-bands and for the two π bands, and the spread in the corresponding gap values is sketched in Fig. 9.14. The pi gap has the approximate value $\Delta_\pi \cong 2.8$meV, and for the larger sigma gap $\Delta_\sigma \cong 6.8$meV. The temperature dependencies of these gaps are of the conventional type, decreasing to zero as the transition temperature is approached from below, as indicated in Fig. 9.15. It is this multigap feature that makes magnesium diboride so interesting as a superconductor, and endows it with some unique properties. The transition temperature T_c is the same for both gaps, and they have the respective reduced gap values $\Delta_\pi/k_BT_c \cong 1.7$ and $\Delta_\sigma/k_BT_c \cong 4$, one being less than and one greater than the BCS value of 3.528.

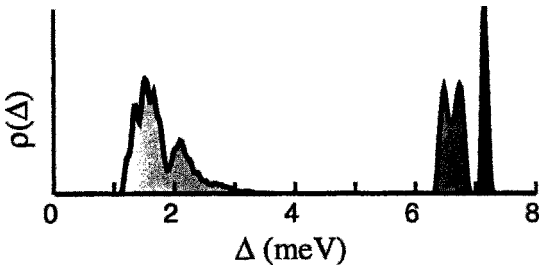

Figure 9.14 Distribution in energy of the lower π-band gap near 2meV and the upper σ-band gap near 7 mV. (Kogan and Bud'ko, 2003, Fig. 5).

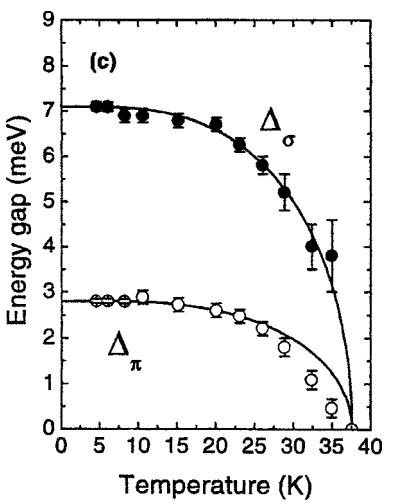

Figure 9.15 Temperature dependence of the pi-band gap Δ_π and the sigma-band gap Δ_σ. The data points determined from experimental conductance measurements are compared to BCS theoretical curves. (Daghero et al., 2003, Fig. 5).

Data from many experiments are easier to explain using a two gap model, such as those involving crystal field, Hall effect, photoemission, Raman scattering, specific heat, thermoelectric power, and tunneling measurements. Electron-phonon coupling calculations have been carried out individually for the σ- and for the π-bands. Many of these results are found in the PhC articles. For example, Daghero *et al.* [2003] found different values for the upper critical field B_{c2} for the two bands, and scanning tunneling spectroscopy for c-plane orientation reveals only the single Δ_σ narrow gap, while ab-plane tunneling resolves two gaps with the larger Δ_π gap dominant, as shown in Fig. 9.16 [Iavarone et al., 2003, Martinez-Samper et al., 2003, Gonnelli et al., 2004].

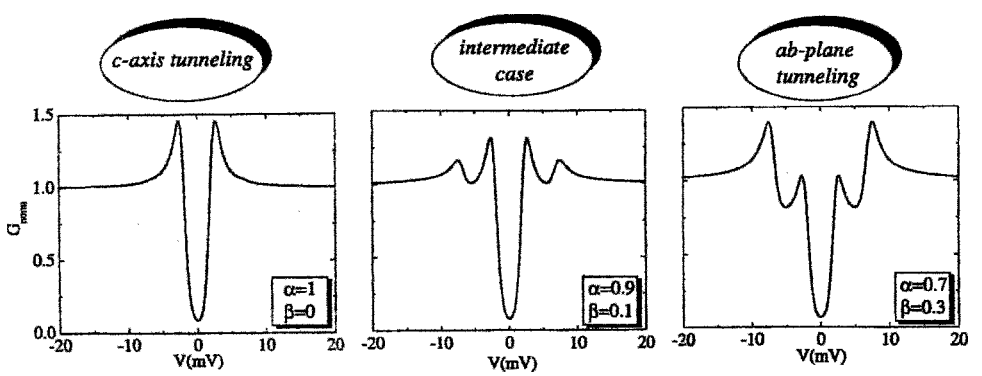

Figure 9.16 Simulated tunneling conductance spectra of MgB_2 for tunneling along the c-axis, in an intermediate case, and in the a, b plane. (Iavarone et al., 2003, Fig. 2).

IV. BOROCARBIDES AND BORONITRIDES

During the preparation of the first edition of this book superconductivity was discovered in a series of quaternary borocarbide compounds, ordinarily referred to simply as borocarbides, with the general formula $(RC)_nM_2B_2$ where R is a transition metal and M is ordinarily Ni. The isostructural boronitride series has the general formula $(RN)_nM_2B_2$ where nitrogen replaces carbon. The subject has been reviewed by Canfield (2000), by Hilscher and Michor (1999), and by Müller and Narozhnyi (2001). The latter review emphasizes the interaction between magnetism and superconductivity in these compounds. Table 9.3 lists the superconducting transition temperatures of a number of borocarbides, and Table 9.4 provides various properties of the two borocarbide superconductors YNi_2B_2C and $LuNi_2B_2C$.

Table 9.3 Superconducting transition temperatures of various borocarbide compounds (see Hilscher and Michor (1999), and Müller and Narozhuyi (2001).)

Compound	$T_c(K)$
$CeNi_2B_2C$	0.1
$DyNi_2B_2C$	6.3
$ErNi_2B_2C$	10.5
$HoNi_2B_2C$	7.8
$LuNi_2B_2C$	16.5
$ScNi_2B_2C$	15.
$ThNi_2B_2C$	8.
$TmNi_2B_2C$	11.
YNi_2B_2C	12.5
$LaPd_2B_2C$	1.8
$ThPd_2B_2C$	14.5
YPd_2B_2C	9.7
$LaPt_2B_2C$	10.
$PrPt_2B_2C$	6.
$ThPt_2B_2C$	6.5
YPt_2B_2C	10.
YRu_2B_2C	9.7
$LaPt_{1.5}Au_{0.5}B_2C$	11.
$PrPt_{1.5}Au_{0.5}B_2C$	6.5
$YPt_{1.5}Au_{0.5}B_2C$	11.
$La_{0.5}Lu_{0.5}Ni_2B_2C$	14.8
$Sc_{0.5}Lu_{0.5}Ni_2B_2C$	15.6
$La_{0.5}Th_{0.5}Ni_2B_2C$	3.9
$La_3Ni_2B_2N_3$	12.

A. Crystal Structure

The RNi_2B_2C compound has the tetragonal structure sketched in Fig. 9.17 in which staggered Ni_2B_2 layers alternate with flat RC planes. Schematic presentations of structures for n = 1, 2, 3, and 4 are sketched in Fig. 9.18. They all have the same Ni_2B_2 layres and RC or RN planes. The Ni atoms are in the center of distorted B_4 tetrahedra which share edges to form slabs held in place by short linear B-C-B bridges, as indicted in Figs. 9.17 and 9.18. The bonding is partly ionic and partly covalent. The distance between nearby nickel atoms in the Ni_2B_2 layers is slightly less than the nearest neighbor distances in atomic nickel, and the Ni-B bonding has a strong admixture of a covalent character. The boron to carbon interatomic distance of 1.47Å suggests that these are double bonds. The resulting rigid three dimensional framework can accommodate various sizes of transition metal atoms R. Larger transition atoms increase the R-C separation in the plane, and compress the B_4 tetrahedra, thereby decreasing the thickness of the R_2B_2 layer, and decreasing the c-parameter. Higher members of the $(RC)_nM_2B_2$ series, with n > 1, stack RC layers one above the other in an NaCl type arrangement, as indicated in Fig. 9.18. The right hand side of Fig. 9.17 provides a more realistic view of the atom packing in the n = 1 structure.

The borocarbides with odd-n have the body-centered tetragonal crystallographic space group I4/mmm, and those with even-n are in the primitive tetragonal space group P4/nmm which has a horizontal reflection plane at the center of the unit cell. The primitive structures have one formula unit per unit cell, while the body centered structures have

Table 9.4 T_c—superconducting transition temperature, B_{c2}—upper critical field at $T = 0$, B_{cl}—lower critical field at $T = 0$, B_c—thermodynamical critical field at $T = 0$, $\xi(0)$—coherence length at $T = 0$, $\lambda(0)$—penetration depth at $T = 0$, $\kappa(0)$ Ginzburg-Landau parameter at $T = 0$, ΔC—specific heat jump at T_c, γ—normal state Sommerfeld constant, $N(E_F)$—density of state at the Fermi level in states per eV and unit cell, υ_F—Fermi velocity, λ_{ph}—electron-phonon coupling constant, μ^*—Coulomb pseudopotential, θ_D—Debye temperature, $\Delta(0)$—quasiparticle energy gap at $T = 0$, l—mean free path, RRR—residual resistance ratio $\rho(300K)/\rho(T \approx T_c)$, T_D—Dingle temperature. (compiled by Müller and Marozhuyi, 2001)

Property	YNi_2B_2C	$LuNi_2B_2C$	Property	YNi_2B_2C	$LuNi_2B_2C$
T_c(K)	15.5	16.5	$N(E_F)$(1/eV)	4.31	4.05
B_{c2}(T)	11	7.5,9	$\upsilon_F(10^5\,ms^{-1})$	0.85, 3.8, 4.2	0.96 . . . 3.7, 4.2
B_{c1}(mT)	30	30, 80	λ_{ph}	0.9, 1.20	0.75, 1.22
B_c(T)	0.23	0.31, 0.54	μ^*	$\approx 0.1, 0.13$	$\approx 0.1, 0.13$
$\xi(0)$(nm)	8 . . . 10, 5.5	6	θ_D(K)	490	360
$\lambda(0)$(nm)	120, 350	130, 71	$\Delta(0)$(meV)	2.2	2.2
$\kappa(0)$	15, 35	22, 12	$\Delta(0)/K_BT_c$	2.1, 1.7	2.2, 1.7
$\Delta C(mJ\,mol^{-1}K^{-1})$	460	695	l(nm)	33	70, 29
$\gamma(mJ\,mol^{-1}K^{-2})$	18.5	19.5, 35	RRR	43	27, 44
$\Delta C/\gamma T_c$	1.77	2.21	T_D(K)	2.8	4

two formula units per unit cell, as is clear from Fig. 9.18. I4/mmm is also the space group of the thallium $Tl_2Ba_2Ca_nCu_{n+1}O_{2n+6}$ and bismuth $Bi_2Sr_2Ca_nCu_{n+1}O_{2n+6}$ series of cuprate high temperature superconductors, whereas cuprates with aligned CuO_2 layers such as $HgBa_2Ca_nCu_{n+1}O_{2n+4}$ belong to primitive tetragonal space group P4/nmm which differs from P4/nmm adapted by even-n borocarbides.

B. Correlations of Superconducting Properties with Structure Parameters

A number of lanthanide nickel borocarbides superconduct when the diameter of the R atom is not too large, and their transition temperatures are listed in Table 9.5 together with the density of states at the Fermi level $D(E_F)$, and the magnetic ordering temperature for ferromagnetic (F) and antiferromagnetic (A) compounds. To obtain correlations with the structure the parameter c' was defined by Baggio-Saitovitch (2001) as the length of the basic six atom RM_2B_2C group along the axial direction for every n in the general chemical formula $(RC)_nM_2B_2$, which means not taking into account extra RC layers in compounds for $n > 1$. We see from Fig. 9.18 that c' is always less than the lattice parameter c, and it has the special value $c' = c/2$ for $n = 1$.

Figure 9.19 shows how the lattice parameters a and c defined in Figs 9.17 and 9.18 depend on the ionic radius of the transition ion R. We see from the figure that a increases approximately linearly with the radius for both $n = 1$ and $n = 2$ compounds. In contrast to this the axial parameter c remains fairly constant for the $n = 2$ series, and decreases with an increase in the radius for the $n = 1$ series. The C-B and Ni-B distances remain approximately the same for different transition ion substitutions, and the decrease in c with an increase in a results from the distortion of the NB_4 tetrahedra, and

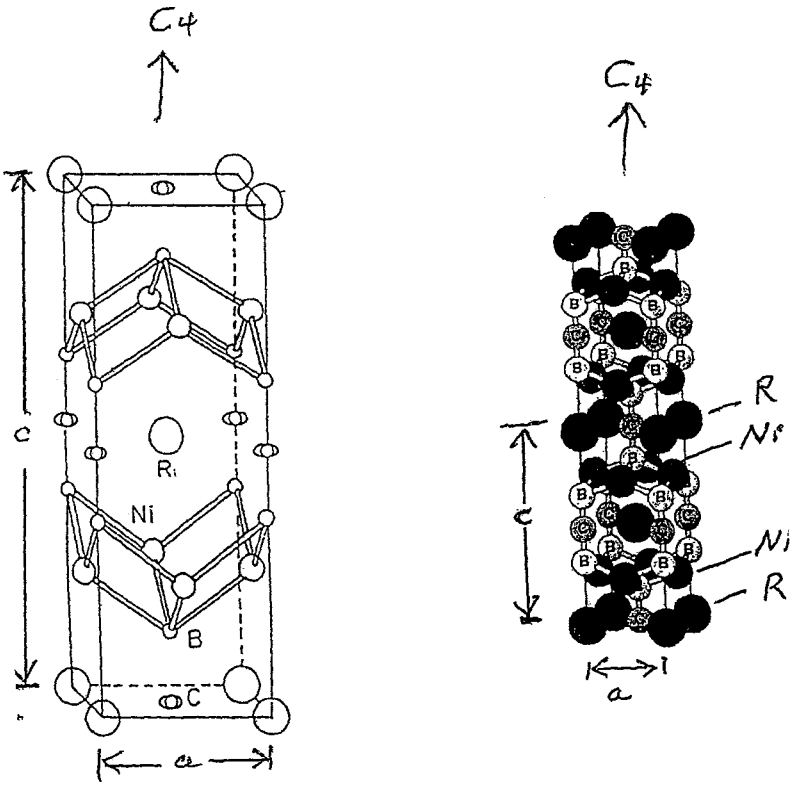

Figure 9.17 Unit cell (left) of the tetragonal structure (space group 14/mmm, D_{4h}") of RNi_2B_2C, and the atom packing arrangement (right). The vertical z axis is a fourfold rotation axis (4, C_4), and the centrally located RC planes are horizonotal reflection planes (m, σ_h). The unit cell also has vertical reflection planes (σ_v), horizontal two-fold axes (2, C_2), and inversion symmetry (i). (Godart et al., 1995; Nagarajan, 2001, Fig. 4; Drechsler et al., 2001, Fig. 1, with kind permission from Springer Science).

the consequent reduction of the thickness of the Ni_2B_2 layer.

C. Density of States

According to Eq. (7–119) of the BCS theory chapter a high value of the superconducting transition temperature T_c is associated with a large density of states $D(E_F)$ at the Fermi level. The LDA band structure calculations carried out by Rosner *et al.* (2001) on YNi_2B_2C show a flat band at the Fermi level near the point X (110) and proceeding from X toward the origin Γ (000) in the Brillouin zone (Winzer et al., 2001). The flatness of the band puts many k-values at the Fermi level so the density of states is high there. Fig. 9.20 plots the total density of states, and the partial densities of states for the electrons associated with the different atoms of YNi_2B_2C. The Ni-3d and Y-4d electrons make the main contribution to $D(E_F)$ at the Fermi level. Divis *et al.* (2001) determined the total density of states for the five compounds RNi_2B_2C with R = Er, Tm, Pr, Nd and Sm, and they found that the first two compounds (Er, Tm) which superconduct have sharp peaks of D(E) at $E = E_F$ which resemble those shown in Fig. 9.20 for YNi_2B_2C. These peaks are missing for the three nonsuperconducting compounds. The

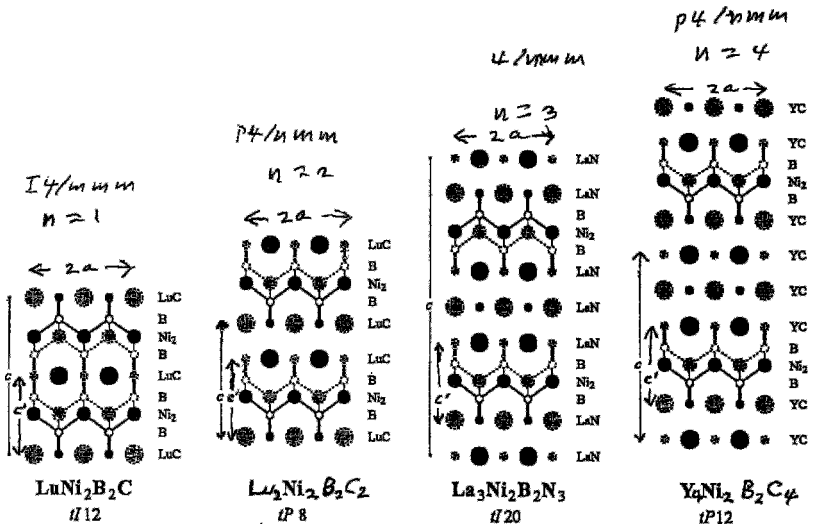

Figure 9.18 Schematic drawings of the members of the structure series $(RC)_nNi_2B_2$ and $(RN)_nNi_2B_2$ for n = 1, 2, 3 and 4 formed by borocarbides and boroonitrides, respectively, with Pearson codes designated. Shading indicates relative height above the plane of the paper. Thick lines connect non-metal atoms and thin lines Ni and B atoms. Compounds with even-n contain one formula unit per vertical distance c, and those with odd-n have two formula units per vertical distance c. (Gladyshevskii in Poole, 2000, Fig. 6.21).

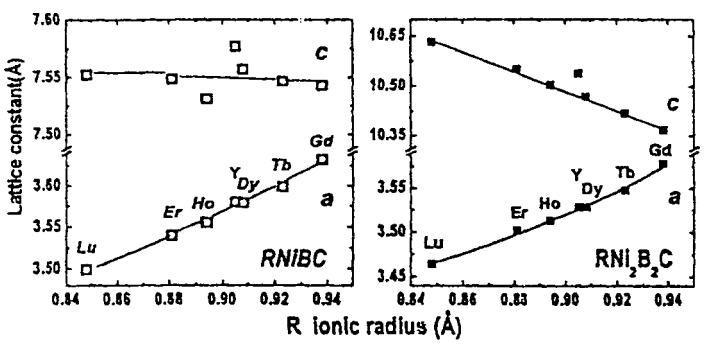

Figure 9.19 Values of lattice constants a, c at room temperature for RNiBC and RNi_2B_2C compounds as a function of the ionic radius of the rare earth. (Baggio-Saitovitch et al., 2001, Fig. 2, with kind permission from Springer Science).

density of states at the Fermi level for several borocarbides is listed in Table 9.5.

We see from the data plotted in Fig. 9.21a that the density of states $D(E_F)$ and the superconducting transition temperature T_c follow a similar dependence on the rare earth transition ion type R over the entire series of borocarbides RNi_2B_2C. The Hoppfield parameter $\eta_\alpha = D_\alpha(E_F)\langle I_\alpha^2\rangle$, where $\langle I_\alpha^2\rangle$ is the average electron-phonon matrix element for atom α, varies with R and α across the borocarbide series in the manner shown in Fig. 9.21b. The dependence of η_{Ni} for the nickel atoms shown at the top of Fig. 9.21b is similar to the dependences of $D(E_F)$ and T_c shown in Fig. 9.21a. We see from these two figures that the highest values of $D(E_{F)}$, T_c and η_{Ni} occur for the higher atomic number

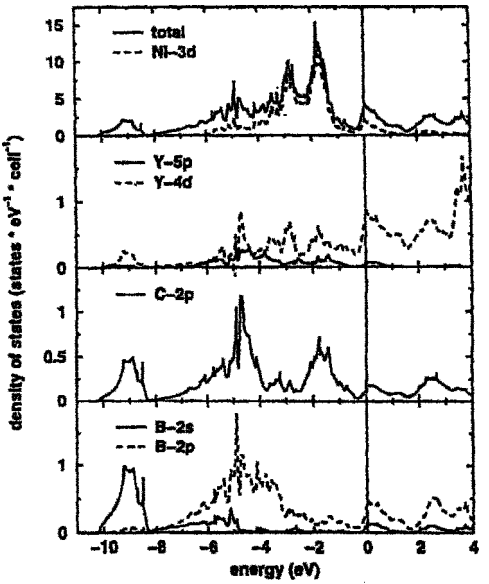

Figure 9.20 Total and partial densities of states for YNi_2B_2C. The Fermi level is at the zero of energy. (Rosner et al., 2001, Fig. 2, with kind permission from Springer Science).

range of the borocarbide series. Figure 9.22 shows how the transition temperature T_c varies with the total density of states at the Fermi level for various borocarbides, using the notation $RC(NiB)_2$ for RNi_2B_2C. The figure compares values calculated by the scalar full potential local orbital method (Drechsler et al. 1999) with experimentally measured values.

D. Thermodynamic and Electronic Properties

The specific heat of the compound YNi_2B_2C is a sum of the Sommerfeld electronic term $\gamma_N T$ and the low temperature Debye term $\beta_D T^3$, as was explained in Sect. VII of Chapter 4.

$$C_p = \lambda_N T + \beta_D T^3$$

The plot of experimentally measured values of C_p/T versus T^2 shown in Fig. 9.23 exhibits the usual jump in value at the transition to the superconducting state, with the transition from the superconducting to the normal state occurring at lower temperatures for increasing applied magnetic fields, as shown on the figure. It is clear that the magnitude of the jump in C_p also decrease with the temperature in the manner discussed in Sect. X. of Chapter 4. The intercept of the extrapolated normal state curve for $T \Longrightarrow 0$ provides an evaluation of the Sommerfeld

Table 9.5 Type of the ground state of RNi_2B_2C compounds: SC—superconducting, AFM—commensurate antiferromagnet structure, SDW—incommensurate antiferromagnet order (spin density wave), WFM—weak ferromagnetism; T_N—magnetic order temperature, T_c—superconducting transition temperature and $N(E_F)$—density of states at the Fermi level. (compiled by Müller and Narozhnyi, 2001)

Compound	Ground state	T_N(K)	T_c(K)	$N(E_F)$
$CeNi_2B_2C$	Mixed valence (SC)	—	(0.1)	2.4
$PrNi_2B_2C$	AFM	4.0	—	2.00
$NdNi_2B_2C$	AFM	4.8	—	2.10
$SmNi_2B_2C$	AFM	9.8	—	2.97
$GdNi_2B_2C$	SDW	19.4	—	3.57
$TbNi_2B_2C$	SDW WFM	15.0	—	4.11
$DyNi_2B_2C$	AFM/SC	11.0	6.2, 6.4	4.16
$HoNi_2B_2C$	AFM/SC	5 . . . 8	8, 7.5	4.04
$ErNi_2B_2C$	SDW (WFM) SC	6 . . . 6.8	10.5	4.32
$TmNi_2B_2C$	SDW/SC	1.5	11	4.02
$YbNi_2B_2C$	Heavy fermion	—	—	

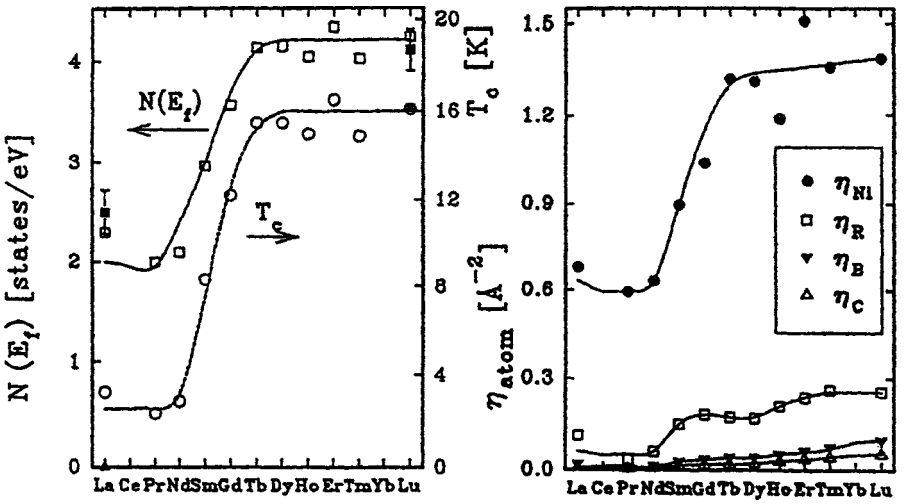

Figure 9.21 Calculated density of states $N(E_F)$ and superconducting transition temperatures T_c on the atom type R in the borocarbide RNi_2B_2C (left panel), and Hoppfield parameters η_α for the four atoms (right panel). (Hilscher et al., 2001, Fig. 1, with kind permission from Springer Science).

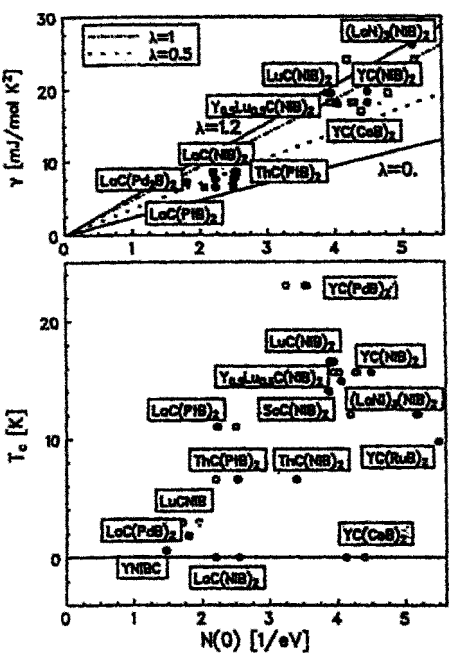

Figure 9.22 Dependence of experimentally determined Sommerfeld constants γ (upper panel) and superconducting transition temperatures T_c (lower panel) on the density of states (DOS) at the Fermi level. Values from the literature (Dreschler et al., 1999) are denoted by open circles. (Dreschler et al., 2001, Fig. 2, with kind permission from Springer Science).

constant $\gamma_N = 20.2\,\mathrm{mJ/moleK^2}$. Figure 9.24 shows how the transition temperature and the Sommerfeld constant vary with the concentration x in the mixed crystal system $Y_xLu_{1-x}Ni_2B_2C$. The figure also presents the variation of the upper and lower limits of the upper critical field B_{c2} versus the concentration x. This mixed crystal system was convenient for study because neither YNi_2B_2C nor $LuNi_2B_2C$ exhibit any ordered magnetic behavior.

Iavarone et al. (2001) used scanning tunneling microscopy and microwave surface impedance measurements to study $LuNi_2B_2C$ thin films grown on several substrates. The STM data provided conductance $G = dI/dV$ versus voltage V plots, and an I versus V plot obtained by integration is shown in the inset to Fig. 9.25. The conductance minima provided the energy gap values plotted in Fig. 9.25, and extrapolation to $T = 0$ gives the gap $2\Delta_0 = 4.0\mathrm{mV}$. Since the transition temperature $T_c = 15.1\mathrm{K}$ this corresponds to the dimensionless ratio $2\Delta_0/k_BT_c = 3.0$, which is slightly less than the BCS value 3.5.

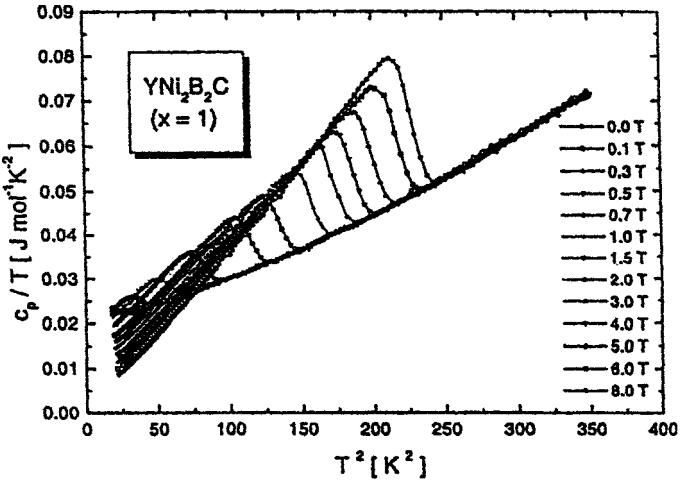

Figure 9.23 Dependence of the specific heat c_p/T of YNi_2B_2C on the temperature squared T^2 for various applied magnetic fields. (Lipp et al., 2001, Fig. 2, with kind permission from Springer Science).

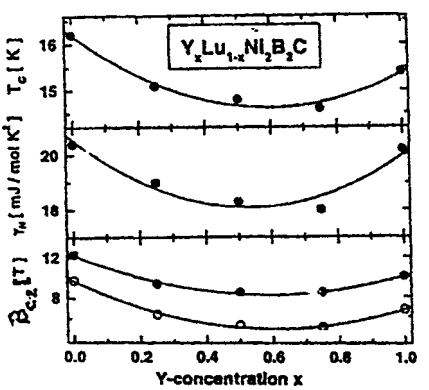

Figure 9.24 Concentration dependence x of the Superconducting transition temperature T_c (upper panel), the Sommerfeld constant γ (middle panel), and the upper and lower bounds of the upper critical field B_{c2} (lower panel) of $Y_xLu_{1-x}Ni_2B_2C$. (Lipp et al., 2001, Fig. 4, with kind permission from Springer Science).

In order to carry out microwave surface impedance measurements superconducting films of $LuNi_2B_2C$ where made end plates of a sapphire (Al_2O_3) cylindrical resonator. Microwave frequency shift measurements Δf provided the values of the penetration depth $\lambda(T)$ which are plotted in Fig. 9.26. It is clear that the data fit the theoretical BCS curve very well. The figure lists the two parameters used for making the BCS fit, namely the low temperature mean free path $\ell = 2\,\text{nm}$, and $T_c = 14.5\text{K}$.

Hall effect measurements were carried out with the two compounds YNi_2B_2C and $LuNi_2B_2C$, and for each compound the Hall resistivity ρ_{xy} was negative in both the normal and the superconducting states. Thus the sign reversal at T_c that is typical for the cuprates was not observed with these two borocarbides.

E. Magnetic Interactions

The borocarbides are a class of compounds in which magnetism and superconductivity can coexist. The magnetism arises from the magnetic moments of the transition ions R, which are proportional to the magneton numbers $g\,[J(J+1)]^{1/2}$ which are plotted in Fig. 9.27 for the rare earth series of atoms. These ions provide local magnetic moments in the lattice at sites between the Ni_2B_2 layers (see Fig. 9.17), and are responsible for the weak ferromagnetism, antiferromagnetism or spin density waves that exist in some of the borocarbides. The magnetic transition

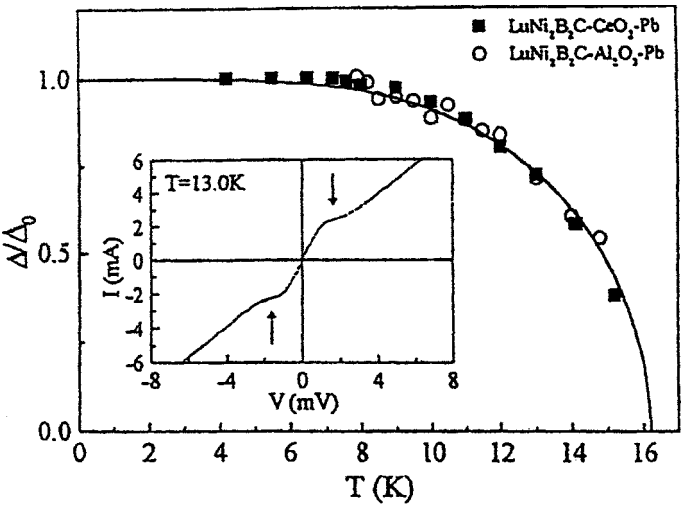

Figure 9.25 Temperature dependence of the superconducting energy gap Δ/Δ_0 for two different $LuNi_2B_2C$ junctions. The inset gives a typical I-V curve with the gap positions indicated by arrows. (Iavarone et al., 2001, Fig. 2, with kind permission from Springer Science).

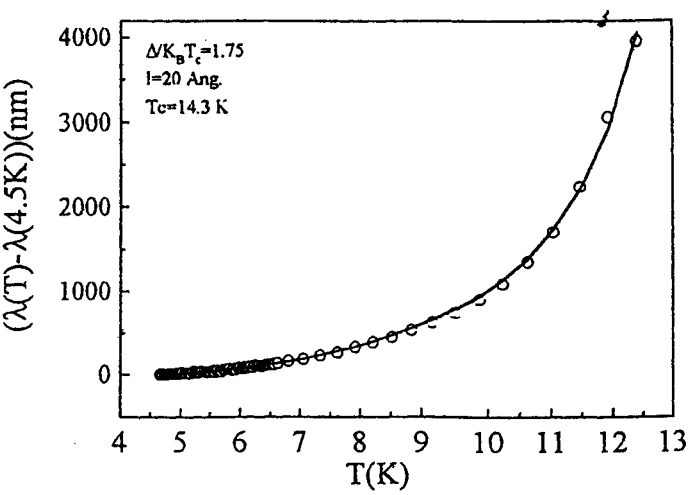

Figure 9.26 Temperature dependence of the penetration depth shift from its value at 4.5K, $\lambda\,(T) - \lambda\,(4.5K)$, for $LuNi_2B_2C$ films grown on copper. The fit parameters to the BCS curve are indicated in the upper left. (Iavarone et al., 2001, Fig. 3, with kind permission from Springer Science).

temperatures T_M to these ordered magnetic states, as well as the nature of the type of magnetic order that is present in particular borocarbide compounds, are listed in Table 9.5. A measure of the effectiveness of local moments on the superconducting properties is given by the de Gennes factor $(g_J - 1)^2 J(J + 1)$ (see Freudenberger *et al.*,

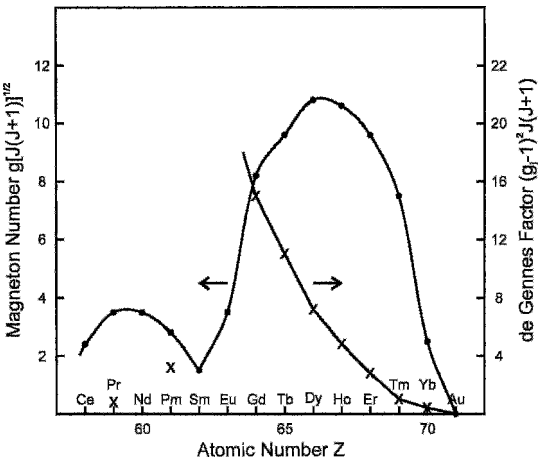

Figure 9.27 Dependence of the magneton number $g(J(J+1))^{1/2}$ and the de Gennes factor $(g_J-1)^2J(J+1)$ on the individual atoms of the rare earth series. (Thanks are due to Michael A. Poole for preparing this figure).

2001, and Hilscher *et al.*, 2001) plotted in Fig. 9.27 for the second half of the lanthanide series, where g_J, is the Landé g-factor, and J is the total angular momentum quantum number. For example gadolinium has a $^6S_{7/2}$ ground state so $J = 7/2$, $g_J = 2$, and $(g_J-1)^2J(J+1) = 15.75$. The magnetic transition temperature T_M correlates with the de Gennes factor in the manner shown in Fig. 9.28 which suggests that the coupling

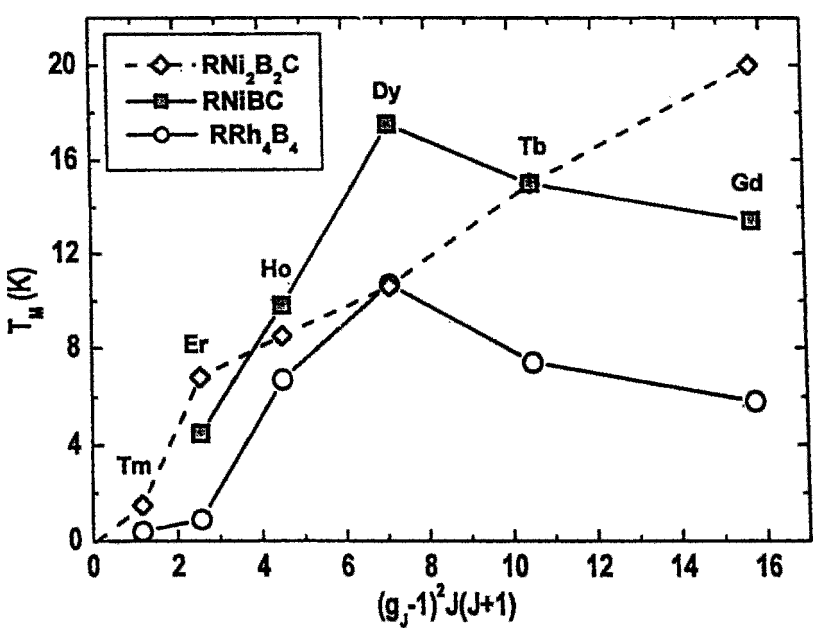

Figure 9.28 Dependence of the magnetic transition temperature T_M on the de Gennes factor $(g_J-1)^2J(J+1)$ for three series of borocarbide compounds. (Baggio-Saitovitch et al., 2001, Fig. 7, with kind permission from Springer Science).

between the 4f electrons of the R atoms involves the RKKY interaction whereby the magnetic interchange between these 4f electrons takes place through the intermediary of magnetization induced in the conduction electrons. We see from the figure that the values of T_M increase linearly with the de Gennes factor for $n = 1$ (RNi_2B_2C), whereas the $n = 2$ (RNiBC) data exhibit a peak for dysprosium, as do the data for the RRh_4B_4 compounds.

The superconducting transition temperature T_c also exhibits a regular variation with the de Gennes factor across the lanthanide series for the $n = 1$ compounds as shown in Fig. 9.29, and has linear correlations with the crystallographic c'/a ratio, as indicated in Fig. 9.30. The latter correlations exist for the usual borocarbide compounds $(RC)_nM_2B_2$, as well as for mixed borocarbides $(R'_xR''_{1-x}C)_nM_2B_2$ which contain two types of rare earth ions R′ and R″. The variation of T_C and T_M with concentration x of dysprosium in the series from nonmagnetic YNi_2B_2C to magnetic $DyNi_2B_2C$ is shown in Fig. 9.31. Figure 4 of Müller and Narozhnyi (2001) highlights the linear variations of T_C and T_M on the de Gennes factor with opposite slopes.

Hall probe measurements were carried out to determine how magnetic flux lines from an applied magnetic field penetrate into an $ErNi_2B_2C$ superconducting crystal using the Hall sensor arrangement sketched at the top of Fig. 9.32. It is clear from the figure that at the temperature of 7.2K, which is between the magnetic ordering temperature $T_M \cong 6K$ and the superconducting transition temperature $T_c = 10.8K$, more magnetic flux penetrates into the sample in the center than at its edges. There is a large gradient of flux between the two sensors 2 and 11 immediately outside the sample and sensors 3 and 10, respectively, located just inside the edge of the crystal due to the shielding currents of density J flowing near the edge, arising from the Maxwell curl expression $\mu_o J = \nabla \times B$. In the absence of appre-

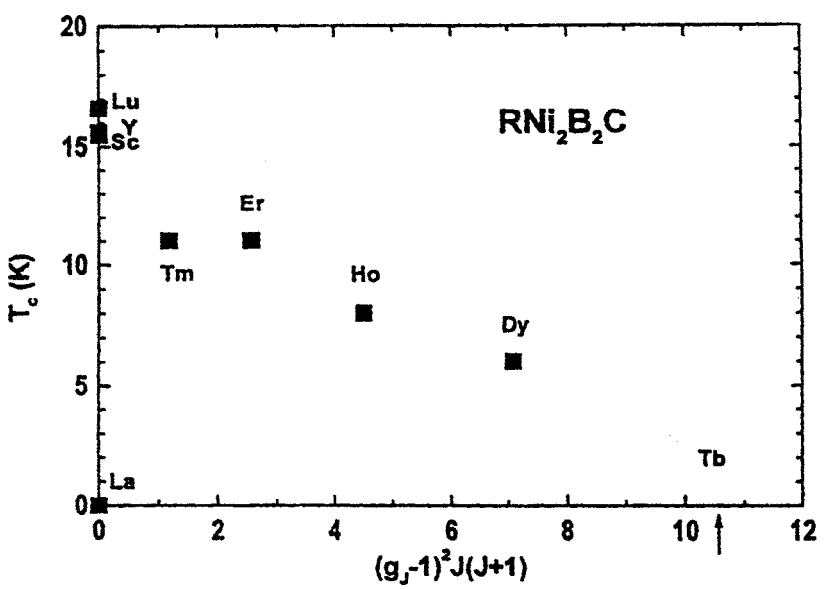

Figure 9.29 Dependence of the magnetic transition temperature T_M on the de Gennes factor $(g_J - 1)^2J(J + 1)$ for RNi_2B_2C compounds. (Baggio-Saitovitch et al., 2001, Fig. 8, with kind permission from Springer Science)

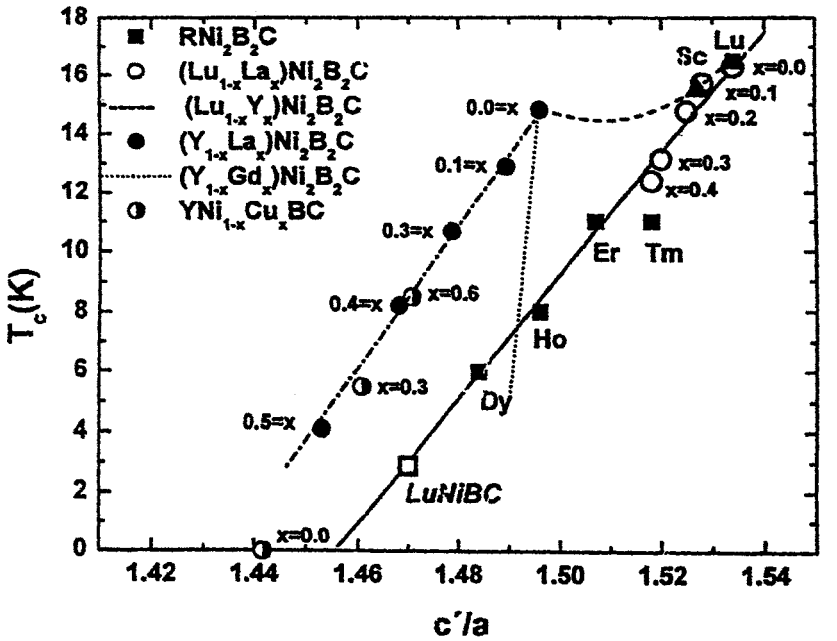

Figure 9.30 Dependence of the superconducting transition temperature T_c on the c'/a ratio for several series of borocarbide compounds. (Baggio-Saitovitch et al., 2001, Fig. 9, with kind permission from Springer Science).

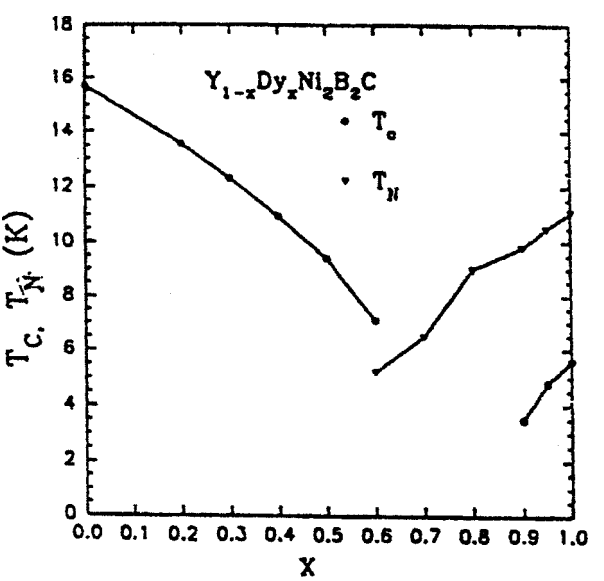

Figure 9.31 Dependence of the superconducting and the magnetic transition temperatures T_c and T_M, respectively, on the concentration x in the $Y_{1-x}Dy_xNi_2B_2C$ series of borocarbide compounds. (Hossain et al., 1999).

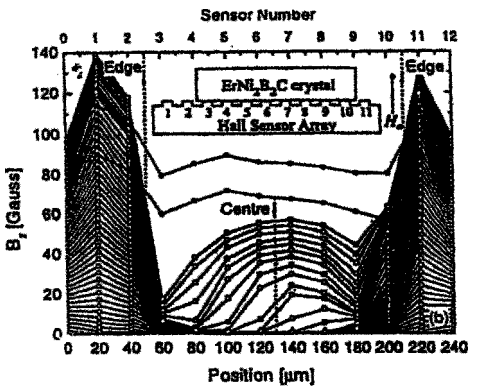

Figure 9.32 Magnetic flux line profiles measured for increasing (open symbols) and decreasing (closed symbols) applied magnetic fields in an $ErNi_2B_2C$ single crystal. The Hall probe sensor positions 0 and 12 represent the applied magnetic field B_{app}. (Dewhurst et al., 2001, Fig. 1, with kind permission from Springer Science).

ciable pinning the flux lines that enter at the surface migrate toward the center and accumulate there, as shown in the figure. Increasing the applied field strength increases the accumulation toward the center, as shown. For a decreasing external field the density of flux lines is fairly uniform across the sample, as shown. When the measurements were repeated at the much lower temperature $T = 2.75K < T_M$, where bulk pinning is appreciable, most of the flux entered at one side of the sample near the edge. For higher applied fields there was a second accumulation of flux on the other side of the sample with an almost flux fee region between the two accumulations. When the external field was gradually decreased under these conditions the flux remained more uniform across the sample, as was the case with the 7.2K measurements.

F. Magnetism of $HoNi_2B_2C$

Some borocarbides exhibit a complicated magnetic behavior, and $HoNi_2B_2C$ is an example. The temperature dependence of the resistivity ρ presented in Fig. 9.33 shows a sharp

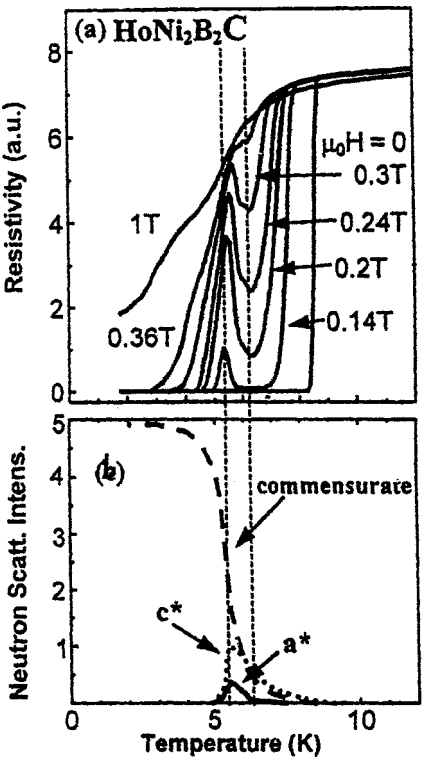

Figure 9.33 Temperature dependence of the resistivity of $HoNi_2B_2C$ (upper panel) in the presence of applied magnetic fields in the range from 0 to 0.3 T, showing the reentrant superconductivity near 6K. The neutron diffraction intensity results (lower panel) identify the presence of the commensurate, the spiral c* incommensurate, and the postulated a* incommensurate structures, sketched in Fig. 35, in the neighborhood of the near reentrant behavior. (Müller et al., 201, Fig. 8, with kind permission from Springer Science).

drop to zero at the transition temperature of 7.8K in zero magnetic field. The application of a magnetic field of 0.14T induces a near-reentrant behavior, namely a finite onset of resistivity below T_C in a magnetic field near the magnetic ordering temperature of $T_M = 5.2K$, and the application of higher fields increases ρ further, as shown. The behavior is called near-reentrant because its onset requires the presence of an applied field. The specific heat plot of Fig. 9.34 confirms that there are additional phases in the sample. Müller *et al.* (2001) interpret these

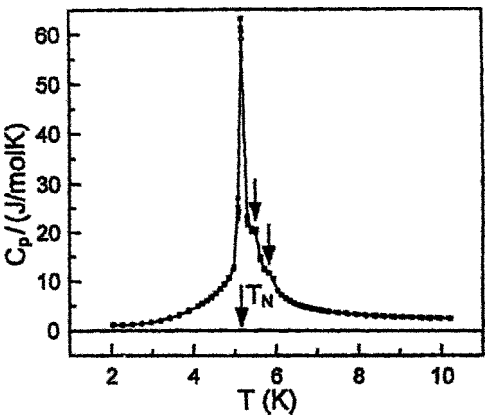

Figure 9.34 Temperature dependence of the specific heat C_p of a 2 mm × 3 mm × 0.1 mm $HoNi_2B_2C$ monocrystal measured in zero magnetic field. The contributions from the three phases that are present are indicated by arrows. (Müller et al., 2001, Fig. 2, with kind permission from Springer Science).

reentrant data in terms of the magnetic structures sketched in Fig. 9.35. Structure (a) is commensurate with ferromagnetically aligned planes antiferromagnetically coupled to each other, and it occurs below 6–7K, as shown by the vertical dashed line in Fig. 9.33b. Figure 9.35b illustrates an incommensurate c* structure with a spiral arrangement of the spins along the c direction, called a spin wave state, which is present in the neighborhood of the reentrant state at 5.2K. The postulated incommensurate structure a* sketched in Fig. 9.35c appears to be more closely related to the reentrant behavior than structure c*. If the Ho atoms are replaced by a small percentage of Y or Lu atoms the spiral c* structure dominates over the commensurate one of Fig. 9.35a, but there is very little change in structure a* at the onset of the near-reentrant behavior. Müller et al. (2001) suggest that the a* structure is associated with the Fermi surface nesting, and is closely related to enhanced pair-breaking induced by the magnetic field applied at the reentrant temperature T_N.

The compound $HoNi_2B_2C$ also has metamagnetic phases with spin orderings ↑ ↑ ↓ and ↑ ↑ → which are intermediate between the ferromagnetic ↑ ↑ ↑ ↑ and antiferromagnetic ↑ ↓ ↑ ↓ types, as well as a paramagnetic phase. Figure 9.36a presents a magnetic phase diagram in the applied magnetic field versus temperature plane when the

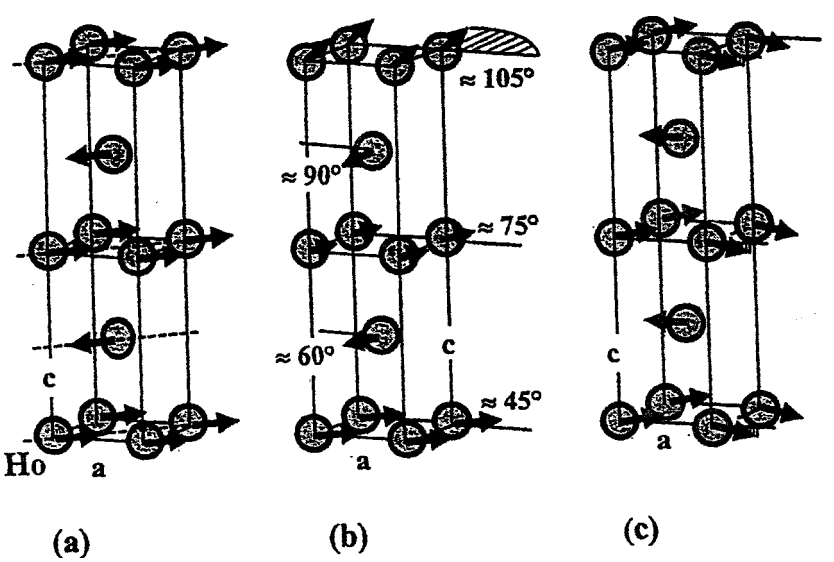

Figure 9.35 Magnetic structures of $HoNi_2B_2C$ determined by neutron diffraction: (a) commensurate, (b) spiral incommensurate c* type, and (c) postulated incommensurate a* type. (Müller et al., 2001, Fig. 4, with kind permission from Springer Science).

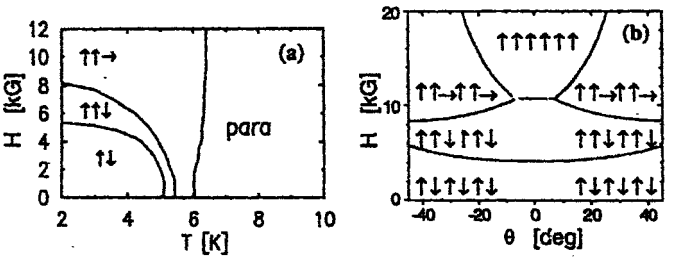

Figure 9.36 Magnetic phase diagrams of $HoNi_2B_2C$: (a) in the applied magnetic field versus temperature plane with the field applied along the tetragonal a axis, and (b) in the applied field versus the angle θ plane, where θ is the angle in the plane perpendicular to the c axis that the applied magnetic field makes with the magnetically easy [001] direction. The regions where the ferromagnetic (↑↑↑↑), antiferromagnetic (↑↓↑↓), metamagnetic (↑↑↓ and ↑↑→) and paramagnetic (para) phases are present are indicated (see Müller and Narozhnyi, 2001). (Canfield et al., 1996).

field is applied along the tetragonal a axis. Figure 9.36b presents a magnetic phase diagram in the applied magnetic field versus angle θ plane when the field is applied perpendicular to the tetragonal c axis, making an angle θ with respect to the magnetically easy [110] direction. Metamagnetic phases are also found in the borocarbide superconductors $TbNi_2B_2C$ and $DyNi_2B_2C$.

V. PEROVSKITES

The main perovskites that superconduct are the two cubic compounds

$$Ba_{1-x}K_xBiO_{3-y} \text{ and } MgCNi_3$$

and a series of lower symmetry perovskites

$$BaPb_{1-x}Bi_xO_3$$

that exhibit superconductivity over part of their ranges of structural stability. In the first two sections we discuss the two cubic examples which differ markedly in their types of superconductivity, and then in the following section we examine the lower symmetry cases which have some affinities to the cuprates.

A. Barium-Potassium-Bismuth Cubic Perovskite

The compound

$$Ba_{1-x}K_xBiO_{3-y},$$

which forms for $x > 0.25$, crystallizes in the cubic pervoskite structure with $a = 4.29$Å (Cava *et al.*, 1988; Jin *et al.*, 1992; Mattheiss *et al.*, 1988). K^+ ions replace some of the Ba^{2+} ions in the C site, and Bi ions occupy the E sites of Eq. (7.2) (Hinks *et al.*, 1988b; Kwei *et al.*, 1989; Pei *et al.*, 1990; Salem-Sugui *et al.*, 1991; Schneemeyer *et al.*, 1988). Some oxygen sites are vacant, as indicated by y. Hinks *et al.* (1989) and Pei *et al.* (1990) determined the structural phase diagram (cf. Kuentzler *et al.*, 1991; Zubkus *et al.*, 1991). We should note from Table 8.1 that the potassium (1.33Å) and barium (1.32Å) ions are almost the same size, and that Bi^{5+} (0.74Å) is close to Ti^{4+} (0.68Å). Bismuth represents a mixture of the valence states Bi^{3+} and Bi^{5+} which share the Ti^{4+} site in a proportion that depends on x and y. The larger size (0.96Å) of the Bi^{3+} ion causes the lattice constant a to expand 7% beyond its cubic $BaTiO_3$ value. Oxygen vacancies help to compensate for the larger size of Bi^{3+}.

The compound $Ba_{1-x}K_xBiO_{3-y}$ was not discovered until after the advent of high-T_c

(Cava *et al.*, 1988; Mattheiss *et al.*, 1988), and is of particular significance for several reasons. It is the first oxide superconductor without copper that has a transition temperature above that of all the *A*15 compounds ($\approx$ 40K for $x \approx 0.4$). This high T_c occurs without the presence of a two-dimensional metal-oxygen lattice. Features of $Ba_{1-x}K_xBiO_{3-y}$, such as the fact that it contains a variable valence state ion and utilizes oxygen vacancies to achieve charge compensation, reappear in the high-temperature superconducting compounds.

Many experimental measurements have been made on this system, such as magnetization (Huang *et al.*, 1991b; Kwok *et al.*, 1989), photoemission (Hamada *et al.*, 1989; Jeon *et al.*, 1990; Nagoshi *et al.*, 1991), x-ray absorption (Salem-Sugui *et al.*, 1991), energy gap (Schlesinger *et al.*, 1989), and the irreversibility line (Shi *et al.*, 1991); a value for the isotope effect exponent $\alpha \approx 0.38$ has been reported (Hinks *et al.*, 1988b, 1989; W. Jin *et al.*, 1991).

Uemura *et al.* (1991) point out that $Ba_{1-x}K_xBiO_{3-y}$ shares with the cuprates, Chevrel phase compounds, heavy fermions, and organic superconductors a transition temperature T_c which is high relative to its N_s/m^* (carrier density-to-effective mass) ratio.

B. Magnesium-Carbon-Nickel Cubic Perovkskite

The perovskite compound $MgCNi_3$, with the unit cell depicted in Fig. 9.37, has carbon atoms in octahedral Ni sites, and the lattice constant a = 3.809. Mao et al. (2003) report the following characteristic parameters: $T_c = 7.63K$, $\kappa = 46$, $\xi_o = 4.6nm$, $\lambda_0 = 213nm$, $\Theta_D = 280K$, $\gamma = 9,2\,mJ/moI\text{-}NiK^2$, $B_{c1} = 13mT$, $B_c = 0.22T$, $B_{c2} = 14.4T$, $2\Delta/k_BT_c = 4.6$, $\Delta C/\gamma T_c = 2.3$. In some cases other researchers have reported values (He et al. 2001; Rosner et al. 2002); which differ from these, such as $\Theta_D = 440K$ by Zhi-Feng et al. (2002). Many of these are typical values which make $MgCNi_3$ seem like a conventional superconductor, but in reality it is an exotic type. There are several reasons for this. Most perovskites are ionic compounds, like $Ba_{1-x}K_xBiO_{3-y}$ which was discussed above, characterized by a strongly electronegative ion F^- or O^{2-} at the F site of Eq. 8-2, and positively charged ions at the C and E sites. In contrast to this $MgCNi_3$ is an intermetallic compound with the metallic ion Ni at the site that is ordinarily occupied by electronegative fluorine or oxygen. The presence of the magnetic Ni ions at the F-sites makes the compound unstable toward ferromagnetism, and hole doping with Co or Fe can bring on the ferromagnetism. Hole doping with 3% Co or Fe lowers T_c by 1K, and electron doping with only 1% Cu destroys the superconductivity altogether. In addition there is a strong singularity in the density of electronic states just below the Fermi level which is associated with a van Hove singularity.

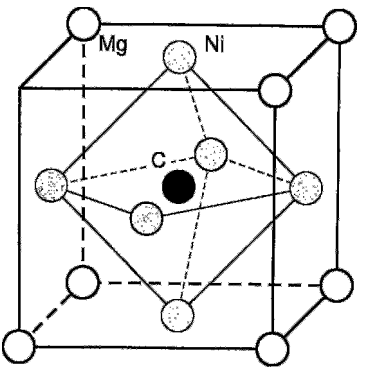

Figure 9.37 Unit cell of the perovskite compound $MgCNi_3$ showing C in the center, Ni at the face centers and Mg at the apices of the cell. (Thanks are due to Michael A. Poole for preparing this figure).

Several properties such as specific heat, nuclear magnetic resonance relaxation rates, and tunneling measurements support an s-wave mechanism of superconductivity. In contrast to this the dominance of non s-wave

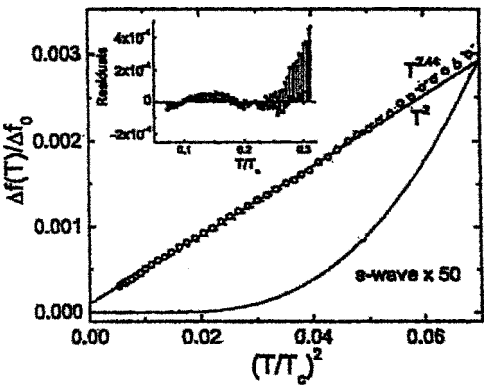

Figure 9.38 Penetration depth of $MgCNi_3$ plotted versus the square of the temperature T^2. The fits of the data to the power laws $T^{2.44}$ (dotted line) and T^2 (solid line) are indicated. The inset shows the residuals for these fits. The standard s-wave curve is included for comparison purposes. (Prozorov et al., 2003, Fig. 3).

pairing is supported by the appearance of a zero-bias conductance peak attributed to Andreev bound states (Mao et al. 2003), and the significant suppression of superconductivity brought about through the introduction of nonmagnetic disorder by irradiation (Karkin et al., unpublished). A more definitive test is the comparison of the temperature dependence of the penetration depth $\Delta\lambda(T) = \lambda(T) - \lambda(T_{min})$ with the standard s-wave BCS behavior shown in Fig. 9.38 (Prozorov et al. 2003). This result indicates the presence of low energy quasiparticles and hence unconventional non s-wave superconductivity which is consistent with d-wave pairing in the presence of strong impurity scattering, although other unconventional mechanisms could possibly explain the observations.

C. Barium-Lead-Bismuth Lower Symmetry Perovskite

In their pioneering article Bednorz and Müller (1986) called attention to the discovery of superconductivity in the mixed-valence compound $BaPb_{1-x}Bi_xO_3$ by Sleight and other researchers. (Bansil and Kaprzyk, 1991; Batlogg *et al.*, 1988; Gilbert *et al.*, 1978; Prassides *et al.*, 1992; Sleight *et al.*, 1975; Sleight, 1987; Suzuki *et al.*, 1981a, b; Thorn, 1987). It was pointed out in these studies that the stoichiometric form of this compound presumably has the composition $Ba_2Bi^{3+}Bi^{5+}O_6$; structurally, it is distorted perovskite.

The metallic compound $BaPbO_3$ is a cubic perovskite with the relatively large lattice constant (Wyckoff, 1964; cf. Nitta *et al.*, 1965; Shannon and Bierstedt, 1970) listed in Table 8.3. At room temperature semiconducting $BaBiO_3$ is monoclinic $\left(a \approx b \approx c/\sqrt{2},\ \beta = 90.17°\right)$, but close to orthorhombic (Chaillout *et al.*, 1985; Cox and Sleight, 1976, 1979; cf. Federici *et al.*, 1990; Jeon *et al.*, 1990; Shen *et al.*, 1989). These two compounds form a solid solution series $BaPb_{1-x}Bi_xO_3$ involving cubic, tetragonal, orthorhombic, and monoclinic modifications. Superconductivity appears in the tetragonal phase, and the metal-to-insulator transition occurs at the tetragonal-to-orthorhombic phase boundary $x \approx 0.35$ (Gilbert *et al.*, 1978; Koyama and Ishimaru, 1992; Mattheiss, 1990; Mattheiss and Hamann, 1983; Sleight, 1987; cf. Bansil *et al.*, 1991; Ekino and Akimitsu, 1989a, b; Papaconstantopoulous *et al.*, 1989).

The compound $BaPb_{1-x}Bi_xO_3$ superconducts in the composition range $0.05 \leq x \leq 0.3$ with T_c up to 13K. Many consider this system, which disproportionates $2Bi^{4+} \rightarrow Bi^{3+} + Bi^{5+}$ in going from the metallic to the semiconducting state, as a predecessor to the LaSrCuO system. The highest T_c of 13K, came with the comparatively low carrier concentration of $2 \times 10^{21} - 4 \times 10^{21}$ (Than *et al.*, 1980). The intensity of the strong vibrational breathing mode near $100\,cm^{-1}$ was found to be proportional to T_c (Bednorz and Müller, 1986; Masaki *et al.*, 1987). These results led Bednorz and Müller to reason that, "Within the BSC system, one may find still higher T_c's in the perovskite type or related metallic oxides, if the electron-phonon interactions

and the carrier densities at the Fermi level can be enhanced further." It was their determination to prove the validity of this conjecture that led to the biggest breakthrough in physics of the latter part of the 20th century. Their choice of materials to examine was influenced by the 1984 article of Michel and Raveau (1984) on mixed-valent Cu^{2+}, Cu^{3+} lanthanum-copper oxides containing alkaline earths.

VI. CHARGE-TRANSFER ORGANICS

Organic compounds and polymers are ordinarily considered as electrical insulators, but it is now known that some of them are also good electrical conductors. For example, the organic compound 7, 7, 7, 8, -tetracyano-*p*-quinodimethane, called TCNQ for short, forms highly conducting salts with a number of compounds, and the properties of these and other organic conductors were widely studied in the 1970s. Several of the $(TMTSF)_2X$ charge-transfer salts superconduct under pressure, where TMTSF is an electron donor and the monovalent counter ion X^- is, for example, AsF_6^-, ClO_4^-, FSO_3^-, PF_6^-, ReO_4^-, SbF_6^-, or TaF_6^-. Figure 9.39 gives the structural formulae of some of the principal organic molecules that play the role of electron donors in conducting and superconducting organics. Figure 9.40 shows the number and range of transition temperatures associated with each.

The electrical properties of organic conductors are often highly anisotropic. TCNQ salts behave as quasi-one-dimensional conductors, and salts of other organics, such as bis(ethylenedithia)tetrathiafulvalene, called BEDT-TTF for short, exhibit low-dimensional behavior (Brooks *et al.*, 1992; Fortune *et al.*, 1992), with T_c reported in excess of 13K (Schirber *et al.*, 1991). In addition, the superconducting properties of the organics, such as the critical fields and the coherence length, are often

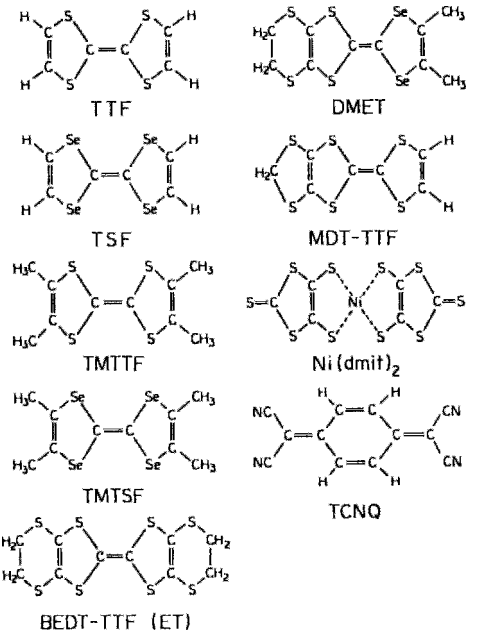

Figure 9.39 Structures of the principal molecules that form organic conductors and superconductors (Ishiguro and Yamaji, 1990, p. 2).

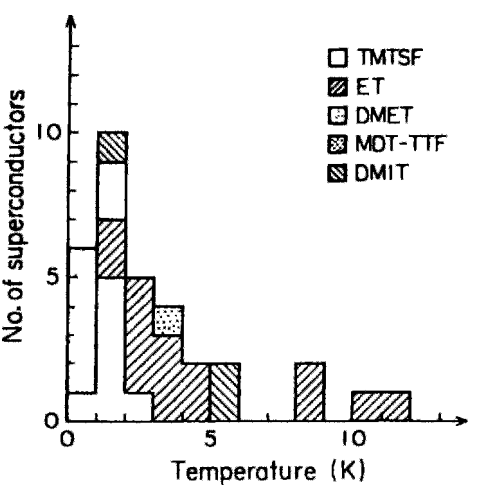

Figure 9.40 Number of known organic superconductors classified by their molecular type as a function of T_c (Ishiguro and Yamaji, 1990, p. 263).

anisotropic. For example, the triclinic compound β–$(ET)_2I_3$ has lower-critical fields $B_{c1} = 5, 9$, and $36\,\mu$T along the a, b, and c crystallographic directions, respectively

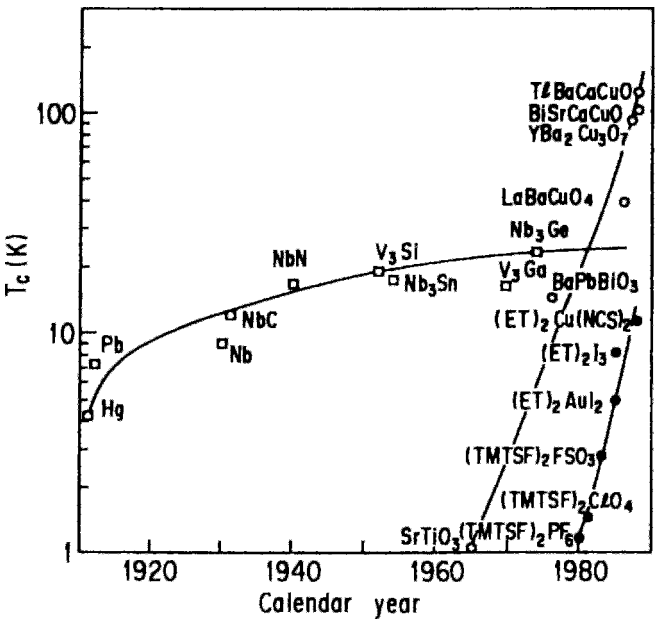

Figure 9.41 Increase in the transition temperature T_c with time (Ishiguro and Yamaji, 1990, p. 259).

and corresponding upper-critical fields $B_{c2} =$ 1.78, 1.70, and 0.08 T (Schwenk *et al.*, 1985; Tokumoto *et al.*, 1985). The coherence lengths are $(\xi)_{\text{plane}} = 350$ Å in the conducting plane and $(\xi)_{\perp} = 23$ Å (Ishiguro and Yamaji, 1990, p. 260). Other anisotropic properties are the plasma frequency (0.89 and 0.48 eV) and the effective mass $m^*/m_c = 2.0$ and $m^*/m_c = 7.0$) parallel to and perpendicular to the (−110) direction, respectively (Kuroda *et al.*, 1988).

The transition temperatures T_c of the organics are in the range of typical classical superconductors as shown in Fig 9.41. Some of the organics, such as BEDT-TTF, exhibit interesting similarities with the cuprates because of their layered structures (Farrell *et al.*, 1990b).

VII. BUCKMINSTERFULLERENES

The compound C_{60}, called buckminsterfullerene, or fullerene for short, consists of 60 carbon atoms at the vertices of the dotriacontahedron (32-sided figure) that is sketched in Fig. 9.42. The term fullerene is used here for a wider class of compounds C_n with n carbon atoms, each of whose carbon

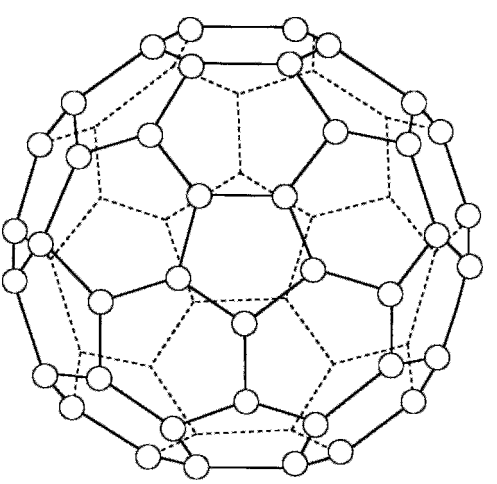

Figure 9.42 Structure of the buckminsterfullerene molecule C_{60}.

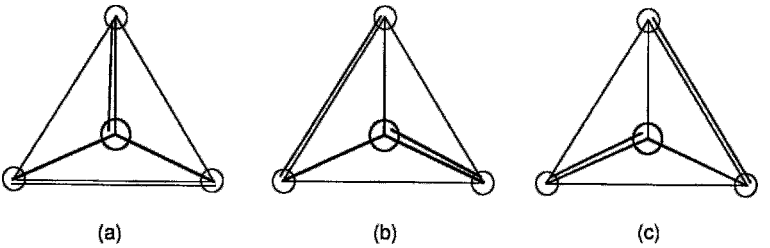

Figure 9.43 The three resonant structures of the (hypothetical) tetrahedral compound C_4.

atoms is bonded to three other carbons to form a closed surface, with the system conjugated such that for every resonant structure each carbon has two single bonds and one double bond. The smallest possible compound of this type is tetrahedral C_4, which has the three resonant structures shown in Fig. 9.43. Cubic C_8 is a fullerene, and we show in Problem 17 that it has nine resonant structures. Icosahedral C_{12} is also a fullerene, but octahedral C_6 and dodecahedral C_{20} are not because their carbons are bonded to more than three neighbors. These hypothetical smaller C_n compounds have not been synthesized, but the larger ones, such as C_{60}, C_{70}, C_{76}, C_{78}, and C_{82}, have been made and characterized. Some of them have several forms, with different arrangements of twelve pentagons and numerous hexagons. Clusters of buckminsterfullerenes, such as icosahedral $(C_{60})_{13}$, have also been studied (T. P. Martin *et al.*, 1993).

The C_{60} molecule might be called the world's smallest soccer ball! Because of its resemblance to the geodesic dome of architect R. Buckminster Fuller it has been referred to as buckminsterfullerene, or fullerene for short. The dual resemblances have prompted the sobriquet buckyball. All sixty carbon atoms are equivalent so the ^{13}C NMR spectrum is a narrow singlet. There are 12 regular pentagons and 20 hexagons with three carbon to carbon band lengths that are slightly longer than the other three.

The outer diameter of the C_{60} molecule is 7.10 Å and its van der Waals separation is 2.9 Å, so that the nearest-neighbor distance (effective diameter) in a solid is 10.0 Å. The bonds shared by a five-membered and a six-membered ring are 1.45 Å long, while those between two adjacent six-membered rings are 1.40 Å long. Above 260K these molecules form a face centered cubic lattice with lattice constant 14.2 Å; below 260K it is simple cubic with $a = 7.10$ Å (Fischer *et al.*, 1991; Kasatani *et al.*, 1993; Troullier and Martins, 1992). When C_{60} is doped with alkali metals to form a superconductor it crystallizes into a face centered cubic lattice with larger octahedral and smaller tetrahedral holes for the alkalis. The C_{60} ions are orientationally disordered in the lattice (Gupta and Gupta, 1993).

The compound C_{60} is not itself a superconductor, but when alkali metals are added it becomes superconducting. The doped compound forms a face-centered cubic lattice with a lattice constant of 10.04 Å. The structure has two tetrahedral holes (sites) and one octahedral hole per C_{60} molecule. If all of these holes are occupied by alkali metals A, the resulting compound is A_3C_{60}. An example of such a compound is K_2RbC_{60} with the potassiums in the smaller tetrahedral holes and the rubidiums in the larger octahedral holes. The transition temperatures of several of these doped fullerenes are given in Table 9.6. The compound Rb_3C_{60} has been

Table 9.6 Transition Temperature T_c of some Alkali Metal-Doped C_{60} Compounds

Compound	T_c, K
K_3C_{60}	19
K_2RbC_{60}	22
Rb_2KC_{60}	25
Rb_3C_{60}	29
Rb_2CsC_{60}	31
Cs_2RbC_{60}	33
Cs_3C_{60}	47

found to have an isotope effect exponent $\alpha = 0.37$ (Ramirez *et al.*, 1992a).

VIII. SYMMETRY OF THE ORDER PARAMETER IN UNCONVENTIONAL SUPERCONDUCTORS

The early suggestion that high temperature superconductors might exhibit unconventional, d-wave pairing, (Annett, Goldenfeld et al. 1991; Monthoux, Balatsky et al. 1991) has lead to a wide variety of new experimental probes with sensitivity sufficient to test this hypothesis. The pioneering work of Hardy and coworkers demonstrated that high resolution measurements of the London penetration depth could detect the presence of nodal quasiparticles characteristic of a *d*-wave pairing state (Hardy, Bonn et al. 1993). Since that time, a large number of new superconductors have been discovered, many of which exhibit nontrivial departures from BCS behavior. For some further reading, the reader is encouraged to explore the following articles: (Desirant and Shoenberg 1948; Carbotte 1990; Van Harlingen 1995; Annett 1997; Hardy, Kamal et al. 1998; Klemm 1998; Maki 1998; Brandow 1999; Timusk and Statt 1999; Tsuei and Kirtley 2000; Carbotte and Marsiglio 2003).

A. Symmetry of the Order Parameter in Cuprates

a. Hole-doped high-T_c cuprates

To our knowledge, the first penetration depth measurement to claim non s-wave superconductivity was that of Gross *et al.* (Gross, Chandrasekhar et al. 1986; Gross-Alltag, Chandrasekhar et al. 1991) on a heavy fermion material, UPt_3. Those authors observed power-law behavior of the penetration depth, $\lambda(T) - \lambda(0) = \Delta\lambda \sim T^n$ with the exponent $n = 1, 2, 3$ depending on the mutual orientation of the vector potential to a p-wave gap vector, and originating from different nodal structures (nodal points and lines) in a 3D Fermi surface.

Early penetration depth measurements in high-T_c cuprates claimed either s-wave pairing, probably due to insufficient sensitivity, or T^2 behavior, due to poor quality samples. Microwave measurements on single crystals YBaCuO by Hardy et. al. (Hardy, Bonn et al. 1993) were the first to show the linear T dependence characteristic of line nodes. By now, this linear variation has been observed in several copper oxides. In Figure 9.44 we show data for a single crystal of optimally doped YBaCuO, measured with a tunnel diode oscillator at a frequency of 12 MHz. The superfluid density

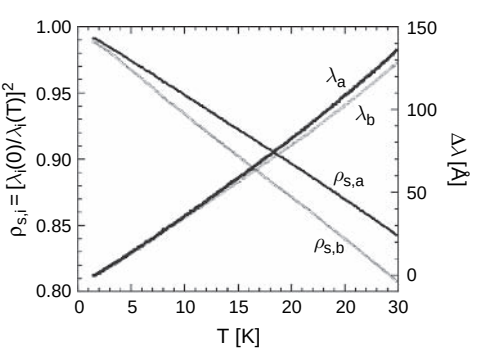

Figure 9.44 Linear temperature dependence of the superfluid density and penetration depth in clean YBCO crystal.

ρ_s and $\Delta\lambda$ are shown with the ac field parallel to both the a and b crystalline axes. ρ_s is linear over a substantially wider range than λ, illustrating the point made earlier that these two quantities have the same T dependence only asymptotically as $T \to 0$. For the optimally doped sample shown here, $d\lambda/dT \approx 4.2\,\text{Å/K}$ in close agreement with the microwave data. Remarkably, this linear variation indicative of nodal quasiparticles has been found to persist, relatively unchanged, even in extremely underdoped YBaCuO samples (Hoessini, Broun et al. 2004). This result remains one of the mysteries of superconductivity in the copper oxides (Lee and Wen 1997; Sheehy, Davis et al. 2004).

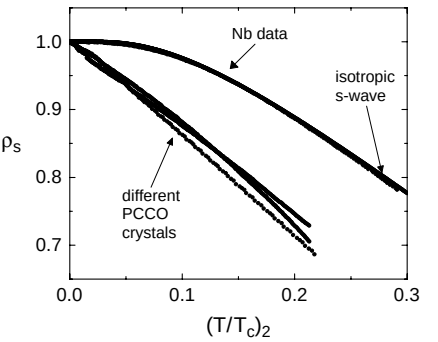

Figure 9.45 Superfluid density in three PCCO crystals plotted versus $(T/T_c)^2$ to emphasize dirty d-wave behaviour. Data for Nb obtained in the same apparatus are also shown, along with the expected behavior for an isotropic s-wave superconductor.

b. Electron-doped cuprates

The situation in electron-doped cuprates has been far more controversial, probably owing to the difficulty in growing high quality single crystals. Early microwave data in $Nd_{2-x}Ce_xCuO_{4-y}$ (NCCO) down to 4.2 Kelvin were interpreted within an s-wave model (Anlage, Wu et al. 1994). However, Cooper suggested that the spin paramagnetism of Nd^{3+} ions could be masking a power law temperature dependence expected if the material were d-wave (Cooper 1996). Lower temperature measurements on single crystals of NCCO clearly showed a vary large spin paramagnetic effect on the penetration depth below 4 K, as we describe later (Alff, Meyer et al. 1999; Prozorov, Giannetta et al. 2000; Prozorov, Giannetta et al. 2000). Additional measurements on nonmagnetic $Pr_{2-x}Ce_xCuO_{4-y}$ (PCCO) down to 0.4 K showed a superfluid density varying as T^2. Our data are shown in Figure 9.45, for several crystals. Data for Nb, a fully gapped s-wave superconductor, are shown for comparison.

The quadratic power law is consistent with a d-wave pairing state exhibiting unitary limit impurity scattering, as we discuss later (Hirschfeld and Goldenfeld 1993, Prozorov, 2000 #202; Kokales, Fournier et al. 2000; Prozorov, Giannetta et al. 2000). Coincident measurements of half-integral flux quanta in PCCO films (Tsuei and J.R. Kirtley 2000) also gave evidence for d-wave pairing in PCCO. Later mutual inductance measurements on PCCO thin films have shown a variety of temperature dependencies ranging from T^3 to T and, more recently, exponential, depending upon the method of film growth and the presence of a buffer layer (Kim, Skinta et al. 2003). Our own measurements on laser ablated thin films of PCCO continue to show a power law behavior that depends upon the oxygen doping level (Snezhko, Prozorov et al. 2004). Figure 9.46 shows data for optimally doped PCCO film and the fit to the disordered d-wave behavior, Eq.(Hirschfeld), which apparently describes the data very well.

To avoid possible demagnetizing effects in the $H \parallel c$ orientation, we also measured the PCCO films with $H \parallel ab$– plane. For films of order λ or less in thickness, the signal is very weak and the data is somewhat noisy, as shown in the inset. Nonetheless, to the best of our knowledge, the inset to Figure 9.46 is the first reported measurement of a thin film in such an orientation. The data are fully

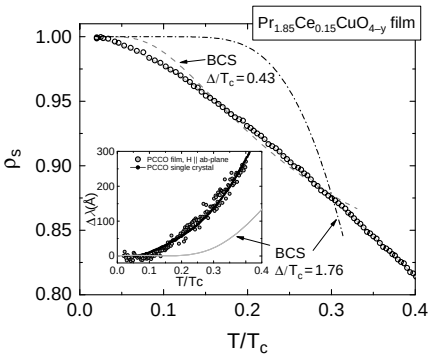

Figure 9.46 (main frame) Superfluid density in optimally doped PCCO film measured in with $H \| c$ - axis; s-wave BCS behaviour is shown by dashed lines, while a fit to Eq. (Hirschfeld) is shown by solid line. The inset shows a comparison between single crystal (solid line) and thin film data, the latter measured in the $H \| ab$ – plane orientation. A standard BCS curve is also shown.

consistent with previous measurements on single crystals.

Tunneling measurements in PCCO show zero bias conductance peaks. These are now believed to arise from Andreev bound states (discussed later) and are thus direct evidence for unconventional pairing. However, the presence of these states appears to depend upon doping so s-wave pairing for some range of parameters is not ruled out (Biswas, Fournier et al. 2002). A large number of and experimental and theoretical works currently support d-wave pairing in the electron-doped cuprates. Raman spectroscopy (Liu, Luo et al. 2005; Qazilbash, Koitzsch et al. 2005), ARPES (Armitage, Lu et al. 2001; Matsui, Terashima et al. 2005) specific heat (Yu, Liang et al. 2005) and Hall effect (Lin and Millis 2005) are all consistent with the d-wave picture. A fuller discussion of this issue is outside the scope of this chapter. We point out that precision penetration depth measurements were the first to call into question the s-wave picture of superconductivity in these materials (Kokales, Fournier et al. 2000; Prozorov, Giannetta et al. 2000; Prozorov, Giannetta et al. 2000).

B. Organic Superconductors

Probably the most thoroughly studied organic superconductors belong to the class generically referred to as κ-$(ET)_2X$ (Ishiguro, Yamaji et al. 1998; Kondo and Moriya 1998; McKenzie 1998; Schmalian 1998; Louati, Charfi-Kaddour et al. 2000). These are highly anisotropic, nearly two dimensional layered superconductors with parameters in the extreme Type II limit. NMR measurements show evidence of a spin gap and d-wave pairing (Mayaffre, Wzietek et al. 1995; Soto, Slichter et al. 1995), somewhat similar to the situation in the copper oxides. We discuss two of the most widely studied compounds, κ-$(ET)_2Cu(NCS)_2$ with $T_c = 10.4\,K$ and κ-$(ET)_2Cu[N(CN)_2]Br$ with $T_c = 11.6\,K$. Both materials superconduct under atmospheric pressure. Early penetration depth measurements claimed s-wave pairing, but lower temperature and higher precision measurements by Carrington *et al.* down to 0.35 K provided strong evidence for nodal quasiparticles (Carrington, Bonalde et al. 1999). That data are shown in Figure 9.47.

The distinction between penetration depth and superfluid density is particularly important here, since λ changes rapidly with temperature, and its absolute value is large. The measured quantity is $\Delta\lambda = \lambda(T) - \lambda(0.36\,K)$, from which the in-plane superfluid density is calculated for several choices of $\lambda(T \approx 0)$. μSR measurements typically give $\lambda(0) \approx 0.8\,\mu m$ (Le, Luke et al. 1992). For any plausible choice of $\lambda(0)$ the data clearly follow a power law. Fits correspond to the dirty d-wave form discussed earlier and yield values of the impurity crossover $T^* \approx 0.8\,K$. The fact that the measurements extend down to $T/T_C = 0.03$ rules out all but an extremely small energy gap. By now, a large number of other measurements

also indicate d-wave pairing (Behnia, Behnia et al. 1998; Arai, Ichimura et al. 2001; Izawa, Yamajuchi et al. 2002; Printeric, Tomic et al. 2002). However, there is still no consensus on the location of the purported nodes on the Fermi surface. In addition, some specific heat measurements do show evidence for an energy gap in these materials (Elsinger, Wosnitza et al. 2000).

Despite this very strong evidence for nodal quasiparticles, the superfluid density is never purely linear, and in fact exhibits an interesting regularity. Figure 9.48 shows the penetration depth itself plotted versus $T^{1.5}$. Over nearly a decade of temperature, samples of both κ-$(ET)_2Cu[N(CN)_2]Br$ (a,b) and samples κ-$(ET)_2Cu(NCS)_2$ (c,d) fit this power law with extraordinary precision. Many samples that have been measured since that time show precisely the same behavior. Although the dirty d-wave functional form can, with an appropriate choice of parameters, appear as a $T^{1.5}$ power law, the fact that every sample measured obeys this law would imply a remarkable regularity in the impurity crossover temperature T^*. We have observed no such regularity in the copper oxides. At the time the data were reported, Kosztin et al. had proposed a Bose-Einstein/BCS crossover theory for the underdoped copper oxides (Kosztin, Chen et al. 1998; Chen, Kosztin et al. 2000). They predicted a superfluid density that would vary as $T + T^{1.5}$, the new $T^{1.5}$ component coming from finite momentum pairs, similar to a Bose-Einstein condensate. However, when plotted as a superfluid density, our data do not fit this power law. Interestingly, more recent measurements on the heavy fermion compound $CeCoIn_5$ also exhibit the same $\Delta\lambda \propto T^{1.5}$ behavior (Özcan, Broun et al. 2003). They speculate that the fractional power law behavior may come from a renormalization of parameters near to a quantum critical point. Several different experiments indicate that $CeCoIn_5$ is also a d-wave superconductor, so the experimental situation is rather analogous to the organics. Chia *et al.* also observed the same power law in this material and believed it can be explained by nonlocal effects (Chia, Van Harlingen et al. 2003). However, nonlocality is unlikely to be relevant for organic superconductors, which exist in an extreme Type II limit.

κ-$(ET)_2Cu[N(CN)_2]Br$ and κ-$(ET)_2Cu(NCS)_2$ are highly anisotropic layered superconductors. By orienting the ac measurement field along the conducting planes,

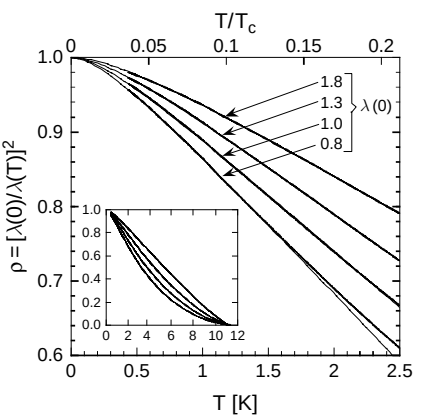

Figure 9.47 In plane superfluid density for different choices of λ(0) in κ-$(ET)_2Cu[N(CN)_2]Br$. Fits to the data use the dirty d-wave interpolation formula. The inset shows data up to T_c (Carrington, Bonalde, et al. 1999).

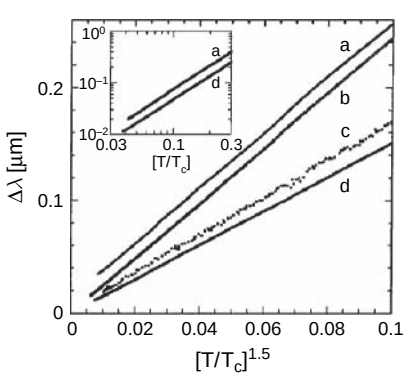

Figure 9.48 Δλ for two samples of κ-$(ET)_2Cu[N(CN)]_2Br$ (a,b) and two samples κ-$(ET)_2Cu(NCS)_2$ (c,d) plotted versus $T^{3/2}$ (Carrington, Bonalde et al. 1999).

the magnetic response is dominated by interplane currents which penetrate in from the edges on a length scale $\lambda_\perp$, the interplane penetration depth. In general, there is no simple formula for $\lambda_\perp$ involving just the gap function and the Fermi surface parameters. This is because $\lambda_\perp$ depends on both the pairing state and the details of the transport between conducting planes. If this transport is coherent, then $\rho_\perp = (\lambda_\perp(0)/\lambda_\perp(T))^2$ will exhibit the same temperature dependence as $\rho_\parallel = (\lambda_\perp(0)/\lambda_\parallel(T))^2$. If not, $\rho_\perp$ will generally follow a higher power law than $\rho_\parallel$ in a d-wave superconductor. The precise exponent can vary from $n = 1$ to $n = 3$ and in special cases, as high as $n = 5$ (Graf, Palumbo et al. 1995; Radtke, Kostur et al. 1996; Hirschfeld, Quinlan et al. 1997; Sheehy, Davis et al. 2004). In most copper oxides one has $1 - \rho_\perp \propto T^{2-2.5}$, indicating incoherent transport between the conducting planes (Hoessini, Broun et al. 2004).

Figure 9.49 shows both $\lambda_\perp$ and the superfluid density $\rho_\perp$ in κ-$(ET)_2Cu(NCS)_2$. $\lambda_\perp(0) \parallel 100\,\mu m$ is sufficiently large that it can be determined directly from the frequency shift of the resonator, as described earlier. We find that $1 - \rho_\perp \propto T^{1.3-1.5}$. Fitting the inplane superfluid density to a pure power law we obtain $1 - \rho_\parallel \propto T^{1.2-1.4}$, which has very nearly the same exponent. (The latter depends somewhat on the choice of $\lambda_\parallel(0)$.) Coherent interplane transport is somewhat surprising given the extreme anisotropy of the ET-class of organic superconductors. Nevertheless, recent magnetoresistive measurements do demonstrate a small but but unequivocal three dimensional character to the Fermi surface. It should also be stressed that the power law variation shown in Figure 9.49 is another very clear demonstration of nodal quasiparticles in the organic superconductors. $\lambda_\perp(0)$ is so large relative to $\Delta\lambda_\perp$ that $\rho_\perp \approx 1 - 2\Delta\lambda_\perp(T)/\lambda_\perp(0)$ is an excellent approximation within the temperature range over which the gap is constant. Therefore, the power law exponent is not particularly sensitive to the choice for $\lambda_\perp(0)$. There is no hint of an energy gap down to the lowest temperatures measured.

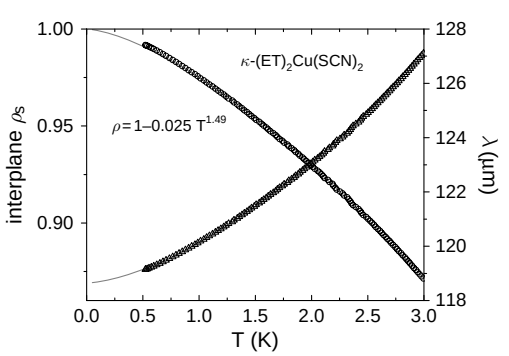

Figure 9.49 Interplane penetration depth and superfluid density for κ-$(ET)_2Cu[SCN]_2$. Fits are to pure power laws.

C. Influence of Bandstructure on Superconductivity

Even conventional s-wave superconductors can exhibit unconventional behaviour if the bandstructure has certain peculiarities. In general, in most superconductors, there is more than one sheet of the Fermi surface. If those were completely independent, one would expect possibly different superconducting gaps with their own T_c and H_c. Usually however, significant interband scattering smears this out resulting in a single effective gap. However, when the dimensionality of different sheets of the Fermi surface differs significantly, the interband scattering is reduced and two-band superconductivity becomes possible. Another important ingredient is the density of states contributed by each sheet of the Fermi surface.

a. MgB_2

There is by now considerable evidence that MgB_2 is a two-band superconductor. By this we mean that each Fermi surface sheet possesses a different gap function. Although strong interband scattering leads to a single T_c, the gap magnitudes on the π and

σ surfaces are significantly different. This was first observed in tunneling measurements where two conductance peaks were observed, one of which was more easily suppressed in a magnetic field (Schmidt, Zasadzinski et al. 2002; Zalk, Brinkman et al. 2006). Penetration depth measurements on MgB_2 wires indicated s-wave pairing but with a gap magnitude significantly smaller than the weak coupling BCS value (Prozorov, Giannetta et al. 2001). Subsequent penetration depth measurements on single crystals by Manzano *et al*. were fit to a two-band α-model discussed previously (eqs. (27,28)). The data and fits are shown in Figure 9.50. The deviation from a single gap picture is very clear. It was found that the larger gap on the σ sheet is $\Delta_\sigma = 75 \pm 5k$ and the π-band gap is $\Delta_\pi = 29 \pm 2K$ (Manzano, Carrington et al. 2002). Measurements by Fletcher *et al*. determined the temperature dependence of the anisotropy in the interplane versus in-plane penetration depth (Fletcher, Carrington et al. 2005). It was found that at low temperatures λ_c/λ_{ab} is approximately unity, and it increases to about 2 at T_c. This is opposite to the temperature dependence of the coherence length anisotropy, which decreases from about 6 to about 2. This observation has provided firm quantitative evidence for a two-gap nature of superconductivity in MgB_2.

Figure 9.50 provides a good example of using two components of the superfluid density and the full temperature range BCS treatment to show the two-gap nature of MgB_2 single crystals. So far, MgB_2 remains the only superconductor with two confirmed distinct gaps, although both vanish at the same temperature.

b. $NbSe_2$

Structurally similar to MgB_2, $NbSe_2$ was also believed to have two distinct gaps. The recent penetration depth measurements performed on different single crystals (Fletcher, Carrington et al. 2006) do not support this conjecture, and lead to the conclusion that there is a single anisotropic s-wave gap, or there is some possibility of two slightly different gaps on 2D Nb sheets of the Fermi surface, but not on the Se 3D sheet (which appears to be fully gapped).

Figure 9.51 plots the in-plane London penetration depth in single crystal $NbSe_2$. A weak coupling BCS behavior with a

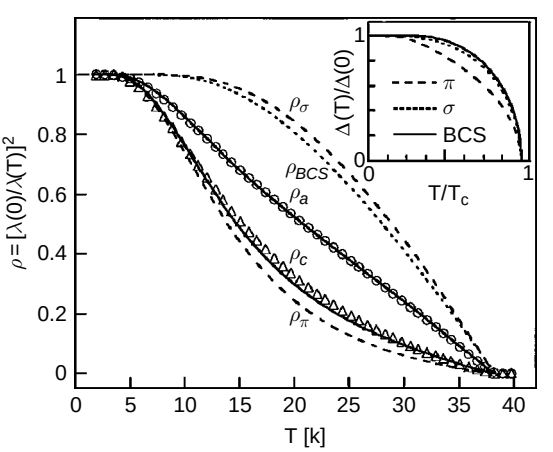

Figure 9.50 Two components of the superfluid density in single crystal MgB_2 (from Fletcher, Carrington et al. 2005). Solid lines are fits to the α-model. The inset shows the temperature dependencies of the two gaps used for the fits.

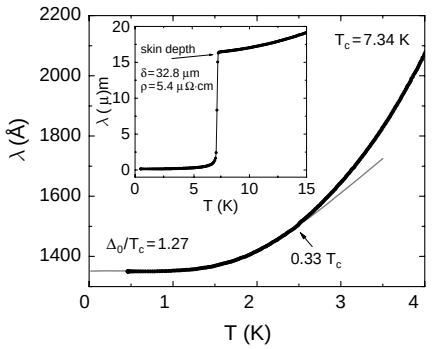

Figure 9.51 London penetration depth in $2H$-$NbSe_2$. Inset shows full temperature range and extracted from the skin depth resistivity.

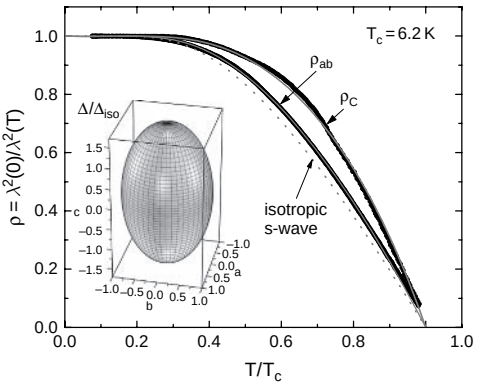

Figure 9.52 Two components of the superfluid density measured in single crystal CaAlSi. Solid lines show the results of a full 3D BCS fit with an ellipsoidal gap shown in the inset as the fit parameter.

slightly reduced gap is indicated. The reduced gap is due to anisotropy. A detailed analysis is given elsewhere (Fletcher, Carrington et al. 2006). Stronger interband scattering and a significantly different density of states on different energy bands are probably responsible for such behaviour.

Another aspect to consider is the stacking sequence of $2H$-$NbSe_2$, where layers are held together only by van der Waals forces. This makes the material closer to layered superconductors where interlayer transport makes the penetration depth appear more gapped than in-plane response (at least in the case of d-wave superconductors (Radtke, Kostur et al. 1996; Hirschfeld, Quinlan et al. 1997; Sheehy, Davis et al. 2004)). The anisotropic electromagnetic response has been analysed in Ref. (Dordevic, Basov et al. 2001). An additional feature of $NbSe_2$ is the incommensurate charge-density wave state observed below 33 K. Currently there is no clear understanding how it might affect the superconducting properties.

c. CaAlSi

A good example of an anisotropic 3D s-wave superconductor is CaAlSi, isostructural with MgB_2 but exhibiting almost ideal weak-coupling BCS behaviour with, an anisotropic 3D gap. In this system both components of the superfluid density were measured, and full temperature range BCS calculations with anisotropic ellipsoidal gap as the fitting parameter were carried out.

Figure 9.52 shows the result of simultaneous fitting two components of the superfluid density in a lower-T_c version of the CaAlSi superconductor. In higher – T_c samples the anisotropy is greatly reduced and most likely the highest – T_c material is an isotropic weak coupling BCS superconductor (Prozorov, Olheiser et al. 2006). Most probably the single gap is due to significant interband scattering and the 3D nature of the in-plane and interplane bands.

D. Some Other Superconductors

a. Heavy-fermion superconductors

In a set of remarkable low-temperature measurements using a SQUID magnetometer, Gross *et al.* obtained power law temperature dependencies of $\lambda(T)$ with different exponents corresponding to different orientations of the sample in the heavy fermion superconductor UBe_{13} (Gross, Chandrasekhar et al. 1986; Gross-Alltag, Chandrasekhar et al. 1991). The measurements provided strong evidence for p-wave

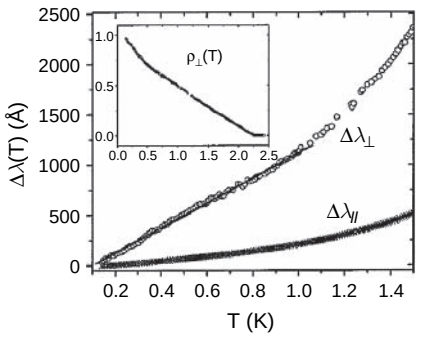

Figure 9.53 Magnetic penetration depth in two orientations in heavy fermion superconductor, $CeCoIn_5$. *Reprinted with permission from Ref. (Chia, Van Harlingen et al. 2003). Copyright: American Physical Society.*

superconductivity for which the theoretical description is complicated by the vector nature of the superconducting gap (it dependence on the mutual orientation of the vector potential and the crystal axes). The general consensus seems to be that these materials have p-wave symmetry of the order parameter (Joynt and Taillefer 2002).

A more recent addition to the heavy fermion superconducting family is $CeCoIn_5$. Figure 9.53 shows the penetration depth measured in two orientations in this material taken from Ref. (Chia, Van Harlingen et al. 2003). Arguing that the effect of impurities should be visible on both components (and, apparently it is not seen in $\lambda_\perp(T)$), it was concluded that a quadratic variation of the in-plane component is due to a non-local response of a superconductor with nodes. A strong-coupling correction have also been suggested.

b. Borocarbides

At some point it seemed that non-magnetic borocarbides are s-wave materials, maybe with some degree of anisotropy. However, most of the single crystals had residual metallic flux, which could mask the true behaviour. Annealing in vacuum could change the behaviour as well. The question of the magnetic penetration depth and pairing symmetry is open, and we are currently working on its resolution. In magnetic borocarbides the penetration depth has a large influence on the underlying magnetic structure and therefore it is useless for establishing the pairing symmetry. However, these systems are very interesting from the point of view of the interplay between superconductivity and magnetism (Ghosh, Krishna et al. 1997; Chia, Bonalde et al. 2001; Chia, Cheong et al. 2005).

c. Sr_2RuO_4

The penetration depth in Sr_2RuO_4 as shown in Fig. 9.54 does not follow a standard s-wave behavior. Moreover, measurements of the NMR Knight shift across the superconducting transition had indicated a triplet pairing state. In that case, the gap is a vector and the data analysis is very difficult. Current debates are between various versions of p- and f- wave pairing (Annett 1999; Bonalde, Yanoff et al. 2000; Won and Maki 2000).

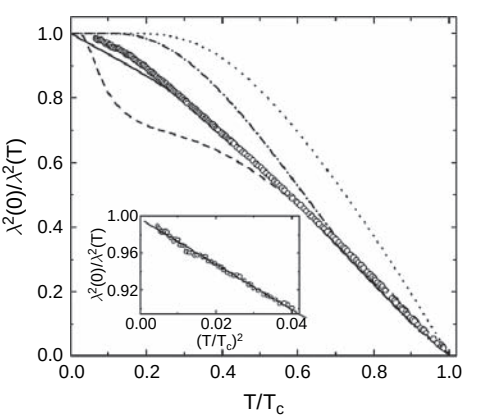

Figure 9.54 Superfluid density in Sr_2RuO_4. Lines show various fits and the Authors concluded that there is a nodal gap and nonlocal quadratic corrections (see Section). *Reprinted with permission from Ref. (Bonalde, Yanoff et al. 2000). Copyright: American Physical Society.*

d. $MgCNi_3$

The recently discovered non-oxide perovskite superconductor $MgCNi_3$ (He, Huang et al. 2001) is viewed as a bridge between high-T_c cuprates and conventional intermetallic superconductors. This material is close to a magnetic instability on hole doping. It was suggested that strong magnetic fluctuations may lead to unconventional pairing (Rosner, Weht et al. 2002). As far as pairing symmetry is concerned, the current experimental situation is controversial. On one hand, evidence for conventional s-wave behavior is found in specific heat measurements (Lin, Ho et al. 2003), although the authors disagree on the coupling strength. The T_1 nuclear spin-lattice relaxation rate of ^{13}C, seems to exhibit a behavior characteristic of an s-wave superconductor (Singer, Imai et al. 2001). On the other hand, a zero-bias conductance peak (ZBCP) attributed to Andreev bound states has been observed, and it was argued that the observed ZBCP could not be due to intergranular coupling or other spurious effects (Mao, Rosario et al. 2003). Nonmagnetic disorder introduced by irradiation was found to significantly suppress superconductivity (Karkin, Goshchitskii et al. 2002). Such suppression is not expected in materials with a fully developed s-wave gap, and is a strong indication of an order parameter with nodes. Theoretical calculations support this conclusion (Granada, da Silva et al. 2002). Furthermore, recent theoretical developments predict the possibility of a unique unconventional state (Voelker and Sigrist 2002), which might reconcile apparently contradictory experimental observations.

It is very difficult to experimentally identify the non-exponential contribution of low-energy quasiparticles due to the presence of nodes in the superconducting gap on the Fermi surface. In the case of thermal measurements, this electronic contribution is masked by a large phonon contribution. For electromagnetic measurements, sensitivity is typically a problem. Precise measurements of the London penetration depth are therefore very important see Fig. 9.55.

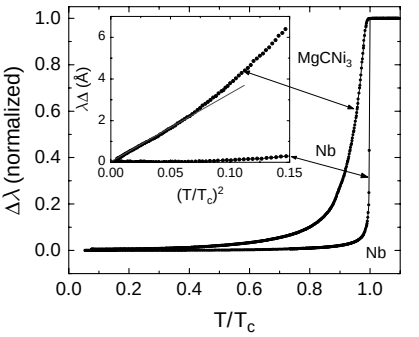

Figure 9.55 Penetration depth measured in $MgCNi_3$ superconductor. The main frame compares the full temperature range to a conventional s-wave (Nb). The inset shows the low temperature regime which clearly indicats a quadratic (non-exponential) behavior of the penetration depth.

IX. MAGNETIC SUPERCONDUCTORS

A. Coexistence of superconductivity and magnetism

Coexistence of superconductivity and magnetism is one of the most interesting subjects in the physics of correlated electrons. Many review books and articles have been published on this subject (Abrikosov, 1988, Bulaevskii, 2984, Buzdin and Bulaevskii, 2986, Fischer and Peter, 1973, Izyumov and Skryabin, 1974, Khan and Raub, 1985, Kulic, 2006, Maple, 1983, Matthias, 1979, Nakanishi, 1984, Whitehead *et al.*, 1985, Fischer 1990). Indeed, in a simple picture, ferromagnetism cannot coexist with singlet pairing, because of the antiparallel spin arrangement. Triplet pairing, on the other hand can coexist with ferromagnetism, and this has been discussed (Matthias, 1979), but there are only few superconductors where triplet pairing is realized and it is not clear if there is an example of a bulk

ferromagnetic triplet superconductor. Most superconductors are singlet (including s, d and g pairing states, and thus all conventional superconductors, borocarbides and cuprates). Therefore it is not surprising that the majority of known magnetic superconductors are antiferromagnetic. There are discussions of so called weak ferromagnetic superconductors, such as ruthenocuprates $R_{z-\delta}Ce_xRuSr_2Cu_2O_y$ (R=Eu and Gd), but it is still unclear whether this is bulk superconductivity (Felner, 2003). A more established example is the low-temperature phase in $ErNi_2B_2C$ (Canfield *et al*., 1997, Kawano-Furukawa, 2001).

Ferromagnetism, however, can coexist with superconductivity if the exchange interaction is indirect. as is the case of elements with partially occupied 4f and 5f orbitals. If such RKKY – type exchange is not strong (so that the ferromagnetic transition temperature, T_{FM}, is only few degrees), ferromagnetism can coexist with superconductivity. In all cases the resulting state is inhomogeneous. If T_{FM} is larger than the superconducting transition temperature, T_c, superconductivity will either not appear at all or will destroy the ferromagnetism, depending on the ratio between the effective molecular magnetic field, I (in energy units) and the superconducting order parameter, Δ_0. If $I < \Delta_0/\sqrt{2}$ superconductivity suppresses ferromagnetism, and in the opposite case it does not. The transition between two states as a function of the parameter I is a first order phase transition. However, even if $I > \Delta_0/\sqrt{2}$ it is possible to have coexisting superconducting and ferromagnetic states. In this case, both magnetic and superconducting order parameters are spatially modulated. This is the so called Larkin-Ovchinnikov-Fulde-Ferrell state (LOFF) (Ovchinnikov, 1964, Fulde and Ferrell, 1964), which has been a goal for experimentalists for the last forty years. Yet no definite experimental evidence for such a state exists, although there are many indirect results in several superconductors such as layered antiferromagnetic $Sm_{1.85}Ce_{0.15}CuO_{4-y}$ or heavy fermion $CeCoIn_x$.

Finally, the most interesting case is when $T_{FM} < T_c$. In this case ferromagnetism develops on a superconducting background, and close to the ferromagnetic transition the spin structure is significantly modified either by helicoidal rotation or by splitting into domains. The exact structure of the coexisting phase is determined by many factors, including the magnetic and superconducting anisotropies. There are only a few well-established examples of ferromagnetic superconductors – the best known and most studied are $HoMo_6S_8$ and $ErRh_4B_4$ (Abrikosov, 1988, Buzdin and Bulaevskii, 1986, Buzdin *et al*., 1984). An example of the AC magnetic susceptibility in the latter in various applied magnetic fields is shown in Figure 9.56.

In zero applied magnetic field, both normal state – superconductor (SC) and superconductor – ferromagnet transitions are very sharp. However, when a magnetic field is applied the behavior in the mixed state is non-trivial, closer to the ferromagnetic transition. An apparent delay or suppression of a superfluid density may be related to a field –

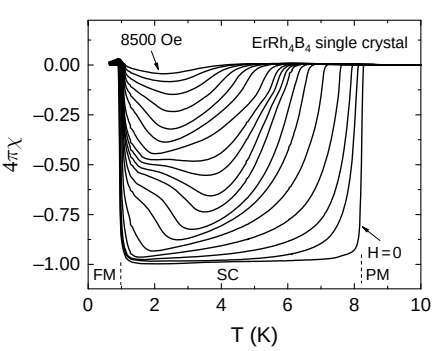

Figure 9.56 The AC susceptibility measured by a tunnel diode superconductor (R. Prozorov and M. W. Vannette) in single crystal $ErRh_4B_4$ (grown by the P. C. Canfield group) in different applied magnetic fields, Normal (paramagnetic, (PM)), superconducting (SC), and ferromagnetic (FM) phases are clearly evident.

dependent vortex core-size, and even to the development of ferromagnetism in the vortex cores. It could also be due to a predicted domain structure or an exotic spin structure. In addition, the FM-SC-FM transition is hysteretic with a distinctly different behavior upon warming or cooling. Clearly, despite a vast literature and tremendous theoretical and experimental efforts, the topic is far from being settled, and more work is needed to understand the coexistence of bulk superconductivity and bulk magnetism.

B. Antiferromagnetic Superconductors

Borocarbides with the general formula RT_2B_2C (R=Sc, Y, La, Th, Dy, Ho, Er, Tm, Lu and T=Ni, Ru, Pd, Pt) constitute a very interesting class of materials. Whereas not all combinations of T and R result in superconductivity, many do. Many Nickel-based (T=Ni) borocarbides exhibit antifferomagnetism coexisting with superconductivity. Some prominent examples are $ErNi_2B_2C$ and $HoNi_2B_2C$ (Canfield *et al*., 1997. With a transition temperature around 16 K and a Neel temperature of about 6 K, $ErNi_2B_2C$ also shows features characteristic of ferromagnetism below 2.3 K, and therefore is believed to be a weak ferromagnetic superconductor. The compound $HoNi_2B_2C$, on the other hand, exhibits several antiferromagnetic structures coexisting with superconductivity, and nearly reentrant behavior at the Néel temperature.

Other examples of antiferromagnetic superconductors include RRh_4B_4 (R=Nd, Tm, Sm), RMo_6S_8 (R=Tb, Dy, Er, Gd, Nd), and $ErMo_6Se_8$. As expected, antiferromagnetic order does not prohibit superconductivity, but certainly influences it. For example, antiferromagnetic superconductors may exhibit gapless superconductivity and a nonmonotonic temperature dependence of the upper critical field (Buzdin and Bulaevskii, 1986). More examples can be found in Fischer (1990).

C. Magnetic Cuprate Superconductor – SmCeCuO

Thus far our discussion has been limited to relatively low-T_c superconductors. Some cuprates also exhibit magnetic ordering, but due to their layered structure superconductivity and magnetism do not coexist in the same volume (we do not discuss weak antiferromagnetic ordering of Cu in Cu–O planes, which is well understood). We restrict ourselves to one example in which a magnetic ordering transition has a profound influence on the penetration depth: The electron-doped copper oxide SCCO (Prozorov *et al*., 2004). In the parent compound Sm_2CuO_4, rare earth Sm^{3+} ions order at 5.95 Kelvin (Jiang *et al*., 1992). The ordering is ferromagnetic within each layer parallel to the conducting planes, and antiferromagnetic from one layer to the next (Sumarlin *et al*., 1993). Ce doping and subsequent oxygen reduction result in a superconductor $Sm_{1.85}Ce_{0.15}CuO_{4-\delta}$ (SCCO) with $T_C \approx 23K$.

Figure 9.57 shows a full-temperature scale variation of the penetration depth in single crystal SCCO in two orientation. The interplane shielding is very weak, yet it exhibits a transition to a more diamagnetic state below about 4 K. The in-plane response shows this effect more clearly. It was tempting to associate this transition to the loss of spin – disorder scattering below the ordering temperature of the Sm^{3+} sublattice. However, the magnetic field dependence is suggesting a different scenario.

Figure 9.58 (left) shows the low temperature penetration depth measured in SCCO for several values of a magnetic field applied along the c-axis. First, there is clear evidence for a phase transition near $T^*(H) \approx 4K$ that is rapidly suppressed by the magnetic field. Second, the penetration depth drops below the transition indicating stronger diamagnetic screening. This enhanced diamagnetism is quite different from the *weaker* screening that results from paramagnetic impurities discussed earlier. The two effects are consistent

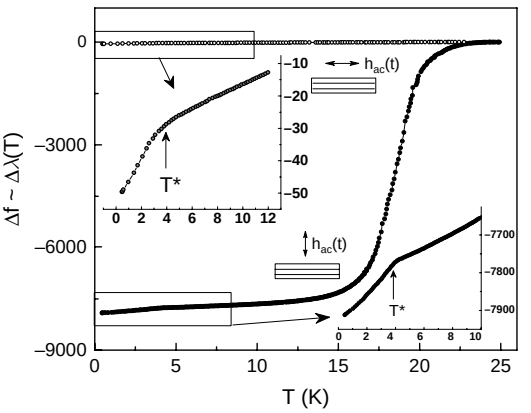

Figure 9.57 Temperature variation of the penetration depth $\Delta\lambda$ in an SCCO superoncductor at two orientations. The insets show low temperature regions where a distinct break of the diamagnetic signal is evident.

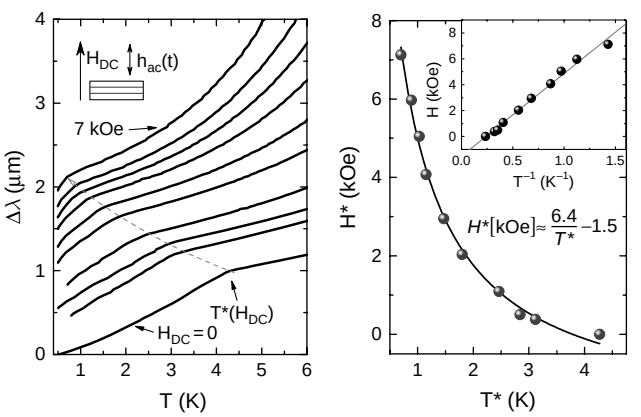

Figure 9.58 Magnetic field dependence of the penetration depth $\Delta\lambda$ in single crystal SCCO (left), and the downturn field H* as a function of the temperature (right). The downturn field is linear in $1/T^*$, as shown by the data replotted in the inset (right),

with a model involved a spin-freezing transition at $T^*(H)$. Work during the 1980's on the effects on the influence of random impurities on superconductive properties showed that while spin fluctuations can be pair breaking, the freezing out of these processes will reduce spin-flip scattering and lead to a sharpened density of quasiparticle states (Schachinger *et al*., 1988). The latter leads, in turn, to stronger diamagnetic screening and a shorter penetration depth. That one must consider a spin-glass type of transition is supported by the rapid suppression of the transition by a magnetic field. An ordinary antiferromagnetic transition is relatively insensitive to fields on this scale. In fact, heat capacity measurements on the parent compound in fields up to 9 T showed only a tiny shift

of the ordering temperature. Therefore, the processes required to induce superconductivity not only reduce the magnetic ordering temperature, but apparently also result in a disordered spin system. It is well known that the transition temperature in spin-glasses is a strong function of the magnetic field. In fact, it was found that the field dependence $T^*(H)$ shown in Figure 9.58 (right) has precisely the functional form observed in $Fe_{92}Zr_8$, a well-known spin glass system (Ryan *et al*., 2001). At this point, it is not known whether the spins actually freezing are the Sm^{3+}. It is possible that the Sm spins interact with Cu^{2+} spins in the conducting layers, for which spin freezing near 4 K is a well-known phenomenon in cuprate superconductors (Lascialfari *et al*., 2003). This example also serves to demonstrate the invaluable role of an external magnetic field in interpreting penetration depth measurements on complex superconductors.

10

Hubbard Models and Band Structure

I. INTRODUCTION

In addition to the phenomenological Ginzburg-Landau theory and the microscopic BCS theory presented in Chapters 5 and 6 respectively, there are other less fundamental theoretical approaches which have been used to explain the presence of superconductivity of some classes of compounds, and to interpret superconducting properties of individual superconductors. This chapter will summarize two of these theoretical approaches, namely the Hubbard model and band structure calculations. Further details of these methods can be found in Chap. 8 of the first edition.

Some of the basic properties of electrical conductivity are clarified very well by the independent electron approximation in which the wave functions are plane waves $e^{i(k\cdot\cdot r-\omega t)}$ and the energy is all kinetic

$$E_k = E_o(a/\pi)^2[k_x{}^2 + K_y{}^2 + k_z{}^2] \qquad (10.1)$$

where $k_x = 2\pi/x$, $k_y = 2\pi/y$, $k_z = 2\pi/z$, and a cubic structure is assumed with lattice spacing a. Energy bands are plots of E_k versus the value of k along various directions of the Brillouin zone.

Many of the most interesting properties of materials, such as magnetic ordering and superconductivity, require theories that go beyond the independent-electron approximation. In order to understand these phenomena it is necessary to take into account

electron correlations. The simplest model of correlated electrons is the one-state Hubbard (1963, 1964) model, and so we will emphasize it.

II. ELECTRON CONFIGURATIONS

Free electron energy bands calculated using the independent electron approximation are an oversimplification of the true state of affairs. For actual compounds there are additional factors to be taken into account. The unit cell contains several atoms with each atom contributing one or more electrons, as listed in Table 10.1. A separate Schrödinger equation is written down for each electron, and these equations are solved self-consistently. An initial guess for the wavefunctions of these electrons is used to calculate the potential, the Schrödinger equations are solved with this potential to obtain new wavefunctions, and these new wavefunctions are then used to provide an improved potential. The process is repeated until the difference between the new potential and the previous potential is less than some predetermined limit.

A. Configurations and Orbitals

Table 10.1 gives the electronic configurations of several atoms that occur commonly in superconductors. For each atom the table gives the total number of electrons, the number of electrons in the core that do not directly enter the calculations, the configuration of the outer electrons, and the configuration of an ion that may be present if

Table 10.1 Electron Configurations of Selected Atoms Commonly Used for Band Structure Calculations of Superconductors[a]

Atom number	Symbol	Core[b, c]	Atom configuration	No. valence elctrons	Ions	Ion configuration	No. electrons
8	O	Be 4	$[2s^2]2p^4$	4	O^{1-}	$2p^5$	5
					O^{2-}	$2p^6$	6
14	Si	Ne 10	$3s^2 3p^2$	4	Si^{4+}	–	0
19	K	Ar 18	$[3p^6]4s$	1	K^{+}	–	0
20	Ca	Ar 18	$4s^2$	2	Ca^{2+}	–	0
23	V	Ar 18	$3d^3 4s^1 4p^1$	5	V^{3+}	$3d^2$	2
29	Cu	Ar 18	$3d^{10}42^1$	11	Cu^{1+}	$3d^{10}$	10
					Cu^{2+}	$3d^9$	9
					Cu^{3+}	$3d^8$	8
38	Sr	Kr 36	$5s^2$	2	Sr^{2+}	–	0
39	Y	Kr 36	$4d^1 5s^2$	3	Y^{3+}	–	0
41	Nb	Kr 36	$4d^3 5s^1 5p^1$	5	Nb^{4+}	$4d^1$	1
50	Sn	– – 46	$5s^2 5p^2$	4	Sn^{4+}	–	0
56	Ba	Xe 54	$[5p^6]6s^2$	2	Ba^{2+}	–	0
57	La	Xe 54	$5d^1 6s^2$	3	La^{3+}	–	0
80	Hg	– – 78	$[5d^{10}]6s^2$	2	Hg^{2+}	$[5d^{10}]$	0
81	Tl	– – 78	$[5d^{10}]6s^2 6p^1$	3	Tl^{3+}	$[5d^{10}]$	0
82	Pb	– – 78	$[5d^{10}]6s^2 6p^2$	4	Pb^{4+}	$[5d^{10}]$	0
83	Bi	– – 78	$[5d^{10}]6s^2 6p^3$	5	Bi^{3+}	$[5d^{10}]6s^2$	2
					Bi^{4+}	$[5d^{10}]6s^1$	1
					Bi^{5+}	$[5d^{10}]$	0

[a] Core electrons listed in square brackets are sometimes included in the basis set.
[b] The core of Sn is Kr plus the fourth transition series ($4d^{10}$) closed shell.
[c] The core of Tl, Pb, and Bi is Xe plus the rare earth ($4f^{14}$} and fifth transition series ($5d^{10}$} closed shells.

a simple ionic picture is adopted. The notation used is nl^N, where n is the principal quantum number corresponding to the level, the orbital quantum number l is 0 for an s state, 1 for a p state and 2 for a d state, and N is the number of electrons in each l state. A full l state contains $2(2l+1)$ electrons, corresponding to 2,6, and 10 for s, p, and d states, respectively. The wavefunctions of these outer electrons are called *orbitals*.

The various s, p, and d orbitals have the unnormalized analytical forms given in Table 10.2, and the electronic charge distribution in space of the d orbital is sketched in Fig. 10.1. Each orbital represents the charge of one electron; the sign on each lobe is the sign of the wavefunction. For example, we see from the table that p_z is given by $r\cos\Theta$, which is positive along the positive z-axis ($\Theta = 0$), negative along the negative z-axis ($\Theta = \pi$), and zero in the x, y-plane $\left(\Theta = \frac{1}{2}\pi\right)$. Linear combinations of atomic orbitals, called *hybrid orbitals*, are used to form covalent bonds that hold the atoms together, as illustrated in Fig. 10.2 for bonding between an oxygen p orbital (p_x) and a copper d orbital $\left(d_{x^2-y^2}\right)$. The figure shows, first, a bonding case in which the signs of the two orbitals that form the hybrid are the same in the region of overlap, second, and antibonding case in which the signs are opposite where overlap occurs, and, third, a nonbonding case where there is no appreciable overlap. Figure 10.3 presents a sketch of a Cu-O_2 plane of a high temperature cuprate superconductor.

Table 10.2 Unnormalized Analytical Expressions in Cartesian and Polar Coordinates for the s, p, and d Orbitals[a]

Orbital	Cartesian form	Polar form
s	1	1
p_x	$\frac{x}{r}$	$\sin\ \Theta\ \cos\ \phi$
p_y	$\frac{y}{r}$	$\sin\ \Theta\ \sin\ \phi$
p_z	$\frac{z}{r}$	$\cos\ \Theta$
d_{xy}	$\frac{xy}{r^2}$	$\sin^2\ \Theta\ \sin\ \phi\ \cos\ \phi$
d_{yz}	$\frac{yz}{r^2}$	$\sin\ \Theta\ \cos\ \Theta\ \sin\phi$
d_{zz}	$\frac{zx}{r^2}$	$\sin\ \Theta\ \cos\ \Theta\ \cos\ \phi$
$d_{x^2-y^2}$	$\frac{x^2-y^2}{r^2}$	$\sin^2\ \Theta\ (\cos^2\ \phi - \sin^2\ \phi)$
d_z	$\frac{3z^2-r^2}{r^2}$	$3\ \cos^2\ \Theta - 1$

[a] $l = 0,\ 1$, and 2, respectively.

Each orbital can accommodate two electrons of opposite spin. In the usual case the two electrons enter the low-lying bonding level to form a chemical bond that holds the atoms together while the anti-bonding level remains empty, as illustrated in Fig. 10.4. The "bonding overlap" case is called a sigma (σ) bond, and a Cu-O bond of this type can be called a $3d_{x^2-y^2} - 2p\sigma$ bond. We will see later that the band structures of superconductors generally consist of many fully occupied bonding levels, called *valence bands*, which lie below the Fermi level, many unoccupied antibonding levels well above it, and one or more partly occupied hybrid orbitals that pass through the Fermi level.

The same approach may be used to treat holes as well as electrons. For example, the copper ion ($3d^9$) may be considered as a filled d shell ($3d^{10}$) plus one $3d$ hole, while the oxygen mononegative ion ($2p^5$) may be treated as a full p shell ($2p^6$) plus one $2p$ hole.

B. Tight-Binding Approximation

In Section I we talked about the nearly free electron case in which the potential energy is small and the eigenfunctions approximate plane waves. Here the energy bands are broad and overlapping. At the beginning of the present section we discussed atomic orbitals, and noted that when the atomic potential energy is dominant the eigenfunctions approximate atomic orbitals centered on individual atoms. This is the case for core electrons whose energy levels lie deep within the atom and do not depend on k.

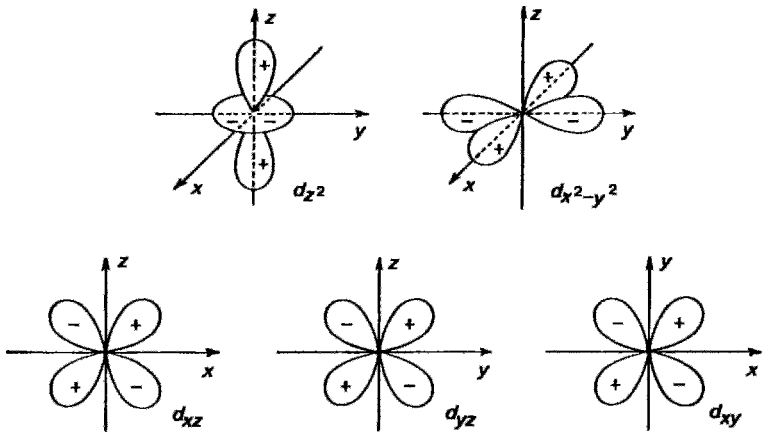

Figure 10.1 Spacial distribution of electron density for the five d orbitals. The signs ($\pm$) on the lobes are for the wavefunction; the sign of the electric charge is the same for each lobe of a particular orbital (Ballhausen, 1962).

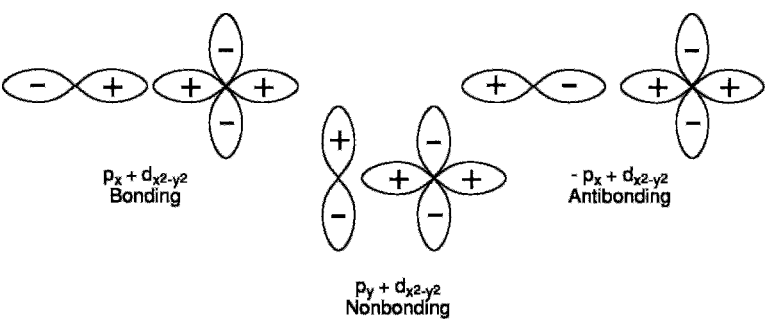

Figure 10.2 Examples of bonding (left), nonbonding (center), and antibonding (right) configurations involving the $d_{x^2-y^2}$ orbital with p_x and p_y orbitals.

In this section we will discuss the intermediate case in which valence-electron orbitals centered on adjacent atoms overlap as shown in Fig. 10.5. Here the isolated atom picture is no longer valid, but the overlap is not sufficiently great to obscure the identity of the individual atomic contribution. This limit, which corresponds to narrow bands with appropriate atomic quantum numbers assigned to each band, is referred to as the tight-binding approximation. This approach is employed in the Hubbard model as well as in the full band structure calculations to be discussed in Sections III – VI.

To clarify the nature of this approach we will examine the case of one atomic state—for example, an s state—which is well isolated in energy from nearby states. A possible basis set for a crystal made up of N such atoms includes states in which the electron is localized on one atom, $\phi(r - \mathrm{R})$, where $\phi(r)$ is an atomic wave function and R is a direct lattice vector. These states overlap and are not orthogonal, and the overlap integral defined by

$$\gamma(R - R') = \int d^3 r \phi^*(r - R)\phi(r - R') \tag{10.2}$$

is a measure of nonorthogonality. When the overlap integral for nearest-neighbor atoms is small, the atomic states are approximately orthogonal.

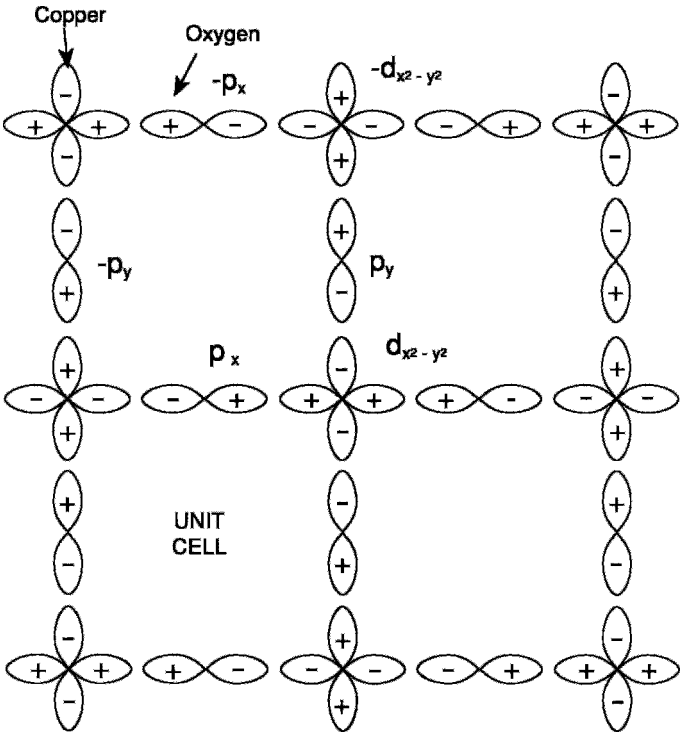

Figure 10.3 Orbitals used for a model of Cu-O planes in a cuprate superconductor. Each copper contributes a $d_{x^2-y^2}$ orbital and each oxygen contributes either a p_x or a p_y orbital, as shown. The unit cell contains one of each type of ion, and hence one of each type of orbital. The figure shows four unit cells.

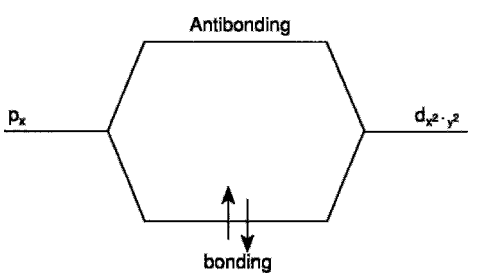

Figure 10.4 Hybridization of a copper $d_{x^2-y^2}$ orbital with an oxygen p_x orbital to form a low-energy bonding configuration and a high-energy antibonding configuration. Two antiparallel electrons that form a chemical bond are shown in the bonding level.

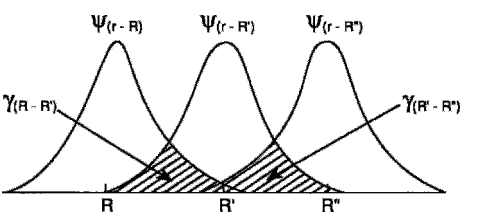

Figure 10.5 Overlap $\gamma(R_i - R_j)$ of atomic wavefunctions for nearby atoms.

These states, however, do not behave under lattice transformations, $\mathrm{r}' \rightarrow \mathrm{r} + \mathrm{R}$, according to Bloch's theorem

$$\Psi_k(r+R) = e^{ik\cdot R}\Psi_k(r). \qquad (10.3)$$

We can remedy this situation by constructing Bloch states, i.e., linear combinations of localized states of the form

$$\Psi_k(r) = (N)^{-1/2}\sum_R e^{ik\cdot r}\phi(r-R). \qquad (10.4)$$

which are orthogonal but not normalized,

$$\int d^3r\Psi^*_{k'}(r)\Psi_k(r) = e^{-i(k-k')\cdot R}\int d^3r\Psi^*_{k'}(r)\Psi_k(r) \tag{10.5}$$

$$= \begin{cases} 0 & k' \le k \\ \Gamma(k) & k' = k. \end{cases} \tag{10.6}$$

We show in Problem 9 that $\Gamma(k)$ is the Fourier transform of the overlap integral

$$\Gamma(k) = \sum_R e^{-ik\cdot R}\gamma(R). \tag{10.7}$$

Since the full Hamiltonian H is symmetric under lattice transformations and the Bloch states $\Psi_k(r)$ for different values of k are orthogonal, it follows that in the simple one-band approximation $\Psi_k(r)$ is an eigenstate of H. The eigenvalue $\varepsilon(k)$ can be evaluated by calculating the expectation value $\int d^3r\Psi^*_{k'}(r)H\Psi_k(r)$. We show in Problem 10 that this gives

$$\varepsilon(k) = \varepsilon_a + \frac{B(k)}{\Gamma(k)}, \tag{10.8}$$

where the energy of an isolated atom ε_a includes a kinetic-energy part $p^2/2m$ and a Coulomb part $u(R)$,

$$u(R) = \int d^3r\phi^*(r-R)[V_a(r-R)]\phi(r-R). \tag{10.9}$$

$\Gamma(k)$ is given by Eq. (10.7) and $B(k)$ is the Fourier transform of the exchange integral $\beta(R)$,

$$B(k) = \sum_R e^{-ik\cdot R}\beta(R), \tag{10.10}$$

$$\beta(R-R') = \int d^3r\phi^*(r-R) \times \left[\sum_{R''} V_a(r-R'')\right]\phi(r-R'), \tag{10.11}$$

where $V_a(r\text{-}R'')$ is the potential due to the nucleus at the lattice position R'' and the summation in Eq. (10.11) excludes the case $R = R'$.

We can see from Fig. 10.5 that overlap integrals fall off very rapidly with distance. The same is true of the exchange integrals. Therefore, we are justified in retaining in 10.7 and 10.10 only terms in which R' is either R or a nearest neighbor to R, which gives

$$\Gamma(k) \approx \gamma_0 + \sum_R e^{-ik\cdot R}\gamma(R) \approx \gamma_0 + 2\gamma_1(\cos k_x a + \cos k_y a) \tag{10.12}$$

and

$$B(k) \approx 2\beta_1(\cos k_x a + \cos k_y a) \tag{10.13}$$

so that

$$\varepsilon(k) \approx \varepsilon_a + \frac{2\beta}{\gamma_0}(\cos k_x a + \cos k_y a) \tag{10.14}$$

where we have assumed that $\beta << \gamma_0$ and $\gamma_1 << \gamma_0$. The width of the band measured along the line $\Gamma - X$, for example, is $\Delta\varepsilon = \varepsilon(0,0)\text{–}\varepsilon(\pi/a, 0) = 4\beta/\gamma_0$. The exchange integral β determines the degree of dispersion in the band. If β is very small, as is the case for well-separated atoms, the bands are nearly flat and centered about the atomic energy level ε_a. Since $\varepsilon(k)$ is a slowly varying function of k, it is possible to form a superposition of states with different k but essentially the same energy. If we wish, we can construct a wave packet that is centered on one atom, and in this way return to our original set of atomic orbitals.

Typical band structure calculations take into account several atomic orbitals $\phi_n(r\text{–}R)$ for each atom, so we can define the Bloch states

$$\Psi_{nk}(r) = (N)^{-1/2}\sum_R e^{ik\cdot r}\phi_n(r-R), \tag{10.15}$$

where n now labels each of the atomic states in the basis. The formalism leading to Eq. 10.8 must now be generalized somewhat to include a greater number of overlap integrals,

$$\gamma_{nm}(R-R') = \int d^3r \phi_n^*(r-R)\phi_m(r-R'), \tag{10.16}$$

and exchange integrals,

$$\beta_{nm}(R-R') = \int d^3r \phi_n^*(r-R) \times \left[\sum_{R^*} V_a(r-R'')\right] \phi_m(r-R'), \tag{10.17}$$

and their respective Fourier transform counterparts $\Gamma_{nm}(k)$ and $B_{nm}(k)$. The eigenstates are linear combinations of atomic orbitals, and the associated method is often referred to as LCAO.

Having covered some background on energy bands and chemical bonding, we will proceed to describe the Hubbard model which, despite its simplicity, exhibits many properties that are characteristic of superconductors (Anderson 1987a; cf. Hirsch 1985a, b, 1987). This will prepare the way for understanding the more complex band structures of the elements, of the $A15$ compounds, and finally, of the high-temperature superconductors.

III. HUBBARD MODEL

The essential principles of the Hubbard Model can be explained by using only one electron orbital, but the use of three such orbitals provides a more realistic description of a cuprate superconductor. We will start with the first and then pass on to the second after saying a few words about the wave functions that are involved.

A. Wannier Functions and Electron Operators

In the tight-binding approximation we made use of the Bloch states $\Psi_k(r)$ as given by Eq. (10.4), which are superpositions of atomic functions $\phi(r–R)$ over lattice positions. These states are orthogonal, and $[\Gamma(k)]^{-1/2}$ from Eq. (10.7) constitutes their normalization constant. A summation of normalized Bloch states over all of the k-states of a band,

$$W(r-R) = [N]^{1/2} \sum_k [\Gamma(k)]^{-1/2} e^{-ik\cdot R} \Psi_k, \tag{10.18}$$

provides a new wavefunction $W(r–R)$ associated with the atom at lattice position R. This wavefunction represents a Wannier state.

The Wannier states are useful because the overlap of two Wannier states at different lattice sites R and R' is zero. For two different bands with indices n and n', the associated Wannier states $W_n(r–R)$ and $W_{n'}(r–R)$ are orthogonal, corresponding to the general orthonormality condition

$$\int d^3r W_n^*(r-R) W_{n'}(r-R') = \delta_{nn'}\delta_{RR'}. \tag{10.19}$$

The Wannier states are also complete:

$$\sum_{r'} \sum_R W_n^*(r-R) W_n(r'-R) = \delta(r-r'). \tag{10.20}$$

If the band is narrow each $W(r–R)$ is localized about one lattice point R. Using Wannier states as a basis, the electron operator for a single band Ψ_σ can be written as

$$\Psi_\sigma(r) = [N]^{-1/2} \sum_R a_\sigma(R) W(r-R). \tag{10.21}$$

The operators $a_\sigma^\dagger(R)$ and $a_\sigma(R)$ are, respectively, the electron creation operator and the

electron annihilation operator, and together they form the number operator $n_\sigma(R)$ for electrons of spin σ in the Wannier state $W(r-R)$,

$$n_\sigma(R) = a^\dagger{}_\sigma(R) a_\sigma(R), \tag{10.22}$$

where no summation is intended. These operators satisfy the anticommutation rule

$$\alpha^\dagger{}_\sigma(R) a_{\sigma'}(R') + a_{\sigma'}(R') a^\dagger{}_\sigma(R) = \delta_{\sigma\sigma'}\delta_{RR'}, \tag{10.23}$$

and have the properties

$$\begin{aligned} a_-|0\rangle &= 0 \\ a_-|-\rangle &= |0\rangle \\ a_-|+\rangle &= 0 \\ a_-|\pm\rangle &= |+\rangle \\ a^\dagger{}_-|0\rangle &= |-\rangle \\ a^\dagger{}_-|-\rangle &= 0 \\ a^\dagger{}_-|+\rangle &= |\pm\rangle \\ a^\dagger{}_-|\pm\rangle &= 0 \end{aligned} \tag{10.24}$$

Similar expressions can be written for the spin-up operators, $a_+{}^\dagger$ and a_+. The wavefunctions $|j\rangle$ correspond to sites occupied by a spin-up electron $|+\rangle$, by a spin-down electron $|-\rangle$, or by two electrons of opposite spin $|\pm\rangle$, while $|0\rangle$ denotes a vacant site. We will use these expressions and extensions of them to the two-electron case $|ij\rangle$ to evaluate the energy of some Hubbard Hamiltonians.

B. One-State Hubbard Model

In a one-state Hubbard model there is one electron orbital per unit cell. To construct this model we begin, as in the tight-binding approximation, with electrons localized in atomic-like states at the positions R of the atoms. We assume that there is only one valence orbital per atom and each atom can accommodate 0, 1, or 2 electrons.

The Hamiltonian consists of a kinetic energy term proportional to a "hopping amplitude" $t > 0$ that represents the electron correlation; a term $-\mu\hat{N}$, where μ is the chemical potential and $\hat{N}$ is the total number of electrons; and an on-site Coulomb repulsion term (10.9), $U > 0$. We thus have

$$\begin{aligned} H = &- t \sum_{R,R',\sigma} [a^\dagger{}_\sigma(R) a_\sigma(R') \\ &+ a^\dagger{}_\sigma(R') a_\sigma(R)] \\ &- \mu \sum_{R,\sigma} a^\dagger{}_\sigma(R) a_\sigma(R) \\ &+ U \sum_{R}^{R,\sigma} n_+(R) n_-(R), \end{aligned} \tag{10.25}$$

where $\mu = 0$ for the undoped case when the orbitals are half filled with electrons. The kinetic energy is the sum of two hermitian conjugates. The "hopping amplitude" t given by

$$t = \frac{\hbar^2}{2m} \int d^3 r \nabla W^*(r-R) \cdot \nabla W(r-R') \tag{10.26}$$

is a measure of the contribution from an electron hopping from one site to another neighboring site. It is assumed that the overlap of Wannier functions separated by more than one lattice spacing is negligible, and that t is the same for all nearest-neighbor pairs R, R'. The chemical potential term is included because we are interested in the change in the properties of the model as the number of electrons is varied. The Coulomb repulsion is assumed to be the same for all sites. The Hamiltonian takes into account only nearest-neighbor correlation and on-site Coulomb repulsion.

The Hamiltonian (10.25), simple as it appears, embodies a great deal of physics. This Hamiltonian, or a generalization of it, is the starting point for a number of theories of high-T_c superconductivity, the Mott insulator transition, and other phenomena related

to highly correlated many-electron systems. Allen (1990) went so far as to state what he called the Hubbard hypothesis: "The fundamental physics of the oxide superconductors is contained in the Hamiltonian (10.25) on a two-dimensional square lattice for small numbers of holes."

In Sections III.D, III.E, and III.F we will discuss examples of the limiting case $U >> t$. Typical values have been given of $t \sim 0.25 - 0.5\,\text{eV}$ and $U \sim 3$–$4\,\text{eV}$ (Ruckenstein *et al.*, 1988). The opposite limit, $U << t$, has also been discussed (e.g., see Varma *et al.*, 1988).

C. Electron-Hole Symmetry

As we shall see, the Hubbard Hamiltonian exhibits an electron-hole symmetry. Such symmetry is of considerable importance, in that most high-temperature superconductors are hole types with a close to a half-full conduction band. To demonstrate this symmetry it is convenient to begin by writing out the generalized Hamiltonian (10.25) in the more symmetric form

$$\begin{aligned} H = &- t \sum_{R,R',\sigma} [a^{\dagger}{}_{\sigma}(R) a_{\sigma}(R') \\ &+ a^{\dagger}{}_{\sigma}(R') a_{\sigma}(R)] \\ &- \mu \sum_{R,\sigma} a^{\dagger}{}_{\sigma}(R) a_{\sigma}(R) \\ &+ U \sum_{R} \left[n_{+}(R) - \frac{1}{2} \right] \left[n_{-}(R) - \frac{1}{2} \right]. \end{aligned} \tag{10.27}$$

This can be done because the extra terms simply shift the chemical potential and the zero point of energy.

The next step is to consider a transformation to "hole" operators by recalling that a site in k-space that is missing an electron is occupied by a hole, so destruction of a hole is equivalent to creation of an electron. Accordingly, we can define the "hole" operators

$$b_{\sigma}{}^{\dagger}(R) = a_{-\sigma}(R), \tag{10.28}$$

where σ and $-\sigma$ denote opposite spin directions. We then have for the number operator, from Eq. (10.22),

$$\begin{aligned} n_{\sigma}(R) &= a^{\dagger}{}_{\sigma}(R) a_{\sigma}(R) \\ &= b_{-\sigma}(R) b^{\dagger}{}_{-\sigma}(R) \qquad (10.29) \\ &= 1 - b^{\dagger}{}_{-\sigma}(R) b_{-\sigma}(R) \\ &= 1 - \tilde{n}_{-\sigma}(R), \qquad (10.30) \end{aligned}$$

where the anticommutation rule (10.23) is applied to obtain the number operator $\tilde{n}_{\sigma}(R) = b^{\dagger}_{\sigma}(R) b_{\sigma}(R)$ for holes. Using these expressions, the Hamiltonian can be written in terms of hole operators,

$$\begin{aligned} H = &t \sum_{R,R',\sigma} [b^{\dagger}{}_{\sigma}(R) b_{\sigma}(R') \\ &+ b^{\dagger}{}_{\sigma}(R') b_{\sigma}(R)] \\ &+ \mu N_{\text{s}} + \sum_{R,\sigma} b^{\dagger}{}_{\sigma}(R) b_{\sigma}(R) \\ &+ U \sum_{R} \left[\tilde{n}_{+}(R) - \frac{1}{2} \right] \left[\tilde{n}_{-}(R) - \frac{1}{2} \right], \end{aligned} \tag{10.31}$$

where N_{s} is the number of sites on the lattice.

The thermodynamic potential Ω is given by

$$\Omega(\mu, T; t, U) = -k_{\text{B}} T \log\{\text{Tr}[e^{-H/kT}]\} \tag{10.32}$$

$$= -2\mu N_{\text{s}} + \Omega(-\mu, T; -t, U). \tag{10.33}$$

If the lattice is bipartite, that is, if it can be decomposed into two sublattices, A and B, with the property that an atom of one sublattice has atoms of the other sublattice as its nearest neighbors, the electron-hole transformation can be modified to

$$b_{\sigma}(R) = \begin{cases} a^{\dagger}_{-\sigma}(R) & R \in A \\ -a^{\dagger}_{-\sigma}(R) & R \in B \end{cases} \tag{10.34}$$

This has the effect $t \to -t$, so that Eq. (10.33) becomes

$$\Omega(\mu, T; t, U) = -2\mu N_s + \Omega(-\mu, T; t, U). \tag{10.35}$$

The average number of particles $N(\mu, T)$ is

$$N(\mu, T) = -d\Omega/d\mu \tag{10.36}$$

$$= 2N_s - N(-\mu, T), \tag{10.37}$$

and for $\mu = 0$ we obtain

$$N(0, T) = N_s, \tag{10.38}$$

that is, one electron per site. Because of the simple relationship (10.37) we need only consider $\mu \geq 0$; the properties of the system for $\mu < 0$ are then easily found by means of the electron-hole transformation (10.34).

D. Half-Filling and Antiferromagnetic Correlations

The high-temperature superconductors and related compounds typically have a set of full low-lying bands, an almost half-full hybrid band near the Fermi level, and a set of empty bands at higher energy. The half-full, one-state Hubbard model stimulates this hybrid band, and thereby provides a simple approximation to the materials. Later, we will see how a three-state Hubbard model more closely approximates the behavior of high-temperature superconductors.

We take $\mu = 0$ so that $\Sigma\langle n_\sigma(\mathrm{R})\rangle = 1$. Thus there is on average one electron per lattice site. If the on-site repulsion is large, $U \gg t$, states with double occupancy will be suppressed. Therefore, let us consider as a subset of all states of the half-filled band those states with exactly one electron at each site. The Coulomb repulsion term $U\Sigma n_+(R)n_-(R)$ only exists for a site that is doubly occupied, so it vanishes in this case. Were it not for the hopping term, these states would all be degenerate with zero energy. Here we show that hopping removes the degeneracy, and, in addition, show by simple perturbation theory that the effect of the hopping term is to lower the energy of an antiferromagnetic pair relative to a ferromagnetic pair of nearest-neighbor electrons.

Consider a nearest-neighbor pair of electrons that occupies one of the two antiferromagnetic states, with antiparallel spins

$$|+-\rangle \text{ and } |-+\rangle, \tag{10.39}$$

or one of the two ferromagnetic states, with parallel spins

$$|++\rangle \text{ and } |--\rangle, \tag{10.40}$$

where $+$ denotes spin up, and $-$ signifies spin down. In addition to these four states, there are two higher energy states

$$|0\pm\rangle \text{ and } |\pm 0\rangle, \tag{10.41}$$

in which both electrons are localized on the same atom.

We wish to apply perturbation theory up to second order for the case $U \gg t$ corresponding to the expression

$$E_i = E_i^{(0)} + E_i^{(1)} + E_i^{(2)} \tag{10.42}$$

for the ith-order energy, where

$$E_i = \langle\Psi_i|H_{\mathrm{Coul}}|\Psi_i\rangle + \langle\Psi_i|H_{\mathrm{hop}}|\Psi_i\rangle + \sum_{j\neq i} \frac{|\langle\Psi_i|H_{\mathrm{hop}}|\Psi_j\rangle|^2}{E_j - E_i}. \tag{10.43}$$

As noted earlier, there is no Coulomb contribution for the four states (10.39) and (10.40), so that the zero-order term vanishes, $E_i^{(0)} = 0$. The first-order energy must be evaluated from the expression

$$E_i^{(1)} - \langle\Psi_i|H_{\mathrm{hop}}|\Psi_i\rangle, \tag{10.44}$$

where the hopping operator H_{hopp} has the explicit form

$$H_{\mathrm{hop}} = -t[a_+^+(1)a_+(2) + a_+^+(2)a_+(1) + a_-^+(1)a_-(2) + a_-^+(2)a_-(1)]. \tag{10.45}$$

Since each term of this operator changes the spin state, the first-order energy (10.44) also vanishes.

Second-order perturbation theory entails evaluating the matrix elements $\langle \Psi_i | H_{\text{hop}} | \Psi_j \rangle$ for $i \neq j$. The only nonvanishing terms are

$$\begin{aligned} \langle +- | H_{\text{hop}} | 0\pm \rangle &= \langle +- | H_{\text{hop}} | \pm 0 \rangle \\ &= \langle -+ | H_{\text{hop}} | 0\pm \rangle \\ &= \langle -+ | H_{\text{hop}} | \pm 0 \rangle \\ &= -t. \end{aligned} \tag{10.46}$$

The denominator $E_j - E_i$ of the second-order term of Eq. (10.43) is $-U$, which gives for the energy of the two antiferromagnetic states

$$E_{+-} = E_{-+} = -\frac{2t^2}{U}. \tag{10.47}$$

Since the energy of the two ferromagnetic states is zero (Problem 17),

$$E_{++} = E_{--} = 0, \tag{10.48}$$

the hopping term has the effect of lowering the energy of an antiferromagnetic pair relative to that of a ferromagnetic pair.

E. *t-J* Model

In one variant of the Hubbard model, called the *t-J*: model, the Coulomb repulsion U term in the Hamiltonian is replaced by the Heisenberg term $J\Sigma \mathrm{S}_i \cdot \mathrm{S}_j$ (Anderson, 1978a, b; Rodriguez and Douçot, 1990; Zhang and Rice, 1988; Halley, 1988, Chapters 15–20). This model may be obtained as the large-U limit ($U \gg t$) of the Hubbard model (Harris and Lange, 1967; Marde *et al.*, 1990). We will justify it in terms of the discussion in the previous section.

If we restrict our attention to states with one electron per site, we can describe the states completely in terms of the spin-$\frac{1}{2}$ operators for the electrons at each site, $S_k(R)$. Although we have employed a basis in which one component of the spin, conventionally the z-component, is diagonal, the Hubbard Hamiltonian is invariant under rotations in spin space. To second order in perturbation theory, the effective Hamiltonian for the subset of states can therefore be written in the Heisenberg form,

$$H_{\text{Heis}} = -J\Sigma \mathrm{S}(R) \cdot \mathrm{S}(R'), \tag{10.49}$$

where the exchange coupling term is

$$J = 4t^2/U. \tag{10.50}$$

Typical values of the parameters, $t \approx 0.4\,\text{eV}$ and $U \approx 3.5\,\text{eV}$ (Ruckenstein *et al.*, 1987), give J close to the experimentally determined value $J \approx 0.14$–$0.16\,\text{eV}$ (Gagliano and Bacci, 1990; Singh *et al.*, 1989). We conclude that at half filling, in the limit $U/t \to \infty$, the ground state of the Hubbard model is equivalent to that of a Heisenberg antiferromagnet.

The Heisenberg term used in the *t-J* model corresponds to the Hamiltonian

$$H = -t\Sigma(a^+_{i\sigma} a_{j\sigma} + a^+_{ja} a_{i\sigma}) + J\Sigma \mathrm{S}_i \cdot \mathrm{S}_j. \tag{10.51}$$

Undoped materials can be understood in terms of the two-dimensional Heisenberg term (Chakravarty *et al.*, 1988; Dagotto *et al.*, 1990), and in the presence of empty sites the hopping matrix element t can represent holes propagating in a fluctuating antiferromagnetic background arising from this $J\Sigma \mathrm{S}_i \cdot \mathrm{S}_j$ term (Poilblanc and Dagotto, 1990; Zotos *et al.*, 1990). Many believe that the *t-J* model embraces the essential features of high-temperature superconductivity (Ohkawa, 1990), and there is an extensive literature on the subject.

The symbol *t-J* is used to designate the two terms in the Hamiltonian (10.51). In the same spirit, the ordinary Hubbard model could be called the *t-U* model, but this notation is never employed. The *t-J*

and Hubbard models have been compared (e.g., Bhattacharya and Wang, 1992; Dagotto *et al.*, 1992).

F. Resonant-Valence Bonds

The Hubbard model is deceptively simple, and while some exact results for the ground state are known in the limit $U/t \to \infty$ and for the case of half filling, the nature of the ground states for arbitrary U and t are not known. An alternate choice of basis for elucidating the nature of the low-lying levels of the model makes use of "resonant-valence-bond" (RVB) states (Anderson, 1987a, b; Emery and Reiter, 1988; Feine, 1993; Kivelson, 1989; Wittmann and Stolze, 1993; and Zhang and Rice, 1988). Electrons at nearest-neighbor sites are paired into "bonds" and linear combinations of the basis states are used to construct eigenstates of the total electronic spin (Allen, 1990).

For two electrons the total spin S can be 1 or 0, and the corresponding triplet (S = 1, $M = 0, \pm 1$) and singlet ($S = M = 0$) wavefunctions are, respectively,

$$|11\rangle = |++\rangle$$
$$|10\rangle = \frac{1}{\sqrt{2}}(|+-\rangle + |-+\rangle)$$
$$\text{triplet}, E = 0 \qquad (10.52)$$
$$|1-1\rangle = |--\rangle$$
$$|VB\rangle = \frac{1}{\sqrt{2}}(|+-\rangle - |-+\rangle)$$
$$\text{singlet}, E = -4t^2/U, \quad (10.53)$$

where we have used the notation $|\text{SM}\rangle$ on the left side. There are two additional ionized states $|\text{A}\rangle$ and $|\text{B}\rangle$ which are both singlets,

$$|A\rangle = \frac{1}{\sqrt{2}}(|0\pm\rangle - |\pm 0\rangle) \quad E = U \qquad (10.54a)$$

$$|B\rangle = \frac{1}{\sqrt{2}}(|0\pm\rangle + |\pm 0\rangle) \quad E = U_l + \frac{4t^2}{U}, \qquad (10.54b)$$

and, of course, a state in which there are no electrons,

$$|\text{vacuum}\rangle = |00\rangle.$$

The singlet state with two electrons labeled $|\text{VB}\rangle$ is the lowest in energy, and it constitutes the "valence bond" state. The energies of these two electron states as given in (10.52)–(10.54b) are sketched in Fig. 10.6

The RVB theory starts by assuming that the ground state of insulating La_2CuO_4 is a linear combination of $|\text{VB}ij\rangle$ states for various pairs of electrons i, j,

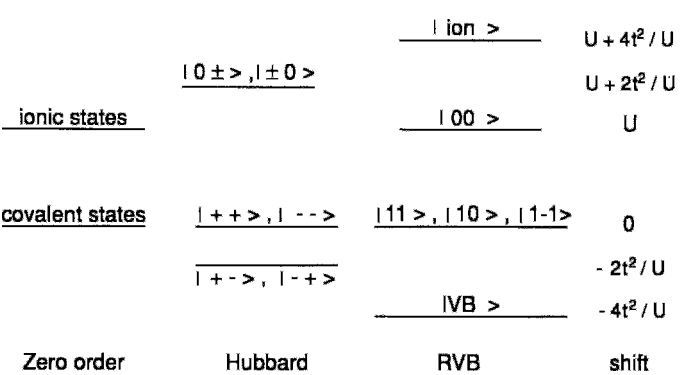

Figure 10.6 Energy levels of the two-site, nearest-neighbor electron-pair problem at half filling, shown for the zero-order (left), Hubbard model (center), and resonant valence-bond (right) approximations.

$$|RVB\rangle = c_{12}|VB12\rangle + c_{34}|VB34\rangle + c_{56}|VB56\rangle + \cdots, \quad (10.55a)$$

and in the presence of a single hole with spin down (h−) paired with a spin-up electron (e+) this becomes

$$|RVB,\ 1\ \text{hole}\rangle = c_{12}|h-\rangle|e+\rangle + c_{34}|VB34\rangle + c_{56}|VB56\rangle + \cdots, \quad (10.55b)$$

where the hole can hop between sites.

G. Spinons, Holons, Slave Bosons, Anyons, and Semions

In the RVB formulation of the two-dimensional large-U Hubbard model, the spin and charge degrees of freedom are separated. The elementary excitations are either neutral spin-$\frac{1}{2}$ solitons (fermion solitary excitations, Doda *et al*., 1982; Doi *et al*., 1992; Drazi and Johnson, 1989; Kivshar, 1991; Rokhsar, 1990; Tighe *et al*., 1993), called *spinons*, or charged boson particles, called *holons* (Allen, 1990; Anderson and Zou, 1988; Kivelon, 1989; Nori *et al*., 1990; Schmeltzer, 1994; Schofield and Wheatley, 1993; Sinha, 1992; Wang, 1989; Xing and Liu, 1991; Zou and Anderson, 1988).

There is a version of the *t-J* model, called the *slave boson representation*, in which the Hamiltonian contains spinon and holon creation and annihilation operators (Schönhammer, 1990; Sheng *et al*., 1990). The so-called slave boson operators are introduced to specify and keep track of empty and singly occupied sites (Arrigoni *et al*., 1990; Jolicoeur and LeGuillou, 1991; Rodriguez and Douçot, 1992). From a more general viewpoint, the slave boson formulation maps a purely fermionic model onto an effective bosonic one (Lilly *et al*., 1990), and the slave boson fields provide a larger quantum mechanical (Fock) space that is subject to constraints involving the slave boson operators (Jolicoeur and LeGuillou, 1991; Rodriguez and Douçot, 1992; Zhang *et al*., 1993; Zou and Anderson, 1988). In addition, the slave bosons carry a conserved quantum number, namely charge (Zou and Anderson, 1988).

In quantum mechanics we learn that the wavefunction $U(r_2, r_1)$ for the exchange of two particles is given by

$$U(r_2, r_1) = e^{i\Theta}U(r_2, r_1) \quad (10.56)$$

where $\Theta = 0$ for bosons which are symmetric under interchange, and $\Theta = \pi$ for fermions which are antisymmetric. Wilczek (1982a, b) coined the word anyon for a particle with some other value Θ in the range $-\pi < \Theta < \pi$, and such a particle is said to have fractional statistics. It violates the usual time reversal (T) and parity (P) conservation laws. Anyons have been used to explain the fractional quantum Hall effect in semiconductor heterojunctions (Arovas *et al*., 1984; Halperin, 1984; Prange and Girvin, 1987). Kalmeyer and Laughlin (1987; Laughlin, 1988a, b) suggested that semions, anyons with $\Theta = \pm\pi/2$,

$$U(r_2, r_1) = iU(r_2, r_1), \quad (10.57)$$

might be the charge carriers responsible for high temperature superconductivity. In principle this can be tested by experiments involving T, P symmetry, but the results have not been encouraging (Shen and Lu, 1993; Zhou and Chen, 1993). Some studies of an anyon gas suggest that its ground state is superconducting, that a collective excitation is a phonon mode, and that a single particle excitation can be identified as a vortex (Choi *et al*., 1992; Gelfand and Halperin, 1992; Mori, 1991; Zhang *et al*., 1990).

H. Three-State Hubbard Model

The one-state Hubbard model that we discussed in Section II.B involved one orbital

per unit cell, with two parameters, a hopping amplitude t and an on-site Coulomb repulsion U. We will now extend the model to a unit cell, shown outlined in Fig. 10.3, containing a Cu atom that contributes a $d_{x^2-y^2}$ orbital, and two oxygens one of which contributes a p_x orbital, the other a p_y orbital (Jefferson *et al.*, 1992). This corresponds to the configuration of the CuO_2 plane shown in the figure, which is believed to be responsible for the super-conducting properties of the cuprates. In this plane each copper has four oxygen nearest neighbors and each oxygen has two copper nearest neighbors. The figure is drawn with the signs on the orbital lobes selected so that all of the overlaps are of the bonding type. The convention chosen for assigning positive (e.g., $+p_x$) and negative (e.g., $-p_y$) signs to the orbitals is given in the figure.

I. Energy Bands

The energy bands calculated by Entel and Zielinksi (1990) are plotted in Fig. 10.7a, and the density of states, together with the partial contributions from the p electrons (n_p) and d electrons (n_d), is plotted in Fig. 10.7b. The conditions for the calculation are clear from the labels in the energy scale of Fig. 10.7a hopping amplitudes $t_p = \epsilon_p = 0$, $t_d = \epsilon_d = 3.6\,\text{eV}$, and Coulomb repulsion terms $U_{pp} = 4\,\text{eV}$, $U_{dd} = 10.5\,\text{eV}$. We see that a predominately p-type band rises above the Fermi level at the corner point M, and that the Fermi surface consists of the p-like pocket of holes indicated in the Brillouin zone shown as an inset to Fig. 10.7a. The low-lying, mainly p-type pair of bonding bands, and the higher, predominately d-type antibonding band, are separated from

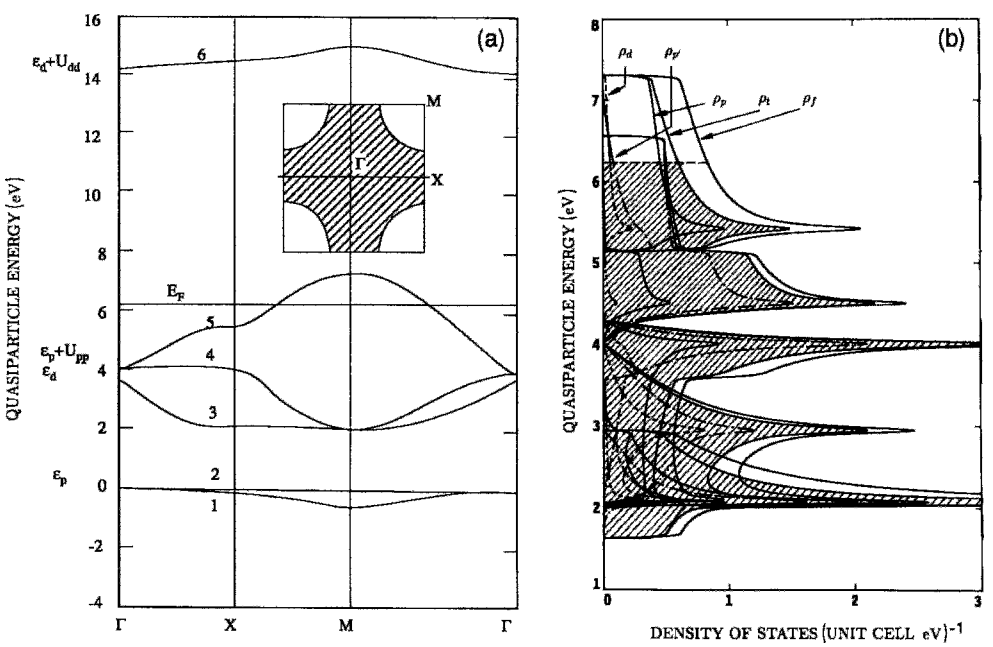

Figure 10.7 Band structure for the three-state Hubbard model for 4.5 electrons per unit cell. The model assumes one d state and two bonding p states per unit cell: (a) Energy bands with the Fermi energy below the gap, (b) density of states, Energies involving hopping amplitudes $\epsilon_p = 0$, $\epsilon_d = 3.6\,\text{eV}$, and Coulomb repulsion terms U_{pp} 4.0 eV, and $U_{dd} = 10.5\,\text{eV}$ are indicated in the ordinate scale of (a). Total density of states ρ_t together with the partial p and d contributions ρ_p and ρ_d are shown. The free-electron result ρ_f is included for comparison. Bands are occupied indicated by cross hatching below the Fermi level $E_F = 6.2\,\text{eV}$, (from Entel and Zielinski (1990)).

the three bands near the Fermi level by insulating gaps.

Since there are three orbitals in the set chosen for the calculation, and since each can contain two electrons of opposite spin, it takes six electrons to fill all of the bands. As electrons are added to the system, the Fermi level rises in the manner shown in Fig. 10.8. Note the two sharp jumps in E_F where the two band gaps are located. The amount of dispersion, or range of energy, over which a band is spread is called the *width* of the band. The width depends on the number of electrons in the unit cell. The predominately p-type band (No. 5) that passes through the Fermi level in Fig. 10.7a for the $n = 4.5$ electron case has the greatest dispersion.

We see from Figs. 10.7a and 10.7b that there are regions where the energy bands are flat, and at these energies the density of states becomes large, corresponding to what are called van Hove singularities (cf. XIII. A). Singularities of this type will be encountered later in the chapter. A DOS peak associated with a CuO_2 plane van Hove singularity can cause a peak in the transition temperature T_c as a function of hole doping (Mahan, 1993; Markiewicz, 1991a, 1991b; Pattnaik *et al.*, 1992; Penn and Cohen, 1992).

The ability to calculate occupation numbers n_i for individual electrons associated with the various bands permits us to determine the contribution of the electrons from each atom in the unit cell of a superconductor to the density of states. In the following sections we will present several such plots of individual atom density of states versus energy.

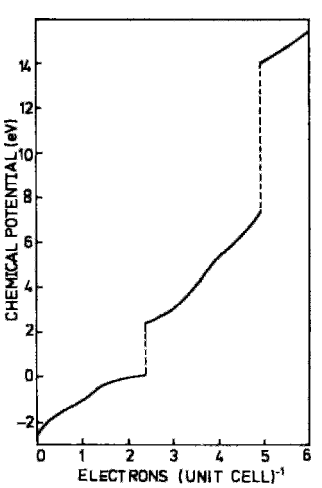

Figure 10.8 Three-state Hubbard model showing the variation with band filling of the Fermi energy (chemical potential) at $T = 100\,\mathrm{K}$, The metal-to-insulator transition occurs at the discontinuity in the Fermi energy near $n = 5$ (Entel and Zielinski, 1990).

J. Metal-Insulator Transition

When the fifth band of Fig. 10.7a is almost full, the Fermi level lies near the top of the band. Adding more electrons fills this band and additional electrons enter the sixth band far above it. This causes the Fermi level to rise above the energy gap to the level of the top band. When this occurs the system undergoes a transition from a metal to an insulator. Evidence for this transition is seen in the discontinuity at the position of the upper energy gap where there are five electrons per cell. Figure 10.9 presents the metal-to-insulator phase diagram, showing the metallic and insulating regions as a function of the p electron Coulomb repulsion energy U_{pp} and the energy difference between the p and d hopping integrals, $\Delta = \frac{1}{2}(t_d - t_p)$, called the *charge-transfer energy* (Entel and Zielinski, 1990). We see from the figure that a charge-transfer insulator (CTI) arising from the presence of a charge-density wave forms for $U_{dd} \gg \Delta$, and that a Mott insulator (MI) forms for $U_{dd} \gg \Delta$. The present calculation is for the ratio $U_{dd}/\Delta = 5.8$, so that it corresponds to the metallic region above the ordinate value $U_{dd}/\gamma > 5$, which could be close to the transition to a charge-transfer insulator. The p orbital Coulomb repulsion energy U_{pp} has much less effect on the phase diagram than its d orbital counterpart U_{dd}. The phase diagram of an actual superconductor

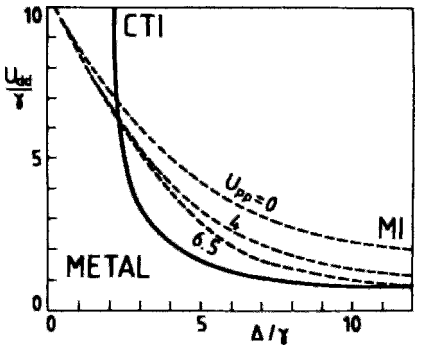

Figure 10.9 Metal-to-insulator phase diagram for the three-state Hubbard model with $V_{dp} = 0$, where the charge transfer energy is given by $\Delta = \frac{1}{2}(t_d - t_p)$. The regions where the charge-transfer insulator (CTI) and the Mott insulator (MI) occur are indicated. For the charge-transfer insulator, which arises from the presence of a charge-density wave, $n_p > n_d$ for the band beneath the gap (Entel and Zielinski, 1990).

can be more complicated, Hebard (1994b) discusses the nature of the superconductor–insulator transition.

The orbital character of the bands depends on U_{pp}. This is shown in Fig. 10.10 for the fifth band when the number of electrons in the unit cell is maintained at the value 4.9. There is a strong dependence of the ratio n_d/n_p on U_{pp} since decreasing U_{pp} from its chosen value of 4 eV to below 3.6 eV raises band 3 above bands 4 and 5. This accords with the proximity of these bands at the point Γ of Fig. 10.7a. It causes the "new fifth band" to become more d-like so that we have $n_d > n_p$ for low values of U_{pp}, as indicated in Fig. 10.10 instead of the opposite ratio $n_d < n_p$ for the large U_{pp} case of Fig. 10.7.

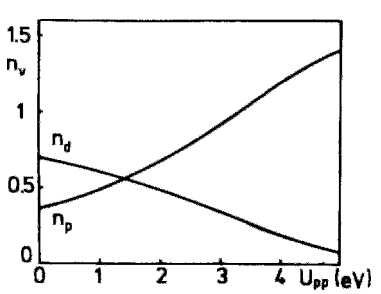

Figure 10.10 Dependence of the occupation numbers n_p and n_d in the band beneath the gap on the intra-atomic Coulomb repulsion energy U_{pp} for $n = 4.9$ electrons per unit cell in the three-state Hubbard model (Entel and Zielinski, 1990).

Now that we have surveyed several varieties of Hubbard models we will proceed to describe the band structure results obtained for several superconductors. Many of the features characteristic of the three-state Hubbard model will be found duplicated in the move sophisticated band structures to be discussed.

IV. BAND STRUCTURE OF $YBa_2Cu_3O_7$

We will begin our discussion of the energy bands of the high-temperature superconductors with the compound $YBa_2Cu_3O_7$ since its structure is of the aligned type; as explained in Chapter 8, Section IV, and hence its Brillounin zone is simpler than those of the cuprates which are body centered. This section will describe the band structure reported by Pickett *et al.* (1990) and Pickett (1989; cf. Costa-Quintana *et al.*, 1989; Curtiss and Tam, 1990; Krakaer *et al.*, 1988; Singh *et al.*, 1990; Wang (1990) J. Yu *et al.*, 1991). The bands reflect the principal structural features of the compound—the presence of two CuO_2 planes containing the Cu(2), O(2), and O(3) atoms, and a third plane containing chains of Cu(1)–O(1) atoms along the b direction, as shown in Fig. 10.11 and described in Chapter 8, Section IV. The *ortho*-rhombic Brillouin zone, also shown in the figure, has a height-to-width ratio

$$(2\pi/c)/(2\pi/a) = a/c \approx 0.33,$$

which is the reciprocal of the height-to-width ratio of the unit cell in coordinate space.

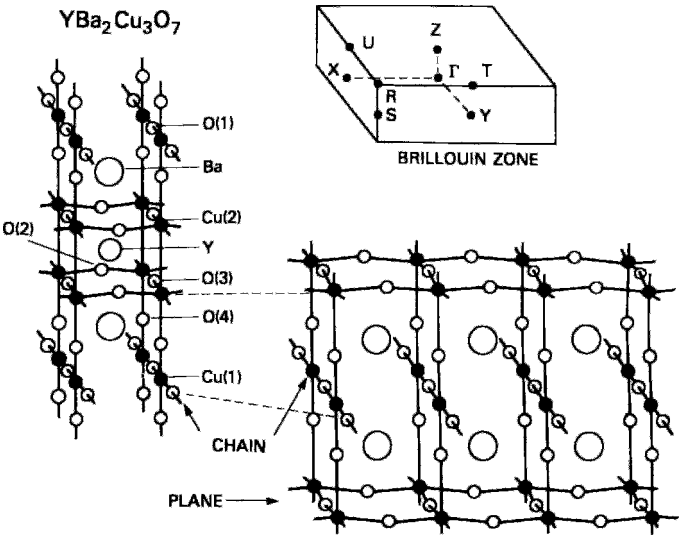

Figure 10.11 Two views of the $YBa_2Cu_3O_7$ unit cell and sketch of the corresponding Brillouin zone (Krakauer *et al.*, 1988).

A. Energy Bands and Density of States

The energy bands of $YBa_2Cu_3O_7$ near the Fermi surface are presented in Fig. 10.12 along the principal directions connecting the symmetry points Γ, X, Y, and S in the central ($k_z = 0$) horizontal plane of the Brillouin zone. The bands change very little at the corresponding symmetry points Z, U, T, and R of the top ($k_z = \frac{1}{2}$) plane. The highest transition temperature is found in the case of a small amount of oxygen deficiency, $\delta \approx 0.1$, in the formula $YBa_2Cu_3O_{7-\delta}$. This slightly less than half-full condition, where $\delta = 0$ for half-full, means that there are missing electrons near E_F, and that the conductivity is of the hole type. This is confirmed by Hall effect measurements, as will be seen in Chapter 16 Section VI.

The two narrow CuO plane-related bands are shown in Fig. 10.12 strongly dispersed, i.e., rising far above the Fermi surface at the corner points S and R of the Brillouin zone of Fig. 10.11. These two bands are almost identical in shape, resembling the Hubbard band that is shown rising above E_F at the corner point M of the Brillouin zone in the inset of Fig. 10.7a. The much broader chain band that is shown strongly dispersed in both the S and the Y (also R and T) or chain directions far above E_F arises from the Cu–O sigma bonds along the chains formed from the oxygen p_y and copper $d_{x^2-y^2}$ orbitals, as illustrated in Fig. 10.13 There is another chain band which undergoes very little dispersion, staying close to the Fermi surface, but it rises slightly above E_F at S and R, as shown in the figure. Oxygen deficiency depopulates the chains, and this is reflected in the absence of chain bands in the semiconducting compound $YBa_2Cu_3O_6$ (Yu *et al.*, 1987).

The lack of appreciable dispersion in the bands along k_z demonstrated by the similarity of Figs. 10.12a and 10.12b means that the effective mass m^* defined by Eq. (1.47),

$$\frac{1}{m^*} = \frac{1}{\hbar^2}\left(\frac{d^2E_k}{dk_z^2}\right)_{E_F}, \qquad (10.58)$$

is very large, and since the electrical conductivity σ from Eq. (1.22) is inversely proportional to the effective mass, this means

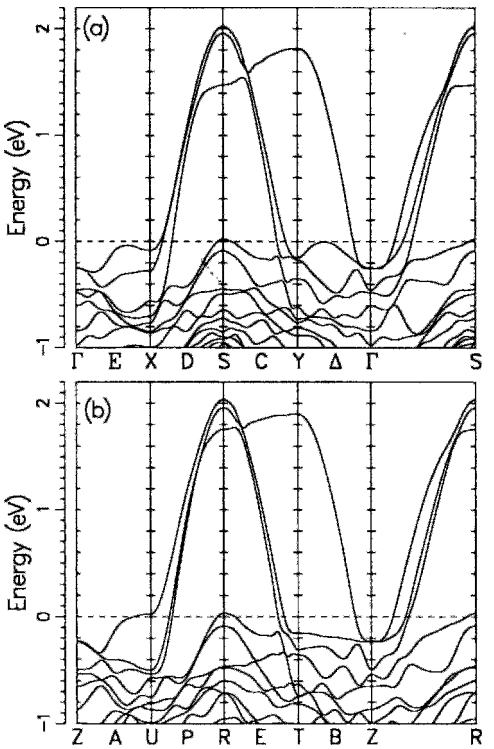

Figure 10.12 Energy bands of $YBa_2Cu_3O_7$ along the principal directions in the Brillouin zone sketched in Fig. 10.11. The two plane bands rise sharply above the Fermi level at points S and R, and the broader chain band is high in energy between S and Y, and between R and T (Pickett *et al.*, 1990).

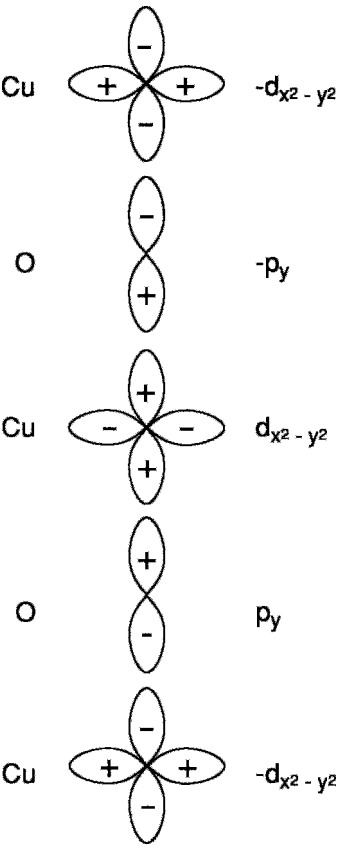

Figure 10.13 Sigma bonding between Cu(1) and O(1) orbitals along chains in the crystallographic b direction of $YBa_2Cu_3O_7$.

that the conductivity is low along the z direction. In contrast, the plane and chain bands appear parabolic in shape along k_x and k_y, corresponding to a much lower effective mass. This explains the observed anisotropy in the normal-state electrical conductivity, $\sigma_c/\sigma_{ab} \approx 20$.

The total density of states and the contribution of each copper and oxygen to $D(E)$ are presented in Fig. 10.14. There are peaks (called *van Hove singularities*, II, I) in the partial DOS of the planar oxygens O(2) and O(3) at energies at which the planar Cu(2) atoms also have peaks, whereas chain Cu(1) have peaks that match those of the O(1) and O(4) oxygens bonded to it. This suggests that the planes and chains are partially decoupled from each other, as we might have expected, since the bridging oxygen O(4) is 1.8 Å from Cu(1) compared to the much longer distance 2.3 Å from Cu(2). Super current can flow along both the planes and chains.

B. Fermi Surface: Plane and Chain Bands

The Fermi surface of $YBa_2Cu_3O_7$ is plotted in Fig. 10.15 for the $k_z = 0$ and $k_z = \pi/a$ horizontal planes of the Brillouin zone, with the symmetry points S and R, respectively, selected as the origin, in accordance with Fig. 10.16. The close similarity

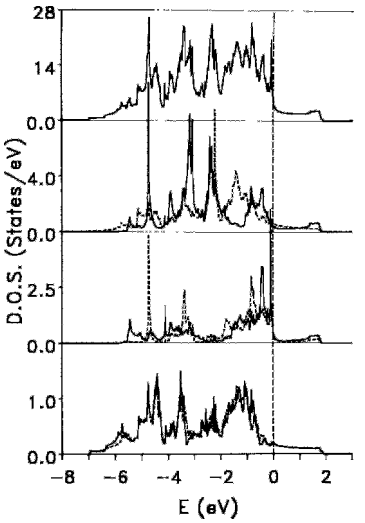

Figure 10.14 Density of states of $YBa_2Cu_3O_7$. The top panel shows the total density of states, the second panel gives the partial DOS of Cu(1) [—] and Cu(2) [----], the third panel presents the same for O(1) [—] and O(4) [----], and the bottom one gives O(2) [—] and O(3) [----] (Krakauer *et al.*, 1988).

between the respective left ($k_z = 0$) and right ($k_z = \pi/a$) panels of the figure confirms that there is very little dispersion in the vertical (k_z) direction. The shapes of these Fermi surfaces can be deduced from where the corresponding bands cross the Fermi surface in Fig. 10.12.

The two plane–band Fermi surfaces presented in the four center panels of Fig. 10.15 consist of large regions of holes in the center, with narrow bands of electrons around the periphery. The surface of one plane band makes contact with the zone boundary between points Y and Γ due to the small maximum that rises above E_F between these points in Fig. 10.12. When 0.2 fewer electrons are present, the Fermi surface is lowered and the contact with the zone boundary extends over a larger range between Y and Γ. Adding 0.2 more electron raises the Fermi surface above the small relative maximum near Y, and the zone boundary is no longer reached. Thus the oxygen content, which determines the electron concentration, influences details of the shape of the Fermi surface. As already noted in Section A, the highest T_c occurs for $\delta \approx 0.1$. The regions of holes around the central points R and S (not shown) resemble their counterpart around point M of the three-state Hubbard model.

The two chain-band Fermi surfaces sketched in the upper and lower pairs of panels of Fig. 10.15 differ considerably. The upper panels show the highly dispersed chain band that lies above E_F everywhere except from Γ to X, where it is below E_F, as shown in Fig. 10.12. This corresponds to a narrow one-dimensional-like slab containing electrons that extends continuously from cell to cell along the direction Γ–X–Γ. . . , and parallel to it there is a wide hole-type slab along Y–S–Y. . . , as shown at the top of Fig. 10.15. The edges of this wide slab are mostly parallel, a condition needed for nesting, but are not close enough to the boundary to create strong nesting, as will be explained in Section VIII. The other chain band lies entirely below the Fermi level except for a narrow region near point S in Fig. 10.12. Figure 10.15 shows this small hole region in the zone centers S and R of the lower two panels.

V. BAND STRUCTURE OF MERCURY CUPRATES

Band structure calculations have been carried out for the aligned Hg-1201 and the Hg-1221 members of the

$$HgBa_2Ca_nCu_{n+1}O_{2n+4+\delta}$$

series of compounds, and we will summarize some of the results that were obtained. The Brillouin zone is the tetragonal anologue of the orthorhombic one sketched in Fig. 10.11 with point y identical with point x, and T identical with u from symmetry.

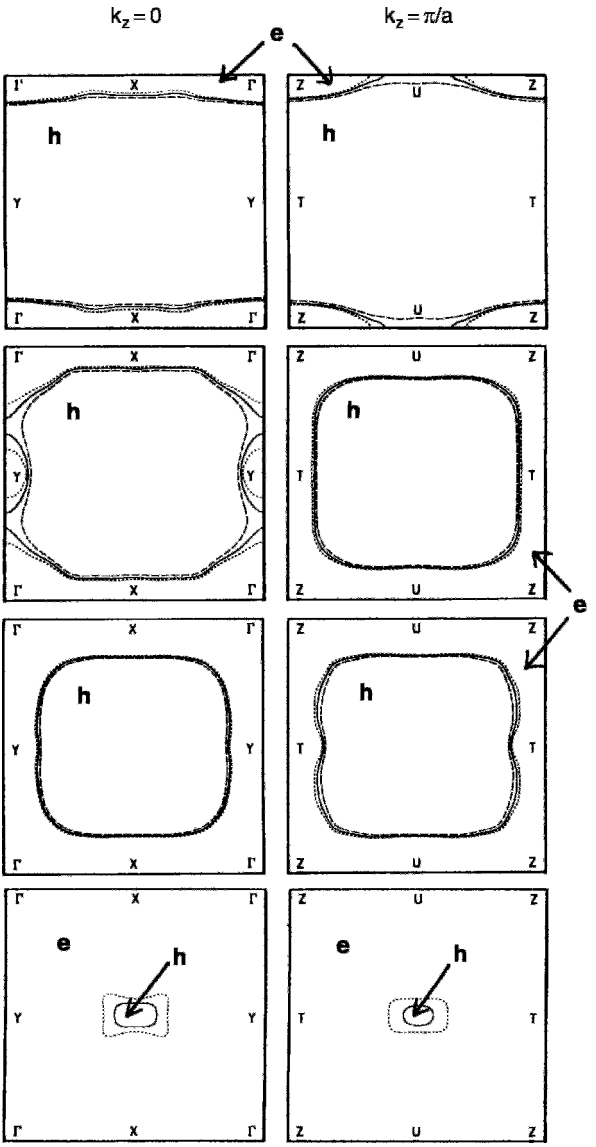

Well dispersed chain band (goes far above E_F).

Plane band which crosses E_F nearest to points X and Y.

Plane band which crosses E_F furthest from points X and Y.

Chain band near E_F.

Figure 10.15 Fermi surfaces of $YBa_2Cu_3O_{7-\delta}$ calculated from the band structure with the electron (e) and hole (h) regions indicated. The left panels are for the midplane of the Brillouin zone ($k_z = 0$) with point S at the center and those on the right are for the top plane ($k_z = \pi/a$) with point R at the center. Points S and R are not labeled. The two top panels show a well dispersed chain band that rises far above the Fermi level. The second pair of panels shows the first plane band; it crosses the Fermi level closest to points X and Y in Fig. 10.12. The third pair of panels presents the second plane band with the crossing further from these points. The bottom panels display the chain band, which is mostly below the Fermi surface, rising above it only near point S (and point R) in Fig. 10.12. The solid lines are for the calculated Fermi surface with $\delta = 0$, the short dashed curve is for $\delta = 0.2$ containing 0.2 fewer electron, and the long-dashed curve is for $\delta = -0.2$ with 0.2 more electron (Krakauer *et al.*, 1988).

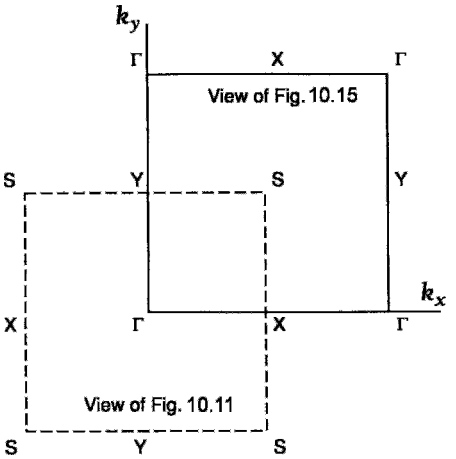

Figure 10.16 Relationship between Brillouin zone boundary in Fig. 10.11 (dashed lines) when point Γ or Z is at the center and Fig. 10.15 (solid lines) when *S* or R is chosen as the center.

The band structure calculations were carried out by adding to the usual orbital set the following upper core level orbitals: Cu $3s$ and $3p$, O $2s$, Ba$5s$ and $5p$, and Hg $5p$ and $5d$, with $\delta = 0$. Ca $3s$ and $3p$ orbitals were added for Hg-1223. Figures 10.17 and 10.18 show the energy bands and density of states for the $n = 0$ compound (Singh, 1993), and Figs. 10.19 and 10.20 present their counterparts for the $n = 2$ compound (Rodriguez, 1994; Singh, 1994). In addition the articles provide Fermi surface across sections for the two compounds.

The bands of $HgBa_2CuO_4$ presented in Fig. 10.17 are highly two dimensional, with very little dispersion in the z direction shown from Γ to Z in the figure. Only one band crosses the Fermi surface, and that is the $pd\sigma^*$ band derived from the CuO_2 planes, which is characteristic of all the layered cuprates. An unoccupied band arising from hybridization of Hg $6p_z$ and O(2) $2p_z$ orbitals lies above the Fermi level, and approaches it without ever crossing it. As a result the $pd\sigma^*$ band is exactly half full, and the stoichiometric compound ($\delta = 0$) is expected to be a Mott insulator. This is in contrast to the case of $Ba_2Tl_2CuO_6$, where the hybridization band does dip below the Fermi level.

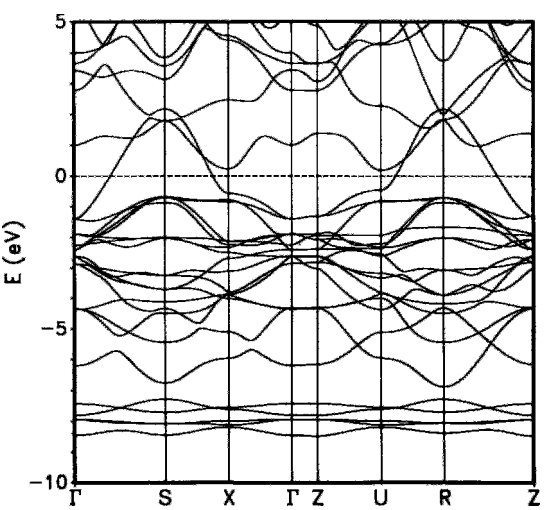

Figure 10.17 Energy bands of stoichiometric $HgBa_2CuO_4(\delta = 0)$ along the Γ–S–*X*–Γ directions defined by Fig. 10.11 for the $k_z = 0$ plane, and along the corresponding Z–U–R–Z directions of the $k_z = \frac{1}{2}$ plane in reciprocal space. The horizontal dashed line at $E = 0$ denotes the Fermi level (Singh *et al*., 1993a).

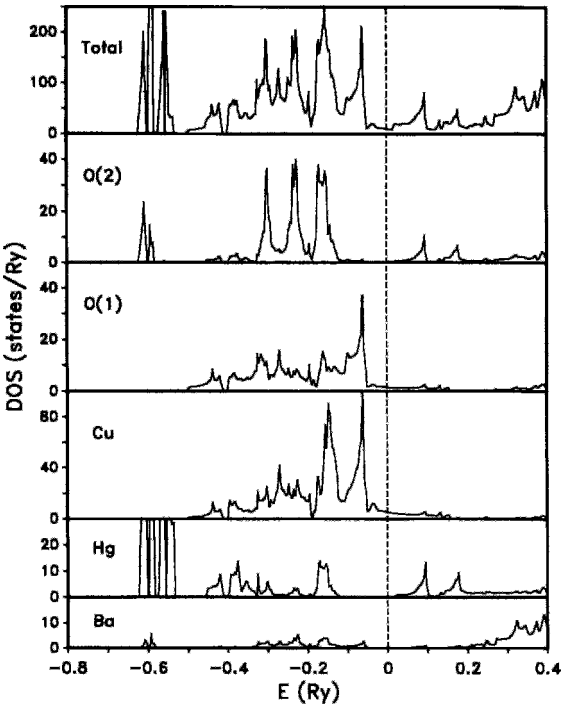

Figure 10.18 Total (top panel) and local site densities of states derived from the band structure of $HgBa_2CuO_4$ shown in Fig. 10.17, where 1 Ry = 13.6 eV, O(1) is in the CuO_2 layer, and O(2) is in the [O–Ba] layer (Singh *et al*., 1993a).

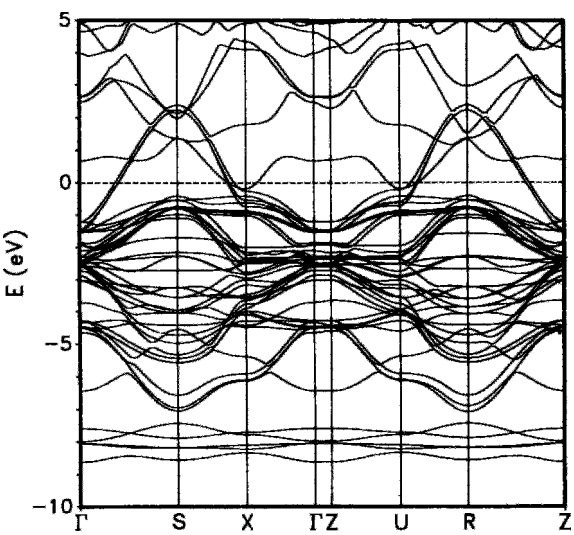

Figure 10.19 Energy bands of stoichiometric compound $HgBa_2Ca_2Cu_3O_8(\delta = 0)$ using the notation of Fig. 10.18. The five lowest energy bands shown are the Hg 5*d* manifold, and because of their flatness they produce the large Hg DOS shown in Fig. 10.20 at $E = 0.6$ Ry (Singh *et al*., 1993b).

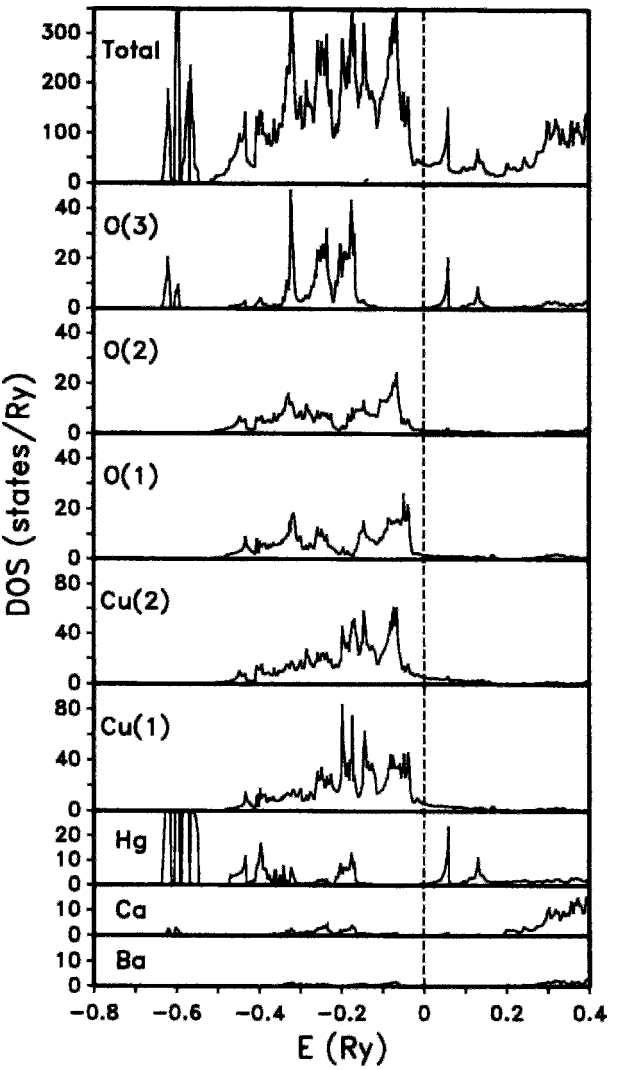

Figure 10.20 Total (top panel) and local site densities of states derived from the bands of $HgBa_2Ca_2Cu_3O_8$ shown in Fig. 10.19 where 1 Ry = 13.6 eV. O(1) is in the central Cu(1) layer, O(2) is in the Cu(2) layer, and apical O(3) is in the [O–Ba] layer (Singh *et al*., 1993b).

We see from Fig. 10.20 that the density of states of $HgBa_2CuO_4$ at the Fermi level is quite small because only the $pd\sigma^*$ band passes through this level, and it is quite steep there. Near but below the Fermi level the DOS arises mainly from the Cu and O(1) atoms of the CuO_2 planes. The hybrid band is largely responsible for the DOS shown above E_F in Fig. 10.20.

The $HgBa_2CuO_{4+\delta}$ calculations were carried out for stoichiometric materials, i.e., $\delta = 0$, so no account was taken of the possibility of the presence of oxygen in the Hg plane at the $\frac{1}{2}\frac{1}{2}0$, $\frac{1}{2}\frac{1}{2}1$ site of O(3) listed

in Table 8.5. The table mentions 11% oxygen occupancy of this site, and this would result in the presence of Cu^{3+} ions as observed, corresponding to hole doping in the CuO_2 planes and metallic behavior.

In addition calculations were carried out of the positron charge density that is predicted for angular correlation of annihilation radiation (ACAR) experiments carried out with positron irradiation, and the resulting contour plots are shown in Fig. 10.21 for two planes of the crystallographic unit cell. The charge density is smallest at the atom positions because the positrons avoid the positively charged atomic cores. It is largest at the empty O(3) site along the ⟨110⟩ direction.

Table 10.3 shows the calculated electric field gradients V_{ii} at all of the $HgBa_2CuO_4$ atom positions, where $V_{xx} = dE_x/dx$, etc. For each site Laplace's equation is obeyed, $V_{xx} + V_{yy} + V_{zz} = 0$, and at sites of tetragonal symmetry $V_{xx} = V_{yy}$. The gradients are smallest in magnitude for Cu in the planar direction, and largest for Hg.

The energy bands of the stoichiometric $HgBa_2Ca_2Cu_3O_{8+\delta}$ compound ($\delta = 0$) are shown in Fig. 10.19 and the density of states plots are in Fig. 10.20. There are some very strong similarities with $HgBa_2CuO_4$, but there are also some marked differences. There are three $pd\sigma^*$ well dispersed antibonding bands that cross the Fermi surface, one for each CuO_2 layer, and they are almost superimposed. The hybrid band dips below the Fermi surface at the X and U points and takes electrons from the $pd\pi^*$, band so there are less electrons in the CuO_2 planes, corresponding to the bands of these planes being less than half full. Thus this three-layer Hg compound is self-doped: the Hg layer produces hole doping of the CuO_2 layers. This is analogous to the $Tl_2Ba_2CuO_6$ case mentioned below.

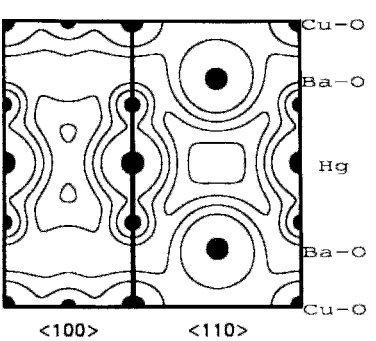

Figure 10.21 Contour plot of positron charge density normalized to one positron per $HgBa_2CuO_4$ unit cell determined by ACAR. Adjacent contours are separated by 0.0005 e^+/a.u. The density is largest in the voids (O(3) site) of the Hg layer. A uniformly distributed positron would have a density 0.00104 e^+/a.u. (Singh *et al*., 1993a).

Table 10.3 Electric Field Gradients at the Atom Sites of $HgBa_2CuO_4$ in Units of $10^{22}V/m^2$. The *x, y, z* Directions Are along the Crystallographic *a, b, c* Directions, Respectively, but for the O(1) Site the *x* Direction is Toward the Neighboring Cu Atoms. Four of the Sites have Tetragonal Symmetry: $V_{xx} = V_{yy}$

Site	V_{xx}	V_{yy}	V_{zz}
Cu	0.096	0.096	−0.192
O(1)	1.31	−0.87	−0.44
Ba	−0.33	−0.33	0.66
O(2)	−0.70	−0.70	1.39
Hg	3.85	3.85	−7.70

We see from Fig. 10.20 that the density of states near but below the Fermi level arises from the three CuO_2 planes, while that slightly above E_F is due to Hg and the oxygen atom O(3) in the Hg plane. Subsequent band structure calculations carried out by Singh and Pickett (1994) showed that oxygen occupation of the $\frac{1}{2}\frac{1}{2}0$, $\frac{1}{2}\frac{1}{2}1$ site produces additional hole doping of the CuO_2 planes. They mentioned that measured values of δ are 0.06, 0.22, and 0.4 for the $n = 0$, $n = 1$, and $n = 2$ mercury compounds, corresponding to 0.12, 0.22, and 0.27 holes per Cu atom, respectively, for these three compounds.

VI. BAND STRUCTURES OF LANTHANUM, BISMUTH, AND THALLIUM CUPRATES

The lanthanum ($(La_{1-x}Sr)_2Cu_2O_4$), bismuth ($Bi_2Sr_2Ca_nCu_{n+1}O_{2+2n}$) and thallium ($Tl_2Ba_2Ca_nCu_{n+1}O_{2+2n}$) cuprate superconducting compounds have body centered crystal structures, and the tetragonal ones have the Brillouin zone sketched in Fig. 10.22. The geometrical relationship between two adjacent Brillouin zones is shown in Fig. 10.23. The body centered cuprates which exhibit a small orthorhombic distortion from tetragonality have a slightly distorted version of this Brillouin zone which is depicted in Fig. 8.42 of the second edition of this text.

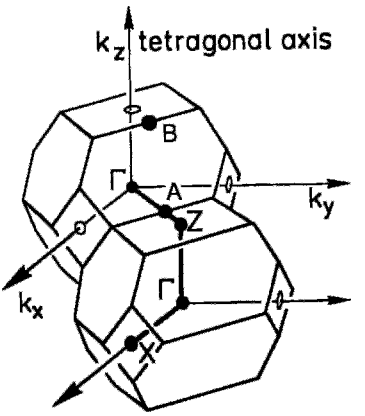

Figure 10.23 Geometrical relationship between adjacent La_2CuO_4 Brillouin zones (Kulkarni *et al.*, 1991). Note that the k_x, k_y axes in this figure are rotated by 45° relative to the axes of Fig. 10.22. The description in the text is in terms of the axes of Fig. 10.22

A. Orbital States

For the undoped compound La_2CuO_4, the copper contributes five d states while each of the four oxygens provides three p states for a total of 17 orbitals. These orbitals are occupied by 33 electrons, which may be counted in one of two ways. Counting by ions, there are nine ($3d^9$) from Cu^{2+} and six ($2p^6$) from each of the four O^{2-} ions. The ionic state La^{3+} has no valence electrons. Counting by atoms, there are three from each La, 11 from Cu, and four from each oxygen. These numbers are listed in Table 10.1. Contour plots of the valence charge density around these atoms in coordinate space that were calculated from the band structure are sketched in Fig. 8.26, and discussed in Chapter 8, Section VII.C.

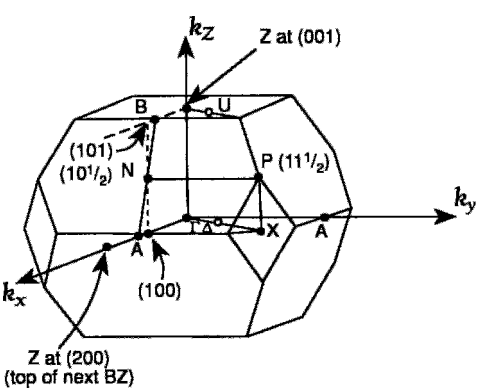

Figure 10.22 Brillouin zone of body-centered La_2CuO_4 with the symmetry points indicated. The symbols Δ and U denote general points along the [110] directions (adapted from Pickett, 1989).

If 10% of the La is replaced by Sr to give the superconducting compound

$$(La_{0.9}Sr_{0.1})_2CuO_4,$$

charge neutrality can be maintained by a change in copper valence to $Cu^{2+}_{0.8}Cu^{3+}_{0.2}$, with an average of $Cu^{2.2+}$. From Table 10.1 we see that Cu^{2+} has the configuration $3d^9$ and Cu^{3+} the configuration $3d^8$, which means that Cu contributes 8.8 electrons, instead of 9, and the total number of electrons is 32.8, not 33. A deficit of oxygen can also contribute to the maintenance of charge neutrality.

B. Energy Bands and Density of States

The energy bands of nonsuperconducting $La_2Cu_2O_4$ are presented in Fig. 10.24. The superconducting doped compound

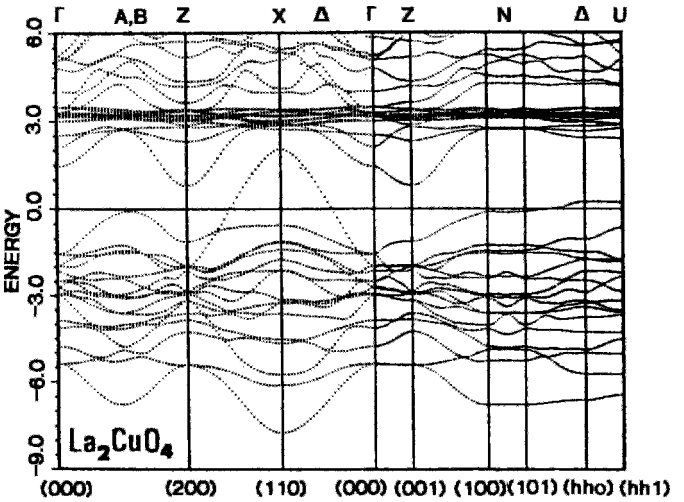

Figure 10.24 Energy bands of La_2CuO_4 along the symmetry directions of the Brillouin zone defined in Fig. 10.22, with E_F taken as the zero of energy. These bands also apply to the doped compound $(La_{0.9}Sr_{0.1})_2Cu_{4-\delta}$. This compound has fewer electrons so its Fermi energy is below (adapted from Pickett *et al.*, 1987).

$(La_{0.9}Sr_{0.1})_2Cu_2O_4$ has the same band configuration, but with the Fermi level slightly lower. In both cases there are 16 low-lying "bonding" bands below the Fermi energy fully occupied by 32 of the 33 valence electrons, one bonding "hybrid" band near E_F and 17 empty higher-energy "antibonding" bands. The hybrid band contains exactly one electron for La_2CuO_4 and 0.8 electron for the doped compound $(La_{0.9}Sr_{0.1})_2CuO_4$, as already noted. Its principal excursion above E_F in the X direction is analogous to that of its counterpart at point M in the three-state Hubbard model of Fig. 10.7a. That the bands are in fact two-dimensional is seen by observing in Fig. 10.24 how flat they are along the vertical paths from Γ to Z ((0,0,0) to (0,0,1)), from (1,0,0) to (1,0,1), and from Δ to U ((h,h,0) to (h, h, 1), where h is arbitrary). We can again argue from Eq. (10.58) that the effective mass m^* is large in the k_z direction, and hence that the electrical conductivity is low for current flow perpendicular to the planes.

The hybrid band that crosses the Fermi surface lies below it at special points Γ and Z so these points are electron-like regions, and at point X the same band rises far above the Fermi surface so this is a hole region, as is clear from the sketch of the Fermi surface in Fig. 10.25. Since doping with strontium lowers E_F the top of the hybrid band at position A, B on Fig. 10.24 rises above the Fermi level, and it transforms from being electron-like to being hole-like at its peak. The result is that the overall configuration of the Fermi surface changes from being electron-type with enclosed holes to being hole-type with enclosed electrons, as shown in Fig. 10.25. In the former case there is an interconnected region of electrons with isolated patches of holes around special point X, and in the latter case there is an interconnected region of holes with isolated islands of electrons at points Γ and Z. This changeover occurs at a Van Hove singularity arising from the hybrid band being fairly flat near points N and A, B of the Fermi level.

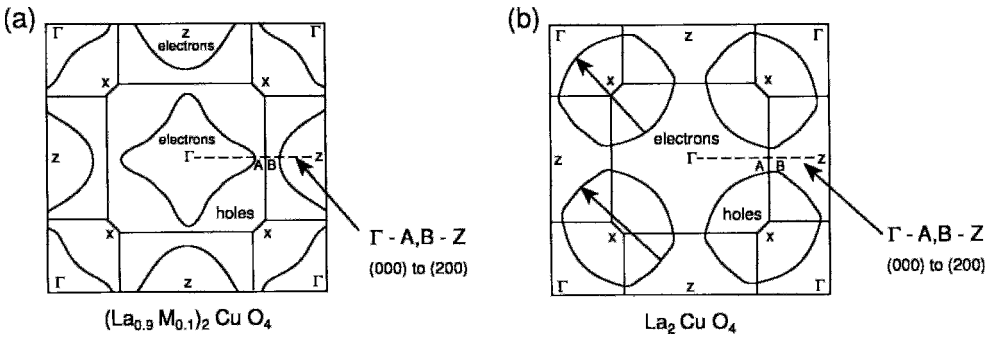

Figure 10.25 Fermi surfaces (a) of La_2CuO_4 with enclosed holes, and (b) of $(La_{0.9}M_{0.1})_2CuO_4$ with enclosed electrons. See Figs. 10.22 and 8.38 for a clarification of the path Γ–*A*–*B*–*Z*. The bold arrows on (b) approximate nesting wave vectors drawn somewhat longer than the Γ–*X* distance. The changeover from enclosed holes to enclosed electrons occurs at a van Hove singularity (Pickett, 1989).

Since the point *Z* is a distance π/c above Γ, as shown in Fig. 10.22, the electron regions of the superconductor $(La_{0.9}Sr_{0.1})_2CuO_{4-\delta}$ extend vertically, from Γ to *Z* to Γ, and so on, forming a cylinder of irregular cross-section (Klemm and Liu, 1991) containing electrons surrounded by holes. The shapes of this cross section around the point Γ and around the point *Z* are shown in Fig. 10.25a. In like manner, the compound La_2CuO_4 has vertical cylinders of holes centered at the point *X* and surrounded by electrons. The change from cylinders of holes to cylinders of electrons is reminiscent of the electron–hole symmetry that was discussed in Section III.C.

The density of states at the Fermi level is highest in regions where the energy bands are fairly flat. It is clear from Fig. 10.26 that this increase of the density of states at E_F when the lowering occurs is mainly associated with the copper and oxygen (O_{xy}) atoms in the CuO_2 planes where the superelectrons are concentrated. Figures 10.27 and 10.28 show that the density of states at the Fermi Levels of the compounds $Bi_2Sr_2CaCu_2O_8$ and thallium $Tl_2Ba_2CuO_6$ is likewise highest in the CuO_2 planes at the copper and oxygen (O(1)) atom positions.

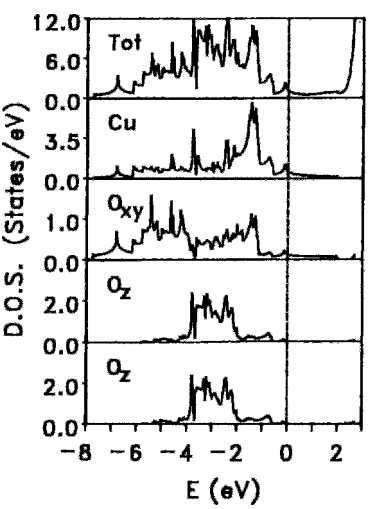

Figure 10.26 Total density of states (top) and partial densities of states for the individual atoms of La_2CuO_4 determined from the band structure. The O_{xy} oxygens are in the CuO_2 planes (Pickett *et al.*, 1987).

The sketch of the "Fermi surface" of La_2CuO_4 in Fig. 10.25 is not in accord with experiment because La_2CuO_4 is an antiferromagnetic insulator with a 2eV energy gap, and hence no Fermi surface may be defined for it. This shows the limitations of band structure calculations.

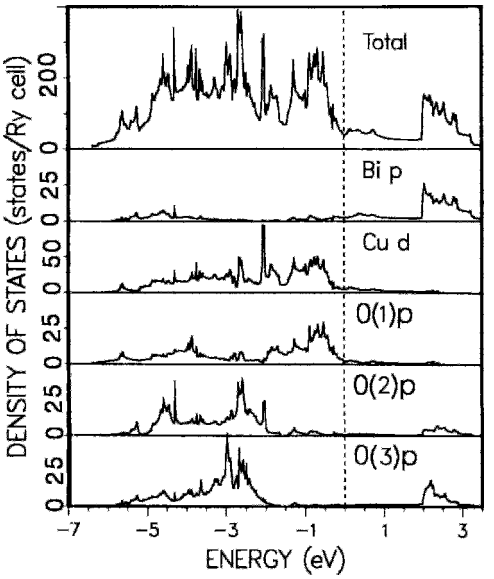

Figure 10.27 Total (top) and partial densities of states from the band structure of $Bi_2Sr_2CaCu_2O_8$. The distributions of Cu and O are similar to those from the other cuprates. Most of the Bi density lies above E_F, but two Bi derived bands do drop to or below E_F (Krakauer and Pickett, 1988).

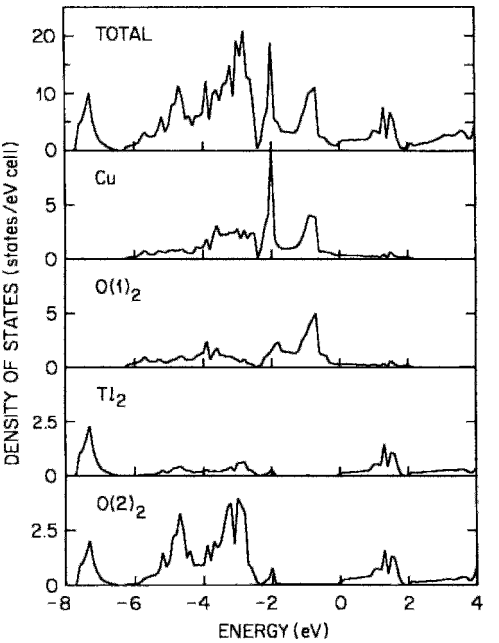

Figure 10.28 Total (top) and partial densities of states from the band structure of $Tl_2Ba_2CuO_6$. The Cu–O densities are similar to those from the other cuprates. The Tl_2 and O(2) spectral density extends just to E_F from above (Hamann and Mattheiss, 1988).

VII. FERMI LIQUIDS

In the independent electron approximation we treat conduction electrons as noninteracting particles obeying Fermi–Dirac statistics, i.e., as constituting a Fermi gas. When the electrons continue to obey FD statistics and interact with each other in such a way that their properties remain close to those of a Fermi gas, they constitute what may be called a Fermi liquid.

Landau (1957) developed a method of taking account of electron–electron interactions in such a manner as to maintain a one-to-one correspondence between the states of a free-electron gas and those of the interacting electron system. The existence of such a one-to-one correspondence constitutes the usual definition of a Fermi liquid. In such a liquid the Pauli exclusion principle permits electrons at the Fermi surface to experience only momentum-changing collisions. Elementary excitations of quasiparticles and quasiholes correspond to those of a Fermi gas. In what are called marginal Fermi liquids, the one-to-one correspondence condition breaks down at the Fermi surface, but many of the properties continue to resemble those of a Fermi liquid (Baym and Pethick, 1991; Levine, 1993; Williams and Carbotte, 1991; Zimanyi and Bedell, 1993).

Transport properties of the cuprates, such as resistivity and the Hall effect, are often described by considering the conduction electrons as forming a normal Fermi liquid (Crow and Ong, 1990; Tsuei *et al.*, 1989). Varma *et al.*, (1989) ascribed anomalies in these normal-state properties to marginal Fermi liquid behavior. Anderson (1987c) attributes the superconductivity of the cuprates to the breakdown of Fermi liquid theory and suggested the applicability of

what are called Luttinger liquids (Anderson, 1990a, b).

VIII. FERMI SURFACE NESTING

The phenomenon of *Fermi surface nesting* occurs when the two sheets of the Fermi surface are parallel and separated by a common reciprocal lattice wave vector $\mathbf{G} = \mathbf{k}_{\text{nest}}$. We see from the bottom of Fig. 10.25 that the two sheets of the Fermi surface of $(La_{1-x}Sr_x)_2CuO_4$ on either side of the hole region are roughly parallel, and that the reciprocal lattice spacing across the region is close to the wave vector $(110)\pi/a$, of length $\sqrt{2}\pi/a$, which is also the distance from Γ to X (Crow and Ong, 1990; Emery, 1987a; Pickett, 1989; Virosztek and Ruvalds, 1991; Wang *et al*., 1990). Two such nesting wave vectors are shown as bold arrows in the figure. The lanthanum compound approaches near-perfect nesting with $\mathbf{k}_{\text{nest}}$ equal to a reciprocal lattice vector.

If more electrons are added to the bands, the hole region contracts and the nesting vector turns out to be less than $\mathbf{G}$. Decreasing the number of electrons enlarges the hole region, but this also leads to an instability in which the Fermi surface switches from the configuration of isolated hole regions shown at the right of the figure to the isolated electron regions in the left drawing. Further doping decreases the size of these electron regions until the spanning vector $\mathbf{k}$ is no longer a reciprocal lattice vector $\mathbf{G}$, and the Fermi surface is no longer nested.

More generally, nesting may lead to instabilities in the Fermi surface even in the absence of this "switchover" instability. This can be seen from the viewpoint of perturbation theory by considering the fact that the energy denominator in the perturbation expression $1/(E_k - E_{k+\mathbf{G}})$ of Eq. (10.43) can approach zero over a wide range of k values for a nesting wave vector $\mathbf{k}_{\text{nest}}$. The result might be the generation of either a charge-density wave (CDW), a spin-density wave (SDW), or both.

The yttrium compound also exhibits a nesting feature, as may be seen from the parallel Fermi surfaces of Fig. 10.15. However, the spanning k-vectors are not close to the reciprocal lattice vectors, the energy denominators $(E_k - E_{k+\mathbf{G}})$ do not become small as in the lanthanum case, and no instability develops.

IX. CHARGE-DENSITY WAVES, SPIN-DENSITY WAVES, AND SPIN BAGS

We noted in Sections V and VI.A contour plots of the charge density around the atoms of a superconductor can be determined from a band-structure calculation. Examples of such plots were given in Figs. 8.14 and 8.26 for the yttrium and lanthanum compounds, respectively. In this section we will be concerned with the charge density of an independent electron gas that is calculated self-consistently (cf. Section III) using the Hartree–Fock approximation referred to in Chapter 1, Section II.

If this method is applied to an independent electron gas using a potential that is periodic in space and independent of spin, self-consistency can be obtained with solutions involving charge density which is periodic in space. In other words, the solution is a charge-density wave. The CDW can have periodicities that are incommensurate with the lattice spacings, and as noted above in Section VIII, CDW is favored by Fermi surface nesting. A crystal structure distortion and the opening up of a gap at the Fermi surface accompany the formation of a CDW and stabilize it by lowering the energy. The presence of the gap can cause the material to be an insulator. Sufficiently high doping of La_2CuO_4 with Sr or Ba disables the nesting

and destabilizes the CDW, thereby converting the material to a metal and making it superconducting.

In quasi-one-dimensional metals the CDW instability that leads to a structural distortion is called a *Peierls instability* (Burns, 1985), a phenomenon which has been discussed in the superconductor literature (e.g., Crow and Ong, 1990; Fesser *et al*., 1991; Gammel *et al*., 1990; Nathanson *et al*., 1992; Ugawa *et al*., 1991; Wang *et al*., 1990). This CDW represents a nonmagnetic solution to the Hartree–Fock equations for an independent electron gas. Solutions with uniform charge densities that are fully magnetized can also be obtained. Overhauser (1960, 1962) assumed an exchange field that oscillates periodically in space and obtained a lower energy solution involving a nonuniform spin density whose magnitude or direction varies periodically in space. This solution corresponds to a spin density wave. Generally, the SDW is incommensurate because its periodicities are not multiples of the crystallographic lattice parameters, and, as noted, a nesting Fermi surface is favorable for the excitation of a SDW state (Burns, 1985). The antiferromagnetic insulator state of La_2CuO_4 mentioned at the end of Section VI.B involves antiparallel nearest-neighbor spins, so that it is the SDW of maximal amplitude and shortest wavelength (Phillips, 1989a). The antiferromagnetism of itinerant electrons, as in a conductor, can be described as a spin-density wave (Kampf and Schrieffer, 1990; Wang *et al*., 1990).

One attempt to understand the mechanism of high-temperature superconductivity has involved the use of what are called *spin bags* (Allen, 1990; Anisimov *et al*., 1992; Goodenough and Zhou, 1990; Schrieffer *et al*., 1988; Weng *et al*., 1990). Consider the case of a half-filled band and an appropriately nested Fermi surface, so that the gap Δ_{SDW} extends over the Fermi surface and the system is an antiferromagnetic insulator. The presence of a quasi-particle alters the nearby sublattice magnetization and forms a region of reduced antiferromagnetic order. Such a region is called a spin bag because it is a metallic domain of depleted spin immersed in a surrounding SDW phase. This spin bag, which moves together with the quasiparticle, has a radius r_{bag} equal to the SDW coherence length, namely $r_{bag} = \hbar v_F/\Delta_{SDW}$ (Kampf and Schrieffer, 1990). Two spin bags attract each other to form a Cooper pair and, as a result, two holes tend to lower their energy by sharing one common bag.

X. MOTT-INSULATOR TRANSITION

If the lattice constant of a conductor is continuously increased, the overlap between the orbitals on neighboring atoms will decrease, and the broad conduction bands will begin to separate into narrow atomic levels. Beyond a certain nearest-neighbor distance what is called a *Mott transition* occurs, and the electrical conductivity of the metal drops abruptly to a very small value. The metal has thus been transformed into what is called a Mott insulator.

One of the chronic failures of band-structure calculations has been an inability to obtain the observed insulating gaps in oxides such as FeO and CoO. In the prototype Mott insulator NiO the calculated gap has been observed to be an order of magnitude too small (Wang *et al*., 1990). The Mott insulator problem involves learning how to accurately predict the electronic properties of materials of this type.

For the large U case the ground state of the undoped ($x = 0$) Hubbard model system is a Mott insulator, sometimes called a Mott-Hubbard insulator. In the cuprates almost all of the Cu ions are in the $3d^9$ state, and there is one hole on each site of the system. There exists a large gap for excitations to levels where two antiparallel holes can occupy the same site. This gap of several eV, called the Mott–Hubbard gap, is too large to permit

significant thermal excitation to occur. The system can, however, lower its energy by having individual holes make virtual hops to and from antiparallel neighbors. This virtual hopping process can be maximized by having the spin system assume an antiferromagnetically ordered configuration. Such ordering has been found experimentally in insulating members of the yttrium and lanthanum families of compounds (Birgeneau *et al*., 1987; Crow and Ong, 1990). Some of the cuprate superconductors order antiferromagnetically at very low temperatures. The Mott transition in high-temperature superconductors has been widely discussed (Aitchison and Mavromators, 1989; Arrigoni and Strinati, 1991; Brandt and Sudbø, 1991; Cha *et al*., 1991; Dai *et al*., 1991; Hallberg *et al*., 1991; Hellman *et al*., 1991; Ioffe and Kalmeyer, 1991; Ioffe and Kotliar, 1990; Kaveh and Mott, 1992; Khurana, 1989; Mila, 1989; Millis and Coopersmith, 1991; Reedyk *et al*., 1992a; Schulz, 1990; Spalek and Wojcik, 1992; Torrance *et al*., 1992).

XI. DISCUSSION

In this chapter we presented the Hubbard model approach and then described band-structure calculations that have been carried out for several types of superconductors. The calculated bands, densities of states, and Fermi surface plots together provide a good explanation of the normal-state properties of the various materials. For example, they describe well the planar nature of the conductivity in the high-temperature superconducting compounds and yield plots of electron density that elucidate the chemical bonding of the atoms. The calculated density of states at the Fermi level does not correlate well with known T_c values in various compounds, however.

Some results of band-structure calculations agree well with experiment, whereas others exhibit rather poor agreement. There are differences in the calculated results published by different investigators. This would appear to indicate that these calculations are unreliable for estimating properties that have not yet been measured, and thus are more descriptive of superconductivity than predictive of it. In particular, investigators have not been successful in anticipating whether or not new compounds will be superconductors, and if so, with how high a T_c. Nevertheless, it is our belief that band structures do provide insight into the nature of superconductors that could not be obtained otherwise, in addition to elucidating their normal-state properties.

FURTHER READING

See the first edition for more details and more references on Hubbard models and bond structure.

PROBLEMS

1. Show that $\Gamma(\mathrm{k})$ is the Fourier transform of the overlap integral $\gamma(\mathrm{R})$ (Eq. (10.7)), where

$$\Gamma(\mathrm{k}) = \sum_{\mathrm{R}} e^{-i\mathrm{k}\cdot\mathrm{R}}\gamma(\mathrm{R}).$$

2. Calculate the expectation value

$$\int d^3r\Psi_k^*,(r)H\Psi_k(r),$$

and show that the energy in the one-band case is given by Eq. (10.8):

$$\epsilon(k) = \epsilon_a + \frac{B(k)}{\Gamma(k)}.$$

3. Write down expressions similar to Eqs. (10.13) and (10.12) for a diatomic lattice of the NaCl or ZnS type. Why are equations of this type not valid for diatomic lattices in general?

4. Show that the only nonvanishing operations involving one-electron number operators are

$$n_+|+\rangle = |+\rangle \quad n_-|-\rangle = |-\rangle$$
$$n_+|\pm\rangle = |\pm\rangle \quad n_-|\pm\rangle = |\pm\rangle$$

5. Why does the first-order energy shift of the hopping term: H_{hop} (10.52) vanish?
6. What is the total number of electrons outside the closed shells in the compound $(La_{0.9}Sr_{0.15})_2CuO_{3.9}$? How many are contributed by each atom and how many/by each ion? What is the average valence of copper?
7. Show that the denominator $E_j - E_i$ of the second-order term in Eq. (10.43) is equal to the Coulomb repulsion term U for the states $|j\rangle = |0\pm\rangle$ and $|\pm 0\rangle$.
8. Prove that the only nonvanishing terms of $\langle\Psi_i|H_{hop}|\Psi_j\rangle$ for $i \neq j$ are given by Eq. (10.46).
9. Show that the energy of the ferromagnetic states (10.40) is zero, as given by Eq. (10.48).
10. Prove Eq. (10.40), namely that $J = 4t^4/U$.
11. Show that in the Hubbard model the ionic states $|0\pm\rangle$ and $|\pm 0\rangle$ have the energy $U + 2t^2/U$, as shown in Fig. 10.6.
12. Show that in the RVB model the two ionic states $|00\rangle$ and $|\text{ion}\rangle$ have the respective energies U and $U + 4t^2/U$, as shown in Fig. 10.6.
13. Show that in the RVB model the states $|\text{VB}\rangle$ and $|\text{ion}\rangle$ mix, and have the eigenenergies $E_i = \frac{1}{2}U \pm (\frac{1}{4}U^2 + 4t^2)^{1/2}$. Show that these reduce to those shown in Fig. 10.6 for the limit $U \gg t$.
14. Find the length of the distances Γ to Z (vertical), Γ to Z (horizontal), Γ to X, Γ to N, Γ to P, and X to P in the Brillouin zone of La_2CuO_4 (Fig. 10.22). Express the answers in $(\text{nm})^{-1}$.
15. Explain why $S = 0.06$, 0.22, and 0.40 for the $n = 0$, 1, 2 Hg compounds $HgBa_2Ca_nCu_{n+1}O_{2n+4}$ give 0.12, 0.22, and 0.27, respectively, holes per Cu atom.

11

Type I Superconductivity and the Intermediate State

I. INTRODUCTION

In Chapters 5, 6, and 7 we showed that the superconducting state can only exist in a material when the external B field at the surface is less than the critical field B_c for a Type I superconductor and less than the upper critical field B_{c2} for a Type II superconductor. For a rod-shaped sample in a parallel external field, the demagnetization factor is zero, so the field H at the surface equals the externally applied field, $H_{in} = H_{app}$, and the situation is not complicated. For other field directions and other sample shapes, the fact that the demagnetization factor does not vanish complicates matters because it raises the question whether the external field can exceed the critical field over part of the surface but not over the remainder. When this occurs with a Type I superconductor, the sample lowers its free energy by going into an intermediate state involving partial penetration of the external field into the interior. In the present chapter we will examine how this happens. We will discuss thin films, the domains that form in thin films in the intermediate state and the magnetic field configurations associated with

thin films. We will also treat the intermediate state induced by transport current in a wire. Most of the chapter will be devoted to these discussions of the intermediate state of a Type I superconductor.

A Type II superconductor exists in what is called the Meissner state of total flux exclusion, $B_{in} = 0$, for applied fields in the range $B_{app} < B_{c1}$ and in the mixed state of partial flux penetration when the applied field is in the range $B_{c1} < B_{app} < B_{c2}$ between the lower and upper critical fields. The way in which the demagnetization factor affects these Meissner and mixed states will be discussed the next chapter. For now, bear in mind that the term, *intermediate state*, applies to Type I superconductors, and the term, *mixed state*, to Type II superconductors.

II. INTERMEDIATE STATE

We learned in Chapter 1 that the magnetic fields inside any material, including a superconductor, satisfy the general expression (1.69)

$$B_{in} = \mu_0(H_{in} + M). \tag{11.1}$$

We saw in Chapter 2 that an ideal Type I superconductor has the following internal magnetic fields:

$$\left.\begin{aligned} B_{in} &= 0 \\ M &= -H_{in} \\ H_{in} &< \frac{B_c}{\mu_0} \end{aligned}\right\} \quad \begin{matrix}\text{Type I} \\ \text{Superconducting State}\end{matrix} \tag{11.2}$$

In this chapter we will see that in the intermediate state of an ideal Type I superconductor, the H_{in} field is pinned at the value B_c/μ_0. This provides us with the relationships

$$\left.\begin{aligned} H_{in} &= \frac{B_c}{\mu_0} \\ \mu_0 M &= B_{in} - B_c \end{aligned}\right\} \quad \begin{matrix}\text{Type I} \\ \text{Intermediate State}\end{matrix} \tag{11.3}$$

for the fields inside. Finally, above T_c the normal state exists with the field configurations

$$\left.\begin{aligned} M &\approx 0 \\ B_{in} &\approx \mu_0 H_{in} \end{aligned}\right\} \quad \begin{matrix}\text{Normal State} \\ \text{Above } T_c\end{matrix} \tag{11.4}$$

where we have written $M \approx 0$ since in the normal state $|\chi| \ll 1$, as we showed in Chapter 1, Section XV.

In Chapter 5 we were concerned with the internal fields of a superconducting ellipsoid in an applied magnetic field, and we made use of expression (10.33),

$$NB_{in} + (1 - N)\mu_0 H_{in} = B_{app}, \tag{11.5}$$

where N is the demagnetization factor. The magnetostatic properties of the intermediate state follow from Eqs. (11.3) combined with (11.5). Since it is not obvious why the internal field H_{in} is pinned at the value B_c/μ_0 in the intermediate state, we will provide some justification for this in the next section before applying Eq. (11.5) to elucidate the properties of this state.

III. SURFACE FIELDS AND INTERMEDIATE-STATE CONFIGURATIONS

We saw in Chapter 5, Section XIII, that the surface field $B_{surf}(\Theta)$ immediately outside a perfectly superconducting sphere has no radial component; it is parallel to the surface, with the value at the angle Θ given by Eq. (5.66) with $\chi = -1$,

$$B_{surf}(\Theta) = \frac{3}{2} B_{app} \sin\Theta. \tag{11.6}$$

If the applied field B_{app} is less than $2B_c/3$, the surface field will be less than B_c for all angles, and the perfectly superconducting state can exist. If, on the other hand, the applied field is greater than $2B_c/3$, we see

from Eq. (11.6) that there will be a range of angles near $\Theta = \pi/2$,

$$\Theta_c < \Theta < \pi - \Theta_c, \tag{11.7}$$

where

$$\Theta_c = \sin^{-1}\left(\frac{2B_c}{3B_{app}}\right), \tag{11.8}$$

for which the surface field will exceed B_c. Thus the sphere is unable to remain perfectly superconducting. In the range of applied fields

$$\frac{2}{3}B_c < B_{app} < B_c, \tag{11.9}$$

the surface field must decompose into superconducting and normal regions that prevent the average internal field H_{in} from exceeding the critical value H_c. In other words, the sphere must enter the intermediate state. For lower applied fields it is perfectly superconducting, whereas for higher applied fields it is in the normal state, as indicated in Fig. 11.1. The arrows in the figure show how the intermediate state can be traversed by varying either the applied magnetic field or the temperature.

One possibility for an intermediate state is for the sphere to go normal in a band around the equator delimited by Θ_c of Eq. (11.8). This, however, would not satisfy the boundary conditions. Another possibility would be for a normal outer layer to surround a superconducting inner region. But such states do not exist because it is energetically more favorable for a sphere to split into small regions of normal material adjacent to regions of superconducting material. We know that below T_c the superconducting state is energetically favored. Thus, the formation of the intermediate state is the way in which a material can continue to possess some of this favorable superconducting-state energy while still satisfying the boundary conditions on the surface field.

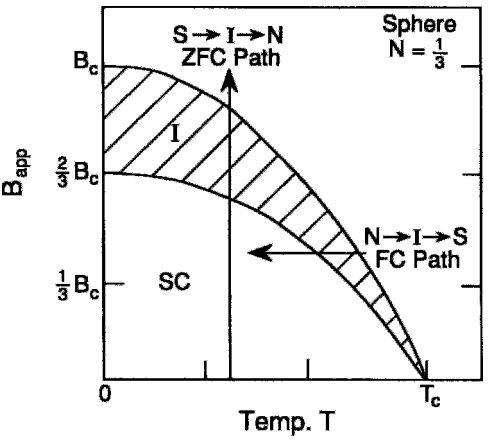

Figure 11.1 Dependence of the critical field $B_c(T)$ of a Type I superconductor on temperature (upper curve), where $B_c = B_c(0)$ is the critical field at 0 K. The figure also plots the curve $\frac{2}{3}B_c(T)$, which is the lower limit of the intermediate state (I) of a superconducting sphere. The vertical arrow indicates the path S → I → N traversed by a zero-field-cooled sphere as increasing applied fields bring it from the superconducting state (SC) at $B_{app} = 0$ through the intermediate state to the normal state (N) that exists for $B_{app} > B_c(T)$. The horizontal path N → I → S traversed by field cooling of the sphere is also shown.

It is easier to picture how the intermediate state forms by considering the case of a Type I superconducting film in a perpendicular magnetic field. We assume a demagnetization factor $N = 0.9$ corresponding to the phase diagram of Fig. 11.2. When the applied field is raised to a value slightly above $0.1B_c(T)$, small regions of normal material appear embedded in a superconducting matrix, as shown in Fig. 11.3a. This is reminiscent of the vortex lattice that forms in Type II superconductors. We see from the sequence of structures in Figs. 11.3a–11.3f that as the applied field increases along the vertical path of Fig. 11.2, normal regions grow at the expense of the superconducting regions. For very high applied fields, as in Fig. 11.3f, when most of the material has become normal, there is still a tendency for the extensive normal regions to be surrounded by what appear to be filaments

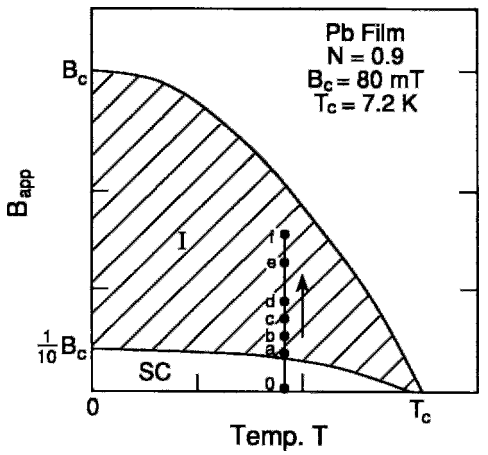

Figure 11.2 Magnetic phase diagram of a film with demagnetization factor $N = 0.9$ in a perpendicular magnetic field. This large demagnetization factor causes the intermediate state to be quite extensive. The vertical isothermal path S → I traversed by the film in passing through the succession of configurations depicted in Figs. 11.3a–11.3f is indicated.

of superconducting material. This has been referred to as a *closed topology*, that is, normal regions surrounded by a superconducting phase (Huebener, 1979).

We have just described the passage through the intermediate state for increasing values of the applied field experienced by a sample that has been precooled in zero field (ZFC) at a particular temperature below T_c. We showed that this S → I path proceeded along the vertical line in Fig. 11.2. Figure 11.1 shows a vertical S → I → N path for a ZFC sphere that starts in the superconducting state, passes through the intermediate state as the field increases at constant temperature, and finally reaches the normal state for $B_{app} > B_c(T)$. Another way of attaining the intermediate state is by field cooling the sphere along the N → I → S path in the same figure. As the sample gradually cools through the intermediate region, it expels flux by forming superconducting regions embedded in a normal matrix, corresponding to what is called an *open topology*, the opposite of what happens in the case S → I → N.

IV. TYPE I ELLIPSOID

Now that we have clarified the nature of the intermediate state, it will be instructive to write down the equations of the internal fields in a perfectly superconducting ellipsoid. For such an ellipsoid the factor $2B_c/3$ in Eq. (11.9) becomes $(1–N)B_c$, and for the purely superconducting state we have, from Eqs. (5.35)–(5.37),

$$B_{app} < (1-N)B_c, \tag{11.10}$$

$$B_{in} = 0, \tag{11.11}$$

$$H_{in} = B_{app}/(1-N)\mu_0, \tag{11.12}$$

$$\mu_0 M = -B_{app}/(1-N), \tag{11.13}$$

$$\chi = -1. \tag{11.14}$$

This states exists over the range given by Eq. (11.10).

The equations for the intermediate state obtained by combining Eqs. (11.3) and (11.5) are

$$(1-N)B_c < B_{app} < B_c, \tag{11.15}$$

$$B_{in} = \frac{1}{N}[B_{app} - (1-N)B_c], \tag{11.16}$$

$$H_{in} = B_c/\mu_0, \tag{11.17}$$

$$\mu_0 M = -\frac{1}{N}(B_c - B_{app}), \tag{11.18}$$

$$\chi = -\frac{1}{N}(1 - B_{app}/B_c). \tag{11.19}$$

The last equation (11.19), will be derived in the following section. The fields given by Eqs. (11.16)–(11.18) are, of course, averages over the normal and superconducting regions, as depicted in Figs. 11.3a–11.3f.

Setting $N = 1/3$ in Eqs. (11.15)–(11.19) recovers the expressions for a sphere. Figures 11.4, 11.5, 11.6, and 11.7 show how the various fields and the susceptibility of a sphere vary with the applied field in the

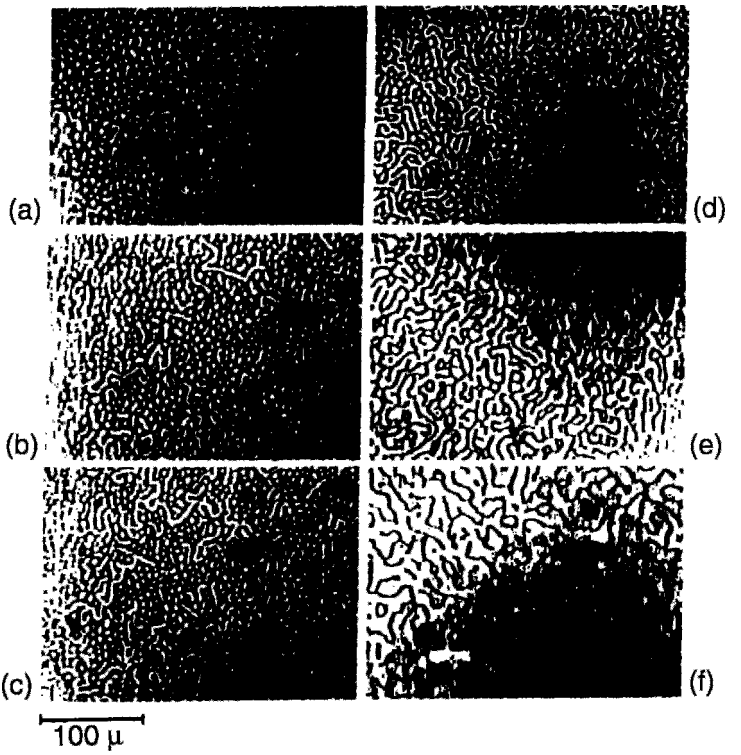

Figure 11.3 Intermediate state domain configurations of a 9.3-μm thick superconducting Pb film in a perpendicular magnetic field at 4.2 K. The structure is shown for the following field values: (a) 9.5 mT, (b) 13.2 mT, (c) 17.8 mT, (d) 21.8 mT, (e) 34.8 mT, and (f) 40.9 mT. The critical field $B_c = 80$ mT for Pb. The photographs were obtained using a magneto-optical method in which normal and superconducting regions are displayed as bright and dark, respectively. Figure 11.2 plots this sequence of increasing fields (Huebener, 1979, p. 22).

perfectly superconducting and intermediate-state ranges. The internal field B_{in} is zero up to $\frac{2}{3}B_c$ and then increases linearly to its normal state value, as shown in Fig. 11.4. Figure 11.5 shows how H_{in} increases at first, and then remains pinned at H_c throughout the intermediate state. The magnitude of the magnetization, presented in Fig. 11.6, increases more rapidly than it would for a parallel cylinder, then drops linearly to zero. We see from Eqs. (11.4) and (11.19) and Fig. 11.7 that the susceptibility stays pinned at the value $\chi = -1$ until the intermediate state is reached and then drops linearly to zero.

V. SUSCEPTIBILITY

We have seen that a material in the intermediate state is an admixture of normal and superconducting regions that coexist at the mesoscopic level. Viewed from a macroscopic perspective, we average over this structure, considering the material to be homogeneous with uniform susceptibility $\chi = M/H_{in}$ given by

$$\chi = \frac{M}{H_c}. \tag{11.20}$$

Substituting the expression from Eq. (11.18) in the latter expression gives Eq. (11.19).

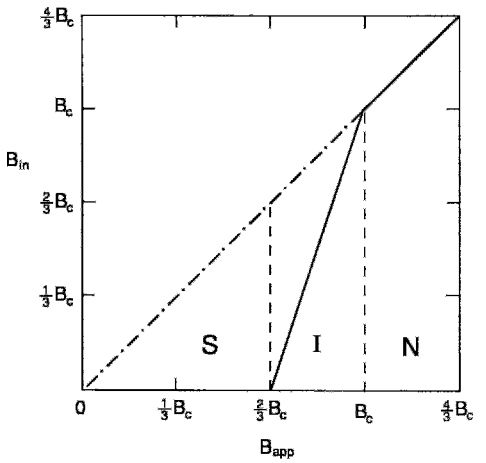

Figure 11.4 Internal magnetic field B_{in} in the Meissner (S) and intermediate (I) states of a Type I superconducting sphere ($N = 1/3$) as a function of the applied field B_{app} (Eqs. (11.11) and (11.16), respectively). In this and Figs. 11.5, 11.6, and 11.7, the solid lines represent the function that is being plotted, vertical dashed lines indicate the boundaries of the Meissner, intermediate, and normal regions, and the unit slope line ($- \cdot - \cdot -$) gives the behavior for zero demagnetization factor ($N = 0$).

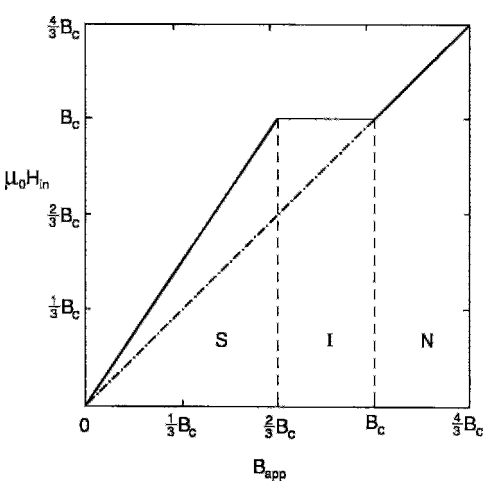

Figure 11.5 Internal field H_{in} (Eqs. (11.12) and (11.17)) for the case of Fig. 11.4.

Since χ is an average of the value -1 in the superconducting regions and 0 in the normal regions, for the intermediate state it lies in the range

$$-1 < \chi < 0, \tag{11.21}$$

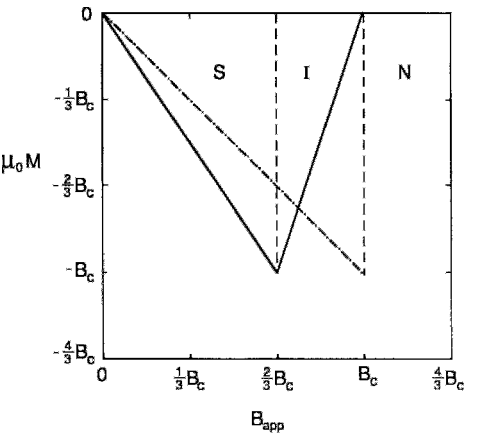

Figure 11.6 Magnetization M (Eqs. (11.13) and (11.18)) for the case of Fig. 11.4.

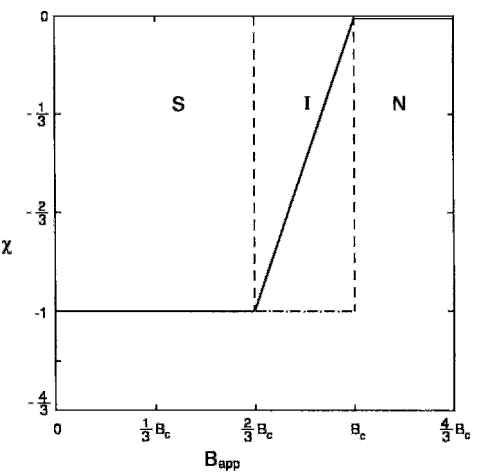

Figure 11.7 Magnetic susceptibility χ (Eqs. (11.14) and (11.19)) for the case of Fig. 11.4.

assuming the value $\chi = -1$ for $B_{app} \leq (1 - N)B_c$ and $\chi = 0$ for $B_{app} \geq B_c$.

Susceptibility is an intrinsic property of a material defined by Eq. (1.77) in terms of the internal field H_{in},

$$\chi = \frac{M}{H_{in}}. \tag{11.22}$$

When the magnetization of a sample is measured in an applied magnetic field $B_{app} = \mu_0 H_{app}$, the experimentally determined susceptibility is often deduced from the expression

$$\chi_{\text{exp}} = M/H_{\text{app}}, \tag{11.23}$$

and the ratio of these gives for the intermediate state

$$\chi = \chi_{\text{exp}} B_{\text{app}}/B_{\text{c}}. \tag{11.24}$$

We can also use a more general expression (10.52),

$$\chi = \chi_{\text{exp}}/(1 - N\chi_{\text{exp}}), \tag{11.25}$$

to obtain χ from χ_{exp}.

VI. GIBBS FREE ENERGY FOR THE INTERMEDIATE STATE

The intermediate state can be described in thermodynamic terms using the formalism for the Gibbs free energy that was developed in Chapter 4, Sections VII–X. In this section we sometimes simplify the notation by writing B for the applied field B_{app} and B_{c} for the critical field $B_{\text{c}}(T)$ at a finite temperature.

Consider the case of a zero-field-cooled Type I superconductor in an applied magnetic field that is isothermally increased from $B_{\text{app}} = 0$ to $B_{\text{app}} = B_{\text{c}}(T)$ along a vertical S $\rightarrow$ I $\rightarrow$ N path of the type shown in Figs. 11.1 and 11.2. To calculate the Gibbs free energy density along this path, we begin by integrating Eq. (4.33),

$$G(B) = K - \int_0^B M dB, \tag{11.26}$$

where K is a constant to be evaluated. For the pure superconducting region, we have from Eq. (11.13),

$$M = -B/\mu_0(1 - N). \tag{11.27}$$

For the intermediate state region M is given by Eq. (11.18),

$$M = -(B_{\text{c}} - B)/N\mu_0, \tag{11.28}$$

where B is the externally applied field. The free energy density is easily calculated for the superconducting region (11.10) by substituting the expression for M from Eq. (11.27) in (11.26). Carrying out the integration we obtain

$$G(B_{\text{app}}) = K + \frac{1}{1 - N}\frac{B_{\text{app}}^2}{2\mu_0}, \tag{11.29}$$

which is an expression that is valid for $B_{\text{app}} < (1 - N)B_{\text{c}}$. For higher applied fields, the interval of integration must be split into two parts,

$$G(B_{\text{app}}) = K - \int_0^{(1-N)B_{\text{c}}} M dB - \int_{(1-N)B_{\text{c}}}^{B} M dB. \tag{11.30}$$

Inserting the appropriate expressions (11.27) and (11.28) for the magnetization and carrying out the two integrations, we obtain after some cancellation of terms

$$G(B_{\text{app}}) = K - (1/2N\mu_0)(B_{\text{c}} - B_{\text{app}})^2 + B_{\text{c}}^2/2\mu_0, \tag{11.31}$$

an expression that is valid for $(1 - N)B_{\text{c}} < B_{\text{app}} < B_{\text{c}}$. At the onset of the normal state ($B_{\text{app}} = B_{\text{c}}$), this reduces to the expression

$$G(B_{\text{c}}) = K + B_{\text{c}}^2/2\mu_0 \tag{11.32}$$

for the free energy density of what is now the normal state. Further integration beyond B_{c} does not yield anything more because in the normal state $\chi \approx 0$, and hence $M \approx 0$, as we showed in Table 1.2.

The constant K is selected as the negative of the condensation energy $B_{\text{c}}^2/2\mu_0$

$$K = -B_{\text{c}}^2/2\mu_0 \tag{11.33}$$

to make the free energy vanish at the upper critical field. This makes $G(B_{\text{app}})$ the free energy of the superconducting state relative to that of the normal state at $T = 0$. The quantity (11.33) is the condensation energy of

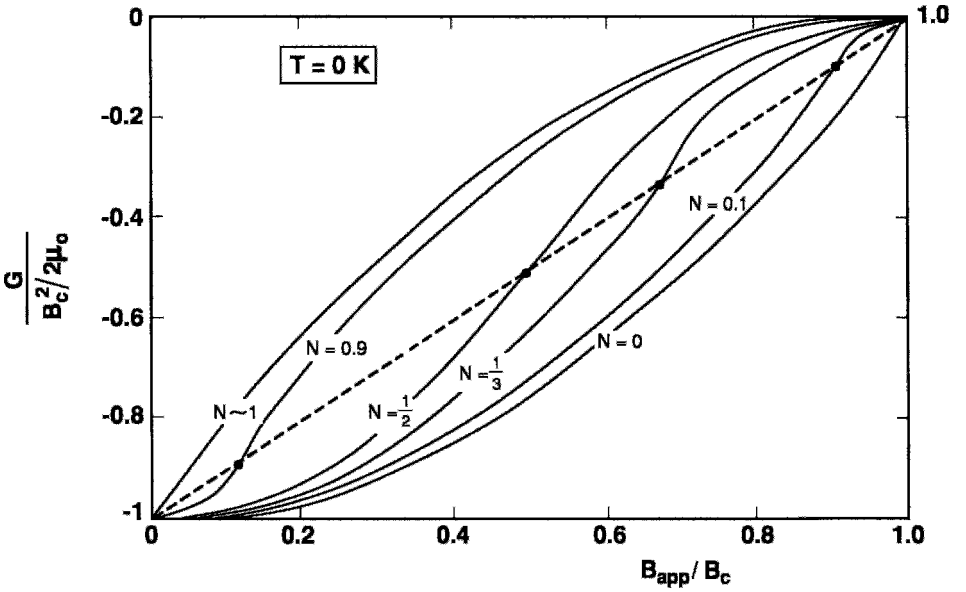

Figure 11.8 Dependence of the Gibbs free energy G on the applied magnetic field B_{app} for six values of the demagnetization factor, N(0, 0.1, 1/3, 1/2, 0.9, and ≈ 1), all at $T = 0$ K. Equations (11.35) were used to plot the curves.

Eq. (6.19) found from the Ginzburg–Landau theory and indicated in Fig. (6.2b).

If we define two normalized quantities

$$g(b) = G(B_{app})/[B_c^2/2\mu_0], \qquad (11.34a)$$

$$b = B_{app}/B_c, \qquad (11.34b)$$

Eqs. (11.29) and (11.31) become, respectively, for the superconducting and intermediate regions at $T = 0$,

$$g(b) = -1 + \frac{b^2}{1-N} \qquad 0 < b < 1-N, \qquad (11.35a)$$

$$g(b) = \frac{-(1-b)^2}{N} \qquad 1-N < b < 1, \qquad (11.35b)$$

with the special values

$$g(b) = \begin{cases} -1 & b = 0 \\ -N & b = 1-N \\ 0 & b = 1 \end{cases} \qquad (11.36)$$

at the boundaries of the various regions.

Equations (11.35) are plotted in Fig. 11.8 for the cases of parallel geometry ($N = 0$), a cylinder in a parallel field ($N = 0.1$), a sphere ($N = \frac{1}{3}$), a long cylinder in a perpendicular field ($N = \frac{1}{2}$), and a disk in a perpendicular field ($N = 0.9$, $N \approx 1$). We see from this figure that a disk or flat plate is in the intermediate state for almost all applied fields below B_c. (This will be discussed in Section VIII.) The transformation from the superconducting to the intermediate state occurs when G crosses the dashed line of unit slope in Fig. 11.8. For each case the superconducting state exists at lower fields (the curve for G below the dashed line in the figure), while the intermediate state exists above the line.

Figure 11.8 presents plots of the Gibbs free energy from Eqs. (11.35) versus the applied field for several demagnetization factors at $T = 0$. Related figures in Chapter 4 (Figs. 4.10, 4.11, 4.15, and 4.19) present plots of the Gibbs free energy versus temperature for several applied fields with $N = 0$.

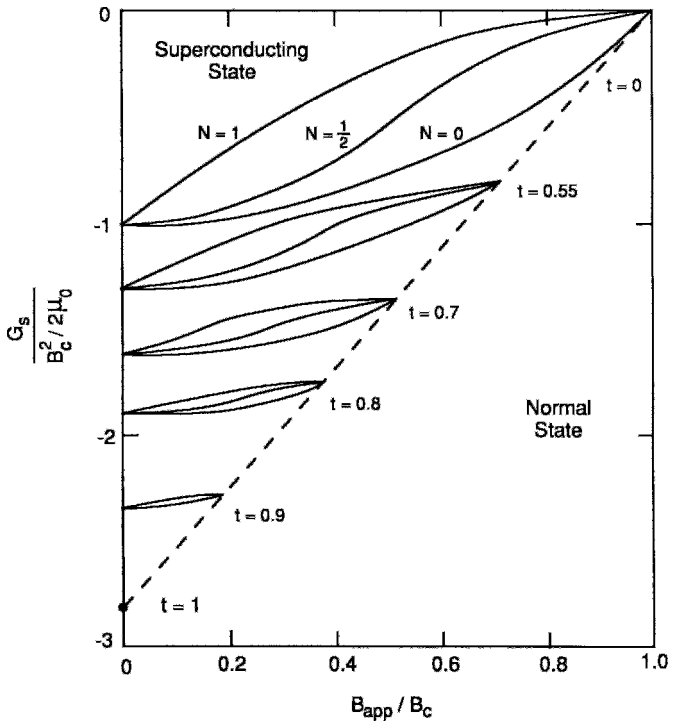

Figure 11.9 Dependence of the Gibbs free energy G on the applied magnetic field B_{app} for demagnetization factors $N = 0$, $\frac{1}{2}$, and 1 at several reduced temperatures $t = T/T_c$, as indicated in Fig. 11.10. The sample is in the superconducting or mixed state to the upper left of the dashed line and in the normal state to the lower right of the line. The figure is drawn for the condition $\mu_0 \gamma\, T_c^2/B_c^2 = 1/\alpha = 2.8$.

Problem 8 shows how to combine the relevant expressions—(11.35) for $T = 0$, and (4.51) for $N = 0$—to obtain more general expressions that are valid in the superconducting and intermediate states when all three quantities T, B_{app}, and N have nonzero values. Using these results, the Gibbs free energy $G(B_{app})$ for $N = 0$, $\frac{1}{2}$, and 1 is plotted in Fig. 11.9 versus the applied field for the reduced temperatures $t = T/T_c = 0$, 0.55, 0.7, 0.8, 0.9, and 1.0, as indicated in Fig. 11.10. We see from these plots that when the temperature is increased, the range of applied fields over which the material superconducts decreases. However, the fraction of this range that is in the intermediate state remains the same since it depends only on the demagnetization factor.

VII. BOUNDARY-WALL ENERGY AND DOMAINS

We have been discussing the field configurations and the Gibbs free energy in superconductors without taking into account the details of the resulting domains. In this and the following two sections we will discuss these domains and their significance. We begin with the case of a Type I superconductor placed in an applied magnetic field which is in the intermediate range (11.15), and then comment on a Type II superconductor in the mixed state with $B_{c1} < B_{app} < B_{c2}$.

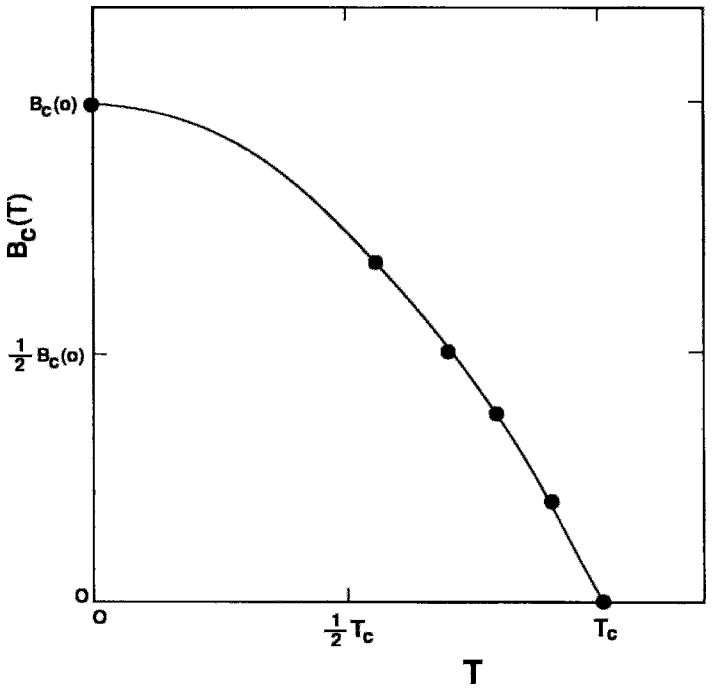

Figure 11.10 Dependence of the critical field $B_c(T)$ of a Type I superconductor on temperature. The points on the curve designate the values of the critical fields for the reduced temperature points indicated on the dashed line of Fig. 11.9.

We adopt the model of a Type I superconductor in the intermediate state that splits into domains of normal material with $\chi \approx 0$ embedded in pure superconducting regions with $\chi = -1$. The boundary between these regions contains a density of magnetic energy $B_c^2/2\mu_0$. The superconducting regions exclude the magnetic field B_{in} and are lower in energy because of the Cooper pair condensation energy. The super electron density n_s extends into the normal region by a distance equal to the coherence length ξ. The magnetic field within the boundary, which is of thickness ξ, contributes a positive energy the magnitude of which is diminished by the effect of the penetration depth λ associated with the decay of the magnetic energy. As a result of this effect, the boundary is effectively shortened, and has thickness

$$d_{bound} \approx (\xi - \lambda). \tag{11.37}$$

The overall energy density per unit area of the boundary layer has the value

$$E_{bound} = \left(\frac{B_c^2}{2\mu_0}\right) d_{bound} \tag{11.38}$$

for a Type I superconductor in the intermediate state.

For Type II superconductors, λ exceeds ξ and the effective domain wall thickness from Eq. (11.37) is negative, so that the boundary energy is negative. In other words, the boundary wall energy is positive for small κ and negative for large κ, where $\kappa = \lambda/\xi$ is the Ginzburg–Landau parameter. For large κ it becomes energetically favorable for the superconducting material to split into domains of large magnetic field strength with positive energies and surrounding transition

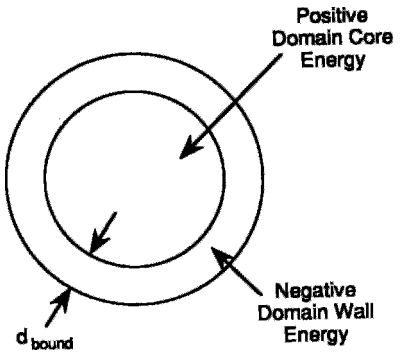

Figure 11.11 Domain core in the normal state with positive energy surrounded by a transition layer boundary of thickness d_{bound} with negative energy for the case $\kappa > 1/\sqrt{2}$.

regions of negative boundary energy, as shown in Fig. 11.11. The crossover between the positive and negative wall energies actually occurs at $\kappa = 1/\sqrt{2}$, so that domain formation becomes energetically favorable for $\kappa > 1/\sqrt{2}$. For the mixed state, which occurs for $\kappa > 1/\sqrt{2}$, the "domains" are, of course, vortices with cores of normal material, as sketched in Fig. 12.7. This energy argument makes it plausible to conclude that the mixed or vortex state forms in Type II superconductors, which have $\kappa > 1/\sqrt{2}$, but does not form in Type I superconductors.

VIII. THIN FILM IN APPLIED FIELD

Many studies have been carried out with films that are thin in comparison with their length and width. When such a material is placed in a magnetic field B_{app} that is oriented perpendicular to its surface, the field penetrates in the intermediate state, as shown in Fig. 11.12. We illustrate the case for $N = \frac{5}{6}$, so the factor $1 - N = \frac{1}{6}$ for this film. Figures 11.13–11.16 show plots of Eqs. (11.10)–(11.19) giving the dependences of B_{in}, H_{in}, M, and χ, respectively, on the applied field. The great extent of the intermediate state is evident from these plots.

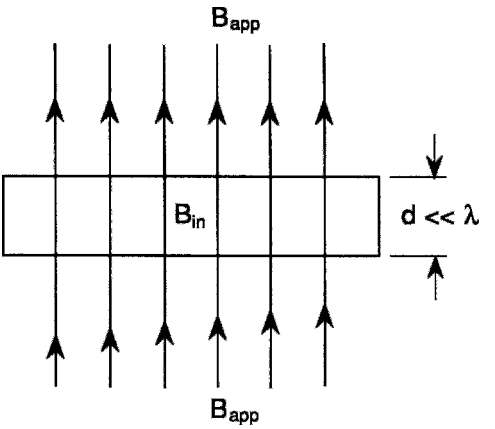

Figure 11.12 Magnetic field penetration through a superconducting thin film whose thickness d is small compared to the penetration depth λ.

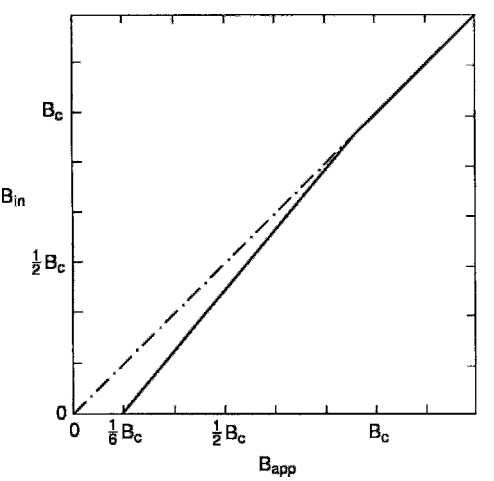

Figure 11.13 Internal magnetic field B_{in} in a superconducting film ($N = 5/6$) as a function of the applied field B_{app} (Eqs. (11.11) and (11.16)) (cf. case of a sphere, Fig. 11.4). Here and in Figs. 11.14 and 11.15, the unit slope line ($- \cdot - \cdot -$) represents the behavior for zero demagnetization factor ($N = 0$).

Let us examine in more detail the case of a disk-shaped film of radius a and thickness $t \ll a$. We know from Table 5.1 and Problem 6 of Chapter 5 that this film has a demagnetization factor $N \approx 1 - \frac{1}{2}\pi t/a$, so that, from Eq. (11.15), the intermediate state extends over the range

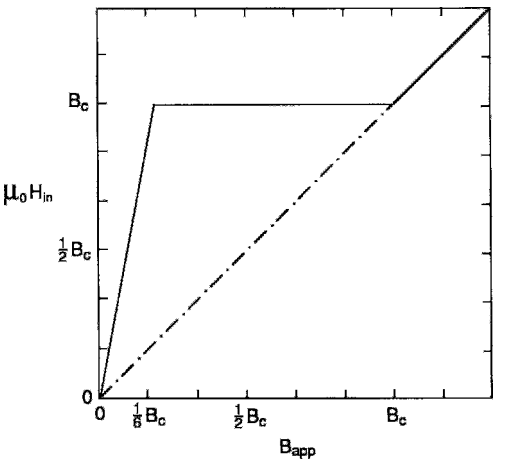

Figure 11.14 Internal field $H_{\rm in}$ (Eqs. (11.12) and (11.17)) in the film sketched in Fig. 11.12.

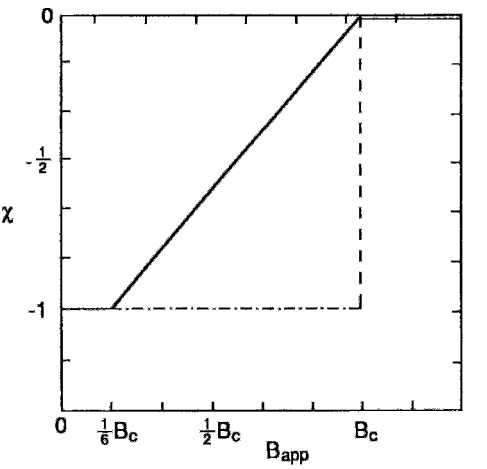

Figure 11.16 Magnetic susceptibility χ (Eqs. (11.14) and (11.19)) of the film sketched in Fig. 11.12.

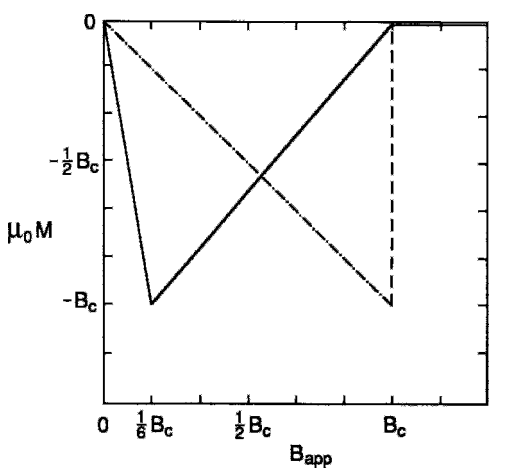

Figure 11.15 Magnetization M (Eqs. (11.13) and (11.18)) for the film sketched in Fig. 11.12.

$$\frac{\frac{1}{2}\pi t}{a} < \frac{B_{\rm app}}{B_{\rm c}} < 1. \qquad (11.39)$$

This means that a superconducting film with a thickness-to-diameter ratio $t/2a = 10^{-3}$ and a lower critical field $B_{\rm c1} = 50\,{\rm mT}$ is driven to the intermediate state by the Earth's typical field of $50\,\mu{\rm T}$. The internal field from Eq. (11.16),

$$B_{\rm in} = B_{\rm app} - \frac{\frac{1}{2}\pi t}{N_a}(B_{\rm c} - B_{\rm app}), \qquad (11.40)$$

is close to the applied field, $B_{\rm in} \approx B_{\rm app}$, over most of the intermediate state to a much greater extent than that shown in Fig. 11.13, since $\pi t/2N_a \ll \frac{1}{6}$. When the film thickness becomes comparable with or less than the penetration depth, the situation is more complicated, however.

IX. DOMAINS IN THIN FILMS

We just saw that a thin film in a perpendicular field below $T_{\rm c}$ is in the intermediate state for almost all applied fields below $B_{\rm c}$. We will proceed to investigate the nature of this state. From the boundary conditions, the macroscopic B fields are continuous across the boundary, as shown in Fig. 11.12.

$$B_{\rm in} = B_{\rm app}. \qquad (11.41)$$

If we take into account the domain structure, a fraction of the material $f_{\rm n}$ will be normal material with $B_{\rm in} = B_{\rm c}$ and a fraction $f_{\rm s}$

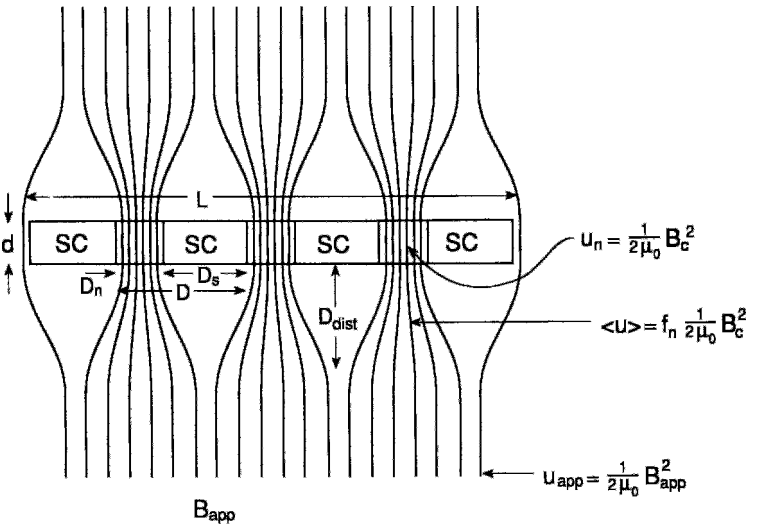

Figure 11.17 Passage of magnetic field lines B of a perpendicular applied field through normal domain regions with diameter D_n of a superconducting thin film. The distortion distance D_{dist}, normal regions in which $B_{in} = B_c$, and superconducting regions (SC) in which $B_{in} = 0$ are shown. The energy densities in the normal regions u_n, in regions far from the film u_{app}, and in regions near the film $\langle u \rangle$ are indicated.

will be perfectly superconducting with $B_{in} = 0$, where

$$f_s + f_n = 1. \tag{11.42}$$

The magnetic field avoids the superconducting parts and passes through the normal regions, as shown in Fig. 11.17. This means that

$$B_{in} = f_n B_c, \tag{11.43}$$

so that

$$B_{app} = f_n B_c, \tag{11.44}$$

from Eq. (11.41). The boundaries or domain walls between the normal and superconducting regions also contain the field B_c, but it is assumed that the fraction of material f_w in the domain walls is small and can be neglected. The figure gives the energy density $u = B^2/2\mu_0$ at three positions in the field.

Figure 11.18 sketches the domain structure in a thin film of length L, width W, and thickness d that is oriented perpendicular to the direction of the applied field. The figure

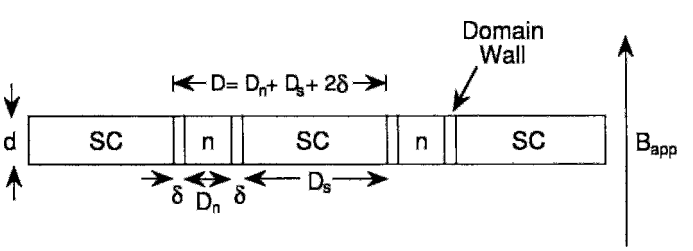

Figure 11.18 Thin film in a perpendicular applied magnetic field showing normal regions (n) of length D_n, superconducting regions (SC) of length D_s, and domain walls of thickness δ separating these regions. The repetition length $D = D_n + D_s + 2\delta$ is also shown.

shows normal regions of width D_n and superconducting regions of width D_s separated by domain walls of thickness δ. In drawing this figure we have assumed that the domains are all the same size and equally spaced. This simplifies the mathematics without changing the physics of the situation. We can define a repetition length D for the domain pattern

$$D_s + D_n + 2\delta = D, \tag{11.45}$$

where each domain has two walls. If we neglect the thickness of the domain walls, as is done on Fig. 11.17, by assuming that $\delta \ll D_s,\ D_n$, we can write

$$D_s + D_n = D, \tag{11.46}$$

where

$$\begin{aligned} D_s &= f_s D, \\ D_n &= f_n D. \end{aligned} \tag{11.47}$$

The number of domains N_d is equal to the length L divided by the domain repetition length D:

$$N_d = L/D. \tag{11.48}$$

The magnitude of the B field is appreciably distorted from its far value $\mathbf{B}_{app}$ only within a distance D_{dist} of the surface given by

$$1/D_{dist} = 1/D_s + 1/D_n, \tag{11.49}$$

and with the aid of Eq. (11.47) we obtain

$$D_{dist} = f_s f_n D \tag{11.50}$$

for the field distortion distance indicated in Fig. 11.17.

Let us try to justify Eq. (11.49) by a hydrodynamic analogy. Consider the B lines as the flow lines of a fluid passing through slots or holes in a barrier, where the density of flow lines represents the speed. The speed changes appreciably near the holes only if the diameter of the holes is small and near the material between the holes only when the holes take up most of the space, as shown in Fig. 11.19. Therefore $D_{dist} \approx D_n$ in the former case, when $D_n \ll D_s$, whereas $D_{dist} \approx D_s$ in the latter case, when $D_n \gg D_s$. Figure 11.19 illustrates the cases $D_s = 3D_n,\ D_s = D_n$, and $D_s = \frac{1}{3}D_n$.

The distortion of the applied magnetic field brought about by the presence of the film, as sketched in Figs. 11.17 and 11.19, serves to increase the Gibbs free energy G of the system. Figure 11.17 shows the magnetic energy densities of each region. The Gibbs free energy is also increased by the magnetic energy stored in the domain walls. A long repetition length reduces the number of domains and decreases the domain wall energy, whereas a short repetition length lessens the distortion of the field and decreases the field distortion energy at the expense of more domain wall energy. An intermediate domain repetition length is best, and we will derive an expression for the optimum value of D.

The magnetic energy stored in each pair of domain walls $2W\delta d(\frac{1}{2}B_c^2/\mu_0)$ gives for the total domain wall contribution to the Gibbs free energy

$$G_w = 2N_d(W\delta d)\left(\frac{1}{2}B_c^2/\mu_0\right) \tag{11.51}$$

$$= 2(WL\delta d/D)\left(\frac{1}{2}B_c^2/\mu_0\right), \tag{11.52}$$

where we have used Eq. (11.48). The change in field energy arises from the difference between energy density near the surface, $\frac{1}{2}f_n B_c^2/\mu_0$, and the energy density far from the film, $\frac{1}{2}B_{app}^2/\mu_0$, where the factor f_n in the former expression takes into account the fact that this field exists only near the normal regions, as shown in Figs. 11.17 and 11.19. This gives for the magnetic field contribution to the Gibbs free energy

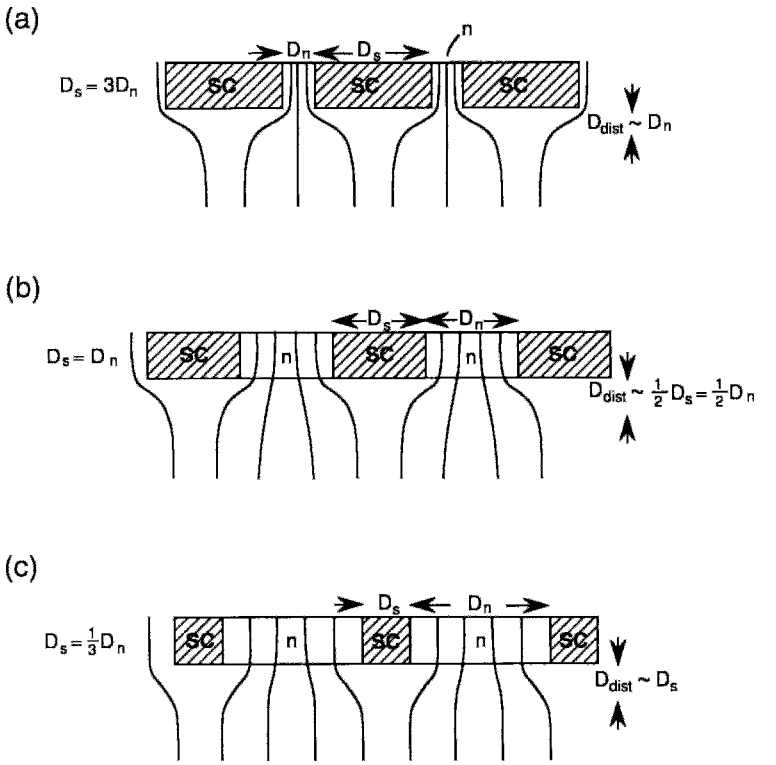

Figure 11.19 Illustration of the distortion distance D_{dist} for the cases $D_s = 3D_n$ with $D_{dist} \approx D_n$(a), $\frac{1}{2}D_n = \frac{1}{2}D_s \approx D_{dist}$(b), and $D_s = \frac{1}{3}D_n$ with $D_{dist} \approx D_s$(c), where the wall thickness δ is negligible, i.e., $\delta \ll D_n,\ D_s$.

$$G_f = 2WLD_{dist}\left[f_n\left(\frac{1}{2}B_c^2/\mu_0\right) - \left(\frac{1}{2}B_{app}^2/\mu_0\right)\right] \quad (11.53)$$

$$= 2(WLD)f_s^2 f_n^2\left(\frac{1}{2}B_c^2/\mu_0\right), \quad (11.54)$$

where we have used Eqs. (11.42), (11.44), and (11.50). The total Gibbs free energy G is the sum of these two, namely $G = G_w + G_f$. Per unit area of film we have

$$G/WL = 2\left(\frac{1}{2}B_c^2/\mu_0\right)(\delta d/D + f_s^2 f_n^2 D). \quad (11.55)$$

The domain repetition distance D obtained by minimizing the total free energy per unit area,

$$\frac{dG}{dD} = 0, \quad (11.56)$$

is equal to

$$D = (d\delta)^{1/2}/f_s f_n, \quad (11.57)$$

where the product $f_s f_n$ is easily deduced from Eqs. (11.42) and (11.44):

$$f_s f_n = B_{app}(B_c - B_{app})/B_c^2. \quad (11.58)$$

The thinner the film, the smaller the value of D and the greater the number of domains. D is large at both ends of the range, where either f_n or f_s is small, corresponding to $B_{app} \ll B_c$ and $B_{app} \approx B_c$, respectively. It is smallest in the middle, where $f_n = f_s = \frac{1}{2}$ and $B_{app} = \frac{1}{2}B_c$.

This derivation assumes that the domain wall thickness δ is much less than the domain sizes D_n and D_s. It does not take into account how the surface energy depresses the value of the critical field. When the film thickness is much greater than the domain wall, $d \gg \delta$, the critical field B_c is shifted to a lower value B_c' given by (Tinkham 1996, p. 29)

$$B_c' = [1 - 2(\delta/d)^{1/2}]B_c \qquad d \gg \delta. \quad (11.59)$$

A similar depression of the lower critical field B_{cl} occurs with Type II superconductors.

X. CURRENT-INDUCED INTERMEDIATE STATE

The intermediate state that we have been discussing arose from the presence of a magnetic field that exceeded the critical field at the surface of the superconductor. We will now examine the intermediate state that forms when a transport current from a current generator produces a magnetic field at the surface of a superconducting wire that exceeds the critical field. In this section we simplify the notation by writing I instead of I_T for the transport current.

We know from Eq. (2.42) that the magnetic field at the surface of a wire of radius a carrying a current I is in the ϕ direction with magnitude

$$H = I/2\pi a. \quad (11.60)$$

This surface field is independent of the distribution of current density inside the wire. When the surface field reaches a particular value, called the critical field $B_c = \mu_0 H_c$, we say that the transport current has attained its critical value I_c, corresponding to

$$H_c = I_c/2\pi a. \quad (11.61)$$

If the current exceeds the critical value, the magnetic field at the surface will exceed H_c and the wire will no longer be able to remain a perfect superconductor. This destruction of pure superconductivity by a transport current is called the *Silsbee effect*. If the wire were to respond by going normal at the surface, the superconducting core would constitute a wire of even smaller radius $r < a$ carrying the same amount of current. From Eq. (11.60) it is clear that the field at the surface of the wire would then be even larger than the field that drove the surface normal. Following this line of reasoning, the entire wire would become normal. There is, however, a second solution to the problem, proposed by F. London (1937; see also F. London, 1950), whereby the wire is assumed to have a core of radius a_i that is in an intermediate state and an outer layer that is normal. We will show how this could occur.

When the total current I exceeds I_c, part of the current I_n flows in the outer normal region and the remainder I_i along a parallel path through the core, which is in the intermediate state,

$$I = I_n + I_i, \quad (11.62)$$

as indicated in Fig. 11.20. The current density J_n in the outer layer is constant, with a value given by

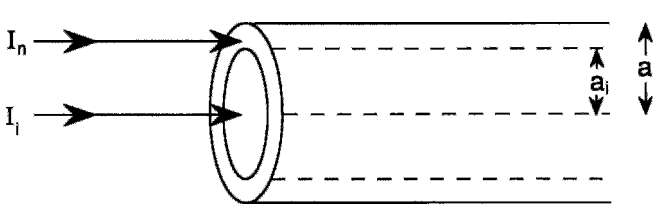

Figure 11.20 Division of applied transport current flowing through a superconducting wire of radius a into a portion I_n flowing in the outer normal region and a portion I_i in the intermediate state flowing in the core of radius a_i.

$$J_n = \frac{I_n}{\pi(a^2 - a_i^2)} \qquad a_i < r < a. \tag{11.63}$$

For this normal current I_n to flow there must be a potential difference between the two ends of the wire, which means that there is an axial electric field E in the normal layer given by Eq. (1.21),

$$E = J_n \rho_n, \tag{11.64}$$

where both J_n and E are unknown.

The intermediate state has regions of superconducting material and regions of normal material, so there is also an electric field $E(r)$ present. All the magnetic fields that are present are independent of time, so from the Maxwell curl relation $\nabla \times \mathbf{E} = -\partial \mathbf{B}/\partial t = 0$, E is also independent of the radial distance r. Therefore, $E(r)$ has the same value E in the normal and in the intermediate state region, and we can write an analogue of Eq. (11.64) for the intermediate state,

$$E = J_i(r)\rho_i(r) \qquad 0 < r < a_i, \tag{11.65}$$

where $J_i(r)$ satisfies the boundary condition for continuity of the current density at $r = a_i$. Thus we obtain

$$J_i(a_i) = J_n, \tag{11.66}$$

$$\rho_i(a_i) = \rho_n. \tag{11.67}$$

We saw in Section II that the intermediate state is characterized by the pinning of the internal field H_{in} at the critical value,

$$H_{in} = H_c \qquad 0 < r < a_i. \tag{11.68}$$

This permits us to write Eq. (11.61) for the intermediate state,

$$H_c = I_i(r)/2\pi r \qquad r < a_i, \tag{11.69}$$

where

$$I_i(r) = \int_0^r J_i(r)(2\pi r)dr. \tag{11.70}$$

We show in Problem 10 that the current density in the intermediate state is given by

$$J_i(r) = (a_i/r)J_n \qquad r \le a_i, \tag{11.71}$$

as illustrated in Fig. 11.21, where

$$H_c = J_n a_i. \tag{11.72}$$

Combining Eqs. (11.64) and (11.72) gives for the radius of the intermediate state region

$$a_i = H_c\, \rho_n/E, \tag{11.73}$$

which depends on the applied current in the manner shown in Fig. 11.22. The resistivity in the intermediate state is proportional to the radius r,

$$\rho_i(r) = \left(\frac{r}{a_i}\right)\rho_n \qquad r \le a_i, \tag{11.74}$$

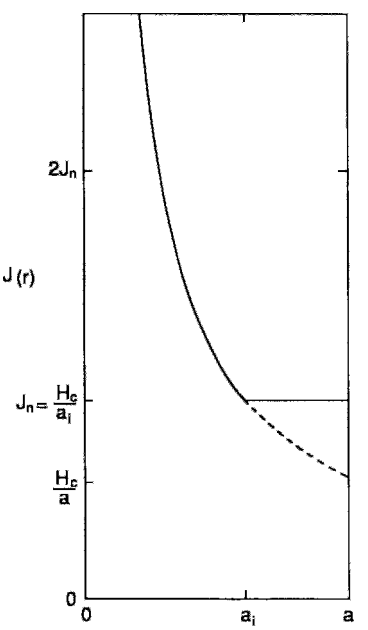

Figure 11.21 Dependence of the current density $J(r)$ on distance r from the center in a superconducting wire of radius a that is in the intermediate state. $J(r)$ decreases with r in the intermediate-state core region of radius a_i and has a constant value $J_n = H_c/a_i$ in the outer layer, where $a_i \le r \le a$, as shown. The extrapolation (– – –) of the core region behavior of $J(r)$ to the value H_c/a at the surface is indicated.

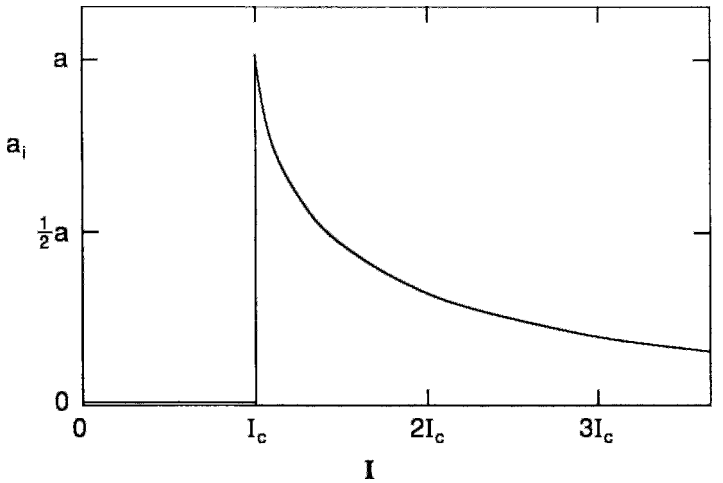

Figure 11.22 Dependence of the core radius a_i of a superconducting wire on the applied transport current I. The intermediate state occurs for transport currents exceeding the value $I_c = 2\pi a H_c$.

as shown in Fig. 11.23 (see Problem 11). This means that the longitudinal path length of the current through the normal region at the radius r is proportional to r. This fits the configuration illustrated in Fig. 11.24, which had been suggested by F. London. In this configuration the core has a sequence of conical regions of superconducting material arranged along the axis with interlaced regions of normal material.

It is shown in Problem 16 that the total current flowing through the wire is given by

$$I = \pi(a^2 + a_i^2)J_n. \tag{11.75}$$

By Eqs. (11.64), (11.72), and (11.73), this may be written as a quadratic equation in terms of the electric field,

$$I(E) = \pi a^2 \frac{E}{\rho_n} + \pi H_c^2 \frac{\rho_n}{E}, \tag{11.76}$$

which has the solution

$$E = \frac{1}{2} I \frac{\rho_n}{\pi a^2} \left\{ 1 \pm \left[1 - (I_c/I)^2 \right]^{1/2} \right\}. \tag{11.77}$$

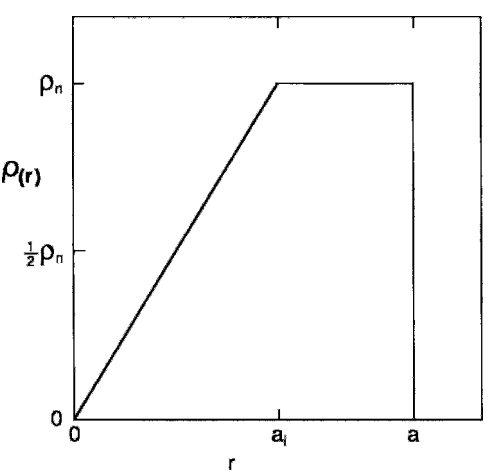

Figure 11.23 Dependence of the resistivity $\rho(r)$ of a superconducting wire in the intermediate state on the radial distance r from the center of the wire. Note that $\rho(r)$ increases linearly with r in the intermediate-state core region, where $r < a_i$, and has the normal state value ρ_n in the outer region, $r > a_i$, of the wire.

The average resistivity $\langle \rho \rangle$ is $E/\langle J \rangle$ and the average current density $\langle J \rangle$ through the wire is $I/\pi a^2$, so we can write

$$\langle \rho \rangle = E(\pi a^2/I), \tag{11.78}$$

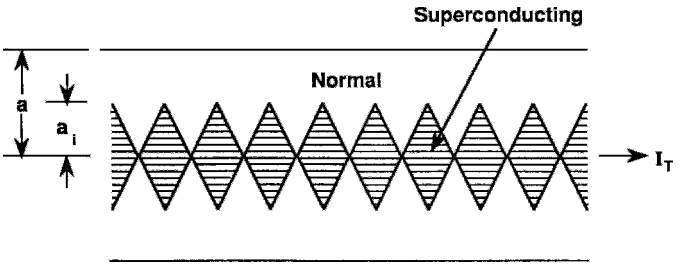

Figure 11.24 London model for the intermediate-state structure of a wire of radius a carrying a transport current in excess of the critical value $I_c = 2\pi a H_c$, where a_i is the radius of the core region (F. London, 1937, 1950).

and Eq. (11.77) gives us the London model expression

$$\frac{\langle\rho\rangle}{\rho_n} = \frac{1}{2}\left\{1+\left[1-\left(\frac{I_c}{I}\right)^2\right]^{1/2}\right\}, \quad (11.79)$$

which is valid for $I > I_c$. The positive sign has been selected in Eq. (11.77) because it gives the proper asymptotic behavior of $\langle\rho\rangle \to \rho_n$ for $I \gg I_c$.

The various resistivity results in the London model can be grouped together as follows:

$$\frac{\langle\rho\rangle}{\rho_n} = \begin{cases} 0 & I < I_c \\ \frac{1}{2} & I = I_c \\ \frac{1}{2}\left\{1+\left[1-(I_c/I)^2\right]^{1/2}\right\} & I > I_c \\ 1-\frac{1}{4}(I_c/I)^2 & I \gg I_c. \end{cases} \quad (11.80)$$

We see that at the point $I = I_c$ the resistivity jumps discontinuously from 0 to the value $\frac{1}{2}\rho_n$. It then slowly approaches ρ_n for higher applied currents in accordance with Eq. (11.80), as shown in Fig. 11.25. Experimental data, such as those plotted in the figure, ordinarily show a larger jump of $\frac{2}{3}$ or more at $I = I_c$ instead of $\frac{1}{2}$. A refined version

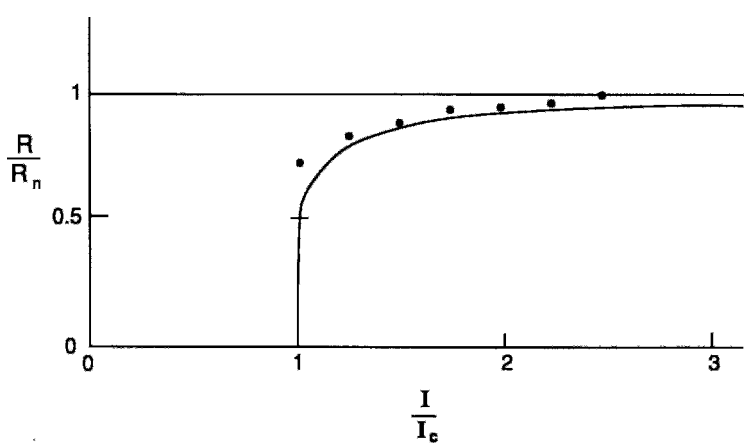

Figure 11.25 London model dependence of the resistance of the intermediate state of a superconducting wire on the value of the transport current I for a fixed temperature T. Experimental data on indium wires at 2.02 K (Watson and Huebener, 1974) are shown for comparison.

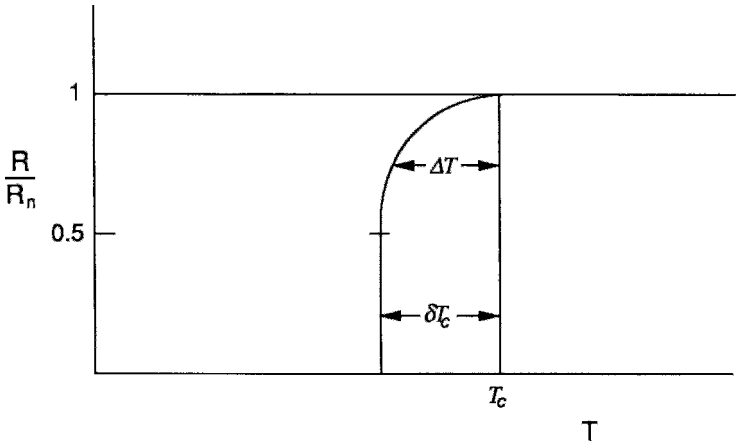

Figure 11.26 Temperature dependence of the resistance in the intermediate state of a current-carrying wire showing T_c decreasing by the variable amount ΔT for resistance in the range $\frac{1}{2}R_n < R < R_n$, and by a fixed amount δT in the range $R < \frac{1}{2}R_n$. The figure is drawn for the case of a constant applied transport current.

of the London model developed by Baird and Mukherjee (1968, 1971) exhibits a larger jump and fits the data better (Huebener, 1979, p. 213; Watson and Huebener, 1974). It is interesting that the intermediate state persists above I_c, and that some superconductivity is predicted to remain in the core region for all finite currents.

Tinkham (1996, p. 34) shows that there is also a dependence of the resistivity on temperature, $\Delta T = T_c - T$, in the neighborhood of the transition temperature, and this is shown in Fig. 11.26.

We have discussed the current-induced intermediate state for superconducting wire of circular cross-section. The same phenomenon can occur with samples of other shapes, such as tapes or thin films, but the mathematical analysis can be more complex.

XI. RECENT DEVELOPMENTS IN TYPE I SUPERCONDUCTIVITY

A. History and General Remarks

The intermediate state has a long history beginning with the pioneering works of Landau (1927, 1038) and continuing to the present day (Reisin and Lipson, 2000, Prozorov *et al.*, 2005, Choksi *et al.*, 2004, Goldstein *et al.*, 1996, Dorsey and Goldstein, 1998, Narayan, 1998, Hernandez and Dominguez, 2002, De Luca, 2000). The topic has been intensively studied from the early 60 s for about 30 years when most of the classical results were obtained and the thermodynamic interpretation was developed. However, the literature of that period, and especially later periods, is full of observations incompatible with the Landau laminar model (Solomon and Harris, 1971, Livingston and DeSorbo, 1969). These results were mostly interpreted to be due to sample imperfections, particular shape, or other special (vs. general thermodynamic) experimental circumstances.

The Type-I problem involves both microscopic mechanisms of superconductivity and the physics of highly nonlinear systems, so exact mathematical solutions do not exist, and various approximations have to be used. Early models based on free energy minimization were insensitive to the manner in which the intermediate

state was prepared, and could not predict the equilibrium *pattern* of flux penetration. During the past decade many new ideas and methods in physics and mathematics of complex and nonlinear systems were developed. These advances resulted in more general approaches to the intermediate state (Liu *et al*., 1991, Hernandez and Dominguez, 2002, Reisin and Lipson, 2000, Dorsey and Goldstein, 1998, Goldstein *et al*., 1996, Jeudy *et al*., 2004, Prozorov *et al*., 2005). In particular, recent contributions considered the evolution of arbitrarily-shaped domains through a current-loop approach (Dorsey and Goldstein, 1998, Goldstein *et al*., 1996, Reisin and Lipson, 2000), analyzed the kinetics of the transition as an important factor determining the structure (Liu *et al*., 1991, Frahm *et al*., 1991), studied the transformation of a tubular to a laminar structure in thin films (Jeudy and Gourdon, 2006), and showed the existence of a topological hysteresis (Prozorov *et al*., 2005).

Applications of the developed ideas are found in many scientific disciplines such as superconductivity and superfluidity, hydrodynamics, reaction-diffusion problems, oceanography, astrophysics, meteorology, combustion, geophysical and biological dynamics, and semiconductors (Walgraef, 1997, Strogatz, 1994, Metlitski, 2005). There is an intense ongoing research effort to explain the formation and evolution of complex patterns observed in these systems. The selection of one pattern over another is an inherently nonlinear evaluation. Amazing similarities between hexagonal structures observed in Type-I superconductors (see Fig 11.27). and some chemical and hydraulic systems provide further evidence of the intimate connection of their formation. Likewise, a well-known Landau laminar structure is not unique for Type-I superconductors. Figure 11.28 shows two very similar patterns. Figure 11.28a shows a pattern obtained as a result of a photochemical reaction after

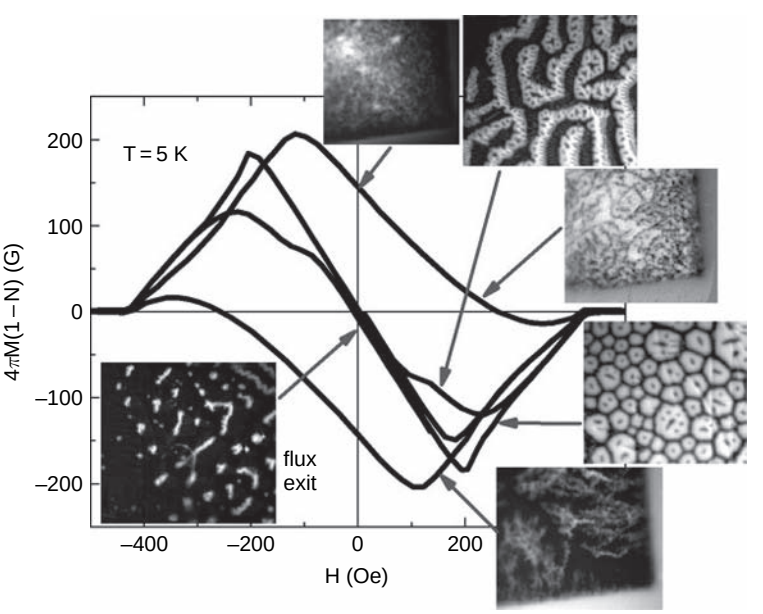

Figure 11.27 Magneto-optical images of the intermediate state (at magnetic field values indicated by arrows) in pure lead, shown together with DC magnetization loops measured at 5 K. The wide hysteretic loop was measured in a cold-worked sample, whereas the inner loop was obtained in a stress-free sample (Prozorov *et al*., 2005).

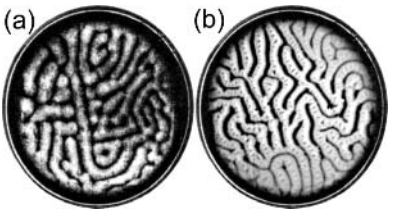

Figure 11.28 Comparison of patterns observed in (a) a photochemical reaction upon irradiation of mercury dithizonate with visible light (from (Walgraef, 1997), page 28) and (b) a laminar intermediate state pattern observed in stress-free lead upon flux exit (Prozorov *et al*., 2005).

mercury dithizonate was irradiated with visible light (picture reproduced from (Walgraef, 1997)), whereas Fig. 11.28b shows a laminar intermediate state pattern in a stress-free pure lead sample upon magnetic flux exit (Prozorov *et al*., 2005). Another example involves the transformation of a closed topology to an open topology patterns, which occurs in one system at different external conditions. Figure 11.29a,b shows an experimental realization of the Turing instability mechanism, based on a nonlinear interaction between reaction and diffusion in a chlorite-iodide-malonic acid reaction in gels. Figure 11.29c,d shows the intermediate state patterns in pure lead upon flux entry (c) and exit (d). Furthermore, closed and open topologies can coexist within one sample. We present two examples of such coexistence: Figure 11.30a depicts the results of a numerical analysis of Hopf bifurcation patterns, whereas Fig. 11.30b shows the transformation of a tubular phase into a laminar structure in pure lead.

To summarize, as of today, the problem of the formation and evolution of the intermediate state in samples of arbitrary shape (especially non-ellipsoidal) and for the arbitrary values of the G-L parameter (as well as other materials parameters) has not yet been settled. Clearly, it cannot be deduced solely from energy minimization arguments,

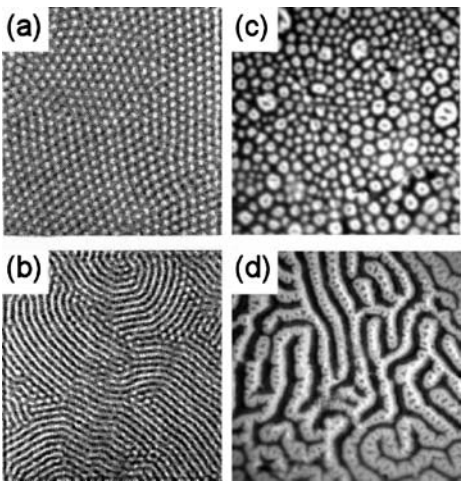

Figure 11.29 (a–b) Turing instability patterns observed in a disk gel reactor (Walgraef, 1997), and (c–d) intermediate state patterns in pure lead upon flux entry (c) and exit (d), after Ref. (Prozorov *et al*., 2005).

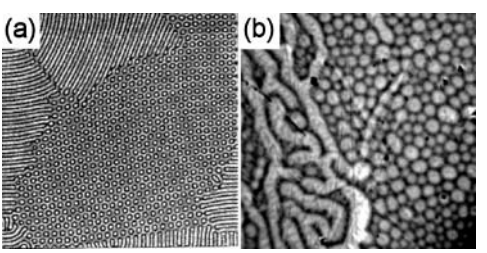

Figure 11.30 Coexistence of closed and open topologies within a single ample: (a) numerical solution of Hopf bifurcation patterns, and (b) disruption of a tubular phase by a defect.

including solving the non-linear G-L equations, and requires methods developed in the field of nonlinear complex systems. On the other hand, the systematic experimental investigation of the pattern formation in Type-I superconductors can influence other, sometimes quite remote, fields of science. An example is new concepts in the physics of neutron stars (Buckley *et al*., 2004). Another very important subject is pattern formation in highly nonlinear systems for which a Type-I superconductor is a perfect model system

(Coullet and Huerre, 1991, Choksi *et al.*, 2004, Walgraef, 1997). It provides a set of characteristics, such as a very small effective mass of the S-N boundary, and easy manipulation by the external magnetic field, unachievable in other, mostly chemical diffusive systems.

B. The Intermediate State

The intermediate state is formed in Type-I superconducting samples when the actual magnetic field at the sample's edge exceeds the critical field, H_c, which occurs for an applied magnetic field of $H = H_c(1 - D)$, and it disappears when the applied field reaches $H = H_c$ (Livingston and DeSorbo, 1969, Huebener, 2001). As illustrated in Fig. 11.31, there are four ways to arrive to a particular point on the magnetic field – temperature, H–T, phase diagram. These four ways are field cooling (FC or $(NI)_H$), zero-field cooling (ZFC or $(SI)_H$), and ascending and descending branches of the magnetization loop, $(SI)_T$ and $(NI)_T$, respectively. We utilize the notation developed in the early literature as it better reflects the specifics of the transition from a Meissner superconducting state (S), or a normal state (N), to an intermediate state (I).

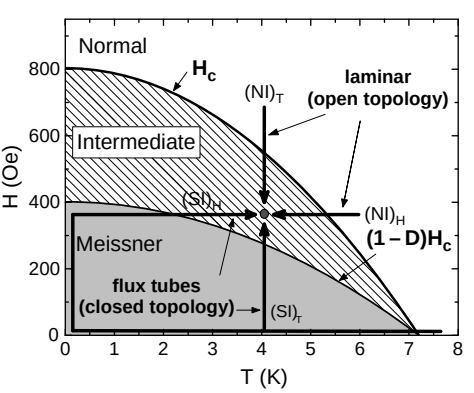

Figure 11.31 Four ways to obtain particular field and temperature responses on an $H-T$ phase diagram. The diagram for a rctangular crossection lead sample with demagnetization factor $D = 0.5$ is shown.

The uncertainty in understanding the formation of an intermediate state already begins at this point. The notion of the demagnetization factor is strictly applicable only to the samples of ellipsoidal shape (Osborn, 1945, Abrikosov, 1988). Only in this case does the magnetic field inside the sample remain uniform and equal to $H/(1 - N)$ (denoted D in Fig. 11.31). Direct visualization of the intermediate state is ordinarily carried out on samples with flat surfaces, usually slabs or disks. There is an ongoing discussion on the effects of this non-ellipsoidal geometry, with no consensus yet achieved (Huebener, 2001, Dorsey and Goldstein, 1998, Castro *et al.*, 1999, Castro *et al.*, 1997).

The thermodynamics of the intermediate state has been the subject of many works (Livingston and DeSorbo, 1969, Huebener, 2001, DeSorbo and Healy, 1964, Clem *et al.*, 1973, Choksi *et al.*, 2004, Farrell *et al.*, 1972). The conventional approach is to assume some geometrical pattern of the intermediate state, and then minimize its free energy by varying the geometrical parameters. The typical and most used structure is the Landau laminar pattern of alternating normal and superconducting regions. The free energy is assumed to consist of the condensation energy loss inside the normal domain, the S-N surface energy, the magnetic field energy, and energy associated with the distortion of the magnetic field outside the sample. The latter has often been analyzed in terms of interactions between the lamellae. The variety of the observed structures as well as the general difficulty of expressing the free energy by taking into account all terms inside and outside of the sample motivated various refinements of these models as well as some adjustments of the geometrical patterns, such as possible branching near the superconductor surface or the lamellae corrugation (Livingston and DeSorbo, 1969). The hexagonal pattern for the intermediate state was also

analyzed (Goren and Tinkham, 1971). The closed topology patterns in the form of flux tubes (typically carrying thousands of flux quanta) were also frequently observed and discussed (Huebener and Gallus, 1973, Huebener and Kampwirth, 1974, Huebener *et al*., 1974, Chimenti and Huebener, 1977, Buck *et al*., 1981, Pavlicek *et al*., 1981, Parisi *et al*., 1983, Fietz *et al*., 1984, Prozorov *et al*., 2005, Pavlicek *et al*., 1982, Livingston and DeSorbo, 1969, Huebener, 2001, Goren and Tinkham, 1971). Typical explanations included the edge barrier in (mostly) thin samples. Recent works concentrate more and more on the question of pattern formation in the intermediate state by studying the dynamics of the S-N (and N-S) transition, and/or considering systems that consist of nuclei that can evolve and change geometry upon interaction with the environment (e.g., the current-loop model) (Liu *et al*., 1991, Doelman and Harten, 1995, Indekeu and van Leeuwen, 1995, Goldstein *et al*., 1996, Castro *et al*., 1997, Dorsey and Goldstein, 1998, Reisin and Lipson, 2000, Blossey, 2001, Abreu and Malbouisson, 2004, Jeudy *et al*., 2004, Choksi *et al*., 2004, Prozorov *et al*., 2005).

It should be noted that we mostly discussed experimental works in which the intermediate state patterns were *directly observed.* There is also an extensive literature involving the use of various indirect techniques. While these works provide important contributions, especially in terms of the analysis and overall consistency of the results with theoretical models, it is difficult to consider particular topological features without literally viewing them.

C. Magneto-Optics with In-Plane Magnetization – a Tool to Study Flux Patterns

The magneto-optical technique is a powerful method for studying the distribution of the magnetic induction B on the surface of a superconductor. Appearing in the late 50 s (Alers, 1957) and greatly improved during the followed decade (Castro *et al*., 1999, Huebener, 1970), it has become a unique tool for the experimental study of these materials. The idea behind the technique is to place a transparent magnetic material (an indicator) on the surface of an object under study. Linearly polarized light propagating throughout the indicator and reflected back is rotated proportionally to the magnetization strength along the direction of travel (Faraday Effect). If an indicator is made of a soft magnetic material, the distribution of the magnetization inside the indicator mimics the distribution of the perpendicular component of the magnetic induction on the surface of the sample under study. Various indicators were used. Most known results obtained on visualization of flux patterns in Type-I superconductors in 60 s–70 s were obtained using Ce^{3+} salts and later EuS-EuF systems (Kirchner, 1973, Habermeier, 2004, Huebener and Clem, 1974, Huebener, 2001). Unfortunately, the former has a very low Verdet constant (how much 1 mm of thickness rotates the polarization plane per unit of magnetic field), and the latter systems have complicated magnetic transitions at low temperatures. Nevertheless, it was possible to successfully utilize these indicators for imaging the intermediate state (Alers, 1957, Kirchner, 1969, Kirchner, 1973, Huebener and Clem, 1974, Huebener, 2001). However, measurements of the actual magnetic induction were too difficult. Another disadvantage of these indicators was the need to deposit them directly onto the surface of superconductors. For reviews of the magneto-optical technique and its applications, see Ref. (Jooss *et al*., 2002, Huebener, 2001, Habermeier, 2004, Livingston and DeSorbo, 1969).

The widespread use of magneto-optics for studying high-T_c superconductors began with the introduction of ferrimagnetic in-plane indicators (Dorosinskii *et al*.,

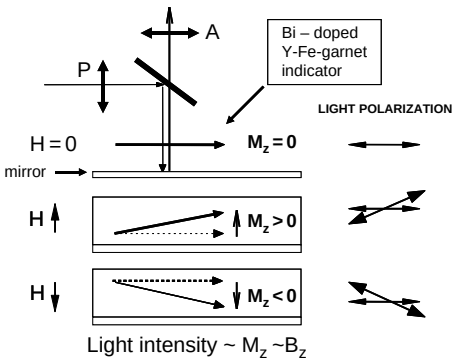

Figure 11.32 Principle of magneto-optical visualization using a Y-Fe-garnet indicator with in-plane spontaneous magnetization.

1993, Vlasko-Vlasov *et al*., 1992, Castro *et al*., 1999), which have a spontaneous magnetization lying in the indicator plane. Figure 11.32 illustrates the principles of operation of such magneto-optical system. A light beam passes through a linear polarizer (P), propagates through the optically transparent indicator film, reflects from a mirror deposited on the bottom surface of an indicator, and finally arrives at an analyzer (A) which is oriented perpendicular to a polarizer. The spontaneous magnetization of a ferrimagnetic indicator (Curie temperature about 400 K) is aligned in the film plane. Faraday rotation only occurs if there is a magnetic moment in the direction of the light beam, therefore without an external magnetic field there is no Faraday rotation. When a perpendicular magnetic field is applied the nonzero perpendicular component (M_z) of the magnetization is induced, and the intensity of the light transmitted through an analyzer increases in proportion to the applied field strength. When such an indicator is placed on a superconductor, the distribution of the out of plane component of magnetization, M_z, inside the indicator is proportional to the distribution of the perpendicular component of the magnetic induction, B_z, on a superconductor surface. Therefore, it can be visualized as a real-time two-dimensional optical picture. The main advantages of this technique are the ability to perform quantitative measurements of the magnetic induction (and even of the magnetic moment), outstanding spatial resolution and magnetic field sensitivity, and the near absence of a temperature dependence below 100 K. Figure 11.27 presents magneto-optical (MO) images of the intermediate state in pure lead, as well as corresponding DC magnetization loops measured at the same temperature on the same sample (Prozorov *et al*., 2005). The wide hysteretic loop was measured in a cold-worked sample and corresponding MO images show dendritic flux penetration and substantial flux trapping upon reduction of the external field to zero. In contrast, the stress-free sample (obtained by homogeneous solidification from the melt) shows two distinct topologies of the intermediate state: a closed topology in the form of flux tubes on flux entry, and an open laminar-type structure upon flux exit. Although, a similar tube phase was observed in the 60 s, it has never been accepted as a possible true equilibrium topology (of thick samples). Moreover, recent experiments on samples of different shapes confirm that in ellipsoidal samples the tubular phase is the stable pattern of the intermediate state, both for flux penetration and flux exit.

Another aspect of magneto-optical imaging is a possibility of obtaining the current density distribution from the measured induction pattern. This is a difficult mathematical problem, because it involves two dimensional inversion of the Biot-Savart integral with kernel singularities (Wijngaarden *et al*., 1996, Jooss *et al*., 2002). Figure 11.33a shows a polygonal pattern obtained in pure lead (note the interesting hexagonal structure of heptagonal inclusions), and Fig. 11.33b shows corresponding current density flow. This information is important since it takes into account the success of the recent current-loop model (Choksi *et al*., 2004, Reisin and Lipson,

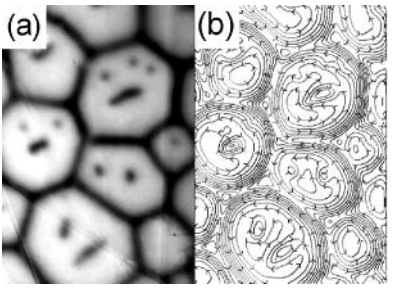

Figure 11.33 (a) Experimental polygonal intermediate state pattern at elevated fields upon flux penetration, and (b) reconstructed current density flow.

2000, Narayan, 1998, Goldstein and Dorsey, 1998, Dorsey and Goldstein, 1998, Goldstein *et al.*, 1996).

D. AC Response in the Intermediate State of Type I Superconductors

At small amplitudes of the excitation fields the response of a superconductor is reversible. In a pure Meissner state the magnetic field penetrates only to the depth determined by the London penetration depth λ, and the magnetic susceptibility of both Type-I and Type-II superconductors also depends only on the London penetration depth, λ. For example, for an infinite slab of width $2w$, $4\pi\chi = \lambda/w \tanh(w/\lambda) - 1$ (Schoenberg, 1952), and this can be generalized for a finite slab (Prozorov *et al.*, 2000). By sweeping the external DC magnetic field it is possible to study the dynamic magnetic susceptibility, *dM/dH*, without affecting the overall field distribution inside a superconductor. In Type-II superconductors if the amplitude of the excitation field is small the Abrikosov vortices are not displaced, but rather they oscillate around their equilibrium positions providing a quasi-elastic response known as the Campbell regime (Campbell and Evetts, 1972, Blatter *et al.*, 1994, Brandt, 1995, Coffey and Clem, 1991). In this regime the effective penetration depth becomes, $\lambda^2 = \lambda_L^2 + \lambda_C^2$, where $\lambda_C^2 = \alpha^{-1} C_{xx}$ is the Campbell penetration depth, C_{xx} is the relevant elastic modulus (either compression or tilt) of the vortex lattice, and α is the Labusch parameter (Coffey and Clem, 1991, Dew-Huges, 1974, Campbell and Evetts, 1972, Brandt, 1995).

Figure 11.34 shows measurements of the small-amplitude AC response in a stress-free lead sample during the sweeping of an external magnetic field. Also shown are MO images. The appearance of the intermediate state manifests itself by an abrupt deviation from the H^2 behavior (due to penetration from the corners (Prozorov *et al.*, 2005)). Clearly the response is hysteretic, but this hysteresis is only related to the topological differences, and to differences in the quasi-elastic response. This conclusion is supported by comparison with the DC magnetization, Figure 11.27, where flux exit corresponds to *smaller* magnetization values, which in Type-II superconductors would correspond to a *larger* penetration depth (Prozorov *et al.*, 2003). In Fig. 11.34 larger values correspond to the flux entry, and indicate a softer phase compared to the laminar structure observed at flux exit. As the field increases the growing flux tubes seem to form a more rigid honeycomb structure, thus leading to a *decrease* of the penetration depth at elevated magnetic fields, as observed in Fig. 11.34. In the cold-worked sample, where the flux penetration is dendritic (see Fig. 11.27), such a non-monotonic behavior is not observed. Thus this distinct feature may serve as a useful tool for the study the intermediate state in samples where direct MO imaging is not possible. Finally, as the field continues to increase, Fig. 11.34 shows that the superconductivity is quenched at H_c, but the penetration depth remains significantly lower than the normal state skin-depth due to the presence of surface superconductivity. Furthermore, the hysteresis of the AC response is observed both for $M(H = \text{const}, T)$ and $M(H, T = \text{const})$ measurements. Another verification of the correspondence of the AC response to

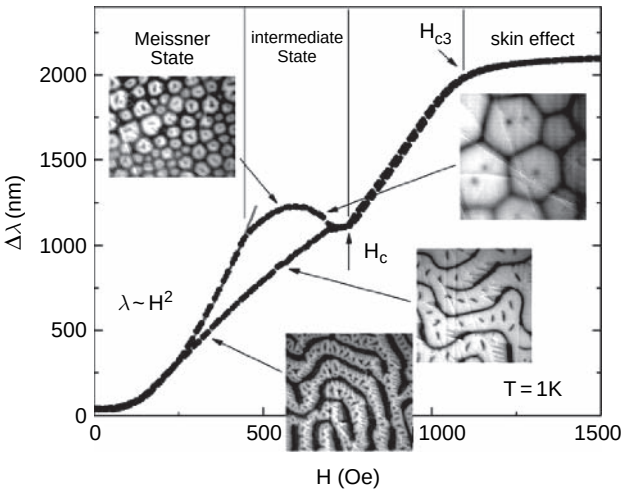

Figure 11.34 Magnetic penetration depth measured by using a tunnel-diode resonator, and the corresponding evolution of intermediate state patterns.

the particular geometry of the intermediate state is the vanishing of the non-monotonic behavior upon the application of an inclined magnetic field (Prozorov *et al.*, 2005). This effect is related to the induced unidirectional anisotropy of the otherwise frustrated intermediate state structure, as first demonstrated by Sharvin (Sharvin and Sedov, 1956, Livingston and DeSorbo, 1969).

Unfortunately, no theory of the quasi-elastic small-amplitude AC magnetic response of the intermediate state of Type-I superconductors is yet available. A theoretical analysis along the lines of the Campbell response, but for Type-I superconductors, is needed. Once a correlation is established and understood, the unique characteristics of the AC response will be very useful in studying ellipsoidal samples, as well as very small samples, which cannot be directly imaged by magneto-optics. Ellipsoidal samples are important because they provide the thermodynamically equilibrium response needed to conclusively answer the basic question of the ground state intermediate state pattern. Recent magneto-optical experiments performed on hemispheres indicate that the tubular structure is the equilibrium pattern of Type-I superconductors.

XII. MIXED STATE IN TYPE II SUPERCONDUCTORS

In this chapter we have been explaining how demagnetization effects in Type I materials produce the intermediate state in an effort to prevent surface fields from exceeding the critical field $B_{c'}$ and driving the material normal. In a Type II super-conductor, when B_{app} becomes large enough to produce surface fields equal to the lower critical field, B_{c1}, vortices appear inside the material near the surface and the mixed state forms at a lower field $B_{c1'}$ than it would under the condition $N = 0$. Ideally, a Type II superconductor is in the $\chi = -1$ or Meissner state for $B_{app} < B_{c1'}$ and in the mixed state above $B_{c1'}$.

The mathematical description of the Meissner state of a Type II superconductor is similar to that of the Type I case that was presented above in Section IV, with B_{c1} replacing B_c at the upper limit of Eq. (11.10).

This limit is the shifted lower critical field $B_{c1'}$ mentioned above,

$$B_{c1'} = (1-N)B_{c1}. \tag{11.81}$$

Thus we can rewrite Eqs. (11.10)–(11.14) for a Type II superconducting ellipsoid in the Meissner state as follows:

$$B_{app} < B_{c1'} \tag{11.82}$$

$$B_{in} = 0, \tag{11.83}$$

$$H_{in} = B_{app}/(1-N)\mu_0, \tag{11.84}$$

$$\mu_0 M = -B_{app}/(1-N), \tag{11.85}$$

$$\chi = -1. \tag{11.86}$$

This state exists over the range given by Eq. (11.82).

When B_{app} exceeds $B_{c1'}$, vortices begin to form and the material enters the mixed state. Since this state can exist for H_{in} greater than $B_{c1'}/\mu_0$, the value of H_{in} does not become pinned at the critical field, as in the Type I case, but continues to increase as the applied field increases. This removes the constraint of Eq. (11.2), so the fields are given by the following more general expressions of Eqs. (5.35)–(5.37):

$$B_{c1'} < B_{app} < B_{c2}, \tag{11.87}$$

$$B_{in} = B_{app}\frac{1+\chi}{1+\chi N}, \tag{11.88}$$

$$H_{in} = \frac{B_{app}}{\mu_0(1+\chi N)}, \tag{11.89}$$

$$M = \frac{B_{app}}{\mu_0}\frac{\chi}{(1+\chi N)}. \tag{11.90}$$

These equations resemble those of the mixed state of a Type II ellipsoid, rather than those, (11.15)–(11.19), of the corresponding Type I intermediate state. The presence of the demagnetization factor N in the denominator of expressions (11.88)–(11.90) causes the internal fields to be larger than they would be for the case $N = 0$ of a cylinder in a parallel applied field.

Pakulis (1990) proposed a mixed state in zero field with normal regions called *thermons* that contain no magnetic flux.

PROBLEMS

1. Find the range of angles for which the magnetic field at the surface of a perfectly superconducting sphere ($\chi = -1$) is (a) greater than, (b) equal to, or (c) less than the applied field B_{app}.
2. What are the smallest and the largest possible values of the angle Θ_c of Eq. (11.8) and at what applied fields do they occur?
3. Deduce the equations for B_{in}, H_{in}, M, and χ in the intermediate state of a Type I superconducting cylinder in a perpendicular magnetic field.
4. Show that the magnetic fields at the surface of a sphere in an applied magnetic field in the intermediate state have the following radial and azimuthal components:

$$B_r = B_{in}\cos\Theta,$$
$$B_\Theta = B_c \sin\Theta.$$

5. Show that the magnetic fields at the surface of a sphere in an applied magnetic field in the perfectly diamagnetic state have the following radial and azimuthal components:

$$B_r = 0$$
$$B_\Theta = \frac{3}{2}B_{app}\sin\Theta.$$

6. Show that the expressions

$$\chi_{exp} = \chi/(1+N\chi),$$
$$\chi = \chi_{exp}/(1-N\chi_{exp}),$$
$$\chi_{exp} = \frac{1}{N}\left(1-\frac{B_c}{B_{app}}\right),$$

are valid for the intermediate state of an ellipsoid.

7. Show that the boundary between the superconducting and intermediate state of an ellipsoid in a magnetic field lies along the dashed line of unit slope shown in Fig. 11.8. Show that along this boundary the Gibbs free energy is $-NB_c^2/2\mu_0$.
8. Show that the normalized Gibbs free energy $g(b, t)$ of an ellipsoid in an applied magnetic field is given by the expressions

$$g(b,t) = -t^2/\alpha - (1-t^2)^2 + b^2/(1-N) \qquad 0 < b < (1-N)(1-t^2)$$

$$g(b,t) = -t^2/\alpha - (1-t^2-b)^2/N \qquad (1-N)(1-t^2) < b < (1-t^2).$$

   These are plotted in Fig. 11.9 for several values of N and t using the BCS expression $1/\alpha = 2.8$.
9. Show that the dashed line of Fig. 11.9 corresponds to the expression $G_s = B_c^2/2\mu_0[(B_{app}/B_c) - 1]$.
10. Derive Eq. (11.71),

$$J_i(r) = J_n(a_i/r) \quad r \le a_i,$$

    and show that

$$J_i(r) = H_c/r \quad r < a_i.$$

11. Derive Eq. (11.74),

$$\rho_i(r) = \rho_n(r/a_i) \quad r \le a_i,$$

    and show that

$$\rho_i(r) = rE/H_c \quad r < a_i.$$

12. Show that the radius a_i of the intermediate-state region of a current-carrying superconducting wire is given by

$$a_i = \frac{aI_c}{I\{1+[1-(I_c/I)]^{1/2}\}}.$$

13. Show that the radius a_i of the intermediate-state region of a current-carrying superconducting wire has the limiting behavior $a_i = a$ for $I = I_c$ and that $a_i \approx aI_c/2I$ for $I \gg I_c$.
14. Show that Eq. (11.77) is the solution to Eq. (11.76).
15. Show that in the intermediate state the current density averaged over the whole wire has the value

$$\langle J \rangle = \frac{H_c}{a_i}\left(1 + \frac{a_i^2}{a^2}\right).$$

    Since this is greater than J_n, we see that the formation of the intermediate state causes more current to flow in the core than would have happened if the wire had become normal.
16. Show that the total current flowing through the intermediate-state region of the wire in Fig. 11.24 is $2\pi a_i^2 J_n$, and that the total current flowing through the wire is given by Eq. (11.75), namely $I = \pi(a^2 + a_i^2)J_n$.

This page intentionally left blank

12

Type II Superconductivity

I. INTRODUCTION

In Chapters 2 and 11 we discussed Type I superconductors, which are superconductors that exhibit zero resistance and perfect diamagnetism. They are also perfect diamagnets for applied magnetic fields below the critical field B_c, and become normal in higher applied fields. Their coherence length exceeds their penetration depth so it is not energetically favorable for boundaries to form between their normal and superconducting phases. The superconducting elements, with the exception of niobium, are all Type I.

We showed in Chapter 6, Section XII, that when the penetration depth λ is larger than the coherence length ξ, it becomes energetically favorable for domain walls to form between the superconducting and normal regions. When such a superconductor, called Type II, is in a magnetic field, the free energy can be lowered by causing domains of normal material containing trapped flux to form with low-energy boundaries created between the normal core and the surrounding superconducting material. When the applied magnetic field exceeds a value referred to as the lower critical field, B_{c1}, magnetic flux is able to penetrate in quantized units by forming cylindrically symmetric domains called *vortices*. For applied fields slightly above B_{c1}, the magnetic field inside a Type II superconductor is strong in the normal cores of the vortices, decreases with distance from the cores, and becomes very small far away. For much higher applied fields the vortices overlap and the field inside

the superconductor becomes strong everywhere. Eventually, when the applied field reaches a value called the upper critical field B_{c2}, the material becomes normal. Alloys and compounds exhibit Type II superconductivity, with mixed-type magnetic behavior and partial flux penetration above B_{c1}. Type II superconductors also have zero resistance, but their perfect diamagnetism occurs only below the lower critical field B_{c1}. The superconductors used in practical applications, which have relatively high transition temperatures, carry large currents and often operate in large magnetic fields, are all of Type II. Their properties will be described in this chapter. In the latter part of the chapter we will examine the properties of the vortices, discussing how they confine flux, how they interact, and how they move about.

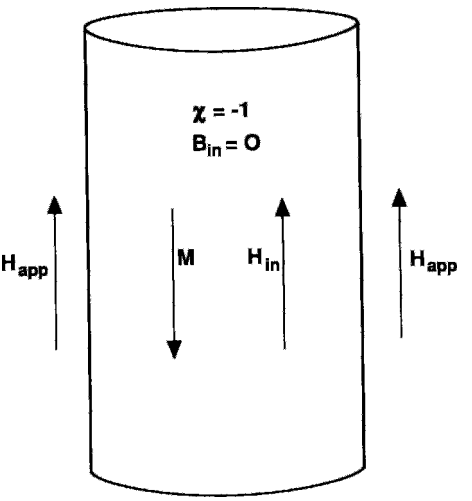

Figure 12.1 Internal fields produced inside a perfectly superconducting cylinder ($\chi = -1$) in an external magnetic field $\mathbf{B}_{app} = \mu_0 \mathbf{H}_{app}$ applied parallel to its axis. This arrangement is referred to as parallel geometry.

II. INTERNAL AND CRITICAL FIELDS

A. Magnetic Field Penetration

The general expression (1.69)

$$\mathbf{B} = \mu_0(\mathbf{H} + \mathbf{M}) \tag{12.1}$$

is valid both inside and outside a superconducting sample in an applied field. For simplicity we will examine the case of an elongated cylindrical superconductor with its axis in the direction of the applied magnetic field, as shown in Fig. 12.1. For this "parallel" geometry the boundary condition (1.74) requires the H fields outside ($H_{app} = B_{app}/\mu_0$) and inside (H_{in}) to be equal at the surface of the sample,

$$H_{app} = H_{in} \tag{12.2}$$

If we apply Eq. (12.1) to the fields inside a Type I superconductivity and recall that $B_{in} = 0$, we obtain for the magnetization in the sample, with the aid of Eq. (12.2)

$$\mu_0 M = -B_{app}. \tag{12.3}$$

Above the critical field B_c the material becomes normal, the magnetization M becomes negligibly small, and $B_{in} \approx B_{app}$. This situation is indicated in Fig. 2.27 and plotted in Fig. 12.2, with the field $\mu_0 H_{in}$ below B_c indicated by a dashed line in the latter figure.

The corresponding diagram for a Type II superconductor has two critical fields, B_{c1}, the field where flux begins to penetrate, and B_{c2}, the field where the material becomes normal. For this case, again applying the boundary condition (12.2), the internal field and magnetization given by

$$\left.\begin{aligned} \mu_0 M &= -B_{app} \\ B_{in} &= 0 \end{aligned}\right\} \quad 0 \le B_{app} \le B_{c1}, \tag{12.4a}$$

$$\mu_0 M = -(B_{app} - B_{in}) \quad B_{c1} \le B_{app} \le B_{c2}, \tag{12.4b}$$

are shown plotted in Figs. 12.3 and 12.4, respectively. The dashed line ($\mu_0 H_{in}$) in Fig. 12.3 represents asymptote of B_{in} as it approaches B_{c2}. Also shown in these two

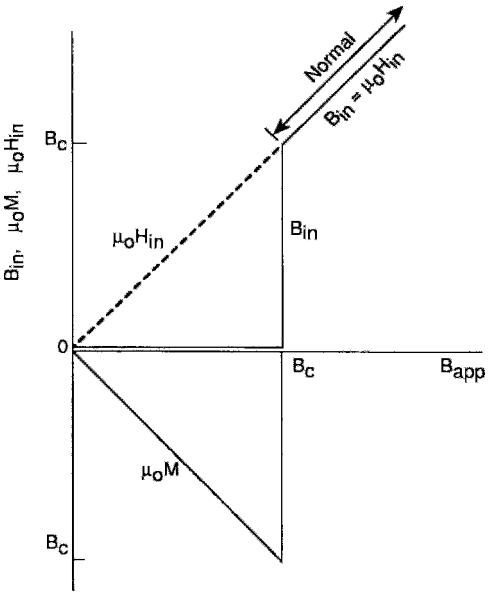

Figure 12.2 Internal fields B_{in} and H_{in} and magnetization M for an ideal Type I superconductor. Use is made of the permeability μ_0 of free space in this and the following two figures so that B_{in}, $\mu_0 H_{in}$, and $\mu_0 M$ have the same units, in accordance with Eq. (12.1).

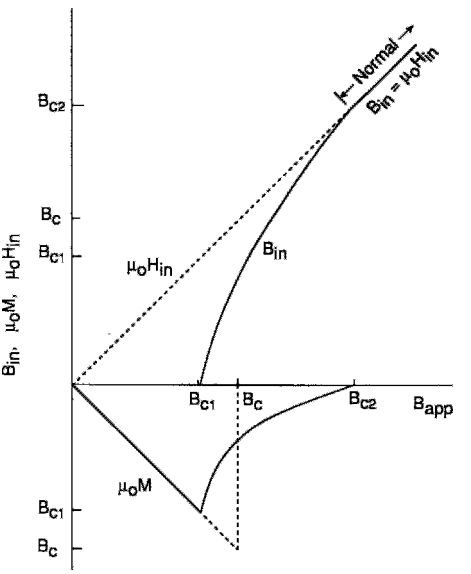

Figure 12.3 Internal fields B_{in} and H_{in} and magnetization M for an ideal Type II superconductor, using the notation of Fig. 12.2.

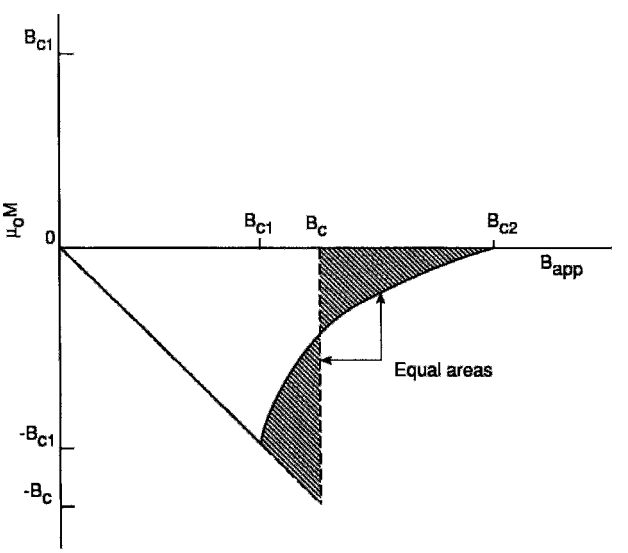

Figure 12.4 Dependence of magnetization M on the applied field for an ideal Type II superconductor. The equality of the areas separated by the thermodynamic critical field B_c is indicated.

figures is the thermodynamic critical field B_c defined by the expression

$$\int_{B_{c1}}^{B_c} (B_{app} + \mu_0 M)\, dB_{app} = \mu_0 \int_{B_c}^{B_{c2}} (-M)\, dB_{app}, \qquad (12.5)$$

which makes the two areas shown shaded in Fig. 12.4 equal. Figures 12.2, 12.3, and 12.4 are idealized cases; in practice, the actual magnetization and internal field curves are rounded, as indicated in Fig. 12.5.

We used the parallel geometry arrangement because it avoids the complications of demagnetization effects; these were discussed later in Chapter 5, Sections X and XI. For this geometry the demagnetization factor N, which is a measure of these complications, is zero.

B. Ginzburg-Landau Parameter

In Chapter 6, Sections V and VII, respectively, we introduced two characteristic length parameters of a superconductor—the coherence length ξ and the penetration

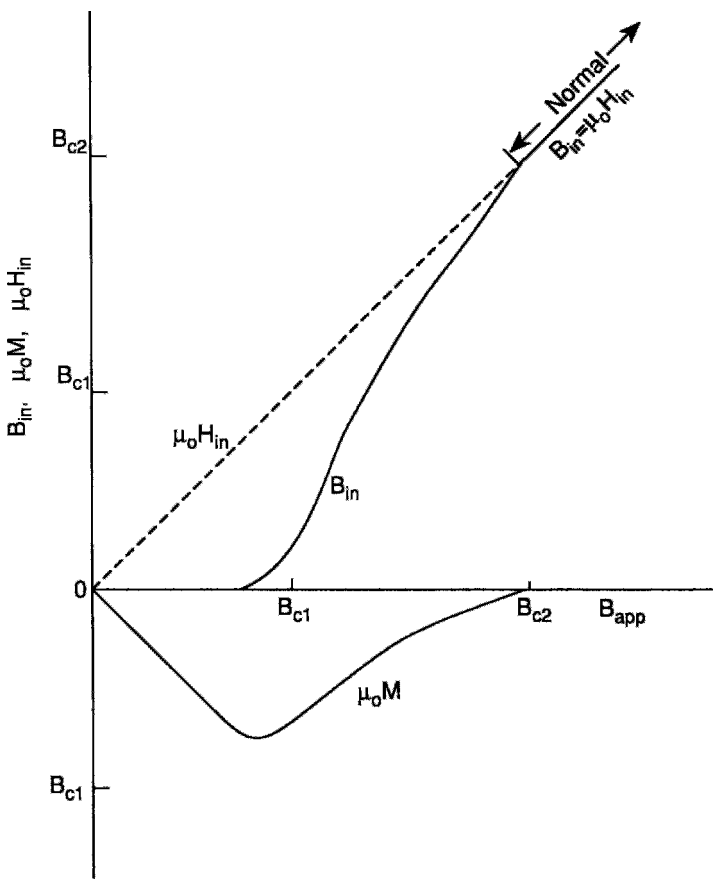

Figure 12.5 Dependence of internal magnetic field B_{in} and magnetization M on an applied field B_{app} for a nonidealized Type II superconductor in which the curves near the lower-critical field are rounded. This is in contrast to the idealized cases of Figs. 12.3 and 12.4 which exhibit abrupt changes in B_{in} and M when the applied field passes through the value B_{c1}.

depth λ. Their ratio is the Ginzburg–Landau parameter κ of Eq. 6.83,

$$\kappa = \frac{\lambda}{\xi}. \tag{12.6}$$

The density of super electrons n_s, which characterizes the superconducting state, increases from zero at the interface with a normal material to a constant value far inside, and the length scale for this to occur is the coherence length ξ. An external magnetic field **B** decays exponentially to zero inside a superconductor, with length scale λ. Figure 12.6 plots these distance dependences of n_s and **B** near the boundary of a superconductor with a normal material for the two cases $\kappa < 1$ and $\kappa > 1$.

For a Type I superconductor the coherence length is the larger of the two length scales, so superconducting coherence is maintained over relatively large distances within the sample. This overall coherence of the superconducting electrons is not disturbed by the presence of external magnetic fields.

When, on the other hand, the material is Type II, the penetration depth λ is the larger of the two length parameters, and external magnetic fields can penetrate to a distance of several or more coherence lengths into the sample, as shown in Fig. 12.6b. Thus, near the interface relatively large magnetic field strengths coexist with high concentrations of superconducting electrons. In addition, inside the superconductor we find tubular regions of confined magnetic flux (the vortices) as already noted. These have an effective radius of a penetration depth beyond which the magnetic field decays approximately exponentially to zero, in the manner

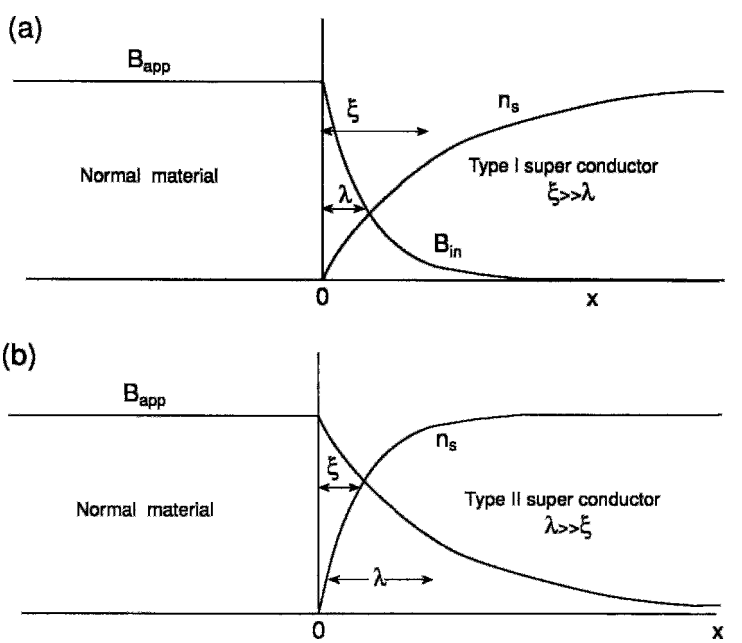

Figure 12.6 Increase in the number of superconducting electrons n_s and decay of the magnetic field B_{in} with distance x from the surface of the superconductor. The coherence length ξ and penetration depth λ associated with the change in n_s and B_{in}, respectively, are shown. (a) Type I superconductor, with $\xi > \lambda$, and (b) Type II superconductor, with $\lambda > \xi$, and $B_{app} < B_{c1}$.

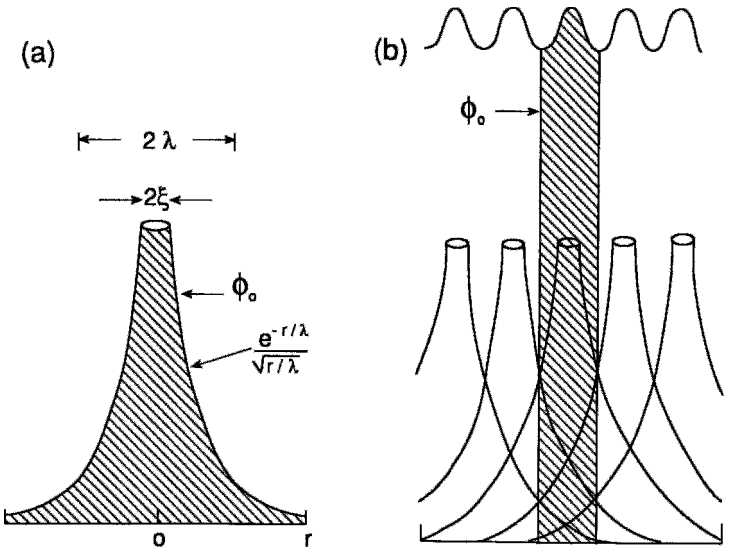

Figure 12.7 Sketch of (a) the magnetic field around an individual vortex, and (b) the field (top) from a group of nearby overlapping vortices (bottom). The coherence-length radius of the core, penetration-depth radius of the field outside the core, and decay of B at large distances are indicated for an individual vortex. The region of fluxoid quantization is cross-hatched for the individual vortex and for one of the overlapping vortices.

illustrated in Fig. 12.7. As the applied field increases, more and more vortices form and their magnetic fields overlap, as indicated in Fig. 12.7b. Type II material is said to be in a mixed state over the range $B_{c1} < B_{app} < B_{c2}$ of applied fields.

Values of ξ, λ, and κ for a number of superconducting materials are given in Table 12.1. Superconductors are classified as Type I or Type II depending on whether the parameter κ is less than or greater than $1/\sqrt{2}$, respectively. We see from the table that all the elements (except for Nb) are Type I and that all the compounds are Type II, with the copper-oxide superconductors having the highest κ values, on the order of 100. Many of the data in the table are averages from several earlier compilations that do not agree very closely. The scatter in the values of ξ and λ listed in Table 12.2 for five of the elements is comparable to that of the high-temperature superconductors in Table III-1 of our earlier work (Poole *et al.*, 1988).

C. Critical Fields

In Chapter 4, Section VIII, and Chapter 6, Section IV, we saw that a Type I superconductor has a critical field B_c, and in Eq. (4.37) we equated the difference $G_n - G_s$ in the Gibbs free energy between the normal and the superconducting states to the magnetic energy $B_c^2/2\mu_0$ of this critical field,

$$G_n - G_s = \frac{B_c^2}{2\mu_0} \tag{12.7}$$

Since this is a thermodynamic expression, B_c is called the *thermodynamic critical field*. Both Type I and Type II superconductors have thermodynamic critical fields. In addition, a Type II superconductor has lower- and upper-critical fields, B_{c1} and B_{c2}, respectively, given by

$$B_{c1} = \frac{\Phi_0 \ln \kappa}{4\pi\lambda^2}, \tag{12.8}$$

$$B_{c2} = \frac{\Phi_0}{2\pi\xi^2}. \tag{12.9}$$

Table 12.1 Coherence Length ξ, Penetration Depth λ, and Ginzburg–Landau Parameter κ of Various Superconductors[a]

Material	T_c (K)	ξ (nm)	λ (nm)	κ (λ/ξ)	Source
Cd	0.56	760	110	0.14	Meservey and Schwartz (1969)
Al[a]	1.18	15.10	40	0.03	Table 9.2
In[a]	3.41	360	40	0.11	Table 9.2
Sn[a]	3.72	180	42	0.23	Table 9.2
Ta	4.4	93	35	0.38	Buckel (1991)
Pb[a]	7.20	82	39	0.48	Table 9.2
Nb[a]	9.25	39	52	1.28	Table 9.2
Pb–In	7.0	30	150	5.0	Orlando and Delin (1991)
Pb–Bi	8.3	20	200	10	Orlando and Delin (1991)
Nb–Ti	9.5	4	300	75	Orlando and Delin (1991)
Nb–N	16	5	200	40	Orlando and Delin (1991)
$PbMo_6S_8$ (Chevrel)	15	2	200	100	Orlando and Delin (1991)
V_3Ga ($A15$)	15	≈2.5	90	≈35	Orlando and Delin (1991)
V_3Si ($A15$)	16	3	60	20	Orlando and Delin (1991)
Nb_3Sn ($A15$)	18	3	65	22	Orlando and Delin (1991)
Nb_3Ge ($A15$)	23.2	3	90	30	Orlando and Delin (1991)
K_3C_{60}	19	2.6	240	92	Holczer *et al.* (1991)
Rb_3C_{60}	29.6	2.0	247	124	Sparn *et al.* (1992)
$(La_{0.925}Sr_{0.075})_2CuO_4$[b]	37	2.0	200	100	Poole *et al.* (1988)
$YBa_2Cu_3O_7$[b]	89	1.8	170	95	Poole *et al.* (1988)
HgBaCaCuO	126	2.3			Gao *et al.* (1993)
$HgBa_2Ca_2Cu_3O_{8+\delta}$	131			100	Schilling *et al.* (1994b)

[a] Figures are rounded averages from Table 12.2.
[b] Averages of the polycrystalline data from our earlier Table III-1 (1988).

Table 12.2 Coherence Length ξ and Penetration Depth λ of Five Superconducting Elements from Several Reports[a]

Parameter	Al	In	Sn	Pb	Nb	Reference
Coherence length ξ, nm		360	175	510	39	Buckel (1991)
	1360	275	94	74		Huebener (1979)
	1600	360	230	90	40	Orlando and Delin (1991)
	1600	440	230	83	38	Van Duzer and Turner (1981)
Penetration depth λ, nm		24	31	32	32	Buckel (1991)
	51	47	52	47		Huebener (1979)
	50	65	50	40	85	Orlando and Delin (1991)
	16	21	36	37	39	Van Duzer and Turner (1981)

[a] Some of the data are reported averages from earlier primary sources. Table 12.1 lists rounded averages calculated from these values, with the entry $\xi = 510\,\text{nm}$ for Pb excluded.

These can be expressed in terms of the thermodynamic critical field B_c, as follows:

$$B_c = \frac{\Phi_0}{2\sqrt{2}\pi\lambda\xi}, \tag{12.10}$$

$$B_{c1} = \frac{B_c \ln\kappa}{\sqrt{2}\,\kappa}, \tag{12.11}$$

$$B_{c2} = \sqrt{2}\,\kappa B_c. \tag{12.12}$$

It is also of interest to write down the ratio and the product of the two critical fields:

$$B_{c2}/B_{c1} = 2\kappa^2/\ln\kappa, \qquad (12.13a)$$

$$(B_{c1}B_{c2})^{1/2} = B_c(\ln\ \kappa)^{1/2}. \qquad (12.13b)$$

Figure 12.3 shows the position of the lower and upper critical fields as well as the thermodynamic critical field on the magnetization curve, and Table 12.3 lists the critical fields of a few Type II superconductors.

Table 12.3 Critical Fields of Selected Type II Superconductors[a]

Material	T_c (K)	B_{c1} (mT)	B_c (mT)	B_{c2} (T)	Reference
Nb wire, RRR = 750	9.3	181.0	0.37	2.0	Roberts (1976)
Nb wire, cold-drawn	9.3	248.0		≈10.0	Roberts (1976)
$In_{0.95}Pb_{0.05}$ (alloy)	3.7	31.8	37.5	0.049	Roberts (1976)
$Mo_{\approx 0.1}Nb_{\approx 0.9}$ (alloy)	6.4	29.0	78.5	0.414	Roberts (1976)
$Mo_{0.66}Re_{0.34}$ (alloy)	11.8	38.1	0.113		Roberts (1976)
$Nb_{0.99}Ta_{0.01}$ (alloy)	8.8	173.0	20.4	0.445	Roberts (1976)
Nb–Ti	9.5			13.0	Orlando and Delin (1991); Van Duzer and Turner (1981)
CTa (NaCl Structure)	≈10.0	22.0	81.0	0.46	Roberts (1976)
Nb–N (NaCl Structure)	16.0	9.3		15.0	Orlando and Delin (1991); Roberts (1976)
Cr_3Ir (*A*15)	0.75	16.8		1.05	Roberts (1976)
V_3Ge (*A*15)	6.8			≈5.0	Roberts (1976)
V_3Ga(*A*15)	15.0			23.0	Orlando and Delin (1991); Van Duzer and Turner (1981)
V_3Si (*A*15)	16.0	55.0	670.0	23.0	Roberts (1976)
Nb_3Sn (*A*15)	18.2	35.0	440.0	23.0	Roberts (1976)
Nb_3Ge (*A*15)	23.1			37.0	Orlando and Delin (1991); Van Duzer and Turner (1981)
HfV_2 (Laves)	9.2	187.0		21.7	Vonsovsky *et al.* (1982, p. 376)
$(Hf_{0.5}Zr_{0.5})V_2$ (Laves)	10.1	197.0		28.3	Vonsovsky *et al.* (1982, p. 376)
ZrV_2 (Laves)	8.5	219.0		16.5	Vonsovsky *et al.* (1982, p. 376)
$NbSe_2$	7.2	7.2	204.0	17.4	Roberts (1976)
$PbMo_6Se_8$ (Chevrel)	3.8			3.8	Vonsovsky *et al.* (1982, p. 420)
$LaMo_6S_8$ (Chevrel)	≈6.5			5.4	Vonsovsky *et al.* (1982, p. 420)
$LaMo_6Se_8$ (Chevrel)	11.0			44.5	Vonsovsky *et al.* (1982, p. 420)
$SnMo_6S_8$ (Chevrel)	11.8			34.0	Vonsovsky *et al.* (1982, p. 420)
$PbMo_6S_8$ (Chevrel)	15.0			60.0	Orlando and Delin (1991)
$U_{0.97}Th_{0.03}Be_{13}$ (heavy fermion)	0.35	4.0			Rauchschwalbe *et al.* (1987)
UPt_3 (heavy fermion)	0.46			1.9	Schenström *et al.* (1989)
$U_{0.985}La_{0.015}Be_{13}$ (heavy fermion)	0.57			3.8	Dalichaouch *et al.* (1991)
UBe_{13} (heavy fermion)	0.9			6.0	Maple *et al.* (1984)
K_3C_{60} (buckyball)	19.0	13.0		32.0	Boebinger *et al.* (1992); Foner *et al.* (1992); Holczer *et al.* (1991); C. E. Johnson *et al.* (1992); Z. H. Wang *et al.* (1993)
Rb_3C_{60} (buckyball)	29.6	12.0		57.0	Foner *et al.* (1992); C. E. Johnson *et al.* (1992); Sparn *et al.* (1992)
$HgBa_2CuO_{4+\delta}$	99		10^3	>35	Thompson *et al.* (1993)

[a] Some of the data are averages from more than one source.

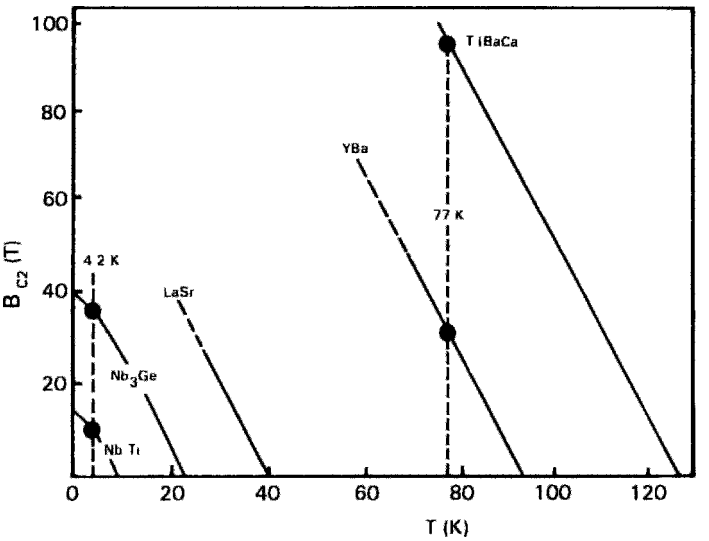

Figure 12.8 Comparison of the temperature dependence of the upper-critical fields B_{c2} of Nb–Ti, Nb_3Ge, LaSrCuO, YBaCuO, and TlBaCaO. The slopes are close to the Pauli limit 1.83 T/K (Poole *et al.* 1988, p. 8).

Section IV gives expressions similar to Eqs. (12.8–12.12) for anisotropic cases.

When the applied magnetic field is perpendicular to the surface of the superconductor, the upper critical field is truly B_{c2}. When it is parallel to the surface, however, it turns out that the superconducting state can persist in a thin surface sheath for applied surface fields up to the higher value $B_{c3} = 1.69\ B_{c2}$ (Saint-James and de Gennes, 1963; Saint-James *et al.*, 1969; Van Duzer and Turner, 1981, p. 319; Walton *et al.*, 1974; Yuan and Whitehead, 1991).

The temperature dependence of the thermodynamic critical field B_c is given in Chapter 2, Section XIII. The lower and upper critical fields of Type II superconductors have a similar temperature dependence. The fields B_{c2} needed to extinguish Type II superconductivity are much larger than those B_c that are sufficient for extinguishing the Type I variety. These large upper-critical fields make Type II superconductors suitable for magnet applications.

Quoted upper-critical fields are usually given for 4.2 K or for extrapolations to 0 K. Values of technological interest are the 4.2 K fields for the low-temperature superconductors and the 77 K fields for the high-temperature superconductors. For example, B_{c2} for the standard magnetic material NbTi is 10 T at 4 K and can be 30 T or more at 77 K for high-temperature superconductors, as shown in Fig. 12.8 (Fischer, 1978; Newhouse, 1969, p. 1268; Vonsovsky *et al.*, 1982, p. 431). Theoretical articles have appeared that discuss upper-critical fields (e.g., Brézin *et al.*, 1990; Estrera and Arnold, 1989; Norman, 1990; Pérez-González and Carbotte, 1992; Pérez-González *et al.*, 1992; Santhanam and Chi, 1988; Theodorakis and Tesanovic, 1989).

III. VORTICES

We have seen that an applied magnetic field B_{app} penetrates a superconductor in the mixed-state, $B_{c1} < B_{app} < B_{c2}$. Penetration occurs in the form of tubes, called vortices (see Fig. 12.9), which serve to confine the flux (Abrikosov 1957; Belitz 1990).

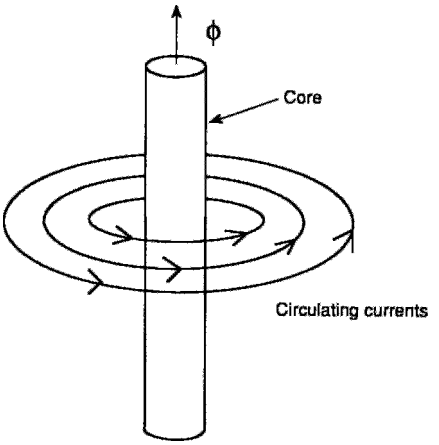

Figure 12.9 Sketch of shielding currents circulating around a vortex core.

The highest field is in the core, which has a radius ξ. The core is surrounded by a region of larger radius λ within which magnetic flux and screening currents flowing around the core are present together, as is clear by comparing Figs. 12.7 and 12.9. The current density J_s of these shielding currents decays with distance from the core in an approximately exponential manner. Analytical expressions for the distance dependence of B and J are derived in the following section for the high-kappa ($\kappa \gg 1$) approximation.

A. Magnetic Fields

Equation (6.39) provides us with an expression for the magnetic flux passing through a region,

$$\int \mathbf{B} \cdot d\mathbf{S} + \frac{\mu_0 m^*}{e^{*2}} \int \frac{\mathbf{J} \cdot d\mathbf{I}}{|\phi|^2} = n\Phi_0, \quad (12.14)$$

where n is the number of vortex cores enclosed by the integrals. For an isolated vortex $n = 1$ because it is energetically more favorable for two or more quanta to form separate vortices rather than to coexist together in the same vortex. Integration of $\mathbf{B}$ over the cross-sectional area of an isolated vortex can be taken from $r = 0$ to $r = \infty$, so the surface integral is numerically equal to the flux quantum Φ_0,

$$\int \mathbf{B} \cdot d\mathbf{S} = \Phi_0, \quad (12.15)$$

and the line integral vanishes because $\mathbf{J}$ become negligibly small at large distances. The quantum condition (12.15) fixes the total magnetic flux in an isolated vortex at one fluxoid, including flux in the core and in the surrounding region. The possibility of vortices containing two or more quanta has been discussed (Buzdin, 1993; Sachdev, 1992; Tokuyasu *et al.*, 1990).

As the applied magnetic field increases, the density of vortices increases and they begin to overlap, making the vortex–vortex nearest-neighbor distance less than the penetration depth. The high-density case can be treated by assuming that the magnetic field at any point is a linear superposition of the fields from all of the overlapping vortices. At high densities B_{in} becomes very large and the variation of the field in the space between the cores becomes very small, as indicated in Fig. 12.10. Nevertheless, the quantization condition still applies and each vortex has, on average, one quantum of flux Φ_0 associated with it, as indicated in Fig. 12.7b. For a regular two-dimensional lattice arrangement of vortices, Eq. (12.15) holds as long as the integration is carried out over the vortex unit cell; the line integral (9.14) of the current density vanishes when it is taken around the periphery of this cell.

When λ is much larger than ξ, as is the case with the high-temperature superconductors, there is considerable overlap of vortices throughout most of the mixed-state range, and the magnetic flux is present mainly in the surrounding region, rather than in the actual cores.

There is no limit to the length of a vortex. Along the axis, which is also the applied field direction, the magnetic field lines are continuous. Thus the flux does not begin and

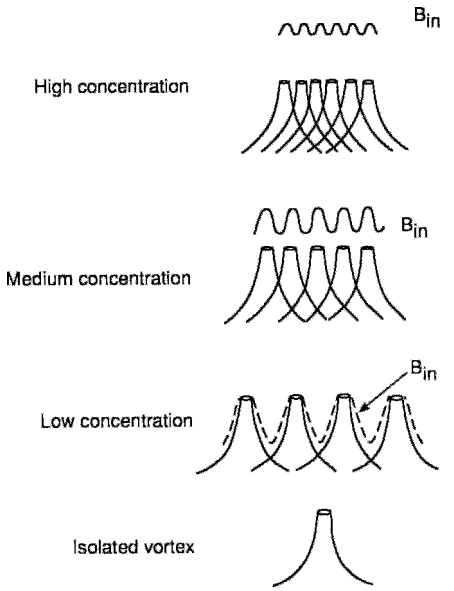

Figure 12.10 Sketch showing how the magnetic field B_{in} inside a superconductor increases as the concentration of vortices increases and their fields increasingly overlap.

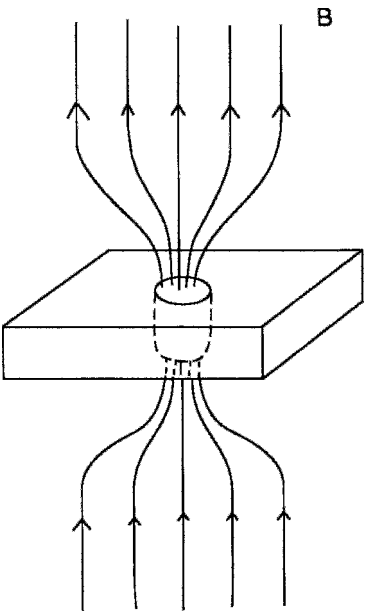

Figure 12.11 Passage of external magnetic field lines through a flat-plat superconductor in the region of a vortex.

end inside the superconductor, but instead enters and leaves at the superconductor surface, which is also where the vortices begin and end. This is illustrated in Fig. 12.11.

We have seen that a vortex has a core radius equal to the coherence length ξ and a surrounding outer region with radius equal to the penetration depth λ. Such an entity can only exist in a Type II superconductor, where λ is greater than ξ. A vortex does not exist, and is not even a meaningful concept under Type I conditions ($\xi > \lambda$).

Scanning tunneling microscope studies of superconducting surfaces (H. F. Hess *et al.*, 1989, 1990, 1991; Karrai *et al.*, 1992; Renner *et al.*, 1991) reveal an enhancement of the differential tunneling conductance (see Chapter 15, Section V) in the vortex core. This has been attributed to the presence of bound states of quasiparticles in the core. As the magnetic field increases, additional vortices form accompanied by the breakup of Cooper pairs, and more and more quasiparticles or normal electrons become localized in the vortex cores (Daemen and Overhauser, 1989; Gygi and Schlüter, 1990a, b, 1991; Klein, 1989, 1990; Overhauser and Daemen, 1989; Shore *et al.*, 1989; Ullah *et al.*, 1990).

B. High-Kappa Approximation

To obtain a description of vortices that is more quantitative in nature as opposed to the rather qualitative description presented in the previous section, it will be helpful to have a closed-form expression for the distance dependence of the confined magnetic fields. For the high-κ limit, $\lambda \gg \xi$, which is valid for the copper-oxide superconductors that typically have $\kappa \approx 100$, we can make use of the Helmholtz equations that were derived from the London formalism in Chapter 6, Section IX. The vortex is assumed to be infinitely long and axially symmetric so that there are no z or angular dependences of its field distribution. The problem is thus

equivalent to the two-dimensional problem of determining the radial dependences.

The magnetic field of the vortex is in the z direction, and its radial dependence outside the vortex core is obtained from the Helmholtz Eq. (6.67). Here we will write the Helmholtz equation in cylindrical coordinates for the two-dimensional case of axial symmetry without assuming any angular dependence,

$$\frac{\lambda^2}{r}\frac{d}{dr}\left(r\frac{d}{dr}\right)\mathbf{B}-\mathbf{B}=0, \qquad (12.16)$$

This equation has an exact solution,

$$B(r)=\frac{\Phi_0}{2\pi\lambda^2}K_0(r/\lambda), \qquad (12.17)$$

where $K_0(r/\lambda)$ is a zeroth-order modified Bessel function. With the aid of Eq. (12.8) this can be written

$$B(r)=B_{c1}\frac{K_0(r/\lambda)}{\frac{1}{2}\ln(\kappa)}. \qquad (12.18)$$

To obtain the current density we substitute Eq. (12.17) in the Maxwell equation for $\mathbf{B}_{in}$,

$$\nabla\times\mathbf{B}_{in}=\mu_0\mathbf{J}_s, \qquad (12.19)$$

to obtain

$$J_s(r)=\frac{\Phi_0}{2\pi\mu_0\lambda^3}K_1(r/\lambda) \qquad (12.20)$$

$$=J_0\frac{K_1(r/\lambda)}{\frac{1}{2}\ln(\kappa)}, \qquad (12.21)$$

where $K_1(r/\lambda)$ is a first-order modified Bessel function, and the characteristic current density J_c is defined in analogy with Eq. (2.51),

$$J_c=B_{c1}/\mu_0\lambda. \qquad (12.22)$$

The function $K_1(r/\lambda)$ results from differentiation of Eq. (12.19), as expected from the modified Bessel function recursion relation $K_1(x)=-dK_0(x)/dx$ (Arfken, 1985, p. 614). The current density also satisfies the Helmholtz equation, Eq. (6.68), expressed in cylindrical coordinates (Eq. 12.16)) as

$$\frac{\lambda^2}{r}\frac{d}{dr}\left(r\frac{d}{dr}\right)\mathbf{J}_s+\mathbf{J}_s=0. \qquad (12.23)$$

Figure 12.12 compares the distance dependence of the modified Bessel functions $K_0(r/\lambda)$ and $K_1(r/\lambda)$ associated with $B(r)$ and $J_s(r)$, respectively.

These modified Bessel functions have asymptotic behaviors at small radial distances,

$$K_0\left(\frac{r}{\lambda}\right)\approx\ln\left(\frac{2\lambda}{r}\right)-\gamma \quad r\ll\lambda, \quad (12.24)$$

$$\approx\ln\left(\frac{1.123\lambda}{r}\right) \quad r\ll\lambda, \quad (12.25)$$

$$K_1\left(\frac{r}{\lambda}\right)\approx\frac{\lambda}{r} \quad r\ll\lambda, \quad (12.26)$$

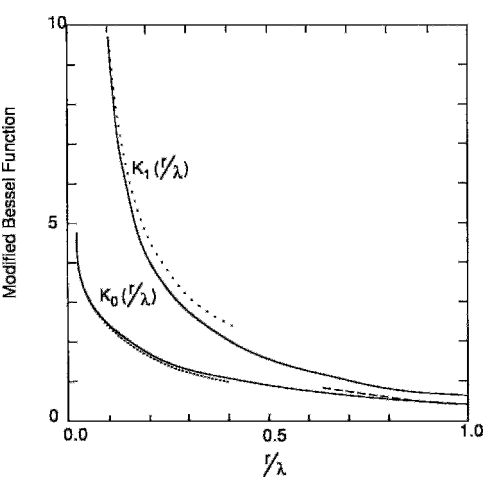

Figure 12.12 Comparison of the distance dependence of the zero-order (K_0) and first-order (K_1) modified Bessel functions associated with the magnetic field and current density, respectively, of a vortex. Asymptotic behavior at short distances (·····) is indicated. Both modified Bessel functions have the same large-distance asymptotic behavior (– – – – –), as shown (Aktas, 1993).

where $\gamma = 0.57721566\ldots$ is the Euler–Mascheroni constant (Arfken, 1985, p. 284) and the factor $2e^{-\gamma} = 1.123$. These expressions show that $K_1(r) \gg K_0(r)$ near the core, where $r \ll \lambda$, as indicated in Fig. 12.12. At large distances the corresponding expressions are

$$K_0\left(\frac{r}{\lambda}\right) \approx \frac{\exp(-r/\lambda)}{(2r/\pi\lambda)^{1/2}} \qquad r \gg \lambda \quad (12.27)$$

$$K_1\left(\frac{r}{\lambda}\right) \approx \frac{\exp(-r/\lambda)}{(2r/\pi\lambda)^{1/2}} \qquad r \gg \lambda. \quad (12.28)$$

Figure 12.12 compares the asymptotic behaviors with the actual functions $K_0(r/\lambda)$ and $K_1(r/\lambda)$. These large-distance expressions permit us to express the magnetic field and current density far from the core in the form

$$B = B_{c1}\frac{(2\pi)^{1/2}}{\ln(\kappa)}\frac{\exp(-r/\lambda)}{(r/\lambda)^{1/2}} \qquad r \gg \lambda, \quad (12.29)$$

$$J_s = J_c\frac{(2\pi)^{1/2}}{\ln(\kappa)}\frac{\exp(-r/\lambda)}{(r/\lambda)^{1/2}} \qquad r \gg \lambda. \quad (12.30)$$

We see from Eqs. 12.24 and (12.26) that both B and J_s are singular at $r = 0$. Since the core is so small in the high-kappa approximation, it is appropriate to remove the singularity by assuming that the magnetic field in the core is constant with the value B(0) given by Eq. (12.17) for $r = \xi$. Even if the mathematical singularity were not removed, the total flux would still remain finite as $r \to 0$, as is proven in Problem 5. In Problem 3 we derive the following expression for the fraction of the total flux of the vortex that is present in the core:

$$\Phi_{core} \approx (\Phi_0/2\kappa^2)\left(\ln 2\kappa + \frac{1}{2} - \gamma\right). \quad (12.31)$$

Figure 12.13 sketches the dependence of Φ_{core}/Φ_0 on k.

Since the magnetic field in the sample is confined to vortices, the total flux is Φ_0 times the number of vortices, and the average internal field B_{in}, given by

$$B_{in} = N_A\Phi_0, \quad (12.32)$$

is proportional to N_A, the number of vortices per unit area. For high applied fields much larger than B_{c1} but, of course, less than B_{c2}, the internal field is approximately proportional to the applied field (see Fig. 12.3), and therefore the density of vortices becomes approximately proportional to the applied field.

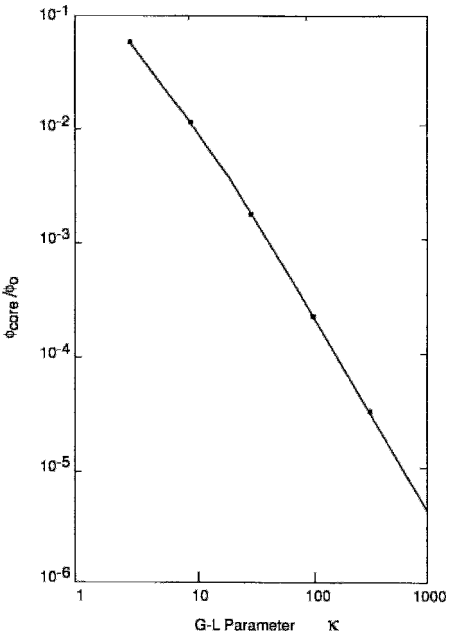

Figure 12.13 Fraction of the total flux quantum, Φ_{core}/Φ_0, present in the core of an isolated vortex as a function of the GL parameter k.

C. Average Internal Field and Vortex Separation

Since interaction between the vortices is repulsive, as we will show in Section V.A, the vortices assume the arrangement that will keep them furthest apart—namely, the two-dimensional hexagonal lattice structure illustrated in Fig. 12.14. To observe this structure

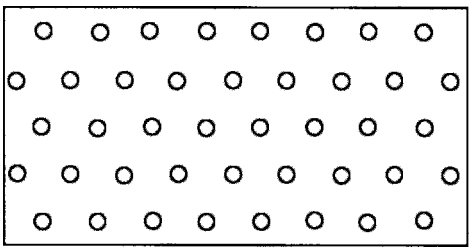

Figure 12.14 Two-dimensional hexagonal lattice of vortex cores.

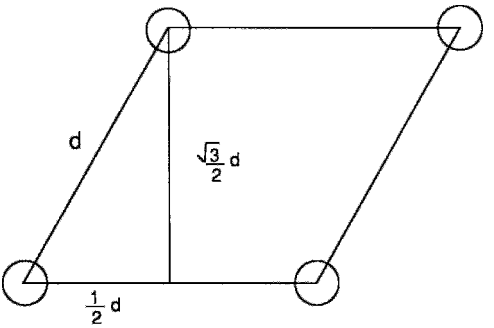

Figure 12.15 Vortex unit cell for the hexagonal lattice of Fig. 12.14. The area of the cell is $\frac{1}{2}\sqrt{3}d^2$.

using what is called the Bitter (1931) technique, the surface is decorated by exposing it to a gas containing tiny suspended magnetic particles that adhere to the vortex cores and show up well on a photographic plate (Dolan *et al.*, 1989; Gammel *et al.*, 1987; Grier *et al.*, 1991; Vinnikov and Grigor'eva, 1988). The imaging can also be done with a scanning-tunneling (H. F. Hess *et al.*, 1989) or scanning-electron microscope, with Lorentz electron microscopy, or with electron holography (Bonevich *et al.*, 1993). Individual vortices have been studied by magnetic force microscopy (Hug *et al.*, 1995; Moser *et al.*, 1995a,b).

The vortices arrange themselves in a hexadic pattern when their density is so high as to make the repulsive interactions between them appreciable in magnitude. Each vortex will then occupy the area $\frac{1}{2}\sqrt{3}d^2$ of the unit cell sketched in Fig. 12.15, where d is the average separation of the vortices. Such a structure has been observed on the surfaces of classical as well as high-temperature superconductors. The average field B_{in} inside the superconductor is given by

$$B_{\text{in}} = \frac{\Phi}{\frac{1}{2}\sqrt{3}d^2}, \tag{12.33}$$

and the number of vortices N equals the total cross-sectional area A_{T} divided by the area per vortex $\frac{1}{2}\sqrt{3}d^2$,

$$N = \frac{A_{\text{T}}}{\frac{1}{2}\sqrt{3}d^2}. \tag{12.34}$$

The vortex lattice structure is not always the hexagonal type depicted in Fig. 12.14 for it can also depend on the magnetic field direction. In low-κ Type II alloys of, for example, Nb, Pb, Tc, or V, the vortices form a square lattice when the magnetic field is parallel to a fourfold crystallographic symmetry axis and a hexagonal lattice when $\mathbf{B}_{\text{app}}$ is along a threefold axis. When $\mathbf{B}_{\text{app}}$ is along a twofold axis direction, a distorted hexagonal lattice is observed (Huebener, 1979, pp. 75ff; Obst, 1971). For $YBa_2Cu_3O_{7-\delta}$ in tilted applied fields, an SEM micrograph shows "a pinstripe array of vortex chains" lying in the $\mathbf{B}_{\text{app}}$, c plane (Gammel and Bishop, 1992), and for the applied field perpendicular to the c direction, chains of oval-shaped vortices are observed (Dolan *et al.*, 1989b).

D. Vortices near Lower Critical Field

When the flux first penetrates the superconductor at $\mathbf{B}_{\text{app}} = \mathbf{B}_{\text{c1}}$ the vortices are near the surface and isolated. As the applied field increases more vortices enter, and their mutual repulsion and tendency to diffuse causes them to migrate inward. Eventually they become sufficiently dense and close enough to experience each others' mutual repulsive forces, so they begin to arrange

themselves into a more or less regular pattern resembling that in Fig. 12.14. For this case we can find an expression for the average internal field $\langle B_{in} \rangle$ in terms of the average separation d by eliminating Φ_0 from Eqs. (12.8) and (12.33)

$$\langle B_{in} \rangle = B_{c1} \frac{8\pi}{\sqrt{3} \ln \kappa} \frac{\lambda^2}{d^2}. \qquad (12.35)$$

Therefore, the separation of vortices when the average internal field equals the lower-critical field is given by

$$d = 2 \left(\frac{\pi}{\sqrt{3} \cdot \frac{1}{2} \ln \kappa} \right)^{1/2} \lambda \qquad (12.36)$$

$$= \frac{3.81\lambda}{\sqrt{\ln \kappa}} \qquad \langle B_{in} \rangle = B_{c1}. \qquad (12.37)$$

Since $\sqrt{\ln 10} = 1.52$ and $\sqrt{\ln 100} = 2.15$, the value of κ does not have much effect on the separation of the vortices. Figure 12.16 shows the dependence of the average internal field on their separation $\frac{1}{2} d/\lambda$.

The process of vortex entry into, and exit from, a superconductor is actually more complicated than this. It can occur in a surface sheath similar to the one that remains superconducting for applied fields in the range $B_{c2} < B_{app} < B_{c3}$, as mentioned in Section II.C. Walton *et al.* (1974) assumed the presence of a surface layer with "nascent" vortices that turn into nucleation sites for the formation of vortices. As the applied field increases, the interface between the surface region containing the vortices and the field-free bulk is able to move inward by diffusion at a velocity proportional to the field gradient (Frahm *et al.*, 1991).

Since it is the applied field rather than the internal field which is known experimentally, it is of interest to determine how the separation of vortices depends on the ratio B_{app}/B_{c1} between the applied field and the lower-critical field. It is assumed that the vortices distribute themselves in a regular manner to produce a uniform internal field, $B_{in} = \langle B_{in} \rangle$. Figure 12.17, an enlargement of the low-field part of Fig. 12.5, shows a typical example illustrating an internal field increasing with increasing applied field in the neighborhood of the lower-critical field. From the slope of the curve of B_{in} versus B_{app}, we conclude that the internal field will reach the value B_{c1} when the applied field approaches the upper limit of the range $B_{c1} < B_{app} < 2B_{c1}$, and we estimate that this might

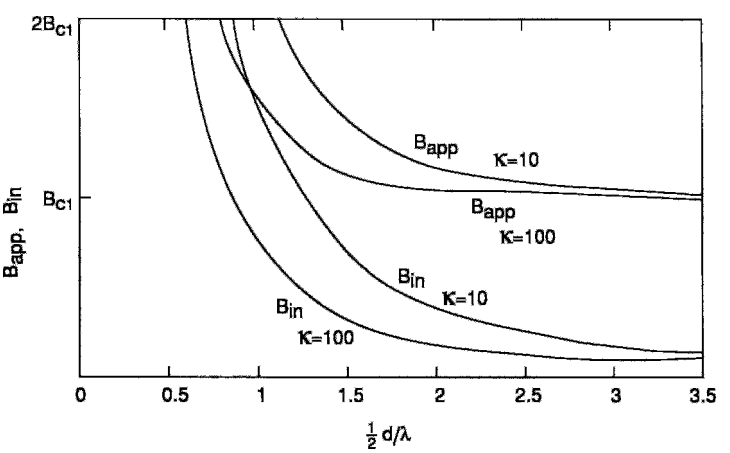

Figure 12.16 Relationship between applied and internal fields, B_{app} and B_{in}, and half the ratio $\frac{1}{2} d/\lambda$ between the vortex separation d and the penetration depth λ, for two values of κ. For much smaller separations $d \ll \lambda$, $\mathbf{B}_{in}$ approaches $\mathbf{B}_{app}$.

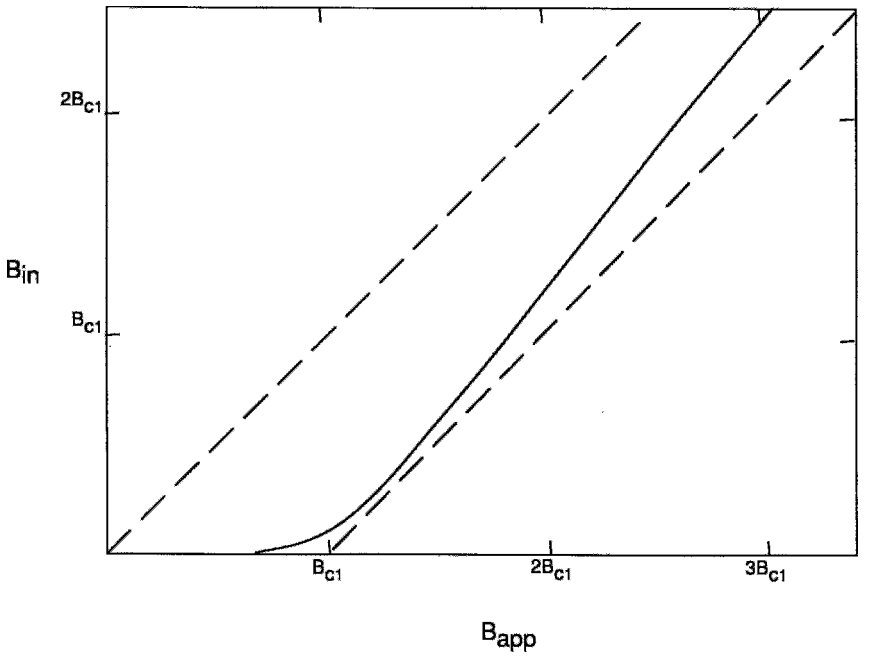

Figure 12.17 The Magnitude of the internal magnetic field B_{in} (solid line) in a Type II superconductor in the neighborhood of the lower-critical field. $\mathbf{B}_{\text{in}}$ approaches the dashed unit slope line through the origin for very high applied fields.

occur for $B_{\text{app}} \approx 1.8B_{\text{c1}}$. Using this figure to convert from B_{in} to B_{app} graphs of B_{app} versus $\frac{1}{2}d/\lambda$ are plotted in Fig. 12.16.

We see from the figure that when the applied field is slightly greater than the lower-critical field, the vortices are much further apart than just one penetration depth. At higher applied fields, the vortices move closer together until near an applied field $B_{\text{app}} \approx 2B_{\text{c1}}$ their separation is about two penetration depths. For higher applied fields appreciable overlap occurs ($\frac{1}{2}d < \lambda$). Thus, relatively low fields produce a concentration of vortices high enough for the vortices to be treated as a continuum rather than as isolated entities.

E. Vortices near Upper Critical Field

When the applied magnetic field approaches the upper-critical field B_{c2} given by Eq. (12.9) the vortices are very close together, with their separation d some what greater than the coherence length ξ. Equating $\langle B_{\text{in}} \rangle$ and B_{c2} in Eqs. (12.9) and (12.33), respectively, we obtain an expression for the vortex nearest-neighbor distance d in terms of the coherence length:

$$d = 2\xi(\pi/\sqrt{3})^{1/2} \tag{12.38}$$

$$\approx 2.69\xi. \tag{12.39}$$

Since $d > 2\xi$, the cores do not quite touch for this highest density case.

F. Contour Plots of Field and Current Density

In Section III.B we wrote down the closed-form expressions (12.17) and (12.20), respectively, for the magnetic field and current density of an isolated vortex, and in Fig. 12.12 we plotted the distance dependence of these quantities for an isolated vortex. In this section we will provide plots that were constructed from calculations of the

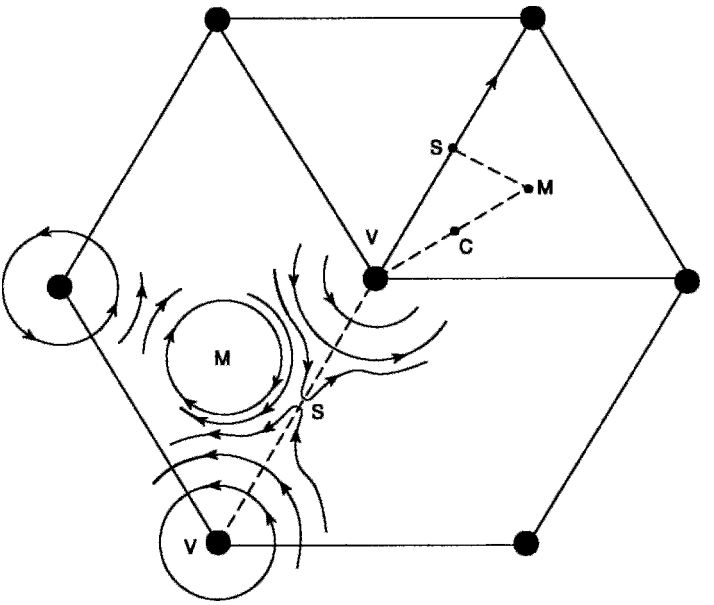

Figure 12.18 Geometrical relationships of a vortex unit cell showing the midpoint M between three vortices V at which the internal field B_{in} is a minimum and the saddle point S midway between two vortices. The triangle V–S–M is the calculational cell, which is one-twelfth the vortex unit cell sketched in Fig. 12.15 and contains all of the information on the fields and currents. Also shown are the current circulation around the vortices V and the midpoint M (Aktas *et al.*, 1994).

position dependence of the field and the current density associated with densely packed vortices (carried out by Aktas, 1993; Aktas *et al.*, 1994). The computations involved adding the contributions of the many overlapping vortices in the neighborhood of a particular vortex, as indicated in Figs. 12.7b and 12.10. This meant taking into account hundreds of vortices, but it was sufficient to carry out the calculations in only one-twelfth of the unit cell because the smaller calculational cell defined by the triangle V–S–M–C–V of Fig. 12.18 replicates itself 12 times in the vortex unit cell of Fig. 12.15.

The magnetic field is a maximum at each vortex position V, of course, and a minimum at the midpoint M between three vortices. Figure 12.19 plots this calculated field change along the path V → S → M → C → V for the case of vortices with "radius" $\lambda = 1000$ Å and separation $d = 400$ Å, which corresponds to considerable overlap. We see from the figure that the field increases along the two paths M → S and M → C. There is a saddle point S midway between the two vortices, with the magnitude of the field decreasing slightly from S to M and increasing appreciably from S to V.

Figure 12.18 portrays the current density encircling the vortex cores V in one direction and flowing around the minimum points M in the opposite direction. Along the path from one vortex to the next the current density passes through zero and reverses direction at the saddle point S. Along the path from the minimum point M to a vortex V there is a curvature change point C at which the current flow switches between clockwise and counterclockwise circulation. Points V, M, and S are well defined geometrically; the

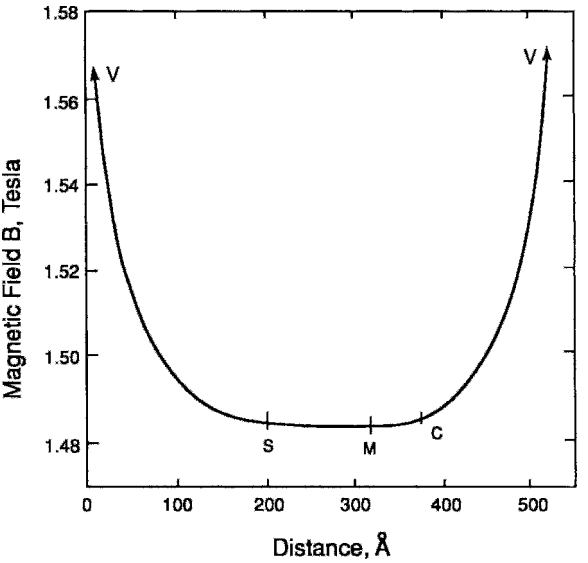

Figure 12.19 Magnitude of internal magnetic field along the three principal directions V → S, S → M, and M → V from the origin at the vortex V in the calculational cell of Fig. 12.18 for $d = 400$ Å and $\lambda = 1000$ Å (Aktas, 1993).

position of point C along the line from V to M has to be calculated. Figure 12.20 plots the current density calculated along the path V → S → M → C → V around the periphery of the calculational cell. A comparison of Figs. 12.19 and 12.20 indicates that the current density tends to be fairly constant over more of the unit cell than is the case with the magnetic field.

The previous few paragraphs describe the internal magnetic field on a mesoscopic scale, with resolution over distances comparable with the penetration depth. Ordinarily, we are interested in the value of the macroscopic internal field, which is an average over these mesoscopic field variations. Forkl *et al.* (1991) used a magneto-optical Faraday effect technique to determine the distribution of the macroscopic internal field inside a disk-shaped sample of $YBa_2Cu_3O_{7-\delta}$; the results are given in Figs. 12.21 and 12.22. Other investigators have published similar internal-field profiles (Flippen, 1991; Glatzer *et al.*, 1992; Mohamed *et al.*, 1989, 1990) and surface-field profiles (Brüll *et al.*, 1991; H. Muller *et al.*, 1991).

G. Closed Vortices

The vortices that we have been discussing are of the open type, in the sense that they begin and end at the surface of the superconductor. Here the flux is continuous with flux entering and leaving from the outside, as indicated in Fig. 12.11. We recall from Figs. 2.36 and 6.19 that a transport current flowing in a superconductor has encircling magnetic field lines, and that the portion of this encircling magnetic flux inside the superconducting material will be in the form of vortices that close in on themselves, basically vortices with loops of totally confined flux. The encircling flux in the region outside the superconductor is not quantized. When both transport and screening current are present, some of the vortices close in on themselves, and some do not.

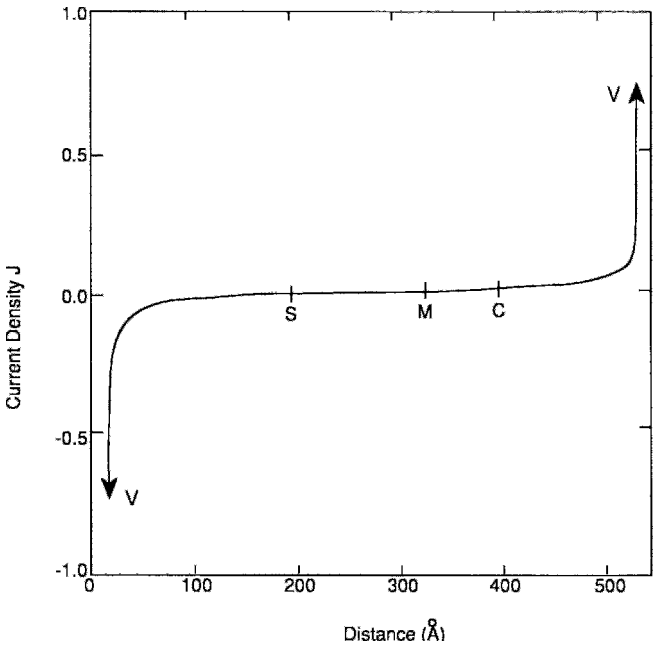

Figure 12.20 Current density along the three principal directions V → S, S → M, and M → V measured from the origin at the vortex V in the calculational cell of Fig. 12.18 for $d = 400\,\text{Å}$ and $\lambda = 1000\,\text{Å}$. The curvature change point C along the path M → V at which the current flow direction shifts from clockwise around V to counterclockwise around M (cf. Fig. 12.18) is indicated. Comparison with Fig. 12.19 shows that the current density exhibits more abrupt changes than the fields (Aktas, 1993).

IV. VORTEX ANISOTROPIES

Section III.B gave expressions for the magnetic field and current densities associated with a vortex in a high-κ isotropic superconductor. Many superconductors, such as those of the high-T_c type, are not isotropic, however, and in this section we will examine the configurations of the resulting vortices. These configurations depend on the coherence length and the penetration depth, which in turn depend on the anisotropies of the carrier effective mass, so we will say a few words about these parameters first. We will emphasize the case of axial symmetry; for this case the a and b directions are equivalent to each other. Such a geometry is exact for tetragonal, and a good approximation for orthorhombic high-temperature superconductors. The reader is referred to the text by Orlando and Delin (1991) for derivations of the various expressions in this section.

An alternative approach to that presented here considers an isolated vortex as having elastic properties that are analogous to those of a string under tension (Hanaguri *et al.*, 1994; Toner, 1991a; Widom *et al.*, 1992). The vortex is assumed to be held in place at its end points by the coupling to the external magnetic field, and when distorted it tends to return to a linear configuration. The flux-line lattice in an anisotropic superconductor is more complicated, and has been treated using anisotropic elasticity theory (Sardella, 1992).

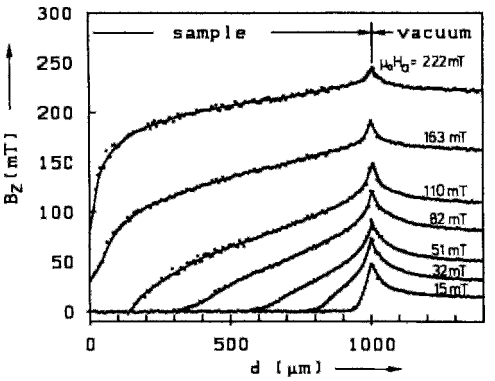

Figure 12.21 Radial distribution of internal magnetic field in a superconducting rod of 1 mm radius for applied fields from 15 mT to 222 mT. The penetration depth $\lambda \approx 20\,\mu$m (Forkl *et al.*, 1991).

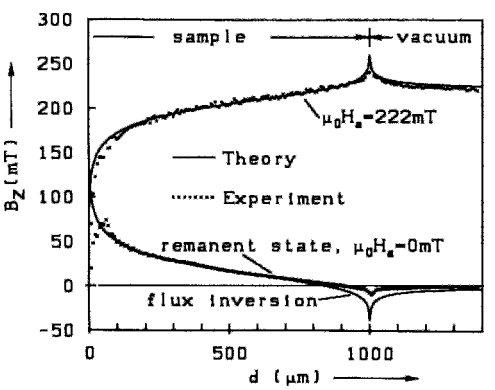

Figure 12.22 Radial distribution of internal magnetic field in the superconducting rod of Fig. 12.21 following application of a field of 222 mT and in the remanent state following removal of this field (Forkl *et al.*, 1991).

A. Critical Fields and Characteristic Lengths

The electron or hole carriers of an anisotropic superconductor have effective masses m^* that depend on the direction, with the principal values m_a, m_b, and m_c along the three principal directions a, b, and c of the crystal. The Ginzburg–Landau theory tells us that, on the basis of Eqs. (6.26) and (6.45), respectively [cf. Eq. 7.123)].

$$\xi^2 = \hbar^2/2m^*|a|, \tag{12.40}$$

$$\lambda^2 = \frac{m^*}{\mu_0 e^{*2}|\phi_\infty|^2}, \tag{12.41}$$

the coherence length ξ is inversely proportional, and the penetration depth λ is directly proportional, to the square root of m^*, where the factors a and ϕ_∞ of the GL theory depend on the temperature. Since the anisotropy arises from the effective mass, to a first approximation we can write for the three principal directions

$$\xi_a\sqrt{m_a} = \xi_b\sqrt{m_b} = \xi_c\sqrt{m_c}, \tag{12.42a}$$

$$\lambda_a/\sqrt{m_a} = \lambda_b/\sqrt{m_b} = \lambda_c/\sqrt{m_c}. \tag{12.42b}$$

Multiplying these expressions together term by term gives

$$\xi_a\lambda_a = \xi_b\lambda_b = \xi_c\lambda_c, \tag{12.43}$$

which is the basic characteristic length relationship of anisotropic superconductors.

Many superconductors, such as the cuprates, are axially symmetric with in-plane ($m_a = m_b = m_{ab}$) and axial-direction (m_c) effective masses. We define the ratio Γ by

$$\Gamma = m_c/m_{ab}, \tag{12.44}$$

with reported values $\Gamma \geq 29$ for $YBa_2Cu_3O_{7-\delta}$ (Farrell *et al.*, 1988), $\Gamma \geq 3000$ for $Bi_2Sr_2CaCu_2O_8$ (Farrell *et al.*, 1989b), and $\Gamma \geq 10^5$ for $Tl_2Ba_2CaCuO_8$ (Farrell *et al.*, 1990a). Using Eqs. (12.42)–(12.44) we can show that the coherence length ξ_{ab} and penetration depth λ_{ab} in the a, b plane are related to their values ξ_c and λ_c along the c direction through the expression (Kes *et al.*, 1991).

$$\Gamma = (\xi_{ab}/\xi_c)^2 = (\lambda_c/\lambda_{ab})^2, \tag{12.45}$$

where for the cuprates (Hikita *et al.*, 1987; Worthington *et al.*, 1987) we have

$$\xi_c < \xi_{ab} \ll \lambda_{ab} < \lambda_c. \tag{12.46}$$

Some reported values of these quantities are listed in Table 12.4.

The GL parameter κ_i for the magnetic field in the ith principal direction is (Chakravarty *et al*., 1990)

$$\kappa_i = \left| \frac{\lambda_j \lambda_k}{\xi_j \xi_k} \right|^{1/2}, \qquad (12.47)$$

which gives for the cuprates with the applied field in the a, b-plane (κ_{ab}) and along the c direction (κ_c), respectively,

$$\kappa_{ab} = \left| \frac{\lambda_{ab} \lambda_c}{\xi_{ab} \xi_c} \right|^{1/2} \qquad (12.48a)$$

$$\kappa_c = \lambda_{ab}/\xi_{ab}. \qquad (12.48b)$$

In the next two sections we will employ these quantities to write down explicit expressions for the core perimeter, magnetic fields, and current densities of vortices in the presence of anisotropies. An average GL parameter $\kappa_{av} = (\lambda_1 \lambda_2 \lambda_3 / \xi_1 \xi_2 \xi_3)^{1/3}$ has also been defined (Clem and Coffey, 1990).

B. Core Region and Current Flow

The vortices described in Section III.B for $\kappa \gg 1$ were axially symmetric, with the shielding current flowing in circular paths around the axis, as illustrated in Fig. 12.9 Axial symmetry is also observed for the cuprates when the applied field is aligned along c. When, however, it is along the b (or a) direction, the core cross-section is an ellipse with semi-axes ξ_{ab} and ξ_c along the a and c directions, as indicated in Fig. 12.23. The current flows in an elliptical path with semi-axes $\alpha\lambda_c$ and $\alpha\lambda_{ab}$, as shown in Fig. 12.24, where α is a numerical factor that depends on the distance of the current from the core. We know from Eq. (12.43) that $\xi_{ab}/\xi_c = \lambda_c/\lambda_{ab}$, so the core and current flow ellipses have the same ratio $\sqrt{\Gamma}$ of semi-major to semi-minor axis, and hence the same eccentricity. The equation for the current flow ellipse with $\alpha = 1$ is

$$\frac{x^2}{\lambda_c^2} + \frac{z^2}{\lambda_{ab}^2} = 1 \qquad \mathbf{B}_{\text{app}} || b, \qquad (12.49a)$$

where x and z are the Cartesian coordinates of points on the perimeter. The corresponding current flow equation for the applied field along the c direction is a circle,

$$\frac{x^2 + y^2}{\lambda_{ab}^2} = 1 \qquad \mathbf{B}_{\text{app}} || c. \qquad (12.49b)$$

Equations (12.49a) and (12.49b) also correspond to loci of constant magnetic field around the vortex. They are plotted on the left and right sides, respectively, of Fig. 12.23 to indicate the relative size of the two vortices. Expressions analogous to Eqs. (12.49) can be written down for the perimeters of the cores.

Since the current paths are ellipses, each increment of current ΔI flows in a channel between a pair of ellipses, in the manner illustrated in Fig. 12.24. When the channel is narrow, as it is at the top and bottom of the figure, the flow is fast, so the current density is large, as indicated. Conversely, in the wider channels on the left and right, the flow is slow and J is small, as indicated. The increment of current ΔI through each part of the channel is the same, so the product J times the width must be constant, and we can write

$$J_x \Delta z = J_z \Delta x. \qquad (12.50)$$

This is a special case of the fluid mechanics expression $J_1 A_1 = J_2 A_2$ for current flow in a pipe of variable cross section A.

C. Critical Fields

The isotropic expressions for the critical fields given in Section III.B can be modified for anisotropy by using the GL parameter κ_i (12.47) for the applied field in the i

Table 12.4 Coherence Lengths ξ_i and Penetration Depths λ_i of Various Superconductors in the Symmetry Plane (called the *a*, *b*-plane) and in the Axial Direction (called the *c*-axis), and Values of the Anisotropy Ratio Γ

Material	T_c (K)	ξ_{ab} (nm)	ξ_c (nm)	λ_{ab} (nm)	λ_c (nm)	$\Gamma(m_c/m_{ab})$	Reference
$NbSe_2$		7.7	2.3	69	230	11	Salamon (1989)
UPt_3 (heavy fermion)	0.46			782	707		Broholm *et al*. (1990)
K-$(ET)_2Cu[NCS]_2$	9			980			Harshman *et al*. (1990)
K-$(ET)_2Cu[NCS]_2$	10					$>4\times10^4$	Farrell *et al*. (1990b)
K-$(ET)_2Cu[N(CN)_2]_2Br$	11.4			650			Lang *et al*. (1992a, b)
K-$ET)_2Cu[N(CN)_2]_2Br$	11.6	3.7	0.4			86	Kwok *et al*. (1990b)
$(La_{0.925}Sr_{0.075})_2CuO_4$	34	2.9					Hase *et al*. (1991)
$(La_{0.91}Sr_{0.09})_2CuO_4$	30	3.3		283			Li *et al*. (1993)
$(Nd_{0.925}Ce_{0.075})_2CuO_4$[a]	21.5			80	100		Wu *et al*. (1993)
$(Nd_{0.9}Ce_{0.1})_2CuO_4$[a]						≈600	O and Markert (1993)
$(Sm_{0.925}Ce_{0.075})_2CuO_{4-\delta}$[a]	11.4	7.9	1.5				Dalichaouch *et al*. (1990b)
$(Sm_{0.925}Ce_{0.075})_2CuO_{4-\delta}$[a]	18	4.8					S. H. Han *et al*. (1992)
$YBa_2Cu_3O_{6.5}$	62	2.0	0.45			19	Vandervoort *et al*. (1991)
$YBa_2Cu_3O_{6.9}$	83			142	>700		Harshman *et al*. (1989)
$YBa_2Cu_3O_{6.94}$	91.2	1.7		150			Ossandon *et al*. (1992a)
$YBa_2Cu_3O_{7-\delta}$	66			260			Lee and Ginsberg (1991)
$YBa_2Cu_3O_{7-\delta}$	90	2.5	0.8			10	Chaudhari *et al*. (1987)
$YBa_2Cu_3O_{7-\delta}$	89	3.4	0.7	26	125	25	Worthington *et al*. (1987)
$YBa_2Cu_3O_{7-\delta}$	92.4	4.3	0.7	27	180	41	Gallagher (1988)
$YBa_2Cu_3O_{7-\delta}$	92	1.2	0.3	89	550	≈27	Salamon (1989)
$YBa_2Cu_3O_{7-\delta}$	90	1.3	0.2	130	450	≈25	Krusin-Elbaum *et al*. (1989)

$YBa_2Cu_3O_{7-\delta}$	92	1.6	0.3				Welp *et al*. (1989)
$EuBa_2Cu_3O_{7-\delta}$	95	2.7	0.6			20	Hikita *et al*. (1987)
$EuBa_2Cu_3O_{7-\delta}$	94	3.5	0.38				Y. Tajima *et al*. (1988)
$TmBa_2Cu_3O_{7-\delta}$	86	7.4	0.9			68	Noel *et al*. (1987)
$Y_{0.8}Pr_{0.2}Ba_2Cu_3O_{7+\delta}$	73	2.4	0.78			9.5	Jia *et al*. (1992)
$Bi_2Sr_2CaCu_2O_8$	84	1.1					Johnston and Cho (1990)
$Bi_2Sr_2CaCu_2O_8$	109				500		Maeda *et al*. (1992)
$Bi_2Sr_2Ca_2Cu_3O_{10}$	109	2.9	0.09				Matsubara *et al*. (1992)
$Bi_2Sr_2Ca_2Cu_3O_{10}$	111	1.0	0.02				Q. Li *et al*. (1992)
$(Bi,\ Pb)_2Sr_2CaCu_2O_8$	91	2.0			178		H. Zhang *et al*. (1992)
$(Bi_{0.9}Pb_{0.1})_2Sr_2CaCu_2O_{8+\delta}$	91.1	2.04	0.037				W. C. Lee *et al*. (1991)
$(Bi_{0.9}Pb_{0.1})_2Sr_2Ca_2Cu_3O_{10+\delta}$	103	1.18					W. C. Lee *et al*. (1991)
$Pb_2Sr_2(Y,\ Ca)CaCu_3O_8$	76	1.5	0.3	258	643	$\approx 12^b$	Reedyk *et al*. (1992b)
$Tl_2Ba_2CaCu_2O_{8-\delta}$	100			182			Ning *et al*. (1992)
$Tl_2Ba_2Ca_2Cu_3O_{10}$	123			173	480	8	Thompson *et al*. (1990)
$Tl_2Ba_2Ca_2Cu_3O_{10}$	100					$\geq 10^5$	Farrell *et al*. (1990a)
$HgBa_2CuO_{4+\delta}$	93	2.1		117			Thompson *et al*. (1993)
$HgBa_2Ca_2Cu_3O_{8+\delta}$	133	1.3		130	3500	730	Schilling *et al*. (1994b)

Note: The axial direction is along the *c*-axis for high temperature superconductors, and along the *a*-axis for typical organic materials.

[a] This is an electron superconductor.

[b] An estimate, since the ratios ξ_{ab}/ξ_c and λ_c/λ_{ab} differ.

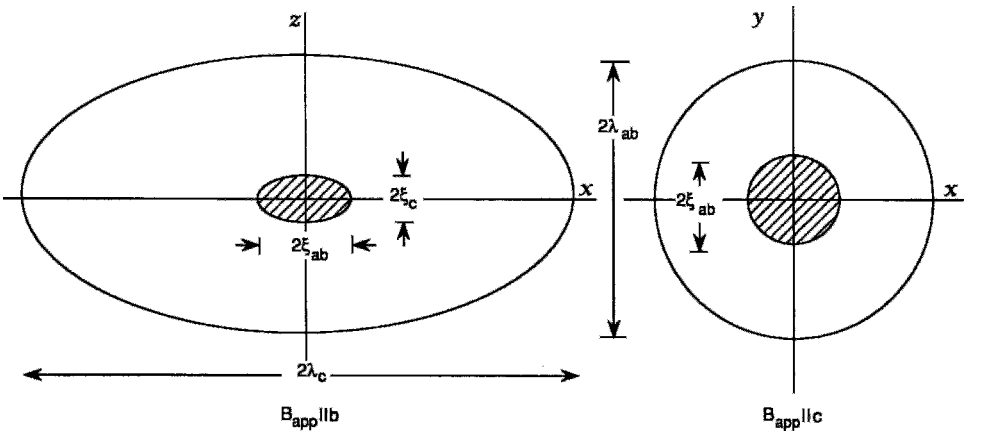

Figure 12.23 Shape of the core (shaded) and the perimeter one penetration length from the center of a vortex for an applied magnetic field along the b (left) and c (right) crystallographic directions, respectively. The magnetic field is constant along each ellipse and along each circle. The figure is drawn for the condition $\lambda_c = 2\lambda_{ab} = 6\xi_{ab} = 12\xi_c$.

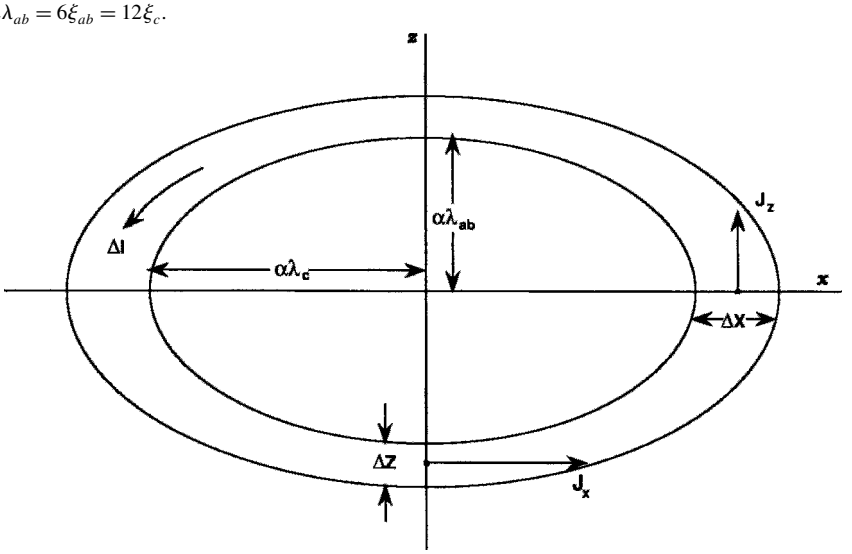

Figure 12.24 Flow of differential current ΔI in an elliptical path around a vortex for an applied magnetic field along the b crystallographic axis. The current densities are $J_x = \Delta I/\Delta z\Delta y$ on the z-axis, and $J_z = \Delta I/\Delta x\Delta y$ on the x-axis.

direction, and inserting the appropriate characteristic lengths for the directions perpendicular to i. When the applied field is along the ith principal direction, expressions (12.8) and (12.9) for the critical fields $B_{c1}(i)$ and $B_{c2}(i)$ become

$$B_{c1}(i) = \frac{\Phi_0 \ln \kappa_i}{4\pi\lambda_j\lambda_k}, \qquad (12.51a)$$

$$B_{c2}(i) = \frac{\Phi_0}{2\pi\xi_j\xi_k} \qquad (12.51b)$$

These can be written in terms of the thermodynamic critical field $\mathbf{B}_c$,

$$B_{c1}(i) = \frac{\ln \kappa_i}{\sqrt{2}\kappa_i} B_c, \qquad (12.52a)$$

$$B_{c2}(i) = \sqrt{2}\kappa_i B_c, \qquad (12.52b)$$

where B_c itself (9.10),

$$B_c = \frac{\Phi_0}{2\sqrt{2}\pi\xi_i\lambda_i}, \tag{12.53}$$

is independent of the direction since, from Eq. (12.43), the product $\xi_i\lambda_i$ has the same value for $i = a, b, c$. The expressions for the ratio

$$B_{c2}(i)/B_{c1}(i) = 2\kappa_i^2/\ln\kappa_i, \tag{12.54}$$

and the product of these critical fields,

$$[B_{c1}(\ell)B_{c2}(i)]^{1/2} = B_c[\ln\kappa_i]^{1/2}, \tag{12.55}$$

are generalizations of Eqs. (12.13). For the particular case of axial symmetry we have for the critical fields in the *a, b*-plane,

$$B_{c1}(ab) = \frac{\Phi_0 \ln\kappa_{ab}}{4\pi\lambda_{ab}\lambda_c}, \tag{12.56a}$$

$$B_{c2}(ab) = \frac{\Phi_0}{2\pi\xi_{ab}\xi_c}, \tag{12.56b}$$

and along the *c* direction,

$$B_{c1}(c) = \frac{\Phi_0 \ln\kappa_c}{4\pi\lambda_{ab}^2}, \tag{12.57a}$$

$$B_{c2}(c) = \frac{\Phi_0}{2\pi\xi_{ab}^2}, \tag{12.57b}$$

where κ_{ab} and κ_c are defined by Eqs. (12.48). The ratio of the upper critical fields,

$$\frac{B_{c2}(ab)}{B_{c2}(c)} = \sqrt{\Gamma}, \tag{12.58}$$

is a particularly simple expression. Table 12.5 provides some experimentally determined values of these critical field anisotropies.

D. High-Kappa Approximation

In Section III.B we wrote down expressions for the radial dependence of the magnetic field and current density associated with a vortex in an isotropic superconductor. Now we will generalize these expressions to account for the presence of anisotropy.

When the applied magnetic field is in the *z* direction, along the *c*-axis, the vortex has axial symmetry and the magnetic field and current densities have the distance dependence,

$$B_z(x, y) = \frac{\Phi_0}{2\pi\lambda_{ab}^2} K_0\left[(x^2+y^2)^{1/2}/\lambda_{ab}\right], \tag{12.59}$$

$$\mathbf{J}_s(x, y) = \frac{\Phi_0}{2\pi\mu_0\lambda_{ab}^3} K_1\left[(x^2+y^2)^{1/2}/\lambda_{ab}\right] \times \left(\frac{y\mathbf{i} - x\mathbf{j}}{(x^2+y^2)^{1/2}}\right), \tag{12.60}$$

where K_0 and K_1 are zeroth- and first-order modified Bessel functions, respectively.

When the applied magnetic field is in the *x* direction, along the *a*-axis, the vortex no longer has axial symmetry, and the distance dependences are more complicated:

$$B_x(y, z) = \frac{\Phi_0}{2\pi\lambda_{ab}\lambda_c} K_0\left[\left(\frac{y^2}{\lambda_c^2} + \frac{z^2}{\lambda_{ab}^2}\right)^{1/2}\right], \tag{12.61}$$

$$\mathbf{J}_s(y, z) = \frac{\Phi_0}{2\pi\mu_0\lambda_{ab}\lambda_c} \times \frac{K_1\left[\left(\frac{y^2}{\lambda_c^2} + \frac{z^2}{\lambda_{ab}^2}\right)^{1/2}\right]}{\left(\frac{y^2}{\lambda_c^2} + \frac{z^2}{\lambda_{ab}^2}\right)^{1/2}} \times \left[\frac{y}{\lambda_c^2}\mathbf{k} - \frac{z}{\lambda_{ab}^2}\mathbf{j}\right]. \tag{12.62}$$

Equation (12.62) is obtained from (12.61) with the aid of relation $\nabla \times \mathbf{B} = \mu_0\mathbf{J}_s$. Analogous expressions can be written down for B_{app} along *y*. The asymptotic equations (12.24)–(12.28) for the modified Bessel functions can also be applied to the anisotropic case.

Table 12.5 Critical Fields of Selected Anisotropic Type II Superconductors

Material	T_c (K)	B_{c1}^{ab} (mT)	B_{c1}^{c} (mT)	B_c (T)	B_{c2}^{ab} (T)	B_{c2}^{c} (T)	$-dB_{c2}^{ab}/dT$ (T/K)	$-dB_{c2}^{c}/dT$ (T/K)	Reference
$CeCu_2Si_2$ (heavy fermion)	0.63				2.0	2.4			Assmus *et al.* (1984)
β-$(ET)_2I_3$ (organic)	1.5	7[a]	36		1.74[b]	0.08			Ishiguro and Yamaji (1990)
β-$(ET)_2I_3$ 1.6 kbar	7.2				25	2.7			Ishiguro and Yamaji (1990)
β-$(ET)_2IBr_2$ (organic)	2.3	390	1600		3.48[c]	1.5			Ishiguro and Yamaji (1990)
β-$(ET)_2AuI_2$ (organic)	4.2	400	2050		≈6.35	≈0.8			Ishiguro and Yamagi (1990)
K-$(ET)_2Cu[N(CN)_2]Br$	11.6						20	2.2	Kwok *et al.* (1990b)
$(Sm_{0.925}Ce_{0.05})_2CuO_4$ (electron type)	11.4				28.2	5.2	3.6	0.1	Dalichaouch *et al.* (1990b)
$(La_{0.95}Ca_{0.05})_2CuO_4$	≈14.0				>20	>13	4	0.3	Hidaka *et al.* (1987)
$(La_{0.9}Ca_{0.1})_2CuO_4$	30			0.2		32		1.5	Li *et al.* (1993)
$(La_{0.93}Ca_{0.07})_2CuO_4$[d]	≈34.0	7	30						Naito *et al.* (1990)
$YBa_2Cu_3O_{6.5}$	62	2.5	8.3	0.38	380	87	8.7	2.0	Vandervoort *et al.* (1991)
$YBa_2Cu_3O_{6.94}$	91.2		32			115		1.8	Ossandon *et al.* (1992a)
$YBa_2Cu_3O_{7-\delta}$		53	520						Dinger *et al.* (1987)
$YBa_2Cu_3O_{7-\delta}$		70	130				≈1.0	0.65	Song *et al.* (1987)
$YBa_2Cu_3O_{7-\delta}$	88.8	≤5	500	2.65	140	29	2.3	0.46	Worthington *et al.* (1987)
$YBa_2Cu_3O_{7-\delta}$	92.4	≤5	500	1.93	240	34	3.8	0.54	Gallagher (1988)
$YBa_2Cu_3O_{7-\delta}$	24	103	≈1.7				14		Salamon (1989)
$YBa_2Cu_3O_{7-\delta}$					110	40	3.4	1.0	Nakao *et al.* (1989)
$YBa_2Cu_3O_{7-\delta}$	90	18	53	≈1.8					Krusin-Elbaum *et al.* (1989)
$YBa_2Cu_3O_{7-\delta}$	92						10.5	1.9	Welp *et al.* (1989)
$EuBa_2Cu_3O_{7-\delta}$	95				190	45	3.0	0.7	Hikita *et al.* (1987)
$EuBa_2Cu_3O_{7-\delta}$	94.8				245	28	3.8	0.41	Y. Tajima *et al.* (1988)
$Y_{0.8}Pr_{0.2}Ba_2Cu_3O_{7-\delta}$	73				174	56	3.4	1.1	Jia *et al.* (1992)
$Bi_2Sr_2CaCu_2O_{8+\delta}$	90	85							Maeda *et al.* (1992)
$(Bi, Pb)_2Sr_2CaCu_2O_8$	91			0.65		≈89		1.4	L. Zhang *et al.* (1992)
$Bi_2Sr_2Ca_2Cu_3O_{10+\delta}$	109						16	0.5	Matsubara *et al.* (1992)
$Pb_2Sr_2(Y, Ca)Cu_3O_8$	76	9.5	50.5	0.80	590	96	11	1.75	Reedyk *et al.* (1992b)
$HgBa_2Ca_2Cu_3O_{8+\delta}$	131		45			190		2.0	Schilling *et al.* (1994b)

Note: Some of the thermodynamic critical fields B_c were calculated from Eq. (12.53) using data from Table 12.4.

[a] Average of $B_{c1}^a = 5\,\text{mT}$, $B_{c1}^b = 9\,\text{mT}$; [b] Average of $B_{c2}^a = 1.78\,\text{T}$, $B_{c2}^b = 1.70\,\text{T}$; [c] Average of $B_{c2}^a = 3.36\,\text{T}$, $B_{c2}^b = 3.60\,\text{T}$; [d] $-dB_{c1}^{ab}/dT = 1.8\,\text{mT/K}$, $-dB_{c1}^{c}/dT = 5.5\,\text{mT/K}$.

When the applied magnetic field is aligned at an oblique angle relative to the c direction, the expressions for the magnetic field and current density in the neighborhood of a vortex become very complicated, and we will not try to specify them.

E. Pancake Vortices

In high-temperature superconductors the coherence length ξ_c along the c-axis is less than the average spacing between the copper-oxide planes, and hence the coupling between the planes tends to be weak. The Lawrence–Doniach model (1971; Bulaevskii, 1973; Bulaevskii *et al.*, 1992; Clem, 1989, 1991) assumes that the superconductor consists of parallel superconducting layers that are weakly Josephson coupled to each other. A vortex perpendicular to these layers, which conventionally would be considered a uniform cylinder of confined flux surrounded by circulating currents, is looked upon in this model as a stacking of two-dimensional (2D) pancake-shaped vortices, one pancake vortex per layer with surrounding, nearly circular current patterns confined to the layer. The stacked 2D Abrikosov vortices shown in Fig. 12.25 are coupled together by means of Josephson vortices whose axes thread through the Josephson junctions between the superconducting layers, stretching from the center of each pancake vortex to the center of the adjacent vortices above and below. The field and current distributions for the individual pancake vortices in this stack, aligned along c, as well as in a "leaning tower" or tilted stack of such vortices have been calculated (Clem, 1991).

Thermal agitation can shake the stack, decouple pancake vortices in adjacent layers, and even cause the stack to break up, as in a Kosterlitz–Thouless-type transition. Figure 12.26 shows a segment of a vortex displaced but still coupled. In this model melting might occur in the direction perpendicular to the layers, with the vortices within each layer forming 2D solids.

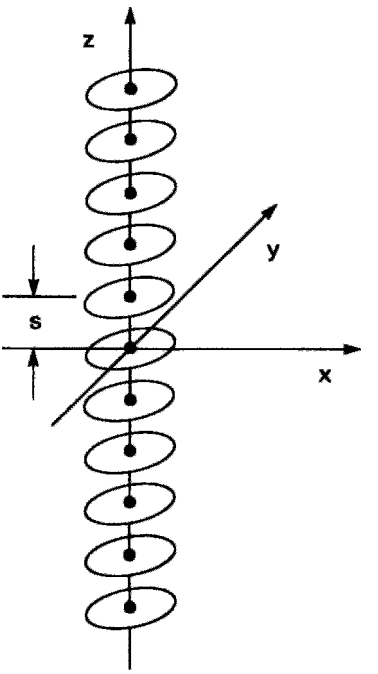

Figure 12.25 Stack of two-dimensional pancake vortices aligned along the c direction (Clem, 1991).

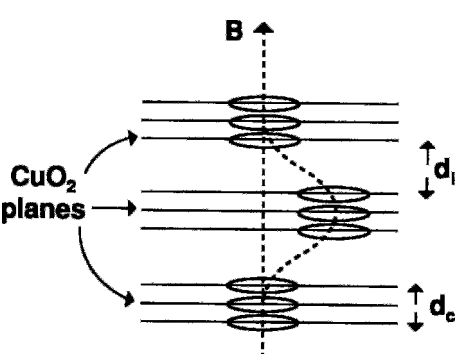

Figure 12.26 Pancake vortex model showing a segment of vortex displaced to the right (Maley, 1991).

F. Oblique Alignment

When the applied magnetic field is inclined at an angle with respect to the c-axis of an anisotropic superconductor, neither the internal magnetic field nor the magnetization is oriented in the same direction as B_{app} (Felner *et al.*, 1989; D. H. Kim *et al.*, 1991b;

Kolesnik *et al*., 1992; L. Liu *et al*., 1992; Tuominen *et al*., 1990; K. Watanabe *et al*., 1991; Welp *et al*., 1989). This complicates the trapping of magnetic flux and alignment of the vortices. Elliptically shaped magnetic field contours around vortices have been published for the case of anisotropy (Thiemann *et al*., 1989). In addition, the upper-critical field and critical current both depend on the orientation (K. Watanabe *et al*., 1991). Transverse magnetization of an Abrikosov lattice, which is absent in an isotropic superconductor, has been determined for the anisotropic case using torque measurements (Farrell *et al*., 1989b; Gray *et al*., 1990).

V. INDIVIDUAL VORTEX MOTION

The mutual-repulsion Lorentz force $\mathbf{J}_i \times \mathbf{\Phi}_j$ between vortices arising from the interaction of the current density $\mathbf{J}_i$ of one vortex with the flux $\mathbf{\Phi}_j$ of another causes the vortices to become arranged in the hexagonal equilibrium configuration of Fig. 12.14. During the equilibration process each moving vortex experiences a frictional or damping force $\mathbf{f} = \beta\mathbf{v}$ that retards its motion, and a second force, called the *Magnus force*, which is given by $\alpha n_s e(\mathbf{v} \times \mathbf{\Phi}_0)$, where n_s is the density of the superconducting electrons. (The origin of the Magnus force will be explained in Section E.) Many vortices become trapped at pinning centers and hinder the motion of nearby vortices. When the pinning forces $\mathbf{F}_P$ are not sufficiently strong to prevent flux motion, the superconductor is called soft; otherwise it is called hard. When transport current $\mathbf{J}_{tr}$ is present, the Lorentz force $\mathbf{J}_{tr} \times \mathbf{\Phi}_0$ acts to unpin the vortices and induce a collective flux motion. When the pinning forces still dominate, this very slow motion is called *flux creep*, and when the Lorentz force dominates, the faster motion is called *flux flow*.

The forces acting on the vortex, such as $\mathbf{F}_P$ and $\mathbf{J} \times \mathbf{\Phi}_0$, are actually forces per unit length, but we have simplified the notation by referring to them as simply forces.

A. Vortex Repulsion

It is shown in electrodynamics texts that the Lorentz force density $\mathbf{f}$ for the interaction between an electric current density $\mathbf{J}$ and a magnetic field $\mathbf{B}$ is given by

$$\mathbf{f} = \mathbf{J} \times \mathbf{B}. \tag{12.63}$$

The force between two vortices may be considered as arising from the interaction between the magnetic field $\mathbf{B}$ of one vortex and the current density $\mathbf{J}$ present at the position of this field and arising from the other vortex, as shown in Fig. 12.27. It is assumed that both vortices are infinitely long and axially symmetric and that they are aligned parallel to each other a distance d apart. Since $\mathbf{f}$ is the force per unit volume, the total force $\mathbf{F}$ is obtained by integrating the current density over the volume containing the $\mathbf{B}$ field,

$$\mathbf{F} = \int \mathbf{J} \times \mathbf{B} r dr d\phi dz, \tag{12.64}$$

where cylindrical coordinates, r, ϕ, and z, have been used, and $r = (x^2 + y^2)^{1/2}$. Since there is no z dependence, it is more appropriate to calculate the force per unit length, which is given by

$$\mathbf{F}/L = \int \mathbf{J}(r') \times \mathbf{B}(r) r dr d\phi, \tag{12.65}$$

where from Fig. 12.28 the distance r' is given by

$$r' = (r^2 + d^2 - 2rd\cos\phi)^{1/2}. \tag{12.66}$$

In the high-κ approximation the expressions in Eqs. (12.17) and (12.20) for $\mathbf{B}(r)$ and $\mathbf{J}(r')$, respectively, can be substituted in the integral,

$$F/L = \frac{\Phi_0^2}{4\pi^2\mu_0\lambda^5} \int K_0\left(\frac{r}{\lambda}\right) K_1\left(\frac{r'}{\lambda}\right) r\, dr\, d\phi, \tag{12.67}$$

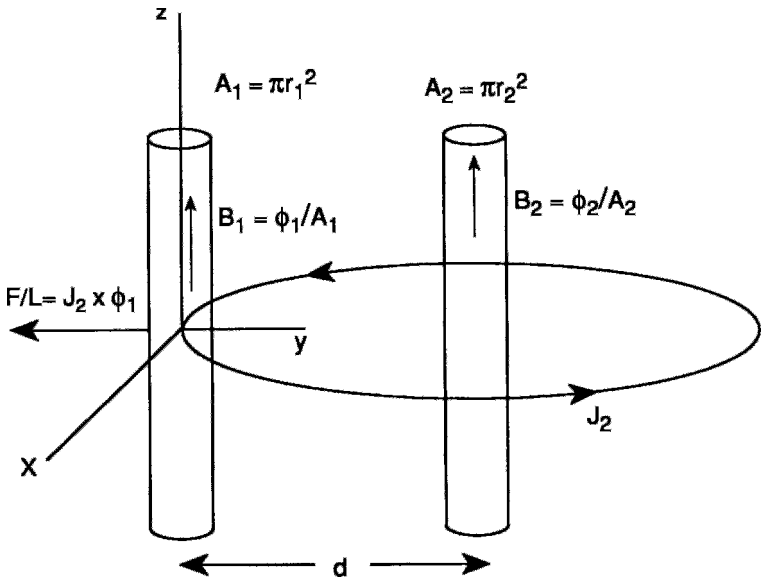

Figure 12.27 Repulsive interaction involving the magnetic field $\mathbf{B}_1$ in a vortex core with current density $\mathbf{J}_2$ from another parallel vortex $\mathbf{B}_2$. The repulsive force $\mathbf{F}/L = \mathbf{J}_2 \times \mathbf{\Phi}_1$ is shown.

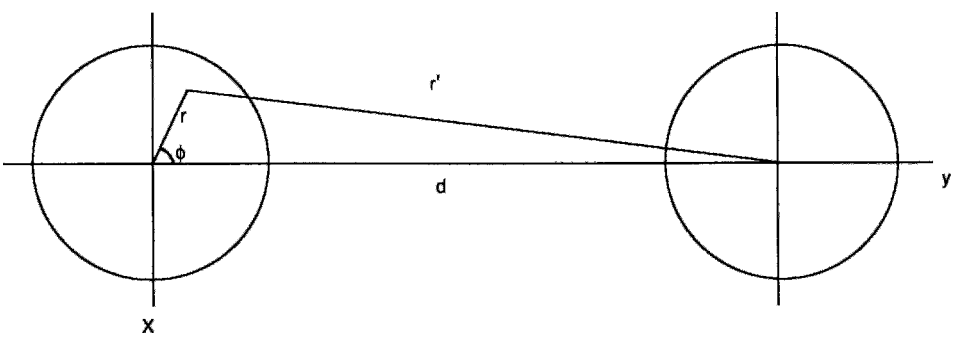

Figure 12.28 Coordinates for calculating the repulsive force between two vortices.

which can be evaluated to give the force per unit length. This force, which is indicated in Fig. 12.27, is repulsive and moves the vortices apart.

The current density and magnetic field strength vary over the region of integration in the manner illustrated in Fig. 12.29, and Eq. (12.67) cannot be integrated in closed form. If the vortices are far enough apart as to make the current density effectively constant throughout the region of integration, $\mathbf{J}(r')$ may be approximated by $\mathbf{J}(d)$ and taken outside the integral,

$$\mathbf{F}/L = \mathbf{J}(d) \times \int \mathbf{B}(r) r \, dr \, d\phi. \qquad (12.68)$$

We know that the magnetic field $\mathbf{B}$ integrated over the cross-section of a vortex equals a fluxoid $\mathbf{\Phi}_0$ oriented along z, giving us

$$\mathbf{F}/L = \mathbf{J} \times \mathbf{\Phi}_0. \qquad (12.69)$$

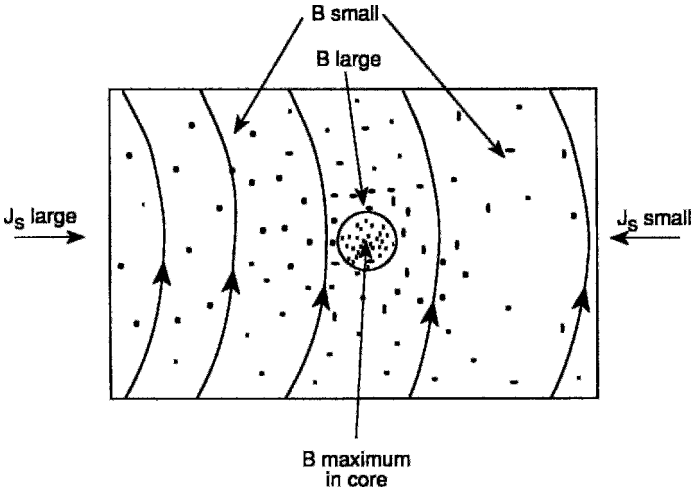

Figure 12.29 Cross section through a vortex core (center) with the strength of its magnitude field **B** directed upward from the page and proportional to the density of the dots. The current density lines $\mathbf{J}_s$ arising from another vortex located to the left become more widely separated toward the right, away from the other vortex. The Lorentz force density $\mathbf{J} \times \mathbf{B}$ is directed to the right and serves to move the two vortices apart.

As before, the force **F** is along the negative y direction, so it is more convenient to write it as a scalar, F. Inserting Eq. (12.20) for $\mathbf{J}(d)$ and using the approximation (12.28) for $r \gg \lambda$, we obtain

$$\frac{F}{L} = \frac{\Phi_0^2}{2\mu_0(2\pi\lambda^5)^{1/2}} \frac{\exp(-d/\lambda)}{\sqrt{d}} \qquad d \gg \lambda. \tag{12.70}$$

Thus the repulsive interaction between vortices is very weak when the vortices are far apart. The forces between vortices are fairly short range with the penetration depth a measure of the range, and they must be sufficiently close together, compared to λ, for their interaction to be appreciable. We saw from Fig. 12.17 that an applied field $B_{\text{app}} \approx 1.8\, B_{c1}$ can be strong enough to bring vortices sufficiently close together for this interaction to be effective.

An analogous case occurs when a wire carrying an electric current $\mathbf{I} = \mathbf{J}A$ interacts with a magnetic field **B**. Equation (12.63) applies to this case also, and we write

$$\mathbf{F}/L = \mathbf{I} \times \mathbf{B}. \tag{12.71}$$

In this case a wire carrying a current I_2 is encircled by magnetic field lines B_2 and a second parallel current I_1 a distance d away interacts with B_2 and experiences a force of attraction,

$$F/L = \frac{\mu_c I_1 I_2}{2\pi d} \tag{12.72}$$

as shown in Fig. 12.30. This represents a much slower fall-off with distance than its vortex counterpart (12.70). Thus there is a close analogy between the interaction of vortices with a current density "field" and the interaction of current-carrying wires with a magnetic field. The vortices confine B and interact with J, while the wires confine J and interact with B. A crucial difference is the sign of the interaction; one repels and the other attracts.

In an anisotropic superconductor the B field of a vortex is not necessarily parallel to the vortex core, but depends on the location of this field relative to the vortex axis and the c direction. There even exist special

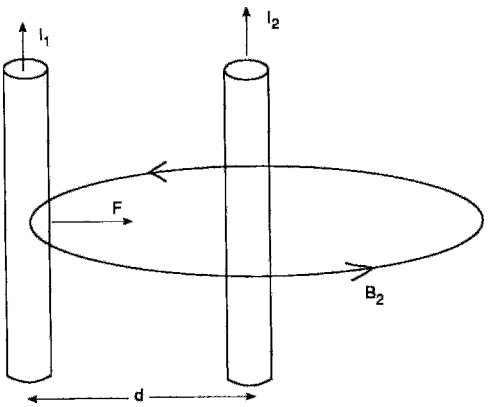

Figure 12.30 Attractive interaction involving a current $\mathbf{I}_1$ and the magnetic field $\mathbf{B}_2$ from a second parallel current $\mathbf{I}_2$ following in the same direction. The force of attraction $\mathbf{F}$ is shown.

applied field orientations that are tilted with respect to the principal axes for which adjacent vortices experience an attractive interaction (Bolle *et al.*, 1991; Daemen *et al.*, 1992; Kogan *et al.*, 1990).

B. Pinning

Pinning forces in general are not well understood, and it will be helpful to make a few qualitative observations. Various models and theories to explain pinning have been proposed (e.g., Brass *et al.*, 1989; Coffey, 1992; Daemen and Gubernatis, 1991; Glyde *et al.*, 1992; Levitovi, 1991; Wördenweber, 1992).

A pinning force F_p is a short-range force that holds the core of a vortex in place at, *inter alia*, a point defect (Giapintzakis *et al.*, 1992; Hylton and Beasley, 1990), columnar defect (Nelson and Vinokur, 1992; Prost *et al.*, 1993), screw dislocation (Ivlev and Thompson, 1992; S. Jin *et al.*, 1991), oxygen vacancy (Chudnovsky, 1990; Feenstra *et al.*, 1992), inclusion (Murakami *et al.*, 1991; Sagdahl *et al.*, 1991; Shi *et al.*, 1989, 1990a, b), grain boundary (Müller *et al.*, 1991), twin boundary (Kwok *et al.*, 1990a; Lairson *et al.*, 1990; J.-Z. Liu *et al.*, 1991; Svensmark and Falicov, 1990), intragranular or intergranular nonsuperconducting region (Davidov *et al.*, 1992; Jung *et al.*, 1990), or praseodymium (Pr) doping (Paulius *et al.*, 1993; Radousky, 1992). The density of pinning centers can be high, with average separations of 100 Å or less (Martin *et al.*, 1992; Tessler *et al.*, 1991). Pinning can be an activated process involving pinning barriers (Campbell *et al.*, 1990; Kopelvich *et al.*, 1991; McHenry *et al.*, 1991; Steel and Graybeal, 1992; Zhu *et al.*, 1992), with typical values between 1 and 12 eV for granular $YBa_2Cu_3O_{7-\delta}$ (Nikolo and Goldfarb, 1989). Vortices can undergo thermally activated hopping between pinning centers (Fisher *et al.*, 1991; Liu *et al.*, 1991; Martin and Hebard, 1991).

The Lorentz force needed to depin a single vortex equals the pinning force. The force per unit length needed to produce this depinning, F_p, has been found to have the temperature dependence

$$F_p = F_p(0)[1 - (T/T_c)]^n, \qquad (12.73)$$

with $F_p(0)$ varying over a wide range from 10^{-12} to 4×10^{-4} N/m and n ranging from 1.5 to 3.5 (Fukami *et al.*, 1991a; Goldstein and Moulton, 1989; O. B. Hyun *et al.*, 1989; O. B. Hyun *et al.*, 1987; Job and Rosenberg, 1992; Park *et al.*, 1992; Shindé *et al.*, 1990; Wadas *et al.*, 1992; Wu and Sridhar, 1990). A distribution of pinning (activation) energies have been reported in the range of hundreds of meV (e.g., Civale *et al.*, 1990; Ferrari *et al.*, 1989; Fukami *et al.*, 1991b; J.-J. Kim *et al.*, 1991a,b; Mohamed and Jung, 1991; Nikolo *et al.*, 1992). Kato *et al.* (1991) suggested that for $T = 0.9T_c = 9$ K, a vortex that is 2λ from a pinning center moves toward it at ≈ 1000 m/sec to be trapped in $\approx 10^{-9}$ sec. Several workers have found the pinning force to be a maximum for applied fields of $\approx \frac{1}{4}\mathbf{B}_{c2}$, with $\mathbf{B}_{app}$ both along and perpendicular to the c direction (Cooley *et al.*, 1992; Fukami *et al.*, 1989; Satchell *et al.*, 1988).

In tetragonal high-temperature superconductors such as the bismuth and thallium types, the dominant pinning mechanism is generally relatively weak interactions between vortices and randomly distributed defects. In orthorhombic superconductors, such as the yttrium compound, twin boundaries provide stronger pinning to the flux lines. High-temperature superconductors tend to have lower pinning forces than classical superconductors (Ferrari *et al.*, 1991).

Some authors take into account a harmonic pinning force $F_p = -kx$ or $F_p = -k\sin(qx)$ or a stochastic force due to thermal fluctuations (Chen and Dong, 1991; Golosovsky *et al.*, 1991, 1992; Inui *et al.* 1989). Harmonic pinning can be important for oscillating applied fields and thermal fluctuations.

Ionizing radiation increases the concentration of pinning centers (Civale *et al.*, 1991b; Fleisher *et al.*, 1989; Gerhäuser *et al.*, 1992; Konczykowski *et al.*, 1991; Weaver *et al.*, 1991), which can have the effect of increasing the critical current density. For example, neutron irradiation of $HgBa_2CuO_{8+\delta}$ increased the area of the high field ($\pm$1T) hysteresis loop, and hence raised the value of J_c, by one or two orders of magnitude (Schwartz *et al.*, 1994). This enhancement of J_c is much greater than that obtained with other cuprates and suggests a scarcity of pinning centers before exposure to the neutron flux. Irradiation can be used to maximize J_c or to optimize the pinning force density for a given applied field B_{app} and superconductor type (Kahan, 1991; Vlcek *et al.*, 1992).

C. Equation of Motion

We will examine the case of an isolated vortex $\mathbf{\Phi}_0$ in a region of constant current density $\mathbf{J}$, as shown in Fig. 12.31. When the pinning force exceeds the Lorentz force,

$$\mathbf{F}_P > \mathbf{J} \times \mathbf{\Phi}_0, \tag{12.74}$$

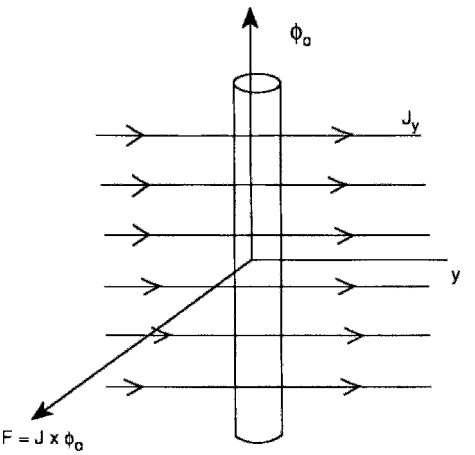

Figure 12.31 Lorentz force $\mathbf{F} = \mathbf{J} \times \mathbf{\Phi}$ exerted on a vortex by a perpendicular transport current $\mathbf{J}$.

the vortex is held in place and no motion can occur. When the Lorentz force exceeds the pinning force, motion begins. The vortex with an effective mass per unit length m_ϕ (Blatter *et al.*, 1991a; Coffey, 1994; Coffey and Clem, 1991; Gittleman and Rosenblum, 1968; van der Zant *et al.*, 1991) is set into motion and accelerated by the Lorentz force $\mathbf{J} \times \mathbf{\Phi}_0$, and the two velocity-dependent forces come into play. One possible equation of motion is

$$\mathbf{J} \times \mathbf{\Phi}_0 - \alpha n_s e(\mathbf{v} \times \mathbf{\Phi}_0) - \beta \mathbf{v} = m_\phi \frac{d\mathrm{v}}{dt}. \tag{12.75}$$

There is an initial period of acceleration that is too short to be observed, followed by steady-state motion at the terminal velocity $v(\infty)$. The steady-state motion is governed by the equation (Heubener, 1979)

$$\mathbf{J} \times \mathbf{\Phi}_0 - \alpha n_s e(\mathbf{v} \times \mathbf{\Phi}_0) - \beta \mathbf{v} = \mathbf{0}, \tag{12.76}$$

with the Lorentz force $\mathbf{J} \times \mathbf{\Phi}_0$ balanced by the two velocity-dependent forces. A more general expression, written in terms of an unspecified dissipative force $\mathbf{f}$,

$$\mathbf{J} \times \mathbf{\Phi}_0 - \alpha n_s e(\mathbf{v} \times \mathbf{\Phi}_0) - \mathbf{f} = \mathbf{0}, \tag{12.77}$$

reduces to Eq. (12.76) for the case $\mathbf{f} = \beta\mathbf{v}$ that is suggested by intuition. We will comment on this more general expression at the end of the section.

D. Onset of Motion

At the onset of motion the velocity is very low and the two velocity-dependent terms in Eq. (12.75) can be neglected. This means that the initial velocity and acceleration are along the $\mathbf{J} \times \mathbf{\Phi}_0$ or x direction. As motion continues the velocity $\mathbf{v}(t)$ increases in magnitude toward a terminal value $\mathbf{v}(\infty) = \mathbf{v}_\phi$ with time constant τ_ϕ as well as shifting direction. We will show below that this terminal velocity vector lies in the x, y-plane in a direction between $\mathbf{J}$ and $\mathbf{J} \times \mathbf{\Phi}_0$.

To estimate the magnitude of τ_ϕ, we recall from hydrodynamics that the time constant for the approach of an object moving in a fluid to its terminal velocity is proportional to the effective mass, and we also know that the effective mass is proportional to the difference between the mass of the object and the mass of fluid which it displaces. In other words, it is proportional to the difference between the density of the object and the density of the medium. Vortex motion involves the movement of circulating super currents through a background medium comprised of super electrons of comparable density, and the closeness of these densities causes m_ϕ, and hence τ_ϕ, to be very small. The terminal velocity is reached so rapidly that only the final steady-state motion need be taken into account. Gurevich and Küpfer (1993) investigated the time scales involved in flux motion and found values ranging from 1 to 10^4 sec. Carretta and Corti (1992) reported an NMR measurement of partial flux melting with correlation times of tens of microseconds.

E. Magnus Force

The Magnus effect involves the force, sometimes called the lift force, that is exerted on a spinning object moving through a fluid medium. This force arises from the Bernoulli equation for streamline (non-turbulent) flow,

$$\frac{1}{2}\rho v^2 + P = \text{const}, \tag{12.78}$$

where $\frac{1}{2}\rho v^2$ is the kinetic energy density, P is the pressure, and the gravity term $\rho g h$ is negligible and hence omitted.

When a vortex is moving through a medium at the speed v_ϕ, as shown in Fig. 12.32a, from the viewpoint of an observer on the vortex the medium is moving at the speed $-v_\phi$, as indicated in Fig. 12.32b. On one side of the vortex the velocity v_s of

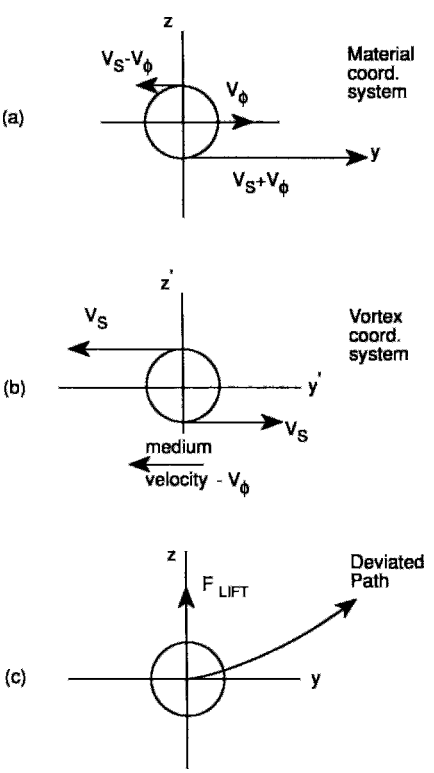

Figure 12.32 Vortex moving in a superconducting medium (a) relative to an x, y coordinate system fixed in the medium, (b) viewed from an x', y' coordinate system fixed on the vortex, and (c) resulting deviated path in the medium arising from the Magnus (lift) force.

the circulating current adds to the velocity of the medium and on the other side it subtracts from it, in accordance with Fig. 12.32a, and for these two cases Eq. (12.78) assumes the scalar form

$$\frac{1}{2}\rho(v_\phi \pm v_s)^2 + P_\pm = \text{const.} \qquad (12.79)$$

Since the kinetic energy is greater for the positive sign, it follows from Eq. (12.79) that $P_+ < P_-$. This pressure difference causes a force F_{lift} to be exerted on the moving vortex in a direction at right angles to its velocity, toward the lower pressure side. The resulting deviated path is shown in Fig. 12.32c. The sideways acting force, called the Magnus force, is given by $-\alpha n_s e(\mathbf{v}_\phi \times \mathbf{\Phi}_0)$, as indicated in Eqs. (12.75)–(12.77). The Magnus coefficient α has different values in different models.

F. Steady-State Motion

For the case of steady-state vortex motion with the viscous retarding force $\mathbf{f}$ given by $\beta\mathbf{v}$, as in Eq. (12.76), the vectors $\beta\mathbf{v}$ and $\alpha n_s e(\mathbf{v} \times \mathbf{\Phi}_0)$ are mutually perpendicular, as illustrated in Fig. 12.33a. The vortex velocity vector shown in Fig. 12.33b has the magnitude v_ϕ given by

$$v_\phi = \frac{J\Phi_0}{[\beta^2(\alpha n_s e\Phi_0)^2]^{1/2}}, \qquad (12.80)$$

and subtends the angle Θ_ϕ, where

$$\tan\Theta_\phi = \alpha n_s e\Phi_0/\beta, \qquad (12.81)$$

with the $\mathbf{J} \times \mathbf{\Phi}_0$ direction. Thus we see that the greater the viscous drag coefficient β and the greater the Magnus force coefficient αn_s, the slower the velocity v_ϕ of the vortices.

Various theories have been proposed to explain steady-state vortex motion. It is common to assume that the core of the vortex is normal, that $T \ll T_c$ (so that normal electrons outside the core can be neglected), that $\alpha = 1$, and that the vortices move freely without any influence from pinning. Relaxation is so rapid that the distance a vortex moves in one relaxation period, τ_ϕ, is small compared to the core radius ξ. Bardeen and Stephen (1965), van Vijfeijken and Niessen (1965a,b), and Nozières and Vinen (1966) have proposed models for steady-state vortex

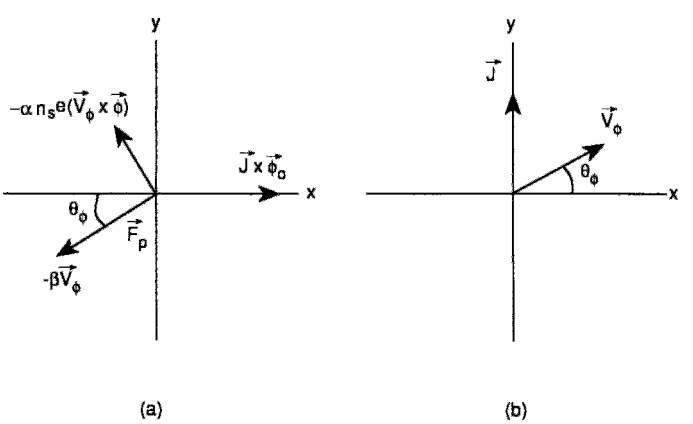

Figure 12.33 Vortex motion at the terminal velocity showing (a) the balance of forces, and (b) the directions of the current flow ($\mathbf{J}$) and vortex motion ($\mathbf{v}_\phi$). These figures are drawn for the case $\mathbf{f} = \beta\mathbf{v}_\phi$ of Eq. (12.77).

motion based on assumptions of this type. Nozières and Vinen assumed that $\alpha = 1$, and wrote Eq. (12.77) in the form

$$n_s e(\mathbf{v}_s - \mathbf{v}_\phi) \times \Phi_0 - \mathbf{f} = 0, \qquad (12.82)$$

asserting that the intuitive choice $\mathbf{f} = \beta \mathbf{v}_\phi$ does not agree with experiment. Another possible choice is $\mathbf{f} = \beta \mathbf{v}_s$. Different theories of vortex motion make predictions of the Hall resistivity and the Hall angle Θ_H of Eq. (1.93) and these predictions can be checked with experiment (Chien *et al*., 1991; Jing and Ong, 1990; Wang and Ting, 1992b). The drag force coefficient β can be looked upon as proportional to a fluxon viscosity. Viscosity coefficients have been determined for the yttrium and bismuth compounds (Golosovsky *et al*., 1992; Matsuda *et al*., 1994).

G. Intrinsic Pinning

Pinning forces were introduced in Section B for the isotropic case. When the applied field is in the c direction there is very little anisotropy in the a and b directions, so that motion proceeds as in the isotropic case. When the field is applied in the a, b-plane, the vortex lines are parallel to the layers. They have their lowest energy when their cores are located between the layers (Carneiro, 1992). In the absence of pinning centers, vortex motion within the layers is uninhibited, but motion perpendicular to the layers is hindered by what is called *intrinsic pinning*. Intrinsic pinning is observable in untwinned $YBa_2Cu_3O_{7-\delta}$ when the applied field is aligned along the a, b-planes (Chakravarty *et al*., 1990; Ivlev and Kopnin, 1990; Ivlev *et al*., 1991a, b; Kwok *et al*., 1991; Tachi and Takahashi, 1989; *vide* also Feinberg and Villard, 1990). The simultaneous presence of two species of vortices, with different orientations, has also been discussed (Daemen *et al*., 1993).

H. Vortex Entanglement

A typical vortex is much longer than its core radius and can be pinned in several places (Niel and Evetts, 1992). For example, a straight vortex aligned along the c direction of a 1.2 μm-thick grain of $YBa_2Cu_3O_7$ has a length of about 1000 unit cells ($c = 1.194$ nm), 500 core radii ($\xi \approx 2.6$ nm), and five penetration depths ($\lambda \approx 0.26\,\mu$m). Such a vortex can twist and turn in the material, and sections of it might move while others remain pinned; it could also undergo a perpendicular excursion along the a, b-plane of a high-temperature superconductor. Another scenario is for two vortices to become entangled, and if this happens they might undergo a reconnection interaction by interchanging segments. These configurations and motions are much harder to handle mathematically in the case of an array of vortices, but they are probably a more accurate representation of the situation than the more idealized case of straight, parallel vortices we have been discussing.

VI. FLUX MOTION

The previous section dealt with the motion of individual vortices. Now we wish to talk about the motion of vortices that are packed together sufficiently densely to be considered as a continuum, or to be thought of as moving about together in groups called *flux bundles*.

A. Flux Continuum

We saw in Section III.D that the vortices in a Type II superconductor are about two penetration depths apart when the applied magnetic field B_{app} reaches a value $\approx 1.8 B_{c1}$. For $B_{app} > 2B_{c1}$ there is a strong overlap of the magnetic fields from neighboring vortices, and the internal field B_{in} exhibits spatial variations about an average value that

are sketched in Figs. 12.7b and 12.10. The overlap is so great that it is reasonable to consider an array of vortices as constituting a continuum of magnetic flux.

When in motion such a continuum has some of the properties of a highly viscous fluid. Many vortices move as a unit or in large groups under the action of perturbing forces. There are two regimes of flux motion, both of which involve dissipation (Palstra *et al*., 1988). The first is flux creep, when the pinning force dominates (Anderson, 1962), and the second flux flow, when the Lorentz force dominates (Kim *et al*., 1964; Tinkham, 1964).

Flux motion is strongly dependent on vortex pinning. Strong pinning centers hold individual vortices in place independently of the presence of the weaker interaction forces from nearby vortices, while weak pinning centers compete with nearby vortices in their ability to hold an individual vortex in place. A large collection of weak pinning centers produces what is called collective pinning (Larkin and Ovchinnikov, 1974; Ovchinnikov and Ivler, 1991). In this case individual vortices cannot move about freely because of constraints from their neighbors so that a relatively small number of pinning centers can restrain the motion of many nearby vortices.

We know that the condensed phases of the liquid and solid state of a particular material are characterized by a fixed density, whereas the gas phase can have a wide range of density. An interesting feature of the condensed vortex phases is that they do not occur for a fixed density, but rather over a range of densities from $\rho_{\min}$ to $\rho_{\max}$. This range may be approximated by the ratio between λ and ξ,

$$\frac{\rho_{\max}}{\rho_{\min}} \approx \kappa^2, \tag{12.83}$$

where the Ginzburg-Landau parameter $\kappa = \lambda/\xi$ enters as a square because the densities ρ are two-dimensional. For high-temperature superconductors with $\kappa \approx 100$ this range of densities is 10^4. Density variations and fluctuations can occur during flux motion.

B. Entry and Exit

The presence of the applied field at the surface of the superconductor induces vortices to form right inside the surface, and a relatively high local concentration can accumulate. An increase in the applied field causes more vortices to enter and move inward by diffusion and by virtue of mutual repulsion, with some of the vortices becoming pinned during migration. The Lorentz force density $\mathbf{J} \times \mathbf{B}$ associated with the interactions between vortices acts like a magnetomechanical pressure serving to push the flux inward. The vortices relax to a new equilibrium distribution consistent with the new screening currents associated with the increase in the applied field.

Foldeaki *et al*. (1989) found that in $YBa_2Cu_3O_{7-\delta}$ there is a large difference between the rate of flux flow in the case of expulsion of flux caused by removal of the applied field $\mathbf{B}_{\text{app}}$ following field cooling versus the rate at which flux penetrates the sample when $\mathbf{B}_{\text{app}}$ is turned on following zero field cooling. The activation energies in the former case, 14–28 meV, are significantly smaller than those, 34 to 67 meV, in the latter case.

C. Two-Dimensional Fluid

Ordinarily, we think of a gas as a collection of molecules that are so widely separated that the interactions between them are negligible, and that the molecules move independently of each other except when undergoing elastic collisions that change their directions and velocities. A liquid is a

collection of molecules that are held closely together by short-range attractive forces, with thermal energy causing them to move around while remaining in contact, thereby preserving short-range order. In the solid state the nearest-neighbor attractive forces dominate over thermal effects, and the molecules become fixed in position in a regular lattice arrangement of the type shown on Fig. 12.14, with long-range order.

Molecules confined to a surface can exist in two-dimensional gas, liquid, and solid states. If some of the molecules in such a two-dimensional fluid become attached to the pinning centers, the motion of the fluid will be restricted by having to flow past the pinned molecules. An array of vortices in a superconductor has many of the properties of these two-dimensional states of matter, but there are some fundamental differences between the two cases. First the interactions between the vortices are repulsive rather than attractive. In addition, the forces have two characteristic lengths, a short coherence length that constitutes a closest-approach distance, and a (much) greater penetration depth which is a measure of the range of the repulsive interaction. The vortices are also much longer than their core diameters so they can become twisted and distorted, as was already mentioned in Section V.H.

When the average separation of vortices is much greater than the penetration depth, they will form a two-dimensional gas in which they are able to move independently of each other, assuming pinning is absent. We can deduce from Fig. 12.16 that applied fields only slightly above the lower-critical field—e.g., $B_{\text{app}} \approx 1.1 B_{\text{c1}}$ for $\kappa \approx 100$—can produce relatively closely spaced vortices (see Problem 6). In addition, the lower-critical field is often not a sharply defined quantity. As a result of these factors, the range of applied fields over which a vortex gas state might be able to exist is too small to be significant. It is the condensed phases which are mainly of interest.

D. Dimensionality

A flux fluid is three-dimensional because it occupies a volume of space, but it moves in a plane perpendicular to the internal field direction, so its motion is often treated as two-dimensional. When the applied field $\mathbf{B}_{\text{app}}$ is along the c direction of a cuprate superconductor, the vortices break up into pancake vortices that are confined to the CuO_2 layers. If the layers then become decoupled from each other, the resulting flux flow can be looked upon as a movement of pancake vortices in each layer that are independent of each other. If a strong pinning center exists in one layer, the pancake vortices in that layer will flow around it. Pancake vortices in the layers above and below will not experience that pinning center, however.

There is also a dimensionality in the super current flow. We see from Fig. 8.30 that the cuprates have groups of closely spaced and, hence, strongly coupled CuO_2 layers. These CuO_2 layers are also more widely separated from the next group above and below, with the coherence length in the c direction less than the distance between pairs of superconducting layers or groups of layers. For example, the $Tl_2Ba_2Ca_nCu_{n+1}O_{6+2n}$ compound has $n+1$ closely spaced CuO_2 planes with intervening Ca ions that are separated from the next such planar group by layers of BaO and TlO. Adjacent groups of planes are uncoupled from each other and conductivity is two-dimensional (2D) whenever the coherence length along the c direction is less than $s/\sqrt{2}$, where s is the spacing between successive planar groups (Bulaevskii, 1973). For example,

$$YBa_2Cu_3O_{7-\delta}$$

at 0 K has $\xi_c(0) \approx 3\,\text{Å}$, and $s = 11.9\,\text{Å}$ is the lattice parameter along c, so $\xi_c \ll s/\sqrt{2}$ and the superconductivity is two-dimensional (2D).

The coherence length $\xi_c(T)$ has the temperature dependence

$$\xi_c(T) \approx \xi_c(0)(1-(T/T_c))^{-1/2}, \quad (12.84)$$

and when $\xi_c(T)$ is equal to $s/\sqrt{2}$ there is a crossover between 2D and 3D behavior, the latter occurring for $\xi_c > s/\sqrt{2}$. Marcon *et al*. (1992) report crossover temperatures of $0.99T_c$ for $Bi_2Sr_2CaCu_2O_{10}$ and $0.88T_c$ for

$$YBa_2Cu_3O_{7-\delta}.$$

The presence of an applied field lowers the critical temperature, $T_c(B) < T_c$, and this depresses the crossover temperature as well (Božovic, 1991; Farrell *et al*., 1990c; Gray *et al*., 1992; Koorevaar *et al*., 1990; Weber and Jensen, 1991).

E. Solid and Glass Phases

When vortices become sufficiently numerous so that their charge and current densities overlap appreciably, they form a condensed phase, either a liquid phase if the temperature is relatively high or a solid near absolute zero. In the absence of pinning and anisotropy the vortices form the hexadic pattern of Fig. 12.14 with each vortex stretched between its two end points like an elastic string, as noted in Section IV. This configuration has long-range order, so the state is called a *flux lattice*. When random pinning centers are present, the spatial structure will reflect their distribution and the long-range order will be disturbed. The result is what is called a *vortex glass* (Chudnovsky, 1991). The portions of the flux lines between the pinning sites are held in place by repulsion from nearby vortices and form local hexadic arrangements, so short-range order is present. Bitter pattern decorations of $YBa_2Cu_3O_7$ crystals display this short-range order (Dolan *et al*., 1989a; Gammel *et al*., 1987).

A flux-glass phase can also form and exhibit short-range order (Chudnovsky, 1989; Fisher, 1989). The positional order of a vortex glass is analogous to the magnetic order of a spin glass (Binder and Young, 1986; Fisher and Huse, 1988). Both a flux lattice and a flux glass are solid phases, since in these phases the vortices remain fixed in place so long as the temperature is low enough, the applied field remains the same, and there is no transport current. Several researchers have reported evidence for a vortex-glass phase in epitaxial films (Koch *et al*., 1989) and monocrystals (Rossel *et al*., 1989a, b), other investigators have studied flux melting and the transition to the vortex-glass state (Charalambous *et al*., 1992; Dekker *et al*., 1992; Dorsey *et al*., 1992; Koka and Shrivastava, 1990a, b; Safar *et al*., 1992; Yeh, 1990; Yeh *et al*., 1992a, b). Mechanical oscillation methods have been employed to study the melting transition (Gammel *et al*., 1989; Gupta *et al*., 1991; F. Kober *et al*., 1991; Luzuriaga *et al*., 1992; E. Rodriguez *et al*., 1990). The subject has also been examined theoretically (Gingras, 1992; Toner, 1991b).

F. Flux in Motion

The very slow flux motion at temperatures far below T_c is referred to as *flux creep*. When a magnetic field is applied to a superconducting sample for $T \ll T_c$, the field penetrates very slowly. Plots of the magnetization versus the logarithm of time tend to be linear, with flux continuing to enter the sample several hours later. Figure 12.34 shows the time dependence of the magnetization in a superconductor that was zero field cooled then exposed to a 5-T field that was subsequently decreased to 3 T. In this experiment (Kung *et al*., 1992; see also Pencarinha *et al*., 1994) the time dependence of the magnetization of $YBa_2Cu_3O_7$ containing Y_2BaCuO_5 particles (green phase) functioning as pinning centers to enhance $\mathbf{J}_c$ was monitored for several hours after the field had been reduced to 3 T. Experimental results are shown for

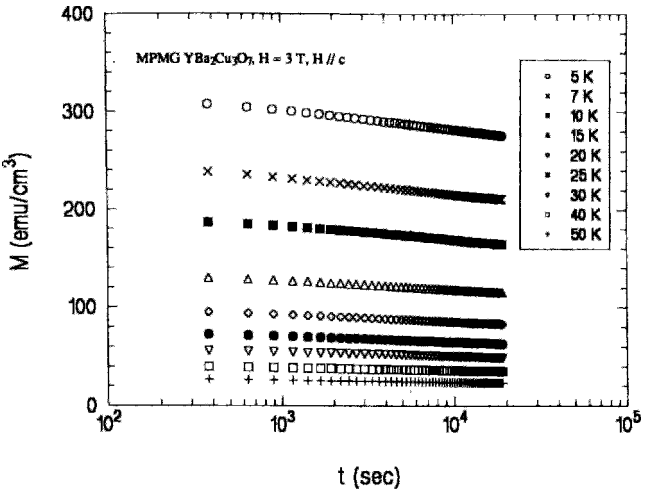

Figure 12.34 Magnetic relaxation of $YBa_2Cu_3O_7$ in a 3-T field showing the linear dependence of magnetization on the logarithm of time for temperatures between 5 K and 50 K (Kung *et al.*, 1992; see also Pencarinha *et al.*, 1994).

temperatures between 5 K and 50 K. Similar results have been obtained with an electron spin resonance surface probe technique (Pencarinha *et al.*, 1994). We see from the figure that the magnetization is greater in magnitude and decays faster at the lower temperatures. The logarithmic time dependence of M, shown at low temperatures as in Fig. 12.34, often becomes nonlogarithmic at higher temperatures (Lairson *et al.*, 1990b; J. Z. Liu *et al.*, 1992; Safar *et al.*, 1989; Shi *et al.*, 1991).

For weak pinning the vortex lattice reacts elastically to an applied force, such as the Lorentz force from a transport current. In the case of strong pinning, untrapped vortices move past trapped vortices and flux flows along channels between regions of trapped flux (Brechet *et al.*, 1990). This latter flow can involve groups of vortices moving cooperatively as a unit, forming what are called *flux bundles* (Geim *et al.*, 1992; C. A. Wang *et al.*, 1992; Zeldov *et al.*, 1989) containing from 4 (Stoddart *et al.*, 1993) to 10^4 (Plaçais and Simon, 1989) vortices. Energy barriers can hinder flux creep (Anderson, 1962; Anderson and Kim, 1964) which involves thermally activated jumps of flux bundles (Cross and Goldfarb, 1991). In high-temperature superconductors the flux creep rate is much greater for flow parallel to the planes than for flow perpendicular to the planes (Biggs *et al.*, 1989).

G. Transport Current in a Magnetic Field

Suppose that a transport current I of uniform density J flows along a superconducting wire located in a transverse magnetic field. If the pinning forces are not sufficiently strong to prevent flux motion, i.e., the superconductor is soft, then: (1) The current exerts a force $\mathbf{J} \times \mathbf{\Phi}_0$ on the vortices, causing them to move from one side of the wire to the other. Viscous drag limits this motion to a constant velocity v_ϕ and the Magnus force causes it to occur at the angle Θ_ϕ shown in Fig. 12.33, as already noted; (2) through Maxwell's equation $\nabla \times \mathbf{B} = \mu_0 \mathbf{J}$ a constant magnetic field gradient is established across the sample. When the applied field is in the

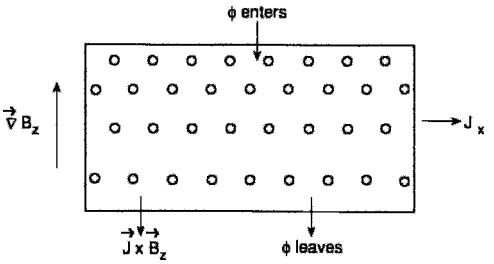

Figure 12.35 Triangular lattice of vortices with gradient $\nabla B_x = dB_z(y)/dy$ in the y direction due to application of a transport current density J_x in addition to the magnetic field B_z. The direction of the Lorentz force $\mathbf{J} \times \mathbf{B}$ is shown. In the absence of pinning forces the current density causes the vortices to move downward at a constant velocity, with new vortices entering the superconductor at the top and old vortices leaving at the bottom. Pinning forces can stop this motion and provide dissipationless current flow. Figure 12.14 shows this vortex lattice in the same applied field but without a transport current.

z direction and the current flows in the x direction, the gradient is given by

$$\frac{d}{dy}B_z(y) = \mu_0 J_x; \tag{12.85}$$

this situation is sketched in Fig. 12.35. (Wilson, 1983); (3) the flux flow corresponds to a magnetic field $\mathbf{B}$ moving across the sample at the constant speed v_ϕ. Such a moving magnetic field generates an electric field

$$\mathbf{E} = \mathbf{v}_\phi \times \mathbf{B} \tag{12.86}$$

in the superconductor which is perpendicular to both $\mathbf{v}_\phi$ and $\mathbf{B}$. The electric field has a component with the same direction as $\mathbf{J}$, giving rise to the ohmic loss $\mathbf{J} \cdot \mathbf{E}$,

$$\mathbf{J} \cdot \mathbf{E} = \mathbf{J} \cdot (\mathbf{v}_\phi \times \mathbf{B}). \tag{12.87}$$

Another way of viewing the situation is to consider flux flow as a rate of change of flux which, by Faraday's law, produces a voltage drop in the superconductor along the direction of the current flow. The resistivity associated with this flow, according to Ohm's law, provides the mechanism for heat dissipation. Pinning of the vortices prevents the flux from flowing, and the result is no voltage drop and zero resistance.

The pinning forces must be weak enough to permit the initial vortex movement required for the establishment of the flux gradient of Eq. (12.85), and strong enough to prevent the continuous vortex motion that produces the heat dissipation of Eq. (12.87). Pinning forces are ordinarily quite weak. Intensive present-day research and development efforts are aimed at achieving sufficiently strong pinning forces for high current densities.

The mutual repulsion between vortices acts to set up a uniform vortex density, and, hence to oppose the establishment of the flux gradient sketched in Fig. 12.35. The pinning must be strong enough to maintain the gradient against these opposing forces. The stronger the pinning, the greater the magnitude of the gradient that can be maintained, and hence, from Eq. (12.85) the greater the current density that can flow without dissipation. This means that the highest current density that can flow in a superconductor, as given by the critical value $\mathbf{J}_c$, increases with an increase in the pinning strength.

H. Dissipation

Transport currents and thermal fluctuations can both induce flux motion and produce dissipation. This can involve, for example, the release and transportation of vortices to other pinning centers (Lairson *et al.*, 1991), and the pinning and depinning of flux bundles.

Heat produced by flux motion flows away from the region of generation toward the boundary of the material. A steady state is established in which the interior of the superconductor is at a somewhat higher temperature. We know from Chapter 2, Sections XII and XVI, that the critical current density J_c

depends on the applied field and the temperature, so the heat that is generated will limit the value of J_c; the sample will go normal if the applied current density exceeds J_c. High critical currents can be attained by preparing samples with favorable distributions of pinning centers. This is especially important for magnet wire, which must carry high currents in the presence of strong magnetic fields.

I. Magnetic Phase Diagram

Figure 12.36 is a simplified phase diagram of the magnetic states of a Type II superconductor based on a Meissner phase of perfect diamagnetism (absence of vortices) at the lowest temperatures and a mixed (vortex-lattice) phase at higher temperatures. From the foregoing discussion it is reasonable to assume that the situation is actually much more complicated, however. Several more realistic phase diagrams have been suggested in the literature (Farrell *et al*., 1991a; Fisher, 1990; Gammel *et al*., 1991; Gerber *et al*., 1992; Glazman and Koshelev, 1991a, b; Huang *et al*., 1991a; Kes *et al*., 1991; Gerber Marchetti and Nelson, 1990; Safar *et al*., 1993; Schaf *et al*., 1989; Zwerger, 1990). We will describe one such diagram (Yeh, 1989, 1991; Yeh and Tsuei, 1989).

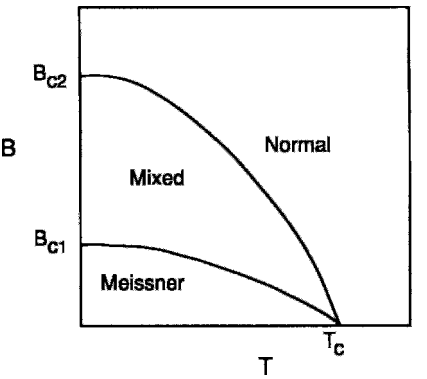

Figure 12.36 Simplified magnetic phase diagram showing the mixed and Meissner states of a Type II superconductor separated by the $B_{c1}(T)$ line.

Figure 12.37 depicts, in addition to the Meissner phase, a flux solid phase with vortices pinned or otherwise held in place,

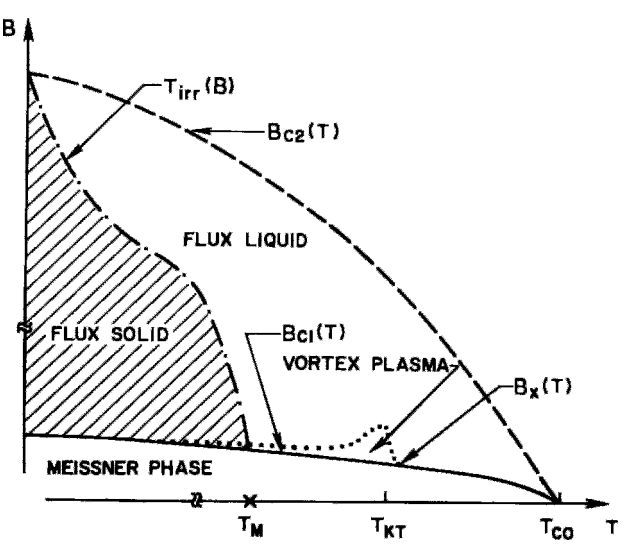

Figure 12.37 More complex magnetic phase diagram showing the Meissner phase, flux solid, and flux liquid regions separated by the irreversibility line (T_{irr}), plasma phase, lower-($B_{c1}(T)$) and upper-($B_{c2}(T)$) critical field curves, and melting (T_M) and Kosterlitz-Thouless (T_{KT}) temperatures (Yeh, 1989; Yeh and Tsuei, 1989).

and a flux liquid phase with many vortices unpinned or free to move reversibly, but with dissipation. These two phases are separated by what is called the *irreversibility line* T_{irr}. In the narrow region, called the *plasma phase*, thermal fluctuations create positively and negatively oriented vortices, called *intrinsic vortices*. These latter vortices are more numerous than the field-induced (extrinsic) vortices we will be describing in the following section.

Some authors call the boundary between the flux liquid and the condensed flux phase the *melting line*; along this line depinning takes place (Hébard *et al*., 1989), and flux creep becomes flux flow.

A number of theoretical treatments involving the structure and dynamics of the various phases of the flux state have appeared. The vortex configurations in these phases have been simulated by Monte Carlo (Hetzel *et al*., 1992; Li and Teitel, 1991, 1992; Minnhagen and Olsson, 1991; Reger *et al*., 1991; Ryu *et al*., 1992) and other calculational methods (Aktas *et al*., 1994; Jensen *et al*., 1990; Kato *et al*., 1993). Computer-generated contour drawings of vortices and vortex motion have been created (Brass and Jensen, 1989; Brass *et al*., 1989; Kato *et al*., 1991; Schenström *et al*., 1989; Tokuyasu *et al*., 1990; Xia and Leath, 1989).

VII. FLUCTUATIONS

Thermal fluctuations can have important effects on the properties of superconductors. In the present section we will give several examples of these effects.

A. Thermal Fluctuations

Thermal fluctuations increase with temperature, and as they do so they increase the extent to which vortices vibrate. Isolated flux lines acting as stretched strings can undergo longitudinal or transverse vibrations, but at higher concentrations the vibrations are more localized along the length of the core with numerous nearby vortices participating. Thermally induced fluctuations are better described as localized vibrations of a flux-line lattice with amplitudes and frequencies that depend on the wave vector dependent shear (c_{66}), bulk (c_B), and tilt (c_{44}) elastic constants (Brandt, 1989, 1990, 1992; Brandt and Sudb, 1991; Houghten *et al*., 1989; Kogan and Campbell, 1989; Shrivastava, 1990; Sudb and Brandt, 1991a, b; Yeh *et al*., 1990). When the vibrations become large enough they cause the solid-flux phase to disorder into a flux liquid consisting of mobile, pulsating vortices (Fisher *et al*., 1991). According to the usual Lindemann criterion, melting occurs when the root mean-square fluctuation amplitude u_{rms} exceeds the quantity $\approx 10^{-1}d$, where d is the average vortex separation introduced in Section III.C (Blatter and Ivler, 1993; Lindemann, 1910; Sengupta *et al*., 1991). The thermal fluctuations can introduce noise and otherwise influence measurements of, for example, electrical conductivity (Jensen and Minnhagen, 1991; Song *et al*., 1992), specific heat (Riecke *et al*., 1989), and NMR relaxation (Bulut and Scalapino, 1992).

In granular samples the superconducting grains can couple together by means of Josephson weak links (cf. Chapter 15, Section VI.A) over a range of coupling energies. When the thermal energy $k_B T$ exceeds the Josephson coupling energy of a pair of grains, the two grains can become uncoupled so that supercurrent no longer flows between them.

B. Characteristic Length

The flux quantum Φ_0 is associated with a characteristic length Λ_T which is determined by equating the quantized flux energy to the thermal energy. The energy U_M of a

magnetic field in a region of volume V is given by

$$U_M = (B^2/2\mu_0)V \tag{12.88a}$$

$$= (\Phi^2/2\mu_0)(V/A^2), \tag{12.88b}$$

where $B = \Phi/A$. If this is equated to the thermal energy $k_B T$ for a quantum of flux, and if we write $A^2/V = 2\pi/\Lambda_T$, we obtain for the characteristic length

$$\Lambda_T = \frac{\Phi_0^2}{4\pi\mu_0 k_B T} \tag{12.89}$$

$$= \frac{1.97}{T}\,\text{cm}, \tag{12.90}$$

where T is the temperature in degrees Kelvin. This is much larger than other characteristic lengths, such as ξ and λ, except in the case of temperatures extremely close to T_c, where Λ_T can become very large (cf. Eq. (2.57), Fig. 2.42). Therefore, fluctuation effects are expected to be weak in superconductors. In the high-temperature cuprates several factors combine to enhance the effects of thermal fluctuations: (1) higher transition temperature, (2) shorter coherence length ξ, (3) large magnetic penetration length λ, (4) quasi-two-dimensionality, and (5) high anisotropy (Fisher *et al.*, 1991; Nelson and Seung, 1989; Vinokur *et al.*, 1990; cf. discussion of Schnack and Griessen, 1992).

C. Entanglement of Flux Lines

At the lowest temperatures a hexagonal flux lattice is expected, perhaps with irregularities due to pinning. At higher temperatures thermal agitation becomes pronounced and can cause an individual vortex that is pinned in more than one place to undergo transverse motion between the pinning sites. This induces a wandering of vortex filaments and leads to an entangled flux liquid phase, as illustrated in Fig. 12.38. A pair of flux lines passing close to each other can be cut, interchanged, or reattached (LeBlanc *et al.*, 1991; Marchetti, 1991; Nelson and LeDoussal, 1990; Nelson and Seung, 1989; Obukhov and Rubinstein, 1990; Sudb and Brandt, 1991a, b).

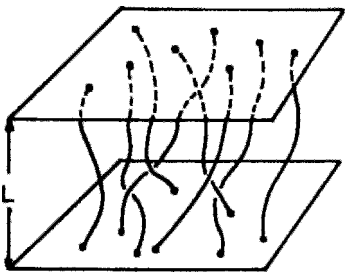

Figure 12.38 Sketch of vortex lines of an entangled flux lattice (Nelson and Seung, 1989).

D. Irreversibility Line

Another characteristic of a glass state is irreversibility. This can manifest itself in resistivity, susceptibility, and other measurable parameters (Ramakrishnan *et al.*, 1991). This history-dependent property was observed by Müller *et al.* (1987) at the beginning of the high-T_c era. The magnetization data plots presented in Fig. 12.39 for the three superconductors $YBa_2Cu_3O_7$, $Bi_2Sr_2CaCu_2O_8$, and $Bi_2Sr_2Ca_2Cu_3O_{10}$ all have a temperature T_{irr} above which the zero-field-cooled and field-cooled points superimpose, and below which the ZFC data are more negative than the FC ones (de Andrade *et al.*, 1991). The irreversibility temperature $T_{irr}(B)$ has been determined for a series of applied fields B, and results for the yttrium sample of Fig. 12.39 are plotted in Fig. 12.40. The linearity of these irreversibility line plots shows that there is a power-law relationship,

$$B \approx a\left[1 - \frac{T_{irr}(B)}{T_c(0)}\right]^n, \tag{12.91}$$

where a is a proportionality constant (Lombardo *et al.*, 1992; Sagdahl *et al.*, 1990;

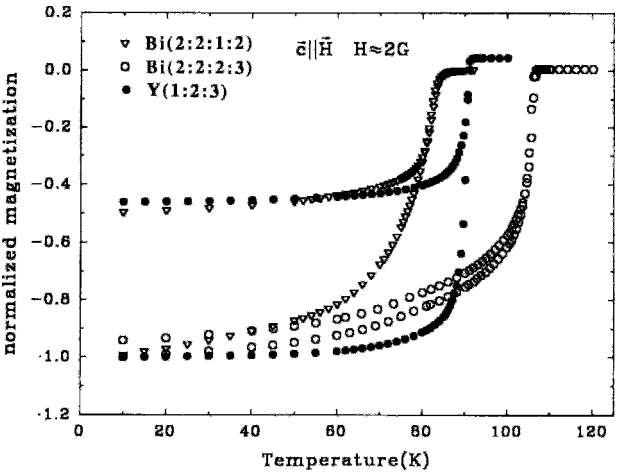

Figure 12.39 Temperature dependence of normalized magnetization of $YBa_2Cu_3O_7$, $Bi_2Sr_2CaCu_2O_8$, and $Bi_2Sr_2Ca_2Cu_3O_{10}$ for a 0.1-mT field applied parallel to the *c*-axis. Both field-cooled (upper curves) and zero-field-cooled (lower curves) data are shown for each superconductor (Y. Xu and Suenaga, 1991).

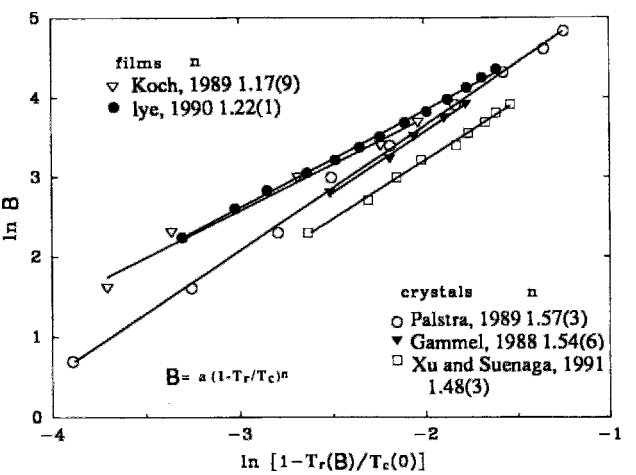

Figure 12.40 Log–Log plot of applied field versus temperature for $YBa_2Cu_3O_7$ films and monocrystals where T_r is the irreversibility temperature (Y. Xu and Suenaga, 1991).

Y. Xu and Suenaga, 1991). The slopes of the lines give $n \approx 1.2$ for thin films and $n \approx 1.5$ for crystals. Analogous plots are available for the flux-lattice melting temperature $T_M(B)$, vortex glass-liquid transition temperature T_g (Koch *et al.*, 1989), and resistive transition temperature $T_R(B)$. The resistivity plots exhibit a similar type of irreversibility as magnetization plots. Some other experimental studies of the irreversibility line of cuprates have been carried out by means of resistivity (Jeanneret *et al.*, 1989; Yeh, 1989; Yeh and Tsuei, 1989) and susceptibility (Geshkenbein *et al.*, 1991; Khoder *et al.*, 1990; Perez *et al.*, 1991; Pureur and Schaf, 1991) measurements. Results are available

for the new mercury superconductors (Chu, 1994; Jwasa *et al.*, 1994b, Huang *et al.*, 1994). Safar *et al.* (1989, 1991) mentioned that the melting and irreversibility lines tend to merge at higher fields, and this trend is clear from Fig. 12.40.

The irreversibility line is not very sensitive to the type and distribution of defects, although these defects have a pronounced effect on the critical current density (Cival *et al.*, 1990, 1991a, b).

Six samples of $YBa_2Cu_3O_{6.38}$ with transition temperatures in the range 7–17 K, adjusted by varying the quenching temperature, were studied, and the irreversibility temperature $T_{irr}(B)$ was found to depend on T_c. Plotting T_{irr}/T_c versus $[1-(T_{irr}/T_c)]$ on a log–log scale, however, caused all of the data to follow the same universal curve (Seidler *et al.*, 1991). This type of scaling of irreversibility curves has been interpreted in terms of the Bean model (Wolfus *et al.*, 1988). The classical superconductors Nb_3Sn and Nb–Ti, when produced in the form of fine multifilamentary wires, exhibit magnetization reversibility with an irreversibility temperature $T_{irr}(B)$ that may be close to the flux-lattice melting temperature (Suenaga *et al.*, 1991; cf. Drulis *et al.*, 1991). This is not the case for the cuprates, for which T_{irr} is interpreted as the depinning temperature.

E. Kosterlitz–Thouless Transition

We mentioned in Section VI.I that thermal fluctuations at low temperatures result in the production of vortex–antivortex pairs, called intrinsic vortices, where the flux and screening currents of an antivortex flow in a direction opposite to that of the vortex. A vortex and antivortex attract each other; at low temperatures they form bound pairs that dissociate at what is called the Kosterlitz–Thouless temperature T_{KT}, indicated in Fig. 12.37 (Berezinskiv, 1971; Creswick *et al.*, 1992; Kosterlitz and Thouless, 1972, 1973; Matlin *et al.*, 1989; Nelson, 1980; Pradhan *et al.*, 1993; Scheidl and Hackenbroich, 1992; Yeh, 1989; Yeh and Tsuei, 1989). In the cuprates the bound pairs tend to reside between planes (Dasgupta and Ramakrishnan, 1991). Experimental evidence for the KT transition in superconductors has been reported, and references to this work are given in the first edition of this book (p. 308).

By way of summary, some of the concepts and processes discussed in the previous sections are visualized in Fig. 12.41 (Brandt, 1990). The original article should be consulted for those parts of the figure that have not been discussed here.

PROBLEMS

1. Consider a Type II superconductor with a Ginzburg–Landau parameter $\kappa = 100$, transition temperature $T_c = 100\,\mathrm{K}$, and Debye temperature of 200 K. Use standard approximation formulae to estimate its upper critical field, lower critical field, thermodynamic field, energy gap, and electronic and vibrational specific heats.
2. Consider three vortices that form an equilateral triangle $3\,\mu\mathrm{m}$ on a side, with one of the vortices pinned. The temperature $T = \frac{1}{4}T_c$ and the penetration depth $\lambda(0) = 3000\,\text{Å}$. What is the force per unit length on each vortex and in what direction will the two unpinned vortices move?
3. Show that for $\kappa \gg 1$, the quantity of magnetic flux in the core of an isolated vortex is given by

$$\Phi_{core} \approx \Phi_0/2\kappa^2(\ln 2\kappa + 1/2 - \gamma),$$

where γ is the dimensionless Euler–Mascheroni constant. What fraction of the total flux is in the core of an isolated vortex of Ti_2Nb, of Nb_3Sn, or of a typical high-temperature superconductor?

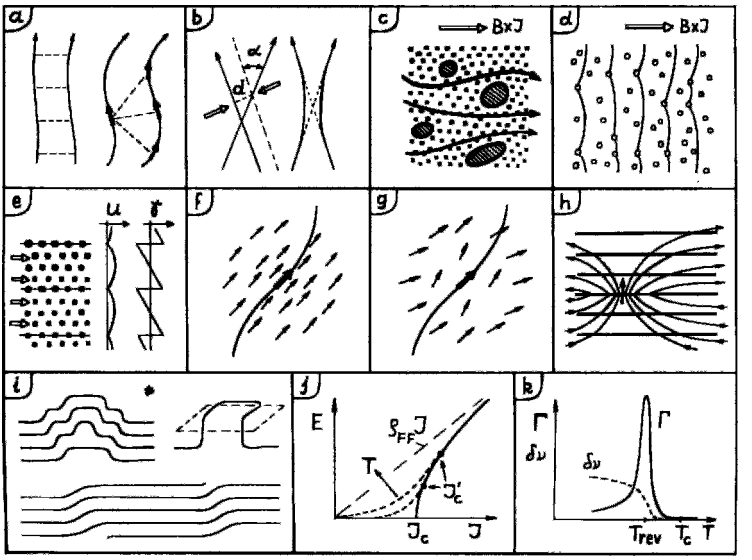

Figure 12.41 Schematic visualization of superconductor concepts and processes. (a) left: simplified 2D interaction between nearly parallel vortex lines, right: more realistic 3D interaction between vortex segments; (b) pair of vortices approaching, crossing, and reconnecting; (c) soft vortex liquid flowing between pinning regions; (d) vortex lattice or liquid, with each vortex pinned by many small pins, subjected to a Lorentz driving force acting toward the right; (e) vortex lattice pinned at equidistant lattice planes parallel to the Lorentz force, which presses it through these channels; plots showing the vortex displacements u and the zigzag shear strain v; (f) magnetic field (small arrows) arising from a vortex segment (dark arrow) in an isotropic superconductor; (g) the same in an anisotropic superconductor; (h) magnetic field lines associated with a point pancake vortex (vertical arrow) on a superconducting layer shown bent by the other layers (horizontal lines) and forced to become parallel to these layers; (i) vortex kinks (upper left), kink pairs (upper right), and a 3D kink structure (lower); (j) current–voltage curves for thermally activated vortex motion; and (k) damping Γ and frequency enhancement $\delta\nu$ of high-temperature superconducting vibrating reed in a longitudinal field. (See original article (Brandt, 1990) for details.)

4. We have seen that parallel vortices inside a superconductor repel each other and become distributed throughout the interior. Show that charges of the same sign inside a normal conductor repel each other and become distributed over the surface. Hint: use Gauss' law and the continuity equation.
5. Show that the integrals of the asymptotic forms of the modified Bessel functions $K_0(r/\lambda)$ and $K_1(r/\lambda)$ of Eqs. (12.24)–(12.26) do not diverge as $r \to 0$, but rather provide finite fields and currents, respectively, in the neighborhood of the origin.
6. For a high-temperature superconductor ($\kappa \approx 100$), how high an applied field $B_{\rm app}$ is needed, relative to $B_{\rm cl}$, to cause the average separation d between nearest-neighbor vortices to reach (a) 100λ, (b) 30λ, (c) 10λ, (d) 3λ, or (e) 1λ?
7. The small argument limit, $r \ll \lambda$, of the zero-order modified Bessel function is given by different authors in different forms:

$$k_0(r/\lambda) \approx -\ln\left(\frac{r}{\lambda}\right) - \gamma + \ln 2$$

Arftken, 1985, pp. 284, 612

$$-\ln\left(\frac{r}{\lambda}\right)$$

Abramowitz and Stegun, eds., 1970, p. 375

$$\ln\left(\frac{r}{2\lambda}\right) - 0.5772\ldots$$

Jackson, 1975, p. 108

$$+\ln\left(\frac{\lambda}{r}\right) + 0.12\ldots$$

Tinkham, 1985, p. 147

$$+\ln\left(\frac{1.123\lambda}{r}\right)$$ Present work

Which of these are equivalent?

8. At what points along the path $V \to S \to M \to C \to V$, starting and ending at the same vortex, V, does the current density pass through zero and at what points does it change sign? Explain these changes, and explain why J has opposite signs at the beginning and at the end of the plot in Fig. 12.20.
9. Derive Eqs. (12.57) and (12.58).
10. The eccentricity e of an ellipse with semi-major and semi-minor axes a and b, respectively, is defined by

$$c = (a^2 - b^2)^{1/2}/a.$$

Show that for a high-temperature superconductor the two expressions

$$a/b = \sqrt{\Gamma}$$
$$e = (\Gamma - 1)^{1/2}$$

are valid for both the core and the current flow ellipses of a vortex, where Γ is the effective mass ratio of Eq. (12.44).

11. Show that for an applied magnetic field aligned along the y direction of a high-temperature superconductor with $(x^2 + z^2)^{1/2} \gg \lambda_c$, the current densities $J_s(x, z)$ of a vortex at points along the x- and z-axes, respectively, are given by

$$\mu_0 \lambda_c J_s(x, 0) = B_y(x, 0)$$
$$\mu_0 \lambda_{ab} J_s(0, z) = B_y(0, z).$$

This page intentionally left blank

13

Irreversible Properties

I. INTRODUCTION

Most of the properties of superconductors are reversible. There are other properties that are irreversible in the sense that when a parameter such as the temperature, the pressure, or the strength of an applied electric or magnetic field is changed in direction the system does not reverse or retrace its former path, but rather hysteretic effects occur. In this chapter we will examine some of these latter cases. The emphasis will be on the Bean Model, a simple model which captures the essential features of some irreversible behaviors of superconductors. Magnetic hysteresis effects will be discussed in some detail.

II. CRITICAL STATES

In Chapter 7 we described the Bardeen–Cooper–Schrieffer (1957) microscopic theory that had been devised to explain the nature of superconductivity, subsequently showing that many of the properties predicted by the BCS theory are satisfied by the classical and by the cuprate superconductors. In Chapter 6 we delineated the Ginzburg–Landau (1950) phenomenological theory, a theory which is helpful for explaining many other properties of superconductors. Chapter 10 presented the Hubbard model and band theory viewpoints on superconductivity. There is yet another approach, introduced

in two works by Bean (1962, 1964), which is too simplified to be called a theory and is instead referred to simply as a model. The Bean model, which has been employed by many experimentalists as an aid in the interpretation of their data, is a type of critical-state model. We begin with a discussion of critical state models in general, and then we apply the Bean model to a number of cases.

These models postulate that for low applied fields or currents, the outer part of the sample is in a so-called "critical state" with special values of the current density and magnetic field, and that the interior is shielded from these fields and currents. The Bean model assumes that the super current density always has the magnitude J_c in the critical state, while the Fixed Pinning model assumes that the pinning force is constant in the critical state. In all the models the magnetic field **B** and the super current density **J** are coupled through the Maxwell relation $\nabla \times \mathbf{B} = \mu_0 \mathbf{J}$, so either one can be calculated from knowledge of the other. When the fields and currents are applied simultaneously and then reversed in direction, they produce modified critical states in the outer parts of the sample, consistent with the assumption of the particular model. High values of the applied fields or currents cause the critical state to penetrate to the innermost parts of the superconductor. The models do not take into account the existence of a lower-critical field B_{c1} or the difference between the Meissner and the mixed states. We do not claim that these models really explain the nature of superconductivity. Rather, they provide a convenient means of describing some experimentally observed phenomena.

In this chapter we will confine our attention to the simple geometry of a solid slab in which the applied magnetic field is parallel to the surface and the demagnetization effects discussed in Chapter 5, Sections X and XI, do not have to be taken into account. The first edition of this work treats cylindrical geometry. The literature can be consulted for critical-state models involving ellipsoidal samples (Bhagwat and Chaddah, 1990, 1992; Chaddah and Bhagwai, 1992; Krasnov, 1992; Krasnov *et al.*, 1991; Navarro and Campbell, 1991).

III. CURRENT–FIELD RELATIONSHIPS

A. Transport and Shielding Current

Electric currents that flow through a superconductor owing to the action of an external current or voltage source are called *transport currents*. Those which arise in the presence of an externally applied magnetic field and cancel the magnetic flux inside the superconductor are called *screening currents*. Figure 13.1a shows the induced shielding current produced by an applied magnetic field and Fig. 13.1b, the induced magnetic field produced by an applied transport current. More complicated cases in which both a transport current and a magnetic field are applied to the superconductor will also be examined. In such cases transport and screening currents are present simultaneously.

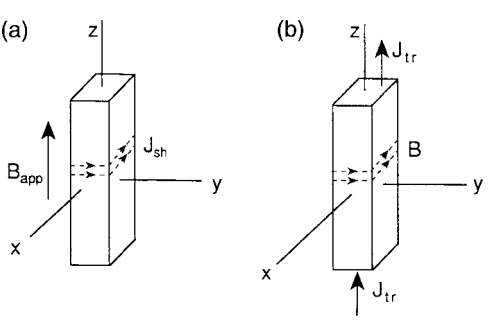

Figure 13.1 (a) Shielding currents J_{sh} induced in a superconducting rod of rectangular cross section by an external magnetic field B_{app} along its axis, and (b) magnetic field B induced in (and around) the same superconducting rod by a transport current J_{tr} flowing along the axis.

B. Maxwell Curl Equation and Pinning Force

We mentioned earlier that the magnetic field and current density that are present in a superconductor are related through the Maxwell curl equation,

$$\nabla \times \mathbf{B} = \mu_0 \mathbf{J}. \tag{13.1}$$

This means that the **B** and **J** vectors are perpendicular at every point in space. We will examine the case of a rectangular slab oriented as shown in Fig. 13.2 in the presence of a magnetic field $\mathbf{B}_{app}$ along the z direction. We assume that the magnetic field inside the slab, $\mathbf{B}_{in} = B_z\mathbf{k}$, is along the z direction and that the current density $\mathbf{J} = J_y\mathbf{j}$ has a component only in the y direction; the current density component J_x at the ends of the loops is neglected. For this case we find from Eq. (13.1) that

$$\frac{d}{dx}B_z(x) = \mu_0 J_y(x), \tag{13.2}$$

which means that the field and current density depend only on x.

The internal magnetic field $B_z(x)$ is equal to the product $n(x)\Phi_0$ of the number of vortices per unit area $n(x)$ times the flux per vortex Φ_0. Equation (13.2) becomes

$$\Phi_0 \frac{d}{dx}n(x) = \mu_0 J_y(x). \tag{13.3}$$

We assume that the vortices in the material are in a static equilibrium configuration. The curl of the magnetic field strength (13.1) produces a gradient in the vortex density (13.3) in a direction perpendicular to the current flow direction, and this is sketched

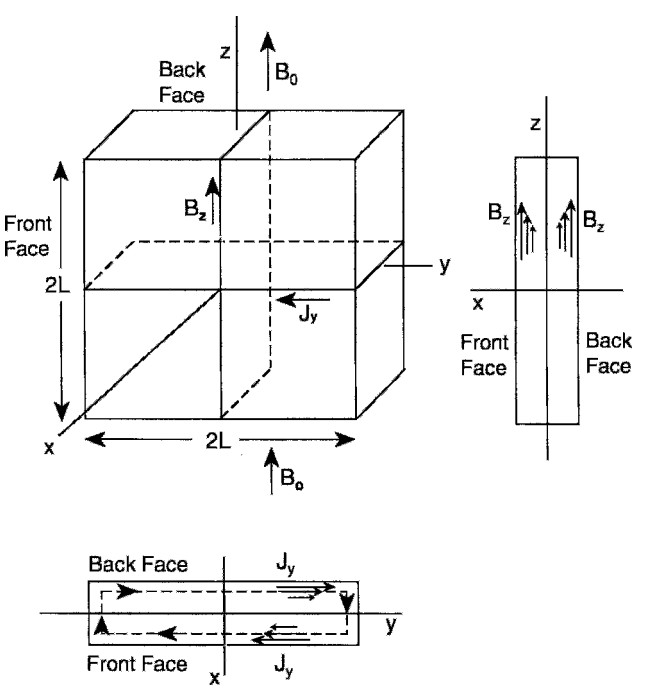

Figure 13.2 Superconducting slab of thickness $2a$ oriented in the y, z-plane with an externally applied magnetic field B_{app} directed along z. The induced shielding current density J_y flowing in the y direction inside the front and back faces is shown.

in Fig. 12.35. The pinning force density $\mathbf{F}_p$ holds the vortices in place, while the Lorentz force density $\mathbf{J} \times \mathbf{B}$ acting on the vortices is balanced by $\mathbf{F}_p$,

$$\mathbf{F_p} = \mathbf{J} \times \mathbf{B} \tag{13.4}$$

$$= (\nabla \times \mathbf{B}) \times \mathbf{B}/\mu_0, \tag{13.5}$$

where we have again used Eq. (13.1). For the present case $\mathbf{F}_p$ only has an x component, with magnitude

$$F_{p_x} = J_y B_z \tag{13.6}$$

$$= \frac{1}{\mu_0} \cdot \frac{dB_z}{dx} B_z \tag{13.7a}$$

$$= \frac{1}{\mu_0} \cdot \frac{d}{dx} \cdot \frac{1}{2} B_z^2. \tag{13.7b}$$

C. Determination of Current–Field Relationships

Equations (13.1)–(13.7) must be satisfied when $\mathbf{B}$ is in the z direction and $\mathbf{J}$ in the y direction. There are many configurations of $B_z(x)$, $J_y(x)$, and $F_p(x)$ that meet this requirement. The Bean model assumes $J_y = \text{const}$, while the Fixed Pinning model assumes $F_p = \text{const}$; all the other models assume a more complex relationship between the internal field and the current density. For most models the relationship between $J_y(x)$ and $B_z(x)$ for the slab geometry is of the form

$$J_y(B_z) = \frac{J_K}{f(B_z)}, \tag{13.8}$$

where $f(B_z)$ is a function of the magnetic field and J_K is independent of the field, but can depend on the temperature. J_y is substituted into Eq. (13.2) and the resultant differential equation is solved to obtain $B_z(x)$, the position dependence of the internal field. Finally, this result is substituted back in Eq. (13.8) to give $J_y(x)$, and Eq. (13.6) immediately provides $F_p(x)$.

IV. CRITICAL-STATE MODELS

A. Requirements of a Critical-State Model

When a magnetic field is turned on it enters a superconductor, its magnitude inside the superconductor decreasing with distance from the surface. If the applied field is weak enough the internal field will be zero beyond a certain distance measured inward from the surface. Critical current flows where the field is present, in accordance with the Maxwell equation (13.1); this is called a *critical state*. As one moves inward, the critical current density generally increases as the field decreases, in accordance with Eq. (13.8). The current density is also zero beyond the point at which the internal field vanishes. When the applied field increases in magnitude, the internal field and current densities penetrate further and for sufficiently strong fields are present throughout the sample. Each critical-state model is based on a particular assumed relationship between the internal field and the critical-current density which satisfies these requirements.

Table 13.1 gives the current–field relationships for several well known critical state models. In these expressions the internal field $B = B(x)$, where x is the distance from the center toward the surface. In most of the models J_c is the critical current in the absence of an applied field.

B. Model Characteristics

Each of the critical-state models depends on a parameter B_K associated with the internal field and a parameter J_K associated with the critical-current density. Both of these parameters can depend on the temperature. The quantity

$$\Theta[B_K - |B(x)|] \tag{13.9}$$

is called the Heaviside step function. One can also write a more general power-law model $J(B) = A|B(x)|^{-n}$ (Askew *et al.*, 1991; Irie

Table 13.1 Current–field relationships corresponding to Eq. (12.8) for several critical state models

$J(B) = J_c$	Bean (1962, 1964)
$J(B) = \dfrac{J_c}{\lvert B(x)\rvert / B_K}$	Fixed Pinning (Ji *et al.*, 1989; Le Blanc and Le Blanc, 1992)
$J(B) = \dfrac{J_c}{\lvert B(x)/B_K\rvert^{1/2}}$	Square Root (Le Blanc and Le Blanc, 1992)
$J(B) = \dfrac{J_c}{1+\lvert B(x)\rvert / B_K}$	Kim (Kim *et al.*, 1962, 1963)
$J(B) = J_c \exp[-\lvert B(x)\rvert / B_K]$	Exponential (Fietz *et al.*, 1964)
$J(B) = J_c - J_c' \lvert B(x)\rvert / B_K$	Linear (Watson, 1968)
$J(B) = \dfrac{J_c}{1+[\lvert B(x)\rvert / B_K]^2}$	Quadratic (Leta *et al.*, 1992)
$J(B) = J_c(1-\lvert B(x)\rvert / B_K)\Theta(B_K - \lvert B(x)\rvert)$	Triangular Pulse (Dersch and Blatter, 1988)
$J(B) = \dfrac{J_c}{[1+\lvert B(x)\rvert / B_K]^\beta}$	Generalized (Lam *et al.*, 1990; M. Xu *et al.*, 1990)

and Yamafuzi, 1967; Yeshurun *et al.*, 1988), which reduces to the Bean, Square Root, and Fixed Pinning models for $n = 0$, $\frac{1}{2}$ and 1, respectively. The Kim model resembles the Fixed Pinning model for high applied fields

$$(|B(x)| \gg B_K), \tag{13.10}$$

while the exponential model, linear model with $J_K = J_K'$, and Kim model all reduce to the Bean model for low applied fields $(|B(x)| \ll B_K)$.

The explicit expressions for $B(x)$ and $J(x)$ that are obtained by solving the differential equation (13.2) for the functions of Eq. 13.8 for various cases depend on boundary conditions, such as the strength of the applied field, the size, shape, and orientation of the sample, and the previous magnetic history. Examples of these solutions will be given for several commonly encountered cases. We will emphasize the Bean model in this chapter.

V. BEAN MODEL

The Bean model (1962, 1964) for super current flow is the simplest, and by far the most widely used of the critical-state models that have been proposed for describing the field and current distribution in a superconductor. The model assumes that wherever the current flows, it flows at the critical density J_c and that the internal magnetic field is given by Eq. (13.1).

A. Low-Field Case

We will first write down solutions for what is called the low-field case. In this case there is a field- and current-free region $(-a' < x < a')$ near the center. In the next section we will provide solutions for the high-field case, i.e., the case in which the fields and currents exist throughout the superconductor.

For the slab geometry of Fig. 13.2 the boundary conditions are that the internal field at the surface, $x = \pm a$, equals the applied field B_0, and that there is a depth, $x = \pm a'$ inside the superconductor at which the internal field drops to zero,

$$B_z(\pm a) = B_0, \tag{13.11a}$$

$$B_z(\pm a') = 0. \tag{13.11b}$$

The differential equation obtained by substituting $J_y(x) = J_c$ in Eq. (13.2) has the solution

$$J_y(x) = J_c \qquad -a \le x \le -a', \quad (13.12a)$$

$$J_y(x) = 0 \qquad -a' \le x \le a', \quad (13.12b)$$

$$J_y(x) = -J_c \qquad a' \le x \le a. \quad (13.12c)$$

Equation (13.2) requires that $B_z(x)$ depend linearly on x in regions where $J_y = \pm J_c$, so that we have for the internal magnetic fields

$$B_z(x) = B_0\left(\frac{a'+x}{a'-a}\right) \qquad -a \le x \le -a', \quad (13.13a)$$

$$B_z(x) = 0 \qquad -a' \le x \le a', \quad (13.13b)$$

$$B_z(x) = B_0\left(\frac{x-a'}{a-a'}\right) \qquad a' \le x \le a. \quad (13.13c)$$

These expressions match the boundary condition $B_z(0) = B_0$ on the two surfaces $x = \pm a$. The quantities J_c and B_0 are related to each other by the expression

$$J_c = \frac{B_0}{\mu_0(a-a')}, \quad (13.14)$$

with the aid of Eq. (13.7), we obtain the pinning forces

$$F_p(x) = J_c B_0\left(\frac{a'+x}{a'-a}\right) \qquad -a \le x \le -a', \quad (13.15a)$$

$$F_p = 0 \qquad -a' \le x \le a', \quad (13.15b)$$

$$F_p(x) = -J_c B_0\left(\frac{x-a'}{a-a'}\right) \qquad a' \le x \le a. \quad (13.15c)$$

These equations for $B_z(x)$, $J_y(x)$, and $F_p(x)$ are plotted in Figs. 13.3a for a finite value of a' and in Fig. 13.3b for $a' = 0$. We see from these figures that $B_z(x)$ is symmetric about the point $x = 0$, while the other two functions $J_y(x)$ and $F_p(x)$ are antisymmetric about this point.

B. High-Field Case

Now that we have explained the low-field Bean model let us introduce its high-field counterpart. The two may be related in terms of a characteristic field B^* proportional to the radius a, as given by

$$B^* = \mu_0 J_c a. \quad (13.16)$$

B^* has the property that when $B_0 = B^*$ the fields and currents are able to reach the center of the slab, as shown in Fig. 13.3b. Thus there are two cases to consider, one for small applied fields,

$$B_0 < B^*, \quad (13.17a)$$

which was discussed in the previous section, and the other for high applied fields,

$$B_0 > B^*. \quad (13.17b)$$

It is easy to show that at high field the currents and fields, respectively, are given by the expressions

$$J_y(x) = J_c \qquad -a \le x \le 0, \quad (13.18a)$$

$$J_y(x) = -J_c \qquad 0 \le x \le a, \quad (13.18b)$$

$$B_z(x) = B_0 - B^*\left(\frac{a+x}{a}\right) \qquad -a \le x \le 0, \quad (13.19a)$$

$$B_z(x) = B_0 + B^*\left(\frac{x-a}{a}\right) \qquad 0 \le x \le a. \quad (13.19b)$$

It is left as an exercise (Problem 3) to write down the pinning forces at high field.

The magnitude of the critical-current density J_c is fixed by the characteristics of the particular superconductor, and depends on such factors as the superconducting material, granularity, twinning, concentration of defect centers, etc. The applied field can be varied, and Fig. 13.3 shows how the internal field, current density, and pinning force vary with the ratio B_0/B^* for the Bean model.

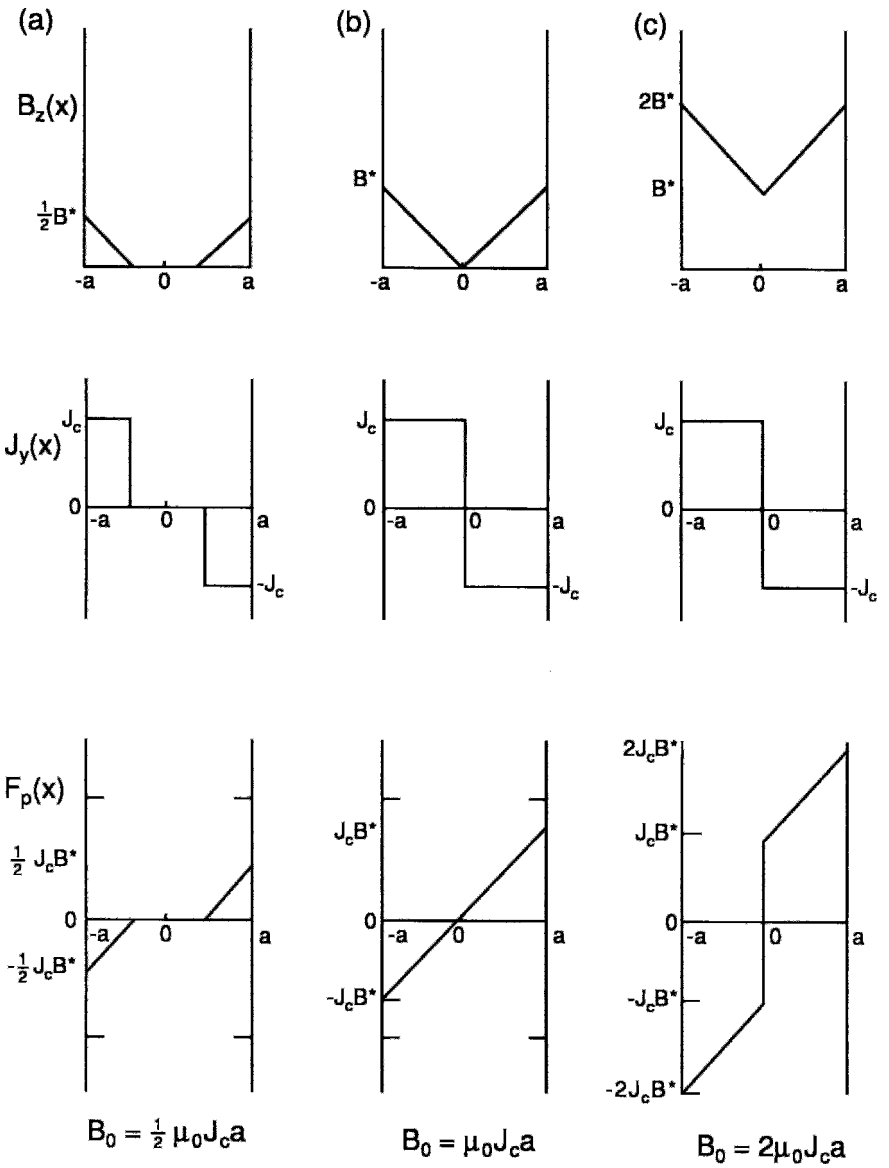

Figure 13.3 Dependence of the internal magnetic field $B_z(x)$, current density $J_y(x)$, and pinning force $F_p(x)$ on the strength of the applied magnetic field B_0 for normalized applied fields given by (a) $B_0/\mu_0 J_c a = \frac{1}{2}$, $B_0/\mu_0 J_c a = 1$, and (c) $B_0/\mu_0 J_c a = 2$. This and subsequent figures are drawn for the Bean model. There is a field free region in the center for case (a), while case (b) represents the boundary between the presence versus the absence of such a region.

Figure 13.3a is for the low-field case $B_0 < B^*$, Fig. 13.3b, with $B_0 = B^*$ the boundary between the two cases, and Fig. 13.3c is for high fields, $B_0 > B^*$.

The figures that we have drawn are for zero-field-cooled samples in which the applied field had been increased from its initial value $B_{app} = 0$ to the value B_0, as shown.

In particular, the three sets of curves drawn in Fig. 13.3 were obtained by increasing the applied field from 0 to $\frac{1}{2}B^*$, then to B^*, and finally to the value $2B^*$. We will see in Section VI that reversing the field leaves some flux trapped, which is reflected in the shape of the plots for $B_z(x)$ versus x.

C. Transport Current

We have discussed the Bean model for a thin slab in an applied magnetic field. Analytic expressions were deduced for the magnetic field, current density, and pinning force for these cases. Let us now apply the same Bean model analysis to the case of a transport current in which a fixed amount of current passes along the slab or wire, and both external and internal magnetic fields are induced by this current.

We will again discuss the case of a slab oriented in the y, z-plane, but this time assuming an applied transport current of magnitude I flowing in the positive y direction, as shown in Fig. 13.4. The current distributes itself in the x, z-cross section in accordance with the Bean model. Thus the critical-current density J_c is adjacent to the outer boundary, between $x = -a$ and $x = -a'$, with zero current in the center, as shown in Fig. 13.5a. Since the cross-sectional area is $2(a - a')L$, the transport current is given by

$$I = 2(a - a')LJ_c. \tag{13.20}$$

This current flow produces internal magnetic fields with the orientations shown in the figure. The external fields that are induced outside the slab will not be of concern to us.

The equations for $B_z(x)$, $J_y(x)$, and $F_p(x)$ for the case of a transport current are the same as Eqs. (13.13)–(13.19) for the

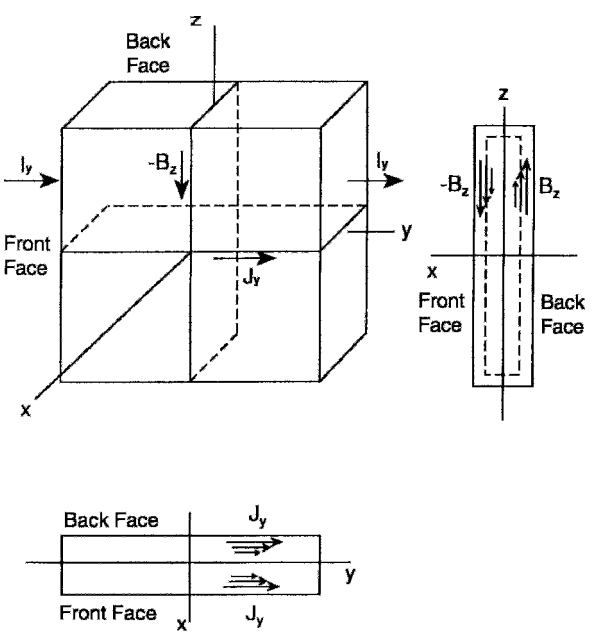

Figure 13.4 Superconducting slab of length $2L$, height $2L$ and thickness $2a$ oriented in the y, z-plane with an applied transport current I_y flowing in the positive y direction. The induced internal magnetic fields B_z are indicated. The induced external fields are not taken into account, and hence are not shown.

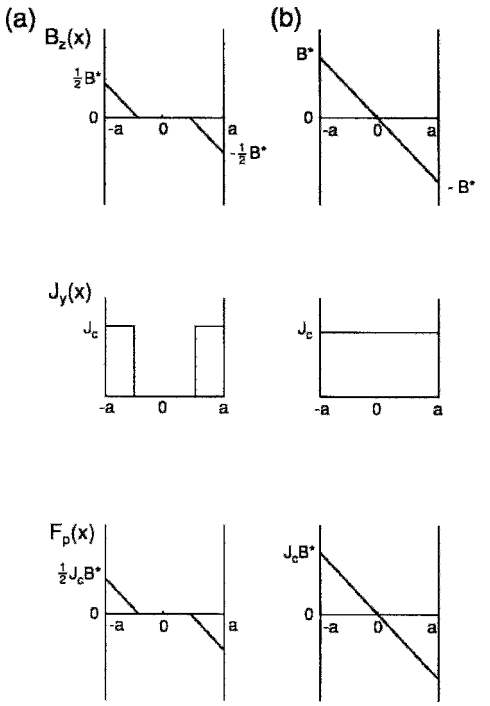

Figure 13.5 Dependence of the internal magnetic field $B_z(x)$, current density $J_y(x)$, and pinning force $F_p(x)$ on the strength of an applied transport current for the Bean model. Figures are drawn for applied currents I that are (a) less than the critical current $I_c = 2aLJ_c$, or (b) equal to the critical current I_c. Applied currents in excess of the critical current cause the wire to go normal.

applied field case, except for several reversals of sign, so we will not bother to write them down. Figures 13.5a provide plots of these three quantities for $I \approx \frac{1}{2}I_c$, where

$$I_c = 2aLJ_c. \tag{13.21}$$

We see from the figure that the induced magnetic field is in opposite directions on either side of the slab, while the internal pinning force has the same direction as in the screening current case. A comparison of Figs. 13.3 and 13.5 shows that B and J reverse their symmetries about the point $x = 0$, B being symmetric and J antisymmetric in the screening case, and B antisymmetric and J symmetric in the transport case; the pinning force F_p is antisymmetric in both cases. This is because in both cases the Lorentz force $\mathbf{J} \times \mathbf{B}$ acts to move the current–field configurations inward, while the pinning force opposes this motion and holds the fields (or vortices) in place. Figure 13.5b shows the field, current density, and pinning force when the wire is carrying its maximum possible transport current (13.16), namely, its critical current I_c.

D. Combining Screening and Transport Current

When both an applied magnetic field and an applied transport current are present, the situation is more complicated. The Bean model conditions still apply—namely, wherever the current flows it flows at the critical density J_c. For the slab geometry, if there is an internal magnetic field $\mathbf{B}_{in}$, it will have a gradient (13.2) equal to $\mu_0\mathbf{J}_c$. Figure 13.6 sketches the slab with an applied external field and a transport current present simultaneously. The induced currents and fields combine with the applied fields to produce the net current densities and magnetic fields, which have the x dependence plotted in Fig. 13.7. This figure is drawn for the high-field case, in which $B_{app} > \mu_0 J_c a$; such a case occurs in magnet wire wound as a solenoid to produce a strong magnetic field.

The difference ΔB between the magnetic fields on the left and right sides of the slab, where $x = -a$ and $x = a$, respectively, is related to the net average current density in the slab arising from the flow of transport current. It is left as an exercise (Problem 7) to show that

$$\Delta B = \mu_0 J_c (x_R - x_L), \tag{13.22}$$

where the notation for this equation is given in the figure.

Section VI.G of the first edition examined more complicated cases involving the simultaneous presence of a transport current and an external field.

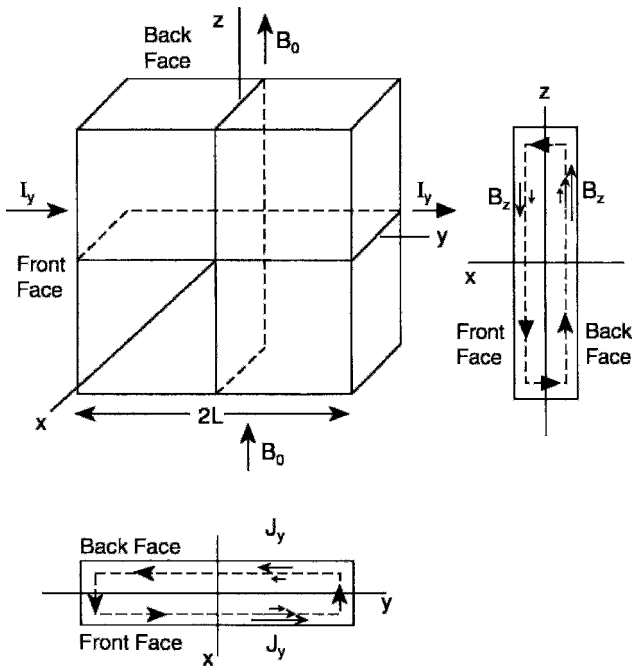

Figure 13.6 Superconducting slab of length $2L$, height $2L$ and thickness $2a$ oriented in the y, z-plane with an applied transport current I_y flowing in the y direction and an applied magnetic field B_0 oriented in the z direction. The internal magnetic fields $B_z(x)$ and current densities $J_y(x)$ shown in the figure are superpositions of those arising from the applied field and the transport current cases of Figs. 13.2 and 13.4 respectively.

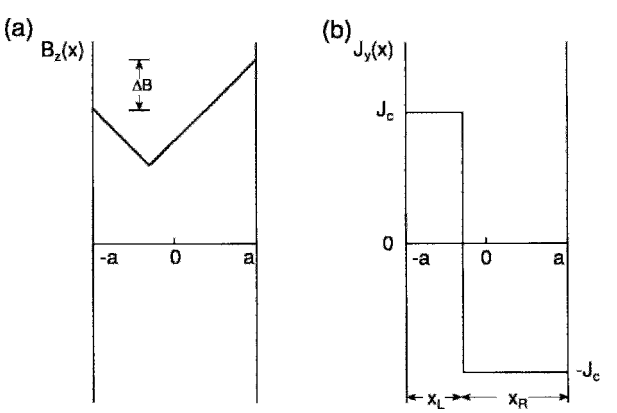

Figure 13.7 Dependence of the internal field $B_z(x)$ and the current density $J_y(x)$ on position x inside the slab of Fig. 13.6 when both a magnetic field and a transport current are applied. The figure is drawn for the high-field case.

E. Pinning Strength

Pinning forces set limits on the amount of resistanceless current that can be carried by a superconductor. We know from Eqs. (13.15) that in the Bean model the pinning force has its maximum magnitude F_p at the edge of the sample, where $x = \pm a$,

$$F_p = J_c B_0. \tag{13.23}$$

We will consider how the value of F_p affects the field and current distributions for a constant applied field B_0. If the slab is a soft superconductor, so that the pinning forces are too weak to hold the vortices in place, from Chapter 12, Section V.C it is clear that F_p is zero in the vortex equation of motion. Setting $F_p = 0$ in Eq. (13.23) gives $J_c = 0$, resistanceless current cannot flow, and, from Eq. (13.2), the magnetic field penetrates the entire cross section, as shown by the curves for "no pinning" in Fig. 13.8. For weak pinning, F_p is small, J_c is small, from Eq. (13.2) the slope dB_z/dx is small, and the magnetic field and current still penetrate the entire sample, but $B_z(x)$ is weaker in the center. If the slab is a hard superconductor, so that F_p is large, J_c is also large, the slope dB_z/dx

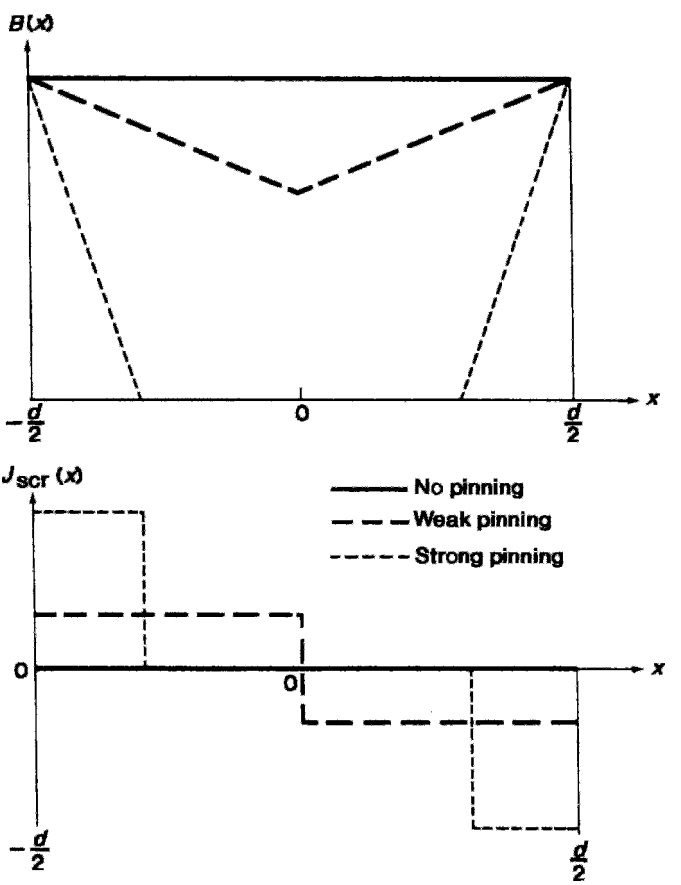

Figure 13.8 Internal magnetic field $B_z(x)$ and current density $J_y(x)$ for strong (- - - - -), weak (– – – –), and zero (—) pinning in a superconducting slab in an external magnetic field, as in Fig. 13.2 (von Duzer and Turner, 1981, p. 338).

is steep, and the field and current only exist near the surface of the sample, as shown by the curves for "strong pinning" in Fig. 13.8. The figure is drawn for the shielding current case, though it can also be concluded that increasing the pinning strength increases the transport supercurrent capacity of a wire (M. B. Cohn *et al.*, 1991).

F. Current-Magnetic Moment Conversion Formulae

The total magnetic moment $\boldsymbol{\mu}$ (denoted here by the symbol M) due to a current density $\mathbf{j}(\mathbf{r})$ in an arbitrary shaped sample is given by

$$\mathbf{M} = \frac{1}{2}\int_V [\mathbf{r}\times\mathbf{j}(\mathbf{r})]d^3\mathbf{r} \qquad (13.24)$$

Assuming that the current density is constant across the sample (simple critical state Bean model) one can calculate the magnetic moment for a plate-shaped sample of arbitrary cross-section. This is very useful because many single crystals can be described by such a geometry, which includes disks (pellets), slabs and odd-shaped flat samples. The formulae below are exact, and do not need be adjusted for example for demagnetization corrections as long as a field-independent critical current is assumed.

Equation (13.24) is an SI formula in which current density j is in amperes per square meter, magnetic field B is in tesla, and lengths are in meters. When practical units are used whereby j is measured in A/cm^2, magnetic field in Gauss, and length in centimeters, the factor $\frac{1}{2}$ in Eq. (13.24) is replaced by 1/20. To convert the formulae below for the magnetic moment to practical units simply divide by 10.

a. Elliptical cross-section

Let us consider a sample of thickness $2d$, which has an elliptical cross-section in the ab-plane (ellipse of semi-major axis b, semi-minor axis w, and volume V):

$$V = 2\pi wbd \qquad (13.25)$$

and

$$M = \frac{jw}{2}\left(1-\frac{w}{3b}\right)V \qquad (13.26)$$

In the particular case of a disk of radius $a = b = R$ we have:

$$V = 2\pi R^2 d \qquad (13.27)$$

and

$$M = \frac{jR}{3}V \qquad (13.28)$$

b. Rectangular cross-section

In the case of a rectangular cross-section of sides $2w$ and $2b$ $(w \le b)$) we find:

$$V = 8wbd \qquad (13.29)$$

and

$$M = \frac{jw}{2}\left(1-\frac{w}{3b}\right)V \qquad (13.30)$$

In the particular case of a square of side $2b = 2w$ we get:

$$V = 8w^2 d \qquad (13.31)$$

and

$$M = \frac{jw}{3}V \qquad (13.32)$$

c. Triangular cross-section

If the sample cross-section is a triangle of sides a, b, n with angles defined as $\alpha = (a\hat{}n)$, $\beta = (b\hat{}n)$ and $\gamma = (a\hat{}b)$, we have: the semi-perimeters $s = (a+b+n)/2$

$$V = 2d\sqrt{s(s-a)(s-b)(s-n)} \equiv 2dA \qquad (13.33)$$

and

$$M = \frac{jA}{3s}V = \frac{2dba^2\sin(\beta)}{3c} \times \left\{\cot\left(\frac{\beta}{2}\right) + \cot\left(\frac{\alpha}{2}\right)\right\} \quad (13.34)$$

or

$$M = \frac{2}{3}jd(s-a)(s-b)(s-n) \quad (13.35)$$

For an equilateral triangle $a = b = n$ we have

$$V = \frac{\sqrt{3}}{2}a^2 d \quad (13.36)$$

$$M = \frac{da^3}{6}j \quad (13.37)$$

In another particular case of triangle of sides $a = b \neq \mathrm{n}$, $\alpha = \beta \neq \gamma$

$$M = \frac{dan^2}{3}j\sin\left(\frac{\alpha}{2}\right) = \frac{dn^3}{12c}j\left(\frac{2a}{n} - 1\right) \quad (13.38)$$

d. General remarks

Note that the formulae for the elliptical and rectangular cases are identical (except for the volumes) if one replaces the ellipse's semiaxes by half widths. It follows that the total magnetic moment, μ, of a sample that was later broken into two pieces will always be greater than sum of the magnetic moments of the individual pieces

$$\mu > \mu + \mu \quad (13.39)$$

For example, if we start with the square sample of side $2b = 2w$ we have for its moment from Eq. (13.32)

$$M = \frac{jb}{3}V \quad (13.40)$$

Now, we cut this sample into two equal pieces. Each has dimensions $b \times 2b \times 2d$, (so $w = b/2$) and the volume of each is just half of the whole. The total magnetic moment of the two pieces is given by Eq. (13.30),

$$2M_1 = 2\frac{jw}{2}\frac{5}{6}\frac{V}{2} = \frac{5}{8}\frac{jb}{3}V = \frac{5}{8}M \quad (13.41)$$

VI. REVERSED CRITICAL STATES AND HYSTERESIS

Up until now we have made the implicit assumption that the sample was zero field cooled and then subjected to an applied field that only increased in value. As the surface field B_o is increased, it begins to proceed inward. Figure 13.9 shows the internal field configurations brought about by a series of six successive increases in the applied field. We know from Eqs. (13.19) that the applied field B^* causes the innermost internal field to just reach the center point $x = 0$; and that twice this surface field, $2B^*$, causes the field at the center point to be B^*, as illustrated in the figure.

The present section will examine what happens when the field decreases from a maximum value. We will not try to write down the equations for all the different cases

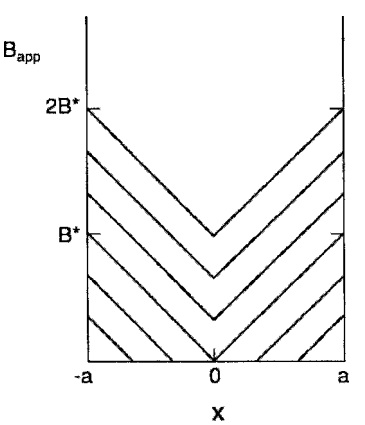

Figure 13.9 Internal field in a superconducting slab for increasing values of the applied field. When B_{app} reaches the value B^*, the internal field reaches the center; when $B_{app} = 2B^*$, the field at the center is B^*.

because they are very complicated, as illustrated in Problem 9, without being very instructive. Instead, we will provide a qualitative discussion by sketching how the field and current configurations change as the field decreases.

A. Reversing Field

The first three panels of Fig. 13.10 show the field and current configurations as the applied field is increased from $0.5B^*$ to $2.5B^*$, while the next three panels show the configurations for a decrease in B_{app} from the maximum value $2.5B^*$ to the minimum $-2.5B^*$. This begins at the surface by a decrease in the internal field there. A B versus x line with the opposite slope moves inward, as shown in Figs. 13.10d and 13.10e. The result is that the flux is trapped inside during the field-lowering process as shown shaded in Fig. 13.11b. Thus the field inside exceeds that at the surface, and the average field inside is larger than the surface value. It will be clear from the discussion below that the amount of trapped flux reaches a maximum when the applied field has decreased through the range $\Delta B = 2B^*$ and that further decreases in the field maintain the amount of trapped flux constant. Finally, the applied field drops below zero and a negative applied field forms a critical state in the opposite direction, as shown. Figure 13.10 also shows the current flow patterns for each step in the field-lowering process.

We see from Fig. 13.10 that increasing the applied field beyond B^* produces a critical state with the maximum amount of shielded flux. The subsequent decrease of the field by $2B^*$ or more produces a critical state with the maximum amount of trapped flux. Figure 13.11 shows these two cases and depicts the shielded and trapped flux as shaded regions. The area of the shaded region

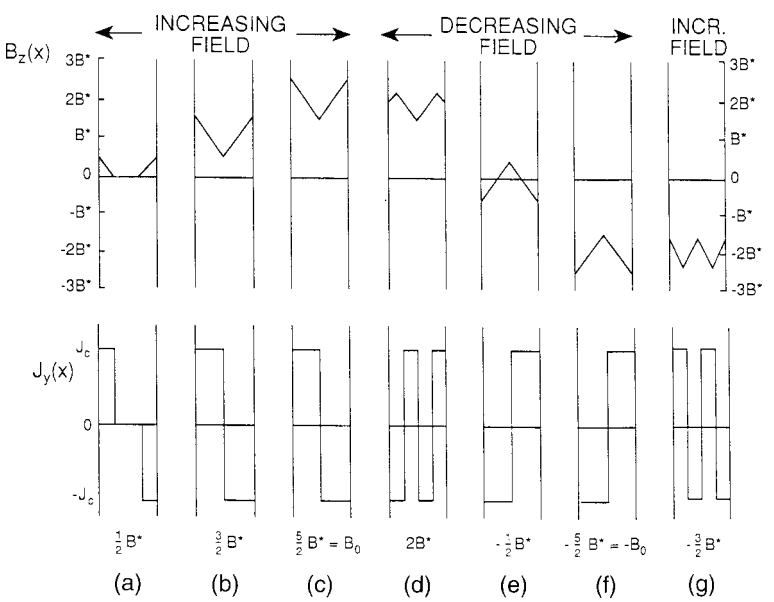

Figure 13.10 Applied field cycle with B_{app} starting at 0, increasing from $0.5B^*$ to $2.5B^*$, decreasing through zero to the negative value $-2.5B^*$, and then beginning to increase again. Plots are shown of the internal field $B_z(x)$ and the current density $J_y(x)$ for successive values of B_{app}.

has the magnitude B^*a, which means that the maximum flux trapped per unit length Φ_{max}/L is

$$\frac{\Phi_{max}}{L} = B^* a. \qquad (13.42)$$

Flux shielding occurs when the average field $\langle B \rangle$ inside the superconductor is lower in magnitude than the applied field, whereas flux trapping occurs when the average internal field exceeds the applied field. It is a simple matter to calculate these averages. Thus we have, for positive $B_0 > B^*$ and $B_{app} > 0$,

$$\langle B \rangle = B_{app} - \tfrac{1}{2}B^* \qquad \text{(shielding)} \quad (13.43a)$$

$$\langle B \rangle = B_{app} + \tfrac{1}{2}B^* \qquad \text{(trapping)}, \quad (13.43b)$$

corresponding to Figs. 13.7a and 13.11 respectively. We see from Fig. 13.10 that these two cases are associated with current flow in opposite directions.

If the applied field is increased from zero to B_0 and then decreased back to zero, the amount of trapped flux will depend on whether the maximum field B_0 is less than B^*, between B^* and $2B^*$, or greater than $2B^*$.

In Eqs. (13.43a) and (13.43b) we gave the average internal fields for the conditions of maximum shielding and maximum trapping when $B_0 > B^*$. The first edition of this work shows how to determine the average internal field throughout a complete raising and lowering cycle.

Figure 13.12 presents a plot of the average field $\langle B \rangle$ versus the applied field B_{app}. There are five special points indicated on the loop: 1) the end points a and a′ where $\langle B \rangle$ is a maximum, 2) point b where $\langle B \rangle = B_{app}$ and the magnetization M is zero, 3) point c where the applied field B_{app} is zero, 4) point d where the average field $\langle B \rangle$ is zero, and 5) point e which appears in Figs. 13.13b and 13.13c as the onset of a linear portion of magnetization versus applied field loop. The definitions of these special points are given in Table 13.2. The first edition provides (Chap. 12, Sect. VI) the information needed to calculate Figs. 13.12 and 12.13.

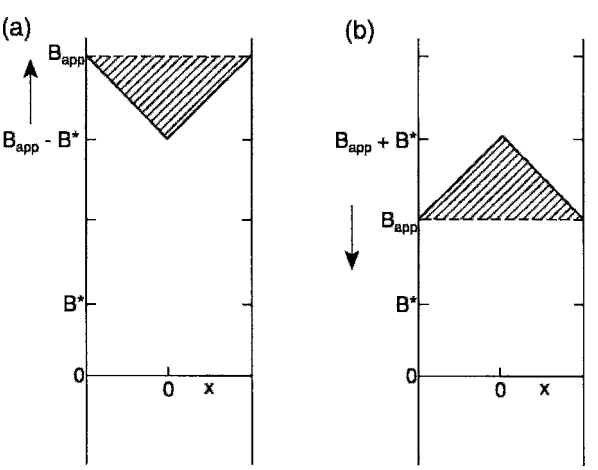

Figure 13.11 Examples of (a) shielded flux (shaded) for an increasing applied field, and (b) trapped flux (shaded) for a decreasing applied field.

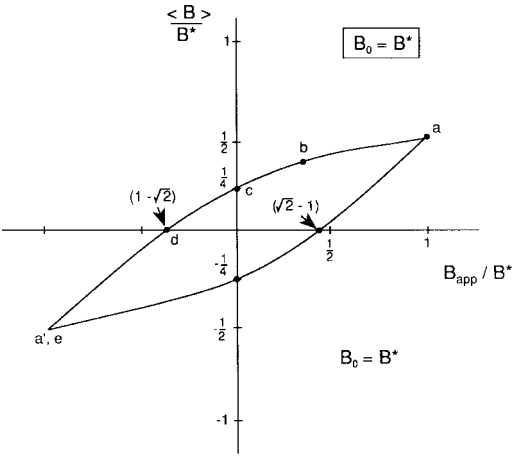

Figure 13.12 Average field $\langle B \rangle$ versus the applied magnetic field B_{app} cycled over the range $-B_0 \leq B_{\text{app}} \leq B_0$ for the case $B_0 = B^*$.

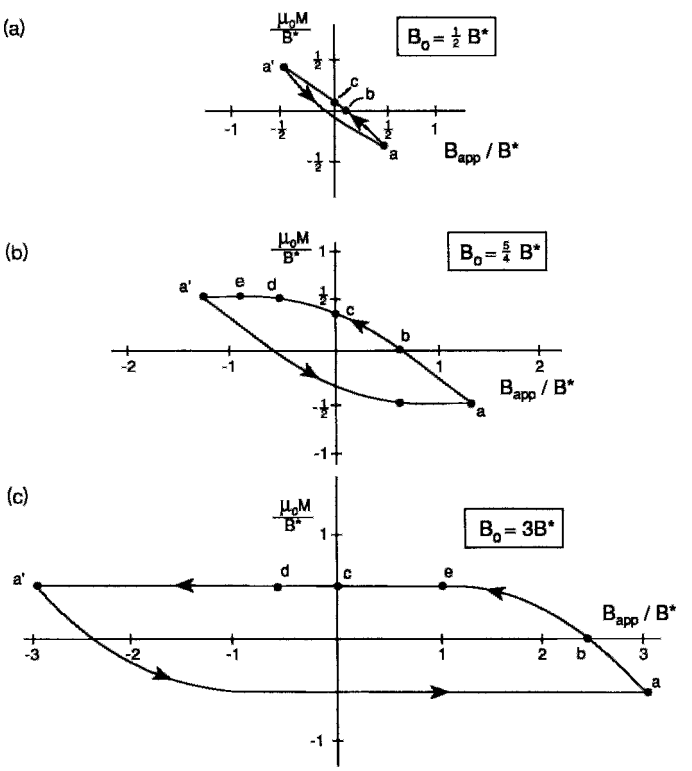

Figure 13.13 Hysteresis loops of magnetization $\mu_0 M$ versus applied magnetic field B_{app} cycled over the range $-B_0 \leq B_{\text{app}} \leq B_0$ for three cases: (a) $B_a = \frac{1}{2}B^*$, (b) $B_0 = \frac{5}{4}B^*$, and (c) $B_0 = 3B^*$. The magnetization has the values listed in Table 12 for the special points a, b, c, d, and e indicated on the loops.

Table 13.2 Definitions of the Special Points a, b, c, d, and e on the Hysteresis Loops of Figs. 13.12, 13.13, and 13.14.

Point	Characteristics	
a	$B_{app} = B_0$	end point of loop
b	$M = 0$	$\langle B \rangle = B_{app}$
c	$B_{app} = 0$	near midpoint of loop
d	$\langle B \rangle = 0$	$\mu_0 M = -B_{app}$
e	onset of linear portion of loop (exists for $B_0 > B^*$ and absent for $B_0 < B^*$)	

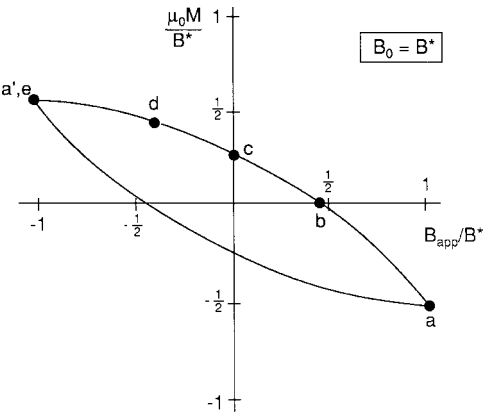

Figure 13.14 Magnetization hysteresis loop for the case $B_0 = B^*$.

B. Magnetization

The magnetization M is given by the relation (1.69),

$$M = \frac{B}{\mu_0} - H. \tag{13.44}$$

For the slab case depicted in Fig. 13.2 the boundary condition (1.76) shows that H is the same outside and inside the superconductor, with the value $\mu_0 H = B_{app}$. Ordinarily, we think of M as the average magnetization, $M = \langle M \rangle$. Bearing this in mind, Eq. (13.44), written for average quantities inside the superconductor, is as follows:

$$\mu_0 M = \langle B \rangle - B_{app}. \tag{13.45}$$

Thus we see that the magnetization determines how great is the difference between the average internal field and the applied field.

C. Hysteresis Loops

A hysteresis loop is a plot of the magnetization M versus the applied field B_{app}. Examples of such loops are presented in Figs. 13.12 to 13.14.

The magnetization loop is narrow and inclined at close to a 45° angle for $B \ll B^*$, in accordance with Fig. 13.13a Figure 13.14 shows the intermediate field case for $B_0 = B^*$. The magnetization saturates at $M = B^*/\mu_0$ over most of the range for the case $B_0 \gg B^*$, as indicated in Fig. 13.13c. The hysteresis loops are labeled with the same points a, b, c, d, and e that were introduced in the previous section; values for the magnetization at these points are given in Table 13.3. The onset of the flat horizontal portion of the loop is indicated by point e. These loops may be compared with their experimentally determined low-field counterparts shown in Figs. 5.5 and 5.6; the former figure illustrates the onset of the saturation phenomenon. The high-field hysteresis loops of Fig. 5.7 are saturated over most of their range, but exhibit the additional feature of a discontinuity at the field B_{c1}, which is not taken into account in the Bean model.

If the magnetization is taken around a cycle of the loop, the net work done by the external field, expressed as the energy loss Q per unit volume, is equal to the area enclosed by the loop:

$$Q = \oint M dB. \tag{13.46}$$

Table 13.3 Expressions for the Average Magnetic Field $\langle B \rangle$ and the Magnetization $\mu_0 M$ at Various Points on the Hysteresis Loops of Figs. 13.12, 13.13 and 13.14 over a Range of Maximum Fields B_0 Relative to the Full Penetration Field B^*. Point e is absent for $B_0 < B^*$

Point	Range of B_0	Applied field B_{app}	Average field $\langle B \rangle$	Magnetization $\mu_0 M$
a	$0 \le B_0 \le B^*$	B_0	$\frac{1}{2}B_0^2/B^*$	$-B_0 + \frac{\frac{1}{2}B_0^2}{B^*}$
a	$B^* \le B_0$	B_0	$B_0 - \frac{1}{2}B^*$	$-\frac{1}{2}B^*$
b	$B_0 \ll B^*$	$\frac{\frac{1}{2}B_0^2}{B^*}$	$\frac{1}{2}B_0^2/B^*$	0
b	$B^* \le B_0$	$B_0 - (2-\sqrt{2})B^*$	$B_0 - (2-\sqrt{2})B^*$	0
c	$0 \le B_0 \le B^*$	0	$\frac{1}{4}B_0^2/B^*$	$\frac{\frac{1}{4}B_0^2}{B^*}$
c	$B^* \le B_0 \le 2B^*$	0	$B_0 - \frac{1}{2}B^* - \frac{\frac{1}{4}B_0^2}{B^*}$	$B_0 - \frac{1}{2}B^* - \frac{\frac{1}{4}B_0^2}{B^*}$
c	$2B^* \le B_0$	0	$\frac{1}{2}B^*$	$\frac{1}{2}B^*$
d	$0 \le B_0 \le \frac{3}{2}B^*$	$B_0 - [2B^*(2B_0 - B^*)]^{1/2}$	0	$-B_0 + [2B^*(2B_0 - B^*)]^{1/2}$
d	$\frac{3}{2}B^* \le B_0$	$-\frac{1}{2}B^*$	0	$\frac{1}{2}B^*$
e	$B^* \le B_0$	$B_0 - 2B^*$	$B_0 - \frac{3}{2}B^*$	$\frac{1}{2}B^*$

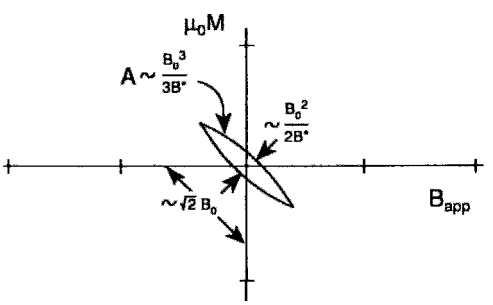

Figure 13.15 Estimating the area of a magnetization hysteresis loop at low field; $B_0 \ll B^*$.

Figure 13.15 shows that the area of the low-field hysteresis loop is proportional to its length $\approx \sqrt{2}B_0$ times its width $\approx B_0^2/2B^*$, using values estimated from Table 13.3. The area may be expressed as

$$Q = \frac{2B_0^2}{\mu_0}\Gamma(\beta), \qquad (13.47)$$

where the loss factor $\Gamma(\beta)$ has the approximate value

$$\Gamma(\beta) \approx \frac{\beta}{3} \qquad \beta < 1 \qquad (13.48)$$

where

$$\beta = \frac{B_0}{B^*}. \qquad (13.49)$$

For high fields, $B_0 \gg B^*$, the area of the loop, to a first approximation, equals its height B^* times the horizontal distance $2B_0$ between the points a and a′, which gives $Q \approx 2B_0B^* = 2B_0^2/\beta$, as may be seen from Fig. 13.13. The correction factor $\approx 4B^{*2}/3$ must be subtracted to account for the rounded part at the ends. Adding these two parts gives the energy loss (13.47), where the energy loss factor $\Gamma(\beta)$ is approximated as

$$\Gamma(\beta) \approx \frac{1}{\beta} - \frac{2}{3\beta^2} \qquad \beta > 1, \qquad (13.50)$$

where β is given by Eq. (13.49). Figure 13.16 shows the dependence of the calculated loss factor $\Gamma(\beta)$ on β for the slab case, which has the limiting approximations (13.48) and (13.50), and also for a cylinder in a

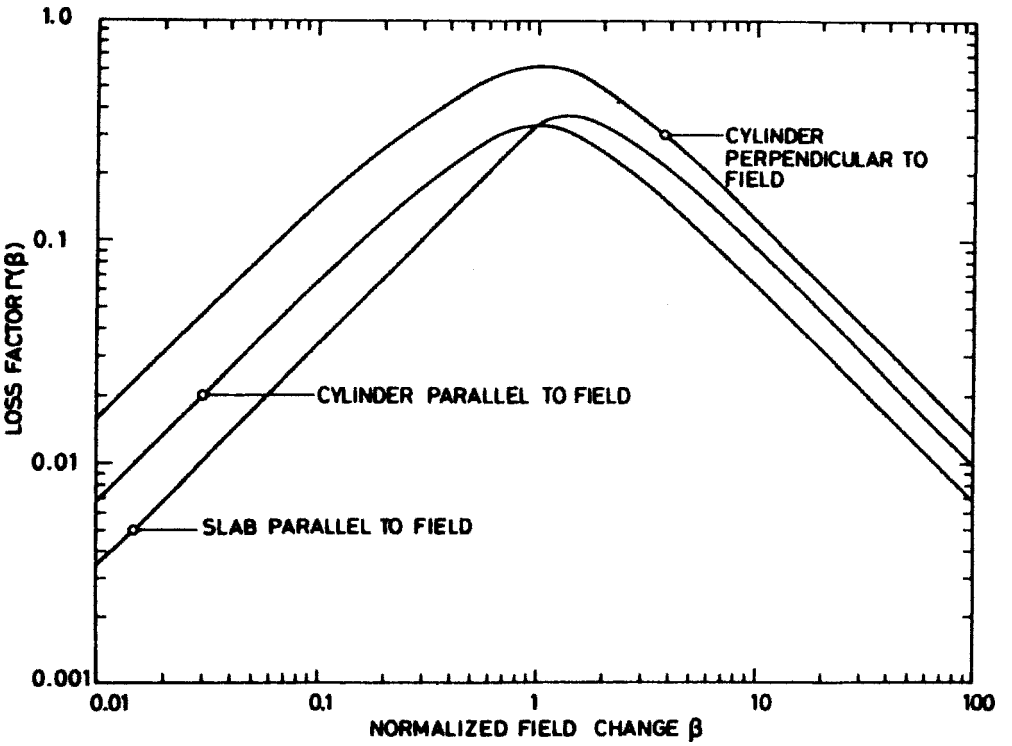

Figure 13.16 Energy loss factor $\Gamma(\beta)$ for different superconductor shapes and orientations in an applied magnetic field. The case of a slab parallel to the applied field is treated in the text, with the low-field side, $B_0 < B^*$ approximated by Eq. (13.48) and the high-field side, $B_0 > B^*$, by Eq. (13.50). Equation (13.51) provides analytical expressions for $\Gamma(\beta)$ in the case of a cylinder oriented parallel to the field (Wilson, 1983, p. 164).

parallel and perpendicular field. The low- and high-field approximations for $\Gamma(\beta)$ of the cylinder are as follows:

$$\Gamma(\beta) \approx \frac{2\beta}{3} - \frac{\beta^2}{3} \qquad \beta < 1, \qquad (13.51a)$$

$$\Gamma(\beta) \approx \frac{2}{3\beta} - \frac{1}{3\beta^2} \qquad \beta > 1. \qquad (13.51b)$$

D. Magnetization Current

We have seen that for high applied fields satisfying the condition $B_{app} \gg B^*$, the average internal field $\langle B \rangle$ varies between $B_{app} + \frac{1}{2}B^*$ and $B_{app} - \frac{1}{2}B^*$, so that the magnetization $\mu_0 M = \langle B \rangle - B_{app}$ varies over the range $\pm\frac{1}{2}B^*$. We know from Eq. (13.34) that

$$B^* = \mu_0 J_c a. \qquad (13.52)$$

A high-field hysteresis loop provides the difference,

$$M_+ - M_- = J_c a, \qquad (13.53)$$

between the upper and lower magnetization plateaux, where

$$\mu_0 M_+ = \tfrac{1}{2}B^*, \qquad (13.54a)$$

$$\mu_0 M_- = -\tfrac{1}{2}B^*, \qquad (13.54b)$$

as indicated in Fig. 13.13c. This gives us an expression for the critical current in terms

of measured values of the magnetization through the Bean model formula,

$$J_c = \frac{2(M_+ - M_-)}{d} \qquad (13.55)$$

$$= 1.59 \times 10^6 \frac{\mu_0 \Delta M}{d} \qquad (\mathrm{A/m^2}), \qquad (13.56)$$

where $\mu_0 \Delta M = \mu_0(M_+ - M)$ is expressed in teslas while d is the diameter of the sample grains, measured in meters. More precisely, this represents a high-field Bean model formula. Such an indirect method of measuring J_c using hysteresis loops is widely employed (Biggs *et al.*, 1989; Crabtree *et al.*, 1987; Frucher and Campbell, 1989; Kohiki *et al.*, 1990; Kumakura *et al.*, 1987; Nojima and Fujita, 1991; Sun *et al.*, 1987; van den Berg *et al.*, 1989; Xiao *et al.*, 1987b), and constitutes one of the most important applications of the Bean model.

Many authors use electromagnetic units for the magnetization, which corresponds to the expression

$$J_c = \frac{30(M_+ - M_-)}{d} \qquad \mathrm{A/cm^2}, \quad (13.57)$$

where d is now in centimeters.

This method has been widely applied for determining J_c. An example is the measurement by Shimizu and Ito (1989) of the critical currents of 16 $YBa_2Cu_3O_{7-\delta}$ samples with a range of particle diameters from 3 to 53 μm. Figure 13.17 shows some of their hysteresis loops. Shimizu and Ito determined the critical current from the plots of ΔM versus d shown in Figs. 13.18 and 13.19 for three applied field strengths at temperatures of 4.2 K and 77 K. The horizontal bar through each datum point gives a range of diameters between 25% and 75% of the diameter distribution. The results were $J_c = 2 \times 10^6\ \mathrm{A/cm^2}$ at 4.2 K in a field of 0.3 T and $7 \times 10^4\ \mathrm{A/cm^2}$ at 77 K in a field of 0.03 T. The experimental results' presented in Figs. 13.18 and 13.19 show that, for small particle diameters, the magnetization is indeed proportional to the diameter (Shimizu and Ito, 1989; Tkaczyk *et al.*, 1992; cf. Babic *et al.*, 1992; Dersch and Blatter, 1988), which means, from Eq. (13.51), that the measured critical current is independent of the diameter. We also see from these figures that the magnetization saturates for particle diameters greater than 20 μm, suggesting that appreciable magnetization current cannot flow through boundaries more than 20 μm wide. Using the Bean expression (13.57) in this saturation region provides values of J_c that are too low.

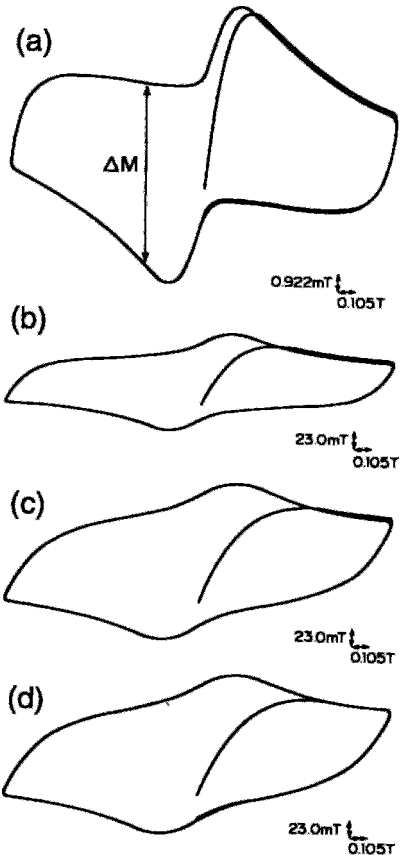

Figure 13.17 Experimental magnetization hysteresis loops of $YBa_2Cu_3O_{7-\delta}$ at 4.2 K used to determine the critical current J_c with powder diameters (a) 3 μm, (b) 15 μm, (c) 36 μm, and (d) 53 μm (Shimizu and Ito, 1989).

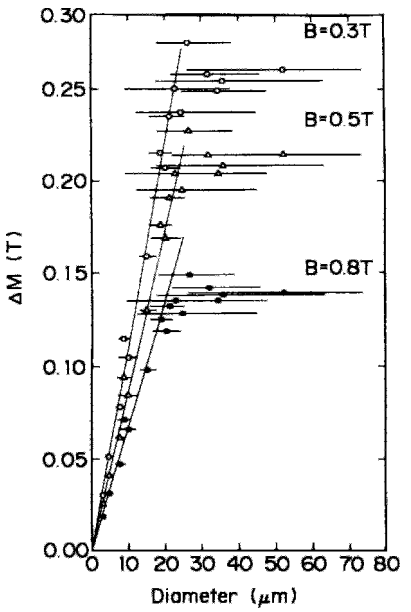

Figure 13.18 Dependence of the magnetization parameter ΔM on the particle diameter d for a series of $YBa_2Cu_3O_{7-\delta}$ samples at 4.2 K. The horizontal lines are a measure of the distribution in diameter, as explained in the text. The critical current is determined from the slope $\Delta M/d$ of the lines on the left using Eq. (13.56) (Shimizu and Ito, 1989).

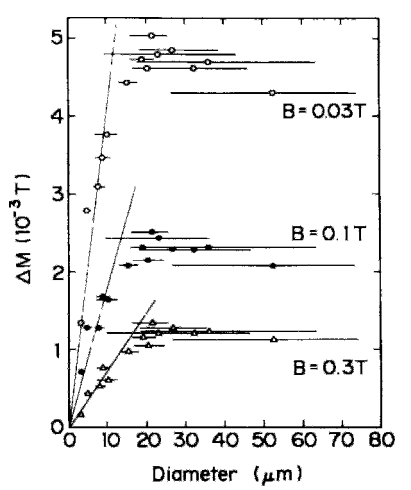

Figure 13.19 Dependence of the magnetization parameter ΔM on the particle diameter d for a series of $YBa_2Cu_3O_{7-\delta}$ samples at 77 K, using the same notation and J_c determination as in Fig. (13.18).

VII. PERFECT TYPE-I SUPERCONDUCTOR

We have been treating various cases in which the magnetization is not reversible, but rather exhibits hysteresis when the magnetic field undergoes a change. Textbooks often discuss a perfect magnetization loop of a superconductor in which the magnetization is linear and reversible during changes in the applied field. To the best of our knowledge there has been no report of an actual measurement of such a material. The problem is the prevalence of all kinds of irreversible contributions that induce a hysteresis and other deviations from the "ideal" shape. These effects can be due to bulk or surface pinning, a geometric barrier, edge geometry, and other deviations from the perfect situation. The recent understanding of possible topological hysteresis, at least in Type-I superconductors, made it unclear whether or not such loop could be measured at all. Figure 13.20 shows the result of an actual measurement performed by using a Quantum Design MPMS on a small sphere which was cast from high purity lead and solidified during free fall in air. Evidently, all characteristic parameters satisfy the description of a perfect Type-I superconducting sphere with the expected demagnetization factor of $N = 1/3$. We are not aware of similar

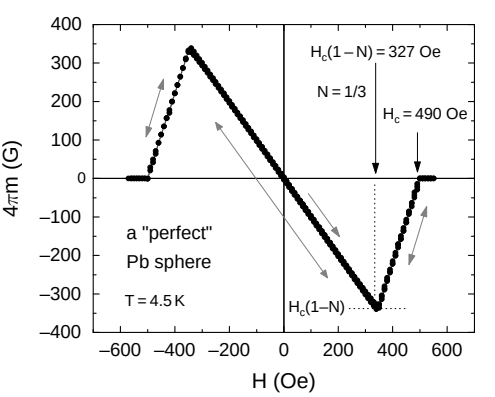

Figure 13.20 Magnetization loop of a "perfect" superconducting Pb sphere.

measurements in Type-II superconductors, although some materials such as $CeCoIn_5$ can be extremely clean, and exhibit almost no hysteresis.

VIII. CONCLUDING REMARKS

The Bean model qualitatively reproduces many of the experimentally observed properties of Type II superconductors, such as the hysteresis loops discussed in Chapter 5, Section IV. It is also widely used in contemporary research for the understanding and interpretation of experimental data. One example is work on time-dependent effects, such as flux creep and magnetic relaxation phenonema. Perhaps the most important application is the determination of critical currents by magnetization measurements, as was explained in Section VI.D.

PROBLEMS

1. Find solutions analogous to Eqs. (13.18) and (13.19) for the Kim model in the high-field case; in this case there is no current-field-free region in the center. Show that this occurs for the condition $B_0 > \mu_0 J_c a$.
2. Show that the expression

$$J_c = \frac{B_0}{\mu_0(a - a')}$$

is valid for both the low-field Kim model and the low-field Bean model. Write down the corresponding expressions for the pinning forces in the high-field Bean model.

3. Show that the condition

$$\frac{I}{L} = \int J_y(x)dx = J_c(a - a')$$

leads to the definition (13.14) of J_c.

4. Draw figures analogous to those shown in Figs. 13.3a, 13.3b, and 13.3c for the Kim model.
5. Draw figures analogous to all those shown in Figs. 13.5a and 13.5b for the Kim model.
6. Derive Eq. (13.22)

$$\Delta B = \mu_0 J_c(x_R - x_L),$$

where the notation is given in Fig. 13.7.

7. The applied field B_{app} is increased from 0 to the value B_0, where $0 < B^* < B_0$. Show that if it is then decreased down into the range

$$-B_0 < B_{app} < B_0 - 2B^*,$$

the average field will have the value

$$\langle B \rangle = B_{app} + \tfrac{1}{2}B^*.$$

What is the magnetization?

8. The applied field B_{app} is increased from 0 to the value B_0, where $0 < B_0 < B^*$. Show that if it is then decreased down into the range $0 < B_{app} < B_0$, the magnetization will be given by

$$\mu_0 M = B_{app} + \frac{(B_0 - B_{app})^2}{4B^*} - \frac{B_0^2}{2B^*}.$$

What is the average field $\langle B \rangle$?

9. Calculate the magnetizations associated with the magnetic field configurations of Figs. 13.13a, b, and c.
10. Show that when $B_0 = B^*$, the point d at which $\langle B \rangle = 0$ occurs at the position $B_{app} = (1 - \sqrt{2})B^*$ (cf. Fig. 13.12).
11. Show that when $B_0 = B^*$, points d and e occur at the same spot on the hysteresis loop.

12. For what values of the ratio B_0/B^* will point e be found between points a′ and d in Fig. 13.13b, and when will it be found between d and c?
13. Find the internal magnetic fields and pinning forces associated with the exponential model.
14. Justify the form of $\Gamma(\beta)$ in Eqs. (13.51a) and (13.51b).

This page intentionally left blank

14

Magnetic Penetration Depth

I. ISOTROPIC LONDON ELECTRODYNAMICS

The notion of a characteristic length for magnetic field penetration into a superconductor was established soon after the discovery of the magnetic field expulsion in tin and lead by W. Meissner and R. Ochsenfeld in 1933. (Meissner and Ochsenfeld, 1933, Meissner and Ochsenfeld, 1983) C. J. Gorter and H. Casimir (GC) introduced a two-fluid model of superconductivity in 1934. (Gorter and Casimir, 1934b, Gorter and Casimir, 1934c, Gorter and Casimir, 1934a) Analysis of the specific heat and critical field data, prompted GC to suggest an empirical form for the temperature dependence of the density of superconducting electrons, $n_s = n(1 - t^4)$, where $t = T/T_c$ and n is the total density of conduction electrons. In 1935 F. and H. London (London and London, 1935) introduced a phenomenological model of superconductivity in which the magnetic field inside a superconductor $\mathbf{B}$ obeys the equation,

$$\lambda_L^2 \Delta \mathbf{B} - \mathbf{B} = 0 \tag{14.1}$$

where λ_L, known as the London penetration depth, is a material-dependent characteristic length scale given by

$$\lambda_L^2 = \frac{mc^2}{4\pi n_s e^2} \tag{14.2}$$

Combining this definition with the GC form for the density of superconducting electrons results in a temperature dependent penetration depth,

$$\lambda(T) = \frac{\lambda(0)}{\sqrt{1-t^4}} \qquad (14.3)$$

It should be noted that although Eq. (14.3) had no microscopic justification, at low temperatures it takes the form $\lambda(T) \approx \lambda(0)(1 + t^4/2 + O(t^8))$. Numerically, the $\lambda(t) \sim t^4$ power law behavior is practically undistinguishable from the exponential behavior $\lambda(t) \sim \exp(-\Delta/T)$ obtained more than 20 years later from the microscopic theory of J. Bardeen, L. N. Cooper and J. R. Schrieffer (BCS). (Bardeen *et al.*, 1957) The GC formula has been extensively used where a simple analytical approximation for $\lambda(t)$ over a full temperature range was needed. However, as shown in Figure 14.1, the GC approximation underestimates the absolute value of the penetration depth by about a factor of two. Some successful attempts were made to generalize the GC approximation to better fit the results of the measurements. (Lewis, 1956). To obtain practical results in the spirit of Eq. (14.3), we solved the full BCS equations for both s- and 2D d-wave symmetries of the order parameter, and found the following approximations:

$$\begin{aligned} \lambda(T) &= \frac{\lambda(0)}{\sqrt{1-t^2}} \qquad -\text{s-wave} \\ \lambda(T) &= \frac{\lambda(0)}{\sqrt{1-t^{4/3}}} \qquad -d\text{-wave} \end{aligned} \qquad (14.4)$$

Figure 14.1 illustrates the behaviour of Eqs. (14.4). Symbols are calculated from Eqs. (14.28) and (14.30) below and solid lines are calculated from Eqs. (14.4). The GC behavior, Eq. (14.3), is also shown. We note that while Eqs. (14.4) are quite good approximations in the entire temperature range, they are not accurate at low temperatures. There, formulae (14.37) and (14.40) should be used instead. In fact, the entire low temperature ($T/T_c \leq 0.35T_c$) region where any rigorous test for the existence of gap nodes must be performed is essentially invisible on Fig. 14.1. It is interesting to note that the best approximation for the s-wave temperature behavior is compatible with the empirical form of the critical field, $H_c = H_c(0)(1-t^2)$ via $H_{c1} = H_c/\sqrt{2}\kappa$, $\lambda = \sqrt{\Phi_0 \ln(\kappa)/4\pi H_{c1}} \sim 1/\sqrt{1-t^2}$.

One of the central issues in early penetration depth measurements was whether all electrons participate in the superconductivity as $T \to 0$. Experiments on pure metals gave values larger than predicted, implying that some electrons remaine normal. Pippard (1953) was the first to suggest a non-local version of London electrodynamics similar to earlier generalizations of Ohm's law. If the microscopic BCS coherence length, $\xi_0 = \hbar v_F/\pi\Delta_0$, is larger than the London penetration depth defined by Eq. (14.2) (denoted by λ_L), the response of a superconductor to a magnetic field is weakened due to the reduction of the vector potential over its length, λ_L, and the effective magnetic penetration depth increases (Tinkham, 1996)

$$\lambda_{eff} \approx a\lambda_L \left(\frac{\xi_0}{\lambda_L}\right)^{1/3} \qquad (14.5)$$

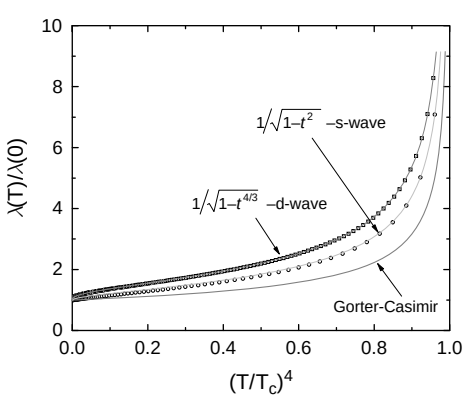

Figure 14.1 Approximate functional forms for the penetration depth in the entire temperature range for the d-wave and s-wave clean limits.

where $a = 0.65$ in an extreme (Type-I) case of $\lambda_L(0) \ll \xi_0$. In the presence of impurities, the effective coherence length is introduced

$$\xi^{-1} = \xi_0^{-1} + \ell^{-1} \tag{14.6}$$

where and ℓ is the mean free path. In this case, the effective penetration depth is (Tinkham, 1996)

$$\lambda_{eff} = \lambda_L \sqrt{1 + \frac{\xi_0}{\ell}} \tag{14.7}$$

Since all non-elemental superconductors are Type-II, the Pippard model is not applicable to our discussion, and from this point on we will assume London electrodynamics ($\lambda/\xi \gg 1$) to hold. For a copper oxide superconductor like YBaCuO one has $\lambda/\xi \approx 100$ even at low temperatures so the London limit is easily satisfied. We note, however, that a different type of nonlocality can arise in unconventional superconductors due to the divergence of the coherence length along nodal directions. (Kosztin and Leggett, 1997)

II. PENETRATION DEPTH IN ANISOTROPIC SAMPLES

The fact that many unconventional superconductors are strongly anisotropic presents some difficulty in determining the basic electromagnetic parameters. We consider the simplest case, in which there are there are now two different penetration depths, λ_{ab} and λ_c. The geometry is shown in Fig. 14.2a. A sample of constant cross section in the x-y plane extends infinitely far in the z-direction. The sample has thickness $2d$, width $2b$ and length $w \to \infty$. A magnetic field is also applied in the z-direction so demagnetizing corrections are absent. To facilitate comparison with the copper oxides we take the y direction along the c-axis and let the x and z directions correspond to the a and b axes. Choosing the coordinate axes to lie along principal axes of the superfluid density tensor we have

$$\lambda_{ii}^2 \Delta j_i = j_i \tag{14.8}$$

For the case considered here, supercurrents flow in the x and y directions. In-plane supercurrents flowing in the x direction penetrate from the top and bottom faces a distance λ_{ab}, as shown. c-axis supercurrents flowing in the y direction penetrate from the left and right edges a distance λ_c.Using (8) and Maxwell's equations it is straightforward to derive the generalized London equation for the magnetic field, (Ginzburg, 1952, Kogan, 1981, Mansky *et al*., 1994)

$$\lambda_c^2 \frac{\partial^2 B_z}{\partial x^2} + \lambda_{ab}^2 \frac{\partial^2 B_z}{\partial y^2} = B_z \tag{14.9}$$

This equation for the field mixes components of the penetration depth, and has a less direct

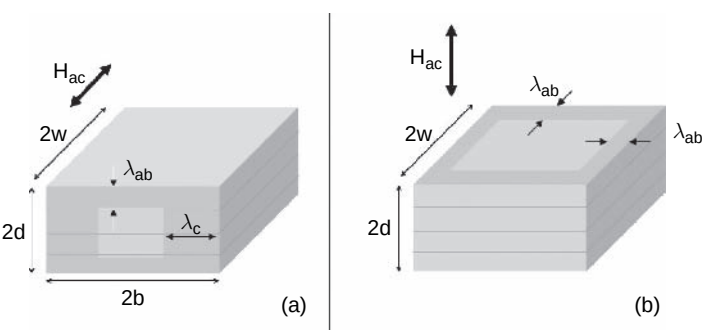

Figure 14.2 Experimental configurations: (a) geometry relevant to Eq. (14.9) when $w \to \infty$, and (b) finite w with the field normal to the conducting planes. The in-plane penetration depth is assumed to be isotropic.

interpretation than Eq. (14.8) for the currents. The full boundary value problem for this case was solved by Mansky et. al. (1994) They obtain a susceptibility,

$$-4\pi\chi = 1 - \frac{\lambda_{ab}}{d}\tanh\left(\frac{d}{\lambda_{ab}}\right) - 2\lambda_c b^2 \sum_{n=0}^{\infty} \frac{\tanh(\tilde{b}_n/\lambda_c)}{k_n^2 \tilde{b}_n^3} \quad (14.10)$$

where $k_n = \pi(1/2 + n)$ and $\tilde{b}_n = b\sqrt{(1+(k_n\lambda_{ab}/d)^2)}$. (Note that Eq. (14.10) has been re-written in a different form compared to (Mansky et al., 1994)). In practice, summation to $n = 50$ suffices. It is easy to show that Eq. (14.10) gives the correct result for limiting cases. For example, if $\lambda_{ab} \ll d$ and $\lambda_c \ll b$ we obtain $\tilde{b}_n \approx b$ and with $\sum_{n=0}^{\infty} k_n^{-2} = 1/2$, $-4\pi\chi = 1 - \lambda_{ab}/d\tanh(d/\lambda_{ab}) - \lambda_c/b\tanh(b/\lambda_c)$ as expected. More often, the in-plane anisotropy is relatively weak (supercurrents along x and y both penetrate by λ_{ab}) whereas λ_c is considerably larger. In organic superconductors, for example, $\lambda_c \approx 100\lambda_{ab}$. In that case, for typical crystal dimensions one has $\lambda_c/d \gg \lambda_{ab}/b$ and the susceptibility in Eq. (14.9) is dominated by λ_c. While the interplane penetration depth is important in its own right, it is often considerably more complicated to interpret than the in-plane depth since it involves poorly understood properties of the interplane transport mechanism. (Radtke *et al.*, 1996, Hirschfeld *et al.*, 1997, Sheehy *et al.*, 2004)

To measure λ_{ab} in highly anisotropic materials one must find either extremely thin samples ($\lambda_c/d \ll \lambda_{ab}/b$) or restrict supercurrents to the conducting planes. The latter approach requires the geometry shown in Fig. 14.2 (b), with the magnetic field normal to the planes. In this case, large demagnetization effects occur, and no closed form solutions of the London equation exist. Strictly speaking, a demagnetizing factor can only be defined for ellipsoidal samples, but for real samples an effective demagnetizing factor can be defined. A more difficult problem is to determine the effective sample dimension by which to normalize the penetration depth in this demagnetizing geometry. A semi-analytical solution for this problem was found for disks and slabs by Prozorov *et al.* (2000a). The susceptibility is given by,

$$-4\pi\chi = \frac{1}{1-N}\left[1 - \frac{\lambda}{\tilde{R}}\tanh\left(\frac{\tilde{R}}{\lambda}\right)\right] \quad (14.11)$$

where $\tilde{R}$ is the effective dimension, and N is the demagnetization factor. For a disk of thickness $2d$ and radius w and a magnetic field applied perpendicular to the plane of the disk (i.e. along d),

$$\tilde{R} \approx \frac{w}{2\left\{1+\left[1+\left(\frac{2d}{w}\right)^2\right]\arctan\left(\frac{w}{2d}\right) - \frac{2d}{w}\right\}} \quad (14.12)$$

In the thin limit, $d \ll w$, $\tilde{R} \approx 0.2w$. The demagnetization correction is given by the expression,

$$\frac{1}{1-N} \approx 1 + \frac{w}{2d} \quad (14.13)$$

The $\tanh(\tilde{R}/\lambda)$ term is an approximation, which only becomes exact for d, $w \to \infty$ whence $\tilde{R} = w/2$. For an infinitely long cylinder the London equation gives $I_1(\tilde{R}/\lambda)/I_0(\tilde{R}/\lambda)$ – the ratio of the modified Bessel functions of the first kind. However, these distinctions are important only close to T_c (more specifically where $\lambda \geq 0.4w$) and even then the results are quite similar. At low temperatures where $\tilde{R}/\lambda \gg 1$ the hyperbolic factor is essentially unity and therefore irrelevant. For rectangular slabs Eqs. (14.12) and (14.13) can be applied with the effective lateral dimension

$$\tilde{W} = \frac{db}{b+2d/3} \quad (14.14)$$

Equation (14.14) was obtained by fitting the numerical solutions of Eq. (14.10) in its isotropic form ($\lambda_c = \lambda_{ab}$) to the Eq. (14.11). A straightforward generalization of Eq. (14.12) would lead to a similar expression, but without factor 2/3 in the denominator. Equation (14.14) is more accurate, because it is obtained for a rectangular slab, not for the disk described by Eq. (14.12).

When large enough single crystals are unavailable penetration depth measurements are often done on granular samples. Very reasonable results can often be obtained by approximating the grains as spherical and using,

$$-4\pi\chi_{Sphere} = \frac{3}{2}\left(1 - \frac{3\lambda}{r}\coth\left(\frac{r}{\lambda}\right) + \frac{3\lambda^2}{r^2}\right) \tag{14.15}$$

where r is the grain radius. This equation is especially useful for small grains, $r \ll \lambda$. For a more accurate measure Eq. (14.15) may be averaged over the grain size distribution, $f(r)$, (Waldram *et al.*, 1994, Porch *et al.*, 1993)

$$-4\pi\langle\chi\rangle = \frac{\int_0^\infty r^3 f(r)\chi(r)dr}{\int_0^\infty r^3 f(r)dr} \tag{14.16}$$

If λ is anisotropic, as is often the case, the grains can be cast in epoxy and aligned with a large magnetic field prior to measurement. (Manzano *et al.*, 2002)

III. EXPERIMENTAL METHODS

Many experimental techniques have been developed to measure the penetration depth. Among other existing techniques we shall mention reversible magnetization, (Hao and Clem, 1991) first critical field, AC susceptibility, microwave cavity perturbation, tunnel-diode oscillator, mutual inductance, kinetic inductance, muon spin relaxation, grain boundary Josephson transport, infrared spectroscopy, electron paramagnetic resonance, and neutron diffraction, as well as various indirect estimations from electromagnetic and thermodynamic quantities. Descriptions of these techniques and their variations (e.g. there are quite a few versions of reversible magnetization measurements) would require a separate review.

Some of the most versatile and sensitive techniques utilize frequency-domain measurements. At microwave frequencies this is called a cavity-perturbation technique. At radio frequencies, it has been developed as a self-resonating LC circuit driven by a tunnel diode (Carrington *et al.*, 1999b, 2001, Prozorov *et al.*, 2000a, 2000b). In the microwave approach (Hardy *et al.*, 1998, Jacobs, 1995 #218, Mao, 1995 #260) a very high quality factor cavity is typically driven externally while its in-phase and quadrature response are measured. In the tunnel diode method, the "cavity" is simply an inductor, typically copper, with a Q of order 100. The coil forms part of an LC tank circuit that is driven to self-resonate with a negative resistance tunnel diode. Tunnel diode oscillators were used early in low temperature physics, but the potential of this approach for very high resolution measurements was first demonstrated by van de Grift. (DeGrift, 1975) By placing a superconducting sample inside the coil, changes in the penetration depth, or more accurately its rf magnetic susceptibility, result in changes of inductance and therefore oscillator frequency. With care, frequency resolution of 10^{-9} in a few seconds counting time can be achieved. For the sub-mm sized crystals characteristic of modern superconductivity research, this resolution translates into changes in λ of order 0.5 Å or smaller. In order to isolate variations of the sample temperature from the oscillator, the sample is attached to a sapphire cold finger (Sridhar *et al.*, 1989) whose temperature can be varied independently from 350 mK to 100 Kelvin. The cold finger stage

can be moved, *in situ*, to determine field and temperature dependent backgrounds, and to calibrate the oscillator response. (Carrington *et al*., 1999b) We mention that Signore *et al*. (1995) used a tunnel diode oscillator to observe unconventional superconductivity in the heavy fermion superconductor UPt_3 More recent variations that provide sample/oscillator thermal isolation have been developed to measure $\lambda(T)$ down to 50 mK. (Chia *et al*., 2003, Bonalde *et al*., 2000a, 2005, Fletcher *et al*., 2006)

A major advantage of the tunnel diode method is that the resonator need not be superconducting so that an external magnetic field can be applied to the sample. This feature was exploited early on by Jacobs *et al*. (1995) to search for possible changes in the penetration depth of YBCO with magnetic field, and to study vortex motion. Tunnel diode oscillators with suitably designed coils are now used in very large and even pulsed magnetic fields. (Coffey *et al*., 2000) The relatively low quality factor of the LC combination means that AC excitation fields can be very small (~ 20 mOe) and thus do not perturb the sample in any significant way. Unless one is very close to T_c, the imaginary part of the sample conductance, and thus the penetration depth, dominates the response. The oscillator approach provides tremendous resolution, but one does not have direct access to the dissipative component of the response, as is possible in a driven cavity or mutual inductance technique.

IV. ABSOLUTE VALUE OF THE PENETRATION DEPTH

One of the important parameters of a superconductor is the absolute value of the magnetic penetration depth extrapolated to zero temperature, $\lambda(0)$, given in simple theory in a clean limit by Eq. (14.2), but it turns out that an effective electron mass (determined by the band structure) given by Eq. (14.25) should be used. It is interesting to note that the clean limit expression for $\lambda(0)$ does not contain any superconducting parameters, and therefore so called Uemura scaling (total superfluid density, $\sim \lambda(0)^{-2}$, vs transition temperature, T_c) is not expected. On the other hand, in a dirty limit the superfluid density is proportional to the superconducting gap via the inverse penetration depth, Eq. (14.7),

$$\frac{1}{\lambda_{eff}^2} \approx \frac{1}{\lambda_L^2}\frac{\ell}{\xi_0} \propto \Delta(0) \propto T_c \qquad (14.17)$$

so it appears that the Uemura scaling is valid only in the dirty limit. It is not surprising that more and more deviations are recently reported indicating that samples have become cleaner.

In principle one could determine $\lambda(0)$ by calculating the expected sample susceptibility as a function of λ, using Eq. (14.11) for example, and then measuring the resulting change in frequency as the sample is removed from the resonator. However, Eq. (14.11) is only approximate and for most situations, $\lambda/\tilde{R} \ll 1$. Moreover the pre-factor cannot be calculated precisely. Therefore, it is not possible to differentiate between a perfectly diamagnetic sample ($\lambda/\tilde{R} = 0$) of arbitrary shape, and one with a finite penetration depth if $\lambda/\tilde{R} \ll 1$. For highly anisotropic materials the interplane penetration depth can be of order of $100\,\mu m$, in which case an approximate value *can* be directly determined by this method. (Carrington *et al*., 1999a) For powder samples in which the grain size distribution is known, Eq. (14.15) can be used to extract the full λ as discussed earlier. (Panagopoulos *et al*., 1997) For thin films, since the geometry is well controlled, it is also possible to determine the full $\lambda(T)$. This is typically done using a mutual inductance technique with drive and pickup coils on opposite sides of the film, well away from any edges. (Fiory *et al*., 1988, Lee *et al*., 1994)

It is possible to obtain $\lambda(0)$ from measurements of the surface impedance $Z_s = R_s + iX_s$. Changes in the frequency and

quality factor of a microwave cavity are directly related to X_s and R_s respectively. In the normal state the sample has skin depth δ, DC conductivity σ_{DC}, and $X_s = R_s = 1/\delta\sigma_{DC}$. In the superconducting state one has $X_s = \omega\mu_0\lambda$. Therefore $X_s(T=0)/R_s(T = T_c^+) = 2\lambda(0)/\delta$. By now measuring the change in X_s, upon cooling from above T_c to $T = 0$, it is possible to obtain $\lambda(0)$, subject to assumptions about the distribution of microwave currents (Mao *et al.*, 1995)

Muon spin rotation (μSR) has been widely used to determine $\lambda(0)$. (Sonier *et al.*, 2000) This met hod actually measures the second moment of the magnetic field distribution around a vortex, which is related to $\lambda(0)$. To extract the penetration depth requires a model for the vortex lattice as well as knowledge of the muon's location. The moment of the field distribution depends in a nontrivial way upon the applied field, so an extrapolation to $H = 0$ is required to yield reliable estimates of $\lambda(0)$.

In the limit that vortex pinning is negligible, the magnetization of a superconductor in the mixed state is a well defined function of the penetration depth. With suitable corrections for vortex core effects, Hao and Clem (1991) showed that the thermodynamic magnetization is given by

$$M = -\frac{\phi_0}{32\pi^2\lambda^2}\ln\left(\frac{\eta H_{c2}}{H}\right) \qquad (14.18)$$

Experimentally, if one can find a region of field over which M is reversible, then (14–15) can be assumed to hold and the penetration depth may be extracted. The difficulty is that only very clean systems exhibit a sufficiently large interval of reversible behavior, and even if they do so, it is often non-logarithmic in H. Understanding such deviations involves an analysis of the field dependence of the effective coherence length and possible nonlocal effects. The general analysis of the reversible magnetization applicable to various large-κ superconductors is currently in progress (Kogan *et al.*, 2006).

Infrared reflectivity measurements can also be used to determine $\lambda(T = 0)$. This method is useful when anisotropy is an issue, since techniques such as μSR or reversible magnetization average over both directions in the conducting plane. This issue is important in YBaCuO where the response can be significantly different for currents along the a and b axes. From the reflectance one obtains the conductivity and the frequency dependent penetration depth, $\lambda(\omega) = 4\pi\omega\sigma(\omega)/c^2$. Since the data begin well above $\omega = 0$ one must either extrapolate backward. or use a sum rule argument to obtain $\lambda(T = 0)$ at $\omega = 0$ (Basov *et al.*, 1995)

Yet another technique that can be used in conjunction with any sensitive enough susceptometer is when the sample under study is coated with a lower-T_c material (typically Al) of known thickness and penetration depth. This has been used with a home-made SQUID magnetometer (Gross-Alltag *et al.*, 1991) and tunnel-diode resonator. (Prozorov *et al.*, 2000b) If the film thickness is smaller than its normal state skin depth, then above T_c(Al) the resonator sees only the sample under study. As one cools below the T_c(Al) the Al film screens the external field from the sample. This is illustrated in Figure 14.3.

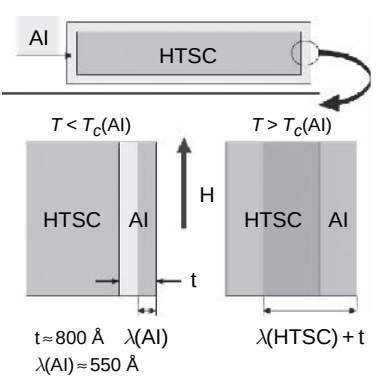

Figure 14.3 Schematics of the experiment used to measure the absolute value of the penetration depth by coating a high-T_c superconductor with low-T_c (Al in this case) material.

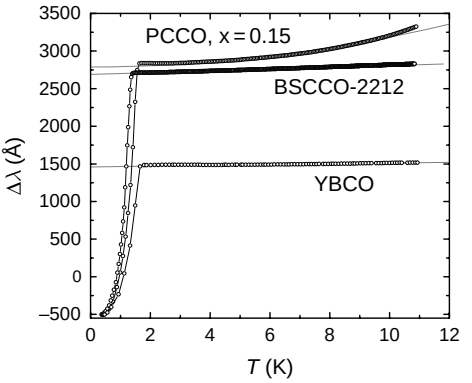

Figure 14.4 Measurements of the absolute value of the penetration depth in $Pr_{1.85}Ce_{0.15}CuO_{4-y}$ (PCCO), $Bi_2Sr_2CaCu_2O_{8+y}$ (BSCCO-2212) and $YBa_2Cu_3O_{7-y}$ (YBCO). The negative initial values correspond to the thickness of the sputtered aluminium layer. For details see Prozorov *et al*. (2000b).

The change in resonator frequency from $T < T_c(\mathrm{Al})$ to just above $T_c(\mathrm{Al})$ then involves total penetration depth of the coated sample, and allows one to extract it via,

$$\lambda(\mathrm{HTSC}) = \lambda(\mathrm{Al}) + \frac{\Delta\lambda - t}{1 - \exp(-t/\lambda(\mathrm{Al}))} \tag{14.19}$$

where $\Delta\lambda$ is the frequency shift measured by warming up above the transition temperature of the Al layer. Figure 14.4 shows the technique applied to three different superconductors for which the absolute values were also established by other techniques (Prozorov *et al*., 2000b). The results are in a good agreement with the literature values for BSCCO and YBaCuO, and provide a new estimate for the electron-doped superconductor PCCO. A drawback to this technique is the need to know the penetration depth of the metallic film coating the sample. Although $\lambda(Al)$ is well known for bulk samples, it is certainly possible that it may differ substantially in thin films.

Values obtained by various methods can differ widely. In the heavy fermion superconductor $CeCoIn_5$, for example, $\lambda(0)$ values derived from μSR were found to differ substantially from those obtained in surface impedance measurements (Özcan *et al*., 2003). While each method has its virtue, none is completely satisfactory. A simple, accurate, model-independent technique for measuring $\lambda(0)$ remains an outstanding experimental challenge.

V. PENETRATION DEPTH AND THE SUPERCONDUCTING GAP

A. Semiclassical Model For Superfluid Density

We will briefly describe the main results of a semiclassical model for the penetration depth given by B. S. Chandrasekhar and D. Einzel (1993) (See also Annett *et al*., 1991). Given a Fermi surface and a gap function, this approach provides a general method for calculating all three spatial components of the penetration depth. It is limited to purely coherent electronic transport, and does not include the effects of scattering.

In the London approximation, the supercurrent **j(r)** is related locally to the vector potential **A(r)** through a tensor equation,

$$\mathbf{j} = -\mathbb{R}\mathbf{A} \tag{14.20}$$

The symmetric response tensor is given by,

$$\mathbb{R}_{ij} = \frac{e^2}{4\pi^3\hbar c}\oint_{FS} dS_\kappa \left[\frac{v_F^i v_F^j}{|\mathrm{v}_F|} \times \left(1 + 2\int_{\Delta(\kappa)}^{\infty} \frac{\partial f(E)}{\partial E}\frac{N(E)}{N(0)}dE\right)\right] \tag{14.21}$$

Here f is the Fermi function and $E = \sqrt{\varepsilon^2 + \Delta^2}$ is the quasiparticle energy. (The normal metal band energy ε is measured from the Fermi level.) $N(E)/N(0) = E/\sqrt{E^2 - \Delta(\mathbf{k})^2}$ is the density of states normalized to its value at the Fermi level in

the normal state and v_F^i are the components of Fermi velocity, $\mathbf{v}_F$. The average is taken over the Fermi surface, with the **k**-dependent superconducting gap $\Delta(\mathbf{k}, T)$ and Fermi velocity. We note that often Fermi surface averaging is used only on the second integral term in Eq. (14.21). This may lead to significant deviations in calculating the superfluid density if Fermi surface is not spherical. In London local electrodynamics one has,

$$\mathbf{j}(\mathbf{r}) = \frac{c}{4\pi}\frac{\mathbf{A}(\mathbf{r})}{\lambda_{ii}^2} \tag{14.22}$$

Using a coordinate system defined by the principal axes of $\mathbb{R}$, penetration depths correspond to the diagnonal components,

$$\lambda_{ii}^2 = \frac{c}{4\pi\mathbb{R}_{ii}} \tag{14.23}$$

The superfluid density is given by,

$$n_{ii}(T) = \frac{cm_{ii}}{e^2}\mathbb{R}_{ii}(T) \tag{14.24}$$

with the effective mass defined as

$$m_{ii} = \frac{e^2 n}{c\mathbb{R}_{ii}(0)} \tag{14.25}$$

which also depends upon the details of the Fermi surface as well of the density of states. For example, assuming a spherical Fermi surface, one obtains the total electron density, $n_{ii}(T \to 0) = n = k_F^3/3\pi^2$. The *normalized* superfluid density is given by

$$\rho_{ii}(T) = \frac{n_{ii}(T)}{n} = \frac{\mathbb{R}_{ii}(0)}{\mathbb{R}_{ii}(T)} = \left(\frac{\lambda_{ii}(0)}{\lambda_{ii}(T)}\right)^2 \tag{14.26}$$

Equation (14.21) provides the connection between the experimentally measured penetration depth and the microscopic superconducting state. Without any further calculation these formulae demonstrate the important point that in the clean limit $\lambda(T = 0)$ is simply a band structure property, unrelated to the gap function. For superconductors with sufficiently strong scattering this statement must be modified. The importance of the gap function becomes evident at non-zero temperatures where it is possible to generate quasiparticle excitations and a paramagnetic current. Several important approximations of Eqs. (14.21) and (14.26) should be considered.

a. Isotropic Fermi surface

In the case of a (2D) cylindrical Fermi surface relevant to the copper oxide superconductors,

$$\rho_{\substack{aa\\bb}} = 1 - \frac{1}{2\pi T}\int_0^{2\pi}\begin{pmatrix}\cos^2(\varphi)\\ \sin^2(\varphi)\end{pmatrix} \times \int_0^{\infty}\cosh^{-2}\left(\frac{\sqrt{\varepsilon^2 + \Delta^2(T,\varphi)}}{2T}\right)d\varepsilon d\varphi \tag{14.27}$$

where $\Delta(\varphi)$ is angle dependent gap function. For a 3D spherical Fermi surface and an anisotropic gap $\Delta(\theta,\ \varphi)$, Eqs. (14.21) and (14.26) become,

$$\rho_{\substack{aa\\bb}} = 1 - \frac{3}{4\pi T}\int_0^1 (1 - z^2)\int_0^{2\pi}\begin{pmatrix}\cos^2(\varphi)\\ \sin^2(\varphi)\end{pmatrix} \times \int_0^{\infty}\cosh^{-2}\left(\frac{\sqrt{\varepsilon^2 + \Delta^2(T,\theta,\varphi)}}{2T}\right)d\varepsilon d\varphi dz \tag{14.28}$$

and

$$\rho_c = 1 - \frac{3}{2\pi T}\int_0^1 z^2\int_0^{2\pi}\cos^2(\varphi) \times \int_0^{\infty}\cosh^{-2}\left(\frac{\sqrt{\varepsilon^2 + \Delta^2(T,\theta,\varphi)}}{2T}\right)d\varepsilon d\varphi dz \tag{14.29}$$

where $z = \cos(\theta)$. For isotropic s-wave pairing both the 2D and 3D expressions give

$$\rho = 1 - \frac{1}{2T}\int_0^\infty \cosh^{-2}\left(\frac{\sqrt{\varepsilon^2+\Delta^2(T)}}{2T}\right)d\varepsilon \tag{14.30}$$

b. Anisotropic Fermi surface, isotropic gap function

This case is useful for treating highly anisotropic Fermi surfaces, and in extreme cases multiband superconductors. Consider two distinct gaps on two different bands indexed by $k = 1, 2$. If Δ^k does not depend on the wavevector, it can be removed from the integral in Eq. (14.21). Using

$$x_{ii} = \frac{X_{ii}^1}{X_{ii}^1 + X_{ii}^2}, \quad X_{ii}^k = \int \frac{\left(v_F^{ik}\right)^2}{v_F^k} dS^k \tag{14.31}$$

we obtain,

$$\rho_{ii}(T) = x_{ii}\rho_1(T) + (1 - x_{ii})\rho_2(T) \tag{14.32}$$

which is related to the so-called α-model (Bouquet *et al*., 2001) with individual superfluid densities calculated for each individual band from Eq. (14.30). This expression was successfully used to model the penetration depth in MgB_2 where two distinct gaps exist.

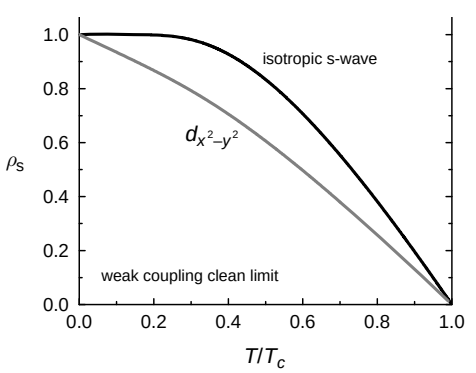

Figure 14.5 Superfluid densities calculated for an isotropic s-wave superconductor, and for a d-wave superconductor.

(Fletcher *et al*., 2005). For the arbitrary case of a highly anisotropic Fermi surface and an anisotropic or nodal gap, the complete version of Eq. (14.21) must be solved.

B. Superconducting Gap

To obtain physically meaningful results from Eqs. (14.21) and (14.26) the temperature dependence of a superconducting gap must be calculated. The self-consistent gap equation depends on the gap symmetry and the details of the Fermi surface. One has,

$$\int_0^{\hbar\Theta_D}\left\langle\left(\frac{\tanh\left(\frac{\sqrt{\varepsilon^2+\Delta^2(T)g^2(\mathbf{k})}}{2T}\right)}{\sqrt{\varepsilon^2+\Delta^2(T)g^2(\mathbf{k})}} - \frac{\tanh\left(\frac{\varepsilon}{2T_c}\right)}{\varepsilon}\right)g^2(\mathbf{k})\right\rangle_{FS} d\varepsilon = 0 \tag{14.33}$$

where $g(\mathbf{k})$ represents a unit-magnitude angular dependence of the superconducting gap. Table 14.1 summarizes $g(\mathbf{k})$ for sev-

Table 14.1 Some representative gap functions for singlet pairing states

G	Notation
1	isotropic s-wave (Nb)
$\frac{1}{\sqrt{1-\varepsilon\cos^2(\theta)}}$	spheroidal anisotropic s-wave
$\frac{\varepsilon}{1+\varepsilon-\cos(4\varphi)}$	Abrikosov's anisotropic s-wave
$\frac{1-\sin^4(\theta)\cos(4\varphi)}{2}$	s + g pairing
$\frac{1+\varepsilon\lvert\cos(6\varphi)\rvert}{1-\varepsilon}$	Anisotropic 6-fold s-wave
$\cos(2\varphi)$	$d_{x^2-y^2}$ (high-T_c cuprates)
$\sin(2\varphi)$	d_{xy}
$\frac{\cos(2\varphi)}{\sqrt{1-\varepsilon\cos^2(\theta)}}$	anisotropic d-wave

eral different gap functions relevant to both the cuprates and some newly discovered superconductors. We include gap functions relevant only to singlet pairing states, for simplicity. There is evidence from penetration depth measurements for triplet, p-wave pairing, most notably in heavy fermion superconductors (Gross *et al*., 1986, Gross-Alltag *et al*., 1991) and in $SrRuO_4$ (Bonalde *et al*., 2000b). For a comprehensive discussion of the representation of the symmetry of the order parameter in singlet and triplet states see, e.g., the review of Joynt and Taillefer (Joynt, 2002).

Strong coupling introduces additional complications for which the full Eliashberg equations must be solved. A discussion can be found in Carbotte et al. (1990). For simple estimates an approximate form can be used. One of the most useful expressions is given by Gross *et al*. (1986)

$$\Delta(T) = \Delta(0)\tanh\left(\frac{\pi}{\Delta(0)}\sqrt{a\left(\frac{T_c}{T}-1\right)}\right) \tag{14.34}$$

where $\Delta(0)$ is the gap magnitude at zero temperature and a is a parameter, both to be determined for each pairing symmetry from Eq. (14.33), as demonstrated in Fig. 14.6.

As shown in Fig. 14.6, Eq.(14.34) provides a very good approximation to an exact solution of the gap equation, Eq. (14.33). In this example, solutions were obtained for s-wave, s + g wave, and d-wave pairing (symbols). The solid lines are the results of numerical fitting to Eq. (14.34). For isotropic s-wave superconductors, $\Delta(0) = 1.76T_c$, $a = 1$, for the pure d-wave case, $\Delta(0) = 2.14T_c$, $a = 4/3$, and for an s + g wave $\Delta(0) = 2.77T_c$, $a = 2$. The temperature dependence and magnitude of the gap depend sensitively on its angular variation, even in an s-wave case.

C. Mixed Gaps

It has been suggested that superconductivity can be complex with various admixtures. Theoretically, such a possibility was suggested as due to orthorhombic distortion in high-T_c cuprates. Gaps of the type $d_{x^2-y^2} + is$ and $d_{x^2-y^2} + id_{xy}$ where proposed. It does not seem that current experiments support this conjecture. For illustration we show in Figure 14.7 the evolution of the superfluid density from a pure d-wave gap to a pure s-wave gap.

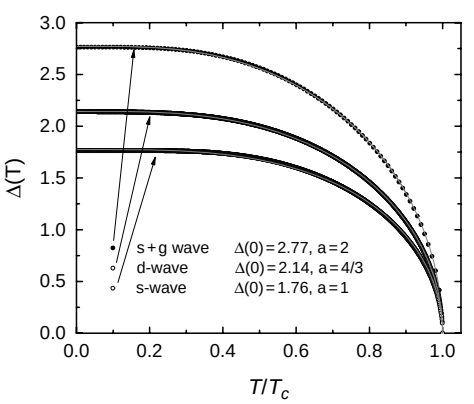

Figure 14.6 Temperature dependence of the superconducting gap for s, d and s + g symmetries obtained from Eq. (14.33) (symbols) and fitting to Eq. (14.34) (solid lines), with the fit parameters indicated.

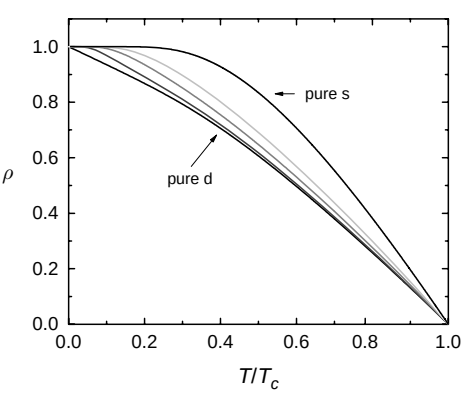

Figure 14.7 Superfluid density for a mixed gap, $d_{x^2-y^2} + is$ for a component content of 0, 10, 20, 30, 40 and 100% (from bottom up). Similar curves are obtained for the $d_{x^2-y^2} + id_{xy}$ case.

D. Low-Temperatures

As Fig. 14.6 illustrates, even for the case of unconventional pairing, the gap function is very nearly constant below some temperature range, typically $T/T_c \approx 0.3$. It is only in this limit where the temperature dependence of the penetration depth allows one to draw general conclusions about the pairing state. At higher temperatures, the temperature dependence of the gap itself cannot be ignored. Since this is model-dependent, the temperature dependence of the penetration depth at higher temperatures is not a reliable guide to the pairing state. In the low temperature limit, things are simpler. Defining $\Delta\lambda = \lambda(T) - \lambda(0)$, Eq. (14.26) can be written as

$$\rho = \left(1 + \frac{\Delta\lambda(T)}{\lambda(0)}\right)^{-2} \approx 1 - 2\frac{\Delta\lambda(T)}{\lambda(0)} \tag{14.35}$$

a. s-wave pairing

For g = 1 we obtain the standard BCS result in the low temperature limit (Abrikosov, 1988)

$$\rho \approx 1 - \sqrt{\frac{2\pi\Delta_0}{T}}\exp\left(-\frac{\Delta(0)}{T}\right) \tag{14.36}$$

The corresponding penetration depth, $\Delta\lambda/\lambda(0) \approx (1-\rho)/2$ is given by,

$$\frac{\Delta\lambda(T)}{\lambda(0)} \approx \sqrt{\frac{\pi\Delta_0}{2T}}\exp\left(-\frac{\Delta(0)}{T}\right) \tag{14.37}$$

The exponentially small value of $\Delta\lambda/\lambda(0)$ justifies the linear approximation of Eq. (14.35), and shows that ρ and λ have the same temperature dependence in this region. However, for a gap function with nodes, λ changes much more rapidly with temperature. Higher order terms in Eq. (14.35) can quickly lead to different T dependences for ρ and λ, even if the gap does not change with temperature. One must then determine the more fundamental quantity, ρ, which requires an additional determination of $\lambda(0)$.

b. d-wave pairing

For a gap function with nodes, ρ depends upon both the gap topology (e.g. point nodes or line nodes) and the detailed functional behavior near the nodes. (Gross *et al.*, 1986) In principle, there are many gap functions consistent with the d-wave pairing symmetry believed to describe the high-T_c cuprates. The widely used form $\Delta = \Delta(0)\cos(2\varphi)$ leads to,

$$\rho = 1 - \frac{2\ln 2}{\Delta(0)}T \tag{14.38}$$

Another possible choice is a two parameter gap function which varies linearly with angle near the nodes and is constant for larger angles:

$$|\Delta(\varphi)| = \begin{cases} \alpha\Delta(0)\varphi, & 0 \le \varphi \le \alpha^{-1} \\ \Delta(0), & \alpha^{-1} \le \varphi \le \pi/4 \end{cases} \tag{14.39}$$

where $\alpha = \Delta^{-1}(0)d|\Delta(\varphi)|/d\varphi|_{\varphi\to\varphi_{node}}$ (Xu *et al.*, 1995). This form leads to,

$$\frac{\Delta\lambda(T)}{\lambda(0)} \approx \frac{2\ln 2}{d\Delta/d\varphi|_{\varphi\to\varphi_{node}}}T = \frac{2\ln 2}{\alpha\Delta(0)}T \tag{14.40}$$

Equation (14.40). reduces to the commonly used Eq. (14.38) if $\Delta = \Delta(0)\cos(2\varphi)$ is used. In either case, the linear T dependence results from the linear variation (near the nodes) of the density of states, $N(E) \sim E$. The importance of low temperature measurements is this direct access to the topological properties of the gap function, independent of other details.

c. p-wave pairing

p-wave and f-wave states are triplet pairing states with a symmetric spin part of the Cooper pair wave function. Therefore any

claim of a such pairing state should include experimental evidence of triplet pairing. The NMR Knight shift has been successfully used for this purpose. When the pairing is singlet, the Knight shift decreases upon entering the superconducting state because the magnetic interaction between the nuclear spi and the conduction electrons is weaker. In the triplet state, however, pairing does not reduce the pair spin, and the Knight shift remains unchanged. One of the recent additions to the triplet state pairing family is the Sr_2RuO_4 superconductor. The well known heavy fermion superconductors, UPt_3 and UBe_{13} are additional examples of the triplet pairing state.

The analysis of the magnetic penetration depth for p-wave pairing is much more difficult, because in this case the gap function is given by

$$\Delta(\mathbf{k}, T) = \Delta(T) f(\mathbf{k} \cdot \mathbf{l}) \qquad (14.41)$$

where $\mathbf{l}$ is the gap axis. The electromagnetic response depends on the mutual orientation of the vector potential and the gap axis, and additionally on the orientation of the crystallographic axes with respect to the crystal faces. A detailed experimental and theoretical study of this situation is presented by Gross *et al*., 1986, and Gross-Alltag *et al*., 1991. The following low-temperature asymptotics were obtained for various cases:

$$\rho_{||,\perp} = 1 - a_{||,\perp} \left(\frac{T}{\Delta(0)} \right)^{n_{||,\perp}} \qquad (14.42)$$

The superfluid density tensor has two eigenvalues – parallel to and perpendicular to the gap axis, $\mathbf{l}$. Note that in this case the current is no longer always parallel to the vector potential. The situation in a p-wave superconductor is summarized in Table 14.2. All low-temperature asymptotics listed in the table have been experimentally observed.

Table 14.2 Various low-temperature coefficients for the p-wave pairing state

	Orientation	A	n
axial $f(\mathbf{k}\cdot\mathbf{1}) = \lvert\mathbf{k}\times\mathbf{1}\rvert$ (two point nodes)	$\|\|$	π^2	2
	$\perp$	$\frac{7\pi^4}{15}$	4
polar $f(\mathbf{k}\cdot\mathbf{1}) = \mathbf{k}\cdot\mathbf{1}$ (equatorial line node)	$\|\|$	$\frac{27\pi\zeta(3)}{4}$	3
	$\perp$	$\frac{3\pi \ln 2}{2}$	1

VI. EFFECT OF DISORDER AND IMPURITIES ON THE PENETRATION DEPTH

A. Non-Magnetic Impurities

Early measurements of the penetration depth in thin films and some crystals of copper oxide superconductors showed a T^2 dependence, instead of the expected linear T dependence for a gap function with line nodes. The problem found its resolution by considering the effect of impurity scattering (Hirschfeld and Goldenfeld, 1993, Preosti *et al*., 1994) It was shown that that resonant (unitary-limit) scattering leads to a nonzero density of quasiparticle states near $E = 0$. In turn, these states lead to a T^2 variation of the penetration depth below a crossover temperature T^*. The reason for considering the unitary limit was the observation that scattering in the Born limit would lead to a rapid suppression of T_c, which was not observed. A useful interpolation between the linear and quadratic regimes was suggested by Hirschfeld and Goldenfeld (1993),

$$\lambda(T) = \tilde{\lambda}(0) + \alpha \frac{T^2}{T + T^*} \qquad (14.43)$$

where $\tilde{\lambda}(0)$ is the effective penetration depth obtained by extrapolation of the linear region of $\lambda(T)$ to $T = 0$. The crossover temperature is given by $k_B T^* \simeq 0.83\sqrt{\Gamma\Delta(0)}$ where $\Gamma = n_i n / \pi N(0)$ is the scattering rate parameter.

n_i is the concentration of impurities, n the electron density and $N(0)$ is the density of states at the Fermi level. $T^* \simeq 0.01 T_c$ is a typical value for high quality YBCO. Impurities also modify the penetration depth at $T = 0$: $\tilde{\lambda}(0)/\lambda(0) \simeq 1 + 0.79\sqrt{\Gamma/\Delta(0)}$. Assuming, for example, a weak coupling BCS result for the d-wave gap, $\Delta(0)/k_B T_c \simeq 2.14$, one has

$$\Gamma \simeq \frac{k_B (T^*)^2}{1.47 T_c} \tag{14.44}$$

The modification of the zero-temperature penetration depth is then given by,

$$\begin{aligned} \tilde{\lambda}(0)/\lambda(0) &= 1 + 0.95 T^*/\Delta(0) \\ &= 1 + 0.44 T^*/T_c \end{aligned} \tag{14.45}$$

which is quite small for clean crystals. This "dirty d-wave" model has been thoroughly studied in both single crystals and thin films of YBaCuO. (Bonn *et al.*, 1994, Lee *et al.*, 1994) In less clean samples the impurity-dominated regime can be a substantial portion of the low temperature region. In that case,

$$\lambda(T) - \tilde{\lambda}(0) = c_2 T^2 \tag{14.46}$$

where,

$$c_2 = 0.83 \frac{\lambda(0)}{\Delta(0)^{3/2} \Gamma^{1/2}} \tag{14.47}$$

This expression will be useful when we compare the effect of impurities to the quadratic temperature dependence arising from nonlocal corrections.

Figure 14.8 shows the temperature dependence of the magnetic penetration depth in a BSCCO-2212 crystal. The impurity crossover occurs at $T^* = 3.5\,K$ while $T_c \approx 92\,K$. The inset shows the normalized superfluid density derived from the penetration depth data and plotted over the entire temperature range up to T_c. The solid lines are the calculated superfluid densities for a clean d-wave case, Eq. (14.27), and for a clean s-wave, Eq. (14.30). The agreement with the d-wave curve is evident.

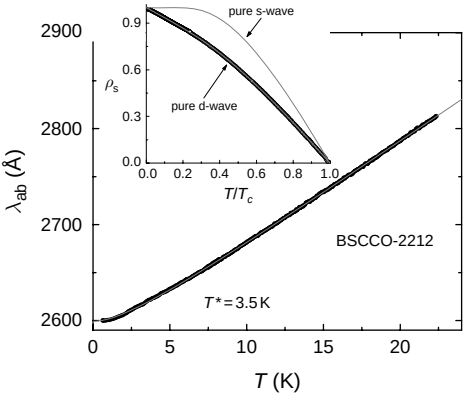

Figure 14.8 In-plane London penetration depth in single crystal BSCCO-2212. The main frame shows the low-temperature part with a fit to Eq. (14.43). The inset shows the full temperature range superfluid density (symbols) and theoretical curves for a clean *d*-wave and an *s*-wave weak coupling involving BCS calculations, based on Eqs. (14.27) and (14.30), respectively.

B. Magnetic Impurities

The ability of magnetic impurities to break Cooper pairs leads to profound effects on all superconductive properties. The most familiar is a suppression of the transition temperature, as first calculated by Abrikosov-Gorkov. Its generalization to unconventional superconductors is beyond the scope of this chapter. Magnetic impurities also affect the penetration depth in a direct way, though a change of permeability when $\mu > 1$. Combining the second London equation, $4\pi\lambda^2 \mathbf{j} = -c\mathbf{B}$, with Maxwell's equations and the constitutive relation $\mathbf{B} = \mu\mathbf{H}$, we obtain a renormalized penetration depth, $\lambda_\mu = \lambda/\sqrt{\mu}$, analogous to the modification of the skin depth in a normal metal. Here λ is the London penetration depth without magnetic impurities, and λ_μ is the physical length scale over which the field changes. However, the change in resonant frequency of an oscillator or cavity involves

a change in energy, which leads to an additional factor of μ. Equation (14.11) then becomes

$$-4\pi\chi = \frac{1}{1-N}\left[1 - \frac{\mu\lambda_\mu}{\tilde{R}}\tanh\left(\frac{\tilde{R}}{\lambda_\mu}\right)\right] \tag{14.48}$$

The extra factor of μ is absent in the argument of the tanh function since the term within the brackets must reduce to $1-\mu$ as $\lambda \to \infty$. At low temperatures the tanh factor becomes unity and the effective penetration depth that one measures is given by

$$\lambda_{eff} = \sqrt{\mu\lambda} \tag{14.49}$$

At low temperatures impurity paramagnetism leads to $\mu \sim T^{-1}$ and therefore a minimum in λ_{eff}. The competing magnetic and superconducting contributions in Eq. (14.49) played an important role in the determining the pairing state in electron-doped cuprates. Early penetration depth measurements in $Nd_{2-x}Ce_xCuO_{4-y}$ (NCCO) extended to 4.2 K where, coincidentally, the competing temperature dependences in Eq .(14.49) lead to a minimum in $\lambda_{eff}(T)$. This made the data appear to saturate, as would be expected for s-wave pairing. Cooper (1996) was the first to point out that the paramagnetic effect could mask a possible power law dependence for $\lambda(T)$.

Figure 14.9 shows $\Delta\lambda_{eff}(T,B) = \lambda_{eff}(T,B) - \lambda_{eff}(T_{\min},B)$ measured in single crystal NCCO at several different magnetic fields aligned parallel to the c-axis. The low-temperature upturn is due to the permeability of Nd^{3+} ions. The fact that the curves collapse together below $T_{\min}$ implies that the permeability is field independent. As the field is increased beyond the valued shown here, the spin system will become more polarized and the permeability should decrease. The field independence below $T_{\min}$ can help to distinguish an upturn in $\lambda(T_{\min})$ from paramagnetic ions from a similar looking upturn due to surface Andreev bound states. As we discuss later, relatively modest fields can quench the upturn from bound states. We have focused on the simplest observable consequence of magnetic impurities on the observed penetration depth. Impurities can have a more profound influence by modifying the gap function itself, and thus the entire temperature dependence of the superfluid density (Carbotte, 1990)

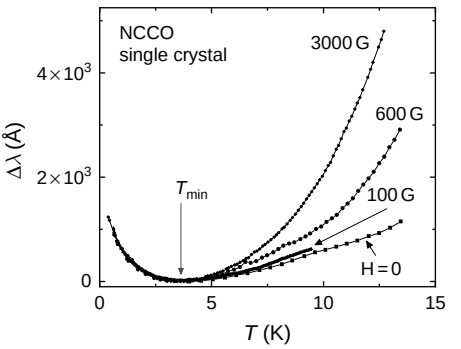

Figure 14.9 Change in the effective penetration depth of the electron-doped superconductor NCCO for different applied fields. The change is measured relative to $T_{\min}$. For $T < T_{\min}$, data at different fields collapse, implying a field-independent permeability for Nd^{3+} ions up to 3 KG.

VII. SURFACE ANDREEV BOUND STATES

The formulae given previously for the superfluid density involve only the absolute square of the gap function. As such, it was believed for some time that penetration depth measurements were insensitive to the phase of the gap function. However this is not true, as is shown theoretically by (Barash *et al*., 2000), and experimentally by (Prusseit *et al*., 1999) and (Carrington *et al*., 2001). Unconventional superconductors support the existence of zero energy, current carrying surface Andreev bound states (ABS). (Bucholtz and Zwicknagl, 1981) These states

are a direct consequence of the sign change in the d-wave order parameter. (Hu, 1994). The zero-bias conductance peak widely observed in ab-planar tunneling is generally associated with these states (Aprili *et al*., 1999). As shown in Fig. 14.10, for $d_{x^2-y^2}$ symmetry, the effect is maximal for a [110] orientation where the nodal directions are perpendicular to the sample surface. A quasiparticle travelling along the trajectory shown by the arrows initially feels a negative pair potential. After reflection it travels in a positive pair potential. This process leads to zero energy bound states that are localized within a few coherence lengths of the surface, and carry current parallel to the surface. As such, they can affect the Meissner screening. The effect is absent for the more common (100) orientation.

Andreev bound states may be observed in penetration depth measurements by orienting the magnetic field along the c-axis, inducing shielding currents that flow along the (110) edges of the sample. Bound states contribute a singular piece to the overall density of current carrying states, $N_{ABS}(E) \sim \delta(E)$. When inserted into Eq. (14.21), this results in a paramagnetic contribution to the penetration depth, $\Delta\lambda_{ABS} \sim 1/T$. This divergent term competes with the linear T dependence from nodal quasiparticles, leading to a minimum in the penetration depth at $T_m \sim T_c\sqrt{\xi_0/\lambda_0}$. For YBaCuO $T_m \sim 10\,K$ for a sample all of whose edges have (110) orientations. The effect is shown in Fig. 14.11 where four YBaCuO crystals with differing amounts of [110] surface were measured. In each case the AC magnetic field was first oriented parallel to the conducting plane (denoted by $\lambda_{ab}^{a,b}$) and then along the c-axis (denoted by λ_{ab}^{c}). The first shows the familiar linear variation characteristic of

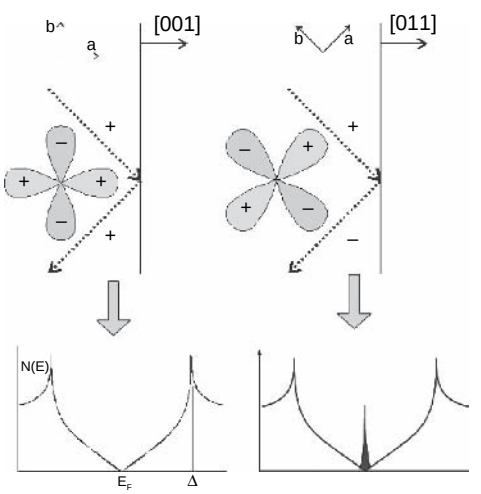

Figure 14.10 Schematic of the origin of surface Andreev bound states. The magnetic field is normal to the surface. Quasiparticles travelling along the trajectory shown by the arrows experiences a sign change in the pair potential **(right)**, resulting in a zero energy bound state localized near the surface. In the other situation **(left)** the effect does not exist. The lower panel shows the corresponding response of the density of states – proliferation of the zero-energy bound (Andreev) states.

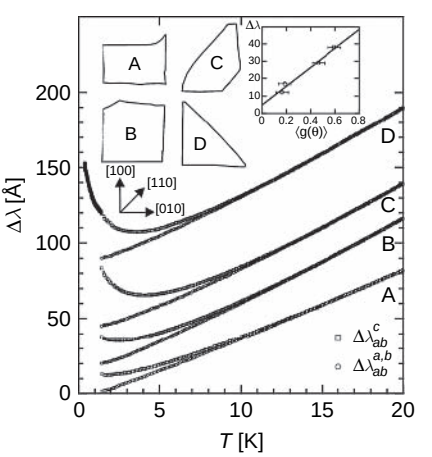

Figure 14.11 λ_{ab} in four YBaCuO crystals. Traces with the AC field along the c-axis exhibit a 1/T upturn, while traces taken with the AC field along conducting planes show no upturn. The inset shows the relative size of the 1/T upturn versus the amount of [110] perimeter surface. $\langle g(\theta)\rangle$. The low temperature portion of trace D was taken in an entirely separate cryostat from the portion above 1.3 K. The symbol λ_{ab}^{c} denotes the in-plane penetration depth with the ac field along the c-axis.

nodal quasiparticles, and the second shows the 1/T upturn from bound states. The bound state signal is largest for the sample exhibiting the largest amount of [110] surface.

Impurity scattering broadens the zero energy peak and reduces the paramagnetic upturn. Another striking feature of the bound state signal is its rapid disappearance in an applied DC magnetic field. Crudely speaking, the Doppler field shifts the zero-energy states, $N(E) \sim \delta\left(E - \frac{e}{c}\mathbf{v}_F\mathbf{A}\right)$, resulting in a field-dependent penetration depth (see Eq. (14.21)),

$$\Delta\lambda_{ABS}(T,H) \sim \frac{1}{T\cosh^2(H/\tilde{H}(T))} \tag{14.50}$$

where $\tilde{H} \simeq H_c T/T_c$ and H_c is the thermodynamic critical field. Figure 14.12 shows the field dependence of the 1/T upturn. Fits to both the single quasiparticle trajectory model (Eq. (14.50)) and the full model of Barash *et. al.* are also shown. The agreement is remarkably good.

These highly distinctive temperature, orientation and field dependences differentiate the signal due to bound states from the paramagnetic upturn from magnetic impurities that was discussed earlier. We reiterate that the bound state effect is inherently phase sensitive, and can distinguish between a nodal order parameter without a sign change from, for example, a d-wave state. These Andreev bound states have also been observed in other superconductors. Figure 14.13 shows the effect in single crystal BSCCO-2212 for several values of the magnetic field, showing the quenching effect just described.

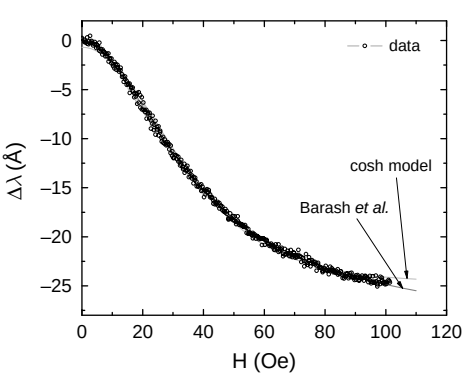

Figure 14.12 Paramagnetic upturn, $\Delta\lambda(H)$, measured at T = 1.34 K in a YBaCuO crystal. "cosh" denotes a fit to Eq. (14.50), and a fit to "Barash *et al.*" (2000), Eq. (26), is indicated.

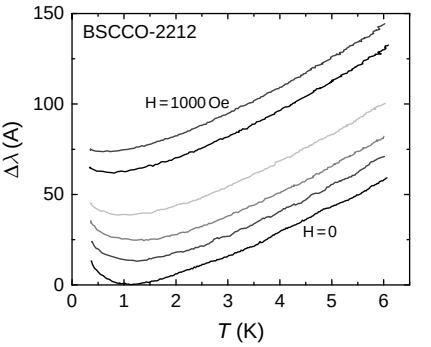

Figure 14.13 Andreev bound states in a BSCCO-2212 single crystal. The curves are offset for clarity.

VIII. NONLOCAL ELECTRODYNAMICS OF NODAL SUPERCONDUCTORS

Since the superconductors under consideration here are typically in the extreme Type II limit $\lambda \gg \xi$, one would not expect nonlocal corrections to the penetration depth to be important. Kosztin and Leggett (1997) pointed out that since the BCS coherence length ($\xi = v_F/\pi\Delta$) formally diverges along nodal directions ($\Delta \to 0$) one may actually have $\xi > \lambda$ near the nodes, and therefore nonlocal corrections to the penetration depth may occur. For a clean d-wave superconductor they predicted that the linear temperature

dependence would crossover to a quadratic dependence below T^*_{NLOC},

$$\lambda(T) - \lambda(0) = \frac{\lambda(0)\ln 2}{T_C T^*_{NLOC}} T^2 \qquad (14.51)$$

and

$$T^*_{NLOC} \simeq \Delta(0)\xi(0)/\lambda(0) \qquad (14.52)$$

For YBaCuO with $T_c \simeq 90\,\mathrm{K}$ this gives $T^*_{NLOC} \simeq 3\,\mathrm{K}$. The nonlocal correction looks very much like the effect from impurity scattering that was discussed earlier. (As in the impurity scenario $\lambda(0)$ is also renormalized, but the predicted change is only of order 1%.) Since the impurity scattering crossover T^* in typical YBaCuO or BSCCO is of the same order as T^*_{NLOC}, the two processes would be difficult to distinguish. However, unlike the effect from impurities, the predicted nonlocality is dependent upon the orientation of the magnetic field and the sample boundaries. One must have $H||c$ – axis to ensure that the wave-vector defining the spatial variation of the vector potential lies in the conducting plane. Recent penetration depth measurements on Sr_2RuO_4 (Bonalde *et al.*, 2000a) and $CeCoIn_5$ (Chia *et al.*, 2003) seem to provide experimental evidence for this mechanism.

IX. NONLINEAR MEISSNER EFFECT

In the presence of a superfluid velocity field $\vec{v}_s$ the energy of a Bogoluibov quasiparticle is changed by $\delta E_{QP} = \vec{v}_s \cdot \vec{p}_F$ where $\vec{p}_F$ is the Fermi momentum. This effect is sometimes called the quasiparticle Doppler shift. Quasiparticles co-moving with $\vec{v}_s$ are shifted up in energy while those moving counter to $\vec{v}_s$ are shifted down. For $T > 0$ the increased population of counter-moving quasiparticles constitutes a paramagnetic current that reduces the Meissner screening. The temperature dependence of λ ultimately derives from this fact. As $\vec{v}_s$ is increased two things occur. First, higher order corrections to the thermal population difference become more important, and second pair breaking effects reduce the gap itself. In a superconductor with a finite energy gap everywhere on the Fermi surface, the supercurrent $\vec{J}_s = -e\rho\vec{v}_s(1 - \alpha(T)(v_s/v_c)^2)$ acquires a correction term quadratic in $\vec{v}_s$. v_c is the bulk critical velocity. Since $\vec{v}_s$ is proportional to the applied magnetic field H, this nonlinearity results in a field-dependent penetration depth,

$$\frac{1}{\lambda(T,H)} = \frac{1}{\lambda(t)}\left[1 - \frac{3\alpha(T)}{4}\left(\frac{H}{H_0(T)}\right)^2\right] \qquad (14.53)$$

$H_0(T)$ is of the order of the thermodynamic critical field. At low temperatures the coefficient $\alpha(T) \sim \exp(-\Delta(0)/T)$. (Xu *et al.*, 1995) This occurs because the Doppler shift must contend with a finite energy gap and so does not affect the quasiparticle population at $T = 0$. The field dependent correction is extremely small since the penetration depth itself is already exponentially suppressed. Any attempt to observe this effect in a conventional type I superconductor must also take account of the very large field dependence that occurs in the intermediate state.

In 1992, Yip and Sauls showed theoretically that the situation would be quite different in a d-wave superconductor. The existence of nodes in the gap function implies that the Doppler shift can change the quasiparticle population at arbitrarily low temperatures so long as $|\delta E_{QP}| \gg k_B T$. In fact, the effect is predicted to be *strongest* at $T = 0$, and to depend upon the orientation of $\vec{v}_s$ relative to the nodal directions. For a d-wave state at $T = 0$, the nonlinearity leads to a nonanalytic correction to the current-velocity relation, $\vec{J}_s = -e\rho\vec{v}_s(1 - |\vec{v}_s|/v_0)\cdot v_0$ is of order the bulk critical velocity. This correction leads to a linear increase in the penetration depth as a function of field.

For a d-wave pairing state at T = 0 the result is, (Yip and Sauls, 1992, Xu *et al.*, 1995)

$$\frac{1}{\lambda(T=0,H)} = \frac{1}{\lambda(0)}\left[1-\tfrac{2}{3}\tfrac{H}{H_0}\right] \quad \vec{H}||node \quad (14.54)$$

$$\frac{1}{\lambda(T=0,H)} = \frac{1}{\lambda(0)}\left[1-\tfrac{1}{\sqrt{2}}\tfrac{2}{3}\tfrac{H}{H_0}\right] \quad \vec{H}||antinode$$

$H_0 = 3\phi_0/\pi^2\lambda\xi$ is of the order of the thermodynamic critical field. The great appeal of this idea lies in the possibility of verifying both the existence of nodes and locating them on the Fermi surface. Yip and Sauls coined the term "nonlinear Meissner effect" (NLME) to describe the phenomenon. As conceived, it results from a field-induced change in quasi-particle populations, and does not include field-induced pair breaking effects on the gap itself. Since the NLME depends upon the quasiparticle energy, and therefore $|\Delta(\vec{k})|^2$, it is a probe of nodes, but it is not inherently sensitive to the phase of the order parameter. This contrasts with the case of surface Andreev bound states which depend for their existence on a sign change of the order parameter.

Despite considerable experimental efforts, the NLME has proven to be extremely difficult to identify. A large number of constraints must be satisfied. First, H must be smaller than the lower critical field to avoid contributions from vortex motion which can also give a linear correction to λ. Using YBaCuO as an example, $H_{C1}/H_0 \sim .01$. With that restriction, the maximum change in λ is of order of 10–15 Angstroms, so the effect is small indeed. Second, unitary limit impurity scattering is predicted to rapidly destroy the NLME so temperatures *above* the impurity crossover T^* are needed. For the best YBaCuO samples, $T^* \approx 1\,\mathrm{K}$. Third, the field dependence is maximal at T = 0, and decreases rapidly once $\delta E_{QP} \ll k_B T$. For YBaCuO, this inequality restricts observation of the effect to temperatures *below* 3–4 K, even at $H = H_{C1}$, the maximum possible field. For higher temperatures the field dependence becomes quadratic and small. The decrease of the linear field dependence with temperature is, however, a distinguishing feature of the NLME for a d-wave state. This point was ignored in some early attempts to identify the effect. In any case, these various conditions place extremely tight constraints on the observability of the NLME.

Several different experiments have been undertaken. The first focuses on the predicted anisotropy in the penetration depth and therefore the magnetic moment of a crystal. Bhattacharya *et al.* (1999, Žutić and Valls, 1998), rotated a sample of YBaCuO and searched for harmonics in the angular dependence of the signal indicative of the nodal anisotropy. They observed anisotropy but well below the predicted amount. The second class of experiments directly measures the penetration depth in a dc magnetic field superimposed on a much smaller ac measurement field. Penetration depth measurements by Maeda and Hanaguri (1998) first reported a linear field dependence, but did not address the question of the temperature dependence. Later measurements by (Carrington *et al.*, 1999b, Bidinosti *et al.*, 1999) reported a linear H dependence but the temperature and sample orientation dependence were completely at odds with the theory. Vortex motion, through the Campbell penetration depth, can easily lead to a linear field dependence. In contrast to the NLME, however, the field dependence coming from vortex motion *increases* with temperature since vortices become more weakly pinned. (Carrington *et al.*, 1999b)

The inability to observe the NLME lead to a re-examination of the original Yip-Sauls argument and to several other suggestions for detecting the effect. Li *et al.* (1998) showed that if the vector potential varies spatially with the wave-vector $\vec{q}$ then nonlocal effects,

similar to those described earlier, suppress the NLME whenever $\vec{v}_s \cdot \vec{q} \neq 0$ (This would occur when the field is oriented normal to the conducting planes, for example.) The suppression occurs for fields $H < H_{C1}$ which effectively renders the effect unobservable. (Li *et al.*, 1998) However, for other field orientations the nonlocal effects should not occur. Experiments have been carried out ror in several orientations and to our knowledge, this nonlocal effect has not been cleanly identified. The tunnel diode method used by the authors was originally developed to search for the NLME. We have routinely searched for a NLME in several different hole- and electron-doped copper oxides, and in the organic superconductors discussed previously. All of these materials show clear evidence, through $\lambda(T)$, for nodal quasiparticles. All show a linear variation, $\Delta\lambda(T, H) \sim \beta(T)H$ with field. However, in all cases, $\beta(T)$ varies with temperature in a manner expected for vortex motion, despite applied fields as low as a few Oe.

Dahm and Scalapino (1999) proposed to exploit the *analytic* corrections to the supercurrent that vary as v_s^2 in order to identify the d-wave state. These terms lead to changes in λ that vary as H^2/T, are apparently less affected by impurity scattering, and can be observed over a wider temperature range. As with the linear-in-H (Yip and Sauls, 1992)) non-analytic corrections, the quadratic corrections are largest at T = 0, and are thus distinguishable from nonlinear effects in an s-wave superconductor. The nonlinear penetration depth leads to harmonic generation and intermodulation frequency generation and so may have relevance in microwave and mixer applications. Recently, intermodulation measurements were performed on a number of microwave stripline resonators made from YBaCuO films. Some of the films exhibit the 1/T upturn predicted for the nonlinear penetration depth in a d-wave state. (Oates *et al.*, 2004) These experiments are the first to observe the low temperature increase in nonlinearity expected for a d-wave superconductor. However, the effect is distinct from the non-analytic, linear-in-H behavior first predicted by Yip and Sauls. To our knowledge, the latter has not yet been observed.

X. AC PENETRATION DEPTH IN THE MIXED STATE (SMALL AMPLITUDE LINEAR RESPONSE)

When Abrikosov vortices are present, the total penetration depth acquires a new contribution due to the motion of vortices. In general this "vortex penetration depth" term can depend upon field, frequency, temperature, orientation, and pinning strength. Vortex motion is a complex subject and we will only touch upon that aspect relating to penetration depth measurements. A simple model for vortex motion treats the displacement $\vec{\mathbf{u}}$ as a damped harmonic oscillator with a restoring force proportional to the curvature of a pinning potential well, a damping proportional to the vortex viscosity, and a driving term from the AC Lorentz force. The inertial term, proportional to the vortex mass, is generally ignored. This is the model first developed by Gittleman and Rosenblum (1966), which shows a crossover from pinning flux motion to flux flow as the frequency is increased. Since the advent of high temperature superconductivity, enormous attention has focused on the new phases of the H-T phase diagram. In particular, it is widely believed that over a substantial portion of the diagram the vortex lattice is melted or at least very weekly pinned, so vortices can be easily displaced. The much higher temperatures that occur in copper oxide superconductors imply that flux flow may be thermally assisted. The effect of this process on the penetration depth was first analyzed by Coffey and Clem

(1991, 1991, 1992) and by Brandt (1991). A good summary is given in (Brandt, 1995). A generalized complex penetration depth in case of small amplitude AC response is given by

$$\lambda^2 = \tilde{\lambda}_L^2 + \frac{B^2}{4\pi}\left(\frac{\alpha_L}{1 - i/\omega\tau} + i\omega\eta\right)^{-1} \approx \lambda_L^2 + \lambda_C^2 \frac{1 - i/\omega\tau}{1 + i\omega\tau_o} \qquad (14.55)$$

where the last expression is obtained for a large barrier for thermal activation, $U \gg k_B T$. In Eq. (14.55), $\tilde{\lambda}_L$ is the field-dependent London penetration depth (see Eq. (14.56)) and λ_C is the Campbell length (discussed below). $\tau = B^2/(\rho_{TAFF}\alpha_L) \approx \tau_0 \exp(U/k_B T)$ is the relaxation time with a flux-flow relaxation time defined as, $\tau_0 = \eta/\alpha_L = B^2/(\rho_{FF}\alpha_L)$. The thermally assisted flux flow resistivity $\rho_{TAFF} = \rho_{FF}\exp(U/k_B T)$ where the bare flux flow resistivity is $\rho_{FF} = B^2/\eta = \rho_n B/H_{c2}$, and $\eta = BH_{c2}/\rho_n$ is the vortex viscosity. In the case of very strong pinning the superconductor behaves as in Meissner state, but with a renormalized penetration depth given by

$$\tilde{\lambda}_L = \frac{\lambda_L}{\sqrt{1 - B/B_{c2}}} \qquad (14.56)$$

(The field dependence is conventional, due to pair breaking, as discussed earlier.) The Campbell length is given by

$$\lambda_C^2 = \frac{C_{nn}}{\alpha_L} \qquad (14.57)$$

where α_L is the Labusch parameter (note that we use pinning force per unit volume, not per unit of vortex length),

$$\alpha_L = \frac{j_c B}{c r_p} \qquad (14.58)$$

where r_p is the radius of the pinning potential determined by the maximum pinning force when the vortex is displaced out of equilibrium, and C_{nn} is the relevant elastic modulus – C_{11} (compressional modulus) for a field parallel to the surface or C_{44} (tilt modulus) for a magnetic field perpendicular to the surface. Both moduli are proportional to B^2 and therefore,

$$\lambda_C^2 = \frac{B^2}{4\pi\alpha_L} \propto \frac{B}{j_c} \qquad (14.59)$$

At low frequencies and not too high temperatures and fields, the response is in-phase with the AC field. The effective penetration depth is given by

$$\lambda^2 = \lambda_L^2 + \lambda_C^2 \qquad (14.60)$$

At low temperatures and for weak pinning, the Campbell contribution rapidly dominates the London depth, leading to $\lambda(B) \sim \sqrt{B}$.

Figure 14.14 shows the typical behavior of a stress-free polycrystalline Nb sample. A crossover to the flux flow regime is seen in both temperature (at different DC fields) and magnetic field (at different temperatures) measurements. We show these data for two reasons. First, if one's focus is the pairing state and the various magnetic field dependent effects that can occur (NLME,

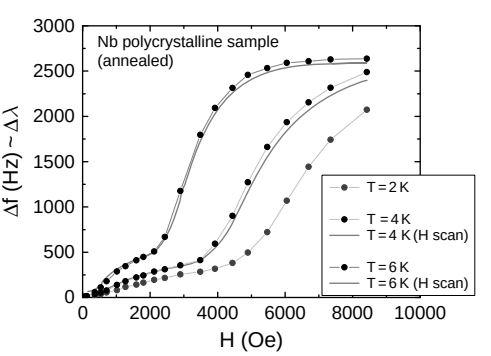

Figure 14.14 Crossover from the pinning to the flux-flow regime as function of the applied magnetic field in a polycrystalline Nb sample. The solid lines correspond to direct field scans, whereas the symbols were obtained from temperature scans at different temperatures.

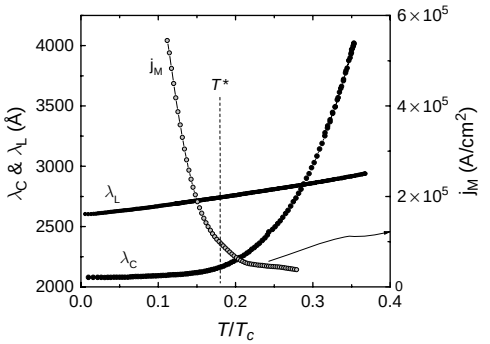

Figure 14.15 London penetration depth, Campbell length, and critical current in BSCCO-2212 single crystal.

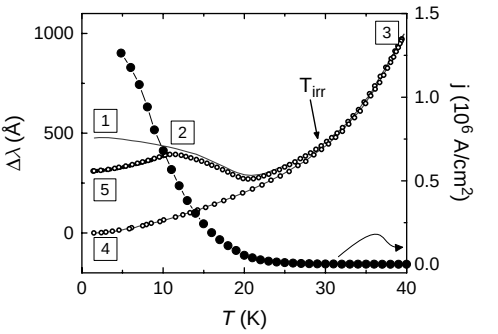

Figure 14.16 Hysteretic magnetic penetration depth measured in single crystal BSCCO-2212. Path 1–2–3 was taken after the magnetic field was applied subsequent to cooling in zero field. Path 3–4 is reversible and corresponds to a homogeneous flux distribution. Path 2–5 was followed when the temperature was reduced after 1–2. Upon warming, it would follow 5–2–3.

bound states, etc.) then the effects of vortex motion can be a significant source of systematic error and must be understood. On the other hand, if vortex motion is the focus of interest, then penetration depth measurements provide a valuable tool to access the true critical current, unaffected by flux creep, since the time window is fixed by the frequency.

Figure 14.15 shows London and Campbell penetration depths as well as the deduced critical current in single crystal BSCCO-2212. Temperature T^* marks a crossover between strong and week pinning regimes.

In the case of a large static gradient due to vortex pinning produced by a DC magnetic field (superimposed on an AC excitation field), the Labusch parameter becomes dependent on the Bean shielding current that biases the vortex position in the pinning well. The first order correction then gives $\alpha(j) = \alpha_0\sqrt{1-j/j_c}$, and

$$\lambda_C^2 = \frac{B^2}{4\pi\alpha\sqrt{1-j/j_c}} \qquad (14.61)$$

which explains many hysteretic phenomena observed with a small amplitude AC response (Prozorov *et al.*, 2003).

Figure 14.16 shows a hysteretic response observed in single crystal BSSCO-2212. After cooling in zero field and the application of a DC magnetic field, a large Bean current causes the penetration depth to increase, according to Eq. (14.61). Warming up (1–2–3) removes this inhomogeneous vortex distribution (and the Bean current) and subsequent cooling follows curve 3–4. If repeated (without turning off the magnetic field), the curve will follow 3–4 both on warming and cooling. Another manifestation of the irreversible behaviour is when the warming is interrupted (1–2) and sample is cooled down. The response follows path 2–5, where the Bean current is decreased, but "frozen". Upon warming from 5, the curve follows 5–2–3. The large circles indicate the critical current density, which drops sharply precisely at the position where the hysteretic response of λ disappears.

XI. THE PROXIMITY EFFECT AND ITS IDENTIFICATION BY USING AC PENETRATION DEPTH MEASUREMENTS

Among the variety of magnetic phenomena that may affect the penetration depth we discuss one last subject, the proximity

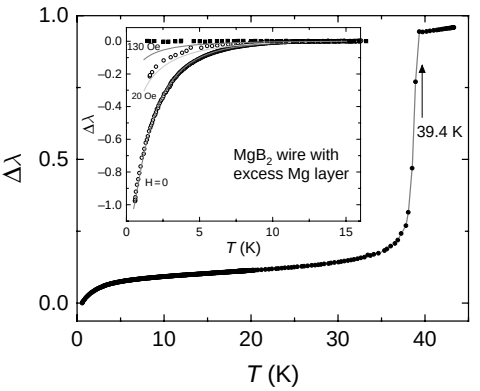

Figure 14.17 Proximity effect induced superconductivity in MgB_2 wires coated with an excess Mg layer. The inset shows the low-temperature part where the field effect on the proximity effect is evident.

effect. As is well known, a superconductor in proximity to a normal metal may induce pairing correlations in the normal metal that extend over a distance ζ_N (de Gennes, 1966) The details depend sensitively on whether the normal metal is in the clean or the dirty limit. In the clean limit, $\xi_N = \hbar v_F/2\pi k_B T$ and the induced pairing correlations can extend over macroscopic distances. Electrons in the normal metal may now carry something similar to a Meissner screening current, and therefore make the combined system appear to have enhanced diamagnetism. Figure 14.17 shows the effect on the penetration depth (Prozorov *et al.*, 2001). The data are shown for a bundle of $180\,\mu m$ diameter MgB_2 wires that were coated with a layer of Mg (roughly $2\,\mu m$ thick) leftover from the growth process. Below approximately 5 Kelvin, λ versus T exhibits a strong negative concavity corresponding to enhanced diamagnetism. In the clean limit, proximity diamagnetism is predicted to turn on at $T \approx 5T_{Andreev}$ where the Andreev temperature is defined by $\xi_N(T_{Andreev}) = d$, the film thickness. (Fauchère and Blatter, 1997) The diamagnetic downturn vanished completely after dissolving the Mg layer away in alcohol. The λ for the MgB_2 wires left behind exhibited the exponential decrease expected for a superconductor whose minimum energy gap is roughly $0.4\Delta_{BCS}$.

The inset to Fig. 14.17 shows the magnetic field dependence of the proximity diamagnetism. A field of roughly 300 Oe was sufficient to entirely quench the effect. The suppression occurs as the external field exceeds the breakdown field $H_B \sim \phi_0 e^{-d/\xi_N}/d\lambda_N$ of the normal metal film. Here d is the film thickness, $\lambda_N = \sqrt{4\pi e^2/m}$ is (formally) the London penetration depth of the normal metal and ϕ_0 is the flux quantum. (Fauchère and Blatter, 1997) Since the film thickness was not uniform, thicker regions with smaller breakdown fields were quenched first, accounting for the gradual suppression of the diamagnetism shown. The fits shown in the inset to Fig. 14.17 assumed a log-normal distribution of Mg thickness d with the mean and variance as free parameters. In addition to being interesting in its own right, proximity diamagnetism is a clear indicator of residual metallic flux that is sometimes left over from the growth process. As Figure 14.17 shows, its presence can lead to serious errors in interpreting the low temperature behavior of $\lambda(T)$.

This page intentionally left blank

15

Energy Gap and Tunneling

I. INTRODUCTION

In Chapter 13 we introduced critical-state models with an emphasis on the Bean model. This gave us a chance not only to provide simple explanations for some of the magnetic phenomena that had been discussed in Chapters 5, 11 and 12, but also to discuss critical currents and, thereby, introduce the area of transport properties, the subject of the present and succeeding chapter. Transport properties are of importance because the principal applications of superconductors are based upon taking advantage of their ability to carry electric current without any loss.

The chapter begins with a discussion of tunneling and super current flow in the absence of externally applied fields. After covering introductory material on tunneling, we will discuss the Josephson effect and macroscopic quantum phenomena. It will be shown how tunneling measurements provide energy gap values. The following chapter will examine several transport processes that involve applied fields and thermal effects.

II. PHENOMENON OF TUNNELING

Tunneling, or barrier penetration, is a process whereby an electron confined to a region of space by an energy barrier is nevertheless able to penetrate the barrier through a quantum mechanical process and emerge on the other side. The example shown in Fig. 15.1 involves electrons with kinetic energy $E_{\mathrm{KE}} = \frac{1}{2}mv^2$ confined to remain on the left side of a barrier by the potential

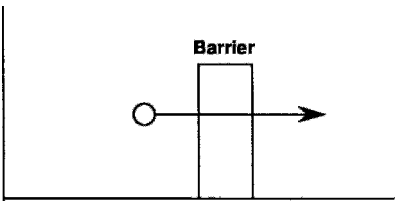

Figure 15.1 Tunneling of electrons through a barrier when the kinetic energy of the electrons is less than the barrier energy eV_b.

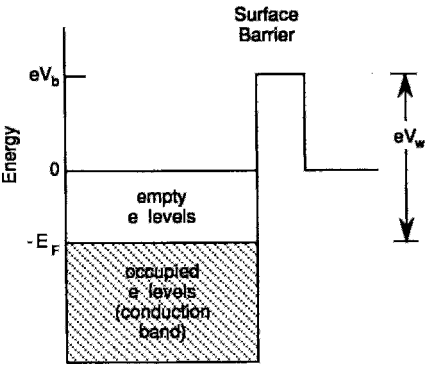

Figure 15.2 Energy-level diagram of a conductor showing the levels occupied below the Fermi energy E_F and the energy barrier eV_b at the surface. The minimum energy (work function) eV_w for extracting an electron is also indicated.

V_b, where $\frac{1}{2}mv^2 < eV_b$. We show in this figure an electron tunneling through the barrier to the right side where it ends up with the same kinetic energy. Such a phenomenon can occur because there is a quantum mechanical probability per unit time that the electron will penetrate the barrier and escape, as explained in standard quantum mechanics texts. Tunneling phenomena are rather common in physics. For example, radioactive decay of nuclei is explained by a barrier penetration model, with half-lives varying from less than nanoseconds to many centuries.

A. Conduction-Electron Energies

The surface of a normal metal has a dipole charge density layer that produces a barrier potential V_b. The conduction electrons inside the metal move in a region where they experience an attractive potential, so that their energies are negative with the value $-|E_F|$, as indicated in Fig. 15.2. At absolute zero the conduction-band levels are filled up to the Fermi level E_F and are empty above, corresponding to Fig. 1.4a. In some of the figures dark shading is used to indicate occupied levels.

To remove an electron from the interior of a metal one must apply a potential equal to or greater than the work function potential V_w. The minimum energy eV_w that can extract an electron is

$$eV_w = eV_b + |E_F|. \qquad (15.1)$$

Metals differ in their eV_w, eV_b, and E_F values, so that a proper treatment of how an electron is transferred between two metals in contact through an insulating barrier should take these factors into account. However, to simplify the mathematics we will ignore these surface potential effects and assume that two metals in contact at the same potential have the same Fermi energy.

Tunneling phenomena are sensitive to the degree of occupation of the relevant energy levels by electrons. Hence, in energy level diagrams it is helpful to include information about the occupation of the levels involved in the tunneling. Figure 1.4b plots the temperature dependence of the Fermi–Dirac distribution function, giving the fractional occupation of levels in the conduction band. We have replotted this function in Fig. 15.3 with energy as the ordinate, $f(E)$ as the abscissa, and electron occupation indicated by shading. Figure 15.4a presents a sketch of a conduction band that is filled at absolute zero and separated from an upper energy band by a gap. Figure 15.4b shows this same diagram at a finite temperature, combined with the distribution function plot of Fig. 15.3 to show the level populations.

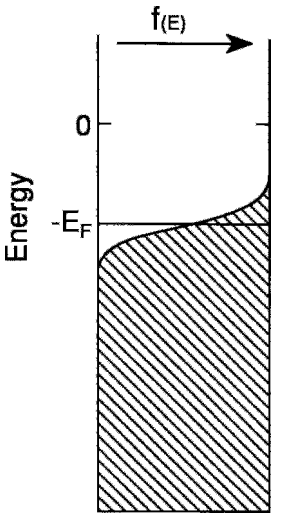

Figure 15.3 Energy-level diagram of a conductor with electron distribution $f(E)$ at a finite temperature near the Fermi level E_F plotted at the top. The shading in this and subsequent figures indicates electron occupancy.

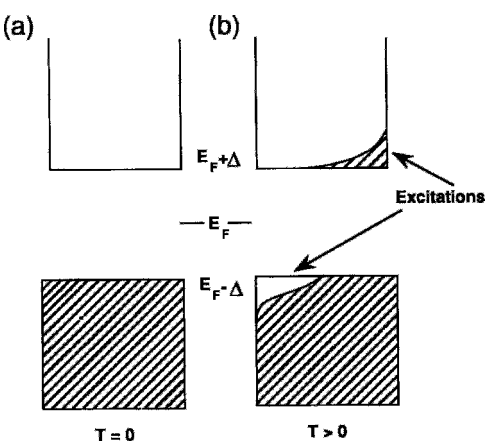

Figure 15.4 Semiconductor representation of the energy level occupancy of a superconductor (a) at $T = 0$, and (b) at $T > 0$. The band gap 2Δ and level populations are shown for each case, using the convention of Fig. 15.3.

B. Types of Tunneling

Tunneling can occur through an insulating layer, I, between two normal materials (N–I–N), such as semiconductors, between a normal metal and a superconductor (N–I–S), or between two superconductors (S–I–S). Proximity junctions (S–N–S), in which the Cooper pair and quasiparticle transfer across the junction via the proximity effect, are discussed in Section VI.F. Junctions involving semiconductors, such as the S-Semicond and S-Semicond-S types, will not be discussed here (Furusaki *et al.*, 1991, 1992; Kastalsky *et al.*, 1991; van Wees *et al.*, 1991). The dc and ac Josephson effects involve particular types of tunneling phenomena across a barrier between two superconductors. In the next several sections we will examine energy level diagrams, and then provide a qualitative picture of various tunneling processes, concluding with a more quantitative presentation.

III. ENERGY LEVEL SCHEMES

Before we discuss the N–I–N, N–I–S, and S–I–S types of tunneling it will be instructive to examine the energy level systems that are involved in each. Two conventions for representing the energy levels will be introduced, called, respectively, the *semiconductor representation* and the *Bose condensation representation*.

A. Semiconductor Representation

A superconductor is considered to have an energy gap $E_g = 2\Delta$ between a lower energy band which is full of super electrons at absolute zero and an upper energy band which is empty at that temperature, as shown in Figs. 15.4a. At higher temperatures some of the electrons are raised from the lower band to the upper band as illustrated in Fig. 15.4b; these excited electrons are often referred to as *quasiparticles*. They act like normal conduction electrons, that is, they behave approximately like free electrons moving at the Fermi velocity v_F, as discussed in Chapter 1, Section II. When an electron jumps down from the bottom of the

quasiparticle band to the top of the super electron band, its energy falls by the amount 2Δ. Following conventional semiconductor terminology, we assign the equivalent Fermi energy to the center of the gap. This single-electron picture, called the semiconductor representation of a superconductor, does not take into account the phenomenon of electron pairing.

B. Boson Condensation Representation

Another way of representing a superconductor at $T = 0$ is by a single level for the super electrons, as shown in Fig. 15.5a. This is justified by the argument that the Cooper pairs which occupy this level are paired electrons with zero spin, and hence are boson particles which obey Bose-Einstein statistics. For bosons there is no Pauli exclusion principle, so it is possible for all of them to have the same energy. Thus the transition to the superconducting state is an example of boson condensation, a phenomenon that is explained in quantum mechanics texts. The condensation takes place when the electrons drop into the single-superconducting level where they exist as Cooper pairs, as shown in Fig. 15.5a. This mode of presenting the energy level diagram is called the *boson condensation representation*.

The Cooper-pair binding energy E_g is shared by two electrons, so that $\Delta = \frac{1}{2}E_g$ is the binding energy per electron. In this representation the Cooper-pair level is located a distance Δ below the bottom of the conduction band, as shown in Fig. 15.5. At absolute zero all the conduction electrons are condensed in the Cooper-pair level. Above absolute zero some of the pairs break up and the individual electrons are excited to the bottom of the conduction band, as shown in Fig. 15.5b. These electrons which are produced by the breakup of Cooper pairs are the quasi-particles mentioned above.

We will find the boson condensation representation a little more convenient than the semiconductor representation for analysis of the tunneling of super electrons. Before proceeding, however, let us say a few words about tunneling in general, after which we will comment on normal electron tunneling.

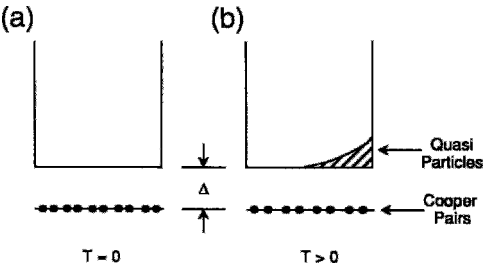

Figure 15.5 Boson condensation representation of the energy level occupancy of a superconductor (a) at $T = 0$, and (b) at $T > 0$, showing the level populations in the quasiparticle band for each case. Figure 15.4 presents the corresponding semiconductor representation.

IV. TUNNELING PROCESSES

We start with a brief qualitative description of the three types of tunneling processes, following it with a more detailed examination.

A. Conditions for Tunneling

Three conditions must be satisfied for tunneling to occur. First, there must be a barrier between the source and destination locations of the tunneling electrons preventing direct electron transport. Second, the total energy of the system must be conserved in the process, which is why single-electron tunneling occurs between levels that have the same energy on either side of the barrier. In two-electron tunneling, one electron gains as much energy as the other electron loses. Third, tunneling proceeds to energy states that are empty since otherwise the Pauli exclusion principle would be violated. A bias voltage that lowers the energy levels

on the positive side relative to levels on the negative side is often applied. This can serve to align occupied energy levels on one side of the barrier with empty levels on the other so as to enable tunneling between the two sides.

There are sign and direction rules that apply to the description of tunneling processes. When a metal (or superconductor) is positively biased relative to another metal, so that its potential is +V, its energy levels are lowered, as shown in Fig. 15.6b. The electron tunneling direction is toward the metal with the positive bias, but the tunneling current flows in the opposite direction, as indicated in the figure. This is because, by convention, current flow is expressed in terms of positive charges so that negatively charged

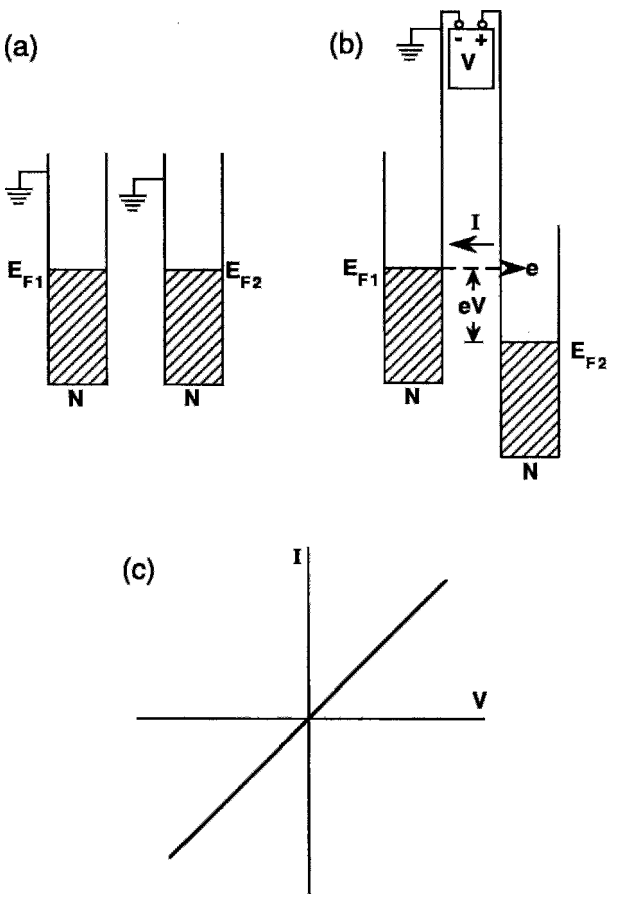

Figure 15.6 Normal metal tunneling showing (a) Fermi levels aligned for zero applied voltage, and hence zero tunneling current, (b) application of a positive bias voltage V to metal 2, lowering its Fermi level by eV relative to metal 1 and causing electrons to tunnel from left to right (metal 1 to metal 2), corresponding to current flow opposite in direction to the electron flow, as indicated by the arrows, and (c) linear dependence of the tunneling current on the applied voltage. Sketch (b) is drawn with metal 1 grounded, so that when the bias is applied, the Fermi level of metal 1 remains fixed while that of metal 2 falls.

electrons must flow in the opposite direction. Thus current flows toward the negative bias, as shown in Fig. 15.6c.

In drawing energy level diagrams, one of the two metals is normally grounded so that its Fermi level does not change when the bias is applied. The Fermi level falls for a metal that is biased positive relative to ground, and raised for one biased negative.

B. Normal Metal Tunneling

Consider two normal metals grounded at absolute zero and separated by an insulating barrier. Their Fermi levels are aligned as shown in Fig. 15.6a, so no tunneling occurs. A positive-bias voltage is then applied to one of the metals, lowering its energy levels, as shown in Fig. 15.6b, so that the electrons are now able to tunnel from the top of the conduction band of the grounded metal to the empty continuum levels of the positively biased metal, as shown. The number of empty levels that can receive electrons is proportional to the bias, so that the current flow is also proportional to it, as shown in Fig. 15.6c. The magnitude of the tunneling current is, of course, small compared to the current that flows in the absence of the barrier. Such a process satisfies the three conditions for tunneling—namely, presence of a barrier, energy conservation, and empty target levels.

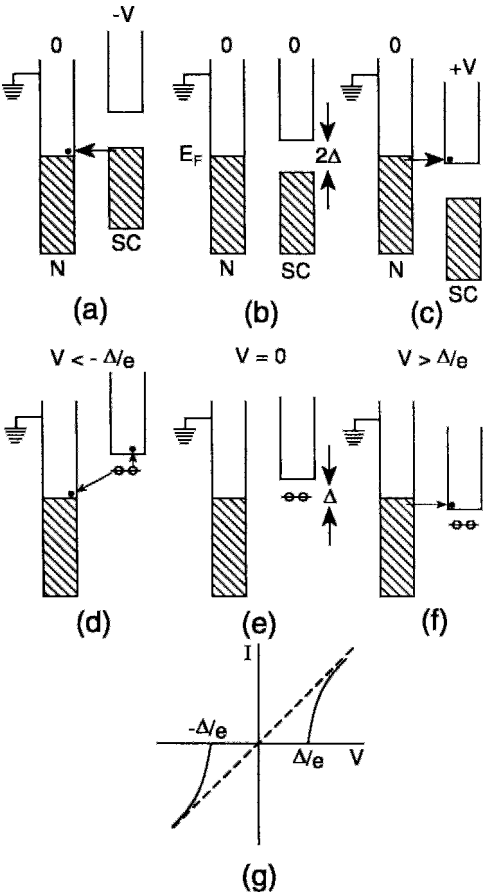

Figure 15.7 Normal metal–superconductor tunneling. The semiconductor representation shows (a) super electron tunneling (SC → N) for $V < -\Delta/e$, (b) zero tunneling current for the $V = 0$ case of the Fermi level in the gap ($-\Delta/e < V < \Delta/e$), and (c) normal electron tunneling (N → SC) for $V > \Delta/e$, which are also shown in the boson condensation representation (d), (e), and (f), respectively. The arrows show the electron tunneling directions, which are opposite to the current flow directions; the current–voltage characteristic is given in (g). The normal metal is grounded so that the superconductor bands shift downward when a positive bias is applied.

C. Normal Metal – Superconductor Tunneling

Next, we consider the case of an insulating barrier between a superconductor and a normal metal. N–I–S tunneling occurs through the processes outlined in Fig. 15.7, where the top three diagrams are the semiconductor representation and the three middle diagrams sketch the boson condensation representation. In the unbiased cases of Figs. 15.7b and 15.7e no tunneling occurs because there is no way for energy to be conserved by electrons tunneling to empty target levels. This is also true for the range $-\Delta/e < V < +\Delta/e$ of biases. For a positive bias, $V \geq \Delta/e$, electrons can tunnel from the conduction

band of the normal metal to the empty states above the gap of the superconductor, as shown in Figs. 15.7c and 15.7f. The figures appear similar in both representations because Cooper pairs do not participate.

For a negative bias, $V \leq -\Delta/e$, the process must be considered more carefully since the explanation is different in the two representations. In the boson condensation picture shown in Fig. 15.7d tunneling involves the breakup of a Cooper pair, with one electron of the pair tunneling down to the top of the normal-metal conduction band and the other jumping upward to the quasiparticle energy band of the superconductor. Thus the paired electrons separate to create a quasiparticle in the superconductor and transfer a conduction electron to the normal metal, with energy conserved in the process (Hu *et al.*, 1990; Rajam *et al.*, 1989; van den Brink *et al.*, 1991; Worsham *et al.*, 1991). Both electrons of the Cooper pair are accounted for. In the semiconductor representation, only the electron that is transferred to the normal metal is taken into account, as shown in Fig. 15.7a. This electron leaves behind it a hole in an otherwise filled band, it is this hole which constitutes the quasiparticle. Figure 15.7g shows how the experimentally measured current flow between the metal and the superconductor depends on the bias.

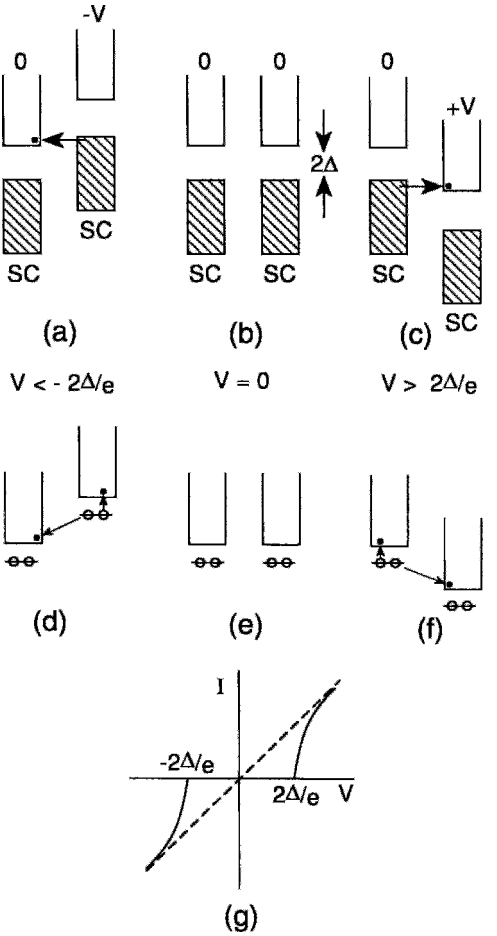

Figure 15.8 Superconductor-to-superconductor tunneling at absolute zero. The semiconductor representation shows (a) super electron tunneling for $V < -2\Delta/e$, (b) zero tunneling current for bias voltages in the range $-2\Delta/e < V < 2\Delta/e$, and (c) opposite-direction super electron tunneling for $2\Delta/e < V$, which are also shown in the boson condensation representation (d), (e), and (f), respectively, where the tunneling arises from the breaking of a Cooper pair. The current–voltage characteristic is given in (g). The arrows show the electron tunneling directions, which are opposite to the current flow directions. The sketches are drawn with the superconductor on the left grounded.

D. Superconductor – Superconductor Tunneling

Finally, let us consider the case of two identical superconductors. S–I–S tunneling occurs through the processes depicted in Fig. 15.8 for the two representations. Over the range of biases $-2\Delta/e < V < +2\Delta/e$ an electron in the semiconductor representation can tunnel from the super-conducting state of one superconductor to become a quasiparticle in the normal state of the other, as shown in Figs. 15.8a and 15.8c. This has its counterpart explanation in Figs. 15.8d and 15.8f where we see how a Cooper pair

in the higher of the two boson condensation levels can break up, with one electron jumping up to become a quasiparticle in its own excited level and the other electron jumping down to become a quasiparticle in the other super-conductor. As the bias voltage increases beyond the range $-2\Delta/e < V < +2\Delta/e$, the current increases abruptly in magnitude and then approaches its normal metal value, as indicated in Fig. 15.8g. The current voltage characteristic for two identical superconductors is, of course, antisymmetric about the point $V = 0$. By antisymmetric we mean that when $V \rightarrow -V$ we will have $I \rightarrow -I$. Note that the onset of tunneling for S–I–S junctions occurs at $V = \pm 2\Delta/e$, which is twice the value for the N–I–S case.

Figure 15.8 was drawn for the case $T = 0$. For a finite temperature there will be some quasiparticles in each superconductor, so that a small tunneling current will flow for bias voltages below $2\Delta/e$, as shown in Fig. 15.9 in the boson condensation representation (a) and in the semiconducting representation (b). The current–voltage characteristic is given in Fig. 15.9c.

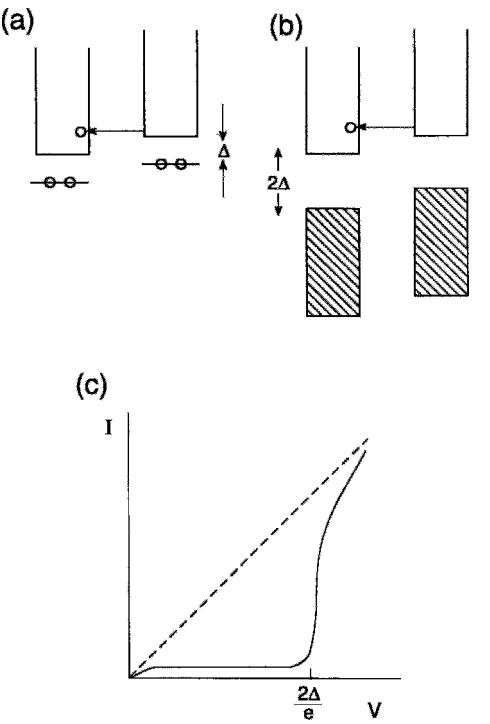

Figure 15.9 Superconductor-to-superconductor tunneling at finite temperatures, $T > 0$. The semiconductor representation (a) and boson condensation representation (b) show finite tunneling between upper quasiparticle levels sparsely populated by thermal excitation. The current–voltage characteristic (c) shows a small current flow for $0 < V < 2\Delta/e$, and the usual larger current flow for $2\Delta/e < V$.

V. QUANTITATIVE TREATMENT OF TUNNELING

The previous section discussed the different tunneling processes in terms of both the boson condensation and the semiconductor representations. The former seems to give a better physical picture of what is happening because it involves the breakup of Cooper pairs, whereas the latter provides a framework for carrying out quantitative calculations of the tunneling current as a function of temperature. We will now apply the Fermi statistics approach of Chapter 1, Section IX, to the semiconductor representation to derive quantitative expressions for the tunneling current.

A. Distribution Function

We explained in Chapter 1, Section IX, that the concentration of conduction electrons as a function of their energy is given by the product of the Fermi–Dirac (F–D) distribution function, *f(E)*, and the density of states, *D(E)*. We begin by expressing the former in a form that is convenient for treating tunneling problems, and then make use of the latter, which we write $D_n(E)$ for the normal electrons involved in the tunneling. The super electrons have a different density of states, $D_s(E)$, which was derived in Chapter 7, Section VI.

In Chapter 1, Section IX, we expressed the energies of a conductor relative to the Fermi energy E_F. In the present discussion it is convenient to select the Fermi level as the zero of energy, i.e., to set $E_F = 0$. With this in mind the F–D distribution of Eq. (1.35) for electrons assumes the form

$$f(E) = \frac{1}{\exp(E/k_B T) + 1}, \tag{15.2}$$

which at absolute zero equals 1 for negative energies and 0 for positive energies. The corresponding distribution function for unoccupied states, sometimes called holes, is $1 - f(E)$. If a bias voltage V is applied, the distribution function for electrons becomes

$$f(E + eV) = \frac{1}{\exp[(E + eV)/k_B T] + 1}, \tag{15.3}$$

and for holes is given by

$$1 - f(E + eV) = \frac{1}{1 + \exp[-(E + eV)/k_B T]}. \tag{15.4}$$

These distributions functions for $T > 0$ are plotted in Fig. 15.10 for zero, positive, and negative biases. Figure 1.4 shows the effect of temperature on the F–D distribution.

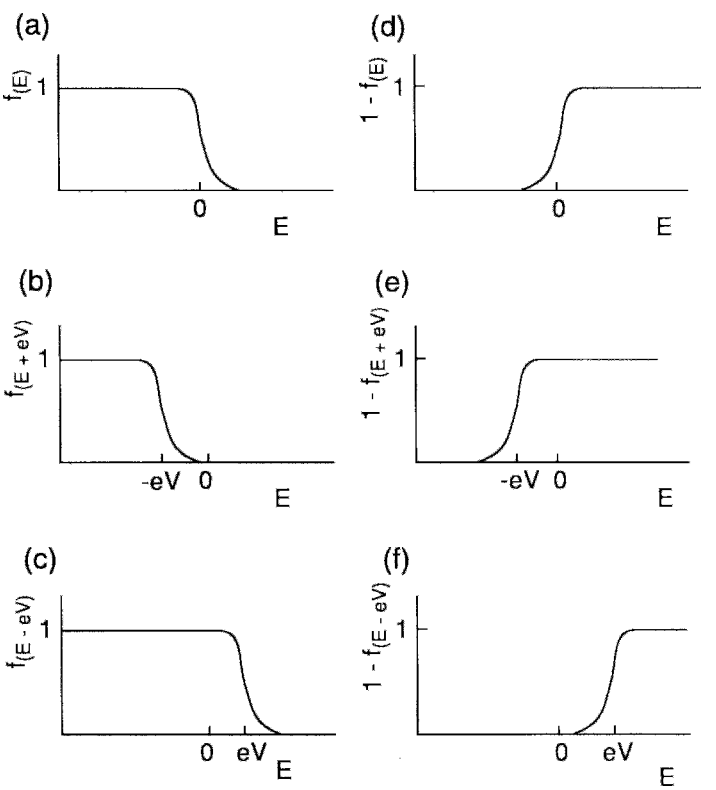

Figure 15.10 The dependence of the Fermi–Dirac distribution function *f(E)* on the energy for zero bias (a), positive bias (b), and negative bias (c). The dependence of the distribution function in the case of holes, $1 - f(E)$, on the energy for the same bias conditions (d, e, and f).

B. Density of States

Now that we have rewritten the F–D distribution functions relative to the zero of energy set at the Fermi level Eq. (1.41) should similarly be rewritten for the density of states $D_n(E)$ of normal electrons with this same zero of energy,

$$D_n(E) = D_n(0)\left(\frac{E_F + E}{E_F}\right)^{1/2}, \qquad (15.5)$$

where $D_n(0)$ is the density of states at the Fermi level ($E = 0$). Plots of $D_n(E)f(E)$ against the energy are shown in Fig. 1.7; we will make use of these plots with the zero of energy set at the Fermi level. Since E in Eq. (15.5) is usually very small compared with the Fermi energy $|E| \ll E_F$, and since the energies of interest are generally limited by the maximum applied bias voltage V_{max}, in tunneling calculations it is usually valid to write

$$D_n(E) \approx D_n(0) \qquad -eV_{max} < E < eV_{max}. \qquad (15.6)$$

The density of states in the superconducting state is given by the BCS expression (7.80)

$$D_s(E) = \begin{cases} \dfrac{D_n(0)|E|}{(E^2 - \Delta^2)^{1/2}} & E < -\Delta \quad (15.7) \\ 0 & -\Delta < E < \Delta \quad (15.8) \\ \dfrac{D_n(0)|E|}{(E^2 - \Delta^2)^{1/2}} & \Delta < E, \quad (15.9) \end{cases}$$

which is plotted in Fig. 7.4.

Another property of the density of states that has important implications for superconductivity is the conservation of states in k-space that was mentioned in Chapter 1, Section X. This is reflected in the conservation of energy levels at the onset of superconductivity. When a material becomes superconducting, an energy gap forms, with some energy states shifting upward above the gap and some falling below it, with the total number of states remaining the same, in the manner illustrated in Fig. 1.9. Comparing Eqs. (15.7) and (15.9) shows that the level spacing is the same just above and just below the gap. The area under the curve for $D(E)$ versus E, which is numerically equal to the total number of energy levels, is unchanged during the passage through T_c,

$$\int_{T>T_c} D_n(E)dE = \int_{T<T_c} D_s(E)dE. \quad (15.10)$$

We will use these expressions for $f(E)$ and $D(E)$ to write down an analytic expression for the tunneling current.

C. Tunneling Current

We begin by deducing a general expression for the tunneling current and then discuss the cases N–I–N, N–I–S, and S–I–S. Note, first, that in our qualitative discussion we were assuming that tunneling takes place in one direction only. A more careful analysis shows that it actually occurs in both directions, and that the net tunneling current is the difference between forward and backward tunneling processes.

Consider the case of a bias voltage V,

$$V = V_1 - V_2, \qquad (15.11)$$

applied to a metal–insulator–metal junction, M_1–I–M_2, as shown in Fig. 15.11, where each M can be a normal metal or a superconductor. To simplify the mathematics we treat the special case of metal 1 at the potential $V_1 = V$ and metal 2 at zero potential, $V_2 = 0$. Electrons can tunnel to the right with the current density J_{12} and to the left with the current density J_{21}, as shown. The tunneling current is, therefore,

$$I = (J_{12} - J_{21})A, \qquad (15.12)$$

where A is the area of the junction. Most electrons that impinge on the barrier from the left are reflected, but a few penetrate it, as

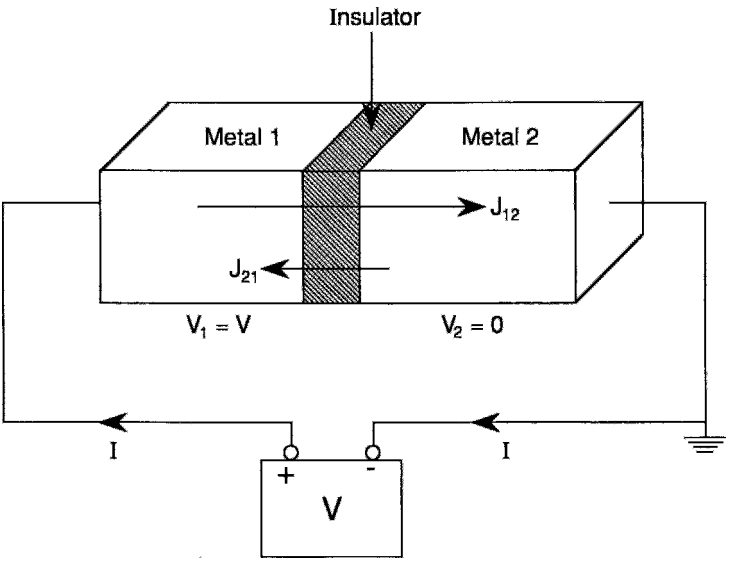

Figure 15.11 Metal-to-metal tunnel junction in the form of a thin uniform insulating layer between two metals M_1 and M_2. Tunneling current densities J_{12} and J_{21} in both directions are shown, with $J_{12} > J_{21}$ for the bias indicated.

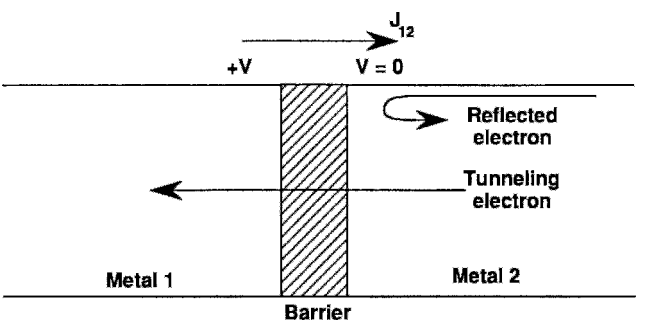

Figure 15.12 One electron reflected from, and another tunneling through, the insulating barrier of a tunnel junction for the bias of Fig. 13.11. The tunneling of the electron is in the direction from the negative to the positive side of the junction, but the corresponding current flow J_{12} is from + to − because it is based on the convention of positive-charge carriers.

illustrated in Fig. 15.12, and contribute to the tunneling current. We recall from quantum mechanics that Fermi's Golden Rule from time-dependent perturbation theory provides the probability per unit time W that an electron will undergo a transition from state 1 to state 2 in the energy range from E to $E+\Delta E$,

$$W_{1\to 2} = (2\pi/\hbar)|\langle 2|H_{\text{pert}}|1\rangle|^2\ \delta_2(E), \tag{15.13}$$

where

$$\delta_2(E) = D_2(E)[1 - f(E)] \tag{15.14}$$

is the "target" density of empty states in the energy range into which the electron tunnels. We assume that the tunneling matrix element H_{T},

$$H_{\text{T}} = H12 = H_{21}^{*}\langle 2|H_{\text{pert}}|1\rangle \tag{15.15}$$

of the perturbation Hamiltonian H_{pert} responsible for the penetration at the barrier can be evaluated. The tunneling current from metal 1 to metal 2 is related to the transition probability through the expression

$$J_{12} = e\int W_{1\to 2} D_1(E-eV) f(E-eV)\,dE$$
$$= \frac{2\pi e}{\hbar}\int |H_T|^2 D_1(E-eV) f(E-eV) \times D_2(E)[1-f(E)]\,dE, \qquad (15.16a)$$

where $W_{1\to 2}$ is given by Eq. (15.13). We note that the integrand is proportional to the overlap between the two densities of states. By the same reasoning, the tunneling current in the reverse direction, J_{21}, is

$$J_{21} = \frac{2\pi e}{\hbar}\int |H_T|^2 D_2(E) f(E) \times D_1(E-eV)[1-f(E-eV)]\,dE, \qquad (15.16b)$$

where again the integrand contains the density of states overlap. Inserting Eqs. (15.16a) and (15.16b) in Eq. (15.12) gives

$$I = \frac{2\pi eA}{\hbar}|H_T|^2 \int D_1(E-eV) D_2(E) \times [f(E-eV)-f(E)]\,dE \qquad (15.17)$$

for the total tunneling current I in the direction from metal 1 to metal 2, where it is assumed that the tunneling matrix element H_T is independent of the energy near $E=0$.

In this expression the density-of-states functions $D_1(E-eV)$ and $D_2(E)$ depend on the nature of the source and target states, whether they are normal or superconducting. The distribution function difference $[f(E-eV)-f(E)]$, on the other hand, depends only on the potential V, being close to 1 for energies between 0 and eV and approaching zero rapidly outside this range. Therefore, strong tunneling can occur only where $D_1(E-eV)$ and $D_2(E)$ are both appreciable in magnitude in this energy range. Weak tunneling could occur in the tails of the function

$$[f(E-eV)-f(E)]$$

just beyond this range. These characteristics will be illustrated in the next three sections for N–I–N, N–I–S, and S–I–S tunneling, respectively.

D. N–I–N Tunneling Current

Normal metal-to-normal metal tunneling depends mainly on the difference in the distribution functions

$$[f(E-eV)-f(E)],$$

since there is very little difference in the two normal metal densities of states. The analysis of this case is left as an exercise (see Problem 1).

E. N–I–S Tunneling Current

For tunneling between a normal metal and a superconductor, the normal-metal density of states $D_n(E-eV)$ can be approximated by $D_n(0)$ and factored out of the integral (15.17). N–I–S tunelling will then occur when the superconducting density of states $D_s(E)$ overlaps with

$$[f(E-eV)-f(E)].$$

At absolute zero $[f(E-eV)-f(E)]$ is 1 in the range $0 \le E \le eV$ and zero outside this range, so that for a positive bias, $V>0$, the integrand of (15.17) becomes

$$D_n(E-eV)D_s(E)[f(E-eV)-f(E)] = \begin{cases} -D_n(0)D_s(E) & \Delta < E < eV \\ 0 & \text{otherwise.} \end{cases} \qquad (15.18)$$

A similar reasoning shows that for a negative bias,

$$D_n(E-eV)D_s(E)[f(E-eV)-f(E)] = \begin{cases} -D_n(0)D_s(E) & -eV < E < -\Delta \\ 0 & \text{otherwise.} \end{cases} \tag{15.19}$$

With the aid of Eqs. (15.7)–(15.9) we see that Eq. (15.17) can be integrated in closed form, as shown in Problem 4, to give

$$I_{ns} = \begin{cases} G_n\left[V^2 - \left(\frac{\Delta}{e}\right)^2\right]^{1/2} & \frac{\Delta}{e} < V \\ 0 & \frac{-\Delta}{e} < V < \frac{\Delta}{e} \\ -G_n\left[V^2 - \left(\frac{\Delta}{e}\right)^2\right]^{1/2} & V < -\frac{\Delta}{e} \end{cases} \tag{15.20}$$

where G_n, which has the value

$$G_n = \left(\frac{2\pi A}{\hbar}\right)|H_T|^2 D_n(0), \tag{15.21}$$

is the normal metal electron tunneling conductance defined by

$$G_n = \frac{1_n}{V} \tag{15.22}$$

and plotted as on asymptotic (dashed) straight line in Figs. 15.7g, 15.8g, and 15.9c. The N–I–S tunneling current (15.20) is shown plotted in Fig. 15.7g. We see that as the voltage increases, the current approaches the normal conductor value. Experimentally determined plots of this type can be used to evaluate the energy gap Δ from N–I–S tunneling measurements.

The expression (15.20) is valid for absolute zero. For $T > 0$ the tails of the distribution function difference,

$$[f(E-eV)-f(E)],$$

produce weak tunneling for potentials $|V|$ in the gap close to the value Δ/e.

The significance of the overlap conditions in producing N–I–S tunneling is illustrated in Fig. 15.13. Figure 15.13a shows the lack of overlap when $|V| \ll \Delta/e$, so that no tunneling occurs. Figure 15.13b indicates the small overlap when V is in the gap near the edges and there is weak tunneling. Finally, Fig. 15.13c shows the strong overlap for $V > \Delta/e$ which produces strong tunneling. These figures should be compared with the more qualitative representations sketched in Fig. 15.7.

F. S–I–S Tunneling Current

Superconductor–superconductor tunneling is treated in a manner similar to the treatment we have just used for the N–I–S case. Unfortunately, in the S–I–S case the tunneling current equation (15.17) cannot be integrated in closed form, and instead we present the more qualitative treatment that is outlined in Fig. 15.14. We select $D_1(E-eV)$ as a superconductor with a small gap Δ_1 and $D_2(E)$ as a superconductor with a larger gap $\Delta_2 > \Delta_1$. As the bias voltage V is increased, the lower bands of D_1 and D_2 are made to coincide at a bias $V = (\Delta_2 - \Delta_1)/e$, as indicated in Fig. 15.14b, and also in the semiconductor and boson condensation representation plots of Fig. 15.15. This coincidence and the overlap of the bands results in weak tunneling because of the very low concentration of electrons in each level, and a small peak appears in the current versus voltage plot of Fig. 15.16b. The current is less on either side of the peak because the amount of overlap of the bands is less. The decrease of I with increasing V beyond the peak at finite temperatures constitutes a negative resistance region of the I-versus-V characteristic of Fig. 15.16b. At absolute zero this current vanishes, as indicated in Fig. 15.16a, because the quasiparticle levels are all empty.

We see from Figs. 15.14c and 15.15b that when the magnitude of the bias reaches the value $V = (\Delta_1 + \Delta_2)/e$, the densities of states $D_1(E)$ and $D_2(E)$ begin to overlap

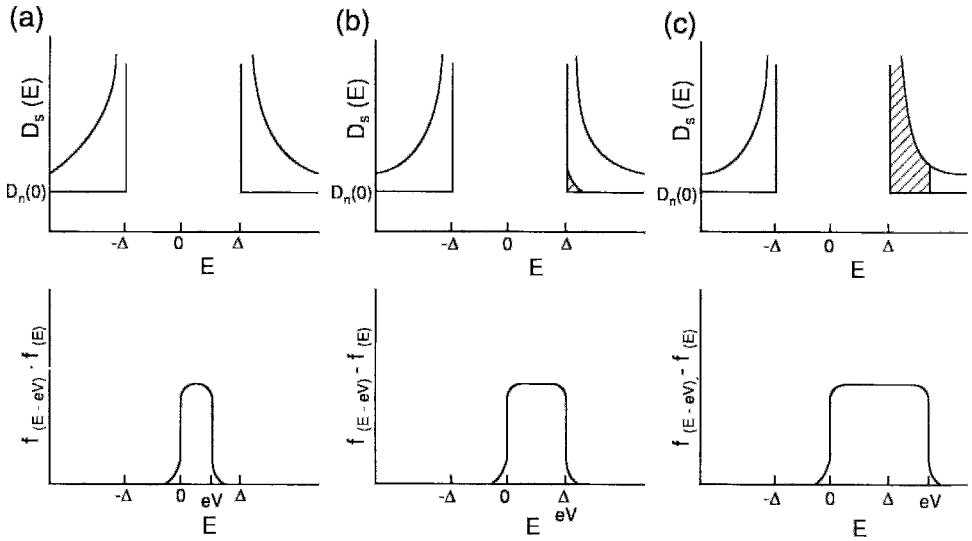

Figure 15.13 Contribution of the occupancy (shaded) of the superconductor density of states $D_s(E)$ to N–I–S tunneling for (a) small positive bias, $0 < V \ll \Delta/e$, and no tunneling current, (b) small bias, $V = \Delta/e$, for which the tail of the distribution function difference $[f(E-eV) - f(E)]$ overlaps $D_s(E)$, the occupancy of $D_s(E)$ is small, and a weak tunneling current flows, and (c) more positive bias, $V > \Delta/e$, producing a strong overlap so that the occupancy of $D_s(E)$ is large near the gap and a strong tunneling current flows.

at their infinity points, and there is a large jump in the tunneling current, as indicated in Figs. 15.16a for $T = 0$ and in Fig. 15.16b for $T > 0$. The tunneling current is now large because it flows from a nearly full level to a nearly empty level. An evaluation of the integral (15.17) at $T = 0$ and $V = (\Delta_1 + \Delta_2)/e$ gives for the jump in current as this bias

$$\Delta I_s = \frac{\pi G_n (\Delta_1 \Delta_2)^{1/2}}{2e}, \tag{15.23}$$

where G_n is the normal tunneling conductance defined by Eq. (15.22). In Problem 5 we show that the ratio of the jump in current ΔI_s to the normal tunneling current I_n at the bias $V = 2\Delta/e$ is given by

$$\Delta I_s / I_n = \frac{\pi}{4}, \tag{15.24}$$

which represents a jump of around 80%. Van Duzer and Turner (1981, p. 87) have shown that, for a finite temperature, this jump has the magnitude

$$\Delta I_s = \frac{\pi G_n \sqrt{\Delta_1 \Delta_2}}{4e} \times \frac{\sinh\left(\dfrac{\Delta_1 + \Delta_2}{2k_B T}\right)}{\left(\cosh \dfrac{\Delta_1}{2k_B T}\right) \cdot \left(\cosh \dfrac{\Delta_2}{2k_B T}\right)}, \tag{15.25}$$

which reduces to Eq. (15.23) for $T = 0$.

If the gaps are the same for the two superconductors, $\Delta_1 = \Delta_2 = \Delta$, there will be no maximum in the weak quasiparticle tunneling current, but such a weak current does flow for $V < 2\Delta/e$, as shown in Fig. 15.9. For $T \ll \Delta/k_B$, this current is given approximately by (Van Duzer and Turner, 1981, p. 87)

$$I_s = \frac{2G_n}{e}(\Delta + eV)\sqrt{\frac{2\Delta}{2\Delta + eV}} \times \sinh\left(\frac{eV}{2k_B T}\right) K_0\left(\frac{eV}{2k_B T}\right) e^{-\Delta/k_B T}, \tag{15.26}$$

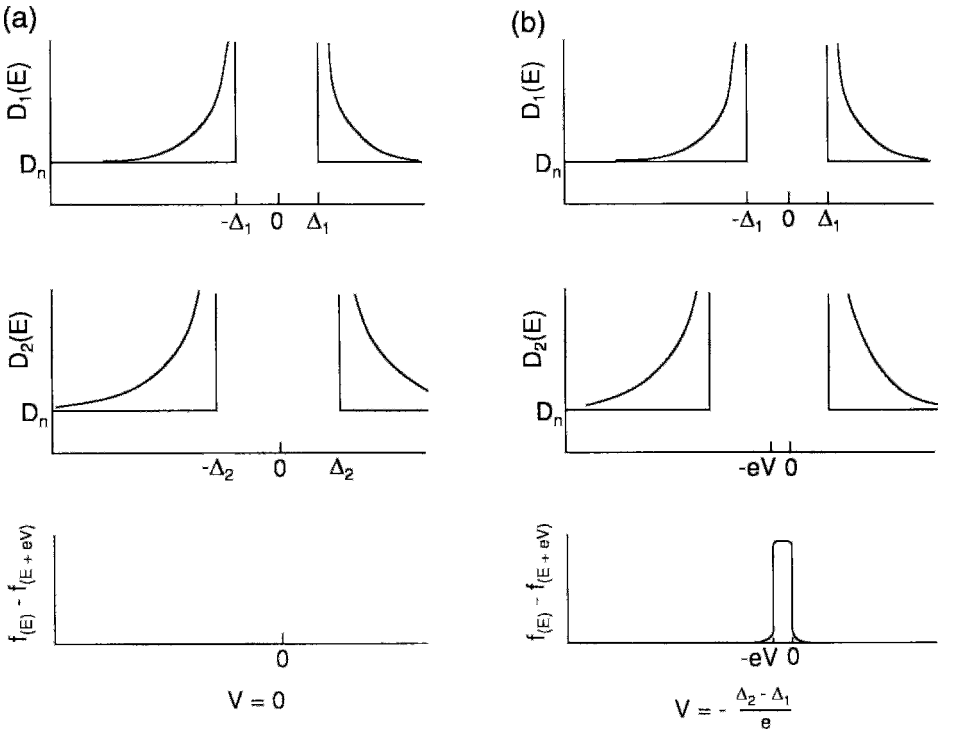

Figure 15.14 Densities of states for superconductor 1 (top) with the gap Δ_1, for superconductor 2 (middle) with the gap Δ_2, and distribution function difference (bottom) for (a) zero bias in which no tunneling current flows, (b) bias $V = (\Delta_2 - \Delta_1)/e$ producing weak tunneling current due to the overlap of the two quasiparticle bands, (c) bias $V = (\Delta_2 + \Delta_1)/e$ for onset of strong tunneling, and (d) bias $V \gg (\Delta_2 + \Delta_1)/e$ producing strong tunneling current due to the large overlap between the occupied superconductor band of the first superconductor and the empty quasiparticle band of the second superconductor. Quasiparticle tunneling (b) arises from the tail of the distribution function difference $f(E) - f(E + eV)$, hence is very weak and vanishes at absolute zero. Figure 13.13 presents energy-level diagrams for these four cases.

where K_0 is the zeroth-order modified Bessel function (cf. Chapter 12, Section III.B).

In Eq. (15.22) we defined the normal metal electron tunneling conductance G_n as the asymptotic slope of the I-versus-V characteristic curve for very large V. We can also define the differential conductance,

$$G_d = \frac{dI}{dV}, \tag{15.27}$$

which is the slope at any point of the I-versus-V curve. Many workers report their tunneling measurements as plots of G_d versus V. This has the advantage of providing greater resolution, since structural features tend to be better resolved in plots of differential conductance than in plots of I versus V (see example in Section VI.C, especially Fig. 15.24).

G. Nonequilibrium Quasiparticle Tunneling

So far we have assumed that the super electrons in the ground energy band and the quasiparticles in the excited band are in thermal equilibrium both between the bands and within each individual band. The tunneling process, of course, disturbs this equilibrium, but this effect is negligible.

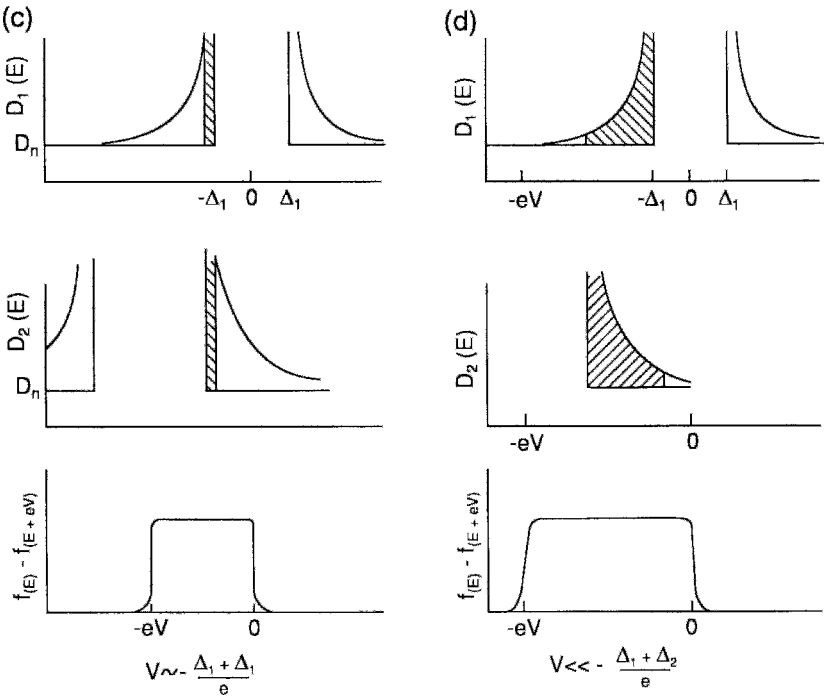

Figure 15.14 (*Continued*)

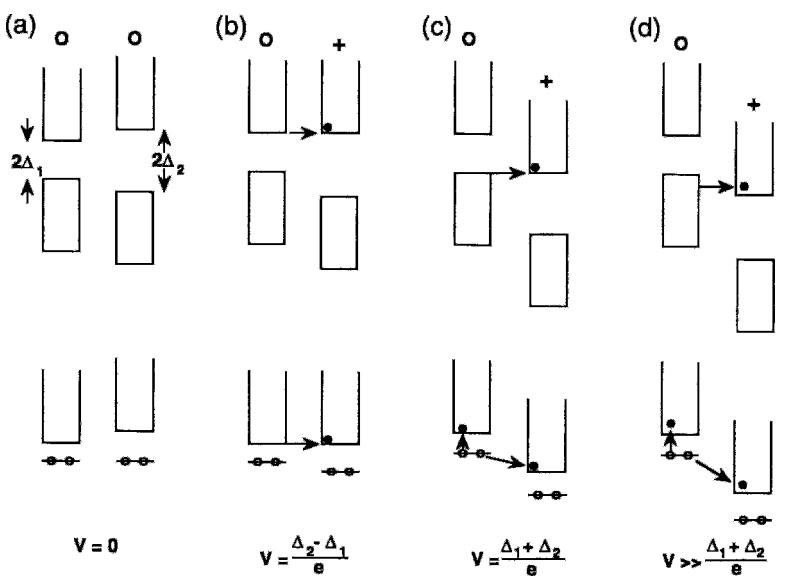

Figure 15.15 Semiconductor (top) and boson condensation (bottom) representations of the S–I–S tunneling cases of Fig. 15.14 for (a) zero bias, (b) quasiparticle band alignment and weak tunneling, (c) onset of Cooper pair tunneling, and (d) strong tunneling of Cooper pair electrons.

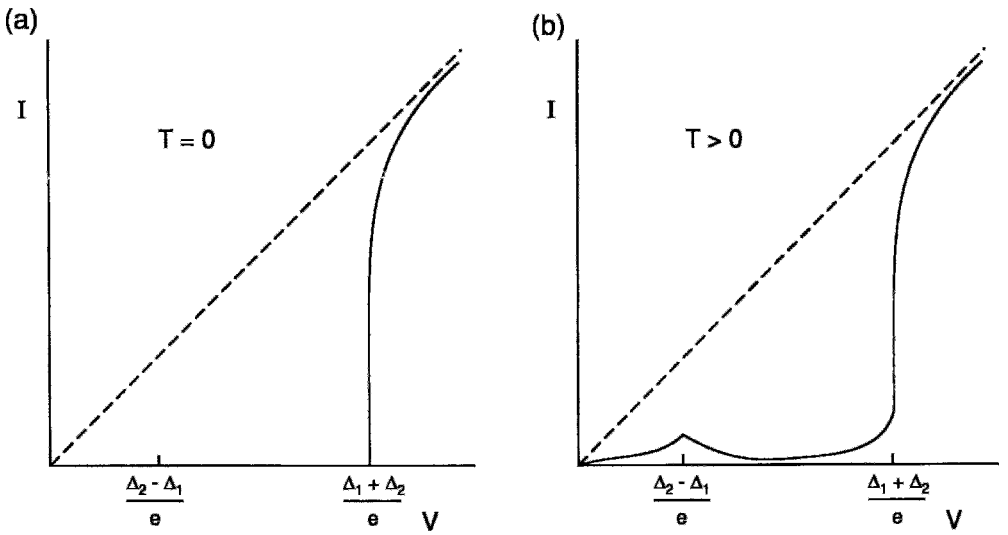

Figure 15.16 Tunneling current versus bias voltage for S–I–S tunneling involving two superconductors with energy gaps $\Delta_2 > \Delta_1$ for (a) $T = 0$, with no tunneling occurring until the bias $V = (\Delta_2 + \Delta_1)/e$ is reached, and (b) $T > 0$, with weak tunneling at the bias $V = (\Delta_2 - \Delta_1)/e$ and strong tunneling for $V > (\Delta_1 + \Delta_2)/e$.

We now wish to treat so-called branch imbalance, in which the number of quasiparticles n_+ with momentum in one direction, $\mathbf{p}_i$, is greater than the number of quasiparticles n_- with momentum in the opposite direction, $-\mathbf{p}_i$, in accordance with Fig. 15.17b. The imbalance $[n_+ - n_-]$ can be brought about by injecting quasiparticles across an N–I–S junction (Clarke, 1972).

When a quasiparticle imbalance exists in the neighborhood of a tunnel junction, a current flows.

$$I = e\frac{d}{dt}[n_+ - n_-], \tag{15.28}$$

to reestablish balance between the positive and negative momentum states in the quasiparticle band. Equilibrium is restored in a time τ_Q, called the *branch imbalance relaxation time*, and we can write

$$[n_+ - n_-] = \frac{I\tau_Q}{e}. \tag{15.29}$$

For temperatures near T_c the relaxation time is predicted, assuming a spacially uniform case, to have the temperature dependence (Schmid, 1968)

$$\tau_Q(T) \approx \tau_Q(T_c)\left(1 - \frac{T}{T_c}\right)^{-1/2}. \tag{15.30}$$

This relation has also been found experimentally (Clarke and Patterson, 1974).

A more extensive discussion of quasiparticle imbalance may be found in the works by Tinkham and Clarke (1972), and by Tilley and Tilley (1986).

H. Tunneling in unconventional superconductors

a. Introduction

Tunneling measurements have proved very useful in studying unconventional superconductors. Both Cooper-pair (Josephson) tunneling and single electron (quasiparticle) tunneling measurements are used. In particular, the measurement of the tunneling current between a superconductor and a normal metal may be utilized for the

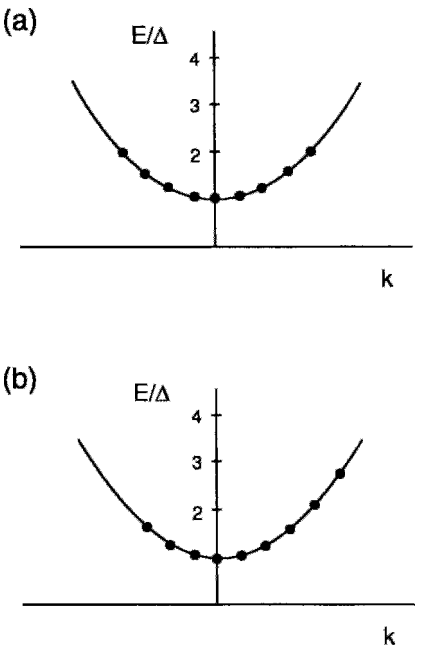

Figure 15.17 Branch imbalance illustrated using a one-electron energy parabola (a) for the usual case of no imbalance where the number of electrons with positive momentum is equal to the number of electrons with negative momentum, and (b) for the branch-imbalance state (number of electrons with positive momentum greater than numbers of electrons with negative momentum).

direct determination of the superconducting gap. If a superconductor is unconventional then directional tunneling measurements help to clarify the superconducting gap structure. Furthermore, Josephson tunneling between two superconductors one of which is unconventional can be used to probe the asymmetry of the superconducting phase, for example, by utilizing corner SQUID junctions (Van Harlingen, 1995, Tsuei and Kirtley, 2000). This is an example of so-called phase-sensitive experiments, which are very important in distinguishing between a highly anisotropic s-wave gap and a d-wave gap. For the former case the order parameter does not change sign anywhere on the Fermi surface, whereas in the latter case it does so.

In a simple tunneling experiment between a normal metal and a superconductor the conductance is related to the density of states, and the bias voltage is related to the energy offset from the Fermi level. Since the quasiparticle energy spectrum is gapped with a superconducting gap Δ, an s-wave superconductor shows technically zero conductance up to $V = \Delta/e$ where e is the electron charge. In unconventional superconductors with nodes the average over the Fermi surface of the quasiparticle energy spectrum is linearly proportional to the energy, and tunneling measurements do indeed reveal this structure. To refine the technique, one can use directional tunneling with small planar or point contacts. In this case the experiments probe the gap structure along a particular direction with respect to crystallographic axes, and reveal the gap anisotropy. Many modifications of tunneling geometries and contacts are employed. Ramp junctions and single grain boundaries, as well as a variety of combinations of insulating layers, have been utilized during the last decade.

As in any type of measurement, there are many complications in performing and interpreting the tunneling experiments. The main problems are the quality of the contacts, an incomplete knowledge of impurity distributions, distortions and stresses at the interface, and the uncertainty of the tunneling current distribution (so-called tunneling cone). As a result, there is still much controversy regarding the interpretation of various experiments. Many, sometimes conflicting, theories claim to describe the results. It will take some time and more experimental statistics on various superconducting systems for the situation to become clear.

b. Zero-Bias Conductance Peak

One of the signatures of a superconductor with nodes in tunneling measurements is the appearance of the zero-bias conductance peak arising from surface Andreev bound states (Greene *et al.*, 1998, Hu, 1998).

If quasiparticles scattered specularly off the interface can be Andreev-reflected by the pair potential then a hole will go back in the direction of the initial quasiparticle trajectory. Multiple scattering events at the interface lead to the formation of zero-energy (with respect to the Fermi level) Andreev bound states. Evidently, this interference with the pair potential is very sensitive to the phase of the superconducting wave function. In a d_{x2-y2} superconductor the effect is maximal for a (110) orientation with respect to the surface. In this case a quasiparticle reflected off the interface experiences a change in sign of the superconducting order parameter (maximum change of the pair potential), and the effect is maximal. As a result, the appearance of a large conductance via these available states at the gap center is possible, and this leads to the formation of the zero bias conductance peak.

The presence of Andreev bound states is not the only explanation for the experimentally observed conductance peak at zero-bias. A trivial explanation is the presence of a mesoscopic superconducting short circuit, and before Andreev physics became established the dominant theory had been the Appelbaum-Anderson model that invoked magnetic impurities at the interface.

A single zero-bias conductance peak is formed only when time-reversal symmetry is preserved. Therefore the application of a magnetic field splits the peak, as was observed experimentally. The problem is that a similar splitting occurs in the Appelbaum-Anderson model as well. In that case, however, it seems that the required fields are much larger, and the field dependence of the splitting is quite different from that in Andreev bound-state physics. Impurities tend to smear the peak, which may be why this peak splitting had not been seen in some earlier experiments carried out with an otherwise "correct" geometry.

Furthermore, in YBaCuO a spontaneous zero-bias conductance peak splitting has been observed below 8 K (Aubin *et al*., 2002, Greene *et al*., 2000, Greene *et al*., 1998). This was interpreted as involving spontaneous time-reversal symmetry breaking, and the creation of mesoscopic surface currents due to the bound states. Such a spontaneous change can be due to the crossover to a mixed symmetry state such as $s + id_{xy}$ or $d_{xy} + id_{x2-y2}$.

c. c-Axis Tunneling

In a pure d-wave superconductor the order parameter has lobes of equal area, but opposite sign. Therefore, the total Cooper pair tunneling current in the c-direction must be zero. However, if there is an s-wave admixture to the order parameter it must lead to the presence of a nonzero c-axis supercurrent. The experimental realization of this simple idea is not straightforward, and until now different groups have reported conflicting results. Various versions of this idea have been explored, including twisted junctions and grain boundaries (Tsuei and Kirtley, 2000).

VI. TUNNELING MEASUREMENTS

Let us now say a few words about the experimental arrangements used in carrying out tunneling experiments, followed by a discussion of representative experimental data that have appeared in the literature.

Tunneling, like photoemission, represents a surface-probe sampling of a region of dimensions determined by the coherence length (Cucolo *et al*., 1991; J.-X. Liu *et al*., 1991; Pierson and Valls, 1992), which, for high-temperature superconductors, can be only one or two unit cell dimensions in magnitude. Lanping *et al*. (1989) constructed a histogram of the distribution of gap parameters Δ determined from tunneling measurements made at 600 different surface locations on the same $YBa_2Cu_3O_{7-\delta}$ sample, obtaining values ranging from 15 to 50 meV, with several data points outside this range.

A. Weak Links

If a superconducting rod is cut at some point and then joined through an intervening insulating section, either (1) the insulating region will turn out to be so thick that the two separated superconducting sections lose contact and have no interaction, or (2) the insulator layer will consist of a monolayer of foreign atoms, so that strong contact is maintained across it, or (3) the section will be intermediate in thickness, so that the superconductors are weakly coupled and electrons can tunnel. The third case, called a *weak link*, is the one that is most commonly used for tunneling studies and Josephson effect measurements (Furusaki and Tsukada, 1991).

B. Experimental Arrangements for Measuring Tunneling

The overall structure at the interface between two superconductors or between a normal metal and a superconductors is called a *microbridge*. The barrier region is the crucial part of the microbridge. A typical barrier thickness is a coherence length or less in magnitude, so that barriers must be much thinner for high-temperature superconductors ($\xi \approx 2\,\text{nm}$) than for an element like lead ($\xi = 80\,\text{nm}$). Beenakker and van Houten (1991) discussed weak links that are quantum point contacts.

The original Zeller and Giaever technique (1969; Fulton *et al*., 1989; Giaever and Zeller, 1968) for making an Al–Al_2O_3–Al sandwich-type tunneling junction was to embed Sn particles in the aluminum oxide since Al oxidizes much faster than Sn, making it easier to form a thin insulating oxide layer on the tin. The preparation method shown in Fig. 15.18 consists in evaporation of a strip of aluminum film on a glass substrate, oxidizing the strip, evaporating tin on the film, and oxidizing once again. Then a second strip of aluminum at right angles to the first strip is evaporated on the substrate, as shown in the figure. An arrangement of the Sn particles for four different samples is shown in the electron micrographs of Fig. 15.19. The final asymmetric feed configuration arrangement is sketched in Fig. 15.20, with the details of the junction area indicated in Fig. 15.21 (Florjanczyk and Jaworski, 1989; Monaco, 1990a, b). To make a tunneling measurement, a bias voltage is applied across the junction using two of the leads, with the current monitored at the other two leads, as shown. Sandwich-tunnel junctions of this type have been made for many S–I–S and N–I–S cases using various

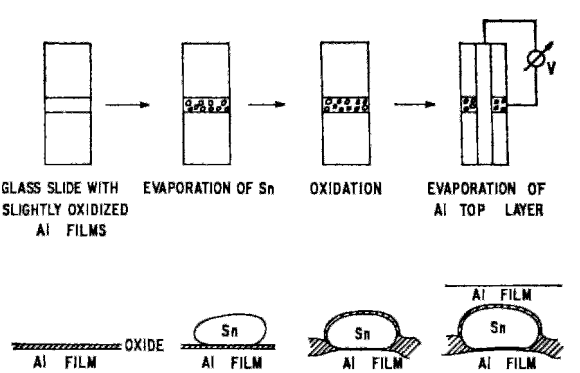

Figure 15.18 Preparation of a tunnel junction containing tin particles. Aluminum oxidizes faster than tin, so that the oxide layer is thicker between the particles than on their surface, as indicated (Zeller and Giaever, 1969).

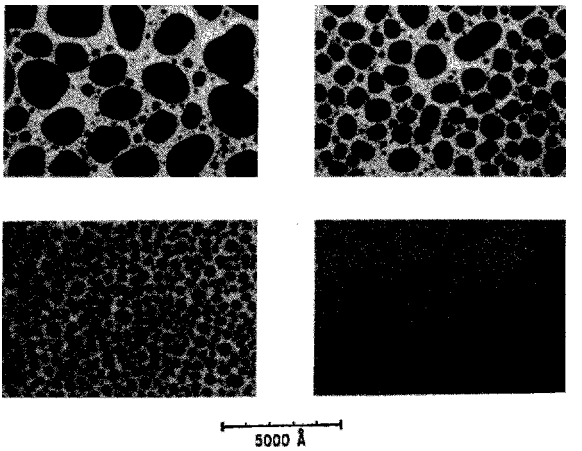

Figure 15.19 Electron micrograph of tin particles on an oxidized aluminum film for four particle sizes (Zeller and Giaever, 1969).

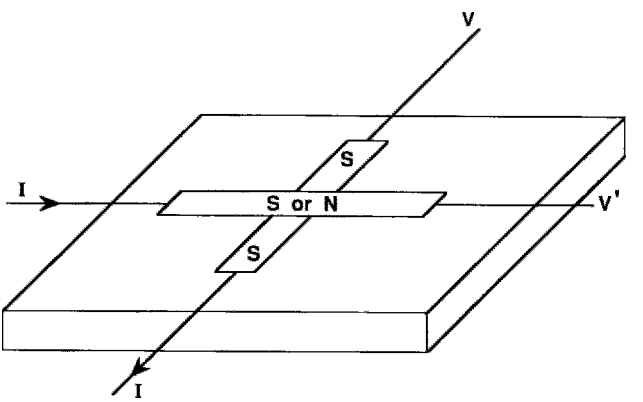

Figure 15.20 Sketch of tunnel junction on a glass substrate, showing current (I) and applied bias voltage (V, V') leads.

combinations of super-conducting and normal metals, but the use of embedded particles, such as Sn, to control the film thickness is not generally employed.

Another common technique for tunneling measurements employs a scanning electron microscope (SEM). A probe ground to a point with a very small tip radius makes contact with the superconductor surface, as indicated in Fig. 15.22a (typical probe materials are Au, Nb, Pt–Rh, Pt–Ir, and W.) The tip touches the surface, or comes very close to it. If contact is made, tunneling probably takes place through a layer of inhomogeneous insulating or semiconducting material, such as the oxide coating the surface. Tunneling can also occur at a constriction, as shown in Fig. 15.22b.

Mooreland's group developed what they call a break junction technique for tunneling measurements (Mooreland *et al.*, 1987a, b). A small piece of bulk material is electromechanically broken under liquid helium and the freshly fractured interfaces

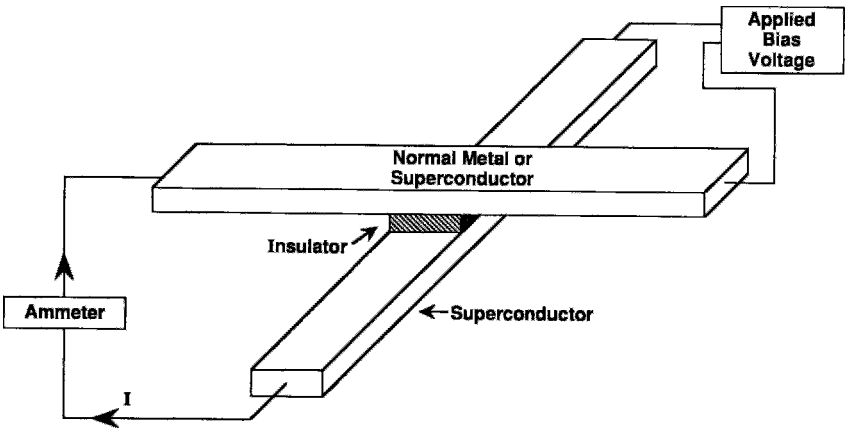

Figure 15.21 Details of the tunnel junction sketched in Fig. 15.20, showing the insulating layer between the metal strips. The ammeter measures the tunneling current produced by the bias voltage.

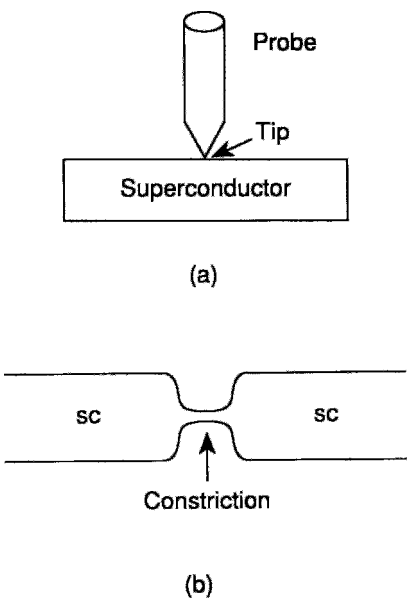

Figure 15.22 Tunnel junction formed from (a) a probe tip in contact with, or almost in contact with, the superconducting surface, and (b) a constricted region in a superconductor.

joined to form a tunneling barrier with the liquid helium acting as insulator.

We will now present some typical experimental tunneling measurements that were made using these techniques.

C. N–I–S Tunneling Measurements

Gallagher *et al.* (1988) made an N–I–S tunneling study of $YBa_2Cu_3O_7$ using a scanning tunneling microscope operating in liquid helium. A coarse-adjust screw and fine-adjust piezoelectric transducer provided the desired tip-to-sample contact, where the tip is embedded in an insulating surface layer with a typical 1 MΩ resistance, which causes the junction to end up in the tunneling regime. Figure 15.23 shows the I-versus-V characteristic made with an Nb tip and Fig. 15.24 the dI/dV-versus-V characteristic for a similar sample made using a W tip. Note the increased resolution of the differential curve.

Ekino and Akimitsu (1989a, b) reported point-contact electron tunneling studies of BiSrCaCuO and BiSrCuO bulk, monocrystal, and sputtered film samples. Figure 15.25 presents the I versus V differential conductance plot for the 2 : 2 : 2 : 3 sample, and we again see that the differential data exhibit much more structure.

D. S–I–S Tunneling Measurements

Figure 15.26 shows some experimental data on tunneling across the $Al–Al_2O_3–Al$ junction formed from an oxide layer between

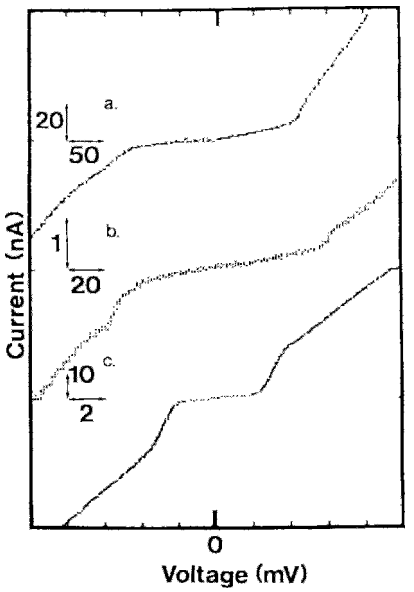

Figure 15.23 Current–voltage characteristics at different positions on the surface of aluminum-doped $YBa_2Cu_3O_{6.5+x}$ determined by scanning tunneling microscopy using an Nb tip at 4.2 K. A jump in the current is observed at 95, 30, and 2.5 mV, respectively. Note the changes in scale for each curve (Gallagher *et al.*, 1988).

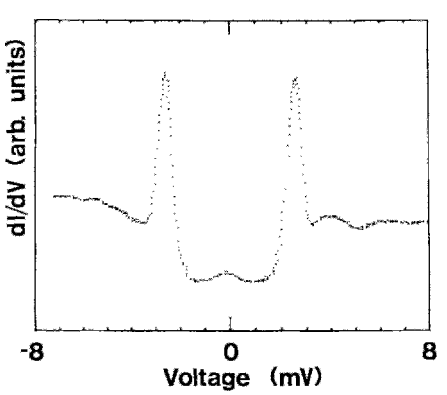

Figure 15.24 Recording of dI/dV obtained for $YBa_2Cu_3O_{6.5+x}$ at 4.2 K using a tungsten tip (Gallagher *et al.*, 1988).

two aluminum samples with $T_c = 1.25$ K. We see from the figure that quasiparticle tunneling is negligible at $T = 0$, becoming dominant just below $T = T_c$. The jump in current at $V = 2\Delta/e$ and $T = 0$ appears to be less than the expected 80%.

E. Energy Gap

We saw in Sections IV.C and IV.D, respectively, that N–I–S tunneling occurs for biases with magnitudes greater than Δ/e, and that S–I–S tunneling occurs for biases exceeding $2\Delta/e$, as indicated in Figs. 15.7 and 15.8. The abrupt rise in current at these biases gives us the superconducting energy gap Δ. When the two superconductors that form an S–I–S junction have different gaps Δ_1 and Δ_2, a finite temperature tunneling measurement can give us the values of both gaps, as pointed out in Section V.F and indicated in Fig. 15.16. Thus a tunneling experiment provides a convenient way of measuring the energy gap.

As an example of a gap determination, note that the peaks on the derivative N–I–S tunneling curve of Fig. 15.24 are separated by 5 meV, which gives $2\Delta \approx 5$ meV. The inset of Fig. 15.25 shows the I^2 versus V^2 plot of Eq. (15.22), giving us the value of the energy gap Δ from the intercept at zero current. The temperature dependence of the energy gap, $\Delta(T)$, obtained by fitting the tunneling data to a broadened BCS density-of-states function,

$$D(E) = \mathrm{Re}\left\{\frac{E - i\Gamma}{[(E - i\Gamma)^2 - \Delta^2]^{1/2}}\right\}, \quad (15.31)$$

where Γ is the gap broadening parameter, provided a good fit to the experimental data for two Bi superconductors, as shown in Fig. 15.27. However, the ratio

$$2\Delta/k_B T_c \approx 10.5$$

is about three times the BCS value of 3.53. Plots similar to Fig. 15.27 have been reported elsewhere (e.g., Ekino and Akimitsu, 1990; Escudero *et al.*, 1989, 1990a; Flensberg and Hansen, 1989).

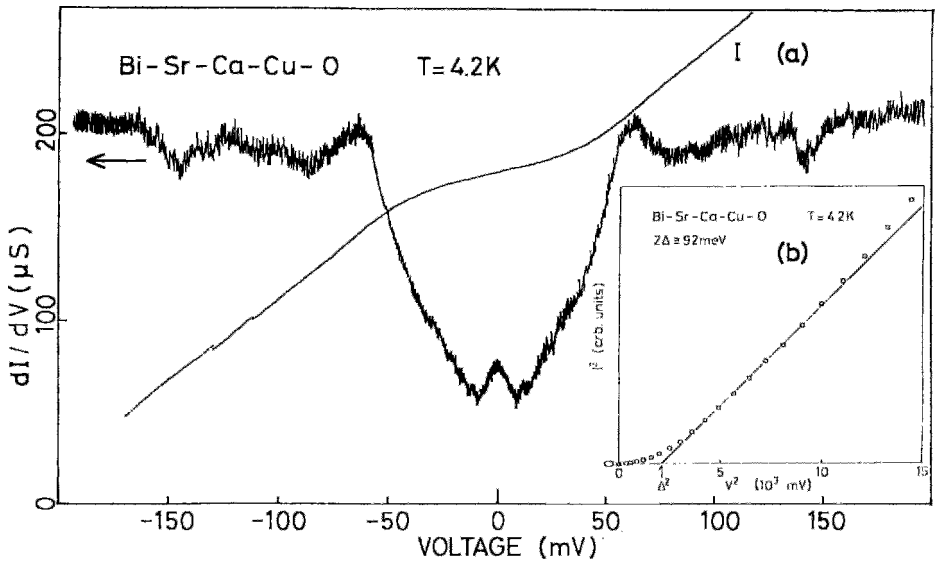

Figure 15.25 Current–voltage and dI/dT characteristic curves of $Bi_2Sr_2Ca_2Cu_3O_{10}$ determined by point contact tunneling. The inset shows a plot of I^2 versus V^2 made from the I-versus-V curve (Ekino and Akimitsu, 1989a).

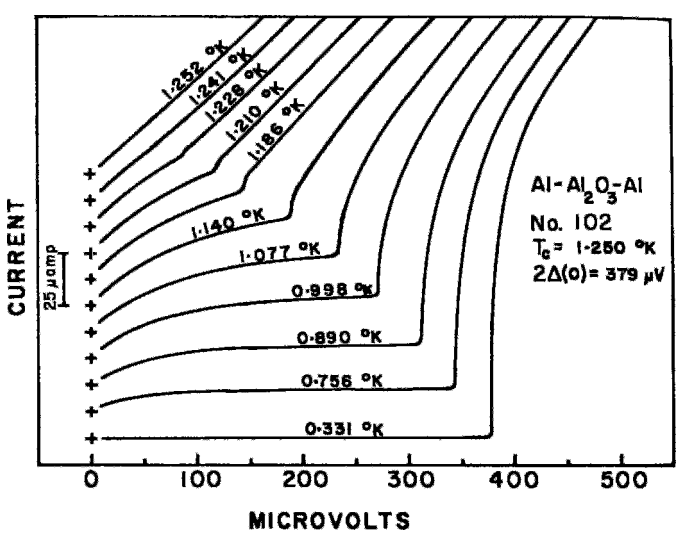

Figure 15.26 Current–voltage measurements on an Al–Al_2O_3–Al tunnel junction. Zero-current positions for each curve are staggered for clarity (Blackford and March, 1968).

Figure 15.26 shows S–I–S tunneling with the sharp rises occurring at the values $2\Delta(T)$. We see from the figure that the gap $2\Delta(T)$ decreases with temperature, as expected. The ratio $2\Delta/k_B T_c = 3.52$ is almost precisely the BCS value.

The ratio $2\Delta(0)/k_B T_c$ has been reported in the range 2–10 for high-temperature super-

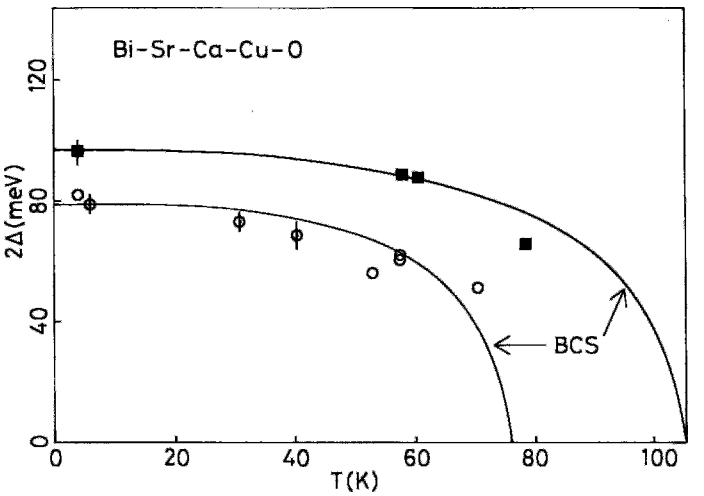

Figure 15.27 Temperature dependence of the energy gap 2Δ of $Bi_2Sr_2CaCu_2O_8$ (○) and $Bi_2Sr_2Ca_2Cu_3O_{10}$ (■) obtained by point-contact tunneling. Some of the data points have vertical error bars. The solid lines are fits to a broadened BCS density of states (Ekino and Akimitsu, 1989a).

conductors (Mattis and Molina, 1991); the older superconductors usually had valves near the range 3–5 (Schlesinger *et al.*, 1990a), much closer to the BCS value of 3.54. Figure 15.28 shows the dependence of $\Delta(0)$ on T_c for several high-temperature superconductors, all with reported ratios $2\Delta(0)/k_BT_c \approx 6$ (Takeuchi *et al.*, 1989).

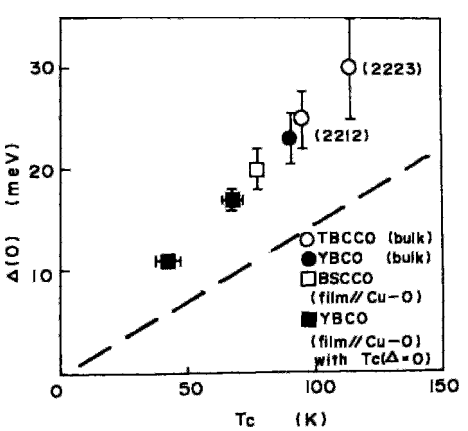

Figure 15.28 Correlation of the energy gap $\Delta(0)$ with the transition temperature T_c for bulk $YBa_2Cu_3O_7$ (YBCO), two $YBa_2Cu_3O_7$ films with tunneling in the Cu–O plane direction, $Bi_2Sr_2CaCu_2O_8$ (BSCCO) film with tunneling in the Cu–O plane direction, bulk $Tl_2Ba_2CaCu_2O_8$ (TBCCO, 2212), and bulk $Tl_2Ba_2Ca_2Cu_3O_{10}$ (2223). The dashed line is drawn for the BCS slope $2\Delta(0)/k_BT_c = 3.53$ (Takeuchi *et al.*, 1989).

The energy gaps of high-temperature superconductors are anisotropic (Bulaevskii and Zyskin, 1990; Mahan, 1989; Spalek and Gopalan, 1989), being much larger in the a, b-plane than in the c direction. Some reported values are $2\Delta_{ab} \approx 6.2k_BT_c$ and $2\Delta_c \approx 2k_BT_c$ for $(La_{1-x}Sr_x)_2CuO_4$ (Kirtley, 1990a, b), $2\Delta_{ab} \approx 8k_BT_c$ and $2\Delta_c \approx 2.5k_BT_c$ for $YBa_2Cu_3O_{7-\delta}$ (Collins *et al.*, 1989a), $2\Delta_{ab} \approx 8k_BT_c$ for $Bi_2Sr_2CaCu_2O_{8-\delta}$, and $2\Delta_{ab} \approx 8k_BT_c$ and $2\Delta_c \approx 4k_BT_c$ for $Ba_{0.6}K_{0.4}BiO_3$ (Schlesinger *et al.*, 1990a; see also Kussmanl *et al.*, 1990; Takada *et al.*, 1989). The existence of these high anisotropies could account for much of the scatter in the reported gaps for the high-temperature superconductors.

F. Proximity Effect

We have been discussing the effect of an insulating layer between a normal metal and a superconductor or between two superconductors. If no intervening layer is present,

another effect, called the *proximity effect*, comes into play. The direct contact at the junction and the overlap of wave functions causes the density n_s of electron pairs to differ in the neighborhood of the surface from its value in the bulk. At an N–S interface some electron pairs leak into the normal metal while some quasiparticles leak into the superconductor, thereby reducing the transition temperature of the superconductor. The proximity effect can cause two superconductors with different T_c that are in contact with each other to exhibit the same intermediate T_c. Theoretical treatments of this effect, such as the tunneling approach of McMillan (DiChiara *et al.*, 1991, 1993; Kadin, 1990; McMillan, 1968; Noce and Maritato, 1989; Stephen and Carbotte, 1991) have been published.

To elucidate this T_c reduction, an experimental study of composite films (Werthamer, 1963) was undertaken, each film consisting of a superconductor of thickness d_s and a normal metal of thickness d_n. Figure 15.29 shows a plot of the critical temperature T_c' of layered PbCu composite relative to $T_c = 7.2\,\mathrm{K}$ of bulk Pb versus the Cu layer thickness d_n for various thickness d_s of Pb. The reduction of the critical temperature is small for super-conductor layer thicknesses greater than the coherence length $\xi = 80\,\mathrm{nm}$ irrespective of the normal layer thickness. The data show that there is a characteristic thickness $L_n \approx 40\,\mathrm{nm}$ of the normal layer beyond which ($d_n > L_n$) there is no additional reduction of the transition temperature. Van Duzer and Turner (1981, p. 301) associate this effect with the diffusion constant D of the normal metal through the expression

$$L_n = (\hbar D/2\pi k_B T)^{1/2}. \qquad (15.32)$$

The thinnest sample studied, $d_s = 7\,\mathrm{nm}$, went normal before this characteristic could be attained. Figure 15.30 shows how the limiting value of T_c' obtained from Fig. 15.29 for the condition $d_n > L_n$ depends on the superconducting layer thickness.

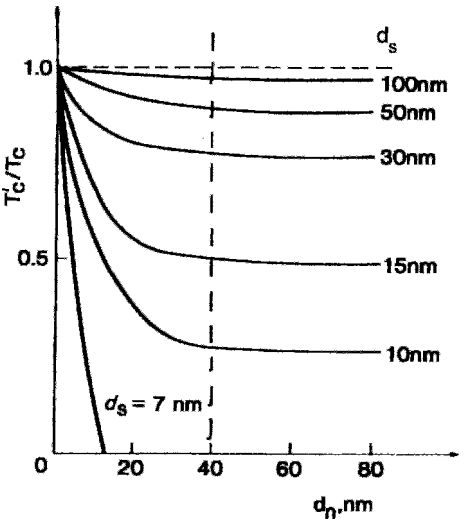

Figure 15.29 Proximity effect for a PbCu composite illustrating how the critical temperature T_c' of superconducting Pb in a copper–lead composite relative to T_c of bulk lead depends on the Cu film thickness d_n for several Pb film thickness d_s from 7 to 100 nm. The vertical dashed line indicates the characteristic thickness L_n (adapted from Werthamer, 1963).

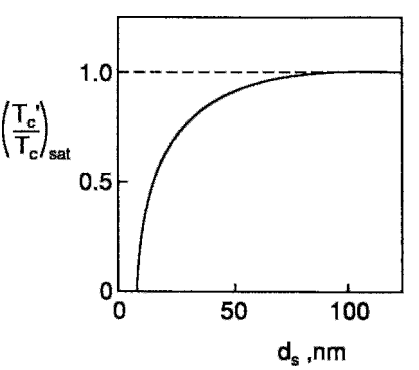

Figure 15.30 Dependence of the limiting value of the relative transition temperature $(T_c'/T_c)_{sat}$ of the PbCu composite of Fig. 15.29 on the thickness d_s of the superconducting component Pb (data from Fig. 15.29).

Similar experiments have been carried out with layers of the superconductor $YBa_2Cu_3O_{7-\delta}$ containing N_y Cu–O layers ($\frac{1}{2}N_y$ unit cells thick) adjacent to N_{Pr} Cu–O layers of the nonsuperconducting material

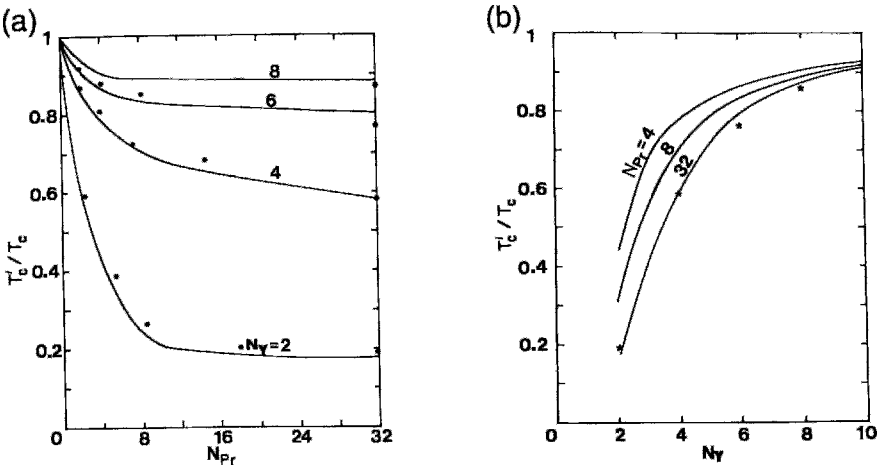

Figure 15.31 Normalized transition temperature T_c'/T_c of $YBa_2Cu_3O_{7-\delta}/PrBa_2Cu_3O_{7-\delta}$ layers plotted (a) versus the number of Cu–O planes N_{Pr} in $PrBa_2Cu_3O_{7-\delta}$, and (b) versus the number of Cu–O planes N_Y in $YBa_2Cu_3O_{7-\delta}$. The calculated curves are drawn to fit the data points (Wu *et al.*, 1991a).

$PrBa_2Cu_3O_{7-\delta}$. The calculations by Wu *et al.* (1991a), which are compared in Fig. 15.31 with the experimental data of Lowndes *et al.* (1990), provide results comparable with those presented in Fig. 15.29. Layered compounds are useful for studying other properties as well, such as resistivity (Minnhagen and Olson, 1992). Radousky (1992) reviewed the superconducting and normal state properties of the $Y_{1-x}Pr_xBa_2Cu_3O_{7-\delta}$ system.

Proximity junctions are (S–N–S) Josephson junctions in which the Cooper pair and quasiparticle transfer arises from the proximity effect (Agrait *et al.*, 1992; Braginski, 1991; Claasen *et al.*, 1991; Gijs *et al.*, 1990a; Han *et al.*, 1990a; Harris *et al.*, 1991; Jung *et al.*, 1990; Klein and Aharony, 1992; Maritato *et al.*, 1988; Polturak *et al.*, 1991; J. Yu *et al.*, 1991). Studies have also been carried out on S-Semicond-S or S-Semicond junctions (Furusaki *et al.*, 1991, 1992; Kastalsky *et al.*, 1991; Kleiner *et al.*, 1992; van Wees *et al.*, 1991) and arrays (Hebboul and Garland, 1991; Kwong *et al.*, 1992; Lerch *et al.*, 1990; Sohn *et al.*, 1992).

G. Even–Odd Electron Effect

Measurements of single-electron tunneling through a small superconducting island of volume 3×10^6 containing 6×10^8 conduction electrons exhibited a $2e$ periodicity in the tunneling current for $T < 0.2T_c$. Such a parity effect arises from the electron pairing, whereby the free energy of the superconducting island depends on whether there is an even or odd number of electrons in the island (Tuominen *et al.*, 1993).

VII. JOSEPHSON EFFECT

Until now we have been discussing the participation of quasiparticles in tunneling. The S–I–S processes that have concerned us included the strong tunneling current that flows between an occupied super electron band and an empty quasiparticle band (S → Q), as well as the relatively weak tunneling between two quasiparticle bands (Q → Q). There is also a third case—tunneling between two occupied super electron bands at zero bias (S → S). In this process there is transfer of Cooper pairs across the junction through an

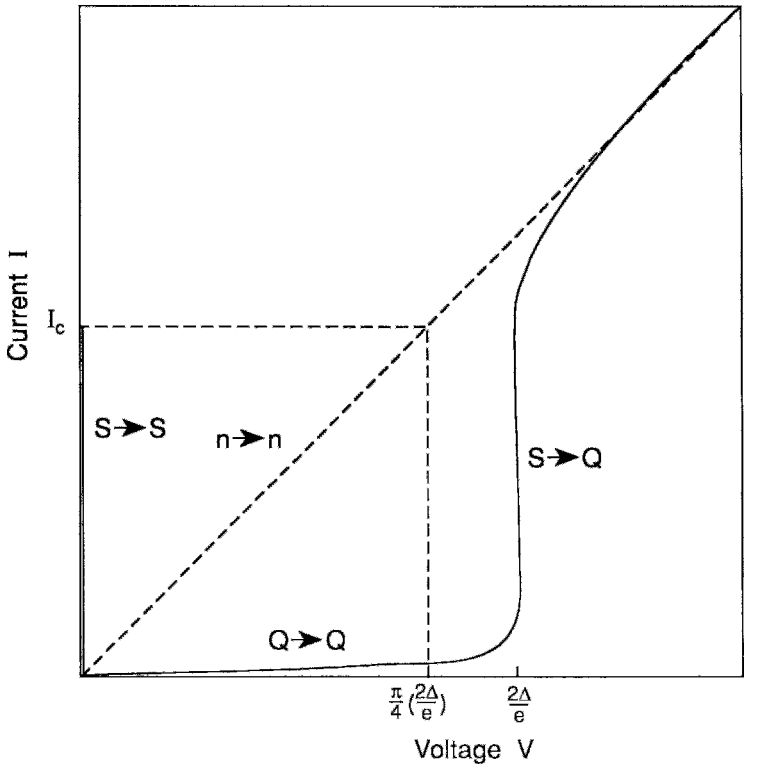

Figure 15.32 Current–voltage characteristic curves for tunneling via the S → S, Q → Q, and S → Q processes. All three processes follow the linear n → n tunneling slope at high voltages, above $2\Delta/e$.

effect predicted by Josephson in 1962 and observed experimentally shortly thereafter (Anderson and Rowell, 1963). Figure 15.32 compares these processes. In the following treatment we assume that the Josephson junction is of the weak-link type referred to in Section VI.A.

A. Cooper Pair Tunneling

When two superconductors are separated by a thin layer of insulating material, electron pairs are able to tunnel through the insulator from one superconductor to the other. There are four modes of pair tunneling: (1) the dc Josephson effect, or flow of a dc current $J = J_0 \sin\phi$ across the junction in the absence of an applied electric or magnetic field, where ϕ is a phase factor and J_0 the maximum zero voltage current, (2) the ac Josephson effect, relating to the flow of a sinusoidal current, $J = J_0 \sin[\phi–(4\pi eVt/h)]$, across a junction with an applied voltage V, where $\nu = 2eV/h$ is the frequency of oscillation, (3) the inverse ac Josephson effect, whereby dc voltages are induced across an unbiased junction by incident radiation or an impressed rf current, and (4) macroscopic quantum interference effects, involving a tunneling current J with an oscillatory dependence on the applied magnetic flux $\sin(\pi\Phi/\Phi_0)$, where Φ_0 is the quantum of magnetic flux.

B. dc Josephson Effect

In deriving the basic equations for the dc Josephson effect we follow the classic

approach of Feynman (1965). Consider two superconductors, 1 and 2, separated by an insulating barrier, as shown in Fig. 15.11. If the barrier is thick enough so that the superconductors are isolated from each other, the time-dependent Schrödinger equation for each side is

$$i\hbar\frac{d\Psi_1}{dt} = H_1\Psi_1, \tag{15.33a}$$

$$i\hbar\frac{d\Psi_2}{dt} = H_2\Psi_2, \tag{15.33b}$$

where Ψ_i and H_i are the wavefunctions and Hamiltonians on either side of the barrier. We assume that a voltage V is applied between the two superconductors. If the zero of potential is assumed to occur in the middle of the barrier between the two superconductors, superconductor 1 will be at the potential $-\frac{1}{2}V$ with Cooper-pair potential energy +eV, while superconductor 2 will be at the potential $+\frac{1}{2}V$ with Cooper-pair potential energy $-eV$. (The factor of $\frac{1}{2}$ does not appear in the potential energy terms because the charge of each Cooper pair is $2e$.)

The presence of the insulating barrier couples together the two equations,

$$i\hbar\frac{d\Psi_1}{dt} = eV\Psi_1 + K\Psi_2, \tag{15.34a}$$

$$i\hbar\frac{d\Psi_2}{dt} = -eV\Psi_2 + K\Psi_1, \tag{15.34b}$$

where K is the coupling constant for the wavefunctions across the barrier. Since the square of each wavefunction is the probability density that super electrons are present, the two wavefunctions can be written in the form

$$\Psi_1 = (n_{s1})^{1/2}e^{i\Theta_1}, \tag{15.35a}$$

$$\Psi_2 = (n_{s2})^{1/2}e^{i\Theta_2}, \tag{15.35b}$$

$$\Phi_1 = \Theta_2 - \Theta_1, \tag{15.35c}$$

where n_{s1} and n_{s2} are the densities of super electrons in the two superconductors and ϕ is the phase difference across the barrier. If the two wavefunctions (15.35a) and (15.34b) are substituted in the coupled wave equations (15.34) and the results separated into real and imaginary parts, we obtain equations for the time dependence of the pair densities and the phase difference:

$$\hbar\frac{d}{dt}n_{s1} = 2K(n_{s1}n_{s2})^{1/2}\sin\phi, \tag{15.36a}$$

$$\hbar\frac{d}{dt}n_{s2} = -2K(n_{s1}n_{s2})^{1/2}\sin\phi, \tag{15.36b}$$

$$\frac{d}{dt}\phi = \frac{2e}{\hbar}V. \tag{15.37}$$

We can specify the current density in terms of the difference between Eqs. (15.36a) and (15.36b) times e

$$J = e\frac{d}{dt}(n_{s1} - n_{s2}), \tag{15.38}$$

which has the value

$$J = J_c\sin\phi, \tag{15.39}$$

where

$$J_c = \frac{4eK(n_{s1}n_{s2})^{1/2}}{\hbar}, \tag{15.40}$$

and the coupling constant K is an unknown quantity. Equations (15.37) and (15.39) are called Josephson relations; they are the basic equations for the tunneling behavior of Cooper pairs. Multiplying Eq. (15.39) by the area A of the junction gives the current $I = JA$,

$$I = I_c\sin\phi \tag{15.41}$$

where $I_c = J_cA$ is the critical current.

Ambegaokar and Baratoff (1963a, b; cf. Aponte *et al.*, 1989) showed that for Cooper-pair tunneling between two identical superconductors with temperature-dependent gaps, $\Delta(T)$, the critical current is given by

$$I_c(T) = \frac{1}{4}\pi G_n[2\Delta(T)/e]\tanh[\Delta(T)/2k_BT], \tag{15.42}$$

where the normal tunneling conductance G_n is given by Eq. (13.22). In the respective limiting cases $T \to 0$ and $T \to T_c$, this is

$$I_c(0) = \frac{1}{4}\pi G_n[2\Delta(0)/e] \qquad T \approx 0 \tag{15.43a}$$

$$I_c(T_c) = \frac{1}{4}\pi G_n[\Delta^2(T)/ek_B T_c] \qquad T \approx T_c. \tag{15.43b}$$

The voltage $\frac{1}{4}\pi(2\Delta/e)$ on the right side of Eq. (15.43) has the physical significance indicated in Fig. 15.32. Thus the maximum Josephson current $I_c(0)$, which occurs for $T = 0$ and $\phi = \pi/2$, is equal to $\frac{1}{4}\pi$, or $\approx$ 80% of the normal-state current at the gap voltage $V = 2\Delta/e$. Figure 15.33 compares the temperature dependence of the maximum zero-voltage tunneling currents of an Sn–I–Sn junction measured by Fiske (1964) with the values predicted by Eq. (15.42). The fit of the Pb–I–Sn Josephson junction data to the same theory is also shown.

Copper-oxide superconductors are often granular in texture with Josephson junctions forming at the intergranular boundaries and perhaps at defect centers as well. Current flows through and between the Josephson junctions, and sometimes the intrajunction phases are favorable for the formation of complete circuits, which can produce flux shielding (Jung *et al.*, 1990; vide Doyle and Doyle, 1993). There is a grain-decoupling (or phase-locking) temperature T_g below which the Josephson junction network exhibits coherent properties, as well as a grain depairing (or critical) temperature T_c below which individual grains superconduct, where $T_g < T_c$ (Sergeenkov and Ausloos, 1993).

C. ac Josephson Effect

We have been discussing the dc effect, whereby a phase difference $\phi = \Theta_2 - \Theta_1$ between either side of a superconductor junction causes a dc current to spontaneously flow at zero voltage. Now let us examine what happens when a dc voltage is applied across the junction.

From Eq. (15.37) we know that a rate of change of phase accompanies the presence of a voltage across a Josephson junction. Since the applied voltage is a constant, this equation can be integrated directly to give

$$\phi(t) = \phi_0 + \left(\frac{2e}{\hbar}\right)Vt, \tag{15.44}$$

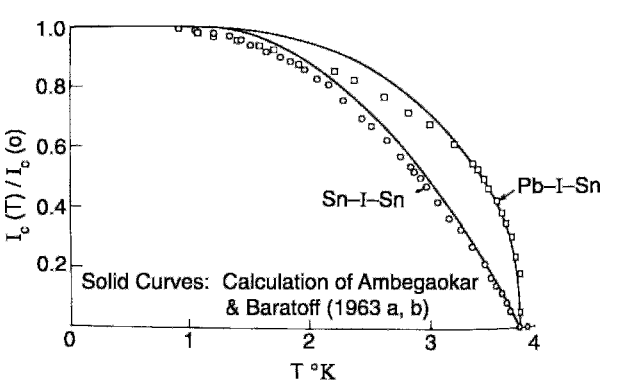

Figure 15.33 Temperature dependence of the maximum zero-voltage current, showing fit of theoretical curves to the experimental tunneling data of Pb–I–Sn (□) and Sn–I–Sn (○) junctions. The normalized tunneling current $I_c(T)/I_c(0)$, is plotted (Fiske, 1964).

which provides a characteristic frequency ν_J known as the Josephson frequency

$$\nu_1 = \frac{2eV}{h} = \frac{V}{\Phi_0} = 483.6 \times 10^{12} V \text{ Hz}, \quad (15.45)$$

where Θ_0 is the quantum of flux (Tsai *et al.*, 1983). A more practical expression to remember is

$$\frac{\nu_J}{V} = 483.6\,\text{MHz}/\mu\text{V}. \quad (15.46)$$

With the aid of these expressions and Eq. (13.39), the critical current density can be written in the form

$$J = J_c \sin(\omega_J t + \phi_0), \quad (15.47)$$

where $\omega_J = 2\pi\nu_J$.

It can be shown that the critical current density J_c depends on the frequency in terms of the voltage and that it reaches a maximum when the applied voltage is equal to the gap voltage, $V = 2\Delta/e$. This voltage dependence of $J_c(V)$, which was predicted by Reidel (1964) and confirmed experimentally by Hamilton (1972), is sketched in Fig. 15.34.

The ac Josephson effect that we have been describing occurs when current flows across a junction at the frequency given by Eq. (15.45) when a dc voltage V is applied across it. There is also an inverse ac Josephson effect, whereby a dc voltage is induced across the junction when an ac current is caused to flow through it, or when an electromagnetic field is incident on it. This will be discussed in Section VII.E.

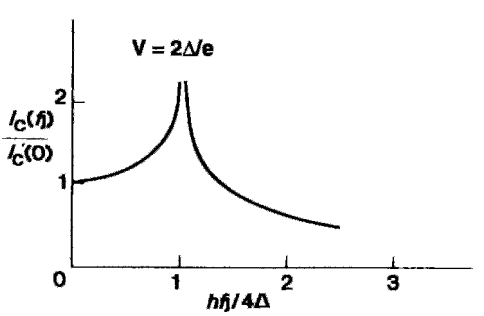

Figure 15.34 Dependence of the critical current on the Josephson frequency, showing the peak at the applied dc voltage $V = 2\Delta/e$ (Van Duzer and Turner, 1981, p. 144).

D. Driven Junctions

The Josephson relations (15.41) and (15.37)

$$I = I_c \sin\phi \quad (15.48)$$

$$\frac{d}{dt}\phi = \frac{2e}{\hbar}V, \quad (15.49)$$

apply to an idealized case in which all the current is carried by electron pairs. In the more general case there can be other types of current flowing, such as displacement current, quasiparticle tunneling current, and perhaps conduction current, if the barrier is not a perfect insulator. It will be instructive to analyze the junction in terms of the equivalent circuit shown in Fig. 15.35, which contains the current source $I_c \sin\phi$ of the junction, a capacitor to represent the displacement current, and a conductance to account for the quasiparticle tunneling and capacitor leakage currents. We assume that the dc current source $I = I(V)$, shown on the left, drives the junction circuit.

The differential equation for the current flow I in the equivalent circuit is

$$I = I_c \sin\phi + GV + C\frac{dV}{dt}, \quad (15.50)$$

where G is assumed to be constant, although in a more general analysis it can be taken as voltage dependent. Equation (15.49) can be used to eliminate the voltage and write the circuit equation in terms of the phase $\phi(t)$:

$$I = \frac{\hbar C}{2e}\cdot\frac{d^2\phi}{dt^2} + \frac{\hbar G}{2e}\cdot\frac{d\phi}{dt} + I_c \sin\phi. \quad (15.51)$$

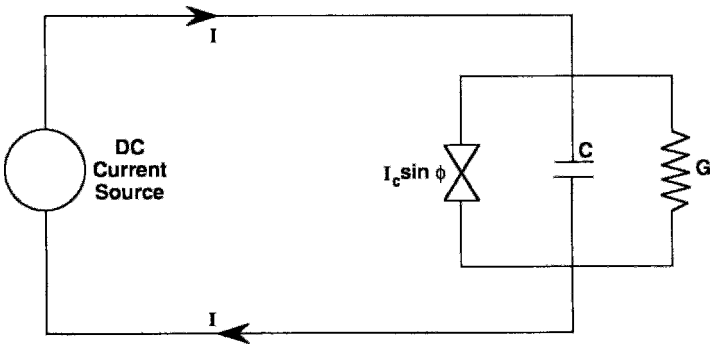

Figure 15.35 Josephson junction represented by the parallel circuit on the right consisting of a junction current source $I_c \sin\phi$, a capacitor C, and a conductance G. The circuit is driven by the dc current source I shown on the left.

With the aid of the Josephson angular frequency $\omega_c = (2e/\hbar)V_c$ for the voltage V_c,

$$V_c = I_c/G, \tag{15.52}$$

obtained from Eq. (15.45), and a new dimensionless variable Θ,

$$\Theta = \omega_c t, \tag{15.53}$$

the circuit equation assumes a simplified form,

$$\frac{I}{I_c} = \beta_c \frac{d^2\phi}{d\Theta^2} + \frac{d\phi}{d\Theta} + \sin\phi, \tag{15.54}$$

where β_c is the admittance ratio,

$$\beta_c = \omega_c C/G. \tag{15.55}$$

The solution to this second-order differential equation exhibit complex time variations of the current. We will not try to interpret these time dependences, and instead we will find the average value of the voltage, from Eq. (15.49)

$$V = \langle V \rangle = \left\langle \frac{d\phi}{dt} \right\rangle \frac{\hbar}{2e}, \tag{15.56}$$

for simple cases. We readily see from the form of Eq. (15.54) that when $I \le I_c$ there is a solution corresponding to Eq. (15.48),

$$I = I_c \sin\phi \qquad I \le I_c, \tag{15.57}$$

with all of the time derivatives equal to zero. In other words, this is the zero-voltage solution. At the other extreme, when $I \gg I_c$, the term $I_c \sin\phi$ becomes negligible, and we can use Eq. (15.49) to obtain the constant-voltage solution

$$I = GV \qquad I \gg I_c, \tag{15.58}$$

where $dV/dt = 0$. Hence, from Eq. (15.49) we have $d^2\phi/dt^2 = 0$ in this limit. The situation is more complex for driving currents that are near the critical current I_c.

The case in which $C \approx 0$, so that $\beta_c \ll 1$, which corresponds to

$$\frac{I}{I_c} = \frac{d\phi}{d\Theta} + \sin\phi \tag{15.59}$$

can be solved analytically (see Problem 9), and has the solution

$$V = 0 \qquad \text{for } I < I_c, \tag{15.60a}$$

$$V = V_c \left[\left(\frac{I}{I_c} \right)^2 - 1 \right]^{1/2} \qquad \text{for } I > I_c, \tag{15.60b}$$

$$V = \frac{I}{G} \qquad \text{for } I \gg I_c. \tag{15.60c}$$

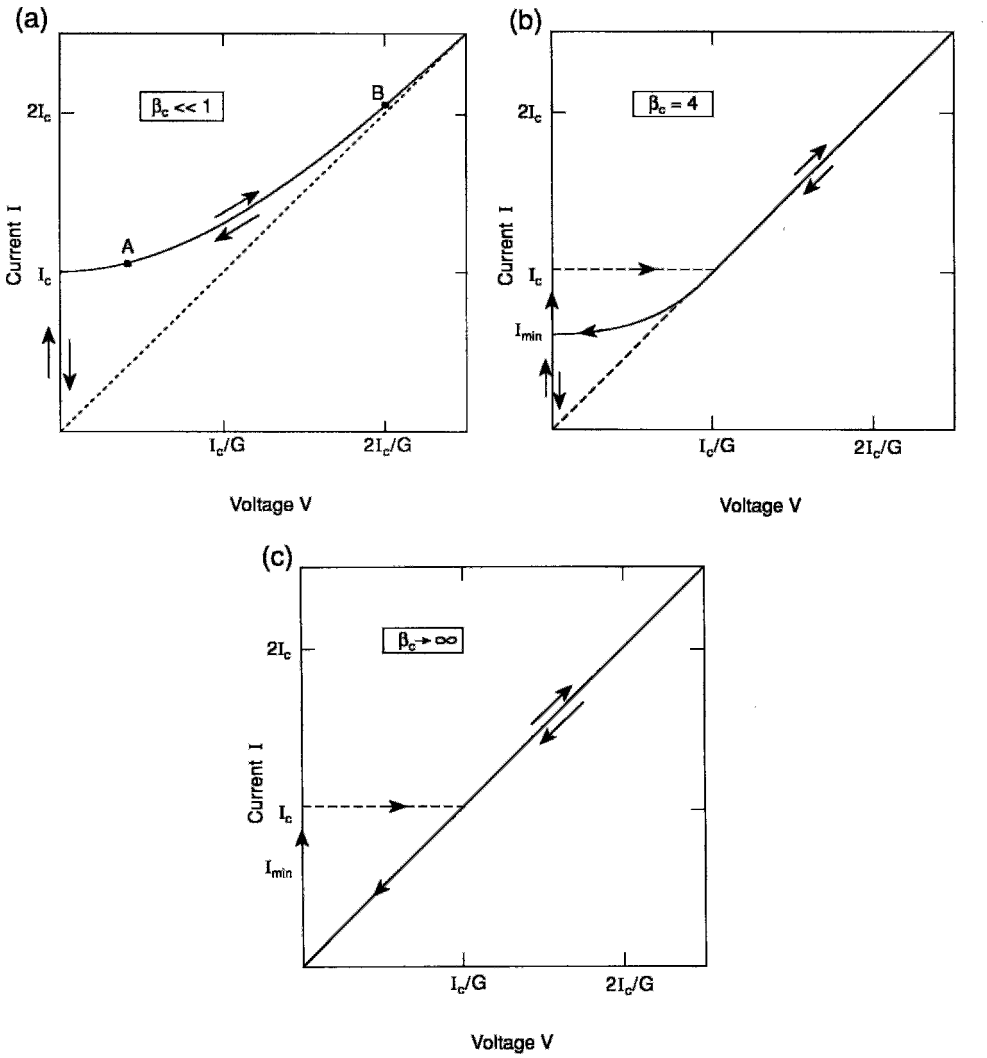

Figure 15.36 Current–voltage characteristics, I, versus V, for the Josephson junction circuit of Fig. 13.35 with: (a) negligible capacitance, $\beta_c \ll 1$, (b) appreciable capacitance, $\beta_c = 4$, and (c) dominating capacitance, $\beta_c \to \infty$, where $\beta_c = \omega_c C/G$.

This is plotted in Fig. 15.36a. Pairs of arrows pointing in opposite directions mean that there is no hysteresis. Figure 15.37 shows how the voltage oscillates with the average values from Eqs. (15.60b) and (15.60c), respectively, indicated by points A and B in Fig. 15.36a (for further details, see Orlando and Delin, 1991, pp. 458ff; Van Duzer and Turner, 1981, pp. 170ff).

When $\beta_c \gg 1$, the two solutions (15.57) and (15.58) apply with $\phi = \pi/2$ so that $\sin\phi = 1$. The I-versus-V characteristic plotted in Fig. 15.36c shows that there is a hysteresis in which V remains pinned at the value $V = 0$ as the current is initially increased from zero until the critical current is reached, at which point the voltage jumps to the value $V = I_c/G$ and there after follows

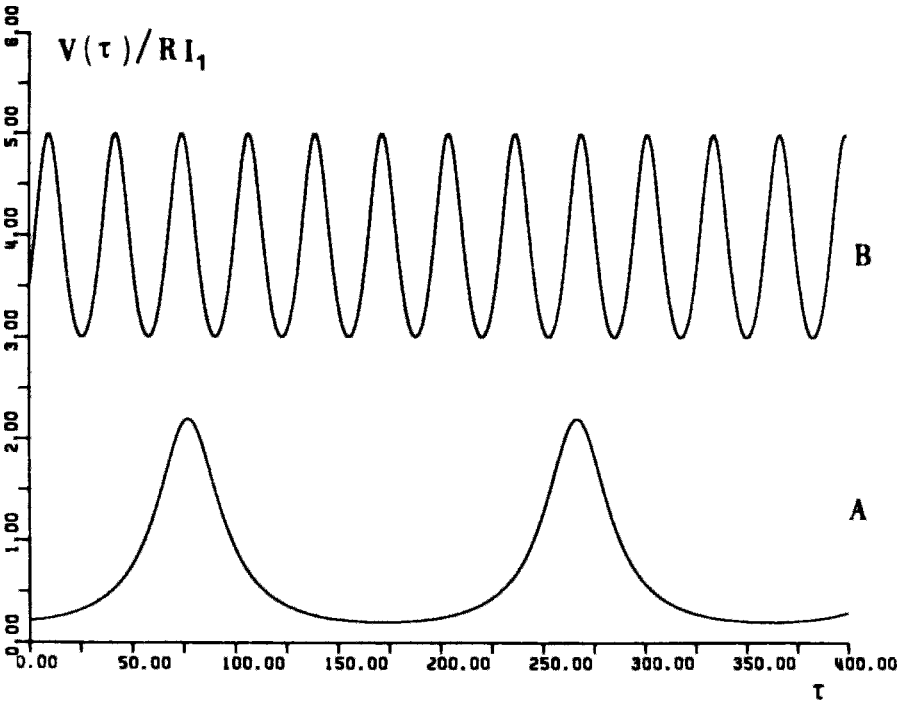

Figure 15.37 Voltage oscillations across the Josephson junction of Fig. 15.35 for the negligible capacitance case $\beta_c \ll 1$, and small and large dc bias voltages as marked at points A and B, respectively, of Fig. 15.36a (Barone and Paterno, 1982, p. 128).

the diagonal line upwards. Subsequent reduction of the voltage follows the diagonal line into the origin.

For immediate values of β_c, the I-versus-V characteristic follows the behavior illustrated in Fig. 15.36b for the case $\beta_c = 4$. Again there is hysteresis, with the initial rise of the current to I_c and its return to the value I_{min} at $V = 0$. Figure 15.38 shows how I_{min} depends on the value of β_c.

The solutions that we have been discussing were average values (15.50) of the voltage V involving a time average $\langle d\phi/dt \rangle$ of the derivative of the phase. The voltage itself oscillates in time, and Fig. 15.37 shows two examples of these oscillations.

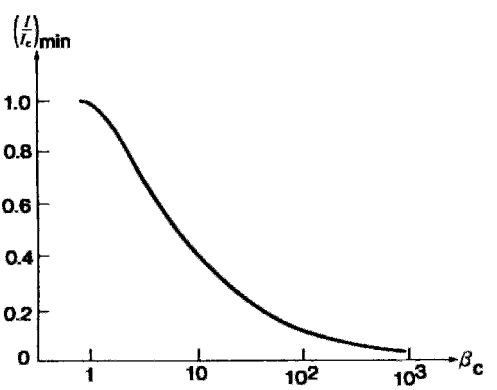

Figure 15.38 Dependence on β_c of the minimum current I_{min} (indicated in Fig. 15.36b) in the circuit of Fig. 15.35 when the current is decreased from values above I_c (Van Duzer and Turner, 1981, p. 173).

E. Inverse ac Josephson Effect

We have found that applying a dc voltage across a Josephson junction causes an ac current to flow. In the reverse ac Josephson experiment, dc voltages are induced across an unbiased junction by introducing an rf current into the junction.

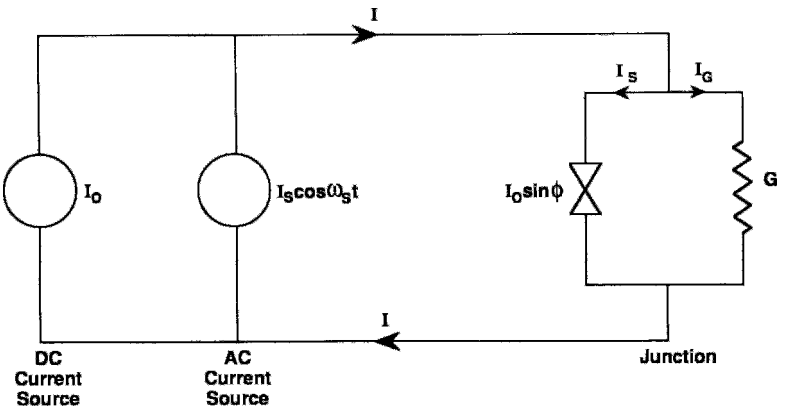

Figure 15.39 Equivalent circuit of a Josephson junction represented by a junction current $I_c \sin\phi$ in parallel with a conductance $G = 1/R$ irradiated with rf power. The junction is shown driven by a dc current source I_0 in parallel with an rf current source $I_s \cos\omega_s t$.

To explain this effect we assume that the Josephson junction can be represented by the parallel equivalent circuit of Fig. 15.39. The circuit consists of the usual Josephson current $I_c \sin\phi$ in parallel with a conductance G. In addition, it has as inputs a dc source current I_0 and an rf source current $I_s \cos\omega_s t$, with the total source current I given by

$$I(t) = I_0 + I_s \cos\ \omega_s t. \qquad (15.61)$$

When $I(t)$ is inserted into Eq. (15.50), a nonlinear differential equation that is difficult to solve results. A numerical solution provides the staircase I versus V characteristic presented in Fig. 15.40. Measurements carried out by Taur *et al.* (1974) with a 35-GHz source satisfying the condition $\omega_s = 0.16\,\omega_c$ compare well with the calculated curves shown in the figure, where the zero rf power curve ($I_s = 0$) is shown for comparison. This staircase pattern, which is referred to as *Shapiro steps* (Eikmans and van Himbergen, 1991; Shapiro, 1963; W. Yu *et al.*, 1992), has been reported by many observers (e.g., Kriza *et al.*, 1991; Kvale and Hebboul, 1991; Larsen *et al.*, 1991; H. C. Lee *et al.*, 1991; Rzchowski *et al.*, 1991; Sohn *et al.*, 1991).

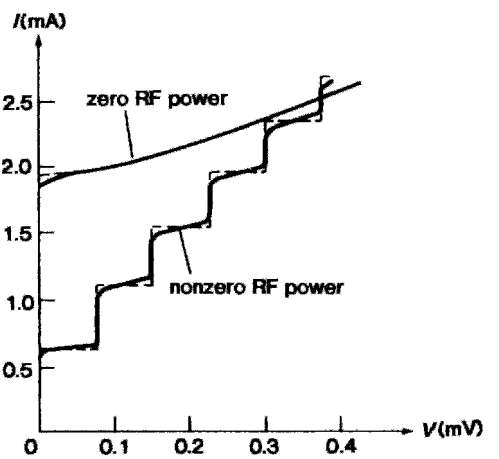

Figure 15.40 Current–voltage characteristics of a point-contact Josephson junction with applied rf power at 35 GHz, for the ac current source of Fig. 15.39. The solid curves calculated for 100 K thermal noise fit the experimental data well. The dashed line is from calculations done without noise (Van Duzer and Turner, 1981, p. 184).

It is mathematically easier to analyze this problem in terms of the circuit of Fig. 15.41 where the source is an applied voltage,

$$V(t) = V_0 + V_s \cos\ \omega_s t. \qquad (15.62)$$

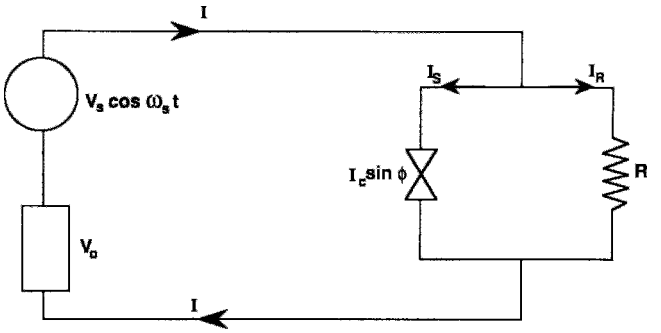

Figure 15.41 Josephson junction of Fig. 15.39 driven by a dc voltage V_0 in series with an rf voltage $V_s \cos \omega_s t$.

It is shown in Van Duzer and Turner (1981; see also Orlando and Delin, 1991) that the current $I(t)$ through the Josephson junction can be written as an infinite series of products of Bessel functions J_n and sine waves,

$$I(T) = I_c \sum_n (-1)^n J_n \left(\frac{2eV_s}{\hbar\ \omega_s} \right) \times \sin[(\omega_J - n\ \omega_s)t + \phi'], \quad (15.63)$$

where ϕ' is a constant of integration. Since the I versus V characteristic is drawn for the average current, $I \approx \langle I(t) \rangle$, and since the sine term averages to zero unless $\omega_J = n\ \omega_s$, there are spikes appearing on this characteristic for voltages equal to

$$V = \frac{n\hbar\ \omega_s}{2e}, \quad (15.64)$$

with the maximum amplitude,

$$I_{max} = J_c J_n \left(\frac{2eV_s}{\hbar\ \omega_s} \right), \quad (15.65)$$

occurring for the phase $\phi' = \pi/2$. Figure 15.42 shows these spikes at intervals proportional to the source frequency and indicates their maximum amplitude range.

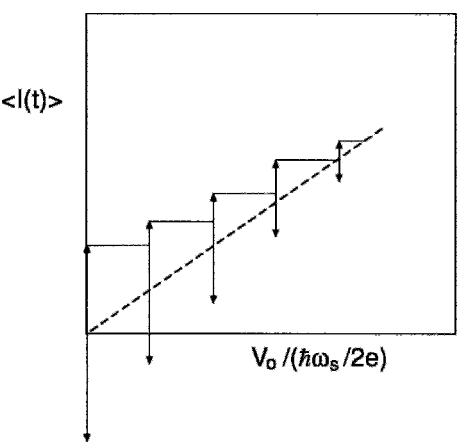

Figure 15.42 I–V characteristic for the dc component of the current versus applied dc voltage V_0 of the equivalent circuit of Fig. 15.41. The value of the current can be anywhere along a particular current spike, depending on the initial phase. The dashed line is for $\langle I(t) \rangle = V_0 G$.

The current can be anywhere along a particular spike, depending on the initial phase (see Orlando and Delin, 1991).

Estéve *et al.* (1987) reported that an LaSrCuO sample with the current–voltage characteristic shown in Fig. 15.43 exhibited the $I - V$ characteristic of Fig. 15.43b when irradiated with x-band (9.4 GHz) microwaves. The microwaves produced the spike-step pattern we have already described. The researchers attributed the results to the

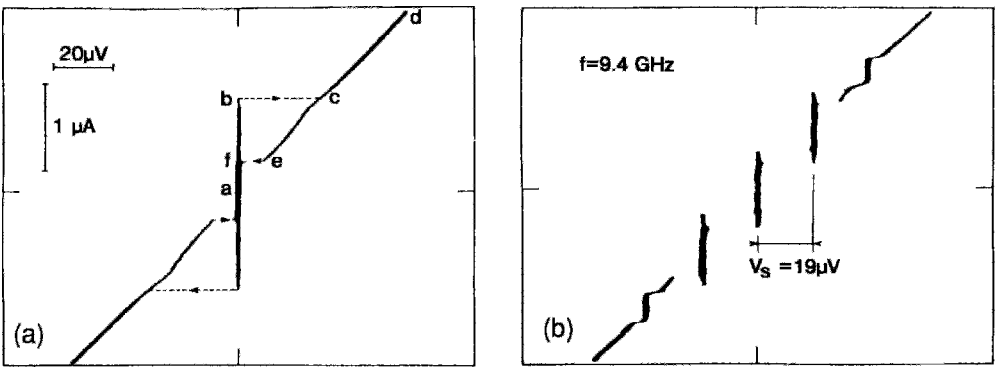

Figure 15.43 Oscilloscope presentation of current-versus-voltage characteristics of a tunnel junction at 4.2 K formed by an Al tip on a $(La_{0.925}Sr_{0.075})_2CuO_4$ sample (Estève *et al.*, 1987). (a) Trace obtained in the absence of rf power, the letters a through f giving the sense of the trace and the dashed lines indicating switching between branches, (b) steps induced by incident microwave radiation at 9.4 GHz (Estève *et al.*, 1987).

beating of the oscillating Josephson supercurrent with the microwaves. The separation in voltage between these steps is proportional to the microwave frequency, and their amplitude is Bessel-like. The Josephson junction characteristics were observed even when the point-contact metal tip was itself superconducting, which indicates that the junction was inside the material underneath the tip.

F. Analogues of Josephson Junctions

Josephson tunneling involves a quantum phenomenon that is difficult to grasp intuitively. This is especially true when we try to picture how the total current flowing through a Josephson junction depends on the phase difference of the electron pairs on either side of the junction. The differential equation for this phase difference ϕ happens to be the same as the differential equation for the rotational motion of a driven pendulum. We will describe this motion and then relate it to the Josephson junction.

Consider a simple pendulum consisting of a mass M attached to a pivot by a massless rod of length R. If a constant torque τ is applied by a motor, it will move the mass through an angle ϕ, as shown in Fig. 15.44. We know from our study of mechanics that the force of gravity acting on the mass m produces a restoring torque $mgR\sin\phi$. For a

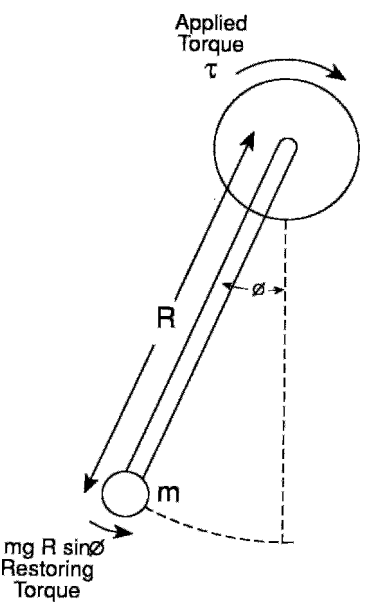

Figure 15.44 Pendulum model of a Josephson junction showing the counterclockwise restoring torque $mgR\sin\phi$ arising from the presence of a clockwise applied torque τ.

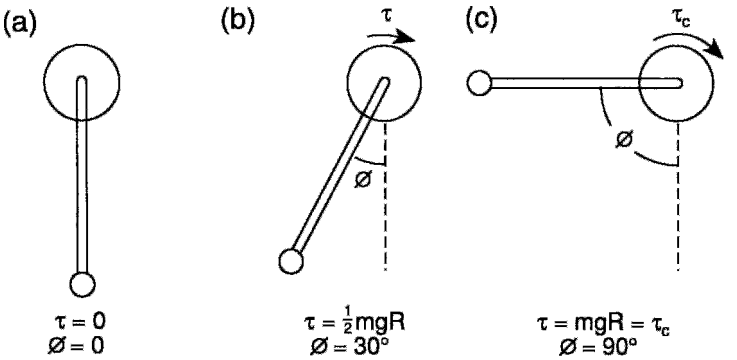

Figure 15.45 Pendulum (a) with no applied torque, $\tau = 0$, (b) with the torque $\tau = \frac{1}{2}mgR$, and (c) with the critical torque applied, $\tau_c = mgR$.

relatively small applied torque the pendulum assumes an equilibrium position at the angle given by

$$\tau = mgR \sin\phi \qquad \left(\frac{d\phi}{dt} = 0\right), \quad (15.66)$$

as indicated in Fig. 15.45b. The greater the torque, the larger the angle ϕ. There is a critical torque τ_c indicated in Fig. 15.45c for the angle $\phi = \pi/2$,

$$\tau_c = mgR. \quad (15.67)$$

If the applied torque exceeds this critical value, the pendulum will continue its motion beyond the angle $\phi = \pi/2$ and rotate continuously as long as the applied torque $\tau > \tau_c$ operates. The motion is fast at the bottom and slow at the top, corresponding to a large angular velocity $\omega = d\phi/dt$ at the bottom and a small ω at the top. For a large torque, $\tau \gg mgR$, the average angular velocity of the motion $\langle\omega\rangle$ increases linearly with the torque, reaching a limit determined by retarding drag forces coming from, for example, the viscosity η of the air or mechanical friction. The drag force is assumed to be proportional to the angular velocity ω, and is written as $\eta\omega$.

The dependence of the average angular velocity on the applied torque is shown in Fig. 15.46. We see from the figure that ω remains zero as the torque τ is increased until the critical value $\tau_c = mgR$ of Eq. (15.67) is reached. Beyond this point ω jumps to a finite value and continues to rise in the way we have already described. If the torque is now decreased down from a large magnitude, once it passes the critical value (15.67)

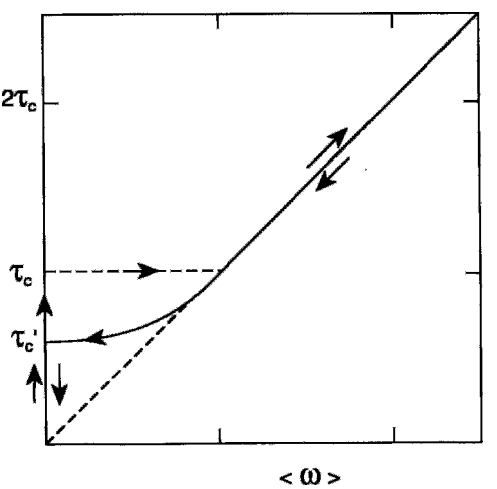

Figure 15.46 Relationship between the average angular velocity of the pendulum $\langle\omega\rangle$ and the applied torque τ. For low applied torques the pendulum oscillates and the average velocity is zero, whereas at high torques, $\tau > \tau_c$, motion is continuous with $\langle\omega\rangle$ proportional to τ. Note the hysteresis for increasing and decreasing torques.

the pendulum will have sufficient kinetic energy to keep it rotating for torques below τ_c, as indicated in the figure. The torque must be reduced much further, down to the value τ_c', before friction begins to dominate and motion stops, as indicated in the figure. Thus we have hysteresis of motion for low applied torques, and no hysteresis for high torques. If we compare Fig. 15.46 with Fig. 15.36b, we see that the torque–angular velocity characteristic curve of the driven pendulum has the same shape as the current–voltage characteristic of the Josephson junction.

The correspondence between the driven pendulum and a Josephson junction can be demonstrated by writing down a differential equation that governs the motion of the pendulum, setting the applied torque τ equal to the rate of change of the angular momentum L,

$$\frac{d}{dt}L = mR^2\frac{d\omega}{dt}, \tag{15.68}$$

and then adding the restoring and damping torques,

$$\tau = mR^2\frac{d^2\phi}{dt^2} + \eta\frac{d\phi}{dt} + mgR\sin\phi, \tag{15.69}$$

where mR^2 is the moment of inertia; here we have made use of the expression $\omega = d\phi/dt$. This equation is mathematically equivalent to its Josephson counterpart (15.51), so we can make the following identifications:

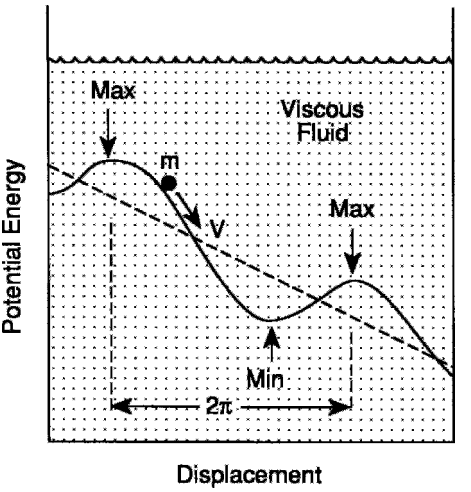

Figure 15.47 Washboard analogue of the Josephson junction showing a particle of mass m descending along a sloped wavy path in a viscous fluid.

This analogue has been found useful in the study of the behavior of Josephson junctions.

Another mechanical device that illustrates Josephson junction-type behavior is the washboard analogue sketched in Fig. 15.47, in which a particle of mass m moves down a sloped sinusoidal path in a viscous fluid, passing through regularly spaced minima and maxima along the way.

Electrical analogues have been proposed (Bak and Pedersen, 1973; Hamilton, 1972; Hu and Tinkham, 1989; cf. Goodrich and Srivastava, 1992; Goodrich *et al.*, 1991) that do not give as much insight into Josephson junction behavior as the mechanical analogues, however, though they are useful for

applied current	I	$\leftrightarrow$	τ	applied torque
average voltage term	$V(2e/\hbar) = d\phi/dt$	$\leftrightarrow$	$\omega = d\phi/dt$	average angular velocity
phase difference	ϕ	$\leftrightarrow$	ϕ	angular displacement
capacitance term	$\hbar C/2e$	$\leftrightarrow$	mR^2	moment of inertia
conductance term	$\hbar G/2e$	$\leftrightarrow$	η	viscosity
critical current	I_c	$\leftrightarrow$	mgR	critical torque

studying the behavior of Josephson junctions when the parameters are varied.

VIII. MAGNETIC FIELD AND SIZE EFFECTS

Until now we have assumed that no magnetic fields are applied, and that the currents circulating in the Josephson junctions produce a negligible amount of magnetic flux. The next few sections examine the effect of applying a magnetic field parallel to the plane of a single Josephson junction as well as perpendicular to a loop containing two such junctions. To determine how the presence of the field affects the phase Θ, we make use of Eq. (6.33):

$$\oint \nabla\Theta \cdot d\mathbf{l} = \frac{2\pi}{\Phi_0} \oint \mathrm{A} \cdot d\mathbf{l}. \qquad (15.70)$$

This shows that $\nabla\Theta$ and the vector potential $\mathbf{A}$ play similar roles in determining the phase. In writing out this expression we have assumed that the line integration is performed over regions of the superconductor where the current density is either zero or makes no contribution to the integral, so that the term $\mathbf{J} \cdot \mathrm{d}\mathbf{l}$ of Eq. (6.33) is omitted. This expression will be applied to several cases.

We begin with a discussion of a short Josephson junction in which the magnetic fields produced by the currents are negligible compared with the externally applied field, and then will treat long junctions where this is not the case. We first examine two-junction loops and arrays of many junctions, followed by ultra-small junctions in which single-electron tunneling is observable. We will conclude with a brief section on superconducting quantum interference devices (SQUIDS).

A. Short Josephson Junction

Consider a weak-link tunnel junction of the type sketched in Fig. 15.11 with a magnetic field $B_0\hat{\mathbf{k}}$ applied along the vertical z direction, as shown in Fig. 15.48. The junction is of thickness d normal to the y-axis with cross-sectional dimensions a and c along x and z, respectively. It is small enough so that the applied magnetic field is larger than the field produced by the currents. One superconductor SC_1 is to the right of the insulating barrier and the other SC_2 to the left, as indicated in the figure.

Because of symmetry, the magnetic field $B_z(y)$ has no x or z dependence, but does

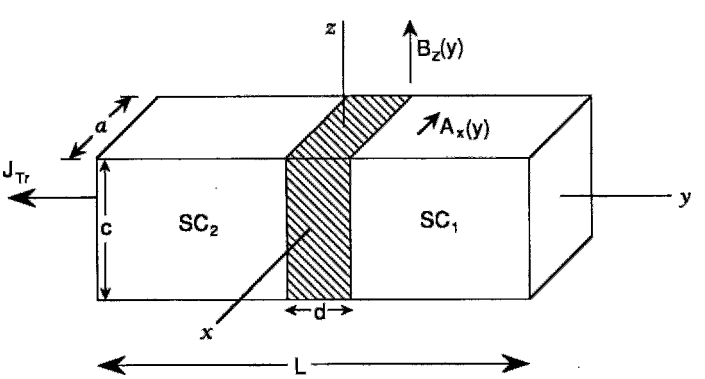

Figure 15.48 Application of a magnetic field $B_0(y)$ transverse to the Josephson junction of Fig. 15.11 with a transport current of density J_{Tr} flowing to the left. The vector potential $A_x(y)$ of the applied field is indicated.

vary with distance along y into the superconductors,

$$\mathbf{B} = B_z(y)\hat{\mathbf{k}}. \tag{15.71}$$

This applied field is derived from the vector potential $\mathbf{B} = \nabla \times \mathbf{A}$,

$$\mathbf{A} = A_x(y)\hat{\mathbf{i}}, \tag{15.72}$$

which has the value (cf. Eq. (6.41)),

$$\mathbf{A} = -yB_0\hat{\mathbf{i}} \qquad |y| \leq \frac{1}{2}d, \tag{15.73}$$

in the barrier layer where the material is normal and $B_z = B_0$, as sketched in Fig. 15.49. We assume that the magnetic field decays exponentially into the superconductors on either side of the barrier, as indicated in Fig. 15.49b. If we proceed far enough inside where B_z drops to zero $\mathbf{A}$ will become constant, as seen from the expression $\mathbf{B} = \nabla \times \mathbf{A}$.

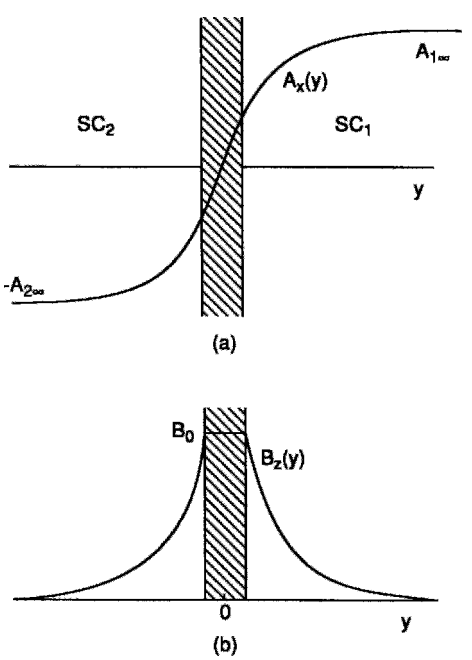

Figure 15.49 Variation of (a) vector potential $A_x(y)$ and (b) magnetic field $B_z(y)$ in the neighborhood of the junction of Fig. 15.48.

We assign it the value $A_{1\infty}$ far inside SC_1 and the value $-A_{2\infty}$ far inside SC_2, as indicated in Fig. 15.49a.

We start by calculating the value for the phase $\Theta_1(x)$ at an arbitrary point x along the interface between the barrier and the superconductor SC_1, as shown in Fig. 15.50. This phase will be found relative to the phase Θ_{10} of $\Theta_1(x)$ at a reference point x_0 on the interface, as indicated. The phase difference $\Theta_1(x) - \Theta_{10}$ may be determined by integrating $\nabla\Theta \cdot d\mathbf{l}$ along the path $A \to B \to C \to D$ in Fig. 15.50, but it is easier to make use of Eq. (15.70) and carry out the equivalent integration of $\mathbf{A} \cdot d\mathbf{l}$ along this same path. Since $\mathbf{A}$ is a vector in the x direction, it is perpendicular to the vertical paths $A \to B$ and $C \to D$, so that the line integral vanishes for these two segments of the path. We already mentioned that the vector potential has the constant value $A_{1\infty}$ along the path $B \to C$, so that integration gives

$$\Theta_1(x) = \Theta_{10} + (2\pi/\Phi_0)A_{1\infty}(x - x_0). \tag{15.74}$$

An analogous expression can be obtained for the other superconductor SC_2 using the path $A' \to B' \to C' \to D'$. Hence we can write for the phase difference $\phi(x)$

$$\phi(x) = \Theta_2(x) - \Theta_1(x) \tag{15.75}$$

$$= \phi_0 + \frac{2\pi}{\Phi_0}[A_{1\infty} + A_{2\infty}]x, \tag{15.76}$$

where $\phi_0 = \Theta_2(x_0) - \Theta_1(x_0) = \Theta_{20} - \Theta_{10}$ at the reference point x_0. The quantity $[A_{1\infty} + A_{2\infty}]$ is evaluated by integrating along a similar closed path that has been enlarged to enclose the entire barrier and extend deep into both superconductors. The resulting line integral equals the total flux through the barrier,

$$\Phi = \int \mathbf{A} \cdot d\mathbf{s}. \tag{15.77}$$

Again, the integrand vanishes for the two vertical paths along which the vectors $\mathbf{A}$ and

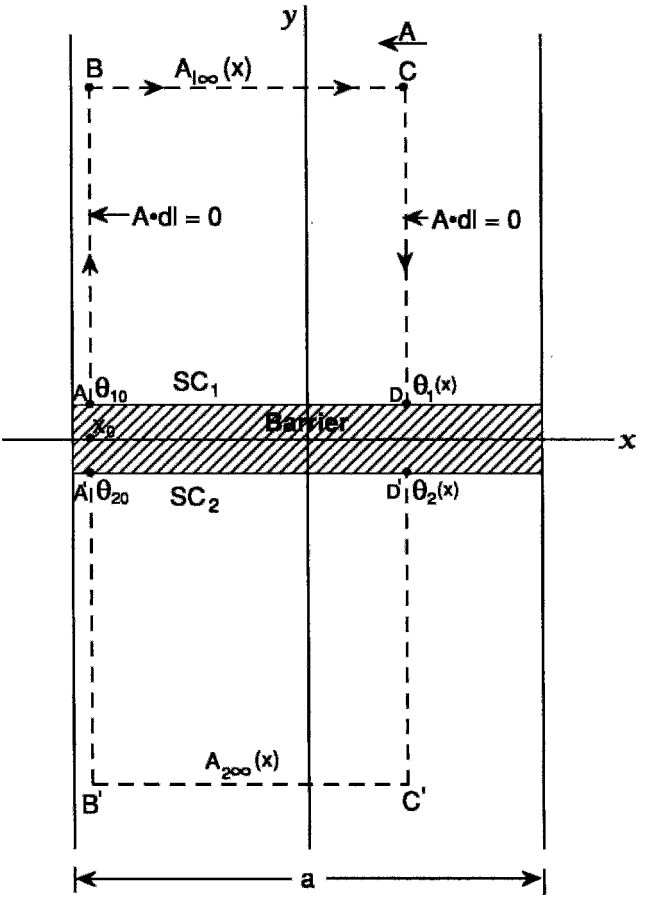

Figure 15.50 Path of integration around the junction of Fig. 15.48 for determining the phase difference $\phi(x) = \Theta_2(x) - \Theta_1(x)$ across the junction at a position x relative to the phase difference $\phi_0 = \Theta_{20} - \Theta_{10}$ at the position x_0 on the left.

$d\mathbf{s}$ are antiparallel. The contributions from the top and bottom paths far inside the two superconductors add to give for the total enclosed flux

$$\Phi = a[A_{1\infty} + A_{2\infty}]. \tag{15.78}$$

This total flux is approximately equal to the applied magnetic field strength B_0 times the effective area of the junction,

$$\Phi = a(d + 2\lambda)B_0. \tag{15.79}$$

The quantity $d + 2\lambda$ constitutes the effective thickness of the junction,

$$d_{\text{eff}} = d + 2\lambda. \tag{15.80}$$

Inserting Eq. (15.78) in (15.76) gives

$$\phi(x) = \phi_0 + \frac{2\pi\Phi}{\Phi_0} \cdot \frac{x}{a}. \tag{15.81}$$

If this is substituted in Eq. (15.39) and integrated over the area $A = ac$ of the junction (see Problem 12),

$$I = J_c \int \sin[\phi(x)]dx\, dz, \tag{15.82}$$

we obtain

$$I = I_c \sin\phi_0 \frac{\sin(\pi\Phi/\Phi_0}{\pi\Phi/\Phi_0}, \qquad (15.83)$$

where $I_c = AJ_c$ is the critical current. This has a maximum for the phase difference $\phi_0 = \pi/2$,

$$I_{max} = I_c \frac{\sin(\pi\Phi/\Phi_0}{\pi\Phi/\Phi_0}, \qquad (15.84)$$

We call this the *Josephson junction diffraction equation*.

The plot of Eq. (15.84) sketched in Fig. 15.51, which has been seen for many samples (e.g., Rosenthal *et al*., 1991; Seidel *et al*., 1991), illustrates how the tunneling current varies with increasing magnetic flux Φ through the junction. Figure 15.52 presents four special cases. When there is no flux, $\Phi = 0$, the current in the junction is uniform, as shown in Fig. 15.52a, and has the critical value I_c. When half a flux quantum is present, $\Phi = \frac{1}{2}\Phi_0$, as in Fig. 15.52b, the average value of the current is the average of a sine wave over a half-cycle, namely $(2/\pi)I_c$. For the next maximum, $\Phi = 3\Phi_0/2$, two of the half-cycles cancel to give the current $I = (2/3\pi)I_c$, which is one-third of the half-cycle case. By induction, the nth maximum of the current $I_c/[\pi(n+\frac{1}{2})]$ occurs at the flux value $\Phi = (n+\frac{1}{2})\Phi_0$. We also deduce from Fig. 15.52c that the current cancels for even cycles, where $\Phi = n\Phi_0$.

For the case of Fig. 15.52c, in which the total phase change across the length of the junction is 2π, one flux quantum fits in it. We see from the directions of the arrows on the figure that the super current flows down across the junction on the left and up on the right. To complete the circuit it flows horizontally within a penetration depth λ inside the superconductor to form closed loops, as illustrated in Fig. 15.53a. These current loops encircle flux, and the resulting configuration is known as a Josephson vortex (Miller *et al*., 1985). There is no core because none is needed; the super current density is already zero in the center.

When the phase change across the junction is $2\pi n$, where n is an integer, there will be n Josephson vortices side by side in the junction, each containing one flux quantum and each having a horizontal length $1/n$ times the length for the single-flux quantum case. Figure 15.53b sketches two fluxons in the gap for $n = 2$, with total phase change of 4π.

Equation (15.83) is mathematically equivalent to the well-known expression for single-slit Fraunhofer diffraction in optics.

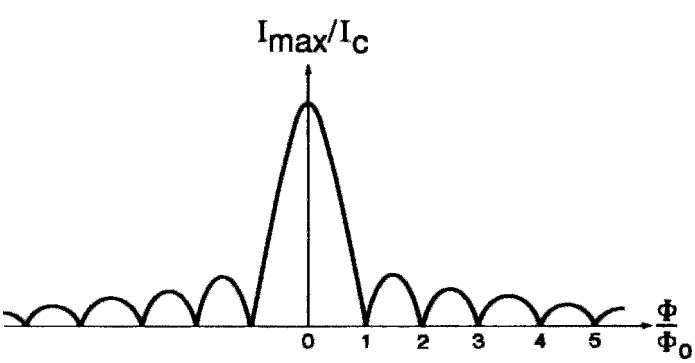

Figure 15.51 Josephson Fraunhofer diffraction pattern showing the maximum normalized zero-voltage current I_{max}/I_c versus Φ/Φ_0 through the parallel junction of Fig. 15.48 when the current density is uniform across the x, z-plane of the junction. The values of I_{max}/I_c at the peaks of the curve, from the center outwards, are $1, 2/3\pi, 2/5\pi, 2/7\pi, \ldots$ (from Van Duzer and Turner, 1981, p. 155).

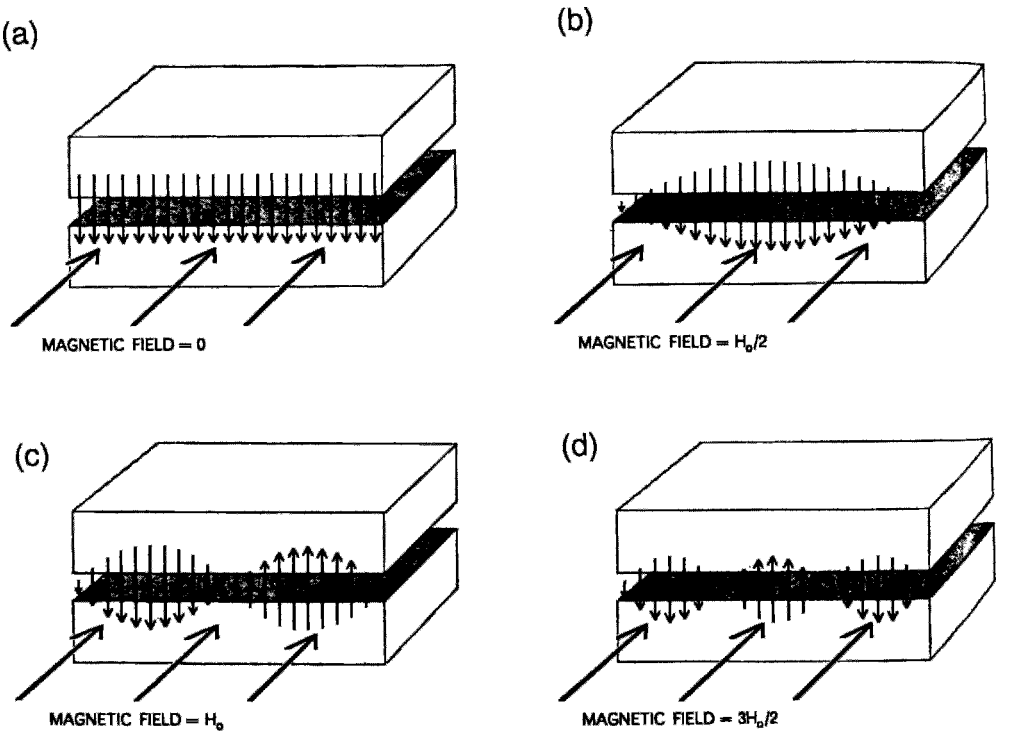

Figure 15.52 Effect of an applied magnetic field on the tunneling-current oscillations across a uniform Josephson junction, where the field $\mu_0 H_0$ corresponds to one flux quantum Φ_0 in the junction (Langenberg *et al.*, 1966).

Peterson and Ekin (1989, 1990; cf. Barone and Paterno, 1982) suggest that an Airy diffraction pattern, in which the quantity $\sin(\pi\Phi/\Phi_0)$ in Eq. (15.83) is replaced by twice a first-order Bessel function, $2J_1(\pi\Phi/\Phi_0)$ more properly characterizes superconductors with grain-boundary barriers in bulk materials. They also give a figure in which the Airy and Fraunhofer diffraction patterns are compared.

B. Long Josephson Junction

We will now examine what are called long Josephson junctions, leaving discussion of the criterion for longness until the next section, VIII.C. We begin by taking the derivative of Eq. (15.81),

$$\frac{d\phi}{dx} = \frac{2\pi\Phi}{\Phi_0 a} = \frac{2\pi B}{\Phi_0} d. \tag{15.86}$$

Although we will not prove it, this expression is more general than (15.81), which may be obtained from it by assuming that Φ arises from a constant magnetic field and then integrating. If we make use of the Maxwell relation $\nabla \times \mathbf{B} = \mu_0 \mathbf{J}$, which for the present case is given explicitly by

$$\frac{dB_z(x)}{dx} = \mu_0 J_y(x), \tag{15.87}$$

we obtain

$$\frac{d^2\phi}{dx^2} = \frac{2\pi\mu_0 J_y(x) d}{\Phi_0}. \tag{15.88}$$

Using Eq. (15.39) this becomes the pendulum equation (which might also be

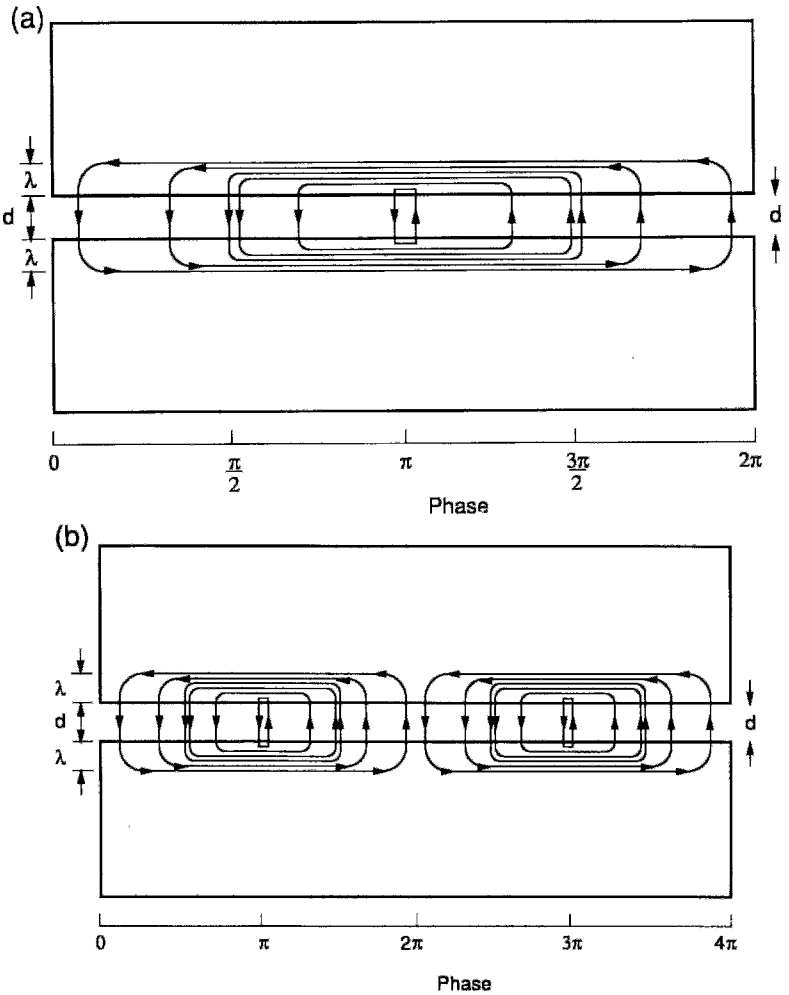

Figure 15.53 Current distribution around Josephson vortices in the junction of Fig. 15.52 for (a) single-vortex case of Fig. 15.52c when the magnetic flux in the junction is Φ_0, and (b) the double-vortex case when the magnetic flux is $2\Phi_0$.

called the stationary sine Gordon equation) (Fehrenbacher *et al.*, 1992).

$$\frac{d^2\phi}{dx^2} = \frac{\sin\phi(x)}{\lambda_J^2}, \tag{15.89}$$

where $\lambda_J = (\phi_0/2\pi\mu_0 J_c d)^{1/2}$ called the Josephson penetration depth, is the natural length scale for the junction. A long junction is one whose length a is greater than λ_J, while for a short junction $a \ll \lambda_J$.

If the time dependence is taken into account, it can be shown that the sine Gordon equation is obtained (Orlando and Delin, 1991, p. 437),

$$\frac{d^2\phi}{dx^2} - \frac{1}{u_p^2}\cdot\frac{d^2\phi}{dt^2} = \frac{\sin\phi(x)}{\lambda_J^2}, \tag{15.90}$$

where u_p, given by

$$u_p = \frac{1}{(\mu_0 \in)^{1/2}}\cdot\frac{d}{d+a\lambda}, \tag{15.91}$$

is the velocity of a transverse electromagnetic (TEM) mode wave in the junction region. This equation has two types of solitary wave (soliton) solutions. The first, called kinks or topological solitons, are able to propagate and have the property that $\phi(x)$ increases monotonically from 0 to 2π as x increases from $-\infty$ to ∞. There are also propagating antikink solutions for which $\phi(x)$ decreases monotonically from 2π to 0 as x increases from $-\infty$ to ∞. Kinks represent magnetic flux quanta Φ_0 in superconductivity (Holst *et al.*, 1990; Kivshar and Soboleva, 1990), and domain walls in the theory of two-dimensional magnetism. The second type of solution, called a *breather*, is a nontopological variety of soliton which is stationary, i.e., does not travel (Dodd *et al.*, 1982; Drazin and Johnson, 1989; Kivshar *et al.*, 1991).

Sometimes, perturbation terms for dissipation and energy (current) input are added to the sine Gordon equation (Grnbech-Jensen *et al.*, 1991; Holst *et al.*, 1990; Malomed, 1989, 1990; Malomed and Nepomnyashchy, 1992; Olsen and Samuelsen, 1991; Pagano *et al.*, 1991; Petras and Nordman, 1989; Ustinov *et al.*, 1992). Phase locking can also occur, in which the fluxon motion in the long junction follows the frequency of the external field, or two such junctions can be phase locked to each other (Fernandez *et al.*, 1990; Grnbech-Jensen, 1992; Grnbech-Jensen *et al.*, 1990; Pedersen and Davidson, 1990). Frequency locking to the external field produces an ordered state and can lead to the appearance of Shapiro steps. The absence of phase locking can produce a disordered state and a condition of chaos (Chi and Vanneste, 1990).

C. Josephson Penetration Depth

Equation (15.89) was obtained from Eq. (15.88) by defining the Josephson penetration depth λ_J,

$$\lambda_J = (\Phi_0/2\pi\mu_0 J_c d_{\text{eff}})^{1/2}, \tag{15.92}$$

which is the length criterion that distinguishes short from long junctions. To obtain a physical significance for this characteristic length, let us compare the energies associated with the stored fields and with the current flow through the junction which is sketched in Fig. 15.48. For a constant magnetic field, the stored magnetic energy U_B is

$$U_B = \int \frac{B^2}{2\mu_0} dx\, dy\, dz \tag{15.93}$$

$$= (B_0^2/2\mu_0) acd_{\text{eff}}$$

$$= \frac{\Phi_0^2}{2\mu_0} \cdot \frac{c}{ad_{\text{eff}}}, \tag{15.94}$$

where we have assumed one Josephson vortex present in the junction, as in Figs. 15.52c and 15.53a, with $B_0 = \Phi_0/ad$. The energy U_J associated with the current flow is

$$U_J = \int JV\, dx\, dy\, dt, \tag{15.95}$$

and, using Eqs. (15.39) and (15.49), this becomes

$$U_J \approx \frac{\Phi_0 J_c ac}{2\pi} \int \sin\phi\; d\phi. \tag{15.96}$$

If we equate the magnetic and current energies, $U_B = U_J$, we obtain

$$a = \lambda_J \left[2\pi^2 / \int \sin\,\phi\, d\phi\right]^{1/2}, \tag{15.97}$$

where the factor in the square brackets is close to but larger than unity. Thus the two energies become comparable when the junction length a approaches the Josephson penetration depth λ_J.

A short junction is one for which $a \ll \lambda_J$, $U_J \ll U_B$, the magnetic fields arising from the current flow are much less than the applied field, and the field B is effectively constant over the junction region. A long junction is one for which $a > \lambda_J$, $U_J > U_B$, etc.

D. Two-Junction Loop

In Section A we derived the diffraction equation (15.84) for a short Josephson junction in the presence of an applied magnetic field. In a typical case applied fields in the millitesla range (see Problem 13) are used to see the current pattern. We will now consider the case of a superconducting loop containing two weak links (short junctions) in parallel, as shown in Fig. 15.54. For this arrangement flux quantization occurs in the area of the loop, which we are assuming to be considerably larger than the area of either junction, so that the system is sensitive to much smaller changes in applied flux.

In analyzing the two-junction loop we are assuming that the individual junction areas are small enough so as to be negligible. Integration of Eq. (15.70) around the dashed path shown in Fig. 15.54 gives

$$(\Theta_{\alpha 2} - \Theta_{\alpha 1}) - (\Theta_{\beta 2} - \Theta_{\beta 1}) = \left(\frac{2\pi\Phi}{\Phi_0}\right), \tag{15.98}$$

where again we are neglecting current flow effects on the phases. Using the phase difference notation of Eq. (15.75), this becomes

$$\phi_\alpha = \phi_\beta + 2\pi\ \Phi/\Phi_0. \tag{15.99}$$

The total current I flowing through this parallel arrangement of weak links is the sum of the individual currents I_α and I_β in the two arms,

$$I = I_\alpha + I_\beta \tag{15.100}$$

and each current satisfies its own individual Josephson equation (15.40), to give

$$I = I_{c\alpha} \sin\phi_\alpha + I_{c\beta} \sin\phi_\beta \tag{15.101}$$

$$= I_{c\alpha} \sin\phi_\alpha + I_{c\beta} \sin\left[\phi_\alpha - 2\pi\left(\frac{\Phi}{\Phi_0}\right)\right] \tag{15.102}$$

where we have used Eq. (15.99). For equal individual currents,

$$I_{c\alpha} = I_{c\beta} = I_c, \tag{15.103}$$

the total current I is maximized by the choice of phase

$$\phi_\alpha = \frac{1}{2}\pi + \pi\Phi/\Phi_0, \tag{15.104a}$$

$$\phi_\beta = \frac{1}{2}\pi - \pi\Phi/\Phi_0, \tag{15.104b}$$

to give for the magnitude of the maximum current

$$I_{max} = 2I_c|\cos(\pi\Phi/\Phi_0)|, \tag{15.105}$$

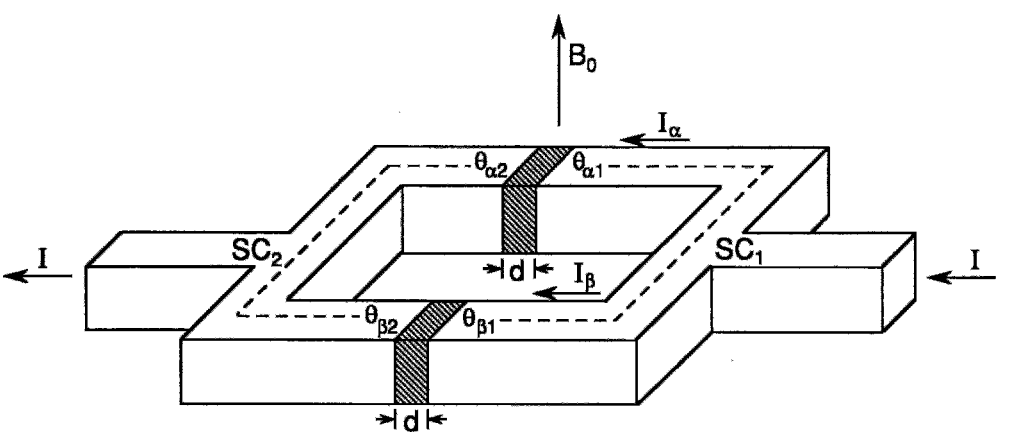

Figure 15.54 Superconducting loop containing two weak links α and β of thickness d showing the phases Θ_{ij} at the junctions and the direction of current flow I. The dashed line indicates the path of integration around the loop.

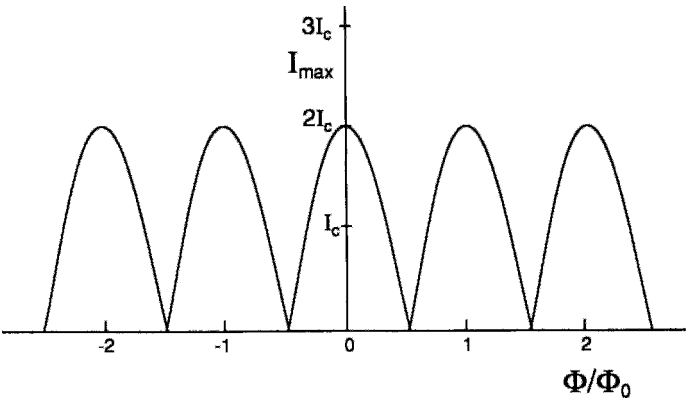

Figure 15.55 Dependence of the current maximum I_{max} of Eq. 15.105 of a balanced Josephson junction loop ($I_{c\alpha} = I_{c\beta}$) on the applied flux Φ normalized relative to the quantum of flux Φ_0.

an expression that we call the *Josephson loop interference equation*. It has its optical analogue in Young's experiment for detecting the interference of light from two identical slits. The phase ϕ_α is an unknown function of the flux in the ring, and adjusts itself to maximize the current. The dependence of I_{max} on the applied flux Φ given by Eq. (15.105) for this equal-current case is plotted in Fig. 15.55.

When the two currents are not the same (Saito and Oshiyama, 1991), it is more complicated to calculate the phase which maximizes the total current (15.101) subject to the condition (15.99). Van Duzer and Turner (1981) give

$$I_{max} = \left[(I_{c\alpha} - I_{c\beta})^2 + 4 I_{c\alpha} I_{c\beta} \cos^2 \left(\frac{\pi \Phi}{\Phi_0} \right) \right]^{1/2} \tag{15.106}$$

This has the minimum and maximum values

$$\text{minimum} = I_{c\alpha} - I_{c\beta} \qquad \Phi = (n + \frac{1}{2})\Phi_0, \tag{15.107a}$$

$$\text{maximum} = I_{c\alpha} + I_{c\beta} \qquad \Phi = n\Phi_0, \tag{15.107b}$$

where we have assumed that $I_{c\alpha} > I_{c\beta}$. The dependence of I_{max} on the applied flux given by Eq. (15.106) for the case $I_{c\alpha} = 2I_{c\beta}$ is plotted in Fig. 15.56 to the same scale as in Fig. 15.55 with the ordinate scale labeled with the limits of Eq. (15.107). Equation (15.106) reduces to Eq. (15.105) for the equal-current case $I_{c\alpha} = I_{c\beta}$.

Equation (15.106) corresponds to the analogue of light interference from two nonidentical slits, but this is rarely studied in optics because it is so easy to make matching slits. Identical Josephson junctions are not so easy to fabricate, so the case of Eq. (15.106) is of interest in superconductivity.

E. Self-Induced Flux

In the previous two sections we tacitly assumed that the flux Φ in the circuits is the applied flux, which meant neglecting the contribution of the currents. We noted in Chapter 2, Section X that the current I_{circ} circulating in a loop can contribute the amount $I_{circ}L$ to the flux, where L is the inductance of the loop. The currents I_α and I_β in the two arms of the loop flow in the same direction,

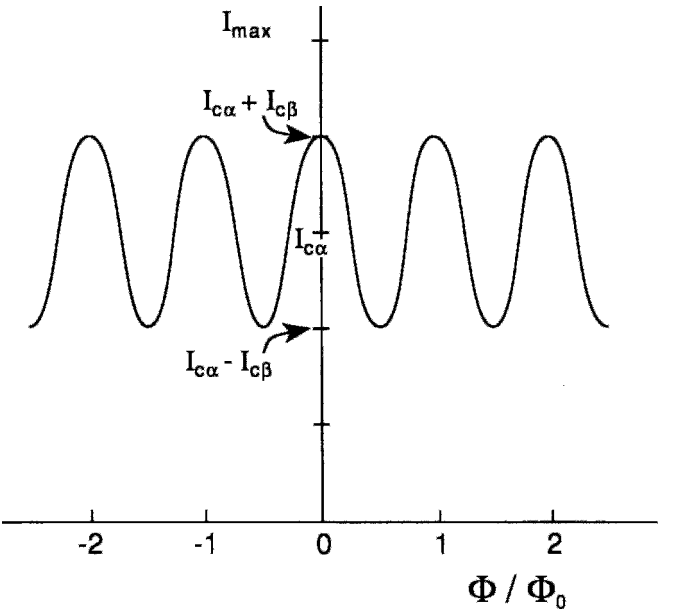

Figure 15.56 Dependence of the current maximum I_{max} of an unbalanced Josephson junction loop ($I_{c\alpha} \neq I_{c\beta}$) on the applied flux Φ normalized relative to the quantum of flux Φ_0. The plot is made for the case of setting $I_{c\alpha} = 2I_{c\beta}$ in Eq. (15.106).

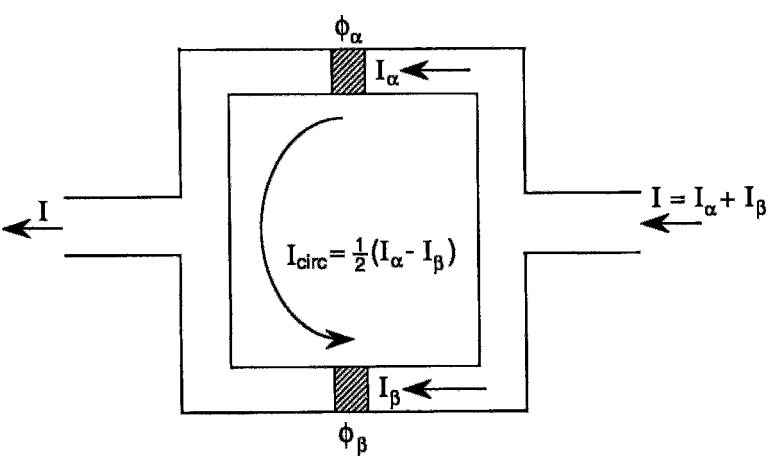

Figure 15.57 Circulating current $I_{circ} = \frac{1}{2}(I_\alpha - I_\beta)$ in an unbalanced Josephson junction loop, $I_\alpha \neq I_\beta$, in the presence of an applied current $I = I_\alpha + I_\beta$.

as indicated in Figs. 15.54 and 15.57, producing magnetic fields (cf. Fig. 2.35) pointed in opposite directions through the loop; for $I_\alpha = I_\beta$ these fields cancel each other. However, when the two currents are not equal, we can decompose them into a symmetrical component $\frac{1}{2}(I_\alpha + I_\beta)$, which flows in the same direction in each arm of the loop and does

not contribute to the flux, and an antisymmetrical circulating component,

$$I_{\text{circ}} = \frac{1}{2}(I_\alpha - I_\beta), \tag{15.108}$$

as indicated in Fig. 15.57, which contributes to the flux. The total flux Φ is then the sum of the applied flux Φ_{app} and the self-induced flux arising from the circulating current,

$$\Phi = \Phi_{\text{app}} + \frac{1}{2}L(I_\alpha - I_\beta). \tag{15.109}$$

This self-induced flux should be taken into account for a proper treatment of Josephson junctions.

F. Junction Loop of Finite Size

As a final example of tunneling we examine a loop in which the two identical junctions are large enough in area so as to contribute to the observed oscillatory current pattern. For this case we can combine the diffraction equation (15.84) for the junction and the interference equation (15.105) for the loop,

$$I = 2I_c \left| \cos(\pi\Phi_L/\Phi_0) \cdot \frac{\sin(\pi\Phi_J/\Phi_0)}{\pi\Phi_J/\Phi_0} \right|, \tag{15.110}$$

where $\Phi_J = B_{\text{app}}A_J$ and $\Phi_L = B_{\text{app}}A_L$ are the amounts of flux in the junctions of area A_J and in the loop of area A_L, respectively, for a particular applied field B_{app}. We can define the critical applied fields B_J and B_L for which one flux quantum Φ_0 is present in the junction and in the loop in terms of their respective areas:

$$B_J = \Phi_0/A_J, \tag{15.111a}$$

$$B_L = \Phi_0/A_L. \tag{15.111b}$$

These expressions permit us to write Eq. (15.110) in terms of the applied field,

$$I = 2I_c \left| \cos(\pi B_{\text{app}}/B_L) \frac{\sin(\pi B_{\text{app}}/B_J)}{\pi B_{\text{app}}/B_J} \right|. \tag{15.112}$$

We call this the *Josephson loop diffraction equation*. Since $A_L \gg A_J$, we have $B_L \ll B_J$, and the expected current pattern is sketched in Fig. 15.58 for the case $B_J = 3B_L$. We see from the figure that the slower individual junction variations constitute an envelope for the more rapid loop oscillations. Figure 15.59a shows some experimental results for a small loop in which the self-induced flux is negligible, so that a pattern similar to the pattern in the center of Fig. 15.58, but with more oscillations, is obtained. Figure 15.59b shows a large loop result in which the self-induced flux is appreciable, so that the minima in the oscillations do not reach zero, as in the pattern of Fig. 15.56. Because this second loop is larger, it has more rapid oscillations, as shown. On each side of Fig. 15.59b we can see traces of the next set of oscillations arising from the second cycles of Eq. (15.112) for the field range $B_J < B_{\text{app}} < 2B_J$, and these are also shown in the pattern of Fig. 15.58.

Equation (15.112) corresponds to the optics analogue of Fraunhofer diffraction from two identical wide slits.

G. Ultrasmall Josephson Junction

When a Josephson junction becomes much smaller than a typical weak link or short junction, new phenomena can appear. As an example, consider an ultra-small junction or nanobridge with area A of $0.01\,\mu m^2$, thickness d of 0.1 nm, and capacitance estimated from the expression $C = \epsilon_0 A/d$ of about 10^{-15} F (Kuzmin and Haviland, 1991; Kuzmin *et al.*, 1991). The change in voltage ΔV brought about by the tunneling of one electron across the junction barrier is given by $\Delta V = e/C = 0.16$ mV, which is an appreciable fraction of a typical junction voltage. This can be enough to impede the tunneling of the next electron. Blocking of current flow has been termed Coulomb blockade (Furusaki and Veda, 1992; Tagliacozzo *et al.*, 1989). Note that it is only in recent

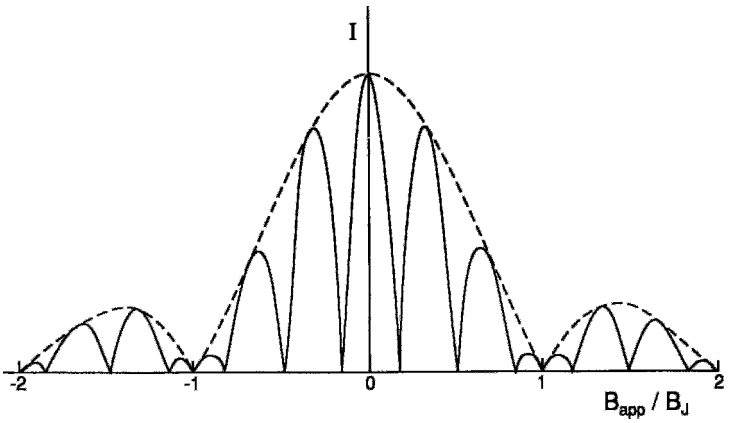

Figure 15.58 Josephson loop diffraction pattern showing the dependence of the super current I flowing through a two-element junction loop of finite size on the magnetic field B_{app}, producing the flux Φ passing through the plane of the loop. The figure is drawn for the case of setting $B_J = 3B_L$ in Eq. (15.112).

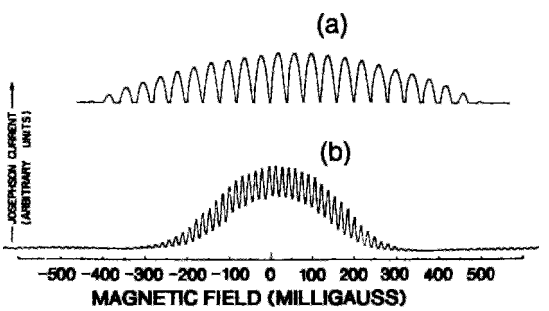

Figure 15.59 Experimentally measured dependence of the Josephson current in a two-element loop on the applied magnetic field. (a) is for the case $B_L \approx 4\,\text{mT}$ and $B_J \approx 50\,\text{mT}$ with negligible self-induced flux ($I_\alpha \approx I_\beta$), so that the oscillations all return to the baseline, as in Fig. 13.58. (b) is for $B_L \approx 1.5\,\text{mT}$ and $B_J \approx 35\,\text{mT}$, so that the self-induced flux is appreciable ($I_\alpha \not\approx I_\beta$) and the rapid oscillations do not return to the baseline (Jaklevic *et al.*, 1965).

decades that techniques such as electron-beam lithography have developed to the point where nanobridges with capacitances in the range 10^{-15}–$10^{-16}\,\text{F}$ can be fabricated (Ralls *et al.*, 1989).

Single-electron tunneling manifests itself by the appearance of fluctuations, called a Coulomb staircase, on an I versus V or dI/dt versus V characteristic, as illustrated in Fig. 15.60 (McGreer *et al.*, 1989).

The Coulomb blockade is a quantum effect that represents the quantization of charge q transferred across a junction. The Hamiltonian, considered as a function of the two conjugate variables q and the phase ϕ, may be written as the sum of a capacitor charging energy, a current bias term, and a Josephson coupling energy.

$$H(q,\phi) = q^2/2C - (\hbar/2e)I\phi - (\pi\hbar/4e^2)(\Delta/R_n)\cos\phi, \tag{15.113}$$

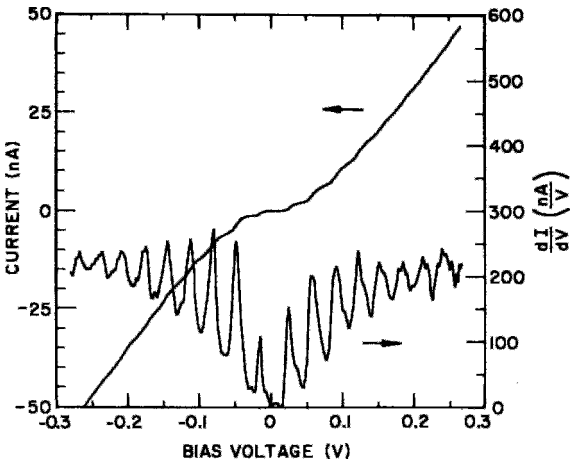

Figure 15.60 Coulomb staircase structure on plots of I versus V and dI/dT versus V of tunneling between a granular lead film and the tip of a scanning tunneling microscope (McGreer *et al.*, 1989).

where I is the bias current, Δ is the energy gap, C is the junction capacitance, and R_n is the normal resistance (Iansiti *et al.*, 1989; Shimshoni and Ben-Jacobs, 1991). For conventional junctions the coupling energy, $(h/8e^2)(\Delta/R_n)\cos\phi$, is dominant and for ultrasmall junctions the charging energy $q^2/2C$ predominates.

There is an uncertainty relationship between the two conjugate variables

$$\Delta\ \phi\ \Delta q \geq e$$

(Graham *et al.*, 1991; Kuzmin *et al.*, 1991). In observing the Coulomb blockade, $q = e$ and the phase (or voltage) fluctuations are large. In the usual dc Josephson effect, which we described in Section VII.B, the phase is well defined and the fluctuations occur in the charge.

In an ultra-small Josephson junction biased by a dc current, correlated tunneling of Cooper pairs can lead to what are called *Bloch oscillations* at the frequency

$$\nu_B = I/2e. \qquad (15.114)$$

One-dimensional N-junction arrays have been used to observe single electron tunneling (Delsing *et al.*, 1989; Kuzmin *et al.*, 1989). A current of $0.01\,\mu\text{A} = 10^{-8}\text{C/s}$ corresponds to a frequency $\approx 3 \times 10^{10}\,\text{Hz}$, which is in the microwave region. Singularities of the observed microwave resistance at the current values corresponding to Eq. (15.114) have provided evidence for the presence of Bloch oscillations (Furusaki and Veda, 1992; Geerligs *et al.*, 1989; Hu and O'Connell, 1993; Kuzmin and Haviland, 1991; Shimshoni *et al.*, 1989). Another type of quantum oscillation is resonant tunneling in the tilted cosine potential illustrated in Fig. 15.61. The figure shows a microwave photon emission accompanying resonant tunneling between levels aligned in adjacent wells (Hata-kenaka *et al.*, 1990; Schmidt *et al.*, 1991).

In an ultra-small junction the effect of a bias current is taken into account by the term $-\hbar I\phi/2e$ in the Hamiltonian (15.113). When the bias current energy $\hbar I_c/2e$ becomes comparable with the charging energy $e^2/2C$, we have $I_c C \approx 3.9 \times 10^{-23}\,\text{AF}$, where I_c is the ideal critical current (Kautz and Martinis, 1990). This relation is satisfied by representative current and capacitance values of some ultra-small junctions.

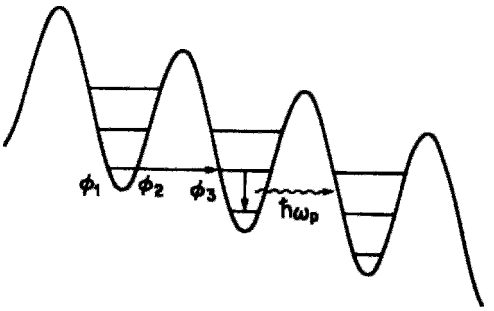

Figure 15.61 Macroscopic resonant tunneling of phase in tilted cosine potential showing the phases ϕ_i at the turning points and the microwave photon emission $\hbar\,\omega$ accompanying the tunneling (Hata-kenaka *et al*., 1990).

H. Arrays and Models for Granular Superconductors

The discussion until now has concerned single Josephson junctions, although we have also examined a pair of junctions. There is an extensive literature on chains, arrays, and layers of Josephson junctions that are coupled together in various ways, and sometimes coupled to an applied current, magnetic field, or radiation (e.g., Eckern and Sonin, 1993; van der Zant *et al*., 1993). High-temperature superconductors can be modeled by arrays of superconducting grains coupled together by Josephson junctions at their interfaces (Babic *et al*., 1991; Cai and Welch, 1992; Deutscher and Chaudhari, 1991; Fishman, 1988, 1989; Majhofer *et al*., 1990; Saslow, 1989; Sugano *et al*., 1992). The junctions in the arrays are often phase locked to each other (cf. Section VIII.B).

I. Superconducting Quantum Interference Device

Flux changes in a loop with two weak lines were shown to produce oscillatory variations in the supercurrent through the loop. A Superconducting Quantum Interference Device (SQUID), is a practical circuit that measures these current variations to quantitatively determine the strength of the applied field. It is more acurate to call such a device a dc SQUID since it measures a slowly changing applied field. A dc SQUID can detect much smaller changes in field than is possible by non-superconducting technology.

One example of a dc SQUID is described in Chapter 5, Section VIII (see Fig. 5.12), and another version is sketched in Fig. 15.62. In the latter arrangement the

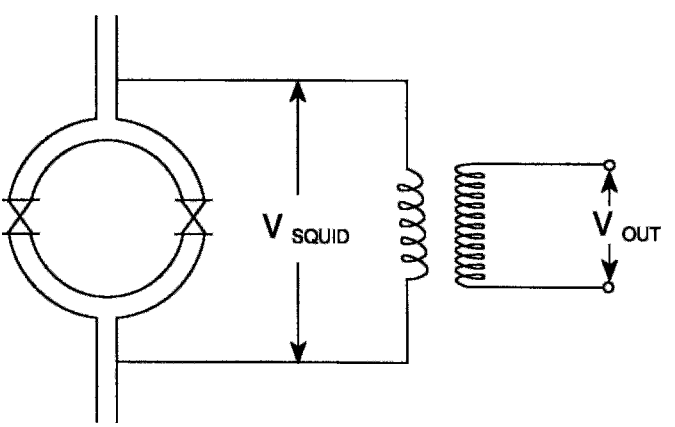

Figure 15.62 Diagram of a Superconducting Quantum Interference Device consisting of two weak links, on the left, showing the voltage V_{SQUID} across them coupled via the transformer to produce the output voltage V_{out}.

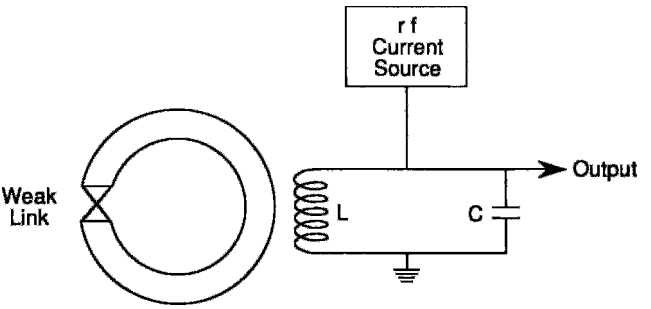

Figure 15.63 An rf SQUID consisting of one weak link coupled to an LC-tuned circuit driven by an rf current source. The rf output voltage is a measure of the change in loading of the tuned circuit produced by a change in flux through the loop.

current change through the weak links is detected as a voltage change across the pair of weak links and then amplified by a step-up transformer followed by further amplification and measurement.

Another type of SQUID, called an rf SQUID, is shown in Fig. 15.63. It consists of a loop with one weak link W coupled to an LC-tuned circuit driven by an rf current source. A change in flux in the loop produces a change in the loading of the tuned circuit, and this is detected by measuring the change in rf voltage across the circuit.

More information on SQUIDs may be obtained from the texts by Van Duzer and Turner (1981) and by Orlando and Delin (1991). SQUIDs have been fabricated from high-temperature superconductors (Gross *et al*., 1990b; Siegel *et al*., 1991; Vasiliev, 1991). Miller *et al*., (1991) discussed a Superconducting Quantum Interference Grating (SQUIG), an interferometer consisting of several Josephson junctions in parallel.

Since a SQUID easily detects a change in one quantum of flux in an area with dimensions in the centimeter range, it is said to measure a macroscopic quantum phenomenon. Orlando and Delin (1991) build on Fritz London's observation that superconductivity is inherently a quantum mechanical phenomenon with macroscopic manifestations in their utilization of a macroscopic quantum model to describe superconductivity.

PROBLEMS

1. Describe N–I–N tunneling in the manner that N–I–S and S–I–S are described in Sections V.E and V.F, respectively. Calculate D_1 and D_2.
2. Derive and justify Eqs. (15.15) and (15.16).
3. Show how to derive the expressions (15.18) and (15.19) for the integrand of Eq. (15.17).
4. Show how to obtain the N–I–S expression (15.20) for I_{ns} from the general tunneling current equation (15.17).
5. Show that in S–I–S tunneling the ratio of the jump in current ΔI_s to the normal tunneling current I_n at the bias $V = 2\Delta/e$ is given by

$$\Delta I_s / I_n = \pi/4,$$

   which is about an 80% jump.
6. Show how Eq. (15.25) for ΔI_s reduces to the simple expression (15.23) in the limit $T \to 0$.

7. Plot $\Delta(T)$ versus T using the data of Fig. 15.26, and compare the plot with Fig. 15.27. How well are the data fit by Eq. (2.65)?
8. Derive Eq. (15.96) from Eq. (15.95).
9. Show how to solve Eq. (15.59):

$$\frac{I}{L} = \frac{d\phi}{d\Theta} + \sin\phi.$$

10. Explain how the washboard analogue sketched in Fig. 15.47 mimics the behavior of a Josephson junction.
11. Justify and derive Eq. (15.70). What is the physical significance of each term?
12. Carry out the integration (15.82) to obtain

$$I = I_c \sin\phi_0 \frac{\sin(\pi\Phi/\Phi_0)}{\pi\Phi/\Phi_0}. \quad (15.83)$$

13. Consider a barrier junction that is 35 μm long and has a 45-nm oxide layer. What applied magnetic field will put one flux quantum in the junction if the superconductors are Nb on one side of the oxide layer and Sn on the other? At what value of the applied field will the first maximum following the principal center maximum appear in the "diffraction pattern"?

This page intentionally left blank

16

Transport Properties

I. INTRODUCTION

In the previous chapter we discussed electron and Cooper pair tunneling, phenomena that constitute important mechanisms of charge transport in superconductors. There are other processes, occurring both above and below T_c, which provide additional information on transport in superconductors, and we will proceed to discuss a number of them. Most of these processes are summarized in Table 16.1.

The chapter begins with a model for ac current flow in superconductors. This is followed by a discussion of the influence of electric and magnetic fields, as well as heat and light, on electrical conductivity. Discussion of the spectroscopic aspects of the interaction with light will be postponed to the next chapter.

II. INDUCTIVE SUPERCONDUCTING CIRCUITS

In earlier chapters, when we remarked that the phenomenon of superconductivity is characterized by a zero-resistance flow of electrical current, we were referring to dc current. There is no heat dissipation when current flows without resistance. We also pointed out, in Chapter 12 Section V.C, that unpinned vortices set into motion by a transport current experience a viscous drag force, and that both ac and dc currents can produce this flux flow dissipation. We will now discuss another process that leads to heat loss.

Table 16.1 Thermoelectric and Thermomagnetic Effects[a]

Effect	Electric field (E or ∇V)	Electric current (I)	Temp. gradient (∇T)	Heat current (dQ/dt)	Magnetic field B_{app}	Figure
Resistivity	Meas. y	Appl. y	0	—	0	2.9
Magnetores. longitud.	Meas. y	Appl. y	0	—	Appl. y	16.16
Magnetores. transv.	Meas. y	Appl. y	0	—	Appl. z	16.16
Thermal cond.	—	0	Meas. y	Appl. y	0	—
Hall	Meas. x	Appl. y	0	—	Appl. z	1.16
Righi-Leduc	—	0	Meas. x	Appl. y	Appl. z	16.47
Seebeck	Meas. y	0	Appl. y	—	0	16.34
Magneto-Seebeck	Meas. y	0	Appl. y	—	Appl. x, y, or z	16.39
Nernst	Meas. x	0	Appl. y	—	Appl. z	16.40
Peltier	—	Appl. y	0	Meas. y	—	16.44
Ettinghausen	—	Appl. y	Meas. x	—	Appl. z	16.45

[a] When the applied quantity is in the y direction, an effect measured longitudinally is also in the y direction, an effect measured transversely is in the x direction, and in most cases an applied magnetic field is in the z direction.

A. Parallel Inductances

In Chapter 2, Section X, we examined a perfect conductor in terms of a simple circuit resistance in parallel with an inductance. Here we wish to consider two possible zero-resistance paths, or channels, through a superconducting grain that can be taken by a super current. Figure 16.1a shows a sketch of the circuit. (It is assumed that the current loops have self and mutual inductance, as in Fig. 16.1b.) The following equations for the two current paths can be deduced from simple circuit analysis by observing that the voltage drop between points A and B of Fig. 16.1b must be the same for the two paths,

$$L_1\frac{dI_1}{dt}+M\frac{dI_2}{dt}=L_2\frac{dI_2}{dt}+M\frac{dI_1}{dt}. \quad (16.1)$$

These can be integrated to give for steady-state current flow

$$(L_1-M)I_1=(L_2-M)I_2. \quad (16.2)$$

In practice, the mutual inductances are negligible, and we have

$$L_1I_1=L_2I_2, \quad (16.3)$$

so that the total current I,

$$I=I_1+I_2, \quad (16.4)$$

splits between the two paths in the inverse ratio of their inductances $I_1/I_2=L_2/L_1$.

B. Inductors

To gain some perspective on the magnitudes of the inductances that are involved in superconducting loops around, for example, the grains of superconductors, it will be helpful to recall some of the expressions that apply to simple inductor geometries with dimensions $\approx 20\,\mu$m. A closely wound N-turn coil of radius r and length d has the inductance

$$L\approx\frac{\pi\mu_0 r^2N^2}{d+0.9r}, \quad (16.5)$$

where the permeability μ_0 is assumed to be that of free space. A long straight wire of length d has the much smaller inductance

$$L\approx\frac{\mu_0 d}{8\pi}. \quad (16.6)$$

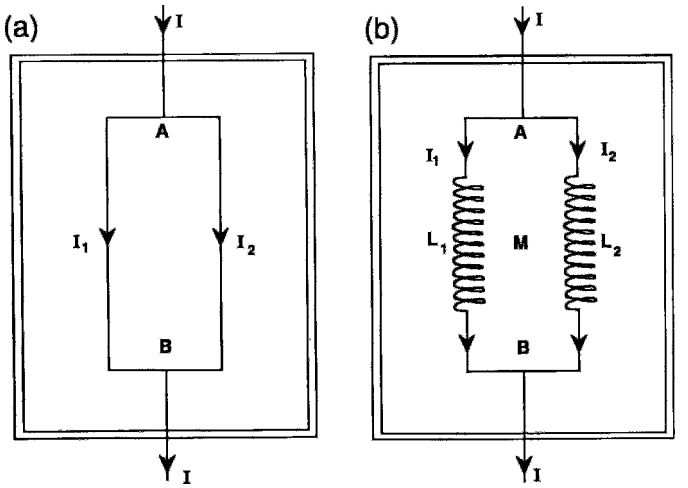

Figure 16.1 A super current I split into two parallel currents I_1 and I_2, perhaps passing through different grains of a superconductor, is shown on the left (a), and the equivalent circuit involving parallel inductances is shown on the right (b).

A loop of wire with the wire radius a and loop radius r has the inductance given by Eq. (2.14), which may be written in the form

$$L \approx \mu_0 r \left(0.0794 + \ln\left(\frac{r}{a}\right)\right), \qquad (16.7)$$

which is small for current paths through grains where r would typically be $20\,\mu$m or less, as is shown in Problem 2.

C. Alternating Current Impedance

When superconducting and normal charge carriers are present during dc current flow, the resistive circuits of the normal carriers will be short-circuited by the zero-resistance circuits of the super current. When the current is alternating, it is assumed that the super current flows in paths with inductance L, and hence with the reactance $i\,\omega L$, and that the normal current flows in paths with the resistance R, as shown in Fig. 16.2. The super current will lag behind the normal current in phase. The voltage drop between points A and B in the figure due to the super current will be the same as that due to the normal current, which corresponds to $I_n R = iI_s\, L\, \omega$. This gives us for the ratio between the magnitudes of the two currents

$$I_n/I_s \approx L\omega/R. \qquad (16.8)$$

The circular loop of Eq. (16.7) has the resistance $R = 2\pi r\rho/\pi a^2$, which gives, inserting the numerical value of μ_0,

$$L/R = 2\pi \times 10^{-7}(a^2/\rho) \times [0.0794 + \ln(r/a)]. \qquad (16.9)$$

We estimate the dimensions $r \approx 30\,\mu$m and $a \approx 3\,\mu$m for typical grain sizes. Using the normal state low-temperature resistivity $\rho \approx 500\,\mu\Omega$ cm of YBaCuO from Table 2.2, we have

$$L/R \approx 2.7 \times 10^{-12} H/\Omega. \qquad (16.10)$$

Equation (16.8) provides an estimate of the dimensionless ratio

$$I_n/I_s \approx 1.7 \times 10^{-11}\nu, \qquad (16.11)$$

where ν is in Hz, so that very little normal current will flow at low frequencies, and

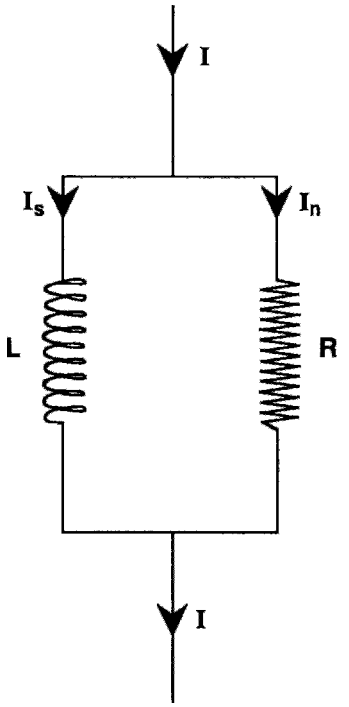

Figure 16.2 Current split similar to that of Fig. 14.1 in which one parallel current, I_s, flows through superconducting material represented by an inductance L, while the other, I_n, flows through normal material represented by a resistance R.

we will have $I \approx I_s$. The current ratio I_n/I_s will be negligible until the frequency exceeds about 10^{11} Hz, at which point ωL becomes comparable to R. At optical frequencies, $\nu > 10^{14}$ Hz, the current flow is mostly normal, $I \approx I_n$. Figure 16.3 shows these frequency dependences of the currents.

The total dissipated power is the power loss due to the normal current in the resistance,

$$P = I_n^2 R. \tag{16.12}$$

From this discussion and Eq. (16.8) we find limiting expressions for the power dissipation at low and high frequencies, respectively:

$$P \approx I^2 R \left(\frac{L\omega}{R}\right)^2 \quad \omega \ll R/L, \tag{16.13a}$$

$$P \approx I^2 R \qquad \omega \gg R/L. \tag{16.13b}$$

Thus the dissipation is negligible at low frequencies, $L\omega \ll R$, while at high frequencies the effective resistance is similar to the normal state value, as in the optical range.

The impedance Z of the parallel L–R circuit shown in Fig. 16.2 has the magnitude and phase angle

$$Z = R\omega L/(R^2 + L^2\omega^2)^{1/2} \tag{16.14}$$

$$\phi = \arctan(R/\omega L), \tag{16.15}$$

with the following limiting values for small and large ω, respectively:

$$Z \approx L\omega, \quad \phi \approx \frac{\pi}{2} \quad \omega \ll \frac{R}{L}, \tag{16.16a}$$

$$Z \approx R \qquad \phi \approx 0 \quad \omega \gg \frac{R}{L}. \tag{16.16b}$$

The result $Z \approx R$ at high frequencies confirms the change to normal state (resistive) behavior that we have already noted.

III. CURRENT DENSITY EQUILIBRATION

Ordinarily, we are interested in equilibrium current flow in which the radial dependence of the current density remains constant along the wire. In this section we will examine what happens when a discontinuity disturbs this regularity. We will find that the disturbance persists for a transition distance along the wire, beyond which spatial equilibrium is restored. For simplicity, we will assume that the undisturbed super current flows with uniform density throughout the entire cross section.

Consider the situation depicted in Fig. 16.4, in which current is flowing in a Type II superconducting wire of radius a. The current enters and leaves the wire radially at the ends, where the radius has been increased to a much larger value c,

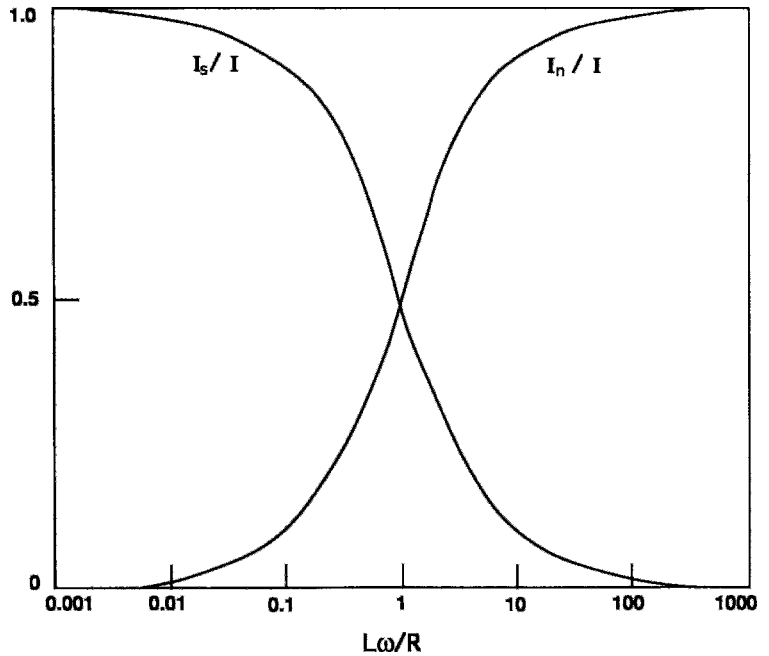

Figure 16.3 Dependence of the superconducting I_s and normal I_n components of the current $I = I_s + I_n$ on the impedance ratio $L\omega/R$ for the loop shown in Fig. 14.2 representing an admixture of superconducting (L) and normal (R) material.

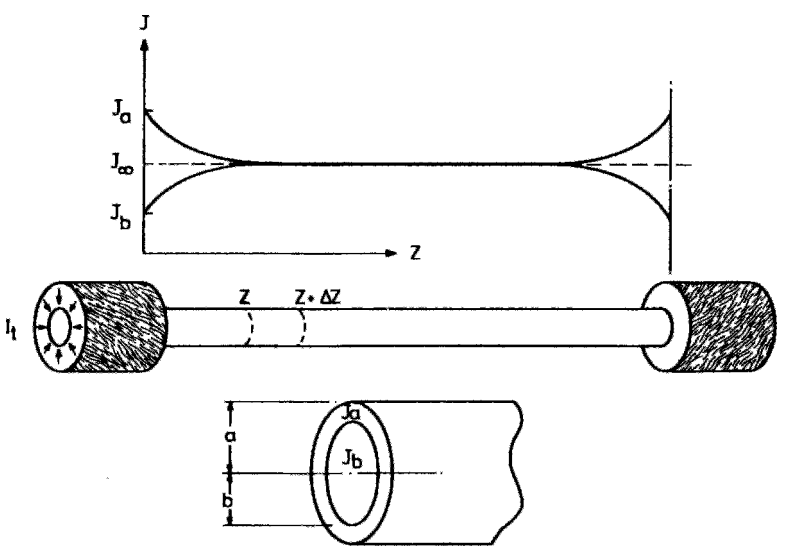

Figure 16.4 Average current densities in the outer (J_a) and inner (J_b) concentric regions of a superconducting wire as a function of the distance z from the junctions at the ends where the current enters and leaves. Within the characteristic distance Λ from the ends $J_a > J_b$ (Wilson, 1983, p. 239).

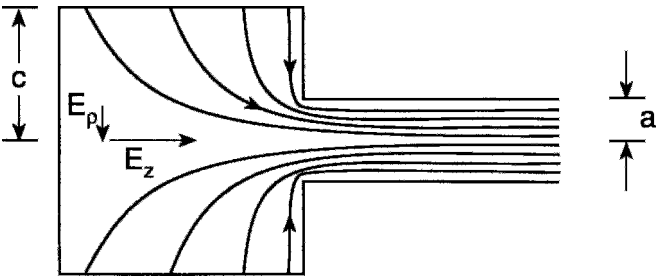

Figure 16.5 Cross section of the current flow contours at one of the junctions of Fig. 14.4. The radial (E_ρ) and axial (E_z) electric fields associated with the current flow in the junction region are indicated.

as indicated in Fig. 16.5. This figure shows how the current-flow contours change gradually from radially directed to longitudinally directed as the current proceeds into the wire. When it enters the narrower part of the wire, it has a greater density toward the surface than in the center. As it proceeds along the wire it gradually becomes uniformly distributed.

To treat this situation quantitatively, we divide the wire into an inner cylinder of radius b and an outer cylindrical shell with inner and outer radii b and a, respectively, as shown in Fig. 16.4. The upper graph in the figure presents a plot of the average current densities J_b and J_a in these two regions, respectively, as a function of the distance z along the wire. The figure shows that uniform-density flow is established after a distance Λ, called the characteristic length. That is, if we wish to measure the critical-current density by gradually increasing the total current until the appearance of a voltage drop ΔV between two electrodes placed along the wire, as shown in Fig. 16.6, care must be taken to locate the electrodes a distance from the ends greater than the characteristic distance Λ.

Near the ends of the wire, where $J_a > J_b$, equilibrium is brought about by the presence of a voltage drop between the inner and outer parts of the wire. The radial electric field component E_ρ associated with this voltage drop, shown in Fig. 16.5, causes an inward current flow, and E_ρ decreases with the approach to uniform density as we proceed along the wire. This situation is treated theoretically by Dresner (1978). Plots made from Dresner's equations, which show how the voltage drop in the wire associated with this radial electric field varies with the distance from the ends, are presented in Fig. 16.7. We see from the figure that as z increases from 0.01Λ to Λ, the radial electric field decreases by over four orders of magnitude to a negligibly small value, confirming that the current density has now become uniform throughout the wire. The three curves in the figure are for the three values of the parameter n occurring in Dresner's model. The results for $z > \Lambda$ are insensitive to n,

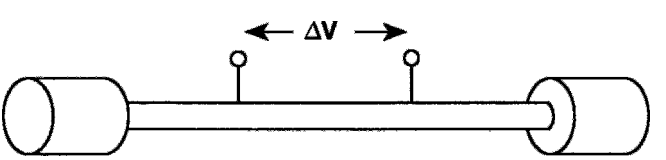

Figure 16.6 Location of the voltage probes on the wire of Fig. 14.4 at positions a distance more than one characteristic length Λ from the junctions.

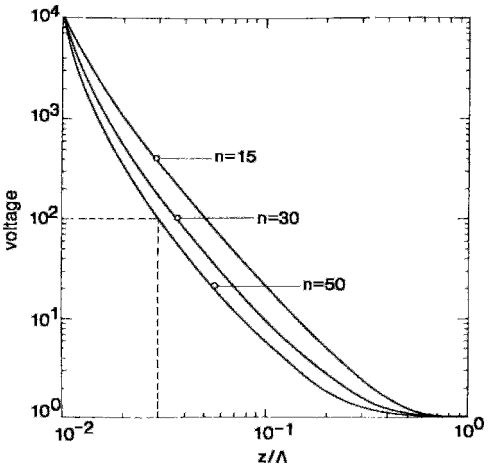

Figure 16.7 Voltage V associated with the radial electric field inside a filamentary wire as a function of the distance z from the junction. Figure 16.5 shows the radial field in the junction and also plots E_ρ in the wire. The constant in Dresner's (1978) equations was selected to make $V = 10^4$ at $z/\Lambda = 10^{-2}$. We see that for all values of Dresner's parameter n, the radial voltage becomes negligibly small within a distance equal to one characteristic length from the junction (Wilson, 1983, p. 241).

since the residual radial field approaches zero for all three choices of n.

We have been assuming that equilibrium current flow occurs with uniform density. There are also cases of a pronounced radial distribution, as in the Bean model, when the penetration depth λ limits the current to a surface layer. When this is the case, λ is the distance that must be traveled to reach the equilibrium state.

IV. CRITICAL CURRENT

The most important transport property of a superconductor is its ability to carry a super current without any dissipation. Chapter 2 discussed transport current and its characteristics of zero resistance and persistence. Some additional understanding of super current flow was provided by the Bean model treatment of Chapter 13. Shielding current was treated at length in Chapters 5, 12, and 13, while the previous chapter discussed current flow through tunnel junctions. The current-induced intermediate state was described in Chapter 11. We now wish to examine the anisotropy of current flow, and its dependence on the magnitude and direction of an applied magnetic field.

A. Anisotropy

Super current flows more easily in the Cu–O planes of high-temperature superconductors than perpendicular to these planes (Gross *et al.*, 1990a). The data in Table 13.4 demonstrate that the critical transport current for flow in the *a, b*-planes is much greater than for flow perpendicular to these planes, i.e., parallel to the *c* direction, $(J_c)_{ab} \gg (J_c)_c$. Because of this high anisotropy, almost all critical current measurements on single crystals or epitaxial films are for flow in the *a, b*-planes.

A good way of showing that J_c in the Cu–O plane is much greater than J_c perpendicular to this plane is to use the magnetization current method of determining J_c, as explained in Chapter 13, Section VI.E. Figure 16.8 shows the temperature dependence of the in-plane magnetization critical current determined by this method for a $Bi_2Sr_2CaCu_2O_8$ monocrystal. The crystal was in the shape of a platelet with the *c*-axis along the short direction, and the magnetic field was applied along *c* for this measurement. When the field was applied parallel to the plane, as indicated in the inset to Fig. 16.9, the current exhibited a similar decrease with increasing temperature. The plot was constructed with the aid of the Bean model, taking into account the difference in the field penetration along the narrow (t) as opposed to along the broad (w) faces, as indicated in the inset. The researchers found that w/t ratios from

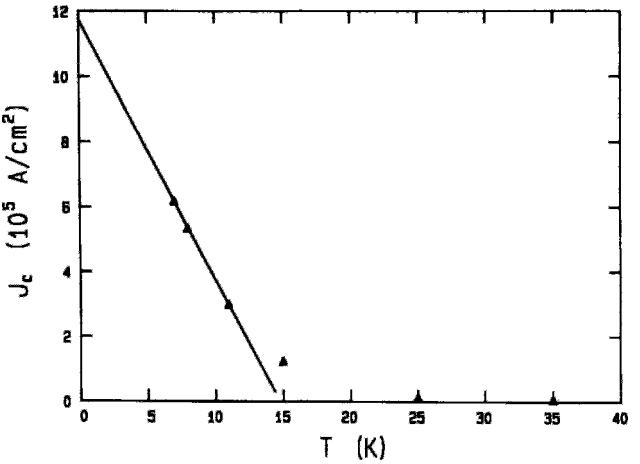

Figure 16.8 Temperature dependence of the critical current J_c determined by magnetization method for a magnetic field applied perpendicular to the Cu–O planes (Biggs *et al.*, 1989).

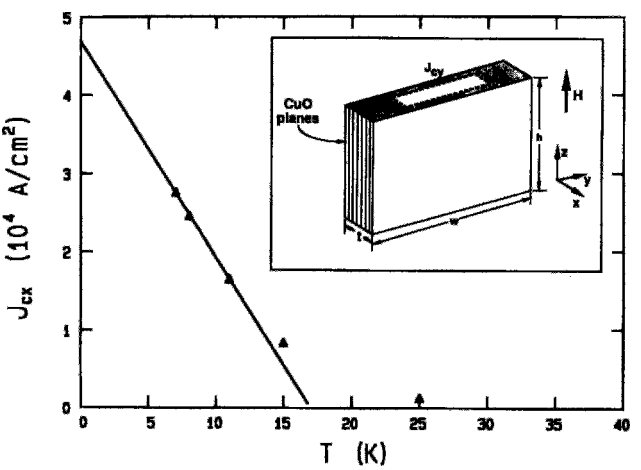

Figure 16.9 Temperature dependence of the critical current J_c determined by the magnetization method for a magnetic field applied parallel to the Cu–O planes. Shaded areas of the inset represent flux penetration (Biggs *et al.*, 1989).

8 to 23 gave the same value of J_c. Of course, for a continuous current flow path, the larger current density, J_{cy} in the figure, is associated with a smaller effective penetration depth, as indicated. Farrell *et al.* (1989a) reported that the magnetization current anisotropy of yttrium cuprate is much larger than those of the lanthanum and thallium cuprates.

B. Magnetic Field Dependence

We will describe the effects of applied magnetic fields on the flow of transport current in the *a, b*-plane of cuprates (Satchell *et al.*, 1988). We see from Fig. 16.10 that for an epitaxial film of $Bi_2Sr_2CaCu_2O_8$ ($T_c \approx 80$ K), the critical current is smaller when the field is applied along *c*, perpendicular to the plane of the film, than when it is applied

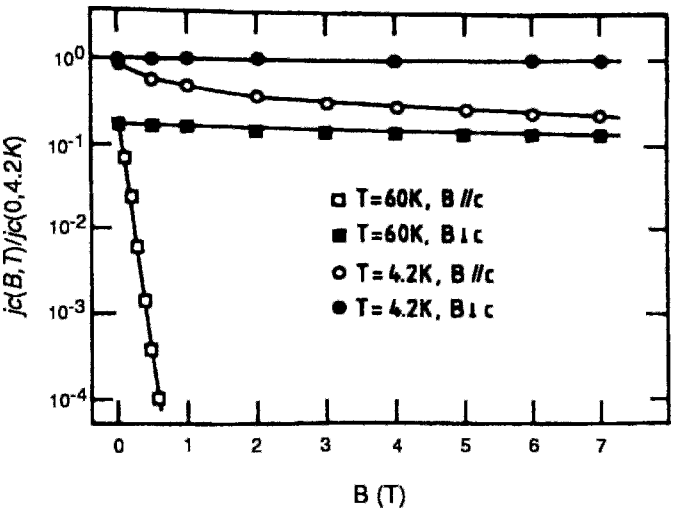

Figure 16.10 Magnetic field dependence of the transport critical current of a $Bi_2Sr_2CaCu_2O_8$ epitaxial film determined at 4.2 K and 60 K for magnetic fields applied parallel to the Cu–O planes, i.e. $\mathbf{B} \perp c$, and perpendicular to the Cu–O planes, i.e. $\mathbf{B} \| c$, (Schmitt *et al.*, 1991).

in the plane. We also see that the drop-off in J_c with increasing field is especially pronounced at 60 K, and much less so at 4.2 K.

Ekin *et al.* (1990, 1991; cf. Lan *et al.*, 1991) made a more comprehensive study of the magnetic field dependence of transport current in grain-aligned

$$YBa_2Cu_3O_{7-\delta}.$$

The grains were platelets, $\approx 5\,\mu$m in diameter, with the c-axis perpendicular to the plane, forming blocks approximately 1 mm × 1 mm in cross section and 15 mm long. Their results, summarized in Figs. 16.11 and 16.12, show that applying the field along the c direction ($B \perp ab$) causes a greater decrease in the current than applying the field in the plane ($B \| ab$). The current decreased much less with increasing field at 4 K than it did at 76 K. In all of these measurements, the applied field and current flow were perpendicular. Force-free values of J_c were determined by rotating the applied field along J_c, which increased the critical current, as indicated in the figures.

The dependence of the critical current on the angle which the applied field makes with the c direction, shown in Fig. 16.13, suggests that J_c depends on $\cos\Theta$ (Maley *et al.*, 1992; Schmitt *et al.*, 1991; Ekin *et al.*, 1991; Fukami *et al.*, 1991b; Miu, 1992). Maley *et al.* (1992) found that the applied field degraded the magnetization currents to a greater extent than did the transport currents, as indicated in Fig. 16.14.

V. MAGNETORESISTANCE

In this section we will discuss the resistivity of a wire in the presence of a magnetic field, which ordinarily is applied transverse to the current direction. This resistivity, called the *magnetoresistivity* ρ_m, is the same as the ordinary zero-field resistivity ρ for some metals, though it has a different value for others. First we will treat the case of a superconductor above and in the neighborhood of its transition temperature, and then we will show that below T_c the resistance can arise from flux flow.

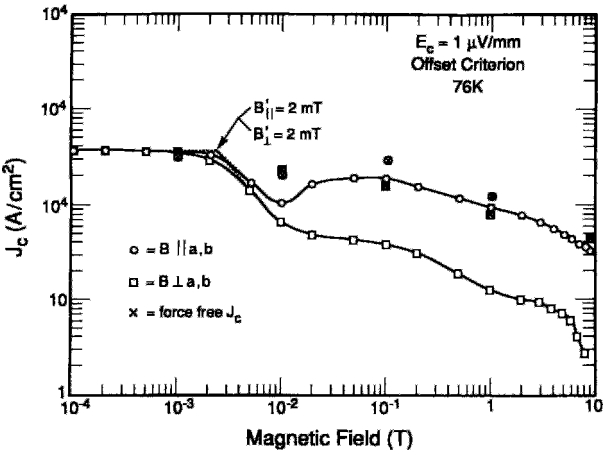

Figure 16.11 Magnetic field dependence of the transport critical current of grain-aligned $YBa_2Cu_3O_{7-\delta}$ determined at 76 K for magnetic fields applied parallel ($\mathbf{B} \parallel a, b$) and perpendicular ($\mathbf{B} \perp a, b$) to the Cu–O planes. The darkened symbols (filled with X) are measurements made with the applied field rotated so as to be directed along the current direction (Ekin *et al.*, 1990).

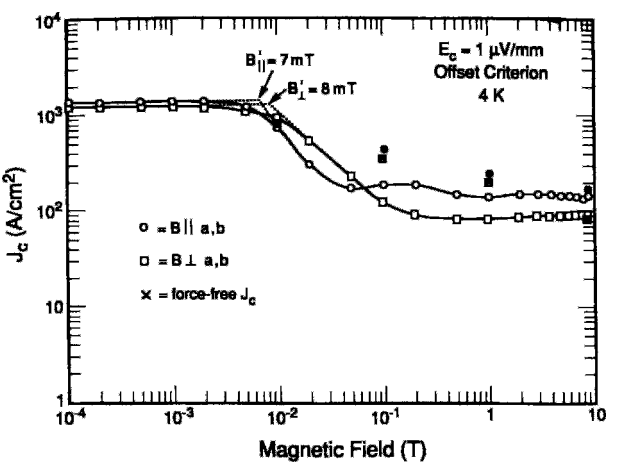

Figure 16.12 Same geometry and physical situation as in Fig. 16.11, at liquid helium temperature (Ekin *et al.*, 1990).

A. Fields Applied above T_c

Consider the current flow situation illustrated in Fig. 1.16 in the absence of a magnetic field. The flowing current produces the potential difference $V_2 - V_1$ between the ends of the wire. The resistance R as given by Ohm's law,

$$R = (V_2 - V_1)/I, \tag{16.17}$$

may be written in terms of the current density $J = I/ad$ and the longitudinal electric field $E_y = (V_2 - V_1)/L$ to give for the resistivity (1.97)

$$\rho = E_y/J, \tag{16.18}$$

which is equivalent to Eq. (1.21).

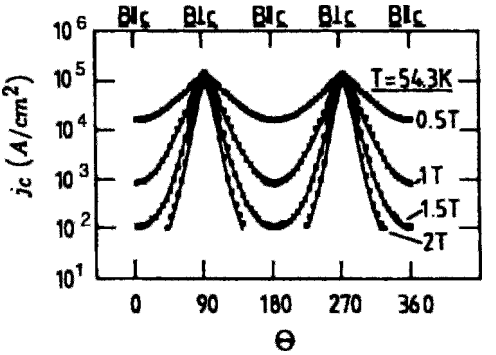

Figure 16.13 Dependence of the critical-current density of a $Bi_2Sr_2CaCu_2O_{8+x}$ epitaxial film on the angle Θ between the applied magnetic field and the *c*-axis. For all angles the field was perpendicular to the current direction (Schmitt *et al.*, 1991).

When a transverse magnetic field is applied, as shown in the figure, a transverse Hall effect field $\mathbf{E}_x = \mathbf{v} \times \mathbf{B}_{\text{app}}$ (see Eq. (1.90)) is induced that separates the charge on either side of the wire, as explained in Chapter 1, Section XVI. A resistance measurement provides the magnetoresistivity ρ_{m},

$$\rho_{\text{m}} = E_y/J, \tag{16.19}$$

which is more precisely called the transverse magnetoresistivity. The longitudinal magnetoresistivity is defined for a magnetic field aligned along the direction of current flow.

For ordinary (normal-state) conductors the applied field does not affect the longitudinal current flow, so that the resistance of a wire is field independent, and ρ_{m} from (16.19) equals the ordinary resistivity from (16.18). However, at very high magnetic fields the trajectories of the electrons deflected by the field can be open, i.e., extending from one Brillouin zone into the next, or they can close on themselves in *k*-space, making the situation complicated. The magnetoresistivity often tends to increase with increasing magnetic field strength, but in some cases it saturates, that is, approaches a field-independent value at the highest fields.

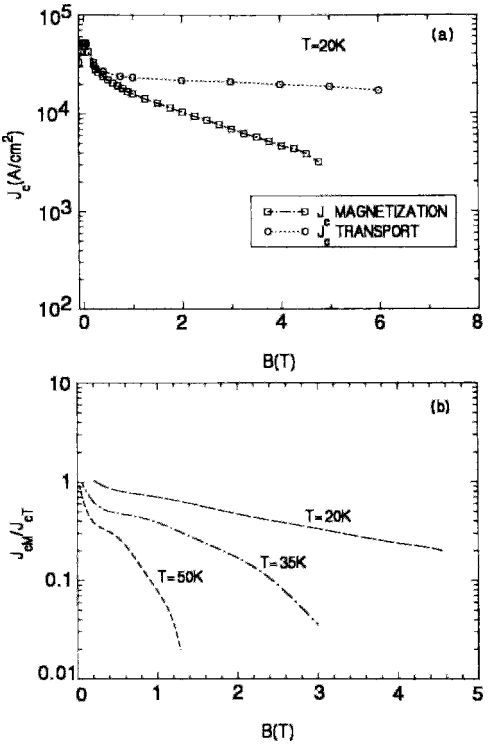

Figure 16.14 Magnetic field dependence of critical-current densities obtained from magnetization and transport measurements of a Pb-doped BiSrCaCuO/Ag superconducting tape showing (a) individual critical current densities at 20 K, and (b) ratio of magnetization to transport critical-current densities at 20 K, 35 K, and 50 K (Maley *et al.*, 1992).

The magnetoresistance of the cuprates in the normal state is not very much affected by the application of small or moderate magnetic fields. This can be seen from Fig. 16.15 for fields up to 7 T applied to $Bi_2Sr_2CaCu_2O_8$ several degrees above T_c (Briceño *et al.*, 1991). A study of $YBa_2Cu_3O_7$ showed very little change in the transverse and longitudinal magnetoresistance for fields up to 10 T and temperatures up to 200 K. For higher fields at 200 K, the longitudinal magnetoresistance was found to increase and its transverse counterpart was found to decrease

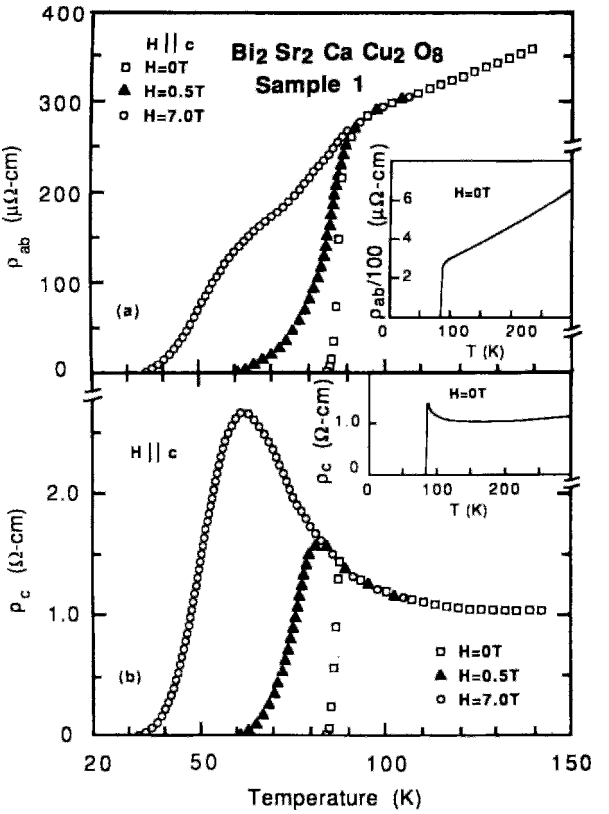

Figure 16.15 Temperature dependence of the magnetoresistance in the a, b-plane (top) and along the c direction (bottom) of a $Bi_2Sr_2CaCu_2O_8$ monocrystal for magnetic fields of 0, 0.5, and 7.0 T applied along the c direction (Briceño *et al.*, 1991).

slightly as the applied field was raised to 43 T (Oussena *et al.*, 1987).

B. Fields Applied below T_c

In the superconducting state the presence of an applied magnetic field shifts the transition temperature downward and broadens the transition in the manner illustrated in Figs. 16.15 and 16.16 for two bismuth cuprates (Ando *et al.*, 1991a, b; Briceño *et al.*, 1991; Fiory *et al.*, 1990; Palstra *et al.*, 1988). Such a downward shift is also to be expected from Fig. 2.46. Similar results have been reported for $(La_{1-\delta}Sr_\delta)_2CuO_4$ (Preyer *et al.*, 1991; Suzuki and Hikita, 1991), $Nd_{1.85}Se_{0.15}CuO_4$ (Suzuzi and Hikita, 1990), $YBa_2Cu_3O_7$ (Blackstead, 1992, 1993; Hikita and Suzuki, 1989; Kwok *et al.*, 1990a), and $Tl_2Ba_2CaCu_2O_8$ (Kim and Riseborough, 1990; Poddar *et al.*, 1989). The zero-field plots of Fig. 16.15 are similar to the $YBa_2Cu_3O_7$ resistivity plots of Fig. 2.7 for ρ_{ab} and ρ_c, with the c-direction resistivity exhibiting a rise slightly above T_c for both compounds. The figures provide ratios $\rho_c/\rho_{ab} \approx 150$ for $YBa_2Cu_3O_7$ and

$$\rho_c/\rho_{ab} \approx 5600$$

for $Bi_2Sr_2CaCu_2O_8$, which demonstrate that the bismuth compound is much more anisotropic. This also constitutes one of

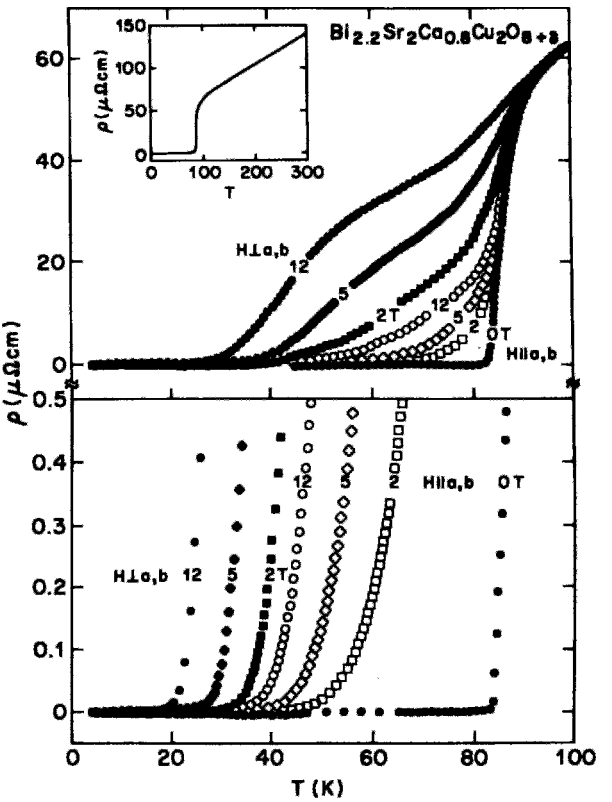

Figure 16.16 Temperature dependence of the magnetoresistance in the a, b-plane of a $Bi_{2.2}Sr_2Ca_{0.8}Cu_2O_{8+\delta}$ monocrystal with magnetic fields of 0, 2, 5, and 12 T applied parallel to and perpendicular to the a, b-plane. The lower part shows the ordinate scale magnified by a factor of about 100 to emphasize the exponential behavior (Palstra *et al.*, 1988).

the principal differences between the two superconductors (Raffy *et al.*, 1991). The n-type superconductor $Nd_{1.85}Se_{0.15}CuO_4$ has $\rho_c/\rho_{ab} \approx 310$, which is closer to the value for the yttrium compound (Crusellas *et al.*, 1991). Figure 16.16 shows that the shift and broadening of the in-plane resistivity (ρ_{ab}) plots are greater for applied fields along the c-axis than for applied fields in the a, b-plane. (The lower part of Fig. 16.16 is magnified by a factor of 100 to emphasize the rapid exponential drop of the resistivity down to zero for all applied field magnitudes and directions.)

We see from Figs. 16.15 and 16.16 that the in-plane magnetoresistivity ρ_{ab} has a bulge halfway down the curve. The expansion of the sharp zero-field resistivity transition of a $YBa_2Cu_3O_7$ monocrystal, shown in Fig. 16.17, reveals that there are actually two very close transition temperatures, $T_{c1} = 90.71$ K and $T_{c2} = 90.83$ K, which separate in applied magnetic fields and are responsible for the observed bulge.

C. Fluctuation Conductivity

The cuprate superconductors exhibit strong temperature and magnetic field

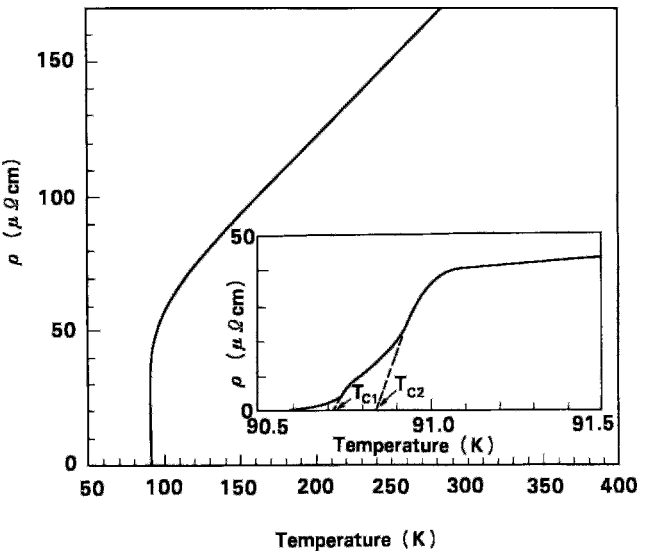

Figure 16.17 Expansion of the region near T_c of a ρ_{ab}-versus-T curve of a $YBa_2Cu_3O_7$ monocrystal showing the two closely spaced critical temperatures T_{c1} and T_{c2} (Hikita and Suzuki, 1989).

dependencies just above T_c that are responsible for the rounding of the resistivity plots of Figs. 16.15, 16.16, and 2.21 at the knee just above T_c. Aronov *et al.* (1989) assumed that the field-dependent part of the electrical conductivity $\Delta\sigma$,

$$\Delta\sigma = \sigma(B) - \sigma(0), \tag{16.20}$$

obtained from the resistivity measurements, where $\sigma = 1/\rho$, is due entirely to the superconductivity fluctuations. Another approach (Bieri and Maki, 1990; D. H. Kim *et al.*, 1991a; Semba *et al.*, 1991; Suzuki and Hikita, 1989) for explaining fluctuation conductivity made use of the Aslamazov–Larkin (Aslamazov and Larkin, 1968) term due to the excess current carried by Cooper pairs and the Maki–Thompson mechanism (Maki, 1968; Thompson, 1970) of forward scattering on quasiparticles due to Cooper pairs. Several researchers have provided plots of $\Delta\sigma$ versus the field or temperature for $La_{2-x}Sr_xCuO_4$ (Suzuki and Hikita, 1989), $YBa_2Cu_3O_7$ (Bieri and Maki, 1990; Matsuda *et al.*, 1989; Osofsky *et al.*, 1991; Semba *et al.*, 1991), $Nd_{1.85}Se_{0.15}CuO_4$ (Kussmaul *et al.*, 1991), and

$$Tl_2Ba_2CaCu_2O_8$$

(Kim *et al.*, 1991a). The Hikami–Larkin approach (Hikami and Larkin, 1988) has been used to obtain values of the coherence length $\xi_{ab} = 15.6\,\text{Å}$ and $\xi_c = 3.6\,\text{Å}$ for $YBa_2Cu_3O_7$ (Andersson and Rapp, 1991).

D. Flux-Flow Effects

When transport current flows in the presence of an applied magnetic field, the vortices arising from the field interact with the current, as was shown in Chapter 12, Section VI.G. This interaction can lead to vortex motion and heat dissipation, and the result is a resistive term called flux-flow resistance. It is a type of magnetoresistance, and limits the achievable critical current in many samples.

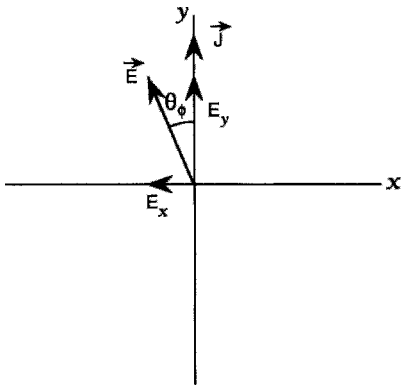

Figure 16.18 Electric field E induced by the motion of a vortex Φ_0 moving at a velocity v_ϕ through an applied magnetic field B_{app} directed upward from the page. The vectors $\mathbf{E}$, $\mathbf{v}_\phi$, and $\mathbf{B}_{app}$ are mutually perpendicular. The vectors for the current density $\mathbf{J}$ and the Lorentz force $\mathbf{J} \times \mathbf{\Phi}_0$ are also indicated.

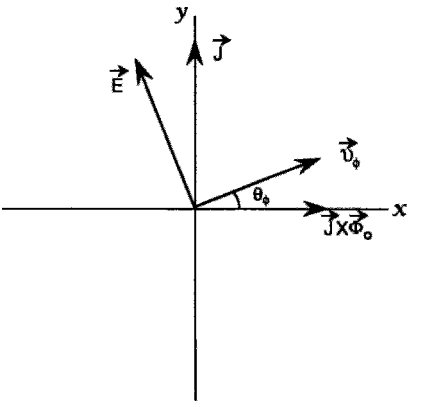

Figure 16.19 Resolution of the induced electric field of Fig. 14.18 into components transverse (E_x) and longitudinal (E_y) to the current density direction ($\mathbf{J}$).

We showed in Chapter 12, Section V.C, that when the Lorentz force $\mathbf{J} \times \mathbf{\Phi}_0$ exceeds the pinning force F_P,

$$|\mathbf{J} \times \Phi_0| > F_p, \tag{16.21}$$

where $\mathbf{\Phi}_0$ is the quantum of flux, the vortices move with the velocity $\mathbf{v}_\phi$ in accordance with the equation of motion Eq. (12.75). The vortex velocity is limited by the frictional drag force $\beta \mathbf{v}_\phi$, while the Magnus force $\alpha n_s e(\mathbf{v} \times \mathbf{\Phi}_0)$ shifts the direction of this motion through an angle Θ_ϕ away from the direction perpendicular to $\mathbf{J}$, as shown in Fig. 16.18.

By Faraday's law, the motion of the vortices transverse to the current density induces a time-averaged macroscopic electric field $\mathbf{E}$, which is given by

$$\mathbf{E} = -\mathbf{v}_\phi \times \mathbf{B}_{in} \tag{16.22}$$

as indicated in Fig. 16.18, where $\mathbf{B}_{in}$ is the average internal field due to the presence of the vortices. The component of this electric field E_y along the current-flow direction,

$$E_y = E \cos \Theta_\phi, \tag{16.23}$$

shown in Fig. 16.19, produces a voltage drop along this direction. The other component of the induced electric field, $E_x = E \sin \Theta_\phi$, produces a Hall effect, as we will show in the following section.

Figure 16.20 shows how the longitudinal voltage drop along the wire depends on the applied current for two $Nb_{1/2}Ta_{1/2}$ samples with different concentrations of pinning centers (Strnad *et al.*, 1964; see also Tilley and Tilley, 1986, p. 229). Beyond the initial curvature, the V versus I curves of Fig. 16.20 may be represented at low voltage by the equation

$$V = R_{ff}(I - I_c), \tag{16.24}$$

where the slopes of the lines provide the flux-flow resistance R_{ff}. The flux-flow resistivity is given by

$$\rho_{ff} = \frac{R_{ff} a d}{L}, \tag{16.25}$$

where the sample dimensions are shown in Fig. 1.16. In Fig. 16.20 we see that the

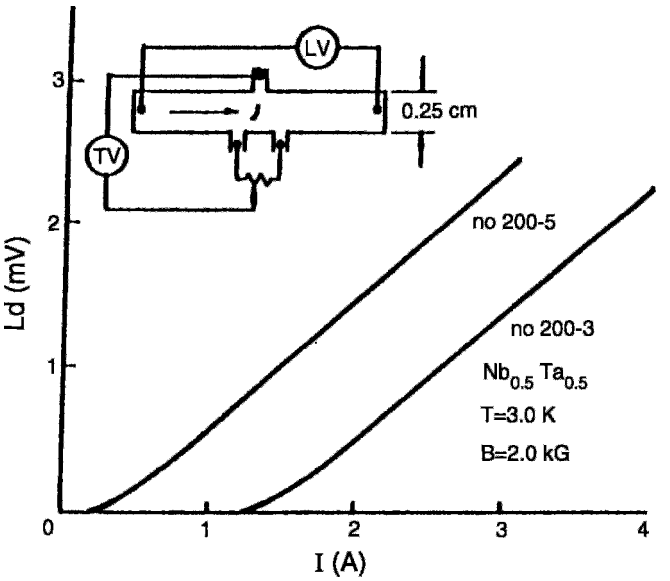

Figure 16.20 Voltage–current characteristics of an $Nb_{1/2}Ta_{1/2}$ superconductor in a magnetic field of 0.2 T at the temperature 3.0 K. The two curves, for samples containing different concentrations of defect pinning centers, have almost the same slope and hence the same flux–flow resistance, but differ in their critical currents I_c. The inset shows the experimental arrangement for the measurements (Strnad *et al.*, 1964).

slopes of the straight lines for the two samples are the same, while the intercepts differ due to the variation in pinning force. Measurements made with different magnetic field strengths, shown in Fig. 16.21, exhibit slopes that increase with the magnetic field (Huebener *et al.*, 1970; see also Huebener, 1979, p. 126). Figure 16.22 shows the magnetic field dependence of the flux-flow resistance for three temperatures.

To a first approximation, the critical-current density J_c is obtained by setting the Lorentz force $\mathbf{J} \times \mathbf{\Phi}_0$ equal to the pinning force $\mathbf{F}_P$,

$$\mathbf{J}_c \times \Phi_0 = \mathbf{F}_p. \tag{16.26}$$

After the onset of flux flow, increasing $\mathbf{J}$ increases the fluxon velocity $\mathbf{v}_\phi$, which may be calculated using the models introduced in Chapter 12, Section V.F. If the Magnus force is neglected, then, as we show in Problem 7, the flux-flow resistivity is

$$\rho_{ff} = \Phi_0 B_0/\beta. \tag{16.27}$$

Strnad *et al.* (1964) found that ρ_{ff} is given by the following empirical relation:

$$\rho_{ff} = \rho_n(B_{in}/B_{c2}). \tag{16.28}$$

The ratio B_{in}/B_{c2} is approximately proportional to the fraction of the material that is "occupied" by the "normal" vortex cores. Thus the resistivity can be imagined as arising from electric current flowing through the normal material that constitutes the vortex cores.

VI. HALL EFFECT

The Hall effect provides information on the sign, concentration, and mobility of

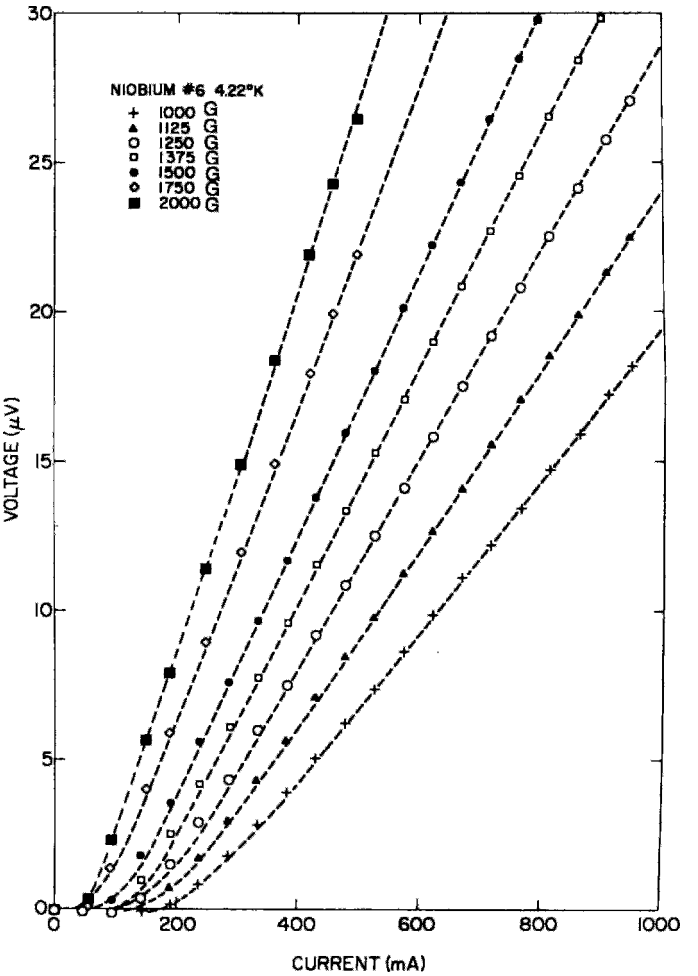

Figure 16.21 Voltage–current characteristics of a niobium foil at 4.22 K in magnetic fields ranging from 0.1 to 0.2 T (1000 to 2000 G), as indicated. The flux-flow resistances evaluated from the linear portions of the plots range from 25 $\mu\Omega$ for the lowest (0.1 T) curve to 64 $\mu\Omega$ for the highest (0.2 T) curve (Huebener *et al.*, 1970).

charge carriers in the normal state, with a positive sign for the Hall coefficient $R_H = E_x/JB_0 = \pm 1/ne$ of Eqs. (1.91) and (1.92) indicating that the majority carriers are holes. In the superconducting state, the Hall voltage arises from the electric field induced by flux motion. Chapter 1, Section XVI, describes a Hall effect measurement made with the experimental arrangement of Fig. 1.16. Hall effect probes have been used to measure the local field at the surface of a superconductor in an applied field B_{app} (Brawner *et al.*, 1993).

A. Hall Effect above T_c

Perhaps the most important result that has been obtained from Hall effect measurements above T_c is that the charge carriers in the copper-oxide planes of most of the high-temperature superconductors are holes. Included in this group are the lanthanum,

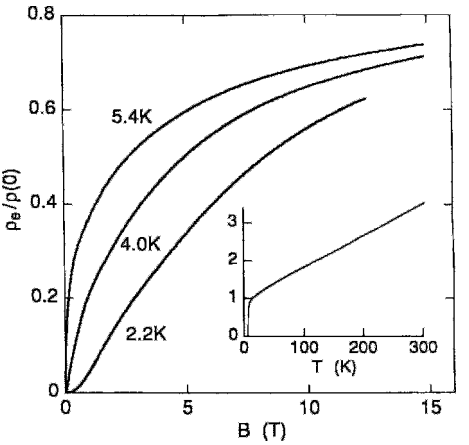

Figure 16.22 Magnetic field dependence of the flux-flow resistivity of $Bi_{2+x}Sr_{2-y}CuO_{6\pm\delta}$ for transport in the *a, b*-plane at three temperatures below the 7 K transition temperature. The inset shows the temperature dependence of the resistivity at zero field. The abscissae are normalized to the value $\rho(0) = 90\,\mu\Omega$ cm (Fiory *et al.*, 1990).

yttrium, bismuth, thallium, and mercury classes of compounds. The major exception is compounds with the Nd_2CuO_4T' structure described in Chapter 8, Section VII.E; their charge carriers are electron-like.

It is easy to argue on the basis of chemical considerations as to why the lanthanum and yttrium compounds are hole-like. Replacing a La^{3+} by a Sr^{2+} without changing the oxygen content can convert a Cu^{2+} to Cu^{3+} on one of the CuO_2 planes, which is the same thing as introducing a hole in a plane. The stoichiometric $YBa_2Cu_3O_7$ compound has an average Cu charge of 2.33, corresponding to one Cu^{3+} and two Cu^{2+} ions, so there is already one trivalent copper ion to contribute a hole. It has also been suggested that the hole might exist on oxygen, corresponding to the ion O^-. From a band structure viewpoint we can say that the hole is in an oxygen $2p$ band.

In contrast, an electron superconductor can be created by doping with a cation having a higher charge, such as substituting Ce^{4+} for Nd^{3+} in $(Nd_{1-x}Ce_x)_2CuO_4$, or substituting a trivalent rare earth such as $R = Gd^{3+}$ for Ca^{2+} in the compound $TlCa_{1-x}R_xSr_2Cu_2O_7$, perhaps to convert Cu^{2+} to Cu^+, or to add an electron to the conduction band. In addition, it has been found that the Hall effect is negative for the applied field aligned in the *a, b*-plane of $YBa_2Cu_3O_7$ (Penney *et al.*, 1988; Tozer *et al.*, 1987). Table X-3 of our earlier work (Poole *et al.*, 1988) summarizes some Hall effect results.

Several research groups have found that the Hall number V_0/R_He of

$$YBa_2Cu_3O_7$$

has a temperature dependence of the form

$$V_0/R_He = A + BT, \qquad (16.29)$$

as shown in Fig. 16.23, where $V_0 = 174$ Å

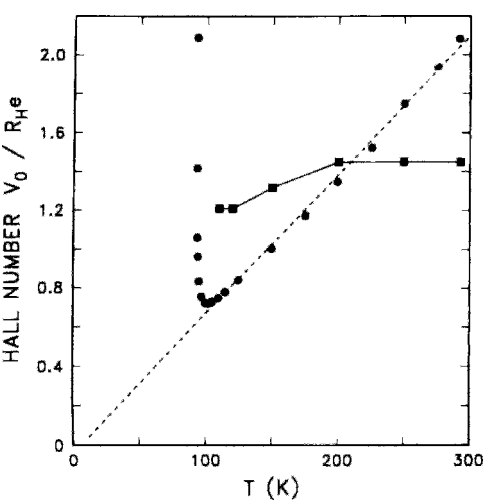

Figure 16.23 Temperature dependence of the Hall number V_0/R_He of $YBa_2Cu_3O_{7-\delta}$. The squares show the nearly temperature independent *n*-type Hall number of one sample for the magnetic field in the *a, b*-plane, while the circles show the *p*-type Hall number for another sample in which the applied field is perpendicular to the *a, b*-plane. The dashed curve is a linear fit to the data above T_c; the solid curve is provided as a visual aid. Near T_c the Hall number diverges, so that the Hall voltage tends to zero (Penney *et al.*, 1988).

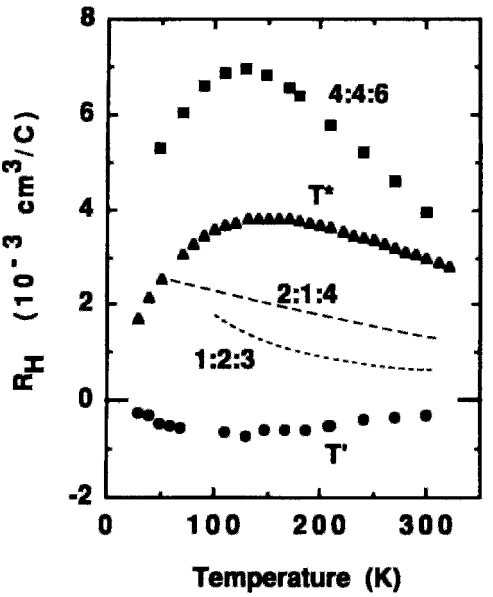

Figure 16.24 Temperature dependence of the Hall coefficient R_H for $(Nb_{0.925}Ce_{0.075})_2CuO_{4-\delta}$ ($T_c = 18$ K, e type, T' phase), $(Nb_{0.7}Ce_{0.1}Sr_{0.2})_2CuO_{4-\delta}$ ($T_c = 23$ K, T* phase), $(Nb_{2/3}Ce_{1/3})_4(Nd_{1/3}Ba_{5/12}Sr_{1/4})_4Cu_6O_y$ ($T_c = 38$ K, 4:4:6 compound), $(La_{0.925}Sr_{0.075})_2CuO_{4-\delta}$ ($T_c = 38$ K, T phase, 2:1:4 compound), and $GdBa_2Cu_3O_{7-\delta}$ (1:2:3 compound) (Cheong *et al.*, 1987; Ikegawa *et al.*, 1990).

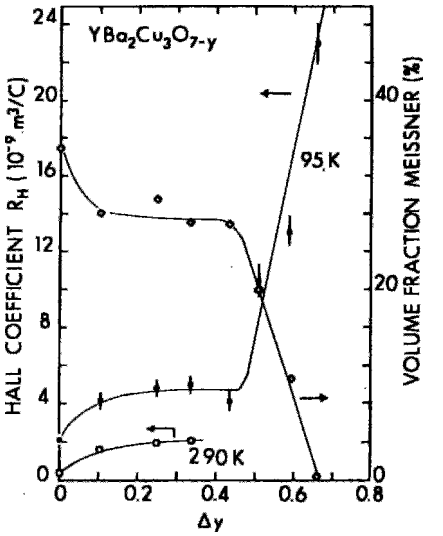

Figure 16.25 Dependence of the Hall coefficient R_H on the oxygen content δ at 77 K (filled circles) and 290 K (open circles). The percentage of the sample exhibiting the Meissner effect is also plotted, with the scale on the right. The solid lines are provided as visual aids (Z. Z. Wang *et al.*, 1987).

and $A \approx 0$ (Penney *et al.*, 1988; *a, b*-plane data from Tozer *et al.*, 1987). The divergence at T_c shown in the figure arises from the Hall voltage (i.e., E_x) going to zero at the transition. Many superconductors do not exhibit the temperature dependence of Eq. (16.29), as the data plotted in Fig. 16.24 demonstrate (Ikegawa *et al.*, 1990; Gd compound data from Cheong *et al.*, 1987). The data for the electron superconductor $(Nd_{0.925}Ce_{0.075})_2CuO_{4-\delta}$ that are plotted in this figure show that R_H is negative, as expected. In Problem 8 it is necessary to show that the other four compounds in this figure are hole-like. The Hall coefficient is also strongly affected by the oxygen content, as shown by the plots in Fig. 16.25.

Mandal *et al.* (1989) compared the Hall numbers per Cu ion for the various high-temperature superconductors. Their results are plotted in Fig. 16.26. We see from the figure that these Hall numbers lie along two straight lines.

Hall effect measurements, like other transport measurements, are affected by sample quality, and hence strongly dependent on factors such as sample preparation, defects, and grain boundaries. This can be deduced from the scatter in some of the data listed in Table X-3 of our earlier work (Poole *et al.*, 1988).

B. Hall Effect below T_c

We have shown that flux flow arising from a transport current in a superconductor below T_c induces an electric field **E** given by Eq. (16.22). The component of this electric field perpendicular to the direction of the

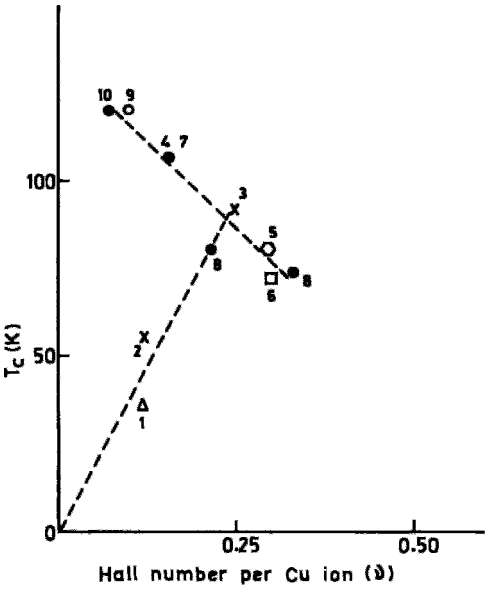

Figure 16.26 Plot of the superconducting transition temperature T_c versus the Hall number per Cu ion, for (1) $(La_{0.925}Sr_{0.075})_2CuO_4$ (Ong *et al.*, 1987), (2) $YBa_2Cu_3O_{6.7}$ (Z. Z. Wang *et al.*, 1987), (3) $YBa_2Cu_3O_7$ (Z. Z. Wang *et al.*, 1987), (4) BiSrCaCuO (Clayhold *et al.*, 1988), (5) $Bi_2(Sr, Ca)_3Cu_2O_{8.35}$ (Takagi *et al.*, 1988), (6) $BiSrCaCu_2O_x$ (Skumryey *et al.*, 1988), (7) $BiSrCaCu_2O_x$ (mixed phase, Mandal *et al.*, 1989), (8) $BiSrCaCu_2O_x$ (85 K phase, Mandal *et al.*, 1989), (9) $Tl_2Ca_2Ba_2Cu_3O_x$ (Clayhold *et al.*, 1988), and (10) $TlCa_3BaCu_3O_x$ (Mandal *et al.*, 1989). The dashed lines are provided as visual aids (figure from Mandal *et al.*, 1989).

current, $E_x = E \sin \Theta_\phi$, shown in Fig. 16.19, produces a Hall-effect voltage. The Hall resistivity ρ_{xy}, defined by Eq. (1.99),

$$\rho_{xy} = E_x/J_y, \tag{16.30}$$

is close to zero for low applied fields in the mixed state below T_c and negative for higher fields. Thereafter, it becomes positive and increases linearly with further increases in field, as shown in Fig. 16.27 for $YBa_2Cu_3O_7$ (Hagen *et al.*, 1990a; Rice *et al.*, 1992). The inset of this figure shows the Hall resistance of a niobium film versus the applied field at $T = 9.16\,\mathrm{K}$, which is slightly below T_c.

We see from Fig. 16.28 that in the mixed state below T_c the Hall mobility $\mu_H = R_H/\rho$ of $Bi_{2+x}Sr_{2-y}CuO_{6\pm\delta}$ increases as the magnetic field is increased and also as the temperature is increased.

VII. THERMAL CONDUCTIVITY

In Chapter 1, Section VIII, we saw that the heat currents carried by conduction electrons are closely related to electrical currents. An additional complication in the heat transport case is that the carriers of heat can be either charge carriers like electrons or electrically neutral phonons, whereas electrical current arises only from charge carrier transport. The transformation to the superconducting state changes the nature of the carriers of the electric current, so it is to be expected that the transport of heat will be strongly affected. In this section we will examine how this comes about. Some theoretical treatments are available (e.g., Oguri and Maekawa, 1990; Peacor *et al.*, 1991a; Tewordt and Wölkhausen, 1989; Wermter and Tewordt, 1991a, b).

A. Heat and Entropy Transport

The thermal current density $\mathbf{U}$ is the thermal energy per unit time crossing a unit area aligned perpendicular to the direction of heat flow. It is a vector representing the transport of entropy density S_ϕ at the velocity $\mathbf{v}$,

$$\mathbf{U} = TS_\phi \mathbf{v}, \tag{16.31}$$

from the hotter to the cooler regions of the material (Maki, 1991). It proportional to the gradient of the temperature ∇T through Fourier's law,

$$\mathbf{U} = -K \nabla T, \tag{16.32}$$

where K is the coefficient of thermal conductivity.

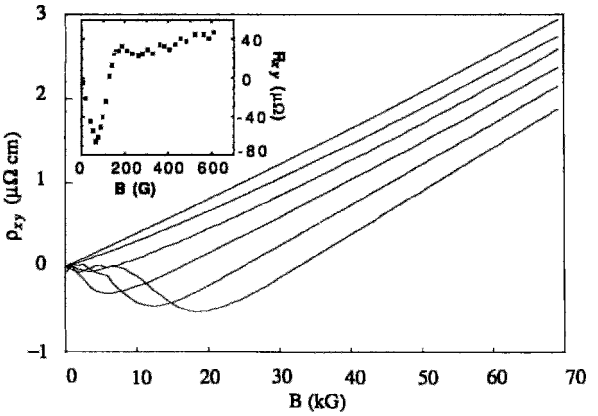

Figure 16.27 Dependence of the Hall resistivity p_{xy} of a $YBa_2Cu_3O_7$ film on the magnetic field from 0 to 7 T for six temperatures near $T_c \approx 90$ K, illustrating the linearity at high field. The temperatures from bottom to top are 88.4, 89.1, 89.8, 90.5, 91.5, and 93.0 K. The inset shows the Hall resistance of a niobium film versus the field from 0 to 60 mT at a temperature of 9.6 K (Hagen *et al.*, 1990a).

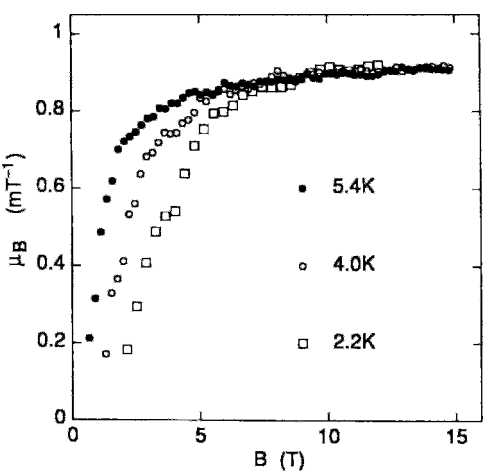

Figure 16.28 Magnetic field dependence of the Hall mobility μ_H in the mixed state of $Bi_{2+x}Sr_{2-y}CuO_{6\pm\delta}$ at three temperatures (Fiory *et al.*, 1990).

In the normal state, electrical conductors are good conductors of heat in accordance with the law of Wiedermann and Franz (1.33). In the superconducting state, in contrast, the heat conductivity can be much lower because, as Uher (1990) points out, Cooper pairs carry no entropy and do not scatter phonons.

B. Thermal Conductivity in the Normal State

The principal carriers of thermal energy through metals in the normal state are conduction electrons and phonons. Heat conduction via each of these two channels acts independently, so that the two channels constitute parallel paths for the passage of heat. A simple model for the conduction of heat between two points A and B in the sample is to represent the two channels by parallel resistors with conductivities K_e and K_{ph} for the electronic and phonon paths, respectively, as shown in Fig. 16.29a. The conductivities add directly, as in the electrical analogue of parallel resistors, to give the total thermal conductivity K,

$$K = K_e + K_{ph}. \qquad (16.33)$$

The electronic path has an electron–lattice contribution K_{e-L}, which is always present, and an impurity term K_{e-I}, which becomes dominant at high defect concentrations. In like manner, the phonon path has a phonon–electron contribution K_{ph-e} plus an additional

contribution $k_{\text{ph}-\text{I}}$ from impurities. Since each pair of terms involves the same carriers of heat, they act in series and add as reciprocals, as in the electrical analogue case of Mattheissen's rule (1.30), where the resistivities (reciprocals of conductivities) add directly. The result is

$$\frac{1}{K_{\text{e}}} = \frac{1}{K_{\text{e}-\text{L}}} + \frac{1}{K_{\text{e}-I}}, \tag{16.34}$$

$$\frac{1}{K_{\text{ph}}} = \frac{1}{K_{\text{ph}-\text{e}}} + \frac{1}{K_{\text{ph}-I}}, \tag{16.35}$$

which corresponds to Fig. 16:29b.

It is shown in standard solid-state physics texts that the electronic contribution to the thermal conductivity has the form

$$K_{\text{e}-\text{L}} = \tfrac{1}{3} v_{\text{F}} l C_{\text{e}} \tag{16.36}$$

$$= \tfrac{1}{3} \gamma v_{\text{F}}^2 \tau T, \tag{16.37}$$

where we have used Eqs. (1.5), the electron mean free path $l = v_{\text{F}}\tau$, and, from (1.51), $C_{\text{e}} = \gamma T$. If we recall from Eq. (1.23) that $\tau \approx T^{-3}$ at low temperatures and $\tau \approx T^{-1}$ at high temperatures, applying the law of Wiedermann and Franz (1.33) gives us

$$K_{\text{e}-\text{L}} \approx \begin{cases} \dfrac{[\text{const}]}{T^2} & T \ll \Theta_{\text{D}} \\ [\text{const}] & T \gg \Theta_{\text{D}} \end{cases} \tag{16.38}$$

for temperatures that are low and high, respectively, relative to the Debye temperature Θ_{D}. In Chapter 1, Section VII, we saw that at the lowest temperatures the electrical conductivity $\sigma(T)$ approaches a limiting value, $\sigma(T) \to \sigma_0$, arising from the impurity contribution. For this term the law of Wiedermann and Franz gives

$$K_{\text{e}-\text{I}} \to [\text{const}]T \qquad T \to 0. \tag{16.39}$$

The temperature dependence of the thermal conductivity of copper, shown in Fig. 16.30, seems to follow this behavior. There is an initial linear region corresponding to Eq. (16.39), a maximum in the curve due

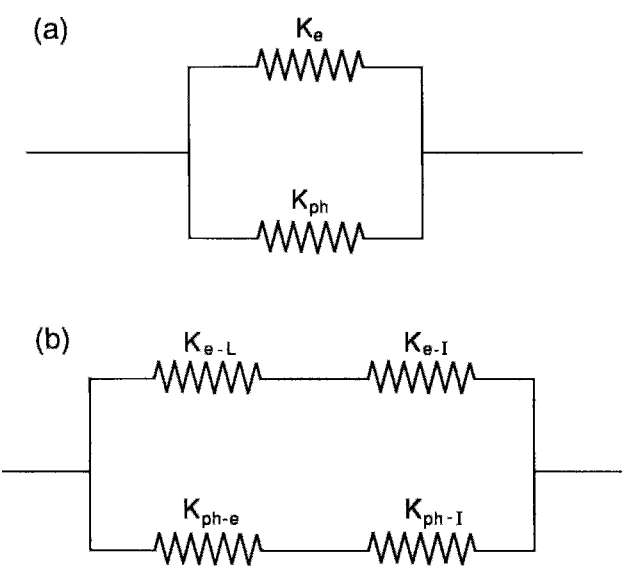

Figure 16.29 Representation of the electron and phonon heat-conduction paths between two points A and B (a) by parallel resistors with respective conductivities K_{e} and K_{ph}, and (b) representation of the interaction mechanisms with the lattice (L) and impurities (I) operative along each of these two paths by a pair of series resistors.

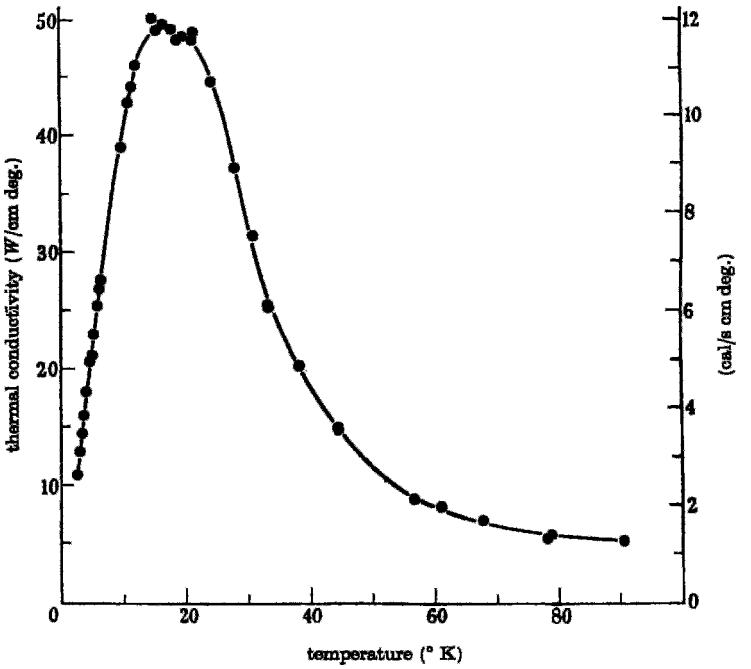

Figure 16.30 Temperature dependence of the thermal conductivity of copper (Berman and MacDonald, 1952).

to the $1/T^2$ term, which should dominate in the intermediate temperature region, perhaps near $T/\Theta_D \approx 0.05$–0.5, and a final asymptotic term at high temperatures.

The lattice contribution to the thermal conductivity has a form which is the phonon analogue of Eq. (16.36),

$$K_{ph-L} = \frac{1}{3} v_{ph} l_{ph} C_{ph}, \qquad (16.40)$$

where Eqs. (1.62a) and (1.62b) give the low- and high-temperature limits of C_{ph}, respectively. The temperature dependence is, however, more complicated than that predicted by the specific heat term, since C_{ph} increases with T, whereas the phonon mean free path l_{ph} decreases with increasing temperature, which not only compensates for C_{ph}, but also tends to cause K_{ph-L} to drop.

In pure metals the electronic contribution to the thermal conductivity tends to dominate at all temperatures, as in the Cu case of Fig. 16.30. When many defects are present, as in disorganized alloys, they affect K_{ph} more than K_e, and the phonon contribution can approach or exceed that of the conduction electrons.

C. Thermal Conductivity below T_c

Thermal conductivity involves the transport of entropy S_ϕ; super electrons, however, do not carry entropy nor do they scatter phonons. We also know from Eq. (4.47) (cf. Fig. 4.8) that below T_c the entropy of a superconductor drops continuously to zero, so that the thermal conductivity can be expected to decrease toward zero also. Figure 16.31 shows this behavior for aluminum (Burns, 1985, p. 657; Scatterthwaite, 1962). The figure plots the ratio of the superconducting state to normal state thermal conductivities K_s/K_n as a function of temperature, where K_n was measured in the presence of a magnetic field $B > B_c$ that

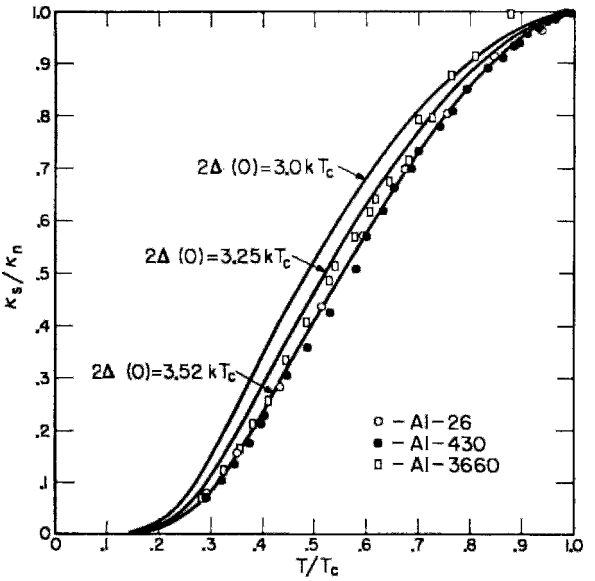

Figure 16.31 Dependence on temperature of the ratio between the electronic thermal conductivity of Al in the superconducting state and its normal-state value. The normal-state data were obtained in a magnetic field that extinguished the superconductivity. The data were fitted by the curve calculated from the BCS theory for $2\Delta/k_BT = 3.52$ (Satterthwaite, 1962).

extinguished the superconductivity. We see from the figure that the data fit the BCS theory very well. The behavior shown in Fig. 16.31 is typical of elemental superconductors. A material of this type could be employed as a heat switch by using a magnetic field to change its thermal conductivity by more than a factor of 100.

In high-temperature superconductors the phonon contribution to the thermal conductivity is predominant above T_c. The onset of superconductivity can have the effect of first increasing the conductivity until it reaches a maximum, beyond which it decreases at lower temperatures, as shown in Fig. 16.32 (Cohn *et al.*, 1992a, c; Heremans *et al.*, 1988; Pillai, 1991; Terzijska *et al.*, 1992; Uher and Huang, 1989; R. C. Yu *et al.*, 1992; cf. Marshall *et al.*, 1992; Szasz *et al.*, 1990). This increase can occur when the thermal conductivity arises mainly from the phonon-electron contribution to K_{ph}. The onset of the superconducting state causes normal electrons to condense into Cooper pairs. These no longer undergo collisions with the phonons and hence do not participate in the phonon–electron interaction. The result is a longer mean free path l_{ph} in Eq. (16.40) and a larger conductivity, as shown in Fig. 16.32 for the unirradiated sample below T_c (Uher, 1990). Irradiating the sample produces defects that limit the mean free paths of the phonons and charge carriers, and leads to a decrease in the thermal conductivity and a suppression of the peak of Fig. 16.32. At lower temperatures, freezing out of the lattice vibrations is reflected in the $C_{ph} \approx AT^3$ term (see Eq. 1.62a) of Eq. (16.40), which becomes negligible relative to the impurity term (16.39). In turn, the latter becomes enhanced by irradiation, and the result is a decrease in K.

Thermal conductivity measurements have been reported, inter alia, on the lan-

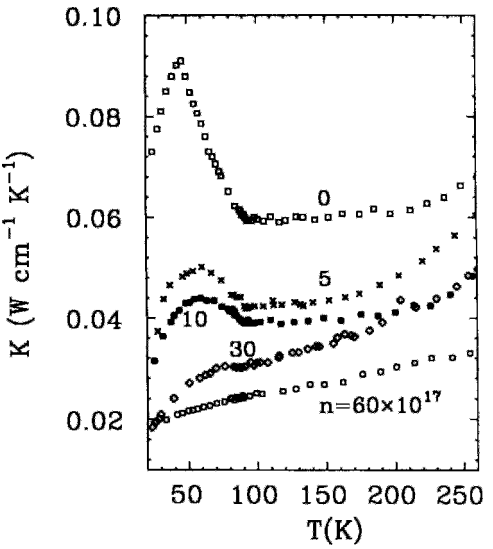

Figure 16.32 Decrease in the thermal conductivity of $YBa_2Cu_3O_{7-\delta}$ brought about by irradiation with fast neutrons at given levels of irradiation, with fluences from 0 up to 6×10^{18} neutrons/cm^2, as indicated (Uher and Huang, 1989).

thanum (Bartkowski *et al.*, 1987), bismuth (Peacor and Uher, 1989; Zhu *et al.*, 1989), and $Ba_{1-x}K_xBi$ superconductors (Peacor *et al.*, 1990).

D. Magnetic Field Effects

In a Type II superconductor the thermal conductivity begins to decrease at the lower-critical field B_{c1}, passing through a minimum and then increasing with increasing field until it reaches its normal-state value at the upper critical field B_{c2} (Zhu *et al.*, 1990), as shown in Fig. 16.33 for the superconductor Bi doped In (Dubeck *et al.*, 1964). This behavior is explained by Uher (1990) as due to the presence of vortices acting as additional scattering centers for phonons, which dominate transport far below T_c, and electronic excitations, which are more important near T_c, where quasiparticles are still plentiful. At the lower critical field, vortices enter the superconductor, degrading the thermal conductivity by inducing increased scattering. As the upper critical field is approached, the electronic excitations associated with the normal core of the vortices begin to enhance the thermal conductivity. The fact that the conductivity is independent of the magnetic field in the Meissner state, where $B_{app} < B_{c1}$, as shown in Fig. 16.33, provides further support for this explanation.

The magnetic field dependence of the thermal conductivity of superconductors has been studied (Peacor *et al.*, 1991b; Regueiro *et al.*, 1991; Richardson *et al.*, 1991); entropy transport due to vortex motion (Palstra *et al.*, 1990) and magnetocaloric cooling (Rey and Testardi, 1991) have been observed in $YBa_2Cu_3O_7$.

E. Anisotropy

The planar structure of high-temperature superconductors makes the thermal conductivity anisotropic. This type of anisotropy has been observed in polycrystalline samples of $YBa_2Cu_3O_{7-\delta}$ with the microcrystallites aligned along the compression axis (Kirk *et al.*, 1989). For a single crystal, the ratio of the in-plane K_{ab} to the out-of-plane (c-axis) K_c thermal conductivity has been observed to have the value

$$K_{ab}/K_c \approx 17$$

for $YBa_2Cu_3O_7$ (Shao-Chun *et al.*, 1991), $K_{ab}/K_c \approx 6$ for $BiSr_2CaCu_2O_8$ (Crommie and Zettl, 1991), and $K_{ab}/K_c \approx 9$ for $Tl_2Ba_2CaCu_2O_8$ (Shao-Chun *et al.*, 1991). The electrical-conductivity anisotropy is much greater, amounting to $\sigma_{ab}/\sigma_c \approx 10^4$ for the bismuth crystal (Crommie and Zettl, 1991).

VIII. THERMOELECTRIC AND THERMOMAGNETIC EFFECTS

A conductor which is open circuited, as shown in Fig. 16.34, and possesses a temperature gradient can develop an electric field

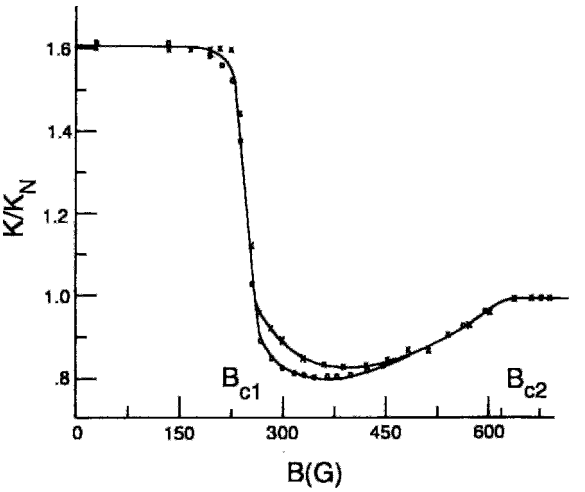

Figure 16.33 Dependence of the thermal conductivity of $In_{0.96}Bi_{0.04}$ normalized to its normal-state value on applied magnetic fields up to 70 mT (700 G). Changes in conductivity occur at the lower- (B_{c1}) and upper- (B_{c2}) critical fields, as indicated (Dubeck *et al*., 1964).

along the gradient direction, called the *thermopower* or *Seebeck effect*, and an electric field perpendicular to this gradient, called the *Nernst effect*. When an isothermal electric current flows, a thermal current can appear flowing parallel to the electric current direction. This is called the *Peltier effect*; an electric current flowing perpendicular to the electric current direction is called the *Ettingshausen effect*. In the two longitudinal effects, Seebeck and Peltier, the central role is played by normal state charge carriers,

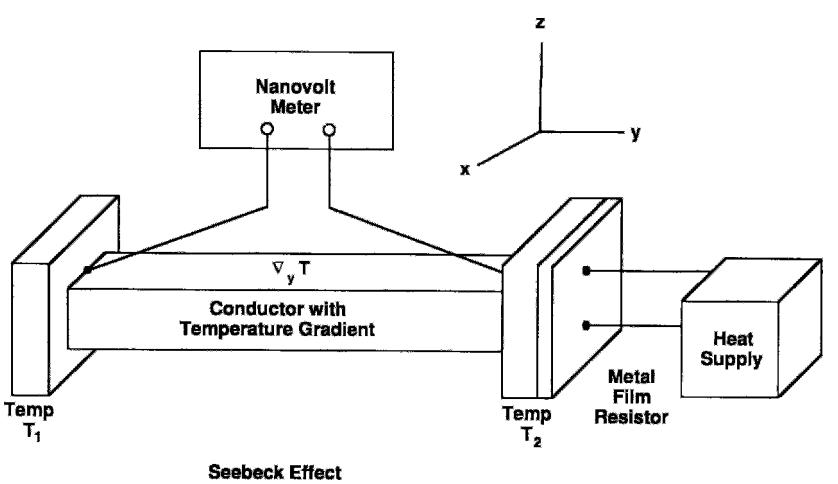

Figure 16.34 Experimental arrangement for measuring the Seebeck effect (thermo-power) voltage across a conductor mounted between two temperature reservoirs T_1 and T_2. The heat dissipation in the metal film raises the temperature T_2 above T_1.

or quasiparticles. The two transverse effects, Nernst and Ettinghausen, require the presence of an applied magnetic field. For superconductors the central role is played by the motion of vortices (Huebener *et al*., 1990; Palstra *et al*., 1990; Ullah and Dorsey, 1990). This means that the Seebeck and Peltier effects are useful for studying superconductors above T_c, whereas the Nernst and Ettinghausen effects provide important information below T_c. Finally, there is a fifth effect, called the *Righi–Leduc effect*, which is the thermal analogue of the Hall effect. This effect can be observed in superconductors below T_c. The characteristics of these five effects are summarized in Table 16.1.

The thermoelectric effects are generally described in solid-state physics texts in terms of bimetallic circuits. A bimetallic circuit can be in the form of a superconducting rod in series with an ordinary conducting wire, such as one made of copper. Since the transverse effects (Nernst, Ettingshausen, Righi–Leduc) occur in the presence of a magnetic field, they are also referred to as thermomagnetic effects. Some articles report more than one transport measurement, such as magnetoresistivity, Hall effect, thermopower, etc., on the same sample (e.g., Burns *et al*., 1989; Freimuth *et al*., 1991; Fujishita *et al*., 1991; Ikegawa *et al*., 1992; Kaiser and Uher, 1988; Ohtani, 1989; Sugiyama *et al*., 1992; Z. H. Wang *et al*., 1993). The polar Kerr effect (Spielman *et al*., 1992) and the magneto optical Faraday effect (Forkl *et al*., 1990) of high-temperature superconductors have also been reported.

A. Thermal Flux of Vortices

In Chapter 12, Section VI, we discussed the motion of vortices in the presence of applied magnetic fields and currents; some of the thermomagnetic effects can be explained in terms of this motion. Vortex motion can also be induced by the presence of a temperature gradient. We will say a few words about the origin of this motion before proceeding to describe the effects themselves.

Consider a Type II superconductor in a uniform applied magnetic field. The density of vortices, which is equal to B_{in}/Φ_0, where Φ_0 is the quantum of flux, is independent of the temperature. If a temperature gradient is established perpendicular to the magnetic field direction, the vortices in the high-temperature regions will have larger radii than those in the low-temperature regions because the effective radius, which is equal to the penetration depth, increases with the temperature, as indicated in Fig. 2.42. We saw in Chapter 12, Section V.A, that the range of the repulsive force between two vortices increases with the penetration length. This means that the vortices at the hot end of a sample will exert a force on their neighbors that pushes them toward the cooler end of the sample. Thus the uniformity of the magnetic field tends to preserve a constant flux density while the thermally induced forces tend to produce flux motion. The result is a continual flux flow, with vortices entering the sample at the hot end and leaving at the cold end. This is illustrated in Fig. 16.35.

From a thermodynamic viewpoint, the force producing flux motion can be looked upon as a thermal force $-S_\phi \nabla T$ equal to the product of what is called the transport entropy S_ϕ (which is measured per vortex unit length) (de Lange and Gridin, 1992; Samoilov *et al*., 1992) and the temperature gradient ∇T. The motion of vortices subject to this force can be described by a vortex equation of motion similar to Eq. (12.75), with the Lorentz force term replaced by the thermal force.

The entropy density within a vortex core, where the material is in the normal state, is higher than it is in the surrounding superconducting medium, causing the vortex to move toward the lower temperature region, where the medium will have a lower entropy density. This pecularity of the entropy density represents one explanation for the flux flow in the presence of

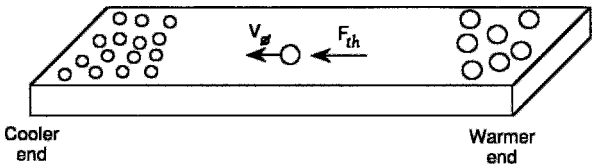

Figure 16.35 Vortex flow from the warmer end of a superconducting slab, where the vortex density is low, to the cooler end, where the density is high, under the action of the thermal force $\mathbf{F}_{\rm th} = -S_\phi \nabla T$. Note that the vortices have larger radii at the warmer end.

a temperature gradient. Increasing the vortex density where the temperature is lower tends to equalize throughout space the average entropy density arising from the superconducting medium plus the vortices with their normal-state cores.

An additional effect can arise from the electrons and holes in the vortex cores, where the material is in the normal state. These will have different thermal distributions in the cores at the hot and cold ends, and the drift velocity of the cores will cause these charge carriers to experience a Lorentz force with the applied magnetic field. This effect can also influence the vortex motion (Wang and Ting, 1992a).

Now that we have seen the ways in which thermal effects can cause vortex motion we are better prepared to understand the thermomagnetic effects that are based on this notion, such as the Seebeck effect arising from thermal diffusion of quasiparticles under the influence of a temperature gradient, and the Nernst effect, which is due to the thermal diffusion of magnetic flux lines (Ri *et al.*, 1993).

B. Seebeck Effect

A conductor which has no electric current flowing through it, but which has a temperature gradient along its length, can develop a steady-state electric field in the gradient direction,

$$\mathbf{E} = S\nabla T. \tag{16.41}$$

This gives rise to an electrostatic potential difference $V_2 - V_1$ between the ends,

$$V_2 - V_1 = S(T_2 - T_1), \tag{16.42}$$

where S is called the thermopower, thermoelectric power, or Seebeck coefficient. We should be careful not to confuse this symbol with the symbol S_ϕ for the transport entropy. A typical experimental arrangement for determining the thermopower, shown in Fig. 16.34, consists of a conducting rod connecting two copper blocks that serve as temperature reservoirs. One block is heated with a metal film resistor that raises its temperature above that of the other block, so that the thermal conductivity of the two copper blocks exceeds that of the conducting rod. A nanovolt meter is employed to measure the thermoelectric voltage between the ends of the rod arising from the longitudinal temperature gradient along the rod.

In the free-electron approximation, the thermopower has the value (Ashcroft and Mermin, 1976, p. 52; MacDonald, 1962)

$$S = \frac{\pi^2}{2} \cdot \frac{k_B}{e} \cdot \frac{T}{T_{\rm F}} \tag{16.43}$$

$$= 142 \left(\frac{T}{T_{\rm F}} \right) \mu{\rm V/K}, \tag{16.44}$$

where the Fermi temperature can be, typically, 10^4 to 10^5 K. Devaux *et al.* (1990) added a temperature-dependent electron diffusion term to this expression. Thermopower

results have been explained using percolation (Rajput and Kumar, 1990) and Hubbard (Oguri and Maekawa, 1990) models. Sergeenkov and Ausloos (1993) discussed thermopower of granular superconductors in terms of the superconductive glass model of Ebner and Stroud (1985). They define a phase locking or grain decoupling temperature below which the grains form a coherent Josephson junction network and above which (but still below T_c) the grains react independently (Mocaër *et al.*, 1991).

A number of workers have reported thermopower measurements on polycrystalline samples of high-temperature superconductors including the mercury compounds (Ren *et al.*, 1993; Subramanian *et al.*, 1994; Xiong *et al.*, 1994), but we will confine our attention to the single crystal and the mixed state results. Figures 16.36, 16.37, and 16.38 compare the temperature dependence of the thermopower measured in the a, b-plane (S_{ab}) and perpendicular to this plane (S_c) for single crystals of $YBa_2Cu_3O_{7-\delta}$, $Bi_2Sr_2CaCu_2O_8$, and TlBaCaCuO. In all these cases the thermopower was zero below T_c and showed a sharp rise in magnitude at the transition tem-

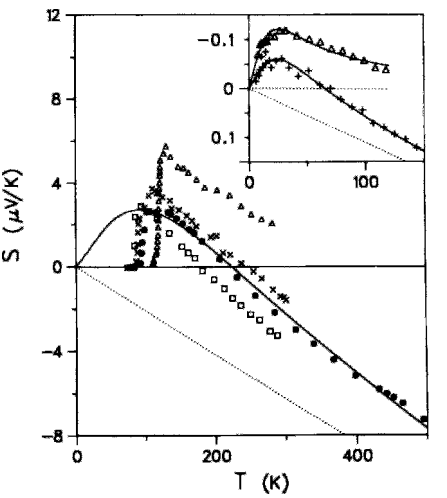

Figure 16.37 In-plane thermopower measurements S_{ab} of sintered $Bi_2Sr_2CaCu_2O_{8+\delta}$ [Pekala *et al.* (1989) (●), Crommie *et al.* (1989) (□), Chen *et al.* (1989) (×), and TlCaBaCuO (Bhatnagar *et al.* (1990) (△)]. Fits to the data are from Pekala *et al.* (1989); the inset data for $Sn_{0.8}Ag_{0.2}$ (△) and $Sn_{0.6}Ag_{0.4}$ (+) are from Compans and Baumann (1987); the figure is from Kaiser and Mountjoy (1991).

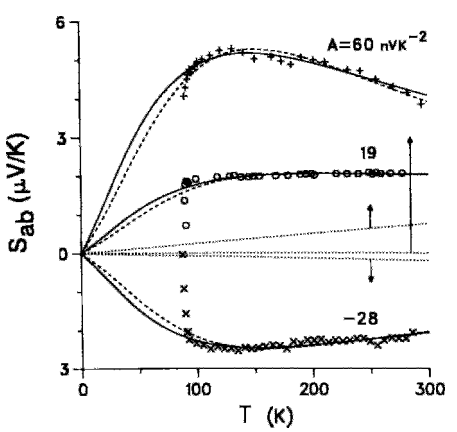

Figure 16.36 In-plane thermopower measurements S_{ab} of $YBa_2Cu_3O_{7-\delta}$ monocrystals. The data are from Lin *et al.* (1989) (+), Sera *et al.* (1988) (◯), and Yu *et al.* (1988) (×); fits to the data are explained in Kaiser and Mountjoy (1991); the figure is from Kaiser and Mountjoy (1991).

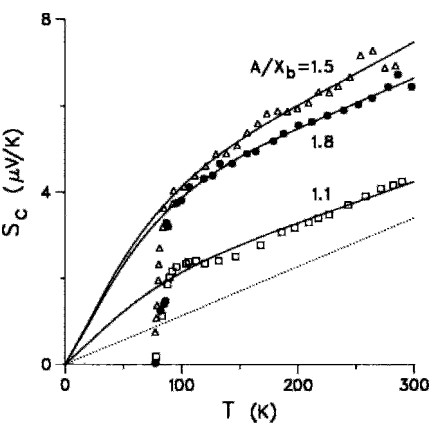

Figure 16.38 Out-of-plane thermopower measurements S_c of monocrystals fitted to a diffusion model (——). The data for $YBa_2Cu_3O_{7-\delta}$ are from Crommie *et al.* (1988) (△), the data for $Bi_2Sr_2CaCu_2O_{8+\delta}$ are from Crommie *et al.* (1989) (□) and Chen *et al.* (1989) (•); the figure is from Kaiser and Mountjoy (1991).

perature. Its subsequent behavior above T_c was not predictable.

Kaiser and Mountjoy (1991) explained these results in terms of the metallic-diffusion approach, an approach that has been successfully applied to other metal systems in which phonon drag is suppressed. They found that the bare thermopower term, which is linear in the temperature, like, the simpler free-electron expression (16.43), is strongly enhanced in high-temperature superconductors by the electron–phonon interaction. Their fits to the data shown in Figs. 16.36, 16.37, and 16.38 are quite good. The figures also show the bare thermopower contribution, which is especially small for the in-plane yttrium data. In the free-electron approximation (16.43), the bare phonon lines of Figs. 16.37 and 16.38 correspond to Fermi temperatures of about 20,000 K and 40,000 K, respectively; actual Fermi temperatures are expected to be smaller than these values. Doyle *et al*. (1992) estimated the Fermi energy of $Bi_{1.6}Pb_{0.4}Sr_2Ca_2Cu_2O_y$ from thermopower measurements.

Single-crystal thermopower results have been reported for the lanthanum (Cheong *et al*., 1989a; Nakamura and Uchida, 1993), yttrium (J. L. Cohn *et al*., 1991, 1992b; Lengfellner *et al*., 1992; Lowe *et al*., 1991), bismuth (Obertelli *et al*., 1992; Song *et al*., 1990), and thallium (Obertelli *et al*., 1992; Shu Yuan *et al*., 1993) compounds and monocrystals of K- and Rb-doped C_{60} (Inabe *et al*., 1992). The thermoelectric power of the Nd–Ce and Nd–Pr electron superconductors was found to be similar in sign (positive) and in terms of temperature dependence to those of hole-type cuprates (Lim *et al*., 1989; Xu *et al*., 1992). The thermopower of the organic superconductor

$$K\text{–}(BEDT\text{–}TTF)_2Cu[N(CN)_2Br$$

was positive along the *a* direction and negative along *c*, suggesting that the carriers in the *a* direction are hole-like, whereas those along *c* are electron-like (J. Yu *et al*., 1991). Electron–phonon enhancement of the thermopower was found in the Chevrel compounds $Cu_{1.8}Mo_6S_{8-x}M_x$, where $M = Se$ or Te (Kaiser, 1987, 1988).

We have been discussing the Seebeck effect in the normal state. Several workers have applied a magnetic field for thermopower measurements to study the mixed state. Figure 16.39 shows the results obtained for $YBa_2Cu_3O_7$ (Hohn *et al*., 1991) with the applied field along the x, y, and z directions, respectively, of Fig. 16.34. Gridin *et al*. (1989) obtained results similar to those shown in Fig. 16.39c for the compound $Bi_2Sr_2CaCu_2O_8$ with the applied field along the z direction. It was found that the area between the curve for the thermopower in a field $\mathbf{B}$ and the curve for zero field ($\mathbf{B} = 0$) (cf. Fig. 16.39c) was proportional to the applied field $\mathbf{B}$. The Seebeck effect in the mixed state has been attributed to counter flow of quasiparticles (normal current) and super current in the presence of a temperature gradient (Huebener *et al*., 1990; Ri *et al*., 1991).

While resistivity and Hall effect experiments determine the density and mobility of charge carriers, thermopower experiments are intended to measure their energy distribution. From Eq. (16.32), we see that the electric field (16.41) associated with the thermopower is proportional to the thermal-energy flux $\mathbf{U}$ of the charge carriers, which, in turn, from Eq. (16.31), is proportional to the entropy flow $S_\phi \mathbf{v}$. Thermopower measurements have been looked upon as measuring the entropy S_ϕ per carrier (Burns *et al*., 1989).

C. Nernst Effect

In the presence of an applied magnetic field, a conductor with a temperature gradient and no electric-current flow can develop a steady-state electric field transverse to

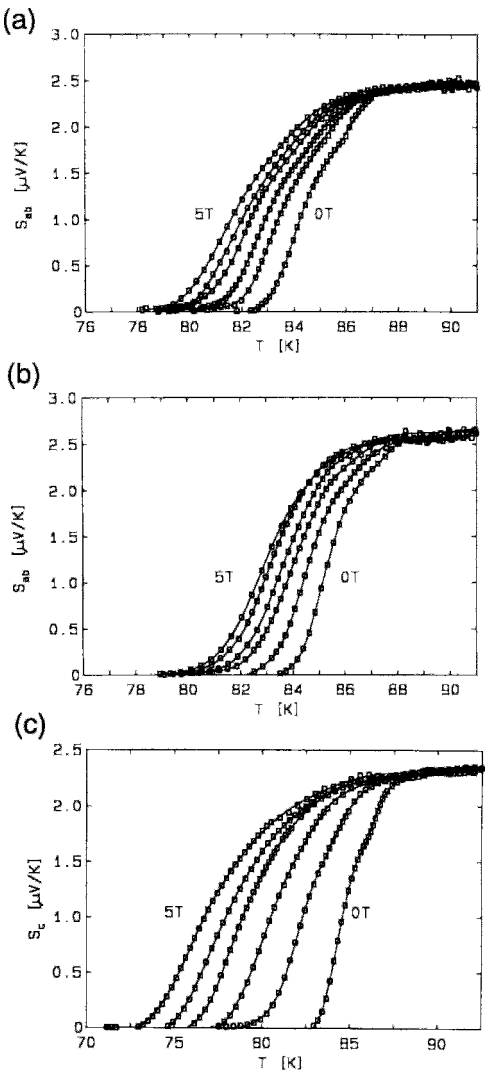

Figure 16.39 Temperature dependence of the magnetothermopower S for the experimental arrangement of Fig. 16.34 in magnetic fields of 1, 2, 3, 4, and 5 T. The c-axis oriented film is in the x, y-plane of Fig. 16.34 so that the temperature gradient $\nabla_y T$ and the measured electric field E_y are both along the y direction. Results are shown for the applied magnetic field oriented (a) in the a, b-plane along the y direction parallel to ∇T, (b) in the a, b-plane, along the x direction perpendicular to ∇T, and (c) perpendicular to the a, b-plane, along the z direction (Hohn *et al.*, 1991).

the gradient direction, a phenomenon that is called the Nernst effect. The effect is very small in normal conductors, but can be appreciable in superconductors if flux flow occurs.

To explain the origin of the transverse electric field, Huebener (1979, pp. 155ff.) made use of the vortex equation of motion (9.76) with the thermal force $-S_\phi \nabla T$ introduced in Section VII.A replacing the Lorentz force $\mathbf{J} \times \mathbf{\Phi}_0$ as the driving force,

$$S_\phi \nabla T + \beta \mathbf{v}_\phi + \mathbf{F}_\mathrm{p} = \mathbf{0}, \tag{16.45}$$

where $\beta \mathbf{v}_\phi$ is the drag force, $\mathbf{F}_\mathrm{p}$ the pinning force, and the Magnus force $\alpha n_s e(\mathbf{v}_\phi \times \mathbf{\Phi}_0)$ is neglected (Zeh *et al.*, 1990). The thermal force does not induce flux flow until it exceeds the pinning force F_p, and this occurs at the critical gradient $(\nabla T)_c$,

$$S_\phi (\nabla T)_\mathrm{C} = -\mathbf{F}_\mathrm{p}, \tag{16.46}$$

to give

$$S_\phi [\nabla T - (\nabla T)_\mathrm{c}] + \beta \mathbf{v}_\phi = 0. \tag{16.47}$$

Therefore, a thermal gradient that exceeds the critical gradient causes vortices to move from the high-temperature end of the material to the low-temperature end, in accordance with Fig. 16.35.

Consider a magnetic field B applied perpendicular to the thermal gradient, as shown in Fig. 16.40. The vortex moving at the velocity v_ϕ in the gradient direction entrains its encircling screening currents, as described in Chapter 2, Section VIII. Let v_e be the velocity of an electron encircling the vortex when the vortex is stationary. Once the vortex starts to move, the velocity of this electron on one side is $v_\mathrm{e} + v_\phi$, and on the other side $v_\mathrm{e} - v_\phi$, as shown in Fig. 16.41. As a result, a Lorentz force $e\mathbf{v} \times \mathbf{B}$ that is stronger on one side of the vortex than on the other comes into play, and the vortices move in a direction perpendicular to both $\mathbf{v}$ and $\mathbf{B}$. This causes a flux gradient to be established along the x direction of Fig. 16.40, producing an electric field $\mathbf{E}$,

$$\mathbf{E} = -\mathbf{v}_\phi \times \mathbf{B}, \tag{16.48}$$

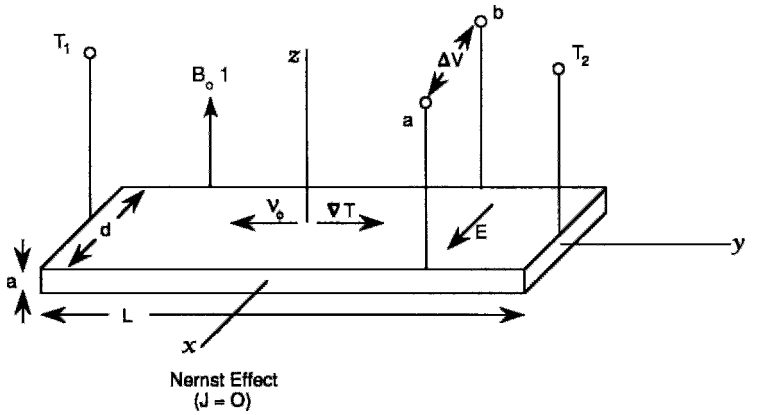

Figure 16.40 Experimental arrangement for measuring the Nernst effect of a superconducting slab in a transverse magnetic field B. The vortices flow to the left with the velocity v_ϕ under the action of the temperature gradient ∇T directed to the right. The temperature (T_1, T_2) and voltage (a, b) measuring leads are indicated.

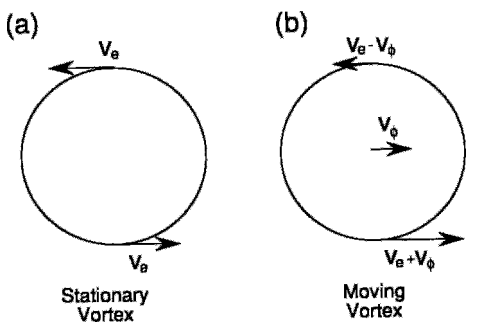

Figure 16.41 Electron circulation around a vortex which is (a) stationary, and (b) moving to the right with the velocity v_ϕ.

which cancels the effect of the magnetic field and causes the flux motion along ∇T to proceed undeflected. An analogous transverse electric field (1.90) arises in the Hall effect. As a result, a voltage difference ΔV, called the Nernst voltage, is established between the terminals a and b on the two sides of the superconductor.

To obtain the equation for the Nernst effect we can substitute v_ϕ from Eq. (16.47) into Eq. (16.48) and write, in scalar notation,

$$\frac{dV}{dx} = -S_\phi(B/\beta)[\nabla T - (\nabla T)_c]. \quad (16.49)$$

We define the Nernst coefficient Q as the ratio between the transport entropy S_ϕ and the vortex friction coefficient β,

$$Q = S_\phi/\beta,$$

and note that the electric field E is the gradient of the potential V in the x direction, and this gives for the Nernst voltage ΔV across a sample of width d

$$\Delta V = -QBd[\nabla T - (\nabla T)_c]. \quad (16.50)$$

Figure 16.42 shows plots of the Nernst voltage measured across thin films of Sn at 2 K ($T_c = 3.7$ K for $B = 0$) for several magnetic field strengths. We see from the figure that the critical thermal gradient $(\nabla T)_c$ is less for higher fields, which is to be expected because the Lorentz force adds to the thermal force in Eq. (16.45) to overcome the pinning. The slopes of the lines $\Delta V/\Delta T$ increase with the applied field, but this increase does not have the proportionality to B predicted by Eq. (16.50).

A measurement of the temperature and field dependence of the Nernst coefficient of $YBa_2Cu_3O_7$ below T_c showed that the vortex

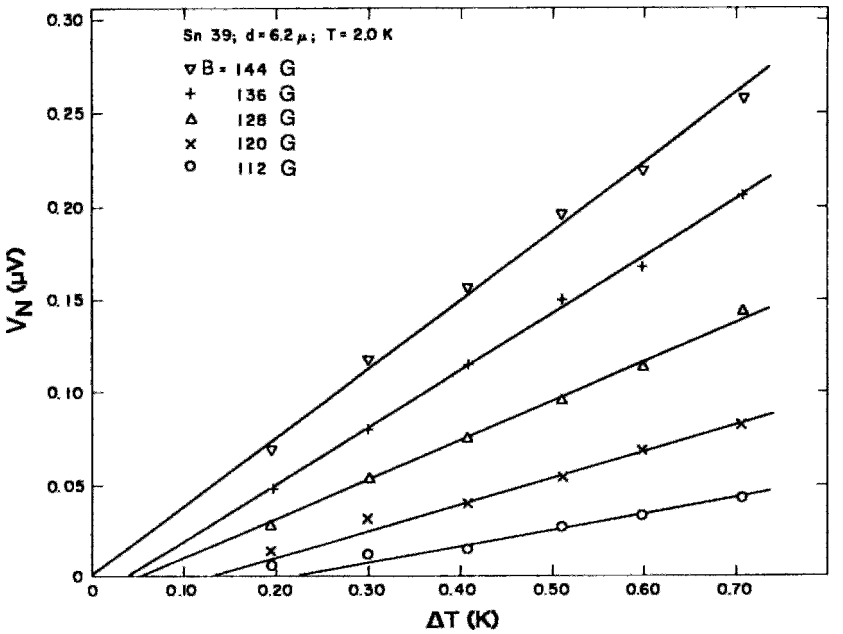

Figure 16.42 Dependence of the Nernst voltage at 2.0 K of a 6.2-μm thick Sn thin film on the longitudinal temperature difference $\Delta T = T_2 - T_1$ for the range of applied magnetic fields from 11.2 to 14.4 mT (110 to 144 G) (Rowe and Huebener, 1969).

entropy per unit length S_ϕ increases with decreasing temperature, with very little field dependence (Hagen *et al.*, 1990b), as shown in Fig. 16.43. The measured magnetoresistance ρ_{xx} together with the expression (Kim and Stephan, 1969)

$$\rho_{xx} = E_x/J_y = \Phi_0 B/\beta \qquad (16.51)$$

have been used to evaluate β and to determine S_ϕ. K. Kober *et al.* (1991) found a pronounced dependence of S_ϕ on B, with the entropy tending to decrease in higher fields. The Nernst effect below T_c has been reported for thallium superconductors (Koshelev *et al.*, 1991; Lengfellner *et al.*, 1990).

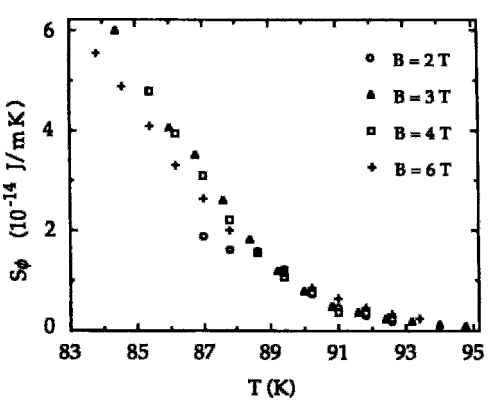

Figure 16.43 Dependence of the vortex entropy per unit length S_ϕ of epitaxial $YBa_2Cu_3O_7$ on the temperature for applied magnetic fields of 2, 3, 4, and 6 T. The entropy was determined from Nernst effect measurements (Hagen *et al.*, 1990b).

The existence of the Nernst effect in the superconducting state indicates the presence of flux flow or vortex motion; flux depinning activation energies can be deduced (Lengfellner and Schnellbögl, 1991) and entropy is transported by a moving flux line. These factors distinguish the effect from the thermoelectric voltage which, since it is produced in the absence of an applied magnetic field, is due to dissipation processes other than flux

motion (Hagen *et al.*, 1990b; Hohn *et al.*, 1991; Lengfellner *et al.*, 1991a).

D. Peltier Effect

When a conductor is maintained at a constant temperature with a uniform electric current flowing through it, the electric current flow is accompanied by a thermal current, a phenomenon called the Peltier effect. (The thermal current serves to carry away the Joule heat generated by the electric current.) The electric current density J and thermal current density U are related by the Peltier coefficient π_P

$$U = \pi_p J. \tag{16.52}$$

This effect is demonstrated experimentally by driving a current through a bimetallic circuit maintained at a constant temperature and measuring the heat absorbed at one junction and released at the other, as shown in Fig. 16.44. Lord Kelvin deduced the relation (Thomson or Kelvin relation)

$$\pi_P = ST \tag{16.53}$$

between the Peltier coefficient π_P and the thermopower S. The Peltier effect is strong in a normal metal but has yet to be observed in a superconductor, perhaps because super current does not carry entropy. In a superconductor the effect could arise from dissipative electric current associated with flux motion carrying Peltier heat across the sample in the mixed state, with the Thomson relation satisfied (Huebener, 1990; Logvenov *et al.*, 1991). The calculations of Maki (1991) provide an extra Peltier effect due to fluctuations.

E. Ettingshausen Effect

When a conductor in an applied magnetic field is maintained at a constant temperature with a uniform electric current flowing through it, heat energy (i.e., a thermal current) can travel in the transverse direction to establish a transverse temperature gradient, a phenomenon called the Ettingshausen effect. This is the transverse analogue of the longitudinal Peltier effect. It is very small in a normal metal, but can be large in a superconductor in the presence of an applied magnetic field because a heat current will be generated by the motion of the vortices in the field. We will analyze this situation for the experimental arrangement of Fig. 16.45, which shows the magnetic field $\mathbf{B}_0$, current density $\mathbf{J}$, and flux flow direction $\mathbf{v}_\phi$, as well

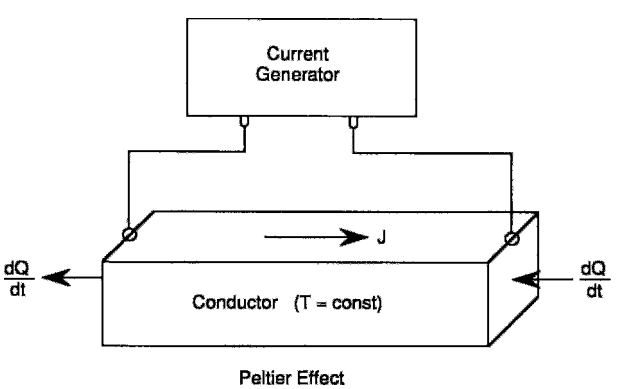

Figure 16.44 Experimental arrangement for the Peltier effect. An electric current is passed through a metal maintained at a constant temperature T, and the heat current dQ/dt that enters at the right and leaves at the left is measured.

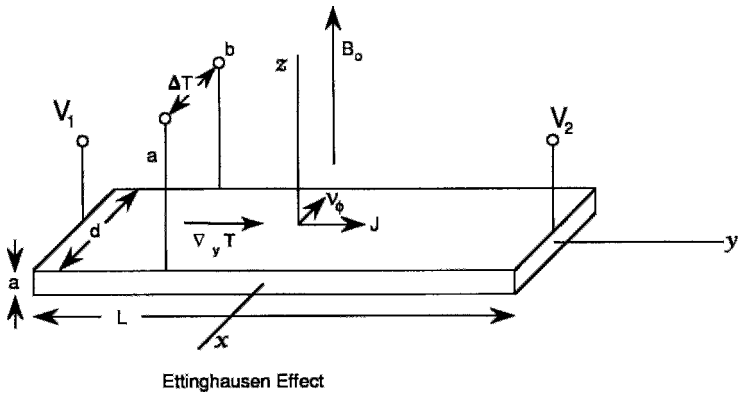

Ettinghausen Effect

Figure 16.45 Experimental arrangement for measuring the Ettingshausen effect of a superconducting slab carrying a transport current density J in a transverse magnetic field B_0. To establish the transverse temperature difference ΔT, the vortices are caused to flow towards the side of the slab with the velocity v_ϕ. The temperature (a, b) and voltage (V_1, V_2) measuring leads are indicated.

as the temperature change ΔT that is developed across the sample.

The electric current flowing through the wire exerts a Lorentz force on the flux structures, which are vortices with quantized flux in the mixed state of Type II superconductors and nonquantized domains in the intermediate state of Type I superconductors, as explained in Chapter 11, Section III. This causes the structures to move with the velocity $\mathbf{v}_\phi$; in addition, their motion is dissipative, as explained in Chapter 12, Section V.C, so that it is accompanied by a flow of heat. The heat-current density $\mathbf{U}_\phi = nTS_\phi \mathbf{v}_\phi$ may be equated to the heat flux $K\boldsymbol{\nabla}T$ through Fourier's law (16.31, 16.32),

$$nTS_\phi \mathbf{v}_\phi = -K\boldsymbol{\nabla}T, \tag{16.54}$$

where n is the number of flux structures per unit area and S_ϕ is the entropy transported per unit length of such a structure. If we substitute v_ϕ from Eq. (16.48) in Eq. (16.54), where $v_\phi = E/B$ (since $\mathbf{v}_\phi$ and $\mathbf{B}$ are mutually perpendicular), and express $\mathbf{E}$ as the gradient of a potential $\boldsymbol{\nabla}V$, we obtain the scalar expression

$$\left|\frac{dT}{dx}\right| = \left(\frac{TS_\phi}{K\Phi}\right)\left|\frac{dV}{dy}\right|, \tag{16.55}$$

which is the fundamental equation for the Ettingshausen effect in the superconducting state. Figure 16.45 clarifies the directions of these gradients, and shows the terminals a and b across which the temperature change is measured. It should be emphasized that the potential gradient $\boldsymbol{\nabla}V$, which is in the $\mathbf{J}$ direction, arises from the motion of the vortices, since the super current flow itself is not accompanied by any potential gradient. The potential difference, $\Delta V = V_2 - V_1$, measured between the two ends of the sample, as shown in Fig. 16.45, provides the magnitude of the gradient $\nabla V = \Delta V/L$.

Figure 16.46 shows some experimental data obtained with the Type II alloy $In_{0.6}Pb_{0.4}$ in several applied magnetic fields. We see from the figure that ΔT is almost linear in $\Delta V = V_2 - V_1$, especially for small applied fields. The slopes of the lines, however, do not exhibit the inverse dependence on the applied field which is expected from Eq. (16.55). Part of this discrepancy is explained by the fact that Φ in Eq. (16.55) is the internal flux, which is not proportional to the applied field (cf. Fig. 12.5). The extra Peltier effect arising from fluctuations (Maki, 1991) gives rise to the Ettingshausen effect in the presence of an applied magnetic field.

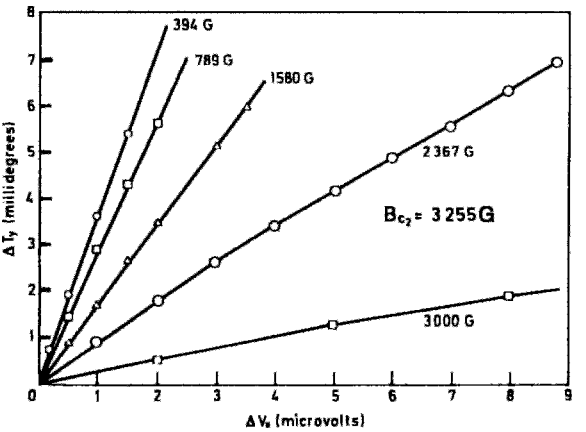

Figure 16.46 Transverse temperature difference ΔT_x arising from the Ettingshausen effect in the Type II superconducting alloy $In_{0.6}Pb_{0.4}$ plotted versus the longitudinal flux-flow voltage ΔV_y for the range of applied magnetic fields 39.4–300 mT (394 to 3000 G) (Solomon and Otter, 1967).

Others have reported Ettingshausen effects in the superconducting state (Freimuth *et al.*, 1991; Palstra *et al.*, 1990; Ullah *et al.*, 1990).

F. Righi–Leduc Effect

The Righi–Leduc effect is the thermal analogue of the Hall effect. One end of the sample is heated and the resulting temperature gradient $\nabla_y T$ in the y direction produces a thermal current of density U_y that flows from the hot end to the cold end, as shown in Fig. 16.47. The application of a magnetic field B_0 along z produces a temperature gradient $\nabla_x T$ along x given by

$$\nabla_x T = R_L B_0 U_y, \tag{16.56}$$

where R_L is the Righi–Leduc coefficient. For metals in which the law of Wiedermann and Franz (1.33) is valid, this coefficient is related to the Hall coefficient R_H (16.28) by the expression

$$R_H = R_L L_0 T, \tag{16.57}$$

where $L_0 = \frac{3}{2}(k_B/e)^2$ is the Lorentz number that appears in Eq. (1.33). The thermal Hall angle Θ_{th} can be defined by analogy to its ordinary Hall effect counterpart (1.93):

$$\tan \Theta_{th} = \nabla_x T / \nabla_y T. \tag{16.58}$$

Figure 16.48 shows that the y direction temperature gradient behaves differently in the Meissner state ($B_{app} < B_{c1}$), the mixed state ($B_{c1} < B_{app} < B_{c2}$), and the normal state ($B_{c2} < B_{app}$).

IX. PHOTOCONDUCTIVITY

Photoconductivity is the increase in electrical conductivity produced by shining light on a material. A related effect, called the *photovoltaic effect* is the inducing of voltages by light. This latter phenomenon is particularly pronounced in semiconductors when the band gap is small and light is able to excite electrons from the full valence band into the empty conduction band.

Figure 16.49 shows the time dependence of the voltage responses of

$$YBa_2Cu_3O_7$$

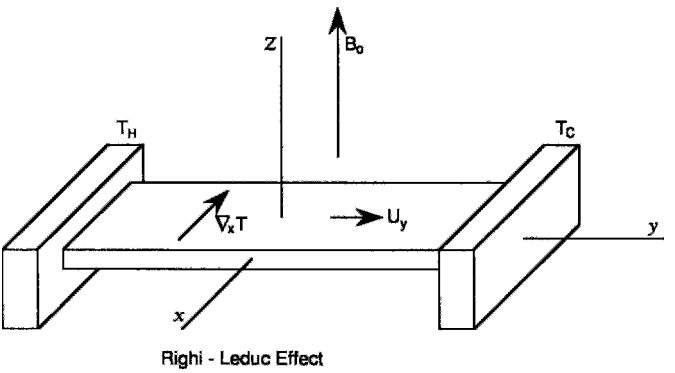

Figure 16.47 Experimental arrangement for measuring the Righi–Leduc effect of a superconducting slab mounted between a cold (T_c) and a hot (T_h) temperature reservoir in a transverse magnetic field B_0. The transverse temperature gradient $\nabla_x T$ and the longitudinal thermal current flow U_y are indicated.

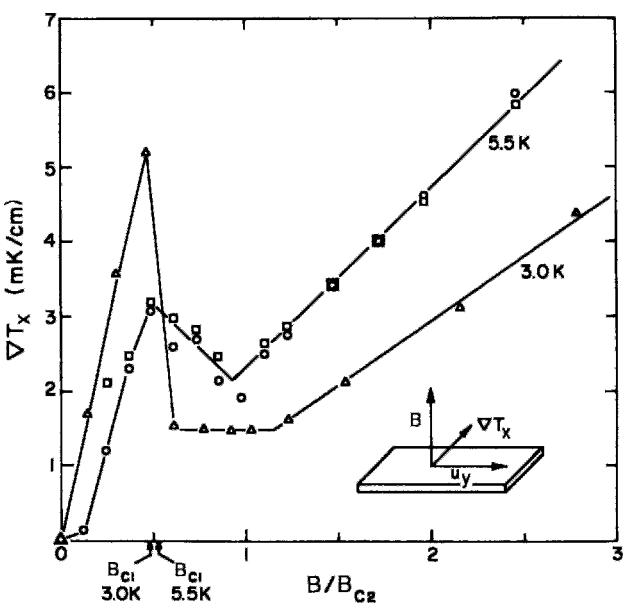

Figure 16.48 Righi–Leduc effect determination of the magnetic field dependence of the transverse temperature gradient for two temperatures. The behavior changes at the lower-critical field B_{c1}, as shown (Stephan and Maxfield, 1973).

to a high-power laser pulse of energy density $2\,\mathrm{mJ/cm^2}$ at 99 K in the normal state. This same laser pulse produced no photoresponse in the superconducting state since more energy was needed. The figure shows the delayed and weaker photoresponse at 57 K obtained with the pulse of higher energy density $4.5\,\mathrm{mJ/cm^2}$ (C. L. Chang *et al.*, 1990).

The compound $YBa_2Cu_3O_{7-\delta}$ is a conductor for δ below about 0.4 and a

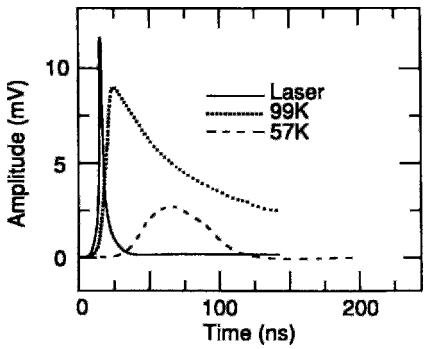

Figure 16.49 Laser intensity in arbitrary units (——) and photoresponse voltages from $YBa_2Cu_3O_7$ above T_c at 99 K (·····) and with higher laser intensity below T_c at 57 K (- - -) (C. L. Chang *et al.*, 1990).

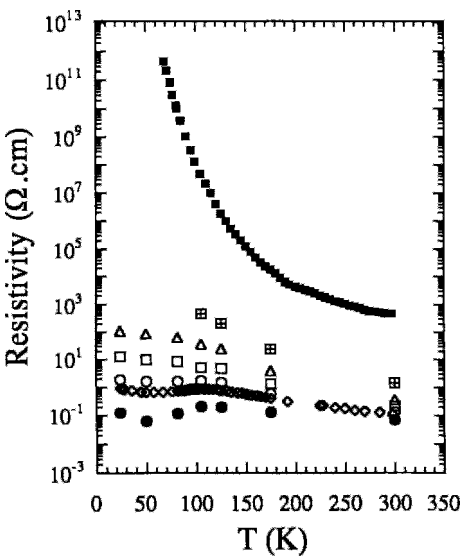

Figure 16.50 Temperature dependence of the photoresistivity in $YBa_2Cu_3O_{6.3}$ for 0.18-eV incident photons with the intensity 10^{13} (⊞), 10^{14} (△), 10^{15} (□), 7×10^{15} (◯), 1.1×10^{16} (◊), and 2.3×10^{16} photons/cm^2 (●). The dark resistivity, with no incident light (■), is also shown (G. Yu *et al.*, 1992).

semiconductor for δ between 0.4 and 1; the quantity δ correlates with the number of charge carriers n_c. Figure 16.50 shows the dramatic lowering of the resistivity of the semiconductor $YBa_2Cu_3O_{6.3}$ from its dark value to its value for several light intensities, with higher intensities producing a

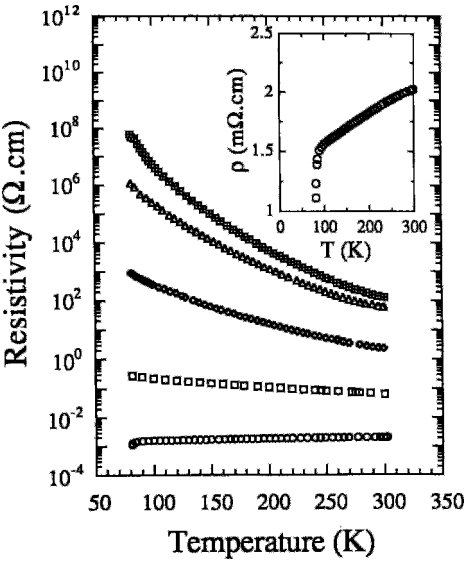

Figure 16.51 Temperature dependence of the dark resistivity of several $DyBa_2Cu_3O_{7-\delta}$ thin films with their oxygen contents increasing over the range from the insulating antiferromagnetic phase at the top to the metallic and superconducting phase at the bottom. The inset shows the resistivity of a $\delta = 0$ superconducting sample on a linear scale (G. Yu *et al.*, 1992).

greater reduction. Figure 16.51 shows how the resistivity of the related superconductor $DyBa_2Cu_3O_{7-\delta}$ decreases as δ decreases, i.e., as the oxygen content increases. Comparing these two figures shows that irradiating the sample has an effect similar to that of increasing the oxygen content, since both processes have the effect of increasing the number of carriers n_c (G. Yu *et al.*, 1990, 1992).

Bluzer (1991) studied transient photoresponse relaxation in $YBa_2Cu_3O_{7-\delta}$ using very short pulses, 0.3 ns in length, and obtained sharply rising signals followed by signals that decreased more slowly, as shown in Fig. 16.52b for the case $T < T_c$. In this temperature regime the response signal is proportional to the derivative of the quasiparticle concentration n_c. According to the n_c-versus-time curve reconstructed from this response and shown in Fig. 16.52a, a laser pulse arrives at time t_0, with each photoabsorbed photon, of energy $E_0 = 2$ eV, splitting

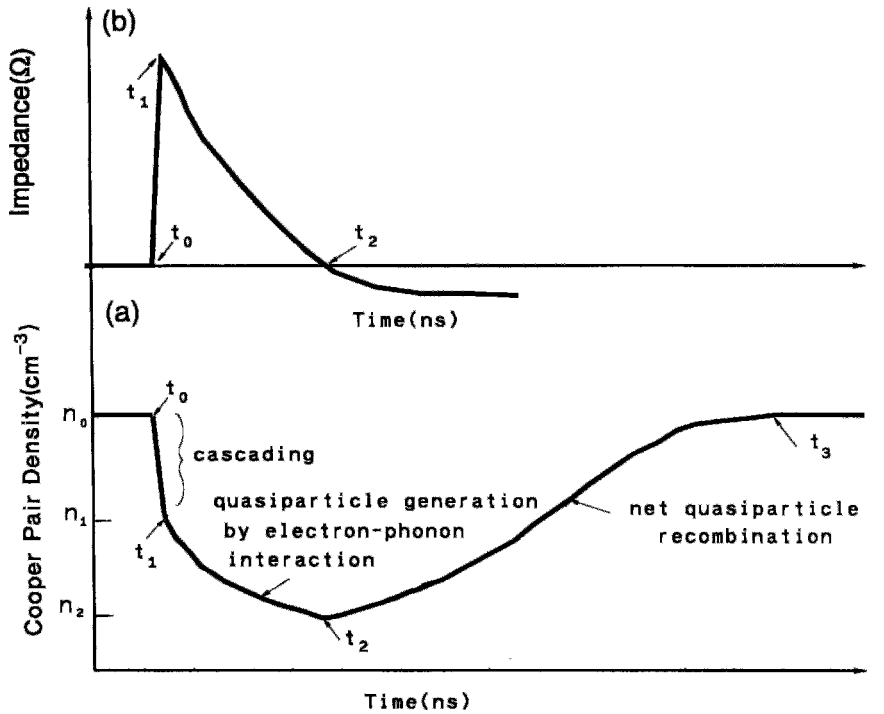

Figure 16.52 (a) Time dependence of the Cooper pair density with the quasiparticle formation and recombination processes indicated, and (b) measured photoresponse produced by these processes. The response signal is proportional to the derivative of the Cooper pair density (Bluzer, 1991).

a Cooper pair to form two quasiparticles. Energetic quasiparticles break up additional Cooper pairs via an avalanche or cascade process that eventually produces, on average, 32 quasiparticles per adsorbed photon by the time t_1 (Han *et al.*, 1990b). Following this cascading process, the lower-energy quasiparticles thermalize between t_1 and t_2 by emitting 40–50 meV phonons, which break up additional Cooper pairs. The subsequent quasiparticle recombination process is detected as a negative photoresponse until the Cooper pair density n_c returns to its initial equilibrium value, as shown in the figure.

Such a cascade process produces quasiparticles at much higher temperatures than the phonons, which are at the lattice temperature. The thermalization process involves electron–phonon interaction; this interaction has been measured by determining the relaxation rate via femtosecond spectroscopy (Brorson *et al.*, 1990; Chekalin *et al.*, 1991; Rice *et al.*, 1993).

We have discussed what might be called transient photoconductivity. Persistent photoconductivity has also been observed, in which the photoinduced conductivity change persists for a long time following excitation (Ayache *et al.*, 1992; Kreins and Kudinov, 1992).

X. TRANSPORT ENTROPY

The principal quantity obtained from thermomagnetic measurements is the transport entropy S_ϕ. Experimentally, flux-flow resistance measurements determine $\Phi_0 B/\beta$ with the aid of Eq. (16.27), the Nernst effect then gives $S_\phi B/\beta$ from Eq. (16.50), and the Ettingshausen effect provides S_ϕ/Φ

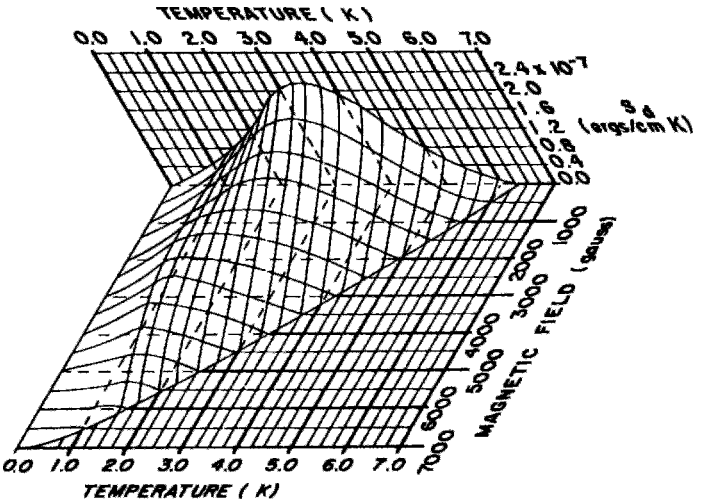

Figure 16.53 Three-dimensional plot showing the dependence of the transport entropy S_ϕ of a vortex per unit length on the magnetic field and the temperature for the Type II alloy $In_{0.6}Pb_{0.4}$ with $T_c = 6.3\,K$ and $B_{c2} = 6500\,G$ (0.65 T) (adapted from Huebener, 1979, p. 161).

from Eq. (16.55). These results provide the entropy per unit length of a vortex in a Type II superconductor.

Figure 16.53 shows how the transport entropy S_ϕ of the Type II alloy $In_{0.6}Pb_{0.4}$ varies with the temperature and magnetic field in the superconducting state. We see from the figure that, for a fixed magnetic field, the entropy increases from zero at $T = 0$, passes through a maximum (at 3.4 K for $B = 0$), and then decreases to zero at $T = T_c(B)$.

PROBLEMS

1. Find the impedance Z of the circuit of Fig. 16.2, and find the ratios I_n/I and I_s/I of the two currents to the total current $I = I_n + I_s$.
2. For the case of relatively small grains, compare the inductances of (a) a 5-turn coil of radius 5 μm and length 10 μm, (b) a straight wire 10 μm long, and (c) a loop of radius 10 μm and wire radius 1 μm.
3. For the case of relatively large grains, compare the inductances of (a) a 10-turn coil of radius 40 μm and length 80 μm, (b) a straight wire 80 μm long, and (c) a loop of radius 80 μm and wire radius 5 μm.
4. For the case of typical electrical circuits, compare the inductances of (a) the coil of Chapter 2, Section IV.B, (b) a straight wire 10 cm long, and (c) a loop of radius 10 cm with wire radius 0.3 mm.
5. Determine the flux-flow resistance determined for each of the V-versus-R curves shown in Fig. 16.21. Make a plot of R versus B.
6. Show that if the Magnus force is neglected, the electric field induced by flux flow is aligned along the transport current direction with the magnitude

$$E \approx 0 \qquad J\Phi_0 < F_p$$

$$E \approx \frac{B_0(J\Phi_0 - F_p)}{\beta} \qquad J\Phi_0 > F_p.$$

7. Show that if the Magnus force is neglected, the differential flux-flow resistivity is given by

$$\rho_{ff} = \frac{\Phi_0 B_0}{\beta}.$$

8. Show that four of the compounds with Hall effect data in Fig. 16.24 are hole-like and that the fifth is electron-like.
9. Derive the Ettinghausen equation (16.55). Deduce the polarity of the potential drop along y (i.e., determine which end is $+$ and which is $-$), and determine which of the two terminals, a or b, is at the higher temperature in Fig. 16.45.
10. Thermopower and Peltier experiments were carried out using the same superconducting rod. In the former experiment the temperature difference ΔT across the sample produced the voltage difference ΔV, and in the latter experiment the input electrical current I produced the thermal current dQ/dt. Show that

$$I\Delta V = \Delta T \frac{dS_\phi}{dt},$$

where the temperature and its gradient are assumed independent of time.
11. Why does the absence of a Peltier effect in a superconductor show that super current does not transport entropy?
12. Derive the Righi–Leduc expression (16.57),

$$R_{\mathrm{H}} = R_{\mathrm{L}} L_0 T.$$

What do you assume about Θ_{th} and Θ_{H}?
13. Describe the details of the quasiparticle production and recombination processes outlined on Fig. 16.52 (consult the original reference).

This page intentionally left blank

17

Spectroscopic Properties

I. INTRODUCTION

Several standard spectroscopic techniques have been widely used for the study of superconductors. We will start by describing the principles of each of these techniques and what can be learned from it, and then present some of the results that have been reported for superconductors.

Most branches of spectroscopy are concerned with the absorption by the sample of an incoming photon of radiation $h\nu$, where h is Planck's constant and ν is the frequency. The photon transfers its energy to the sample by inducing a transition from a ground state E_0 into an excited state E_e. The difference in energy between the two states is equal to the energy of the photon,

$$E_e - E_0 = h\nu, \tag{17.1}$$

as indicated in Fig. 17.1. The intensity of light I_0 incident on the sample is partly transmitted, I_t, and partly reflected, I_r, so that the amount absorbed is given by

$$I_a = I_0 - I_r - I_t, \tag{17.2}$$

as shown in Fig. 17.2. Transmission spectrometers measure I_t, generally when I_r is small, while reflectance spectrometers measure I_r, generally when I_t is small. Either way, the spectrometer provides the frequency dependence of the ratio I_a/I_0, a maximum in I_a indicating the center of an absorption line. In a single-beam measurement, I_a itself is determined, while in a double-beam technique the absorption of a sample is measured relative to that of a reference material. Superconductors tend to be opaque at infrared and visible frequencies, so that reflectance

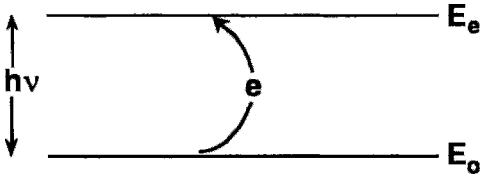

Figure 17.1 Incoming photon $h\nu$ inducing an electron to jump from a ground state energy level E_0 into an excited state level E_e.

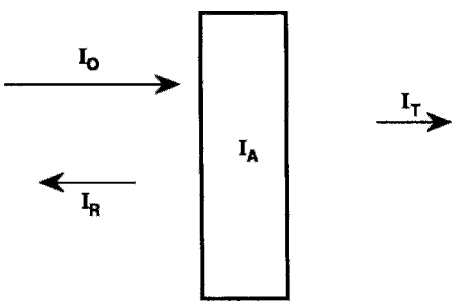

Figure 17.2 Absorbed (I_A), transmitted (I_T), and reflected (T_R) components of an incident light beam of intensity I_0.

techniques apply; higher frequencies in the x-ray region can penetrate, and transmission is often employed here. In the next section we will say a few words about reflection before proceeding to the various individual spectroscopies.

A number of acronyms, such as ACAR, ARPES, BIS, EELS, EPR, ESR, EXAFS, IPS, IR, μSR, NMR, NQR, PAS, PES, UPS, UV, XAFS, XANES, and XPS, in common use in the field will be defined in the appropriate sections. In addition, spectroscopists report their results in terms of different energy units. If we had standardized this chapter, by for example, converting all energies to joules, it would have been difficult to compare the results we wish to present with those found in the literature. The appropriate conversion factors are

$$1000\,\mathrm{cm}^{-1} \equiv 0.124\,\mathrm{eV} \equiv 30\,\mathrm{THz} \equiv 10^5\,\text{Å}. \qquad (17.3)$$

II. VIBRATIONAL SPECTROSCOPY

Vibrational spectroscopy involves photons that induce transitions between vibrational states in molecules or solids. These transitions generally fall within the frequency band of infrared (IR) spectrometers, typically from 2×10^{13} to 12×10^{13} Hz, but sometimes over a wider range. It is customary for workers in the field to use the unit of reciprocal centimeters, which corresponds to 650 to 4000 cm^{-1} for the above range. The conversion factor between the two is the velocity of light, 2.9979×10^{10} cm/s.

The energy gaps of high-temperature superconductors are in the infrared region, so that a change in the absorption can occur when the vibrational frequency equals the energy gap,

$$h\upsilon = E_g \qquad (17.4)$$

which gives us a value of $E_g = 2\Delta$, (see Chapter 7, Section VI, F).

A. Vibrational Transitions

In infrared spectroscopy, an IR photon $h\nu$ is absorbed directly to induce the vibrational transition (17.1), while in the case of Raman spectroscopy an incident optical photon of frequency $h\nu_{inc}$ is absorbed and a second optical photon $h\nu_{emit}$ is emitted, with the transition induced by the difference frequency $h\nu$,

$$h\upsilon = |\hbar\nu_{inc} - \hbar\nu_{emit}|, \qquad (17.5)$$

where $\nu_{inc} > \nu_{emit}$ for what is called a Stokes line and $\nu_{inc} < \nu_{emit}$ for an anti-Stokes line. The fundamental vibrational energy levels E_n have the energies

$$E_n = (n_v + \frac{1}{2})h\nu_0, \qquad (17.6)$$

where the vibrational quantum number $n_v = 0, 1, 2, 3, \ldots$ is a positive integer and ν_0 is

the characteristic frequency for a particular vibrational mode. Transitions occur for the condition

$$\nu = (n'_{\mathrm{v}} - n_{\mathrm{v}})\nu_0. \qquad (17.7)$$

The lowest frequency transition with $n'_{\mathrm{v}} - n_{\mathrm{v}} = 1$ is called a fundamental band.

B. Normal Modes

Molecular vibrations occur in what are called normal modes. These involve the coherent oscillations of atoms in the unit cell relative to each other at a characteristic frequency. The oscillations occur in such a manner that the center of gravity is preserved. The normal modes of $Tl_2Ba_2CaCu_2O_8$ (also isomorphous $Bi_2Sr_2CaCu_2O_8$; cf. Kulkarni *et al.*, 1989, 1990; R. Liu *et al.*, 1992b; Prade *et al.*, 1989) are sketched in Fig. 17.3, with the arrows indicating the motion of the various atoms during a normal mode oscillation. Analogous mode diagrams have been published for the compounds La_2CuO_4 (Mostoller *et al.*, 1990; Pintschovius *et al.*, 1989), $(Nd, Ce)_2CuO_4$ (Zhang *et al.*, 1991a), and $YBa_2Cu_3O_6$, and $YBa_2Cu_3O_7$ (Bates, 1989). Isomorphous compounds have the same normal modes, but different frequencies of oscillation because of the differences in the masses and bonding strengths of the atoms.

Spectroscopists have developed a notation for these modes based on characteristics of the oscillations. The one-dimensional A and B modes refer to atom motions parallel to the *c*-axis, i.e., in the vertical (z) direction. The A mode is symmetrical for a 90° rotation about z, which means that all of the arrows on the atoms of Fig. 17.3 are coincident under this operation. The B mode is antisymmetrical under this 90° rotation, so that the arrows reverse direction. The subscript 1 is for a mode which is symmetrical for a 180° rotation about x or y, while the subscript 2 is for a mode which is antisymmetrical for this rotation. We see from the figure that there is a center of inversion, so that atoms interchange positions under the inversion operation $x \rightarrow -x$, $y \rightarrow -y$, and $z \rightarrow -z$. The even, or gerade (g), vibrations, which preserve this center of symmetry, are said to be symmetric with respect to inversion, and the odd, or ungerade (u), vibrations are antisymmetric with respect to inversion.

There are also two-dimensional modes E_g and E_u involving atom motions in the *a, b*-plane, but these are more difficult to characterize.

C. Soft Modes

A phase transition in which the low- and high-temperature crystal structures differ by only small lattice displacements is often accompanied by what are called soft vibrational modes (Burns, 1985, Section 14-3). Most vibrational modes increase in frequency as the temperature is lowered, but the soft modes decrease in frequency as the transition temperature is approached from above, reaching very low frequencies near the transition. Further cooling below the transition temperature causes the modes to increase in frequency again, and sometimes a split into two modes occurs. Phase transitions associated with high-temperature superconductors often involve orthorhombic-to-tetragonal changes in crystal structure, in which individual atoms undergo very small shifts in position, so that soft modes are to be expected.

D. Infrared and Raman Active Modes

Two important characteristics of a vibrating system are its electric dipole moment and its polarizability. The electric dipole moment μ_{D} arises from the separation of charge. For point charges $-Q$ and $+Q$ separated by the distance d, it is

$$\mu_{\mathrm{D}} = dQ. \qquad (17.8)$$

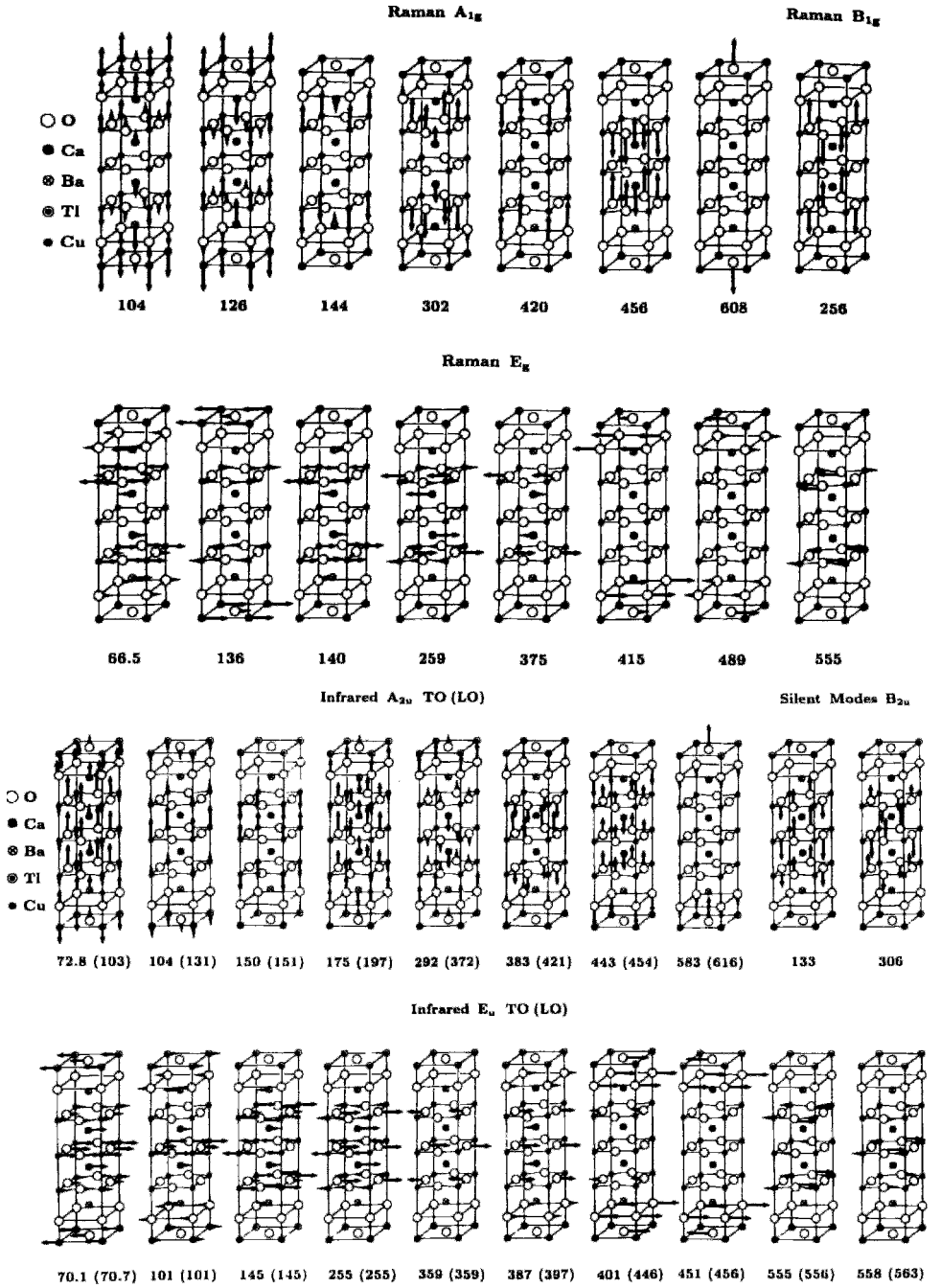

Figure 17.3 Raman-active (top panels) and infrared-active (bottom panels) normal vibrational modes of $Tl_2Ba_2CaCu_2O_8$, a body-centered tetragonal compound. For the infrared-active modes, the transverse optical (TO) frequencies, in cm^{-1}, are given first, followed by the corresponding longitudinal optical (LO) values in parentheses. The lengths of the arrows, although not drawn to scale, are indicative-of the relative vibrational amplitudes (Kulkarni *et al*., 1989, 1990).

The polarizability P causes the electric vector of an incident light wave to induce a dipole moment μ_{ind}. It is defined as the ratio of the induced moment to the applied field,

$$P = \mu_{\text{ind}}/E. \tag{17.9}$$

Therefore, the polarizability is a measure of the deformability of the electron cloud of the molecule in the presence of an electric field. Infrared spectral lines are due to a change in the electric dipole moment of the molecule, while Raman lines appear when there is a change in the polarizability. These two spectroscopies are complementary to each other because some vibrational transitions are IR active while others are Raman active. Infrared active modes are of odd (u) type, where the oscillating atoms produce a dipole moment, while Raman active modes are of even (g) type, having no moment themselves, though a moment is induced by the electric field of the incident radiation. Thomsen and Cardona (1989) give lists of infrared and Raman active modes for some high-temperature superconductors. Kulkarni *et al.* (1989) obtained good agreement between calculated vibrational frequencies of $Tl_2Ba_2CaCu_2O_8$ and experimental values from infrared and Raman studies.

E. Kramers-Kronig Analysis

Infrared and optical reflectance measurements of superconductors can provide information on the conductivity. In this section we will explain how the conductivity is obtained from these data.

The reflectance (or reflectivity) R represents the fraction of reflected light,

$$R = \frac{I_r}{I_0}. \tag{17.10}$$

For normal incidence it is related to the relative dielectric constant ϵ through the expression

$$R = \frac{|\sqrt{\epsilon} - 1|}{|\sqrt{\epsilon} + 1|}, \tag{17.11}$$

where ϵ has real and imaginary parts ϵ' and ϵ'',

$$\epsilon = \epsilon' + i\epsilon'', \tag{17.12}$$

corresponding to dispersion and absorption, respectively. The limiting dielectric constant for large ω, ϵ_∞, is obtained from a fit to the data, so that it is a limiting value for the range of frequencies under investigation, rather than the ultimate limit $\epsilon_\infty = 1$ of free space. Equation (17.11) is more complicated for oblique incidence. A Kramers–Kronig analysis (Wooten, 1972) can be performed to extract the frequency dependence of $\epsilon'(\omega)$ and $\epsilon''(\omega)$, and the data can sometimes be fitted to an expression containing Drude-like terms such as

$$\epsilon(\omega) = \epsilon_\infty - \frac{f_p\omega_{\text{p}}^2}{\omega^2 - i\omega/\tau} + \sum_i \frac{f_i\omega_i^2}{(\omega_i^2 - \omega^2) - i\omega/\tau_i}, \tag{17.13}$$

where f_i is the oscillator strength and the relaxation times τ and τ_i provide the broadening of the resonances. The summation terms are Lorentz oscillator types that account for features arising, for example, from vibrational absorption lines. The second term corresponds to Eq. (1.27), with the damping factor $i\omega/\tau$ added, where ω_{p} is the plasma frequency (1.28),

$$\omega_{\text{p}} = (ne^2/\epsilon_0 m)^{1/2}, \tag{17.14}$$

which was introduced in Chapter 1, Section V.

Some experimentalists report their data as plots of $\epsilon'' = Im[\epsilon(\omega)]$ versus the frequency. Others present plots of the high-frequency conductivity σ_1,

$$\sigma_1(\omega) = (\omega\epsilon''/4\pi). \tag{17.15}$$

We see from a comparison of Figs. 17.4a and 17.4b that the ϵ'' (or σ_1) plots are superior to reflectance plots for determining the

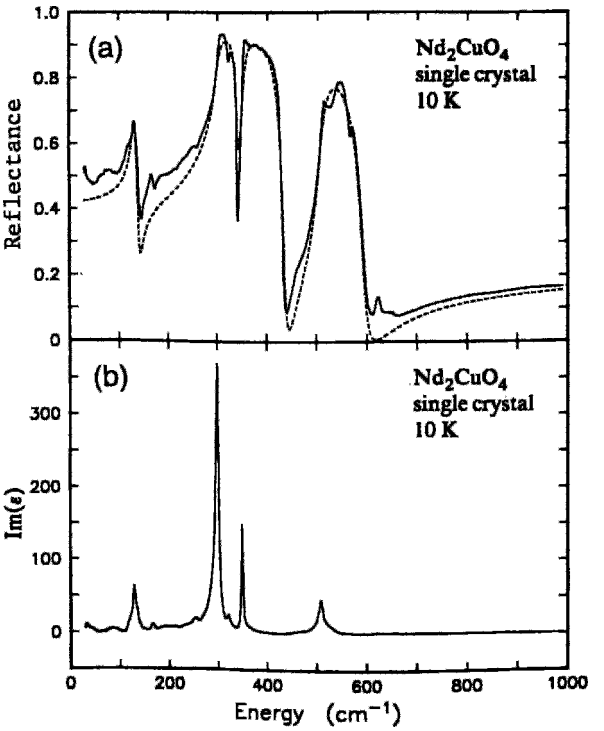

Figure 17.4 Infrared spectrum of an Nd_2CuO_4 single crystal at 10 K showing (a) the reflectance, and (b) the imaginary part of the dielectric constant ϵ'' determined by a Kramers–Kronig analysis using the value $\epsilon_\infty = 6.8$ (Crawford *et al.*, 1990a).

positions and widths of individual absorption lines arising from the summation terms of Eq. (17.13). To see why this is so, consider the real and imaginary parts of one of the terms in the summation of Eq. (17.13),

$$f_i\omega_i^2\left[\frac{\omega_i^2-\omega^2}{(\omega_i^2-\omega^2)^2+(\omega/\tau_i)^2} + i\frac{\omega/\tau_i}{(\omega_i^2-\omega^2)^2+(\omega/\tau_i)^2}\right], \quad (17.16)$$

which, in the usual limit of narrow lines, $\omega_i\tau_i \gg 1$, can be written

$$\frac{2(\omega_i-\omega)\tau_i}{4(\omega_i-\omega)^2\tau_i^2+1} + i\frac{1}{4(\omega_i-\omega)^2\tau_i^2+1}, \quad (17.17)$$

where the factor $f_i\omega_i\tau_i$ has been omitted. This corresponds to a Lorentzian line shape. The sketches of this function in Fig. 17.5 show that the real (dispersion) and imaginary (absorption) parts produce resonant lines centered at ω_i, where $1/\tau_i$ is the linewidth. The reflectance plotted in Fig. 17.4a is a mixture of absorption and dispersion, hence it cannot provide the resonant frequencies ω_i with any precision.

F. Infrared Spectra

Figure 17.4 shows an example of an infrared spectrum of Nd_2CuO_4 with the T' structure in the far-infrared region where the fundamental band vibrations are found. Figure 17.6 shows a much broader scan for this same compound, from 50 to 32,000 cm^{-1} (4 eV), and Fig. 17.7 presents

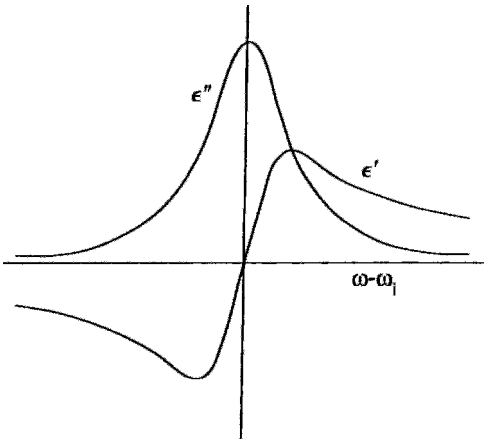

Figure 17.5 Normalized line shape of the dielectric constant $\epsilon = \epsilon' + i\epsilon''$ showing the real part ϵ', called the dispersion, and the imaginary part ϵ'', called the absorption.

the conductivity of three R_2CuO_4 compounds, where R = Nd, Sm, or Gd, calculated from their infrared reflectances. The mid-infrared spectrum is devoid of features that are typical of an insulating compound. What is referred to as a charge-transfer transition appears at $12{,}000\,cm^{-1}$ (1.5 eV).

The far-infrared reflectance and conductivity spectra of $YBa_2Cu_3O_{7-\delta}$ in the normal (at 110 K) and superconducting (at 2 K) states are compared for ceramic samples in Figs. 17.8 and 17.9 (Bonn *et al.*, 1988). The ranges of reflectance and conductivity values are much higher than in the Nd_2CuO_4 case of Figs. 17.6 and 17.7, and data for single crystals and oriented films have even higher reflectances. The low-frequency conductivity $2100\,(\Omega\,cm)^{-1}$ of Fig. 17.9 approaches the measured dc value of $3300\ (\Omega\,cm)^{-1}$. The plasma frequency ω_p is $6{,}000\,cm^{-1}$ (0.75 eV), and $1/\tau = 300\,cm^{-1}$.

Isotopic substitutions have been employed to identify modes. For example, it was observed that enriching $YBa_2Cu_3O_{7-\delta}$ with the heavy isotope ^{65}Cu causes the $148.6\,cm^{-1}$ line, which involves Cu vibrations, to shift downward in energy by $1.8\,cm^{-1}$, whereas the $112.5\,cm^{-1}$ line, which does not involve Cu motion, remained at the same frequency. A similar result

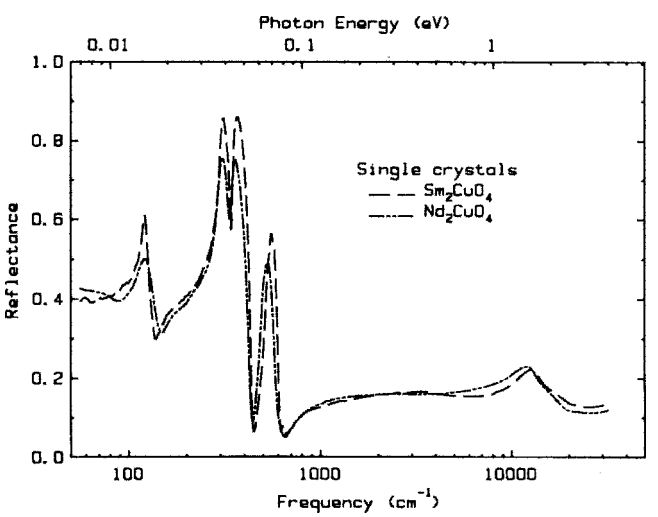

Figure 17.6 Frequency dependence of the reflectance of Sm_2CuO_4 (- - -) and Nd_2CuO_4 (–·–·–·–) in the infrared and visible regions (Herr *et al.*, 1991).

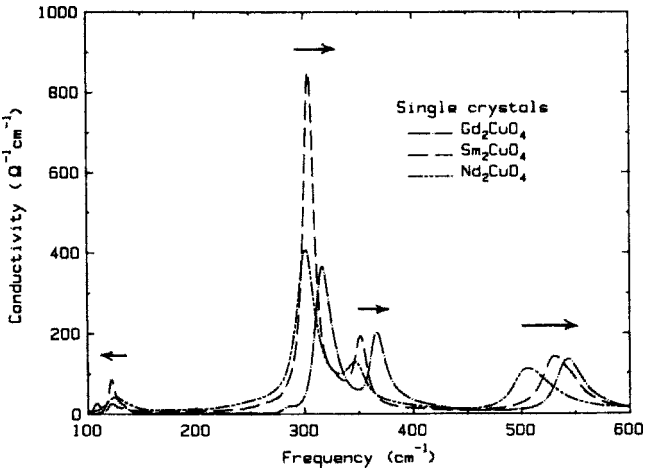

Figure 17.7 Frequency dependence of the conductivity of three monocrystals determined from a Kramers–Kronig analysis. The arrows indicate the shift direction with increasing mass Nd → *Sm* → Gd (Herr *et al.*, 1991).

occurs with ^{18}O enrichment of

$$(Pr_{1-x}Ce_x)CuO_4,$$

where three modes involving oxygen vibrations were observed to shift downward by 3–4%, whereas a fourth mode, which involves Pr vibrations, did not change. These downward shifts occur because classically, the vibrational frequency depends on the mass, in accordance with the expression

$$\nu_0 = (1/2\pi)(k/m)^{1/2} \qquad (17.18)$$

where k is the spring constant, so that higher masses produce lower frequencies, assuming that the substitution does not change k. Table 17.1 lists spring constants for various atom pairs in

$$(La_{0.925}Sr_{0.75})_2CuO_4$$

and $YBa_2Cu_3O_7$ that were deduced from measured vibrational frequencies (Bates, 1989; Brun *et al.*, 1987).

We see from Fig. 17.7 and Table 17.2 how the low-frequency infrared line shifts downward in frequency from 126 to 121 cm^{-1} as R of the compound R_2CuO_4 changes in the order Pr–Nd–Sm–Gd of increasing mass. This is expected behavior for a mass change effect. At higher field, the other three lines shift in the opposite direction, which may be attributed to the decrease in bond length with a consequent increase in the spring constant in the order Pr–Nd–Sm–Gd, with the spring constant effect dominating in Eq. (17.18).

G. Light-Beam Polarization

In conventional Raman spectroscopy, an incident unpolarized light beam simultaneously excites many of the A_g, B_g, and E_g Raman active modes. Polarized light enhances some of these modes and diminishes or eliminates others. A variety of directions and polarizations of the incident and scattered light beams can be employed to sort out and identify the modes.

To label the polarized spectra we will use the notation $k_i(E_i, E_s)k_s$ to denote the orientations of the incident (i) and scattered

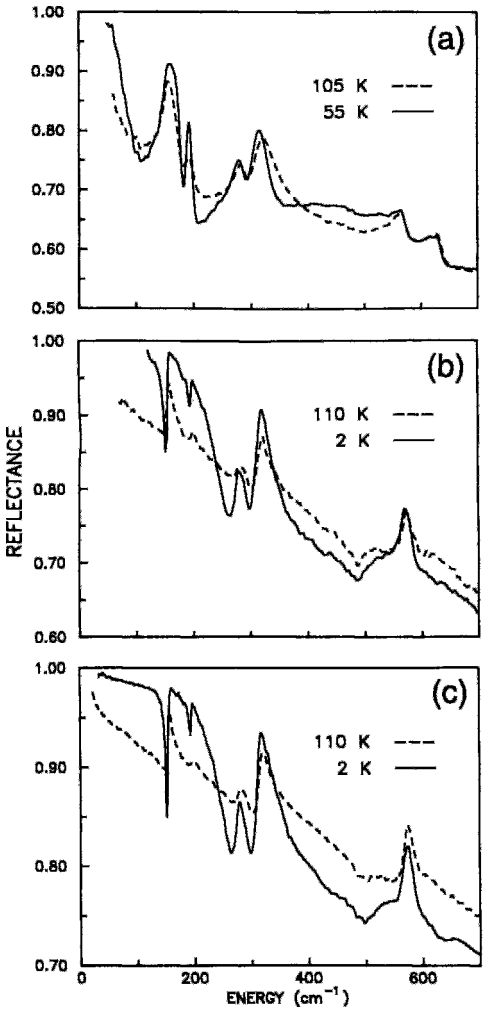

Figure 17.8 Optical reflectance of $YBa_2Cu_3O_{7-\delta}$ in the superconducting state (dashed curves) and in the normal state (solid curves) for (a) polished sample, (b) unpolished sample following several days exposure to the air, and (c) unpolished sample immediately after annealing in oxygen (Bonn *et al.*, 1988).

(s) light propagation directions **k** and electric vector **E** polarizations. Sometimes, the polarization will be along x', y'-axes that are oriented at 45° with respect to the x, y-axes, as shown in the inset of Fig. 17.10. A horizontal bar will be printed over the coordinate (e.g., $\bar{x}$) to denote the negative (e.g., $-x$) direction. Figure 17.10 illustrates the $z(x', y')z$ case, in which an incident light beam travels along z and is polarized along x', while a scattered beam departs along z and is polarized along y'. Some authors (e.g., Weber *et al.*, 1988) use a shorthand notation, specifying only the polarization directions, writing $x'y'$ for the case of Fig. 17.10.

H. Raman Spectra

In the previous section, we discussed that the Raman active modes can be sorted by using polarized light sources and detectors. For example, $YBa_2Cu_3O_7$ has five observed A_g modes, at 116, 149, 335, 435, and 495 cm^{-1}, plus some weaker B_{2g} and B_{3g} modes. Figures 17.11a, 17.11b, and 17.11c show how to distinguish between these modes by changing the polarization conditions. For example, the $z(y', x')\bar{z}$ spectrum contains only the 335 cm^{-1} line, while $y(zz)\bar{y}$ exhibits only the other four A_g types. These spectra were obtained with twin-free monocrystals. B_{2g} and B_{3g} are essentially the same modes with atomic vibrations along a and b, respectively, and are detectable using the respective polarizations $y(z, x)\bar{y}$ and $x(z, y)\bar{x}$. These two modes differ because of the chains running along the b direction.

Weber and Ford (1989) published a Raman study of undoped La_2CuO_4 in which they demonstrated the superiority of single crystal samples by means of the spectra presented in Fig. 17.12. This figure compares a powder sample with micrometer-sized particles with the freshly broken surface of a ceramic sample composed of 1–10 μm grains, and an optically polished single crystal. Figure 17.13 shows a soft mode at 104 cm^{-1} observed below the transition temperature 573 K from the high-temperature tetragonal phase to the low-temperature *ortho*-rhombic phase. Figure 17.14 shows the pronounced decrease in frequency of this soft mode as the transition temperature

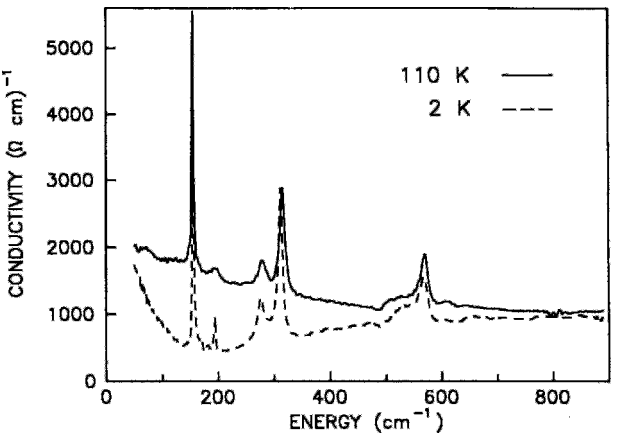

Figure 17.9 Real part of the conductivity of $YBa_2Cu_3O_{7-\delta}$ determined from a Kramers–Kronig analysis of the reflectance of the unpolished sample of Fig. 17.8 immediately after annealing in oxygen, shown in the superconducting state (dashed curve) and in the normal state (solid curve) (Bonn *et al.*, 1988).

Table 17.1 Bond Lengths and Effective Spring Constants (k_{eff}) of Atom Pairs in Lanthanum and Yttrium Compounds

$(La_{0.925}Sr_{0.075})_2CuO_4$			$YBa_2Cu_3O_{7-\delta}$		
Bond	**Length[a] Å**	**k_{eff}[b] N/m**	**Bond**	**Length[c] Å**	**k_{eff}[c] N/m**
Cu–O(2)	1.89	85	Cu(1)–O(2)	1.83	176
Cu–O(2)	2.40	20	Cu(1)–O(1)	1.94	152
La–O(1)	2.64	160	Cu(2)–O(3)	1.93	155
La–O(2)	2.39	105	Cu(2)–O(4)	1.96	149
La–O(2)	2.73	50	Cu(2)–O(2)	2.33	103
La–La		30	Ba–O(2)	2.75	58
La–Cu		10	Ba–O(1)	2.91	55
O(1)–O(1)	2.67	20	Ba–O(3)	2.94	54
O(2)–O(2)	3.77	7	Ba–O(4)	2.94	54
O(1)–O(2)	3.05	4	Y–O(4)	2.38	79
			Y–O(3)	2.42	77

[a] From Collin and Comes (1987).
[b] From Brun *et al.* (1987).
[c] From Bates (1989).

is approached from below. We see from Fig. 17.15, which compares spectra of the superconductor $(La_{1.85}Sr_{0.15})_2CuO_4$ at room temperature and at 8 K below T_c, that there is no sign of a phonon mode associated with the superconducting transition.

Table 17.3 compares frequencies of the Raman active modes of several of the high-temperature superconductors. Each mode in the table is labeled with the atom that dominates the particular vibration. Figure 17.16 shows the

Table 17.2 Shift of Infrared Frequency ω_i of the Series of Tetragonal R_2CuO_4 Compounds (R Changing in the Order Pr, Nd, Sm, and Gd of Increasing Mass Number)

Atom	Mass number	Lattice constant, Å		Infrared frequency, cm^{-1}			
		a	c	ω_1	ω_2	ω_3	ω_4
Pr[a]	140.9	3.95	12.17	126	299	336	495
Nd[b]	144.2	3.94	12.15	127	301	346	510
Sm[b]	150.4	3.91	11.93	123	304	351	534
Gd[b]	157.3	3.89	11.85	121	318	368	545

[a] From Crawford *et al.* (1990b).
[b] Lattice constants from Wyckoff (1965); IR frequencies from Burns (1989).

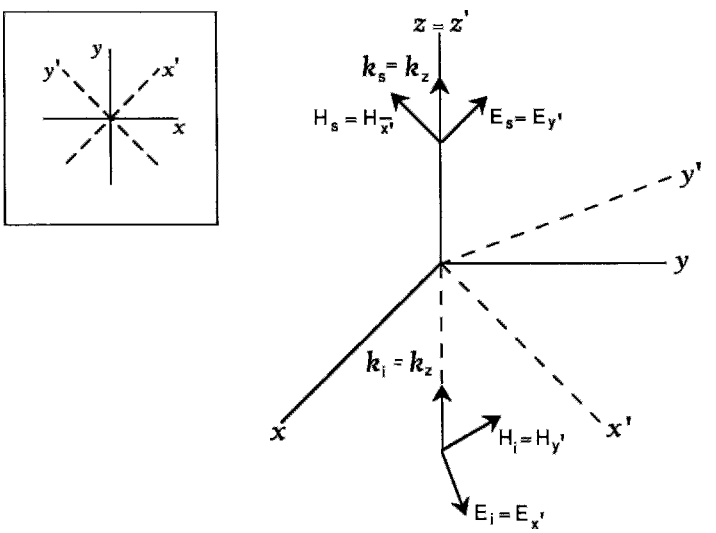

Figure 17.10 Experimental conditions for a $z(x', y')z$ polarization measurement. (The abbreviated notation $x'y'$ is sometimes employed.) The inset shows the orientation of the x'-y'-axes relative to x-y-axes.

$$Bi_2Sr_2Ca_nCu_{n+1}O_{2n+6}$$

Raman spectra for $n = 0$ and $n = 1$ (M. J. Burns *et al.*, 1989), the frequencies of which are presented in the table.

I. Energy Gap

Tunneling and vibrational spectroscopy are complementary ways of determining the energy gap of a superconductor (see Chapter 15, Section VI.E, for a discussion of tunneling spectroscopy and energy gaps). In the present section we will say a few words concerning the spectroscopic determination of gaps.

For a superconductor at absolute zero, we expect light with frequencies lower than $2\Delta/h$ to be transmitted and light with frequencies $\nu > 2\Delta/h$ to be reflected, as in the case of a normal metal. Above absolute zero these latter frequencies can excite quasiparticles and induce a

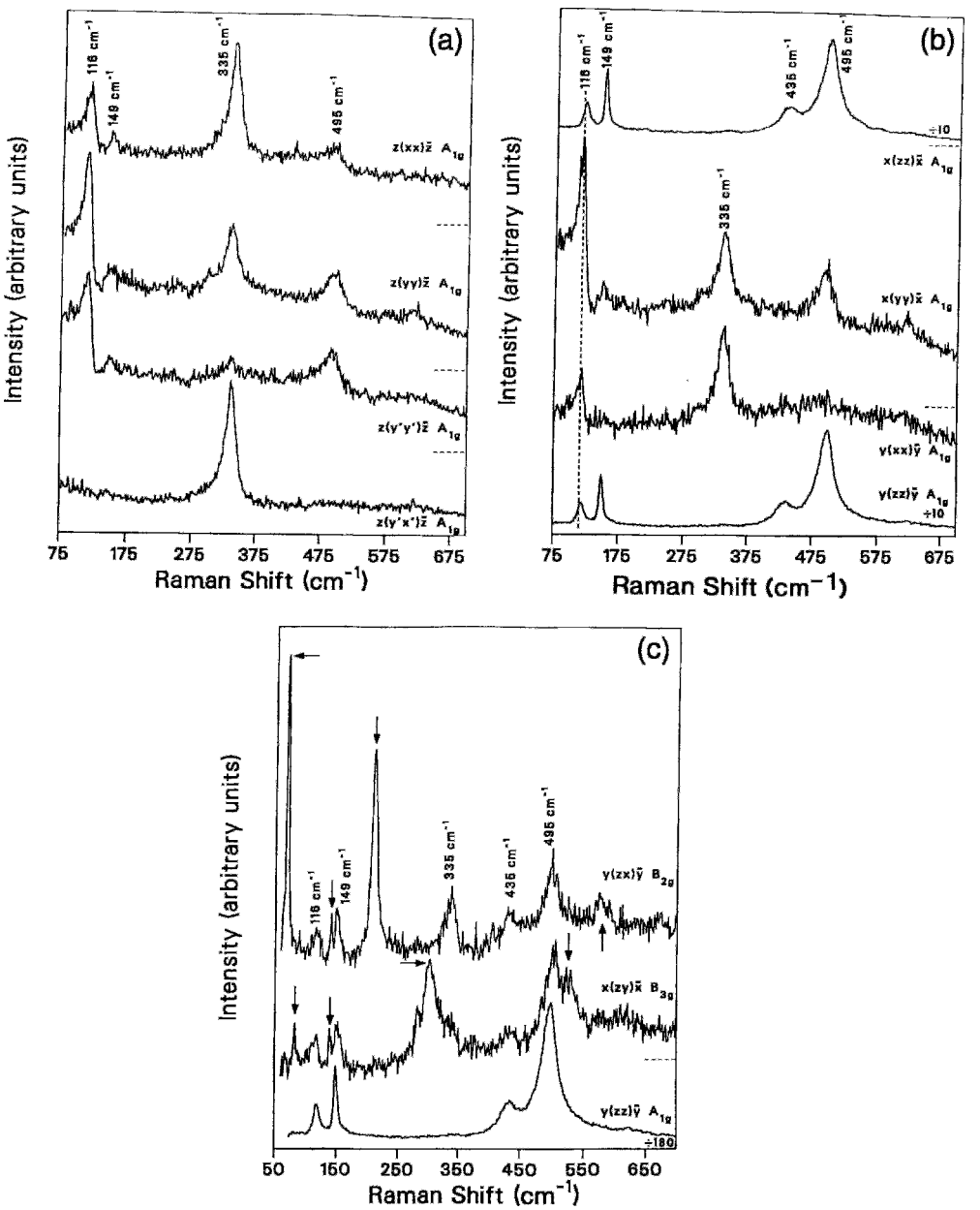

Figure 17.11 (a) Raman spectra of twin-free $YBa_2Cu_3O_7$ recorded with the laser beam directed along the *c*-axis and the indicated polarizations. The *x*-axis is the base line for the power spectrum, while the dotted lines indicate the base lines of the three upper spectra (McCarty *et al*., 1990a, b). (b) Raman spectra of twin-free $YBa_2Cu_3O_7$ recorded with the laser beam propagating in the *x*, *y*-plane, using the notation of Fig. 17.11a. Note the scale factor change for the two middle spectra (McCarty *et al*., 1990a, b). (c) Raman spectra of twin-free $YBa_2Cu_3O_7$ recorded with the laser beam directed along the *c*-axis, and the indicated polarizations selected to enhance the B_{2g} (top spectrum) and B_{3g} (middle spectrum) modes. Note the scale factor change for the lower A_g mode spectrum. The five A_g modes, with their frequencies labeled, appear on the upper spectrum due to polarization leakage (McCarty *et al*., 1990a, b).

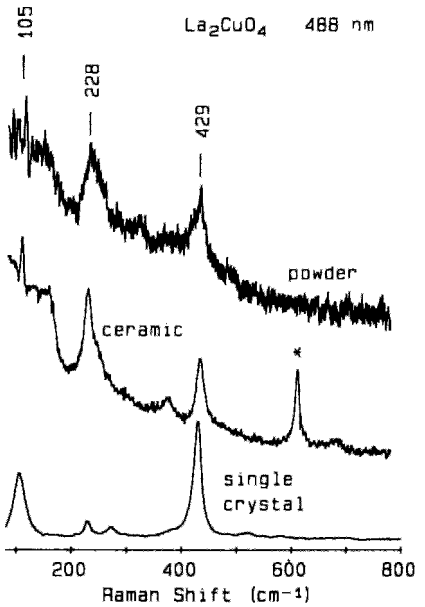

Figure 17.12 Raman spectra of La_2CuO_4. The laser powers and exposure times were 15 mW and 50 min for the powder, 15 mW and 10 hr for the ceramic (1–10 μm grains), and 50 mW and 50 min for the single crystal. Different polarization conditions were used, and the spectra have a common baseline (Weber *et al.*, 1989).

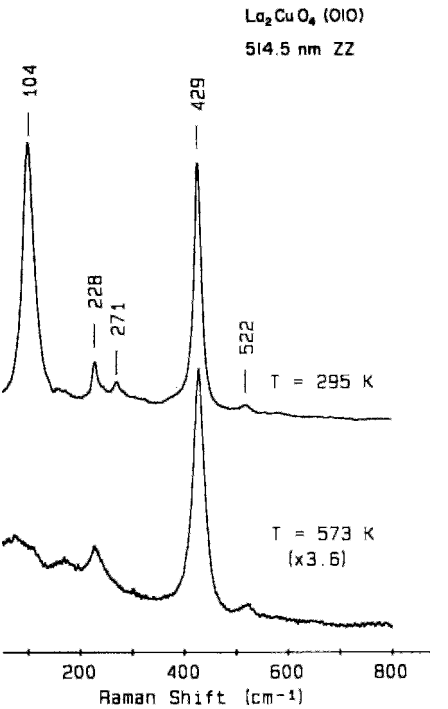

Figure 17.13 Low-frequency zz spectra from the [010] surface of orthorhombic La_2CuO_4 at 295 K (top), and tetragonal La_2CuO_4 at 573 K (bottom). A 50 mW, 514.5 nm laser was employed (Weber *et al.*, 1989).

photoconductive response. Figure 17.17 shows low-temperature experimental data for reflection of infrared radiation at frequencies below the gap value $2\Delta \sim 70\,\text{cm}^{-1}$, with a drop to zero reflectivity for frequencies above this value for the superconductor $Ba_{0.6}K_{0.4}BiO_3$ (Schlesinger *et al.*, 1989). The figure also shows the drop in reflectivity when the temperature is increased, and also when a magnetic field is applied. Figure 17.18 presents infrared reflectivity (reflectance) spectra for two single-domain (untwinned) $YBa_2Cu_3O_{7-\delta}$ crystals arising from the Cu–O planes when the electric field is polarized parallel to the *a*-axis, and with possible contributions from the chains as well for polarization parallel to *b* (Schle-singer *et al.*, 1990b; vide also Friedl *et al.*, 1990; McCarty *et al.*, 1991). In both cases, the superconducting-to-normal state resistivity ratios R_s/R_n, obtained at the temperatures 35 K and 100 K, respectively, peak near $\approx 500\,\text{cm}^{-1}$, indicative of an energy gap. Brunel *et al.* (1991) measured the sharp infrared reflectivity discontinuity at the gap for the superconductor $Bi_2Sr_2CaCu_2O_8$.

III. OPTICAL SPECTROSCOPY

Visible (13,000 to 25,000 cm^{-1}, or 1.6 to 2.5 eV) and ultraviolet (UV) (3.1 to $\approx$ 40 eV) spectroscopy, both often referred to as optical spectroscopy, have been employed to detect crystal field-split electronic energy levels in insulating solids containing transition ions and to determine energy gaps in semiconductors as well as the locations of impurity levels within these gaps. The response of metals to incident optical radiation depends on the plasma

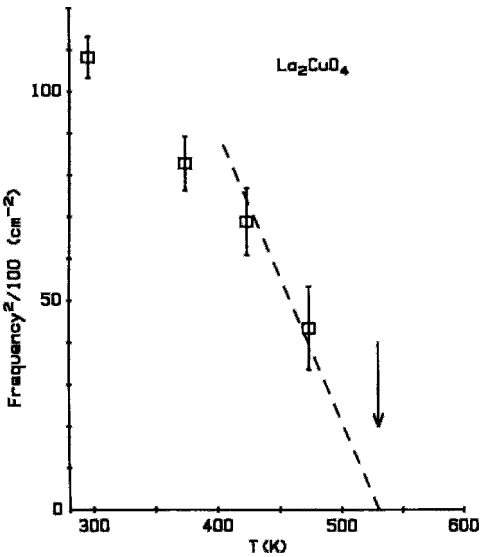

Figure 17.14 Plot of frequency squared versus T for the soft phonon observed in La_2CuO_4 for zz scattering under the same conditions as Fig. 17.13 (Weber *et al.*, 1989).

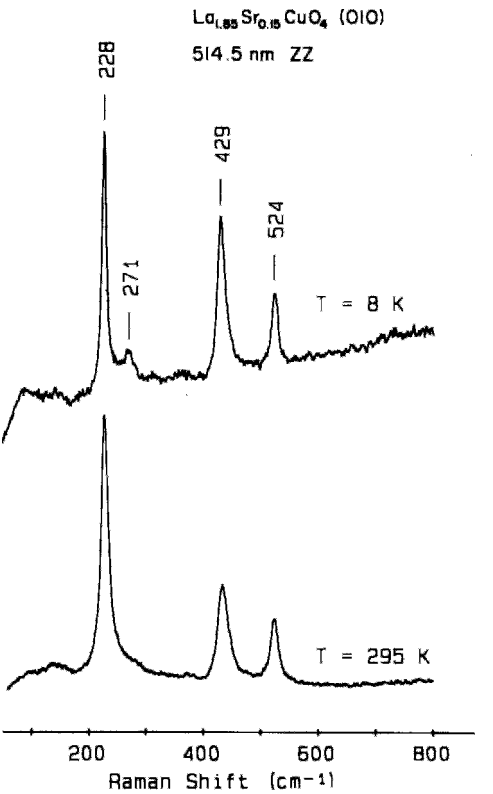

Figure 17.15 Raman spectra from the orthorhombic form of $(La_{0.925}Sr_{0.075})_2CuO_4$ at 8 K (top), and from the tetragonal form at 295 K, for the same conditions as Fig. 17.13 (Weber *et al.*, 1989).

frequency ω_p (17.14) which, as noted in Section II, lies in the near-infrared region for the high-temperature superconductors.

A study was made of the optical reflectance (reflectivity) of the series of $La_{2-x}Sr_xCuO_4$ compounds prepared for the range of compositions indicated in Fig. 17.19. The broad spectral scan, up to 37 eV, which is shown in Fig. 17.20 exhibits three reflectivity edges. The highest frequency edge, near 30 eV, falls off as $1/\omega^4$, which was attributed to excitations involving some of the valence electrons. The midfrequency band, from 3 to 12 eV, was assigned to interband excitations from O $2p$ valence bands to La $5d/4f$ orbitals, with the semiconductor La_2CuO_4 having an optical energy gap of ≈ 2 eV (Uchida *et al.*, 1991). The low-frequency edge is absent in the $x = 0$ insulating compound and present in the two doped conductors. Figure 17.21 presents a set of Bi compound spectra in the range 0.1–3 eV. The superconductor $Bi_2Sr_2CaCu_2O_8$ and the metal $Bi_2Sr_2(Ca,\ Nd)Cu_2O_8$ both exhibit the absorption edge near 1.1 eV, whereas the other two compounds, which are semiconductors, do not.

A Kramers–Kronig analysis carried out for the reflectance spectra of Fig. 17.20 provided the conductivity spectra presented in Fig. 17.22 for the low-energy region. At the low-frequency limit $\sigma(\omega)$ increases continuously with the level x of doping, being low for the insulators ($x = 0,\ 0.02,\ 0.06$), high for the superconductors ($x = 0.1,\ 0.15,\ 0.2$), and highest for the nonsuperconducting metal ($x = 0.34$). (Recall that $La_{2-x}Sr_xCuO_4$ is a hole superconductor.) A similar set of spectra obtained for the electron superconductor $Nd_{2-x}Ce_xCuO_{4-y}$ exhibited the same depen-

Table 17.3 Measured Raman Frequencies in cm^{-1} of the A_{1g} and B_{1g} Modes of High-Temperature Superconductors[a]

$(La_{1-x}Sr_x)_2CuO_4$[b]	$Bi_2Sr_2Ca_nCu_{n+1}O_{6+2n}$		$Tl_2Ba_2Ca_nCu_{n+1}O_{6+2n}$		$YBa_2Cu_3O_7$[c]	$TlBa_2CaCu_2O_7$[c,d]
$x = 0.075$	$n = 0$	$n = 1$	$n = 1$	$n = 2$		
				92		
	196 Bi	164 Bi	134 Tl	129 Tl	108 Ba	120 Ba
			157 Cu_p		152 Cu_p	148 Cu_p
226 La	309 Sr	292 Sr				
		282			340	278
			409 O_p		440 O_p	
430 O_z	455 O_z	464 O_z	493 O_z	498 O_z	504 O_z	525 O_z
	625 O_0	625 O_0	599 O_0	599 O_0		

[a] Most of the modes are labeled with their dominant vibrating atom; Cu_p and O_p denote copper and oxygen atoms in the planes; O_0, oxygens centered in an axially distorted octahedron of six heavy-atom nearest neighbors; and O_z, oxygens on the *c*-axis above and below the Cu atoms. From Burns *et al*. (1989).

[b] An Sr atom replacing La in the compound $(La_{1-x}Sr_x)_2CuO_4$ is expected to have its frequency raised from 226 to $284\,cm^{-1}$.

[c] Isostructural compound.

[d] $T_c = 60\,K$.

dence of the low-frequency conductivity on x as in the hole case.

The rare-earth ions have crystal-field energy-level splittings in the optical region, and transitions between them can be observed. As an example, the energy levels of six erbium compounds are given in Fig. 17.23, and the optical transitions in the green region of the visible spectrum are shown in Fig. 17.24 for three of them (Jones *et al*., 1990). This technique could be employed for checking the purity of a sample.

IV. PHOTOEMISSION

Photoemission spectroscopy (PES) measures the energy distribution of the electrons emitted by ions in various charge and energy states. These electrons have energies characteristic of particular atoms in particular valence states. We will describe the technique, say something about the energy states that are probed, and describe what the technique tells us about superconductors.

A. Measurement Technique

To carry out this experiment, the material is irradiated with ultraviolet light or x-rays, and the incoming photons cause electrons to be ejected from the atomic energy levels. The emitted electrons, called *photoelectrons*, have a kinetic energy KE which is equal to the difference between the photon energy $h\nu_{ph}$ and the ionization energy E_{ion} required to remove an electron from the atom, as follows:

$$KE = h\nu_{ph} - E_{ion}. \tag{17.19}$$

The detector measures the kinetic energy of the emitted electrons, and since $h\nu_{ph}$ is known, the ionization energy is determined from Eq. (17.19). Each atomic energy state of each of the ions has a characteristic ionization energy, so that the measured kinetic energies provide information about the valence states of the atoms. In addition, many ionization energies are perturbed by the surrounding lattice environment, so that this environment is also probed by the measurement.

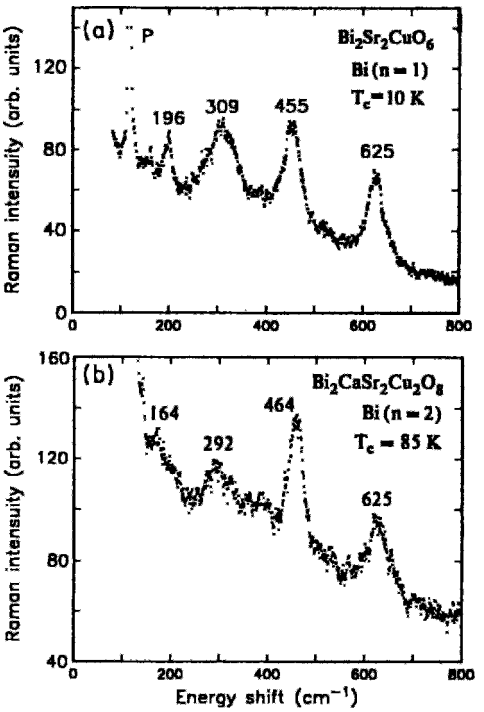

Figure 17.16 Polarized Raman spectra obtained at room temperature from single crystal $Bi_2Sr_2CuO_6$ (2201, a) and $Bi_2Sr_2CaCu_2O_8$ (2212, b) (Burns *et al.*, 1989).

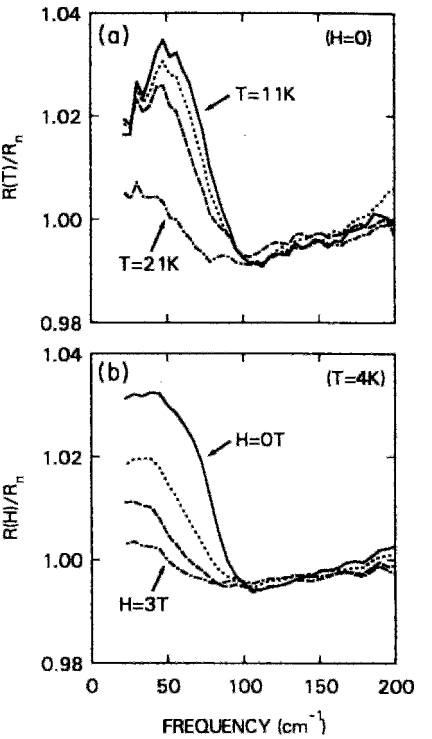

Figure 17.17 The frequency dependence of the reflectivity R in the superconducting state of $Ba_{0.6}K_{0.4}BiO_3$ normalized relative to its normal state value R_n showing the low frequency enhancement associated with the superconducting energy gap. The suppression of the low frequency enhancement by (a) a change in temperature ($T = 11,\ 14.\ 17,\ 21$ K) in zero field $B_{app} = 0$, and (b) the effect of applying a field ($B_{app} = 0,\ 1,\ 2,\ 3\ T$) at the temperature 4 K are shown. (Schlesinger *et al.*, 1989).

In ultraviolet photoemission spectroscopy (UPS), the excitation energy comes from a high-intensity UV source, such as the 21.2-eV resonance line (He–I) or the higher-frequency 40.8-eV line (He–II) of a helium-gas discharge tube. In the x-ray analogue (XPS), the radiation used to excite the photoelectrons is obtained from an Mg–K_α (1253.6), Al–K_α, (1486.7 eV) or other convenient x-ray source.

It is also possible to carry out the reverse experiment, called inverse photoelectron spectroscopy (IPS), in which the sample is irradiated with a beam of electrons and the energies of the emitted photons are measured. When UV photons are detected, the method is sometimes called bremsstrahlung isochromat spectroscopy (BIS). A related experiment is electron energy-loss spectroscopy (EELS) in which the decrease in energy of the incident electron beam is measured. Another technique, called Auger electron spectroscopy is based on a radiationless transition, whereby an x-ray photon generated within an atom does not leave the atom as radiation, but instead ejects an electron from a higher atomic level.

B. Energy Levels

We know from the quantum theory of atoms that, to first order, the frequency ν

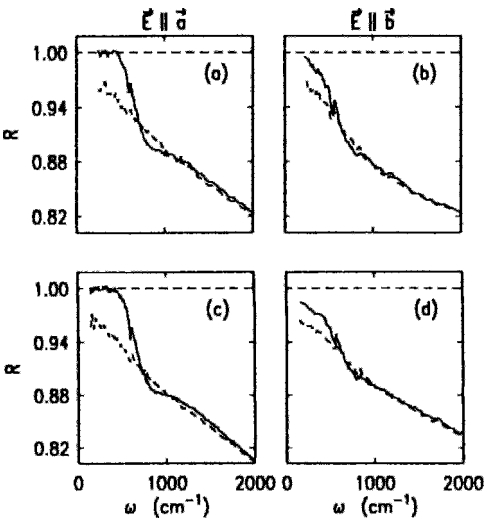

Figure 17.18 Polarized infrared reflectance spectra for two untwinned $YBa_2Cu_3O_{7-\delta}$ samples in the normal state ($T = 100$ K, dashed curves) and in the superconducting state ($T = 35$ K, solid curves). Polarization parallel to the *a*-axis is on the left, while polarization parallel to the *b*-axis is on the right. Two samples were used, spectra (a) and (b) from one of them and spectra (c) and (d) from the other (Schlesinger *et al.*, 1990b).

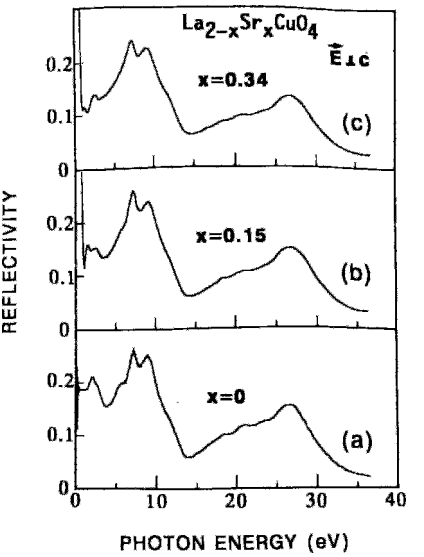

Figure 17.20 Optical reflectivity (reflectance) spectra with the **E** vector polarized in the *a, b*-plane for $La_{2-x}Sr_xCuO_4$ single crystals with three of the compositions x indicated in Fig. 17.19 (Uchida *et al.*, 1991)

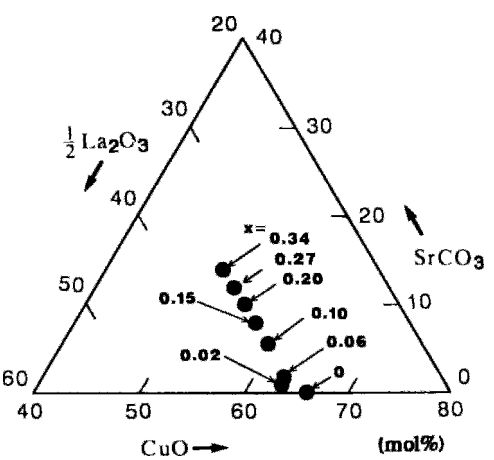

Figure 17.19 Compositions of the starting materials La_2O_3, $SrCO_3$, and CuO used to grow single crystals of $La_{2-x}Sr_xCuO_4$ with the indicated x values (Uchida *et al.*, 1991).

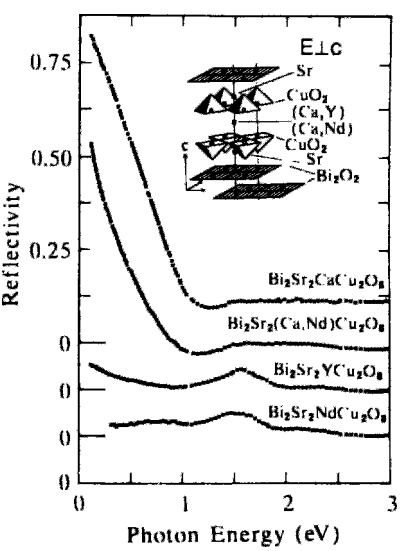

Figure 17.21 Room-temperature optical reflectivity (reflectance) spectra for four Bi-cuprates with the electric field E of the incident light polarized in the *a, b*-plane (Terasaki *et al.*, 1990a,b).

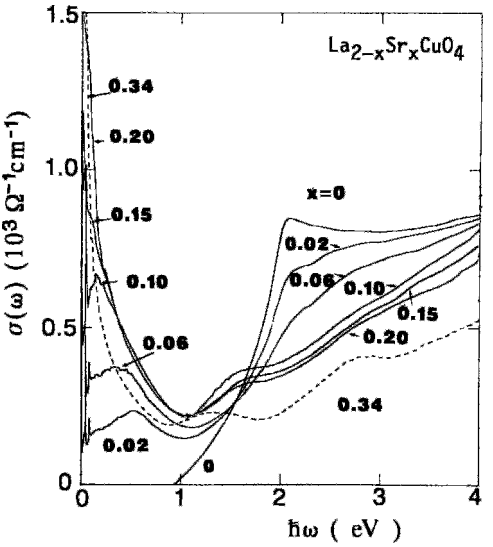

Figure 17.22 Frequency dependence of the optical conductivity $\sigma(\omega)$ of $La_{2-x}Sr_xCuO_4$ obtained from a Kramers–Kronig analysis of reflectance spectra for the **E** vector polarized in the *a, b*-plane. Results for several compositions x from Fig. 17.19 are shown (Uchida *et al.*, 1991).

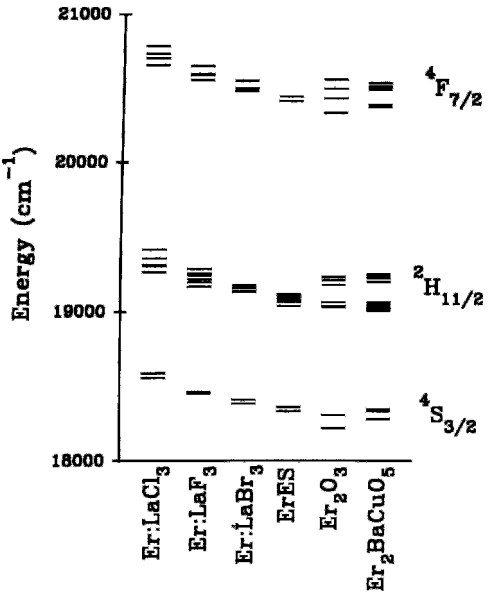

Figure 17.23 Crystal-field energy levels of Er^{3+} in several compounds, including the erbium green-phase Er_2BaCuO_5, which has levels close to those of the oxide Er_2O_3. ErES denotes erbium ethyl sulphate (Jones *et al.*, 1990).

of a transition from the energy level with principal quantum number n_1 to the level n_2 is

$$\nu = \frac{me^4Z^2}{8\epsilon_0^2h^3}\left(\frac{1}{n_1^2}, \frac{1}{n_2^2}\right), \qquad (17.20)$$

where Z is the atomic number and the other symbols have their usual meaning. Figure 17.25 gives the energy level scheme for molybdenum, with additional finestructure splittings not included in Eq. (17.20). For the atomic number (Z) dependence of the K_α line, which represents the innermost x-ray transition from $n_1 = 1$ to $n_2 = 2$, Eq. (17.20) gives Moseley's law

$$\sqrt{\nu} = a_K(Z - 1). \qquad (17.21)$$

The factor $(Z - 1)$ in Eq. (17.21) in place of Z takes into account shielding of the nucleus by the remaining $n_1 = 1$ electron, whose apparent charge falls to $(Z - 1)$. A similar

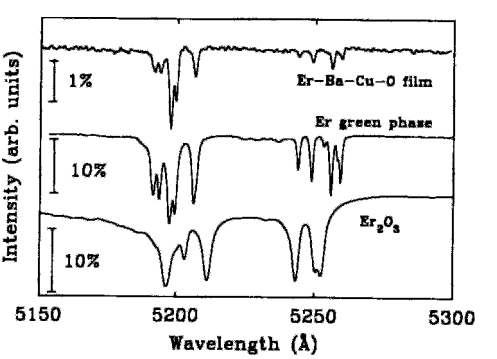

Figure 17.24 Optical spectra for the $^4I_{15/2} \rightarrow {}^2H_{11/2}$ transition in $ErBa_2Cu_3O_{7-\delta}$ (top), Er_2BaCuO_5 (middle), and Er_2O_3 (bottom) (Jones *et al.*, 1990).

expression applies to the next highest frequency L_α line, which has $n_1 = 2$ and $n_2 = 3$.

Figure 17.26 presents a plot of $\sqrt{\nu}$ versus the atomic number Z for the experimentally measured K_α and L_α lines of the

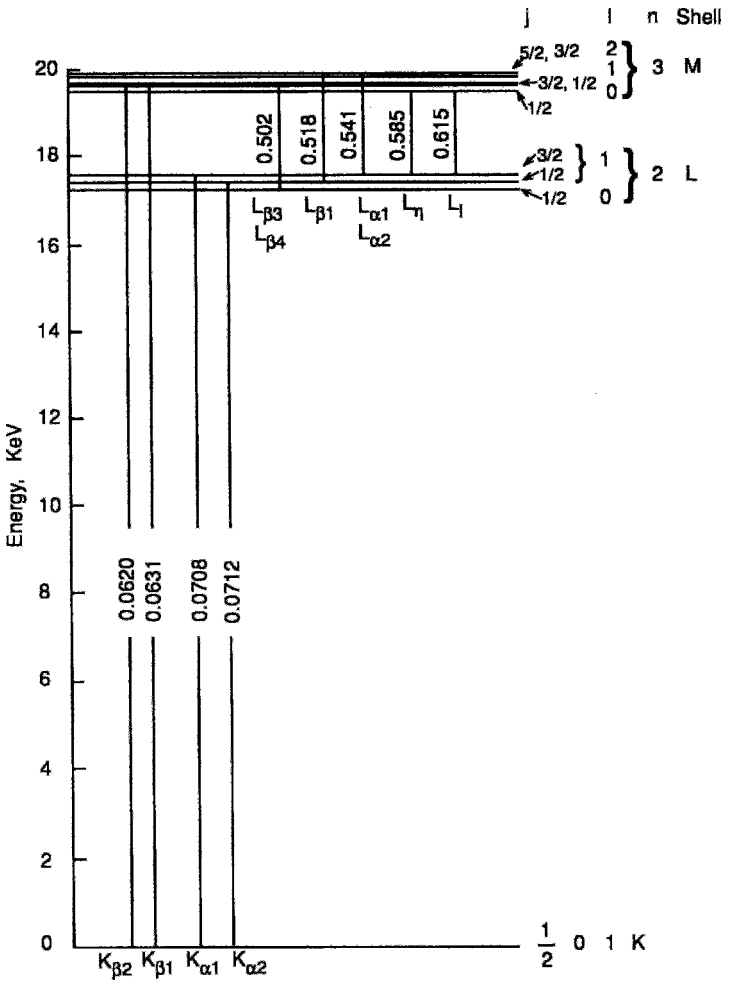

Figure 17.25 Energy-level diagram of Mo showing the wavelengths, in nanometers, of the K and L series lines, each of which is labeled using the Siegbahn notation. The j, l, and n quantum number is given for each energy level.

elements in the periodic table from $Z = 15$ to $Z = 60$, showing that Moseley's law is obeyed. These inner-level transitions are very little disturbed when the atom is bound in a solid because of shielding by the outer electrons, so that the regularity of Moseley's law applies to bound as well as free atoms, permitting atoms to be unambiguously identified. This law only holds for the innermost atomic electrons, however.

The ionization energies of the outer electrons of atoms are more dependent on the number of electrons outside the closed shells than on the atomic number, as shown by the data in Fig. 17.27. The ionization energies are in the visible or near-ultra-violet region. When the atom is bound in a solid, its valence electrons form ionic or covalent bonds, drastically modifying their upper energy level schemes and ionization energies. Atomic

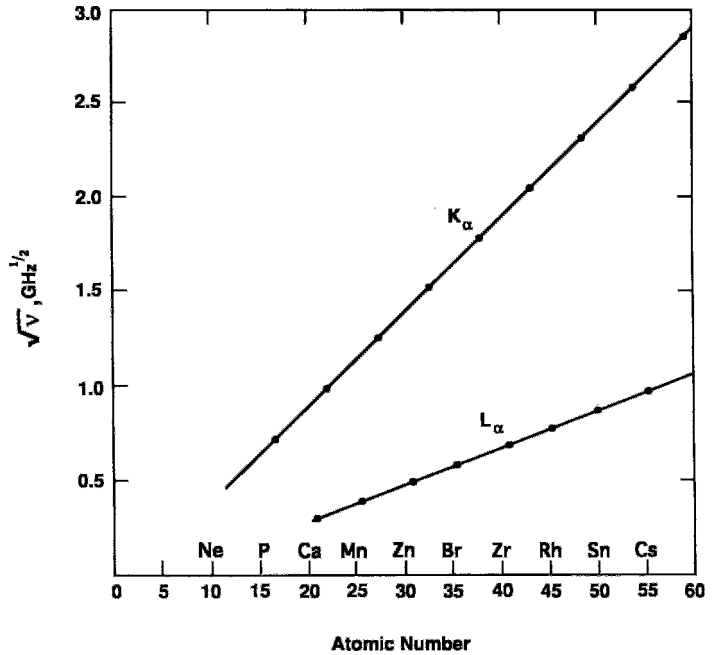

Figure 17.26 Moseley plot of the K_α and L_α characteristic x-ray lines of a number of elements in the atomic number range from 17 to 59.

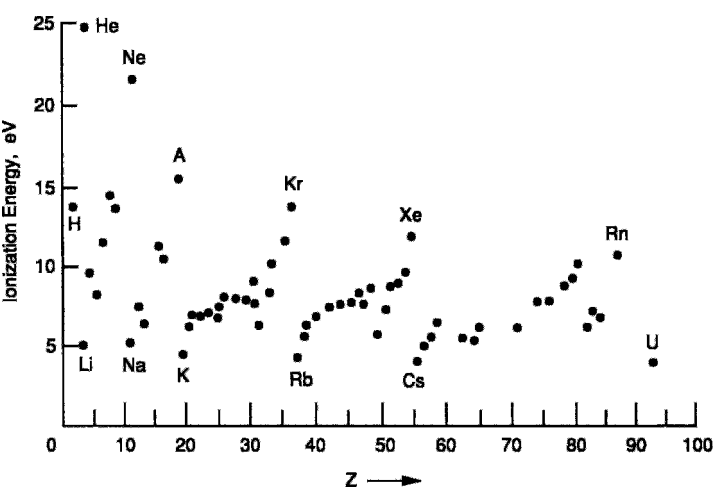

Figure 17.27 Experimentally determined ionization energy of the outer electron in various elements (Eisberg and Resnick, 1974, p. 364). Copyright © 1974. Reprinted by permission of John Wiley & Sons, Inc.

electrons below the valence electrons but not in the deepest levels undergo shifts in energy that are intermediate between the two extreme cases of the outermost and innermost electrons.

C. Core-Level Spectra

The four parts of Fig. 17.28b presents core-level XPS spectra arising from the atoms Ba, Cu, O, and Y of $YBa_2Cu_3O_7$ (Steiner *et al.*, 1987). Figure 17.29 gives corresponding spectra from Bi, O, and Sr of $Bi_2(Sr, Ca)_3Cu_2O_{8+\delta}$ (Fujimori *et al.*, 1989). The latter figure shows the decomposition of each line into components. Figure 17.30 shows how the lines in the Cu($2p_{3/2}$) spectral region with binding energy from 934 to 937 eV vary in position and intensity for the four compounds $LaCuO_3$, La_2CuO_4, CuO, and Cu_2O. The Cu($2p_{1/2}$) transition is near 954 eV. (Allan *et al.* (1990), and Yeh *et al.* (1990) show similar Cu($2p$) spectra for $YBa_2Cu_3O_{7-\delta}$ at three temperatures in the superconducting region.) The lines, near 944 and 963 eV in the spectra of Fig. 17.30, are satellites of the two main lines. Several researchers have studied the photoemission of the oxides Cu_2O, CuO, and $NaCuO_2$, which have monovalent, divalent, and trivalent Cu, respectively, for comparison with cuprate spectra (Brandow, 1990; Ghijsen *et al.*, 1990; Karlsson *et al.*, 1992; Sacher and Klemberg-Sapieha, 1989; Shen *et al.*, 1990).

The shapes of photoemission core spectra provide information on various sample characteristics.

1. The spectra from the six atoms in the compound $Bi_2Sr_2Ca_{1-x}Y_xCu_2O_y$ are presented in Fig. 17.31 for $x = 0$, 0.5, 0.8, and 1.0, with the $x = 0$ scan omitted for Y (Itti *et al.*, 1991). The decline in the intensity of the Ca line for these four x values is evident. Figure 17.32 clarifies how the various line positions shift toward higher values with the increase in x.
2. The core spectra from the four atoms of $YBa_2Cu_3O_{7-\delta}$ are compared in Fig. 17.33 for no pretreatment, following two high-temperature heat treatments in an ultra-high vacuum (UHV), and following heating and annealing in oxygen (Frank *et al.*, 1991). The decomposition into component lines arising from the surface and from the bulk is shown for three of the spectra. As the treatment proceeds, the bulk fraction increases relative to the surface fraction, as shown.
3. A combined photoelectron microscopy and spectroscopy experiment compared the Bi spin-orbit split $d_{5/2}$, $d_{3/2}$ doublet

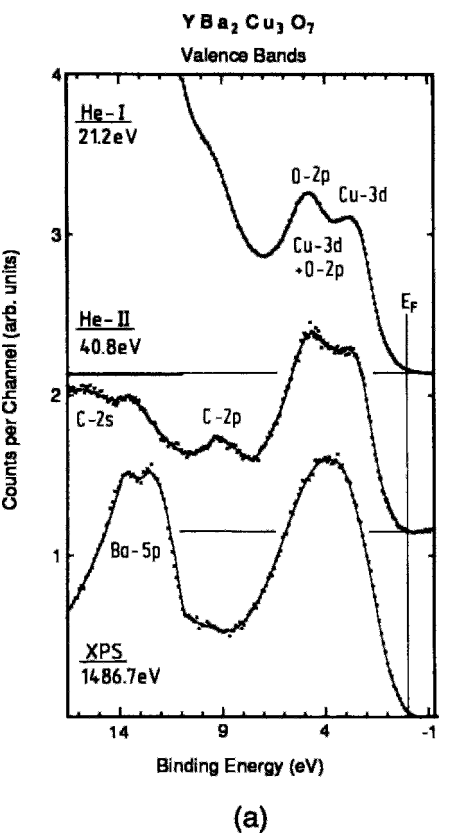

Figure 17.28 Photoemission spectra of $YBa_2Cu_3O_7$, showing (a) valence band spectra at low energies, and (b) core-level x-ray spectra (XPS) (Steiner *et al.*, 1987). (*Continues*)

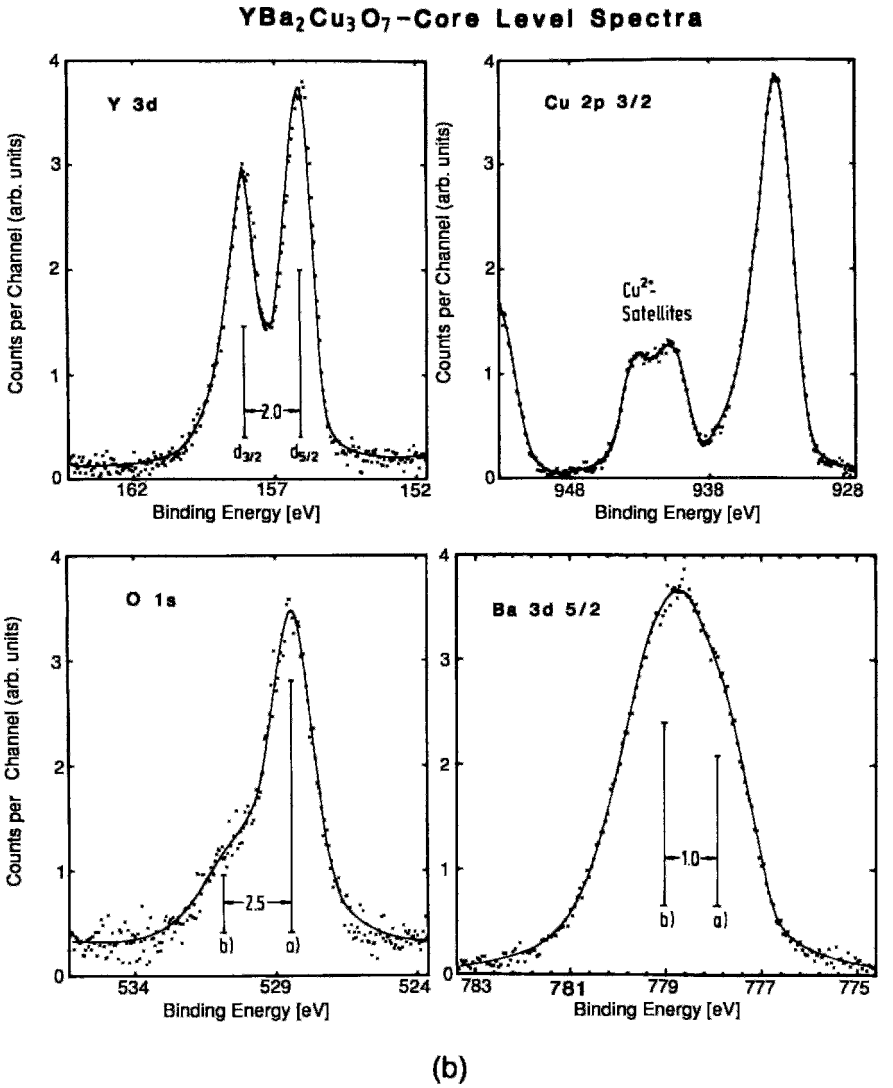

Figure 17.28 (*Continued*)

obtained from different regions, $\approx 20\,\mu$m in diameter, on the surface of cleaved monocrystals of $Bi_2Sr_{2-x}Ca_{1+x}Cu_2O_{8+\delta}$. The spectra are given in Fig. 17.34 (Komeda *et al.*, 1991).

We see that some spectra exhibit a doublet from a highly oxidized form of Bi shifted by about 2 eV to higher binding energies. The change in the Bi oxidation state at the crystal edges could degrade the superconducting properties.

D. Valence Band Spectra

The spectra of the outer, or valence, electrons occur at lower energies, 0 to 16 eV, as shown on the panel of Fig. 17.28a. The overlapping of the O2p and Cu3d bands depends on the conditions under which they

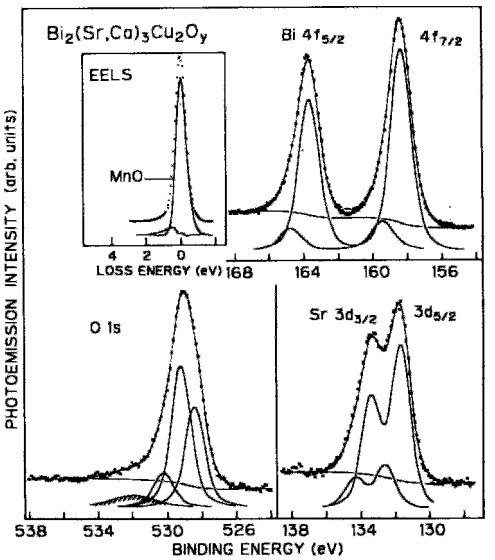

Figure 17.29 Core-level XPS spectra of $Bi_2(Sr,Ca)_3Cu_2O_y$ shown fit with calculated line shapes. The weak shaded part of the O-1*s* spectrum is due to contamination. The inset shows the elastic peak of the electron energy loss spectrum (EELS, dots, $E_0 \approx 2\,kV$) decomposed into a dominant, purely elastic part characteristic of the wide-gap insulator MnO and a weak residual signal (Fujimori *et al.*, 1989).

are obtained, and these conditions can be varied to enhance certain features relative to others. For example, Fig. 17.35 shows angle-resolved photoemission spectra (ARPES) obtained from $(Bi_{0.8}Pb_{0.2})_2Sr_2CaCu_2O_8$ single crystals cleaved *in vacuo* for electron-emission angles in the range from 30° to 61.5° (Böttner *et al.*, 1990), while Fig. 17.36 (Arko *et al.*, 1989) presents spectra of $YBa_2Cu_3O_{6.9}$ for different incident-photon energies between 14 and 70 eV. The peaks B to F in Fig. 17.35 are associated with flat regions of the energy bands. The A and D peaks of Fig. 17.36, which vary in the extent of their resolution, are assigned to the O2*p* and Cu3*d* states, respectively. From Fig. 17.36 it is clear that the discontinuity in intensity at the absorption edge itself, the zero of energy, is small compared with the atomic absorptions that start near 1 eV. This edge has been resolved using UPS with the 21.7-eV exciting line (Imer *et al.*, 1989). Figure 17.37 illustrates how excitation with the photon energies of one element, O1*s* in this case, enhances the spectral features from another element, the Cu3*d* lines at 13 eV

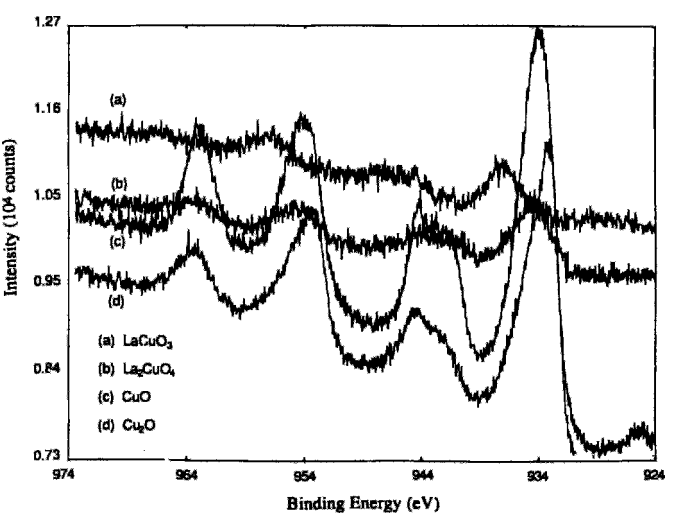

Figure 17.30 XPS spectra of the Cu $2p_{3/2}$ ($\approx$ 935 eV) and Cu $2p_{1/2}$ ($\approx$ 954 eV) regions of four copper oxides: CuO, Cu_2O, La_2CuO_4, and $LaCuO_3$. The lines near $\approx$ 944 eV and $\approx$ 963 eV are satellites (Allan *et al.*, 1990).

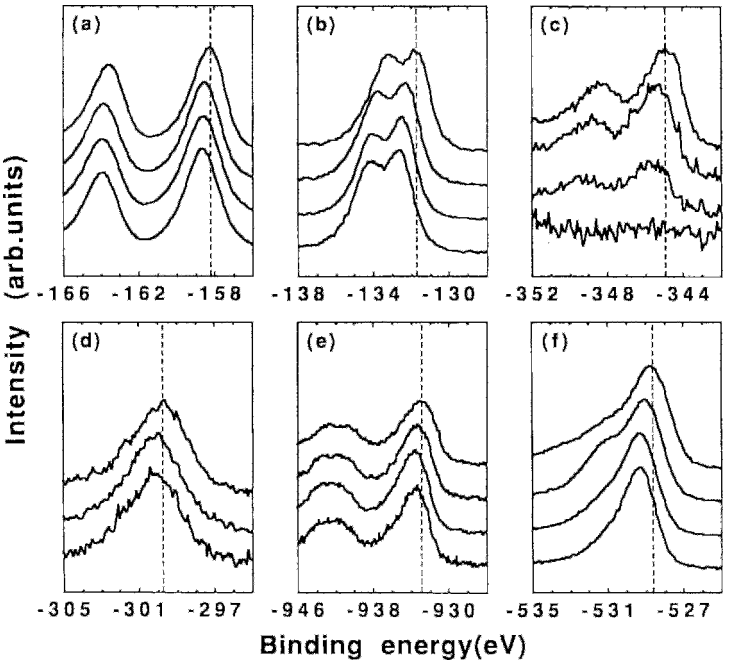

Figure 17.31 XPS core spectra of $Bi_2Sr_2Ca_{1-x}Y_xCu_2O_y$, with $x = 0$, 0.5, 0.8, and 1.0 from top to bottom, for the atoms: (a) Bi $4f$, (b) Sr $3d$, (c) Ca $2p$, (d) Y $3p$, (e) Cu $2p_{3/2}$, and (f) O $1s$. There is, of course, no $x = 0$ spectrum for Y (Itti *et al.*, 1991).

(Sarma *et al.*, 1989). The figure also shows an Auger signal (Bar-Deroma *et al.*, 1992; Cota *et al.*, 1988).

Angle resolved photoemission spectra have been analyzed by Fermi liquid theory (Kim and Riseborough, 1990). Some typical articles on valence bands are (Brookes *et al.*, 1989; Dessau *et al.*, 1991; Matsuyama *et al.*, 1989; Mehl *et al.* 1990; Wells *et al.*, 1990).

E. Energy Bands and Density of States

Various investigators have employed photoemission to obtain information on, for example, energy bands (Dessau *et al.*, 1992; Liu *et al.*, 1992a; Takahashi *et al.*, 1989), the Fermi surface (Campuzano *et al.*, 1991; Mazin *et al.*, 1992; Tobin *et al.*, 1992), and the Eliashberg function $\alpha^2 D_{\rm ph}(W)$ (Arnold *et al.*, 1991; Bulaevskii *et al.*, 1988) of high-temperature superconductors.

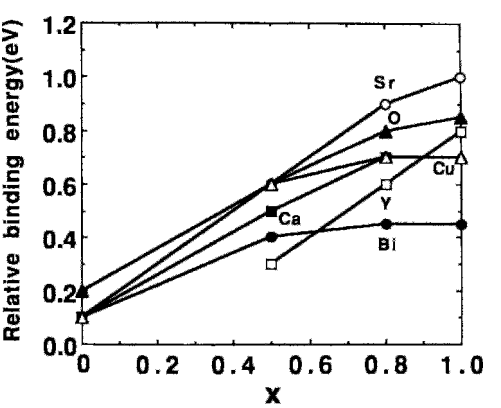

Figure 17.32 Shift of the binding energy of each core level with the Y content x obtained from the spectra of Fig. 17.31. The vertical axis indicates the shift in binding energy relative to the offset values of 158.1 (Bi $4f_{7/2}$), 131.6 (Sr $3d_{5/2}$), 344.8 (Ca $2p_{3/2}$), 299.4 (Y $2p_{3/2}$), 932.7 (Cu $2p_{3/2}$), and 528.4 eV (O $1s$) (Itti *et al.*, 1991).

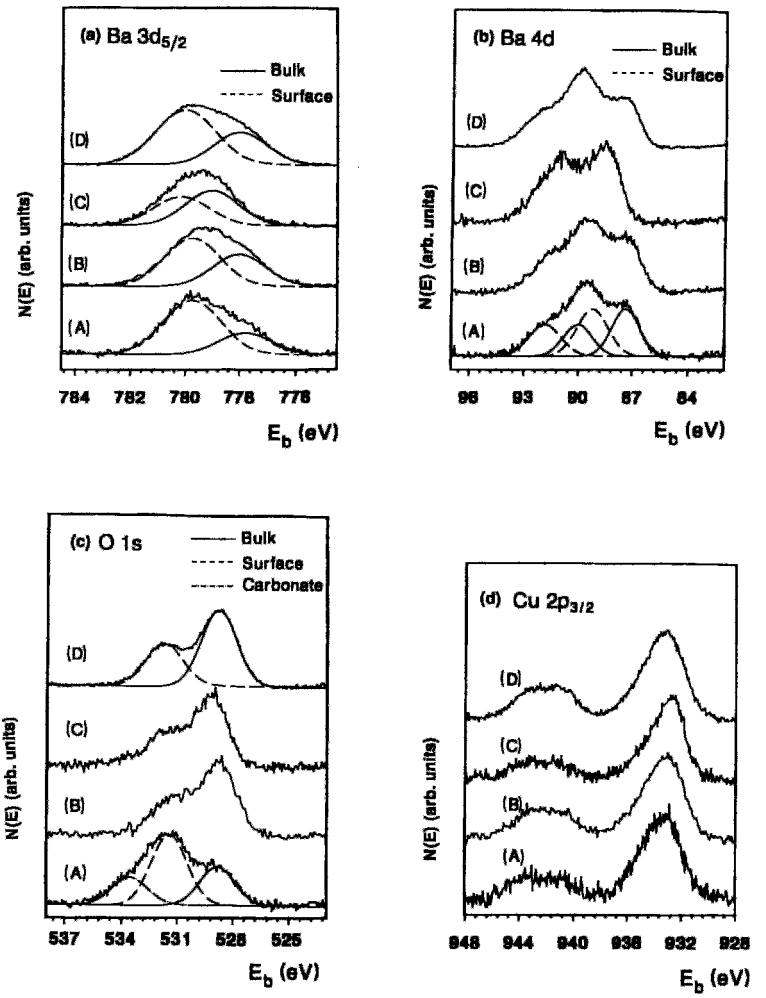

Figure 17.33 XPS spectra and line shape decomposition of three atoms in $YBa_2Cu_3O_{7-\delta}$: (a) Ba $3d_{5/2}$, (b) Ba $4d$, (c) O $1s$, and (d) Cu $2p_{3/2}$. Spectra are presented for samples before pretreatment (A), after heating *in vacuo* to 520 K (B), after heating *in vacuo* to 650 K (C), and after annealing in pure oxygen at 700 K (D). The spectra were recorded at room temperature *in vacuo*, and both the S-shaped background and the $K_{\alpha 3,4}$ satellite contributions have been subtracted out (Frank *et al*., 1991).

V. X-RAY ABSORPTION EDGES

A. X-ray Absorption

An energetic photon is capable of removing electrons from all occupied atomic energy levels with ionization energies less than the photon energy. When the photon energy drops below the highest ionization energy, which corresponds to the K-level, the $n = 1$ electron can no longer be removed and the x-ray absorption coefficient abruptly drops. It does not, however, drop to zero, because the x-ray photon is still energetic enough to knock out electrons in the $L(n = 2)$, $M(n = 3)$, etc., levels, as is clear from Fig. 17.25. The abrupt drop in the absorption coefficient is referred

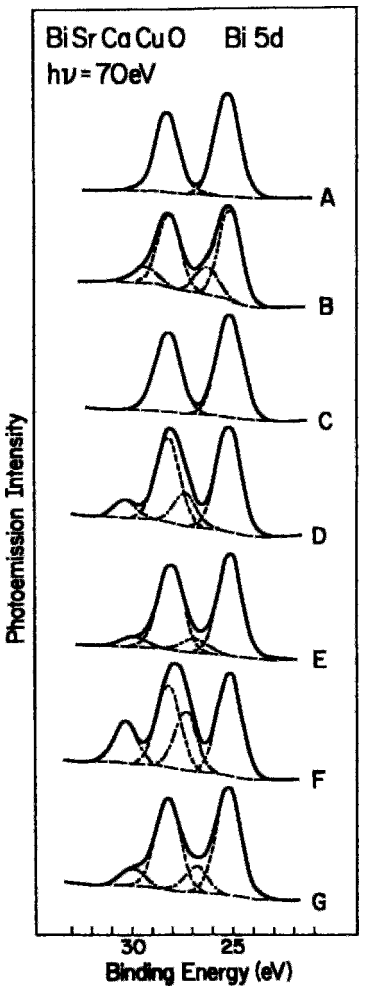

Figure 17.34 Core-level photoemission energy distribution curves for Bi $5d_{3/2}$ and $5d_{5/2}$ lines in $Bi_2Sr_{2-x}Ca_{1+x}Cu_2O_{8+\delta}$. Spectra were obtained from seven $\approx 20\,\mu$m diameter regions located at different places on an electron micrograph of the surface (not shown). Regions A and C, which are representative of the clean surface, exhibit a single Bi doublet. Regions B and D–G, which are situated near the border between the monocrystal stacks, show a second-position dependent component suggestive of highly oxidized Bi (Komeda *et al.*, 1991).

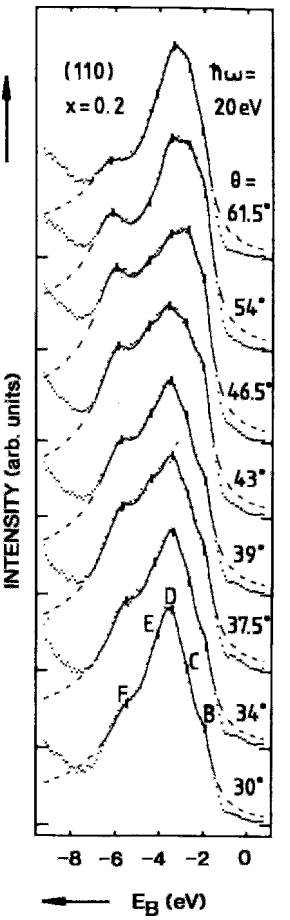

Figure 17.35 Angle-resolved photoemission spectra (ARPES) of $(Bi_{0.8}Pb_{0.2})_2Sr_2CaCu_2O_8$ single crystals for emission angles between 30° and 61.5°. Calculated curves fit to the spectra are shown as solid lines inside the fit range and as dashed lines outside. Calculated peak positions are shown as tick marks labeled B, C, D, E, and F (Böttner *et al.*, 1990).

to as an absorption edge; in this case, it is a K-absorption edge.

A photon with energy slightly below the ionization energy can raise the $n = 1$ electron to a higher unoccupied level, such as a $3d$ or $4p$ level. Transitions of this type provide what is called fine structure on the absorption edge, furnishing information on the bonding states of the atom in question. The resolution of individual fine-structure transitions can be improved with the use of polarized x-ray beams (Abbate *et al.*, 1990). Among the specialized x-ray absorption spectroscopy (XAS)

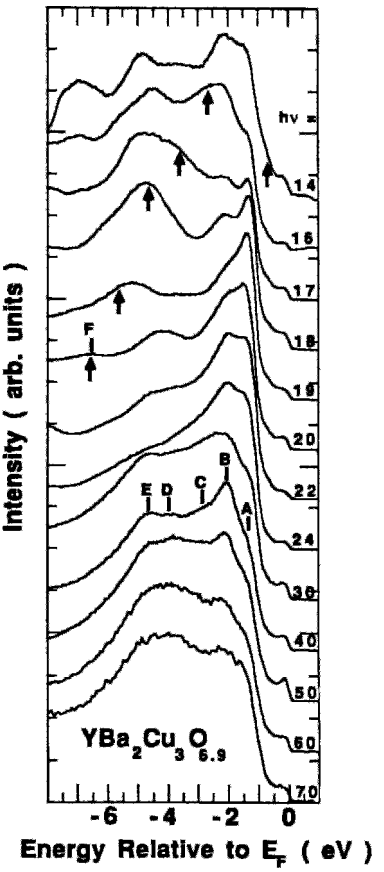

Figure 17.36 Valence-band photoemission spectra of $YBa_2Cu_3O_{6.9}$ for a series of incident photon energies from 14 to 70 eV, normalized to equal maximum intensities. The symbols A, B, C, D, E, and F indicate identifiable peaks. Peak F, which shifts with *hv* to apparent higher binding energies, is labeled by arrows. The O 2*p* intensity is strongly concentrated in peaks A and B, while the Cu 3*d* intensity is partly centered on peak D, and partly distributed throughout the valence bands (Arko *et al*., 1989).

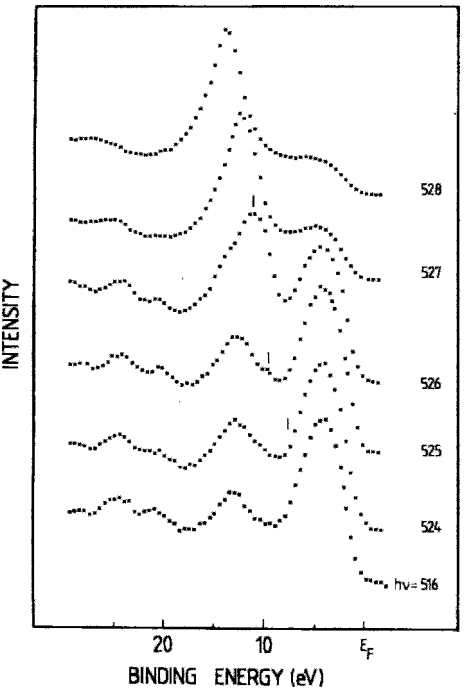

Figure 17.37 Valence-band photoemission spectra of $YBa_2(Cu_{0.9}Fe_{0.1})_3O_{6.9}$. The oxygen Auger line is indicated by a vertical tick on three of the spectra (Sarma *et al*., 1989).

techniques that have been used we may note x-ray absorption near-edge structure (XANES), x-ray absorption fine-structure (XAFS), and extended x-ray absorption fine-structure (EXAFS) spectroscopy.

Figure 17.38 shows the O 1*s* x-ray absorption edges obtained with twin-free monocrystals of

$YBa_2Cu_3O_7$ and $YBa_2Cu_4O_8$

for the case of polarization parallel to the *a* and *b* directions (Krol *et al*., 1992). The difference spectrum is also shown. The XAS spectrum for E||*a* is due to the O(2) atoms in the CuO_2 planes, while that for E||*b* arises from the O(3) atoms in the planes and the O(1) atoms in the chains. For $YBa_2Cu_3O_7$, the O(1) and apex oxygen O(4) binding energies determined from the absorption edge were found to be 0.4 and 0.7 eV, respectively, both of which is lower than the binding energies of the oxygens O(2,3).

Figure 17.39 shows how varying the angle between the incident beam and the *c*-axis of $YBa_2Cu_3O_{6.9}$ monocrystals resolves oxygen–hole structure into a small, lower-energy peak (A) at 526.4 eV attributed

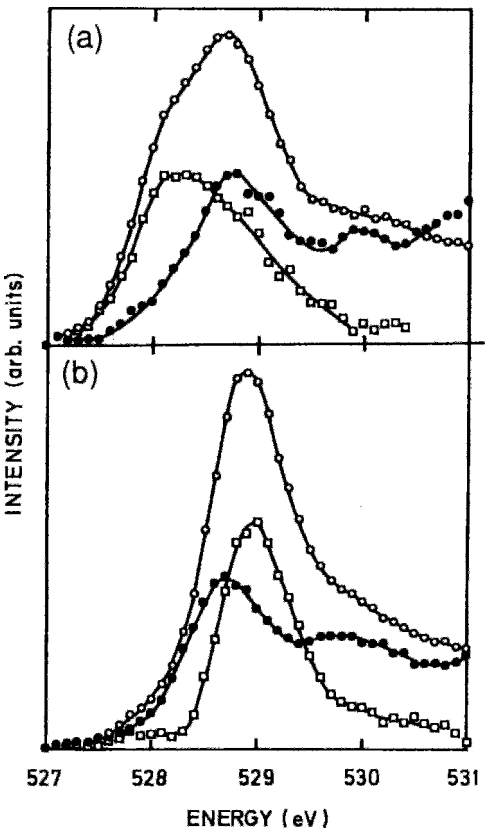

Figure 17.38 X-ray absorption spectrum of the O 1*s* line of (a) $YBa_2Cu_3O_7$, and (b) $YBa_2Cu_4O_8$ for E$\|a$(•), E$\|b$(•), and difference spectrum E$\|b-$Ea(•) (Krol *et al.*, 1992).

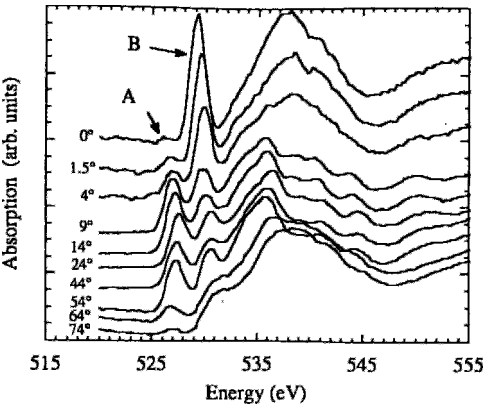

Figure 17.39 Energy dependence of the x-ray absorption of $YBa_2Cu_3O_{6.9}$ by O 1*s* electrons for a series of angles between the electric field and the *c*-axis. Peak A arises from the oxygens O(2) and O(3) in the CuO_2 planes, while peak B is from O(4) along the chains (Alp *et al.*, 1989b).

to holes on O(2) and O(3) in the CuO_2 planes and a more prominent (B) peak at 529.2 eV assigned to holes on O(4) along the chains (Alp *et al.*, 1989b).

The XANES spectra presented in Fig. 17.40 show the effect of doping the hole superconductor LaSrCuO and the electron superconductor NdCeCuO by comparing the absorption with that of the respective undoped compounds. The results indicate that substitution has less effect on the Cu bonding in La_2CuO_4 than in Nd_2CuO_4, and suggest that electron doping occurs mainly at the Cu atom of CuO_2 in the Nd compound, mainly at the O atom in the La compound.

Substitution of first-transition ions for Cu in $YBa_2Cu_3O_{7-\delta}$ produces the changes in the *K*-absorption edge that are shown in Fig. 17.41. These changes provide evidence that Fe and Co substitute for Cu(1) in the linear chain site, Zn occupies only the in-plane position at Cu(2) and Ni resides in both.

Superconductors have also been studied by related x-ray techniques, such as Rutherford backscattering (Sharma *et al.*, 1991).

B. Electron-Energy Loss

Another technique for obtaining absorption edges, called electron-energy loss spectroscopy (EELS), involves irradiating a thin film with a beam of monoenergetic electrons with energies of, for example, 170 keV. As the electrons pass through the film, they exchange momentum with the lattice and lose energy by exciting or ionizing the atoms. An electron-energy analyzer is then used to determine the energy E_{abs} that is absorbed. This energy corresponds to a transition of the type shown in the energy level diagram of Fig. 17.25, and equals the difference between

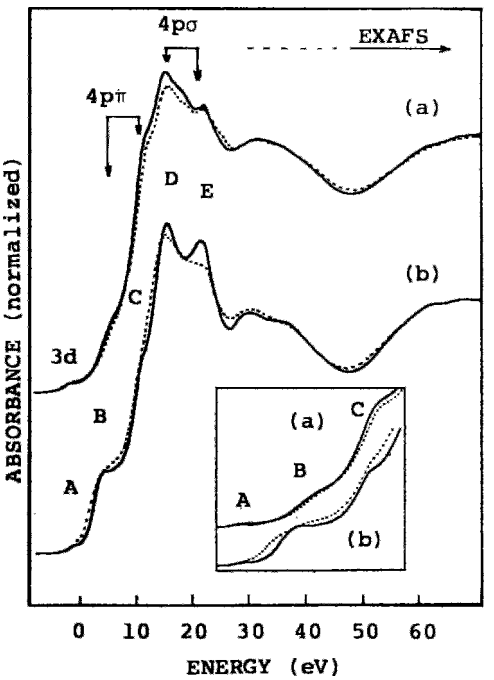

Figure 17.40 X-ray absorption CuK near-edge spectra (XANES) for (a) La_2CuO_4 (solid line) and $(La_{0.925}Sr_{0.075})_2CuO_4$ (dashed line), and (b) Nd_2CuO_4 (solid line) and $(Nd_{0.925}Ce_{0.075})_2CuO_4$ (dashed line). The inset presents the 1s 3d and 1s 4$p\pi$ regions on a magnified scale. The excitation energy was measured relative to the first inflection point of the Cu foil K-edge (Kosugi *et al*., 1990).

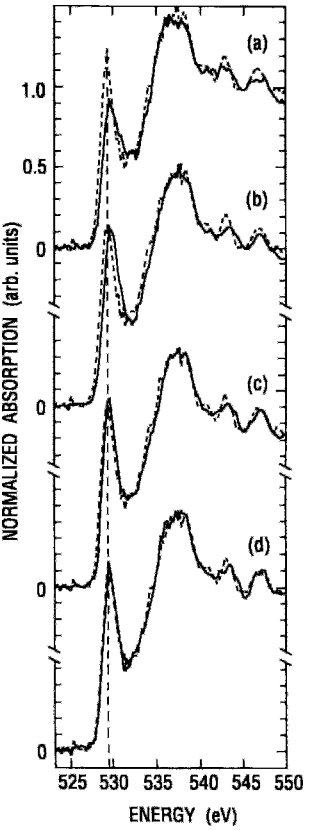

Figure 17.41 Comparison of the x-ray absorption oxygen K near-edge absorption spectra of $YBa_2(Cu_{0.96}M_{0.04})_3O_{7-\delta}$ for the metal substitutions M given by (a) Fe, (b) Co, (c) Ni, and (d) Zn. The 4%-doped (solid curves) and undoped (dashed curves) spectra are compared for each case (C. Y. Yang *et al*., 1990).

the kinetic energy KE_0 of the incident electrons and the kinetic energy KE_{sc} of the scattered electrons

$$E_{abs} = KE_0 - KE_{sc}. \qquad (17.22)$$

In a plot of the intensity of the scattered electrons as a function of the absorbed energy, peaks will be found at the binding energies of the various electrons in the sample.

An analogue of optical and x-ray polarization experiments can be obtained from EELS by varying the direction of the momentum transfer **q** between the incoming electron and the lattice relative to the c-axis of the crystal. The vector **q** plays the role of the electric polarization vector **E** in photon spectroscopy.

VI. INELASTIC NEUTRON SCATTERING

A neutron is a particle with almost the same mass as a proton, but, unlike the proton, it is electrically neutral. Despite this lack of charge, it has a magnetic moment, which enables it to interact with local magnetic moments as it passes through matter. When it scatters elastically, it has the same kinetic energy after the scattering event as it had beforehand. In nonmagnetic materials, neutrons scatter elastically off atomic nuclei; coherent scattering

experiments, called neutron diffraction, are similar to their x-ray diffraction counterparts, likewise helping to determine crystal structures. Neutrons interact strongly with the magnetic moments of any transition ions that are present, and the resulting diffraction pattern provides the spin directions, as illustrated in Fig. 5.23, for antiferromagnetic alignment.

When neutrons scatter inelastically in matter, their kinetic energy changes through the creation (+) or absorption (−) of a phonon with energy $\hbar\omega_{\text{ph}}$,

$$\frac{1}{2}mv^2 = \frac{1}{2}mv'^2 \pm \hbar\omega_{\text{ph}}, \qquad (17.23)$$

so that energy is exchanged with the lattice vibrations. A measurement of the angular distribution of neutrons scattered at various energies provides detailed information about the phonon spectrum, such as the dispersion curves and the phonon density of states $D_{\text{ph}}(\omega)$. The latter determines the dimensionless electron–phonon coupling constant λ through the Eliashberg relation (7.96),

$$\lambda = 2\int \frac{\alpha^2(\omega)D_{\text{ph}}(\omega)d\omega}{\omega}, \qquad (17.24)$$

where $\alpha(\omega)$ is the electron–phonon coupling strength; $\alpha^2(\omega)\mathrm{D}_{\text{ph}}(\omega)$ is called the Eliashberg function. Inelastic scattering has also resolved spin waves in La_2CuO_4 (Aeppli *et al.*, 1989). Thus inelastic neutron scattering measurements can provide us with important information about superconductors. We will give some representative results obtained using this experimental tool. Figure 17.42 presents the dispersion curves, determined by inelastic neutron scattering, of the low-lying phonon branches for the superconductor

$$(La_{1-x}Sr_x)_2CuO_4.$$

Phonon dispersion curves were determined over a much broader energy range for the isomorphous nonsuperconducting compound La_2NiO_4. A soft mode (cf. Section II.C) exists in La_2NiO_4 at the point X (point $(\frac{1}{2}, 0, \frac{1}{2})$) in the Brillouin zone sketched in Fig. 10.22. Figure 17.43 shows that this soft mode decreases in frequency by 15% when the temperature is reduced from 300 K to 12 K. Phase transitions in crystals often involve soft modes, as was mentioned in Section II.C.

The experimental phonon density of states $D_{\text{exp}}(\omega)$ corresponding to the phonon dispersion curves of Li_2NiO_4 is plotted in Fig. 17.44. The calculated values, also shown in the figure, are in moderate agreement with experiment. The corrected density of states $D_{\text{ph}}(\omega)$ is obtained from the experimental DOS by weighting the vibrations of the ith atom with the ratio σ_i/M_i, where σ_i is the neutron-scattering cross section and M_i is the mass of the ith atom. The result is plotted in Fig. 17.45.

The phonon DOS for the cubic superconductor $Ba_{0.6}K_{0.4}BiO_3$, is presented in Fig. 17.46 together with its counterpart, which was calculated by molecular dynamics simulation (Loong *et al.*, 1989, 1991, 1992). The random nature of the substitution of K on the Ba sites of this compound causes the experimental spectrum to be broader and less well resolved than the calculated spectrum. The partial DOS calculated for the atoms Ba, Bi, and K, shown in Fig. 17.47, are responsible for the peaks seen in the total DOS at around 11 and 15 meV, while the more spread-out region beyond 20 meV arises from the oxygen atoms. The phonon density of states reported here is analogous to the more familiar electron density of states discussed at length in Chapter 10.

We see from these figures that the replacement of ^{16}O by ^{18}O shifts the phonon DOS frequencies to lower values. This shift gives an isotope effect exponent of $\alpha = 0.42$, which is close to the two values of $\alpha = 0.35$ and $\alpha = 0.41$ obtained from the variation of T_c (Hinks *et al.*, 1988b).

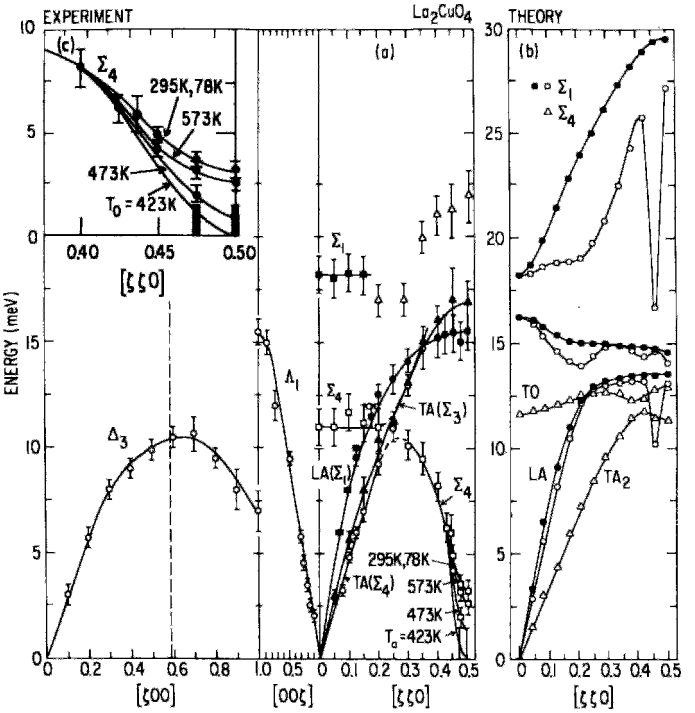

Figure 17.42 Low-lying phonon branches in $(La_{1-x}Sr_x)\ CuO_4$ with the models labeled according to Weber (1987), showing (a) experimental results, (b) calculated dispersion curves, and (c) inset, measured temperature dependence near the X point. The dispersion curves are only weakly temperature dependent, except for the TO phonon near the X point shown in inset (c). The filled symbols show unrenormalized bare phonons, and the open circles indicate Σ_1 symmetry phonons renormalized by interactions with conduction electrons (Böni *et al.*, 1988).

Phonons $\hbar\omega$ are also capable of probing the phonon spectrum by inelastic scattering. This is monitored by measuring the frequency shifts,

$$\hbar\omega = \hbar\omega' \pm \hbar\omega_{\text{ph}}, \tag{17.25}$$

and scattering angles. When the emitted or absorbed phonon $\hbar\omega_{\text{ph}}$ is acoustic, the process is called *Brillouin scattering*, and when it is optical, it is referred to as *Raman scattering*.

VII. POSITRON ANNIHILATION

In positron annihilation spectroscopy (PAS), a sample is irradiated by a radioactive source, such as ^{22}NaCl, which emits high-energy (545-keV) electrons with positive charges e^+, called *positrons* (Benedek and Schüttler, 1990, Chakraborty, 1991). When the positron enters the solid, it rapidly loses most of its kinetic energy and approaches thermal energy, $\approx \frac{3}{2}k_B T \approx 0.04\,\text{eV}$, in 0.001 to 0.01 ns. Following thermalization, the positron diffuses like a free particle, although its motion is correlated with nearby conduction electrons, until it encounters an electron e^- and annihilates in about 0.1 ns, producing two 0.51-MeV gamma (γ) rays in the process

$$e^+ + e^- \rightarrow \gamma + \gamma. \tag{17.26}$$

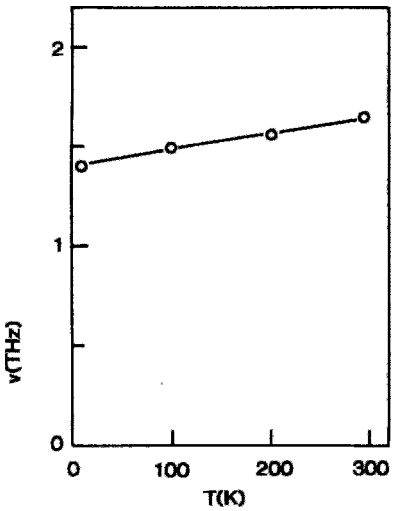

Figure 17.43 Temperature dependence of the frequency of the soft mode of La_2NiO_4 at $q = (\frac{1}{2}, 0, \frac{1}{2})$ (Pintschovius *et al.*, 1989).

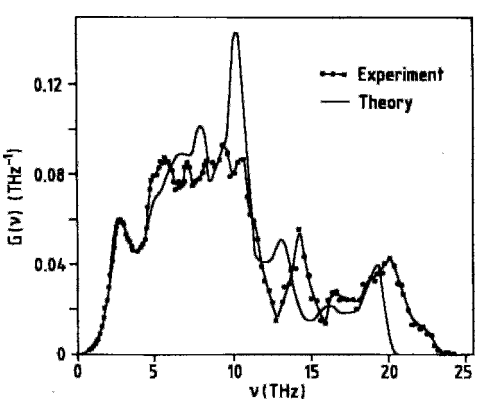

Figure 17.44 Comparison of the phonon density of states experimentally determined by inelastic neutron scattering (····) and calculated (——) (Pintschovius *et al.*, 1989).

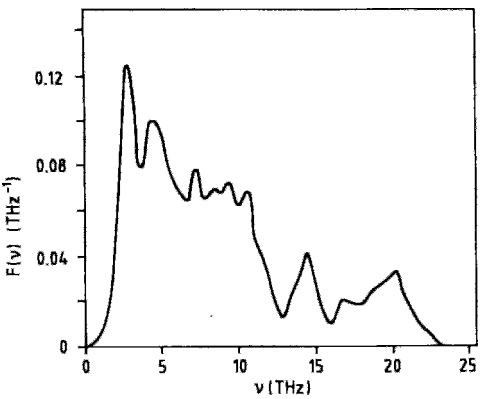

Figure 17.45 Corrected phonon density of states of La_2NiO_4 obtained by applying corrections to the experimentally determined curve of Fig. 17.44 (Pintschovius *et al.*, 1989).

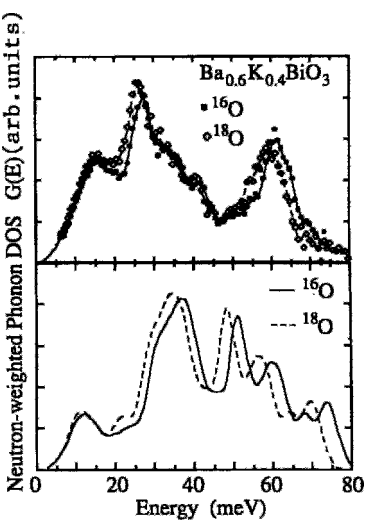

Figure 17.46 Comparison of the phonon density of states of $Ba_{0.6}K_{0.4}BiO_3$ (a) determined experimentally by inelastic neutron scattering, and (b) calculated by molecular dynamics simulations (Loong *et al.*, 1991, 1992).

The electron has much more momentum than the positron, and momentum balance causes the two gamma rays, to make a slight angle with respect to each other as they depart in opposite directions. The Angular Correlation of this Annihilation Radiation (ACAR) is one of the important parameters which is measured in this technique. The positron lifetime, τ, is determined by the time delay between the 1.28-MeV gamma ray emitted by the radioactive ^{22}Na simultaneously with the positron, and the pair of 0.51-MeV gamma

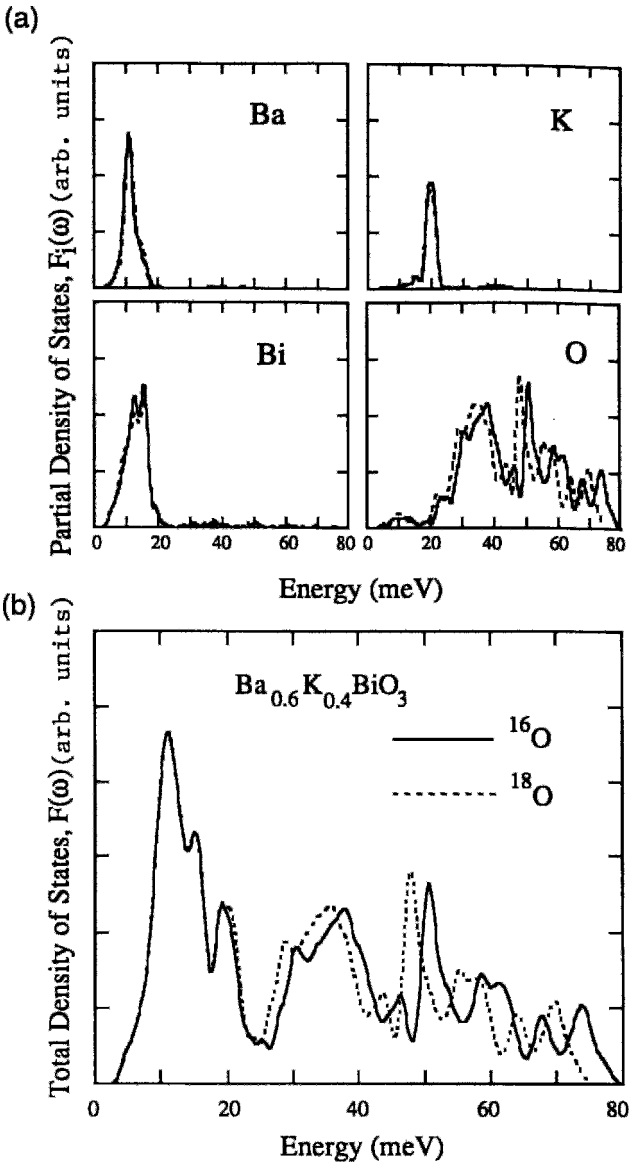

Figure 17.47 $Ba_{0.6}K_{0.4}BiO_3$ partial phonon density of states calculated for the atoms Ba, K, Bi, and O (upper panels), and the total density of states (lower panel). Isotopic substitution of ^{18}O for ^{16}O shifts the oxygen partial DOS and the total DOS in the oxygen region, but does not affect the Ba, K, or Bi partial DOS curves (Loong *et al.*, 1991, 1992).

rays produced by the annihilation event. The emitted gamma rays have a spread in energy due to Doppler broadening. The positrons can become trapped in vacancies before annihilation, with oxygen vacancies the likely trapping sites in high-temperature superconductors. A positron is sensitive to the details of the local electronic environment, which

are reflected in its mean lifetime τ, its angular correlation, and its Doppler broadening parameters S and W. In $YBa_2Cu_3O_{7-\delta}$ there is a life-time $\tau_1 \approx 0.2$ ns due to a shoft-lived component, perhaps from annihilation in the grains, and a lifetime $\tau_2 \approx 0.7$ ns of a long-lived component, perhaps from annihilation at grain surfaces. These parameters exhibit discontinuities at the transition temperature (Barbiellini *et al.*, 1991; Huang *et al.*, 1988; McMullen, 1990; Tang *et al.*, 1990; Wang *et al.*, 1988). Figure 17.48 shows four of these discontinuities for the superconductor $YBaCu_3O_{7-\delta}$ with a midpoint $T_c = 85.7$ K. One theoretical study has suggested that BCS pairing could be responsible for the measured shifts in positron properties near T_c (Benedek and Schüttler, 1990).

The positron annihilation characteristics are determined by the overlap of the positron and electron densities (Bharathi *et al.*, 1990; Sundar *et al.*, 1990b). Figure 17.49 shows the positron densities in the [020] vertical plane of the three $Tl_2Ba_2Ca_nCu_{n+1}O_{2n+6}$ superconductors 2201, 2212, and 2223. In the 2201 compound, the positron density is quite generally spread out, while in the other two compounds it is concentrated within the sets of copper-oxide layers, especially between the layers where the calcium atoms are located. The lack of concentration in the CuO_2 layers in the former case is consistent with the electron density plot for the 2201 Tl

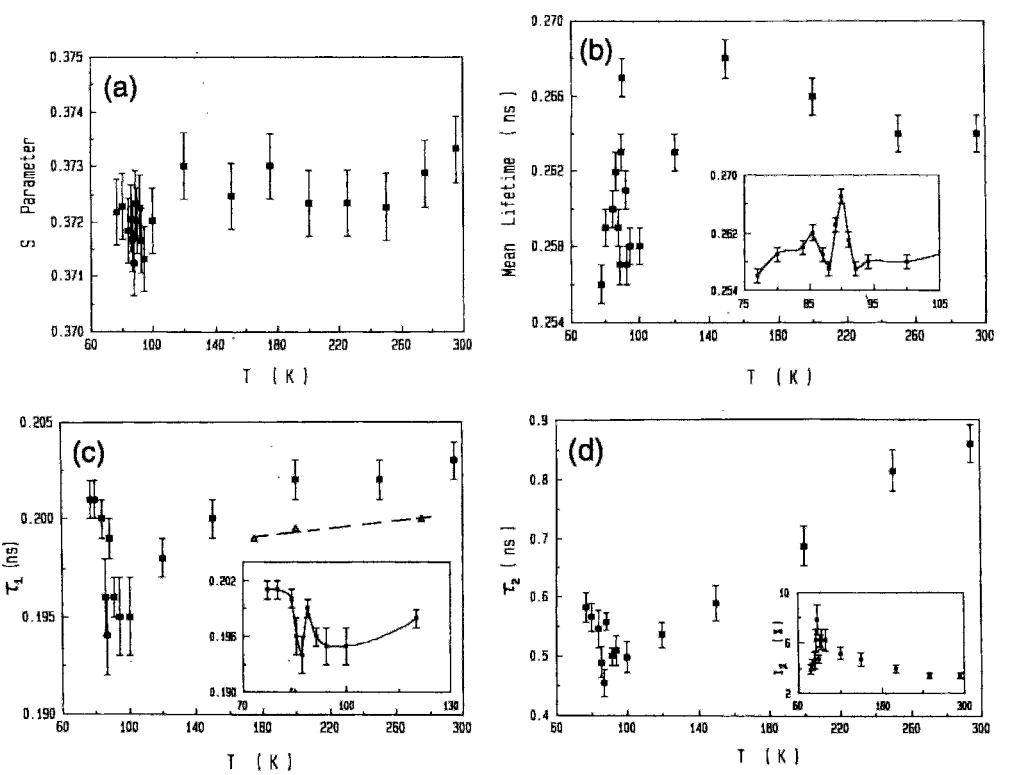

Figure 17.48 Temperature dependence of positron annihilation results obtained with a $YBa_2Cu_3O_{7-\delta}$ sample showing (a) Doppler broadening line shape parameter S, (b) mean lifetime τ, (c) lifetime τ_1 of short-lived component, and (d) lifetime τ_2 of long-lived component. The insets of (b) and (c) show data on an expanded scale. The inset of (d) shows the temperature dependence of the relative intensity of the long-lived component. The dashed curve of (c) represents "delayed" data taken 40 hours later. The curves are drawn as visual aids (Wang *et al.*, 1988).

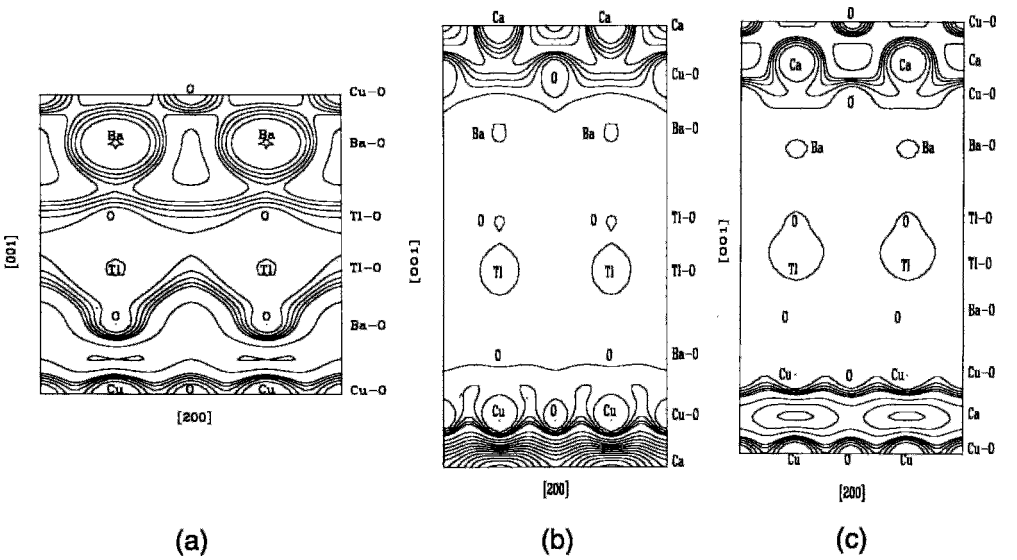

Figure 17.49 Contour plots of the positron density distribution in the [020] vertical plane of (a) $Tl_2Ba_2CuO_6$, (b) $Tl_2Ba_2CaCu_2O_8$ and (c) $Tl_2Ba_2Ca_2Cu_3O_{10}$ crystals. See Fig. 8.31 for corresponding charge density plots of $Tl_2Ba_2CuO_6$ (Sundar *et al.*, 1990b).

compound that is presented in Fig. 8.31. In contrast to the situation in the hole-type thallium superconductors, the positron density is found to be fairly generally distributed throughout the unit cell of the electron superconductor $(Nd_{0.925}Ce_{0.075})_2CuO_{3.98}$ (Sundar *et al.*, 1990a).

The upper half of each positron density plot of Fig. 17.49 shows the Ba of the Ba–O and the O of Tl–O; the lower halves show the Tl of the Tl–O and the O of Ba–O. A comparison with the unit cells of Figs. 8.29 and 8.30 shows that this is in accord with the atom positions.

A two-dimensional angular correlation technique, called 2D-ACAR, is designed to sample the anisotropy of the conduction electron motion, thus providing information on the topology of the Fermi surface (Barbiellini *et al.*, 1991; Rozing *et al.*, 1991). For example, Bansil *et al.*, (1991) published plots of Fermi surface sheets of $YBa_2Cu_3O_7$ similar to some of those presented in Fig. 10.15 and Tanigawa *et al.* (1988) provided three-dimensional sketches of the first Brillouin zone of $La_2CuO_{4-\delta}$, a zone that exhibits electron regions at the point Γ similar to the regions in the upper part of Fig. 10.25 2D-ACAR studies have been reported for single crystals of $YBa_2Cu_3O_{6.9}$ (Smedskjaer *et al.*, 1992).

VIII. MAGNETIC RESONANCE

Another branch of spectroscopy that has provided valuable information on superconductors is magnetic resonance, the study of microwave and radio frequency transitions. We will comment on several types of magnetic resonance, including nuclear magnetic resonance (NMR), nuclear quadrupole resonance (NQR), electronspin resonance (ESR or EPR), microwave absorption, muon spin resonance (μSR), and Mössbauer resonance, all of which have been used to study superconductors, and we will discuss some of the results that have been obtained.

Magnetic resonance measurements are made in fairly strong magnetic fields, typ-

ically $\approx 0.33\,\mathrm{T}$ for ESR and $\approx 10\,\mathrm{T}$ for NMR, which are considerably above the lower-critical field B_{c1} of a high-temperature superconductor. At these fields most of the external magnetic flux penetrates into the sample, so that the average value of B inside is not very different from the value of B outside.

A. Nuclear Magnetic Resonance

Nuclear magnetic resonance involves the interaction of a nucleus possessing a nonzero nuclear spin I with an applied magnetic field B_{app}, giving the energy level splitting into $2I+1$ lines with energies

$$E_m = \hbar\gamma B_{app} m, \tag{17.27}$$

where γ is the gyromagnetic ratio, sometimes called the magnetogyric ratio, characteristic of the nucleus and m assumes integer or half-integer values in the range $-I < m < I$, depending on whether I is an integer or a half-integer (Poole and Farach, 1987). Figure 17.50 shows the energy levels and the NMR transition for the case $I = \frac{1}{2}$, $m = \pm\frac{1}{2}$. Typical NMR frequencies range from about 60 to 400 MHz. Several nuclei common to superconductors are listed in Table 17.4 together with their spins, natural abundances and other characteristics. The isotopes of Tl and Y are particularly favorable for NMR because they have nuclear spin $I = 1/2$, so that they lack a quadrupole moment and their lines are not broadened by noncubic crystalline electric fields. The dominant isotope of oxygen, ^{16}O, which is 99.76% abundant, has $I = 0$, so that it does not exhibit NMR. Zero-spin nuclei are not listed in the table.

The importance of NMR arises from the fact that the value of γ is sensitive to the local chemical environment of the nucleus. It is customary to report the chemical shift δ,

$$\delta = \frac{\gamma - \gamma_R}{\gamma_R}, \tag{17.28}$$

which is the extent to which γ deviates from γ_R, the value of a reference sample, where, for proton reference samples, $\gamma_R/2\pi$ is close to 42.576 MHz/T. Chemical shifts are small, and are usually reported in parts per million (ppm). In addition, spin–spin interactions with neighboring nuclei can split the line into a multiplet, providing further information on the coordination to surrounding atoms.

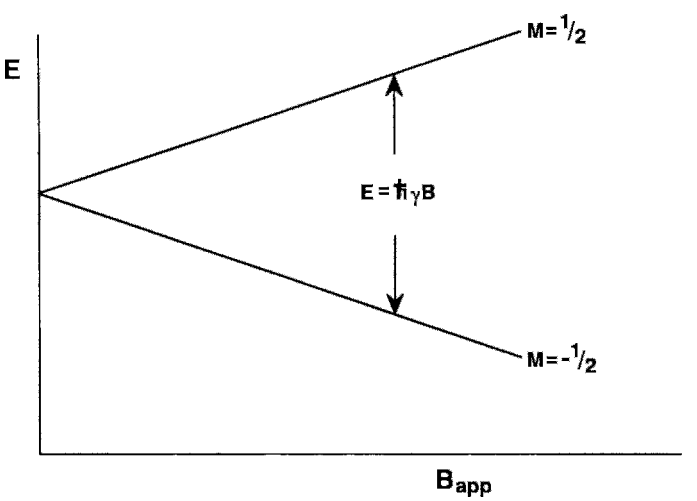

Figure 17.50 Zeeman splitting of a spin-$\frac{1}{2}$ energy state in a magnetic field.

Table 17.4 NMR Data on Nuclei Commonly Found in High-temperature Superconductors[a]

Z	A	Elem	*I*	%Abund	Mag Mon[b]	MHz/T[c]	Sensit/B[d]	Sensit/f[e]	*eqQ*[f]
1	1	H	1/2	99.985	2.79268	42.5759	1.000	1.000	0
1	2	D	1	0.015	0.85739	6.5357	0.00965	0.409	0.0029
6	13	C	1/2	1.108	1.216	10.705	0.016	2.51	0
8	17	O	5/2	0.037	−1.8930	−5.7719	0.0291	1.58	−0.26
19	39	K	3/2	93.08	0.39094	1.987	0.0005	0.233	0.049
20	43	Ca	7/2	0.145	−1.3153	−2.8646	0.0640	1.41	−0.065
29	63	Cu	3/2	69.09	2.2206	11.285	0.0931	1.33	−0.209
29	65	Cu	3/2	30.91	2.3790	12.090	1.14	1.42	−0.195
38	87	Sr	9/2	7.02	−1.0893	1.845	0.00269	1.43	0.15
39	89	Y	1/2	100.0	−0.13682	2.086	0.000118	0.0005	0
41	93	Nb	9/2	100.0	6.1435	10.407	0.482	8.07	−0.36
56	135	Ba	3/2	6.59	0.83229	4.230	0.0049	0.497	0.18
56	137	Ba	3/2	11.32	0.93107	4.732	0.00686	0.556	0.28
57	139	La	7/2	99.911	2.7615	6.014	0.0592	2.97	0.22
60	143	Nd	7/2	12.20	−1.25	2.72	0.00549	1.34	−0.48
60	145	Nd	7/2	8.30	−0.78	1.7	0.00133	0.838	−0.25
80	199	Hg	1/2	16.9	0.498	7.60	0.0057	0.178	0
81	203	Tl	1/2	29.5	1.5960	24.332	0.187	0.571	0
81	205	Tl	1/2	70.5	1.6115	24.570	0.192	0.577	0
82	207	Pb	1/2	22.1	0.5837	8.899	0.00913	0.209	0
83	209	Bi	9/2	100.0	4.0389	6.842	0.137	5.30	−0.46

[a] The nucleus ^{16}O (99.8%) has no nuclear spin ($I = 0$) and thus cannot be observed. Data from Harris (1981); see also Emsley, Feeney, and Sutcliffe (1965), and Poole and Farach (1994).
[b] Magnetic moment in units of nuclear magneton.
[c] Resonant frequency for a field of 1 T in units of MHz.
[d] Relative sensitivity at constant field.
[e] Relative sensitivity of constant frequency.
[f] Quadrupole moment eqQ in units of $10^{-24}\,cm^2$. Data from Landolt–Börnstein, New Series III/20a, 1988.

Relaxation-time measurements determine the efficiency of spin-energy transfer to the lattice (Poole and Farach, 1971).

Pulsed NMR of ^{89}Y nuclei has been observed in $YBa_2Cu_3O_{7-\delta}$ at 12.2 MHz and 5.9 T in the temperature range from 59 to 295 K (Mali *et al.*, 1987; Markert *et al.*, 1987). The value of $T_c = 86$ K at 5.9 T was determined by the onset of line broadening from a width of 0.31 mT above T_c to 0.71 mT ten degrees below T_c. This broadening arises from the spatial variation in the internal field, as sketched at the top of Fig. 12.10, which causes each ^{89}Y nucleus to experience a slightly different local field. The fraction of ^{89}Y detected decreased from 100% above T_c to about 80% at 59 K due to incomplete rf penetration in the mixed state. The spin-lattice relaxation time T_1 increased below T_c. Preparation conditions influence the Y site, since different ^{89}Y chemical shifts have been observed under different conditions (slowly cooled, rapidly cooled, or water-exposed $YBa_2Cu_3O_{7-\delta}$).

Most NMR studies are carried out with the isotope ^{63}Cu (nuclear spin $I = 3/2$) since it is 69% abundant. Figure 17.51 presents the ^{63}Cu NMR spectra obtained at 100 K for the applied field parallel to c and in the a, b-plane. The resonances attributed to the four-coordinated chain Cu(1) sites and to the five-coordinated plane Cu(2) sites are indicated. Nuclei in metals have their frequency ν_m shifted in position relative to its value ν_i in a diamagnetic insu-

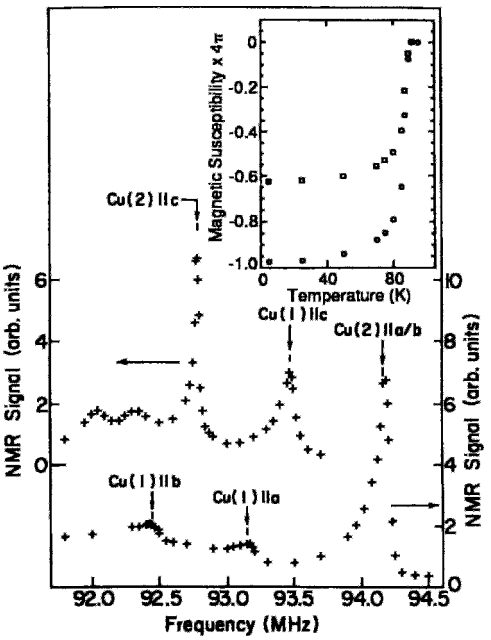

Figure 17.51 NMR spectrum of ^{63}Cu in $YBa_2Cu_3O_{7-\delta}$ at 100 K with the applied magnetic field parallel to the c-axis (above) and with the applied field in the a, b-plane (below). The resonances attributed to Cu(1) in the chains and to Cu(2) in the planes are indicated. The inset shows the magnetization for zero field cooling (open circles) and field cooling in 1.6 mT (open squares), with the sharp superconducting transition evident (Barrett *et al.*, 1990).

lator by their nuclear spin interaction with the spin paramagnetism of the conduction electrons and the relative frequency shift $K = (\nu_m - \nu_i)/\nu_i$ is called the Knight shift (Lane, 1962; Pennington and Slichter, 1990). When normal conduction electrons convert to super electrons as the temperature is lowered in the range below T_c the Knight shift K is expected to decrease. Figure 17.52 shows this decrease for Cu(1) and Cu(2) nuclei in the temperature range from 0 to 120 K. These shifts were found to obey BCS expressions for a strong coupling-spin singlet state (Barrett *et al.*, 1990). NMR of ^{63}Cu provided the energy-gap ratio $E_g/k_BT_C = 1.3$ in

$$(La_{0.915}Sr_{0.085})_2CuO_{4-\delta}$$

(Lee *et al.*, 1987).

Several high-temperature superconductors enriched with the rare isotope ^{17}O, which has nuclear spin $I = 5/2$, have been studied by NMR. The broad-scan room-temperature spectrum of $YBa_2Cu_3O_{7-\delta}$ presented in Fig. 17.53 exhibits 20 lines from the various oxygens and these are identified in the caption. The use of aligned grains considerably increased the resolution of this spectrum, indicating a considerable amount of anisotropy. The narrower scans of Fig. 17.54 show that the compounds

$$(La_{0.925}Sr_{0.075})_2CuO_4,$$

$$Bi_2Sr_2CaCu_2O_{8+\delta},$$

and $Tl_2Ba_2CaCu_2O_{8+\delta}$, all of which have similar structures (cf. Chapter 8), exhibit similar spectra. These spectra differ from those of the compounds $(Ba_{0.6}K_{0.4})BiO_3$ and $YBa_2Cu_3O_{7-\delta}$, which have different structures. This result is to be expected, since NMR probes the local environment of the nucleus.

NMR spectroscopy has been instrumental in confirming the structures of the fullerenes, such as C_{60} and C_{70}. The room-temperature ^{13}C NMR spectrum of C_{60}, shown at the top of Fig. 17.55, is a single narrow line with a chemical shift of 143 ppm relative to the standard compound tetramethylsilane (TMS), confirming the equivalence of all of the carbons as well as demonstrating that the molecule is rapidly and isotropically reorientating. We see from the figure that when the molecule is cooled, the NMR line broadens. At 77 K its spectrum is a typical asymmetric chemical shift pattern with the principal values 220, 186, and 25 ppm, which are typical of aromatic hydrocarbons. This suggests that the molecules are now stationary and randomly oriented in the solid. The chemical shift tensor is expected to have one principal value in the direction perpendicular to the approximate plane of the sp^2 hybrid CC_3 group. Within this plane the three C–C bonds are not equivalent, since two of them connect a five-membered

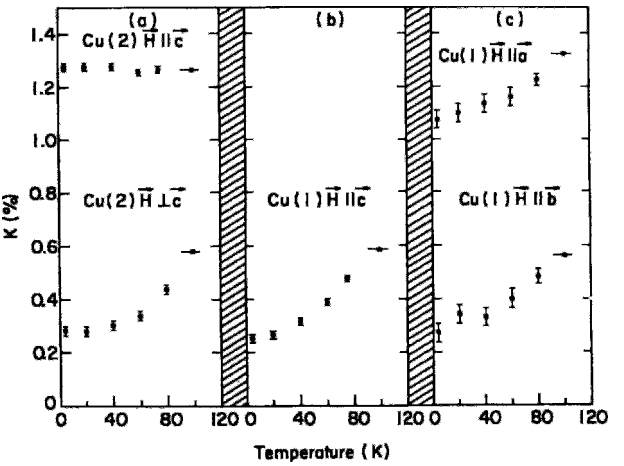

Figure 17.52 Temperature dependence below T_c of the five NMR signals of Fig. 17.51 arising from ^{63}Cu in the planes and chains with the applied field along the *a*-, *b*-, and *c*-axes, as indicated (Barrett *et al*., 1990).

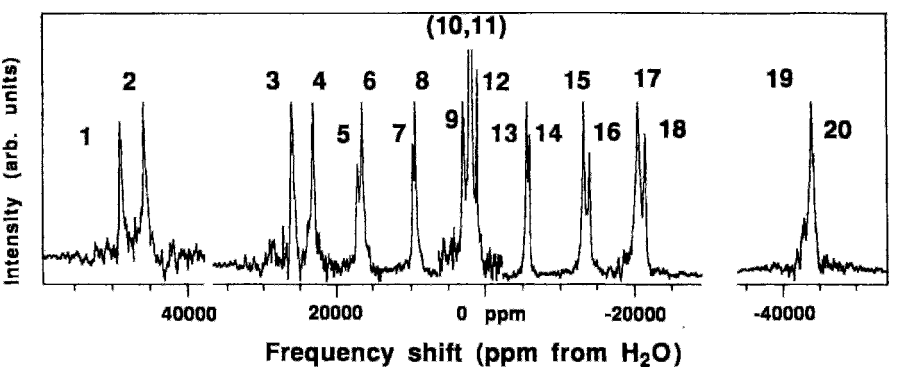

Figure 17.53 Room-temperature ^{17}O NMR spectra at 48.8 MHz (8.45 T) of $YBa_2Cu_3O_{7-\delta}$ magnetically aligned in a field parallel to the *c*-axis. The measured relative intensities for central and satellite transitions have the expected 9 : 8 : 5 ratio, but here the peak intensities have been equalized for clarity. All but one of the 20 expected transitions, five lines from each of the four oxygens, are shown: peaks 2, 4, 12, 18, and 19 from O(1), peaks 5–8, (10, 11), 13–16 from O(2, 3), and peaks 1, 3, 9, 17, and 20 from O(4) (Oldfield *et al*., 1989).

and a six-membered ring, whereas the third connects two six-membered rings, thereby explaining the lack of axial symmetry in the chemical-shift powder pattern.

The fullerene C_{70} has the five inequivalent carbons labeled a, b, c, d, and e on the left side of Fig. 17.56, giving rise to five lines in the ^{13}C NMR spectrum displayed at the top of Fig. 17.56. These lines have the respective intensity ratios 10 : 10 : 20 : 20 : 10, corresponding to the numbers of their respective carbon atoms in the C_{70} molecule. The two-dimensional spectrum given in the figure provides the measured spin–spin coupling constants between the carbons. The C–C bond lengths of

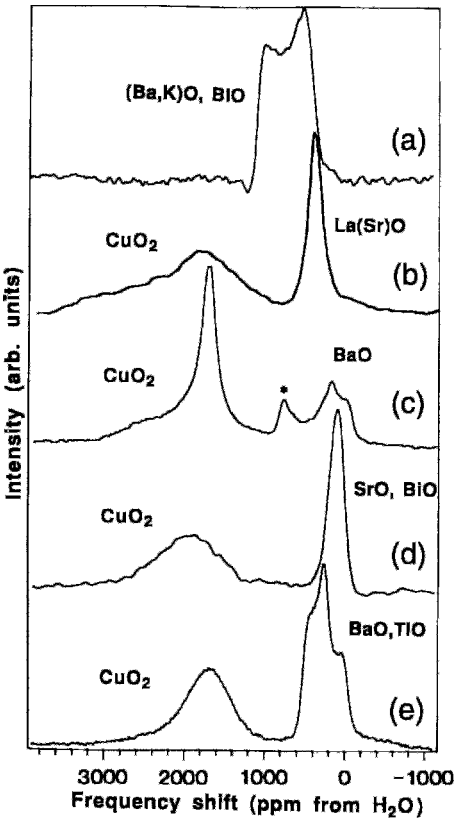

Figure 17.54 Room-temperature ^{17}O NMR spectra at 67.8 MHz (11.7 T) of (a) $(Ba_{0.6}K_{0.4})BiO_3$, (b) $(La_{0.925}Sr_{0.075})_2CuO_4$, (c) $YBa_2Cu_3O_{7-\delta}$, (d) $Bi_2Sr_2CaCu_2O_{8+\delta}$, and (e) $Tl_2Ba_2CaCu_2O_{8+\delta}$. The $*$ line in (c) arises from O(1) sites in a small population of aligned crystallites, which also contribute to the absorption at 18 ppm (Oldfield *et al.*, 1989).

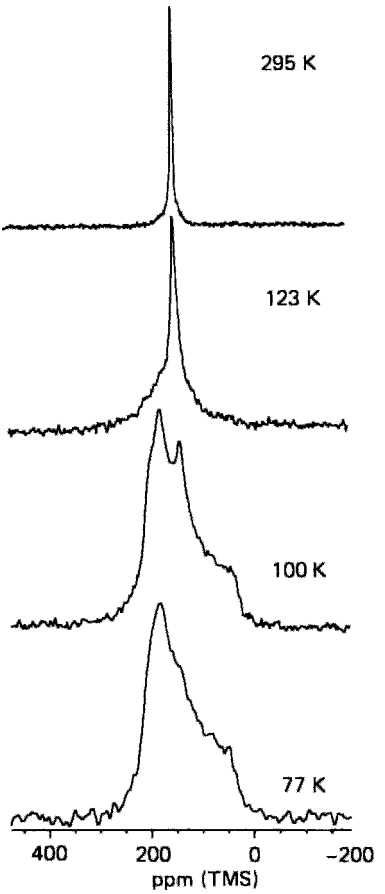

Figure 17.55 Temperature dependence of the 15-MHz ^{13}C NMR spectrum of C_{60}. The single narrow line at room temperature shows that all of the carbons are equivalent. The sequence of spectra suggests rapid reorientation at room temperature and the lack of rotational motion at liquid nitrogen temperature on the NMR timescale of $\tau \approx 0.1$ ms (R. D. Johnson *et al.*, 1992).

C_{60} and C_{70} determined by NMR agreed with those deduced from crystallographic studies.

The ^{13}C NMR of alkali metal-doped fullerenes, such as K_xC_{60}, which are both conducting and superconducting, exhibit a second narrow ^{13}C resonance at 186 ppm in addition to the usual resonance at 143 ppm. This resonance appears for $0 < x < 3$ and arises from K_3C_{60} molecules with the K^+ ions at interstitial sites adjacent to the C_{60}^{3-} ions. The C_{60}^{3-} ions rotate rapidly at room temperature to average out the chemical shift anisotropy. Thus K_xC_{60} constitutes a two-phase system. The chemical shift is identified with a Knight shift arising from hyperfine coupling between the ^{13}C nuclei and the conduction electrons (Tycko *et al.*, 1991, 1992).

Some relevant articles on NMR are: ^1H (DeSoto *et al.*, 1993; Le Dang *et al.*, 1989; Maniwa *et al.*, 1991b), $^9Be(3/2)$ (Tien and Jiang, 1989), ^{13}C (Antropov *et al.*, 1993 (t)), $^{17}O(5/2)$ (Asayama *et al.*,

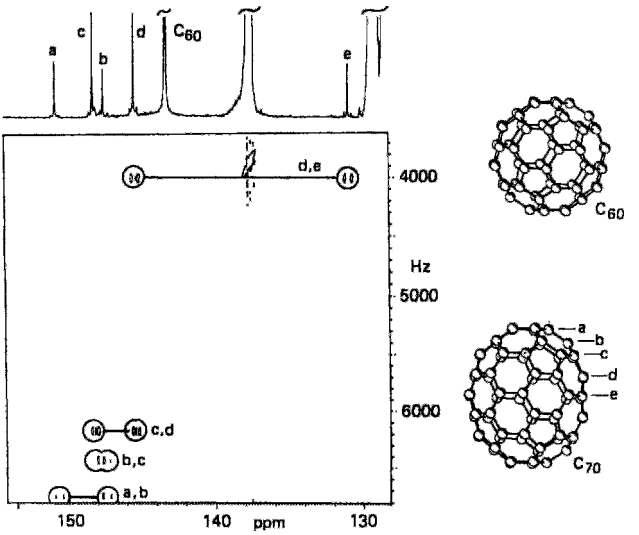

Figure 17.56 The upper trace is the 125.7-MHz ^{13}C NMR spectrum of a ^{13}C enriched mixture of C_{60} and C_{70}. The C_{60} line and the five C_{70} lines labeled a, b, c, d, and e with the respective relative intensities 10 : 10 : 20 : 20 : 10 are indicated. The two-dimensional spectrum presented on the lower left shows doublets arising from the various bonded carbon pairs. Reprinted by permission from R. D. Johnson *et al.*, 1992. Copyright (1992) by the American Chemical Society.

1991; Coretsopoulos *et al.*, 1989; Howes *et al.*, 1991; Reveu *et al.*, 1991; Trokiner *et al.*, 1990, 1991), $^{63,65}Cu(3/2)$ (Horvatic *et al.*, 1993; Millis and Monien, 1992; Millis *et al.*, 1990 (t), Walstedt *et al.*, 1990, 1992), ^{89}Y (Alloul *et al.*, 1993; Barrett *et al.*, 1990; Carretta and Corti, 1992; Carretta *et al.*, 1992; Millis and Monien, 1992; Millis *et al.*, 1990 (t)), $^{139}La(7/2)$ (Hammel *et al.*, 1990), $^{203,205}Tl$ (Fujiwara *et al.*, 1991; Kitaoka *et al.*, 1991; Song *et al.*, 1991a). Articles on NMR relaxation include $^{17}O(5/2)$ (Barrett *et al.*, 1991; Hammel *et al.*, 1989; Takigawa *et al.*, 1991a), $^{63,65}Cu(3/2)$ (Anikenok *et al.*, 1991; Borsa *et al.*, 1992; Martindale *et al.*, 1992; Mila and Rice, 1989 (t); Pennington *et al.*, 1989; Reyes *et al.*, 1991; Takigawa *et al.*, 1991b; Walstedt *et al.*, 1991), ^{89}Y (Adrian, 1988, 1989; Alloul *et al.*, 1989; Z. P. Han *et al.*, 1991, 1992), $^{141}Pr(5/2)$ (Teplov *et al.*, 1991), ^{169}Tm (Bakharev *et al.*, 1991; Teplov *et al.*, 1991), ^{195}Pt (Vithayathil *et al.*, 1991), and $^{203,205}Tl$ (Lee *et al.*, 1989; Nishihara *et al.*, 1991; Song *et al.*, 1993). (Theory and calculation articles are indicated by (t); the nuclear spin is given when it is not $\frac{1}{2}$.)

B. Quadrupole Resonance

A nucleus with spin $I > \frac{1}{2}$ has an electric quadrupole moment. Several such nuclei are listed in Table 17.4. The crystalline electric fields at an atomic site with symmetry less than cubic split the nuclear-spin levels in a manner that depends on the site symmetry, and the spacings between the levels are measured experimentally by nuclear quadrupole resonance (NQR). The frequencies used for making these measurements are similar to those employed for NMR. Table VI-14 of our earlier work (Poole *et al.*, 1988) lists the point symmetries for the occupied atomic sites in some of the high-temperature superconductors. Babu and Remakrishna (1992) reviewed the NQR of superconductors.

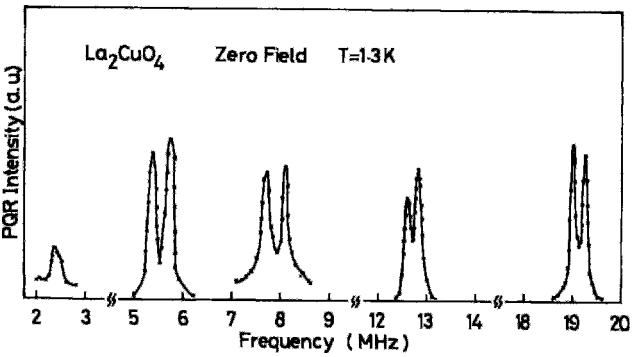

Figure 17.57 Nuclear quadrupole resonance spectrum of ^{139}La in La_2CuO_4 in zero field at 1.3 K. Reprinted by permission from Kitaoka *et al.*, 1987a. Copyright (1987) American Chemical Society.

The ^{139}La NQR spectrum of the prototype compound La_2CuO_4 in zero magnetic field at 1.3 K is shown in Fig. 17.57. It has five main lines from 2.4 to 19.3 MHz, arising from the five $m \rightarrow m'$ transitions $-\frac{1}{2} \rightarrow \frac{1}{2}, +\frac{1}{2} \rightarrow \pm\frac{3}{2}, -\frac{1}{2} \rightarrow \pm\frac{3}{2}, \pm\frac{3}{2} \rightarrow \pm\frac{5}{2}$, and $\pm\frac{5}{2} \rightarrow \pm\frac{7}{2}$ of the $I = \frac{7}{2}$ ^{139}La nucleus. Additional doublet splittings are caused by internal magnetic fields that arise from the magnetic ordering of the copper ions occurring below 240 K (Kitaoka *et al.*, 1987a). The doublet splittings are not resolved in the barium- and strontium-substituted compounds, as shown in Fig. 17.58, suggesting that the internal magnetic fields decrease with alkaline earth doping. The internal field parallel to c is about 35 mT for low barium contents ($\approx 1\%$) in the superconducting region (Kitaoka *et al.*, 1987b). The electric field gradient at the La site also changes on passing from the normal to the super-conducting state (Watanabe *et al.*, 1989). Cho *et al.*, (1992) used ^{139}La NQR relaxation to study magnetic ordering in $(La_{1-x}Sr_x)_2CuO_4$.

The room-temperature ^{63}Cu NQR spectrum of $YBa_2Cu_3O_x$ presented in Fig. 17.59 consists of one line at 22.1 MHz arising from Cu(1) in the chains and another at 31.2 MHz arising from Cu(2) in the basal plane (Vega *et al.*, 1989a). The ^{65}Cu isotope produces NQR lines shifted 6.7% lower in frequency;

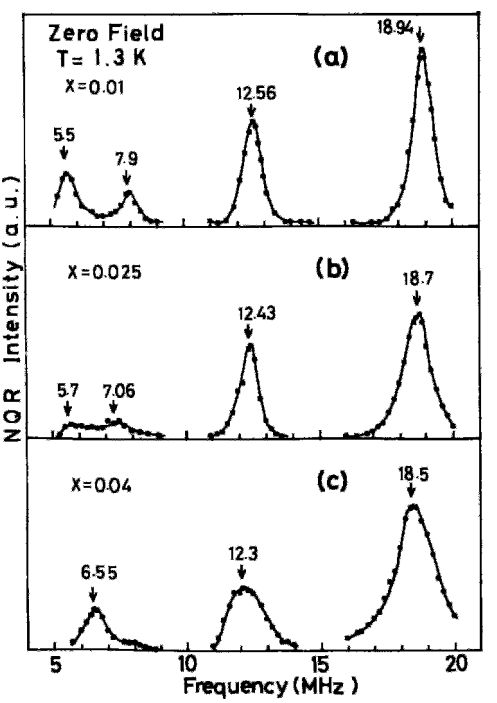

Figure 17.58 Nuclear quadrupole resonance spectrum at 1.3 K of ^{139}La in $(La_{1-x}Ba_x)_2CuO_4$ for (a) $x = 0.01$, (b) $x = 0.025$, and (c) $x = 0.04$. The calculated resonant frequencies are indicated by arrows (Kitaoka *et al.*, 1987a).

these are not shown. The symmetry was found to be close to axial for Cu(2), deviating considerably from axial for Cu(1), as

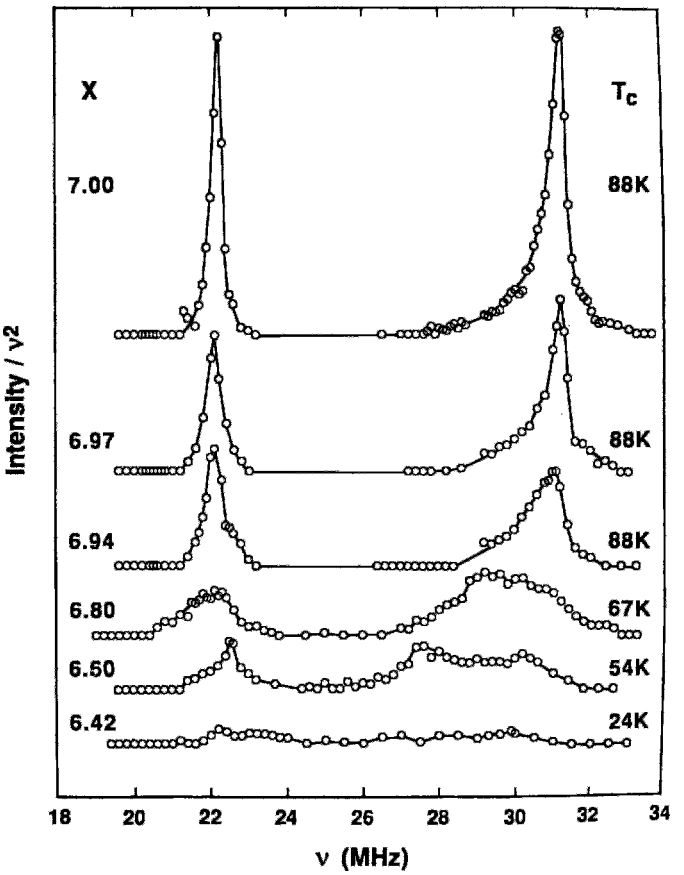

Figure 17.59 Short T_1 components of the NQR spectrum of ^{63}Cu in high-temperature quenched $YBa_2Cu_3O_x$ with the indicated x and T_c values. The 22.1 MHz line arises from Cu(1) in the chains, while the 31.2 MHz line is from Cu(2) in the planes (Vega *et al.*, 1989a).

would be expected from an examination of the structural drawings in Figs. 8.8, 8.10, and 8.11. We see from Fig. 17.59 that the linewidth strongly depends on the oxygen content. The sharpest line occurs in the stoichiometric compound $YBa_2Cu_3O_7$. Removal of oxygen lowers the symmetries of the two sites, broadening the lines and shifting them toward each other. This means that oxygen is being removed adjacent to both sites.

When the temperature of the sample is gradually lowered from room temperature to 20 K, the $^{63}Cu(1)$ resonance decreases in frequency by 0.5% while the $^{63}Cu(2)$ line increases in frequency by 1.1% (Mali *et al.*, 1987), as shown in Fig. 17.60. The variation in the electric field gradients at the two Cu sites can be accounted for by lattice compression. There is no discontinuity at the transition temperature.

NQR articles for several nuclei are ^{17}O (Sahoo *et al.*, 1990), $^{63,65}Cu$ (Carretta *et al.*, 1992; Fujiwara *et al.*, 1991; Ishida *et al.*, 1991; Kitaoka *et al.*, 1991; Pennington *et al.*, 1988, 1990; Pieper, 1992; Reyes *et al.*, 1990; Saul and Weissmann, 1990; Song

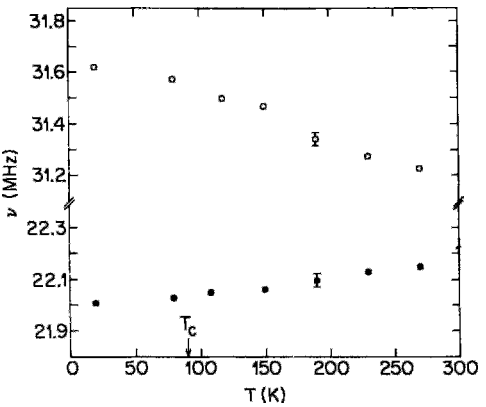

Figure 17.60 Temperature dependence of the ^{63}Cu nuclear quadrupole frequencies arising from Cu(1) (•) in the chain sites and Cu(2) (○) in the planar sites of $YBa_2Cu_3O_{7-\delta}$ (Mali *et al.*, 1987).

et al., 1991b; Sulaiman *et al.*, 1991; Vega *et al.*, 1989b), $^{69,71}Ga$ (Pieper, 1992), ^{135}Ba (Sulaiman *et al.*, 1992), ^{139}La (Song and Gaines, 1991; Sulaiman *et al.*, 1992), ^{141}Pr (Erickson, 1991).

C. Electron-Spin Resonance

Electron-spin resonance (ESR) detects unpaired electrons in transition ions, especially those with odd numbers of electrons, such as $Cu^{2+}(3d^9)$ and $Gd^{3+}(4f^7)$. Free radicals, like those associated with defects or radiation damage, can also be detected. The Zeeman energy level diagram of Fig. 17.50 also applies to ESR, except that the energies or resonant frequencies are three orders of magnitude higher for the same magnetic field. A different notation is employed for the energy,

$$E_m = g\mu_B B_{app} m, \qquad (17.29)$$

where μ_B is the Bohr magneton and g is the dimensionless g-factor; g has the value 2.0023 for a free electron. Equations (17.27) and (17.29) are related through the expression $g\mu_B = \hbar\gamma$ (Poole, 1983; Poole and Farach, 1987).

Some oxide superconductors exhibit an ESR signal, with g in the range from $\approx$ 2.05 to $\approx$ 2.27, arising from the divalent copper ions. This signal does not appear in high-purity samples, so that its appearance indicates the presence of a nonsuperconducting fraction, such as the green-phase Y_2BaCuO_5 admixed with $YBa_2Cu_3O_{7-\delta}$. We say that the high-temperature superconductors are ESR silent so far as the Cu^{2+} signal is concerned (McKinnon *et al.*, 1987, 1988; Simon *et al.*, 1993).

The magnetic field inside a superconducting sample was probed by placing one free radical marker on the face of a sample normal to the magnetic field direction and another free radical marker on the face of the sample parallel to the external magnetic field (Bontemps *et al.*, 1991; Davidov *et al.*, 1992; Farach *et al.*, 1990; Frait *et al.*, 1988a, b; Koshta *et al.*, 1993; Maniwa *et al.*, 1990; Poole *et al.*, 1988; Rakvin *et al.*, 1989; Shvachko *et al.*, 1991). In the superconducting state the two markers experience different local magnetic fields, so that the resonant positions of the lines shift in the manner shown in Fig. 17.61. The observed shift occurs because the free radicals respond to the surface field, which differs from the applied field in accordance with Eq. (5.35). Thus the observed shift in line position is a measure of the magnitude of the internal field B_{in} within the sample. With this result we are able to determine the temperature dependence of the susceptibility, with the results presented in Fig. 17.62. A related NMR method of probing the surface measures proton signals in a silicone oil coating (Maniwa *et al.*, 1991a).

The ESR spectrum of the compound LaC_{82}, illustrated in Fig. 17.63, consists of an unresolved hyperfine octet. This is well resolved by dissolving the LaC_{82} in degassed 1,1,2,2-tetrachloroethane, as shown. The spectrum is interpreted as arising from an unpaired electron delocalized in the π-electron system of the triply negative

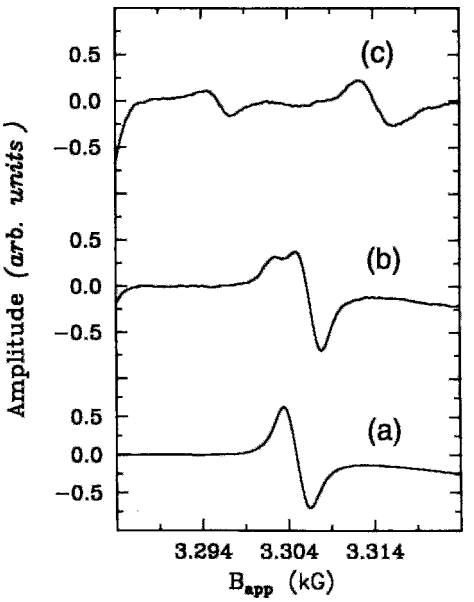

Figure 17.61 Shift of the ESR signals of paramagnetic markers located on the side and end of a $YBa_2Cu_3O_{7-\delta}$ sample from their superposed position (a) above T_c to different field positions (b,c) below T_c. The separation of the lines is proportional to the susceptibility (Farach *et al.*, 1990).

fullerene anion $(C_{82})^{3-}$ and interacting with the La^{3+} inside (i.e. endohedral). The 99.9%-abundant ^{139}La nucleus has spin $I = 7/2$, which gives the $2I + 1 = 8$ observed hyperfine multiplet. The hyperfine coupling is only 0.125 mT, indicating that the interaction with the La nucleus is very weak.

Acrivos *et al.* (1994) used ESR dynamic measurements to compare the paramagnetic and antiferromagnetic properties of various superconducting oxides.

D. Nonresonant Microwave Absorption

Below the transition temperature a superconductor has a microwave absorption signal that increases in amplitude as the temperature is lowered. There are often superimposed fluctuations that exhibit regularities, as shown in Fig. 17.64. These closely spaced oscillations have been attributed to Josephson junctions in the sample. Irradiating a Josephson junction with microwaves induces an oscillating voltage that depends on the microwave power and frequency. This phenomenon, called the inverse Josephson effect, was explained in Chapter 15, Section VII.E. If the magnetic field is scanned through zero to negative fields, the absorption exhibits a hysteresis, as shown in Fig. 17.65. The absorption is called nonresonant because it does not involve transitions

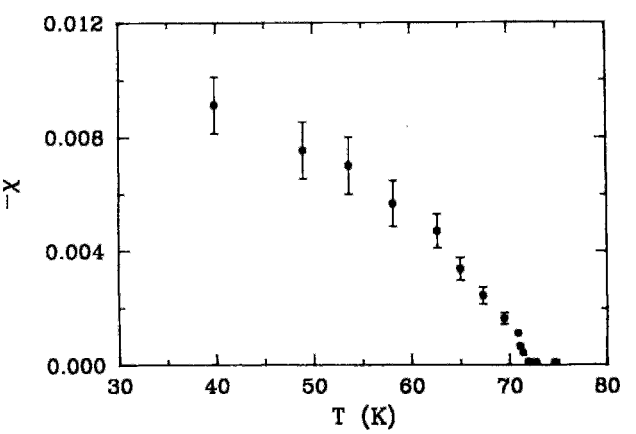

Figure 17.62 Temperature dependence of the susceptibility of $YBa_2Cu_3O_{7-\delta}$ determined by the ESR method of Fig. 17.61 (Farach *et al.*, 1990).

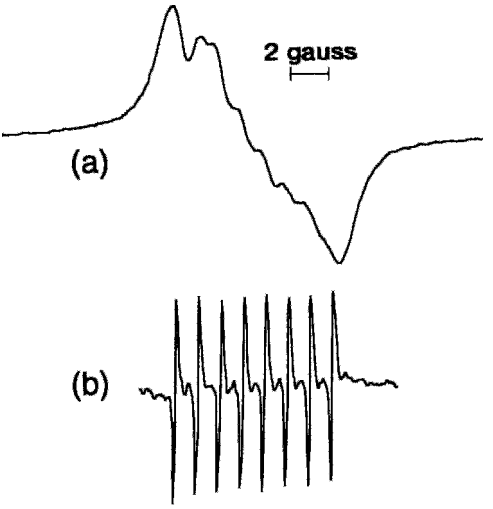

Figure 17.63 Electron-spin resonance spectrum of LaC_{82} mixed with C_{60} and C_{70} with the La inside the C_{82} fullerene cage. The poorly resolved octet (a) in the solid-state spectrum becomes well resolved (b) after the compound has been dissolved in degassed 1,1,2,2-tetrachloroethane solution. The linewidth is 12.5 μT and $g = 2.0010$ in the latter case (R. D. Johnson *et al.*, 1992).

between the Zeeman energy levels such as those which are characteristic of NMR and ESR absorption lines.

Xia and Stroud (1989) suggested that the absorption takes place in superconducting grains whose dimensions are small compared with the penetration depth and which are coupled together in closed loops. Imperfect monocrystalline sample could also contain weakly linked loops. These loops support screening currents in response to an external magnetic field. The presence of a dc field perpendicular to the plane of the loop and an incident microwave field can cause phase slips via jumps from one energy state into another as the flux through the loop changes with time. The phase slip generates a voltage difference between neighboring grains, and hence leads to energy absorption.

Blazey *et al.* (1987) identified the field B_{max} in which the low-field absorption reaches a maximum as the field where flux slippage starts to occur. This phenomenon

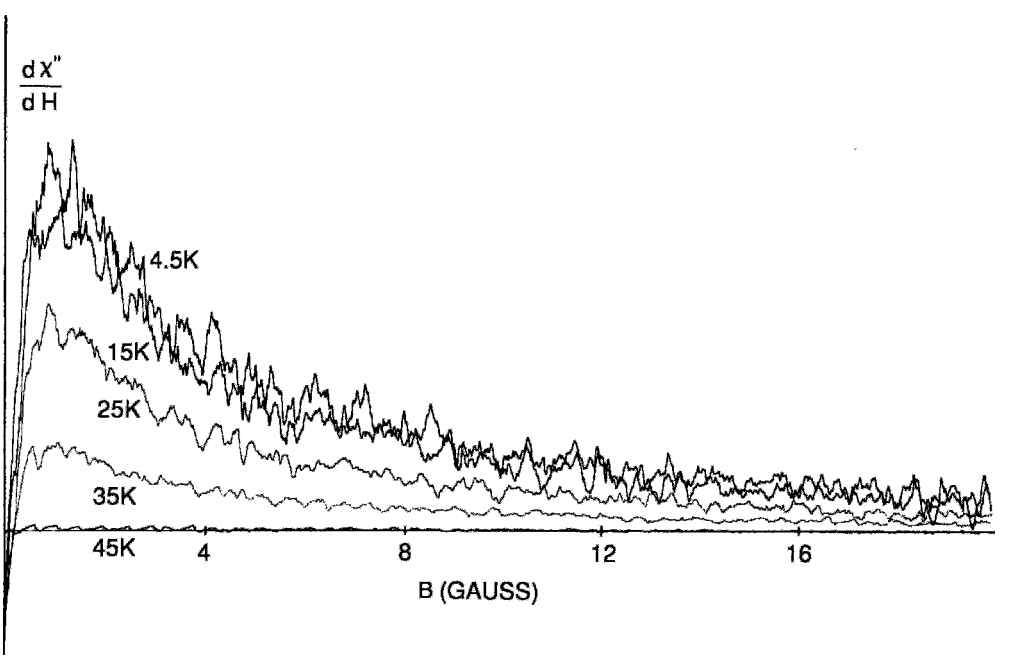

Figure 17.64 Low-field microwave absorption of $La_{2.8}Sr_{0.2}Cu_2O_7$ after field cooling at several temperatures in the range 4.5–45 K. Reprinted with permission from Blazey *et al.*, 1987. Copyright (1987) American Chemical Society.

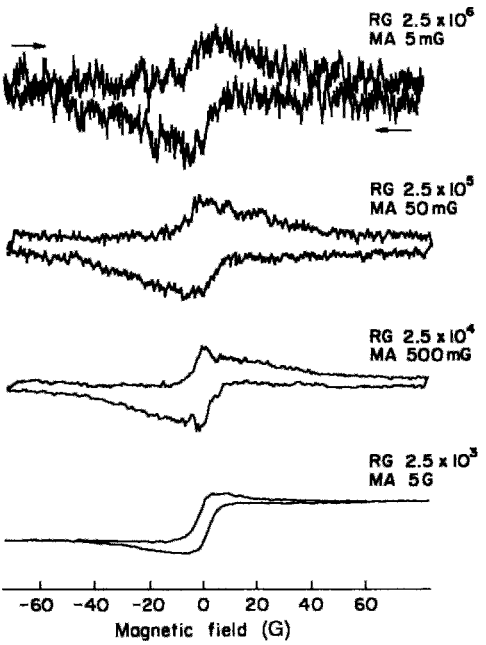

Figure 17.65 Hysteresis loops for microwave absorption of $YBa_2Cu_3O_{7-\delta}$ single crystals at 56 K cycled through zero field for four different modulation amplitudes (MA). Higher receiver gain (RG) settings were needed for the lower modulation amplitudes due to the decrease in sensitivity (Dulčic *et al.*, 1989).

was used to estimate the average radius r_L of the superconducting loops,

$$\pi r_L^2 = \frac{\phi_0}{2B_{max}}. \qquad (17.30)$$

Various samples gave loop radii in the range 0.6–2.5 μm. Zero field cooled samples exhibit a minimum absorption at zero field; stored flux shifts this minimum in field cooled samples (Mzoughi *et al.*, 1992).

E. Microwave Energy Gap

Energy gaps of superconductors with low transition temperatures, $T_c < 1$ K, occur in the microwave region. Since a temperature of 1 K is equivalent to 20.8 GHz, we can estimate from the BCS result $E_g/k_BT_c = 3.53$ that 1 K corresponds to an energy gap of ≈ 74 GHz, which is in the upper range of readily available microwave frequencies. Most microwave absorption studies of the type described in the previous section were carried out at ≈ 9 GHz, which is almost three orders of magnitude below the energy gap frequency of a high-temperature superconductor.

A study made of the temperature dependence of the normalized microwave resistivity of aluminum ($T_c = 1.2$ K) for a range of microwave frequencies of 12–80 GHz, shown in Fig. 17.66a, illustrates how the gap can be estimated (Biondi and Garfunkel, 1959). Each curve is labeled with its equivalent k_BT_c value. The curves for photon energies less than $3k_BT_c$ extrapolate to zero,

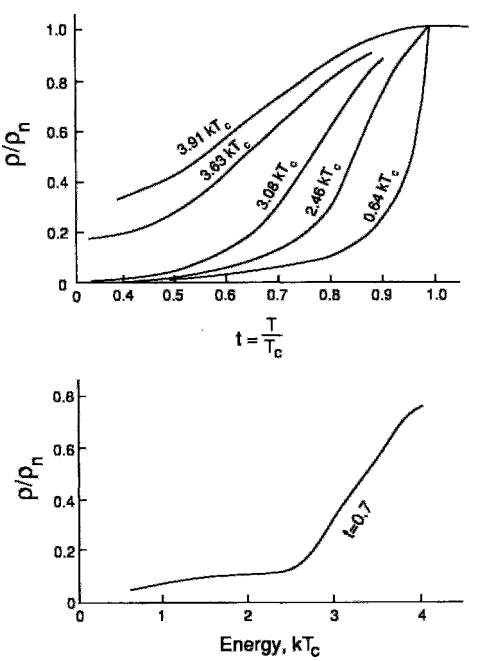

Figure 17.66 Temperature dependence of the normalized microwave resistivity ρ/ρ_n of aluminum (top) for a range of microwave frequencies, where ρ_n is the normal-state resistivity. Each curve is labeled with its equivalent k_BT_c value. The plot of the normalized resistivity versus k_BT_c (bottom) exhibits a break in the curve at the temperature $T = 0.7T_c$ corresponding to the energy gap $E_g \approx 2.6\,k_BT_c$ (Biondi and Garfunkel, 1959).

which indicates that super electrons are not excited above the gap for microwave energies less than $3k_BT_c$. Above this energy the curves extrapolate to a finite resistivity, indicative of the presence of excited quasiparticles. In carrying out this experiment the lowest temperatures, $\approx 0.3\,K$, were reached with the aid of a He^3 refrigerator.

To determine the gap energy a plot was made of the microwave resistivity of each frequency at the temperature $T = 0.7T_c$ versus the energy, as shown in Fig. 17.66b. We see from the plot that the resistivity has a small slope up to the energy $2.6k_BT_c$ and a larger slope beyond this point, indicating that the gap energy is $E_g \approx 2.6k_BT_c$. The more rapid rise in resistivity beyond this point arises from super electrons that have become excited to the quasiparticle state.

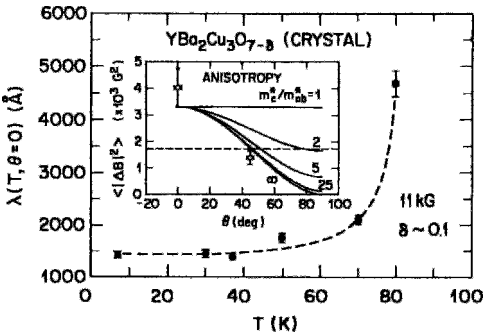

Figure 17.67 Temperature dependence of the penetration depth λ in a single crystal of $YBa_2Cu_3O_{7-\delta}$ for a 1. 1-T magnetic field aligned along the c-axis, showing measured data points and fits to the data (dashed curves). The inset shows the average field squared $\langle|\Delta B|^2\rangle$ for two data points and several calculated mass anisotropy curves m_c^*/m_{ab}^* as a function of the angle Θ of the magnetic field relative to the c-axis. The data were obtained from muon spin relaxation (Harshman *et al.*, 1989).

F. Muon-Spin Relaxation

The negative muon μ^- acts in all respects like an electron and the positive muon μ^+ like a positron except for each having a mass 206.77 times larger (Poole, 1983). In this experiment positive polarized muons are implanted into a sample that had been placed in a magnetic field. The precession of the muons at $\gamma_\mu/2\pi = 135.5\,MHz/T$ provides a microscopic probe of the distribution of the local magnetic fields (Budnick *et al.*, 1987). In particular, the width of the muon spin relaxation (μSR) signal from a superconductor provides an estimate of this field distribution and of the penetration depth λ (Ansaldo *et al.*, 1991a; Pümpin *et al.*, 1990). The measurements are carried out in an external field that is significantly larger than the lower-critical field, so that the separation between the vortices is smaller than λ, and the μSR signal represents a simple average over the internal field in different parts of the sample.

As an example of a penetration depth determination we present in Fig. 17.67 the temperature dependence measured using a single crystal of $YBa_2Cu_3O_{7-\delta}$ with an 11-T applied magnetic field aligned parallel to the c-axis ($\Theta = 0$). The distribution of the internal magnetic field B_{in} depends on the anisotropy in the fall-off of the magnetic field in various directions around a vortex. The fall-off is, in turn, governed by the corresponding penetration depth in the plane perpendicular to the field direction. Figure 17.67 compares the temperature dependence of the measured values λ_{ab} with the dependence expected from Eq. (2.57),

$$\lambda = \lambda(0)\left[1 - \left(\frac{T}{T_c}\right)^4\right]^{-1/2} \qquad (17.31)$$

with $\lambda(0) = 141.5\,nm$. We see that the fit to the data is good.

We saw in Chapter 12 Section IV.A, that for a high-temperature superconductor $m_{ab}^* < m_c^*$, and hence that $\lambda_{ab} < \lambda_c$. We can conclude from a comparison of Eqs. (12.59) and (12.61) that the area enclosed by a vortex within a distance from the origin that satisfies Eq. (12.49) and makes the modified Bessel function assume the value $K_0(1)$ is larger when the magnetic field is aligned

in the *a, b*-plane than when B_{app} is along *c* (see Fig. 12.23). This means that the vortices overlap more when the applied field is in the *a, b*-plane than when it is along the *c* direction; the variation in space of the internal field ΔB about its average value, shown plotted in Fig. 12.19, is also less for the former case. An intermediate amount of overlap, and hence of ΔB, will occur for intermediate angular orientations.

To check the anisotropy, Harshman *et al.* (1989) oriented the applied magnetic field at an angle $\pi/4$ relative to the *c* direction and found that the measured variation in the average field squared $\langle|\Delta B|^2\rangle$ had decreased. The result is compared in the inset of Fig. 17.67 with representative curves calculated for various rations m_c^*/m_{ab}^* that show the existence of strong anisotropy, since $m_c^*/m_{ab}^* > 25$. This means that $\lambda_c/\lambda_{ab} > 5$; in other words, $\lambda_c > 700\,\text{nm}$. The effective mass m_c^* relative to the electron rest mass m_0 was also determined and it was found that $m_c^* \approx 10m_0$.

G. Mössbauer Resonance

Mössbauer resonance measures gamma rays emitted by a recoilless nucleus when it undergoes a transition from a nuclear ground state to a nuclear excited state. For ^{57}Fe the emitted gamma ray has an energy of 14.4 KeV and a linewidth typically of 5×10^{-9} eV. The gamma ray can shift in energy, called an isomer shift, or its spectrum can split into a multiplet by hyperfine interaction from the nuclear spin, by crystal field effects, or by the quadrupole interaction. Line broadening and relaxation provide additional information. These factors are sensitive to the chemical environment of the nucleus in the lattice. Mössbauer workers frequently quote energy shifts in velocity units, mm/s.

In a typical experiment, one of the atoms of a superconductor such as Cu, Y, or Tl, is partially replaced by a small concentration of a nucleus, such as ^{57}Co, ^{57}Fe, ^{151}Eu, or ^{119}Sn, any one of which is favorable for Mössbauer studies. Sometimes, the replacement is 100%, as in the compound $EuBa_2Cu_3O_{7-\delta}$. The partial substitution can have the effect of lowering the transition temperature, particularly when Cu is being replaced, as shown in Fig. 17.68. The spectra provide information on the valence state of the nucleus (e.g., Fe^{2+} or Fe^{3+}), for example, whether it is high spin (e.g., $S = 5/2$) or low

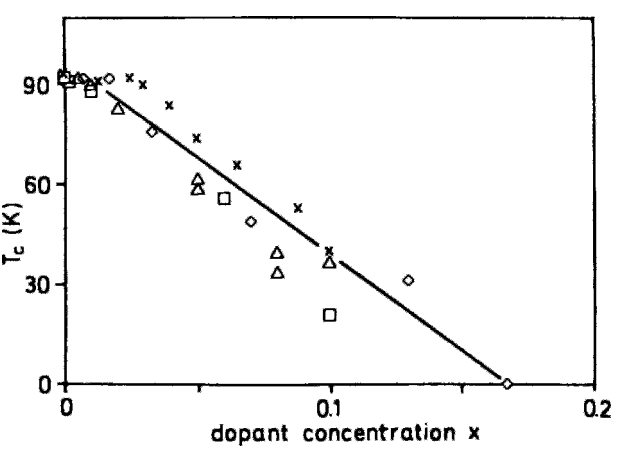

Figure 17.68 Dependence of the zero-resistance midpoint transition temperature T_c on the concentration x of the transition ion dopant M in $YBa_2(Cu_{1-x}M_x)_3O_{7-\delta}$ for: (a) Fe (□) (Bottán *et al.*, 1988), (b) Fe (Δ) (Oda *et al.*, 1987), (c) Fe (◊) (Tarascon *et al.*, 1988a), and (d) Co (×) (Langen *et al.*, 1988) (figure from Bottayán *et al.*, 1988).

spin (e.g., $S = 1/2$), which is the dominant substitutional site (e.g., Cu(1) or Cu(2)), etc. Perhaps of greater interest is the information that Mössbauer gives us about the magnetic changes that occur.

Mössbauer data from $YBa_2Cu_3O_{7-\delta}$ with ^{57}Fe substituted for 10% of the Cu are shown in Fig. 17.69. The Fe is magnetically ordered at low temperature, with the ordering identified as antiferromagnetic since turning on a magnetic field of 5 T has the effect of broadening and producing a small inside shift of the outer lines of the spectrum, as shown in the figure. Increasing the temperature produces a decrease in the magnetic splitting accompanied by relaxation-time broadening. The onset of magnetic splitting occurs at 50 K; it appears in the wings in Figs. 17.69c and 17.69d, and is resolved in Figs. 17.69a and 17.69b. Below T_c, which from Fig. 17.69 is about 25 K for 10% Fe, the spectra of Fig. 15.69 appear more spread out. Bottyan *et al.* (1988) conclude that there are four Fe species that appear as the oxygen content (δ) and the Fe/Cu ratio of Fe varies, with three high-spin Fe^{4+} and one high-spin Fe^{3+}, with a preference for the Cu(1) sites. Pissas *et al.* (1992) found Fe equally distributed between the chain and plane Cu sites, being high-spin ($S = 5/2$) at the latter site.

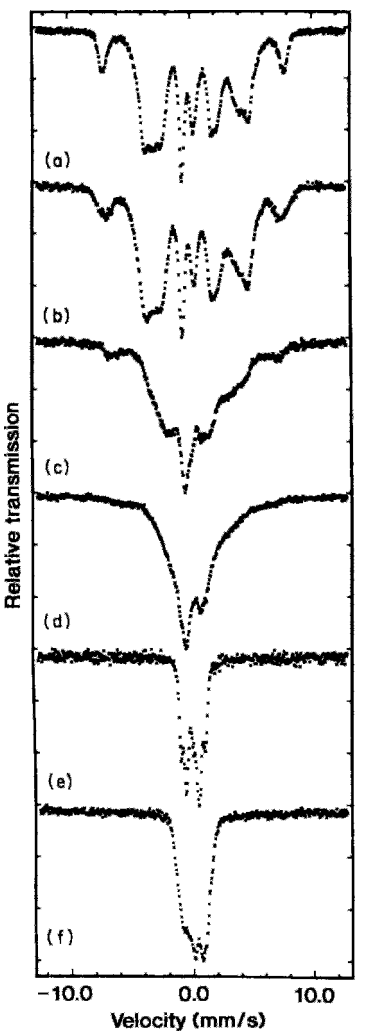

Figure 17.69 Comparison of Mössbauer absorption spectra of $YBa_2(Cu_{0.9}Fe_{0.1})_3O_7$ in zero field below T_c at (a) 4.2 K, (c) 15 K, and (d) 19 K, and above T_c at (e) 100 K. Spectra are also shown in a 5-T magnetic field at (b) 4.2 K, and (f) 100 K (Bottyán *et al.*, 1988).

Shinjo and Nasu (1989) reviewed magnetic order at very low temperatures in the superconductors

$$YbBa_2Cu_3O_7 \quad \text{and} \quad GdBa_2Cu_3O_7.$$

The isomer shift values indicate that the conduction-electron densities in the rare-earth ions are close to zero (Smit *et al.*, 1987), and suggest that they do not contribute to the electrical conductivity. The pronounced change in the spectrum with the temperature, shown in Figs. 17.70 and 17.71 for the two compounds, indicates the change from a low-temperature ordered state into a high-temperature paramagnetic-type state with the respective Néel temperatures T_N of 0.35 K and 2.5 K, both of which are far below the superconducting transition temperature $T_c \approx 90$ K. The authors suggest that the rare earth sheets sandwiched by superconducting layers may be an ideal two-dimensional magnetic lattice.

Relevant Mössbauer articles on several isotopes are, for ^{119}Sn (Kuzmann *et al.*,

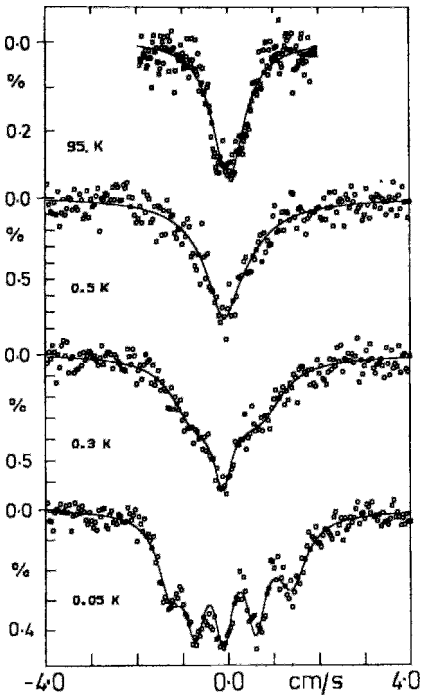

Figure 17.70 Mössbauer spectra of ^{170}Yb in $YbBa_2Cu_3O_7$ at four temperatures showing resolution of structure in the millidegree region (Hodges *et al.*, 1987).

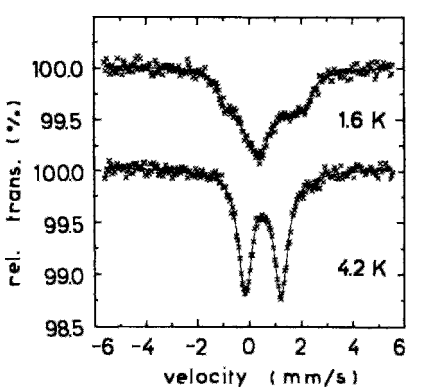

Figure 17.71 Mössbauer spectra of ^{155}Gd in $GdBa_2Cu_3O_7$ at 1.6 K and 4.2 K, showing resolved structure at the lower temperature (van den Berg *et al.*, 1987; Smit *et al.*, 1987).

1989; Matsumoto *et al.*, 1991; Nishida *et al.*, 1990a,b; Shiujo *et al.*, 1989; Shinjo and Nasu, 1989; Smith *et al.*, 1992), for ^{121}Sb (Smith *et al.*, 1992), for ^{151}Eu (Kuzmann *et al.*, 1989; Malik *et al.*, 1988; Shinjo and Nasu, 1989; Stadnik *et al.*, 1989, 1991; Yoshimoto *et al.*, 1991), for ^{155}Gd (Bornemann *et al.*, 1991; Shinjo and Nasu, 1989), and for ^{170}Yb (Shinjo and Nasu, 1989). The literature on ^{57}Fe studies is extensive.

PROBLEMS

1. What are the real and imaginary parts of $\sqrt{\epsilon}$ if $\epsilon = 2 + 3j$?
2. A metal is opaque for incident radiation below 2 eV and transparent for higher incident energies. Find the plasma frequency and the density of conduction electrons.
3. An ionically bonded molecule A^+B^- with the bond length 0.17 nm has polarizability $2 \times 10^{-16}\,\mathrm{cm}^2/\mathrm{V}$. It is irradiated with light with the power density $3\,\mathrm{W/m}^2$. Find the permanent and induced dipole moments.
4. Calculate the frequency and the energy of the $n = 1$ to $n = 4$ transition of Cu. Find the Moseley law constant for this transition.
5. A neutron moving through a lattice at the velocity $v = 2 \times 10^5\,\mathrm{m/sec}$ creates a phonon of frequency $5 \times 10^{11}\,\mathrm{Hz}$. Find its new velocity v'.
6. Show that Eq. (17.16) reduces to Eq. (17.17) in the limit $\omega_i \tau_i \gg 1$. Show that $1/\tau_i$ is the linewidth for the real and imaginary parts of the expression.
7. A molecule with the vibrational frequency $\nu_0 = 10^{12}\,\mathrm{Hz}$ is irradiated with visible light of wavelength $600\,\mu\mathrm{m}$. What are the first five Stokes line frequencies in the Raman spectrum?
8. What is the gyromagnetic ratio γ for a Cu^{2+} ion with $g = 2.17$? What will be its ESR frequency in a magnetic field of 0.3 T?
9. Derive an expression for the dependence of the shift in the resonant lines

of Fig. 17.62 on the applied field for the sample geometry of Fig. 5.17, taking into account the demagnetization factor.

10. A material has a characteristic vibrational frequency $\nu_0 = 3 \times 10^{12}$ Hz and an index of refraction $n = 2$. Find the energies E of the three lowest vibrational transitions, the frequency ν of the fundamental vibrational band, the spring constant k and the reflection coefficient R for normal incidence.
11. Sketch the energy level diagram and indicate all of the transitions appearing on the ^{139}La nuclear quadrupole resonance spectrum of Fig. 17.57.

References

M. Abramowitz and I. A. Stegun, Eds., "Handbook of Mathematical Functions," NBS, U. S. Gov. Printing Off., Washington, DC, 1964.

A. A. Abrikosov, Zh. Eksp. Teor. Fiz. 35, 1442 (1957); Sov. Phys. JETP 5, 1174 (1957).

A. A. Abrikosov, Fundamentals of the Theory of Metals, Pt. 2: Elsevier (1988).

D. Achkir, D. Poirier, C. Bourbonnais, G. Quirion, C. Lenoir, P. Batail, and D. Jerome, Phys. Rev. B 47, 11595 (1993).

S. Adachi, A. Tokiwa-Yamamoto, M. Itoh, K. Isawa, and H. Yamauchi, Physica C 214, 313 (1993).

F. J. Adrian, Phys. Rev. Lett. 61, 2148 (1988); see also 63, 688, 690 (1989).

F. J. Adrian, Chem. Eng. News Dec. 21, 24 (1992).

G. Aeppli, S. M. Hayden, H. A. Mook, Z. Fisk, S.-W.Cheong, D. Rytz, J. P. Remeika, G. P. Espinosa, and A. S. Cooper, Phys. Rev. Lett. 62, 2052 (1989).

N. Agrait, J. G. Rodrigo, and S. Vieira, Phys. Rev. B46, 5814 (1992).

N. Agrait, J. G. Rodrigo, and S. Vieira, Phys. Rev. B47, 12345 (1993).

M. Akera and T. Andu, in "Proc. 8th Int. Conf. on Elect. Prop, of 2-Dimensional Systems," Grenoble, France, 1989.

J. Akimitsu, S. Suzuki, M. Wantanabe, and H. Sawa, Jpn. J. Appl. Phys. 27, L1857 (1988).

S. Aktas, "A Numerical Study of Magnetic Vortices in High Kappa Superconductors," Ph.D. thesis, University of South Carolina, 1993.

S. Aktas, C. P. Poole, Jr., and H. A. Farach, J. Phys. Condens. Matter 6, 7373 (1994).

N. E. Alekseevskii, N. M. Dobrovolskii, D. Ekkert, and V. I. Tsebro, JETP 72, 1145 (1977).

L. Alff, S. Meyer, S. Kleefisch, U. Schoop, A. Marx, H. Sato, M. Naito, and R. Gross, Phys. Rev. Lett. 83 2644 (1999).

E. Alleno, Z. Hossain, C. Godart, R. Narajan and L. C. Gupta, Phys. Rev. B 52, 7428 (1995).

A. A. Aligia, Phys. Rev. B 39, 6700 (1989).

K. Allan, A. Campion, J. Zhou, and J. B. Goodenough, Phys. Rev. B 41, 11572 (1990).

P. B. Alien, in "High-Temperature Superconductivity" (J. W. Lynn, Ed.), Chap. 9, Springer-Verlag, Berlin, (1990).
H. Alloul, T. Ohno, and P. Mendels, Phys. Rev. Lett. 63, 1700 (1989).
H. Alloul, A. Mahajan, H. Casalta, and O. Klein, Phys. Rev. Lett. 70, 1171 (1993).
C. C. Almasan, J. Estrada, C. P. Poole, Jr., T. Datta, H. A. Farach, D. U. Gubser, S. A. Wolf, and L. E. Toth, Mater. Res. Soc. Symp. Proc. 99, 451 (1987).
C. C. Almasan and M. B. Maple, in "Chemistry of High Temperature Superconductors" (C. N. R. Rao, Ed.), World Scientific, Singapore, 1991.
C. C. Almasan, S. H. Han, E. A. Early, B. W. Lee, C. L. Seaman, and M. B. Maple, Phys. Rev. B 45, 1056 (1992).
E. E. Alp, J. C. Campuzano, G. Jennings, J. Guo, D. E. Ellis, L. Beaulaigue, S. Mini, M. Faiz, Y. Zhou, B. W. Veal, and J. Z. Liu, Phys. Rev. B 40, 9385 (1989).
V. Ambegaokar and A. Baratoff, Phys. Rev. Lett. 10,468 (1963a); 11, 104 (1963b).
V. Ambegaokar and U. Eckern, Phys. Rev. B 44, 10358 (1991).
J. R. Anderson, D. A. Papaconstantopoulis, J. W. McCaffrey, and J. E. Schirber, Phys. Rev. B 7, 5115 (1973).
P. W. Anderson, Phys. Rev. 112, 1900 (1958).
P. W. Anderson, Phys. Rev. B 115, 2 (1959).
P. W. Anderson, Phys. Rev. Lett. 9, 309 (1962).
P. W. Anderson and J. M. Rowell, Phys. Rev. Lett. 10, 230 (1963).
P. W. Anderson and Y. B. Kirn, Rev. Mod. Phys. 36, 39 (1964).
P. W. Anderson, Science 235, 1196 (1987a); Phys. Rev. Lett. 59, 2497 (1987b). P.
P. W. Anderson, in "Frontiers and Borderlines of Many Particle Physics," Int. School of Physics "Enrico Fermi," North-Holland, Varenna, 1987.
P. W. Anderson and Z. Zou, Phys. Rev. Lett. 60, 132 (1988). (Reprinted in Halley, 1988).
P. W. Anderson, Phys. Rev. Lett. 64, 1839 (1990a); 65, 2306 (1990b).
P. W. Anderson, Physica C 185–189, 11 (1991).
P. W. Anderson and R. Schrieffer, Physics Today, June 1991, p. 54.
P. W. Anderson, Science 256, 1526 (1992).
P. W. Anderson, "A Career in Theoretical Physics," World Scientific, Singapore, 1994a.
P. W. Anderson, Amer. Scientist 82, 379 (1994b).
M. Andersson and O. Rapp, Phys. Rev. B 44, 7722 (1991).
Y. Ando, N. Motohira, K. Kitazawa, J. Takeya, and S. Akita, Jpn. J. Appl. Phys. 30, LI 635 (1991a); Phys.Rev. Lett. 67, 2737 (1991b).
B. Andraka, J. S. Kirn, G. R. Stewart, K. D. Carlson.H. H. Wang, and J. M. Williams, Phys. Rev. B 40, 11345 (1989).
M. Angst, R. Puzniak, A. Winiewski, J. Roos, H. Keller, P. Miranovic, J. Jun, S. M. Kazarov, J. Karpinski, Physica C 385, 143, (2003).
O. A. Anikeenok, M. V. Eremin, Sh. Zhdanov. V. V. Naletov, M. P. Rodionova, and M. A. Teplov, JETP Lett. 54, 149 (1991).
V. I. Anisimov, M. A. Korotin, J. Zaanen, and P. L. Andersen, Phys. Rev. Lett. 68, 345 (1992).
S. M. Anlage, M. Pambianchi, A. T. Findikoglu, C. Doughty, D.-H. Wu, J. Mao, S.-N. Mao, X. X. Xi, T. Venkstesan, J. L. Peng, and R. L. Greene, Proc. SPIE Conf. on Oxide Superconductivity, Vol 2158 (D. Pavuna, Ed.), 1994.
S. Anlage, D-H Wu, J. Mao, S. N. Mao, X. X. Xi, T. Venkatesan, J. L. Peng, and R. L. Greene, Phys. Rev. B 50 523 (1994).
J. F. Annett, NATO ASI Ser., Ser., 332405 (1997).
J. F. Annett, N. Goldenfeld, and S. R. Renn. "Temperature Superconductors" (D. M. Ginsberg, Ed.), Vol. 2, Chap.9, World Scientific, Singapore, 1990.
J. F. Annett, N. Goldenfeld, and S. R. Renn, Phys. Rev. B 43, 2778 (1991).
J. F. Annett, Physica C 317 1–8 (1999).
J. F. Annett, G. Litak, B. L. Gyorffy, and K. Li. Wysokinski, Phys. Rev. B 66, 134514 (2002)
J. F. Annett, B. L. Gyorffy, G. Litak, and K. I. Wysokinski, Eur. Phys. J. B 36, 301 (2003).
E. J. Ansaldo, C. Niedermayer, H. Gliickler, C E-Stronach, T. M. Riseman, R. S. Gary, D. R. Noakes, X. Obradors, A. Fuetes, J. M. Navarro. P. Gomez, N. Casan, B. Martinez, F. Perez, J. Rodriguez-Carvajal, and K. Chow, Physica C 735–189, 1213 (1991a).
E. J. Ansaldo, C. Niedermayer, and C. E. Stronact Nature 353, 121 (1991b).
V. P. Antropov, I. I. Mazin, O. K. Andersen, A. I. Liechtenstein, and O. Jepsen, Phys. Rev. B 47 12373 (1993).
J. Aponte, H. C. Abache, A. Sa-Neto, and M. Octavio, Phys. Rev. B 39, 2233 (1989).
M. Aprili, E. Badica, and L. H. Greene, Phys. Rev. Lett. 83, 4630 (1999).

T. Arai, K. Ichimura, K. Nomura, S. Takasaki, J. Yamada, S. Nakatsuji, and H. Anzai, Phys. Rev. B 63 104518 (2001).
T. Arai, K. Ichimura, K. Nomura, S. Takasaki, J. Yamada, S. Nakatsuji, and H. Anzai, Phys. Rev. B 63 104518 (2001).
B. Arfi, Phys. Rev. B 45, 2352 (1992).
G. Arfken, "Mathematical Methods for Physicists 3rd ed., Wiley, New York, 1985.
T. A. Arias and J. D. Joannopoulos, Phys. Rev. B 39, 4071 (1989).
D. N. Aristov, S. V. Maleyev, and A. G. Yashenkin. Phys. Rev. B 48, 3527 (1993).
A. J. Arko, R. S. List, R. J. Bartlett, S.-W. Che Z. Fisk, J. D. Thompson, C. G. Olson, A.-B. Yang, R. Liu, C. Gu, B. W. Veal, J. Z. Liu, A. P. Plaulikas, K. Vandervoort, H. Claus, J. C. Campuzano, L J. E. Schirber, and N. D. Shinn, Phys. Rev. B 40, 2268 (1989).
N. P. Armitage, D. H, Lu, D. L. Feng, C. Kirn, A. Damascelli, K. M. KShen, F. Ronning, Z-X., Shen, Y. Onose, Y. Taguchi, and Y. Tokura, Phys. Rev. Lett. 86 1126 (2001).
G. B. Arnold, F. M. Mueller, and J. C. Swihart. Phys. Rev. Lett. 67, 2569 (1991).
A. G. Aronov, S. Hikami, and A. I. Larkin, Phys. Rev. Lett. 62, 965, 2236(E), (1989).
D. Arovas, J. R. Schrieffer, and F. Wilczek. Phys. Rev. Lett. 53, 722 (1984).
E. Arrigoni, G. Strinati, and C. Castellani, Phys. Rev. B 41, 4838 (1990).
K. Asayama, G.-Q. Zheng, Y. Kitaoka, K. Ishida, and K. Fujiwara, Physica C 178, 281 (1991).
N. W. Ashcroft and N. D. Mermin, "Solid State Physics," Saunders, Philadelphia, 1976.
M. Ashida, S. Aoyama, J. Hara, and K. Nagai, Phys. Rev. B 40, 8673 (1989).
J. Ashkenazi, S. E. Barnes, F. Zuo, G. C. Vezzoli, and B. M. Klein, Eds., "High Temperature Superconductivity," Plenum, New York, 1991.
T. R. Askew, R. B. Flippen, K. J. Leary, M. N. Kunchur, J. Mater. Res. 6, 1135 (1991).
L. G. Aslamazov and A. I. Larkin, Fiz. Tverd. Tela 10, 1104 (1968) [Sov. Phys. Solid State 10, 875(1968)].
W. Assmus, M. Herrmann, U. Rauchschwalbe, S. Riegel, W. Lieke, H. Spille, S. Horn, G. Weber, F. Steglich, and G. Cordier, Phys. Rev. Lett. 52, 469 (1984).
K. S. Athreya, O. B. Hyun, J. E. Ostenson, J. R. Clem, and D. K. Finnemore, Phys. Rev. B 38, 11846 (1988).
A. Auerbach, "Interacting Electrons and Quantum Magnetism," Springer-Verlag, Berlin, 1994.
B. Aurivillus, Ark. Kemi 1, 463, 499 (1950).
B. Aurivillus, Ark. Kemi 2, 519 (1951).
B. Aurivillus, Ark. Kemi 5, 39 (1952).
C. Ayache, I. L. Chaplygin, A. I. Kirilyuk, N. M. Kreines, and V. I. Kudinov, Solid State Commun. 81, 41 (1992).
J. Azoulay, Phys. Rev. B 44, 7018 (1991).
E. Babic, M. Prester, D. Drobac, Z. Marohnic, and N. Biskup, Phys. Rev. B 43, 1162 (1991).
E. Babic, M. Prester, D. Drobac, Z. Marohnic, P. Nozar, P. Stastny, F. C. Matacotta, and S. Bernik, Phys. Rev. B 45, 913 (1992).
P. K. Babu and J. Ramakrishna, Supercond. Rev. 1, 75 (1992).
E. M. Baggio-Saitovitch, D. R. Sanchez, and H. Micklitz, (K. H. Muller and V. Narozhnyi, Eds.), Rare Earth Transition Metal Borocarbides (Nitrides); Superconducting Magnetic and Normal State Properties, p. 51, Kluwer Acad. Publ. Dordrecht, (2001)
D. C. Baird and B. K. Mukherjee, Phys. Rev. Lett. 21, 996 (1968).
D. C. Baird and B. K. Mukherjee, Phys. Rev. 3, 1043 (1971).
C. K. Bak and N. F. Pedersen, Appl. Phys. Lett. 22, 149 (1973).
O. N. Bakharev, A. V. Dooglav, A. V. Egorov, V. V. Naletov, M. P. Rodionova, M. S. Tagirov, and M. A. Teplov, Appl. Magn. Reson. 2, 559 (1991).
J. Bala and A. M. Oles, Phys. Rev. B 47, 515 (1993).
C. J. Ballhausen, "Introduction to Ligand Field Theory," McGraw-Hill, New York, 1962.
M. Ban, T. Ichiguchi, and T. Onogi, Phys. Rev. B 40, 4419 (1989).
A. Bansil, P. E. Mijnarends, and L. C. Smedskjaer, Phys. Rev. B 43, 3667 (1991).
A. Bansil and S. Kaprzyk, Phys. Rev. B 43, 10335 (1991).
Y. S. Barash, M. S. Kalenkov, and J. Kurkijarvi, Phys. Rev. B 62, 6665 (2000).
A. Baratoff and G. Binnig, Physica B 188, 1335 (1981).
B. Barbiellini, P. Genoud, J. Y. Henry, L. Hoffmann, T. Jarlborg, A. A. Manuel, S. Massidda, M. Peter, W. Sadowski, H. J. Scheel, A. Shukla, A. K. Singh, and E. Walker, Phys. Rev. B 43, 7810 (1991).

J. Bardeen, L. N. Cooper, and J. R. Schrieffer, Phys. Rev. 108, 1175 (1957).
J. Bardeen and M. P. Stephen, Phys. Rev. A 140, 1197 (1965).
J. Bardeen, L. N. Cooper and J. R. Schrieffer, Phys. Rev. B 62, 6665 (2000).
R. Bar-Deroma, J. Felsteiner, R. Brener, J. Ashkenazi, and D. van der Marel, Phys. Rev. B 45, 2361 (1992).
C. Barlingay, V. Garcia-Vazquez, C. M. Falco, S.Mazumdar, and S. H. Risbud, Phys. Rev. B 41, 4797 (1990).
A. Barone and G. Paterno, "Physics and Applications of the Josephson Effect," Wiley, New York, 1982.
S. E. Barrett, D. J. Durand, C. H. Pennington, C. P. Slichter, T. A. Friedmann, J. P. Rice, and D. M. Ginsberg, Phys. Rev. B 41, 6283 (1990).
S. E. Barrett, J. A. Martindale, D. J. Durand, C. H. Pennington, C. P. Slichter, T. A. Friedmann, J. P. Rice, and D. M. Ginsberg, Phys. Rev. Lett. 66, 108 (1991).
J. C. Barry, Z. Iqbal, B. L. Ramakrishna, H. Eck-hardt, F. Reidinger, and R. Sharma, Appl. Phys.Lett. No. 71.70-b (1989).
K. Bartkowski, R. Horyn, A. J. Zaleski, Z. Bukowski, M. Horobiowski, C. Marucha, J. Rafalowicz, K. Rogacki, A. Stepien-Damm, C. Sulkowski, E. Trojnar, and J. Klamut, Phys. Status Solidi 103, K 37 (1987).
D. N. Basov, R. Liang, D. A. Bonn, W. N. Hardy, B. Dabrowski, M. Quijada, D. B. tanner, J. P. Rice, D. M. Grinsberg and T. Timusk, Phys. Rev. Lett. 74, 598 (1995).
F. E. Bates, Phys. Rev. B 39, 322 (1989).
B. Batlogg, A. P. Ramirez, R. J. Cava, R. B. van Dover, and E. A. Reitman, Phys. Rev. B 35, 5340 (1987).
B. Batlogg, R. J. Cava, L. W. Rupp, Jr., A. M. Mujsce, J. J. Krajewski, J. P. Remeika, W. F. Peck, Jr., A. S. Cooper, and G. P. Espinosa, Phys. Rev. Lett. 61, 1670 (1988).
B. W. Batterman and C. S. Barrett, Phys. Rev. Lett. 13, 390 (1964).
G. Baym and C. Pethick, "Landau Fermi–Liquid Theory," Wiley, New York, 1991.
C. P. Bean, Phys. Rev. Lett. 8, 250 (1962).
C. P. Bean, Rev. Mod. Phys. 36, 31 (1964).
M. R. Beasley, R. Labusch, and W. W. Webb, Phys. Rev. 181, 682 (1969).
J. G. Bednorz and K. A. Miiller, Z. Phys. B 64, 189 (1986).
J. G. Bednorz and K. A. Muller (Eds.), "Earlier and Recent Aspects of Superconductivity," Springer-Verlag, Berlin, 1990.
C. W. J. Beenakker and H. van Houten, Phys. Rev.Lett. 66, 3056 (1991).
V. P. Belash, E. Z. Kurmaev, and S. A. Nemnonov, Fiz. Met. Metalloved 37, 659 (1974).
S. Behnia, K. Behnia, and A. Deluzet, Phys. Rev. Lett. 81 4728 (1998)
D. Belitz, in "High Temperature Superconductivity" (J. W. Lynn, Ed.), Chap. 2, Springer-Verlag, Berlin, 1990.
R. Benedek and H.-B. Schuttler, Phys. Rev. B 41, 1789 (1990).
M. A. Beno, L. Soderholm, D. W. Capone II, D. G. Hinks, J. D. Jorgensen, J. D. Grace, I. K. Schuller, C. U. Segre, and K. Zhang, Appl. Phys. Lett. 51,57 (1987).
V. L. Berezinskii, Sov. Phys. JETP 34, 610 (1972).
D. D. Berkley, E. F. Skelton, N. E. Moulton, M. S. Osofsky, W. T. Lechter, V. M. Browning, and D. H. Liebenberg, Phys. Rev. B 47, 5524 (1993).
A. J. Berlinsky, C. Kallin, G. Rose, and A.-C. Shi, Phys. Rev. B 48, 4074 (1993).
R. Berman and D. K. C. MacDonald, Proc. R. Soc. London Ser. A 211, 122 (1952).
R. Beyers and T. M. Shaw, Solid State Phys. 42, 135 (1989).
R. Beyers and B. T. Ahn, Annu. Rev. Mater. Sci. 21, 335 (1991).
R. Bhagavatula, C. Ebner, and C. Jayaprakash, Phys. Rev. B 45, 4774 (1992).
K. V. Bhagwat and P. Chaddah, Physica C 166, 1 (1990).
K. V. Bhagwat and P. Chaddah, Physica C 190C, 444 (1992).
A. Bharathi, C. S. Sundar, W. Y. Ching, Y. C. Jean, P. H. Hor, Y. Y. Xue, and C. W. Chu, Phys. Rev. B 42, 10199 (1990).
A. K. Bhatnagar, R. Pan, D. G. Naugle, P. J. Sqattrito, A. Clearfleld, Z. Z. Sheng, Q. A. Shams, and A. M. Hermann, Solid State Commun. 73, 53 (1990).
R. N. Bhatt, Phys. Rev. B 16, 1915 (1977).
R. N. Bhatt, Phys. Rev. B 17, 2947 (1978).
A. Bhattacharya and C. S. Wang, Phys. Rev. B. 45, 10826 (1992).
A. Bhattacharya, I. Zutic, O. T. Valls, A. M. Goldman. U. Welp, and B. Veal, Phys. Rev. Lett. 82, 3132 (1999).

C. P. Bidinosti, W. N. Hardy, A. D. Bonn, and R. Liang, Phys. Rev. Lett. 83, 3277 (1999).

J. B. Bieri and K. Maki, Phys. Rev. B 42, 4854 (1990).

B. D. Biggs, M. N. Kunchur, J. J. Lin, S. J. Poon, T. R. Askew, R. B. Flippen, M. A. Subramanian, J. Gopalakrishnan, and A. W. Sleight, Phys. Rev. B39, 7309 (1989).

S. J. L. Billinge, G. H. Kwei, and J. D. Thompson, in "Strongly Correlated Electronic Materials" (K. S. Bedell, Ed.) Addison-Wesley, New York, 1994.

K. Binder and A. P. Young, Rev. Mod. Phys. 58, 801 (1986).

B. Binnig, A. C. Castellano, M. De Santis, P. Rudolf, P. Lagarde, A. M. Frank, and A. Marcelli, Solid State Commun. 63, 1009 (1980).

M. A. Biondi and M. P. Garfunkel, Phys. Rev. 116,853 (1959).

R. J. Birgeneau, C. Y. Chen, D. R. Gabbe, H. P. Jenssen, M. A. Kastner, C. J. Peters, P. J. Picone, T. Thio, T. R. Thurston, H. L. Tuller, A. D. Axe, P. Boni, and G. Shirane, Phys. Rev. Lett. 59, 1329 (1987).

P. Birrer, F. N. Gygax, B. Hitti, E. Lippelt, A. Schenck, M. Weber, D. Cattani, J. Cors, M. Decroux, and O. Fischer, Phys. Rev. B 48, 15689 (1993).

D. Bishop, C. M. Varma, B. Batlogg, E. Bucher, Z. Fisk, and J. L. Smith, Phys. Rev. Lett. 53, 1009 (1984).

A. Biswas, P. Fournier, M. M. Qazilbash, V. N. Smolyaninova, H. Balci, and R. L. Greene, Phys. Rev. Lett. 88 207004 (2002).

F. Bitter, Phys. Rev. 38, 1903 (1931).

B. L. Blackford and R. H. March, Canad. J. Phys. 46, 141 (1968).

H. A. Blackstead, J. Supercond. 5, 67 (1992).

H. A. Blackstead, Phys. Rev. B 47, 11411 (1993).

G. Blatter, J. Rhyner, and V. M. Vinokur, Phys. Rev.B 43, 7826 (1991a).

G. Blatter, V. B. Geshkenbein, and V. M. Vinokur, Phys. Rev. Lett. 66, 3297 (1991b). G. Blatter, B. I. Ivlev, and J. Rhyner, Phys. Rev. Lett. 66, 2392 (1991c).

G. Blatter and B. Ivlev, Phys. Rev. Lett. 70, 2621 (1993).

K. W. Blazey, K. A. Miiller, J. G. Bednorz, W. Berlinger, G. Amoretti, E. Buluggiu, A. Vera, and F. C. Matacotta, Phys. Rev. B 36, 7241 (1987).

J. E. BJendell, C. K. Chiang, D. C. Cranmer, S. W. Freiman, E. R. Fuller, Jr., E. Drescher-Krasicka, W. L. Johnson, H. M. Ledbetter, L. H. Bennett, L. J. Swartzendruber, R. B. Marinenko, R. L. Mykleburst, D. S. Bright, and D. E. Newbury, ACS Symp. Ser. 557, 240 (1987).

N. Bluzer, Phys. Rev. B 44, 10222 (1991).

G. S. Boebinger, T. T. M. Palstra, A. Passner, M. J. Rosseinsky, D. W. Murphy, and I. I. Mazin, Phys. Rev. B 46, 5876 (1992).

C. A. Bolle, P. I. Gammel, D. G. Grier, C. A. Murray, D. J. Bishop, D. B. Mitzi, and A. Kapitulnik, Phys. Rev. Lett. 66, 112 (1991).

I. Bonalde, B. D. Yanoff, M. B. Salamon, D. J. Van Harlingen, E. M. E. Chia, Z. Q. Mao, and Y. Maeno, Physical Review Letters 85 4775 (2000).

I. Bonalde, B. D. Yanoff, D. J. Van Harlingen, M. B. Salamon, and Y. Maeno, Physica C 341–348, 1695 (2000).

I. Bonalde, B. D. Yanoff, D. J. Van Harlingen, M. B. Salamon, and Y. Maeno, Superconductivity and its Applications (Amsterdam) 341, 1695 (2000)

J. E. Bonevich, K. Harada, T. Matsuda, H. Kasai, T. Yoshida, G. Pozzi, and A. Tonomura, Phys. Rev. Lett. 70, 2952 (1993).

P. Boni, J. D. Axe, G. Shirane, R. J. Birgeneau, D. R. Gabbe, H. P. Jenssen, M. A. Kastner, C. J. Peters, P. J. Picone, and T. R. Thurston, Phys. Rev. B 38, 185 (1988).

E. Bonjour, R. Calemczuk, J. Y. Henry, and A. F. Khoder, Phys. Rev. B 43, 106 (1991).

D. A. Bonn, A. H. O'Reilly, J. E. Greedan, C. V. Stager, T. Timusk, K. Kamaras, and D. B. Tanner, Phys. Rev. B 37, 1574 (1988).

D. A. Bonn, S. Kamal, K. Zhang, R. Liang, D. J. Baar, E. Klein, and W. N. Hardy, Phys. Rev. B 50, 4051 (1994).

N. Bontemps, D. Davidov, P. Monod, and R. Even, Phys. Rev. B 43, 11512 (1991).

P. Boolchand, C. Blue, K. Elgaid, I. Zitkovsky, D. McDaniel, W. Huff, B. Goodman, G. Lemon, D. E. Farrell, and B. S. Chandrasekhar, Phys. Rev. B 38, 11313 (1988).

P. Boolchand, S. Pradhan, Y. Wu, M. Abdelgadir, W. Huff, D. Farrell, R. Coussement, and D. McDaniel, Phys. Rev. B 45, 921 (1992).

P. Bordet, C. Chaillout, J. Chenavas, J. L. Hodeau, M. Marezio, J. Karpinski, and E. Kaldis, Nature (London) 334, 596 (1988).

H. J. Bornemann, D. E. Morris, C. Steinleitner, and G. Czjzek, Phys. Rev. B 44, 12567 (1991).
F. Borsa, A. Rigamonti, M. Corti, J. Ziolo, O. Hyun, and D. R. Torgeson, Phys. Rev. Lett. 68, 698 (1992).
I. Bose, Phys. Rev. B 43, 13602 (1991).
R. Bottner, N. Schroeder, E. Dietz, U. Gerhardt, W. Assmus, and J. Kowalewski, Phys. Rev. B 41, 8679 (1990).
L. Bottyan, B. Molnar, D. L. Nagy, I. S. Sziics, J. Toth, J. Dengler, G. Ritter, and J. Schober, Phys. Rev. B 38, 11373 (1988).
F. Bouquet, Y. Wang, R. A. Fisher, D. G. Hinks, J. D. Jorgensen, A. Junot, and N. E. Phillips, Europhys. Lett. 56, 856 (2001).
R. Boyn, K. Lobe, H.-U. Habermeier, and N. PruB, Physica C 181, 75 (1991).
I. Bozovic, J. Supercond. 4, 193 (1991).
A. I. Braginski, Physica C 780, 642 (1991).
B. H. Brandow, J. Solid State Chem. 88, 28 (1990).
B. Brandow, International Journal of Modern Physics B 13 3482 (1999).
E. H. Brandt, Physica C 162C–164C, 1167 (1989).
E. H. Brandt, Physica B 165–166, 1129 (1990); Int. Conf. Low Temperature Phys., Brighton, U. K., August 1990.
E. H. Brandt, Phys. Rev. Lett. 67, 2219 (1991).
E. H. Brandt, Phys. Rev. Lett. 69, 1105 (1992).
E. H. Brandt, Rep. on Prog. in Phys. 58, 1465 (1995).
A. Brass, H. J. Jensen, and A. J. Berlinsky, Phys. Rev.B 39, 102 (1989).
A. Brass and H. J. Jensen, Phys. Rev. B 39, 9587 (1989).
D. A. Brawner, A. Schilling, H. R. Ott, R. J. Haug, K. Ploog, and K. von Klitzing, Phys. Rev. Lett. 71, 785 (1993).
Y. J. M. Brechet, B. Doucot, H. J. Jensen, and A.-C. Shi, Phys. Rev. B 42, 2116 (1990).
E. Brezin, A. Fujita, and S. Hikami, Phys. Rev. Lett.65, 1949 (1990).
G. Briceno, M. F. Crommie, and A. Zettl, Phys. Rev. Lett. 66, 2164 (1991).
M. B. Brodsky, R. C. Dynes, K. Kitazawa, and H. L. Tuller (Eds.), "High Temperature Superconductors," Vol. 99, Materials Research Society, Pittsburgh, (1988).
C. Broholm, G. Aeppli, R. N. Kleiman, D. R. Harshman, D. J. Bishop, E. Bucher, D. LI. Williams, E. J. Ansaldo, and R. H. Heffner, Phys. Rev. Lett. 65, 2062 (1990).
N. B. Brookes, A. J. Viescas, P. D. Johnson, J. P. Remeika, A. S. Cooper, and N. V. Smith, Phys. Rev. B 39, 2736 (1989).
J. S. Brooks, C. C. Agosta, S. J. Klepper, M. Tokumoto, N. Kinoshita, H. Anzai, S. Uji, H. Aoki, A. S. Perel, G. J. Athas, and D. A. Howe, Phys. Rev. Lett. 69, 156 (1992).
S. D. Brorson, A. Kazeroonian, J. S. Moodera, D. W. Face, T. K. Cheng, E. P. Ippen, M. S. Dresselhaus, and G. Dresselhaus, Phys. Rev. Lett. 64, 2172 (1990).
P. R. Broussard, Phys. Rev. B 43, 2783 (1991).
P. Brull, D. Kirchgassner, and P. Liederer, Physica C 182, 339 (1991).
T. Brun, M. Grimsditch, K. E. Gray, R. Bhadra, V. Maroni, and C. K. Loong, Phys. Rev. B 55, 8837 (1987).
L. C. Brunei, S. G. Louie, G. Martinez, S. Labdi, and H. Raffy, Phys. Rev. Lett. 66, 1346 (1991).
L. J. Bucholtz, and G. Zwicknagl, Phys. Rev. B 23, 5788 (1981).
W. Buckel, "Superconductivity, Fundamentals and Applications," VCH, Weinheim, Germany, (1991).
J. I. Budnick, A. Golnik, Ch. Niedermayer, E. Recknagel, M. Rossmanith, A. Weidinger, B. Chamber-land, M. Filipkowski, and D. P. Yang, Phys. Lett. A 124, 103 (1987).
L. N. Bulaevskii, Zh. Eksp. Teor. Fiz. 64, 2241 (1973); Sov. Phys. JETP (Engl. Trans.) 37, 1133 (1988).
L. N. Bulaevskii, O. V. Dolgov, and M. O. Ptitsyn, Phys. Rev. B 38, 11290 (1988).
L. N. Bulaevskii and M. V. Zyskin, Phys. Rev. B 42, 10230 (1990).
L. N. Bulaevskii, M. Ledvij, and V. G. Kogan, Phys. Rev. B 46, 366, 11807 (1992).
N. Bulut and D. J. Scalapino, Phys. Rev. B 45, 2371 (1992).
G. Burns, P. Strobel, G. V. Chandrashekhar, F. H. Dacol, F. Holtzberg, and M. W. Shafer, Phys. Rev. B 39, 2245 (1989).
G. Burns and A. M. Glazer, "Space Groups for Solid State Scientists," Academic Press, San Diego, 1990.
G. Burns, "High Temperature Superconductivity: An Introduction," Academic Press, Boston, 1992.
M. J. Burns, Phys. Rev. B 40, 5473 (1989).
R. Busch, G. Ries, H. Werthner, G. Kreiselmeyer, and G. Saemann-Ischenko, Phys. Rev. Lett. 69, 522 (1992).

A. Bussmann-Holder and A. R. Bishop, Phys. Rev. B44, 2853 (1991).
A. I. Buzdin, Phys. Rev. B 47, 11416 (1993).
B. Cabrera, C. E. Cunningham, and D. Saroff, Phys. Rev. Lett. 62, 2040 (1989).
Z.-X. Cai and D. O. Welch, Phys. Rev. B 45, 2385 (1992).
J. Callaway, "Energy Band Theory," New York, 1964.
H. B. Callen, "Thermodynamics and Introduction to Thermostatics," Wiley, New York, 1964.
I. A. Campbell, L. Fruchter, and R. Cabanel, Phys. Rev. Lett. 64, 1561 (1990).
J. C. Campuzano, G. Jennings, M. Faiz, L. Beaulaigue, B. W. Veal, J. Z. Liu, A. P. Paulikas. K. Vandervoort, H. Claus, R. S. List, A. J. Arko and R. L. Bartlett, Phys. Rev. Lett. 64, 2308 (1990).
J. C. Campuzano, L. C. Smedskjaer, R. S. Benedek, G. Jennings, and A. J. Bansil. Phys. Rev. B 43, 2788 (1991).
P. C. Canfield, S. L. Bud'ko, and B. K. Cho, Physica C, 262, (1996).
P. C. Canfield, S. L. Bud'ko, B. K. Cho, A. Lacerda, D. Farrell, E. Johnston-Halperin, V. A. Kalasky, and V. L. Prokosky, Phys. Rev. B 55, 970 (1997).
P. C. Canfield, S. L. Bud'ko, and D. K. Finnemore, Physica C385, 1, (2003)
P. C. Canfield, Chap. 5, Section G in Handbook of Superconductivity, C. P. Poole, Jr., Editor, Academic Press, Boston, (2000).
J. J. Capponi, C. Chaillout, A. W. Hewat, P. LeJay, M. Marezio, N. Nguyen, B. Raveau, J. L. Soubeyroux, J. L. Tholence, and R. Tournier Europhys. Lett. 3, 1301 (1987).
J. P. Carbote, Rev. of Mod. Phys. 62, 1027 (1990).
J. P. Carbotte, Rev. Mod. Phys. 62, 1027 (1990)
J. P. Carbotte, Reviews of Modern Physics 62 1027 (1990).
J. R. Carbotte and C. Jiang, Phys. Rev. B 48, 4231 (1993).
J. P. Carbotte, and F. Marsiglio, *Phys*. of Superconductors 1 233 (2003).
G. Carneiro, Phys. Rev. B 45, 2391 (1992)
P. Carretta and M. Corti, Phys. Rev. Lett. 68, 1236 (1992).
P. Carretta, M. Corti, A. Rigamonti, R. De Renzi, F. Licci, C. Paris, L. Bonoldi, M. Sparpaglione, and L. Zini, Physica C 191C, 97 (1992).
A. Carrington, I. J. Bonalde, R. Prozorov, R. W. Giannetta, A. M. Kini., J. Schlueter, H. H. Wang, U. Geiser, and J. M. Williams, Phys. Rev. Lett. 83, 4172 (1999).
A. Carrington, R. W. Giannetta, J. T. Kim, and J. Giapintzakis, Phys. Rev. B: Condens. Matter Mater. Phys. 59 R14173 (1999).
A. Carrington, F. Manzano, R. Prozorov, R. W. Giannetta, N. Kameda, and T. Tamegai, Phys. Rev. Lett. 86 1074 (2001)
R. J. Cava, B. Batlogg, T. Siegrist, J. J. Krajewski, W. F. Peck Jr., S. Carter, R. J. Felder, H. Takagi and R. B. van Dover, Phys. Rev. B 49, 12384 (1994)
R. J. Cava, B. Batlogg, J. J. Krajewski, R. Farrow, L. W. Rupp, Jr., A. E. White, K. Short, W. F. Pick, and T. Kometani, Nature 332,814 (1988).
R. J. Cava, A. Santoro, D. W. Johnson, Jr. and W. W. Rhodes, Phys. Rev. B 35, 6716 (1987)
R. J. Cava, Nature 367, 252 (1994).
M.-C. Cha, M. P. A. Fisher, S. M. Girvin, M. Wallin, and A. P. Young, Phys. Rev. B 44, 6883 (1991).
P. Chaddah, K. V. Bhagwat, and G. Raulkumaer, Physica C 159C, 570 (1989).
P. Chaddah and K. Bhagwat, in "High Temperature Superconductivity" (S. K. Mali and S.S. Shah, Eds.), Nova Science, New York, 1992.
C. Chaillout, J. P. Remeika, A. Santoro, and M. Marezio, Solid State. Commun. 36, 829 (1985).
T. K. Chaki and M. Rubinstein, Phys. Rev. B 36, 7259 (1987).
B. Chakraborty, Phys. Rev. B 43. 378 (1991).
S. Chakravarty, B. I. Halperin, and D. R. Nelson, Phys. Rev. Lett. 60, 1057 (1988).
S. Chakravarty, B. I. Ivlev, and Y. N. Ovchinnkov, Phys. Rev. B 42, 2143 (1990).
S. Chakravarty, A. Sudbo, P. W. Anderson, and S. Strong, Science 261, 337 (1993).
L. P. Chan, D. R. Harshman, K. G. Lynn, S. Massidda, and B. D. Mitzi, Phys. Rev. Lett. 67, 1350 (1991).
B. S. Chandrasekhar, and D. Einzel, Annalen der Physik (Berlin, Germany) 2 535 (1993).
B. S. Chandrasekhar, Appl. Phys. Lett. 1, 1 (1962).
C. L. Chang, A. Kleinhammes, W. G. Moulton, and L. R. Testardi, Phys. Rev. B 41, 11564 (1990).
C. L. Chang, C. V. Tomy, D. McK Paul and C. Ritter, Phys. Rev. B 54, 9031, (1996).

M. Charalambous, J. Chaussy, and P. Lejay, Phys. Rev. B 45, 5091 (1992).

T. Chattopadhyay, P. J. Brown, B. C. Sales, L. A. Boatner, H. A. Mook, and H. Maletta, Phys. Rev. B 40, 2624 (1989).

P. Chaudhari, R. T. Collins, P. Freitas, R. J. Gambino, J. R. Kirtley, R. H. Koch, R. B. Laibowitz, F. K. LeGoues, T. R. McGuire, T. Penney, Z. Schlesinger, A. P. Segmiiller, S. Foner, and E. J. McNiff, Jr., Phys. Rev. B 36, 8903 (1987).

S. V. Chekalin, V. M. Farztdinov, V. V. Golovlyov, V. S. Letokhov, Yu. E. Lozovlk, Yu. A. Matveets, and A. G. Stepanov, Phys. Rev. Lett. 67, 3860 (1991).

D.-X. Chen, R. B. Goldfarb, J. Nogues, and K. V. Rao, J. Appl. Phys. 63, 980 (1988).

G. H. Chen, J. H. Wang, D. N. Zheng, Y. F. Yan, S. L. Jia, Q. S. Yang, Y. M. Ni, and Z. X. Zhao, Mod. Phys. Lett. B 3, 295 (1989).

H. Chen and J. Callaway, Phys. Rev. B 40, 8800 (1989).

C. H. Chen, in "Physical Properties of High Temperature Superconductors" (D. M. Ginsberg, Ed.), Vol. 2, Chap. 4, World Scientific, Singapore, 1990.

J. H. Chen, Solid State Commun. 75, 557, 563, 567, 573 (1990a); Phys. Rev. B 42, 3952, 3957 (1990b).

Q. Chen, I. Kosztin, and K. Levin, Phys. Rev. Lett. 85 2801 (2000).

D.-X. Chen, A. Sanchez, J. Nogues, and J. S. Munoz, Phys. Rev. B 41, 9510 (1990a).

D.-X. Chen, A. Sanchez, and J. Munoz, J. Appl. Phys. 67, 3430 (1990b).

D.-X. Chen, A. Sanchez, T. Puig, L. M. Martinez, and J. S. Munoz, Physica C 168C, 652 (1990c).

C. Y. Chen, R. J. Birgeneau, M. A. Kastner, N. W. Preyer, and T. Thio, Phys. Rev. B 43, 392 (1991).

D.-X. Chen, J. A. Brug, and R. B. Goldfarb, IEEE Trans. Magn. 27, 3601 (1991).

D.-X. Chen and A. Sanchez, J. Appl. Phys. 70, 5463 (1991).

C.-C. Chen, S. P. Kelty, and C. M. Lieber, Science 253, 886 (1991).

B. Chen and J. Dong, Phys. Rev. B 44, 10206 (1991).

C. T. Chen, L. H. Tjeng, J. Kwo, H. L. Kao, P. Rudolf, F. Sette, and R. M. Fleming, Phys. Rev. Lett. 68, 2543 (1992).

T.-P. Chen, Z. X. Zhao, H. D. Yang, E. L. Wolf, R. N. Shelton, and P. Klavins, Phys. Rev. 45, 7945 (1992).

Q. Y. Chen, in "Magnetic Susceptibility of Superconductors and other Spin Systems" (R. A. Hein, T. L. Francavilla, and D. H. Liebenberg, Eds.), Plenum, New York, (1992).

L. Chengren and D. C. Larbalestier, Cryogenics 27,171 (1987).

S.-W. Cheong, S. E. Brown, Z. Fisk, R. S. Kwok, J. D. Thompson, E. Zirngiebl, G. Gruner, D. E. Peterson, G. L. Wells, R. B. Schwarz, and J. R. Cooper, Phys. Rev. B 36, 3913 (1987).

S.-W. Cheong, M. F. Hundley, J. D. Thompson, and Z. Fisk, Phys. Rev. B 39, 6567 (1989a).

S.-W. Cheong, Z. Fisk, J. D. Thompson, and R. B. Schwarz, Physica C 159C, 407 (1989b).

H.-F. Cheung, Y. Gefen, E. K. Riedel, and W.-H. Shih, Phys. Rev. B 37, 6050 (1988).

X.-F. Chen, M. J. Marone, G. X. Tessema, M. J. Skove, M. V. Nevitt, D. J. Miller, and B. W. Veal, Phys. Rev. B 48, 1254 (1993).

C. C. Chi and C. Vanneste, Phys. Rev. B 42, 9875 (1990).

E. E. M. Chia, I. Bonalde, B. D. Yanoff, D. J. Van Harlingen, M. B. Salamon, S. I. Lee, and H. J. Kirn, Journal of Magnetism and Magnetic Materials 226; 230 (2001)

E. E. M. Chia, D. J. Van Harlingen, M. B. Salamon, B. D. Yanoff, I. Bonalde, and J. L. Sarrao, Phys. Rev. B 67 14527 (2003)

E. E. M. Chia, W. Cheong, T. Park, M. B. Salamon, E-M. Choi, and S. Lee, Phys. Rev. B 72 214505 (2005)

T. R. Chien, T. W. Jing, N. P. Ong, and Z. Z. Wang, Phys. Rev. Lett. 66, 3075 (1991).

B. K. Cho, P. C. Canfield, and D. C. Johnston, Phys. Rev. B 52 3676 (1995).

B. K. Cho, P. C. Canfield, and D. C. Johnston, Phys. Rev. B 52 R3844 (1995).

B. K. Cho, P. C. Canfield, and D. C. Johnston, Phys. Rev. B 53 8499 (1996).

J. H. Cho, F. Borsa, D. C. Johnston, and D. R. Torgeson, Phys. Rev. B 46, 3179 (1992).

H. J. Choi, D. Roundy, H. Sun M. L. Cohen, and S. G. Louie, Nature 418, 758, (2002).

M. Y. Choi and S. Kirn, Phys. Rev. B 44, 10411 (1991).

M. Y. Choi, C. Lee, and J. Lee, Phys. Rev. B 46, 1489 (1992).

C. W. Chu, P. H. Hor, R. L. Meng, L. Gao, and Z. J. Huang, Science 255, 567 (1987).

C. W. Chu, P. H. Hor, R. L. Meng, L. Gao, Z. J. Huang, and Y. Q. Wang, Phys. Rev. Lett. 58, 405 (1987).
C. W. Chu, P. H. Hor, R. L. Meng, L. Gao, Z. J. Huang, J. Bechtold, M. K. Wu, and C. Y. Huang, Mater. Res. Soc. Symp. Proc. 99, 15 (1987).
C. W. Chu, J. Bechtold, L. Gao, P. H. Hor, Z. J. Huang, R. L. Meng, Y. Y. Sun, Y. Q. Wang, and Y. Y. Xue, Phys. Rev. Lett. 60, 941 (1988).
C. W. Chu, L. Gao, F. Chen, Z. J. Huang, R. L. Meng, and Y. Y. Xue, Nature 565, 323 (1993b).
C. W. Chu, J. Superconductivity 7, 1 (1994).
C. W. Chu, "Unusual High Temperature Superconductors," Proc. Symp. Quantum Theory of Real Materials, Berkeley, California, Aug. (1994).
E. M. Chudnovsky, Phys. Rev. B 40, 11355 (1989).
E. M. Chudnovsky, Phys. Rev. Lett. 65, 3060 (1990).
E. M. Chudnovsky, Phys. Rev. B 43, 7831 (1991).
F. Chung and S. Sternberg, Amer. Scientist 81, 56 (1993).
L. Civale, A. D. Marwick, M. W. McElfresh, T. K. Worthington, A. P. Malozemoff, F. H. Holtzberg, J. R. Thompson, and M. A. Kirk, Phys. Rev. Lett. 65, 1164 (1990).
L. Civale, T. K. Worthington, and A. Gupta, Phys. Rev. B 43, 5425 (1991).
L. Civale, A. D. Marwick, T. K. Worthington, M. A. Kirk, J. R. Thompson, L. Krusin-Elbaum, Y. Sun, J. R. Clem, and F. Holtzberg, Phys. Rev. Lett. 67, 648 (1991).
J. H. Claassen, J. F. Evetts, R. E. Somekh, and Z. H. Barber, Phys. Rev. B 44, 9605 (1991).
J. Clarke, Phys. Rev. Lett. 28, 1363 (1972).
J. Clarke and J. L. Paterson, J. Low Temp. Phys. 15, 491 (1974).
J. Clayhold, N. P. Ong, P. H. Hor and C. W. Chu, Phys. Rev. B 38, 7016 (1988).
J. R. Clem, Physica C 162–164, 1137 (1989).
J. R. Clem and M. W. Coffey, Phys. Rev. B 42, 6209 (1990).
J. R. Clem and M. W. Coffey, Physica C185–189, 1915 (1991).
J. R. Clem, Phys. Rev. B 43, 7837 (1991).
J. Clem, "A. C. Losses in Type-II Superconductors, Chap, in Magnetic Susceptibility of Superconductors and Other Spin Systems," (R. A. Hein, T. L. Francavilla, and D. H. Liebenberg, Eds.), Plenum, New York, 1992.
J. R. Clem and Z. Hao, Phys. Rev. B 48, 13774 (1993).
A. M. Clogston and J. Jaccarino, Phys. Rev. 121, 1357 (1961).
A. M. Clogston, Phys. Rev. Lett. 9, 266 (1962).
M. W. Coffey and J. R. Clem, Phys. Rev. B 44, 6903 (1991).
M. W. Coffey and J. R. Clem, Phys. Rev. B 45, 9872 (1992)
M. W. Coffey, Phys. Rev. B 46, 567 (1992).
M. W. Coffey and J. R. Clem, Phys. Rev. Lett. 67, 386 (1991); Phys. Rev. B 44, 6903 (1991).
M. W. Coffey, Phys. Rev. B 47, 12284 (1993).
M. W. Coffey, Phys. Rev. B 49, 9774 (1994).
T. Coffey, Z. Bayindir, J. F. DeCarolis, M. Bennett, G. Esper, and C. C. Agosta Rev. Sci. Inst. 71 4600 (2000).
R. W. Cohen, G. D. Cody, and L. J. Vieland, in Electronic Density of States, NBS Spec. Publ. (U.S.) 323, 767 (1971).
M. L. Cohen, in "Novel Superconductivity" (S. A.Wolf and V. Z. Kresin, Eds.), p. 1095. Plenum, New York, 1987. M. L. Cohen and D. R. Penn, Phys. Rev. B 42, 8702 (1990).
J. L. Cohn, S. A. Wolf, V. Selvamanickam, and K. Salama, Phys. Rev. Lett. 66, 1098 (1991).
M. B. Cohn, M. S. Rzchowski, S. P. Benz, and C. J. Lobb, Phys. Rev. B 43, 12823 (1991).
J. L. Cohn, S. A. Wolf, and T. A. Vanderah, Phys. Rev. B 45, 511 (1992).
J. L. Cohn, E. F. Skelton, S. A. Wolf, J. Z. Liu, and R. N. Shelton, Phys. Rev. B 45, 13144 (1992).
J. L. Cohn, E. F. Skelton, S. A. Wolf, J. Z. Liu, and R. N. Shelton, Phys. Rev. B 45, 13140 (1992).
B. R. Coles, Cont. Phys. 28, 143 (1987).
G. Collin and R. Comes, C. R. Acad. Sci. Paris 304, 1159 (1987).
R. T. Collins, Z. Schlesinger, F. Holtzberg, and C. Feild, Phys. Rev. Lett. 63, 422 (1989).
R. T. Collins, Z. Schlesinger, G. V. Chandrasehekhar, and M. W. Shafer, Phys. Rev. B 39, 2251 (1989).
R. T. Collins, Z. Schlesinger, F. Holtzberg, P. Chaudhari, and C. Feild, Phys. Rev. B 39, 6571 (1989).
R. T. Collins, Z. Schlesinger, F. Holtzberg, C. Feild, U. Welp, G. W. Crabtree, J. Z. Liu, and Y. Fang, Phys. Rev. B, 43, 8701 (1991).

S. J. Collocott, R. Driver, and E. R. Vance, Phys. Rev.B 41, 6329 (1990a).
S. J. Collocott, N. Sawides, and E. R. Vance, Phys. Rev. B 42, 4794 (1990b).
S. Collocott, R. Driver, and C. Andrikidis, Phys. Rev. B 45, 945 (1992).
R. Combescot, Phys. Rev. Lett. 67, 148 (1991a); Phys. Rev. B 42, 7810 (1991b).
E. Compans and F. Baumann, Jpn. J. Appl. Phys. 26 Suppl. 3, 805 (1987).
L. D. Cooley, G. Stejic, and D. C. Labalestier, Phys. Rev. B 46, 2964 (1992).
J. R. Cooper, A. Carrington, P.J. Meeson, E. A. Yelland, N. E. Hussey, L. Balicas, S. Tajima, S. Lee, S. M. Kazakov, and J. Karpinski, Physiva C 385, 75 (2003).
L. N. Cooper, Phys. Rev. 104, 1189 (1956).
J. R. Cooper, Phys. Rev. B: Cond. Matt. 54 R3753 (1996).
C. Coretsopoulos, H. C. Lee, E. Ramli, L. Ravea, T. B. Rauchfuss, and E. Oldfield, Phys. Rev. B 39.781 (1989).
D. L. Cox and M. B. Maple, Phys. Today, February 1955. p. 32.
L. A. Curtiss and S. W. Tarn, J. Mater. Res. 3, 1209 (1988).
J. Costa-Quintana, F. Lopez-Aguilar, S. Balle, and R. Salvador, Phys. Rev. B 39, 9675 (1989).
L. Cota, L. Morales de la Garza, G. Hirata, L. Martinez, E. Orozco, E. Carrillo, A. MendooLJ. L. Albarran, J. Fuentes-Maya, J. L. Boldu, J. G. Perez-Ramirez, R. Perez, J. Reyes Gasga, M. An-los, and M. Jose-Yacaman, J. Mater. Res. 3, 417 (1988).
R. Cote and A. Griffin, Phys. Rev. B 48, 10404 (1993).
F. A. Cotton, "Chemical Applications of Group Theory." Wiley, New York, 1963.
D. E. Cox and A. W. Sleight, Solid State Commun. 19, 969 (1976).
D. E. Cox and A. W. Sleight, Acta Cryst. B 35, 1 (1979).
D. L. Cox and M. B. Maple, Phys. Today, February 1995, p. 32.
G. W. Crabtree, J. Z. Liu, A. Umezawa, W. K. Kwok, C. H. Sowers, S. K. Malik, B.
W. Veal, D. J. Lam, M. B. Brodsky, and J. W. Downey, Phys. Rev. B36, 4021 (1987).
M. K. Crawford, G. Burns, G. V. Chandrashekhar, F. H. Dacol, W. E. Farneth, E. M. McCarron III, and R. J. Smalley, Phys. Rev. B 41, 8933 (1990a).
M. K. Crawford, G. Burns, G. V. Chandrashekhar, F. H. Dacol, W. E. Farneth, E. M. McCarron III, and R. J. Smalley, Solid State Commun. 73, 507 (1990b).
R. J. Creswick, H. A. Farach, C. P. Poole, Jr., "Introduction to Renormalization Group Methods in Physics," Wiley, New York, 1992.
M. Crisan, Phys. Lett. A 124, 195 (1987).
M. F. Crommie, A. Zettl, T. W. Barbee, III, and M. L. Cohen, Phys. Rev. B 37, 9734 (1988).
M. F. Crommie, G. Briceno, and A. Zettl, Physica C 162–164, 1397 (1989).
M. F. Crommie and A. Zettl, Phys. Rev. B 43, 408 (1991).
R. W. Cross and R. B. Goldfab, Appl. Phys. Lett. 58, 415 (1991).
J. E. Crow and N.-P. Ong, in "High Temperature Superconductivity" (J. W. Lynn, Ed.), Chap. 7, Springer-Verlag, Berlin, 1990.
M. A. Crusellas, J. Fontcuberta, S. Pinol, T. Grenet, and J. Beille, Physica C 180, 313 (1991).
A. M. Cucolo, R. Di Leo, P. Romano, L. F. Schneemeyer, and J. V. Waszczak, Phys. Rev. B 44, 2857 (1991).
S.-M. Cui and C.-H. Tsai, Phys. Rev. B 44, 12500 (1991).
J. C. Culbertson, U. Strom, S. A. Wolf, P. Skeath, E. J. West, and W. K. Burns, Phys. Rev. B 39, 12359 (1989).
J. C. Culbertson, U. Strom, S. A. Wolf, and W. W. Fuller, Phys. Rev. B 44, 9609 (1991).
L. A. Curtiss and S. W. Tarn, J. Mater. Res. 3, 1269 (1988).
L. L. Daeman, L. J. Campbell, and V. G. Kogan, Phys. Rev. B 46, 3631 (1992).
L. L. Daemen, L. J. Campbell, A. Yu Simonov, and V. G. Kogan, Phys. Rev. Lett. 70, 2948 (1993).
L. L. Daemen and A. W. Overhauser, Phys. Rev. B40, 10778 (1989).
D. Daguero, R. S. Gonnelli, G. A. Ummarino, V. A. Stepanov, J. Jun, S. M. Kazakov and J. Karpinski, Physica C 385, 255 (2003).
E. Dagotto, A. Moreo, R. Joynt, S. Bacci, and E. Gagliano, Phys. Rev. B 41, 2585, (1990).
E. Dagotto, Rev. Mod. Phys. 66, 763 (1994).
E. Dagotto, A. Moreo, F. Ortolani, D. Poilblanc, and J. Riera, Phys. Rev. B 45, 10741 (1992).
T. Dahm, and D. J. Scalapino, Phys. Rev. B 60 13125 (1999)

Y. Dalichaouch, M. B. Maple, J. Y. Chen, T. Kohara, C. Rossel, M. S. Torikachvili, and A. L. Giorgi, Phys. Rev. 41, 1829 (1990a).
Y. Dalichaouch, B, W. Lee, C. L. Seaman, J. T. Markert, and M. B. Maple, Phys. Rev. Lett. 64, 599 (1990b).
Y. Dalichaouch, B. W. Lee, S. E, Lambert, M. P. Maple, J. L. Smith, and Z. Fisk, Phys. Rev. B 43, 299 (1991).
C. Dasgupta and T. V. Ramakrishnan, Physica C 183C, 62 (1991).
T. Datta, C. P. Poole, Jr., H. A. Farach, C. Almasan, J. Estrada, D. U. Gubser, and S. A. Wolf, Phys. Rev. B 37, 7843 (1988).
M. Daumling and G. V. Chandrashekhar, Phys. Rev. B 46, 6422 (1992).
D. Davidov, P. Monod, and N. Bontemps, Phys. Rev. B 45, 8036 (1992).
M. C. de Andrade, C. C. Almasan, Y. Dalichaouch, and M. B. Maple, Physica C 184C, 378 (1991).
P. G. De Gennes, C. R. Acad. Sci. Paris, 247 1836, (1958).
P. G. De Gennes, Rev. Mod. Phys. 36, 225 (1964).
P. G. De Gennes, "Superconductivity of Metals and Alloys," Benjamin, New York, 1966.
L. Degiorgi, P. Wachter, G. Griiner, S.-M. Huang, J. Wiley, and R. B. Kaner, Phys. Rev. Lett. 69, 2987 (1992).
S. K. Dhar, R. Naragajan, Z. Hossain, B. Tominez, C. Godart, L. C. Gupta, and R. Vijayaraghavan, Solid State Commun. 98 985 (1996).
C. V. DeGrift, Rev. Sci. Instrum. 46 599 [25] (1975)
C. Dekker, W. Eidelloth, and R. H. Koch, Phys. Rev. Lett. 68, 3347 (1992).
O. L. de Lange and V. V. Gridin, Phys. Rev. B 46, 5735 (1992).
P. Delsing, K. K. Likharev, L. S. Kuzmin, and T. Claeson, Phys. Rev. Lett. 63, 1180, 1861 (1989).
P. Derrenagas, J. Stassis, A. I. Goldman, P. C. Canfield, and B. K. Cho, Physica, B212, (1995); Phys. Rev. B 53 8506, (1996).
H. Dersch and G. Blatter, Phys. Rev. B 38, 11391 (1988).
M. Desirant, and D. Shoenberg, Proceedings of the Physical Society, London 60 413 (1948).
S. M. DeSoto, C. P. Slichter, H. H. Wang, U. Geiser, and J. M. Williams, Phys. Rev. Lett. 70, 2956 (1993).
D. S. Dessau, B. O. Wells, Z.-X. Shen, W. E. Spicer, A. J. Arko, R. S. List, D. B. Mitzi, and A. Kapitul-nik, Phys. Rev. Lett. 66, 2160 (1991).
D. S. Dessau, Z.-X. Shen, B. O. Wells, D. M. King, W. E. Spicer, A. J. Arko, L. W. Lombardo, D. B. Mitzi, and A. Kapitulnik, Phys. Rev. B 45, 5095 (1992).
C. Detlefs, A. I. Goldman, C. Stassis, P. C. Canfield, B. K. Cho, J. P. Hill, and D. Gibbs, Phys. Rev. B 53 6355, (1996).
C. Detlefs, A. H. M. Z. Islam, A. I. Goldman, C. Stassis, P. C. Canfield, J. P. Hill, and D. Gibbs, Phys. Rev. B 55 R680, (1997).
C. Detlefs, F. Bourdarot, P. Burlet, P. Dervenagas, S. L. Bud'ko, and P. c. Canfield, Phys. Rev. B 61, 14916 (2000).
G. Deutscher and P. Chaudhari, Phys. Rev. B 44, 4664 (1991).
F. Devaux, A. Manthiram, and J. B. Goodenough, Phys. Rev. B 41, 8723 (1990).
F. W. de Wette, A. D. Kulkarni, J. Prade, U. Schroder, and W. Kress, Phys. Rev. B 42, 6707 (1990).
M. J. DeWeert, D. A. Papaconstantopoulos, and W. E. Pickett, Phys. Rev. B 39, 4235 (1989).
C. D. Dewhurst, S. S. James, N. Saha, R. Surdeanu, Y. Paltiel, E. Zeldov, and D. McK Paul; K. H. Muller and V. Narozhnyi (eds.) Rare Earth Transition Borocarbides (Nitrides): Superconducting, Magnetic and Normal State Properties, 347, Kluwer, (2001).
L. M. Dezaneti, Y. Y. Xue, Y. Y. Sun, K. Ross and C. W. Chu, Physica, C334, 123 (2002).
A. DiChiara, F. Fontana, G. Peluso, and F. Tafuri, Phys. Rev. B 44, 12026 (1991).
A. DiChiara, F. Fontana, G. Peluso, and F. Tafuri, Phys. Rev. B 48, 6695 (1993).
F. Diederich and R. L. Whetten, Ace. Chem. Res. 25, 119 (1992).
H.-Q. Ding, Phys. Rev. Lett. 68, 1927 (1992).
T. R. Dinger, T. K. Worthington, W. J. Gallagher, and R. L. Sandstrom, Phys. Rev. Lett. 58, 2687 (1987).
M. Divis, K. Schawrz, P. Blaha, G. Hilscher, M. Michor, and S. Khmelevski, Phys. Rev. B 62 6774, (2000).
M. Divis, M. Michor, S. Khmelevski, P. Blaha, G. Hilscher, and K. Schwarz, K. H. Muller and V. Narozhnyi (eds.) Rare Earth Transition Borocarbides (Nitrides): Superconducting,

Magnetic and Normal State Properties, 83, Kluwer, (2001).
M. Divis, unpublisd, (2001).
M. I. Dobroliubov and S. Yu. Khlebnikov, Phys. Rev.Lett. 67, 2084 (1991).
R. K. Dodd, J. C. Eilbeck, J. D. Gibbon, and H. C. Morris, "Solitons and Nonlinear Wave Equations.", Academic Press, New York, 1982.
I. Doi, K. Sano, and K. Takano, Phys. Rev. B 45, 274 (1992).
G. J. Dolan, G. V. Chandrashekhar, T. R. Dinger, C. Feild, and F. Holtzberg, Phys. Rev. Lett. 62, 827 (1989a).
G. J. Dolan, F. Holtzberg, C. Feild, and T. R. Dinger, Phys. Rev. Lett. 62, 2184 (1989b).
S. Doniach, in "Proceedings Los Alamos Symposium, High Temp. Supercond.," p. 406. Addison-Wesley, New York, 1989.
S. Doniach and M. Inui, Phys. Rev. B 41, 6668 (1990).
G. Dopf, A. Muramatsu, and W. Hanke, Phys. Rev. Lett. 68, 353 (1992).
S. V. Dordevic, D. N. Basov, R. C. Dynes, and E. Bucher, Phys. Rev. B 64, 161103 (2001).
M. M. Doria, J. E. Gubernatis, and D. Rainer, Phys. Rev. B 41, 6335 (1990).
A. T. Dorsey, M. Huang, and M. P. A. Fisher, Phys. Rev. B 45, 523 (1992).
S. X. Dou, H. K. Liu, A. J. Bourdillon, M. Kviz, N. X. Tan, and C. C. Sorrell, Phys. Rev. B 40, 5266 (1989).
R. A. Doyle, O. L. deLange, and V. V. Gridin, Phys. Rev. B 45, 12580 (1992).
T. B. Doyle and R. A. Doyle, Phys. Rev. B 47, 8111 (1993).
P. G. Drazin and R. S. Johnson, "Solitons: An Introduction" Cambridge Univ. Press Cambridge, U.K., 1989.
S. L. Drechsler, S. V. Shulga, R. H. Muller, G. Fuchs, J. Freudenberger, G. Behr, H. Eschrig, L. M. Schultz, M. S. Golden, H. V. Lips, J. Fink, V. N. Narozhnyi, H. Rosner, P. Zahn, A. Gladun, D. Lipp, A. Kreyssig, M. Loewenhaupt, K. Koepernik, K. Winzer and K. Krug, Physica, C 317, 117 (1999).
S. L. Drechsler, H. Rosner, S. V. Shulga, I. Opahle, and H. Eschrig, L. Dresner, Cryogenics, May, p. 285, 1978. K. H. Muller and V. Narozhnyi (eds.) Rare Earth Transition Borocarbides (Nitrides): Superconducting, Magnetic and Normal State Properties, 83, Kluwer, (2001).
M. S. Dresselhaus, G. Dresselhaus, and R. Saito, in "Physical Properties of High Temperature Superconductors" (D. M. Ginsberg, Ed.), Vol. 4, Chap. 7, World Scientific, Singapore, 1994.
H. Drulis, Z. G. Xu, J. W. Brill, L. E. De Long, and J.-C. Hou, Phys. Rev. Lett. 44, 4731 (1991).
Q. Du, M. D. Gunzberger, and J. S. Peterson, Phys. Rev. B 46, 9027 (1992).
L. Dubeck, P. Lindenfeld, E. A. Lynten, and H. Rohrer, Rev. Mod. Phys. 36, 110 (1964).
A. Dulcic, R. H. Crepeau, and J. H. Freed, Phys. Rev. B 39, 4249 (1989).
A. C. Dumar, K. D. D. Rathnayaka, D. G. Naugle, and P. C. Canfield, Int. J. Mod. Phys. B 12 3264, (1998).
B. D. Dunlap, L. N. Hall, F. Behroozi, G. H. Crabtree, and D. G. Niarchos, Phys. Rev. B 29, 6244, (1984).
B. D. Dunlap, M. Slaski, Z. Sungaila, D. G. Hinks, K. Zhang, C. Segre, S. K. Malik, and E. E. Alp, Phys. Rev. B 37, 592 (1988).
C. Duran, J. Yazyi, F. de la Cruz, D. J. Bishop, D. B. Mitzi, and A. Kapitulnik, Phys. Rev. B 44, 7737 (1991).
D. E. Eastman, Solid State Commun. 7, 1697 (1969).
C. Ebner and D. Stroud, Phys. Rev. B 31, 165 (1985).
C. Ebner and D. Stroud, Phys. Rev. B 39, 789 (1989).
U. Eckern and E. B. Sonin, Phys. Rev. B 47, 505 (1993).
G. L. Eesley, J. Heremans, M. S. Meyer, G. L. Dol and S. H. Liou, Phys. Rev. Lett. 65, 3445 (1990).
H. Eikmans and J. E. van Himbergen, Phys. Rev. B 44, 6937 (1991).
H. Eisaki, H. Takagi, R. J. Cava, B. Batlog, J. J. Krajewski, W. F. Peck Jr., K. Mizuhashi, J. O. Lee, and S. Uchida, Phys. Rev. B 50, 647 (1994).
R. Eisberg and R. Resnick, "Quantum Physics," Wiley, New York, 1974.
J. W. Ekin, H. R. Hart, and A. R. Gaddipati, J. Appl. Phys. 68, 2285 (1990).
J. W. Ekin, K. Salama, and V. Selvamanickam, Appl. Phys. Lett. 59, 360 (1991).
T. Ekino and J. Akimitsu, Phys. Rev. B 40, 6902, 7364 (1989a).
T. Ekino and J. Akimitsu, J. Phys. Soc. Jpn. 58, 2135 (1989b).

T. Ekino and J. Akimitsu, Phys. Rev. B 42, 8049 (1990).
T. Ekino, H. Fujii, M. Kosugi, Y. Zenitani and J. Akimitsu, Phys. Rev. B 53, 5640 (1996).
G. M. Eliashberg, Zh. Eksp. Teor. Fiz. 38, 966 (1960a) G. M. Eliashberg, Zh. Eksp. Teor. Fiz. 39, 1437 (1960b).
B. Ellman, J. Yang, T. F. Rosenbaum, and E. Bucher.Phys. Rev. Lett. 64, 1569 (1990).
M. El Massalami, S. L. Bud'ko, B. Giordanengo, and E. M. Baggio-Saitovitch, Physica C 244 41 (1995).
M. El Massalami, R. E. Rapp and G. J. Nieuwenhuys Physica C 304 184 (1998).
E. Elsinger, J. Wosnitza, S. Wanka, J. Hagel, D. Schweitzer, and W. Strunz, Phys. Rev. Lett. 84 6098 (2000).
V. J. Emery, Phys. Rev. Lett. 58, 2794 (1987) (reprinted in Halley, 1988, p. 227).
V. J. Emery and G. Reiter, Phys. Rev. B 38, 4547 (1988).
J. W. Emsley, J. Feeney, and L. H. Sutcliffe, "High Resolution Nuclear Magnetic Resonance Spectroscopy, Pergamon, New York, Vol. 1. (1965)
D. Emin, Phys. Rev. B 49, 9157 (1994).
P. Entel and J. Zielinski, Phys. Rev. B 42, 307 (1990)
O. Entin-Wohlman and Y. Imry, Phys. Rev. B 40.6731 (1989).
L. E. Erickson, Phys. Rev. B 43, 12723 (1991).
R. Escudero, E. Guarner, and F. Morales, Physica C 162–164, 1059 (1989).
R. Escudero, F. Morales, and E. Guarner, Physica C 166C, 15 (1990).
D. Esteve, J. M. Martinis, C. Urbina, M. H. Devoret G. Collin, P. Monod, M. Ribault, and A. Revcolevschi, Europhys. Lett. 3, 1237 (1987).
J. P. Estrera and G. B. Arnold, Phys. Rev. B 39, 2094 (1989).
L. M. Falicov and C. R. Proetto, Phys. Rev. B 47, 14407 (1993).
M. M. Fang, J. E. Ostenson, D. K. Finnemore, D. E. Farrell, and N. P. Bansal, Phys. Rev. B 39, 222 (1989).
H. A. Farach, E. Quagliata, T. Mzoughi, M. A. Mesa, C. P. Poole, Jr., and R. Creswick, Phys. Rev. B 41, 2046 (1990).
D. E. Farrell, B. S. Chandrasekhar, M. R. DeGuire, M. M. Fang, V. G. Kogan, J. R. Clem, and D. K. Finnemore, Phys. Rev. B 36, 4025 (1987).
D. E. Farrell, C. M. Williams, S. A. Wolf, N. P. Bansal, and V. G. Kogan, Phys. Rev. Lett. 61, 2805 (1988).
D. E. Farrell, M. M. Fang, and N. P. Bansal, Phys. Rev. B 39, 718 (1989a).
D. E. Farrell, S. Bonham, J. Foster, Y. C. Chang, P. Z. Jiang, K. G. Vandervoort, D. J. Lam, and V. G. Kogan, Phys. Rev. Lett. 63, 782 (1989b).
D. E. Farrell, R. G. Beck, M. F. Booth, C. J. Alien, E. D. Bukowski, and D. M. Ginsberg, Phys. Rev. B42, 6758 (1990a).
D. E. Farrell, C. J. Alien, R. C. Haddon, and S. V. Chichester, Phys. Rev. B 42, 8694 (1990b).
D. E. Farrell, J. P. Rice, D. M. Ginsberg, and J. Z. Liu, Phys. Rev. Lett. 64, 1573 (1990c).
D. E. Farrell, J. P. Rice, and D. M. Ginsberg, Phys. Rev. Letts. 67, 1165 (1991).
A. L. Fauchere and G. Blatter, Phys. Rev. B 56, 14102 (1997).
R. Fazio and G. Schon, Phys. Rev. B 43, 5307 (1991).
J. F. Federici, B. I. Greene, H. Hartford, and E. S. Hellman, Phys. Rev. B 42, 923 (1990).
R. Feenstra, D. K. Christen, C. Klabunde, and J. D. Budai, Phys. Rev. B 45, 7555 (1992).
R. Fehrenbacher, V. B. Geshkenbein, and G. Blatter, Phys. Rev. B 45, 5450 (1992).
D. Feinberg and C. Villard, Phys. Rev. Lett. 65, 919 (1990).
L. F. Feiner, M. Grilli, and C. DiCastro, Phys. Rev. B 45, 10647 (1992).
L. F. Feiner, Phys. Rev. B 48, 16857 (1993).
I. Feiner, U. Yaron, Y. Yeshurun, G. V. Chandrashekhar, and F. Holtzberg, Phys. Rev. B 40, 5329 (1989).
J. C. Fernandez, R. Grauer, K. Pinnow, and G. Reinisch, Phys. Rev. B 42, 9987 (1990).
M. J. Ferrari, M. Johnson, F. C. Wellstood, J. Clarke, D. Mitzi, P. A. Rosenthal, C. B. Eom, T. H. Geballe, A. Kapitulnik, and M. R. Beasley, Phys. Rev. Lett. 64, 72 (1989).
M. J. Ferrari, F. C. Wellstood, J. J. Kingston, and J. Clarke, Phys. Rev. Lett. 67, 1346 (1991).
K. Fesser, U. Sum, and H. Biittner, Phys. Rev. B 44, 421 (1991).
A. L. Fetter and J. D. Walecka, "Quantum Theory of Many Particle Systems." McGraw-Hill, New York, 1971.
R. P. Feynman, "Lectures on Physics," Vol. 3, Chap.21. Addison-Wesley, New York, 1965.

W. A. Fietz, M. R. Beasley, J. Silcox, and W. W. Webb, Phys. Rev. 136, A 335 (1964).
A. T. Fiory, M. Gurvitch, R. J. Cava, and G. P. Espinosa, Phys. Rev. B 36, 7262 (1987).
A. T. Fiory, G. P. Espinosa, R. M. Fleming, G. S. Grader, M. Gurvitch, A. F. Hebard, R. E. Howard, J. R. Kwo, A. F. J. Levi, P. M. Mankiewich, S. Martin, C. E. Rice, L. F. Schneemeyer, and A. E. White, International Conference on Electronic Materials, Tokyo, 1988.
A. T. Fiory, A. F. Hebard, P. M. Mankiewich, and R. E. Howard, App. Phys. Lett. 52 2165 (1988).
A. T. Fiory, S. Martin, R. M. Fleming, L. F. Schneemeyer, J. V. Waszczak, A. F. Hebard, and S. A. Sunshine, Physica C 162C–164C, 1195 (1989).
A. T. Fiory, M. A. Paalanen, R. R. Ruel, L. F. Schneemeyer, and J. V. Waszczak, Phys. Rev. B 41, 4805 (1990).
O. Fischer, Appl. Phys. 16, 1 (1978).
O. Fischer, in "Earlier and Recent Aspects of Superconductivity" (J. G. Bednorz and K. A. Miiller,Eds.), p. 96, Springer, Berlin, 1990.
P. Fischer, K. Kakurai, M. Steiner, K. N. Clausen, B. Lebech, F. Hulliger, H. R. Ott, P. Briiesch, and P. Unternahrer, Physica C 152C, 145 (1988).
J. E. Fischer, P. A. Heiney, A. R. McGhie, W. J. Romanow, A. M. Denenstein, J. P. McCauley, Jr., and A. B. Smith, III, Science 252, 1288 (1991).
J. E. Fischer, P. A. Heiney, and A. B. Smith, III, Acc. Chem. Res. 25, 97 (1992).
K. H. Fischer, Physica C 178C, 161 (1991).
D. S. Fisher and D. A. Huse, Phys. Rev. B 38, 373 (1988).
M. P. A. Fisher, Phys. Rev. Lett. 62, 1415 (1989).
R. A. Fisher, S. Kirn, B. F. Woodfield, N. E. Phillips, L. Taillefer, K. Hasselbach, J. Flouquet, A. L.Giorgi, and J. L. Smith, Phys. Rev. Lett. 62, 1411 (1989).
M. P. A. Fisher, Phys. Rev. Lett. 65, 923 (1990).
D. S. Fisher, M. P. A. Fisher, and D. A. Huse, Phys. Rev. B 43, 130 (1991).
R. S. Fishman, Phys. Rev. B 38, 11996 (1988).
R. S. Fishman, Phys. Rev. Lett. 63, 89 (1989).
Z. Fisk, P. C. Canfield, W. P. Beyermann, J. D. Thompson, M. F. Hundley, H. R. Ott, E. Felder, M. B. Maple, M. A. Lopez de la Torre, P. Visani, and C. L. Seaman, Phys. Rev. Lett. 67, 3310 (1991).
M. D. Fiske, Rev. Mod. Phys. 36, 221 (1964).
R. L. Fleisher, H. R. Hart, Jr., K. W. Lay, and F. E. Luborsky, Phys. Rev. B 40, 2163 (1989).
J. D. Fletcher, A. Carrington, O. J. Taylor, S. M. Kazakov, and J. Karpinski, Phys. Rev. Lett. 95 97005 (2005)
J. D. Fletcher, A. Carrington, P. Piener, P. Rodiuere, J. P. Brison, R. Prozorov, T. Olheiser, and R. W. Giannetta, Cond. Matt. (2006)
R. B. Flippen, Phys. Rev. B 44, 7708 (1991).
M. Florjanczyk and M. Jaworski, Phys. Rev. B 40, 2128 (1989).
R. Fliikiger and W. Klose, "Landolt-Bornstein, Group III Solid State Physics," Vol. 21, Superconductors. Springer-Verlag, Berlin/New York, 1993.
M. Foldeaki, M. E. McHenry, and R. C. O'Handley, Phys. Rev. B 39, 2883 (1989).
S. Foner, E. J. McNiff, Jr., D. Heiman, S.-M. Huang, and R. B. Kaner, Phys. Rev. B 46, 14936 (1992).
A. Forkl, T. Dragon, and H. Kronmiiller, J. Appl. Phys. 67, 3047 (1990).
A. Forkl, H. U. Habermeier, B. Liebold, T. Dragon, and H. Kronraiiller, Physica C 180C, 155 (1991).
M. Forsthuber and G. Hilscher, Phys. Rev. B 45, 7996 (1992).
N. A. Fortune, K. Murata, K. Ikeda, and T. Takahashi, Phys. Rev. Lett. 68, 2933 (1992).
C. M. Foster, K. F. Voss, T. W. Hagler, D. Mihailovic, A. S. Heeger, M. M. Eddy, W. L. Olsen, and E. J. Smith, Solid State Commun. 76, 651 (1990).
H. Frahm, S. Ullah, and A. T. Dorsey, Phys. Rev. B 43 3067 (1991).
Z. Frait, D. Fraitova, and L. Pust, J. Phys. Colloque C 8, 2235 (1988a)
Z. Frait, D. Fraitova, E. Pollert, and L. Pust, Phys. Status Solidi 746, K119 (1988b).
J. P. Franck, in "Physical Properties of High Temperature Superconductors," (D. M. Ginsberg, Ed.), Vol. 4, Chap. 4, World Scientific, Singapore (1994).
G. Frank, Ch. Ziegler and W. Gopel, Phys. Rev. B 43,2828 (1991).
A. Freimuth, C. Hohn, and M. Galffy, Phys. Rev. B 44, 10396 (1991).

T. Freltoft, G. Shirane, S. Mitsuda, J. P. Remeika, and A. S. Cooper, Phys. Rev. B 37, 137 (1988).
T. Freltoft, H. J. Jensen, and P. Minnhagen, Solid-State Commun. 78, 635 (1991).
T. A. Friedmann, J. P. Rice, J. Giapintzakis, and D. M. Ginsberg, Phys. Rev. B 39, 4258 (1989).
J. Freudenberger, G. Fuchs, K. Nenkov, S. L. Drescheler, K. H. Muller, L. Schultz, A. Kreyssig, and M. Loewenhaupt, K. H. Muller and V. Narozhnyi (eds.) Rare Earth Transition Borocarbides (Nitrides): Superconducting, Magnetic and Normal State Properties, 275, Kluwer, (2001).
T. A. Friedmann, M. W. Rabin, J. Giapintzakis, J. P. Rice, and D. M. Ginsberg, Phys. Rev. B 42, 6217 (1990).
B. Friedl, C. Thomsen, and M. Cardona, Phys. Rev. Lett. 65, 915 (1990).
H. Frohlich, Phys. Rev. 79, 845 (1950).
L. Fruchter and I. A. Campbell, Phys. Rev. B 40, 5158 (1989).
A. Fujimori, S. Takekawa, E. Takayama-Muromachi, Y. Uchida, A. Ono, T. Takahashi, Y. Okabe and H. Katayama-Yoshida, Phys. Rev. B 39, 2255 (1989).
H. Fujishita, M. Sera, and M. Sato, Physica C 175, 165 (1991).
K. Fujiwara, Y. Kitaoka, K. Ishida, K. Asayama, Y. Shimakawa, T. Manako, and Y. Kubo, Physica C 184. 207 (1991).
T. Fukami, T. Kamura, A. A. Youssef, Y. Hori, and S. Mase, Physica C 759, 427 (1989).
T. Fukami, K. Hayashi, T. Yamamoto, T. Nishizaki, Y. Horie, F. Ichikawa, T. Aomine, V. Scares, and L. Rinderer, Physica C 184, 65 (1991a).
T. Fukami, T. Yamamoto, K. Hayashi, T. Nishizaki, Y. Hori, F. Ichikawa, and T. Aomine, Physica C 185. 2255 (1991b).
T. A. Fulton, P. L. Gammel, D. J. Bishop, L. N. Dunkleberger, and G. J. Dolan, Phys. Rev. Lett. 63, 1307 (1989).
A. Furusaki, H. Takayanagi, and M. Tsukada, Phys. Rev. Lett. 67, 132 (1991).
A. Furusaki and M. Tsukada, Phys. Rev. B 43, 10164 (1991).
A. Furusaki and M. Ueda, Phys. Rev. B 45, 10576 (1992).
A. Furusaki, H. Takayanagi, and M. Tsukada, Phys. Rev. B 45, 10563 (1992).
M. Furuyama, N. Kobayashi, and Y. Muto, Phys. Rev. B 40, 4344 (1989).
E. Gagliano and S. Bacci, Phys. Rev. B 42, 8772 (1990).
M. C. Gallagher, J. G. Adler, J. Jung, and J. P. Franck, Phys. Rev. B 37, 7846 (1988).
W. J. Gallagher, J. Appl. Phys. 63, 4216 (1988).
C. F. Gallo, L. R. Whitney, and P. J. Walsh, in "Novel Superconductivity" (S. A. Wolf and V. Z. Kresin, Eds.), p. 385, Plenum, New York, 1987.
C. F. Gallo, L. R. Whitney, and P. J. Walsh, Mater. Res. Soc. Symp. Proc. 99, 165 (1988).
P. L. Gammel, D. J. Bishop, G. J. Dolan, J. R. Kwo. C. A. Murray, L. F. Schneemeyer, and J. V. Waszczak, Phys. Rev. Lett. 59, 2592 (1987).
P. L. Gammel, L. F. Schneemeyer, J. K. Waszczak, and A. J. Bishop, Phys. Rev. Lett. 61, 1666 (19881
P. L. Gammel, A. Hebard, and D. J. Bishop, Phys. Rev. B 40, 7354 (1989).
J. T. Gammel, R. J. Donohoe, A. R. Bishop, and B. I. Swanson, Phys. Rev. B 42, 10566 (1990).
P. L. Gammel, L. F. Schneemeyer, and D. J. Bishop. Phys. Rev. Lett. 66, 953 (1991).
P. L. Gammel, D. J. Bishop, T. P. Rice, and D. M. Ginsberg, Phys. Rev. Lett. 68, 3343 (1992).
F. Gao, G. L. Carr, C. D. Porter, D. B. Tanner. S.Etemad, T. Venkatesan, A. Inam, B. Dutta, X. D. Wu, G. P. Williams, and C. J. Hirschmugl, Phys. Rev. B 43, 10383 (1991).
L Gao, R. L. Meng, Y. Y. Xue, P. H. Hor and C. W. Chu, Appl. Phys. Lett. 58, 92 (1991).
U Gao. Z. J. Huang, R. L. Menag, J. G. Lin, F. Chen, L. Beauvais, Y. Y. Sun, Y. Y. Xue, and C. W. Chu, Physica C 213, 261 (1993).
M. M. Garland, J. Mater. Res. 3, 830 (1988).
P. Garoche, R. Brusett, D. Jerome, and K. Bech-gaard, J. Physique Lett. 43, L147 (1982).
L. J. Geerligs, M. Peters, L. E. M. de Groot, A. Verbruggen, and J. E. Mooij, Phys. Rev. Lett. 63, 326 (1989).
L L Geguzin, I. Ya. Nikiforov, and G. I. Alperovitch, Fiz. Tverd. Tela. 75, 931 (1973).
C. Geibel, S. Thies, D. Kaczorowski, A. Mehner, A. Grauel, B. Seidel, U. Ahlheim, R. Helfrich, K. Petersen, C. D. Bredl, and F. Steglich, Z. Phys. B, Cond. Matt. 83, 305 (1991a).
C. Geibel, C. Schank, S. Thies, H. Kitzawa, C. D. Bredl, A. Bohm, M. Rau, A. Grauel, R. Caspary, R. Helfrich, U. Anlheim, G. Weber, and F. Steglich, Z. Phys. B, Cond. Matt. 84, 1 (1991b).

C. Geibel, U. Ahlheim, C. D. Bredl, J. Diehl, A. Grauel, R. Helfrich, H. Kitazawa, R. Kohler, R. Modler, M. Lang, C. Schank, S. Thies, F. Steglich, N. Sato, and T. Komatsubara, Physica C 185, 2651 (1991c).

A. K- Geim, I. V. Grigorieva, and S. V. Dubonos, Phys. Rev. B 46, 324 (1992).

R. Y. Gelfand and B. I. Halperin, Phys. Rev. B 45, 5517 (1992).

A. Geiber, Th. Grenet, M. Cyrot, and J. Beille, Phys. Rev. B 45, 5099 (1992).

W. Gerhauser, G. Ries, H. W. Neumuller, W. Schmidt, O. Eibl, G. Saemann–Ischenko, and S. Klaumfinzer, Phys. Rev. Lett. 68, 879 (1992).

V. B. Geshkenbein, V. M. Vinokur, and R. Fehrenbacher, Phys. Rev. B 43, 3748 (1991).

J. Ghijscn, L. H. Tjeng, H. Eskes, G. A. Sawatzky, and R. L. Johnson, Phys. Rev. B 42, 2268 (1990).

P. K. Ghosh, N. M. Krishna, and K. N. Shrivastava, Journal of Physics: Condensed Matter 9, L 663 (1997).

L Giaever and H. R. Zeller, Phys. Rev. Lett. 20, 1504 (1968).

J. Giapintzaiis, W. C. Lee, J. P. Rice, D. M. Ginsbeig, L M. Robertson, R. Wheeler, M. Kirk, and M.-Q. Ruault, Phys. Rev. B 45, 10677 (1992).

M. A. M. Gijs, D. Scholten, Th. van Rooy, and A. M.Genits, Phys. Rev. B 41, 11627 (1990a).

M. A. M. Gijs, A. M. Gerrits, and C. W. J. Beenakker, Phys. Rev. B 42, 10789 (1990b).

L R. Gilbert, R. Messier, and R. Roy, Thin Solid Filns 54, 129 (1978).

D. B. Gingol and C. J. Lobb, Phys. Rev. B 42, 8220 (1990).

M. J. P. Gingras, Phys. Rev. B 45, 7547 (1992).

D. M. Ginsberg (Ed.), "Physical Properties of High Temperature Superconductors," Vol. 1, 1989; Vol. 2, 1990; Vol. 3, 1992; Vol. 4, 1994, World Scientific, Singapore.

V. L. Ginzburg and L. Landau, Zh. Eksp. Teor. Fiz.20, 1064 (1950).

V. L. Ginzburg, Zh. Eksp. Teor. Fiz. 23 326 (1952).

V. L. Ginzburg and D. A. Kirzhnits, "High Temperature Superconductivity," Nauka, Moscow, 1977 [Engl. Transl. Consultants Bureau, New York, 1982].

J. I. Gittleman and B. Rosenblum, Phys. Rev. Lett. 16, 734 (1966).

J. I. Gittleman and B. Rosenblum, J. Appl. Phys. 39, 2617 (1968).

S. H. Glarum, L. F. Schneemeyer, and J. V. Waszczak, Phys. Rev. B 41, 1837 (1990).

R. Gladyshevskii, and K. Cenzual, Handbook of Superconductivity, C. P. Poole Jr. (Edt.) Academic Oress (2000).

N. E. Glass and D. Rogovin, Phys. Rev. B 39, 11327 (1989).

D. Glatzer, A. Forkl, H. Theuss, H. U. Habermeier, and Kronmiiller, Phys. Status Solidi 170, 549 (1992).

L. I. Glazman and A. E. Koshelev, Phys. Rev. B 43, 2835 (1991a); Physica C 173, 180 (1991b).

H. R. Glyde, L. K. Moleko, and P. Findeisen, Phys. Rev. B 45, 2409 (1992).

C. Godart, L. C. Gupta, R Nagarajan, S. K. Dhar, H. Noel, M. Potel, C. Mazundar, Z. Hossain, C. Levy-Clement, G. Schiffmacher, B. D. Padalia, R. Vijayaraghavan, Phys. Rev. B 51 489 (1995).

A. Gold and A. Ghazali, Phys. Rev. B 43, 12952 (1991).

R. B. Goldfarb, A. F. Clark, A. I. Braginski, and A. J. Panson, Cryogenics 27, 475 (1987a).

R. B. Goldfarb, A. F. Clark, A. I. Braginski, and A. J. Panson, in "High Temperature Superconductors" (D. U. Grubser and M. Schluter, Eds.), p. 261, Mater. Res. Soc., Pittsburgh (1987b).

D. Goldschmidt, Phys. Rev. B 39, 2372 (1989).

M. J. Goldstein and W. G. Moulton, Phys. Rev. B 40, 8714 (1989).

M. Golosovsky, D. Davidov, E. Farber, T. Tsach, and M. Schieber, Phys. Rev. B 43, 10390 (1991).

M. Golosovsky, Y. Naveh, and D. Davidov, Phys. Rev. B 45, 7495 (1992).

R. S. Gonnelli, D. Daghero, G. A. Ummarino, V. A. Stepanov, J. Jun, S. M. Kazalkov, and Karpinski, Phys. Rev. Lett. 89, 247004 (2002).

J. B. Goodenough and J.-S. Zhou, Phys. Rev. B 42, 4276 (1990).

J. B. Goodenough, J.-S. Zhou, and J. Chan, Phys. Rev. B 47, 5275 (1993).

L. F. Goodrich, A. N. Srivastava, and T. C. Stauffer, J. Res. NIST 96, 703 (1991).

L. F. Goodrich and A. N. Srivastava, Supercond. Industry, Spring, 28 (1992).

L. P. Gor'kov, Zh. Eksp. Teor. Fiz. 36, 1918. [Sov. Phys. JETP 36, 1364] (1959).

L. P. Gor'kov, Sov. Phys. JETP 38, 830 (1973).
L. P. Gor'kov, Sov. Phys. JETP Lett. 20, 260 (1974).
C. J. Gorter, and H. Casimir, Physica, 1 306 (1934).
C. J. Gorter, and H. Casimir, Zeitschrift fuer Technische Physik, 15 539 (1934).
C. J. Gorter, and H. Casimir, Phys. Z., 35 963 (1934).
U. Gottwick, R. Held, G. Sparn, F. Steglich, H. Rietschel, D. Ewert, B. Renker, W. Bauhofer, S. von Molnar, M. Wilhelm, and H. E. Hoenig, Europhys. Lett. 4, 1183 (1987).
C. E. Gough, M. S. Colclough, E. M. Forgan, R. G. Jordan, M. Keene, C. M. Muirhead, A. I. M. Rae, N. Thomas, J. S. Abell, and S. Sutton, Nature 326, 855 (1987).
M. E. Gouvea, G. M. Wysin, A. R. Bishop, and F. G. Mertens, Phys. Rev. B 39, 11840 (1989).
G. S. Grader, P. K. Gallagher, and E. M. Gyorgy, Appl. Phys. Lett. 51, 1115 (1987).
J. E. Gaebner, R. C. Haddon, S. V. Chichester, and S. M. Glarum, Phys. Rev. B 41, 4808 (1990).
M. J. Graf, M. Palumbo, D. Rainer, and J. A. Sauls, *Phys. Rev. B* 52, 10588 (1995).
R. Graham, M. Schlautmann, and D. L. Shepelyansky, Phys. Rev. Lett. 67, 255 (1991).
C. M. Granada, C. M. da Silva, and A. A. Gomes Solid State Commun 122, 269 (2002).
K. E. Gray, R. T. Kampwirth, and D. E. Farrell, Phys. Rev. B 41, 819 (1990).
K. E. Gray, D. H. Kirn, B. W. Veal, G. T. Seidler, T. F. Rosenbaum, and D. E. Farrell, Phys. Rev. B 45, 10071 (1992).
R. L. Greene, in "Organic Superconductivity" (V. Z. Kresin and W. A. Little, Eds.), p. 7. Plenum, New York, 1990.
E. Gregory, T. S. Kreilick, J. Wong, A. K. Ghosh, and W. B. Sampson, Cryogenics 27, 178 (1987).
V. V. Gridin, P. Pernambuco-Wise, C. G. Trendall, W. R. Datars, and J. D. Garrett, Phys. Rev. B 40, 8814 (1989).
D. G. Grier, C. A. Murray, C. A. Bolle, P. L. Gammel, D. J. Bishop, D. B. Mitzi, and A. Kapitulnik, Phys. Rev. Lett. 66, 2770 (1991).
R. Griessen, Phys. Rev. Lett. 64, 1674 (1990).
M. Grilli, R. Raimondi, C. Castellani, C. DiCastro, and G. Kotliar, Phys. Rev. Lett. 67, 259 (1991).
N. Gronbech-Jensen, Phys. Rev. B 45, 7315 (1992).
N. Gronbech-Jensen, N. F. Pedersen, A. Davidson, and R. D. Parmentier, Phys. Rev. B 42, 6035 (1990).
N. Gronbech-Jensen, S. A. Hattel, and M. R. Samuelsen, Phys. Rev. 45, 12457 (1991).
R. Gross, P. Chaudhari, M. Kawasaki, and A. Gupta, Phys. Rev. B 42, 10735 (1990a).
R. Gross, P. Chaudhari, M. Kawasaki, M. B. Ketchen, and A. Gupta, Appl. Phys. Lett. 57, 727 (1990b).
F. Gross-Alltag, B. S. Chandrasekhar, D. Einzel, P. J. Hirschfeld, and K. Andres, Zeitschrift fuer Physik B: Condensed Matter 82, 243 (1991).
F. Gross, B. S. Chandrasekhar, D. Einzel, K. Andres, P. J. Hirschfeld, H. R. Ott, J. Beuers, Z. Fisk, and J. L. Smith, Zeitschrift fuer Physik B: Condensed Matter 64, 175 (1986).
D. Y. Gubser and M. Schluter, Eds., "High Temperature Superconductors," Proc. Symp., Spring Meet., Anaheim, CA, Apr. 1987, Mater. Res. Soc., Pittsburgh, 1987.
F. Guinea and G. Zimanyi, Phys. Rev. B 47, 501 (1993).
B. Gumhalter and V. Zlatic, Phys. Rev. B 42, 6446 (1990).
J. Guo, D. E. Ellis, E. E. Alp, and G. L. Goodman, Phys. Rev. B 42, 251 (1990).
R. P. Gupta and M. Gupta, Phys. Rev. B 47, 11635 (1993a); Phys. Rev. B 48, 16068 (1993b).
L. C. Gupta, R. Ngarajan, Z. Hossain, Ch. Mazundar, S. K. Dhar, C. Godart, C Levy-Clement B. D. Padalia, and R Vijayaraghavan, J. Magn. Mater. 140 2053 (1995).
A. Gurevich and H. Kiipfer, Phys. Rev. B 48, 6477 (1993).
M. Gurvitch and A. T. Fiory, Phys. Rev. Lett. 59, 1337 (1987a); Appl. Phys. Lett. 51, 1027 (1987b) in "Novel Superconductivity" (S. A. Wolf and V. Z. Kresin, Eds.), p. 663, Plenum, New York.1987c.
M. Gurvitch, A. T. Fiory, L. F. Schneemeyer, R. J. Cava, G. P. Espinosa, and J. V. Waszczak, Physica C. 153–155, 1369 (1988).
H. Gutfreund and W. A. Little, in "Highly Conducting One Dimensional Solids" (J. T. Devreese, R. P. Evrard, and V. E. van Doren, Eds.), Chap. 7, Plenum, New York, 1979.
F. Gygi and M. Schluter, Phys. Rev. Lett. 65, 1820 (1990a); Phys. Rev. B 41, 822 (1990b); B 43, 7609 (1991).
R. C. Haddon, Ace. Chem. Res. 25, 127 (1992).

S. J. Hagen, T. W. Jing, Z. Z. Wang, J. Horvath, and N. P. Ong, Phys. Rev. B 37, 7928 (1988).
S. J. Hagen, C. J. Lobb, R. L. Greene, M. G. Forrester and J. H. Kang, Phys. Rev. B 41, 11630 (1990a).
S. J. Hagen, C. J. Lobb, R. L. Greene, M. G. Forrester and J. Talvacchio, Phys. Rev. B 42, 6777 (1990b).
R. R. Hake, Phys. Rev. 166, 471 (1968).
J. W. Halley, (Ed.), "Theories of High Temperature Superconductivity," Addison Wesley, Reading MA, 1988.
B. I. Halperin, Phys. Rev. Lett. 52, 1583, 2390 (1984).
N. Hamada, S. Massidda, A. J. Freeman, and J. L. Redinger, Phys. Rev. B 40, 4442 (1989).
D. R. Hamann and L. F. Mattheiss, Phys. Rev. B 38, 5138 (1988).
P. D. Hambourger and F. J. Di Salvo, Physica B 99, 173 (1980).
C. A. Hamilton, Phys. Rev. B 5, 912 (1972).
P. C. Hammel, M. Takigawa, R. H. Heffner, Z. Fis, and K. C. Ott, Phys. Rev. Lett. 63, 1992 (19891
P. C. Hammel, A. P. Reyes, Z. Fisk, M. Takigawa J. D. Thompson, R. H. Heffner, W. -W.Cheong, and J. E. Schirber, Phys. Rev. B 42, 6781 (1990)
D. P. Hampshire, X. Cai, J. Seuntjens, and D. C. Larbalestler, Supercond. Sci. Technol. 1, 12 (1988).
S. Han, L. F. Cohen, and E. L. Wolf, Phys. Rev. B 42, 8682 (1990a).
S. G. Han, Z. V. Vardeny, K. S. Wong, and O. G. Symko, Phys. Rev. Lett. 65, 2708 (1990b).
Z. P. Han, R. Dupree, D. McK Paul, A. P. Howes, and L. W. J. Caves, Physica C 181, 355 (1991).
Z. P. Han, R. Dupree, A. Gencten, R. S. Liu, and P. P. Edwards, Phys. Rev. Lett. 69, 1256 (1992).
S. H. Han, C. C. Almasan, M. C. de Andrade, Y. Dalichaouch, and M. B. Maple, Phys. Rev. B 46, 14290 (1992).
T. Hanaguri, T. Fukase, I. Tanaka, and H. Kojima, Phys. Rev. B 48, 9772 (1993).
Z. Hao, J. R. Clem, M. W. McElfresh, L. Civale, A. P. Malozemoff, and F. Holtzberg, Phys. Rev. B 43, 2844 (1991).
Z. Hao, and J. R. Clem, Phys. Rev. Lett. 67, 2371 (1991)
J. Hara, M. Ashida, and K. Nagai, Phys. Rev. B 47, 11263 (1993).
W. N. Hardy, D. A. Bonn, D. C. Morgan, R. Liang, and K. Zhang, Physical Review Letters 70, 3999 (1993).
W. N. Hardy, S. Kamal, and D. A. Bonn, NATO AS1Series, Series B: Physics 371, 373 (1998).
A. B. Harris and R. V. Lange, Phys. Rev. 157, 295 (1967).
R. K. Harris, "Nuclear Magnetic Resonance Spectroscopy," Halsted, 1986.
D. C. Harris, S. T. Herbert, D. Stroud, and J. C. Garland, Phys. Rev. Lett. 67, 3606 (1991).
D. R. Harshman, L. F. Schneemeyer, J. V. Waszczak, G. Aeppli, R. J. Cava, B. Batlogg, L. W. Rupp, E. J. Ansaldo, and D. LI. Williams, Phys. Rev. B 39, 851 (1989).
D. R. Harshman, R. N. Kleiman, R. C. Haddon, S. V. Chichester-Hicks, M. L. Kaplan, L. W. Rupp, Jr., T. Pfiz, D. LI. Williams, D. B. Mitzi, Phys. Rev. Lett. 64, 1293 (1990).
D. R. Harshman and A. P. Mills, Jr., Phys. Rev. B 45, 10684 (1992).
M. Hase, I. Terasaki, A. Maeda, K. Uchinokura, T. Kimura, K. Kishio, I. Tanaka, and H. Kojima, Physica C 185–189, 1855 (1991).
T. Hasegawa, H. Ikuta, and K. Kitazawa, in "Physical Properties of High Temperature Superconductors" (D. M. Ginsberg, Ed.), Vol. 3, Chap. 7, World Scientific, Singapore, 1992.
S. Hasegawa, T. Matsuda, J. Endo, N. Osakabe, M. Igarashi, T. Kobayashi, M. Naito, A. Tonomura, and R. Aoki, Phys. Rev. B 43, 7631 (1991).
N. Hatakenaka, S. Kurihara, and H. Takayanagi, Phys. Rev. B 42, 3987 (1990).
J. Hauck, S. Denker, H. Hindriks, S. Ipta, and K. Mika, Z. Phys. B 84, 31 (1991).
D. B. Haviland, Y. Liu, and A. M. Goldman, Phys. Rev. Lett. 62, 2180 (1989).
R. M. Hazen, L. W. Finger, R. J. Angel, C. T. Prewitt, N. L. Ross, H. K. Mao, C. G. Hadidiacos, P. H. Hor, A. L. Meng, and C. W. Chu, Phys. Rev. B 35, 7238 (1987).
R. M. Hazen, L. W. Finger, R. J. Angel, C. T. Prewitt, N. L. Ross, C. G. Hadidiacos, P. J. Heaney, D. R. Veblen, Z. Z. Sheng, A. El Ali, and A. M. Hermann, Phys. Rev. Lett. 60, 1657 (1988).
R. M. Hazen, in "Physical Properties of High Temperature Superconductors" (D. M. Ginsberg, Ed.), Vol. 2, Chap. 3, World Scientific, Singapore, 1990.

T. He, Q. Huang, A. P. Ramirez, Y. Wang, K. A. Regan, N. Rogado, M. A. Hayward, M. K. Haas, J. S. Slusky, K. Inumaru, H. W. Zandbergen, N. P. Ong, and R. J. Cava, Nature 411, 54 (2001).

A. F. Hebard, P. L. Gammel, C. E. Rice, and A. F. J. Levi, Phys. Rev. B 40, 5243 (1989).

A. F. Hebard and M. A. Paalanen, Phys. Rev. Lett. 65, 927 (1990).

A. F. Hebard, M. J. Rosseinsky, R. C. Haddon, D. W. Murphy, S. H. Glarum, T. T. M. Palstra, A. P. Ramirez, and A. R. Kortan, Nature, 350, 600 (1991).

A. F. Hebard, in "Proc. R. L. Orbach Symp. Random Magnetism and High Tc Supercond.," World Scientific, Singapore, 1994.

A. F. Hebard, in "Strongly Correlated Electronic Materials" (K. S. Bedell, Ed.), Addison-Wesley, New York, 1994.

S. E. Hebboul and J. C. Garland, Phys. Rev. B 43, 13703 (1991).

R. Heid, Phys. Rev. B 45, 5052 (1992).

R. A. Hein, T. L. Francavilla, and D. H. Liebenberg (Eds.), "Magnetic Susceptibility of Superconductors and Other Spin Systems," Plenum, New York, 1991.

M. Heinecke, and K. Winzer Phys. B 98, 147 (1995).

C. S. Hellberg and E. J. Mele, Phys. Rev. B 48, 646 (1993).

F. Hellman and T. H. Geballe, Phys. Rev. B 36, 107 (1987).

N. F. M. Henry and K. Lonsdale, "International Tables for X-Ray Crystallography," Kynboh, Birmingham, England, 1965.

J. Heremans, D. T. Morelli, G. W. Smith, and S. C. Strite III, Phys. Rev. B 37, 1604 (1988).

F. Herman, R. V. Kasowski, and W. Y. Hsu, Phys. Rev. B 36, 6904 (1987).

A. M. Hermann and J. V. Yakhmi, "Thallium Based High Temperature Superconductors," Dekker, Basel, 1993.

S. L. Herr, K. Kamaras, D. B. Tanner, S.-W. Cheong, G. R. Stewart, and Z. Fisk, Phys. Rev. B 43, 7847 (1991).

D. W. Hess, T. A. Tokuyasu, and J. A. Sauls, Phys. Condens. Matt. 1, 8135 (1989).

H. F. Hess, R. B. Robinson, R. C. Dynes, J. M. Valles, Jr., and J. V. Waszczak, Phys. Rev. Lett. 62, 214 (1989).

H. F. Hess, R. B. Robinson, and J. V. Waszczak, Phys. Rev. Lett. 64, 2711 (1990).

H. F. Hess, R. B. Robinson, and J. V. Waszczak, Physica B 769, 422 (1991).

J. D. Hettinger and D. G. Steel, in "High Temperature Superconducting Science" (D. Shi, Ed.), Pergamon, New York, 1994.

R. E. Hetzel, A. SudbO, and D. Huse, Phys. Rev. Lett. 69, 518 (1992).

E. T. Heyen, R. Liu, C. Thomsen, R. Kremer, M. Cardona, J. Karpinski, E. Kaldis, and S. Rusiecki, Phys. Rev. B 41, 11058 (1990a).

E. Heyen, M. Cardona, J. Karpinski, E. Kaldis, and S. Rusiecki, Phys. Rev. B 43, 12958 (1991).

Y. Hidaka, Y. Enomoto, M. Suzuki, M. Oda, and T. Murakami, Jpn. J. Appl. Phys. 26, L377 (1987).

S. Hikami and A. I. Larkin, Mod. Phys. Lett. B 2, 693 (1988).

M. Hikita, Y. Tajima, A. Katsui, Y. Hidaka, T. Iwata, and S. Tsurumi, Phys. Rev. B 36, 7199 (1987).

M. Hikita and M. Suzuki, Phys. Rev. B 39, 4756 (1989).

G. Hilscher, H. Michor, N. M. Hong, T. Holubar, W. Perthold, M. Vybornov, and P. Rogl, in Int. Conf. Strongly Correlated Electron Systems, Amsterdam, Netherlands, Aug. (1994).

G. Hilscher, H. Michor, and M. Divis, K. H. Muller and V. Narozhnyi (eds.) Rare Earth Transition Borocarbides (Nitrides): Superconducting, Magnetic and Normal State Properties, p. 347, Kluwer, (2001).

G. Hilscher, and H. Michor, Superconductivity and Magnetism in Quatemary Borocarbides, Studies on High Temperature Superconductors, vol 28, p. 241, A. V. Narlikar (ed.), New York: Nova Science (1999).

D. G. Hinks, D. R. Richards, B. Dabrowski, D. T. Marx, and A. W. Mitchell, Nature 335, 419 (1988).

D. G. Hinks, B. Dabrowski, D. R. Richards, J. D. Jorgensen, S. Pel, and J. F. Zasadzinski, Mat. Res. Soc. Symp. Proc. 756, 357 (1989).

J. E. Hirsch, Phys. Rev. B 31, 4403 (1985a); Phys. Rev. Lett. 54, 1317 (1985b).

J. E. Hirsch, Phys. Rev. Lett. 59, 228 (1987).

P. J. Hirschfeld, and N. Goldenfeld, Phys. Rev. B 48, 4219 (1993).

P. J. Hirschfeld, S. M. Quinlan, and D. J. Scalapino, Phys. Rev. B 55, 12742 (1997).

T. Hocquet, P. Mathieu, and Y. Simon, Phys. Rev. B 46, 1061 (1992).

J. A. Hodges, P. Imbert, and G. Jehanno, Solid State Commun. 64, 1209 (1987).
U. Hofmann and J. Keller, Z. Phys. B. Cond. Matter 74, 499 (1989).
C. Hohn, M. Galffy, A. Dascoulidou, A. Freimuth, H. Soltner, and U. Poppe, Z. Phys. B 85, 161 (1991).
K. Holczer, O. Klein, G. Gruner, J. D. Thompson, F. Deiderich, and R. L. Whetten, Phys. Rev. Lett.67, 271 (1991).
T. Holst, J. B. Hansen, N. Gronbech-Jensen, and J. A. Blackburn, Phys. Rev. B 42, 127 (1990).
T. Hoist and J. B. Hansen, Phys. Rev. B 44, 2238 (1991).
X. Q. Hong and J. E. Hirsch, Phys. Rev. B 46, 14702 (1992).
T. Honma, K. Yamaya, F. Minami, and S. Takekawa, Physica C 776, 209 (1991).
B. Hopfengartner, B. Hensel, and G. Saemann-Ischenko, Phys. Rev. B 44, 741 (1991).
M. L. Horbach, F. L. J. Vos, and W. van Saarloos, Phys. Rev. B 48, 4061 (1993).
M. L. Horbach, F. L. J. Vos, and W. van Saarloos, Phys. Rev. B 49, 3539 (1994).
M. Horvatic, T. Auler, C. Berthier, Y. Berthier, P. Butaud, W. G. Clark, J. A. Gillet, P. Segransan, and J. Y. Henry, Phys. Rev. B 47, 3461 (1993).
Z. Hossain, S. K. Dhar, R. Nagarajan, L. C. Gupta, C. Godart, and R Vijayaraghavan, IEEE trans. Mag. 31, 4133 (1995).
Z. Hossain, R. Nagarajan, S. K. Dhar, L. C. Gupta, Physica B 259–261 606 (1999).
A. Houghton, R. A. Pelcovits, and A. SudbO, Phys. Rev. B 40, 6763 (1989); 41, 4785 (E) (1990).
A. P. Howes, R. Dupree, D. McK Paul, and S. Male, Physica C 185–189, 1137 (1991).
T. C. Hsu and P. W. Anderson, Physica C 162–164, 1445 (1989).
Y. Y. Hsu H. C. Chang, and H. C. Ku, J. Appl. Phys. 83, 6789 (1998).
C-R. Hu, Phys. Rev. Lett. 72 1526 (1994).
Q. Hu and M. Tinkham, Phys. Rev. B 39, 11358 (1989).
Q. Hu, C. A. Mears, P. L. Richards, and F. L. Lloyd, Phys. Rev. Lett. 64, 2945 (1990).
G. Y. Hu and R. F. O'Connell, Phys. Rev. B 47, 8823 (1993).
W. F. Huang, P. J. Ouseph, K. Fang, and Z. J. Xu, Solid State Commun. 66, 283 (1988).
Z. J. Huang, Y. Y. Xue, P. H. Hor, and C. W. Chu, Physica C 776, 195 (1991a).
Z. J. Huang, H. H. Fang, Y. Y. Xue, P. H. Hor, C. W. Chu, M. L. Norton, and H. Y. Tang, Physica C 180, 331 (1991b).
M.-Z. Huang, Y.-N. Xu, and W. Y. Ching, Phys. Rev. B 46, 6572 (1992).
Z. J. Huang, Y. Y. Xue, R. L. Meng, and C. W. Chu, Phys. Rev. B 49, 4218 (1994).
J, Hubbard, Proc. Royal Soc. London A 276, 238 (1963).
J. Hubbard, Proc. Royal Soc. London A 281, 401 (1964).
R. P. Huebener, R. T. Kampwirth, and A. Seher, J. Low Temp. Phys. 2, 113 (1970).
R. P. Huebener, Physica C 168, 605 (1990).
N. H. Hur, H.-G. Lee, J.-H. Park, H.-S. Shin, and I-S. Yang, Physica C 218, 365 (1993).
N. H. Hur, N. H. Kirn, S. H. Kim, Y. K. Park, and J. C. Park, Physica C, 231, 227 (1994).
M. S. Hybertsen, E. B. Stechel, W. M. C. Foulkes,and M. Schliiter, Phys. Rev. B 45, 10032 (1992).
T. L. Hylton and M. R. Beasley, Phys. Rev. B 41, 11669 (1990).
O. B. Hyun, D. K. Finnemore, L. Schwartzkopf, and J. R. Clem, Phys. Rev. Lett. 58, 599 (1987).
O. B. Hyun, J. R. Clem, and D. K. Finnemore, Phys.Rev. B 40, 175 (1989).
M. lansiti, M. Tinkham, A. T. Johnson, W. F. Smith, and C. J. Lobb, Phys. Rev. B 39, 6465 (1989).
M. Iavarone, A. Andreone, A. Cassinese, R. Dicapua, L. Gianni, R. Vaglio, Y. De Wilde, and G. W. Crabtree, K. H. Muller and V. Narozhnyi (eds.) Rare Earth Transition Borocarbides (Nitrides): Superconducting, Magnetic and Normal State Properties, 347, Kluwer, (2001).
M. Iavarone, G. Karapetrov, A. E. Koshelev, W. K. Kwok, G. W. Crabtree, D. G. Hinks, R. Cook, W. N. Kang, E. M. Choi, H. J. Kim, and S. I. Lee, Physica C 385, 215 (2003).
H. Ihara, R. Sugise, K. Hayashi, N. Terada, M. Jo, M. Hirabayashi, A. Negishi, N. Atoda, H. Oyanagi, T. Shimomura, and S. Ohashi, Phys. Rev. B 38, 11952 (1988).
H. Ihara, M. Hirabayashi, H. Tanino, K. Tokiwa, H. Ozawa, Y. Akahama, and H. Kawamura, Jpn. J. Appl. Phys. 32, L1732 (1993).
J. Ihm and B. D Yu, Phys. Rev. B 39, 4760 (1989).

S. Ikegawa, T. Wada, A. Ichinose, T. Yamashita, T. Sakurai, Y. Yaegashi, T. Kaneko, M. Kosuge, H. Yamauchi, and S. Tanaka, Phys. Rev. B 41, 11673 (1990).

S. Ikegawa, T. Wada, T. Yamashita, H. Yamauchi, and S. Tanaka, Phys. Rev. B 45, 5659 (1992).

J.-M. Imer, F. Patthey, B. Dardel, W. D. Schneider, Y. Baer, Y. Petroff, and A. Zettl, Phys. Rev. Lett. 62, 336 (1989).

T. Inabe, H. Ogata, Y. Maruyama, Y. Achiba, S. Suzuki, K. Kikuchi, and I. Ikemoto, Phys. Rev. Lett. 69, 3797 (1992).

S. E. Inderhees, M. B. Salamon, J. P. Rice, and D. M.Ginsberg, Phys. Rev. Lett. 66, 232 (1991).

Y. Inoue, Y. Shichi, F. Munakata, and M. Yamanaka, Phys. Rev. B 40, 7307 (1989).

M. Inui, P. B. Littlewood, and S. N. Coppersmith, Phys. Rev. Lett. 63, 2421 (1989).

Z. Iqbal, J. C. Barry, and B. L. Ramakrishna, in "Studies in High Temperature Superconductors" (A. V. Narlikar, Ed.), Nova Sci., New York, 1989.

Z. Iqbal, G. H. Kwei, B. L. Ramakrishna, and E. W. Ong, Physica C 767, 369 (1990).

Z. Iqbal, R. H. Baughman, B. L. Ramakrishna, S.Khare, N. S. Murthy, H. J. Bornemann, and D. E.Morris, Science 254, 826 (1991).

Z. Iqbal, Supercond. Rev. 1, 49 (1992).

Z. Iqbal, T. Datta, D. Kirven, A. Longu, J. C. Barry, F. J. Owens, A. G. Rinzler, D. Yang, and F. Reidinger, Phys. Rev. B 49, 12322 (1994).

F. Irie and K. Yamafuji, J. Phys. Soc. Jpn. 23, 255 (1976).

E. D. Isaacs, D. B. McWhan, R. N. Kleiman, D. J.Bishop, G. E. Ice, P. Zschack, B. D. Gaulin, T. E.Mason, J. D. Garrett, and W. J. L. Buyers, Phys. Rev. Lett. 65, 3185 (1990).

K. Isawa, A. Tokiwa-Yamamoto, M. Itoh, S. Adachi, and H. Yamauchi, Physica C 217, 11 (1993).

K. Isawa, A. Tokiwa-Yamamoto, M. Itoh, S. Adachi, and H. Yamauchi, Physica C 222, 33 (1994a).

K. Isawa, T. Higuchi, T. Machi, A. Tokiwa-Yamamoto, S. Adachi, M. Murakami, and H. Yamauchi, Appl. Phys. Lett. 64, 1301 (1994b).

T. Ishida and R. B. Goldfarb, Phys. Rev. B 41, 8937 (1990).

T. Ishida, R. B. Goldfarb, S. Okayasu, and Y. Kazu-mata, Physica C 185–189, 2515 (1991).

T. Ishiguro and K. Yamaji, "Organic Superconductors," Springer-Verlag, Berlin, 1990.

A. Isihara, "Statistical Physics," Academic Press, New York, 1971.

Y. Ishii and J. Ruvalds, Phys. Rev. B 48, 3455 (1993).

T. Itoh and H. Uchikawa, Phys. Rev. B 39, 4690 (1989).

M. Itoh, A. Tokiwa-Yamamoto, S. Adachi, and H. Yayauchi, Physica C 212, 271 (1993).

R. Itti, F. Munakata, K. Ikeda, H. Yamauchi, N. Koshizuka, and S. Tanaka, Phys. Rev. B 43, 6249 (1991).

B. I. Ivlev and N. B. Kopnin, Phys. Rev. Lett. 64, 1828 (1990).

B. I. Ivlev, N. B. Kopnin, and M. M. Salomaa, Phys. Rev. B 43, 2896 (1991a).

B. I. Ivlev, Yu. N. Ovchinnikov, and R. S. Thompson, Phys. Rev. B 44, 7023 (1991b).

B. I. Ivlev and R. S. Thompson, Phys. Rev. B 45, 875 (1992).

Y. lye, T. Tamegai, T. Sakakibara, T. Goto, and N. Miura, Physica C 153–155, 26 (1988).

Y. lye, S. Nakamura, T. Tamegai, T. Terashima, K. Yamamoto, and Y. Bundo, "High-Temperature Superconductors: Fundamental Properties and Novel Materials Processing" (D. Christen, J. Narayan, and L. Schneemeyer, Eds.), MRS Symposia Proceedings, No. 169, p. 871. Material Research Soc., Pittsburgh, 1990.

Y. lye, in "Physical Properties of High Temperature Superconductors" (D. M. Ginsberg, Ed.), Vol. 3, Chap. 4, World Scientific, Singapore, 1992.

J. D. Jackson, "Classical Electrodynamics," 3rd Ed. Wiley, New York, 1999.

H. M. Jaeger, D. B. Haviland, B. G. Orr, and A. M. Goldman, Phys. Rev. 40, 182 (1989).

T. Jacobs, S. Sridhar, Q. Li, G. D. Gu, and N. Koshizuka, Phys. Rev. Lett. 75 4516 (1995).

R. C. Jaklevic, J. Lambe, J. E. Mercereau, and A. H. Silver, Phys. Rev. A 140, 1628 (1965).

G. M. Japiassu, M. A. Continentino, and A. Troper, Phys. Rev. B 45, 2986 (1992).

M. Jarrell, H. R. Krishnamurthy, and D. L. Cox, Phys. Rev. B 38, 4584 (1988).

B. Jeanneret, Ph. Fliickiger, J. L. Gavilano, Ch. Leemann, and P. Martinoli, Phys. Rev. B 40, 11374 (1989).

C. S. Jee, B. Andraka, J. S. Kirn, H. Li, M. W. Meisel, and G. R. Stewart, Phys. Rev. B 42, 8630 (1990).
J. H. Jefferson, H. Eskes, and L. F. Feiner, Phys. Rev. B 45, 7959 (1992).
C. D. Jeffries, Q. H. Lam, Y. Kirn, C. M. Kirn, A. Zettl and M. P. Klein, Phys. Rev. B 39, 11526 (1989).
H. J. Jensen, A. Brass, An-C. Shi, and A. J. Berlinsky, Phys. Rev. B 41, 6394 (1990).
H. J. Jensen and P. Minnhagen, Phys. Rev. Lett. 66, 1630 (1991).
Y. Jeon, G. Liang, J. Chen, M. Croft, M. W. Ruck-man, D. Di Marizo, and M. S. Hegde, Phys. Rev. B 41, 4066 (1990).
Y. X. Jia, J. Z. Liu, M. D. Lan, P. Klavins, R. N. Shelton, and H. B. Radousky, Phys. Rev. B 45, 10609 (1992).
C. Jiang and J. P. Carbotte, Phys. Rev. B 45, 10670 (1992a).
C. Jiang and J. P. Carbotte, Phys. Rev. B 45, 7368 (1992b).
H. Jiang, Y. Huang, H. How, S. Zhang, C. Vittoria, A. Widom, D. B. Chrisey, J. S. Horwitz, and R. Lee, Phys. Rev. Lett. 66, 1785 (1991).
P. J. Jiang, M. S. Lin, J. H. Shieh, Y. B. You, H. C. Ku, and J. C. Ho, Phys. Rev. B 51 16436 (1995).
W. Jin, C. K. Loong, D. G. Hinks, P. Vashishta, R. K. Kalia, M. H. Degani, D. L. Price, J. D. Jorgensen, and B. Dabrowski, Mat. Res. Soc. Symp. Proc. 209, 895 (1991).
S. Jin, G. W. Kammlott, S. Nakahara, T. H. Tiefel, and J. Graebner, Science 253, 427 (1991).
S. Jin, T. H. Tiefel, R. C. Sherwood, M. E. Davis, R. B. van Dover, G. W. Kammlott, R. A. Fastnacht, and H. D. Keith, Appl. Phys. Lett. 52, 2074 (1988).
W. Jin, M. H. Dagani, R. K. Kalia, and P. Vashishta, Phys. Rev. B 45, 5535 (1992).
T. W. Jing and N. P. Ong, Phys. Rev. B 42, 10781 (1990).
R. Job and M. Rosenberg, Supercond. Sci. Technol. 5, 7 (1992).
R. D. Johnson, D.S. Bethune, and C. S. Yannoni, Acc. Chem. Res. 25, 169 (1992).
C. E. Johnson, H. W. Jiang, K. Holczer, R. B. Kaner, R. L. Whetten, and F. Diederich, Phys. Rev. B 46, 5880 (1992).
D. C. Johnston, H. Prakash, W. H. Zachariasen, and R. Viswanathan, Mat. Res. Bull. 8, 111 (1973).
D. C. Johnston and J. H. Cho, Phys. Rev. B 42, 8710 (1990).
Th. Jolicoeur and J. C. LeGuillou, Phys. Rev. B 44, 2403 (1991).
M. L. Jones, D. W. Shortt, and A. L. Schawlow, Phys. Rev. B 42, 132 (1990).
J. D. Jorgensen, M. A. Beno, D. G. Hinks, L. Soderholm, K. J. Volin, R. L. Hitterman, J. D. Grace, I. K. Schuller, C. U. Segre, K. Zhang, and M. S. Kleefisch, Phys. Rev. B 36, 3608 (1987a); see also Schuller et al. (1987).
J. D. Jorgensen, B. W. Veal, W. K. Kwok, G. W. Crabtree, A. Umezawa, L. J. Nowicki, and A. P. Paulikas, Phys. Rev. B 36, 5731 (1987b).
J. D. Jorgensen, B. W. Veal, A. P. Paulikas, L. J.Nowicki, G. W. Crabtree, H. Claus, and W. K.Kwok, Phys. Rev. B 41, 1863 (1990).
B. D. Josephson, Phys. Lett. 1, 251 (1962).
J. Jung, M. A.-K. Mohamed, S. C. Cheng, and J. P. Franck, Phys. Rev. B 42, 6181 (1990).
A. Junod, A. Bezinge, and J. Muller, Physica C 752, 50 (1988).
A. Junod, in "Physical Properties of High Temperature Superconductors" (D. M. Ginsberg, Ed.), Vol. 2, Chap. 2, World Scientific, Singapore, 1990.
A. Junod, D. Sanchez, J.-Y. Genoud, T. Graf, G. Triscone, and J. Muller, Physica C 185–189, 1399 (1991).
V. V. Kabanov and O. Yu. Mashtakov, Phys. Rev. B47, 6060 (1993).
K. K. Kadish and R. S. Ruoff, (Eds.), "Recent Advances in the Chemistry and Physics of Fullerenes and Related Materials," Electrochemical Society, Pennington, N. J., 1994.
A. Kadin, Phys. Rev. B 41, 4072 (1990).
A. Kahan, Phys. Rev. B 43, 2678 (1991).
A. B. Kaiser, Phys. Rev. B 35, 4677 (1987).
A. B. Kaiser and C. Uher, Aust. J. Phys. 41, 597 (1988).
A. B. Kaiser, Phys. Rev. B 37, 5924 (1988).
A. B. Kaiser and G. Mountjoy, Phys. Rev. B 43, 6266 (1991).
E. Kaldis, P. Fischer, A. W. Hewat, E. A. Hewat, J. Karpinski, and S. Rusiecki, Physica C 159, 668 (1989).
C. Kallin, A. J. Berlinsky, and W.-K. Wu, Phys. Rev. B 39, 4267 (1989).

V. Kalmeyer and R. B. Laughlin, Phys. Rev. Lett. 59, 2095 (1987).
A. Kampf and J. R. Schrieffer, Phys. Rev. B 41, 6399 (1990).
K. Kanoda, H. Mazaki, T. Mizutani, H. Hosoito, and T. Shinjo, Phys. Rev. B 40, 4321 (1989).
S. G. Kaplan, T. W. Noh, A. J. Sievers, S.-W. Cheongand, and Z. Fisk, Phys. Rev. B 40, 5190 (1989).
V. R. Karasik, N. G. Vasil'ev, and V. G. Ershov, Zh. Eksp. Teor. Fiz. 59, 790 (1970); Sov Phys–JETP 32, 433 (1971).
K. Karlsson, O. Gunnarsson, and O. Jepsen, Phys. Rev. B 45, 7559 (1992).
K. Karra'i, E. J. Choi, F. Dunmore, S. Liu, H. D. Drew, Q. Li, D. B. Fenner, Y. D. Zhu, and F.-C. Zhang, Phys. Rev. Lett. 69, 152 (1992).
H. Kasatani, H. Terauchi, Y. Hamanaka, and S. Nakashima, Phys. Rev. B 47, 4022 (1993).
A. Kastalsky, A. W. Kleinsasser, L. H. Greene, R. Bhat, F. P. Milliken, and J. P. Harbison, Phys. Rev. Lett. 67, 3026 (1991).
K. D. D. Kathnayaka, D. G. Naugle, B. K. Cho, and P. C. Canfield, Phys. Rev. B 53, 5688 (1996).
R. Kato, Y. Enomoto, and S. Maekawa, Phys. Rev. B44, 6916 (1991).
R. Kato, Y. Enomoto, and S. Maekawa, Phys. Rev. B47, 8016 (1993).
K. Katti and S. H. Risbud, Phys. Rev. B 45, 10155 (1992).
R. L. Kautz and J. M. Martinis, Phys. Rev. B 42, 9903 (1990).
H. Kawano, H. Takeya, H. Yoshizawa, and K. Kadowaki, J. Phys. Chem. Sol. 60 1053 (1999).
Z. A. Kazei and I. B. Krynetskii, "Landolt-Bornstein, Group III", Solid State Physics, Vol. 27, Subvol. f2, Springer, Heidelberg, 1992.
A. Kebede, C. S. Jee, J. Schwegler, J. E. Crow, T. Mihalisin, G. H. Myer, R. E. Salomon, P. Schlottmann, M. V. Kuric, S. H. Bloom, and R. P.Guertin, Phys. Rev. B 40, 4453 (1989).
F. J. Kedves, S. Meszaros, K. Vad, G. Halasz, B. Keszei, and L. Mihaly, Solid State Commun. 63, 991 (1987).
O. Keller, Phys. Rev. B 43, 10293 (1991).
P. H. Kes, C. J. van der Beek, M. P. Maley, M. E. McHenry, D. A. Huse, M. J. V. Menken, and A.A. Menovsky, Phys. Rev. Lett. 67, 2383 (1991).
I. B. Khalfin and B. Ya. Shapiro, Phys. Rev. B 46, 5593 (1992).
A. F. Khoder, M. Couach, and J. L. Jorda, Phys. Rev. B 42, 8714 (1990).
A. F. Khoder and M. Couach, in "Magnetic Susceptibility of Superconductors and Other Spin Systems" (R. A. Hein, T. L. Francavilla, and D. H. Liebenberg, Eds.), Plenum, New York, 1992.
Y. B. Kim, C. F. Hempstead, and A. R. Strnad, Phys. Rev. Lett. 9, 306 (1962).
Y. B. Kim, C. F. Hempstead, and A. R. Strand, Phys. Rev. 729, 528 (1963). B. Kim and M. J. Stephan, in "Superconductivity" (R. D. Parks, Ed.), Vol. 2, p. 1107, Dekker, New York, 1969.
D. H. Kim, K. E. Gray, R. T. Kampwirth, K. C. Woo, D. M. McKay, and J. Stein, Phys. Rev. B 41, 11642 (1990).
D. H. Kim, K. E. Gray, R. T. Kampwirth, and D. M.McKay, Phys. Rev. B 42, 6249 (1990); 43, 2910 (1991a).
D. H. Kim, D. J. Miller, J. C. Smith, R. A. Holoboff, J. H. Kang, and J. Talvacchio, Phys. Rev. B 44, 7607 (1991b).
J.-J. Kim, H.-K. Lee, J. Chung, H. J. Shin, H. J. Lee, and J. K. Ku, Phys. Rev. B 43, 2962 (1991).
D. M. King, Z.-X. Shen, D. S. Dessau, B. O. Wells, W. E. Spicer, A. J. Arko, D. S. Marshall, J. Di-Carlo, A. G. Loeser, C. H. Park, E. R. Ratner, J. L. Peng, Z. Y. Li, and R. L. Greene, Phys. Rev. Lett. 70, 3159 (1993).
K. Kinoshita, F. Izumi, T. Yamada, and H. Asano, Phys. Rev. B 45, 5558 (1992).
W. P. Kirk, P. S. Kobiela, R. N. Tsumura, and R. K. Pandey, Ferroelectrics 92, 151 (1989).
T. R. Kirkpatrick and D. Belitz, Phys. Rev. Lett. 68, 3232 (1992).
J. R. Kirtley, R. T. Collins, Z. Schlesinger, W. J. Gallagher, R. L. Sandstrom, T. R. Dinger and D. A. Chance, Phys. Rev. B 55, 8846 (1987).
J. R. Kirtley, Phys. Rev. 41, 7201 (1990a); Int. J. Mod. Phys. B 4, 201 (1990b).
T. J. Kistenmacher, Phys. Rev. B 39, 12279 (1989).
Y. Kitaoka, S. Hiramatsu, T. Kohara, K. Asayama, K. Ohishi, M. Kikuchi, and N. Kobayashi, Jpn. J. Appl. Phys. 26, L397 (1987a).

Y. Kitaoka, S. Hiramatsu, K. Ishida, T. Kohara, and K. Asayama, J. Phys. Soc. Jpn. 56, 3024 (1987b).
Y. Kitaoka, K. Fujiwara, K. Ishida, K. Asayama, Y. Shimakawa, T. Manako, and Y. Kubo, Physica C779, 107 (1991).
K. Kitazawa and S. Tajima, in "Some Aspects of Superconductivity," (L. C. Gupta, Ed.), Nova Sci., New York, 1990.
C. Kittel, "Introduction to Solid State Physics," 8th Ed. Wiley, New York, 2004.
S. Kivelson, Phys. Rev. B 39, 259 (1989).
Y. S. Kivshar and T. K. Soboleva, Phys. Rev. B 42, 2655 (1990).
Y. S. Kivshar, B. A. Malomed, Z. Fei, and L. Vazquez, Phys. Rev. B 43, 1098 (1991).
A. K. Klehe, A. K. Gangopadhyay, J. Diederichs, and J. S. Schilling, Physica C 213, 266 (1992).
K. Klehe, J. S. Schilling, J. L. Wagner, and D. G. Hinks, Physica C 223, 313 (1994).
B. M. Klein, L. L. Boyer, D. A. Papaconsantopoulos, and L. F. Mattheiss, Phys. Rev. B 18, 6411 (1978).
B. M. Klein, L. L. Boyer, and D. A. Papaconstantopoulos, Phys. Rev. Lett. 42, 530 (1979).
U. Klein, Phys. Rev. B 40, 6601 (1989); 41, 4819 (1990).
D. J. Klein, T. G. Schmalz, M. A. Garcfa-Bach, R. Valenti, and T. P. Zivkovic, Phys. Rev. B 43, 719 (1991).
L. Kleion and A. Aharony, Phys. Rev. B 45, 9926 (1992).
R. Kleiner, F. Steinmeyer, G. Kunkel, and P. Muller, Phys. Rev. Lett. 68, 2394 (1992).
A. Kleinhammes, C. L. Chang, W. G. Moulton, and L. R. Testardi, Phys. Rev. B 44, 2313 (1991).
A. W. Kleinsasser and T. N. Jackson, Phys. Rev. B 42, 8716 (1990).
R. A. Klemm and S. H. Liu, Phys. Rev. B 44, 7526 (1991).
R. A. Klemm, Phys. Rev. B 47, 14630 (1993).
F. Kober, H.-C. Ri, R. Gross, D. Koelle, R. P. Huebener, and A. Gupta, Phys. Rev. B 44, 11951 (1991).
J. Kober, A. Gupta, P. Esquinazi, H. F. Braun, E. H. Brandt, Phys. Rev. Lett. 66, 2507 (1991).
R. H. Koch, V. Foglietti, W. J. Gallagher, G. Koren, A. Gupta, and M. P. A. Fisher, Phys. Rev. Lett. 63, 1511 (1989).
B. N. Kodess, Ph. D. thesis, Penn State University, Penn. Cited as Ref. 6. 130 of Vonsovsky et al. (1982).
V. G. Kogan, Phys. Rev. B 24 1572 (1981).
V. G. Kogan, M. M. Fang, and S. Mitra, Phys. Rev. B38, 11958 (1988).
V. G. Kogan, Phys. Rev. B 38, 7049 (1988).
V. G. Kogan and L. J. Campbell, Phys. Rev. Lett. 62, 1552 (1989).
V. G. Kogan, N. Nakagawa, and S. L. Thiemann, Phys. Rev. B 42, 2631 (1990).
V. G. Kogan, and S. L. Bud'ko, Physica C 385 131 (2003)
V. G. Kogan, R. Prozorov, S. L. Bud'ko, P. C. Canfield, J. R. Thompson, and J. Karpinsky, to be published.
S. Kohiki, S.-I. Hatta, K. Setsune, K. Wasa, Y. Higashi, S. Fukushima, and Y. Gohshi, Appl. Phys. Lett. 56, 298 (1990).
S. Koka and K. Shrivastava, Physica B 165–166, 1097 (1990).
S. Kolesnik, T. Skoskiewicz, J. Igalson, and Z. Korczak, Phys. Rev. B 45, 10158 (1992).
T. Komeda, G. D. Waddill, P. J. Benning, and J. H. Weaver, Phys. Rev. B 43, 8713 (1991).
M. Konczykowski, F. Rullier-Albenque, E. R. Yacoby, A. Shaulov, Y. Yeshurun, and P. Lejay, Phys. Rev. B 44, 7167 (1991).
J. Konior, Phys. Rev. B 47, 14425 (1993).
R. Konno and K. Ueda, Phys. Rev. B 40, 4329 (1989).
P. Koorevaar, J. Aarts, P. Berghuis, and P. H. Kes, Phys. Rev. B 42, 1004 (1990).
Y. Kopelevich, A. Gupta, P. Esquinazi, C.-P. Heidmann, and H. Miiller, Physica C 183, 345 (1991).
P. Kopietz, Phys. Rev. Lett. 70, 3123 (1993).
A. E. Koshelev, G. Yu. Logvenov, V. A. Larkin, V. V. Ryazanov, and K. Ya. Soifer, Physica C 177, 129 (1991).
A. A. Koshta, Yu. N. Shvachko, A. A. Romanyukha, and V. V. Ustinov, Zh. Eksp. Teor. Fiz. 103, 629 (1993); Transl. Sov. Phys. JETP 76, 314 (1993).
I. Z. Kostadinov, V. G. Hadjiev, J. Tihov, M. Mateev, M. Mikhov, O. Petrov, V. Popov, E. Dinolova, Ts. Zheleva, G. Tyuliev, and V. Kojouharov, Physica C 156, 427 (1988).
J. M. Kosterlitz and D. Thouless, J. Phys. C 5, L124 (1972); 6, 1181 (1973).
N. Kosugi, Y. Tokura, H. Takagi and S. Uchida, Phys. Rev. B 41, 131 (1990).

I. Kosztin, and A. J. Leggett, Phys. Rev. Lett. 79 135 (1997).
Y. Koyama and M. Ishimaru, Phys. Rev. B 45, 9966 (1992).
H. Krakauer, W. E. Pickett, D. A. Papaconstantopoulos, and L. L. Boyer, Jpn. J. Appl. Phys. 26, Suppl. 26-3. (1987)
H. Krakauer, W. E. Pickett and R. E. Cohen, J. Supercond. 1, 111 (1988).
H. Krakauer and W. E. Pickett, Phys. Rev. Lett. 60, 1665 (1988).
V. M. Krasnov, V. A. Larkin, and V. V. Ryazanov, Physica C 174, 440 (1991).
V. M. Krasnov, Physica C 190, 357 (1992).
N. M. Kreines and V. I. Kudinov, Mod. Phys. Lett. B 6, 6 (1992).
V. Z. Kresin and S. A. Wolf, in "Novel Superconductivity" (S. A. Wolf and V. Z. Kresin, Eds.), p. 287, Plenum, New York, 1987.
V. Z. Kresin, and S. A. Wolf, "Fundamentals of Superconductivity," Plenum, New York, 1990.
V. Z. Kresin and W. A. Little (Eds.), "Organic Superconductivity," Plenum, New York, 1990.
V. Z. Kresin, H. Morawitz, and S. A. Wolf, "Mechanisms of Conventional and High Tc Superconductivity," Oxford Univ. Press, Oxford, 1993.
A. Krimmel, P. Fischer, B. Roessli, H. Maletta, C. Geibel, C. Schank, A. Grauel, A. Loidl, and F. Steglich, Z. Phys. B 86, 161 (1992).
G. Kriza, G. Quirion, O. Traetteberg, W. Kang, and D. Jerome, Phys. Rev. Lett. 66, 1922 (1991).
E. Kriiger, Phys. Stat. Sol. B 756, 345 (1989).
L. Krusin-Elbaum, A. P. Malozemoff, Y. Yeshurun, D. C. Cronemeyer and F. Holtzberg, Phys. Rev. B39, 2936 (1989).
H. C. Ku, H. D. Yang, R. W. McCallum, M. A. Noack, P. Klavins, R. N. Shelton, and A. R. Moodenbaugh, in "High Temperature Superconductors" (U. Gubser and M. Schluter, Eds.), p. 177, Mater. Res. Soc., Pittsburgh, (1987).
H. C. Ku, C. C. Lai, Y. B. You, J. H. Shieh and W. Y. Guan, Phys. Rev. B 50 351 (1994).
R. Kuentzler, C. Hornick, Y. Dossmann, S. Wegner, R. El Farsi, and M. Drillon, Physica C 184, 316 (1991).
M. L. Kulic and R. Zeyher, Phys. Rev. B 49, 4395 (1994).
J. Kulik, Y. Y. Xue, Y. Y. Sun, and M. Bonvalot, J. Mater. Res. 5, 1625 (1990).
A. D. Kulkarni, J. Prade, F. W. de Wette, W. Kress, and U. Schroder, Phys. Rev. B 40, 2642 (1989).
A. D. Kulkarni, F. W. de Wette, J. Prade, U. Schroder, and W. Kress, Phys. Rev. B 41, 6409 (1990).
A. D. Kulkarni, F. W. de Wette, J. Prade, U. Schroder, and W. Kress, Phys. Rev. B 43, 5451 (1991).
H. Kumakura, M. Uehara, and K. Togano, Appl. Phys. Lett. 51, 1557 (1987).
G. R. Kumar and P. Chaddah, Phys. Rev. B 39, 4704 (1989).
N. Kumar and A. M. Jayannavar, Phys. Rev. B 45, 5001 (1992).
M. N. Kunchur and S. J. Poon, Phys. Rev. B 43, 2916 (1991).
P. J. Kung, M. P. Maley, M. E. McHenry, J. O. Willis, J. Y. Coulter, M. Murakami, and S. Tanaka, Phys. Rev. B 46, 6427 (1992).
E. Z. Kurmaev, V. P. Belash, S. A. Nemnonov, and A. S. Shulakov, Phys. Stat. Solid B 61, 365 (1974).
H. Kuroda, K. Yakushi, H. Tasima, A. Ugawa, Y. Okawa, A. Kobayashi, R. Kato, H. Kobayashi, and G. Saito, Synth. Metals A 27, 491 (1988).
A. Kussmaul, J. S. Moodera, G. M. Roesler, Jr., and P. M. Tedrow, Phys. Rev. B 41, 842 (1990).
A. Kussmaul, J. S. Moodera, P. M. Tedrow, and A. Gupta, Physica C 177, 415 (1991).
A. L. Kuzemsky, in Int. Conf. Supercond. and Strongly Correlated Electron Systems, Amalfi, Italy, (1993).
E. Kuzmann, Z. Homonnay, A. Vertes, M. Gal, K. Torkos, B. Csakvari, G. K. Solymos, G. Horvath, J. Bankuti, I. Kirschner, and L. Korecz, Phys. Rev. B39, 328 (1989).
L. S. Kuzmin, P. Delsing, T. Claeson, and K. Likharev, Phys. Rev. Lett. 62, 2539 (1989).
L. S. Kuzmin, Yu. V. Nazarov, D. B. Haviland, P. Delsing, and T. Claeson, Phys. Rev. Lett. 67, 1161 (1991).
L. S. Kuzmin and D. Haviland, Phys. Rev. Lett. 67, 2890 (1991).
M. Kvale and S. E. Hebboul, Phys. Rev. B 43, 3720 (1991).
G. H. Kwei, J. A. Goldstone, A. C. Lawson, Jr., J. D. Thompson, and A. Williams, Phys. Rev. B 39, 7378 (1989).

G. H. Kwei, R. B. Von Dreele, S.-W. Cheong, Z. Fisk, and J. D. Thompson, Phys. B 41, 1889 (1990).
W. K. Kwok, U. Welp, G. W. Crabtree, K. G. Vandervoort, R. Hulscher, Y. Zheng, B. Dabroski, and D. G. Hinks, Phys. Rev. B 40, 9400 (1989).
W. K. Kwok, U. Welp, G. W. Crabtree, K. G. Vandervoort, R. Hulscher, and J. Z. Liu, Phys. Rev. Lett. 64, 966 (1990a).
W. K. Kwok, U. Welp, K. D. Carlson, G. W. Crabtree, K. G. Vandervoort, H. H. Wang, A. M. Kini, J. M. Williams, D. L. Stupka, L. K. Montgomery, and J. E. Thompson, Phys. Rev. B 42, 8686 (1990b).
H. S. Kwok, J. P. Zheng, and S. Y. Dong, Phys. Rev. B 43, 6270 (1991).
Y. K. Kwong, K. Lin, M. Park, M. S. Isaacson, and J. M. Parpia, Phys. Rev. B 45, 9850 (1992).
J. Labbe, Phys. Rev. 158, 647, 655 (1967a).
J. Labbe, S. Barisic, and J. Friedel, Phys, Rev. Lett. 19, 1039 (1967b).
C. C. Lai, M. S. Lin, Y. B. You and H. C. Ku, Phys. Rev. B 51, 420 (1994).
B. M. Lairson, S. K. Streiffer, and J. C. Bravman, Phys. Rev. B 42, 10067 (1990a).
B. M. Lairson, J. Z. Sun, J. C. Bravman, and T. H. Geballe, Phys. Rev. B 42, 1008 (1990b).
B. M. Lairson, J. Z. Sun, T. H. Geballe, M. R. Beasley, and J. C. Bravman, Phys. Rev. B 43, 10405 (1991).
R. Lal and S. K. Joshi, Phys. Rev. B 45, 361 (1992).
Q. H. Lam, Y. Kim, and C. D. Jeffries, Phys. Rev. B42, 4846 (1990).
M. D. Lan, J. Z. Liu, and R. N. Shelton, Phys. Rev. B44, 233 (1991).
L. D. Landau, Sov. Phys. JETP 3, 920 (1957a); 5, 101 (1957b).
C. T. Lane, "Superfluid Physics," Chap. 9, McGraw-Hill, New York, 1962.
M. Lang, N. Toyota, T. Sasaki, and H. Sato, Phys. Rev. Lett. 69, 1443 (1992a); Phys. Rev. B 46, 5822 (1992b).
J. Langen, M. Veit, M. Galffy, H. D. Jostarndt, A. Erie, S. Blumenroder, H. Schmidt, and E. Zirngiebl, Solid State Commun. 65, 973 (1988).
D. N. Langenberg, D. J. Scalapino, and B. N. Taylor, Sci. Amer. 274, 30 (May 1966).
W. Lanping, H. Jian, and W. Guowen, Phys. Rev. B 40, 10954 (1989).
D. C. Larbalestier, M. Daeumling, X. Cai, J. Suentjens, J. McKinnell, D. Hampshire, P. Lee, C. Meingast, T. Willis, H. Muller, R. D. Ray, R. G. Dillenburg, E. E. Hellstrom, and R. Joynt, J. Appl. Phys. 62, 3308 (1987a).
D. C. Larbalestier, M. Daeumling, P. J. Lee, T. F. Kelly, J. Seuntjens, C. Meingast, X. Cai, J. McKinnell, R. D. Ray, R. G. Dillenburg, and E. E. Hellstrom, Cryogenics 27, 411 (1987b).
A. I. Larkin and Yu. N. Ovchinnikov, Sov. Phys. JETP 38, 854 (1974).
A. Larsen, H. D. Jensen, and J. Mygind, Phys. Rev. B 43, 10179 (1991).
R. B. Laughlin, Phys. Rev. Lett. 60, 2677 (1988a).
R. B. Laughlin, Science 242, 525 (1988b).
W. E. Lawrence and S. Doniach, in "Proc. 12th Int. Conf. Low Temp. Phys. Kyoto, 1970" (E. Kanda, Ed.), p. 361. Keigaku, Tokyo, (1971).
M. A. R. LeBlanc, D. LeBlanc, A. Golebiowski, and G. Pillion, Phys. Rev. Lett. 66, 3309 (1991).
D. LeBlanc and M. A. R. LeBlanc, Phys. Rev. B 45, 5443 (1992).
K. Le Dang, J. P. Renard, P. Veillet, E. Velu, J. P. Burger, J. N. Daou, and Y. Loreaux, Phys. Rev. B 40, 11291 (1989).
E. Lederman, L. Wu, M. L. denBoer, P. A. van Aken, W. F. Muller, and S. Horn, Phys. Rev. B 44, 2320 (1991).
J. Y. Lee, K. M. Paget, T. R. Lemberger, S. R. Foltyn, and X. Wu, Phys. Rev. B 50, 3337 (1994).
T.-K. Lee, J. L. Birman, and S. J. Williamson, Phys. Rev. Lett. 39, 839 (1977a); Phys. Lett. A 64, 89 (1977b).
T.-K. Lee and J. L. Birman, Phys. Rev. B 17, 4931 (1978).
M. Lee, M. Yudkowsky, W. P. Halperin, J. Thiel, S.-J. Hwu, and K. R. Poeppelmeier, Phys. Rev. B 36, 2378 (1987).
M. Lee, Y.-Q. Song, W. P. Halperin, L. M. Tonge, T. J. Marks, H. O. Marcy, and C. R. Kannewurf, Phys. Rev. B 40, 817 (1989).
S. Lee, H. Mori, T. Masui, Yu. Rlsev, A. Yamamoto, S. Tajima, J. Phys. Soc. Jpn. 70, 2255 (2001).
S. Lee, Physica C 385, 31 (2003).
S. J. Lee and J. B. Ketterson, Phys. Rev. Lett. 64, 3078 (1990).

S.-I. Lee, Y. H. Jeong, K. H. Han, Z. S. Lim, Y. S. Song, and Y. W. Park, Phys. Rev. B 41, 2623 (1990).
W. C. Lee and D. C. Johnston, Phys. Rev. B 41, 1904 (1990).
H. C. Lee, R. S. Newrock, D. B. Mast, S. E. Hebboul, J. C. Garland, and C. J. Lobb, Phys. Rev. 44, 921 (1991).
W. C. Lee and D. M. Ginsberg, Phys. Rev. B 44, 2815 (1991).
W. C. Lee, J. H. Cho, and D. C. Johnston, Phys. Rev. B 43, 457 (1991).
S. Lenck, S. Wermbter, and L. Tewordt, J. Low Temp. Phys. 80, 269 (1990).
S. Lenck and J. P. Carbotte, Phys. Rev. B 49, 4176 (1994).
H. Lengfellner, A. Schnellbogl, J. Betz, W. Prettl, and K. F. Renk, Phys. Rev. B 42, 6264 (1990).
H. Lengfellner, A. Schnelbogl, J. Betz, K. Renk, and W. Prettl, Appl. Phys. Lett. 60, 1991 (1991a).
H. Lengfellner and A. Schnellbogl, Physica C 174, 373 (1991).
H. Lengfellner, G. Kremb, A. Schnellbogl, J. Betz, K. F. Renk, and W. Prettl, Appl. Phys. Lett. 60 501 (1992).
Y. Le Page, T. Siegrist, S. A. Sunshine, L. F. Schneemeyer, D. W. Murphy, S. M. Zahurak, J. V.Waszczak, W. R. McKinnon, J. M. Tarascon, G. W. Hull, and L. H. Greene, Phys. Rev. B 36, 3617 (1987).
Ph. Lerch, Ch. Leemann, R. Theron, and P. Martinoli, Phys. Rev. B 41, 11579 (1990).
J. Lesueur, L. H. Greene, W. Feldmann, and A. Inam, Physica C 191, 325 (1992).
B. G. Levi, Phys. Today 19 (May 1988), p. 19.
G. Levin, Phys. Rev. B 47, 14634 (1993).
L. Levitov, Phys. Rev. Lett. 66, 224 (1991).
J. A. Lewis, C. E. Platt, M. Wegmann, M. Teepe, J. L. Wagner, and D. G. Hinks, Phys. Rev. B 48, 7739 (1993).
H. W. Lewis, Phys. Rev. 102, 1508 (1956).
C. Li, M. Pompa, S. D. Longa, and A. Bianconi, Physica C 778, 421 (1991).
J. Q. Li, C. Chen, D. Y. Yang, F. H. Li, Y. S. Yao, Z. Y. Ran, W. K. Wang, and Z. X. Zhao, Z. Phys. B. 74, 165 (1989).
J. Q. Li, X. X. Xi, X. D. Wu, A. Inam, S. Vadlamannati, W. L. McLean, T. Venkatesan, R. Ramesh,D. M. Hwang, J. A. Martinez, and L. Nazar, Phys. Rev. Lett. 64, 3086 (1990).
M. R. Li, P. J. Hirschfeld, and P. Wolfle, Phys. Rev. Lett. 81, 5640 (1998).
Q. Li, M. Suenaga, T. Hikata, and K. Sato, Phys. Rev. B 46, 5857 (1992).
Q. Li, M. Suenaga, T. Kimura, and K. Kishio, Phys. Rev. 47, 11384 (1993).
Y.-H. Li and S. Teitel, Phys. Rev. Lett. 66, 3301 (1991).
Z.-Z. Li and Y. Qiu, Phys. Rev. B 43, 12906 (1991).
A. I. Liechtenstein, I. I. Mazin, C. O. Rodriguez, O. Jepsen, O. K. Andersen, and M. Methfessel, Phys. Rev. B 44, 5388 (1991).
L. Lilly, A. Muramatsu, and W. Hanke, Phys. Rev. Lett. 65, 1379 (1990).
Z. S. Lim, K. H. Han, S.-I. Lee, Y. H. Jeong, S. H. Salk, Y. S. Song, and Y. W. Park, Phys. Rev. B 40, 7310 (1989).
S.-Y. Lin, L. Lu, H.-M. Duan, B.-H. Ma, and D. -L. Zhang, Int. J. Mod. Phys. B 3, 409 (1989).
J. J. Lin, Phys. Rev. B 44, 789 (1991).
F. Lindemann, Phys. Z. 11, 609 (1910).
D. Lipp, M. Schneider, A. Gladun, S.-L. Drechesler, J. Freudenberger, G. Fucks, K. Nenkov, K.-H. Muller, T. Cichorek, P. Gegenwart, (K. H. Muller and V. Narozhnuy, Eds.), Rare Earth Transition Metal Borocarbides (Nitrides); Superconducting Magnetic and Normal State Properties, p. 89, Kluwer Acad. Publ. Dordrecht, (2001)
G. Litak, J. F. Annett, B. L. Gyorffy, and K. I. Wysokinski, (K. H. Muller and V. Narozhnuy, Eds.), Rare Earth Transition Metal Borocarbides (Nitrides); Superconducting Magnetic and Normal State Properties, p. 307, Kluwer Acad. Publ. Dordrecht, (2001)
G. Litak, J. F. Annett, B. L. Gyorffy, and K. I. Wysokinski, Phys. Stat. Sol. (b) 241, No. 5 983 (2004).
W. A. Little and R. D. Parks, Phys. Rev. Lett. 9, 9 (1962).
J.-X. Liu, J.-C. Wan, A. M. Goldman, Y. C. Chang, and P. Z. Jiang, Phys. Rev. Lett. 67, 2195 (1991).
J.-Z. Liu, Y. X. Jia, R. N. Shelton, and M. J. Fluss, Phys. Rev. Lett. 66, 1354 (1991).
J. Z. Liu, L. Zhang, M. D. Lan, R. N. Shelton, and M. J. Fluss, Phys. Rev. B 46, 9123 (1992).
L. Liu, J. S. Kouvel, and T. O. Brun, Phys. Rev. B 43, 7859 (1991).

R. Liu, B. W. Veal, A. P. Paulikas, J. W. Downey, H. Shi, C. G. Olson, C. Gu, A. J. Arko, and J. J. Joyce, Phys. Rev. B 45, 5614 (1992).
R. Liu, M. V. Klein, P. D. Han, and D. A. Payne, Phys. Rev. B 45, 7392 (1992).
L. Liu, J. S. Kouvel, and T. O. Brun, Phys. Rev. B 45, 3054 (1992).
G. Yu. Logvenov, V. V. Ryazanov, A. V. Ustinov, and R. P. Huebener, Physica C 175, 179 (1991).
L. W. Lombardo, D. B. Mitzi, A. Kapitulnik, and A. Leone, Phys. Rev. B 46, 5615 (1992).
F. London and H. London, Proc. Roy. Soc. (London) A 141, 71 (1935).
F. London, and H. London Proc. R Soc. London, Ser. A 149, 71 (1935).
P. London, "Une Conception Nouvelle de la Superconductibilite," Hermann, Paris, 1937.
F. London, "Superfluids," Wiley, New York, Vol. 1, 1950; Vol. 2, 1954, Dover, New York, 1961.
J. M. Longo and P. M. Raccah, J. Solid State Chem. 6, 526 (1973).
C.-K. Loong, P. Vashishta, R. K. Kalia, M. H. Degani, D. L. Price, D. J. Jorgensen, D. G. Hinks, B. Dabrowski, A. W. Mitchell, D. R. Richards, and Y. Zheng, Phys. Rev. Lett. 62, 2628 (1989).
C.-K. Loong, D. G. Hinks, P. Vashishta, W. Jin, R. K. Kalia, M. H. Degani, D. L. Price, J. D. Jorgensen, B. Dabrowski, A. W. Mitchell, D. R. Richards, and Y. Zheng, Phys. Rev. Lett. 66, 3217 (1991).
C.-K. Loong, P. Vashishta, R. K. Kalia, W. Jin, M. H.Degani, D. G. Hinks, D. L. Price, J. D. Jorgensen, B. Dabrowski, A. W. Mitchell, D. R. Richards, and Y. Zheng, Phys. Rev. B 45, 8052 (1992).
Y. Lou, X. Lu, G. H. Dai, W. Y. Ching, Y.-N. Xu, M.-Z. Huang, P. K. Tseng, Y. C. Jean, R. L.Meng, P. H. Hor, and C. W. Chu, Phys. Rev. B 46, 2644 (1992).
A. J. Lowe, S. Regan, and M. A. Howson, Phys. Rev. B 44, 9757 (1991).
D. H. Lowndes, D. P. Norton, and J. D. Budai, Phys. Rev. Lett. 65, 1160 (1990).
J. P. Lu, K. Arya, and J. L. Birman, Phys. Rev. B 40, 7372 (1989).
J.-T. Lue and J. S. Sheng, Phys. Rev. B 47, 5469 (1993).
G. M. Luke, L. P. Le, B. J. Sternlieb, Y. J. Uemura, J. H. Brewer, R. Kadono, R. F. Kiefi, S. R. Kreitzman, T. M. Riseman, C. E. Stronach, M. R. Davis, S. Uchida, H. Takagi, Y. Tokura, Y. Hidaka, T. Murakami, J. Gopalakrishnan, A. W. Sleight, M. A. Subramanian, E. A. Early, J. T. Markert, M. B. Maple, and C. L. Seaman, Phys. Rev. B 42, 7981 (1990).
G. M. Luke et al., Nature 394, 558 (1998).
J. Luzuriaga, M.-O. Andre, and W. Benoit, Phys. Rev. B 45, 12492 (1992).
J. W. Lynn, T. W. Clinton, W.-H. Li, R. W. Erwin, J. Z. Liu, K. Vandervoort, and R. N. Shelton, Phys. Rev. Lett. 63, 2606 (1989).
J. W. Lynn, (Ed.), "High Temperature Superconductivity," Springer-Verlag, Berlin, 1990a.
J. W. Lynn, "High Temperature Superconductivity," Chap. 8, Springer-Verlag, Berlin, 1990b.
J. W. Lynn, J. Alloys Compd. 181, 419 (1992).
J. W. Lynn, S. Skanthakumar, Q. Huang, S. K. Sinha, Z. Hossain, L. C. Gupta, R. Nagarajan, And C. Godart, Phys. Rev. B 55, 6584 (1997).
E. A. Lynton, "Superconductivity," Methuen, London, 1962.
D. K. C. MacDonald, "Thermoelectricity, An Introduction to the Principles," Wiley, New York, 1962.
H. Maeda, Y. Tanaka, M. Fukutomi, and T. Asano, Jpn. J. Appl. Phys. Lett. 27, 209 (1988).
A. Maeda, T. Shibauchi, N. Kondo, K. Uchinokura, and M. Kobayashi, Phys. Rev. B 46, 14234 (1992).
Y. Maeno, T. Tomita, M. Kyogoku, S. Awaji, Y. Aoki, K. Hoshino, A. Minami, and T. Fujita, Nature 328, 512 (1987).
A. Maeda, and T. Hanaguri, Supercond. Rev. 3, 1 (1998).
Y. Maeno, H. Hashimoto, K. Yoshida, S. NishiZaki, T. Fujuta, J. G. Bednorz, and F Lichtenberg, Nature 372, 532 (1994).
S. Magalo, M. Michor, M. El-Hagarty, G. Hilscher and E. Schachinger, Phys. Rev. B 63, 104508 (2001).
G. D. Mahan, Phys. Rev. B 40, 11317 (1989).
G. D. Mahan, Phys. Rev. B 48, 16557 (1993).
R. Mailfert, R. W. Batterman, and J. J. Hanak, Phys. Lett. A 24, 315 (1967).
A. Majhofer, L. Mankiewicz, and J. Skalski, Phys.Rev. B 42, 1022 (1990).
K. Maki, Prog. Theoret. Phys. 39, 897 (1968).
K. Maki, Phys. Rev. B 43, 1252 (1991); erratum, B 43, 13685 (1991).
K. Maki, E. Puchkaryov and G. F. Wang, (S.-L. Dreschsler and T. Mishonov, eds.),

High-Tc Superconductors and Related Materials, 199, Kluwer Academic Publishers. Printed in the Netherlands (2001).
H. Maletta, A. P. Malozemoff, D. C. Cronemeyer, C. C. Tsuei, R. L. Greene, J. G. Bednorz, and K. A. Miiller, Solid State Commun. 62, 323 (1987).
M. P. Maley, J. Appl. Phys. 70, 6189 (1991).
M. P. Maley, P. J. Kung, J. Y. Coulter, W. L. Carter, G. N. Riley, and M. E. McHenry, Phys. Rev. B 45, 7566 (1992).
M. Mali, D. Brinkmann, L. Pauli, J. Roos, H. Zimmermann, and J. Hulliger, Phys. Lett. A 124, 112 (1987).
S. K. Malik, C. V. Tomy, D. T. Adroja, R. Nagarajan, R. Prasad, and N. C. Soni, Solid State Commun. 66 (10), 1097 (1988).
B. A. Malomed, Phys. Rev. B 39, 8018 (1989).
B. A. Malomed, Phys. Rev. B 41, 2616 (1990).
B. A. Malomed and A. Weber, Phys. Rev. B 44, 875 (1991).
B. A. Malomed and A. A. Nepomnyashchy, Phys. Rev. B 45, 12435 (1992).
V. Manivannan, J. Gopalakrishnan, and C. N. R. Rao, Phys. Rev. B 43, 8686 (1991).
Y. Maniwa, H. Sato, K. Mizoguchi, and K. Kune, Jpn.J. Appl. Phys. 29, 268 (1990).
Y. Maniwa, T. Mituhashi, K. Mizoguchi, and K. Kume, Physica C 775, 401 (1991a).
Y. Maniwa, S. Sato, T. Mituhaski, K. Mizoguchi, and K. Kume, Physica C 185–189, 1761 (1991b).
P. A. Mansky, P. M. Chaikin, and R. C. Haddon, Phys. Rev. B 50, 15929 (1994).
F. Manzano, A. Carrington, N. E. Hussey, S. Lee, A. Yamamoto, and S. Tajima Phys. Rev. Lett. 88 47002 (2002).
J. Mao, D. H. Wu, J. L. Peng, R. L. Greene, and S. M. Anlage, Phys. Rev. B 51, 3316 (1995).
Z. Q. Mao, M. M. Rosario, K. D. Nelson, K. Wu, I. G. Deac, P Schiffer, and Y. Liu, Phys. Rev. B 67, 94502 (2003).
M. B. Maple, J. W. Chen, S. E. Lambert, Z. Fisk, J. L. Smith, and H. R. Ott, cited in Stewart (1984).
M. C. Marchetti and D. R. Nelson, Phys. Rev. B 41, 1910 (1990).
M. C. Marchetti, Phys. Rev. B 43, 8012 (1991).
R. Marcon, R. Fastampa, M. Giura, C. Matacotta, Phys. Rev. B 39, 2796 (1989).
R. Marcon, E. Silva, R. Fastampa, and M. Giura, Phys. Rev. B 46, 3612 (1992).
J. Marcus, C. Escribe-Filippini, C. Schlenker, R. Buder, J. Devenyi, and P. L. Reydet, Solid State Commun. 63, 129 (1987).
M. Marder, N. Papanicolaou, and G. C. Psaltakis, Phys. Rev. B 41, 6920 (1990).
J. T. Markert, T. W. Noh, S. E. Russek, and R. M. Cotts, Solid State Commun. 63, 847 (1987).
R. S. Markiewicz, Physica C 777, 171 (1991).
R. S. Markiewicz, Int. J. Mod. Phys. B 5, 2037 (1991).
P. Marsh, R. M. Fleming, M. L. Mandich, A. M. DeSantolo, J. Kwo, M. Hong, and L. J. Martinez-Miranda, Nature 334, 141 (1988).
C. D. Marshall, I. M. Fishman, R. C. Dorfman, C. B. Eom, and M. D. Payer, Phys. Rev. B 45, 10009 (1992).
F. Marsiglio and J. E. Hirsch, Phys. Rev. B 44, 11960 (1991).
F. Marsiglio, Phys. Rev. B 44, 5373 (1991).
F. Marsiglio and J. E. Hirsch, Phys. Rev. B 49, 1366 (1994).
S. Martin, A. T. Fiory, R. M. Fleming, L. F. Schneemeyer, and J. V. Waszczak, Phys. Rev. Lett. 60, 2194 (1988).
S. Martin, A. T. Fiory, R. M. Fleming, G. P. Espinosa, and A. S. Copper, Phys. Rev. Lett. 62, 677, (1989); see 63, 582 (1989) for comment by P. C. E. Stampand a reply by the authors. S. Martin, A. T. Fiory, R. M. Fleming, L. F. Schneemeyer, and J. V. Waszczak, Phys. Rev. B 41, 846 (1990).
S. Martin and A. F. Hebard, Phys. Rev. B 43, 6253 (1991).
M. Martin, C. Kendziora, L. Mihaly, and R. Lefferts, Phys. Rev. B 46, 5760 (1992).
M. C. Martin, D. Roller, and L. Mihaly, Phys. Rev. B 47, 14607 (1993).
T. P. Martin, U. Naher, H. Schaber, and U. Zimmermann, Phys. Rev. Lett. 70, 3079 (1993).
C. Martin, M. Hervieu, M. Huve, C. Michel, A. Maignan, G. van Tendeloo, and B. Raveau, Physica C 222, 19 (1994).
J. A. Martindale, S. E. Barrett, C. A. Klug, K. E. O'Hara, S. M. DeSoto, C. P. Slichter, T. A. Friedmann, and D. M. Ginsberg, Phys. Rev. Lett. 68, 702 (1992).
P. Marinez-Samper, J. G. Rodrigo, G. Rubio-Bolinger, H. Suderw, S. Viera, S. Lee, and S. Tajima, Physica C 385 233 (2003).
J. L. Martins and N. Troullier, Phys. Rev. B 46, 1766 (1992).

A. Masaki, H. Sato, S. -I. Uchida, K. Kitazawa, S. Tanaka, and K. Inoue, Jpn. J. Appl. Phys. 26, 405 (1987).
H. Mathias, W. Moulton, H. K. Ng, S. J. Pan, K. K. Pan, L. H. Peirce, L. R. Testardi, and R. J. Kennedy, Phys. Rev. B 36, 2411 (1987).
P. Mathieu and Y. Simon, Europhys. Lett. 5, 67 (1988).
I. Matsubara, H. Tanigawa, T. Ogura, H. Yamashita, M. Kinoshita, and T. Kawai, Phys. Rev. B 45, 7414 (1992).
Y. Matsuda, N. P. Ong, Y. F. Yan, J. M. Harris, and J. B. Peterson, Phys. Rev. B 49, 4380 (1994).
Y. Matsumoto, M. Katada, and T. Nishida, Physica C 185, 1229 (1991).
T. Matsuura and K. Miyake, Jpn. J. Appl. Phys. 26, L 407 (1987).
H. Matsuyama, T. Takahashi, H. Katayama-Yoshida, Y. Okabe, H. Takagi, and S. Uchida, Phys. Rev. B 40, 2658 (1989).
L. F. Mattheiss, Phys. Rev. B 1, 373 (1970).
L. F. Mattheiss and D. R. Hamann, Phys. Rev. B 28, 4227 (1983).
L. F. Mattheiss, Jpn. J. Appl. Phys. 24(2), 6 (1985).
L. F. Mattheiss and D. R. Hamann, Solid State Commun. 63, 395 (1987).
L. F. Mattheiss, Phys. Rev. Lett. 58, 1028 (1987).
L. F. Mattheiss, E. M. Gyrogy, and D. W. Johnson, Jr., Phys. Rev. B 37, 3745 (1988).
L. F. Mattheiss and D. R. Hamann, Phys. Rev. Lett. 60, 2681 (1988).
L. F. Mattheiss and D. R. Hamann, Phys. Rev. B 39, 4780 (1989).
L. F. Mattheiss, Phys. Rev. B 42, 359 (1990).
B. Matthias, Phys. Rev. 92, 874 (1953).
B. Matthias, Phys. Rev. 97, 74 (1955).
D. C. Mattis and M. Molina, Phys. Rev. B 44, 12565 (1991).
E. Maxwell, Phys. Rev. 78, 477 (1950).
I. I. Mazin, O. Jepsen, O. K. Andersen, A. I. Liechtenstein, S. N. Rashkeev, and Y. A. Uspenskii, Phys. Rev. B 45, 5103 (1992).
I. I. Mazin, and V. P. Antropov, Physica C 385, 49 (2003).
K. F. McCarty, D. S. Ginley, D. R. Boehme, R. J. Baughman, and B. Morosin, Solid State Commun. 68, 77 (1988).
K. F. McCarty, B. Morosin, D. S. Ginley, and D. R. Boehme, Physica C 757, 135 (1989).
K. F. McCarty, J. Z. Liu, R. N. Shelton, and H. B. Radousky, Phys. Rev. B 41, 8792 (1990a); B 42, 9973 (1990b).
K. F. McCarty, H. B. Radousky, J. Z. Liu, and R. N. Shelton, Phys. Rev. B 43, 13751 (1991).
K. A. McGreer, J.-C. Wan, N. Anand, and A. M. Goldman, Phys. Rev. B 39, 12260 (1989).
M. E. McHenry, S. Simizu, H. Lessure, M. P. Maley, J. Y. Coulter, I. Tanaka, and H. Kojima, Phys. Rev. B 44, 7614 (1991).
W. R. McKinnon, J. R. Morton, K. F. Preston, and L. S. Selwyn, Solid State Commun. 65, 855 (1988).
W. L. McMillan, Phys. Rev. 167, 331 (1968).
T. McMullen, Phys. Rev. B 41, 877 (1990).
G. A. Medina and M. D. N. Regueiro, Phys. Rev. B 42, 8073 (1990).
N. I. Medvedeva, S. A. Turzhevsky, V. A. Gubanov, and A. J. Freeman, Phys. Rev. B 48, 16061 (1993).
D. Mehl, A. R. Koymen, K. O. Jensen, F. Gotwald, and A. Weiss, Phys. Rev. B 41, 799 (1990).
W. Meissner, and R. Ochsenfeld, Naturwissenschaften 21 787 (1933).
W. Meissner, and R. Ochsenfeld (English translation by A. M. Forrest) Eur. J. Phys. 4, 117 (1983).
K. Mendelssohn, "Cryophysics," Chap. 6, Interscience, New York, 1960.
R. L. Meng, Y. Y. Sun, J. Kulik, Z. J. Huang, F. Chen, Y. Y. Xue, and C. W. Chu, Physica C 214, 307 (1993a).
R. L. Meng, L. Beauvais, X. N. Zhang, Z. J. Huang, Y. Y. Sun, Y. Y. Zue, and C. W. Chu, Physica C 216, 21 (1993b).
R. Meservey and B. B. Schwartz, in "Superconductivity" (R. D. Parks, Ed.), Vol. 1, Chap. 3, Dekker, New York, 1969.
J. Metzger, T. Weber, W. H. Fietz, K. Grube, H. A. Ludwig, T. Wolf, and H. Wiihl, Physica C 214, 371 (1993).
H. M. Meyer III, D. M. Hill, T. J. Wagener, Y. Gao, J. H. Weaver, D. W. Capone II, and K. C. Goretta, Phys. Rev. B 38, 6500 (1988).
P. F. Miceli, J. M. Tarascon, L. H. Greene, P. Barboux, M. Giroud, D. A. Neumann, J. J. Rhyne, L. F. Schneemeyer, and J. V. Waszczak, Phys. Rev. B 38, 9209 (1988).
C. Michel and B. Raveau, Rev. Chim. Miner. 21, 407 (1984).

C. Michel, M. Hervieu, M. M. Borel, A. Grandin, F. Deslandes, J. Provost, and B. Raveau, Z. Phys. B. Cond. Matt. 68, 421 (1987).
H. Michor, T. Holubar, C. Dusek, and G. Hilscher, Phys. Rev. B 52, 16165 (1995).
H. Michor, R. Krendelsberger, P. Rogl, and H. W. Zandbergen, Phys. Rev. B 54, 9408 (1996).
R. Micnas, J. Ranninger, and S. Robaszkiewicz, Phys. Rev. B 36, 4051 (1987).
A. R. Miedema, J. Phys. (Paris) F3, 1803 (1973).
A. R. Miedema, J. Phys. (Paris) F4, 120 (1974).
F. Mila and T. M. Rice, Physica C 757, 561 (1989).
S. L. Miller, K. R. Biagi, J. R. Clem, and D. K. Finnemore, Phys. Rev. B 31, 2684 (1985).
J. H. Miller, Jr., G. H. Gunaratne, J. Huang, and T. D. Golding, Appl. Phys. Lett. 59, 3330 (1991).
A. J. Millis, H. Monien, and D. Pines, Phys. Rev. B 42, 167 (1990).
A. J. Millis and H. Monien, Phys. Rev. B 45, 3059 (1992).
L. Mingzhu, T. Weihua, M. Xianren, L. Zhenjin, H. Wei, T. Qingyun, R. Yanru, and L. Zhenxing, Phys. Rev. B 41, 2517 (1990).
P. Minnhagen and P. Olsson, Phys. Rev. Lett. 67, 1039 (1991).
P. Minnhagen and P. Olsson, Phys. Rev. B 45, 5722 (1992).
P. Miranovic, K. Machida, and V. G. Kogan, Cond. Mat. 0207146
L. Miu, A. Crisan, S. Popa, V. Sandu, and L. Nistor, J. Supercond. 3, 391 (1990).
L. Miu, Phys. Rev. B 45, 8142 (1992).
P. Mocaer, L. Tessler, M. Lagues, F. Laher-Lacour, C. Lacour, U. Dai, N. Hess, and G. Deutscher, Physica C 185–189, 2505 (1991).
M. A. K. Mohamed, J. Jung, and J. P. Franck, Phys. Rev. B 39, 9614 (1989).
M. A. K. Mohamed, J. Jung, and J. P. Franck, Phys. Rev. B 41, 4286, 6466 (1990).
M. A.-K. Mohamed and J. Jung, Phys. Rev. B 44, 4512 (1991).
R. Monaco, Int. J. Infrared. Millimeter Waves II, 533 (1990a); J. Appl. Phys. 68, 679 (1990b).
H. C. Montgomery, J. Appl. Phys. 42, 2971 (1971).
P. Monthoux and D. Pines, Phys. Rev. B 49, 4261 (1994).
J. S. Moodera, R. Meservey, J. E. Tkaczyk, C. X. Hao, G. A. Gibson, and P. M. Tedrow, Phys. Rev. B 37, 619 (1988).
H. A. Mook, D. McK Paul, B. C. Sales, L. A. Boatner, and L. Cussen, Phys. Rev. B 38, 12008 (1988).
J. Moreland, A. F. Clark, H. C. Ku, and R. N. Shelton, Cryogenics 27, 227 (1987).
J. Moreland, J. W. Ekin, L. F. Goodrich, T. E. Capobianco, A. F. Clark, J. Kwo, M. Hong, and S. H.Liou, Phys. Rev. B 35, 8856 (1987).
H. Mori, Phys. Rev. B 43, 5474 (1991).
D. E. Morris, J. H. Nickel, J. Y. T. Wei, N. G. Asmar, J. S. Scott, U. M. Scheven, C. T. Hultgren, A. G.Markelz, J. E. Post, P. J. Heaney, D. R. Veblen, and R. M. Hazen, Phys. Rev. B 39, 7347 (1988).
D. E. Morris, N. G. Asmar, J. Y. T. Wei, J. H. Nickel, R. L. Sid, J. S. Scott, and J. E. Post, Phys. Rev. B 40, 11406 (1989).
A. Moser, H. J. Hug, I. Parashikov, B. Stiefel, O. Fritz, H. Thomas, A. Baratoff, H.-J. Guntherodt, and P. Chaudhari, Phys. Rev. Lett. 74, 1847 (1995).
M. Mostoller, J. Zhang, A. M. Rao, and P. C. Eklund, Phys. Rev. B 41, 6488 (1990).
R. Movshovic, M. F. Hundley, J. D. Thompson, P. C. Canfield, B. K. Cho, and A. V. Chubukov, Physica C 227, 381 (1994).
H. Mukaida, K. Kawaguchi, M. Nakao, H. Kumakura, D. Dietderich, and K. Togano, Phys. Rev. B 42, 2659 (1990).
K. A. Miiller, M. Takashige, and J. G. Bednorz, Phys. Rev. Lett. 58, 1143 (1987).
K.-H. Muller, Physica C 159, 717 (1989).
K.-H. Muller and A. J. Pauza, Physica C 161, 319 (1989).
K.-H. Muller, IEE Trans. Magn. March (1991).
K.-H. Muller, M. Nikolo, and R. Driver, Phys. Rev. B 43, 7976 (1991).
K.-H. Muller, and V. N. Narozhnyi, Rep. Prog. Phys. 64, 943 (2001).
K.-H. Muller, J. Freudenberger, G. Fuchs, K. Nenkov, A. Kreyssig, and M. Loewenhaupt, (K. H. Muller and V. Narozhnyi, Eds.), Rare Earth Transition Metal Borocarbides (Nitrides); Superconducting Magnetic and Normal State Properties, p. 255, Kluwer Acad. Publ. Dordrecht, (2001)
H. Muller, M. Suenaga, and Y. Yokoyama, J. Appl. Phys. 70, 4409 (1991).
M. Murakami, H. Fujimoto, S. Gotoh, K. Yamaguchi, N. Koshizuka, and S. Tanaka, Physica C 185–189, 321 (1991).

M. Murakami, in "Studies of High Temperature Superconductors" (A. V. Narlikar, Ed.), Vol. 9, Nova Sci., New York, 1991.
D. W. Murphy, S. Sunshine, R. B. van Dover, R. J. Cava, B. Batlogg, S. M. Zahurak, and L. F. Schneemeyer, Phys. Rev. Lett. 58, 1888 (1987).
P. Muzikar, D. Rainer, and J. A. Sauls, Proc. NATO Adv. Study Inst. Vortices in Superfluids, Cargese, Corsica (N. Bontemps, Ed.), Kluwer, Dordrecht, 1994.
J. A. Mydosh, Phys. Scripta T19, 260 (1987).
T. Mzoughi, H. A. Farach, E. Quagliata, M. A. Mesa, C. P. Poole, Jr., and R. Creswick, Phys. Rev. B 46, 1130 (1992).
J. Nagamatsu, N. Nakagawa, T. Muranaka, Y. Zenitani, and J. Akimitsu, Nature 410, 63 (2001).
N. Nagaosa and P. Lee, Phys. Rev. B 43, 1233 (1991).
R. Nagarajan, L. C. Gupta, Ch. Mazumdar, Z. Hossain, S. K. Dhar, C. Godart, B. D. Padalia, and R. Vijayaraghavan, J. Alloys Compd. 225, 571 (1995).
R. Nagarajan, (K. H. Muller and V. Narozhnyi, Eds.), Rare Earth Transition Metal Borocarbides (Nitrides); Superconducting Magnetic and Normal State Properties, p. 1, Kluwer Acad. Publ. Dordrecht, (2001)
M. Nagoshi, Y. Fukuda, T. Suzuki, K. Ueki, A. Tokiwa, M. Kikuchi, Y. Syono, and M. Tachiki, Physica C 185, 1051 (1991).
M. Naito, A. Matsuda, K. Kitazawa, S. Kambe, I. Tanaka, and H. Kojima, Phys. Rev. B 41, 4823 (1990).
Y. Nakamura and S. Uchida, Phys. Rev. B 47, 8369 (1993).
K. Nakao, N. Miura, K. Tatsuhara, H. Takeya, and H. Takei, Phys. Rev. Lett. 63, 97 (1993).
A. V. Narlikar, Ed., "Studies of High Temperature Superconductors," Nova Sci., New York, 1989.
K. Nasu, Phys. Rev. B 42, 6076 (1990).
B. Nathanson, O. Entin-Wohlman, and B. Muhlschlegel, Phys. Rev. B 45, 3499 (1992).
R. Navarro and L. J. Campbell, Phys. Rev. B 44, 10146 (1991).
D. R. Nelson, in "Fundamental Problems in Structural Mechanics V" (E. G. D. Cohen, Ed.), North-Holland, Amsterdam, 1980.
D. L. Nelson, M. S. Whittingham, and T. F. George, Eds., "Chemistry of High-Temperature Superconductors," ACS Symposium Series No. 351, American Chemical Society, Washington, DC, 1987.
D. R. Nelson and H. S. Seung, Phys. Rev. B 39, 9153 (1989).
D. R. Nelson and P. Le Doussal, Phys. Rev. B 42, 10113 (1990).
D. R. Nelson and V. M. Vinokur, Phys. Rev. Lett. 68, 2398 (1992).
E. Nembach, K. Tachikawa, and S. Takano, Philos. Mag. 21, 869 (1970).
S. A. Nemnonov, E. Z. Kurmaev, and V. I. Minin, IMF Akad. Nauk. USSR (Kiev) 1, 87 (1969).
S. J. Nettel and R. K. MacCrone, Phys. Rev. B 47, 11360 (1993).
M. V. Nevitt, G. W. Crabtree, and T. E. Klippert, Phys. Rev. B 36, 2398 (1987).
V. L. Newhouse, in "Superconductivity" (R. D. Parks, Ed.), Vol. 2, p. 1283, Dekker, New York, 1969.
E. J. Nicol and J. P. Carbotte, Phys. Rev. B 43, 10210 (1991).
E. J. Nicol and J. P. Carbotte, Phys. Rev. B 47, 8205 (1993).
Ch. Niedermayer, H. Gluckler, A. Golnik, U. Binninger, M. Rauer, E. Recknagel, J. I. Budnick, and A. Weidinger, Phys. Rev. B 47, 3427 (1993).
L. Niel and J. E. Evetts, Supercond. Sci. Technol. 5, S347 (1992).
G. Nieva, E. N. Martinez, F. de la Cruz, D. A.Esparza, and C. A. D'Ovidio, Phys. Rev. B 36, 8780 (1987).
M. Nikolo and R. B. Goldfarb, Phys. Rev. B 39, 6615 (1989).
M. Nikolo, W. Kiehl, H. M. Duan, and A. M. Hermann, Phys. Rev. B 45, 5641 (1992).
H. Ning, H. Duan, P. D. Kirven, A. M. Hermann, and T. Datta, J. Supercond. 5, 503 (1992).
T. Nishida, M. Katada, and Y. Matsumoto, Physica B165–167, 1327 (1990a); Jpn. J. Appl. Phys. 29, 259 (1990b).
H. Nishihara, T. Ohtani, Y. Sano, and Y. Nakamura, Physica C 185–189, 2733 (1991).
T. Nitta, K. Nagase, S. Hayakawa, and Y. Iida, J. Am. Ceram. Soc. 48, 642 (1965).
R. K. Nkum and W. R. Datars, Physica C 192, 215 (1992).
C. Noce and L. Maritato, Phys. Rev. B 40, 734 (1989).

H. Noel, P. Gougeon, J. Padiou, J. C. Level, M. Potel, O. Laborde, and P. Monceau, Solid State Commun. 63, 915 (1987).
T. Nojima and T. Fujita, Physica C 178, 140 (1991).
F. Nori, E. Abrahams, and G. T. Zimanyi, Phys. Rev. B 41, 7277 (1990).
M. R. Norman, Phys. Rev. B 42, 6762 (1990).
D. L. Novikov, V. A. Gubanov, and A. J. Freeman, Physica C 191, 399 (1992).
P. Nozieres and W. F. Vinen, Philos. Mag. 14, 667 (1966).
N. Niicker, H. Romberg, M. Alexander, and J. Fink, in "Studies of High Temperature Superconductors" (A. V. Narlika, Ed.), Nova Sci., New York, 1992.
B.-H. O and J. T. Markert, Phys. Rev. B 47, 8373 (1993).
D. E. Oates, S. H. Park, and G. Koren, Phys. Rev. Lett. 93, 197001 (2004).
S. D. Obertelli, J. R. Cooper, and J. L. Tallon, Phys. Rev. B 46, 14928 (1992).
B. Obst, Phys. Status Solidi B 45, 467 (1971).
S. P. Obukhov and M. Rubinstein, Phys. Rev. Lett. 65, 1279 (1990).
Y. Oda, H. Fujita, H. Toyoda, T. Kaneko, T. Kohara, I. Nakada, and K. Asayama, Jpn. J. Appl. Phys. 26, L1660 (1987).
T. Oguchi, Jpn. J. Appl. Phys. 26, L417 (1987).
A. Oguri and S. Maekawa, Phys. Rev. B 41, 6977 (1990).
K. Ohbayashi, N. Ogita, M. Udagawa, Y. Aoki, Y. Maeno, and T. Fujita, Jpn. J. Appl. Phys. 26, L423 (1987).
F. J. Ohkawa, Phys. Rev. B 42, 4163 (1990).
Y. Ohta and S. Maekawa, Phys. Rev. B 41, 6524 (1990).
T. Ohtani, Mater. Res. Bull. 24, 343 (1989).
N. Okazaki, T. Hasegawa, K. Kishio, K. Kitazawa, A. Kishi, Y. Ikeda, M. Takano, K. Oda, H. Kitaguchi, J. Takada, and Y. Miura, Phys. Rev. B 41, 4296 (1990).
E. Oldfield, C. Coretsopoulos, S. Yang, L. Reven, H. C. Lee, J. Shore, O. H. Han, E. Ramli, and D. Hicks, Phys. Rev. B 40, 6832 (1989).
O. H. Olsen and M. R. Samuelsen, Phys. Rev. B 43, 10273 (1991).
N. P. Ong, Z. Z. Wang, J. Clayhold, J. M. Tarascon, L. H. Greene, and W. R. McKinnon, Phys. Rev. B 55, 8807 (1987).
N. P. Ong, Phys. Rev. B 43, 193 (1991).
H. Kamerlingh Onnes, Leiden Commun., 120a, 122b, 124c (1911).
M. Onoda, S. Shamoto, M. Sato, and S. Hosoya, Jap. J. Appl. Phys. 26, L363 (1987).
T. P. Orlando and K. A. Delin, "Foundations of Applied Superconductivity," Addison-Wesley, Reading, MA, 1991.
J. A. Osborn, Phys. Rev. 67, 351 (1945).
S. B. Oseroff, D. C. Vier, J. F. Smyth, C. T. Sailing, S. Schultz, Y. Dalichaouch, B. W. Lee, M. B. Maple, Z. Fisk, J. D. Thompson, J. L. Smith, and E. Zirngiebl, in "Novel Superconductivity" (S. A. Wolf and V. Z. Kresin, Eds.), p. 679, Plenum, NewYork, 1987.
M. S. Osofsky, H. Rakoto, J. C. Ousset, J. P. Ulmet, J. Leotin, S. Askenazy, D. B. Crisey, J. S. Horwitz, E. F. Skelton, and S. A. Wolf, Physica C 182, 257 (1991).
J. G. Ossandon, J. R. Thompson, D. K. Christen, B. C. Sales, Y. Sun, and K. W. Lay, Phys. Rev. B 46, 3050 (1992).
J. G. Ossandon, J. R. Thompson, D. K. Christen, B. C. Sales, H. R. Kerchner, J. O. Thomson, Y. R. Sun, K. W. Lay, and J. E. Tkaczyk, Phys. Rev. B 45, 12534 (1992).
S. B. Ota, Phys. Rev. B 35, 8730 (1987).
S. B. Ota, V. S. Sastry, E. Gmelin, P. Murugaraj, and J. Maier, Phys. Rev. B 43, 6147 (1991).
C. E. Otis and R. W. Dreyfus, Phys. Rev. Lett. 67, 2102 (1991).
H. R. Ott, H. Rudigier, Z. Fisk, and J. L. Smith, Phys. Rev. Lett. 50, 1595 (1983).
H. R. Ott, in "Novel Superconductivity" (S. A. Wolf, and V. Z. Kresin, Eds.), p. 187, Plenum, NewYork. H. R. Ott, "Ten Years of Superconductivity: 1980–1990," Kluwer, 1993.
M. Oussena, S. Senoussi, G. Collin, J. M. Broto, H. Rakoto, S. Askenazy, and J. C. Ousset, Phys. Rev. B 36, 4014 (1987).
Yu. N. Ovchinnikov and B. I. Ivlev, Phys. Rev. B 43, 8024 (1991).
A. W. Overhauser, Phys. Rev. Lett. 4, 462 (1960).
A. W. Overhauser, Phys. Rev. 128, 1437 (1962).
A. W. Overhauser and L. L. Daemen, Phys. Rev. Lett. 62, 1691 (1989).
F. J. Owens, Physica C 178, 456 (1991).
F. J. Owens, Physica C 195, 225 (1992).
M.-A. Ozaki and K. Machida, Phys. Rev. B 39, 4145 (1989).
S. Ozcan, D. M. Broun, B. Morgan, R. K. W. Haselwimmer, J. L. Sarrao, S. Kamal, C.

P. Bidinosti, and P. J. Turner M, Lett. 62, 412 (2003).
S. Pagano, B. Ruggiero, and E. Sarnelli, Phys. Rev. B 43, 5364 (1991).
A. Paitskar, N. K. Budras, W. P. Beyemann, P. C. and S. L. Bud'ko, Phys. Rev. B 54, R3772 (1996).
E. J. Pakulis, Phys. Rev. B 42, 10746 (1990).
T. T. M. Palstra, A. A. Menovsky, and J. A. Mydosh; Coles (1987); Phys. Rev. B 33, 6527 (1988).
T. T. M. Palstra, B. Batlogg, L. F. Schneemeyer, and J. V. Waszczak, Phys. Rev. Lett. 61, 1662 (1988).
T. T. M. Palstra, B. Batlogg, R. B. Van Dover, L. F. Schneemeyer, and J. V. Waszczak, Appl. Phys. Lett. 54, 763 (1989).
T. T. M. Palstra, B. Batlogg, L. F. Schneemeyer, J. V. Waszczak, Phys. Rev. Lett. 64, 3090 (1990).
T. T. M. Palstra, R. C. Haddon, A. F. Hebard, and J. Zaanen, Phys. Rev. Lett. 68, 1054 (1992).
T. T. M. Palstra and R. C. Haddon, Solid State Commun., 92, 71 (1994).
W. Pan and S. Doniach, Phys. Rev. B 49, 1192 (1994).
C. Panagopoulos, J. R. Cooper, T. Xiang, G. B. Peacock, I. Gameson, and P. P. Edwards, Phys. Rev. Lett. 79, 2320 (1997).
D. A. Papaconstantopoulos, A. Pasturel, J. P. Julien, and F. Cyrot-Lackmann, Phys. Rev. B 40, 8844 (1989).
M. Paranthaman, J. R. Thompson, Y. R. Sun, and J. Brynestad, Physica C 213, 271 (1993).
M. Paranthaman, Physica C 222, 7 (1994).
G. S. Park, C. E. Cunningham, B. Cabrera, and M. E. Huber, Phys. Rev. Lett. 68, 1920 (1992).
R. D. Parks and W. A. Little, Phys. Rev. 133, A97 (1964).
R. D. Parks, Ed. "Superconductivity," Vols. 1 and 2, Dekker, New York, 1969.
P. C. Pattnaik, C. L. Kane, D. M. Newns, and C. C. Tsuei, Phys. Rev. B 45, 5714 (1992).
D. McK Paul, H. A. Mook, A. W. Hewat, B. C. Sales, L. A. Boatner, J. R. Thompson, and M. Mostoller, Phys. Rev. B 37, 2341 (1988).
D. McK Paul, H. A. Mook, L. A. Boatner, B. C. Sales, J. O. Ramey, and L. Cussen, Phys. Rev. B 39, 4291 (1989).
L. Pauling and E. B. Wilson, "Introduction to Quantum Mechanics," McGraw-Hill, New York, 1935.
L. M. Paulius, C. C. Almasan, and M. B. Maple, Phys. Rev. B 47, 11627 (1993).
S. D. Peacor and C. Uher, Phys. Rev. B 39, 11559 (1989).
S. D. Peacor, R. Richardson, J. Burm, C. Uher, and A. Kaiser, Phys. Rev. B 42, 2684 (1990).
S. D. Peacor, J. L. Cohn, and C. Uher, Phys. Rev. B 43, 8721 (1991).
S. D. Peacor, R. A. Richardson, F. Nori, and C. Uher, Phys. Rev. B 44, 9508 (1991).
W. B. Pearson, "Handbook of Lattice Spacings and Structures of Metals," p. 79, Pergamon, New York, 1958.
M. J. Pechan and J. A. Horvath, Am. J. Phys. 58, 642 (1990).
N. F. Pedersen and A. Davidson, Phys. Rev. B 41, 178 (1990).
S. Pei, J. D. Jorgensen, B. Dabrowski, D. G. Hinks, D. R. Richards, A. W. Mitchell, J. M. Newsam, S. K. Sinha, D. Vaknin, and A. J. Jacobson, Phys. Rev. B 41, 4126 (1990).
K. E. Peiponen and E. Vartiainen, Phys. Rev. B 44, 8301 (1991).
M. Pekala, K. Pekala, and A. Pajaczkowska, Phys. Status Solidi B 152, Kl (1989).
M. T. Pencarinha, C. P. Poole, Jr., H. A. Farach, and O. A. Lopez, J. Phys. Chem. Solids 56, 301 (1995).
D. R. Penn and M. L. Cohen, Phys. Rev. B 46, 5466 (1992).
T. Penney, S. von Molnar, D. Kaiser, F. Holtzberg, and A. W. Kleinsasser, Phys. Rev. B 38, 2918 (1988).
C. H. Pennington, D. J. Durand, D. B. Zax, C. P. Slichter, J. P. Rice, and D. M. Ginsberg, Phys. Rev. B 37, 7944 (1988).
C. H. Pennington, D. J. Durand, C. P. Slichter, J. P. Rice, E. D. Bukowski, and D. M. Ginsberg, Phys. Rev. B 39, 274, 2902 (1989).
C. H. Pennington and C. P. Slichter, in "Physical Properties of High Temperature Superconductors" (D. M. Ginsberg, Ed.), Vol. 2 Chap. 5, World Scientific, Singapore, 1990.
C. H. Pennington and C. P. Slichter, Phys. Rev. Lett. 66, 381 (1991).
S. J. Pennycook, M. F. Chisholm, D. E. Jesson, D. P. Norton, D. H. Lowndes, R. Feenstra, H. R. Ker-chner, and J. O. Thomson, Phys. Rev. Lett. 67, 765 (1991).
F. Perez, X. Obradors, J. Fontcuberta, M. Vallet, and J. Gonzalez-Calbet, Physica C 185–189, 1843 (1991).

A. Perez-Gonzalez and J. P. Carbotte, Phys. Rev. B 45, 9894 (1992).
A. Perez-Gonzalez, E. J. Nicol, and J. P. Carbotte, Phys. Rev. B 45, 5055 (1992).
R. L. Peterson and J. W. Ekin, Physica C 757, 325 (1989).
R. L. Peterson and J. W. Ekin, Phys. Rev. B 42, 8014 (1990).
M. F. Petras and J. E. Nordman, Phys. Rev. B 39, 6492 (1989).
B. W. Pfalzgraf and H. Spreckels, J. Phys. C 27, 4359 (1987).
J. C. Phillips, Phys. Rev. B 36, 861 (1987).
J. C. Phillips, "Physics of High-Tc Superconductors," Academic Press, New York, 1989a.
J. C. Phillips, Phys. Rev. B 40, 7348, 8774 (1989b).
J. C. Phillips, Mater. Lett. 18, 106 (1993).
N. E. Phillips, R. A. Fisher, and J. E. Gordon, Prog. Low Temp. Phys. 19 (1991).
T. Pichler, M. Matus, J. Kiirti, and H. Kuzmany, Phys. Rev. B 45, 13841 (1992).
W. E. Pickett, H. Krakauer, D. A. Papaconstantopoulos, and L. L. Boyer, Phys. Rev. B 35, 7252 (1987).
W. E. Pickett, Rev. Mod. Phys. 61, 433 (1989).
W. E. Pickett, R. E. Cohen, and H. Krakauer, Phys. Rev. B 42, 8764 (1990).
W. E. Pickett, H. Krakauer, R. E. Cohen, and D. J. Singh, Science 255, 46 (1992).
M. W. Pieper, Physica C 190, 261 (1992).
S. W. Pierson and O. T. Vails, Phys. Rev. B 45, 2458 (1992).
C. G. S. Pillai, Solid State Commun. 80, 277 (1991).
W. Pint and E. Schachinger, Phys. Rev. B 43, 7664 (1991).
L. Pintschovius, J. M. Bassat, P. Odier, F. Gervais, G. Chevrier, W. Reichardt, and F. Gompf, Phys. Rev. B 40, 2229 (1989).
A. B. Pippard, Proc. R. Soc. London A 216, 547 (1953).
M. Pissas, G. Kallias, A. Simopoulos, D. Niarchos, and A. Kostikas, Phys. Rev. B 46, 14119 (1992).
F. Pistolesi and G. C. Strinati, Phys. Rev. B 49, 6356 (1994).
B. Plaqais and Y. Simon, Phys. Rev. B 39, 2151 (1989).
B. B. Plapp and A. W. Hubler, Phys. Rev. Lett. 65, 2302 (1990).
A. Poddar, P. Mandal, K. G. Ray, A. N. Das, B. Ghosh, P. Choudhury, and S. Lahiri, Physica C 759, 226 (1989).
D. Poilblanc and E. Dagotto, Phys. Rev. B 42, 4861 (1990).
C. Politis, V. Buntar, W. Krauss, and A. Gurevich, Europhys. Lett. 17, 175 (1992).
A. Pomar, A. Diaz, M. V. Ramallo, C. Torron, J. A. Veira, and F. Vidal, Physica C 218, 257 (1993).
C. P. Poole, Jr., and H. A. Farach, "Relaxation in Magnetic Resonance," Academic Press, New York, 1971.
C. P. Poole, Jr., "Electron Spin Resonance," 2nd ed., Wiley, New York, 1983.
C. P. Poole, Jr., and H. A. Farach, "Theory of Magnetic Resonance," 2nd ed., Wiley, New York, 1987.
C. P. Poole, Jr., T. Datta, and H. A. Farach, "Copper Oxide Superconductors," Wiley, New York, 1988.
C. P. Poole, Jr. and H. A. Farach, Magn. Reson. Relat. Phenom., Proc. 24th Ampere Congr., Poznan, p. 601 (1988).
C. P. Poole, Jr., T. Datta, and H. A. Farach, J. Supercond. 2, 369 (1989).
C. P. Poole, Jr., and H. A. Farach, Eds., "Handbook of Electron Spin Resonance," Amer. Inst. Phys., New York, 1994.
A. Poppl, L. Kevan, H. Kimura, and R. N. Schwartz, Phys. Rev. B 46, 8559 (1992).
A. Porch, J. R. Cooper, D. N. Zheng, J. R. Waldram, A. M. Campbell, and P. A. Freeman, Physica C 214 350 (1953)
A. M. Portis, K. W. Blazely, and F. Waldner, Physica C 153, 308 (1988).
J. Prade, A. D. Kulkarni, and F. W. de Wette, U. Schroder, and W. Kress, Phys. Rev. B 39, 2771 (1989).
A. K. Pradhan, S. J. Hazell, J. W. Hodby, C. Chen, Y. Hu, and B. M. Wanklyn, Phys. Rev. B 47, 11374 (1993).
R. Prange and S. Girvin, Eds., "The Quantum Hall Effect," Springer-Verlag, Heidelberg, 1987.
K. Prassides, M. J. Rosseinsky, A. J. Dianoux, and P. Day, J. Phys. Condens. Matter 4, 965 (1992).
K. Prassides, A. Lappas, M. Buchgeister and P. Verges, Europhys. Lett. 29, 641 (1995).
G. Preosti, H. Kim, and P. Muzikar, Phys. Rev. B 50, 1259 (1994).

N. W. Preyer, M. A. Kastner, C. Y. Chen, R. J. Birgeneau, and Y. Hidaka, Phys. Rev. B 44, 407 (1991).
D. Prost, L. Fruchter, I. A. Campbell, N. Motohira, and M. Konczykowski, Phys. Rev. B 47, 3457 (1993).
R. Prozorov, E. R. Yakoby, I. Felner and Y. Yeshurun, Physica, C 233, 367 (1994).
R. Prozorov, R. W. Giannetta, A. Carrington, and F. M. Araujo-Moreira, Phys. Rev. B 62 115 (2000).
R. Prozorov, R. W. Giannetta, A. Carrington, P. Fournier, R. L. Greene, P. Guptasarma, D. G. Hinks, and A. R. Banks, App. Phys. Lett. 77 4202 (2000).
R. Prozorov, R. W. Giannetta, S. L. Bud'ko and P. C. Canfield, Phys. Rev. B 64, 180501 (2001).
R. Prozorov, A. Snezhko, T. He, and R. J. Cava, Phys. Rev. B 60, 180502 (2003).
R. Prozorov, R. W. Giannetta, N. Kameda, T. Tamegai, J. A. Schlueter and P. Founier, Phys. Rev. B 67, 18450 (2003).
W. Prusseit, H. Walter, R. Semerad, H. Kinder, W. Assmann, H. Huber, B. Kabius, H. Burkhardt, D. Rainer, and J. A. Sauls, Physica C 318, 396 (1999.)
T. Puig, L. M. Martinez, M. T. Aurell, A. Sanchez, D.-X. Chen, and J. S. Munoz, in "Physics and Materials Science of High-Temperature Superconductivity" (R. Kossowsky, S. Methfessel, and D. Wohlbeben, Eds.), p. 467, Kluwer Academic, Dordrecht, 1990.
B. Pumpin, H. Keller, W. Kundig, W. Odermatt, I. M. Savic, J. W. Schneider, H. Simmler, P. Zimmer-mann, E. Kaldis, S. Rusiecki, Y. Maeno, and C. Rossel, Phys. Rev. B 42, 8019 (1990).
P. Pureur and J. Schaf, Solid State Commun. 78, 723 (1991).
S. N. Putilin, I. Bryntse, and E. V. Antipov, Mater. Res. Bull. 26, 1299 (1991).
S. N. Putilin, E. V. Antipov, E. V. Chmaissem, and M. Marezio, Nature 362, 266 (1993).
D. S. Pyun and T. R. Lemberger, Phys. Rev. B 44, 7555 (1991).
K. F. Quader and E. Abrahams, Phys. Rev. B 38, 11977 (1988).
R. M. Quick, C. Esebbag, and M. de Llano, Phys. Rev. B 47, 11512 (1993).
M. Rabinowitz and T. McMullen, Chem. Phys. Lett. 218, 437 (1994).
H. B. Radousky, J. Mater. Res. 7, 1917 (1992).
R. J. Radtke, K. Levin, H.-B. Shiittler, and M. R. Norman, Phys. Rev. B 48, 653 (1993).
R. J. Radtke, V. N. Kostur, and K. Levin, Phys. Rev. B 53, R522 (1996).
D. Rainer and J. A. Sauls, "Proc. 1992 Spring School on Cond. Matter Phys., Trieste, Italy," World Scientific, Singapore, 1994.
A. K. Rajagopal and S. D. Mahanti, Phys. Rev. B 44, 10210 (1991).
P. F. Rajam, C. K. Subramaniam, S. Kasiviswanathan, and R. Srinivasan, Solid State Commun. 71, 475 (1989).
R. Rajput and D. Kumar, Phys. Rev. B 42, 8634 (1990).
B. Rakvin, M. Pozek, and A. Dulcic, Solid State Commun. 72, 199 (1989).
B. Rakvin, T. A. Mahl, A. S. Bhalla, Z. Z. Sheng, and N. S. Dalai, Phys. Rev. B 41, 769 (1990).
K. S. Rails, D. C. Ralph, and R. A. Buhrman, Phys. Rev. B 40, 11561 (1989).
S. Ramakrishnan, R. Kumar, P. L. Paulose, A. K. Grover, and P. Chaddah, Phys. Rev. B 44, 9514 (1991).
R. Ramakumar, R. Kumar, K. P. Jain, and C. C. Chancey, Phys. Rev. B 48, 6509 (1993).
S. Ramasesha and C. N. R. Rao, Phys. Rev. B 44, 7046 (1991).
A. P. Ramirez, T. Siegrist, T. T. M. Palstra, J. D. Garrett, E. Bruck, A. A. Menovsky, and J. A. Mydosh, Phys. Rev. B 44, 5392 (1991).
A. P. Ramirez, A. R. Kortan, M. J. Rosseinsky, S. J. Duclos, A. M. Mujsce, R. C. Haddon, D. W. Murphy, A. V. Makhija, S. M. Zahurak, and K. B. Lyons, Phys. Rev. Lett. 68, 1058 (1992a).
A. P. Ramirez, M. J. Rosseinsky, D. W. Murphy, and R. C. Haddan, Phys. Rev. Lett. 69, 1687 (1992b).
J. Rammer, Phys. Rev. B 36, 5665 (1987).
J. Rammer, Phys. Rev. B 43, 2983 (1991).
C. N. R. Rao, P. Ganguly, A. K. Raychaudhuri, R. A. Mohan Ram, and K. Sreedhar, Nature 326, 856 (1987).
K. V. Rao, D.-X. Chen, J. Nogues, C. Politis, C. Gallo, and J. A. Gerber, in "High Temperature Superconductors" (D. U. Gubser and M. Schluter, Eds.), p. 133, Mater. Res. Soc., Pittsburgh, 1987.
C. N. R. Rao, Philos. Trans. R. Soc. London Ser. A336, 595 (1991).
C. N. R. Rao, A. K. Santra, and D. D. Sarma, Phys. Rev. B 45, 10814 (1992).

U. Rauchschwalbe, F. Steglich, G. R. Stewart, A. L. Giorgi, P. Fulde, and K. Maki, Europhys. Lett. 3, 751 (1987).
J. Redinger, A. J. Freeman, J. Yu, and S. Massidda, Phys. Lett. A 124, 469 (1987).
M. Reedyk, C. V. Stager, T. Timusk, J. S. Xue, and J. E. Greedan, Phys. Rev. B 45, 10057 (1992b).
M. E. Reeves, S. E. Stupp, T. Friedmann, F. Slakey, D. M. Ginsberg, and M. V. Klein, Phys. Rev. B 40, 4573 (1989).
J. D. Reger, T. A. Tokuyasu, A. P. Young, and M. P. A. Fisher, Phys. Rev. B 44, 7147 (1991).
M. N. Regueiro, B. Salce, R. Calemczuk, C. Marin, and J. Y. Henry, Phys. Rev. B 44, 9727 (1991).
W. Rehwald, M. Rayl, R. W. Cohen, and G. D. Cody, Phys. Rev. B 6, 363 (1972).
F. Reif, "Fundamentals of Statistical and Thermal Physics," McGraw-Hill, New York, 1965.
Y. T. Ren, J. Clayhold, F, Chen, Z. J. Huang, X. D. Qiu, Y. Y. Sun, R. L. Meng, Y. Y. Xue, and C. W. Chu, Physica C 217, 6 (1993).
B. Renker, F. Gompf, E. Gering, D. Ewert, H. Rietschel, and A. Dianoux, Z. Phys. B 73, 309 (1988).
Ch. Renner, A. D. Kent, Ph. Niedermann, O. Fischer, and F. Levy, Phys. Rev. Lett. 67, 1650 (1991).
L. Reven, J. Shore, S. Yang, T. Duncan, D. Schwartz, J. Chung, and E. Oldfield, Phys. Rev. B 43, 10466 (1991).
C. M. Rey and L. R. Testardi, Phys. Rev. B 44, 765 (1991).
A. P. Reyes, D. E. MacLaughlin, M. Takigawa, P. C. Hammel, R. H. Heffner, J. D. Thompson, J. E. Crow, A. Kebede, T. Mihalisin, and J. Schwegler, Phys. Rev. B 42, 2688 (1990).
A. P. Reyes, D. E. MacLaughlin, M. Takigawa, P. C. Hammel, R. H. Heffner, J. D. Thompson, and J. E. Crow, Phys. Rev. B 43, 2989 (1991).
C. A. Reynolds, B. Serin, W. H. Wright, and L. B. Nesbitt, Phys. Rev. 78, 487 (1950).
H.-C. Ri, F. Kober, R. Gross, R. P. Huebener, and A. Gupta, Phys. Rev. B 43, 13739 (1991).
H.-C. Ri, J. Kober, A. Beck, L. Alff, R. Gross, and R. P. Huebener, Phys. Rev. B 47, 12312 (1993).
J. K. Rice, S. W. McCauley, A. P. Baronavski, J. S. Horwitz, and D. B. Chrisey, Phys. Rev. B 47, 6086 (1993).
J. P. Rice, N. Rigakis, D. M. Ginsberg, and J. M. Mochel, Phys. Rev. B 46, 11050 (1992).
T. M. Rice, and M. Sigrist J. Phys. : Condens. Matter 7, L643 (1995).
P. L. Richards and M. Tinkham, Phys. Rev. 119, 575 (1960).
R. A. Richardson, S. D. Peacor, F. Nori, and C. Uher, Phys. Rev. Lett. 67, 3856 (1991).
C. T. Riecke, Th. Wolkhausen, D. Fay, and L. Tewordt, Phys. Rev. B 39, 278 (1989).
E. Riedel, Z. Naturforsch A. 790, 1634 (1964).
E. K. Riedel, H.-F. Cheung, and Y. Gefen, Phys. Scr. T 25, 357 (1989).
P. S. Riseborough, Phys. Rev. B 45, 13984 (1992).
B. Roas, L. Schultz, and G. Saemann-Ischenko, Phys. Rev. Lett. 64, 479 (1990).
B. W. Roberts, J. Phys. Chem. Ref. Data 5, 581 (1976).
C. O. Rodriguez, Phys. Rev. B 49, 1200 (1994).
E. Rodriguez, J. Luzuriaga, C. D'Ovidio, and D. A. Esparza, Phys. Rev. B 42, 10796 (1990).
J. P. Rodriguez, Phys. Rev. B 36, 168 (1987).
J. P. Rodriguez and B. Doucot, Phys. Rev. B 42, 8724 (1990).
J. P. Rodriguez and B. Doucot, Phys. Rev. B 45, 971 (1992).
C. T. Rogers, K. E. Myers, J. N. Eckstein, and I. Bozovic, Phys. Rev. Lett. 69, 160 (1992).
D. S. Rokhsar, Phys. Rev. Lett. 65, 1506 (1990).
M. Rona, Phys. Rev. 42, 4183 (1990).
A. C. Rose-Innes and E. H. Rhoderick, "Introduction to Superconductivity," Pergamon, Oxford, 1994.
P. A. Rosenthal, M. R. Beasley, K. Char, M. S. Colclough, and G. Zaharchuk, Appl. Phys. Lett. 59, 3482 (1991).
H. Rosner, S.-L. Drechsler, K. Koernik, I. Opahle, and H. Eschrig, (K. H. Muller and V. Narozhnyi, Eds.), Rare Earth Transition Metal Borocarbides (Nitrides); Superconducting Magnetic and Normal State Properties, p. 71, Kluwer Acad. Publ. Dordrecht, (2001)
H. Rosner, R. Weht, M. D. Johannes, W. E. Pickett, and E. Tosatti, Phys. Rev. Lett. 88, 27001 (2002).
J. Rossat-Mignod, P. Burlet, M. J. G. M. Jurgens, J. Y. Henry, and C. Vettier, Physica C 152, 19 (1988).
M. J. Rosseinsky, A. P. Ramirez, S. H. Glarum, D. W. Murphy, R. C. Haddon, A. F. Hebard, T. T. M. Palstra, A. R. Kortan, S. M. Zahurak,

and A. V. Makhija, Phys. Rev. Lett. 66, 2830 (1991).
C. Rossel, Y. Maeno, and I. Morgenstein, Phys. Rev. Lett. 62, 681 (1989a); C. Rossel, Y. Maeno, and F. H. Holtzberg, IBM J. Res. Dev. 33, 328 (1989b); C. Rossel, O. Pena, H. Schmitt, and M. Sargent, Physica C 181, 363 (1991).
C. S. J. Rothman, J. L. Routbort, U. Welp, and J. E. Baker, Phys. Rev. B 44, 2326 (1991).
V. A. Rowe and R. P. Huebener, Phys. Rev. 785, 666 (1969).
J. M. Rowell and R. C. Dynes, in "Phonons" (M. A. Nusimovici, Ed.), Flammarion, Sciences, Paris, 1972.
G. J. Rozing, P. E. Mijnarends, A. A. Menovsky, and P. F. de Chatel, Phys. Rev. B 43, 9523 (1991).
A. E. Ruckenstein, P. J. Hirschfeld, and J. Appel, Phys. Rev. B 36, 857 (1987); reprinted in "Theories of High Temperature Superconductivity" (J. W. Halley, Ed.), p. 137. Addison-Wesley, Reading, MA, 1988.
S. Ryu, S. Doniach, G. Deutscher, and A. Kapitulnik, Phys. Rev. Lett. 68, 710 (1992).
M. S. Rzchowski, L. L. Sohn, and M. Tinkham, Phys. Rev. B 43, 8682 (1991).
S. Sachdev and Z. Wang, Phys. Rev. B 43, 10229 (1991).
S. Sachdev, Phys. Rev. B 45, 389 (1992).
E. Sacher and J. E. Klemberg-Sapieha, Phys. Rev. B 39, 1461 (1989).
C. A. R. Sa de Melo, Z. Wang, and S. Doniach, Phys. Rev. Lett. 68, 2078 (1992).
H. Safar, C. Duran, J. Guimpel, L. Civale, J. Luzuriaga, E. Rodriguez, F. de la Cruz, C. Fainstein, L. F. Schneemeyer, and J. V. Waszczak, Phys. Rev. B 40, 7380 (1989).
H. Safar, H. Pastoriza, F. de la Cruz, D. J. Bishop, L. F. Schneemeyer, and J. Waszczak, Phys. Rev. B 43, 13610 (1991).
H. Safar, P. L. Gammel, D. J. Bishop, D. B. Mitzi, and A. Kapitulnik, Phys. Rev. Lett. 68, 2672 (1992).
H. Safar, P. L. Gammel, D. A. Huse, D. J. Bishop, W. C. Lee, J. Giapintzakis, and D. M. Ginsberg, Phys. Rev. Lett. 70, 3800 (1993).
L. Sagdahl, S. Gjolmesli, T. Laegreid, K. Fossheim, and W. Assmus, Phys. Rev. B 42, 6797 (1990).
L. Sagdahl, T. Laegreid, K. Fossheim, M. Murkami, H. Fujimoto, S. Gotoh, K. Yamaguchi, H. Ya-mauchi, N. Koshizuka, and S. Tanaka, Physica C 172, 495 (1991).
N. Sahoo, S. Markert, T. P. Das, and K. Nagamine, Phys. Rev. B 41, 220 (1990).
D. Saint-James and P. D. de Gennes, Phys. Lett. 7, 306 (1963).
D. Saint-James, E. J. Thomas, and G. Sarma, "Type II Superconductivity," Pergamon, Oxford, 1969.
K. Saitoh and T. Nishino, Phys. Rev. B 44, 7070 (1991).
S. Saito and A. Oshiyama, Phys. Rev. Lett. 66, 2637 (1991).
M. B. Salamon and J. Bardeen, Phys. Rev. Lett. 59, 2615 (1987).
M. B. Salamon, in "Physical Properties of High Temperature Superconductors," (D. M. Ginsberg, Ed.), Vol. 1, Chap. 2, World Scientific, Singapore, 1989.
S. Salem-Sugui, Jr., E. E. Alp, S. M. Mini, M. Ramanathan, J. C. Campuzano, G. Jennings, M. Faiz, S. Pei, B. Dabrowski, Y. Zheng, D. R. Richards, and D. G. Hinks, Phys. Rev. B 43, 5511 (1991).
A. V. Samoilov, A. A. Yurgens, and N. V. Zavaritsky, Phys. Rev. B 46, 6643 (1992).
P. Samuely, P. Szabo, J. Kacmarcik, T. Klein, and A. G. M. Jansen, Physica C 385, 244 (2003). Ft
B. A. Sanborn, P. B. Alien, and D. A. Papaconstantopoulos, Phys. Rev. B 40, 6037 (1989).
A. Sanchez and D.-X. Chen, in "Susceptibility of Superconductors and Other Spin Systems" (T. Francavilla, R. A. Hein, and D. Leiberger, Eds.), Plenum, New York, 1991.
A. Sanchez, D.-X. Chen, J. Munoz, and Y.-Z. Li, Physica C 175, 33 (1991).
P. Santhanam and C. C. Chi, Phys. Rev. B 38, 11843 (1988).
A. Santoro, in "High Temperature Superconductivity" (J. W. Lynn, Ed.), Chap. 4, Springer-Verlag, Berlin, 1990.
E. Sardella, Phys. Rev. B 45, 3141 (1992).
D. D. Sarma, P. Sen, C. Carbone, R. Cimino, and W. Gudat, Phys. Rev. B 39, 12387 (1989).
J. L. Sarrao, M. C. de Andrade, J. Herrman, S. H. Han, Z. Fisk, M. B. Maple, and R. Cava, Physica C 229, 65 (1994).
W. M. Saslow, Phys. Rev. B 39, 2710 (1989).
J. S. Satchel), R. G. Humphreys, N. G. Chew, J. A. Edwards, and M. J. Kane, Nature 334, 331 (1988).

N. Sato, T. Sakon, N. Takeda, T. Komatsubara, C. Geibei, and F. Steglich, J. Phys. Soc. Jpn. 61, 32 (1992).
S. Satpathy and R. M. Martin, Phys. Rev. B 36, 7269 (1987).
C. B. Satterthwaite, Phys. Rev. 125, 873 (1962).
A. Saul and M. Weissmann, Phys. Rev. B 42, 4196 (1990).
J. Schaf, P. Pureur, and J. V. Kunzler, Phys. Rev. B 40, 6948 (1989).
S. Scheidl and G. Hackenbroich, Phys. Rev. B 46, 14010 (1992).
A. Schenstrom, M-F. Xu, Y. Hong, D. Bein, M. Levy, B. K. Sarma, S. Adenwalla, Z. Zhao, T. Tokuyasu, D. W. Hess, J. B. Ketterson, J. A. Sauls, and D. G. Hinks, Phys. Rev. Lett. 62, 332 (1989).
A. Schilling, M. Cantoni, J. D. Guo, and H. R. Ott, Nature 363, 56 (1993).
A. Schilling, M. Catoni, O. Jeandupeux, J. D. Guo, and H. R. Ott, in "Advances in Superconductivity" (T. Fujita and Y. Shiohara, Eds.), Vol. 6, Springer-Verlag, Berlin, 1994a.
A. Schilling, O. Jeandupeux, S. Biichi, H. R. Ott, and C. Rossel, Physica C 235, (1994b).
J. E. Schirber, D. L. Overmyer, K. D. Carlsan, J. M. Williams, A. M. Kini, H. H. Wang, H. A. Charlier, B. J. Love, D. M. Watkins, and G. A. Yaconi, Phys. Rev. B 44, 4666 (1991).
Z. Schlesinger, R. L. Greene, J. G. Bednorz, and K. A. Miiller, Phys. Rev. B 35, 5334 (1987).
Z. Schlesinger, R. T. Collins, J. A. Calise, D. G. Hinks, A. W. Mitchell, Y. Zheng, B. Dabrowski, N. E. Bickers, and D. J. Scalapino, Phys. Rev. B 40, 6862 (1989).
Z. Schlesinger, R. T. Collins, F. Holtzberg, C. Feild, G. Koren, and A. Gupta, Phys. Rev. B 41, 11237 (1990a).
Z. Schlesinger, R. T. Collins, F. Holtzberg, C. Feild, S. H. Blanton, U. Welp, G. W. Crabtree, Y. Fang,and J. Z. Liu, Phys. Rev. Lett. 65, 801 (1990b).
D. Schmeltzer, Phys. Rev. B 49, 6944 (1994).
A. Schmid, Phys. Kondens. Mat. 8, 129 (1968).
J. M. Schmidt, A. N. Cleland and J. Clarke, Phys. Rev. B 43, 229 (1991).
P. Schmitt, P. Kummeth, L. Schultz, and G. Saemann-Ischenko, Phys. Rev. Lett. 67, 267 (1991).
H. Schnack and R. Griessen, Phys. Rev. Lett. 68, 2706 (1992).
L. F. Schneemeyer, J. K. Thomas, T. Siegrist, B. Batlogg, L. W. Rupp, R. L. Opila, R. J. Cava, and D. W. Murphy, Nature 335, 421 (1988).
T. Schneider, Z. Phys. B 85, 187 (1991).
T. Schneider, Z. Gedik, and S. Ciraci, Z. Phys. B 83, 313 (1991).
T. Schneider, Physica C 195, 82 (1992).
T. Schneider and H. Keller, Phys. Rev. Lett. 69, 3374 (1992).
A. J. Schofield and Wheatley, Phys. Rev. B 47, 11607 (1993).
K. Schonhammer, Phys. Rev. B 42, 2591 (1990).
J. R. Schrieffer, "Theory of Superconductivity," Addison-Wesley, New York, 1964.
J. R. Schrieffer, X.-G. Wen, and S.-C. Zhang, Phys.Rev. Lett. 60, 944 (1988).
E. A. Schuberth, B. Strickler, and K. Andres, Phys.Rev. Lett. 68, 117 (1992).
I. K. Schuller, D. G. Hinks, M. A. Beno, S. W. Capone II, L. Soderholm, J. P. Locquet, Y. Bruynseraede, C. U. Segre, and K. Zhang, Solid State Commun. 63, 385 (1987).
J. Schwartz, S. Nakamae, G. W. Raban, Jr., J. K. Heuer, S. Wu, J. L. Wagner, and D. G. Hinks, Phys. Rev. B 48, 9932 (1994).
H. Schwenk, F. Gross, C. P. Heidmann, K. Andres, D. Schweitzer, and H. Keller, Mol. Cryst. Liq. Cryst.119, 329 (1985); Phys. Rev. B 31, 3138 (1985).
P. Seidel, E. Heinz, M. Siegel, F. Schmidl, K. J. Zach, and H.-J. Kohler, in "Proc. 4th Int. Conf. on Superconducting and Quantum Effect Devices and Their Applications," Berlin, June 1991.
G. T. Seidler, T. F. Rosenbaum, D. L. Heinz, J. W. Downey, A. P. Paulikas, and B. W. Veal, Physica C 183, 333 (1991).
G. T. Seidler, T. F. Rosenbaum, and B. W. Veal, Phys. Rev. B 45, 10162 (1992).
K. Semba, T. Ishii, and A. Matsuda, Phys. Rev. Lett. 67, 769 (1991).
S. Sengupta, C. Dasgupta, H. R. Krishnamurthy, G. I. Menon, and T. V. Ramakrishnan, Phys. Rev. Lett. 67, 3444 (1991).
S. Senoussi, M. Oussena, and S. Hadjoudi, J. Appl. Phys. 63, 4176 (1988).
A. Sequeira, H. Rajagopal, P. V. P. S. S. Sastry, J. V.Yakhmi, R. M. lyer, and B. A. Dasannacharya, Physica B 180–181, 429 (1992).
M. Sera, S. Shamoto, and M. Sato, Solid State Commun. 68, 649 (1988).

S. Sergeenkov and M. Ausloos, Phys. Rev. B 47, 14476 (1993).
R. D. Shannon and P. E. Bierstedt, J. Am. Ceram. Soc. 58, 635 (1970).
C. Shao-Chun, Z. Dong-Ming, Z. Dian-Lin, H. M. Duan, and A. M. Hermann, Phys. Rev. B 44, 12571 (1991).
B. Ya. Shapiro, Phys. Rev. B 48, 16722 (1993).
S. Shapiro, Phys. Rev. Lett. 80 (1963).
R. P. Sharma, L. E. Rehn, and P. M. Baldo, Phys.Rev. B 43, 13711 (1991).
T. P. Sheahen, "Introduction to High Tc Superconductivity," Plenum, New York, 1994.
D. E. Sheehy, T. P. Davis, and M. Franz Phys. Rev. B 70, 54510 (2004).
S.-Q. Shen and W. Lu, Phys. Rev. B 48, 1105 (1993).
Z.-X. Shen, P. A. P. Lindberg, B. O. Wells, D. S. Dessau, A. Borg, I. Lindau, W. E. Spicer, W. P. Ellis, G. H. Kwei, K. C. Ott, J.-S. Kang, and J. W. Alien, Phys. Rev. B 40, 6912 (1989).
Z.-X. Shen, R. S. List, D. S. Dessau, F. Parmigiani, A. J. Arko, R. Bartlett, B. O. Wells, I. Lindau, and W. E. Spicer, Phys. Rev. B 42, 8081 (1990).
Z.-Y. Shen, "High Temperature Superconducting Microwave Circuits," Artech House, Norwood, Massachusetts, 1994.
Z. Z. Sheng, A. M. Hermann, A. El Ali, C. Almasan, J. Estrada, T. Datta, and R. J. Matson, Phys. Rev. Lett. 60, 937 (1988).
Z. Z. Sheng and A. M. Hermann, Nature 332, 55 (1988).
D.-N. Sheng, Z.-B. Su, and L. Yu, Phys. Rev. B 42, 8732 (1990).
D. Shi, M. S. Boley, U. Welp, J. G. Chen, and Y. Liao, Phys. Rev. B 40, 5255 (1989).
D. Shi, M. Xu, M. M. Fang, J. G. Chen, A. L. Cornelius, and S. G. Lanan, Phys. Rev. B 41, 8833 (1990a).
D. Shi, M. Xu, A. Umezawa, and R. F. Fox, Phys.Rev. B 42, 2062 (1990b).
D. Shi, X. S. Ling, M. Xu, M. M. Fang, S. Luo, J. I. Budnick, B. Dabrowski, D. G. Hinks, D. R. Richards, and Y. Zheng, Phys. Rev. B 43, 3684 (1991).
D. Shi and M. Xu, Phys. Rev. B 44, 4548 (1991).
D. Shi, Ed., "High Temperature Superconducting Materials Science and Engineering," Elsevier, Oxford, 1994.
J. S. Shier and D. M. Ginsberg, Phys. Rev. 147, 384 (1966).
E. Shimizu and D. Ito, Phys. Rev. B 39, 2921 (1989).
E. Shimshoni, Y. Gefen, and S. Levit, Phys. Rev. 40, 2147 (1989).
E. Shimshoni and E. Ben-Jacob, Phys. Rev. B 43, 2705 (1991).
S. L. Shinde, J. Morrill, D. Goland, D. A. Chance, and T. McGuire, Phys. Rev. B 41, 8838 (1990).
T. Shinjo, T. Mizutani, N. Hosoito, T. Kusuda, T.Takabatake, K. Matsukuma, and H. Fujii, Physica C 759, 869 (1989).
T. Shinjo and S. Nasu, in "Mechanisms of High Temperature Superconductivity" (H. Kamimura and A. Oshiyama, Eds.), p. 166, Springer Series in Material Science, Springer-Verlag, Heidelberg, 1989.
K. N. Shrivastava, Phys. Rev. B 41, 11168 (1990).
J. D. Shore, M. Huang, A. T. Dorsey, and J. P. Sethna, Phys. Rev. Lett. 62, 3089 (1989).
S. V. Shulga, S. -L. Drechsler, G. Fuchs, K.-H Muller, K. Winzer, M. Heinecke, and K. Krug, Phys. Rev. Lett. 80, 1730 (1998).
L. Shu-yuan, L. Li, and Z. Dian-lin, H. M. Duan, W. Kiel, and A. M. Hermann, Phys. Rev. B 47, 8324 (1993).
Yu. N. Shvachko, A. A. Koshta, A. A. Romanyukha, V. V. Ustinov, and A. I. Akimov, Physica C 174, 447 (1991).
Y. Sidis, M. Braden, P. Bourges, B. Hennion, S. NishiZaki, Y. Maeno, and Y. Mori, Phys. Rev. Lett. 83, 3323 (1999).
M. Siegel, F. Schmdl, K. Zach, E. Heinz, J. Borck, W. Michalke, and P. Seidel, Physica C 180, 288 (1991).
T. Siegrist, S. Sunshine, D. W. Murphy, R. J. Cava, and S. M. Zahurak, Phys. Rev. B 35, 7137 (1987).
T. Siegrist, S. M. Zahurak, D. W. Murphy, and R. S. Roth, Nature 334, 231 (1988).
P. J. C. Signore, B. Andraka, M. W. Meisel, S. E. Z. Brown, A. L. G. Fisk, J. L. Smith, F. Gross-Alltag, E. A. Schuberth, and A. A. Menovsky, Phys. Rev. B 52, 4446 (1995).
P. Simon, J. M. Bassat, S. B. Oseroff, Z. Fisk, S.-W. Cheong, A. Wattiaux, and S. Schultz, Phys. Rev.Lett. 48, 4216 (1993).
R. R. P. Singh, P. A. Fleury, K. B. Lyons, and P. E. Sulewski, Phys. Rev. Lett. 62, 2736 (1989).
D. Singh, W. E. Pickett, E. C. von Stetten, and S. Berko, Phys. Rev. B 42, 2696 (1990).
D. J. Singh, Physica C 212, 228 (1993a).
D. J. Singh, Phys. Rev. B 48, 3571 (1993b).

D. J. Singh and W. E. Pickett, Phys. Rev. Lett., 73, 476 (1994).
K. Sinha, Ind. J. Phys. 66A, 1 (1992) in K. P. Sinha, "Magnetic Superconductors; Recent Developments," Nova, New York, 1989.
S. Skanthakumar, H. Zhang, T. W. Clinton, W. -H. Li, J. W. Lynn, Z. Fisk, and S.-W. Cheong, Physica C 160, 124 (1989).
H. L. Shriver and I. Mertig, Phys. Rev. B 41, 6553 (1990).
V. Skumryev, R. Puzniak, N. Karpe, H. Zheng-he, M.Pout, H. Medelius, D.-X. Chen, and K. V. Rao, Physica C 152, 315 (1988).
V. Skumryev, M. R. Koblischka, and H. Kronmiiller, Physica C 184, 332 (1991).
A. W. Sleight, J. L. Gillson, and P. E. Bierstedt, SolidState Commun. 17, 27 (1975).
A. W. Sleight, Am. Chem. Soc. Symp. Ser. 351, 2 (1987).
L. C. Smedskjaer, A. Bansil, U. Welp, Y. Fang, and K. G. Bailey, Phys. Rev. B 46, 5868 (1992).
H. H. A. Smit, M. W. Dirken, R. C. Thiel, and L. J. de Jongh, Solid State Commun. 64, 695 (1987).
M. G. Smith, A. Manthiram, J. Zhou, J. B. Goode-nough, and J. T. Markert, Nature 351, 549 (1991).
M. G. Smith, J. B. Goodenough, A. Manthiram, R. Taylor, W. Peng, C. Kimball, J. Solid State Chem. 98, 181 (1992).
J. O. Sofo, C. A. Balseiro, and H. E. Castillo, Phys. Rev. B 45, 9860 (1992).
L. L. Sohn, M. S. Rzchowski, J. U. Free, S. P. Benz, M. Tinkham, and C. J. Lobb, Phys. Rev. B 44, 925 (1991).
L. L. Sohn, M. S. Rzchowski, J. U. Free, M. Tinkham, and C. J. Lobb, Phys. Rev. 45, 3003 (1992).
P. R. Solomon and F. A. Otter, Phys. Rev. 164, 608 (1967).
S. N. Song, Q. Robinson, S.-J. Hwu, D. L. Johnson, K. R. Poeppelmeier, and J. B. Ketterson, Appl. Phys. Lett. 57, 1376 (1987).
Y. S. Song, H. Park, Y. S. Choi, Y. W. Park, M. S. Jang, H. C. Lee, and S. I. Lee, J. Korean Phys. Soc. 23, 492 (1990).
Y. Song and J. R. Gaines, J. Phys. Condens. Matter. 3, 7161 (1991).
Y.-Q. Song, M. Lee, W. P. Halperin, L. M. Tonge, and T. J. Marks, Phys. Rev. B 44, 914 (1991a).
Y.-Q. Song, M. A. Kennard, M. Lee, K. R. Poeppelmeier, and W. P. Halperin, Phys. Rev. B 44, 7159 (1991b).
Y. Song, A. Misra, P. P. Crooker, and J. R. Gaines, Phys. Rev. B 45, 7574 (1992).
Y.-Q. Song, W. P. Halperin, L. Tonge, T. J. Marks, M. Ledvij, V. G. Kogan, and L. N. Bulaevskii, Phys. Rev. Lett. 70, 3127 (1993).
J. E. Sonier, J. H. Brewer, and R. F. Kiefl, Rev. Mod Phys. 72, 769 (2000).
J. Spalek and W. Wojcik, Phys. Rev. B 45, 3799 (1992).
G. Sparn, J. D. Thompson, R. L. Whetten, S.-M. Huang, R. B. Kaner, F. Diederich, G. Griiner, and K. Holczer, Phys. Rev. Lett. 68, 1228 (1992).
P. N. Spathis, M. P. Soerensen, and N. Lazarides, Phys. Rev. B 45, 7360 (1992).
S. Spielman, J. S. Dodge, L. W. Lombardo, C. B. Eom, M. M. Fejer, T. H. Geballe, and A. Kapitulnik, Phys. Rev. 68, 3472 (1992).
S. Sridhar, D-H Wu, and W. Kennedy, Phys. Rev. Lett. 63, 1873 (1989).
Z. M. Stadnik, G. Stroink and R. A. Dunlap, Phys. Rev. B 39, 9108 (1989).
Z. M. Stadnik, G. Stroink, and T. Arakawa, Phys. Rev. B 44, 12552 (1991).
B. W. Start and A. Griffin, Phys. Rev. B 48, 619 (1993).
D. G. Steel and J. M. Graybeal, Phys. Rev. B 45, 12643 (1992).
F. Steglich, J. Aarts, C. D. Bredl, W. Lieke, D. Meschede, W. Franz, and H. Schafer, Phys. Rev. Lett. 43, 1892 (1979).
P. Steiner, V. Kinsinger, I. Sander, B. Siegwart, S. Hufner, and C. Politis, Z. Phys. B Cond. Mat. 67, 19 (1987).
B. Stemlieb, C. Stassis, A. I. Goldman, P. Canfield, and S. Shapiro, J. Appl. Phys. 81, 4937 (1997).
C. H. Stephan and B. W. Maxfield, J. Low Temp. Phys. 10, 185 (1973).
W. Stephan and J. P. Carbotte, Phys. Rev. B 43, 10236 (1991).
G. R. Stewart, Rev. Mod. Phys. 56, 755 (1984).
G. R. Stewart, Z. Fisk, J. O. Willis, and T. J. Smith, Phys. Rev. Lett. B 52, 679 (1984).
G. R. Stewart, J. O'Rourke, G. W. Crabtree, K. D. Carlson, H. H. Wang, J. M. Williams, F. Gross, and K. Andres, Phys. Rev. B 33, 2046 (1986).
S. T. Stoddart, H. I. Mutlu, A. K. Geim, and S. J. Bending, Phys. Rev. B 47, 5146 (1993).

E. C. Stoner, Phil. Mag. 36, 803 (1945).
H. T. C. Stoof, Phys. Rev. B 47, 7979 (1993).
J. A. Stratton, "Electromagnetic Theory," McGrawHill, New York, 1941.
S. K. Streiffer, B. M. Lairson, C. B. Eom, B. M. Clemens, J. C. Bravman, and T. H. Geballe, Phys. Rev. B 43, 13007 (1991).
A. R. Strnad, C. F. Hempstead, and Y. B. Kim, Phys. Rev. Lett. 13, 794 (1964).
S. E. Stupp, M. E. Reeves, D. M. Ginsberg, D. G. Hinks, B. Dabrowski, and K. G. Vandervoort, Phys. Rev. B 40, 10878 (1989).
S. E. Stupp, T. A. Friedmann, J. P. Rice, R. A. Schweinfurth, D. J. Van Harlingen, and D. M. Ginsberg, Phys. Rev. B 43, 13073 (1991).
C. K. Subramanian, M. Paranthaman, and A. B. Kaiser, Physica C 222, 47 (1994).
M. A. Subramanian, C. C. Torardi, J. C. Calabrese, J. Gopalakrishnan, K. J. Morrissey, T. R. Askew, R. B. Flippen, U. Chowdhry, and A. W. Sleight, Science 239, 1015 (1988a).
M. A. Subramanian, J. C. Calabrese, C. C. Torardi, J. Gopalakrishnan, T. R. Askew, R. B. Flippen, K. J. Morrissey, U. Chowdhry, and A. W. Sleight, Nature 332, 420 (1988b).
A. Sudbo and E. H. Brandt, Phys. Rev. B 43, 10482 (1991a); Phys. Rev. Lett. 67, 3176 (1991b).
M. Suenaga, A. K. Ghosh, Y. Xu, and D. O. Welch, Phys. Rev. Lett. 66, 1777 (1991).
R. Sugano, T. Onogi, and Y. Murayama, Phys. Rev. B 45, 10789 (1992).
J. Sugiyama, S. Tokuono, S.-I. Koriyama, H. Yamauchi, and S. Tanaka, Phys. Rev. B 43, 10489 (1991).
J. Sugiyama, K. Matsuura, M. Kosuge, H. Yamauchi, and S. Tanaka, Phys. Rev. B 45, 9951 (1992).
S. B. Sulaiman, N. Sahoo, T. P. Das, O. Donzelli, E. Torikai, and K. Nagamine, Phys. Rev. B 44, 7028 (1991).
S. B. Sulaiman, N. Sahoo, T. P. Das and O. Donzelli, Phys. Rev. B 45, 7383 (1992).
P. E. Sulewski, A. J. Sievers, R. A. Buhrman, J. M. Tarascon, L. H. Greene, and W. A. Curtin, Phys. Rev. B 35, 8829 (1987).
P. E. Sulewski, P. A. Fleury, K. B. Lyons, S. -W. Cheong, and Z. Fisk, Phys. Rev. B 41, 225 (1990).
J. Z. Sun, D. J. Webb, M. Naito, K. Char, M. R. Hahn, J. W. P. Hsu, A. D. Kent, D. B. Mitzi, B. Oh, M. R. Beasley, T. H. Geballe, R. H. Hammond, and A. Kapitulnik, Phys. Rev. Lett. 58, 1574 (1987).
K. Sun, J. H. Cho, F. C. Chou, W. C. Lee, L. L. Miller, D. C. Johnston, Y. Hidaka and T. Mu-rakami, Phys. Rev. B 43, 239 (1991).
C. S. Sundar, A. Bharathi, Y. C. Jean, P. H. Hor, R. L. Meng, Z. J. Huang, and C. W. Chu, Phys. Rev. B 42, 426 (1990a).
C. S. Sundar, A. Bharathi, W. Y. Ching, Y. C. Jean, P. H. Hor, R. L. Meng, Z. J. Huang and C. W. Chu, Phys. Rev. B 42, 2193 (1990b).
C. S. Sundar, A. Bharathi, W. Y. Ching, Y. C. Jean, P. H. Hor, R. L. Meng, Z. J. Huang, and C. W. Chu, Phys. Rev. B 43, 13019 (1991).
C. Surgers, H. v. Lohneysen, and L. Schultz, Phys. Rev. B 40, 8787 (1989).
M. Suzuki, Y. Enemoto, T. Murakami, and T. Inamura, "Proc. 3rd Meeting Ferro-electric Materials and Their Applications," Kyoto, 1981a.
M. Suzuki, Y. Enemoto, T. Murakami, and T. Inamura, Jpn. J. Appl. Phys. 20, Suppl. 20–24, 13 (1981b).
M. Suzuki and M. Hikita, Jpn. J. Appl. Phys. 28, L1368 (1989).
M. Suzuki and M. Hikita, Phys. Rev. B 41, 9566 (1990).
M. Suzuki and M. Hikita, Phys. Rev. B 44, 249 (1991).
H. Svensmark and L. M. Falicov, Phys. Rev. B 42, 9957 (1990).
A. Szasz, J. Hajdu, J. Kojnok, Z. Dankhazi, W. Krasser, T. Trager, and J. Bankuti, J. Super-cond. 3, 425 (1990).
B. Szpunar and V. Smith, Jr., Phys. Rev. B 45, 10616 (1992).
M. Tachiki and S. Takahashi, Solid State Com-mun. 70, 291 (1989).
A. Tagliacozzo, F. Ventriglia, and P. Apell, Phys. Rev. B 40, 10901 (1989).
S. Tajima, S. Uchida, A. Masaki, H. Takaki, K. Kitazawa, S. Tanaka, and A. Katsui, Phys. Rev. B 32, 6302 (1985).
S. Tajima, S. Uchida, H. Ishii, H. Takagi, S. Tanaka, U. Kawabe, H. Hasegawa, T. Aita, and T. Ishiba, Mod. Phys. Lett. B 1, 353 (1988).
Y. Tajima, M. Hikita, T. Ishii, H. Fuke, K. Sugiyama, M. Date, A. Yamagishi, A. Katsui, Y. Hidaka, T. Iwata, and S. Tsurumi, Phys. Rev. B 37, 7956 (1988).

S. Tajima and K. Kitazawa, in "Some Aspects of Superconductivity" (L. C. Gupta, Ed.) Nova Scientific Publ., New York, 1990.

J. Takada, T. Terashima, Y. Bando, H. Mazaki, K. Lijima, K. Yamamoto, and K. Hirata, Phys. Rev. B 40, 4478 (1989).

Y. Takada, Phys. Rev. B 39, 11575 (1989).

H. Takagi, H. Eisaki, S. Uchida, A. Maeda, S. Tajima, K. Uchinokura, and S. Tanaka, Nature 332, 236 (1988).

H. Takagi, R. J. Cava, H. Eisaki, J. O. Lee, K. Mizuhashi, B. Batlogg, S. Uchida, J. J. Krajewski, and W. F Peck Jr., Physica C 228, 389 (1994).

T. Takahashi, H. Matsuyama, H. Katamaya-Yoshida, Y. Okabe, S. Hosoya, K. Seki, H. Fujimoto, M. Sato, and H. Inokuchi, Phys. Rev. B 39, 6636 (1989).

I. Takeuchi, J. S. Tsai, Y. Shimakawa, T. Manako, and Y. Kubo, Physica C 158, 83 (1989).

M. Takigawa, A. P. Reyes, P. C. Hammel, J. D. Thompson, R. H. Heffner, Z. Fisk, and K. C. Ott, Phys. Rev. B 43, 247 (1991).

M. Takigawa, J. L. Smith, and W. L. Hulls, Phys. Rev. B 44, 7764 (1991).

T. Tamegai, K. Koga, K. Suzuki, M. Ichihara, F. Sadai, and Y. Iye, Jpn. J. Appl. Phys. Lett. 2, 28, L112 (1989).

Z. Tan, J. I. Budnick, W. Q. Chen, D. L. Brewe, S.-W. Cheong, A. S. Cooper, and L. W. Rupp, Jr., Phys. Rev. B 42, 4808 (1990).

Z. Tan, J. I. Budnick, S. Luo, W. Q. Chen, S.-W. Cheong, A. S. Cooper, P. C. Canfield, and Z. Fisk, Phys. Rev. B 44, 7008 (1991).

Y. Tanaka and M. Tsukada, Phys. Rev. B 40, 4482 (1989a); Solid State Commun. 69, 195, 491 (1989b).

Y. Tanaka and M. Tsukada, Phys. Rev. B 42, 2066 (1990).

Y. Tanaka and M. Tsukada, Phys. Rev. B 44, 7578 (1991).

S. Tanda, M. Honma, and T. Nakayama, Phys. Rev. B 43, 8725 (1991).

C. Q. Tang, B. R. Li, and A. Chen, Phys. Rev. B 42, 8078 (1990).

X. X. Tang, D. E. Morris, and A. P. B. Sinha, Phys Rev. B 43, 7936 (1991).

T. Tani, T. Itoh and S. Tanaka, J. Phys. Soc. Jpn. Suppl. A 49, 309 (1980).

S. Tanigawa, Y. Mizuhara, Y. Hidaka, M. Oda, M. Suzuki, and T. Murakami, Mater. Res. Soc. Symp. Proc. 99, 57 (1988).

D. B. Tanner and T. Timusk, in "Physical Properties of High Temperature Superconductors" (D. M. Ginsberg, Ed.), Vol. 3, Chap. 5, World Scientific, Singapore, 1992.

H. J. Tao, A. Chang, F. Lu, and E. L. Wolf, Phys. Rev. B 45, 10622 (1992).

J. M. Tarascon, L. H. Greene, W. R. McKinnon, and G. W. Hull, Phys. Rev. B 35, 7115 (1987a).

J. M. Tarascon, W. R. McKinnon, L. H. Greene, G. W. Hull, and E. M. Vogel, Phys. Rev. B 36, 226 (1987b).

J. M. Tarascon, L. H. Greene, W. R. McKinnon, G. W. Hull, and T. H. Geballe, Science 235, 1373 (1987c).

J. M. Tarascon, P. Barboux, P. F. Miceli, L. H. Greene, D. W. Hull, M. Eibschutz, and S. A. Sunshine, Phys. Rev. B 37, 7458 (1988a).

J. M. Tarascon, Y. LePage, P. Barboux, B. G. Bagley, L. H. Greene, W. R. McKinnon, G. W. Hull, M. Giroud, and D. M. Hwang, Phys. Rev. 37, 9382 (1988b).

J. M. Tarascon, E. Wang, L. H. Greene, B. G. Bagley, G. W. Hull, S. M. D'Egidio, P. F. Miceli, Z. Z. Wang, T. W. Jing, J. Clayhold, D. Brawner, and N. P. Ong, Phys. Rev. B 40, 4494 (1989a).

J. M. Tarascon, Y. LePage, W. R. McKinnon, E. Tselepis, P. Barboux, B. G. Bagley, and R. Ramesh, in "Proc. Mater. Res. Soc. Symp.," San Diego, Apr. 23–28, 1989b.

V. V. Tatarskii, M. Paranthaman, and A. M. Hermann, Phys. Rev. B 47, 14489 (1993).

Y. Taur, P. L. Richards, and T. Auracher, Low Temp. Phys. 3, 276 (1974).

W. M. Temmerman, G. M. Stocks, P. J. Durham, and P. A. Sterne, J. Phys. F 17, L135 (1987).

M. A. Teplov, O. N. Bakharev, A. V. Dooglav, A. V. Egorov, M. V. Eremin, M. S. Tagirov, A. G. Volodin, and R. Sh. Zhdanov, Physica C 185–189, 1107 (1991).

I. Terasaki, T. Nakahashi, S. Takebayashi, A. Maedaand K. Uchinokura, Physica C 765, 152 (1990a).

I. Terasaki, S. Tajima, H. Eisaki, H. Takigi, K. Uchinokura, and S. Uchida, Phys. Rev. B 41, 865 (1990b).

B. M. Terzijska, R. Wawryk, D. A. Dimitrov, Cz. Marucha, V. T. Kovachev, and J. Rafalowicz, Cryogenics 32, 53 (1992).

Z. Tesanovic and M. Rasolt, Phys. Rev. B 39, 2718 (1989).

Z. Tesanovic, M. Rasolt, and L. Xing, Phys. Rev. B 43, 288 (1991).
Z. Tesanovic, Phys. Rev. B 44, 12635 (1991).
L. R. Tessler, J. Provost, and A. Maignan, Appl. Phys. Lett. 58, 528 (1991).
L. Tewordt, S. Wermbter, and Th. Wolkhausen, Phys. Rev. B 40, 6878 (1989).
L. Tewordt and Th. Wolkhausen, Solid State Commun. 70, 839 (1989).
T. D. Thanh, A. Koma, and S. Tanaka, Appl. Phys. 22, 205 (1980).
S. Theodorakis and Z. Tesanovic, Phys. Rev. B 40, 6659 (1989).
S. L. Thiemann, Z. Radovic, and V. G. Kogan, Phys. Rev. B 39, 11406 (1989).
T. Thio, T. R. Thurston, N. W. Preyer, P. J. Picone, M. A. Kastner, H. P. Jenssen, D. R. Gabbe, C. Y. Chen, R. J. Birgeneau, and A. Aharony, Phys. Rev. B 38, 905 (1988).
G. Thomas, M. Capizzi, J. Orenstein, D. Rapkine, A. Millis, P. Gammel, L. Gammel, L. F. Schneemeyer, and J. Waszczak, in "Proc. Int. Symposium on the Electronic Structure of High Tc Superconductors, " p. 67, (A. Bianconi, Ed.) Pergamon Press, Oxford, 1988.
R. S. Thompson, Phys. Rev. B 1, 327 (1970).
J. R. Thompson, J. Brynestad, D. M. Kroeger, Y. C. Kirn, S. T. Sekula, D. K. Christen, and E. Specht, Phys. Rev. B 39, 6652 (1989).
J. R. Thompson, D. K. Christen, H. A. Deeds, Y. C. Kim, J. Brynestad, S. T. Sekula, and J. Budai, Phys. Rev. B 41, 7293 (1990).
J. R. Thompson, J. G. Ossandon, D. K. Christen, B. C. Chakoumakos, Y. R. Sun, M. Paranthaman, and J. Brynestad, Phys. Rev. B 48, 14031 (1993).
R. J. Thorn, ACS Symp. Ser. 351, Chap. 3, (1987).
C. Tien and I. M. Jiang, Phys. Rev. B 40, 229 (1989).
T. S. Tighe, M. T. Tuominen, J. M. Hergenrother, and M. Tinkham, Phys. Rev. B 47, 1145 (1993).
D. R. Tilley and J. Tilley, "Superfluidity and Superconductivity," Hilger, Boston (1986).
M. Tinkham, Phys. Rev. Lett. 13, 804 (1964).
M. Tinkham and J. Clarke, Phys. Rev. Lett. 28, 1366 (1972).
M. Tinkham, "Introduction to Superconductivity", (New York: McGraw-Hill Book Co.) (1996).
J. E. Tkaczyk, R. H. Arendt, M. F. Garbauskas, H. R. Hart, K. W. Lay, and F. E. Luborsky, Phys. Rev. B45, 12506 (1992).
J. G. Tobin, C. G. Olson, C. Gu, J. Z. Liu, F. R. Solal, M. J. Fluss, R. H. Howell, J. C. O'Brien, H. B. Radousky, and P. A. Sterne, Phys. Rev. B 45, 5563 (1992).
B. H. Toby, T. Egami, J. D. Jorgensen, and M. A. Subramanian, Phys. Rev. Lett. 64, 2414 (1990).
K. Togano, H. Kumakura, K. Fukutomi, and K. Tachikawa, Appl. Phys. Lett. 51, 136 (1987).
A. Tokiwa, M. Nagoshi, and Y. Syono, Physica C 170, 437 (1990).
A. Tokiwa, Y. Syono, T. Oku, and M. Nagoshi, Physica C 185–189, 619 (1991).
A. Tokiwa-Yamamoto, K. Isawa, M. Itoh, S. Adachi, and H. Yamauchi, Physica C 216, 250 (1993).
A. Tokumitu, K. Miyake, and K. Yamada, Phys. Rev. B 47, 11988 (1993).
M. Tokumoto, H. Bando, H. Anzai, G. Saito, K. Murata, K. Kajimura, and T. Ishiguro, J. Phys. Soc. Jpn. 54, 869 (1985).
T. A. Tokuyasu, D. W. Hess, and J. A. Sauls, Phys. Rev. B 41, 8891 (1990);
T. A. Tokuyasu and J. A. Sauls, Physica B 165–166, 347 (1990).
J. C. Toledano, A. Litzler, J. Primot, J. Schneck, L. Pierre, D. Morin, and C. Daguet, Phys. Rev. B 42, 436 (1990).
B. Tominez, P. Berger, E. Alleno, B. Decamps, G. Schiffmacher, M. Bohn and C. Godart, J. Alloys Compd 275–7123 (1998).
C. V. Tomy, M. R. Lees, L. Afalfiz, G. Balakrishan, and D. D. McK Paul, Phys. Rev. B 52, 9186 (1995).
J. Toner, Phys. Rev. Lett. 66, 2523 (1991a).
J. Toner, Phys. Rev. Lett. 67, 2537 (1991b); see comment by T. Nattermann and I. Lyuksyutov, and reply 68, 3366 (1992).
C. C. Torardi, M. A. Subramanian, J. C. Calabrese, J. Gopalakrishnan, K. J. Morrissey, T. R. Askew, R. B. Flippen, U. Chowdhry, and A. W. Sleight, Science 240, 631 (1988a).
C. C. Torardi, M. A. Subramanian, J. C. Calabrese, J. Gopalakrishnan, E. M. McCarron, K. J. Morrissey, T. R. Askew, R. B. Flippen, U. Chowdhry, and A. W. Sleight, Phys. Rev. B 38, 225 (1988b).
J. B. Torrance, J. Solid State Chem. 96, 59 (1992).
H. Totsuji, Phys. Rev. B 43, 5287 (1991).
M. Touminen, A. M. Goldman, Y. Z. Chang, and P. Z. Jiang, Phys. Rev. B 42, 412 (1990).

S. W. Tozer, A. W. Kleinsasser, T. Penney, D. Kaiser, and F. Holtzberg, Phys. Rev. Lett. 59, 1768 (1987).

J. M. Tranquada, in "Early and Recent Aspects of Superconductivity" (J. G. Bednorz and K. A. Miiller, Eds.), p. 422, Springer-Verlag, Berlin, 1990.

J. M. Tranquada, P. M. Gehring, G. Shirane, S. Shamoto, and M. Sato, Phys. Rev. B 46, 5561 (1992).

A. Tressaud, K. Amine, J. P. Chaminade, J. Etourneau, T. M. Due, and A. Sartre, J. Appl. Phys. 68, 248 (1990).

J.-M. Triscone, O. Fischer, O. Brunner, L. Antognazza, A. D. Kent, and M. G. Karkut, Phys. Rev. Lett. 64, 804 (1990).

V. N. Trofimov, A. V. Kuznetsov, P. V. Lepeschkin, K. A. Bolschinskov, A. A. Ivanov, and A. A. Mikhailov, Physica C 183, 135 (1991).

A. Trokiner, R. Mellet, A. M. Pougnet, D. Morin, Y. M. Gao, J. Primot, and J. Schneck, Phys. Rev. B 41, 9570 (1990).

A. Trokiner, L. LeNoc, J. Schneck, A. M. Pougnet, R. Mellet, J. Primot, H. Savary, Y. M. Gao, and S. Aubry, Phys. Rev. B 44, 2426 (1991).

N. Troullier and J. L. Martins, Phys. Rev. B 46, 1754 (1992).

S. A. Trugman, Phys. Rev. Lett. 65, 500 (1990).

J.-S. Tsai, A. K. Jain, and J. E. Lukens, Phys. Rev. Lett. 51, 316 (1983).

S.-F. Tsay, S.-Y. Wang, and T. J. W. Yang, Phys. Rev. B 43, 13080 (1991).

C. C. Tsuei, A. Gupta, and G. Koren, Physica C 767, 415 (1989).

M. Touminen, A. M. Goldman, Y. Z. Chang, and P. Z. Jiang, Phys. Rev. B 42, 412 (1990).

M. T. Tuominen, J. M. Hergenrother, T. S. Tighe, and M. Tinkham, Phys. Rev. B 47, 11599 (1993).

I. Tutto, L. M. Kahn and J. Ruvalds, Phys. Rev. B 20, 952 (1979).

R. Tycko, G. Dabbagh, M. J. Rosseinsky, D. W. Murphy, R. M. Fleming, A. P. Ramirez, and J. C. Tully, Science 253, 884 (1991).

R. Tycko, G. Dabbagh, M. J. Rosseinsky, D. W. Murphy, A. P. Ramirez, and R. M. Fleming, Phys. Rev. Lett. 68, 1912 (1992).

S. Uchida, H. Takagi, K. Kitazawa and S. Tanaka, Jpn. J. Appl. Phys. 26, L1 (1987).

S. Uchida, T. Ido, H. Takagi, T. Arima, Y. Tokura and S. Tajima, Phys. Rev. B 43, 7942 (1991).

Y. J. Uemura, L. P. Le, G. M. Luke, B. J. Sternlieb, W. D. Wu, J. H. Brewer, T. M. Riseman, C. L. Seaman, M. B. Maple, M. Ishikawa, D. G. Hinks, J. D. Jorgensen, G. Saito and H. Yamochi, Phys. Rev. Lett. 66, 2665 (1991).

A. Ugawa, K. Iwasaki, A. Kawamoto, K. Yakushi, Y. Yamashita, and T. Suzuki, Phys. Rev. B 43, 14718 (1991).

C. Uher and W.-N. Huang, Phys. Rev. B 40, 2694 (1989).

C. Uher, in "Physical Properties of High Temperature Superconductors" (D. M. Ginsberg, Ed.), Vol. 3, Chap. 3, World Scientific, Singapore, 1992.

S. Ullah, A. T. Dorsey, and L. J. Buchholtz, Phys. Rev. B 42, 9950 (1990).

S. Ullah and A. T. Dorsey, Phys. Rev. Lett. 65, 2066 (1990).

J. S. Urbach, D. B. Mitzi, A. Kapitulnik, J. Y. T. Wei, and D. E. Morris, Phys. Rev. B 39, 12391 (1989).

A. V. Ustinov, T. Doderer, R. P. Huebener, N. F. Pederson, B. Mayer, and V. A. Oboznov, Phys. Rev. Lett. 69, 1815 (1992).

J. M. Valles, Jr., R. C. Dynes, and J. P. Garno, Phys. Rev. B 40, 6680 (1989).

J. M. Valles, Jr., R. C. Dynes, A. M. Cucolo, M. Gurvitch, L. F. Schneemeyer, J. P. Garno, and J. V. Waszczak, Phys. Rev. B 44, 11986 (1991).

J. van den Berg, C. J. van der Beek, P. H. Kest, J. A. Mydosh, M. J. V. Menken, and A. A. Menovsky, Supercond. Sci. Tech. I, 249 (1989).

J. van den Berg, C. J. van der Beek, P. H. Kes, J. A. Mydosh, G. J. Nieuwenhuys, and L. J. de Jongh, Solid State Commun. 64, 699 (1987).

A. M. van den Brink, G. Schon, and L. Geerligs, Phys. Rev. Lett. 67, 3030 (1991).

D. Van Der Marel, Physica C 765, 35 (1990).

H. P. van der Meulen, A. de Visser, J. J. M. Franse, T. T. J. M. Berendschot, J. A. A. J. Perenboom, H. van Kempen, A. Lacerda, P. Lejay, and J. Fouquet, Phys. Rev. B 44, 814 (1991).

H. S. J. van der Zant, F. C. Fritschy, T. P. Orlando, and J. E. Mooij, Phys. Rev. Lett. 66, 2531 (1991).

K. G. Vandervoort, U. Welp, J. E. Kessler, H. Claus, G. W. Crabtree, W. K. Kwok, A. Umezawa, B. W. Veal, J. W. Downey, A. P. Paulikas, and J. Z. Liu, Phys. Rev. B 43, 13042 (1991).

H. S. J. van der Zant, F. C. Fritschy, T. P. Orlando, and J. E. Mooij, Phys. Rev. B 47, 295 (1993).

R. B. VanDover, E. M. Gyorgy, A. E. White, L. F. Schneemeyer, R. J. Felder, and J. V. Waszczak, Appl. Phys. Lett. 56, 2681 (1990).

T. Van Duzer and C. W. Turner, "Principles of Superconductive Devices and Circuits," Elsevier, New York (1981).

A. G. Van Vijfeijkenand and A. K. Niessen, Philips Res. Rep. 20, 505 (1965a); Phys. Lett. 76, 23 (1965b).

B. J. van Wees, K.-M. H. Lenssen, and C. J. P. M. Harmans, Phys. Rev. B 44, 470 (1991).

C. M. Varma, S. Schmitt-Rink, and E. Abrahams, in "Theories of High Temperature Superconductivity" (J. W. Halley, Ed.), p. 211, Addison Wesley, Reading, MA, 1988.

C. M. Varma, P. B. Littlewood, S. Schmitt-Rink, E. Abrahams, and A. E. Ruckenstein, Phys. Rev. Lett. 63, 1996 (1989).

V. Vasiliev, J. Supercond. 4, 271 (1991).

D. R. Veblen, P. J. Heaney, R. J. Angel, L. W. Finger, R. M. Hazen, C. T. Prewitt, N. L. Ross, C. W. Chu, P. H. Hor, and R. L. Meng, Nature 332, 334 (1988).

A. J. Vega, W. E. Farneth, E. M. McCarron, and R. K. Bordia, Phys. Rev. B 39, 2322 (1989a).

A. J. Vega, M. K. Crawford, E. M. McCarron, and W. E. Farneth, Phys. Rev. B 40, 8878 (1989b).

E. L. Venturini, D. S. Ginley, J. F. Kwak, R. J. Baughman, J. E. Schirber, and B. Morosin, in "High Temperature Superconductors" (D. U. Gubser and M. Schluter, Eds.), p. 97, Mater. Res. Soc., Pittsburgh, 1987.

R. Vijayaraghavan, A. K. Ganguli, N. Y. Vasanthacharya, M. K. Rajumon, G. U. Kulkarni, G. Sankar, D. D. Sarma, A. K. Sood, N. Chandrabhas, and C. N. R. Rao, Supercond. Sci. Technol. 2, 195 (1989).

P. Villars and J. C. Phillips, Phys. Rev. B 37, 2345 (1988).

L. Ya. Vinnikov and I. V. Grigor'eva, JETP Lett. 47, 106 (1988).

V. M. Vinokur, M. V. Feigel'man, V. B. Geshkenbein, and A. I. Larkin, Phys. Rev. Lett. 65, 259 (1990).

V. M. Vinokur, M. V. Feigel'man, and V. B. Geshkenbein, Phys. Rev. Lett. 67, 915 (1991).

A. Virosztek and J. Ruvalds, Phys. Rev. Lett. 67, 1657 (1991).

J. P. Vithayathil, D. E. MacLaughlin, E. Koster, D. LI. Williams, and E. Bucher, Phys. Rev. B 44, 4705 (1991).

B. M. Vlcek, M. C. Frischherz, S. Fleshier, U. Welp, J. Z. Liu, J. Downey, K. G. Vandervoort, G. W. Crabtree, M. A. Kirk, J. Giapintzakis, and J. Farmer, Phys. Rev. Lett. 46, 6441 (1992).

N. V. Volkenshteyn et al., Fiz. Met. Metalloved 45, 1187 (1978).

A. R. von Hippel, "Dielectrics and Waves," p. 255, MIT Press, Cambridge, MA, 1954.

S. von Molnar, A. Torresson, D. Kaiser, F. Holtzberg, and T. Penney, Phys. Rev. B 37, 3762 (1988).

F. von Oppen and E. K. Riedel, Phys. Rev. Lett. 66, 84 (1991).

S. V. Vonsovsky, Yu. A. Izyumov, and E. Z. Kurmaev, "Superconductivity in Transition Metals," Springer, New York (1982).

A. Wadas, O. Fritz, H. J. Hug, and H.-J. Giintherodt, Z. Phys. B 88, 317 (1992).

J. R. Waldram, A. Porch, and H. M. Cheah, Physica C 232 189 (1994).

M. Wallin, Phys. Rev. B 41, 6575 (1990).

R. E. Walstedt and W. W. Warren, Jr., Science 248, 1082 (1990).

R. E. Walstedt, W. W. Warren, Jr., R. F. Bell, R. J. Cava, G. P. Espinosa, L. F. Schneemeyer, and J. V. Waszczak, Phys. Rev. B 41, 9574 (1990).

R. E. Walstedt, R. F. Bell, L. F. Schneemeyer, J. V. Waszczak, and G. P. Espinosa, Phys. Rev. B 45, 8074 (1992).

B. L. Walton, B. Rosenblum, and F. Bridges, Phys. Rev. Lett. 32, 1047 (1974).

Z. Wang, N. Zou, J. Pang, and C. Gong, Solid State Commun. 64, 531 (1987).

Z. Z. Wang, J. Clayhold, N. P. Ong, J. M. Tarascon, L. H. Greene, W. R. McKinnon, and G. W. Hull, Phys. Rev. 36, 7222 (1987).

S. J. Wang, S. V. Naidu, S. C. Sharma, D. K. De, D. Y. Jeong, T. D. Black, S. Krichene, J. R. Reynolds, and J. M. Owens, Phys. Rev. B 37, 603 (1988).

Y. R. Wang, Phys. Rev. B 40, 2698 (1989).

C-P. S. Wang, in "High Temperature Superconductivity" (J. W. Lynn, Ed.), Chap. 5, Springer-Verlag, Berlin, 1990.
Y.-Y. Wang, G. Feng, and A. L. Ritter, Phys. Rev. B 42, 420 (1990).
T. Wang, K. M. Beauchamp, D. D. Berkley, B. R. Johnson, J.-X. Liu, J. Zhang, and A. M. Goldman, Phys. Rev. B 43, 8623 (1991).
Y. Wang, A. M. Rao, J. -G. Zhang, X. -X. Bi, P. C. Eklund, M. S. Dresselhaus, P. P. Nguyen, J. S. Moodera, G. Dresselhaus, H. B. Radousky, R. S. Glass, M. J. Fluss, and J. Z. Liu, Phys. Rev. B 45, 2523 (1992).
Z. D. Wang and C. S. Ting, Phys. Rev. 46, 284 (1992b).
Z. D. Wang and C. -R. Hu, Phys. Rev. B 44, 11918 (1991).
C. A. Wang, R. L. Wang, H. C. Li, H. R. Yi, C. G. Cui, S. L. Li, X. N. Jing, J. Li, P. Xu, and L. Li, Physica C 191, 52 (1992).
Z. H. Wang, A. W. P. Fung, G. Dresselhaus, M. S. Dresselhaus, K. A. Wang, P. Zhou, and P. C. Eklund, Phys. Rev. B 47, 15354 (1993).
N. L. Wang, Y. Chong, C. Y. Wang, D. J. Huang, Z.Q. Mao, L. Z. Cao, and Z. J. Chen, Phys. Rev. B 47, 3347 (1993).
Y. Watanabe, Z. Z. Wang, S. A. Lyon, D. C. Tsui, N. P. Ong, J. M. Tarascon, and P. Barboux, Phys. Rev. B 40, 6884 (1989).
Y. Watanabe, D. C. Tsui, J. T. Birmingham, N. P. Ong, and J. M. Tarascon, Phys. Rev. B 43, 3026 (1991).
K. Watanabe, S. Awaji, N. Kobayashi, H. Yamane, T. Hirai, and Y. Muto, J. Appl. Phys. 69, 1543 (1991).
J. H. P. Watson, J. Appl. Phys. 39, 3406 (1968).
H. L. Watson and R. P. Huebener, Phys. Rev. B 10, 4577 (1974).
C. H. Watson, D. A. Browne, J.-C. Xu, and R. G. Goodrich, Phys. Rev. B 40, 8885 (1989).
W. J. Wattamaniuk, J. P. Tidman, and R. F. Frindt, Phys. Rev. Lett. 35, 62 (1975).
B. D. Weaver, J. M. Pond, D. B. Chrisey, J. S. Horwitz, H. S. Newman, and G. P. Summers, Appl. Phys. Lett. 58, 1563 (1991).
W. Weber, Phys. Rev. Lett. 58, 1371 (1987).
W. Weber, Z. Phys. B 70, 323 (1988).
H. Weber and P. Minnhagen, Phys. Rev. B 38, 8730 (1988).
W. H. Weber, C. R. Peters, B. M. Wanklyn, C. Chen, and B. E. Watts, Phys. Rev. B 38, 917 (1988).
W. H. Weber, C. R. Peters, and E. M. Logothetis, J. Opt. Soc. Am. B 6, 455 (1989).
H. Weber and H. J. Jensen, Phys. Rev. B 44, 454 (1991).
M. Weger, Rev. Mod. Phys. 36, 175 (1964).
B. O. Wells, Z.-X. Shen, D. S. Dessau, W. E. Spicer, C. G. Olson, D. B. Mitzi, A. Kapitulnik, R. S. List, and A. Arko, Phys. Rev. Lett. 65, 3056 (1990).
U. Welp, W. K. Kwok, G. W. Crabtree, K. G. Vandervoort, and J. Z. Liu, Phys. Rev. Lett. 62, 1908(1989); Phys. Rev. B 40, 5263 (1989).
U. Welp, S. Fleshier, W. K. Kwok, J. Downey, Y.Fang, G. W. Crabtree, and J. Z. Liu, Phys. Rev. B 42, 10189 (1990).
Z. Y. Weng, C. S. Ting, and T. K. Lee, Phys. Rev. B 41, 1990 (1990).
F. Wenger and S. Ostlund, Phys. Rev. B 47, 5977 (1993).
S. Wermbter and L. Tewordt, Phys. Rev. B 44, 9524 (1991); Physica C 183, 365 (1991).
N. R. Werthamer, Phys. Rev. 132, 2440 (1963).
M.-H. Whangbo and C. C. Torardi, Acct. Chem. Res. 24, 127 (1991).
J. M. Wheatley, T. C. Hsu, and P. W. Anderson, Phys. Rev. B 37, 5897 (1988).
A. Widom, Y. N. Srivastava, C. Vittoria, H. How, R. Karim, and H. Jiang, Phys. Rev. B 46, 1102 (1992).
F. Wilczek, Phys. Rev. Lett. 48, 1144 (1982a).
F. Wilczek, Phys. Rev. Lett. 49, 957 (1982b). N. K. Wilkin and M. A. Moore, Phys. Rev. B 48, 3464 (1993).
P. J. Williams and J. P. Carbotte, Phys. Rev. B 43, 7960 (1991).
M. N. Wilson, "Superconducting Magnets," Clarendon Press, Oxford, 1983. A. Wittlin, L. Genzel, M. Cardona, M. Bauer, W. Konig, E. Garcia, M. Barahona, and M. V. Cabanas, Phys. Rev. B 37, 652 (1988).
K. Winzer, and K. Krug, (K. H. Muller and V. Narozhnyi, Eds.), Rare Earth Transition Metal Borocarbides (Nitrides); Superconducting Magnetic and Normal State Properties, p. 63, Kluwer Acad. Publ. Dordrecht, (2001)
T. Wittmann and J. Stolze, Phys. Rev. B 48, 3479 (1993).
S. A. Wolf and V. Z. Kresin, Eds., "Novel Superconductivity," Plenum, New York, 1987.
Y. Wolfus, Y. Yeshurun, I. Felner, and H. Sompolinsky, Phys. Rev. B 40, 2701; see B 39, 11690 (1989).

H. Won and K. Maki, Phys. Rev. B 49, 1397 (1994).
H. Won and K. Maki, Europhys. Lett., 52(4), 427 (2000). Phys. Rev. B 49, 1397 (1994).
R. F. Wood and J. F. Cooke, Phys. Rev. B 45, 5585 (1992).
F. Woolen, "Optical Properties of Solids," p. 244, Academic Press, New York, 1972.
R. Wordenweber, Phys. Rev. B 46, 3076 (1992).
A. H. Worsham, N. G. Ugras, D. Winkler, D. E. Prober, N. R. Erickson, and P. F. Goldsmith, Phys. Rev. Lett. 67, 3034 (1991).
T. K. Worthington, W. J. Gallagher, and T. R. Dinger, Phys. Rev. Lett. 59, 1160 (1987).
M. K. Wu, J. R. Ashburn, C. J. Torng, P. H. Hor, R. L. Meng, L. Gao, Z. J. Huang, Y. Q. Wang, and C. W. Chu, Phys. Rev. Lett. 58, 908 (1987).
J. Z. Wu, C. S. Ting, and D. Y. Xing, Phys. Rev. B 40, 9296 (1989).
D.-H. Wu and S. Sridhar, Phys. Rev. Lett. 65, 2074 (1990).
J. Z. Wu, C. S. Ting, W. K. Chu, and X. X. Yao, Phys. Rev. B 44, 411 (1991a).
J. Z. Wu, P. Y. Hsieh, A. V. McGuire, D. L. Schmidt, L. T. Wood, Y. Shen, and W. K. Chu, Phys. Rev. B 44, 12643 (1991b).
D. H. Wu, J. Mao, S. N. Mao, J. L. Peng, X. X. Xi, T. Venkatesan, R. L. Greene, and S. M. Anlage, Phys. Rev., Lett. 70, 85 (1993).
R. W. G. Wyckoff, "Crystal Structures," Vol. 1, 1963; Vol.2 1964; Vol.3 1965; Vol. 4; 1968; Wiley, New York.
K. I. Wysokinski, G. Litak, J. F. Annett, and B. L. Gyorffy, Phys. Stat. Sol. (b) 236, No. 2, 325 (2003).
D. G. Xenikos and T. R. Lemberger, Phys. Rev. B 41, 869 (1990).
T.-K. Xia and D. Stroud, Phys. Rev. B 39, 4792 (1989).
W. Xia and P. L. Leath, Phys. Rev. Lett. 63, 1428 (1989).
G. Xiao, F. H. Streitz, A. Gavrin, Y. W. Du, and C. L. Chien, Phys. Rev. B 35, 8782 (1987a).
G. Xiao, F. H. Streitz, A. Gavrin, M. Z. Cieplak, J. Childress, M. Lu, A. Zwicker, and C. L. Chien, Phys. Rev. B 36, 2382 (1987b).
G. Xiao, M. Z. Cieplak, and C. L. Chien, Phys. Rev. B 40, 4538 (1989).
D. Y. Xing and M. Liu, Phys. Rev. B 43, 3744 (1991).
D. Xu, S. K. Yip, and J. A. Sauls, Phys. Rev. 551 16233 (1995).
Y. Xu, M. Suenaga, Y. Gao, J. E. Crow, and N. D. Spencer, Phys. Rev. B 42, 8756 (1990).
M. Xu, D. Shi, and R. F. Fox, Phys. Rev. B 42, 10773 (1990).
Y. Xu and M. Suenaga, Phys. Rev. B 43, 5516 (1991).
Y.-N. Xu, M.-Z. Huang, and W. Y. Ching, Phys. Rev. B 44, 13171 (1991).
X-Q. Xu, S. J. Hagen, W. Jiang, J. L. Peng, Z. Y. Li, and R. Greene, Phys. Rev. B 45, 7356 (1992).
J. V. Yakhmi and R. M. Iyer, in "High Temperature Superconductors" (S. K. Malik and S. S. Shah, Eds.), Nova Sci., New York, 1992.
J. V. Yakhmi, "Chemistry and Physics of Fullerenes," in "Atomic and Molecular Physics," (S. A. Ahmad, Ed.) Narosa Publishing, New Delhi, India, 1994.
K. Yamada, K. Kakurai, Y. Endoh, T. R. Thurston, M. A. Kaster, R. J. Birgeneau, G. Shirane, Y. Hidaka, and T. Murakami, Phys. Rev. B 40, 4557 (1989).
K. Yamamoto, H. Mazaki, H. Yasuoka, S. Katsuyama, and K. Kosuge, Phys. Rev. 46, 1122 (1992).
K. Yamamoto, H. Mazaki, and H. Yasuoka, Phys. Rev. B 47, 915 (1993).
H. Yamasaki, K. Endo, S. Kosaka, M. Umeda, S. Yoshida, and K. Kajimura, Phys. Rev. Lett. 70, 3331 (1993).
Y. Yan and M. G. Blanchin, Phys. Rev. B 43, 13717 (1991).
K. N. Yang, J. M. Ferreira, B. W. Lee, M. B. Maple, W.-H. Li, J. W. Lynn, and R. W. Erwin, Phys. Rev. B 40, 10963 (1989).
C. Y. Yang, A. R. Moodenbaugh, Y. L. Wang, Y. Xu, S. M. Heald, D. O. Welch, D. A. Fischer, and J. E. Penner-Hahn, Phys. Rev. B 42, 2231 (1990).
A. Yatskar, N. K. Budraa, W. P. Beyermann, P. C. Canfield, and S. L. Phys. Rev. Lett. 78, 935 (1996).
Z. Ye, H. Umezawa, and R. Teshima, Phys. Rev. B 44, 351 (1991).
W.-J. Yeh, L. Chen, F. Xu, B. Bi, and P. Yang, Phys. Rev. B 36, 2414 (1987).
N.-C. Yeh and C. C. Tsuei, Phys. Rev. B 39, 9708 (1989).
N.-C. Yeh, Phys. Rev. B 40, 4566 (1989).
N.-C. Yeh, Phys. Rev. B 42, 4850 (1990).

N.-C. Yeh, Phys. Rev. B 43, 523 (1991).
N.-C. Yeh, W. Jiang, D. S. Reed, A. Gupta, F. Holtzberg, and A. Kussmaul, Phys. Rev. B 45, 5710 (1992b).
N.-C. Yeh, D. S. Reed, W. Jinag, U. Kriplani, F. Holtzberg, A. Gupta, B. D. Hunt, R. P. Vasquez, M. C. Foote, and L. Bajuk, Phys. Rev. B 45, 5654 (1992a).
Y. Yeshurun, A. P. Malozemoff, F. Holtzberg, and T. R. Dinger, Phys. Rev. B 38, 11828 (1988).
S. K. Yip, and J. A. Sauls, Phys. Rev. Lett. 69 2264 (1992).
M. Yoshimoto, H. Koinuma, T. Hashimoto, J. Tanaka, S. Tanabe, and N. Soga, Physica C 181, 284 (1991).
M. Yoshimura, H. Shigekawa, H. Nejoh, G. Saito, Y. Saito, and A. Kawazu, Phys. Rev. B 43, 13590 (1991).
J. Yu, A. J. Freeman, and S. Massidda, in "Novel Superconductivity" (S. A. Wolf and V. Z. Kresin, Eds.), p. 367, Plenum, New York, 1987.
R. C. Yu, M. J. Naughton, X. Yan, P. M. Chaikin, F. Holtzberg, R. L. Greene, J. Stuart, and P. Davies, Phys. Rev. B 37, 7963 (1988).
G. Yu, C. H. Lee, A. J. Heegar, N. Herron, and E. M. McCarron, Phys. Rev. Lett. 67, 2581 (1990).
J. Yu, A. J. Freeman, R. Podloucky, P. Herzig, and P. Weinberger, Phys. Rev. B 43, 532 (1991).
X.-J. Yu and M. Sayer, Phys. Rev. B 44, 2348 (1991).
R. C. Yu, J. M. Williams, H. H. Wang, J. E. Thompson, A. M. Kini, K. D. Carlson, J. Ren, M.-H. Whangbo, and P. M. Chaikin, Phys. Rev. B 44, 6932 (1991).
W. Yu, E. B. Harris, S. E. Hebboul, J. C. Garland, and D. Stroud, Phys. Rev. B 45, 12624 (1992).
B. D. Yu, H. Kirn, and J. Ihm, Phys. Rev. B 45, 8007 (1992).
G. Yu, C. H. Lee, A. J. Heeger, N. Herron, E. M. McCarron, L. Cong, G. C. Spalding, C. A. Nordman, and A. M. Goldman, Phys. Rev. B 45, 4964 (1992).
R. C. Yu, M. B. Salamon, J. P. Lu, and W. C. Lee, Phys. Rev. Lett. 69, 1431 (1992).
B. J. Yuan and J. P. Whitehead, Phys. Rev. B 44, 6943 (1991).
K. Yvon and M. Francois, Z. Phys. B 76, 413 (1989).
A. A. Zakhidov, A. Ugawa, K. Imaeda, K. Yakushi, H. Inokuchi, K. Kikuchi, I. Ikemoto, S. Suzuki, and Y. Achiba, Solid State Commun. 79, 939 (1991).
M. Zeh, H.-C. Ri, F. Kober, R. P. Huebener, J. Fischer, R. Gross, H. Muller, T. Sermet, A. V. Ustinov, and H.-G. Wener, Physica C 167, 6 (1990).
E. Zeldov, N. M. Amer, G. Koren, A. Gupta, R. J. Gambino, and M. W. McElfresh, Phys. Rev. Lett. 62, 3093 (1989).
H. R. Zeller and I. Giaever, Phys. Rev. 181, 789 (1969).
X. C. Zeng, D. Stroud, and J. S. Chung, Phys. Rev. B 43, 3042 (1991).
R. Zeyher, Phys. Rev. B 44, 10404 (1991).
F. C. Zhang and T. M. Rice, Phys. Rev. B 57, 3759 (1988).
L. Zhang, M. Ma, and F. C. Zhang, Phys. Rev. B 42, 7894 (1990).
Z. Zhang, C.-C. Chen, and C. M. Lieber, Science 254, 1619 (1991).
H. Zhang, J. W. Lynn and D. E. Morris, Phys. Rev. B 45, 10022 (1992).
L. Zhang, J. Z. Liu, and R. N. Shelton, Phys. Rev. B 45, 4978 (1992).
L. Zhang, J. K. Jain, and V. J. Emery, Phys. Rev. B 47, 3368 (1993).
Z. Zhang and C. M. Lieber, Phys. Rev. B 47, 3423 (1993).
H. Zhang and H. Sato, Phys. Rev. Lett. 70, 1697 (1993).
Z. Zhao, L. Chen, Q. Yang, Y. Huang, G. Chen, R. Tang, G. Liu, C. Cui, L. Chen, L. Wang, S. Guo, S. Li, and J. Bi, in "Cooper Oxide Superconductors" (C. P. Poole, Jr., T. Datta, and H. A. Farach, Eds.), p. 274, Wiley, New York, 1987.
B.-R. Zhao, S. -I. Kuroumaru, Y. Horie, E. Yanada, T. Aomine, X. -G. Qiu, Y.-Z. Zhang, Y. -Y. Zhao, P. Xu, L. Li, H. Ohkubo, and S. Mase, Physica C 179, 138 (1991).
G. L. Zhao and J. Callaway, Phys. Rev. B 49, 6424 (1994).
C. Zhaojia, Z. Yong, Y. Hongshun, C. Zuyao, Z. Donquin, Q. Yitai, W. Baimei, and Z. Qinii, Solid State Commun. 64, 685 (1987).
H. Zheng, M. Avignon, and K. H. Bennemann, Phys. Rev. B 49, 9763 (1994).
X. Zhengping, J. Chunlin, and Z. Lian, J. Supercood. 3, 421 (1990).
W. Zhi-Feng, C. Xiao-Long, C. Guang-Can, W. Fu-Ming, L. Wen-Chao, and H. Meng, Chinese Phys. Lett. 19, 249 (2002).

J. Zhou and S. G. Chen, Phys. Rev. B 47, 8301 (1993)

D.-M. Zhu, A. C. Anderson, E. D. Bukowski, and D. M. Ginsberg, Phys. Rev. B 40, 841 (1989)

D.-M. Zhu, A. C. Anderson, T. A. Friedmarm, and D. M. Ginzberg, Phys. Rev. B 41, 6605 (1990).

S. Zhu, D. K. Christen, C. E. Klabunde, J. R. Thompson, E. C. Jones, R. Feenstra, D. H. Lowndes, and D. P. Norton, Phys. Rev. B 46, 5576 (1992).

Y. Zhu in "High Temperature Superconducting Materials Science and Engineering," (D. Shi, Ed.) Pergamon, New York, 1994.

G. T. Zimanyi and K. S. Bedell, Phys. Rev. B 48, 6575 (1993).

P. Zolliker, D. E. Cox, J. B. Parise, E. M. McCarron III, and W. E. Farneth, Phys. Rev. B 42, 6332 (1990).

X. Zotos, P. Prelovsek, and I. Sega, Phys. Rev. B 42, 8445 (1990).

Z. Zou and P. W. Anderson, Phys. Rev. B 37, 627 (1988); (reprinted in Halley, 1988, p. 163).

V. E. Zubkus, E. E. Tornau, S. Lapinskas, and P. J. Kundrotas, Phys. Rev. B 43, 13112 (1991).

I. Zutic, and O. T. Vails, Phys. Rev. B 58, 8738 (1998).

W. Zwerger, Phys. Rev. B 42, 2566 (1990).

Index